CO_2 Capture Project

Carbon Dioxide Capture for Storage in Deep Geologic Formations

Results from the CO_2 Capture Project

5

Volume Five: CCS Technology Development and Demonstration Results (2015-2022)

Edited by Karl F Gerdes

Carbon Dioxide Capture for Storage in Deep Geologic Formations – Results from the CO_2 Capture Project

Volume 5

CCS Technology Development
and Demonstration Results (2015-2022)

Edited by

Karl F. Gerdes

2022

Published in the UK by the CO_2 Capture Project.

CO_2 Capture Project (CCP) Phase 4 members: BP, Chevron, and Petrobras. For further information on the work of the CO_2 Capture Project, please visit www.co2captureproject.org.

The various chapters contained in this collected work relate to CCP4 activities and are protected under the copyright laws of the countries of the respective authors or their employers. This collective work is also protected under appropriate copyright laws.

The following conditions apply to use of this work and the individual contributions:

Single copies of single chapters may be made for personal use as allowed by national copyright laws. All other rights are reserved, and no permission is given for any other use or copying of this work and the individual contributions.

CCP or any of their affiliates or members accept no responsibility or liability of whatsoever nature to any party to whom this report, or any part thereof, is made known. Any such party relies on the report at their own risk. CCP or any of their affiliates or members make no representations, guarantees or warranties, express or implied, as to the accuracy, quality, fitness for purpose, or completeness of the information contained in the book. Any use of this book and the information contained therein is at the sole risk of the user.

CCP or any of their affiliates or members shall have no duty of care or liability to any person or party in connection with the book and its contents. By using the book, the user agrees to indemnify and hold CCP and any of their affiliates and members completely harmless from any claims arising from any loss, damage, or injury (including but not limited to loss or damage to property and death) to the user, its employees and representatives and/or any third party, whether direct or indirect and whether caused by tort (including negligence) or otherwise (even if foreseeable) that may arise in connection with the use of the book and the information therein by the user. This does not affect CCP's liability in so far as it cannot be excluded or limited under applicable law.

First edition 2022
British Library Cataloguing in Publication Data
A catalogue record is available from the British Library
ISBN: 978-1-3999-4078-8

Volume 4 of this series was published by CPL Scientific Publishing Services Ltd ISBN: 978-1-872691-68-8
Volume 3 of this series was published by CPL Scientific Publishing Services Ltd ISBN: 978-1-872691-49-7
Volumes 1&2 of this series were published by Elsevier BV ISBN: 0-08-044570-5 (2 volume set)

Printed in the UK by Short Run Press Limited

PREFACE

Tony Espie
Chair Executive Board, CO_2 Capture Project, BP International Limited, Sunbury on Thames, UK

The CO_2 Capture Project (CCP) was established more than two decades ago to accelerate the deployment of CO_2 capture and storage (CCS) technology as a viable option for use by the oil and gas industry to manage CO_2 emissions. Throughout this period, CCP members and partners have collaborated to share expertise, facilities, and assets to close gaps in knowledge and verify relevant technologies from a user's perspective. This volume documents results from the fourth and final phase of CCP.

CCP Members determined early on that for CCS to realise its potential there must be a high level of knowledge transfer between the different players. CCP has remained committed to sharing knowledge beyond our member companies. In this volume, you will find detailed reports from our four Teams–Capture, Storage, Policy, and Communications–covering the fourth phase of our activity (CCP4 2015–2022).

Since Phase 4 began in 2015, there has been an upswing in momentum for CCS after a period of uncertainty following the 2008 financial crisis. Several events of note:

- The COP21 Paris agreement in 2015, because of which governments across the world committed to significant cuts in man-made CO_2 emissions.
- Policy changes in Europe and, especially in the US, where the Budget Bill of 2018 contained an extension and enlargement to the US tax credit for CCS and CCUS, known as 45Q and further incentives were part of the Inflation Reduction Act of 2022.
- The coming to prominence in 2018 of Extinction Rebellion and other movements–which, allied with major climate-linked events over recent years, focused attention like never before on our changing environment.
- The October 2018 IPCC Special Report on Global Warming at 1.5°C stated that CCS and negative emissions technologies (coupled to CCS) are critical to achieving both the 2°C and 1.5°C goals.
- Publication of the sixth Climate Change Assessment Report by the IPCC in 2021, with its stark warnings about the threats facing mankind.

The final phase of CCP has kept a practical focus on finding viable CCS solutions for use by our industry–for oil refining, gas power generation, and natural gas production. We continued to work closely with government, academic bodies, and innovative technology suppliers. And we have together delivered a number of important studies, demonstrations, and field trials to make a major contribution to our industry's understanding of the application of CCS.

Capture Overview

The Capture Team focused in Phase 4 on reducing the cost of CO_2 capture from refining operations, post-combustion capture with emphasis on natural gas power generation, and CO_2 separation from natural gas production. Following the screening of more than 200 capture technologies in Phase 1 (2000–2003), and further development and assessment in Phase 2 (2004-2009), the first CCP capture demonstrations were part of Phase 3 (2010-2014). Both implemented Oxyfiring–a pilot-scale Fluid

Catalytic Cracking (FCC) catalyst regenerator and an oil-field once-through steam generator (OTSG) boiler. Phase 3 also included a significant effort to develop an economic model with greater clarity–comparing baseline costs for oxy-firing, post-combustion and pre-combustion across the main oil & gas capture scenarios.

Highlights of the Capture Team's work through the four phases of CCP are shown in Table 1.

Table 1. Capture Team Highlights 2000–2022.

CCP1: 2000–2004 Screening proof of concept	CCP2: 2004–2009 Intensive development	CCP3: 2009–2014 Demonstration	CCP4: 2015-2022 Continued development
• Screened 200 capture technologies. • Identified pre-combustion, post-combustion and oxy-firing technologies to deliver significant capture cost reduction.	• Further developed most promising capture technologies from CCP1, with two potentially ready for field demonstration. • Identified novel capture technologies.	• Field demonstrated FCC and OTSG oxy-firing capture technologies. • Continued development of novel technologies including Chemical Looping Combustion and Membrane Water Gas Shift. • Developed economic baseline modelling for all scenarios.	• Two different pilot campaigns for post-combustion capture solvent piperazine. • Field demonstration of novel fast-cycle Temperature Swing Adsorption process from Svante. • Testing of novel 3D printed structured adsorbents. • Initial testing and assessment of sub-sea CO_2 separation from natural gas. • Techno-economic assessments of promising capture technologies.

Storage, Monitoring & Verification Overview

In Phase 4, the focus of the SMV program was to demonstrate the viability of monitoring tools in the field and to develop robust leakage detection, characterization and if needed, intervention protocols. The latter was pioneered late in Phase 3. The program has largely maintained its general themes: "Assurance", "Surveillance", "Optimization", and "Risk Assessment" which evolved to include "Field Trialing" and "Contingencies".

The aim of the Storage Team has been to build a robust knowledge base around the storage of CO_2 and to trial monitoring technologies. An important aspect of the work is to develop information that assures stakeholders that secure CO_2 storage can be achieved. The Storage Team was comprised of experts in subsurface exploration, production, and site decommissioning with decades of experience in the oil and gas industry. Highlights of work by the Storage Team are shown in Table 2.

In Phase 3, a contingencies program was established to increase confidence around storage integrity by improving the industry's ability to manage unexpected migration of CO_2 from storage sites.

The Phase 4 work on Assurance focused on assessing the risks of using depleted oil and gas reservoirs for CO_2 storage. CCP4 continued Contingencies-themed work to detect, characterize, and mitigate leakage events in storage reservoirs. The projects under the Optimization banner studied ways to optimize design and operations of storage projects and included two extensive reviews of storage projects to document lessons learned and analyse cost reductions through experience. The major focus of CCP4 was on Surveillance (how to detect where stored CO_2 is moving in a storage setting) and Field Trials.

Table 2. Storage Team Highlights 2000–2022.

CCP1: 2000–2004 Screening proof of concept	CCP2: 2004–2009 Intensive development	CCP3: 2009–2014 Demonstration	CCP4: 2015-2022 Continued development
• Pioneered risk-based approach for geological site selection, operation and closure. • Developed new storage monitoring tools.	• Strengthened the science of storage with a focus on well integrity, through systematic R&D. • Published a definitive book on storage.	• Storage R&D and trialling of field monitoring technologies. • Developed Certification Framework. • Completed modelling of storage contingencies.	• Tested leak mitigation in a purposely-damaged cemented and cased demo well. • Deployed novel surveillance tools at Aquistore. • Modeling study of impact of EOR operations on subsequent use as a storage reservoir.

Policy & Incentives Overview

The CCP Policy & Incentives (CCP P&I) Team continued to focus on gaining understanding of policies and incentives that could enable wider deployment of CCS projects around the world. The P&I Team surveyed existing and emerging policies and incentives and analysed both national and subnational policies. The team examined how policies and regulations for CO_2 enhanced oil recovery can transition into CO_2 storage regulations, executed a deep dive on the detailed regulations two subnational jurisdictions of interest to the CCP member companies, and conducted a global analysis of whether CCS commitments and deployments are included in the "nationally determined contributions" of nations that are Parties to the Paris Agreement.

The Team provided the technical and economic insights needed by stakeholders to inform the development of legal and policy frameworks. This work has been shared with the industry at conferences, including the UN climate change conferences, and is available online in the CCP's publication section. The scope of work carried out by the Policy & Incentives Team during the four phases of CCP is characterized by the highlights shown in Table 3.

Table 3. Policy & Incentives Team Highlights 2000–2022.

CCP1: 2000–2004 Screening proof of concept	CCP2: 2004–2009 Intensive development	CCP3: 2009–2014 Demonstration	CCP4: 2015-2022 Continued development
• Surveyed existing policies, regulations, and incentives affecting CCS projects. • Identified gaps in the regulatory and policy framework that inhibit CCS deployment. • Established outreach effort to inform the policy debate.	• Conducted study to assess issues of financing a CO_2 pipeline infrastructure. • Surveyed issues and concerns of stakeholders, including general public, policy makers, NGOs, investors, and others.	• Updated survey of regulatory issues facing CCS. • Documented lessons learned from real CCS projects from a variety of jurisdictions. • Updated stakeholder concerns and added granularity. • Studied types and effectiveness of local benefit sharing as a means to gain support for CCS projects.	• Documented Best Practice in Transitioning from CO_2 EOR to CO_2 Storage. • Review of CO_2 EOR regulations transitioning to CO_2 storage in Texas and Alberta. • Role of CCS in the Energy Transition as projected by bodies such as IPCC, IEA, and EU. • Survey of CO_2 Storage Regulations

Communications Overview

Communication activities during CCP4 continued the tradition of sharing updates and results from the work of the Technical and Policy teams using a variety of means. There has been an increased focus on peer-to-peer communication through conferences and events. As CCP comes to a close, there has been a focused effort to establish a lasting record of CCS knowledge and insights, derived from the entire body of CCP work and available to all. The main avenues of communication have been Technical Factsheets, Annual Reports, Policy Reports, and participation in and sponsorship of international conferences. The CCP website–www.co2captureproject.org–will be maintained until 2026 as an accessible source of the technical and policy work products of the project. Highlights of the Communication Team's work through the four phases of CCP are shown in Table 4.

Table 4. Communications Team Highlights 2000–2014.

CCP1: 2000–2004 Screening proof of concept	CCP2: 2004–2009 Intensive development	CCP3: 2009–2014 Demonstration	CCP4: 2015-2022 Continued development
• Launched an official website with a vast resource and registrant database. • Participated in international conferences. • Published a book of the CCP Phase 1 results. • Developed a Phase 1 results brochure.	• Published a comprehensive technical guide to CO_2 geological storage. • Developed a meter-long In Depth leaflet that provides a spatial perspective of CO_2 storage. • Published a book of the CCP Phase 2 results. • Participated in international conferences.	• Developed regular project overview factsheets. • Participant at key UNFCCC COP, GHGT, and CCUS conferences. • Launched an educational website that explains CCS to the broader audience. • Created an interactive, digital version of the In Depth leaflet. • Published a book of the CCP Phase 3 results.	• Published Annual Reports of CCP progress. • Published four major Policy reports. • Participated in and sponsored key international CCS meetings and conferences. • Continued to update the CCP website. • Published a book of CCP Phase 4 results.

Concluding Remarks

CCP has continued to be a leading participant in the response of the oil and gas industry to the challenge of de-carbonizing the energy system. During CCP Phase 4, emerging technologies have been tested and assessed that have great potential to lower the cost of post-combustion capture. A new initiative examined improved ways to deal with CO_2 separation and storage for offshore natural gas production. On the CO_2 storage side, novel monitoring technologies have been tested and assessed, and mitigation methods to de-risk possible leakage pathways have been field-trialled at the Swiss Mont Terri underground laboratory. All this work is aimed as assuring long-term storage security.

ACKNOWLEDGEMENTS

Tony Espie, BP International Limited, Chertsey Road, Sunbury-on-Thames, TW16 7LN, United Kingdom, Chair Executive Board, CO_2 Capture Project Phase 4

The CO_2 Capture Project has provided a unique, collaborative forum for an evolving group of major energy companies to develop practical CCS knowledge and solutions specifically tailored to the needs of the oil and gas industry. Since its founding in 2000, the engine driving CCP's efforts has been expert Technical Teams, comprised of engineers, scientists, and geologists from member companies. Over the time of the Project, almost 200 projects have been executed to increase understanding of the science, economics, and practical engineering applications of CCS. The Teams cover four areas of activity (1) Capture, (2) Storage, Monitoring and Verification, (3) Policy and Incentives, and (4) Communications.

CCP's work was carried out in phases, with the partnership having now completed its fourth and final phase. During Phase 1, eight corporate partners engaged with governments to develop the initial program. Phase 2 followed in 2004 with eight corporate members to the full program, two additional partners, and four participating governments. Phase 3 began in late 2009 with seven corporate members and an Associate member: EPRI. In the third phase, the CCP worked closely with a wide range of national and regional bodies, industry partners, academic organizations, and global research institutes. CCP was recognised by the Carbon Sequestration Leadership Forum (CSLF) for its contribution to the advancement of CCS. Phase 4 began in 2015 with four corporate members: BP, Chevron, Petrobras, and Suncor. Suncor later withdrew from the program.

Phase 4, as in previous phases, engaged technical experts seconded from the member organizations to CCP working teams. These teams have been led by Raja Jadhav (Chevron)–Capture Team Lead, Scott Imbus (Chevron) followed by Harvey Goodman (Chevron) and Dean Thornton (Chevron)–Storage Team Leads, Arthur Lee (Chevron)–Policy & Incentives Team Lead, and Mark Crombie (BP) followed by Simon Taylor (Pulse Brands) as Communications Team Leads. The teams were governed by the Executive Board with representatives from each corporate member: Jonathon Forsyth followed by Tony Espie for BP as CCP Chairmen, Rodolfo Dino followed by Anna Musse for Petrobras, and Vincent Kwong followed by Raja Jadhav for Chevron, and Stephen Kaufman (Suncor). Additionally, the teams are guided by an independent Technical Advisory Board (TAB) made up of CCS industry experts, led by Vello Kuuskraa. The TAB participants for Phase 4 were Michael Celia and Dale Simbeck. The Advisory Board provided independent peer reviews of CCP activities and respective programs to ensure efforts remain true to the partnership's aims.

Sincere thanks are extended to all of CCP's external collaborators for their support through generous government contributions, expert research and development, and technical project associations. CCP and Phase 4 will be remembered for identifying promising technology, nurturing its development, and the successful delivery of demonstration trials.

Special thanks to all reviewers of the technical contributions found in this book as their voluntary efforts have helped this book deliver valuable information to the CCP members and the broader industrial community. The CCP extends thanks to Karl F Gerdes, who edited this book, as well as Volume 4 of the series.

Please see the section "Contributors to CCP4" for a listing of the individuals from the CCP Member Companies who planned and guided this work, a listing of all technology providers contributing to the success of CCP4, and a listing of the individuals who provided peer review of the technical chapters. Individual chapter authors are listed in the Author Index.

CONTENTS

Carbon Dioxide Capture for Storage in Deep Geological Formations, Volume 5
Karl F Gerdes (Editor)
© 2022 BP. All rights reserved.

INTRODUCTION

Tony Espie[1] and Karl F Gerdes[2]
[1]Chair Executive Board, CO_2 Capture Project, BP International Limited, Sunbury on Thames, UK
[2]Editor, Karl F Gerdes Consulting, Davis, California, USA

BACKGROUND

The CO_2 Capture Project (CCP) is an international partnership of major energy companies, collaborating with specialists from industry, technology providers, and academia to advance technologies to lower the cost of CO_2 capture and to ensure secure and safe geological storage. The overarching goal is to accelerate the deployment of Carbon Capture and Storage (CCS) as a viable option for CO_2 mitigation in the oil and gas industry.

The CCP has completed the fourth and final phase of activity, which commenced in 2015. Phase 1 of the project, CCP1 (2000-2004), conducted screening reviews of nearly 300 capture and storage technologies to identify those that could deliver significant capture cost reduction and increased assurance of long-term storage. Of particular note was pioneering work on a risk-based approach for geological site selection, operation and closure, and identification of storage monitoring tools for further development [1, 2].

Phase 2 of the project, CCP2 (2004-2009), pushed further development of promising capture technologies, with two technologies readied for demonstration. CCP developed the concept of a Certification Framework for storage site assessment and completed a landmark CO_2-exposed well study, which provided valuable data on the type and extent of alteration and factors influencing alteration of the well integrity [3].

Phase 3 of the project, CCP3 (2009-2014), demonstrated selected CO_2 capture and storage monitoring technologies [4]. Two different oxy-firing capture technologies were demonstrated–oxy-fired catalyst regeneration in an integrated Fluid Catalytic Cracking pilot unit at a Brazilian facility and oxy-fired operation of a once-through steam generator at a Canadian production facility. On the Storage, Monitoring, and Verification (SMV) front, several important demonstrations and studies were completed. A modular borehole monitoring system was successfully deployed at the Citronelle site, and InSAR satellite technology was deployed to detect surface deformation from CO_2 storage at Decatur, USA. A key contribution to CO_2 storage assurance was CCP3-SMV's launch of the "CO_2 Storage Contingencies Initiative" to better define approaches to detection, characterization, and intervention of unexpected leakage [5].

Phase 4 of the project, CCP4 (2015-2022), continued to develop pioneering CCS technology and knowledge for potential application in the oil and gas industry. The CCP4 program aimed to continue work on CO_2 capture solutions and understanding of deployment opportunities in the context of specific application scenarios, similar to the approach in previous phases of CCP. The CCP4 scenarios are refinery and Post-Combustion Capture with emphasis on natural gas power generation, and CO_2 separation from natural gas production. The storage program continued to demonstrate safe and secure geological containment through testing of field-based well integrity sealing methods, monitoring, and development of robust intervention protocols.

A few highlights of CCP4 include:

- Demonstrated in two different pilot campaigns that the Piperazine with Advanced Stripper (PZAS^{TM}) capture process has a wide range of application–from NGCC to coal-fired flue gas.
- Used a series of Techno-Economic Assessments (TEA) to compare innovative capture technologies for NGCC and identified use of Molten Carbonate Fuel Cells (MCFC) as a low-cost option.
- Supported testing of structured adsorbents with potential for higher productivity (kg CO_2/ m^3hr) and lower pressure drop than conventional packed bed adsorbents. Applications include Sorbent Enhanced Water Gas Shift (SEWGS) to improve economics of low-carbon H_2 production and post-combustion capture.
- Demonstrated Svante's innovative adsorption-based CO_2 capture system at a pilot scale of 1 tonne per day (TPD) at Lafarge Canada's Richmond cement plant, which has a CO_2 concentration similar to SMR flue gas.
- Supported testing of polymeric membranes for CO_2 separation at the harsh conditions necessary to implement subsea wellhead processing and CO_2 reinjection as part of the COMPMEM project.
- Conducted two modelling studies related to storage assurance–one examined operational management of stresses in an EOR reservoir to preserve caprock integrity for subsequent use CO_2 storage, and the second looked at the ability to detect leakage associated with a degraded plugged and abandoned well.
- Completed a study combining modelling with lab experiments assessed the ability of a silica gel agent injected into a storage formation to prevent or mitigate leakage.
- Compiled a database of the early operating experience of storage projects–ranging from pilots to demonstrations to commercial operation. Lessons learned were extracted from incidents and unanticipated variances between expected and actual performance.
- Conducted two field experiments at the Mont Terri Underground Laboratory–one to test various injected sealants injected to mitigate leakage in a purposely-damaged well, and the second to examine possible effects of fluid injection on fault slippage with implications for fluid leakage.
- Modelled novel technologies based on the ongoing Aquistore saline storage project to assess surveillance capabilities of (1) time lapse borehole gravity and (2) borehole to surface electromagnetics.

ABOUT THIS BOOK

This book is a collection of peer-reviewed scientific chapters that describe the technological advances made during CCP4. This is the fifth volume in the series, with the first two published in 2005, documenting progress during CCP1 [1, 2], the third volume published in 2009 covering CCP2 [3] and the fourth volume published in 2015 covering CCP3 [4].

All chapters of this book are available to download for free after registration at the CCP website at www.co2captureproject.org.

Introductory Material

This chapter provides background on CCP4, including accomplishments and organizational structure. Following this introduction is a chapter by the chair of CCP's independent Technical Advisory Board, Vello Kuuskraa, which offers the perspective of the Advisory Board concerning the accomplishments of CCP.

CO_2 Capture

The section following the introductory material documents work on **CO_2 Capture**, comprising 20 chapters. Chapter 1 introduces the CCP4 capture program and provides an executive summary of the results. Thereafter are three groupings of chapters dedicated to the CO_2 capture application scenarios of CCP4:

- **Refining Scenario** (Chapters 2–6). The focus of the refining scenario in CCP4 was on CO_2 capture from hydrogen production by Steam Methane Reforming (SMR)–the global workhorse technology for H_2 production from natural gas. Chapter 2 is a summary of a well-documented study from the IEAGHG R&D Program to characterize the cost of CO_2 capture by several options from SMR H_2 plants [6]. Chapters 3-4 document development efforts and assessment of a novel structured material fabricated using 3D printing to reduce the cost and improve the performance of the Water Gas Shift step by combining WGS catalysis and CO_2 adsorption. Chapter 5 describes further development of advanced, rapid cycle adsorption for CO_2 capture from SMR furnace flue gas. Chapter 6 summarizes a preliminary techno-economic study of SMR flue gas capture using a developmental graphene oxide-based membrane.
- **Post-Combustion Capture Scenario** (Chapters 7–17). These chapters document economic assessments and development work aimed at mitigating CO_2 emissions from industrial emissions sources.

  Natural Gas Combined Cycle (NGCC) power generation is the focus of Chapters 7–11 and 17. Chapter 7 compares the estimated cost of capture for four emerging technologies to the cost using mature flue gas solvent scrubbing. Chapter 8 extends the analysis for the most promising capture technology identified in Chapter 7–integration of a Molten Carbonate Fuel Cell (MCFC) with the NGCC combustion turbine. Chapter 9 is a techno-economic assessment of the use of aqueous piperazine (PZ) solvent for CO_2 capture in several process configurations. Chapters 10–11 describe pilot demonstration and design studies in support of deployment of PZ solvent for NGCC applications. Chapter 17 provides a techno-economic assessment of MHI's KS-1™ solvent applied to CO_2 capture from an NGCC power plant.

  Other Post-combustion Capture is the focus of Chapters 12–16. Chapter 12 documents pilot testing for a new, non-amine solvent. Chapter 13 assesses MCFC for CO capture from smaller emission sources–in this case, MW-scale internal combustion engines. Chapter 14 is a computational study to compare capture performance using a packed bed of conventional adsorbent beds to a structured adsorbent (related to the materials described in Chapters 3–4). Chapter 15 documents a comparison of chemical and physical solvents for post-combustion CO_2 capture applied to NGCC power generation using a simplified model to optimize the process for each solvent. Chapter 16 describes development, fabrication, and testing of novel graphene oxide-based membrane materials for CO_2 capture.
- **Natural Gas Treating** (Chapters 18-19) Chapter 18 provides a state-of-the-art review of technology for CO_2 removal from natural gas in an offshore setting. Chapter 19 describes progress towards deployment of a subsea system for fluid separation and membrane-based CO_2 separation from natural gas.

Chapter 20 completes the Capture section with conclusions and recommendations for further work.

Storage, Monitoring, and Verification

The next section of the book describes CCP4 work on **Storage, Monitoring, and Verification** (SMV). Chapter 21 provides an executive summary of the SMV work. This is followed by a series of chapters grouped by themes.

- **Subsurface Assurance**. The focus of this work in CCP4 was to gain insight into the risks of using depleted oil and gas reservoirs for CO_2 storage. Chapter 22 describes a modelling study to elucidate how operational management of stresses in an EOR reservoir can preserve seal integrity for subsequent use CO_2 storage. Chapter 23 assesses the ability to detect leakage associated with a degraded plugged and abandoned well using electromagnetic and seismic data.
- **Contingencies.** CCP4 continued work to detect, characterize, and mitigate leakage events in storage reservoirs. Chapter 24 summarizes a study that combined reservoir modelling with targeted lab experiments to assess injection of a silica gel agent into a storage formation to prevent or mitigate leakage.
- **Optimization.** This theme considers ways to optimize design and operations of storage projects. Chapter 25 documents a modelling study of the Cranfield Oil field in Mississippi to assess how the various operating modes of EOR affect storage and oil recovery. The start-up and early operating experience of storage pilots, demonstrations and commercial projects provide lessons learned in Chapter 26. Chapter 27 provides a substantive analysis of cost reductions in storage projects via experience gained in moving from First-of-a-kind to Nth-of-a-kind.
- **Surveillance and Field Trials.** The major focus of CCP4 efforts on SMV was here. Two field experiments at the Mont Terri Underground Laboratory in Switzerland contribute learning about purposely-induced well damage and leak mitigation (Chapters 28–30) and about the impact of fluid injection on fault slippage (Chapter 31). The Aquistore saline storage project in Canada provided the opportunity to deploy two novel tools for surveillance of the injected CO_2 plume, as documented in Chapters 32 (borehole gravity) and 33 (borehole to surface electromagnetics).

The final chapter of the SMV section, Chapter 34, offers a summary of key findings from the work of CCP3, technology gaps remaining, and recommendations for addressing them.

Policy and Incentives/Communications

The book concludes with two chapters which describe the work completed by CCP's Policy and Incentives (P&I) and Communications teams.

Chapter 35 documents four studies undertaken to elucidate policies and incentives that could enable wider deployment of CCS projects around the world at a time of increasing interest in CCS technology development and increasing activity in policymaking and creation of incentives to enable CCS project deployment. The CCP P&I Team surveyed both existing and emerging policies and incentives and analyzed national and subnational policies. The chapter summarizes the goals and key findings of the four studies:

- Best Practice in Transitioning from CO_2 EOR to CO_2 Storage
- Review of CO_2 EOR Transitioning to CCS in Texas and Alberta
- Role of CCS in the Energy Transition
- Survey of CO_2 Storage Regulations

Chapter 36 describes the communication activities which CCP undertook to continue sharing of updates and results from the work of the Technical and Policy teams through a variety of platforms. In CCP4, there has been an increased focus on peer-to-peer communication through conferences and events. As the 20+ year CCP program came to a close, the establishment of a lasting legacy of CCS knowledge and insights, derived from the entire body of CCP work and available to all, became an overarching aim. The main avenues of communication have been Technical Factsheets, Annual Reports, Policy Reports, and participation in and sponsorship of international conferences. The CCP website–www.co2captureproject.org–will be maintained until 2026 as an accessible source of the technical and policy work products of the project.

CCP4 STRUCTURE

CCP4 members took part in all activities, its working teams, and had representation on the Executive Board.

Structure and Management Process

Executive Board

Each member organisation had a representative on the CCP Executive Board, which exercised overall control and governance of the program, as well as prioritizing specific projects to be undertaken and funded. The Board typically met quarterly.

Technical Advisory Board

A Technical Advisory Board (TAB) assisted CCP by conducting independent peer reviews on the activities of the CCP teams and their respective programs. TAB recommendations helped to keep the program on track and shape its future direction. The TAB was comprised of independent, international technical experts from industry and academia.

Program Management

The Program Manager provided direction to the teams for the delivery of the program goals within the overall budget and timeframe set by the Executive Board.

Teams

The detailed activities of CCP were planned and carried out by four teams–Capture; Storage, Monitoring & Verification; Policy & Incentives; and Communications. The teams were comprised of engineers, geologists and other subsurface specialists, policy and regulatory specialists, and communications experts drawn from each of the member organisations.

Each of the technical teams was led by a designated team leader. The technical teams were assigned the following broad goals within their areas:

- **Capture:** Reducing the cost of CO_2 capture from operations in the oil and gas industry and in natural gas power generation.
- **Storage, Monitoring & Verification:** Increasing understanding and developing methods for safely storing and monitoring CO_2 in the subsurface.
- **Policy & Incentives:** Providing technical, economic, and social insights to inform the development of legal and policy frameworks and to help public understanding.

- **Communications:** Taking content from the ongoing work of other teams and delivering it to government, industry, NGOs, and the general public.

Technology Providers

CCP4 engaged a variety of technology providers to carry out the specifics of the technical program. The technology providers include academic institutions, research companies, CCP4 participants, national laboratories, and expert consulting firms. These providers worked with the CCP teams to deliver the program results.

CCS TECHNOLOGIES IN CCP4

As noted in the Background section of this chapter, the technology program of CCP4 was built on results from the previous phases of the project. The guiding principles used by CCP for selecting technologies on which to work are:

- Likelihood to achieve target cost reduction relative to existing (baseline) technology.
- Health, Safety, and Environmental requirements–safe for people and the environment, and reliable–must be met.
- Relevant to the CCP Member companies' operations.
- Likelihood to meet the time schedule set for CCP4 and to be achievable with the resources available from CCP4 members and partner organizations and agencies.
- Acceptable to government and public stakeholders.

REFERENCES

1. Thomas, D.C. (editor), (2005) *Carbon Dioxide Capture for Storage in Deep Geologic Formations – Results from the CO_2 Capture Project*, Vol 1 *Capture and Separation of Carbon Dioxide From Combustion Sources*; ISBN 0-08-044570-5, Elsevier Publihsing, UK.
2. Benson, S.M. (editor, (2005) *Carbon Dioxide Capture for Storage in Deep Geologic Formations – Results from the CO_2 Capture Project*, Vol 2 *Geologic Storage of Carbon Dioxide with Monitoring and Verification*; ISBN 0-08-044570-5, Elsevier Publishing, UK.
3. Eide, L.I. (editor), (2009) *Carbon Dioxide Capture for Storage in Deep Geologic Formations – Results from the CO_2 Capture Project*, Vol 3 *Advances in CO_2 Capture and Storage Technology - Results (2004-2009)* ; ISBN 0-08-044570-5, CPL Press, UK.
4. Gerdes, K.F. (editor), (2015) *Carbon Dioxide Capture for Storage in Deep Geologic Formations – Results from the CO_2 Capture Project*, Vol 4 *Development and Demonstration Resulss (2009-2014).* ISBB 978-1-872691-68-8, CPL Press, UK.
5. Imbus, S., *et al.*, (2013) "CO_2 Storage Contingencies Initiative: Detection, Intervention, and Remediation of Unexpected CO_2 Migration," at GHGT-11, *Energy Procedia*, **37**, 7802-7814.
6. IEAGHG, (2017) *Techno-Economic Evaluation of SMR Based Standalone (Merchant) Plant with CCS.* 2017/02, February, 2017.

Carbon Dioxide Capture for Storage in Deep Geological Formations, Volume 5
Karl F. Gerdes (Editor)
© 2022 BP. All rights reserved.

STRATEGIC ACCOMPLISHMENTS OF THE CO_2 CAPTURE PROJECT: A TWENTY-YEAR PERSPECTIVE

Vello A. Kuuskraa[1], Dale Simbeck[2], Michael A. Celia[3]
[1]Advanced Resources International, Arlington, VA USA
[2]Independent Consultant
[3]Department of Civil and Environmental Engineering, Princeton University

ABSTRACT: The CO_2 Capture Project (CCP) was initiated in 2000 by eight of the world's leading energy companies. The two major themes that guided the CCP research and development program were: (1) to identify and further develop lower cost CO_2 capture technologies; and (2) to improve the performance and public acceptance of CO_2 storage in geologic formations. To assist in ensuring the quality of results produced by CCP, a Technology Advisory Board (TAB), made up of external experts, was established by CCP. In this chapter, the TAB endeavors to appraise the impact of CCP over its more than 20-year existence.

KEYWORDS: CO_2 capture, CO_2 Storage, CCS.

BACKGROUND

The CO_2 Capture Project (CCP), founded in Year 2000 by eight of the world's leading energy companies, has been in operation for two decades. Since its inception, the CCP has pursued two themes: (1) identify and support the development of lower cost CO_2 capture technologies and (2) develop information that would improve the performance and public acceptance of CO_2 storage.

As part of its commitment to quality project management, the CCP Executive Board (containing representatives from each of the participating companies) established a Technical Advisory Board (TAB). At key decision points, CCP projects and priorities were peer reviewed by the TAB. The TAB also provided external benchmarking and assurance that "best technical practices" were used in the pursuit and performance of projects. The TAB consisted of independent experts from industry and academia and, during its initial years, representatives from the three government funding agencies—the European Commission's Clean Energy Ministerial, the US Department of Energy's Fossil Energy R&D Program, and the Norwegian Research Council.

This section provides the CCP TAB's appraisal of how the strategic accomplishments of the CCP have shaped the status and acceptance of CO_2 Capture and Storage (CCS) as a major option for controlling greenhouse gas emissions and lowering the costs of addressing climate change.

RECOGNIZING STRATEGIC ACCOMPLISHMENTS

To assess the strategic accomplishments and value of the CO_2 Capture Project, the TAB has taken a longer-term view, asking the following questions:

- What was the commercially viable status and acceptance of CO_2 Capture and Storage at the turn of the twenty-first century?

- How have the work and investments of the CO_2 Capture Project helped change the status and acceptance of CO_2 Capture and Storage? and
- Now, twenty years later, what is the commercially viable status and public acceptance of CO_2 Capture and Storage as a major climate change mitigation option?

Status of CO_2 Capture and Storage at the Turn of the Century

Twenty years ago, CO_2 Capture and Storage was a concept, a concept that might, at some point in the future and with advances in technology, enable power plants, refineries, and other industrial facilities and processes to manage their CO_2 emissions. However, little rigorous information was available on the actual performance and costs of the host of potential CO_2 capture technologies discussed in the technical literature.

In addition, even more uncertainty existed on the perceived viability and safety of long-term storage of the captured CO_2 in geologic formations. Little information existed on the location of favorable settings and the storage capacities of geologic (saline) formations. The general perception was that storing CO_2 in underground saline formations was a high-risk undertaking.

As such, the energy and environmental community, for the most part, discounted the potential of using CO_2 Capture and Storage as a viable climate mitigation option.

Phases 1 and 2 of the CCP (2000-2004 and 2004-2009)

To overcome these perceptions and barriers, the CCP's Capture Team, during Phase 1 of the CCP, conducted in-depth reviews of nearly 200 novel CO_2 capture concepts and technologies, identifying a handful of promising technologies that offered potential for significantly lowering the costs of CO_2 capture [1]. The Capture Team also developed a "common economic model" to assess the economic viability of these capture technologies on a uniform and transparent basis [2].

In parallel, the CCP's Storage Team sponsored a series of studies to expand the knowledge base on geological storage. These studies were based on laboratory and field data with a focus on storage reliability and security [3]. The Storage Team also developed and rigorously used a risk-based methodology for assessing the viability and integrity of storing CO_2 in geologic (saline) formations [4]. Collectively, these actions help build better public understanding and acceptance of CO_2 storage in geologic formations.

The Policies and Incentives Team reviewed existing regulations, policies, and incentives to help define a more supportive policy framework for CO_2 Capture and Storage while the Communications Team began to distribute the work of the CCP to the public.

During Phase 2, the CCP Capture Team conducted more intensive investigations of promising CO_2 capture technologies, targeting two technologies for further evaluation and field testing. The targeted applications were innovative pre-combustion capture (hydrogen firing) on a natural gas-fired power plant in Europe [5] and oxyfiring a fluid catalytic cracker operation at a refinery in Brazil [6]. The Capture Team continued to pursue cost reductions for previously identified promising capture technologies. In addition, the Capture Team identified and provided support to several novel capture technologies, such as Chemical Looping Combustion and Membrane Water Gas Shift.

To help gain public understanding and acceptance of CO_2 storage in geologic (saline) formations, the CCP Storage Team, during Phase 2 of the CCP, authored and published the report, *A Technical Basis for Carbon Dioxide Storage* [7]. This report compiled the 50 years of subsurface expertise by the oil and gas industry, as well as research by more than 50 academic institutions on safe storage of CO_2. This report also provided detailed guidance on how to assess and manage commercial-scale

subsurface CO_2 storage projects. A notable highlight by the Storage Team was the coring of a well and its cement that had been exposed to CO_2 for more than twenty years, providing key information on longer-term wellbore integrity [8].

The Policy and Incentives Team engaged with stakeholders and public officials to identify barriers that were limiting initiation of commercial-scale CO_2 Capture and Storage. The Communications Team ensured that the work and information from the CCP studies and investments were available to the larger public.

A Mid-Point Review

A mid-point review, 10 years after the launch of the CCP, showed that much had been accomplished. However, even with these accomplishments, much still remained to be done before CO_2 Capture and Storage would be accepted as the third main option, along with efficiency and renewables, for reducing CO_2 emissions and mitigating climate change. The words of then Chairman of the CCP Executive Board, Mr. Gardiner Hill of BP, succinctly captured the status of CO_2 Capture and Storage at the mid-point of the CCP:

> *"A strong dose of realism is required on both the costs and timescales needed to structure what will be complex commercial-scale projects and the exploration, appraisal, and development of necessary commercial-scale storage sites."*

Phases 3 and 4 of the CCP (2009-2014 and 2015-2022)

Phase 3 of the CCP started with a recognition of the need to accelerate the commercial-scale application of CO_2 Capture and Storge. With new research institutes and other entities entering the CCS arena, such as the US Department of Energy's Regional Partnerships, the CCP began to concentrate on CO_2 capture technologies and demonstrations of direct use by the oil and gas industry, such as CO_2 capture from refineries, from heavy oil operations, from production of hydrogen, and from higher CO_2 content offshore gas fields.

The CCP Capture Team, recognizing the abundance of domestic natural gas supplies, the increasing importance of low carbon intensity power generation, and the steady progress in amine and sorbent systems, began to give priority to post-combustion CO_2 capture technology for natural gas-fired power.

Notable CCP Phases 3 and 4 technology demonstrations supported by the CCP Capture Team were the field demonstrations of CO_2 capture from Fluid Catalytic Cracking (FCC) at the Petrobras refinery test unit in Brazil [9], from an oxy-fired steam generator at a heavy oil field site in Canada [10], and from a cement plant in Canada using a novel solid adsorption system [11].

During Phase 3, the CCP Storage Team began to give more emphasis to key technical issues facing management of CO_2 storage, including fluid leakage pathways, plume and pressure monitoring, geomechanical stability, and caprock integrity [12]. In addition, the Storage Team continued to progress the theme of risk management as the foundation for its scientific, technical, and field storage projects [13].

Building on success of its well integrity and other CO_2 storage projects, the CCP Storage Team during Phase 4 of the CCP, began to address some of the more challenging areas surrounding the management of storage, such as monitoring and remediation of CO_2 leakage from previously drilled wells and reactivated fault systems. The storage integrity work at the Mont Terri underground test site in Switzerland was and remains a truly pioneering effort.

CCP's Policy & Incentives Team defined and communicated consistent and enabling regulatory and policy frameworks, at both national and international levels, supportive of commercial-scale CCS. The CCP's Communications Team ensured that a steady stream of information on CCP's accomplishments was available to an increasingly diverse audience ranging from the scientific community to the general public.

To recognize its numerous accomplishments, the CCP received the Carbon Sequestration Leadership Forum (CSLF) Global Achievement Award in 2015 "as an exemplary model of science-based research, development, and demonstration."

STATUS OF CO_2 CAPTURE AND STORAGE TODAY

With advances in technology, introduction of incentives, and calls for materially lower CO_2 emissions from all sectors of industry, the acceptance and technical readiness of capturing CO_2 and storing it in geologic formations is dramatically different today than two decades ago. While commercial-scale CCS projects are still too few, the Global CCS Institute's "Global Status of CCS 2021" report lists 27 operating CCS projects, with another 108 in the pipeline. A significant portion of these projects were added just in the past year, with 41 new facilities added in North America and 25 added in Europe [14].

The ability to manage underground CO_2 storage safely and securely, beyond its use and storage in oil fields, is now widely accepted in the scientific community and much of the public. The CO_2 storage capacity in North America has been shown to be vast, with government programs such as Carbon SAFE helping identify, characterize, and pre-deploy geologic settings for safe, secure, and low-cost CO_2 storage. The North Sea has become the preferred site for storing CO_2 captured in Europe, helping overcome the issues surrounding onshore CO_2 storage. Many other countries, including Australia, Canada, and Japan, have begun to define and characterize their CO_2 storage options and capacity.

CLOSING COMMENTS

Today, the need for CO_2 Capture and Storage is even more compelling than two decades ago. Much of the industry has set goals for dramatically reducing CO_2 emissions and becoming net carbon neutral during the next two to three decades. Toward this goal, CCS will enable greater use of hydrogen in the transportation sector, will help lower CO_2 emission by steel, cement, and petrochemical industries, and will provide more efficient and cost-effective options for management of CO_2 emissions by electric power generators, oil refineries, and oilfield operations.

The two decades of CCP activity helped build the scientific foundation and public acceptance of CO_2 Capture and Storage. With continuing policy and financial support, steady technological advances, and improvements in geologic understanding, CCS will be able to achieve its long-sought goal–becoming the third essential greenhouse gas mitigation option and a valuable partner to increased efficiency and use of renewables.

REFERENCES

1. Thomas, D.C. (ed.), (2005), *Carbon Dioxide Capture for Storage in Deep Geologic Formations – Results from the CO_2 Capture Project, Vol 1 Capture and Separation of CO_2 from Combustion Sources*. Elsevier.
2. Melien, T., Economic and Cost Analysis for CO_2 Capture Costs in the CO_2 Capture Project Scenarios. In: Thomas, D.C. (ed.), (2005), *Carbon Dioxide Capture for Storage in Deep Geologic Formations – Results from the CO_2 Capture Project, Vol 1 Capture and Separation of CO_2 from Combustion Sources*. Elsevier.

3. Imbus, S., Technical Highlights of the CCP Research Program on Geological Storage of CO_2, In: Benson, S., (ed.), (2005) *Carbon Dioxide Capture for Storage in Deep Geologic Formations – Results from the CO2 Capture Project, Vol 2 Geologic Storage of CO_2 with Monitoring and Verification*. Elsevier.
4. Wildenborg, A., Leijnse, A., Kreft, M., Nepveu, M., Obdam, A., Orlic, B., Czernichowski-Lauriol, I., Torfs, P. and Wojcik, R., Risk Assessment Methodology for CO_2 Storage: The Scenario Approach. In: Benson, S., (ed.), (2005) *Carbon Dioxide Capture for Storage in Deep Geologic Formations – Results from the CO_2 Capture Project, Vol 2 Geologic Storage of CO_2 with Monitoring and Verification*. Elsevier.
5. Beavis, R., Introduction to CACHET – A Pre-Combustion Technology Development Program Co-Funded by the EU and CCP. In: Eide, L.I. (ed.), (2009) *Carbon Dioxide Capture for Storage in Deep Geologic Formations – Results from the CO_2 Capture Project, Vol 3 (2004-2009),* CPL Press.
6. de Mello, L., Moure, G., Pravia, O., Gearhart, L. and Milios, P., Oxy-Combustion for CO_2 Capture from Fluid Catalytic Crackers (FCC), In: Eide, L.I. (ed.), (2009) *Carbon Dioxide Capture for Storage in Deep Geologic Formations – Results from the CO_2 Capture Project, Vol 3 (2004-2009),* CPL Press.
7. CO_2 Capture Project, *A Technical Basis for Carbon Dioxide Storage.* CPL Press, ISBN: 978-1-872691-48-0, 2009. Available online at https://www.co2captureproject.org/
8. Crow, W., Williams, D., Carey, J., Celia, M., and Gasda, S., Well Integrity Evaluation of a Natural CO_2 Producer, In: Eide, L.I. (ed.), (2009) *Carbon Dioxide Capture for Storage in Deep Geologic Formations – Results from the CO_2 Capture Project, Vol 3 (2004-2009),* CPL Press.
9. de Mello, L., Gobbo, R., Moure, G., and Miracca, I, FCC Oxy-Fuel Demonstration at Petrobras Shale Industrial Business Unit, In: Gerdes, K.F. (ed.), (2015) *Carbon Dioxide Capture for Storage in Deep Geologic Formations – Results from the CO_2 Capture Project, Vol 4 (2009-2014),* CPL Press.
10. McGeean, C., Paton, C., Grimard, J., Pugsley, T., Tian, K., Laux, S., Bool, L., and Catesw, L., OTSG Oxy-Fuel Demonstration Project, In: Gerdes, K.F. (ed.), (2015) *Carbon Dioxide Capture for Storage in Deep Geologic Formations – Results from the CO_2 Capture Project, Vol 4 (2009-2014),* CPL Press.
11. Perera, L., Henkel, B., Liu, A., and Giguere, J., Project CO_2MENT: CO_2 Capture from a Cement Plant, In: Gerdes, K.F. (ed.), (2022) *Carbon Dioxide Capture for Storage in Deep Geologic Formations – Results from the CO_2 Capture Project, Vol 5 (2015-2022),* BP.
12. Imbus, S., Dodds, K., Busch, A., and Chan, M., CCP3-Storage, Monitoring and Verification (SMV) Overview., In: Gerdes, K.F. (ed.), (2015) *Carbon Dioxide Capture for Storage in Deep Geologic Formations – Results from the CO_2 Capture Project, Vol 4 (2009-2014),* CPL Press.
13. Oldenburg, C., Nicot, J., Jordan, P., Zhang, Y., Pan, L., Houseworth, J., Meckel, T., Carr, D., and Bryant, S., Health, Safety, and Environmental Risk Assessment of Geologic Carbon Sequestration: Overview of the Certification Framework, Example Application and Selected Special Studies 2010-2014, In: Gerdes, K.F. (ed.), (2015) *Carbon Dioxide Capture for Storage in Deep Geologic Formations – Results from the CO_2 Capture Project, Vol 4 (2009-2014),*CPL Press.
14. Global CCS Institute, 2021, *Global Status of CCS 2021*, Australia. https://www.globalccsinstitute.com/resources/global-status-report/

Carbon Dioxide Capture for Storage in Deep Geological Formations, Volume 5
Karl F. Gerdes (Editor)
© 2022 BP. All rights reserved.

Chapter 1

INTRODUCTION TO THE CCP4 CAPTURE TECHNOLOGY PORTFOLIO

Raja Jadhav
Chevron Technical Center, 100 Chevron Way, Richmond, CA, USA

ABSTRACT: This chapter describes the portfolio of CO_2 capture technology projects carried out by the CCP4 (2015-2022) and provides a summary of program objectives, project descriptions and key results achieved by industry and academic research partners. In CCP4, projects were developed based on the three application scenarios–Refinery, Post Combustion, and Natural Gas Treating.

KEYWORDS: CO_2 capture; NGCC; SMR; natural gas treating; post-combustion; solvents; membranes; adsorbents; techno-economic assessment (TEA)

INTRODUCTION

Since the inception of CCP in 2000, significant progress has been made in development of CO_2 capture technologies, with the focus on reducing the cost of capture. A few commercial projects have also been in operation since then that have provided valuable industrial experience of capture technologies at a large scale. However, the high cost of CO_2 capture remained a key challenge at the beginning of CCP4 for widespread deployment of CCS projects, especially for small and dilute CO_2 sources from oil and gas operations. Therefore, a key objective of CCP4's capture program was to continue support for further advancement of technolgies to reduce the cost of CO_2 capture. CCP4 supported desktop, lab, bench, and pilot scale studies to increase the understanding of existing, emerging, and breakthrough CO_2 capture technologies and targeted a reduction in the CO_2 capture cost by more than 50%.

The goal of this chapter is to:

- Provide an overview of how the CCP4 Capture program was developed, progressing from the learnings of the previous three phases of CCP.
- Describe the application scenarios considered in CCP4 for assessing the selected capture technologies.
- Summarize the objectives, activities, and results of projects in CCP4.

OVERVIEW OF THE CCP CAPTURE PROGRAM

The CCP has completed four phases of work since its inception in 2000. The highlights and achievements of the Capture program are given following:

CCP1 (2000-2004)–Screening/Proof of Concept [1]

- Nearly 200 CO_2 capture technologies were screened.
- Based on the technology screening, a small number of pre-, post- and oxy-combustion technologies were identified that showed promise to deliver significant cost reduction for CO_2 capture.

CCP2 (2004-2009)–Intensive Development [2]

- The most promising capture technologies identified in CCP1 were further developed, and two projects identified for field demonstration in the next phase.
- Several promising novel technologies were identified.

CCP3 (2009-2014)–Demonstration [3]

- Field demonstrations of an oxy-fired Fluid Catalytic Cracker (FCC) Catalyst Regenerator and a Once-Through Steam Generator (OTSG) confirmed technical feasibility of oxy-firing for these two applications.
- Bench- and pilot-scale testing of several novel technologies was completed along with techno-economic assessments (TEA).
- Economic baseline modeling of various capture technologies applied to three scenarios (Oil Refinery, Heavy Oil Production, and NGCC Power Generation) was completed.

CCP4 (2015-2022)–Further Advancement

- Work continued to further advance CO_2 capture technology deployment and knowledge for the oil and gas industry by supporting lab, bench, and pilot scale projects and carrying out techno-economic assessment of novel technologies.
- A new scenario of natural gas treating was included to support development of CO_2 removal technologies for offshore production application.

CCP4 SCENARIOS

Three industrial application scenarios were defined in CCP4 to provide a realistic context for assessing capture technologies chosen for development. The scenarios are:

- Oil refinery
- Post-Combustion
- Natural gas treating

In the following section, the various capture technology projects and assessments in these scenarios are described.

CCP4 PROGRAM SUMMARY

Oil Refinery Scenario: CO_2 Capture from Oil Refineries

A typical oil refinery has multiple and distributed CO_2 sources, including fired heaters, boilers, cogeneration units, and process units such as FCCs and hydrogen plants. The previous phases of CCP targeted all these major CO_2 emission sources. The work in CCP4 was more narrowly focused on capture from steam methane reformer (SMR) hydrogen plants, which were identified in CCP3 as one of the lowest cost CO_2 capture opportunities. This is because CO_2 capture can be implemented on the

high pressure shifted syngas gas stream for partial capture of the SMR emissions. Alternatively, for a high degree of capture, the flue gas from the reforming furnace has a higher concentration of CO_2 than does a typical fired furnace, which lowers the cost. It should also be noted that SMR is one of the largest single point sources of CO_2 in a refinery.

The following projects were studied in the Oil Refinery scenario.

Techno-Economic Assessment of CO_2 Capture from an SMR Plant

In Chapter 2, a study carried out in collaboration with IEA's Greenhouse Gas R&D Program (IEAGHG), is summarized. CCP4 performed a TEA of CO_2 capture from the:

- Shifted syngas stream upstream of the hydrogen purification unit (HPU).
- Tail-gas exiting the HPU.
- Reformer furnace flue gas, which includes the purification unit tail gas.

These three locations each offer distinct advantages and disadvantages. The shifted syngas has the highest partial pressure of CO_2, although contains only about 55-60% of the total CO_2 produced by the SMR–the balance being produced by fuel combustion in the reformer furnace. The tail gas has the highest concentration of CO_2 and capture from this location will not impact the HPU, although this stream is similar to shifted syngas in that it contains only the process-generated CO_2. The reformer furnace flue gas has 100% of the CO_2 produced by the SMR in a single stream, although it is at the lowest pressure of the three and is diluted with nitrogen and contains oxygen from the furnace operation. Based on a detailed evaluation by an engineering contractor, the IEAGHG study showed that an MDEA solvent-based process implemented upstream of the HPU had the lowest CO_2 avoided cost while an MEA solvent-based process implemented on the reformer flue gas had the highest cost of CO_2 avoided [4].

Manufacturing and Testing of 3D-Printed CO_2 Capture Materials for Productivity Step Change (3D-CAPS)

The goal of the 3D-CAPS project was to reduce the size of equipment needed for CO_2 capture using solid adsorbents by manufacturing materials with vastly improved heat and mass transfer characteristics. As described in Chapter 3, the objectives of the 3D-CAPS project were to:

- Achieve a 10-fold productivity increase for two sorbent-based technologies.
- Optimize sorbent shapes with Computational Fluid Dynamics (CFD) and other modelling tools, followed by their manufacturing and testing under relevant conditions.

Two types of structured sorbents were manufactured and evaluated in the project:

- Amine functionalised silica-supported sorbents (ImmoAmmo) for application in post-combustion CO_2 capture in the 40-130 °C temperature range
- Hydrotalcite (HTC) sorbent suitable for CO_2 capture at elevated pressure (up to 30 bar) in the 350-550 °C temperature range, as part of the sorption-enhanced water gas shift (SEWGS) process

The structured adsorbents were 3D-printed using Digital Light Processing (DLP). Good quality printed structures of silica (as support for ImmoAmmo sorbents) were repeatedly obtained. However, 3D-printing of HTC materials was more challenging, and structures could only be prepared in small batches and thus highlighted the need for further development work. Lab-scale experiments on the structured sorbents showed marked productivity increase compared to conventional packed beds. Models were developed in the project to understand the performance of structured sorbents, which

were validated with the results from lab-scale tests. These models were also used in developing and analysing capture system designs.

In Chapter 4, a preliminary TEA of the SEWGS process for CO_2 capture from SMR plants is documented. Based on the assumed capital cost savings in the SEWGS process, a 15% lower CO_2 avoided cost over that of an MDEA-based process was estimated. The SEWGS process also resulted in a higher CO_2 avoidance rate.

The project concluded that a targeted productivity increase of a factor 10 can be obtained, which can lead to more compact equipment, and reduced cost of CO_2 capture. To achieve this productivity increase, a balanced combination of material sorption properties, structural details and process design for the targeted CO_2 capture application is required.

Pilot Testing of Structured Adsorbent For CO_2 Capture From Cement Flue Gas

Chapter 5 summarizes recent progress by Svante in developing a novel rapid cycle, temperature swing adsorption (RC-TSA) process. A Metal Organic Framework (MOF)-based structured adsorbent was evaluated for CO_2 capture from the flue gas of a cement plant at a pilot scale of 1 tonne per day (TPD). The adsorbent was deployed in a novel rotating bed apparatus to implement the RC-TSA process. The cycle time for capture and release of pure CO_2 is less than 60 seconds, compared to hours for conventional adsorption-based technologies. Although the pilot plant was deployed on a cement plant flue gas, the concentration of CO_2 in cement plant emissions is about 18-20 mol %, similar to flue gas from modern SMR plants, and the pilot results are equally applicable to SMR plants.

The pilot project achieved steady state performance with high purity CO_2 product (> 95%) and met the key performance indicators (KPIs), including productivity and steam ratio. A new Waste Heat Recovery (WHR) cycle concept was designed to reduce the plant steam consumption and overall steam ratio.

TEA Of a Graphene Oxide (GO)-Based Membrane for CO_2 Capture From An SMR

As part of the main project that involved lab-scale development of the GO-based membrane and testing on synthetic NGCC and other flue gases, a TEA of CO_2 capture from the flue gas of an SMR plant was carried out as described in Chapter 6. The preliminary economic results, based on the assumed cost of the novel membranes, indicated that the levelized cost of hydrogen (LCOH) and CO_2 avoided cost of an SMR plant employing the GO-based membrane process were lower than that for a conventional MEA solvent-based process.

Post-Combustion Scenario: CO_2 Capture Using Post-Combustion Technologies

A post-combustion scenario was developed in CCP4 to group the capture technologies targeting CO_2 present in the flue gas of various combustion sources. Detailed techno-economic work in CCP3 [3] highlighted that post-combustion solvent-based technology provided the lowest CO_2 avoided cost for the sources evaluated. The main focus in CCP4 was CO_2 capture from natural gas combined cycle (NGCC) power plants because they can provide low-carbon, baseload power in the near future to complement the projected larger penetration of renewable power that is intermittent. However, capture of CO_2 from NGCC power plants is challenging because of the low concentration of CO_2 in the flue gas (~4 vol%) at atmospheric pressure and high concentration of O_2 in the flue gas (~ 12–14 vol%), which results in larger equipment size and higher energy consumption compared to capture from streams with a higher concentration of CO_2. Although CCP4 was focused on identifying and developing novel technologies that can capture CO_2 from NGCC power plants at reduced costs, other CO_2 sources considered included SMR flue gas, gas engine exhaust, and biomass-fired flue gas.

TEA of Novel Technologies for Post-combustion Capture of CO_2 from NGCC Power Plants

Using a common technical and economic framework, TEAs of four technologies were carried out for NGCC capture as detailed in Chapter 7. The technologies were molten carbonate fuel cell (MCFC), gas separation membrane, pressurized CO_2 absorption, and supersonic anti-sublimation. The study basis was the same as the 2011 EU benchmark study [5] – a state-of-the-art NGCC power plant without CO_2 capture was the Reference case, and the same NGCC plant with an MEA capture unit was the Base case. The analysis showed that a combined cycle integrated with MCFC was the most attractive technology, with considerable reduction in energy penalty and costs compared to the Base case and the other emerging technologies.

MCFC-based Capture from NGCC

Chapter 8 provides more detail on use of MCFC for capture from an NGCC. An integrated case is compared to a non-integrated case. The non-integrated case places the MCFC downstream of the Heat Recovery Steam Generator as might be the case for a retrofit.

TEA Of Piperazine Solvent for NGCC Capture

Building from the Chapter 7 comparison of novel technologies for NGCC capture, Chapter 9 documents a TEA study of the concentrated (5m) piperazine (PZ) solvent that has been under development at UT Austin for more than a decade [6]. The intent of the study was to provide an updated benchmark for flue gas capture by a chemical solvent to replace MEA. Several configurations of the capture system were assessed. The work was a collaboration between the LEAP group and UT-Austin, where specific testing produced data to tune the simulation model used to estimate the performance of the PZ-based capture plant.

Pilot Testing of Piperazine Solvent with the Advanced Stripper (PZAS™)

Chapter 10 describes development work on PZAS™, a second-generation amine scrubbing technology for CO_2 capture that has superior kinetics, favourable vapor-liquid characteristics, large operational CO_2 carrying capacity, and good resistance to thermal and oxidative degradation. A project was developed to test the technology on NGCC-specific flue gas (~4 vol% CO_2) at the pilot scale at the National Carbon Capture Center (NCCC) in Alabama, US. The main goals of the project were to (a) demonstrate the application of PZAS™ to low-CO_2 flue gas streams can achieve high capture rate at reasonable energy consumption; (b) generate data for model evaluation for scale-up, especially under different process conditions and configurations, and (c) demonstrate long-term operability of PZAS™, while evaluating emissions, degradation, corrosion, and other operational performance.

The pilot test campaign carried out performance testing under different operating conditions. New process configurations for absorber intercooling and process intensification concepts to combine direct contact cooler with absorber cooling were also tested and confirmed. The results showed faster kinetics for the solvent than MEA (allowing shorter contacting towers) with regeneration energy as low as 2.3 GJ/tonne of CO_2 depending on process conditions. The pilot test demonstrated long-term operation with a hot inlet flue gas and produced data on solvent degradation, corrosion, and amine emissions.

Alternative Absorber Design Study for PZAS^{TM} Capture Process

One of the major equipment items in a flue gas capture plant is the absorber where the CO_2 is scrubbed from the huge volume of flue gas. Chapter 11 documents a design study to develop a cost estimate for

a circular absorber as an alternative to the rectangular absorber used in a detailed design study funded by US DOE [7]. The rectangular design has been used in a very large capture demonstration plant in Texas, USA [8]. The circular tower is estimated to be 8% lower cost.

Pilot Testing of a Novel Non-Amine Solvent-Based Process

Chapter 12 describes ongoing development of a transformational non-amine solvent-based technology for CO_2 capture by C-Capture with potential to greatly reduce energy requirements compared to amine-based systems. The process was tested at pilot scale on biomass-fired flue gas at Drax Power Station in the UK. The objectives of the pilot work were to (a) validate C-Capture's process and develop scaleup data, (b) generate results on solvent's flue gas compatibility and ageing, and (c) analyse the emission products from the capture plant.

To meet the above objectives, a pilot plant designed to capture up to 1 tonne CO_2/day was constructed and operated at Drax on a slipstream from the power plant. The pilot plant included a conventional packed column and a 10-column-in-series spray absorber. Although the solvent was found to be compatible with the biomass-derived flue gas, and solvent ageing was found to be very minimal at the testing conditions, both the packed column and the spray absorber showed lower than expected capture performance. This has led to C-Capture refocussing on further investigating the absorption mechanism and developing an appropriate absorber design for the novel solvent.

TEA Of MCFC For CO_2 Capture from Natural Gas-Fired IC Engines

Following from chapter 7, Chapter 13 summarizes assessment of MCFC capture technology for CO_2 capture from small (~1 MW scale) internal combustion (IC) gas engines and combustion turbines that are widely used in providing shaft power in oil and gas production operations. The cost of CO_2 capture for these smaller CO_2 sources (~ 100 tonnes/day or lower) is generally higher for conventional solvent-based post-combustion capture technologies since most of these technologies are characterized by a strong economy of scale. As the MCFC systems are modular in nature, they can have an economic advantage when applied to CO_2 capture from smaller sources. Therefore, a TEA of the MCFC technology for capturing CO_2 from a cluster of reciprocating gas engines was carried out. The assessment indicated that the MCFC generated additional ~20% low-carbon electricity, which can be utilized or sold, while capturing 90% of the CO_2 emissions from the gas engines. The cost of CO_2 avoided was estimated to be in the range of $100–110/tonne of CO_2 depending on the process configuration, which is expected to be much lower than that for a conventional solvent-based capture technology at this small scale.

Model-Based Optimization of VSA System Based on Structured Adsorbents (3D-CAPS)

Chapter 14 documents a comparison of 3D-printed structured adsorbents to a conventional packed bed for two applications – FCC catalyst regenerator flue gas (15% CO_2) and SMR flue gas (21% CO_2). A model of the VSA cycle is used to develop the optimized cycle for each adsorbent and application. The structured absorbent has potential increase volumetric productivity by 3-fold and reduce energy consumption by 38%, which translates to a 1.8 times reduction in the plot space required.

TEA of New Solvents for CO_2 Capture

Chapter 15 proposes a screening method to compare post-combustion CO_2 capture solvents. To understand the cost saving potential of novel solvents, a high-level approach was developed in this project to rapidly screen both physical and chemical solvents, including ionic liquids and two new proprietary solvents. A conventional CO_2 capture plant treating a flue gas stream containing either 4

or 8 vol% CO_2 was considered, with the higher concentration corresponding to an Exhaust Gas Recirculation (EGR) case. The total annualised cost, including capital and operating cost, was estimated to rank the screened solvents. The process conditions were optimized for each solvent. The ionic liquid solvents were estimated to have higher capture cost compared to generic MEA solvent. The preliminary analysis showed that a power plant with an EGR scheme had potential for reducing capture costs, although further work will be required to understand its full impact.

Development of a Graphene Oxide (GO)-Based Membrane for CO_2 Capture

The development of a novel membrane for flue gas capture is the focus of Chapter 16. Membranes are potentially attractive for this application because of their operational simplicity and potential for lower capital investment, particularly for smaller scale applications due to their modular nature. In this project, ultrathin graphene oxide (GO)-based membranes with grafted, brush-like CO_2-philic agents were prepared onto a porous polymeric substrate for highly efficient CO_2 separation from other flue gas components. Amine-based CO_2-philic agents were introduced into the GO nanochannels with physical/chemical bonding. Both hollow fiber and flat sheet supports were used for depositing GO-based membranes.

Because of the facilitated transport of CO_2 molecules between the GO nanochannels, these membranes exhibited excellent separation performance under simulated flue gas conditions with CO_2 permeance of greater than 1,000 GPU and CO_2/N_2 selectivity of 300, demonstrating their potential for CO_2 capture from flue gas streams. The project also demonstrated scalability of the membrane up to 1,000 cm^2, which delivered separation performance similar to that of the smaller membranes.

TEA of CO_2 Capture from an NGCC Power Plant using MHI's KM CDR Process™

An economic baseline for a state-of-the-art capture technology is necessary to measure the performance of other novel capture technologies. Chapter 17 describes a study commissioned with Mitsubishi Heavy Industries (MHI) to develop an Engineering, Procurement and Construction (EPC) cost estimate for their KM CDR Process™. Based on an NGCC reference case [5] producing 830 MWe net electric power, the Total Plant Cost (TPC) for the capture plant was estimated. Using an economic methodology developed in CCP4, the costs of CO_2 captured and avoided were estimated to be \$65 and \$76/tonne of CO_2, respectively.

Field Demonstration of CO_2 Capture from Oilfield Engines Using a Turbocharger/Membrane Process

Reciprocating engines used in upstream oil and gas production are a significant source of CO_2 emissions. However, capture of CO_2 from these distributed and small sources of CO_2 using conventional amine solvent-based technology is expensive. Therefore, CCP4 supported a project to demonstrate a novel turbocharger process integrated with a membrane to capture CO_2 form oilfield engines.

However, the developer sold the technology and field pilot equipment prior to the final installation and commissioning of the pilot skids, which ended CCP4's involvement in the project, and therefore the project results are not presented here. CCP4 played an enabling role to de-risk this modular technology by completing the bulk of the design and equipment selection/procurement activities for the field pilot.

Natural Gas Treating Scenario: CO_2 Removal During Natural Gas Production

CCP4 created a new scenario–natural gas treating–to address the need of novel, cost-effective and modular technologies for separation of CO_2 during offshore natural gas production. The basic thrust of this work was to identify treating technology which integrated well with subsequent CO_2 storage.

Technology Screening Study for CO_2 Removal in Offshore Natural Gas Production

Chapter 18 documents a study to evaluate the current state-of-the-art and emerging technologies for removal of CO_2, with a specific focus on the technology landscape for offshore CO_2 removal from natural gas. Based on an extensive literature search and discussions with technology providers and experts, the study concluded that membrane technology was a leading, established technology for offshore CO_2 separation applications. Chemical solvent was prohibitively expensive at high CO_2 feed concentrations. Of the emerging technologies evaluated, a novel gas-liquid contactor utilizing hollow fibre membranes for solvent scrubbing was assessed to be the most promising, especially for applications where weight and space constraints imposed high costs. The chapter also provides guidance on the suitability of the various technologies at varying CO_2 and hydrocarbon compositions.

Development of Membrane-Based CO_2 Separation for Subsea Processing

Chapter 19 summarizes a project by a CCP-supported consortium to validate the concept of using membrane-based CO_2 separation on the sea floor, with subsequent reinjection of the CO_2 into an oil reservoir for enhanced oil recovery (EOR). Four membranes were evaluated at lab scale at the conditions relevant to subsea gas separation over a broad range of temperature, pressure and CO_2 content in the feed gas. The compatibility of the polymeric membrane and potting materials for exposure to fluids and chemicals expected during gas production was also tested. Based on the results of the experimental programs, two membranes were qualified for further testing at a pilot scale.

SUMMARY AND CONCLUSIONS

Please refer to Chapter 20 for key findings and recommendations for future work in the field of CO_2 capture in light of the findings of CCP.

REFERENCES

1. Thomas, D.C. (editor), (2005) *Carbon Dioxide Capture for Storage in Deep Geologic Formations–Results from the CO_2 Capture Project*, Vol 1 *Capture and Separation of Carbon Dioxide From Combustion Sources*; ISBN 0-08-044570-5, Elsevier Publihsing, UK.
2. Eide, L.I. (editor), (2009) *Carbon Dioxide Capture for Storage in Deep Geologic Formations–Results from the CO_2 Capture Project*, Vol 3 *Advances in CO_2 Capture and Storage Technology-Results (2004-2009)* ; ISBN 0-08-044570-5, CPL Press, UK.
3. Gerdes, K. (Editor), (2015) *Carbon Dioxide Capture for Storage in Deep Geologic Formations–Results from the CO_2 Capture Project, Vol.4-CCS Technology Development and Demonstration Results (2009-2014)*, CPL Press, UK.
4. IEAGHG, *Techno-Economic Evaluation of SMR Based Standalone (Merchant) Plant with CCS*. 2017.
5. CAESAR, 2011. European best practice guidelines for assessment of CO_2 capture technologies, EU project 213206 Deliverable D4.9, Feb 2011.
6. Rochelle G.T., Chen E., Freeman S., Van Wagener D., Xu Q., and Voice A. (2011) Aqueous piperazine as the new standard for CO_2 capture technology. *Chem. Eng. J.* **171** (3), 725−733.
7. F. Closmann, T. Gao, A. Suresh Babu, M. Abreu, B. Drewry, G.T. Rochelle, FEED for Piperazine with the Advanced Stripper on NGCC at Denver City, Texas. *Proceedings* of the

15th International Conference on Greenhouse Gas Control Technologies (GHGT-15), SSRN-id3819272, 2021.
8. Patel, S., Capturing Carbon and Seizing Innovation: Petra Nova is Power's Plant of the Year, *Power,* Aug 1, 2017.

Carbon Dioxide Capture for Storage in Deep Geological Formations, Volume 5
Karl F. Gerdes (Editor)
© 2022 BP. All rights reserved.

Chapter 2

TECHNO-ECONOMIC EVALUATION OF CO_2 CAPTURE FROM SMR PLANTS

Ibrahim Ali[1], Betty Pun[2], Paulo Prunzel[3]
[1]BP International Ltd, ICBT Chertsey Road, Sunbury-on-Thames, UK
[2]Chevron Energy Technology Co, Richmond, CA USA
[3]Petrobras Research Center, Avenida Horácio Macedo, Rio de Janeiro, Brazil

ABSTRACT: The third phase of the CO_2 Capture Project (CCP3) identified CO_2 capture from hydrogen production, particularly from Steam Methane Reforming (SMR), as one of the lowest cost CO_2 capture opportunities for oil refineries and heavy oil upgrading applications. Building on the results from CCP3, CCP4 focused on advancing the development and deployment of lower cost CO_2 capture technologies, especially those that show the potential for deployment in the nearer term. This chapter summarizes a study carried out by the IEA Greenhouse Gas R&D programme (IEAGHG), with support from CCP4 [1]. The study evaluated several cases of CO_2 capture at three different locations in an SMR plant–(i) the shifted syngas stream upstream of the hydrogen purification unit (PSA), (ii) the tail-gas from hydrogen purification, and (iii) the flue gas from the steam methane reforming furnace. Each of the three locations has its advantages and disadvantages. Capturing before the hydrogen purification gives the advantage of a higher CO_2 partial pressure and compact CO_2 capture equipment. However, it does not address the CO_2 emissions from the reformer flue gases. Hence, the total CO_2 capture rate is around 55%. Capturing from the reformer flue gas offers the opportunity to achieve a high rate of capture (90% or greater), but it entails handling the large volumetric flow rate of atmospheric pressure flue gas with costly post-combustion capture technology. The IEAGHG study concluded that an MDEA process implemented before the hydrogen purification unit has the lowest CO_2 avoided cost (€47/tonne of CO_2 avoided), while an MEA process implemented on the reformer flue gas has the highest cost of CO_2 avoided (€70/tonne) despite achieving a 90% CO_2 capture rate. A review of the current state of the art in CO_2 capture from hydrogen production is also included.

KEYWORDS: CCS, hydrogen plant, syngas, CO_2 capture, pre-combustion, post-combustion, steam methane reforming (SMR), CO_2 avoided cost, pressure-swing adsorption (PSA), LCOH

INTRODUCTION

The IEA Greenhouse Gas R&D Programme (IEAGHG) carried a techno-economic assessment of a SMR-based standalone H_2 plant with CO_2 Capture [1]. The study provides an up-to-date assessment of the performance and costs of a modern SMR-based H_2 plant without and with CCS producing 100,000 Nm^3/h (~90 MMSCFD) H_2. Six different cases were evaluated. These include:

1. Base case: modern SMR without CCS
2. Case 1A: SMR with CO_2 capture from the shifted syngas using MDEA
3. Case 1B: SMR with H_2-rich fuel firing the SMR furnace and CO_2 capture from shifted syngas using MDEA
4. Case 2A: SMR with CO_2 Capture from PSA Tail Gas using MDEA

5. Case 2B: SMR with CO_2 capture fro.m PSA tail gas using cryogenic and membrane technology
6. Case 3: SMR with CO_2 capture from the refomer flue gas using MEA

Details of the above study have been published by IEAGHG [1]. The report included a preliminary equipment list with no detailed cost breakdown, overall CAPEX and OPEX, levelised cost of hydrogen (LCOH), and the cost of CO_2 avoided. In collaboration with CCP4, IEAGHG undertook additional analysis to generate a detailed cost breakdown for the reference case (SMR without CCS) and Case 1A (SMR with CO2 capture from the shifted syngas using MDEA). These details are presented in this chapter.

SUMMARY OF THE SIX CASES EVALUATED

Base Case–Modern SMR Without CCS

The base case is a modern SMR reference plant (without CCS) consisting of the following main units:

- Feedstock pretreatment
- Pre-reformer
- Primary reformer
- High temperature water gas shift unit
- Pressure-swing adsorption (PSA) for hydrogen purification

A simplified block diagram for the base case plant is shown in Figure 1.

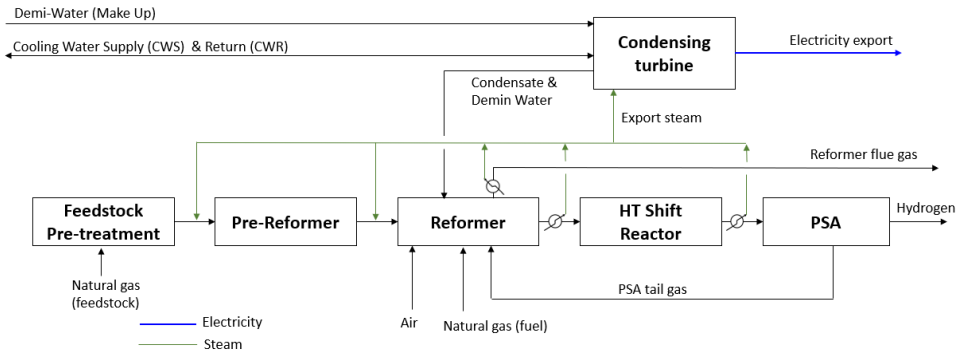

Figure 1. Base case–SMR plant without CCS producing 100,000 Nm^3/h H_2

The key features of the base case SMR plant are presented in Table 1. The hydrogen plant is designed to optimize heat recovery by the integration of a high-temperature air preheating system and the use of a pre-reformer and further preheating of the pre-reformed feed to the SMR. These heat recovery features reduce the steam production capacity of the plant. All the excess steam generated is delivered to the power island to generate electricity for use in the plant and export to the grid.

Table 1. Key features of the base case SMR plant.

Capacity	100,000 Nm^3/h H_2
Syngas capacity	188,000 Nm^3/h syngas (wet)
Residual CH_4 (after SMR)	3.4 mole % (dry basis)
Residual CO (after HTS)	3.7 mole % (dry basis)
PSA efficiency (H_2 recovery)	89%
H_2 product purity	99.99+ mol%
CO_2 concentration in SMR flue gas	21.2 mol%
Specific CO_2 emissions	9 kg CO_2/kg H_2

Case 1A–SMR with CO_2 Capture from Shifted Syngas using MDEA

Case 1A is based on the base case hydrogen plant with CO_2 capture using chemical absorption with methyldiethenolamine (MDEA) on the shifted syngas upstream of the PSA. The hydrogen and syngas production capacity of the plant are kept constant at 100,000 Nm^3/h H_2 and ~188,000 Nm^3/h wet syngas respectively. The PSA handles a smaller volume of syngas than for the base case due to the removal of the CO_2 from the shifted syngas. Figure 2 presents a simplified block flow diagram of this case. The basis for all the capture cases presented in this chapter for new build integrated facilities (greenfield projects) rather than retrofit for the CO_2 capture.

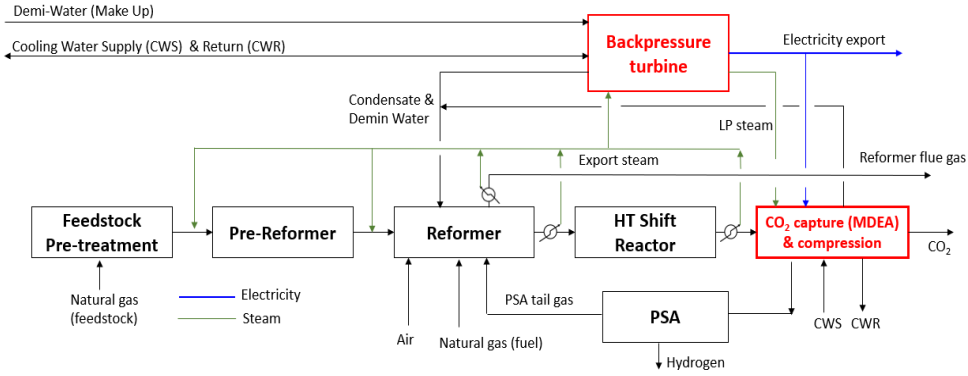

Figure 2. Case 1A–SMR plant with CO_2 capture from shifted syngas.

The main changes to the hydrogen plant relative to the base case are indicated in red boxes (as shown in Figure 2). The capture plant is designed based on MDEA solvent (supplied by Dow Chemical–UCARSOL AP806).

The addition of a CO_2 capture facility also resulted in some changes to the hydrogen plant and the power island relative to the base case. These include:

- Primary reformer burners would require burner tuning adjustment to accommodate the PSA tail gas with higher LHV, and to ensure that NOx emissions regulations are met.

- Some of the heat exchangers and steam generation coils are slightly enlarged/modified to accommodate the production of steam required by the CO_2 capture plant.
- The power island is now based on a back pressure steam turbine rather than a condensing steam turbine.

The steam demand to regenerate the solvent of the CO_2 capture plant is about 64.4 t/h of low-pressure (LP) steam. This is provided by increasing the consumption of natural gas (as supplementary fuel). Due to the extraction of the LP steam and the additional electricity required for the CO_2 capture and compression plant, the amount of electricity exported to the grid has decreased from 9.92 MW (base case) to 1.49 MW.

Case 1B–SMR with H_2-Rich Fuel Firing SMR Furnace & CO_2 Capture from Shifted Syngas using MDEA

Case 1B is a modification of Case 1A intended to increase the CO_2 capture rate of Case 1A by burning H_2-rich (lower carbon) fuel instead of natural gas in the reforming furnace. The net hydrogen production capacity has been kept constant at 100,000 Nm^3/h H_2. However, the syngas production of the SMR plant has been increased to ~238,500 Nm^3/h to deliver the CO_2-lean supplementary fuel. Case 1B uses 9% more natural gas for feedstock and fuel and represents an increase of ~27% in syngas production capacity relative to Case 1A. Figure 3 presents a simplified block flow diagram of Case 1B.

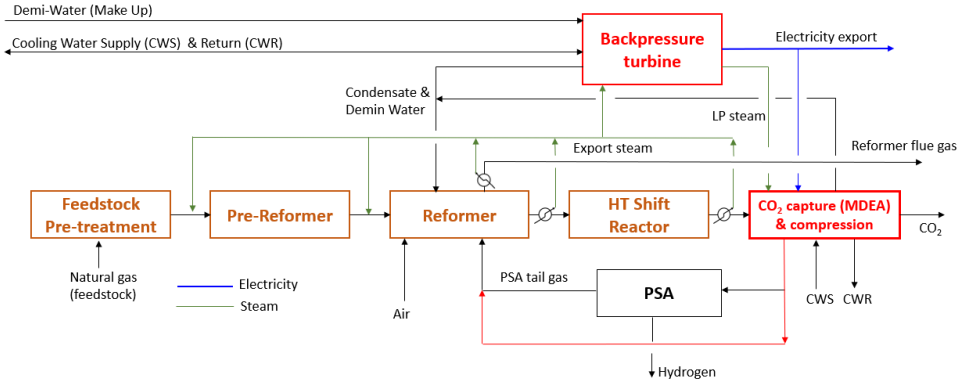

Figure 3. Case 1B–SMR plant with H_2-rich furnace firing and CO_2 capture from shifted syngas.

Maintaining the same CO_2 capture process as in Case 1A, the syngas production unit capacity has been expanded to accommodate the extra syngas needed to supply the SMR's supplementary fuel (as indicated in brown boxes as shown in Figure 3). Around 21% of the sweet syngas (or "raw hydrogen" gas) from the CO_2 capture plant is used as supplementary fuel to the SMR. The steam demand to regenerate the solvent of the CO_2 capture plant is about 77.8 t/h of LP steam.

As in Case 1A, the power island is based on a back-pressure steam turbine to produce electricity. Due to the steam and power demand of the CO_2 capture and compression plant, the amount of surplus electricity exported to the grid is reduced to 1.54 MW compared to 9.92 MW for the base case even with the larger syngas production.

Case 2A–SMR with CO_2 Capture from PSA Tail Gas using MDEA

The hydrogen production unit is identical to the base with both the hydrogen and syngas production capacity of the plant kept constant at 100,000 Nm^3/h H_2 and ~188,000 Nm^3/h wet syngas respectively. The main difference between this case and Case 1A is that CO_2 is captured from the PSA tail gas, rather than from the PSA feed. The CO_2 capture plant uses the same MDEA process as in Case 1A.

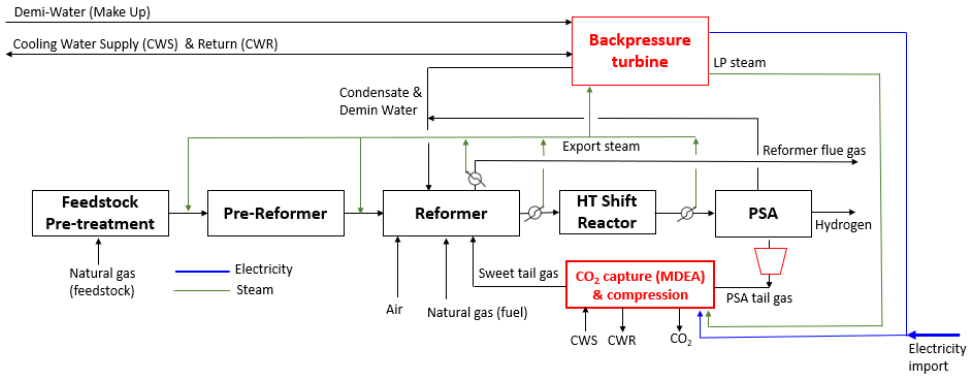

Figure 4–Case 2A–SMR plant with CO_2 capture from PSA tail gas using MDEA.

To allow CO_2 capture based on the MDEA solvent, the PSA tail gas is compressed to around 10 bar. In addition to the electricity demand of the CO_2 capture and compression plant, the compression of the PSA tail gas results in a deficit for electricity production. Therefore, this case requires import of electricity from the grid of about 1.1MW. Pressure energy is not recovered from the CO_2-depleted tail gas used as fuel in the reformer. The total steam demand to regenerate the solvent of the CO_2 capture plant is 66.9 t/h of LP steam.

Case 2B–SMR with CO_2 Capture from PSA Tail Gas using Cryogenic and Membrane Separation

This case features the same CO_2 capture location as in Case 2A. However, the CO_2 capture process is based on cryogenic and membrane separation. A simplified block flow diagram of the process is presented in Figure 5.

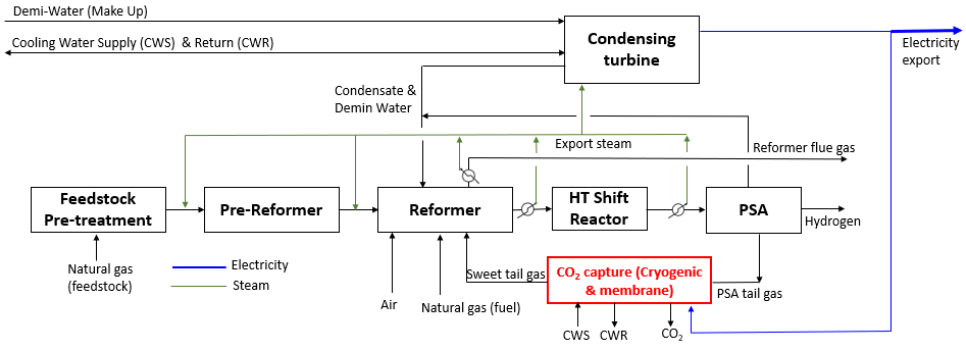

Figure 5. Case 2B–SMR plant with CO_2 capture on PSA tail gas using cryogenic and membrane separation.

The CO_2 capture plant is based on low temperature CO_2 separation and with additional CO_2 being captured from the vent stream of the cold box using a commercially available membrane process. The CO_2 removal system has the following features:

- The PSA tail gas is compressed and dehydrated using a 2-bed TSA system to feed to the low temperature CO_2 separation system.
- CO_2 compression is integrated into the CO_2 removal system.
- Cold box is based on an autorefrigeration cycle usinsg impure CO_2 as the refrigerant and has 3 stages of partial condensation and flash.
- Purity of the product CO_2 is about 99.6%.
- The lowest temperature within the system is about -55°C. This is the temperature of the feed to the third flash vessel after an expansion valve.
- The vent from the cold box (gas from 2nd flash vessel) is sent to the membrane. The CO_2-rich permeate is recycled back to the cold box. The non-permeate CO_2-lean gas from the membrane is pre-heated using the heat recovered from the CO_2 compressors before being expanded and sent to the SMR as fuel.

Since the tail gas from the CO_2 capture plant has a higher heating value than in the base case, the result is slightly better combustion efficiency in the SMR furnace. In addition, there is no steam demand by the CO_2 capture plant. This results in the overall natural gas consumption of the SMR plant with capture to be around 0.032 MJ/Nm^3 H_2 less than for the base case.

The power island for this case is the same configuration as the base case (condensing steam turbine). However, because of the additional electricity required by the CO_2 capture plant, the amount of electricity exported is reduced to around 0.29 MW, compared to the base case at 9.92 MW.

Case 3–SMR with CO_2 Capture from the Reformer Flue Gas using MEA

The hydrogen plant in this case is like the base case process. However, to increase the fraction of CO_2 capture for the whole process, the CO_2 capture is implemented on the reforming furnace flue gas. As this stream contains both the CO_2 generated by the process, due to the PSA tail gas use as fuel in the furnace, and the additional natural gas fuel, a high CO_2 capture rate is achieved. The CO_2 capture process is based on chemical absorption using MEA (MDEA is not applicable due to the low CO_2 partial pressure). A simplified block flow diagram of the process is presented in Figure 6.

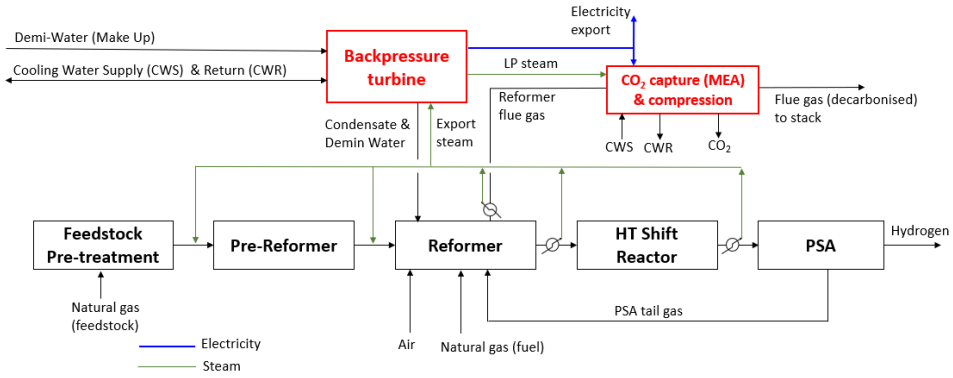

Figure 6. Case 3–SMR plant with CO_2 capture from the reformer furnace flue gas.

The changes to the H_2 plant are indicated in red boxes in Figure 6. The CO_2 capture plant is designed based on a proprietary MEA process using a split flow configuration.

To meet the steam demand of the CO_2 capture plant, natural gas consumption has been increased and several of the heat exchangers and steam generating coils of the reformer are enlarged. Due to the requirement to extract LP steam, a back-pressure steam turbine is used. The total steam demand to regenerate the solvent is about 96.4 t/h. The additional electricity demand of the CO_2 capture and compression plant results in a reduction of the electricity exported to the grid to 0.43 MW compared to 9.9 MW for the base case.

PLANT PERFORMANCE SUMMARY

A summary of the performance of the H_2 plants is presented in Table 2.

The following should be noted on the performance of the processes:

- The H_2 plant without CO_2 capture (base case) is designed to optimize heat integration and uses a pre-reformer. The deployment of the pre-reformer reduces the duty of the SMR furnace, thereby prolonging the life of the reformer tubes. However, the use of pre-reformer and the air pre-heating system reduces the amount of steam produced from the plant.
- This study opted for an SMR design without a low-temperature shift (LTS) reactor downstream of the HTS. This decision is a trade-off between CAPEX and OPEX. The addition of an LTS requires more CAPEX but reduces feedstock consumption by producing more hydrogen and also increases the steam generation capacity of the syngas cooler. Typically, the use of LTS is only attractive if the feedstock is expensive.

Table 2. Summary of Case Studies.

	Units	Base Case	Case 1A	Case 1B	Case 2A	Case 2B	Case 3
Inlet stream							
Natural gas (NG) feedstock	t/h	26.2	26.3	33.3	26.2	26.2	26.2
Natural gas fuel	t/h	4.3	5.3	0.0	5.6	4.3	7.3
Total NG input	t/h	30.6	31.6	33.3	31.8	30.5	33.6
Total NG thermal input	MW (thermal, LHV)	394.8	407.7	430.6	411.1	393.9	433.7
Product stream							
H_2 product to battery limit	t/h	9.0	9.0	9.0	9.0	9.0	9.0
H_2 product to battery limit	Nm^3/h	10^5	10^5	10^5	10^5	10^5	10^5
Thermal power in H_2 product	$MW_{thermal}$ (LHV)	300	300	300	300	300	300
LHV thermal efficiency	%	76.0	73.6	69.7	73.0	76.2	69.2
Power balance							
Gross output from COGEN	MW_{el}	11.50	6.70	8.00	6.90	11.00	11.70
H_2 plant consumption	MW_{el}	-1.22	-1.26	-1.58	-1.26	-1.22	-1.31
COGEN auxiliaries, BOP	MW_{el}	-0.37	-0.38	-0.44	-0.40	-0.51	-1.68
CO_2 capture consumption	MW_{el}	0.00	-0.57	-0.72	-3.44	-8.99	-2.00
CO_2 compression consumption	MW_{el}	0.00	-3.01	-3.72	-2.87	**Note 1**	-6.28
Power export to grid	MW_{el}	9.92	1.49	1.54	-1.07	0.28	0.43
Specific NG consumption							
NG feedstock	MJ/Nm^3 H_2	12.2	12.2	15.5	12.2	12.2	12.2
NG fuel	MJ/Nm^3 H_2	2.0	2.5	0.0	2.6	2.0	3.4
Total (feedstock + fuel)	MJ/Nm^3 H_2	14.2	14.7	15.5	14.8	14.2	15.6
CO_2 emissions							
Specific CO_2 emissions	kg CO_2 /Nm^3 H_2	0.809	0.370	0.292	0.387	0.377	0.089
Specific CO_2 emissions	kg CO_2/kg H_2	9.0	4.1	3.2	4.3	4.2	1.0
CO_2 emissions	t/h	80.9	37.0	29.2	38.7	37.7	8.9
Overall CO_2 capture rate	%	0.0	55.7	66.9	54.1	53.2	90.0
Overall CO_2 avoidance rate (vs base case)	%	0.0	54.2	63.9	52.2	53.4	89.0

Note 1-Included in the CO_2 capture plant.

- The H_2 plant without CO_2 capture consumes about 14.2 MJ/Nm3 H_2 and emits about 0.81 kg CO_2/Nm^3 H_2. It has a surplus of about 9.92 MW electricity which is exported to the grid.
- For Cases 1A, 2A and 3, the CO_2 capture is based on chemical absorption technology and achieves overall CO_2 capture rates from 55% to 90%. CO_2 capture increases natural gas consumption relative to the base case by 0.46 to 1.40 MJ/Nm^3 H_2. The extra fuel is largely needed to produce the steam required for solvent regeneration. The steam is extracted from the back-pressure steam turbine, which reduces power production. In addition, the CO_2 capture and compression plant requires power, resulting in a significant reduction of exported electricity (with Case 2A requiring import of ~1.07 MW).
- For Case 1B, the overall CO_2 capture rate is increased to about 64%, compared to Case 1A at 54%. This is achieved by burning H_2-rich fuel instead of natural gas as furnace fuel. The H_2 rich fuel is obtained from the sweet syngas coming from the CO_2 Capture Plant. For this case, the raw syngas capacity of the SMR and associated equipment is increased by around 27% to maintain a fixed production capacity of 100,000 Nm^3/h H_2.
- For Case 2B, the CO_2 is captured from the PSA tail gas using low temperature CO_2 separation and membrane technology. In this case, the natural gas consumption has reduced slightly by 0.03 MJ/Nm^3 H_2 compared to the Base Case. The electricity required by the CO_2 capture plant reduced the net electricity that could be exported.

TECHNO-ECONOMIC ANALYSIS SUMMARY

The main assumptions for the techno-economic evaluations are:

- Greenfield site, Netherlands coastal location
- 9°C ambient temperature
- Seawater cooling
- Natural Gas (with 5 ppmv H_2S) at 6 €/GJ LHV Basis
- 4Q 2014 costs
- Discount rate: 8% (constant money value)
- Operating life: 25 years
- Construction time: 3 years
- Capacity factor: 95%
- CO_2 transport and storage cost: €10/t stored
- Electricity cost: €80/MWh

Capital Cost (CAPEX)

The capital cost estimates were derived in general accordance with the practice of IEAGHG in estimating cost of the plant without and with CO_2 capture. The capital cost is presented as the Total Plant Cost (TPC) and the Total Capital Requirement (TCR).

TPC is defined as the installed cost of the plant, including project contingency. It is broken down into:

- Direct materials
- Construction
- Engineering, procurement and construction (EPC) services
- Other costs
- Contingency

TCR is defined as the sum of:

- Total plant cost (TPC)
- Interest during construction
- Owner's costs
- Spare parts cost
- Working capital
- Start-up costs

For each of the cases, the TPC has been determined through a combination of licensor/vendor quotes, the use of Wood's (formerly Amec Foster Wheeler) in-house database, and the development of conceptual estimating models based on the specific characteristics, materials, and design conditions of each item of equipment in the plant. The other components of the TCR have been estimated mainly as percentages of other cost estimates in the plant. The overall accuracy of the estimate is in the range of -15/+35%.

The capital cost of each case is summarised in Table 3, and the breakdown of the total plant cost is shown in Figure 7. To implement capture of CO_2 from an SMR plant, the increase in the specific capital cost per Nm^3/h H_2 ranges from 18 to 42% compared to the base case for partial capture of 53-65%. On the other hand, for 90% CO_2 capture from an SMR plant, the increase in the specific capital cost is about 78% compared to the base case.

Table 3. Capital costs of SMR-based H_2 plants (4Q 2014, Netherlands coastal location).

	Total plant cost (TPC) (€million)	**Total capital requirement (TCR) (€million)**	**% TPC increase (vs base case)**
Base case	171.0	222.9	
CO_2 capture from shifted syngas			
Case 1A	201.8	263.9	18.0%
Case 1B	228.5	298.7	33.7%
CO_2 capture from PSA tail gas			
Case 2A	226.1	292.2	32.2%
Case 2B	241.4	313.9	41.2%
CO_2 capture from reformer flue gas			
Case 3	305.3	398.5	78.6%

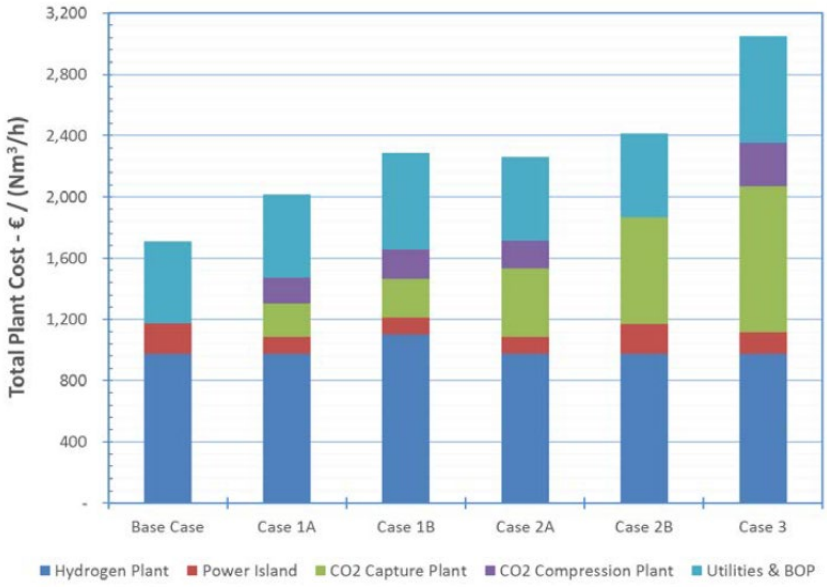

Figure 7. Specific total plant costs (TPC) for SMR-based hydrogen plants.

Operating Cost (OPEX)

The OPEX of the plant includes the cost for labour, maintenance, natural gas, catalyst, and chemicals. Table 4 summarises the OPEX for all the cases. The biggest factors that increase the operating cost of the plant with CO_2 capture are the cost of incremental natural gas, maintenance (proportional to CAPEX), and loss of revenue from the sale of electricity.

Table 4. Operating costs of SMR-based H_2 plants.

	Base Case	Case 1A	Case 1B	Case 2A	Case 2B	Case 3
Fixed operating costs (€million/year)						
Direct labour	2.28	2.58	2.58	2.58	2.58	2.58
Admin. & overheads	0.99	1.13	1.18	1.18	1.21	1.32
Insurance & local taxes	1.71	2.00	2.28	2.26	2.41	3.06
Maintenance	2.56	3.00	3.42	3.39	3.61	4.59
Subtotal	**7.55**	**8.72**	**9.46**	**9.42**	**9.81**	**11.55**
Variable operating costs (€million/year; availability = 95%)						
NG (feedstock & fuel)	70.98	73.28	77.39	73.91	70.80	77.97
Water makeup	0.10	0.10	0.13	0.10	0.10	0.07
Chemicals & catalysts	0.42	0.42	0.51	0.42	0.42	0.42
Subtotal	**71.50**	**73.80**	**78.03**	**74.43**	**71.32**	**78.46**
Total operating costs	79.05	82.53	87.48	83.85	81.14	90.01
Revenues (€million/year)						
Electricity	-6.60	-0.99	-1.03	0.71	-0.19	-0.28
Total OPEX (Note 1)	**79.05**	**82.53**	**87.48**	**84.56**	**81.14**	**90.01**

Note 1–The total OPEX row includes electricity cost, where electricity is imported (Case 2A), but does not include the revenue from electricity sale.

Levelized Cost of Hydrogen (LCOH)

The levelized cost of hydrogen (LCOH) is a measure of the net present cost of producing hydrogen over the lifetime of the plant. It is price of hydrogen which enables the present value from all sales of hydrogen (including the additional revenue from the sale of electricity) over the economic lifetime of the plant to equal the present value of all costs of building, maintaining, and operating the plant over its lifetime.

The LCOH in this study is calculated assuming constant (in real terms) prices for fuel and other costs and constant operating capacity factors throughout the plant lifetime, apart from lower capacity factors in the first year of operation. The assumptions presented at the beginning of this section feed into the LCOH calculations.

Cost of CO_2 Avoided

The CO_2 capture cost is based on the CO_2 captured per net Nm^3 H_2 produced. The cost of CO_2 avoided is based on the CO_2 reduction to the atmosphere per net Nm^3 H_2 – accounting for additional utility usage for capture and loss of efficiency for the overall plant. It is calculated as the ratio of the difference in LCOH with capture and without (reference plant) to the difference in emissions intensity for the reference and plant with capture. This is given in Equation 1:

$$Cost\ of\ CO_2\ avoided\ (CCA) = \frac{LCOH_{CCS} - LCOH_{Reference}}{CO_2\ Emissions_{Reference} - CO_2\ Emissions_{CCS}} \quad (1)$$

Where:

- CCA is expressed in € per tonne of CO_2 avoided.

- LCOH is expressed in € per Nm^3 H_2.
- CO_2 emissions are expressed in tonne of CO_2 per Nm^3 H_2.

The levelised costs of hydrogen (LCOH) and cost of CO_2 avoided (CCA) are shown in Table 4 and Figure 8 for the cases evaluated.

Table 4. Techno-economic analysis summary: LCOH and cost of CO_2 avoided.

Case	LCOH (€/Nm^3)	CCA (€/tonne CO_2)
Base case	0.114	-
Case 1A	0.135	47.1
Case 1B	0.146	62.0
Case 2A	0.142	66.3
Case 2B	0.140	59.5
Case 3	0.165	69.8

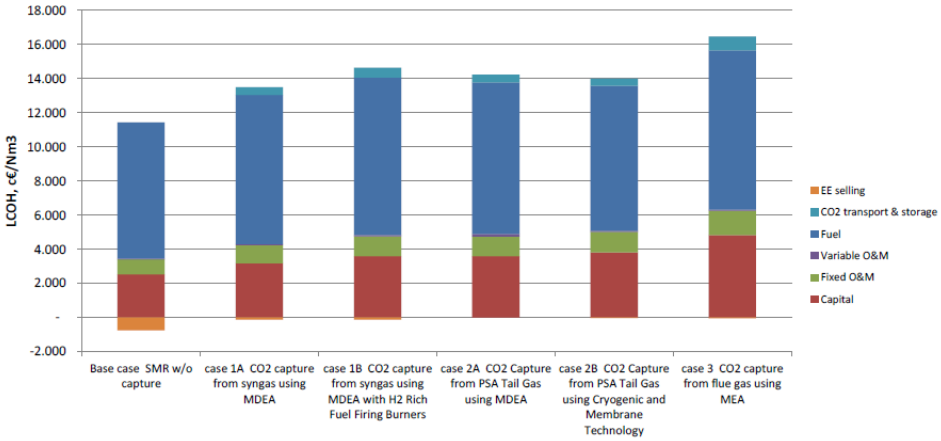

Figure 8. Levelised cost of hydrogen (LCOH) for the different cases.

CURRENT STATE OF THE ART IN HYDROGEN PRODUCTION WITH CCS

The previous sections focus on CO_2 capture from three locations identified for SMR. As has been already discussed, a key limitation of CO_2 capture from an SMR from the syngas stream can only capture a maximum of 65%, even with hydrogen firing in the furnace (Case 1B). There are other technologies that reduce the proportion of CO_2 in the flue gas relative to the process gas, such as gas heated reforming that can be added to the SMR process to improve efficiency [3]. However, to achieve overall CO_2 capture rate of 90% or above in an SMR process, the CO_2 capture needs to be located on the flue gas stream from the reformer and this is more expensive than capturing from the process stream (Case 3).

There are other hydrogen production technologies from natural gas that do not require external heating of the natural gas reforming and hence do not generate a separate, low-pressure CO_2-rich flue gas stream. These include partial oxidation (POX), autothermal reforming (ATR) and ATR integrated

with gas-heated reformers (GHR). These processes can incorporate CO_2 capture with greater than 90% overall CO_2 capture rate on the higher-pressure process gas stream.

ATR combines the endothermic methane reforming reaction and the highly exothermic partial combustion of natural gas inside a single reactor vessel, therefore yielding a process that is thermally neutral (autothermal). Pure oxygen is used for the partial combustion of natural gas in an ATR to produce H_2. A cryogenic air separation unit (ASU) is required, and this is the major cost center for an ATR system. The ASU loses economies of scale at lower capacities, and this limits the minimum practical size of an oxygen-blown ATR [4]. There is disagreement among some recent studies on costs for ATR versus SMR [1,3,6]. IEA [1] estimates that ATR is lower cost above about 220,000 Nm^3/hr or 200 MM SCFD of H_2. Site specific factors, especially utility costs, strongly affect which option in lower cost.

The key advantage of the ATR relative to SMR is the ability to achieve a higher CO_2 capture rate at lower marginal costs especially in scenarios where greater than 90% capture rate is required. In addition, ATR processes can be combined a GHR to increase efficiency and reduce CAPEX, although this has only been practiced at modest scale for retrofits.

KEY FINDINGS AND CONCLUSIONS

The study summarised in this chapter provides an assessment of the performance and costs of a modern SMR-based hydrogen plant with and without CCS producing 100,000 Nm^3/h hydrogen. The study is based on a new build merchant plant without any integration to an industrial complex. The design was optimized to minimize excess steam production, with any excess used to generate power.

Several options for capturing CO_2 from an SMR Based H_2 plant were assessed. Case 1A is based on capturing CO_2 from the shifted syngas using MDEA solvent. This represents one option for SMR-based H_2 plants that is currently in commercial operation.

- This plant consumes about 14.67 MJ/Nm^3 NG (both as feedstock and fuel) and captures around 56% of the total CO_2 emitted (avoiding around 54% CO_2 as compared to the base case).
- The levelized cost of hydrogen for Case 1A is € 0.135/Nm^3 which is about €0.021/Nm^3 higher than the base case. This case achieved the lowest LCOH among the options considered. The increase in the LCOH is predominantly contributed by the increased CAPEX and and higher NG consumption. A smaller impact is loss of revenue from electricity sale.

Four other CO_2 capture options were also evaluated. These include the use of H_2-rich burner in conjunction with CO_2 capture from shifted syngas (Case 1B), CO_2 capture from PSA tail gas using MDEA (Case 2A) or the use of Cryogenic and Membrane Separation (Case 2B) and CO_2 capture from SMR flue gas using MEA (Case 3).

- The incorporation of CO_2 capture increases the natural gas consumption by 0.46 to 1.40 MJ/Nm^3 H_2 (with the exception of Case 2B where natural gas consumption decreases slightly).
- Similarly, all plants with CO_2 capture resulted in a significant reduction of the surplus electricity exported to grid (with Case 2A requiring an additional import from the grid of around 1.1 MW).
- The LCOH for the plants with CCS ranges from €0.145 - €0.165 /Nm^3 H_2. This is about 27-45% higher than the SMR H_2 plant without CCS (0.114 €/Nm^3). The cost of CO_2 avoided is in the range of 47 -70 €/t (including the cost of transport and storage at 10 €/t).

Case 3 achieves a high rate of CO_2 capture. This case has the highest CAPEX, OPEX, LCOH and cost of CO_2 avoided. However, there is no CO_2 tax considered in the analysis. A CO_2 tax of about €80 - €90/tonne CO_2 makes Case 3 competitive with Cases 1A, 2A and 2B.

Case 2B has a slightly lower natural gas consumption than the base case. It may be attractive in scenarios where the cost of natural gas is very high. Furthermore, there is the option to increase hydrogen yield with Case 2B. This has not been taken into account in the current analysis.

ACKNOWLEDGEMENTS

IEAGHG for permission to publish summary material from the 2017 study [1].

REFERENCES

1. IEAGHG, *Techno-Economic Evaluation of SMR Based Standalone (Merchant) Plant with CCS*. 2017.
2. IEAGHG, *Techno-economic evaluation of deploying CCS in an SMR-based H2 production using natural gas as feedstock and fuel*, Report no. 2015-08, 2015.
3. Element Energy Ltd (for the UK Department of Business, Energy & Industrial Strategy (BEIS), Hydrogen Supply Chain Evidence Base. Novmeber 2018.
4. Tesch, Morosuk, and Tsatsaronis, "Comparative Evaluation of Cryogenic Air Separation Units from the Exergetic and Economic Points of View," IntechOpen Journal, DOI:http://dx.doi.org/10.5772/intechopen.85765 , 2019.
5. IEA, Reference Data and Supporting Literature Reviews for SMR-Based H2 Production with CCS, March 2017.
6. Pun, B., and Butler, D., "Technoeconomic Evaluation of Carbon Dioxide Capture from Refinery Heaters and Boilers," in *Carbon Dioxide Capture for Storage in Deep Geologic Formations – Results from the CO2 Capture Project Volume 4 CCS Technology Development and Demonstration Results (2009-2014)*, K. Gerdes (ed) CPL Press 2015.

Carbon Dioxide Capture for Storage in Deep Geological Formations, Volume 5
Karl F. Gerdes (Editor)
© 2022 BP. All rights reserved.

Chapter 3

3D-PRINTING OF HYDROTALCITE-BASED SORBENTS FOR INCREASED PRODUCTIVITY IN CARBON CAPTURE APPLICATIONS

Soraya Sluijter[1] and Carlos A. Grande[2]
[1]TNO, Westerduinweg 3, 1755 LE Petten, The Netherlands
[2]SINTEF Industry, Forskningsveien 1, 0373 Oslo, Norway

ABSTRACT: The overall goal of the 3D-CAPS project is to improve the economics of CO_2 capture using adsorption by greatly improving the adsorbent productivity, as characterized by kg CO_2/m^3h. Two adsorbents for CO_2 capture are targeted for enhancement by use of 3D-structured monoliths of the sorbent materials. This chapter describes the 3D-printing of a potassium-promoted hydrotalcite (K-HTC) sorbent for the sorption-enhanced water–gas shift (SEWGS) application and the investigation of relevant properties to obtain this productivity increase. Specifically, the effects of printing and of post-processing, which consists of a washing step and heat treatment, on the properties of the printed materials are studied. The capacity measurements of the materials at relevant temperature and pressure (400°C and 20 bara(a)) after printing and post-processing show that the printed and post-processed K-HTC materials keep the original CO_2 capture capacity compared to the starting sorbents. The pressure drop over the monolithic structures is lower than that for conventional pelletized adsorption beds (< 60 mbar/m vs > 200 mbar/m at 1 m/s velocity), as expected. Test results can be used to validate modelling discussed in Chapter 4. The effect of 3D-structuring of the sorbent material on the productivity appears promising.

KEYWORDS: CO_2 capture, pre-combustion, structured sorbent, 3D-printing

INTRODUCTION

The commercialization of adsorbent based capture technologies would benefit from improvements in both the size of equipment and the energy associated with the carbon abatement. The 3D-CAPS project aims to address these challenges by significantly increasing the productivity (kg CO_2/m^3hr) of two adsorbents by structuring through 3D-printing. This chapter describes the 3D-printing of the hydrotalcite materials as well as the characterisation and relevant properties of the resulting structured materials to obtain this productivity increase for the sorption-enhanced water–gas shift (SEWGS) technology. The designs used in this chapter are partly determined by the modelling described in Chapter 4 of this volume, which also covers the techno-economic assessment for application in CO_2 capture from hydrogen plants. In addition, the amine functionalised silica sorbents part of the 3D-CAPS project is discussed in Chapter 14.

In SEWGS, the water–gas shift reaction (WGS) is combined with in situ adsorption of CO_2, typically at about 400°C and pressure up to 30 bar. Potassium-promoted hydrotalcite (K-HTC) functions both as a catalyst for the WGS reaction and sorbent of CO_2 in the SEWGS process [1]. The CO_2 is released during periodic regeneration of the K-HTC. Thus, the overall process directly converts syngas into separate streams of H_2 and CO_2, which makes the SEWGS process exceptionally suitable for pre-combustion CO_2 capture mitigating greenhouse gas emissions. One of the challenges of this and other pressure swing adsorption (PSA) technologies using traditional packed-beds is the trade-offs among

flow rate through the reactor, pressure drop and kinetics of the adsorption process. 3D-printing will allow bespoke material configuration solutions not available with current production technologies, allowing maximum interplay between these three competing and complementary elements.

Structured adsorbents and catalysts have recently gained significant interest owing to the advantages of lower pressure drop and faster mass transfer compared to conventional shaped materials [2-4]. Additive manufacturing (3D-printing) allows production of structured materials with tailored channel sizes and wall thickness, having improved heat and mass-transfer characteristics, that are not available through traditional material preparation routes. For a standard packed-bed adsorption system, as the flow rate increases, ideal plug-flow starts to become disperse, which reduces mass transfer performance, and pressure drop increases. Reduced mass transfer efficiency requires more frequent regeneration. The shorter time on stream in adsorption mode at constant regeneration times reduces the effective productivity. Similarly, cycling times can be limited by pressure drop over the column, as is also described in Chapter 4. By using optimized 3D-printed sorbents with good mass transfer and lower pressure drop characteristics, flow rates can be increased to enhance the productivity.

The K-HTC material, which is a complex material consisting of a double layered hydroxide with carbonate and water groups in between the layers, is fabricated into structured form by a 3D-printing method, Digital Light Processing (DLP). DLP is an indirect slurry-based printing process, that uses a photo-active material to initiate binding (Figure 1). After printing the structure layer by layer by illuminating cross-sections of the design, a debinding and sintering step is required to obtain the final structured adsorbents. The printing and the post-processing, which consists of a washing step and heat treatment, may have an effect on the properties of the printed materials. Specifically, heat is known to have a large effect on hydrotalcites. The structure decomposes at higher temperatures by dehydration, dehydroxylation and decarbonation, spinel formation and K_2CO_3 decomposition [5].

In this chapter, the effect of printing and post-treatment on the sorbent material is discussed. The adsorption capacity of the printed material is derived from breakthrough measurements carried out at relevant conditions, 400°C and 20 bar, and compared to non-printed base material. Furthermore, the effect of structuring of the sorbent on the pressure drop is assessed.

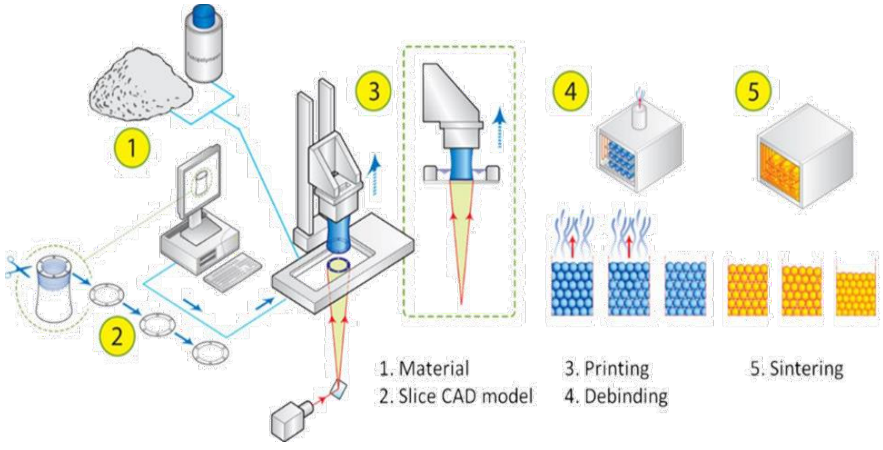

Figure 1. Overview of DLP AM process: 1. Paste development, 2: slice design, 3. Printing, 4: thermal debinding and 5: sintering.

CHARACTERISATION OF PRINTED HYDROTALCITE MATERIALS

3D-Printing Materials and Post-Treatment

The slurries for 3D-printing are provided by the company Admatec and consist of the K-HTC material (Sasol Pural KMG30 powder), resin (di and tri-acrylates), a photo initiator and additives (plasticizers, surfactants). The adsorbent structures are printed on a dedicated Admaflex 130 DLP printer. After successful printing, the resulting structures are washed with either ethanol, isopropanol or acetone (by submerging them in the solvent overnight at 50°C with stirring). After drying in air, the brown/green structures are measured, weighed, and calcined in air (12°C/h to 420°C (2 h dwell), 12°C /h to 470 or 550°C (2h dwell)) in a Nabertherm C440/450 oven. After sintering the final structures are again measured and weighed.

SEM and EDX

Scanning electron microscopy (SEM) was used to examine the microscopic structure of the printed materials. The printed structures were analysed on a Hitachi S3700-N SEM (Figure 5). Elemental mapping was performed by energy dispersive x-ray (EDX) analysis on the same machine to determine the potassium content on the sorbent after washing with various solvents.

CO_2 Capacity of Printed Materials

To determine the CO_2 sorption capacity of the various adsorbents after 3D-printing and post-treatment, experimental runs at high pressure (20 bar) were conducted on the high-pressure multi reactor rig ('Spider') shown in Figure 2. Gas bottles connected to Mass Flow Controllers (MFC) were used to produce the desired gas mixtures in the buffer vessel at a pressure of 30 bar. Separate MFCs control the flow into each reactor. The MFC connects to a three-way valve which can be instantaneously switched between the feed mixture from the buffer vessel or inert gas (argon in this case, N_2 in figure 2). The sampling intake can be switched between the feed from the buffer vessel or the reactor effluent and can be changed between the reactors. The analytical system consists of a single Mass Spectrometer (MS) with the inlet flow being diluted with helium.

Most experiments used six reactors in parallel, each 9.3 mm internal diameter and electrically heated. The reactors were loaded with 2.5 g of printed and then crushed material (212-425 μ) and reference materials. The bottom of each reactor was filled with silicon carbide particles up to the level of the test section. The test section of the reactor was filled with the sample and topped with a layer of silicon carbide. The test section sits completely within the reactor oven. The samples were dried at 150°C prior to weighing. A pre-treatment under N_2 (5°C/min to 450°C and 4h at 450°C) was done to dry the HTC. During adsorption testing, the reactors were each fed 150 NmL/min of gas mixtures at 400°C and 20 bar(a) pressure. The feed gas consisted of 25% of H_2O and 25%, 10% or 3% of CO_2 balanced with N_2. Adsorbent regeneration consisted of periodic switching to the same composition with argon instead of CO_2. For every mixture, the adsorption and the regeneration were measured for each sample by GC-MS. Gas analysis was performed by mass spectrometry (MS), which measured hydrogen (m/z=2), water (m/z=18), carbon monoxide/nitrogen (m/z=28), argon (m/z=40) and carbon dioxide (m/z=44).

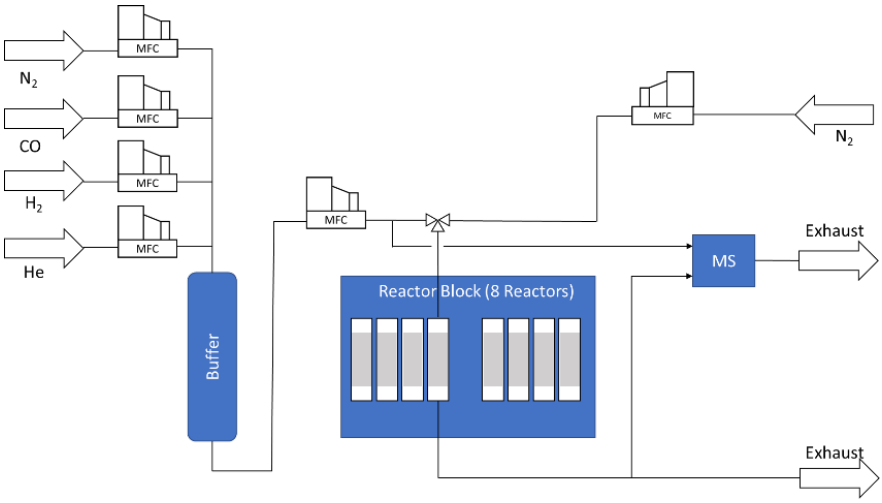

Figure 2. High pressure multi-column unit called the 'Spider'.

Pressure Drop of Printed Structures

The pressure drop (Δp) as a function of the flow was measured at TNO using N_2 at room temperature as the working fluid. The cylindrical printed samples to be measured were inserted in a standard one-inch external diameter tube for Δp measurements. To prevent bypass flow and to fix the structures within the tube, the samples were wrapped in ceramic (ZrO_2) cloth. The velocity of the gas passing through the tube, was varied and controlled by a series of Bronkhorst mass flow controllers with the appropriate operating ranges. The pressure drop was measured on a Bronkhorst EL-press. When the pressure drop was too low for the detection limits of this system a more sensitive set-up was used at SINTEF.

The unit at SINTEF used to measure pressure drop is shown in Figure 3. All the measurements were made using compressed air without further treatment. The operation of the unit was previously described in the literature [6]. The design includes two mass flow controllers to accurately control the velocity over two different ranges.

All measurements of pressure drop were made at 295 K. During each experiment, the air flow was increased in steps and the following data was acquired:

- Δp measured using Testo 435-4 internal differential pressure sensor (accuracy ±0.02 hPa low-range and ±1% mv in remaining range).
- Flow rate and temperature of the exit stream was measured by an electronic bubble flow meter and a K-thermocouple.
- The flow was increased to cover the velocity range 0–5 m/s.

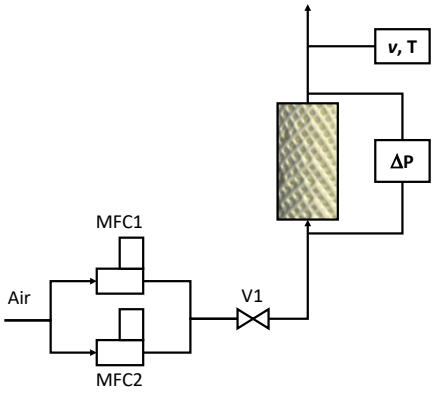

Figure 3. Equipment used to measure pressure drop. Terminology: MFC: mass flow controllers; v,T: velocity and temperature measurement; V1: on-off valve; ΔP: differential pressure meter.

RESULTS FOR CHARACTERISATION OF PRINTED HYDROTALCITE MATERIALS

The K-HTC sorbent was successfully printed, post-processed and tested for pressure drop and mass transfer kinetics. During the printing process, issues arising due to viscosity variation and reduced photo-activity over time were successfully resolved. However, several challenges remain to be addressed – specifically, reproducibility and the appearance of cracks during post-processing.

Over the course of the project, monolithic structures *1-6*, having various channel and strut sizes (Table 1) have been fabricated and tested. Also, a monolith having zig-zag channels was investigated ("zz" image in Table 1). This structure had to be printed in two halves to avoid connection gaps. *Monolith 1* and *4* could be printed, however during post-processing there were problems with cracking, due to the walls being too thin (*Monolith 1*) or debris in the narrow channels (*Monolith 4*). *Monolith 6* was designed based on modelling results in Chapter 4, which indicated that this structure would potentially deliver an 8-fold productivity increase. In addition, a foam structure was printed to study the performance of a regular reticular structure in terms of mixing and pressure drop (Figure 4) [6].

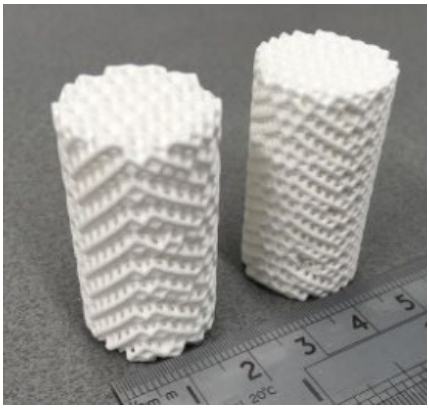

Figure 4. Isoreticular Foam structures.

3-D printing using DLP is known to have high resolution [2]. Indeed, when printing the structures, low deviations (<20 μ) were observed (except when the structures were cracked or had other defects). The measured reduction in mass upon sintering corresponds with the volume per cent of solid material in the slurry and indicates that all organics from the paste are burned away in the process. The shrinkage in width and height was around 15-20% depending on the concentration of K-HTC in the paste. SEM pictures of *Monolith 6* and reference materials are depicted in 5. Although there are some

cracks present in the printed structure (more than in the reference Pural KMG30 pellets from Sasol), the particles are fused together.

Table 1: Various monolithic structures that were printed with various properties. Below the table are images of the printed monolith structures.

Structure	Wall thickness *t* (mm)	Channel radius *a* (mm)	channel size *b*	Bed Voidage	External surface area (cm^2/cm height)	Bulk Density (kg/m^3)	# channels
Packed bed	-	-	-	~0.38	-	~1200	-
Monolith 1	0.3	0.9	1.56	0.48	16.2	973	30
Monolith 2	0.9	0.9	1.56	0.30	10.26	1297	19
Monolith 3	0.9	1.8	3.11	0.44	7.56	1032	7
Monolith 4	0.9	0.45	0.78	0.17	11.34	1547	42
Monolith 5	1.58	0.9	1.56	0.22	7.56	1444	14
Monolith 6	0.5	0.5	0.86	0.31	19.2	1275	64
Monolith zz	1.58	0.9	1.56	0.22	17.56	1444	14

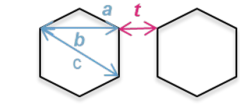

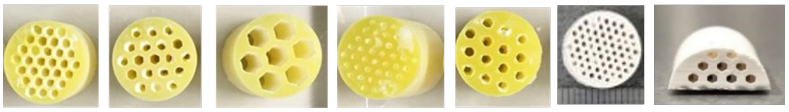

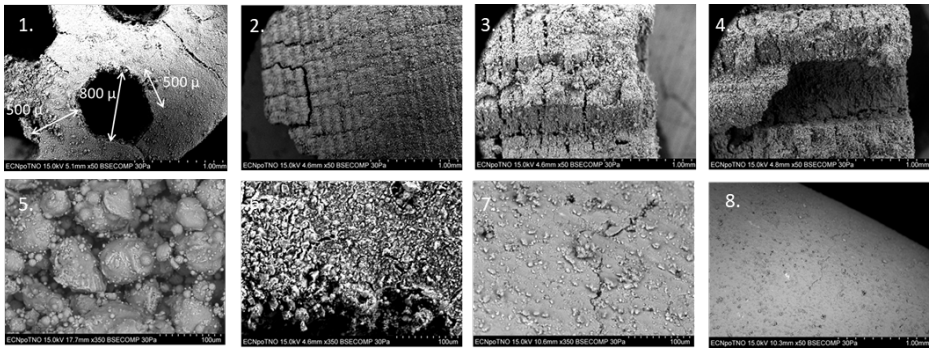

Figure 5. SEM pictures of Monolith 6 sintered at 470°C and reference powder and pellet. (1) channels in *Monolith 6*. (2) Side view (round). (3) & (4). Broken area. (5) Pural KMG30 powder. (6) 3D-printed *Monolith 6*. (7) & (8) enlargements of Pural KMG30 pellet.

Effect of Printing and Post-Treatment on the Sorbent

Generally, 3D-printed ceramics prepared by DLP were washed with water after printing. Because of the high solubility of K_2CO_3 in water, we investigated the effect of washing the structures with various solvents (ethanol, isopropyl alcohol (IPA) and acetone). IPA seemed to give the best results in terms of minimizing cracking after washing, drying, and sintering at 470°C, although SEM pictures of monoliths washed with IPA showed some cracks (Figure 5). EDX measurements did not indicate any significant loss of K_2CO_3 upon washing with IPA and therefore, IPA was chosen as the solvent for washing the 3D-printed HTC materials.

Capacity of 3D-Printed Structures

The capacity measurements of the materials after printing and post-processing at relevant temperature and pressure (400°C and 20 bar(a)) give no indication of reduced capacity due to the printing process compared to the reference materials (Pural KMG30 pellets), as can be seen in Figure 6. Neither the slurry that was used nor the sintering temperature seems to have an effect on the capacity. In addition, the bulk density of the structured materials is in the same range or higher compared to the packed bed (Table 1), thus the capacity per volume is also not reduced and productivity can theoretically be increased by increasing the flow rate.

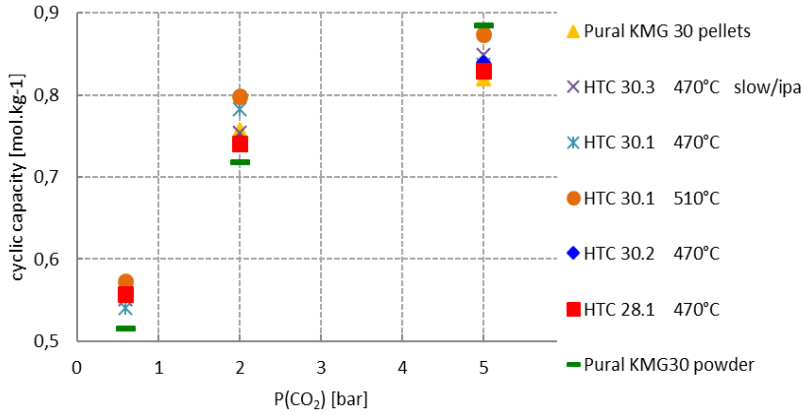

Figure 6. Capacity of printed structures compared to reference pellets or powder at 400°C and 20 bar(a).

Effect of Structuring on Pressure Drop and Other Productivity-Related Parameters

As expected, the pressure drop for flow through monoliths is lower than in a similar column filled with pellets. In columns packed with pellets, the flow tends to be turbulent, as the fluid must flow around each pellet structure. In monoliths the gas flow tends to be laminar, as the fluid moves straight through the channels. This is illustrated by the fact that the monolith Δp was too low to measure for the set-up at TNO. For flows up to 20 L/min (~3 m/s), the observed pressure drop remained below 0.01 bar for samples of ~ 2 cm in length. The measurements at Sintef (Figure 7) confirm the low pressure drop over the monoliths. As expected, the size of the channels has a significant effect on the pressure drop.

Preliminary experiments were done to study the effect of HTC structuring on the adsorbent productivity at ambient pressure. Adsorption/desorption trials compared the *Monolith 6* and

isoreticular foam with pellets of various sizes. These early results indicate better mass transfer and potentially more efficient regeneration for the 3D-structured materials compared to the packed bed, showing a steeper normalized breakthrough curve. These comparisons need replication at higher pressure to be conclusive. After cyclic tests (225 cycles) were performed, the monolith structures were

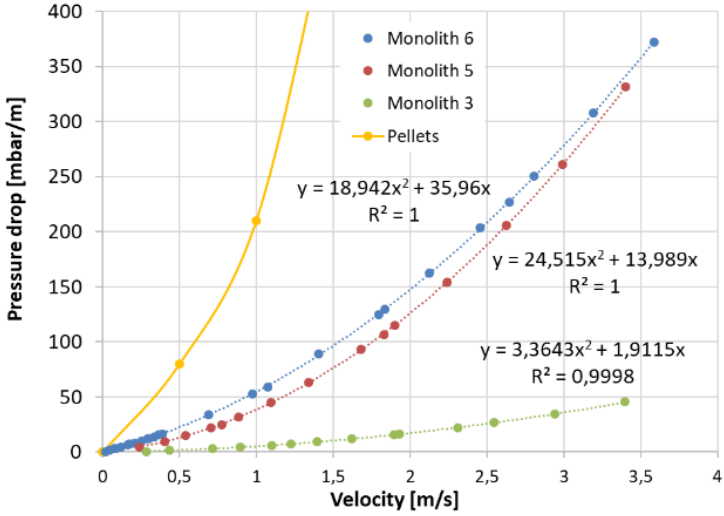

Figure 7. Pressure drop as a function of gas velocity in selected 3D-printed "green" HTC monoliths with various channel sizes and pellets.

still intact, and no significant capacity change was observed during the measurements. The foam structure, on the other hand, could not be recovered intact from the reactor. This reinforces the need for improved understanding of 3D-printing and post-processing procedures for K-HTC materials.

CONCLUSIONS AND RECOMMENDATIONS

Several structured hydrotalcite sorbents in the form of monoliths and foam structures have been prepared by 3D-printing using DLP for the first time. The foam structures cannot be prepared by traditional manufacturing methods (e.g., extrusion). The slurry and post-processing recipes need adjustment to improve reproducibility and the quality of the structured sorbents (strength and cracking), especially for larger scale fabrication. Research into the further development of the printing procedure continues, including testing the effect of adding binder to the slurry. Importantly, the printing and post-processing methods developed for the preparation of 3D-structured K-HTC sorbents do not affect the CO_2 capture capacity of the material at the relevant SEWGS conditions.

Preliminary testing on the effect of structuring the materials on the SEWGS process was performed. As expected, the pressure drop over the monoliths is significantly lower than over a packed bed. The effect of structuring of the materials on axial dispersion and mass transfer needs to be further investigated. Overall, the combined results in the preparation of 3D-printed K-HTC and modelling of structured SEWGS (Chapter 4) indicate that a marked productivity increase is possible by structuring. Compared to a conventional packed bed, the structured adsorbents maintain a steep (or sharp)

breakthrough curve at higher flowrates and achieve more efficient regeneration in combination with low pressure drop. Research continues to further quantify and optimize these benefits, validate modelling assumptions, prove the technology on larger scale and improve the understanding of the effect of structuring on the productivity.

ACKNOWLEDGEMENTS

The ACT 3D-CAPS project # 271503 has received funding from RVO (NL), RCN (NO), UEFISCDI (RO), and is co-funded by the CO_2 Capture Project (CCP) and the European Commission under the Horizon 2020 programme ACT, Grant Agreement No 691712.

REFERENCES

1. Boon J.; Cobden P. D.; van Dijk H. A. J.; Hoogland C.; van Selow E. R.; van Sint Annaland M., Isotherm Model for High-Temperature, High-Pressure Adsorption of CO_2 and H_2O on K-Promoted Hydrotalcite. *Chem. Eng. J.* (2014) **248**, 406–414. https://doi.org/10.1016/J.CEJ.2014.03.056.
2. Chen Z.; Li Z.; Li J.; Liu C.; Lao C.; Fu Y.; Liu C.; Li Y.; Wang P.; He Y., 3D Printing of Ceramics: A Review. *J. Eur. Ceram. Soc*. (2019) **39** (4), 661–687. https://doi.org/10.1016/j.jeurceramsoc.2018.11.013.
3. Parra-Cabrera C.; Achille C.; Kuhn S.; Ameloot R., 3D Printing in Chemical Engineering and Catalytic Technology: Structured Catalysts, Mixers and Reactors. *Chem. Soc. Rev.* (2018) **47** (1), 209–230. https://doi.org/10.1039/C7CS00631D.
4. Sireesha M.; Lee J.; Kranthi Kiran A. S.; Babu V. J.; Kee B. B. T.; Ramakrishna S. A Review on Additive Manufacturing and Its Way into the Oil and Gas Industry. *RSC Adv.* (2018) **8** (40), 22460–22468. https://doi.org/10.1039/C8RA03194K.
5. Dijk, van; Coenen K.; Gallucci F.; Cobden P.; van Dijk E.; Hensen E.; van Sint Annaland M. Influence of Material Composition on the CO_2 and H_2O Adsorption Capacities and Kinetics of Potassium-Promoted Sorbents Citation for Published Version (APA): Influence of Material Composition on the CO_2 and H_2O Adsorption Capacities and Kinetics of Potassium-Promoted Sorbents. *Chem. Eng. J.* (2017) **334**, 2115–2123. https://doi.org/10.1016/j.cej.2017.11.161.
6. Bastos Rebelo N. F.; Andreassen K. A.; Suarez Ríos L. I.; Piquero Camblor J. C.; Zander H. J.; Grande C. A. Pressure Drop and Heat Transfer Properties of Cubic Iso-Reticular Foams. *Chem. Eng. Process. - Process Intensif.* (2018) **127**, 36–42. https://doi.org/10.1016/j.cep.2018.03.008.

Carbon Dioxide Capture for Storage in Deep Geological Formations, Volume 5
Karl F. Gerdes (Editor)
© 2022 BP. All rights reserved.

Chapter 4

STRUCTURED SORBENTS FOR CO_2 CAPTURE FROM HYDROGEN PLANTS: MODELLING AND TECHNO-ECONOMIC ANALYSIS

Jebin James[1] and Ibrahim Ali[2]
[1]TNO, Westerduinweg 3, 1755 LE Petten, The Netherlands
[2]BP International Ltd, ICBT Chertsey Road, Sunbury-on-Thames, Middlesex, TW16 7LN, UK

ABSTRACT: The multi-column model developed by TNO for a Sorption-Enhanced Water Gas Shift (SEWGS) process has been adapted to describe a structured adsorbent. The modified model has adopted the linear driving force approximation for intraparticle mass transfer resistance and includes an axial dispersion coefficient and a pressure drop term. The structured bed is assumed to be entirely made up of potassium-promoted hydrotalcite (K-HTC) material. The monolith has a large number of channels with hexagonal cross section. The 3D-SEWGS system consists of 6 or 8 columns with structured adsorbent, depending on the gas flowrate, and the process cycle includes a co-current rinse and two pressure equalization steps. The optimum process parameters to achieve the highest productivity of 10 mols/(kg·hr) for a design with 6 columns were $(Steam/Carbon)_{rinse}$ =0.1 mole/mole and $(Steam/Carbon)_{purge}$ =1.25 mole/mole, while meeting a CO_x (CO and CO_2) capture rate target of 85 mol% on a dry basis and a CO_2 purity target of 95 mol% on a dry basis. This CO_X removal rate at the 3D-SEWGS operation corresponds to an overall CO_2 avoided of 60% for the full system. A preliminary technoeconomic evaluation carried out on the capture process has shown that it is competitive with aMDEA for CO_2 capture from a hydrogen plant, with a potential to achieve about 15% saving in the cost of CO_2 avoided.

KEYWORDS: hydrogen plant, CO_2 capture, pre-combustion, 3D-CAPS, structured sorbent, steam methane reforming, SMR, avoided cost

INTRODUCTION

The “Three-Dimensional Printed Capture Materials for Productivity Step-Change” (3D-CAPS) project aims to achieve a productivity increase of an order of magnitude in two sorbent-based technologies for carbon capture (Figure 1). It is envisaged that this will lead to substantial decrease in overall equipment size and costs. The two types of sorbent material explored are hydrotalcites (HTC) for CO_2 capture under high temperature and high pressure conditions and amine functionalised silica-supported sorbents for post-combustion capture conditions of low pressure and mildly elevated temperatures. This chapter covers the techno-economic assessment of structured hydrotalcites, while the experimental results are covered in Chapter 3. The assessment of amine-functionalised silica-supported sorbents is covered in Chapter 14.

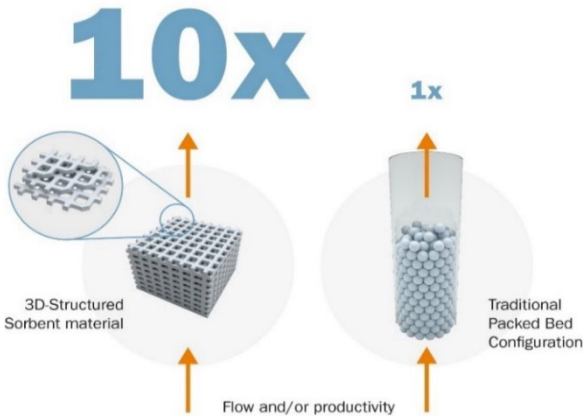

Figure 1. Representation of step change targeted with 3D-CAPS.

Steam Methane Reforming

Around 90% of hydrogen produced globally is from fossil fuels and a large part of that is through steam methane reforming [1]. A simplified overview of the process is shown in Figure 2. Natural gas is used as feedstock and fuel in the process. Natural gas that is used as feedstock is first treated to remove any sulphur species, as these are poisonous to downstream catalysts. The purified feed is mixed with steam and fed to a pre-reformer, where heavier hydrocarbons are converted to CH_4 and other co-products. Next, the products from the pre-reformer are mixed with some more steam and fed to the reformer, where most of the CH_4 is converted to an equilibrium mixture of H_2, CO, CO_2, CH_4 and H_2O. After heat recovery, the product stream is sent to a catalytic High Temperature Shift (HT-Shift) reactor where CO is reacted with H_2O to produce CO_2 and H_2. This reaction is equilibrium limited and residual amounts of CO remain. The products of the HT-Shift reactor are cooled to recover heat and then sent to a Pressure Swing Adsorption (PSA) unit. The PSA unit recovers between 85% - 90% of the H_2 and produces a H_2 product with a purity of > 99.9%. The PSA also produces a tail gas that is used as fuel in the reformer. The heat required for the endothermic reforming reaction is supplied by combustion of natural gas and PSA tail gas. The combustion results in production of more heat than required by the plant. After heat integration, excess heat is exported in the form of high-pressure saturated steam at about 40 bara. This steam is used to generate electricity to meet system demands and for export to other process units, typically.

The flow sheet for a typical SMR plant (Figure 2) has several locations where CO_2 capture can be implemented. They are after the HT-Shift Reactor, on the PSA tail gas, and on the flue gas exiting the reformer furnace. A detailed study has been performed for each option, including some variations and these are reported in [1]. The Sorption-Enhanced Water Gas Shift (SEWGS) system can be placed either at the exit of the HT-Shift or on the tail gas exiting from the PSA. The latter option would require compression and steam addition. The former option is already at an elevated temperature and pressure, suitable for SEWGS.

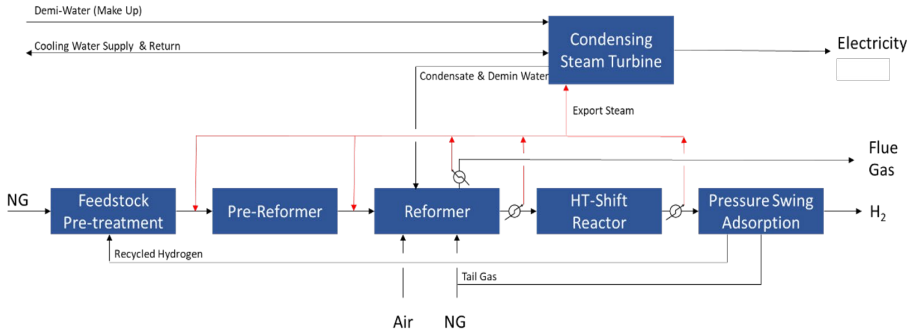

Figure 2. Hydrogen production from natural gas using steam methane reforming [1].

Sorption Enhanced Water Gas Shift (SEWGS)

The goal of the WGS step downstream of the reforming furnace is to maximize conversion of CO to CO_2 and H_2. The WGS reaction is shown by equation 1:

$$CO + H_2O \leftrightarrow CO_2 + H_2 \quad (1)$$

Depending on the level of CO conversion required, multiple shift-reactors at different temperature levels are used. A common arrangement uses a high-temperature shift (HTS), followed by cooling and water removal and then a low-temperature shift (LTS). This is followed by cooling and removal of the CO_2 using absorption with a suitable solvent.

In the Sorption Enhanced Water Gas Shift (SEWGS) concept, the LTS is integrated with a capture unit and the process occurs at pressure between 10-40 bara and temperatures between 300 and 500°C [2]. The number of process steps is reduced, as shown in Figure 3. Note however that the conventional

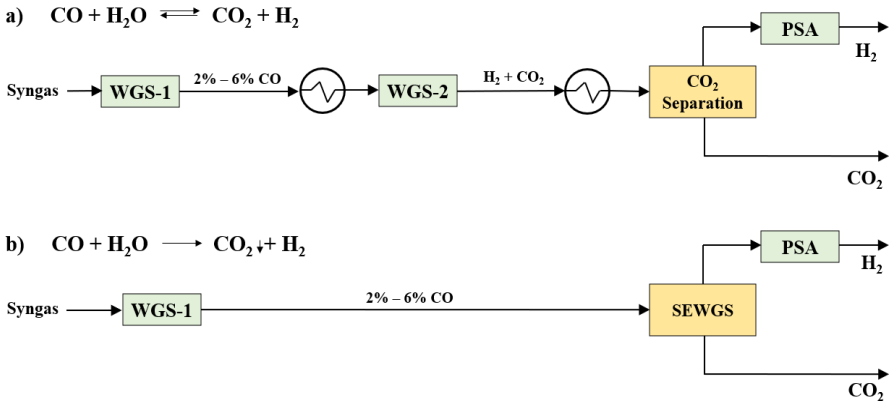

Figure 3. Process for hydrogen production based on: a) conventional WGS ; b) SEWGS.

process (HTS-LTS-PSA) produces very pure hydrogen while the SEWGS process may need an additional H_2 purification step, depending on the H_2 use.

The SEWSG process functions by using a CO_2 adsorbent that is catalytically active for WGS reaction. A frequently studied material with these properties is potassium promoted hydrotalcite [3]. Due to the finite capacity of the sorbent for CO_2, multiple parallel columns are required, such that when one column is saturated and enters regeneration, another column can be used for adsorption. For efficient CO conversion and CO_2 separation, the process cycle includes multiple steps shown in Figure 4. The steps for the cycle studied here are adsorption, rinse, pressure equalization (decreasing pressure), blowdown, purge, pressure equalization (increasing pressure) and repressurisation.

During adsorption, feed gas enters the adsorption column at the top. The CO in the gas is converted to CO_2 and H_2, while CO_2 is adsorbed. This simultaneous conversion and adsorption lead to a higher CO conversion than achievable using just an LTS catalyst, due to removal of one of the reaction products. Next, a high pressure co-current rinse is performed, in which part of the unconverted syngas in the column is replaced by H_2O. The use of a rinse originates from PSA cycle design and is known to improve the CO_2 purity. After the rinse step, several pressure equalization steps are carried out, in which a high-pressure column is connected to a lower pressure column, to exchange gas from columns at higher pressure to columns in a lower pressure part of the cycle. This serves to reduce the amount of gas fed to the column for repressurisation and, therefore, the compression energy required. During the pressure equalization, CO_2 that is released largely readsorbs further downstream in the column rather than transferring to another column. This serves to maintain a high carbon capture ratio during the next cycle. Additionally, the rinse gas is expanded, which prevents residual syngas from contaminating the CO_2 product by sweeping it to another column about to undergo the conversion and adsorption step. During the blowdown step, relatively pure CO_2 product is collected. To further desorb CO_2, a low-pressure counter-current purge step follows. The purge steam effectively functions to sweep the top part of the column of residual CO_2, which reduces the CO_2 slip to the H_2 product stream and maintains a high capture ratio.

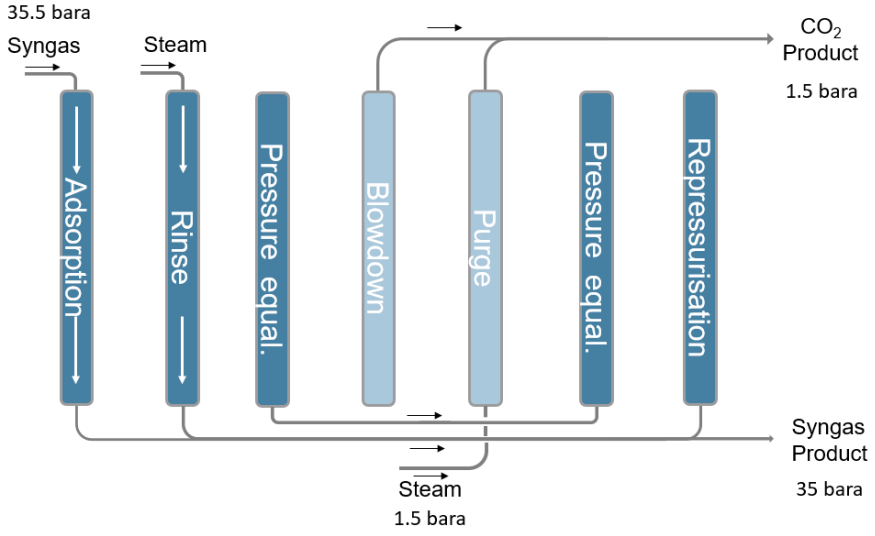

Figure 4. Steps of a SEWGS cycle with co-current steam rinse.

This multi-step batch process is transformed into a quasi-continuous process by using multiple columns which are operated in cycles resembling those of a pressure swing adsorption process, allowing the constant production of separate H_2-rich and CO_2-rich streams.

The focus of this work is to evaluate the performance of the SEWGS cycle using structured adsorbents. Key performance metrics are the Carbon Capture Ratio (CCR), CO_2 purity (CP) and Productivity, as defined in Table 1 by equations 2, 3 and 4. The evaluation is done based on the model developed by Boon *et al.* (2015) [2] for a packed bed. The model was modified to account for a structured adsorbent.

Table 1. Definition of Key Performance Indicators.

Carbon Capture Ratio	$\frac{\boldsymbol{CO_x\ in\ CO_2\ product}}{\boldsymbol{CO_x\ in\ feed}}$	(2)
CO_2 Purity	$\frac{\boldsymbol{CO_2\ in\ CO_2\ product}}{\boldsymbol{Total\ CO_2\ product - H_2O\ in\ CO_2\ product}}$	(3)
Productivity	$\frac{\boldsymbol{CO_2\ product\ flow\ \left(\frac{mol}{hr}\right)}}{\boldsymbol{Total\ sorbent\ mass\ (kg)}}$	(4)

MODELLING

Reactor Model

Modelling in this context refers to dynamic reactor modelling using mathematical equations and approximations. The column model is built up from a set of conservation equations comprising mass, momentum and energy balance equations along with appropriate rate descriptors. An adsorption process is an unsteady state process, and the model equations are a set of partial differential equations. The equations are simplified based on the following assumptions:

1. Axially dispersed plug flow model
2. Validity of ideal gas law
3. Absence of radial gradients
4. Uniformity of the ads orbent properties throughout the column
5. Instantaneous thermal equilibrium between gas and solid phases

Based on the above assumptions, for n components in the feed, there are n-1 component mass balance equations, 1 continuity or total mass balance equation, 1 energy balance, 1 momentum balance and n intraparticle mass transfer rate equations. The packed bed multicycle model for SEWGS process, developed by Boon *et al.* [2] is summarised in Table 2. Several phenomena are described differently for structured adsorbents compared than for a packed bed. Specifically, mass transfer, axial dispersion and pressure drop are affected because of the structured geometry. Therefore, the model is changed by modifying these three elements. The equations used for these adaptations are described in the sections below.

Table 2. Column model equations.

Continuity	$$\frac{\partial \rho}{\partial t} = -\frac{\partial \rho v}{\partial z} + \frac{1-\epsilon_b}{\epsilon_b} a_b \sum_i M_i N_i$$	(5)
Momentum	$$0 = -\frac{\partial p}{\partial z} - f\frac{|u|u}{d_p}$$	(6)
Heat balance	$$\left(\epsilon_b \rho C_p + (1-\epsilon_b)\rho_p C_{p,\mathrm{p}}\right)\frac{\partial T}{\partial t} = -\rho C_p u \frac{\partial T}{\partial z} + \frac{\partial}{\partial z}\left(\lambda \frac{\partial T}{\partial z}\right) + \frac{4U(T_w - T)}{d_c} - (1-\epsilon_b)\rho_p \left((-\Delta H_r) r_{WGS} + \sum_i \left(-\Delta H_{a,i} \frac{d\langle q_i \rangle}{dt} \right) \right)$$	(7)
Mass balance	$$\frac{\partial(\rho \omega_i)}{\partial t} = -\frac{\partial \rho v \omega_i}{\partial z} + \frac{\partial}{\partial z}\left(D_z \rho \frac{\partial \omega_i}{\partial z}\right) + \frac{1-\epsilon_b}{\epsilon_b} a_b M_i N_i$$	(8)
Intraparticle mass transfer	$$\frac{dq_i}{dt} = k_{LDF_i} \cdot \left(q_i^* - q_i\right)$$	(9)

Parametric Study

Cycle modelling of SEWGS is a complex undertaking given the large number of degrees of freedom in the design. The introduction of additional parameters to describe the geometry of the microstructure (i.e., 3D Printed structure) adds an additional complexity. Therefore, it is important to understand the influence of microstructure dimensions before embarking on a process cycle design. This can be done by performing a sensitivity study on the performance parameters known to be affected by geometry to identify optimum microstructure dimensions. The premise of the parametric study is that if the overall target is an order of magnitude increase in productivity, then these parameters must also improve by an order of magnitude.

First, it's important to understand the assumptions and definitions around productivity such that the correct parameters can be selected for study. Productivity is defined with units of mol of CO_2 captured per kg of sorbent per hour. It can also be expressed as shown in Equation 10, which is analogous to saying that the productivity is proportional to the working capacity (*WC*) over the cycle time (Equation 11). In other words, the productivity is proportional to how quickly the working capacity (WC) can be used.

$$Productivity = \frac{n_{CO_2}}{m_{ads}} \cdot \frac{1}{t_{cycle}} \tag{10}$$

$$Productivity \propto \frac{WC}{t_{cycle}} \tag{11}$$

Based on the isotherm provided in Boon *et al.* [3] the maximum working capacity under the conditions found in SEWGS can be estimated to be around 0.52 mol/kg. Therefore, following the previous assertion, if this working capacity can be accessed in one hour, the productivity will be 0.52 mol/kg/hr. if accessed in 1 minute, the productivity capacity will be 31 mol/kg/hr.

The working capacity will only be achieved if sufficient CO_2 is available for adsorption. Increased productivity requires two conditions: (1) fast loading and unloading of the material and (2) sufficient CO_2 available to be adsorbed and desorbed (i.e., high feed flow). Thus, an order of magnitude increase in productivity (e.g., going from 1 mol $CO_2/kg_{sorbent}/hr$ to 10 mol $CO_2/kg_{sorbent}/hr$) for the SEWGS system will require higher velocity than is achievable in a conventional adsorption bed. Higher velocities increase pressure drop and the length of the mass transfer zone (MTZ). For adsorption and regeneration, a lower pressure drop and a shorter MTZ are preferred. As the velocity increases, both the pressure drop and the length of the MTZ increase. The adsorbent productivity relationship in Equation 11, which incorporates the adsorbent's maximum working capacity, does not include the negative effects of pressure drop and mass transfer zone on the actual working capacity. A modification to this expression was proposed by Rezaei *et al.* [4] and is adopted for use within our modelling. The modification is shown in Equation 12 [5]. Here, the definition of productivity includes two functions, one relating to pressure drop and the other to mass transfer zone. Both the pressure drop and the MTZ functions will be related to the geometry of the structured adsorbent. Therefore, the productivity can be connected to geometric parameters. In this work we do not rigorously find the function f1 and f2 but use Equation 12 as a guide to understanding how productivity can be increased. We explore how pressure drop, mass transfer zone (resulting from mass transfer coefficient and dispersion) are influenced by geometry of a structured adsorbent.

$$Productivity = k\frac{WC - f_1(dP) - f_2(MTZ)}{t_{cycle}} \tag{12}$$

f_1 is a function of pressure drop. The relation of the pressure drop to velocity for a packed bed is represented by the well-known Ergun equation. An analogous expression for structured packing is suggested by Patton *et al.* [5].

f_2 is more complex due to the multiple phenomena that define the mass transfer zone. In principle, the mass transfer zone is influenced by the isotherm, the mass transfer mechanism and axial dispersion mechanism. Here we assume that the isotherm will be identical regardless of geometry and method of creating the geometry (i.e., 3D Printing), allowing us to focus only on mass transfer and axial dispersion.

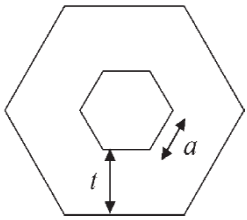

Figure 5. Hexagonal channel definition.

Mass Transfer

The mass transfer rate is modelled using a linear driving force (LDF) approximation and for a packed bed. The approximation consists of the LDF mass transfer coefficient multiplied by the driving force. The LDF mass transfer coefficient is often obtained experimentally but in some specific cases can also be derived with some simplifying assumptions (e.g., Boon *et al.* [3]). The theoretical derivation for the K_{LDF} includes a pre-factor (k) that is dependent upon geometry, porosity and intraparticle diffusivity. We assume for the sake of simplicity that the physical characteristics of the sorbent (porosity and intraparticle diffusivity) remain constant. Therefore, the only parameter that varies with geometry is *k,* the pre-factor to the K_{LDF}. The derivation of the pre-factor for spherical particles and monolith channels can be found in Patton *et al.* [5].

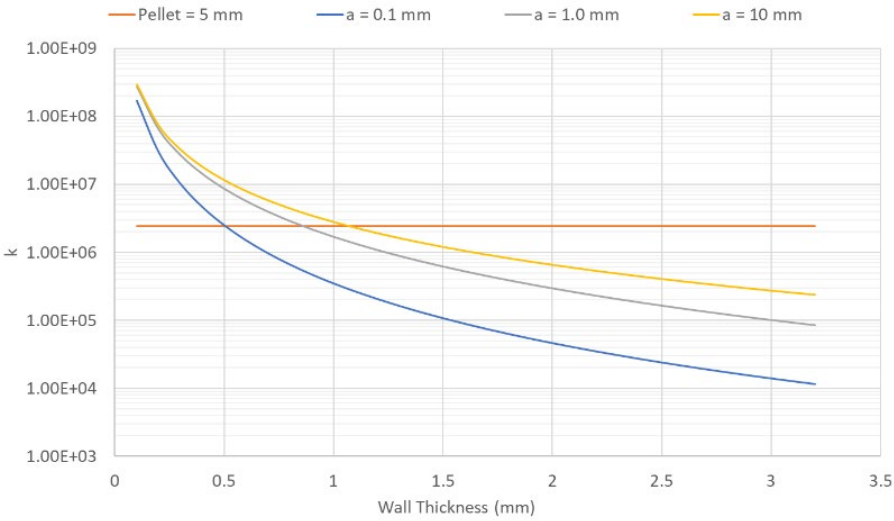

Figure 6. Effect of Monolith dimensions on K_{LDF} pre-factor (k) for a hexagonal channel.

It is possible to compare how these pre-factors vary for a hexagonal channel as a function of its dimension and compare it to that of a 5x5 mm pellet. The dimensions of the hexagonal channel are defined by the wall thickness (t) and circumradius (a), as shown in Figure 5. Figure 6 shows how the pre-factor varies with wall thickness and channel size (circumradius).

This analysis shows that to achieve an order of magnitude increase in *k*, the wall thickness should be maintained below 0.25 mm. The effect of circumradius in this region of wall thickness is limited.

Axial Dispersion Coefficient

The axial dispersion coefficient in a porous media can be represented by two terms – the first represents dispersion due to molecular diffusion (D_m) and the second represents the summation of effects due to turbulence, dead zones and other flow deviations [6]. A similar expression for a hexagonal channel can also be derived. It is important to note that the axial dispersion coefficient represents only a part of the overall dispersion seen at the outlet of the reactor, which results from the contributions of both the advective and the dispersive transport mechanisms.

The axial dispersion coefficient for a hexagonal monolith is shown by Equation 13. The coefficient is sensitive to hydraulic diameter(d_h) and fluid velocity. The velocity is determined by the monolith geometric parameters *t* and *a*, since they define the open area for a given column size and flow rate.

$$D_{ax} = D_m + (v_z^2 \cdot d_h^2)/(192 \cdot D_m) \quad (13)$$

However, instead of making this relation explicit, it is explored implicitly by looking at the relationship between axial dispersion, circumradius and velocity (as represented by Eq. 13). The results of varying velocity and the hydraulic diameter are shown in Figure 7. The molecular diffusion coefficient (D_m) used is 9.54 x 10^{-6} m^2s^{-1}.

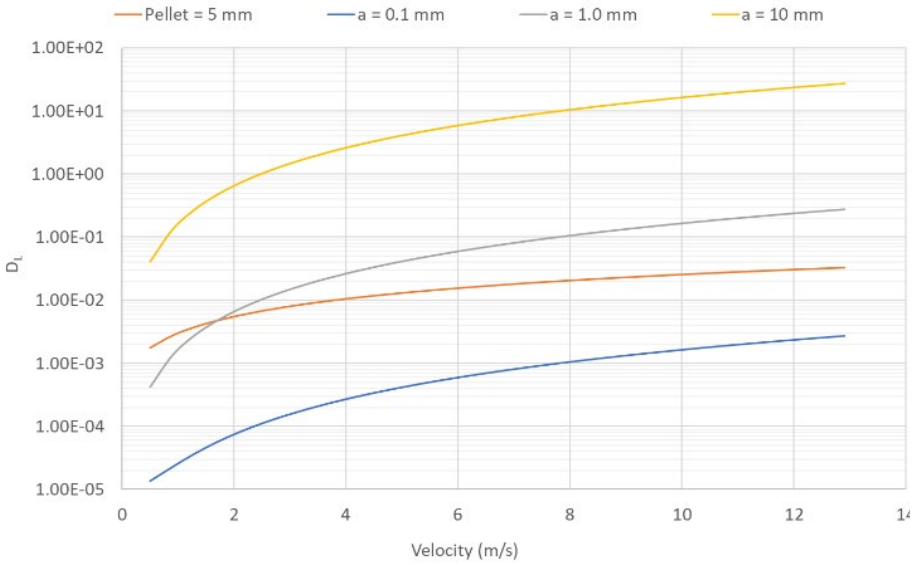

Figure 7. Effect of velocity and circumradius (a) on axial dispersion coefficient (D_L) for a hexagonal channel.

The modeling indicates that a smaller circumradius reduces the axial dispersion coefficient and that a lower velocity also reduces the coefficient. The influence of velocity on axial dispersion coefficient is limited compared to the effect of circumradius. These results indicate that a circumradius of 0.1 mm is the best choice to reduce the axial dispersion coefficient. Combining this with the result from K_{LDF} analysis, the ideal hexagonal channel dimensions would be a = 0.1 mm and t = 0.25 mm. However, these results neglect the effect of pressure drop.

Pressure Drop

The pressure drop correlation by Heck *et al.* [7] derived from the energy balance can be used to calculate the pressure drop across the monolith structure along its axial direction. The pressure drop equation for a monolith is shown below, in which f is fanning friction factor, Re is Reynolds number, Q is fluid volumetric flowrate (m^3/s), μ is the viscosity of the gas mixture, A_{ch} is channel cross-section area (m^2), g_c is the gravitational constant (=1) and d_h is hydraulic diameter.

$$\frac{\Delta P}{L} = \frac{2fReQ\mu}{A_c g_c d_h^2} \tag{14}$$

The pressure drop factors that are sensitive to structure geometry are hydraulic diameter (d_h) and interstitial velocity. Calculations of pressure drop with varying velocity for a hexagonal channel (a=0.5 mm and t=0.25 mm) and for pellets are shown in Figure 8. The graph also shows the value of the dispersion coefficient calculated for the same geometry and velocity (equation 13). The selected hexagon with a = 0.5 mm and t = 0.25 mm has a pressure drop lower than the packed bed and will also have lower axial dispersion if the velocity is maintained below 6 m/s.

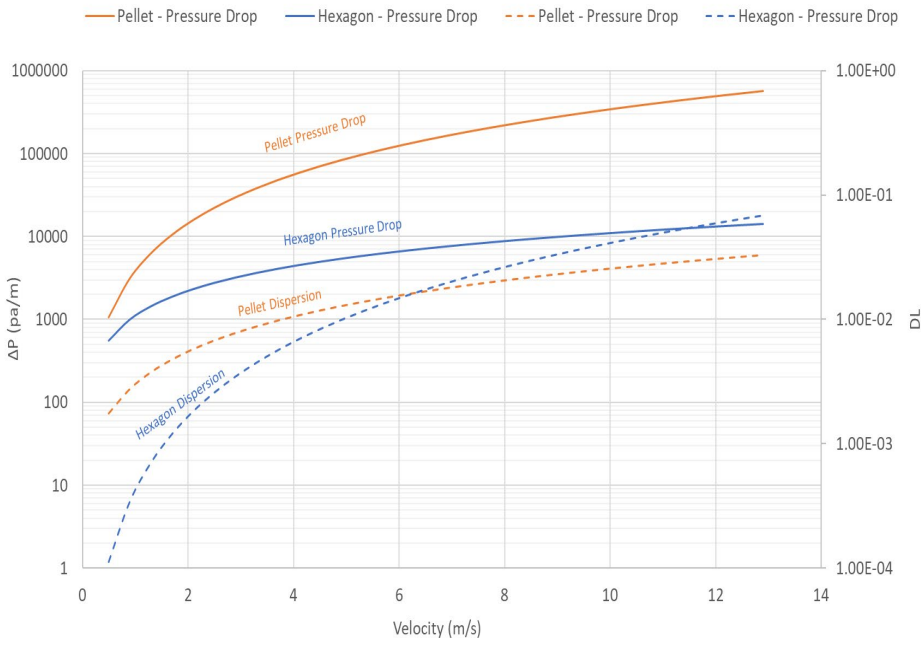

Figure 8. Pressure drop and Dispersion for pellets vs. monolith with hexagonal channels having dimensions a=0.5 mm and t=0.25 mm.

Velocity

For the packed bed, assuming flows corresponding to the SMR design basis of 101,000 Nm^3/h H_2, two column diameters (1.5 m and 3 m) were investigated. The interstitial velocity in the 1.5 m column (single train) is 7.12 m/s, while in a 3 m column the velocity is 1.78 m/s. Figure 9 shows how velocity changes at fixed flow rate as a function of wall thickness for the hexagonal channels in the 1.5 m diameter column (top) and the 3 m diameter column (bottom). In the structured bed, for a fixed feed rate the velocity varies with the wall thickness and the circumradius. As discussed previously, based on mass transfer and pressure drop, the most promising dimensions for the hexagonal channel are a circumradius of 0.5 mm and a wall thickness of 0.25 mm. For the 3 m monolith column, the velocity will be similar to that of the packed bed. Note that both the packed bed and the hexagonal channels have similar void fractions (38% for packed bed vs 44% for the hexagonal channels). The mass transfer, pressure drop and dispersion for the monolith will be orders of magnitude larger and the separation efficiency would improve compared to the packed bed, but the productivity will not see a large improvement. This is because no changes have resulted in faster access to the working capacity. As defined before, the productivity will increase if we can access the working capacity faster. To do this, the capture system must be operated at higher velocities. Maintaining the hexagonal channel dimensions, we can vary the velocity by varying the column diameter.

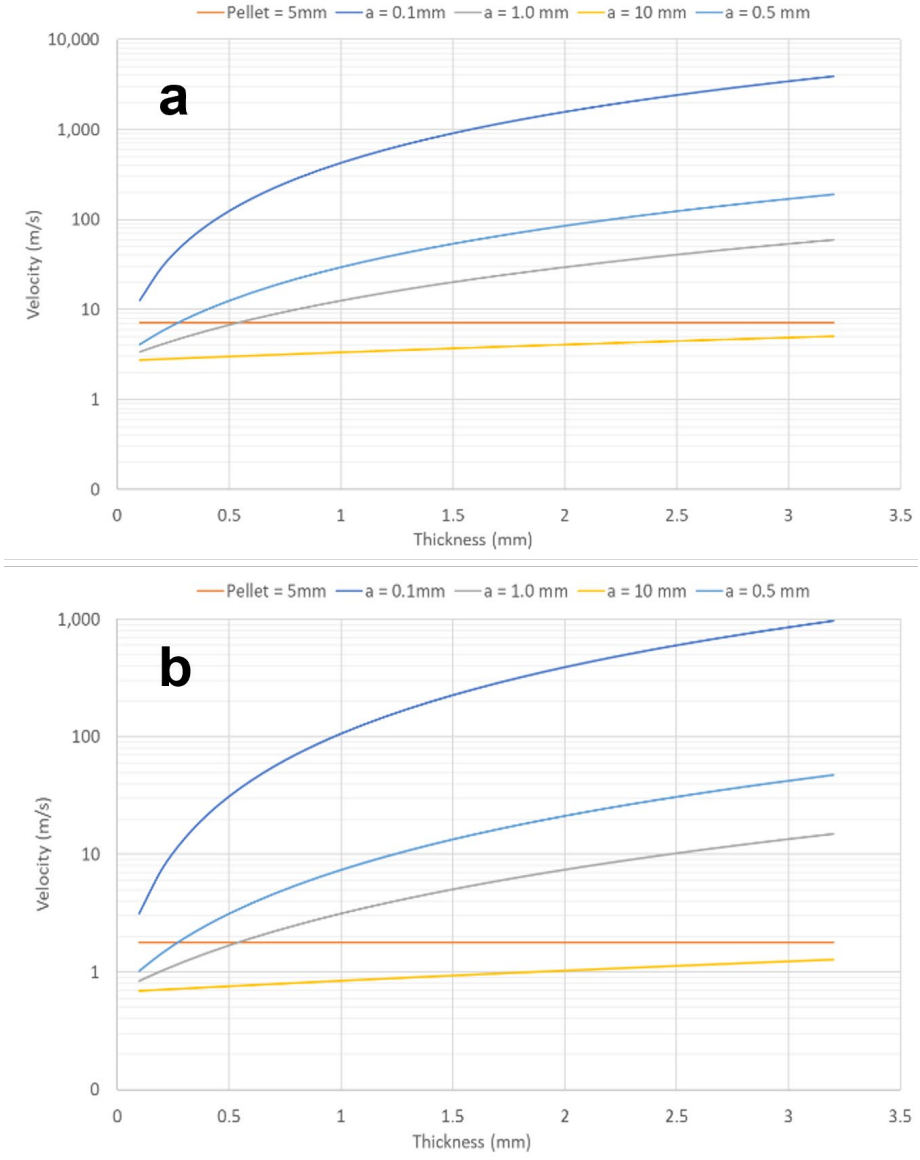

Figure 9. Velocity variation for a column of 1.5 m diameter (a) and 3 m diameter (b) with packed and structured bed.

More specifically when considering the 1.5 m column, having a = 0.5 mm and t = 0.25 mm will result in a velocity of 7.12 m/s. At this velocity, based on Figures 6 and 8, we can infer that the separation efficiency could be maintained due to the higher mass transfer and lower pressure drop even with the moderately worse dispersion characteristic. This would, in theory, result in a significantly higher productivity. To test this hypothesis, cycle modelling was carried out, as discussed in the following section.

Cycle Modelling

Modelling the SEWGS cycle involved a sensitivity study with respect to total flowrate (as a proxy for velocity), total cycle time, steam consumption (purge and rinse) and purge duration. However, for the sake of brevity, only the final result and some key observations are reported below. The final dimensions selected to achieve the high productivity of 10 mol/kg/s based on modelling are shown in Table 3. The cycle chosen for study employs two pressure equalization (PEQ) steps with product repressurisation. The total cycle time is 120 s. This system achieved a CO_2 purity of 95.1 mol% on a dry basis with a carbon capture rate of 84%.

For this study, the process cycle and reactor sizing were optimised for productivity. The cost of this is reflected by the high steam consumption with a molar ratio of Steam/Carbon Fed (S/C) of 1.35 It is possible to optimise towards a lower productivity and decrease the steam consumption. This has not been considered in the current scope of the study. The overall carbon capture rate achieved is 84% with respect to the CO_2 and CO entering the SEWGS system. For shorter cycle times, the slip of CO increases as the kinetics of the WGS reaction becomes limiting. This causes the overall capture rate to decrease, even if there is no slip of CO_2. This indicates that to achieve a high CCR at higher productivities, the kinetics of WGS reaction must be further explored. Finally, an interesting observation regarding the cycle design is the ratio of purge time to adsorption time. A sensitivity study performed at decreasing the purge time, indicated that a faster regeneration did not negatively affect the carbon capture rate. In a traditional packed bed system, reducing the purge time at high purge ratios leads to a much higher pressure drop, which results in poor regeneration of the sorbent. In a structured bed, this limitation is overcome.

Table 3. Process Parameters for Modelling (Plant Scale: 101,000 Nm^3/h H_2).

		Reactor specifications		Mass flow	Number of columns	S/C rinse	S/C purge
		Height	**Diameter**				
Structured bed		10 m	1.5 m	30 kg/s	6	0.1	1.25
Hexagon:	a = 0.5 mm						
	t = 0.25 mm						

SYSTEM ANALYSIS

Heat Integration & Electricity Balance

The integration of the 3D-SEWGS unit into the SMR flowsheet requires the balancing of heat demands across the plant and the capture unit. In the reference system, excess heat is used for electricity generation and therefore, the integration will need to evaluate heat and electricity balance in tandem. The integrated process is shown in Figure 10.

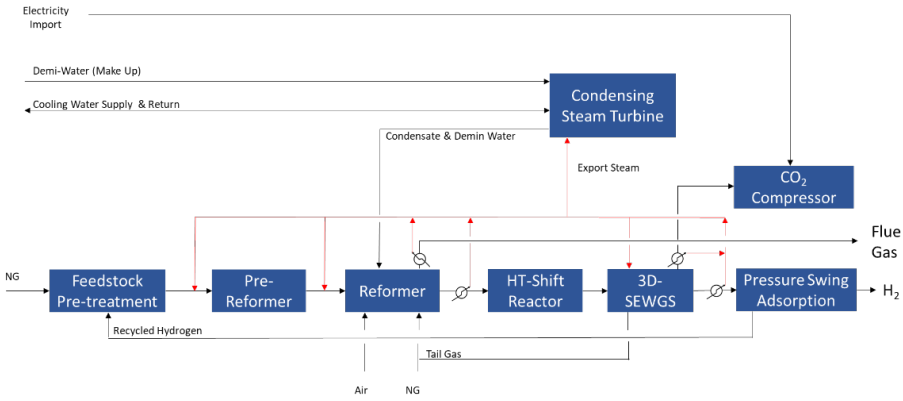

Figure 10. Hydrogen production with carbon capture from natural gas using steam methane reforming.

The 3D-SEWGS feed stream from the HT-WGS enters at 412°C. The two product streams are hydrogen-rich and CO_2-rich streams at 466°C and 382°C, respectively. In addition, steam at 420°C is required for rinse and purge steps for the process to achieve the desired purity and capture rate (CO_2 and CO capture rate of 84% and target CO_2 purity = 95 mol% on a dry basis). The steam is raised internally from Boiler Feed Water (BFW) at 25°C. The grand composite curves (GCCs) resulting from the combination of the temperature-enthalpy curves for the 5 aforementioned streams are shown in Figure 11 (Top). From the GCC, it is evident that the heat demand for heating up the cold streams is fully satisfied by extracting heat from the hot streams. Some additional cooling at about 125°C is required. If this integration is used with respect to the full system, there will be an overall heat deficit, because parts of the front-end system in the original integration used heat extracted by cooling the outlet of the HT-Shift to the required temperature for PSA. Therefore, the heat demand equivalent to this must also be satisfied. This is achieved by adding the temperature-enthalpy curve of the HT-Shift outlet as an additional hot stream that requires cooling. The result of including this is shown in Figure 11 (Bottom). Now, it becomes evident that when the additional heat demand is taken into account, there is a heat deficit. This additional heat required is satisfied using some of the high-pressure steam, resulting in a lower export of high-pressure steam.

The electricity demand of the SMR plant with 3D-SEWGS is shown in Table 4. The H_2 Plant demand and auxiliary cogeneration demands are taken from the reference case [1]. The CO_2 capture plant does not have any major electricity demand, unlike the MDEA system, which requires large recirculation pumps. The CO_2 compression (to 110 bar) and drying electricity demand has been scaled linearly from the reference case with respect to the volumetric flow of CO_2.

The original system without capture generates 11.5 MW of electricity from the high-pressure steam export. However, in the 3D-SEWGS capture case, 68.9% of the steam is consumed internally, leaving enough steam to generate 3.58 MW of electricity. When combined with the total electricity demand, we note that 1.52 MW of electricity import is required. This is shown in Table 5.

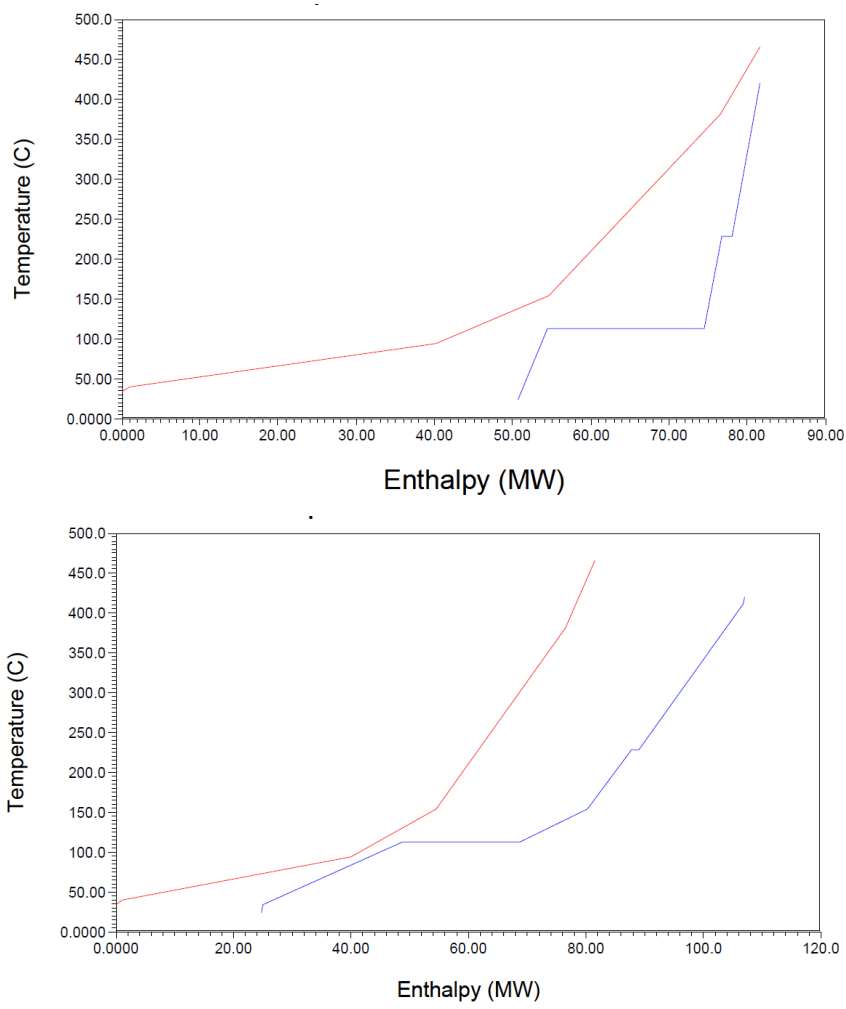

Figure 11. Grand Compositive Curve of SEWGS only (Top) and integrated system (Bottom).

Table 4. Breakdown of Electricity Demand for SMR with SEWGS.

Electricity Demand		
H_2 Plant Demand	-1.26	MWe
COGEN Aux.	-0.38	MWe
CO_2 Capture Plant	0	MWe
CO_2 Compression & Drying	-3.47	MWe
Total Demand	-5.10	MWe

Table 5. Electricity Balance.

Electricity Generation	3.58	MWe
Electricity Demand	-5.10	MWe
Electricity Balance	-1.52	MWe

TECHNOECONOMIC EVALUATION

A preliminary technoeconomic evaluation was conducted on the 3D-SEWGS process based on the block flow diagrams and the mass and energy balances from the process modelling presented in the previous section. For comparison, CO_2 capture from hydrogen production using activated MDEA (aMDEA) on the shifted syngas is the base case. This provides a direct comparison of the SEWGS process with the more mature aMDEA. Both scenarios do not include CO_2 capture from the SMR furnace flue gas. The base aMDEA case information is from IEAGHG Case 1A [1]. The reference process is the steam methane reformer (SMR) without capture and is documented in the same report.

A summary of the main process parameters comparing the reference case, the base case and the 3D-CAPS SEWGS process is presented in Table 6. The SMR with SEWGS produces slightly more hydrogen (about 1%) than the reference SMR without capture and the base case from the same natural gas feed rate to the reformer. This is due to the extra water-gas shift reaction that takes place in the SEWGS reactors relative to the conventional WGS steps. This also leads to more CO_2 being captured than the base case. Due to the lower electricity generation and the higher parasitic load of the 3D-CAPS SEWGS process, the plant requires a net electricity import (the SEWGS process has an electricity penalty of 0.83 GJ_e/tonne CO_2 vs 0.70 GJ_e/tonne CO_2 for the aMDEA process). The carbon intensity of the imported power is accounted for in the calculation of the cost of CO_2 avoided.

Table 6. A summary of the main parameters comparing the reference case, base case and the 3D-CAPS SEWGS process.

		Reference (no capture)	Base case (capture with aMDEA)	Capture with 3D-CAPS SEWGS
Natural gas (feedstock)	tonnes/h	26.2	26.3	26.2
Natural gas (fuel)	tonnes/h	4.3	5.3	5.1
Natural gas (total)	tonnes/h	30.6	31.6	31.3
H_2 production	**Nm^3/h**	**100,000**	**100,000**	**101,122**
Gross power (cogen)	MW_e	11.5	6.7	3.6
Parasitic power load	MW_e	-1.6	-5.2	-5.1
Net power export	**MW_e**	**9.9**	**1.5**	**-1.5**
CO_2 emissions	**Million tonnes/year**	**0.67**	**0.31**	**0.26**
CO_2 avoidance	**%**	**0%**	**54%**	**60%**
Electricity penalty due to capture	**GJ_e/tonne CO_2**	NA	0.70	0.83

Cost Estimation

The main equipment items of the SEWGS process were sized based on the process mass and energy balances generated in the previous section. The equipment list is the basis for a preliminary cost estimate for the process. A key factor for the cost SEWGS estimates the rather high design temperatures, compared to the MDEA-based process, required for the adsorption towers. This can limit the choice of the material of construction for the towers.

Table 7 presents a cost estimate of the major equipment items in the 3D-CAPS SEWGS process and the aMDEA process. The total direct material cost includes the equipment cost, the bulk items cost

Table 7. Estimated major equipment cost of 3D-CAPS SEWGS process and base-case aMDEA (Million €, 2014 Basis, escalated to 2020 using CEPCI).

	aMDEA	3D-CAPS SEWGS
Major equipment cost	6.2	4.7
Bulk items cost	2.9	3.1
Freight cost	0.5	0.5
Total direct material cost (2014 basis)	**9.6**	**8.3**
Total direct material cost (2020)	**10.0**	**8.5**

and the freight cost. Bulk items include steel structures, piping materials, instrument and control systems and electricals. Note that the original cost estimates were based on 2014 data. The costs were escalated to 2020 based on the Chemical Engineering Plant Cost Index (CEPCI–2014: 576.1 and 2020: 596.2).

As shown in Table 7, the total direct material cost for the 3D-CAPS SEWGS process is about 15% lower than that of the aMDEA process. This is due to a lower cost for the major equipment items for the SEWGS. Although the SEWGS process has a larger number of vessels (7 adsorption towers) than the aMDEA (a single absorber and a stripper) and the vessels have higher design temperatures and pressures, the diameters are considerably smaller, and no large pumps are required for the process. These details contribute to a lower overall cost for the major equipment items in the 3D-CAPS SEWGS process. It should be noted that the SEWGS capital costs are very preliminary with several assumptions. They are therefore subject to higher uncertainties than for the aMDEA case, which is a commercial technology.

A breakdown of the major cost components that comprise the total plant cost for all the sections of the hydrogen plant and the 3D-CAPS CO_2 capture process is given in Table 8. The total plant cost (TPC) for the CO_2 capture process is small compared to the total cost for the whole complex (only about 9% of the total), and it is similar to the cost of the CO_2 compression.

Table 8. Cost Built-up for SMR hydrogen plant with 3D-CAPS SEWGS CO_2 capture process (Million €, 2014 basis, escalated to 2020 in the economic analyses using CEPCI).

	H_2 plant	**CO_2 Capture**	**CO_2 Compression**	**Power Island**	**Utilities and Balance of Plant**	**Total**
Direct material (D)	40.7	8.3	8.6	2.2	19.3	82.4
Construction (C)	25.7	5.0	4.3	1.4	18.2	56.8
Direct field cost (DFC = D+C)	66.4	13.2	12.9	3.7	37.5	133.7
Other costs (O)	1.9	0.4	0.3	0.1	1.3	4.0
EPC services (E)	12.8	2.2	2.0	0.5	6.6	24.1
Total installed cost (TIC = DFC+O+E)	81.0	15.8	15.3	4.3	45.4	161.8
Project contingency (PC)	16.2	3.2	3.1	0.9	9.1	32.4
Total plant cost (TPC = TIC + PC) [2014 basis]	**97.2**	**18.9**	**18.3**	**5.2**	**54.5**	**194.1**
TPC (2020 basis)	**100.6**	**19.6**	**18.9**	**5.4**	**56.4**	**200.8**

Techno-economic Evaluations

The cost estimates and the mass and energy balances presented in the previous sections were used to estimate the levelized cost of hydrogen production (LCOH) for the processes with and without CO_2 capture. A summary of the main assumptions used in the discounted cash flow (DCF) model for

determining the LCOH is in Table 9. These assumptions are the same as those used in the IEAGHG 2017 report on SMR with CO_2 capture [1] to enable a consistent comparison.

Table 9. Techno-economic assumptions for discounted cash flow (DCF) model.

OPEX	Fixed O&M	No. of personnel (base case)	**38**	
		Extra staff (CO_2 capture)	**5**	
		Operator salary	**60000**	€/yr
		Indirect labour cost	**30%**	of direct & maintenance labour
		Maintenance materials	**0.9%**	of total plant cost (TPC)/yr
		Maintenance labour	**0.6%**	
		Insurance	**0.5%**	
		Local taxes and fees	**0.5%**	
	Variable O&M	Chemicals and Catalysts	**0.4**	€ million/yr
	Fuel cost		**6.0**	€/GJ
			6.3	€/MMBTU
	Electricity price		**80.0**	€/MWh
	Operating hours (95% operating factor)		**8328**	hours/yr
Other Costs	Transport and storage costs		**10**	€/t_{CO2}
	CO_2 emissions tax		**0**	€/t_{CO2}
FINANCIALS	Inflation rate		**0.0%**	%
	Discount rate		**8%**	%
	Time horizon (from start of operations)		**25**	Years
	CAPEX basis year		**2014**	
	CAPEX escalation		**2020**	

The LCOH and cost of CO_2 avoided for both the SEWGS and aMDEA capture processes are presented in Table 10. The two capture processes yield very similar LCOH. The lower capital cost and the slightly higher hydrogen production of SEG+WGS capture are partly offset by the higher energy requirement. However, an advantage of the SEWGS process appears to be the higher CO_2 avoidance rate (60% vs 54% for the aMDEA process). This is reflected in the cost of CO_2 avoided (CCA) of the SEWGS process, which is around 14% lower than that of aMDEA. It should be noted that it may not be possible to substantially lower the CCA because the capital cost of the CO_2 capture section is only a small fraction of the total capital cost of the whole hydrogen production plant. This means that the ability to influence the CCA through cost reduction in the SEWGS process is limited. A major area of uncertainty in the current analysis is the cost of the 3D-printed structures for the 3D-CAPS SEWGS process.

Table 10. Levelised cost of hydrogen (LCOH) and CO_2 avoided cost for the 3D-CAPS SEWGS process compared with the reference and base cases (aMDEA)[1] [costs escalated to 2020 basis].

		Reference Case (No capture)	Base Case (aMDEA)	3D-CAPS SEWGS
CAPEX (Total Plant Cost: CO_2 Capture)	€million	-	22.8	19.6
CAPEX (Total Plant Cost: Whole Complex)	€million	176.9	208.8	200.9
CAPEX (Total Capital Requirement)	€million	230.7	273.1	262.7
Levelised Cost of Hydrogen (LCOH)	**€/Nm^3**	**0.1154**	**0.1363**	**0.1356**
Cost of CO_2 Avoided	**€/tonne**	**-**	**47.6**	**41.0**
SEWGS Cost of CO_2 Avoided vs aMDEA			-	86.2%

For this study, the cost of the structured adsorbent was assumed to be no more than the cost of the amines for the aMDEA process. A sensitivity analysis carried out by increasing the structured sorbent cost by 100% (i.e., 2x its initial value) increases the cost of CO_2 avoided for the SEWGS process from €41.0/tonne to €42.0/tonne.

CONCLUSIONS AND RECOMMENDATIONS

The following conclusions may be drawn from the modelling of the 3D-SEWGS Process:

- A process intensified SEWGS system using a monolith absorbent has potential to achieve a productivity of 10 mol/kg/hr. To achieve this performance increase, understanding and selecting the correct microstructure for the intensified system is critical.
- In a 3D-SEWGS system operating at high throughput, the limiting factor in achieving high rates of carbon capture shifts from limiting the slip of CO_2 to ensuring effective conversion of CO.

Future work should aim at validating the performance predicted by the simplified models. Further study is needed to limit the slip of CO in high throughput systems.

The preliminary techno-economic evaluation of the 3D-SEWGS process showed:

- In this study, the configuration of the 3D-SEWGS process was optimized to achieve high productivity. Logically, this should lead to lower CAPEX due to a more compact process. However, this approach significantly reduces steam export (and electricity production), and the process becomes a net electricity consumer (compared to the aMDEA process which exports electricity). The assumption of high electricity cost (€80/MWh) will tend to make the 3D-SEWGS process less attractive.
- The contribution of the capture plant cost as a proportion of the total cost of the hydrogen plant with capture is small, which limits the ability to substantially decrease the levelized cost of hydrogen (LCOH) and the cost of CO_2 avoided through improving the productivity of the 3D-SEWGS plant.

- If the capital cost savings in the 3D-SEWGS process estimated here are realised, a cost of CO_2 avoided that is about 15% lower than that of aMDEA may be achieved. This is mainly due to the higher CO_2 avoidance in the SEWGS process.

Given the conclusions above, an important area of investigation for the future is a configuration of the plant that aims to maximise energy efficiency rather than CO_2 capture productivity. Further work should also be carried out on estimating the cost of the 3D-printed structures. Another area of further work is the quantification of the benefit of the SEWGS system on the PSA. The PSA cost has been assumed to be the same but there is a potential benefit due the lower mass flow rate into the PSA because of the conversion of the CO to CO_2 in the SEWGS unit.

ACKNOWLEDGEMENTS

The authors would like to thank Ionela Dumbrava and Ana-Maria Cormos of Babes-Bolyai University for their contribution on 3D-SEWGS modelling. They would also like to thank Jurriaan Boon, and Francesco Sebastiani for the valuable discussions and insight on the modelling.

This work is a part of the ACT 3D-CAPS project. The ACT 3D-CAPS project # 271503 has received funding from RCN (Norway, 276322), RVO (The Netherlands, 271503) and UEFISCDI, (Romania, 87/2017) and is co-funded by the CO_2 Capture Project (CCP) and the European Commission under the Horizon 2020 programme ACT, Grant Agreement No 691712.

REFERENCES

1. IEAGHG, Techno-Economic Evaluation of SMR Based Standalone (Merchant) Plant with CCS. 2017.
2. Boon, J., *et al.*, High-temperature pressure swing adsorption cycle design for sorption-enhanced water–gas shift. *Chemical Engineering Science*, 2015. 122: p. 219-231.
3. Boon, J., *et al.*, Isotherm model for high-temperature, high-pressure adsorption of CO_2 and H_2O on K-promoted hydrotalcite. *Chemical Engineering Journal*, 2014. 248: p. 406-414.
4. Rezaei, F. and P. Webley, Optimum structured adsorbents for gas separation processes. *Chemical Engineering Science*, 2009. 64(24): p. 5182-5191.
5. Patton, A., Crittenden, B. D., & Perera, S. P. (2004). Use of the Linear Driving Force Approximation to Guide the Design of Monolithic Adsorbents. *Chemical Engineering Research and Design*, **82**(8), 999-1009. doi:10.1205/0263876041580749.
6. Ruthven, D. M. (1984). *Principles of Adsorption and Adsorption Processes*. New York: John Wiley & Sons.
7. Müller-Steinhagen, H., and Heck, K., (1986) A simple friction pressure drop correlation for two-phase flow in pipes, *Chem Engr & Proc*, **20**(6).

Carbon Dioxide Capture for Storage in Deep Geological Formations, Volume 5
Karl F. Gerdes (Editor)
© 2022 BP. All rights reserved.

Chapter 5

PROJECT CO_2MENT: CO_2 CAPTURE FROM A CEMENT PLANT

Linal Perera, Brett Henkel, Andrew Liu, and Julie Giguere
Svante Inc., 8528 Glenlyon Pkwy #143, Burnaby, BC V5J 0B6

ABSTRACT: The goal of Project CO_2MENT is to demonstrate Svante's innovative adsorption-based carbon dioxide (CO_2) capture system on Lafarge Canada's Richmond cement plant at a pilot scale of 1 tonne per day (TPD). The concentration of CO_2 in cement plant emissions is about 20 mol %. This is similar to the concentration in flue gas from a modern Steam Methane Reformer (SMR) which uses Pressure Swing Adsorption (PSA) to purify H_2 and recycles the unconverted CH_4, CO and the process-generated CO_2 as fuel for the furnace. For this demonstration, Svante built the world's first VeloxoTherm™ 200 Series, capable of capturing up to 1 TPD of CO_2 using CALF-20, a Metal Organic Framework (MOF) sorbent material. In a later phase of the project, the captured purified CO_2 will be liquefied to demonstrate utilization in value-added applications.
The project scope consists of three phases:

Phase 1 -- Flue gas pre-treatment and contaminant-mitigation system design, construction, and testing.
Phase 2 -- CO_2 capture plant design, construction, and testing.
Phase 3 -- CO_2 liquefaction and utilization systems design, construction, and testing.

Results for Phase 1 demonstrated that a scrubber unit alone could achieve flue gas cooling, SO_X removal and particulate matter reduction. A guard bed may be required, depending on NO_X concentration in the feed and sensitivity of the carbon capture system used. Operation of the CO_2 capture unit in Phase 2 achieved steady state with high purity CO_2 product (>95%). The key performance metrics extracted from these results were consistent with expectations, considering actual operating conditions.

KEYWORDS: CO_2 capture, adsorption, structured sorbent, pre-treatment, liquefaction, utilization technology, climate change, cement, emissions, carbon, GHG targets.

INTRODUCTION

Capture of CO_2 from industrial operations using chemical solvents is technically proven, but the costs in terms of capital and energy use are sufficiently high to prompt developers to seek other technological approaches. One avenue showing promise is the use of solid adsorbents. Svante has developed the VeloxoTherm™ system based on a rapid-cycle Temperature Swing Adsorption (TSA) process that captures CO_2 directly from industrial sources and releases pure CO_2 with a cycle time of less than 60 seconds, compared to hours for other technologies, and requiring about half their capital cost. The capture process is implemented via a device similar to a Ljungström® air preheater, in which a proprietary structured adsorbent is arranged on a circular rotating structure. The device simultaneously exposes different segments of the structure to each step of the TSA cycle. A key advancement is the development of innovative adsorbent materials which enable the use of a rapid temperature swing cycle.

Production of cement –the universal binding agent employed in concrete buildings, roads, sidewalks, sanitary sewers, and much of the unseen infrastructure that forms the foundation of modern life–accounts for more than 5% of global CO_2 emissions. For every tonne of cement produced, more than three-quarters of a tonne of CO_2 is released into the atmosphere. The inherent chemistry required to produce cement, in which limestone is heated to produce lime, releases CO_2, in addition to the CO_2 generated from fuel combustion to drive the reaction. This presents a hurdle for the cement industry striving to achieve lower CO_2 emissions.

Project CO_2MENT centers around Lafarge Canada's Richmond cement plant. Operating since 1956, the Lafarge Richmond cement plant is currently pursuing initiatives to increase its usage of lower-carbon fuels and improve energy efficiency while, in parallel, investigating solutions to address process emissions.

Project CO_2MENT has engaged a diverse group of organizations with interest in seeing CO_2 capture and CO_2 reuse technologies successfully demonstrated. Svante, LafargeHolcim, and TotalEnergies are the primary sponsors of Project CO_2MENT, with further support from CCP in Phases 1 and 2. The demonstration of the VeloxoTherm™ capture technology on cement plant emissions is of interest to CCP because the CO_2 concentration, at about 20 mol %, is similar to that in flue gas from a modern SMR H_2 plant utilizing PSA for H_2 purification.

FOCUS OF PROJECT CO_2MENT

The objective of Project CO_2MENT is to promote the development and demonstration of integrated solutions to capture and reuse CO_2 in value-added applications. The goal of Phases 1 and 2 of this project was to develop and demonstrate a customized-for-cement version of Svante's carbon capture technology at pilot scale. Future work to be completed during Phase 3 will support the development of CO_2 utilization technologies.

By using Project CO_2MENT to prove the technologies' applicability to actual cement-kiln emissions and further identify utilization options for the extracted CO_2, this project could lead to several desirable outcomes, including:

- The development of low-cost capture solutions for industrial CO_2 emissions from cement plants, which at commercial scale could make a meaningful contribution to British Colombia's 2050 GHG targets and have global scale impacts on the world's GHG emissions.
- The demonstration of a capture technology that is also applicable to Steam-Methane Reformer flue gas, which has similar CO_2 concentration.
- The identification of viable options to utilize captured CO_2.

PROJECT CO_2MENT RESULTS

Phase 1-CO_2MENT Project Results

Scrubbing System and Flue Gas Contaminants

The objective of Phase 1 was to build and test a pre-conditioning process to remove particulates and control NO_X and SO_X from the kiln flue gas before entering the Svante CO_2 capture unit. The phase 1 pre-treatment system includes a third-party (Tri-Mer) supplied scrubber unit to remove almost all SO_X, followed by a guard bed unit to remove almost all NO_X. The scrubber unit was also designed to remove most of the entrained particles from the cement plant flue gas.

Figure 1. Tri-Mer Pre-Treatment System at the Lafarge Richmond Cement Plant.

Phase 1 operation of Project CO_2MENT commenced in Q4-2019 with the installation of the kiln flue gas pre-treatment system to remove solid particulates, as well as SO_X and NO_X impurities. The plant was started and tested during the period of November 2019 to March 2020. Ultimately, the Phase 1 unit proved it was possible to control SO_2 to < 5ppm and NO_2 to < 10ppm, which are the maximum impurities requirements for the Svante carbon capture system. The pre-treatment system consists of a Direct Contact Cooler (DCC) using caustic scrubbing, and Svante's proprietary guard bed using activated carbon Structured Adsorbent Beds (SABs) (Figures 1 and 2). The field trials demonstrated a recovery of 90% for solid particles greater than 10 microns and the removal of SO_2 and NO_2 to less than 3 ppmv and 1 ppmv, respectively, from the flue gas entering the CO_2 capture system.

SOx/NOx Removal

The SO_2 present in Lafarge Richmond flue gas (20-50 ppmv) was reduced to below 3 ppmv, largely by a single stage scrubber without the use of caustic soda. Addition of chemicals (e.g., NaOH) improved removal of SO_2 to less than 1.5 ppmv. Figure 3 shows SO_2 removal with a scrubber solution having about neutral pH. The measured concentration of NO_2 was higher after the scrubber, which might be related to conversion of NO to NO_2 in the presence of water and oxygen in the flue gas. While running the scrubber at neutral condition (pH ~7), NaOH consumption was minimized, and wastewater production was reduced to a fraction of vendor design specifications. It is important to note that the fuel used at Lafarge Richmond kiln was a mixture of various waste materials and coal which caused large fluctuations in flue gas composition, including NO_X and SO_X as can be seen in Figure 3. The removal of NO_2 was performed by a guard bed designed and built by Svante. The guard bed was able to completely remove the NO_2 passing through the scrubbers, while NO was not removed.

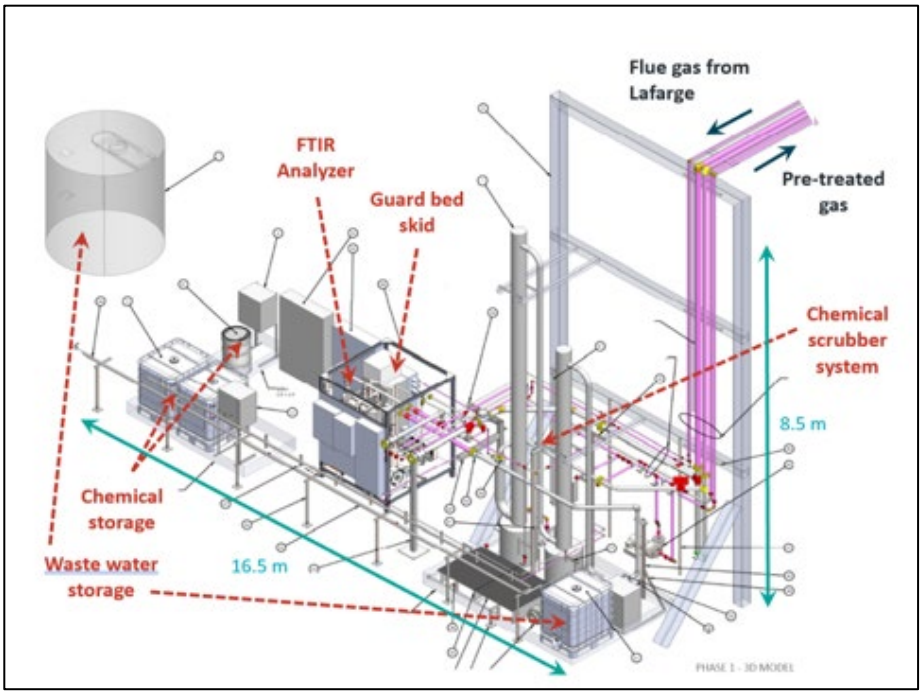

Figure 2. Schematic of Pre-Treatment System for Project CO_2MENT.

Particulate Removal

Total particulate content in the flue gas was monitored during a 3-week testing period and an average of about 3.5 mg/m^3 of P10 (less than 10 microns) was detected in the flue gas upstream of the Tri-Mer scrubber. Downstream from the scrubber, the P10 particulate matter dropped to about 0.2 mg/m^3, as shown in Figure 4. This represents a reduction of more than 90%. It is also important to note that the size of the particulates remaining in the flue gas (<10µm) is much smaller than the gas flow

channel height of the structure laminate in the capture unit, so no solids buildup leading to flow restriction is expected.

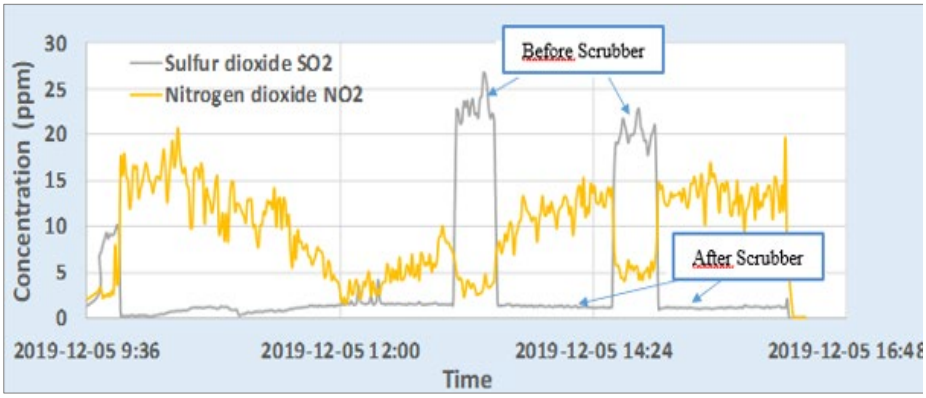

Figure 3. SO_2/NO_2 Removal by Tri-Mer Scrubbers at pH of ~7.

Proposed Commercial Pre-Treatment Scheme

Based on the above results, a scrubber unit alone could also serve as a DCC to handle process cooling in addition to SO_X removal and particulate matter reduction. A guard bed may be required, depending on the NO_2 concentration in the feed and sensitivity of the carbon capture system used. Figure 5 shows the suggested configuration. Svante has planned and coordinated internal and third-party testing on the stability of the Svante MOF adsorbent (CALF-20) to SO_X and NO_X, and based on primary results it is not anticipated that a guard bed will be necessary. Further testing is currently in progress at the Lafarge Richmond site to confirm this configuration.

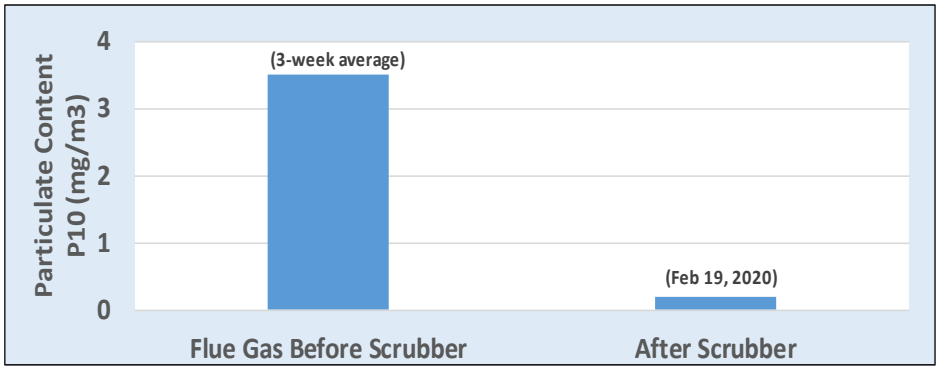

Figure 4. Particulate (<10 μm) Removal by Tri-Mer Scrubbers.

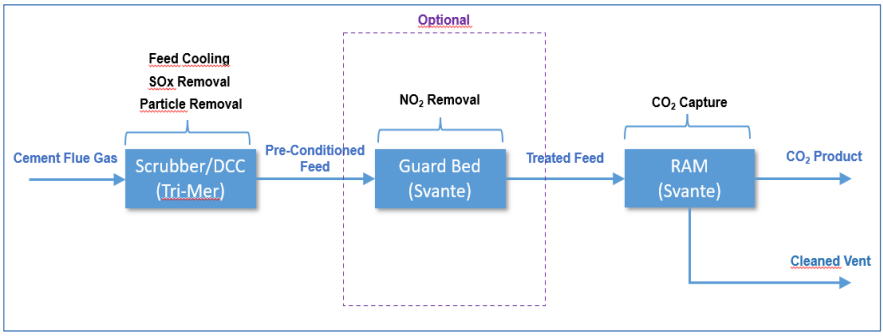

Figure 5. Svante's Pre-Treatment System Configuration.

CO_2 Capture Plant Process Description

The Svante carbon capture process consists of a series of steps which include: passage of flue gas, regenerating steam, and conditioning air through structured adsorbent beds in a specific order.

I. Adsorption: The first step in the process is the introduction of the feed gas into the structured adsorbent beds, where CO_2 is adsorbed onto the surface of the adsorbent while the remainder of the flue gas–mainly N_2, O_2 and H_2O–is sent to the stack as spent/exhaust gas.

II. Regeneration: The CO_2-rich adsorbent bed then rotates to a sector of the process where low pressure steam flows through the adsorbent bed, requiring only a small amount of superheat to overcome heat losses from the system. This is the first regeneration step, where steam regenerates the adsorbent releasing a stream composed primarily of CO_2 and steam.

III. Conditioning: After regeneration with steam, the bed rotates through a sector of the process where heated ambient air is used to condition and cool the structured adsorbent. The ambient air stream, termed Conditioning Gas, removes most of the water vapor from the adsorbent.

The adsorption, regeneration, and conditioning functions described above are integrated and implemented in a rotating system, as shown in Figure 6. The adsorbent material is secured within a rotating cylindrical frame, known as a Rotary Adsorption Machine (RAM). The construction of the RAM is based on a technology similar to that of regenerative air heaters, widely used in power plants. The frame is divided into distinct zones to allow for the adsorption, regeneration, and conditioning steps of the carbon capture process.

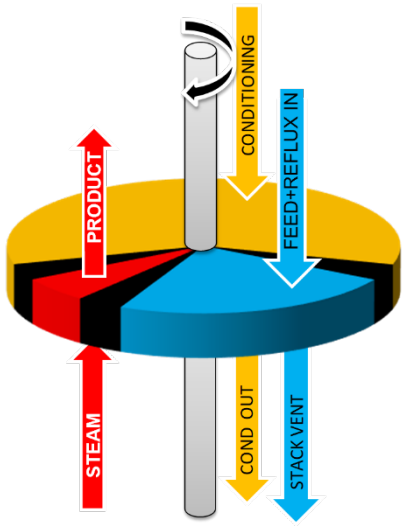

CYCLE STEP	PURPOSE
FEED	CO_2 is adsorbed from the flue-gas.
STACK	Gases, primarily N_2, O_2 and H_2O, are exhausted to the stack after CO_2 has been adsorbed from the Feed.
STEAM PUSH	Steam is introduced to regenerate the adsorbent and pushes out the high purity CO_2 product.
PRODUCT	CO_2 product and moisture are produced.
CON-DITIONING	Ambient air is used to remove moisture and cool down the bed for adsorption.

Figure 6. Standard 3-step RAM Process Cycle.

Phase 2-CO_2MENT Project Results

Phase 2 of Project CO_2MENT started in Q2-2020. For this demonstration, Svante built the world's first VeloxoTherm™ 200 Series, capable of capturing up to 1 TPD of CO_2 using CALF-20, a Metal Organic Framework (MOF) sorbent material [1]. Commissioning was completed in Q1-2021 and operation with kiln flue gas commenced in Q2-2021. Figure 7 shows the carbon capture plant overview and Figure 8 illustrates the 3D layout of Phase 2, installed at the Lafarge Richmond cement plant.

This plant is the world's first CO_2 capture demonstration unit to use MOF sorbent material (CALF-20), and first to be commissioned, operated and tested for cement flue gas application.

Figure 7. Svante's CO_2 Capture Plant (Phase 1 + Phase 2) at the Lafarge Cement Plant in Richmond, British Colombia.

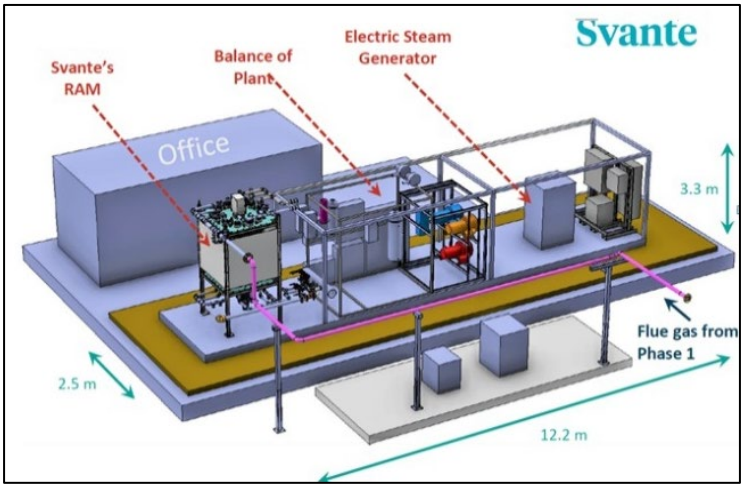

Figure 8. 3D Rendering of the Phase 2 Carbon Capture Plant Based on Svante's Rotary Adsorption Machine (RAM).

Performance Testing

A 7-day continuous test run was conducted with actual flue gas from the Lafarge Richmond cement plant, and CO_2 feed content varying from 10 to 20%. Figure 9 shows a nearly 2-day (43-hour) steady state operation for both the pre-treatment and CO_2 capture units, as part of the 7-day continuous operation. For this period, the flue gas CO_2 concentration fluctuated only slightly (within ±0.5%), with an average concentration of 18.7 vol%.

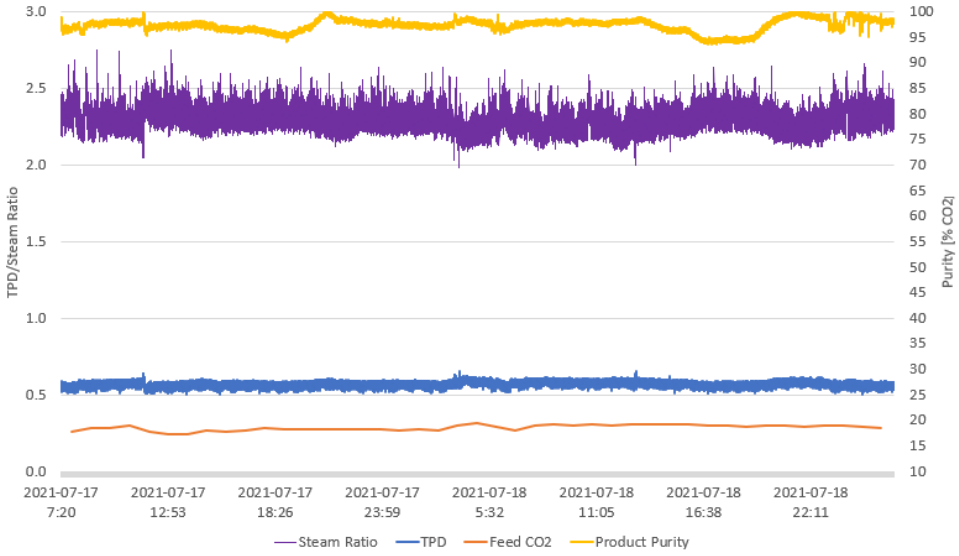

Figure 9. 43-hour continuous operation trends for Svante's CO_2 capture plant.

Key Performance Indicators (KPIs) extracted from this steady state period are summarized in Table 1. During the 2-day operation, the actual purity (~97%) was higher than the target (95%), due to cycle tuning. This resulted in a slightly higher steam ratio than the expected value derived from the lab test unit. For a typical commercial liquid amine system, the steam ratio is normally in the range of 1.1-1.5. Nevertheless, the Svante technology has a great potential to optimize both the MOF adsorbent material and the process cycle to improve the overall KPIs, including minimizing the steam ratio. The 3-5 years goal will be to reach 1.2-1.3 steam ratio for cement applications. Some ongoing R&D development will be integrated into the on-going testing, as described below.

Table 1. Test KPIs from Phase 2 Steady State Operation. Flue Gas CO_2:16-18%

KPIs	Productivity [TPD/m^3]*	Steam Ratio (kg/kg)**	Product Purity [%]
CALF-20 Test Data	10.6	2.3 ± 0.2	97 ± 2
Base Design Target	>8	1.9 ± 0.3	>95

*Tonnes CO_2/m^3 bed/ Day

** Amount of steam usage (kg)/amount of CO_2 produced (kg)

A new Waste Heat Recovery (WHR) cycle concept has been designed, which recycles steam generated from waste heat for CO_2 recovery. The objective of this cycle is to reduce the plant steam consumption and overall steam ratio. This new cycle modification is currently undergoing testing, and has shown a significant reduction in steam ratio ~20%.

Durability Testing

Durability testing was conducted on a reduced number of beds (24). This test used a standard cycle based on the original design and was intended to evaluate performance stability and adsorbent degradation, as well as wear on the beds, rotary valve seal, etc.

Figure 10 shows the durability test results for the first ~460 hours. Most of the performance variations are closely related to CO_2 feed concentration, which was in the range of 10-20% during the testing period. In general, lower CO_2 feed concentration results in lower productivity and higher steam ratio.

The balance of plant was initially designed for a maximum production rate of 0.7 TPD for another application. Upgrades would be required for various pieces of equipment, excluding the RAM, to reach the rate of 1 TPD. However, this has not impacted the utility of the operational data for this study or Svante's larger scale-up strategy towards commercialization.

Performance degradation related to flue gas contaminates (NO_X and SO_X) and particles are closely monitored and will be evaluated throughout the duration of durability test. It is expected that the MOF adsorbent will not suffer any thermal, condensation or oxidation related degradation in the operating temperature range.

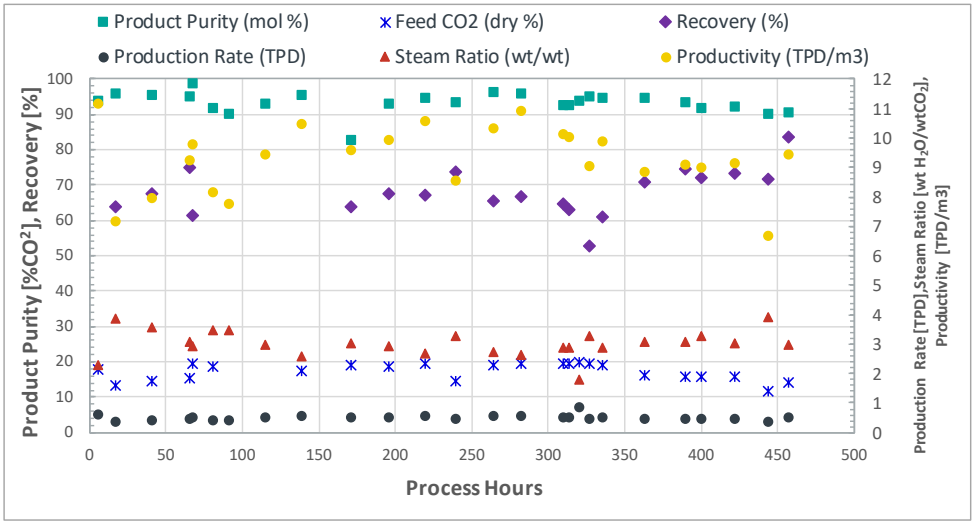

Figure 10. Durability test results of Svante's CO_2 capture plant.

The design basis for this system was for a feed CO_2 of 17-18%. However, the actual feed CO_2 varied between 10-20% during testing which resulted in a wide range of recoveries. For future tests, a more consistent operation at higher feed CO_2 will be selected to demonstrate the target CO_2 capture ratio without impacting KPIs. To support this, Svante is implementing additional cycle adjustments to simultaneously improve capture efficiency and bed CO_2 saturation at the end of the capture step. This

results in higher CO_2 recovery while maintaining other KPIs and will allow to demonstrate Svante's competitive position within the carbon capture space.

Phase 3-CO_2MENT Project Objectives

Phase 3 of Project CO_2MENT is expected to begin in 2022, with the goal of demonstrating utilization technologies where CO_2 is permanently sequestered into concrete. A CO_2 liquefaction unit will be installed downstream of the capture plant to pressurize the CO_2 product gas and liquefy the captured CO_2 for storage and utilization.

Solidia, a leading US based utilization company, will use Svante's captured CO_2 to cure concrete in a neighbouring pre-cast plant. Carbon Upcycling Technologies (CUT), a Canadian based company making carbon derived additives, will use Svante's captured CO_2 to inject into fly-ash for use in concrete production.

SUMMARY

Project CO_2MENT delivered promising operational results. Most notably:

- Successfully meeting CO_2 capture KPIs, specifically:
  - ✓ CO_2 purity >95%
  - ✓ Productivity > 8 Tonnes CO_2/m^3 bed/ Day
- Steam ratio demonstrated as 2.3 ± 0.2 and new WHR cycle design to be tested to reduce plant steam consumption and overall steam ratio.
- Positive results enabled continuation of Project CO_2MENT to development and execution of Phase 3, to further demonstrate and develop utilization technologies.
- Promising technology and operation demonstrated for the cement industry, prompting future scale-ups and CO_2 mitigation projects.

ACKNOWLEDGMENTS

Svante acknowledges funding support from the BC Government's Innovative Clean Energy (ICE) fund, the Canadian Federal Government Industrial Research Assistance (IRAP program), and co-funding from the CO_2 Capture Project (CCP), Total, and LafargeHolcim.

REFERENCES:

1. Omid Ghaffari-Nika, Laurent Mariacb, Andrew Liua, Brett Henkela, Stefan Marxd, Pierre Hovingtona, "Rapid Cycle Temperature Swing Adsorption Process Using Solid Structured Sorbent for CO_2 capture from Cement Flue Gas", 15th International Conference on Greenhouse Gas Control Technologies (GHGT-15), 15th-18th March 2021 Abu Dhabi, UAE

Carbon Dioxide Capture for Storage in Deep Geological Formations, Volume 5
Karl F Gerdes (Editor.)
© 2022 BP. All rights reserved.

Chapter 6

TECHNO-ECONOMIC ANALYSIS OF A GRAPHENE OXIDE-BASED MEMBRANE PROCESS FOR FLUE GAS CO_2 CAPTURE FROM AN SMR PLANT

Weiwei Xu,[1] Huanghe Li,[2] Miao Yu,[2] Yuhao Wang,[1] Howard Meyer,[1] Shiguang Li[1]
[1]GTI Energy, Des Plaines, IL 60018, USA
[2]Rensselaer Polytechnic Institute (RPI), Troy, NY 12180, USA

ABSTRACT: A techno-economic analysis (TEA) of CO_2 capture from the flue gas of a steam methane reforming (SMR)-based merchant H_2 plant using a graphene oxide (GO)-based membrane process is described. The economic results are compared with benchmark CO_2 capture technology using monoethanolamine (MEA) solvent absorption. The levelized cost of hydrogen (LCOH) and CO_2 avoided cost of a SMR H_2 plant employing the GO-based membrane process are estimated to be \$0.214/Nm^3 (\$2.3/kg) and \$70.5/t, which are ~9% and ~30% less, respectively, than for CO_2 capture using MEA. These TEA results indicate that the GO membrane-based process has potential to serve as an optional platform for capturing CO_2 from SMR H_2 plant flue gas.

KEYWORDS: steam methane reforming, techno-economic analysis, CO_2 capture, graphene oxide gas separation membrane

INTRODUCTION

CO_2 Capture from SMR Plant

A typical SMR-based H_2 plant mainly consists of four sections: (1) feedstock pre-reformer, (2) steam reformer, (3) water gas shift (WGS) Reactor, and (4) pressure swing adsorption (PSA) unit.

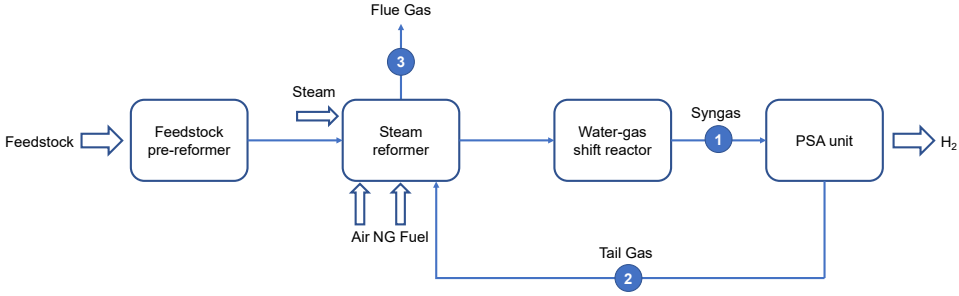

Figure 1. Simplified block flow diagram of an SMR plant with three possible locations for CO_2 capture.

The simplified block flow diagram, shown in Figure 1, is typical of an SMR plant. The feedstock pre-reformer is primarily designed to take over part of the overall reforming duty of the SMR plant.

In the pre-reforming section, the treated feedstock is mixed with high pressure superheated steam to convert any heavy hydrocarbons in the feed to CH_4 and other co-products, such as CO_2, CO, and H_2. The product gas of the pre-reformer is then mixed with the second stream of high-pressure superheated steam and sent to the steam reformer tubes where the steam reforming reaction occurs to produce a mixture of H_2, CO, CO_2, CH_4, and H_2O. The syngas leaving the steam reformer is then fed into the WGS reactor where the excess steam converts most of the CO to CO_2 and H_2. The shifted syngas is then cooled to condense water and fed to the PSA unit to remove the impurities to produce a high-purity H_2 product.

As illustrated in Figure 1, CO_2 is generated from two sets of reactions in a typical SMR plant: (1) the steam reforming and WGS reactions that generates about 55-60% of the CO_2; and (2) the combustion of the natural gas and the residual CO in the PSA tail gas in the SMR furnace that generates the remaining 40-45% of CO_2 [1]. There are three options for capturing CO_2 generated in the SMR plant: (1) from the syngas after the WGS reactor; (2) from the PSA tail gas; and (3) from SMR flue gas. To achieve capture rates greater than 60% in an SMR plant, Option 3 must be included. Studies in this chapter will be focused on Option 3 – capturing CO_2 only from the flue gas of the SMR plant.

Scope of the Study

The objective of this study was to perform a techno-economic analysis (TEA) for capturing CO_2 from the flue gas of an SMR-based merchant H_2 plant with an innovative graphene oxide (GO)-based membrane process and to compare it with a reference case published in the International Energy Agency Greenhouse Gas (IEAGHG) technical report, "Techno-Economic Evaluation of SMR-based Standalone Hydrogen Plant with CCS" [1]. The reference case captures CO_2 from SMR's flue gas using a MEA solvent absorption process. The economic comparison is reported in terms of 2014 euros.

The key design parameters of the SMR-based H_2 plant are summarized in Table 1. The plant is designed to produce 100,000 Nm^3/h of H_2 from natural gas as feedstock and fuel. The technical design basis, economic evaluation criteria, and assumptions of this TEA study are based on the guidelines provided in the IEAGHG technical report [1]. The graphene oxide (GO)-based membrane capture process is based on capture of 90% of the CO_2 from the SMR flue gas, which is the same as the reference Case 3.0 using benchmark MEA chemical absorption technology.

Table 1. Design basis for IEA Reference Case [1].

Point Source	Steam Methane Reformer
Scale (Nm^3/hr hydrogen)	100,000
Total Flue Gas Flow (kmol/h)	8,659.4
Pressure (bara)	1.2
Temperature (°C)	136
Composition (mol%)	
CO_2	21.23
N_2	60.83
O_2	1.02
H_2O	16.92

BENCHMARK SMR FLUE GAS CO_2 CAPTURE TECHNOLOGY USING MEA SOLVENT ABSORPTION PROCESS

The block flow diagram in Figure 2 shows the main process units and the relevant inlet/outlet streams in a new-build SMR H_2 plant with flue gas CO_2 capture using the MEA technology. The SMR H_2 plant consists of five units: (1) H_2 plant; (2) CO_2 capture plant. (3) Co-generation (COGEN) unit; (4) demineralized (DEMI) water unit; and (5) balance of plant (BoP) including additional utilities and facilities to support the operation of the whole plant.

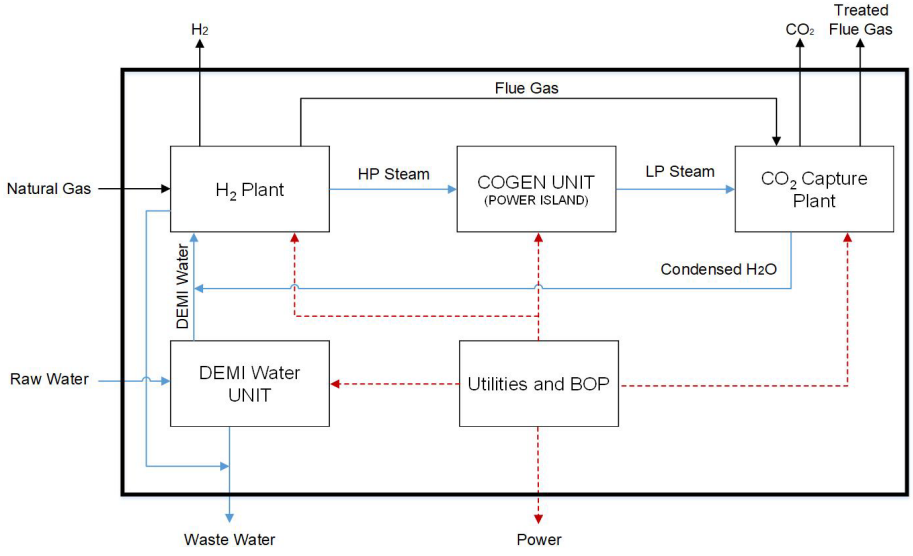

Figure 2. Overall block flow diagram of SMR plant with CO_2 capture. Black lines represent gas streams, blue lines represent water streams, and the red-dashed lines represent power streams [1].

H_2 Plant

In this unit, the natural gas is supplied as feedstock and fuel to produce 100,000 Nm^3/h of H_2. The flue gas generated in the H_2 plant is sent to the CO_2 capture plant for further treatment, and the excess superheated steam is delivered to COGEN unit for power generation.

CO_2 Capture Plant (MEA-based Chemical Absorption Unit)

The SMR flue gas is treated in this unit. About 90% of the CO_2 from the flue gas is captured and compressed and dehydrated. The treated flue gas passes through a water wash to minimize the loss of amine and emissions of degradation products and is then vented.

The capture plant includes gas-gas heat exchange, quench scrubber, absorber column, lean/rich amine heat exchangers, flash drum, stripper column, various trim coolers, filters, and pumps. If necessary, the SMR flue gas goes through a quench scrubber for desulfurization to reduce the SO_x level below 1 ppm. The flue gas is then sent to the absorber column where CO_2 is absorbed by a counter-current contacting with an amine solution. The CO_2-rich solution is pumped to the stripper column for CO_2 regeneration, the low pressure (LP) steam coming from the COGEN unit is used to heat the stripper column reboiler, and the condensed steam from the reboiler is recycled to the H_2 plant steam system.

COGEN Unit

The superheated steam exported from the H_2 plant drives a condensing steam turbine in the COGEN unit. The power generated by the COGEN unit supplies the electricity required by the H_2 Plant, CO_2 capture plant, DEMI water unit, and other utilities. Surplus electricity from the COGEN unit can be exported to the local grid. LP steam exported from the COGEN unit is sent to the stripper reboiler of the CO_2 capture plant.

DEMI-Water Unit

Raw water is treated in a reverse-osmosis system and electro-deionization system to provide demineralized water required for steam production. The treated DEMI-water is also used in the closed-circuit cooling water system.

Balance of Plant

Balance of plant includes additional utilities and facilities supporting the operation of the SMR-based H_2 plant, such as the instrument/plant air system, nitrogen system, flare system, drain system, utility interconnections, and buildings.

Plant Performance with MEA Capture

The performance of an SMR without CO_2 capture (Base Case) and a newly built SMR with flue gas CO_2 capture by using the MEA absorption process (Case 3.0) are shown in Table 2 [1]. This table summarizes consumption, production, and emissions relevant to the SMR-based H_2 plant. Compared with the Base Case (no capture), the H_2 plant with CO_2 capture uses more natural gas, since supplementary fuel is required to generate steam for the CO_2 capture plant. Due to the power consumption for CO_2 capture, CO_2 compression, and additional utilities, the surplus electricity, which could be exported to the local electricity grid, is reduced from 9.9 MW for the Base Case to 0.43 MW for the H_2 plant with CO_2 capture using MEA. Adding the additional CO_2 capture section also increases the total capital cost (TCR) and annual operation and maintenance (O&M) cost for the SMR-based H_2 plant. For this study, we convert 2014 euro, which is used as the economic analysis basis in IEAGHG technical report, to 2018 US $, the levelized cost of hydrogen (LCOH), increases

from \$ 0.163/Nm^3 for the reference case to \$ 0.236/Nm^3 for the capture case. The LCOH was calculated by a cash flow analysis.

Table 2. SMR Performance Without and With CO_2 Capture (MEA) [1].

Inlet Streams	**Units**	**SMR Plant Base Case**	**SMR with CO_2 Capture Using MEA**
Nat. Gas (Feedstock)	t/h	26.231	26.231
Nat Gas (Fuel)	t/h	4.332	7.348
TOTAL Nat Gas	t/h	30.563	33.579
Nat Gas LHV	MJ/kg	46.5	46.5
Total Energy Input	MW_{th} LHV	394.77	433.72
Outlet Streams			
H_2 Production	t/h	8.994	8.994
	$Nm^{3/h}$	100000	100000
H_2 LHV	MJ/kg	119.96	119.96
Total Energy in H_2	MW_{th} LHV	299.7	299.7
Power Balance			
Gross COGEN Power Gen	MW	11.5	11.7
H_2 Plant Power Use	MW	-1.216	-1,314
Utilities/BOP Power Use	MW	-0.366	-1.677
CO_2 Capture Power Use	MW	0	-2.001
CO_2 Compression Power	MW	0	-6.282
Power Balance	MW	9.918	0.426
Specific Consumption			
Nat Gas (Feedstock)	$GJ/10^3\ Nm^3\ H_2$	12.197	12.197
Nat Gas (Fuel)	$GJ/10^3\ Nm^3\ H_2$	2.014	3.416
Feed + Fuel	$GJ/10^3\ Nm^3\ H_2$	14.212	15.614
Cost			
Total Plant Cost	10^6 2018 \$	244.9	437.3
Annual O&M Cost	10^6 2018 \$/year	103.7	138.0
LCOH	2018 \$/Nm^3	0.163	0.236
CO_2 Avoided Cost	2018 \$/t		100.0

TEA OF GO-BASED MEMBRANE PROCESS FOR SMR FLUE GAS CO_2 CAPTURE

The purpose of this study is to produce a techno-economic analysis (TEA) of CO_2 capture from the flue gas of an SMR H_2 plant using a novel graphene oxide (GO)-based membrane process.

GO-based Membrane Technology

The GO-based membrane technology reported here builds on previous work on ultrathin, GO-based membranes [3]. A laboratory-scale program supported by the United States Department of Energy (US DOE project DE-FE0026383) further developed GO-based membranes for CO_2 capture from flue gases. The high-selectivity membranes showed CO_2 permeances as high as 1,020 GPU with a CO_2/N_2 selectivity of 680, as summarized in Zhou *et al.* [4]. A bench-scale GO-based membrane process (designated as "GO^2"), a current DOE supported program (DE-FE0031598), focuses on integrating high-selectivity GO-1 membranes and high-flux GO-2 membranes is being developed for post-combustion CO_2 Capture (see Chapter 16 of the present volume). This process is planned for testing in 2022 at the National Carbon Capture Center (NCCC) in Alabama, US.

Process Simulation for the GO-based Membrane Process

A GO membrane with a CO_2 permeance of 1,500 GPU and CO_2/N_2 selectivity of 300, determined by laboratory testing results, was specified for the process simulation. A standalone membrane model was used to estimate the multicomponent gas permeation in the GO membrane module and integrated with Aspen Plus® to perform the process simulation for the SMR flue gas carbon capture process. The membrane model describes a flat sheet membrane configuration. The equations, assumptions, and detailed equation solving procedures of the membrane model are listed in Appendix A.

The CO_2 capture operation conditions for the process modeling are listed in Table 3. We assumed the same membrane properties when scaled to the commercial-scale plate-and-frame modules under real application conditions. The process simulation results indicate that a one-stage CO_2 capture process is sufficient to achieve 90% CO_2 capture rate and CO_2 product purity > 95% from the flue gas of the merchant-scale SMR H_2 plant.

Table 3. GO membrane properties and CO_2 capture conditions.

CO_2 Permeance	CO_2/N_2 Selectivity	Feed Pressure	Permeate Pressure	Operating Temperature	CO_2 Product Pressure
1500 GPU	> 300	5.0 bara	0.2 bara	80 ˚C	110 bar

An Aspen Plus® simulation of the CO_2 capture process shown in Figure 3 indicates that a one-stage capture process can achieve 90% CO_2 capture and greater than 95% CO_2 purity. The flue gas (Stream 1) exported from the SMR H_2 plant is cooled to 65°C by heat exchange (HeatEx1). The flue gas is then pressurized by a blower to 5.0 bara and cooled down to operation temperature before being fed to the GO membrane unit (Stream 5). The membrane unit separates the feed gas into a CO_2-depleted retentate (Stream 6), and a CO_2 enriched permeate (Stream 7). The permeate side of the membrane unit is maintained at a 0.2 bara vacuum. The permeate stream (Stream 7) containing 82% CO_2, 3% N_2, and 15% H_2O (Table 4, > 95% CO_2 on a dry basis) is cooled to partially condense water and sent (Stream 10) to the CO_2 compression and dehydration train. The treated flue gas (Stream 6) that has 90% CO_2 removed is then exhausted to the stack.

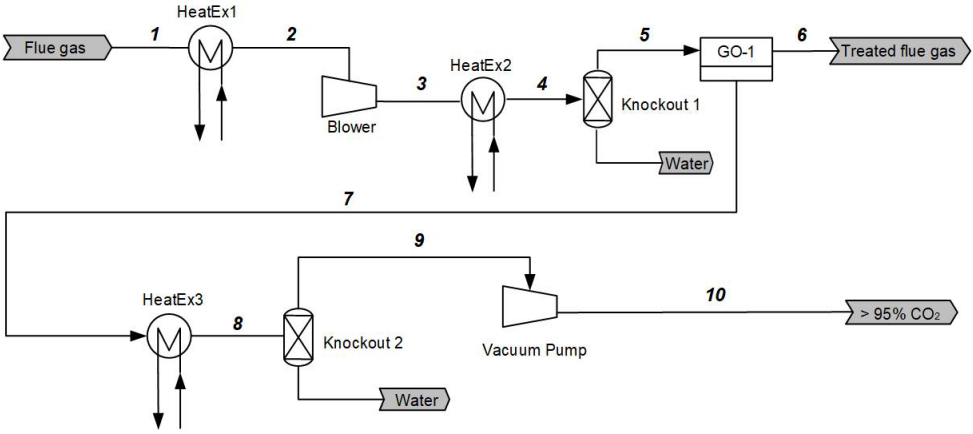

Figure 3. Process flow diagram of the GO-based one-stage membrane process for CO_2 capture from SMR flue gas.

Table 4. Material Balance for GO-based membrane process.

Stream	1	2	3	4	5	6	7	8	9	10
Temperature, °C	136	65	187	80	80	80	80	25	25	80
Pressure, bara	1.2	1.2	5	5	5	5	0.2	0.2	0.2	1
Flow (kmol/sec)	2.41	2.41	2.41	2.41	2.19	1.63	0.56	0.56	0.54	0.54
CO_2	0.51	0.51	0.51	0.51	0.51	0.05	0.46	0.46	0.46	0.46
N_2	1.49	1.49	1.49	1.49	1.49	1.48	0.02	0.02	0.02	0.02
H_2O	0.41	0.41	0.41	0.41	0.19	0.11	0.09	0.09	0.06	0.06
Mole Fraction										
CO_2	0.21	0.21	0.21	0.21	0.23	0.03	0.82	0.82	0.85	0.85
N_2	0.62	0.62	0.62	0.62	0.68	0.90	0.03	0.03	0.03	0.03
H_2O	0.17	0.17	0.17	0.17	0.09	0.07	0.15	0.15	0.12	0.12

Table 4 shows the stream compositions generated by integrating the standalone membrane model and Aspen Plus® model for the GO-based one-stage membrane process. A GO membrane with an area of 2.68×10^4 m^2 is required to meet the CO_2 recovery and purity target.

The performance of the SMR H_2 plant with flue gas CO_2 capture using GO membrane process is shown in Table 5. Since no additional steam is required for the membrane-based CO_2 capture process

and assuming the power requirements of the GO-based plant can be provided by the electricity exported from the COGEN unit, the total natural gas consumption, in this case, is the same as an SMR plant without CO_2 capture (Table 2, Base Case). The gross power generated in the COGEN unit and the energy consumption by H_2 plant and BoP are identical to the Base Case. The power consumption of the CO_2 capture plant was estimated by the Aspen Plus® process simulation, and the power consumption of the following 6-stage CO_2 compression and dehydration train was ratioed on CO_2 volume from IEA Case 3.0. The energy used by the CO_2 capture plant is 13.964 MW, mainly due to about 11.8 MW demand for the blower and about 2.2 MW for the vacuum pump. Including electricity consumed by all five sections of the SMR H_2 plant, an extra 9.762 MW of electricity needs to be imported from the local grid for the CO_2 capture process.

Table 5. CO_2 Capture with MEA [1]vs GO Membranes.

Inlet Streams	**Units**	**SMR with CO_2 Capture Using MEA**	**SMR with CO_2 Capture Using GO Membranes**
Nat. Gas (Feedstock)	t/h	26.231	26.231
Nat Gas (Fuel)	t/h	7.348	4.332
TOTAL Nat Gas	t/h	33.579	30.563
Nat Gas LHV	MJ/kg	46.5	46.5
Total Energy Input	MW_{th} LHV	433.72	394.77
Outlet Streams			
H_2 Production	t/h	8.994	8.994
	Nm^3/h	100000	100000
H_2 LHV	MJ/kg	119.96	119.96
Total Energy in H_2	MW_{th} LHV	299.7	299.7
Power Balance			
Gross COGEN Power Gen	MW	11.7	11.5
H_2 Plant Power Use	MW	-1,314	-1.216
Utilities/BOP Power Use	MW	-1.677	-0.366
CO_2 Capture Power Use	MW	-2.001	-13.964
CO_2 Compression Power	MW	-6.282	-5.716
Power Balance	MW	0.426	-9.762
Specific Consumption			
Nat Gas (Feedstock)	$GJ/10^3\ Nm^3\ H_2$	12.197	12.197
Nat Gas (Fuel)	$GJ/10^3\ Nm^3\ H_2$	3.416	2.014
Feed + Fuel	$GJ/10^3\ Nm^3\ H_2$	15.614	14.212
Specific Emissions			
CO_2 Emissions	$t/1000\ Nm^3\ H_2$	0.0888	0.0809
CO_2 Captured	$t/1000\ Nm^3\ H_2$	0.8004	0.7282

TEA for GO-based Membrane Process

The cost estimating methodology, technical design basis, economic evaluation criteria, and basic assumptions used for the TEA were based on the guidelines provided in the IEAGHG technical report [1]. The Base Case and Case 3.0 published in the IEAGHG technical report were used as reference for this study. The cost of major equipment items, such as blower, heat exchangers, and vacuum pump associated with the GO membrane-based CO_2 capture process were estimated in 2018 US $ by the Aspen Process Economic Analyzer. Since the IEAGHG cost and economic study was reported in 2014 €, the total plant cost, annual O&M cost, LCOH, and CO_2 avoided cost for the Base Case and Case 3.0 were adjusted to 2018 US $ by accounting for inflation from 2014 to 2018 and the euro-to-dollar currency exchange rate (Table 6). Other parameters for the TEA, such as natural gas price, CO_2 transportation and storage (T&S) cost, electricity price, membrane cost, and membrane replacement cost, are also converted to the 2018 US dollar and listed in Table 6.

Table 6. Cost basis adjustment parameters.

Adjustment from 2014 euro to 2018 US dollar cost basis	
2014-2018 Inflation Rate	6.1%
2014 Currency Exchange Rate ($/€)	1.35
Natural Gas Price (2018 $/GJ LHV)	8.59
CO_2 T&S (2018 $/tonne)	14.3
Electricity (2018 $/MWh)	115
Membrane Cost (2018 $/m^2)[1]	30
Membrane Replacement (2018 $/m^2/year)[2]	5

Notes:
1. The membrane element cost is \$20/m^2 based on the current market price for desalination membranes. \$5/m^2 is used for the module housing. The installation material cost for the module is \$5/m^2.
2. The \$5/m^2 annual membrane replacement cost was estimated by spreading out \$20/m^2 membrane element cost evenly over the membrane lifetime of 4 years [6].

Total Plant Cost (TPC)

The TPC is defined as the total installed cost of the plant and includes contingencies. For the SMR-based H_2 plant with CO_2 capture, the TPC (Table 7) is estimated by breaking down the whole plant into different process units: H_2 plant, power island, CO_2 capture plant, CO_2 compression unit, and other utilities/balance of the plant (BoP).

Since the total natural gas consumption for a SMR H_2 plant with GO membrane-based CO_2 capture is same as the plant without CO_2 capture (Base Case), the TPC for the H_2 plant, BoP, and power island is the same as the base case. The TPC for the CO_2 capture plant is calculated based on:

- Direct material cost
- Construction cost
- EPC service cost
- Other costs
- Contingency

Table 7. TPC for SMR with GO membrane CO_2 capture.

	Description	H_2 Plant (10^6 2018 $)	Utilities (10^6 2018 $)	Power Island (10^6 2018 $)	CO_2 Capture (10^6 2018 $)	CO_2 Compress (10^6 2018 $)	Total Cost (10^6 2018 $)
1	Direct Material	58.3	27.0	12.3	15.3	17.4	130.2
2	Construction	36.8	25.5	8.1	2.0	8.6	81.0
3	Direct Field Cost	95.1	52.5	20.3	17.4	26.0	211.3
4	Other Costs	2.7	1.8	0.7	1.0	0.7	7.8
5	EPC Svcs.	18.3	9.7	3.0	1.9	3.8	35.6
6	TIC	116.0	64.0	24.0	20.3	30.4	254.8
7	Project Contingency	23.2	12.8	4.8	1.9	6.1	48.8
8	TPC	139.2	76.8	28.8	22.2	36.5	303.6

As noted above, for the capture plant Aspen Process Economic Analyzer was used to estimate major equipment costs. The direct and indirect cost of the CO_2 capture plant are calculated based on methodology from Peters *et al.* [5] and summarized in Table B-1 in Appendix B. The TPC for CO_2 compression unit is ratioed on CO_2 volume from IEA Case 3.0. It should be noted that the TPC for the GO membrane-based capture was estimated using a different, simplified methodology that was used for the IEA case studies.

Annual Variable and Fixed Costs

The variable and fixed operating costs for the SMR H_2 plant with GO membrane-based CO_2 capture are summarized in Table 8. The yearly variable operating cost includes consumption of:

- Natural gas
- Raw make-up water
- Cooling water
- Electricity
- Cost of membrane replacement ($5/(m^2 year))
- Other chemicals

The yearly fixed operation cost includes:

- Operating labor cost is based on 38 staff for the SMR plant and 8 for the CO_2 capture plant with an average labor cost for each of $86,000/year.
- Maintenance cost, which is estimated to be 1.5% of TPC.
- Insurance & local taxes, which is estimated to be 1% of TPC.
- Overhead cost, which is 30% of the sum of operation labor cost and maintenance labor cost.

Table 8. Yearly variable and fixed cost for SMR Plant with CO_2 capture from flue gas using one-stage GO membrane process.

Capacity Factor		95%
Yearly Variable Operating Cost		
Consumables		Operating Cost (10^6 2018 $)
Nat Gas as Feedstock and Fuel		101.64
Raw Make-up Water		0.14
Cooling Water		0.52
Electricity		9.31
Membrane Replacement		0.13
Chemicals and Catalyst		0.57
Total Yearly Variable Cost		112.32
Yearly Fixed Operating Cost		
Operating Labor	SMR (38 P)	3.27
	CO_2 Capture (8P)	0.69
Labor Subtotal		3.95
Maintenance Labor		1.82
Maintenance Material		2.73
Maintenance Subtotal		4.55
Insurance and Local Taxes		3.04
Overhead		1.73
Total Yearly Fixed Cost		13.28

Total Capital Requirement (TCR)

The TCR for SMR H_2 plant with GO membrane-based CO_2 capture is summarized in Table 9. The TCR is the sum of:

- Total plant cost (TPC)
- Spare parts cost, which is assumed to be 0.5% of TPC
- Start-up cost, 2% of TPC, cost for supplying four months feedstock, and one month labor cost
- Owner's cost, which is 7% of TPC
- Working capital cost, including the cost for supplying one month feed stock, fuel electricity, make-up and cooling water, and chemicals
- Financing cost, which is 2.7% of TPC

Table 9. TCR for SMR with Flue Gas Capture Using GO Membranes.

Total Capital Requirement (TCR)	
Item	**(10^6 2018 $)**
Total Plant Cost	303.6
Spare Parts	1.5
Start-up Cost	14.6
Owner's Cost	21.3
Working Capital Cost	9.3
Financing Cost	8.2
TCR	358.5

Annual Operation and Maintenance (O&M) Cost

The annual O&M cost (Table 10) is estimated by adding the total fixed cost, variable cost, CO_2 Transportation and Storage (T&S) cost and subtracting the revenue from the exported electricity.

The LCOH accounts for both the annual operating cost and the annualized cost of capital:

$$LCOH = \frac{CCF \times TCR + O\&M\ Cost}{H_2\ Produced} \quad (3)$$

where: CCF is capital charge factor [2]. The CO_2 avoided cost, which includes CO_2 transportation and storage (T&S) cost, is calculated using the usual relationship:

$$CO_2\ Avoided\ Cost = \frac{LCOH_{ccs} - LCOH_{Reference}}{CO_2\ Emissions_{Reference} - CO_2\ Emissions_{ccs}} \quad (4)$$

The levelized cost of hydrogen (LCOH) of the SMR H_2 plant using the GO-based membrane for flue gas CO_2 capture is estimated to be \$0.214/Nm^3 (Table 10), which is about 9% lower than that for the SMR with MEA capture. The CO_2 avoided cost for the SMR H_2 plant using GO-based membrane for CO_2 capture is \$70.5/t, which is about 30% less than that achieved using MEA capture.

TEA Sensitivity Study

Table 10. Cost breakdown for SMR with and without CO_2 capture.

	SMR Base Case [1]	SMR with MEA Capture [1]	SMR with GO Membrane Capture
Total Fixed Cost (10^6 2018 $/year)	10.8	16.6	13.3
Total Variable Cost (10^6 2018 $/year)	102.4	112.4	112.3
Other Revenue (10^6 2018 $/year)	9.4	0.4	0
CO_2 T&S (10^6 2018 $/year)	0.0	9.5	8.7
Annual O&M Cost (10^6 2018 $/year)	103.7	138.0	134.3
TPC (10^6 2018 $)	244.9	437.3	358.5
LCOH (2018 $/Nm3)	0.163	0.236	0.214
CO_2 Avoided Cost (2018 $/tonne)	-	100.0	70.5

Table 11. Sensitivity study variables and ranges.

Variable	Base Value	Sensitivity Range
Natural Gas Price (2018 $/GJ LHV)	8.6	2.9 to 25.8
CO_2 T&S (2018 $/tonne)	14.3	-28.6 to 57.3
Electricity (2018 $/MWh)	114.6	28.6 to 143.2
Membrane cost (2018 $/$m^2$)	30.0	10 to 100
Membrane Replacement (2018 $/$m^2$/year)	5.0	1 to 20

Note: Negative CO_2 T&S cost could represent income received from CCS operations (i.e., EOR revenues, any incentives or tax credits from authorities.

A sensitivity study was conducted to assess the impact on LCOH and CO_2 avoided cost of various cost components, such as natural gas price, CO_2 T&S cost, electricity price, initial membrane cost, and membrane replacement cost. The ranges of the cost elements are listed in Table 11. The impact of natural gas and electricity costs on LCOH of the reference case without CO_2 capture was published in the IEAGHG technical report [1]. Since the other three factors—the CO_2 T&S cost, the membrane cost, and the membrane replacement cost—have no effect on the capital cost of the SMR H_2 plant, the LCOH of the reference case without CO_2 capture does not change.

The tornado plot of the LCOH sensitivity study is shown in Figure 4. The natural gas price has the largest impact on the LCOH of the SMR using GO-based membrane for flue gas CO_2 capture. The influence of electricity price, membrane cost, and membrane replacement costs is negligible. Figure 5 shows the tornado plot of the CO_2 avoided cost sensitivity study, which suggests that the cost of CO_2 T&S has a larger effect on the CO_2 avoided cost.

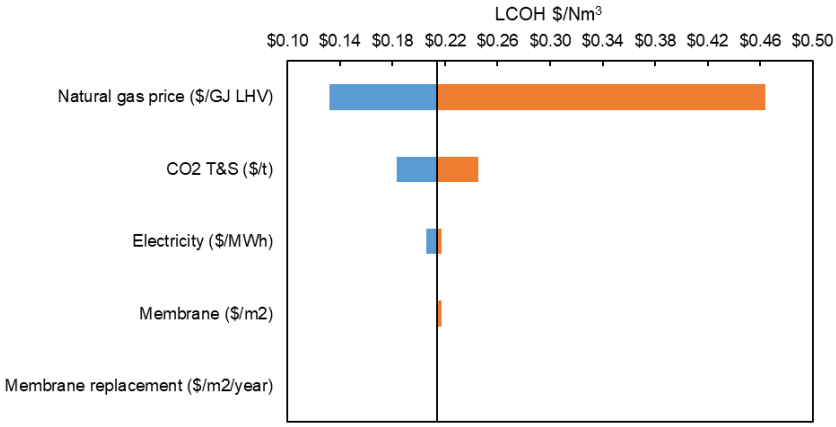

Figure 4. Tornado plot of LCOH sensitivity study to natural gas price, CO_2 T&S cost, electricity price, installed membrane cost, and membrane replacement cost.

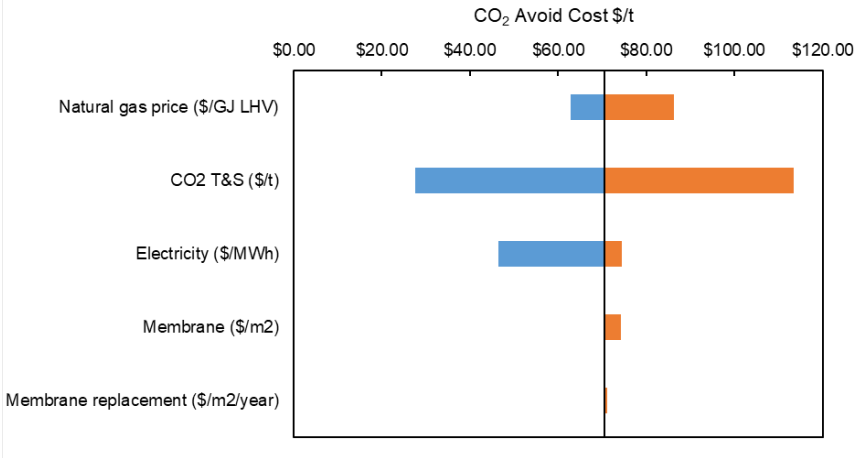

Figure 5. Tornado plot of CO_2 avoided cost sensitivity study to natural gas price, CO_2 T&S cost, electricity price, membrane, and membrane replacement cost.

CONCLUSIONS

The techno-economic analysis performed in this study indicates potential for a GO membrane-based CO_2 capture process on an SMR to significantly reduce the CAPEX compared to use of MEA absorption. The TPC of the SMR plant using the membrane process was estimated to be about 31% lower than the solvent-based IEA Case 3 ($304 MM vs. $437 MM) [1]. As shown in Figure 6, the MEA-based CO_2 capture plant with a cost of $136 MM accounts for 31% of TPC, while the membrane-based process is estimated to cost about $22.2 MM, and only accounts for 7% of TPC. Since no additional steam is required for the membrane-based CO_2 capture process, the natural gas consumption, CO_2 emission, and corresponding captured CO_2 (Table 5) of the SMR plant employing membrane-based CO_2 capture are smaller than required for the MEA technology, leading to about an 9% reduction in CO_2 compression cost ($36 MM vs. $40 MM).

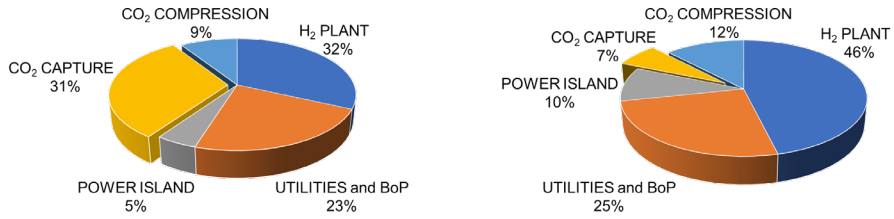

Figure 6. Comparison of TPC for SMR plant with CO_2 capture using MEA and GO membrane-base process.

Compared to the MEA CO_2 adsorption technology, the simpler GO membrane-based process with lower natural gas consumption is estimated to reduce OPEX by about 3% ($134 MM vs. $138 MM).

The reduced CAPEX and OPEX for the GO membrane-based CO_2 capture process leads to lower LCOH and CO_2 avoided cost. The LCOH of a SMR H_2 plant employing the GO-based membrane process is estimated to be $0.214/Nm^3, and the CO_2 avoided cost is $70.5/t, which are about 9% and 30% less, respectively, than those for the MEA process. This analysis indicates that the GO membrane-based process has potential to reduce the cost of capturing CO_2 from SMR H_2 plant flue gas.

ACKNOWLEDGEMENTS

We gratefully acknowledge support by the CCP4 (CCP4-CAP-013) and the US Department of Energy (Contract Numbers DE-FE-0004787). We thank Dr. Betty Pun and Dr. Raja Jadhav at Chevron, Dr. Ibrahim Ali at BP, Dr. Paulo Frederico Prunzel at Petrobras, and DOE/NETL Project Manager Dustin Brown for their assistance and many valuable discussions.

REFERENCES

1. IEAGHG, “Techno-Economic Evaluation of SMR Based Standalone (Merchant) Hydrogen Plant with CCS”, 2017/02, Feburary, 2017.
2. DOE NETL, “Cost and performance baseline for fossil energy plantsVolume 1: bituminous coal and natural gas to electricity”, 2019/09, Sepetember, 2019.
3. Li H, Song ZN, Zhang XJ, Huang Y, Li SG, Mao YT, *et al.* Ultrathin, Molecular-Sieving Graphene Oxide Membranes for Selective Hydrogen Separation. *Science* 2013, 342(6154): 95-98.

4. Zhou FL, Tien HN, Xu WW, Chen JT, Liu QL, Hicks E, *et al.* Ultrathin Graphene Oxide-Based Hollow Fiber Membranes with Brush-Like CO_2-Philic Agent for Highly Efficient CO_2 Capture. *Nature Communications* 2017, 8(1): 1-8.
5. Peters M., Timmer Haus, K., West, R. (2003) *Plant Design and Economics for Chemical Engineers* 5th Edition, McGraw-Hill.
6. Han Y and Ho W.S.W. Design of Amine-Containing CO2-Selective Membrane Process for Carbon Capture from Flue Gas. *Industrial & Engineering Chemistry Research* 2020, 59, 5340–5350.

Appendix A: The standalone GO membrane model used for SMR H_2 plant flue gas CO_2 capture process simulation.

A one-dimensional membrane model was used to estimate the multicomponent gas permeation in a membrane module with vacuum applied on the permeate side. The schematic drawing of the membrane module is shown in Figure A-1.

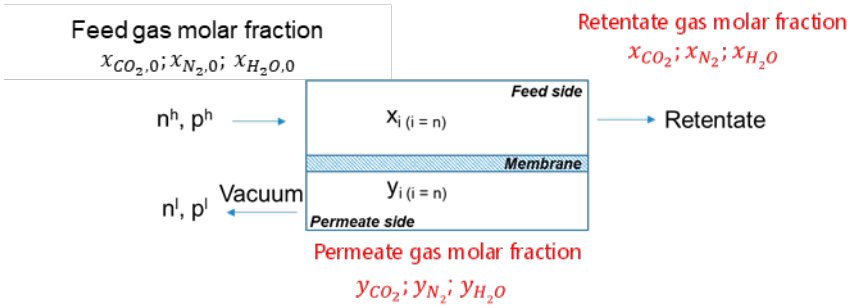

Figure A-1. Schematic drawing of vacuum applied membrane separation module.

A plug flow is assumed on the feed side of membrane, and the pressure drop between feed and retentate side is negligible. The mass balance across the membrane is governed by following equations:

$$\frac{dn^h}{dA} = -J \tag{1}$$

$$\frac{dx_{CO_2}}{dA} = -\frac{1}{n^h}\left[\frac{P_{CO_2}}{l}\left(p^h x_{CO_2} - p^l y_{CO_2}\right) - x_{CO_2} \times J\right] \tag{2}$$

$$\frac{dx_{N_2}}{dA} = -\frac{1}{n^h}\left[\frac{P_{N_2}}{l}\left(p^h x_{N_2} - p^l y_{CO_2}\right) - x_{N_2} \times J\right] \tag{3}$$

$$\frac{dx_{H_2O}}{dA} = -\frac{1}{n^h}\left[\frac{P_{H_2O}}{l}\left(p^h x_{H_2O} - p^l y_{H_2O}\right) - x_{H_2O} \times J\right] \tag{4}$$

And $J = \frac{P_{CO_2}(x_{CO_2})}{l}\left(p^h x_{CO_2} - p^l y_{CO_2}\right) + \frac{P_{N_2}(x_{N_2})}{l}\left(p^h x_{N_2} - p^l y_{N_2}\right) + \frac{P_{H_2O}(x_{CO_2})}{l}\left(p^h x_{H_2O} - p^l y_{H_2O}\right)$

Where n^h is feed side molar flow rate, $\frac{P_{CO_2}}{l}$, $\frac{P_{N_2}}{l}$ and $\frac{P_{H_2O}}{l}$ are the permeance of CO_2, N_2 and H_2O, $x_{CO_2}, x_{N_2}, x_{H2O}$ and $y_{CO_2}, y_{N2}, y_{H2O}$ are the molar fraction of each species on feed and permeate sides, respectively, p^h is feed side pressure, p^l is permeate side pressure, and J is the total flux.

When vacuum is applied on the permeate side, a crossflow pattern is assumed, and the material balance on the permeate side of membrane is governed by following equations:

$$y_{CO_2} + y_{N_2} + y_{H_2O} = 1 \tag{5}$$

$$y_{N_2} = \frac{x_{CO_2}\frac{P_{N_2}}{P_{CO_2}}}{\frac{p^l}{p^h}\left(\frac{P_{N_2}}{P_{CO_2}}-1\right)+\frac{x_{CO_2}}{y_{CO_2}}} \tag{6}$$

$$y_{H_2O} = \frac{x_{H_2O}\frac{P_{H_2O}}{P_{CO_2}}}{\frac{p^l}{p^h}\left(\frac{P_{H_2O}}{P_{CO_2}}-1\right)+\frac{x_{CO_2}}{y_{CO_2}}} \tag{7}$$

$$n^l = n^h|_{A=0} - n^h|_{A=A_t}\,; A_t = total\ membrane\ area \tag{8}$$

The permeate side total molar flow rate n^l can be obtained by the overall mass balance (equation 8).

Combing equations (1)-(8) completes the modelling of gas permeation in the membrane module. The highly coupled ordinary differential equations and algebraic equations are solved in MATLAB. The MATLAB program solves the membrane model with an incremental step size dA. Given the initial gas composition at A=0, the molar fraction at the permeate side can be calculated by solving the algebraic equations (5)-(7). The set of x's and y's are substituted to calculate J. The feed gas composition as well as the flow rate at A=dA can then be calculated with equations (1)-(4) by approximating the derivative using a finite difference. Similarly, the molar fraction on the permeate side at A=dA is calculated using the feed composition. Following this logic, for a given set of feed gas flow rate, feed gas compositions, operation pressure and membrane area, the permeate and retentate gas compositions as a function of the membrane area could be calculated by the membrane model in an iterative manner. The implementation of membrane model in the SMR flue gas carbon capture process simulation requires the estimation of required membrane area for given CO_2 capture rate and product purity. The product purity is the molar fraction of CO_2 relative to CO_2 and nitrogen in the permeate. The CO_2 capture rate is the total amount of CO_2 that passed through the membrane divided by the total amount in the feed. Product purity and capture rate are defined in equations (9) and (10), respectively:

$$y_{CO2}/(y_{co2} + y_{N2}) \tag{9}$$

$$\frac{y_{CO2}(n^h_{(A=0)} - n^h_{(A=At)})}{n^h_{(A=0)} * xco2{,}0} \tag{10}$$

When estimating the membrane area given a specific requirement, the algorithm checks the criteria values in each incremental step dA. The integrated process calculates the fraction of a component on the feed side and the permeate side as a function of the membrane area. The product purity at A=Ai in equation (9) is calculated based on the average molar fraction from A=0 to A=Ai on the permeate side. The CO_2 capture rate at A=Ai is calculated as:

$$\frac{\int y_{CO_2}(A) dn^h_A}{n^h_{(A=0)} * x_{CO_2,0}} \tag{11}$$

The integral in the numerator is the total amount of CO_2 through the membrane and is approximated by finite difference in each dA step as:

$$\frac{\sum_{i=2}^{n}\left[\frac{y_{CO_2}{}^{(i)}+y_{CO_2}{}^{(i-1)}}{2}\right]\left[n^{h}_{(A=A_i)}-n^{h}_{(A=A_{i-1})}\right]}{n^{h}_{(A=0)}*x_{CO_2,0}} \tag{12}$$

The given condition may not satisfy the two criteria at the same time. The algorithm will stop when both criteria are met.

Appendix B: Direct/indirect cost for CO_2 capture unit of the SMR H_2 plant using GO membrane for CO_2 capture.

Table B-1: Direct/indirect cost for CO_2 capture [1]

Direct Cost	Description			Cost
	Equipment	CO_2 capture	$	6,003,040.00
	Total Equipment Cost		$	6,003,040.00
	Installed cost	*(0.47 * equipment cost)*	$	2,821,428.80
	Piping Cost	*(0.66 * equipment cost)*	$	3,962,006.40
	Instrumentation Cost	*(0.18 * equipment cost)*	$	1,080,547.20
	Electrical	*(0.11 * equipment cost)*	$	660,334.40
	Material Cost	*(membrane cost 30/m2)*	$	802,920.00
	Total Direct Cost		$	15,330,276.80
Indirect Cost				
	Engineering and supervision	*(0.32 * equipment cost)*	$	1,920,972.80
	Construction expenses	*(0.34 * equipment cost)*	$	2,041,033.60
	Total Indirect Cost		$	3,962,006.40
	Total Direct and Indirect Cost		$	19,292,283.20
	Contingency	*(0.1 x direct & indirect cost)*	$	1,929,228.32
	Contractor fee	*(0.05 * direct & indirect cost)*	$	964,614.16
	Total Fixed Capital Investment		$	22,186,125.68

Note 1: TPC of CO_2 removal is calculated based on methodology from "Peters, M.; Timmer Haus, K.; West, R. Plant Design and Economics for Chemical Engineers 5th Edition."

Carbon Dioxide Capture for Storage in Deep Geological Formations, Volume 5
Karl F. Gerdes (Editor)
© 2022 BP. All rights reserved.

Chapter 7

PRELIMINARY PERFORMANCE AND COST EVALUATION OF FOUR ALTERNATIVE TECHNOLOGIES FOR POST-COMBUSTION CO_2 CAPTURE IN NATURAL GAS-FIRED POWER PLANTS

Manuele Gatti[1]*, Emanuele Martelli[1], Federico Capra[1,2], Daniele Di Bona[2], Marco Gabba[2], Francesco Magli[1,2], Roberto Scaccabarozzi[1], Maurizio Spinelli[2], Federico Viganò[1], Stefano Consonni[1,2]
[1] Politecnico di Milano, Department of Energy, Via Lambruschini 4, 20156, Milano
[2] LEAP, Via Nino Bixio 27C, 29121, Piacenza
* Corresponding author

ABSTRACT: The objective of this study is to assess the technical and economic potential of four alternative technologies suitable for post-combustion CO_2 capture from natural gas-fired power plants. These include: (1) CO_2 permeable membranes; (2) Molten Carbonate Fuel Cells (MCFC); (3) Pressurized CO_2 Absorption integrated with multi-shaft gas turbine and Heat Recovery Steam Cycle; and (4) Supersonic Flow-driven CO_2 Anti-sublimation and inertial separation. A common technical and economic framework is defined, and the performance and costs of the systems are evaluated based on process simulations and preliminary equipment sizing. A state-of-the-art NGCC without CO_2 capture is taken as the reference case, and the same NGCC designed with CO_2 capture using MEA absorption is used as a base capture case. The analysis concludes that a combined cycle integrated with MCFC is the most attractive technology, both in terms of energy penalty and economics, with an estimated CO_2 avoided cost of 49 $\$/t_{CO2}$ avoided and SPECCA (Specific Primary Energy Consumption per unit of CO_2 Avoided) equal to 0.31 MJ_{LHV}/kg_{CO2} avoided. The second-best capture technology is the base case amine scrubbing (SPECCA = 3.34 MJ_{LHV}/kg_{CO2} avoided and cost of CO_2 avoided = $\$75/t_{CO2}$ avoided), followed by the supersonic flow driven CO_2 anti-sublimation and inertial separation system and CO_2 permeable membranes.

KEYWORDS: CO_2 capture and storage; post-combustion CO_2 capture; molten carbonate fuel cells; membrane separation; natural gas combined cycle

INTRODUCTION

The IEA views CO_2 Capture and Storage (CCS) as a key technology to reduce power plan CO_2 emissions in an economically sustainable way [1]. To accelerate the pace of deployment, several R&D institutions, industrial technology providers and operators are currently pursuing R&D programs and activities aimed at reducing the CO_2 avoidance cost while demonstrating and improving the commercial maturity of various CCS technologies [2,3].

The CO_2 Capture Project (CCP) views post-combustion CO_2 capture from natural-gas-fired combined cycle (NGCC) operations as a key CCS application [4,5]. This chapter presents the outcome of a preliminary techno-economic study to assess the advantages of four novel post-combustion technologies and to benchmark their performance against conventional technology, namely post-combustion capture by monoethanolamine (MEA). An early version of this work, "Preliminary Performance and Cost Evaluation of Four Alternative Technologies for Post-Combustion CO_2

Capture in Natural Gas-Fired Power Plants", was published by the authors in 2020 (https://doi.org/10.3390/en13030543).

OVERVIEW OF NOVEL CAPTURE TECHNOLOGIES

While successful demonstration of CO_2 capture by amine solvents at large-scale has been invaluable in showing the technical readiness level of this approach [6], the high CO_2 avoidance cost remains a barrier to the adoption of CO_2 capture and storage (CCS) as a climate change mitigation measure [7]. This has spurred the development of different innovative technologies with the objective of improving performance and/or reducing costs [8]. Examples of such technologies are membranes [9], Molten Carbonate Fuel Cells (MCFC) [10,11], capture from pressurized combustion (e.g., as developed by Sargas AS, Norway) [12], and supersonic flow-driven anti-sublimation [13].

Membranes

Selective gas permeable membranes are considered a promising technology for the post-combustion capture of CO_2 from NGCCs. Merkel *et al*. [9] proposed a flow scheme which implements "selective flue gas recirculation" to enhance the application of polymeric CO_2 permeable membranes for CO_2 capture. The flue gas discharged from a combined cycle is cooled down to near ambient temperature, removing most of its water content, and then compressed to a moderate pressure (1.1–3 bar) for feed to a first membrane separator for CO_2 capture. With a cross-flow configuration, this device produces a stream of highly concentrated CO_2, which is sent to a purification step prior to export. However, the first membrane does not completely remove the CO_2, so a significant amount remains in the flue gas, which is fed to a second membrane separator. This second stage utilizes the turbine combustion air as a sweep gas to achieve removal of almost all the remaining CO_2. After the second separation stage, the CO_2-depleted flue gas, optionally expanded in a turbine, is discharged into the atmosphere. The stream of CO_2-enriched air, with a CO_2 content in the range 8.8–16.2 mol%, is used as the oxidant in the gas turbine. The benefits of the selective flue gas recirculation are: (i) the concentration of CO_2 in the flue gas is increased, which reduces the energy penalty for its capture; (ii) the excessive dilution of the air stream at the inlet of the gas turbine that occurs with conventional flue gas recirculation is avoided, since the use of a CO_2-selective membrane minimizes the recycle of other species than CO_2. In particular, (ii) is the crucial aspect of this approach, which makes possible recirculating a high flow rate of CO_2, increasing the CO_2 in the flue gas from 4% to 15%–20% on a molar basis, while keeping the concentration of O_2 in the CO_2-enriched air high enough to be suitable for the normal, albeit off-design, operation of the gas turbine, without requiring significant modification in its design.

Molten Carbonate Fuel Cells (MCFC)

Molten Carbonate Fuel Cells (MCFC) are direct fuel conversion systems, which can be efficiently exploited both as active CO_2 separators and as electricity generators. The concept of using MCFCs as CO_2 concentrators relies on their inherent capability to transfer CO_2 as an oxygen carrier, in the form of carbonate ions (CO_3^{2-}), from the cathode to the anode side, where CO_2 is concentrated because of both this mass transfer and fuel oxidation.

In more detail, at the cathode, O_2 and CO_2 molecules form carbonate ions ($½O_2 + CO_2 + 2e^- = CO_3^{2-}$) by a catalytic reaction promoted by the nickel oxide (NiO) cathode [14}. These ions, produced on the porous surface of the cathode, are then transferred through a selective membrane, where the electrolyte (a liquid potassium/lithium carbonate retained in a $LiAlO_2$ ceramic matrix) conducts the ions to the anode. Fuel to drive the MCFC operation is reformed to produce CO and hydrogen, and Water Gas Shift also produces more H_2, and the reformed mixture flows to the anode. At the anode, CO_3^{2-} ions react with H_2, producing water and carbon dioxide ($CO_3^{2-} + H_2 \leftrightarrow CO_2 + H_2O + 2e^-$). For each CO_3^{2-} ion transferred through the fuel cell membrane, two electrons flow externally in the

opposite direction, generating a current flow. These electrochemical reactions result in CO_2 removal from the cathode stream of the MCFC and concentration in the gaseous effluent exiting the anode side. The removal efficiency depends on the CO_2 utilization factor, which is in turn related to the MCFC area and operating conditions. The anode effluent contains water and unconverted syngas (produced by CH_4 reforming within the cell) in addition to CO_2. The CO_2 can easily be removed from the CO/H_2, which is recycled for fuel use.

One of the most interesting advantages of MCFCs is that the operating temperature, close to 650°C, closely matches with the exhaust conditions of heavy-duty gas turbines (GTs), making the process integration easier. Moreover, nickel surfaces within the fuel cell catalyse the internal fuel reforming of the natural gas (NG) feed to the MCFC.

The use of MCFCs as CO_2 capture devices has been widely studied for applications in coal power plants, IGCC, NGCC and other industrial applications [10], showing the potential for high capture rates with limited energy penalty, especially in the NGCC case. The MCFC can be located between the gas turbine (GT) and heat recovery steam generator (HRSG) of the modified NGCC, where the bottoming steam cycle recovers the heat from both the GT and MCFC [10]. In this configuration, the MCFC can capture up to 80-90% of the total CO_2 released by the fuel combustion and can increase the electric output of the power plant by around 25% [15].

More details of the inner workings of MCFCs and integration with NGCC is found in Chapter 8 of this volume.

Currently, the main issues with use of MCFCs are reliability (tests still ongoing to prove 10 years operation for 1.4 MW_{el} stacks, the basic building blocks of an MCFC system), their limited onstream factor (latest installations [16] are targeting 8000 equivalent hours per year with 95% availability), and costs, which are difficult to predict because there is not yet a mature market [17]. Ahmed *et al*. reports MCFC costs of around 2000 $\$/kW_{el}$ expected at an annual manufacturing volume of 5 MW_{el}, projected to reduce to 1250 $\$/kW_{el}$ if the annual production increases to 50 MW_{el}. Preliminary CCS performance estimates released by FCE [18] (the largest MCFC manufacturer, and focused on CCS from coal) report a CO_2 avoided cost lower than 40 $\$/t_{CO2}$ avoided.

High-Pressure Combustion and Capture

Christensen *et al*. [12] recently proposed a method to remove the CO_2 from NGCC flue gas while it is still at high pressure. In the proposed scheme, a multi-shaft gas turbine (for this study, a GE LMS100 model [19]) is split into a gas generator, producing a stream of flue gas at high pressure and temperature (8 bar and 800°C), and a final expansion stage. For a conventional NGCC, the hot, high-pressure combustion gases are directly expanded to generate power. Instead, the hot, high-pressure stream is cooled by generating steam in a Heat Recovery Steam Generator (HRSG) for a recuperative steam cycle, which produces a significant portion of the electrical power of the overall plant. In an alternative configuration, a pressurized natural gas-fired boiler further heats the hot gases, ahead of the HRSG, while increasing the CO_2 concentration up to 9% mol [12]. In either configuration, a pressurized solvent-based capture system decarbonizes the cooled flue gas, which is then heated via waste heat recovery and finally expanded to atmospheric pressure to generate additional electric power. The capture unit is a hot potassium carbonate solvent-based Benfield absorption scheme designed and licensed by UOP [20]. Other technologies favored by the high CO_2 partial pressure may be applicable. The developers report that the potential advantages of this scheme are: (i) the high CO_2 partial pressure at the inlet of the CO_2 capture section, which should reduce the energy penalty due to capture; (ii) the compact size of the HRSG and of the CO_2 capture section due to higher pressure; and (iii) the maturity of the technology, which involves only conventional units (the LMS100 gas turbine, the well-known Benfield process and a Heat Recovery Steam Cycle).

Compared to other approaches, this technology is readily implementable as a short-term CCS option, with limited investment required for research.

Supsonic Anti-Sublimation

Balepin and Castrogiovanni [21] and Castrogiovanni [13] proposed a process aimed at exploiting the auto-refrigeration of a supersonic acceleration and expansion of flue gas to separate the CO_2 as a solid phase. This concept is not completely new in the field of gas purification, since a similar system has been recently designed and installed for natural gas conditioning [22]. Nevertheless, its application as a post-combustion CO_2 capture technique is new and entails different design and operating conditions. According to the patent [23], flue gas can be derived either from natural gas or coal combustion, and CO_2 is captured via anti-sublimation, followed by inertial separation, both resulting from the supersonic expansion of the gas mixture.

The key equipment of the process is an "Inertial CO_2 Extraction System," which consists of a De Laval nozzle followed by a diffuser [13]. The system is currently being tested and developed, at the bench scale, by Orbital ATK and ACENT Laboratories. Dehydrated pressurized flue gas enters the convergent tube section (subsonic nozzle) of the CO_2 extraction system and passes through a throat designed to achieve sonic conditions. This is followed by a divergent tube section (supersonic nozzle), where the expansion occurs, and supersonic velocities and very low temperatures and pressures are achieved. As a result, the CO_2 freezes into solid particles which migrate to the wall of the tube, as a result of the combination of induced swirl (a large tangential velocity component is induced at the tube entrance by vanes) and higher density of the solid phase compared to the gas. Then a cyclone removes the collected particles such that the remaining gas stream is decarbonized. At the end of this section, another convergent tube (supersonic diffuser) followed by a sonic throat and a divergent tube (subsonic diffuser) discharge the CO_2-depleted flue gas at nearly atmospheric pressure. In both the diffusers, deceleration provides pressure recovery and temperature increase. According to the developers[13], the main advantages of the technology are: (i) the very reduced footprint compared to an amine plant of similar capacity (with potentially less than half of the area required for the installation of the whole system); (ii) the lower energy penalties and cost of CO_2 avoided, estimated to be near to 50 $\$/t_{CO2}$ avoided for the application of the technology to a coal-fired power plant.

OUTLINE OF THE CHAPTER

This study of CO_2 capture from flue gas produced from natural gas sources was commissioned by CCP4 and carried out by a group of LEAP (Laboratorio Energia e Ambiente Piacenza) and GECOS (Group of Energy Conversion Systems) - Politecnico di Milano researchers together with the CCP4 team. This work originates from the initial study reported by Forsyth *et al*. [24] and focuses on the preliminary assessment of the following four promising technologies for post-combustion CO_2 capture from NGCCs:

- CO_2 permeable membranes (MEM)
- Molten Carbonate Fuel Cells (MCFC)
- Pressurized CO_2 absorption integrated with multi-shaft gas turbine and Heat Recovery Steam Cycle (HPS)
- Supersonic flow driven CO_2 anti-sublimation and inertial separation (SSD)

Figure 1 depicts the CO_2 capture concept for each of the novel technologies evaluated.

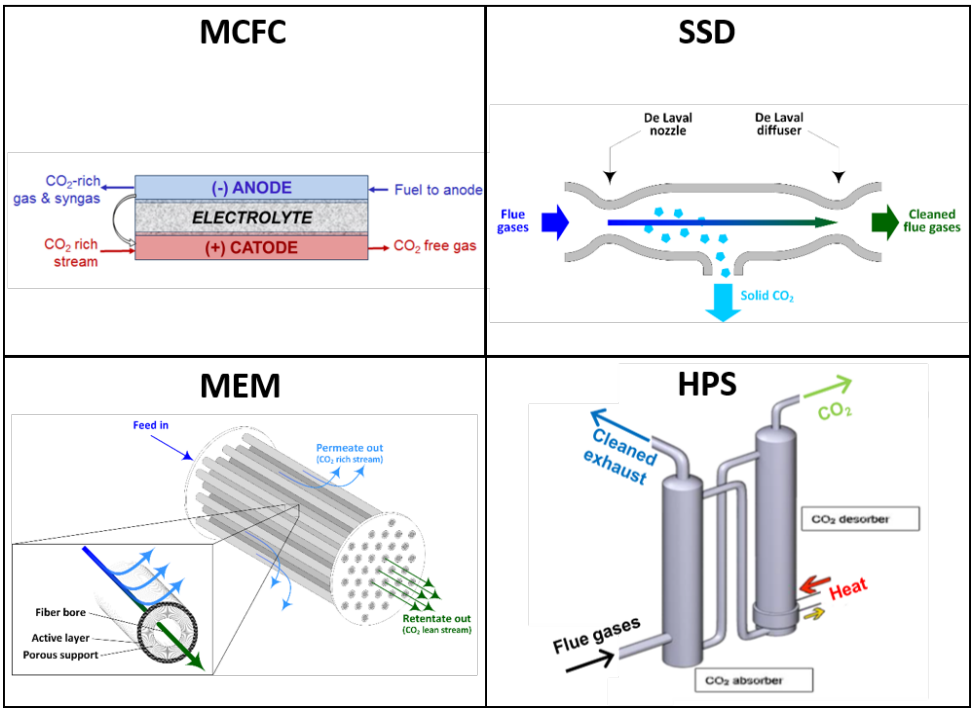

Figure 1. Conceptual representation of the CO_2 capture processes behind the four technologies evaluated in this study.

The chapter is structured as follows. First, the technical and economic framework for the comparative analysis is presented in the next section, which also reports a description, performance and cost figures for the reference NGCC without and with CCS. The following three sections describe in detail the process flow diagram and modelling approach followed to evaluate each of the four novel technologies. Finally, we compare the performance and costs of all the schemes evaluated. Conclusions are presented in the final section.

TECHNICAL AND ECONOMIC FRAMEWORK

Accurate process models (built in Aspen Plus® v8.8 [25], Thermoflex® v24 [26] and GS [27]) are used to make a systematic assessment of the energy and economic performance of the four technologies. The key performance data needed to correctly size and model the equipment used in the capture processes have been provided by the main technology providers or assumed based on the engineering judgment of the participants in this study and their industrial partners. The most significant cost and performance assumptions, for which no industrial feedback or literature data are available, are highlighted and discussed in the process modelling and results sections. The purpose of this high-level evaluation is to perform a consistent comparison between alternative options, while providing recommendations on areas for future work concerning further development of the technologies and their integration with natural gas-fired power plants.

The baseline system of this study is the Natural Gas Combined Cycle described in the CCS European Benchmarking Task Force (EBTF) report [28], which is thought to be representative of the

state-of-the-art of this power generation technology. Table 1 reports the main technical assumptions of the EBTF NGCC (named NGCC w/o capture) study.

Table 1. Key assumptions for the performance evaluation of the NGCC baseline.

Assumption	Units	Value
Plant type	-	Green-field
Location	-	North America - US Gulf Coast (i.e., no particular issues that would alter performance and installation/indirect costs)
Air supply		
Temperature	°C	15
Pressure	bara	1.013
Relative humidity	%	60
Fuel supply		
Temperature	°C	10
Pressure	bar	70
Gas turbine details		
Two F class machines		
Pressure ratio		18.1
Turbine inlet temperature	°C	1360
Net Electric Efficiency	% LHV	38.25
Natural gas pre-heat	°C	160
Heat recovery steam cycle details		
Three pressure levels	bar	130 / 35 / 4
Superheat level	°C	565
Condensing pressure	bar	0.048
Cooling water temperature	°C	18
Flue Gas details (GT exhaust)		
Flow rate	kg/s	1330.6
Pressure	bar	1.04
Temperature	°C	608
Composition		
N_2	%mol	74.38
O_2	%mol	12.39
CO_2	%mol	3.96
H_2O	%mol	8.38
Ar	%mol	0.89

Methodology for Performance Evaluation

The large-capacity, high efficiency gas turbine-based combined cycle (NGCC w/o capture) is designed to generate 830 MW_{el} of net electric power at full load and features a net electric efficiency of 58.30% on a LHV basis. The NGCC uses two "F class" gas turbines paired with two triple-pressure-level Heat Recovery Steam Generators (HRSGs) and a single steam turbine. The performance and the detailed design features (e.g., turbine geometry, cooling system, etc.) of the GTs have been calculated

with the detailed expander model described in Chiesa and Macchi [29]. This approach is consistent with the CCS European Benchmarking Task Force report [28], since the same GT model and assumptions are adopted here. Given the R&D efforts needed to modify the design of a GT, the GT geometry is kept fixed throughout the whole study. Thus, when necessary, the off-design performance of the EBTF gas turbine was assessed with the detailed model from Chiesa and Macchi [29]. This off-design calculation of the GT performance was necessary for the schemes involving flue gas recycle – the MCFC and the membranes. The control strategy adopted for off-design operation uses the compressor Variable Inlet Guide Vanes (VIGV) to adjust the inlet mass flow rate of air while maintaining the turbine inlet temperature at design condition. This control strategy allows the maximization of the turbine electrical efficiency. Assuming that there is sufficient margin in the compressor load to prevent a stall in the compressor stages, the gas turbine is able to work at the same pressure ratio as the design condition (operating without flue gas recycle). For the cooled expansion, the necessary cooling flow rates have been calculated to maintain the same blade metal temperature. These minor adjustments of the cooling flow rates compared to the design condition can be easily performed in practice without redesigning the GT cooling system (e.g., by tuning the control valves placed on the cooling flow circuit). The same HRSC (HRSG and steam turbine) configuration as the EBTF study has been adopted. However, the HRSC performance has not been calculated in the off-design mode. Since this study is based on a green-field plant, the HRSG tube banks, steam turbine and condenser are re-sized for each plant scheme. The HRSC performance has been calculated with the GS code and the model described by Chiesa and Macchi [29].

Three of the four novel technologies (i.e., MEM, MCFC, and SSD) assessed in this work are based on the same GT set of the NGCC w/o capture case, and they include an HRSC as well. The only exception is the High-pressure solvent absorption case (HPS), where the GE LMS100 GT has been adopted, since the HPS case requires an inter-cooled multi-shaft GT.

For the NGCC equipped with capture, the base case utilizes 30% w/w MEA solvent absorption downstream of the EBTF NGCC. The process assumptions and performance results are taken directly from project CAESAR [28]. The steam used to drive the CO_2 desorption from the loaded solvent is taken from the steam turbine between the intermediate and low pressure sections. An electric-drive compressor is used to deliver CO_2 at high pressure (110 bar) ready for pipelining and subsequent geological sequestration or enhanced oil recovery. The key assumptions for this baseline can be seen in **Table 1**. The target purity specification for the CO_2 stream is shown in **Table 2**.

The baseline configurations without and with CCS are defined:

- The Reference plant is the natural gas combined cycle without capture (NGCC w/o capture) described in CAESAR [28].
- The Base plant is the NGCC with MEA-based capture (NGCC + MEA) described in CAESAR [28].

According to CAESAR [28], when MEA-based capture is added to the Reference NGCC, there is a 77 MW_{el} reduction in the gross power generated by the steam turbine, due to steam extraction for solvent regeneration, and the net power is further reduced by 43 MW_{el} required for the CO_2 capture operation, including the CO_2 compressor. The combined effect is a reduction in the net output of the base case by 120 MW_{el} compared to the reference plant and the overall impact is to reduce the net efficiency of the plant from 58% to 50% on a Lower Heating Value (LHV) basis. This is summarised in **Table 3**.

Table 2. Product CO_2 specification for EOR applications.

Parameter	Units	Value
T	°C	30
P	bar	110
Concentration limits	-	-
CO_2	$\%_{mol}$	> 97
H_2O	ppm_v	< 50
N_2 + Ar	$\%_{mol}$	< 3
O_2	ppm_v	< 75

Table 3. Performance of EBTF plant with and without capture.

	EBTF w/o CO_2 capture (reference plant)	**EBTF w/ MEA CO_2 capture (base plant)**
Fuel input, MW_{LHV}	1422.6	1422.6
Gas turbine net power (2 units), MW_{el}	544.2	544.2
Steam cycle net power, MW_{el}	285.7	207.9
CO_2 compressors, MW_{el}	-	-22.6
Other auxiliaries (capture section), MW_{el}	-	-19.9
Power Consumption of capture section, MW_{el}	-	-42.5
Overall net power, MW_{el}	829.9	709.7
Net electric efficiency, $\%_{LHV}$	58.3	49.9
CO_2 captured, %	-	90.5
CO_2 avoided, %	-	88.8
Regeneration thermal energy specific requirement, GJ/t_{CO2}	-	3.96
SPECCA, $MJ_{LHV}/kg_{CO2\text{-}avoided}$	-	3.34
CO_2 emissions, kg_{CO2}/MWh_{el}	351.8	39.3

The novel CO_2 capture technologies were simulated with specific modelling software selected based on the capture process. SSD was simulated with Aspen Plus® [25], MCFC and MEM with GS [27], and HPS with Aspen Plus® [25] and Thermoflex® [26]. The key general assumptions are outlined in **Table 4**, while details on process modelling and specific assumptions for each technology are described in sections which follow. The energy and mass balances calculated for each novel technology flowsheet were used to determine the energy and economic performance of the overall plant.

Table 4. Key assumptions for evaluation of novel capture technologies.

Temperature at outlet of coolers, °C	28
Electric consumption of auxiliaries for cooling, expressed as a % of the heat rejected, %	2
Polytropic efficiency of flue gas compressors, %	90
Polytropic efficiency of flue gas expanders, %	90
Polytropic efficiency of vacuum pumps, %	85
Polytropic efficiency of CO_2 compressors, %	85
Polytropic efficiency of air blowers, %	85
Hydraulic efficiency of CO_2 pumps, %	75
Electric-mechanical efficiency of motor-drivers, %	95
Minimum temperature difference gas-gas heat exchangers, °C	25
Minimum temperature difference liquid-gas heat exchangers, °C	10
Relative pressure drop of heat exchangers - gas side, %	2
Relative pressure drop of heat exchangers - liquid side, bar	0.4

The performance summary tables also report net power output, net electric efficiency, specific CO_2 emissions, and the Specific Primary Energy Consumption for CO_2 Avoided, defined as (Eq. 1):

$$SPECCA\left[\frac{MJ_{LHV}}{kg_{CO2\ avoided}}\right] = \frac{\left(\frac{1}{\eta_{CCS}} - \frac{1}{\eta_{REF}}\right)}{E_{REF} - E_{CCS}} \cdot 3600 \quad (1)$$

Where η denotes the net electric efficiency and E the specific CO_2 emission rate [kg_{CO2} / MWh_e] of the plant. Subscript "REF" refers to the indices of the reference plant NGCC w/o capture, and "CCS" refers to the NGCC equipped with the CO_2 capture technology under investigation.

Methodology for Cost Estimation

For each technology assessed, the cost is estimated using a "bottom-up" approach, where the total plant cost is built up from the equipment items that make up the overall system. This approach reflects the methodology used by EBTF (CaESAR [28], CCP3 [30] and several other research groups [11]). The methodology entails the following steps:

1. Break-down the power plant into basic equipment units or plant subsections.
2. Assume a sizing and cost model for each item defined in step 1.
3. Add installation costs, indirect costs, escalation and contingencies.
4. Compute the operating costs, the First Year Cost of Electricity (COE) and the Cost of CO_2 Avoided (CCA).

The analysis and important economic and financial assumptions are depicted in Figure 2.

The overall capital expenditure required to build the plant on a green-field basis is the Total Plant Cost (TPC). After dividing the power plant flowsheet into relevant subsystems, the Total Equipment Cost (TEC) of each subsystem is calculated. For each piece of equipment, the TEC is calculated, based on size, according to the well-known power-law relationship (Eq. 2):

$$TEC\ [M\$] = C_0 \left(\frac{S}{S_0}\right)^f \quad (2)$$

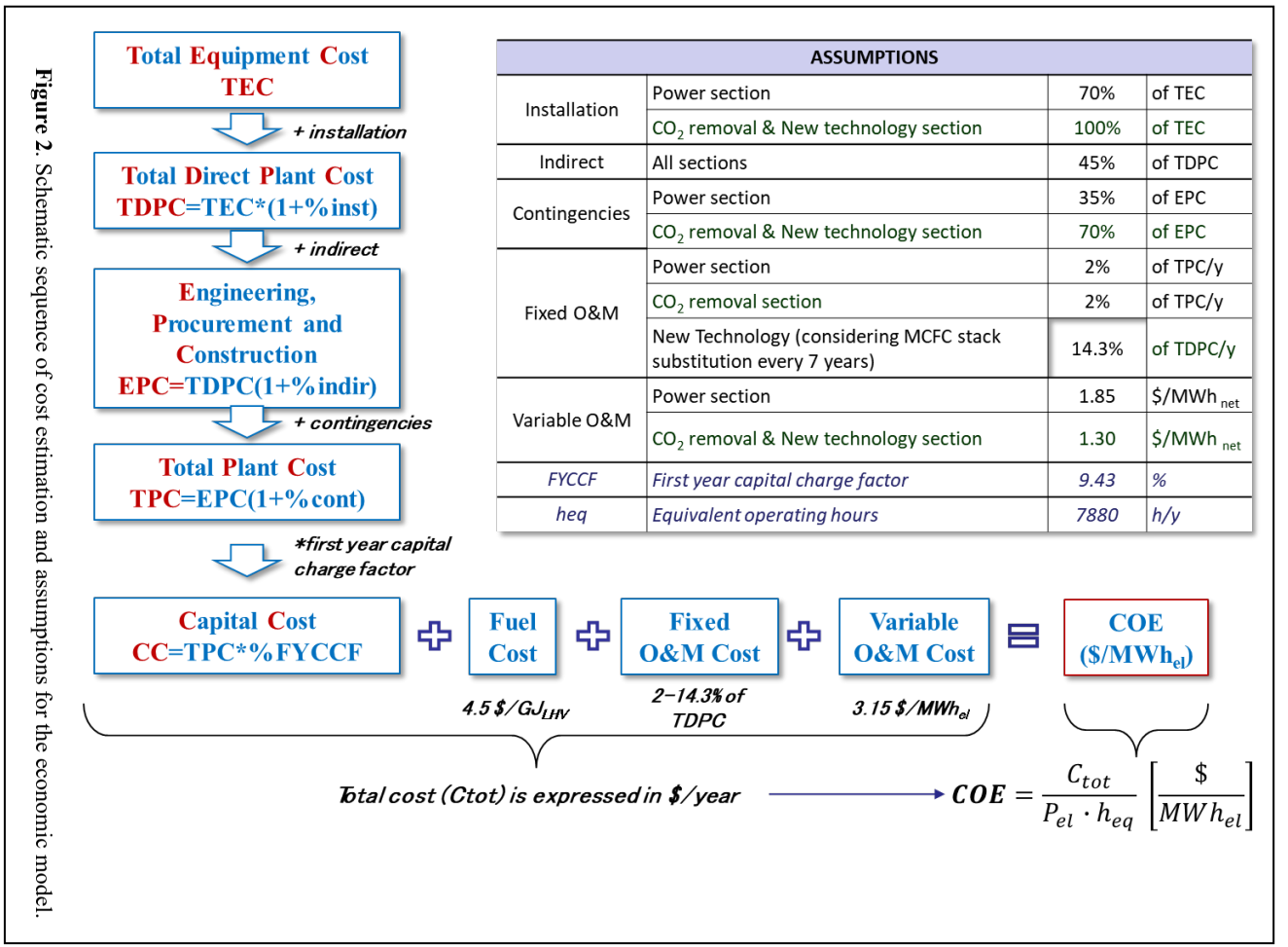

ASSUMPTIONS			
Installation	Power section	70%	of TEC
	CO_2 removal & New technology section	100%	of TEC
Indirect	All sections	45%	of TDPC
Contingencies	Power section	35%	of EPC
	CO_2 removal & New technology section	70%	of EPC
Fixed O&M	Power section	2%	of TPC/y
	CO_2 removal section	2%	of TPC/y
	New Technology (considering MCFC stack substitution every 7 years)	14.3%	of TDPC/y
Variable O&M	Power section	1.85	$/MWh net
	CO_2 removal & New technology section	1.30	$/MWh net
FYCCF	*First year capital charge factor*	*9.43*	*%*
heq	*Equivalent operating hours*	*7880*	*h/y*

Figure 2. Schematic sequence of cost estimation and assumptions for the economic model.

Where *TEC* is the cost in million of $, *S* is the actual size, *f* is the scale factor, and. S_0 and C_0 are the appropriate reference size and cost for the component.

As shown in Figure 2, the installation, indirect and project cost contingency are expressed as a fraction of TEC, TDPC and EPC values. Hence, the Total Plant Cost is obtained by multiplying the TEC by a series of incremental factors (%inst, %indir, %cont in Figure 2). Since the technology readiness level (TRL) of the specific plant sections reflects the extent of engineering and deployment (if any), the contingency percentage factors are different for each of the plant sections. Some components can be reasonably classified as mature technologies (e.g., GT), while other components/subsections (CCS equipment) are still characterized by a lower level of confidence from both the engineering and economic perspectives. As an example, the contingency associated with the capture section is much higher than the value for the power section (70% vs 35%), because the operations in the carbon capture section are characterized by a lower TRL and more limited industrial experience for some key pieces of equipment or plant sections (e.g., MCFC, cryogenic unit, etc.) compared to conventional operations.

Table 5 reports the equipment costs and references adopted for the Base and Reference cases. All the cost values from different sources have been referenced to the same year (2014) by means of the CEPCI escalation index [31] while a 1.329 $/€ exchange rate has been assumed (average value for year 2014).

Table 5. Basis for TEC estimation of the reference NGCC.

Plant component	Scaling parameter	Reference Size S_0		EBTF w/o capture S	EBTF with capture S	Reference Cost C_0	Scale factor f
		Units	Value	Value	Value	M$2014	
GT and auxiliaries	GT Net Power	MW_{el}	272.4	272.12	272.12	67.0	n.a.
HRSG, ducting and stack	UA*	$MW_{th}/{}^{o}K$	10.06	10.675	10.675	31.6	0.67
eST and auxiliaries	ST Gross Power	MW_{el}	293.2	292.8	215.7	49.0	0.67
Cooling water system and BoP	Heat Released	MW_{th}	436.6	470	546	15.5	0.67

*Note: UA is a scaling parameter of heat exchanger (related to the physical size of the unit), defined as the product of the global heat transfer coefficient (U) and the overall heat transfer area (A) of the HRSG.

For the novel technologies, when standard equipment units are considered (e.g., compressors, turbines, pumps, shell & tube heat exchangers, etc.), cost assumptions are made either in agreement with the current industrial state-of-the-art or using Thermoflex® and its cost database PEACE®. Costs of unconventional pieces of equipment were tentatively estimated as described for each technology in the following sections.

Once the TEC is estimated, the installation costs, indirect costs, owner costs and contingencies are estimated using multiplicative factors defined by combining the authors' experience and authoritative

sources such as NETL [32,33], IEA [34] and EIA (U.S. Energy Information Administration)[35]. The location assumed for these cost estimates is North America - US Gulf Coast (a site without any special issues that would alter installation/indirect costs).

The Total Plant Cost (TPC) is calculated from the TEC as described in Figure 2.

1. *Installation cost (INST)*, which accounts for piping, erection, Outside Battery Limits equipment, etc.:
   $INST = A \cdot TEC$ (3)
2. *Indirect Cost (IC),* which accounts for yard improvement, service facilities, buildings, engineering, etc.:
   $IC = B \cdot (1 + A) \cdot TEC$ (4)
3. *Engineering, Procurement and Construction (EPC) cost,* which includes both Direct and Indirect Costs:
   $EPC = TEC + INST + IC = (1 + A) \cdot (1 + B) \cdot TEC$ (5)
4. *Owner's Cost and Contingencies (OCC)*, which accounts for plant planning, commissioning and contingencies:
   $OCC = C \cdot EPC = C \cdot (1 + A) \cdot (1 + B) \cdot TEC$ (6)
5. *Total Plant Cost (TPC)*:
   $TPC = EPC + OCC = (1 + A) \cdot (1 + B) \cdot (1 + C) \cdot TEC$ (7)

The values assumed for the coefficients A, B and C are reported in Figure 2. The power section (i.e., the NGCC) and the CO_2 Removal Section feature different levels of design and capital cost uncertainty, since NGCC plants are technologically mature, whereas CCS plants are not. For this reason, in this work we make a distinction between the "Power section" and the "CO_2 removal section", and the coefficients A, B and C of the latter are significantly higher.

Once the TPC is obtained, the calculation of the First Year Cost of Electricity (COE) includes contributions from the total capital cost, and the cost of fuel, consumables and O&M. These cost values are calculated according to the technical and financial assumptions in **Table 6** and the CCP methodology described in [30]. The analysis is then concluded by calculating the cost of CO_2 Avoided (CCA–eq.8), which is generally recognized as a key metric for the techno-economic evaluation of power systems with CCS. The CCA [\$/t_{CO2}] can be calculated as the ratio between the marginal cost of the electricity for the MCFC+NGCC power plant and the avoided specific CO_2 emission:

$$CCA = \frac{(COE)_{CCS} - (COE)_{REF}}{(e_{CO2})_{REF} - (e_{CO2})_{CCS}} \quad \left[\frac{\$2014}{t_{CO2\ avoided}}\right] \tag{8}$$

The Cost of CO_2 Avoided is determined as follows:

$$CCA\left[\frac{\$}{t_{CO2\ avoided}}\right] = \frac{(COE)_{CCS} - (COE)_{REF}}{(kg_{CO2}kWh^{-1})_{REF} - (kg_{CO2}kWh^{-1})_{CCS}} \tag{9}$$

This cost estimate methodology is meant to reflect industry standards. However, the performance and cost estimates do not include first-of-a-kind costs or exceptional-case risk premiums or contingencies that might be needed for demonstration or first commercial CCS projects.

Based on these assumptions, the capital and operating costs of the reference and base case were estimated.

Table 6. Financial assumptions.

Assumption	Value
Cost and financial	
Location basis	US Gulf Coast
Plant type	Green-field
Cost year basis	2014
Base currency used, $	US Dollars
Average exchange rate (2014), $/€	1.329
Investment lifetime, years	25
Inflation rate, %	2
Discount rate, %	10
First year capital charge factor, %	9.43
Fuel cost, $/GJ (2014)	4.5
Number of equivalent hours, hours equivalent at full load/year	7880

For the Base case plant of this study, the specific total plant cost (i.e., TPC of the full plant with NGCC + MEA units + CO_2 compression and dehydration system) was assumed equal to an average value of 2181 $\$_{2014}$/kW, a figure aligned with the estimates of the most authoritative industrial references (EIA [36], NETL [32], IEAGHG[37]).

The capital cost increase of the "Base" relative to the "Reference" plant is nearly 75% (TPC increases from 879 M$ to 1548 M$), and the Cost of CO_2 avoided is 75 $\$/t_{CO2}$ at a CO_2 capture rate of 90%. These results, which exclude CO_2 transport and storage charges (as all other CCA estimates in this paper), are comparable with the results of similar studies published by the US DOE National Energy Technology Laboratory [32] and the IEA GHG Research and Development programme [37].

SPECIFIC CAPTURE TECHNOLOGY DISCUSSION

CO_2 Permeable Membranes

Polymeric membrane technology has been successfully commercialised for CO_2 separation from natural gas. Such membranes have typically been used where the natural gas contains greater than 10% CO_2 and the feed gas is available at high pressure [38]. In such circumstances the performance and cost of the technology can be more attractive than amine or other types of solvent. However post-combustion CO_2 capture from NGCCs represents a significantly more challenging set of process conditions.

A scheme similar to that proposed by Merkel *et al*. [9] and shown in Figure 3 has been assessed. CO_2 permeable membranes perform three different functions in the flow sheet: (1) to provide selective recirculation of CO_2 to the gas turbine inlet; (2) to separate CO_2 from the CO_2-enriched exhaust gas; and finally, (3) to help separate CO_2 from the incondensable gas stream in the final CO_2 purification section, which also uses a distillation column that separates out CO_2 at -30 °C and 27 bar. In the case considered in this paper, a combination of feed compression to 3 bar and a permeate vacuum of 0.3 bar is used to generate a pressure ratio of 10 for the membrane capture step.

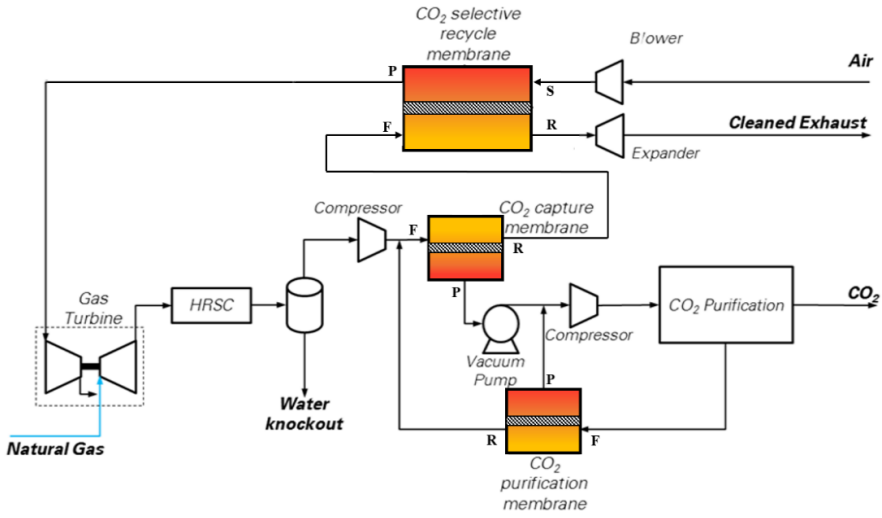

Figure 3. CO_2 capture scheme using CO_2 permeable membranes. Nomenclature of membrane inlet/outlet streams: F = Feed; P = Permeate; R = Retentate; S = Sweep

The following process schemes have been studied and evaluated:

- *MEM-0*: a scheme very similar to the original one published by Merkel *et al*. [9] with only one minor difference: the retentate stream coming from the CO_2 purification membrane is sent downstream of the main flue gas compressor (and not upstream of the water knock-out) as shown in Figure 3. This saves some compression power. The membrane area has been adjusted to reach a high CO_2 removal rate (i.e., 94% CCL).
- *MEM-1*: same configuration as MEM-0 but with a smaller membrane area, adjusted to reach 90% CCL.
- *MEM-2*: same configuration as MEM-0 scheme but featuring lower pressure levels for both the feed (1.7 bar) and the backpressure of capture membrane (0.2 bar). This design explores the performance and economics trade-offs between membrane feed pressure and membrane area. The membrane area has been adjusted to reach 94% CCL.
- *MEM-3*: same as option MEM-2 but featuring a smaller membrane area, reduced so as to reach a CCL equal to 90%.

Hence, one of the goals of this analysis is to understand whether there are economic benefits (i.e., lower CO_2 avoidance costs) from increasing the CCL from the target value of 90% reported by Merkel *et al*. [9].

The EBTF gas turbine was modelled in off-design operation (combustion air diluted with recycled CO_2) with the GS code [27]. The HRSG and steam cycle configuration/design, ambient temperature, cooler exit temperatures, condensing temperature of steam cycle and refrigeration loop were changed to align the assumptions with the EBTF study. The HRSG and steam cycle are re-designed specifically for the flue gas composition, temperature and mass flow rate for the respective cases. The CO_2 purification operation is further discussed in the Results Section and Appendix with regard to achieving the very low residual O_2 specification on the exported CO_2.

Molten Carbonate Fuel Cells

The MCFC power island has been integrated with the baseline NGCC as depicted in Figure 4. Fuel Cell Energy, a provider of MCFC technology, provided guidance on the MCFC equipment, performance, operating conditions, and costs assumed in this study. More detail can be found in [39]. As shown in Figure 4, the anode of the MCFC is fed a mixture of natural gas, recycled unconverted fuel and steam, which undergoes a reforming process. Natural gas and the unconverted fuel are first preheated up to 300°C, sent to the zinc-oxide sulfur removal unit [40] and then heated up to the anode inlet temperature (450°C) by direct mixing with superheated steam (565°C) extracted from the LP section of the steam cycle. In the proposed configuration, the MCFC is placed between the gas turbine and the heat recovery steam generator (HRSG), and separates the CO_2 from the high temperature GT exhaust directly fed to the cathode side of the fuel cell at a temperature of 608°C. This technical choice minimizes the energy penalty associated with the CO_2 capture section, because the cathode reactants (GT exhausts) do not need to be pre-heated to the MCFC's working temperature, and the waste heat released by the fuel cell is recovered for steam production in the HRSG. This MCFC-NGCC integrated scheme exploits synergies between the MCFC and the NGCC and should deliver improved thermodynamic performance relative to either of the stand-alone MCFC and NGCC power plants with post-combustion capture. In this integrated arrangement, the anode exhaust, which contains unconverted H_2 and CO, and the CO_2-rich flow, first produces steam in a HRSG and, then enters the GPU section, where CO_2 is separated from the fuel stream via a cryogenic, auto-refrigerated process similar to the one described by Campanari *et al*. [10]. The unconverted fuel, separated as a vapor phase by the GPU, contains nearly all the H_2 and CO released at the anode, some CH_4 and also a residual amount of CO_2, and is subsequently recycled back to the fuel cell anode. In this way, all the fuel fed to the fuel cell is eventually converted into electricity. As a result, the overall fuel utilization factor approaches 100%, even though the single-pass utilization factor across the MCFC anode is 80%. The anode-side heat recovery section has been designed to avoid metal dusting, which may damage carbon steel surfaces, affecting the durability of the heat recovery section [41,42]. To avoid metal dusting, the mixture of CO_2 and unconverted fuel leaving the MCFC anode is cooled by a quench boiler followed by an economizer (as shown in HEX3 of Figure 4), which raises IP steam at a temperature of 254°C (@35 bara). The high heat transfer coefficient of this quench boiler ensures a wall temperature lower than 350°C, which is generally recognized as a safety limit to prevent metal dusting.

To reduce the MCFC active area and the related investment cost, the fuel cell is assumed to operate with a current density of 1500 A/m^2. The cell is simulated with the GS software, and the voltage and performance are calculated by means of an ad hoc correlation developed on the basis of experimental testing at FCE laboratories. The laboratory fuel cell test rig, which consists of a single cell with an active layer of 250 cm^2, was operated over a wide range of current densities (from 800 up to 1600 A/m^2) using NGCC flue gas and other combustion effluents (CO_2 concentration ranging from 4% to 20%$_{mol}$) as cathode reactants [39]. The MCFC performance correlation computes the Nernst voltage as a function of the average partial pressures of the anode/cathode reactants and of the average temperature. In addition, voltage losses are also evaluated as a function of the composition of the reactants, temperature and current density, which strongly influences the ohmic resistance of the fuel cell. The anode is fed with a mixture of natural gas and recovered syngas, to which is added sufficient steam to achieve a S/C ratio equal to 2. As stated above, the amount of fuel converted in a single pass of the MCFC (U_F) is assumed equal to 80%, whereas the CO_2 utilization factor is limited in order to leave a CO_2 concentration of 1% at cathode outlet to avoid excessive concentration overpotential inside the MCFC.

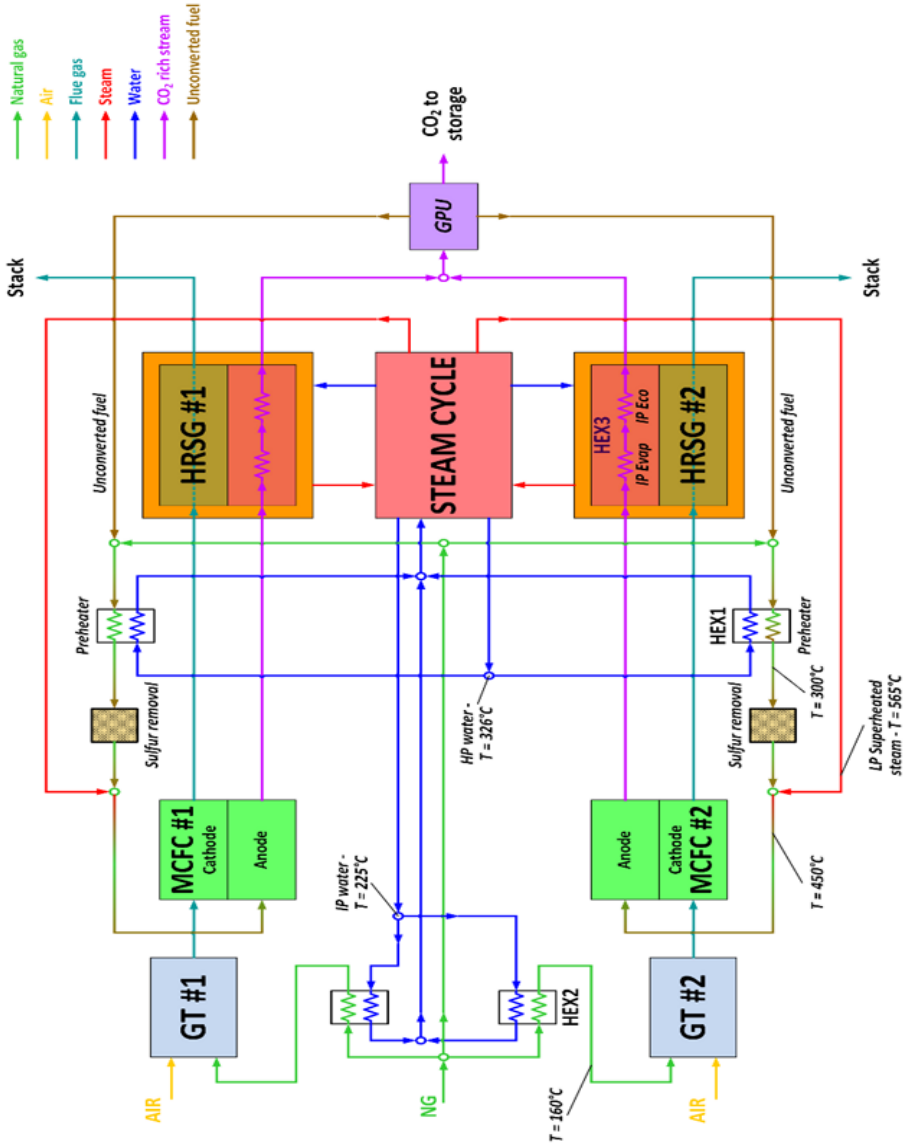

Figure 4. Process flow diagram of the NGCC-MCFC integrated plant.

Long-term experimental tests have shown that the MCFC can achieve such a low CO_2 concentration at the cathode outlet, as reported in the work by Ghezel-Ayagh *et al*.[43]. During these trials, the cathode of a short MCFC stack was fed coal combustion effluent (13.5%$_{mol}$ CO_2 at the cathode inlet), and the CO_2 utilization was maintained constantly higher than 90% (corresponding to a CO_2 concentration at cathode outlet close to 1%$_{mol}$). Furthermore, the flux of CO_2 separated has been varied significantly from 100 up to 180 Ncm^3/m^2/s, where the upper value corresponds to current densities close to 1600 A/m^2. According to Ghezel-Ayagh *et al*. [43], during the long-term experiment, no additional voltage losses (i.e., the polarization curve remains fairly constant over time) or significant material degradation were observed. However, during this test campaign, the short stack was operated with a low current density (~1000A/m^2) for most of the runtime (~8000 h of the total 16000 h). Hence, further long-term experimental testing should be dedicated to demonstrating the durability of MCFC materials, as well as stable operation without significant performance degradation, when both high current densities and high CO_2 utilizations are selected as design parameters.

In the present work, since the MCFC cathode receives the CO_2 in the NGCC exhaust (@3.98% CO_2, 12.39% O_2), the resulting CO_2 utilization is 75.9%. The oxygen utilization (U_{O2}=12.1%) is a direct consequence of the assumption on CO_2 utilization, because each mole of CO_2 transferred from the fuel cell cathode to the anode involves the permeation of 0.5 mol of oxygen, due to the formation of the CO_3^{2-} ion. In this operating condition, the resulting MCFC voltage is 0.7 V, and this determines the waste heat released by the electrochemical process, which is partially exploited to drive the natural gas reforming internal to the MCFC. Because of this heat generation, the anode and cathode streams leave the fuel cell at a temperature of 652°C and are both used for steam production in the HRSC.

Pressurized CO_2 Absorption Integrated with Multi-shaft Gas Turbine and Heat Recovery Steam Cycle (HPS)

An approach to tackle the low concentration of CO_2 in NGCC exhaust gases is to remove the CO_2 from the flue gas via solvent absorption at pressure prior to the final gas turbine expansion stage. This concept [12], shown in Figure 5, is based on a gas turbine which is split into a mechanically-balanced gas generator, which includes two expansion stages, followed by a low pressure expansion section. Among the heavy duty GT sets available, the multi-shaft, intercooled GE LMS100 model is likely to be suitable for this purpose, since it is designed with a three-shaft structure making it theoretically possible to be split into a gas generator (mechanically balanced) and a last expansion stage (LP-GT) which generates a net electric output of 105.6 MW$_{el}$ at ISO conditions (GEpower, [19]).

The gas generator produces hot flue gas at 8 bar and 800°C, and it is followed by a customized heat recovery cycle. Then, the CO_2 capture section, based on the well-known hot potassium carbonate process [20,44], decarbonizes the flue gas. Finally, the CO_2-depleted flue gas, re-heated to 300°C at the exit of the CO_2 capture section, is expanded in the LP-GT to atmospheric pressure.

Two different configurations have been considered in this study:

- HPS-0a, which is based on the flowsheet of Figure 5 and does not include supplementary firing.
- HPS-0b, which features supplementary firing in the pressurized heat recovery steam generator (HPS) located downstream of the gas generator. The additional CO_2, which further increases the flue gas CO_2 concentration, is captured by the downstream post-combustion capture unit.

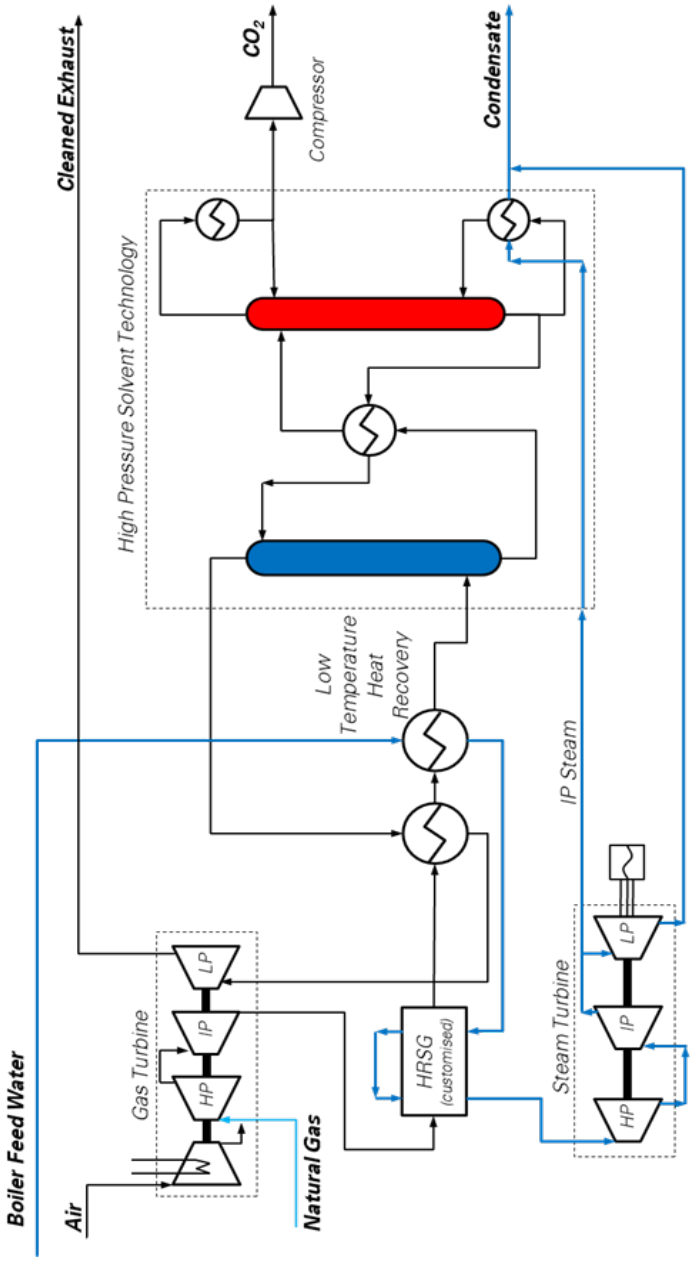

Figure 5. Simplified process flow diagram of the pressurized CO_2 solvent absorption integrated with multi-shaft gas turbine and Heat Recovery Steam Cycle

The energy and mass balances of the HPS unit have been evaluated with detailed Aspen Plus® and Thermoflex® models. The gas turbine performance has been simulated using Thermoflex®, which reproduced the performance of the commercial LMS100PA GT model, including the cooling flows of the expanders. The pressurized boiler and HRSG have been designed according to the EBTF guidelines [28] for advanced Ultra SuperCritical steam cycles (USC), to account for the large amount of thermal power transferred in the HRSG at high temperature (starting from nearly 800°C). The steam cycle features regenerative water pre-heating up to 315°C and requires very high steam turbine inlet temperatures and pressures (e.g., 300 bar and 600°C with re-heat at 60 bar) to fully exploit the thermodynamic potential of the heat transferred in the HRSG.

The hot potassium carbonate solvent scrubbing system was not modelled and cost-assessed in detail, since reliable thermodynamic and transport properties for the solvent and the proprietary activator are not available in the public domain. Therefore, the following assumptions have been made to predict its performance:

- The net specific thermal consumption for solvent regeneration is 2.76 MJ/kg CO_2 separated [44], supplied via LP steam extracted from the steam cycle cross-over at 6 bar.
- The specific electric consumption of the capture process is 308.3 kJ/kg CO_2 separated. This is the average electric consumption of the process reported in the patent by Christensen *et al*. [12].
- Assumed process operating conditions are: absorption at 8 bar, 75°C, CO_2 capture level (CCL) of 90%, and captured CO_2 made available at the top of the stripper at 1.5 bar for subsequent compression. The power consumption for CO_2 compression has been simulated in Aspen Plus® according to EBTF assumptions.

Supersonic Flow Driven CO_2 Anti-Sublimation and Inertial Separation (SSD)

The block flow diagram of the Supersonic flow driven CO_2 anti-sublimation process evaluated in this work is depicted in Figure 6. The scheme resembles those proposed in several studies [23, 45, 46, 47, 48]. The power island is the reference NGCC, which discharges the flue gas directly into the capture island. The flue gas is dehydrated in two stages by first, bulk water condensation and removal in a cooler (operating at 28°C) with a knock-out drum, followed by deep water removal in a molecular sieve drier to achieve the target moisture content of 10 ppm_v. The dried flue gas is compressed using a mulit-stage, inter-cooled compressor to 2 to 5 bar, the operational pressure required at the inlet of the supersonic extraction system, according to Balepin *et al*. [23]. A chiller may be included to pre-cool the compressed gases, which allows CO_2 separation at a lower pressure compared to the case without cooling. Finally, the "Inertial CO_2 Extraction System" carries out the CO_2 separation to produce CO_2 ready for compression, transport and storage, as well as decarbonized flue gas at conditions suitable for the stack.

The performances of this plant (NGCC + SSD) was estimated as follows. The NGCC section is identical to the reference case, and therefore produces 1330.6 kg/s of flue gas at 1.01 bara, 87°C, containing 3.96%$_{mol}$ of CO_2 (corresponding to 81.63 kg/s of CO_2). The conventional equipment units of the capture section (namely, gas cooler, water knock-out drum and intercooled compressor) have been modelled in detail with Aspen Plus®, while the power consumption of the unconventional units (the molecular sieve drier and the auxiliary system for flue gas refrigeration) have been estimated through the assumptions reported in **Table 4**.

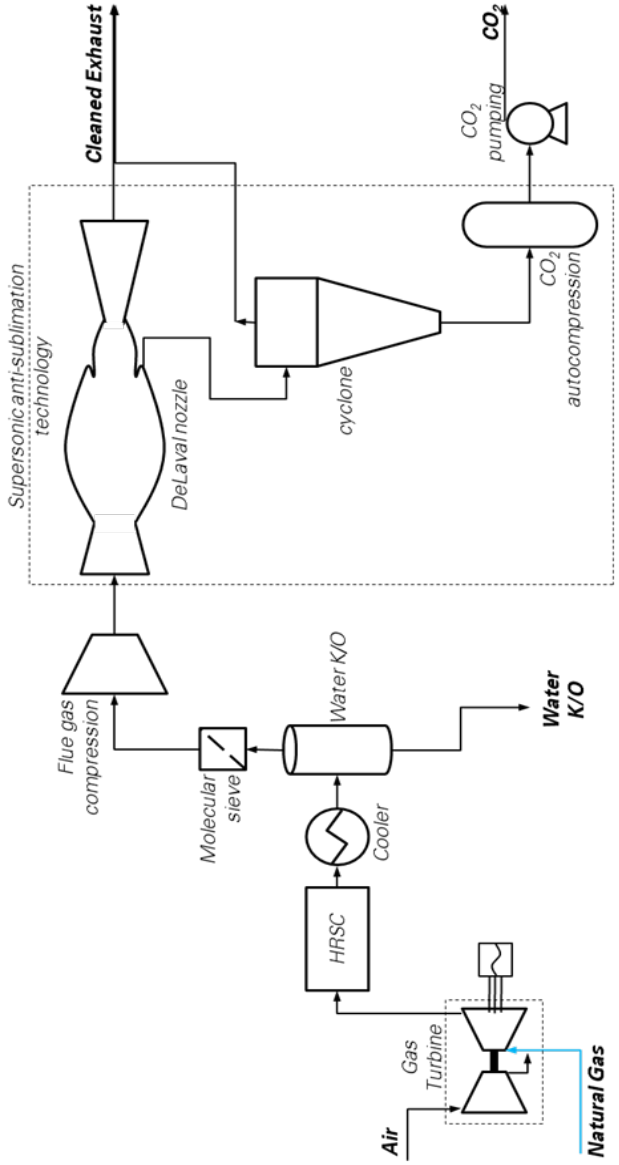

Figure 6. CO_2 capture by supersonic flow-driven deposition (SSD).

It is important to note that accurate modelling of the supersonic CO_2 separator is extremely challenging. The technology is still in early development at the bench scale (TRL-4 according to the developers [13]), and its geometry, set up and balance of plant are likely to be modified in the future. Within the device, many complex physical phenomena occur, including phase-transition in a

multicomponent mixture with particle nucleation and growth, thermodynamic non-equilibrium effects, shock-waves, and marked three-dimensionality of velocity and temperature profiles. Several approaches have been proposed in the literature for the performance assessment of supersonic separators, and they can be classified as follows:

a) Detailed modelling and simulation of the system with a CFD and/or multi-physics approach [47, 49, 50];
b) High level analysis of the system, assuming experimentally-measured performance as an input of the overall technology evaluation (see Hammer *et al*.[48]; Sipocz *et al*., [51]).

Given the existing uncertainty on the configuration of the system, as well as the lack of relevant experimental data required for CFD model calibration, a high-level analysis has been adopted for this analysis. We have assumed the correlation between achievable CO_2 capture level and inlet conditions of the nozzle (pressure and temperature) found by Hammer *et al*.[48]. However, the capture limits and operating conditions adopted in this paper were estimated by Hammer *et al*. [47] from process simulations based on a simplified model (assuming homogeneous phase-equilibrium) and should be taken as theoretical calculations, since they have not yet been confirmed with experimental investigation at the conditions of interest. The difficulty in accurate performance estimation is illustrated by the work of Balepin *et al*. [52]. They reported experimental results from a 3-years R&D project involving several bench-scale test campaigns and process modelling activities aimed at investigating the potential of a "supersonic post-combustion Inertial CO_2 Extraction System". They tested flue gas with CO_2 concentrations ranging from 2.1% to 9.9 %mass but were not able to identify a clear correlation between feed CO_2 concentration, inlet pressure and temperature and achievable CO_2 removal levels. The CO_2 removal was quite variable (half of the tests achieved CCL>50% and only one third of the tests reported CCL>80%). Should relevant experimental data become available in the future, the accuracy of the performance analysis for this technology may be substantially improved.

For this study, five different operating conditions were evaluated by varying the inlet nozzle pressure and temperature within the theoretical ranges identified by Hammer *et al*. [48] and Sipocz *et al*. [51]. The matrix of the cases is reported in **Table 7**, along with the capture rate assumptions. According to Castrogiovanni [13], the supersonic separator should include internal cold recovery (i.e., the solid CO_2 is pressurized and then liquefied by supplying the heat recovered from the flue gas before it is refrigerated) and a so-called "posimetric compressor". Due to the lack of data, no cold recovery has been considered here, and we assume that the CO_2 solid particles are adiabatically compressed from 0.1 to 10 bar as solids, then liquefied and adiabatically pumped to 110 bar in the liquid phase. This results in an overall electricity consumption for CO_2 compression of 13.2 kJ/kg of CO_2 captured. The overall parasitic load for CO_2 capture includes: flue gas compressor power; electric consumption for heat removal from pre-, inter- and after-coolers (equal to 2% of the thermal load); electric consumption by the chiller (where required); electric consumption of the afore-mentioned solid and liquid pumps; electric consumption of drier auxiliaries, assumed equal to 4250 kW_{el}/(ton water removed/h) (IEA[57]).

Table 7. List of the SSD cases evaluated.

	SSD-2.4	SSD-2.7	SSD-3	SSD-4	SSD-5
Pressure at supersonic nozzle inlet, bara	2.4	2.7	3	4	5
Temperature at supersonic nozzle inlet, °C	-7	2	11	28	28
CO_2 capture rate (Hammer *et al*., 2014), %	90	90	90	90	90

RESULTS AND DISCUSSION

CO_2 Permeable Membranes

For this study, membrane calculations were based on a CO_2 permeance of 2200 gpu across the membrane, and on selectivities back-calculated from Merkel *et al*. [9] and reported in **Table 8**.

Table 8. Membrane selectivity with respect to CO_2.

	CO_2/N_2	CO_2/O_2	CO_2/Ar	CO_2/H_2O
Selectivity	50	25	50	0.6

Based on these selectivities, the compositions of the key process streams for the three main cases assessed are shown in **Table 9**.

Table 9. Purities of relevant streams across the CO_2 capture membrane and of the dense-phase CO_2 purified by the cryogenic separation unit.

	Feed stream CO_2 capture membrane			Permeate stream CO_2 capture membrane			Purified CO_2 stream after cryogenic/ membrane purification		
Case	CO_2 [%mol]	O_2 [%mol]	Balance [%mol]	CO_2 [%mol]	O_2 [%mol]	Balance [%mol]	CO_2 [%mol]	O_2 [%mol]	Balance [%mol]
MEM1	22.48%	8.22%	69.30%	82.83%	2.20%	14.97%	97.39%	0.77%	1.84%
MEM2	18.07%	8.47%	73.46%	72.41%	3.27%	24.32%	97.37%	0.79%	1.84%
MEM3	18.86%	8.42%	72.72%	73.91%	3.02%	23.07%	97.37%	0.79%	1.84%

Table 10 summarizes the thermodynamic performance for the membrane-based options evaluated. None of the membrane cases achieve as low an energy penalty for CO_2 avoidance as the base case amine. The SPECCA for the membrane options ranged between 3.4 and 4.3 $MJ_{LHV}/kg\ CO_2$-avoided compared to the Base case value of 3.34 (**Table 3**). As shown in **Table 10**, the energy penalty caused by the auxiliary power consumption of the membrane capture section is between 8.5 and 10.5% of the fuel input (LHV basis). This results in net electric efficiency of the membrane cases less than 50%. Increasing the CO_2 Capture Level (CCL) from 90% to 94% does not provide significant benefits in terms of SPECCA, since larger membranes with greater pressure losses and higher auxiliary power

are required. The most significant thermodynamic penalty items are flue gas compression (between 40 and 60% of the overall penalty) and subsequent CO_2 purification and liquefaction within a dedicated GPU. Depending on the application, further CO_2 purification may be needed. For example, if EOR applications are envisaged (see **Table 2**), the purity of the CO_2 captured with membranes does not meet the specifications, especially for O_2 content (**Table 9**), which is two orders of magnitude above the 75 ppm_v limit typically required for EOR. In this case, a more sophisticated purification system is required, which affects both the overall performance and costs, compared to the cases studied in this work. This is further discussed below.

The cost analysis of cases MEM-1, MEM 2 and MEM-3 is reported in **Table 11**, and the COE and the Cost CO_2 Avoided (CCA) are presented in **Table 12**. The equipment cost of the membrane module is assumed equal to 50 $\$/m^2$, an optimistic value which is the target reported by polymeric membrane manufactures (Merkel *et al*. [9] identifies 50-500 $\$/m^2$ as a realistic range). O&M costs assume that the membrane material is durable and capable of long service life (a full module replacement every 10 years has been assumed).

The COE of membrane configurations (**Table 12**) lies in a range between 71 and 78 $\$/MWh_{el}$. MEM-1 is the configuration with the lowest CCA (86 $\$/t_{CO2}$ avoided) due to smaller EGR membrane and CO_2 membrane area. Cases with 90% CCL show lower CO_2 avoidance costs compared to 94% CCL cases, which are affected by the higher cost of the CO_2 capture and EGR membrane area. Although the case studies which assumed lower flue gas compression and lower pressure on the permeate side of the CO_2 Capture membrane were more energy efficient, they had higher CCA, due to higher equipment cost.

In cases MEM-0, through MEM-3, the CO_2 purification unit consists of a simple cryogenic column operating at a bottom temperature of -30°C and 25 bar and a purification membrane that pulls out a further portion of the CO_2 in the overhead gas and recycles the remaining to the front of the process. As shown in **Table 9**, the CO_2 product fails to meet the O_2 specification of < 75 ppm for EOR operations. The Appendix documents a follow-on study considering the optimization of the purification unit to meet CO_2 specification.

Table 10. Summary of thermodynamic performance for membrane-based capture.

	MEM-0	MEM-1	MEM-2	MEM-3
Fuel input, MW_{LHV}	1515.33	1517.85	1488.48	1494.68
Gas turbine net power (2 units), MW_{el}	542.52	542.90	538.18	539.18
Steam cycle net power, MW_{el}	340.44	341.35	330.07	332.42
Flue gas compression / expansion, MW_{el}	-92.81	-92.19	-53.28	-53.18
Vacuum pump, MW_{el}	-13.24	-12.61	-19.67	-18.37
Air blower, MW_{el}	-9.31	-9.33	-10.03	-9.98
CO_2 compressors, MW_{el}	-26.91	-25.58	-31.75	-29.24
CO_2 purification unit, MW_{el}	-9.80	-9.60	-10.26	-9.77
Other auxiliaries (capture section), MW_{el}	-7.17	-7.13	-6.56	-6.50
Power Consumption of capture section, MW_{el}	-159.24	-156.44	-131.55	-127.04
Overall net power, MW_{el}	723.7	727.8	736.7	744.5
Net electric efficiency, $\%_{LHV}$	47.8	48.0	49.5	49.8
Specific CO_2 emission, g/kWh_{el}	25.8	42.8	24.9	41.2
CCL, %	94.0	90.0	94.0	90.0
CO_2 avoided, %	92.7	87.8	92.9	88.3
SPECCA, $MJ_{LHV}/kg_{CO2\text{-}avoided}$	4.19	4.33	3.37	3.40

Table 11. Main results of equipment cost assessment for membrane.

	MEM-1	**MEM-2**	**MEM-3**
CO_2 capture membrane area, m^2	68466	217520	188640
EGR membrane area, m^2	734600	2248000	1944480
Purification membrane area, m^2	352	711	602
Equipment cost of GT, M$	167	166	166
Equipment cost of Steam Cycle, M$	143	142	141
Total Equipment Cost of power section, M$	310	308	307
Equipment cost of capture and purification membrane, M$	3	11	9
Equipment cost of EGR membrane, M$	37	112	97
Equipment cost of CO_2 compressors	20	24	22
Equipment cost of CO_2 purification unit	10	11	10
Equipment cost of CO_2 removal section auxiliaries, M$	64	45	47
Total Equipment Cost of CO_2 removal section, M$	135	203	186

Table 12. Membrane economic evaluation of membrane-based schemes.

Parameter	Unit	EBTF w/o capture	MEM-1	MEM-2	MEM-3
Power Section TEC	[M$2014]	264	310	308	307
Power Section TPC	[M$2014]	879	1033	1024	1022
CO_2 Removal Section TEC	[M$2014]	-	135	203	186
CO_2 Removal Section TPC	[M$2014]	-	664	999	919
Total TPC	[M$2014]	879	1697	2022	1941
Net Power	[MW_{el}]	829.90	727.8	736.7	744.6
Efficiency LHV	[%]	58.30	48.00	49.50	49.80
Fuel cost	[M$]	182	194	190	191
Fixed O&M	[M$]	18	38	53	50
Variable O&M	[M$]	12	18	18	18
First year capital charge	[M$]	294	410	452	442
COE	[$/$MWh_{el}$]	45.0	71.4	77.8	75.3
CO_2 captured	[kg/s]	-	79.23	79.72	76.65
CO_2 emissions	[kg/s]	-	9.09	5.55	8.99
Specific CO_2 emissions	[kg/MWh_{el}]	351.80	44.97	27.14	43.48
Specific CO_2 avoidance	[kg/MWh_{el}]	-	306.83	324.66	308.32
CCA	[$/t]	-	86.1	101.2	98.4

Molten Carbonate Fuel Cells

The energy performance of the MCFC integrated with NGCC is shown in **Table 13**. MCFC power production is basically defined by the choice of the current density (1500 A/m^2) and the mass flow rate of CO_2 captured, which is almost 80% of the carbon introduced with the natural gas to fuel the gas turbine and the fuel cell section. The choice of the current density defines the MCFC voltage, as characterized by the polarization curve, The flow rate of CO_2 transferred from cathode to anode determine the total current circulating within the MCFC modules. For the case studied here, the fuel cell has a capacity of 179.1 MW_{el}. Most of the energy losses caused by the over-potential within the MCFC are recovered in the Heat Recovery Steam Cycle (HRSC) unit, because the waste heat released by the fuel cell is exploited for steam production within the HRSC. The added steam production increases the HRSC power output with respect to the baseline EBTF case, reaching a value of 306 MW_{el}, and the overall power increases to 983.4 MW_{el} (+18.5%). Due to the high efficiency of the capture section, the SPECCA index is very low (0.31 MJ_{LHV}/kg_{CO2} avoided), with a CO_2 capture rate close to 80%. Interestingly, if the power consumption of CO_2 purification and compression are excluded, the SPECCA index could become negative, with the overall net electric efficiency exceeding the reference NGCC and CO_2 avoided larger than the CO_2 capture rate. However, the gas purification unit is essential for the operation of the plant, not only for bringing the CO_2-rich stream to the storage conditions, but also for recovering the unconverted syngas leaving the MCFC anode. If the system was operated without the auxiliary flash separation, the fuel utilization factor would be limited by the single passage utilization factor inside the MCFC (U_F=0.8), resulting in loss of 20% of the energy in the NG fed to the fuel cell modules.

Table 13. MCFC Performance evaluation outcomes (MCFC-1).

NGCC Fuel input, MW_{LHV}	1423.1
Gas turbine net power (2 units), MW_{el}	542.9
Steam cycle net power, MW_{el}	305.6
MCFC Fuel Input, MW_{LHV}	286.3
MCFC net power, MW_{el}	179.1
Flue gas fan, MW_{el}	-2.35
CO_2 compressors, MW_{el}	-41.58
Other auxiliaries (pumps), MW_{el}	-0.224
Total fuel input, MW_{LHV}	1709.4
Overall net power, MW_{el}	983.38
Net electric efficiency, %LHV	57.5
Specific CO_2 emission, g/kWh_{el}	72.1
CCL, %	79.8
CO_2 avoided, %	79.5
SPECCA, $MJ_{LHV}/kg_{CO2\text{-}avoided}$	0.31

The equipment cost estimates of both the NGCC and MCFC units are shown in **Table 14**. The specific equipment cost of the MCFC + BoP section is considerably higher than calculated for the GT+HRSC section (555 $/kW_{el}$ vs 316 $/kW_{el}$). The equipment cost of the compression and purification unit is less than 50% of the MCFC investment. The specific total plant cost (specific TPC, see Table 15) of the MCFC system, including all BoP items, is 3300 $/kW_{el}$ (TPC of MCFC+BoP+blower+heaters+ quench boiler equal to 591 M$ with a net MCFC power output of 179.1 MW_{el}) a figure close to the lower bound of the installed cost-range, 3500-5500 $/kW_{el}$, reported by DOE [53]). This reported range is assumed to represent year 2010 market status for a 2.8 MW_{el} CHP system, at a production volume of 30 MW_{el} per year. According to DOE projections made in 2011, the 10 year-forward specific installed cost target was 1500 $/kW_{el}$, assuming a production volume of 100 MW_{el} per year. Even though the MCFC cost level has decreased remarkably over the last 20 years [11], according to DOE targets [53] there is potential for further cost improvements in the future.

Table 14. MCFC cost evaluation outcomes.

Equipment cost of GT, M$	134
Equipment cost of Steam Cycle, M$	136
Total Equipment Cost of power section, M$	269
Equipment cost of MCFC + BOP, M$	99
Equipment cost of CO_2 purification unit, M$	44
Equipment cost of flue gas blower, M$	2
Equipment cost of fuel heaters, M$	7
Equipment cost of quench boilers, M$	13
Total Equipment Cost of CO_2 removal section, M$	164

Even though the integration of the MCFC (with BoP and CO_2 purification auxiliaries) causes a 94% increase in the overall capital cost, the high efficiency of the added power output from the MCFC (i.e., only 0.8 percentage points lower than the reference NGCC w/o CCS) of this combination achieves attractive economics. As reported in **Table 15**, the cost of electricity shows a moderate increase with respect to the Reference case (58.8 $/MWh_{el}$, about 30% higher than EBTF [28]),

resulting in a cost of CO_2 avoided less than 50 $/t$_{CO2}$. This cost is considerably lower than the base capture technology (NGCC with MEA-based capture).

In this evaluation, the integration of MCFC with the NGCC appears to be competitive in terms of power production efficiency and capture cost, although a large proportion of the cost is for the new technology section, which is characterized by a high degree of cost uncertainty. In particular, the fuel cell cost assumed in the present estimate, though not too far from current market values, is based on future mass-production of the stack components (i.e., hundreds of MW_{el} per year). Furthermore, the economics are calculated assuming a conventional MCFC lifetime (i.e., 7 years), even though the MCFC operating conditions in this application reflects the CCS requirements (high CO_2 utilization factor, U_{CO2} = 80% and low voltage, 0.7 V) which have not yet been tested for sustained operations. In particular, high over-potential and the related waste heat could affect the integrity of the electrolyte and the electrodes. The durability of these critical components should be demonstrated by long period testing under CCS conditions. With the understanding that the MCFC integration with the combined cycle needs development and demonstration, we can conclude that:

- The MCFC integration provides an increase in power plant output, as well as a strong decrease in specific CO_2 emissions (-80%) with only a low power production efficiency penalty;
- Metal dusting represents an issue for the materials of the heat exchanger network and adds complexity to the design of the anode gas heat recovery section (CO-rich exhausts);
- The maximum CO_2 capture efficiency is limited by the constraint on the minimum CO_2 concentration at the cathode outlet ($X_{CO2,MIN}$=1%) and reaches a value close to 80%.
- The key technical and economic performance indicators look promising: SPECCA = 0.3 $MJ_{LHV}/kg_{CO2\text{-}avoided}$, CCA = 50 $/t$_{CO2}$.
- The long-term durability of electrolyte materials should be proven experimentally for the present case, where the MCFC is operated in CCS conditions (i.e., high CO_2 utilization factor) and with high current density (Ic=1500 A/m^2).

Table 15. MCFC general performance and costs evaluation.

Parameter	Units	EBTF w/o capture	MCFC-1
Power Section TEC	[M$2014]	264	269
Power Section TPC	[M$2014]	879	879
CO_2 Removal Section TEC	[M$2014]	-	164
CO_2 Removal Section TPC	[M$2014]	-	823
Total TPC	[M$2014]	879	1702
Net Power	[MW_{el}]	829.9	983.38
Efficiency LHV	[%]	58.30	57.53
Fuel cost	[M$]	182	218
Fixed O&M	[M$]	18	53
Variable O&M	[M$]	12	24
First year capital charge	[M$]	294	456
COE	[$/$MWh_{el}$]	45.0	58.8
CO_2 captured	[kg/s]	-	77.8
CO_2 emissions	[kg/s]	-	19.70
Specific CO_2 emissions	[kg/MWh_{el}]	351.8	72.12
Specific CO_2 avoidance	[kg/MWh_{el}]	-	279.7
CCA	[$/t]	-	49.4

Pressurized CO_2 Absorption Integrated with Multi-shaft Gas Turbine and Heat Recovery Steam Cycle (HPS)

Table 16 reports the performance metrics of the HPS configurations analyzed. Since detailed analysis of the concept requires specification of a specific type of gas turbine that is different from the one used for the reference case, the results cannot be directly compared with the original EBTF NGCC scheme. For this HPS scheme, the LMS100 GT power output is smaller than that of the turbine specified for the EBTF reference case. In the case with supplementary firing HPS-0b, the steam cycle power output increases by 300% compared to the base case HPS-0a. For both HPS options, the steam cycle generates most of the power. This is a characteristic of the HPS concept that differs from standard NGCCs with and without CO_2 capture.

This assessment reveals that the supplemental firing case (HPS-0b) has slightly better energy performance than the base case (HPS-0a) for the following reasons:

- Higher concentration of CO_2 in the flue gas (9.0% for HPS-0b compared to 3.9% for HPS-0a).
- Improved heat integration between hot flues gases and steam cycle.

However, these two positive effects for case HPS-0b are offset by the pressure losses due to the post-combustor and by the reduction of flue gas mass flow rate. The increased pressure losses in the flue gas line cause a reduction in the pressure ratio of the LP gas expander (since CO_2 lean gas expansion begins at a lower pressure compared to the base case, HPS-0a, decreasing from 7.7 bar to 7.2 bar). Furthermore, in HPS-0b, the removal of CO_2 and water across the capture unit causes a considerable decrease of mass flow rate of flue gas entering the LP gas expander (from 407.6 kg/s of HPS-0a to 363.0 kg/s of HPS-0b). The combination of these two effects leads to the reduction of the gas turbine power output from 95.2 MW_{el} to 83.7 MW_{el}.

For both cases, the overall plant efficiency is around 40%, which is lower than the base solvent case. The main reason for such low efficiency is the large flue gas temperature drop of 500°C between the exit of the gas generator (high-pressure expander) and the inlet of the power expander (low pressure expander).

Table 16. High Pressure Capture performance metrics.

	HPS-0a Base Case	**HPS-0b Sup. Firing**
Fuel input, MW_{LHV}	488.30	1087.22
Gas turbine net power (2 units), MW_{el}	95.16	83.72
Steam cycle net power, MW_{el}	114.55	384.61
CO_2 compressors, MW_{el}	-9.36	-20.76
CO_2 purification unit, MW_{el}	-7.78	-17.24
Power Consumption of capture section, MW_{el}	-17.14	-38.00
Overall net power, MW_{el}	192.57	430.33
Net electric efficiency, %LHV	39.44	39.58
Specific CO_2 emission, g/kWh_{el}	53.5	53.1
CCL, %	90.0	90.0
CO_2 avoided, %	84.78	84.89
SPECCA, $MJ_{LHV}/kg_{CO2\text{-}avoided}$	9.91	9.79

The results of the economic analysis are shown in **Table 17** and **Table 18**. The most uncertain cost figures are the hot potassium carbonate plant cost and the pressurized HRSG cost. For the first item, we used a specific $\$/t_{CO2}$ value reported by UOP [44]. For the second item, we corrected the cost estimate of a standard HRSG with a pressure factor typically used for heat exchangers [54].

The capture section, including the pressurized steam generator, represents around 20% of the total equipment cost of the plant, while, as expected, the cost of the steam cycle more than doubles in the supplementary firing case (HPS-0b).

Table 17. HPS main results of equipment cost assessment.

	HPS-0a Base Case	**HPS-0b Sup.Firing**
Benfield plant CO_2 captured flow rate, kg/s	25.77	57.13
Pressurized HRSG exchange area, m^2	17436	26305
Equipment cost of GT, M$	89	89
Equipment cost of Steam Cycle, M$	33	75
Total Equipment Cost of power section, M$	121	164
Equipment cost of hot potassium carbonate plant, M$	7	14
Equipment cost of Pressurized HRSG, M$	7	10
Equipment cost of CO_2 compressors, M$	10	18
Equipment cost of CO_2 removal section auxiliaries, M$	3	3
Total Equipment Cost of CO_2 removal section, M$	27	44

Due to economy of scale, mainly related to the large steam cycle system, the supplementary firing configuration has better economic performance than the base case. **Table 18** shows that the cost of

electricity decreases from 86.1 $/MWh$_{el}$ to 71.0 $/MWh$_{el}$ and the Cost CO_2 Avoided is almost 40% better compared to the case HPS-0a, dropping from 137.9 $/t$_{CO2}$ to 87.1 $/t$_{CO2}$.

Table 18. Economic evaluation of HPS schemes.

Parameter	Units	EBTF w/o capture	HPS-0a Base Case	HPS-0b Sup.Firing
Power Section TEC	[M$2014]	264	121	164
Power Section TPC	[M$2014]	879	404	544
CO_2 Removal Section TEC	[M$2014]	-	27	44
CO_2 Removal Section TPC	[M$2014]	-	135	216
Total TPC	[M$2014]	879	539	760
Net Power	[MW]	829.90	192.60	430.30
Efficiency LHV	[%]	58.30	39.40	39.60
Fuel cost	[M$]	182	62	139
Fixed O&M	[M$]	18	11	15
Variable O&M	[M$]	12	7	15
First year capital charge	[M$]	294	131	241
COE	[$/MWh$_{el}$]	45.0	86.1	71.0
CO_2 captured	[kg/s]	-	25.77	57.13
CO_2 emissions	[kg/s]	-	2.86	6.35
Specific CO_2 emissions	[kg/MWh$_{el}$]	351.80	53.52	53.10
Specific CO_2 avoidance	[kg/MWh$_{el}$]	-	298.28	298.70
CCA	[$/t]	-	137.9	87.1

Supersonic Flow Driven CO_2 Anti-Sublimation and Inertial Separation (SSD)

The performance metrics for cases with SSD separator inlet pressures ranging from 2.4 to 5 bar are summarized in Table 19. The dominant energy penalty for this technology is the power consumption for flue gas compression from 1 bar to the SSD inlet pressure, which accounts for 79% to 95% of the overall energy penalty. When the SSD inlet pressure is increased from 2.4 bar to 5 bar, the SPECCA increases from 4.36 to 8.14 MJ$_{LHV}$/kg CO_2-avoided, indicating that the best option from an energy perspective is the 2.4 bar case, which also requires the smallest axial compressor with fewer stages.

However, according to the most recent experimental investigations [13], an SSD inlet pressure close to 2 bar is considered too low to achieve 90% capture. Given the lack of data on the SSD sub-system cost, an economic assessment has been carried out only for one representative case, SSD-3, and results are reported in **Table 20** and **Table 21**. It is important to note that the estimated equipment cost of the SSD sub-system (100 M$), which is the cost of the units within the dotted rectangle in the flowsheet of Figure 6, should be taken just as an order of magnitude estimate, given the very limited TRL of the technology and the uncertainties in the full-scale design of the separator. The cost estimates of compressors and other auxiliaries of the capture island are more accurate since these are conventional pieces of equipment.

The resulting CCA cost (equal to 97.1 $/t$_{CO2}$ for the case at 3 bar) highlights the need to improve SSD performance to increase its competitiveness as a stand-alone post-combustion capture technology for NGCC plants. However, given the large uncertainty affecting the technology, it is difficult to draw conclusions on its economic performance.

Table 19. SSD performance metrics.

	SSD-2.4	**SSD -2.7**	**SSD -3**	**SSD -4**	**SSD -5**
Fuel input, MW_{LHV}	1422.6	1422.6	1422.6	1422.6	1422.6
Gas turbine net power (2 units), MW_{el}	544.2	544.2	544.2	544.2	544.2
Steam cycle net power, MW_{el}	285.7	285.7	285.7	285.7	285.7
Flue gas compressor, MW_{el}	-127.2	-143.2	-157.9	-192.0	-226.7
SSD system auxiliary consumption, MW_{el}	-22.1	-17.5	-14.2	-10.4	-11.2
Power consumption of capture section, MW_{el}	-149.3	-160.7	-172.1	-202.4	-237.9
Overall net power, MW_{el}	680.6	669.2	657.8	627.5	592.0
Net electric efficiency, $\%_{LHV}$	47.8	47.0	46.2	44.1	41.6
Specific CO_2 emission, g/kWh_{el}	43.2	43.9	44.7	46.8	49.6
CCL, %	90	90	90	90	90
CO_2 avoided, %	87.8	87.6	87.4	86.8	86.0
SPECCA, $MJ_{LHV}/kg_{CO2\text{-}avoided}$	4.36	4.78	5.22	6.48	8.14

Table 20. SSD equipment costs.

	SSD-3
SSD system flue gas flow rate, kg/s	1260
Equipment cost of GT, M$	134
Equipment cost of Steam Cycle, M$	130
Total Equipment Cost of power section, M$	264
Equipment cost of flue gas compressor, M$	46
Equipment cost of SSD system, M$	100
Equipment cost of CO_2 removal section auxiliaries, M$	13
Total Equipment Cost of CO_2 removal section, M$	159

Table 21. SSD economic evaluation.

Parameter	Units	EBTF w/o capture	SSD -3
Power Section TEC	[M$2014]	264	264
Power Section TPC	[M$2014]	879	879
CO_2 Removal Section TEC	[M$2014]	-	159
CO_2 Removal Section TPC	[M$2014]	-	782
Total TPC	[M$2014]	879	1661
Net Power	[MW_{el}]	829.90	657.80
Efficiency LHV	[%]	58.30	46.20
Fuel cost	[M$]	182	182
Fixed O&M	[M$]	18	33
Variable O&M	[M$]	12	16
First year capital charge	[M$]	294	388
COE	[$/$MWh_{el}$]	45.0	74.8
CO_2 captured	[kg/s]	-	73.46
CO_2 emissions	[kg/s]	-	8.16
Specific CO_2 emissions	[kg/MWh_{el}]	351.80	44.66
Specific CO_2 avoidance	[kg/MWh_{el}]	-	307.14
CCA	[$/t]	-	97.1

CONCLUSIONS

This section compares the preliminary technical and economic assessments of four alternative technologies suitable for post-combustion CO_2 capture from NGCC exhaust gases.

Figure 7 compares the thermodynamic performance (SPECCA) of the cases investigated. Based on the results of this assessment, the only technology superior to the base case is MCFC, which has a very low SPECCA index (0.31 MJ_{LHV}/kg CO_2-avoided). The most promising configuration of membranes is estimated to achieve an energy penalty comparable to the base case (3.37 MJ_{LHV}/kg CO_2-avoided for MEM-3 vs 3.34 MJ_{LHV}/kg CO_2-avoided for EBTF). Supersonic flow driven deposition is ranked third in energy performance, with a SPECCA of 5.22 MJ_{LHV}/kg CO_2-avoided in the most representative case (SSD inlet pressure of 3 bar). However, SSD is by far the least developed CO_2 capture concept among the candidates considered, and the system implementation and overall process integration may be further improved by the technology developers in the future. An optimistic outlook for SSD was reported by Balepin *et al*. [52], concluding that progress was made in the understanding and maturing of this technology, and promise remains for applications requiring bulk CO_2 capture (around 50%) from gas streams with CO_2 concentrations of the order of 8 mol %. The schemes based on HPS are less attractive from the point of view of energy performance, since they deliever lower net electric efficiencies compared to the base case (39.6% in the HPS most attractive configuration versus 49.9%).

The Cost of CO_2 Avoided is considered here as the most relevant economic metric. CCA for the various technologies is reported in Figure 8 as a function of the Specific Total Plant Cost ($/$kW_{el}$),

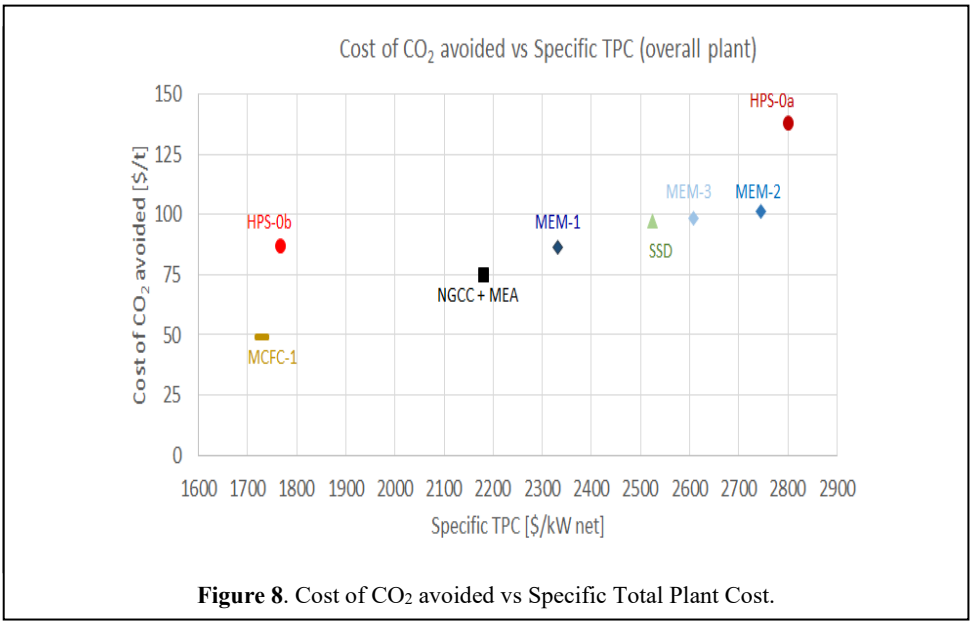

Figure 8. Cost of CO_2 avoided vs Specific Total Plant Cost.

and in Figure 8 in relation to the Specific TPC per CO_2 avoided ($/kg CO_2/s). The specific indexes are provide a way to compare the investment costs of plants with different sizes and rates of CO_2 avoided. In Figure 8, the most attractive plants are the ones positioned close to the bottom-left corner (low operating and small specific investment costs). Both Figure 8 and 9 show that MCFC is the only technology among those considered in this study which achieves a cost of CO_2 avoided appreciably lower than the base case, with a reduction of about 35%. The base high pressure captutre case (HPS-0b) has a specific investment cost less than Base case but the cost of CO_2 avoided is higher than the base case (87 vs 75 $/$t_{CO2}$). Membrane cases that performed at a similar level to the EBTF plant in terms of SPECCA have both a Specific TPC and a CCA larger than the base case. Table 22 compares

the key performance and cost metrics of the best case for each of the four analyzed technologies to the metrics for the reference- and base-plants.

In summary, MCFC is estimated to achieve improvement relative to the Base CCS technology for both energy performance and cost. A more detailed assessment is encouraged to verify technical feasibility and cost assumptions. In this study, CO_2 permeable membranes are shown to be less attractive than amines for deep CO_2 removal from NGCC flue gas due to the large membrane area and resultant high capital costs. Membrane technology may be competitive for lower capture rate applications (less than the 90%). High-pressure solvent absorption from high-pressure exhaust gas, though a well-known and low risk technology, does not outperform benchmark capture technology on performance. Although a decrease of specific investment cost appears to be achievable with supplementary firing (which increases the power output), the cost of CO_2 avoided is affected by the lower net electric efficiency. Supersonic flow-driven CO_2 deposition is the technology with the lowest TRL among those studied here, and the results of this study suggest that the energy performance can be competitive to the MEA benchmark case only if acceptable CO_2 removal levels can be achieved using moderate flue gas compression ratios. SSD application to post-combustion capture from NGCCs looks challenging due to the low CO_2 concentration in the flue gas. However, given the large uncertainty with this technology, it is difficult to draw definitive conclusions on its economic performance.

Since the energy and economic performance of CO_2 capture technologies are strongly dependent on the application (e.g., flue gas composition, plant size, mass and energy integration with the power plant) and the modelling assumptions, the results and considerations found in this work cannot be generalized. As an example, for applications featuring higher CO_2 concentrations (such as coal-fired steam cycles, cement plants, refineries, smelters, etc.), technologies based on physical separation processes, such as HPS, SSD and MEM, are expected to be more competitive.

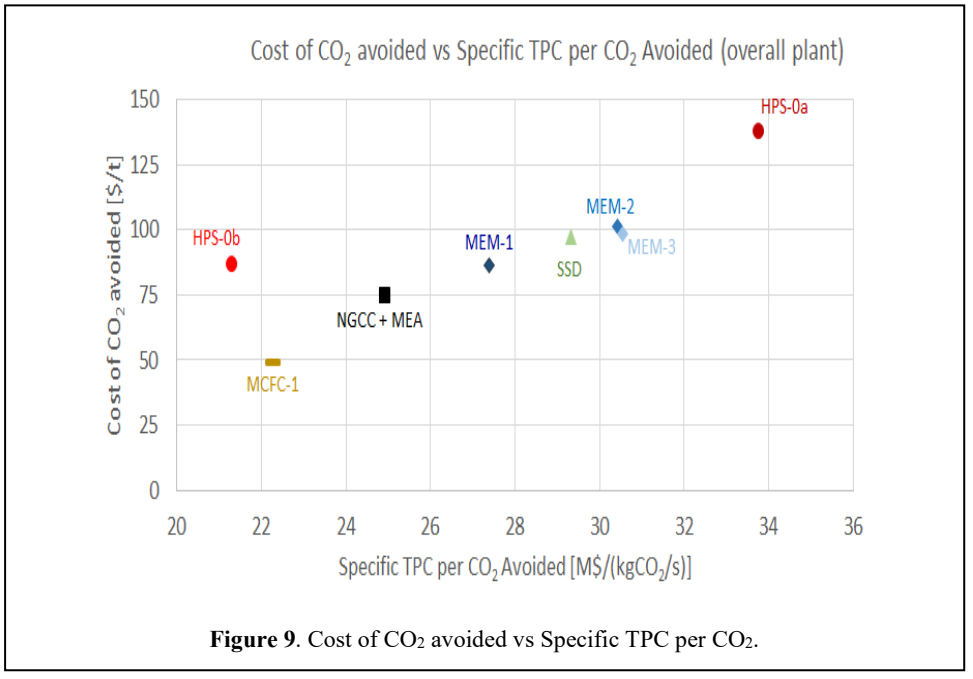

Figure 9. Cost of CO_2 avoided vs Specific TPC per CO_2.

Table 22. Summary table of performance and costs of the CCS technologies assessed.

Case Name	Net electric efficiency	SPECCA index	Total Plant Cost specific per unit of net power	CO_2 Avoidance Cost
Units	**%LHV**	**MJ_{LHV}/ Kg CO_2-avoided**	**\$2014/kW_{el}**	**\$/t_{CO2}**
NGCC without capture (Reference plant)	58.3	-	1059	-
NGCC + MEA Amine (Base plant)	49.9	3.34	2181	75
CO_2 permeable membranes (MEM-1)	48.0	4.33	2331	86
Molten carbonate fuel cell (MCFC)	57.5	0.31	1731	49
High-pressure solvent absorption from high-pressure exhaust gas (HPS-0b)	39.6	9.79	1767	87
Supersonic deposition technology (SSD-3)	46.2	5.22	2525	97

REFERENCES

1. International Energy Agency (IEA), 2019. World Energy Outlook 2019.
2. DOE, 2020. *2020 Carbon Capture Program R&D Compendium of Carbon Capture Technology*, Report 05.2020-1000, May 2020 [Web Document].
3. Global CCS Institute, 2021. *Global Status of CCS 2021* [Web Document].
4. CCP, 2017. Carbon Capture Project (CCP) [Web Document].
5. Crombie, M., Imbus, S., Jadhav, R., 2016. CO_2 Capture Project - 16 years of CCS development & collaboration to build knowledge GHGT-13. GHGT-13 Conf.
6. Stéphenne, K., 2014. Start-up of World's First Commercial Post-combustion Coal Fired CCS Project: Contribution of Shell Cansolv to SaskPower Boundary Dam ICCS Project. *Energy Procedia* 63, 6106–6110. doi:10.1016/j.egypro.2014.11.642
7. Rubin, E.S., Davison, J.E., Herzog, H.J., 2015. The cost of CO_2 capture and storage. *Int. J. Greenh. Gas Control* 40, 378–400. doi:10.1016/j.ijggc.2015.05.018
8. Mathieu, P., Bolland, O., 2013. Comparison of Costs for Natural gas Power Generation with CO_2 Capture. *Energy Procedia* 37, 2406–2419. doi:10.1016/j.egypro.2013.06.122
9. Merkel, T.C., Wei, X., He, Z., White, L.S., Wijmans, J.G., Baker, R.W., 2013. Selective Exhaust Gas Recycle with Membranes for CO_2 Capture from Natural Gas Combined Cycle Power Plants. *Ind. Eng. Chem. Res.* 52, 1150–1159. doi:10.1021/ie302110z
10. Campanari, S., Manzolini, G., Chiesa, P., 2013. Using MCFC for high efficiency CO_2 capture from natural gas combined cycles: Comparison of internal and external reforming. *Appl. Energy* 112, 772–783. doi:10.1016/j.apenergy.2013.01.045
11. Campanari, S., Chiesa, P., Manzolini, G., Bedogni, S., 2014. Economic analysis of CO_2 capture from natural gas combined cycles using Molten Carbonate Fuel Cells. *Appl. Energy*

130, 562–573. doi:10.1016/j.apenergy.2014.04.011
12. Christensen, T., Børseth, K., Hamrin, S., De Meyer, H., 2013. JET ENGINE WITH CARBON CAPTURE. US 2013/0119667 A1.
13. Castrogiovanni, A., 2016. Supersonic Post-Combustion Inertial CO_2 Extraction System. Bench Scale Project Status Update. 2016 NETL CO_2 Capture Technology Project Review Meeting, Pittsburgh, PA
14. Vielstich, W., Gasteiger, H.A., Lamm, A., Yokokawa, H., 2009. *Handbook of Fuel Cells: Fundamentals, Technology and Applications*.
15. Campanari, S., Chiesa, P., Manzolini, G., 2010. CO_2 capture from combined cycles integrated with Molten Carbonate Fuel Cells. *Int. J. Greenh. Gas Control* 4, 441–451. doi:://doi.org/10.1016/j.ijggc.2009.11.007
16. Ohmer, M., 2016. Industrial heat supplied by an integrated 1.4 MW fuel cell CHP plant. https://www.youtube.com/watch?v=Y4NlrX7sm28
17. Ahmed, S., Papadias, D., Ahluwalia, R., Hua, T., Roh, H.-S., 2015. Performance and Cost Analysis for a 300 kW Tri-generation Molten Carbonate Fuel Cell System. FY2015 Annual Progress Report, DOE Hydrogen and Fuel Cell Program.
18. Ghezel-Ayagh, H., 2016. Pilot Test of Novel Electrochemical Membrane System for Carbon Dioxide Capture and Power Generation. Pittsburgh (PA). 2016 NETL CO_2 Capture Technology Meeting August 8-12, 2016.
19. GEpower, 2016. GE factsheet - LMS100 POWER PLANTS. (www.ge.com)
20. UOP Publication, Milidovich, S., Tanislav, Zbacnik, E., 2013. Increasing Efficiency of Hot Potassium Carbonate CO_2 Removal Systems (www.uop.com).
21. Balepin, V., Castrogiovanni, A., 2011. A High Efficiency Inertial CO_2 Extraction System (ICES). NETL CO_2 Capture Technology Meeting, Pittsburgh, PA, 2011.
22. Schinkelshoek, P., Epsom, H.D., 2008. Supersonic gas conditioning - Commercialisation of Twister technology. *GPA Annual Conv. Proc*., 739–745.
23. Balepin, V., Castrogiovanni, A., Girlea, F., Robertson, A., Sforza, P., 2012. Inertial extraction system. US2013/0228076 A1.
24. Forsyth, J., Lodge, S., Consonni, S., Di Bona, D., Gatti, M., Martelli, E., Scaccabarozzi, R., Viganò, F., 2017. Evaluation of Five Alternative CO_2 Capture Technologies with Insights to Inform Further Development. *Energy Procedia* 114, 2599–2610. doi:10.1016/J.EGYPRO.2017.03.1419
25. AspenTech, 2016. Aspen Plus v8.8.
26. Thermoflow, 2014. Thermoflex, v24. //www.thermoflow.com/combinedcycle_TFX.html.
27. Politecnico di Milano, 2012. Software presentation: GS (Gas-Steam Cycles).
28. CAESAR, 2011. European best practice guidelines for assessment of CO_2 capture technologies, EU project 213206 Deliverable D4.9, Feb 2011.
29. Chiesa, P., Macchi, E., 2004. A Thermodynamic Analysis of Different Options to Break 60% Electric Efficiency in Combined Cycle Power Plants. *J. Eng. Gas Turbines Power* 126, 770. doi:10.1115/1.1771684
30. Gerdes, K. (ed), 2015, *Carbon Dioxide Capture for Storage in Deep Geologic Formations – Results from the CO_2 Capture Project Volume 4: CCS Technology Development and Demonstration; Results (2009-2014),* CPL Press.
31. *Chemical Engineering*, 2014. CEPCI, The Chemical Engineering Plant Cost Index. www.chemengonline.com/site/plant-cost-index/ [last accessed on April 1st 2017].
32. Fout, T., Zoelle, A., Keairns, D., Turner, M., Woods, M., Kuehn, N., Shah, V., Chou, V., Pinkerton, L., 2015. *Cost and Performance Baseline for Fossil Energy Plants Volume 1a: Bituminous Coal (PC) and Natural Gas to Electricity Revision 3*. Natl. Energy Technol. Lab. 1a, 240. doi:DOE/NETL-2010/1397
33. Zoelle, A., Turner, M.J., Chou, V., 2015. DOE/NETL *Quality Guidelines for Energy System*

Studies Performing a Techno-economic Analysis for Power Generation Plants.
34. Rubin, E., Booras, G., Davison, J.E., Ekstrom, K., Matuszewski, M., McCoy, S., Short, C., 2013. *Toward a common method of cost estimation for CO_2 capture and storage at fossil fuel power plants* (No. 2013/TR2).
35. EIA (U.S. Energy Information Administration), 2017. Annual Energy Outlook 2017.
36. EIA (U.S. Energy Information Administration), 2013. Updated Capital Cost Estimates for Utility Scale Electricity Generating Plants.
37. IEAGHG, 2012. CO_2 Capture at gas fired power plants, 2012/8.
38. Kohl, A.L., Nielsen, R., 1997. *Gas purification*, Fifth. ed. Elsevier.
39. Spinelli, M., Campanari, S., Consonni, S., Romano, M.C., Kreutz, T., Ghezel-Ayagh, H., Jolly, S., 2018. Molten Carbonate Fuel Cells for Retrofitting Postcombustion CO_2 Capture in Coal and Natural Gas Power Plants. *J. Electrochem. Energy Convers. Storage* 15(3), 31001. doi:10.1115/1.4038601.
40. Farooque, M., Daly, J., Wang, J., 2014. Contaminants Control for Fuel Cells – FCE Experience, ANL Conference, Chicago, March 2014.
41. Grabke, H.J., 1995. Metal Dusting of Low- and High-Alloy Steels. *Corrosion* 51, 711–720.
42. Martelli, E., Kreutz, T.G., Gatti, M., Chiesa, P., Consonni, S., 2013. Numerical optimization of steam cycles and steam generators designs for coal to FT plants. *Chem. Eng. Res. Des.* 91, 1467–1482. doi:10.1016/j.cherd.2013.02.026.
43. Ghezel-Ayagh, H., Jolly, S., Patel, D., Steen, W., 2017. Electrochemical Membrane Technology for Carbon Dioxide Capture from Flue Gas. *Energy Procedia* 108, 2–9. doi:10.1016/j.egypro.2016.12.183.
44. UOP Publication, Bartoo, R.K., Furukawa, S.K., 1997. Improved Benfield Process for Ammonia Plant. Intern. UOP Tech. Pap., www.uop.com .
45. Calayag, B., Castrogiovanni, A., 2014. A high efficiency inertial CO_2 extraction system — ICES. Proj. US DOE Off. Foss. Energy NETL Program.
46. Balepin, V.,Castrogiovanni, A., Robertson, A., Calayag, B., 2014. "Supersonic Post-Combustion Inertial CO_2 Extraction System," 2014 NETL CO_2 Capture Technology Meeting, Pittsburgh, 30 July 2014.
47. George, E., Jarry, A., Pale, M., Saysset, S., 2014. Fundamental and Applied Numerical Approaches for CO_2 Capture in Flue Gases within a Supersonic Nozzle, in: *International Gas Union Research Conference* 2014.
48. Hammer, M., Wahl, P.E., Anantharaman, R., Berstad, D., Lervåg, K.Y., 2014. CO_2 Capture from Off-shore Gas Turbines Using Supersonic Gas Separation. *Energy Procedia* 63, 243–252. doi:10.1016/j.egypro.2014.11.026
49. Castier, M., 2014. Modeling and simulation of supersonic gas separations. *J. Nat. Gas Sci. Eng.* 18, 304–311. doi:10.1016/j.jngse.2014.03.014
50. Rajaee Shooshtari, S.H., Shahsavand, A., 2013. Reliable prediction of condensation rates for purification of natural gas via supersonic separators. *Sep. Purif. Technol.* 116, 458–470. doi:10.1016/j.seppur.2013.06.009
51. Sipocz, N., Fritz, J.M., Gonzalez, S.M.A., Nazelle, C. DE, Du, R., Shisler, R.A., Lissianski, V.V., Michelassi, V., 2013. Method and systems for CO_2 separation with cooling using converging-diverging nozzle. doi:WO 2013162915 A1
52. Balepin Vladimir (Orbital ATK), 2017. Supersonic Post-combustion Inertial CO_2 Extraction System - Final Report DOE-OA-13122. www.netl.doe.gov/File%20Library/Research/Coal/carbon%20capture/post-combustion/Final-Report-ATK-FE0013122-April-2017.pdf.
53. Spendelow, J., Nguyen, T., Houchins, C., Martin, K.E., Papageorgopoulos, D., 2012. Medium-scale CHP Fuel Cell System Targets. https://www.hydrogen.energy.gov › 11014_medium_scale_chp_target

54. Ulrich, D.G., Vasudevan, P.T., 2004. *Chemical Engineering Process Design and Economics*: *A Practical Guide,* 2nd ed. Process Publishing.
55. Häring, H.W. 2008. Industrial Gas Processing, Weinheim, Germany: WILEY-VCH Verlag Gmbh & CO. KGaA.
56. Yan, J. *et al*. 2011 "CO_2 processing experience for oxyfuel combustion CO_2 capture – based on results from Vattenfall's 30 MW_{th} oxyfuel pilot plant," 2d Oxyfuel Combustion Conference, IEAGHG, Queensland, Australia, Sept 2011.
57. IEA, "Evaluation and analysis of the performance of dehydration units for CO_2 capture", 2014/04, April 2014.

APPENDIX

Impact of Enhanced CO_2 Purification for Membrane CO_2 Removal

In the Membrane CO_2 removal cases studied here, the outlet stream from the CO_2 Capture Membrane contains 78-85% CO_2 (See **Table 9**). The CO_2 Purification Unit specified for these cases can reduce N_2 and H_2O to meet CO_2 specification shown in **Table 2** (CO_2 content >97%), but not the O_2 specification. Therefore, a study was carried out to understand the options for CO_2 purification in a membrane-based CO_2 capture process. Given the operating characteristics of the selective flue gas recycling process for an NGCC power plant, and the assumed performance of the MTR membrane, the capture membrane outlet stream to be purified contains up to 15% N_2, up to 4% O_2, and up to 4% H_2O.

Absorption solvents have high affinity towards CO_2 and are most suitable for applications where CO_2 is a contaminant. In this case, solvent absorption of CO_2 as the bulk phase, rather than as a contaminant, would require large energy consumption and high costs. An adsorption approach is technically feasible for CO_2 purification, but a preferential adsorbent for O_2 over CO_2 for industrial purification of CO_2, which would be best for this application, is not commercially available. As shown already, available CO_2 removal membranes also fall short on CO_2/O_2 selectivity.

Cryogenic or phase change technologies are considered suitable for separating the non-condensable species (N_2 and O_2) from CO_2, after a dehydration step. CO_2 purification via phase change at temperatures near -56 °C (the CO_2 freeze-out limit) is a standard industrial practice [55] and has been used in CCS pilot projects [56]. A block flow diagram of the cryogenic purification unit is shown in Figure A-1. Water removal is done in stages, first by interstage cooling in the compression train, followed by triethylene glycol (TEG) or molecular sieve adsorption to achieve the desired water content.

Two categories of cryogenic technologies are considered: (1) flash separation and (2) stripping/distillation-based separation. As with all cryogenic processes, heat integration is key to energy efficiency. Performance metrics are reported in Table A-1.

Cryogenic separation using flashing only is capable of satisfying the specification on CO_2 purity, but not the O_2 content (75 ppm in **Table 2** and < 10 ppm for some EOR/pipeline specifications). Therefore, flash-based technologies must be coupled with an oxygen removal step such as catalytic oxidation or chemisorption, or a distillation column must be added, either of which will add energy and capital to the purification section. Energy consumption for CO_2 purification is small compared to that required for compression (typically less than 5%). However, 3.5% (flash configuration) to 14% (distillation configuration) of the stream entering the purification unit needs to be recycled to the capture section, which has implications for the size of the capture unit and the overall process CapEx

and OpEx. The process performance and economic analysis of the membrane case was not revisited for this side study.

Table A-1. Performance of cryogenic purification units for CO_2.

	2-stage flash (option 1)	**2-stage flash (option 2)**	**Flash + Distillation**
Specific electricity consumption (kJ/kg CO_2)	472.0	489.7	579.0
CO_2 recovery (%)	96.7	96.4	86.2
CO_2 purity (%)	96.0	96.8	>99.9
O_2 content in CO_2 stream (ppm)	10800	9100	9.0
N_2 content in CO_2 stream (%)	2.57	2.05	<1 ppm

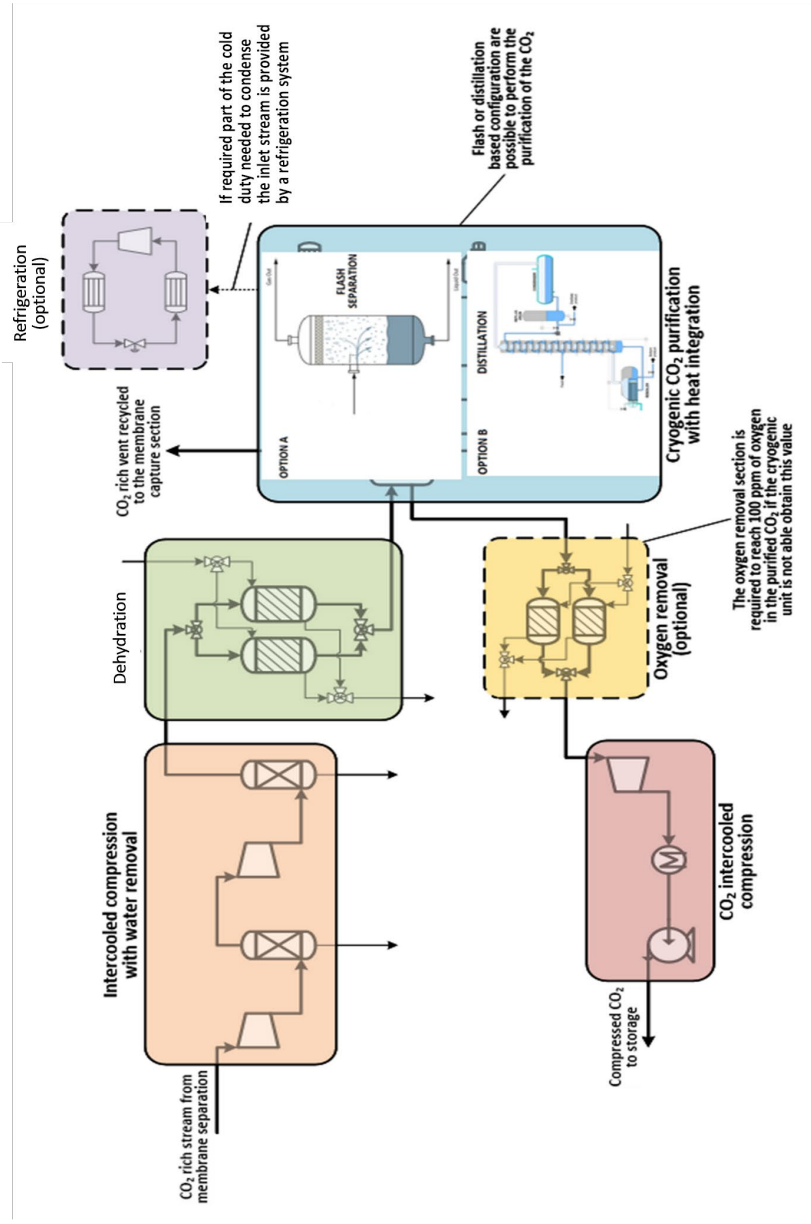

Figure A-1. CO_2 purification section block flow diagram.

Carbon Dioxide Capture for Storage in Deep Geological Formations, Volume 5
Karl F. Gerdes (Editor)
© 2022 BP. All rights reserved.

Chapter 8

ASSESSING THE POTENTIAL OF MCFC-BASED CO_2 CAPTURE IN NATURAL GAS-FIRED COMBINED CYCLE POWER PLANTS

Maurizio Spinelli[1], Daniele Di Bona[1], Manuele Gatti[2], Emanuele Martelli[2], Stefano Consonni[2]
[1]LEAP, Via Nino Bixio 27C, 29121, Piacenza, Italy
[2]Politecnico di Milano, Department of Energy, Via Lambruschini 4, 20156, MI, Italy

ABSTRACT: This work explores two configurations of natural gas-fired combined cycles (NGCC) with molten carbonate fuel cells (MCFC) for CO_2 capture. Special attention is devoted to the selection of MCFC operating conditions (trade-off between CO_2 capture and voltage losses), technical issues, heat integration, fuel use and CO_2 purification. Two options are assessed: (i) an "integrated" version with MCFC modules installed between the gas turbine (GT) and the heat recovery steam generator (HRSG) to maximize the efficiency of the integrated power plant; and (ii) a "non-integrated" version, with the MCFC section located downstream of the HRSG, and a regenerative heat exchanger is used to preheat cathode reactants up to the MCFC working temperature (around 600°C). The present study includes a full techno-economic analysis of the two options based on a preliminary sizing of the key-components, and a sensitivity analysis of the CO_2 utilization factor. The techno-economic analysis shows that, compared to a benchmark amine (MEA) scrubbing process, the "integrated" configuration shows considerably better energy and economic performance (Specific Primary Energy Consumption for CO_2 Avoided – SPECCA = 0.31 MJ/kg; Cost of CO_2 avoided – CCA = 50 \$/t_{CO2}). The "non-integrated" solution shows better performance than the benchmark system but similar CO_2 avoidance cost (SPECCA = 2.4 MJ/kg; CCA = 76 \$/t_{CO2}).

KEYWORDS: CO_2 capture and storage, post-combustion CO_2 capture, molten carbonate fuel cells, natural gas combined cycle

INTRODUCTION

The benchmark technology for post-combustion CO_2 capture in natural gas-fired power plants is chemical absorption with amine-based solvents [5]. However, the high investment cost and energy penalty of amine scrubbing processes are barriers to deployment for CO_2 capture. A very promising capture alternative with the MCFC has led to industrial interest in advancing the technology [11].

In an earlier study [12] and as documented in Chapter 7, the MCFC-based capture system integrated with the NGCC shows promise when compared to post-combustion scrubbing with amines, as well as to three novel CO_2 capture systems. In this chapter, the integrated capture system described in Chapter 7 is more fully analyzed.

As conceptually illustrated in Figure 1, CO_2 can be removed from a CO_2-rich flue gas, which also must contain O_2, on the cathode side of an MCFC, where the electrochemical reaction of O_2 and CO_2 form a carbonate ion occurs. The carbonate ion migrates through the liquid carbonate electrolyte retained in a ceramic matrix. On the anode side of the MCFC, where fuel is fed, reforming takes place to make H_2 which reacts with the carbonate ion to form CO_2 and H_2O. The anode reactions produce electrons which flow externally to the cathode to satisfy the demand of the carbonate formation,

producing a current flow. Thus, the MCFC separates CO_2 from the NGCC flue gas while simultaneously generating additional electric power from additional fuel fed to the MCFC with high efficiency.

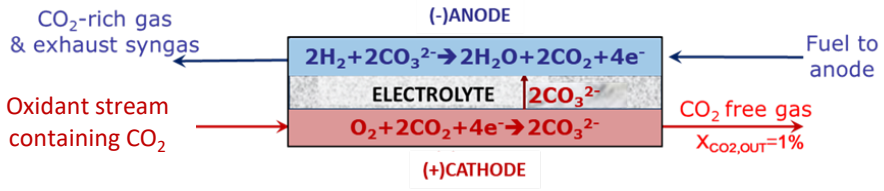

Figure 1. MCFC working principle and general electrochemical anode/cathode reactions.

Various MCFC-based configurations for CCS have been proposed in the power sector for retrofitting coal and natural gas-fired power plants and for greenfield integrated applications, showing promising results according to recent modelling studies. Examples include natural gas combined cycles (NGCC) [14-17], coal-fired plants [7, 10, 18], integrated coal gasification combined cycles (IGCC) [19], and biogas plants.

For NGCC's, Campanari [24] concluded that the most efficient way to integrate an NGCC with an MCFC is to install the fuel cell between the gas turbine (GT) and the heat recovery steam generator (HRSG) of the combined cycle plant. This "integrated" NGCC+MCFC solution was also analyzed by Greppi *et al.* [25], where a synergistic operation of MCFC and membranes was proposed. However, in that study, technological constraints imposed by use of a separate reformer for the fuel fed to the MCFC and by a stack maximum temperature, limited the proposed layout to about 60% carbon capture and resulted in only an additional 11% net power output. The thermal integration of the natural gas reformer with the MCFC modules is advantageous since the high MCFC operating temperature and presence of large nickel anode surfaces catalyzes reforming. This allows elimination of a separate fuel reformer. Further, the endothermic reforming reaction reduces the temperature increase across the MCFC and allows the operation of the fuel cell with higher CO_2 utilization factors which generates more heat, resulting in larger MCFC active area and higher power output. Campanari *et al.* [16] compared internal and external reforming and identified a promising NGCC+MCFC configuration that achieves a high carbon capture rate (up to 85%) and a significant increase of the power plant electricity output (+20%) with a specific energy consumption for CO_2 avoided (SPECCA) of 0.4 MJ/kg_{CO2}.

The downstream retrofit (also called "bolt-on") layout proposed by Spinelli *et al.* [26] explores post-combustion capture using an MCFC island for NGCCs and for pulverized coal-fired steam cycles (PCC). This "non-integrated" layout is more amenable to retrofit application, because it minimizes the changes to the baseline power plant and yields a significant carbon capture rate (>80%) and a very limited (<3%) decrease in efficiency with respect to the baseline NGCC.

The main objective of this work is to provide a comprehensive comparison between the integrated and non-integrated (also referred to as "fully-retrofitable") NGCC+MCFC solutions, assessing the two configurations with the same basis of design. The techno-economic analysis of both configurations takes into account the following:

- Updated polarization curves integrated within a recent 0D MCFC model, which includes indirect and direct internal reforming (IIR and DIR), as described in [26].

- The effect of possible metal dusting on the design of the heat exchanger network, especially concerning the anode and cathode preheating sections.
- The specific engineering design and cost assessment of pieces of heat transfer equipment.
- The effect of CO_2 utilization factor on the power plant performance and cost.

The energy and economic performance of the MCFC-based power plants are compared with those of a benchmark amine scrubbing post-combustion processes (Chapter 7). An early version of this work, "Assessing the potential of molten carbonate fuel cell-based schemes for carbon capture in natural gas-fired combined cycle power plants", was published by the authors in 2020 (https://doi.org/10.1016/j.jpowsour.2019.227223).

MCFC WORKING PRINCIPLE

The schematic of a standalone MCFC fed with natural gas is shown in Figure 2. The key components of the fuel cell are the two electrodes, made of nickel-based alloys (e.g., Ni-Al-Cr) at the anode and high porosity oxides (NiO-MgO) at the cathode, and a liquid carbonate electrolyte, capable of transporting CO_3^{2-} ions, retained in a ceramic matrix [27]. CO_2-rich flue gas is fed to the fuel cell cathode while a mixture of natural gas and steam is fed to the anode side. Natural gas is converted to hydrogen by a first *indirect* internal reforming process (IIR, which occurs in a separate layer interposed between two different MCFC active layers) and a second *direct* reforming process (DIR) occurring at the MCFC anode and driven by the progressive H_2 consumption.

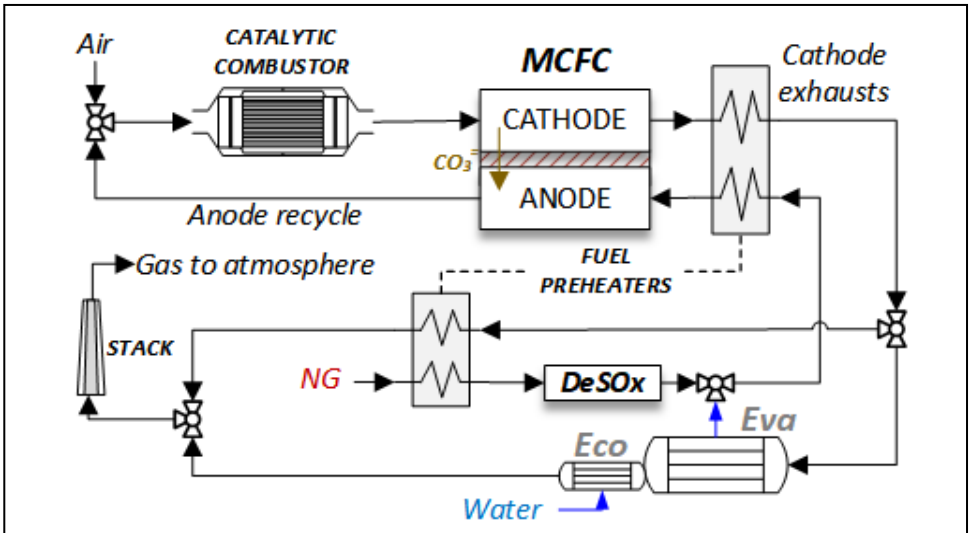

Figure 2. Simplified layout of the MCFC standalone application. The source for the CO_2 fed to the cathode is the anode effluent coming from the fuel cell itself (internal recycle anode ➔ cathode). Before being introduced to the cathode, the unconverted syngas contained in anode exhausts is oxidized in a catalytic combustor. Hot cathode effluents preheat natural gas and water in the economizer (ECO) and raise LP steam in the evaporator (EVA).

The performance of an MCFC depends on the current density (electric current per unit of active electrolyte area), the composition of the feed streams (anode and cathode) and the excess of reactants fed to the fuel cell with respect to the minimum stoichiometric requirement. For design purposes, the focus is typically on the utilization factors (denoted U_{O2}, U_{CO2}, U_{H2}), defined as the fraction of O_2, CO_2, H_2 consumed by the reactions with respect to the total amount fed to the MCFC, rather than on the excess of reactants.

The performance of the fuel cell can be modelled using the potential of an ideal fuel cell as reference (E_{Nernst}, also called Nernst potential) and subtracting the voltage losses due to the reaction activation mechanism ΔV_{Act}, the ohmic losses ΔV_{Ohm}, and the non-homogenous reactant concentrations ΔV_{Conc} [27]:

$$V = E_{Nernst} - \Delta V_{Act} - \Delta V_{Ohm} - \Delta V_{Conc} \quad (1)$$

E_{Nernst} is related to the Gibbs free energy associated with the electrochemical reactions, corrected with a function of operating temperature and of the partial pressures of the reactants:

$$E_{Nernst} = \frac{\Delta G}{nF} + \frac{RT}{nF} ln\left(\frac{p_{H_2}an \left(p_{O_2}ct\right)^{0.5} p_{CO_2}ct}{p_{H_2O}an\, p_{CO_2}an}\right) \quad (2)$$

Since the average partial pressures of all the reactants at the anode (p_{H2an} and p_{H2Oan}) and at the cathode ($p_{O2,ct}$, $p_{CO2,ct}$ and $p_{H2O,ct}$) sides of the MCFC depend on the inlet and outlet stream compositions, the ideal Nernst voltage is significantly influenced by the utilization factors of all the species.

Once the potential V is known, the gross power produced by the MCFC can be calculated as:

$$P_{el,MCFC} = V \cdot IC \cdot A \quad [W] \quad (3)$$

where IC is the current density and A is the active MCFC area.

The voltage (as well as the cell efficiency) depends on the current density IC, reactants inlet concentrations and utilization factors. To achieve high voltage, the MCFC should operate with low current density (to limit the ohmic losses) and high inlet reactant concentrations (beneficial for the Nernst potential and concentration losses).

In the stand-alone application (without CO_2 capture), the MCFC cathode is fed with air and recycled anode exhausts to provide both the O_2 and the CO_2 required for sustaining electrochemical reactions (see Figure 1). Since targeting complete fuel conversion (100% fuel utilization factor) would lead to excessive concentration losses and shorter fuel cell life, the MCFC anode is fed excess fuel (the typical fuel utilization factor U_F is 70-80%), and the unconverted syngas (largely H_2O, CO and H_2) is mixed with air and oxidized in a catalytic combustor before being fed to the cathode. In this way, the thermal energy generated by the syngas combustion increases the temperature of cathode stream up to the MCFC working condition. On the anode side of the fuel cell, the cathode exhaust is cooled by preheating NG and water fed.

Since all the anode effluents are recycled back to the MCFC cathode, the inlet CO_2 partial pressure at the cathode side is quite high (y_{CO2ct}~ 15-20%) and allows the fuel cell to work with high voltage (see eq. 2) and high electric efficiency, which is further enhanced by the low CO_2 utilization factor. Under these conditions, the MCFC can reach high voltages (e.g., around 0.8 V) even in case of high current densities (I_c=1500-1600 A/m^2).

When the MCFC is operated in a carbon capture configuration (Figure 3), the fuel cell operates as an active CO_2 concentrator, and the CO_2 partial pressure at the cathode inlet is usually lower, because it is defined by the composition of combustion effluents coming from the source combustion process

(in the present case NGCC exhaust at 4 mol% CO_2). In addition, the desired high CO_2 utilization factor (required to match the targeted CO_2 capture levels of 80-90%) brings the average CO_2 concentration across the cathode down to low values. For this reason, if the fuel cell is operated with the same current density as the standalone capture configuration (e.g., I_c=1500 A/m^2), the voltage will be lower than that observed in the standalone case (e.g., 0.7 V) [12].

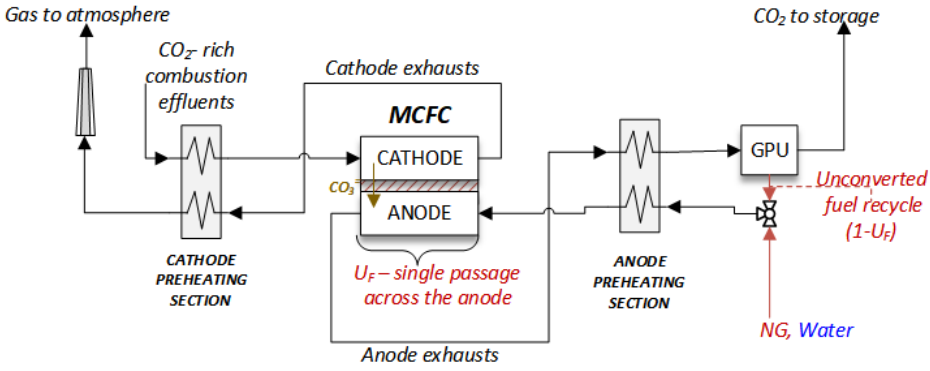

Figure 3. Simplified layout of the MCFC carbon capture application. The scheme shows that, owing to the gas processing unit which separates the unconverted fuel (or exhaust syngas) from the CO_2 stream leaving the anode, the fraction (1-U_F) can be recycled to the anode inlet, bringing the overall fuel utilization close to 100%.

MCFC MODEL

A 0D fuel cell model was implemented using GS software source code [28], a proprietary simulation program based on a lumped parameter approach. In particular, the MCFC model includes:

- Coupling mass/energy balances with the MCFC electrochemical reactions.
- Calibrated voltage correlations.
- Simulation of the direct and indirect internal reforming processes (respectively DIR and IIR, Figure 4).

The fuel conversion in the pre-reformer layer can be specified in the model, which can then calculate the energy balance for the whole stack, the total current and power produced by the MCFC, and the global active area of the fuel cell stack. The MCFC voltage is estimated using a correlation based on a polarization curve interpolated from data gathered by Fuel Cell Energy Inc. (FCE) using simulated coal and NG power plant effluents [12, 26]. The correlation computes the MCFC voltage as the difference between the Nernst potential and all the polarization losses (Equation 1). The current density and the utilization factors are specified input values. The average compositions of the streams flowing through the anode and cathode are used to compute Nernst potential and voltage losses and is specified by the inlet compositions and the values of U_{CO2}/U_{O2}/U_F.

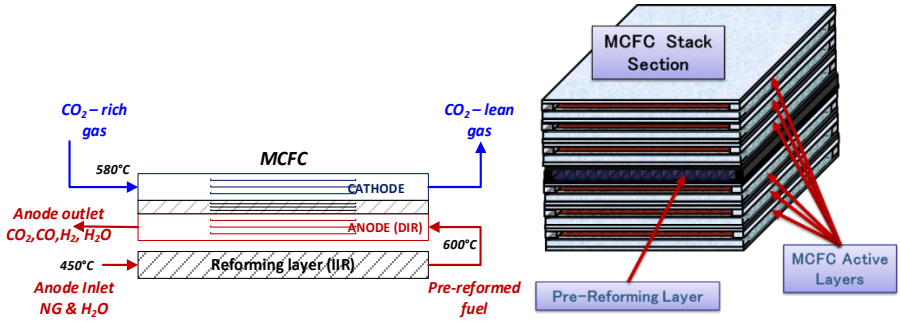

Figure 4. Fuel cell stack composition: reforming layers and active MCFC layer.

Effect of CO_2 partial pressure

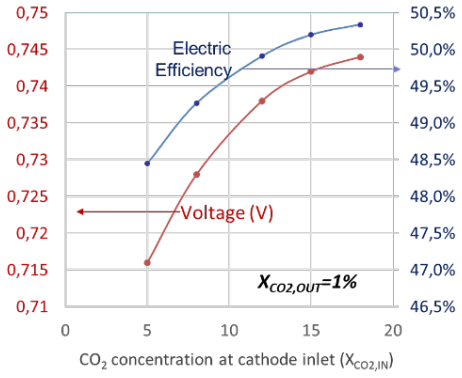

Effect of current density and fuel utilization

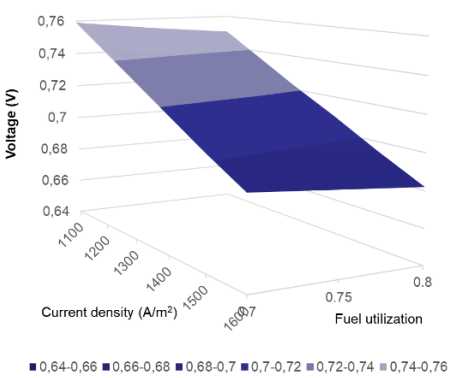

Figure 5. MCFC voltage and gross efficiency variation as a function of CO_2 concentration at the cathode inlet (left side) and as a function of current density/fuel utilization (right side).

Figure 5-A illustrates the resulting MCFC voltage and efficiency as a function of CO_2 concentration at the cathode inlet. Figure 5-B shows the effect of current density and fuel utilization factor on the MCFC voltage for a case representative of the MCFC integration to NGCCs (X_{CO2}=4% at the cathode inlet). Since the ohmic polarization is directly proportional to the value of current density, the MCFC voltage shows a linear decrease as current density (I_c) increases. Likewise, a minor voltage loss is also observed as the fuel utilization factor (U_F) increases, because of the progressively lower average H_2 partial pressure across the anode.

It is important to highlight that the Fuel Utilization values on the x-axis of Figure 5-B represent the once-through conversion of fuel through the MCFC. As explained in the next section and illustrated in Figure 6, the unconverted syngas can be recycled from the anode outlet to the anode inlet, increasing the overall fuel utilization (up to 100%) and the electric efficiency of the capture system. This efficient configuration is enabled by the need to separate unconverted fuel from the CO_2-rich anode exhaust to meet the specifications of the CO_2 exported to storage.

The MCFC operating conditions assumed for the NGCC+MCFC configurations assessed here are listed in Table 1, reflecting the current state of technology developed by FCE. The selected current density (Ic=1500 A/m^2,) is chosen to maximize the power density and minimize the MCFC active area and the related investment cost. High current density raises the ohmic overpotential, which causes a decrease in the fuel cell voltage and a consequent efficiency penalty for the MCFC-based capture system. As illustrated in 5-B, if the current density is increased from 1100 A/m^2 to 1500 A/m^2 the higher ohmic resistance of the fuel cell decreases the voltage from 0.75 V to 0.7 V. This voltage percentage decrease is less significant than the corresponding current density increase. For this reason, the higher current density translates into a higher power density (P_{spec}=V*I_C=1050 W/m^2) and a lower investment cost. The high over-potential and related waste heat caused by high current density and high utilization factors could affect the integrity of the electrolyte and the electrodes, the durability of which should be experimentally demonstrated in long duration testing at conditions representative of the CCS application.

Table 1. Fuel cell operating parameters [12]

Fuel utilization factor (single pass)	75%
Steam to carbon ratio (S/C)	2
Current density	1500 A/m^2
Oxygen mol fraction at cathode outlet (X O_2)	1%
Inlet temperature (reforming layer)	450°C
Inlet temperature (anode and cathode)	580°C
Pressure drops on anode/cathode	3/2 kPa
Heat losses (% input thermal power)	1%
DC/AC converter efficiency	94%

The once-through fuel utilization factor of the MCFC (U_F) is assumed equal to 75%. The input value for the CO_2 utilization factor (U_{CO2}) is set by the assumption that the CO_2 concentration at the cathode outlet is 1 mol%, in order to avoid a large concentration overpotential in the MCFC. In this example, since the MCFC cathode feed is the NGCC exhaust (3.98% CO_2, 12.39% O_2), the resulting CO_2 utilization to leave 1% at the outlet is approximately U_{CO2}=76%. In the final sensitivity analysis presented later, the outlet CO_2 concentration is varied between 0.5 and 2%, leading to U_{CO2} values between 50 and 90%.

PROPOSED NGCC-MCFC SCHEMES

Two schemes to couple MCFC and NGCC–one integrated and one non-integrated–have been defined and analyzed in this work. The simplified flow sheets are illustrated in Figure 6 and Figure 7.

INTEGRATED NGCC-MCFC

The first option to use MCFC for CO_2 capture from an NGCC–previously discussed in Chapter 7 and [12]–is one of the most efficient CCS power plant concepts, because of the combination of high MCFC electric efficiency and favorable heat integration. The MCFC is placed between the gas turbine (GT) and the heat recovery steam generator (HRSG) and separates the CO_2 from the high temperature GT exhaust. This placement of the fuel cell reduces the energy penalty associated with CO_2 capture, because the temperature of the cathode inlet stream (GT exhaust is 608°C) matches well with the MCFC's working temperature (580°C). Because no preheat is needed for the cathode feed, much of the heat generated by the MCFC is recovered from the hot cathode exhaust (650°C) by generating steam in the HRSG, which increases the power output of the bottoming Rankine cycle.

On the anode side of the MCFC, reactants (natural gas, recycled unconverted fuel, and H_2O) are first preheated to 300°C by hot high-pressure water from the HRSG and then desulphurized. Finally, this stream is mixed with superheated steam extracted from the HRSG, to achieve a steam-to-carbon ratio and inlet temperature required by the pre-reformer layer integrated into the MCFC.

The stream leaving the anode, which contains captured CO_2 and unconverted syngas stream, first produces steam in a segregated section of the HRSG (to avoid the self-defeating dilution with cathode reactants) and then enters the gas processing unit (GPU). The GPU separates CO_2 from the unconverted fuel via a double-flash cryogenic gas separation described later. This step is designed to meet the CO_2 purity specifications for transport and storage. To maximize the overall fuel utilization and the efficiency of the fuel cell section, the unconverted fuel recovered by the cryogenic section is recycled back to the fuel cell anode. The recycled fuel is mixed with supplemental natural gas feed and heated to 300°C prior to the zinc-oxide sulfur removal unit [29]. The mixture is then heated to the anode inlet temperature (450°C) by direct mixing with superheated steam (565°C) extracted from the low pressure (LP) section of the steam cycle. The steam injection rate is set to achieve a steam-to-carbon ratio of 2.

The heat exchanger network has been optimized to achieve the maximum heat recovery (maximum generation of steam for power generation), while avoiding metal dusting [30], which may affect the anode side heat exchangers. Since the anode inlet and outlet streams contain CO and H_2 with a carbon activity greater than 1 in the temperature range 450-800°C (in absence of H_2S), severe carburization may occur, which causes progressive corrosion of the heat exchanger To prevent this damage, the tube metal temperature of the heat exchangers is kept below 450°C by generating steam or preheating liquid water, since the high heat transfer coefficient keeps the tube wall temperature close to the boiling water temperature.

Non-Integrated NGCC-MCFC

In the non-integrated, retrofit option, Figure 7, the MCFC is placed downstream the HRSG to avoid the need to modify the NGCC and to minimize the impact on the operation of the baseline power plant. The non-integrated option is less invasive but also inherently less efficient than the integrated one, because fuel fed to the MCFC is converted to electricity with a lower efficiency, due to absence of a steam cycle for power production in this MCFC configuration. In this “bolt-on” configuration, the fuel cell does not employ a steam bottoming cycle since all the heat recovered by cooling the MCFC effluent is needed to preheat the MCFC feeds. As explained in the results section, the relative simplicity of the non-integrated scheme is partly counterbalanced by a more complicated heat exchanger network, which contributes to the higher capital cost of the CO_2 capture section.

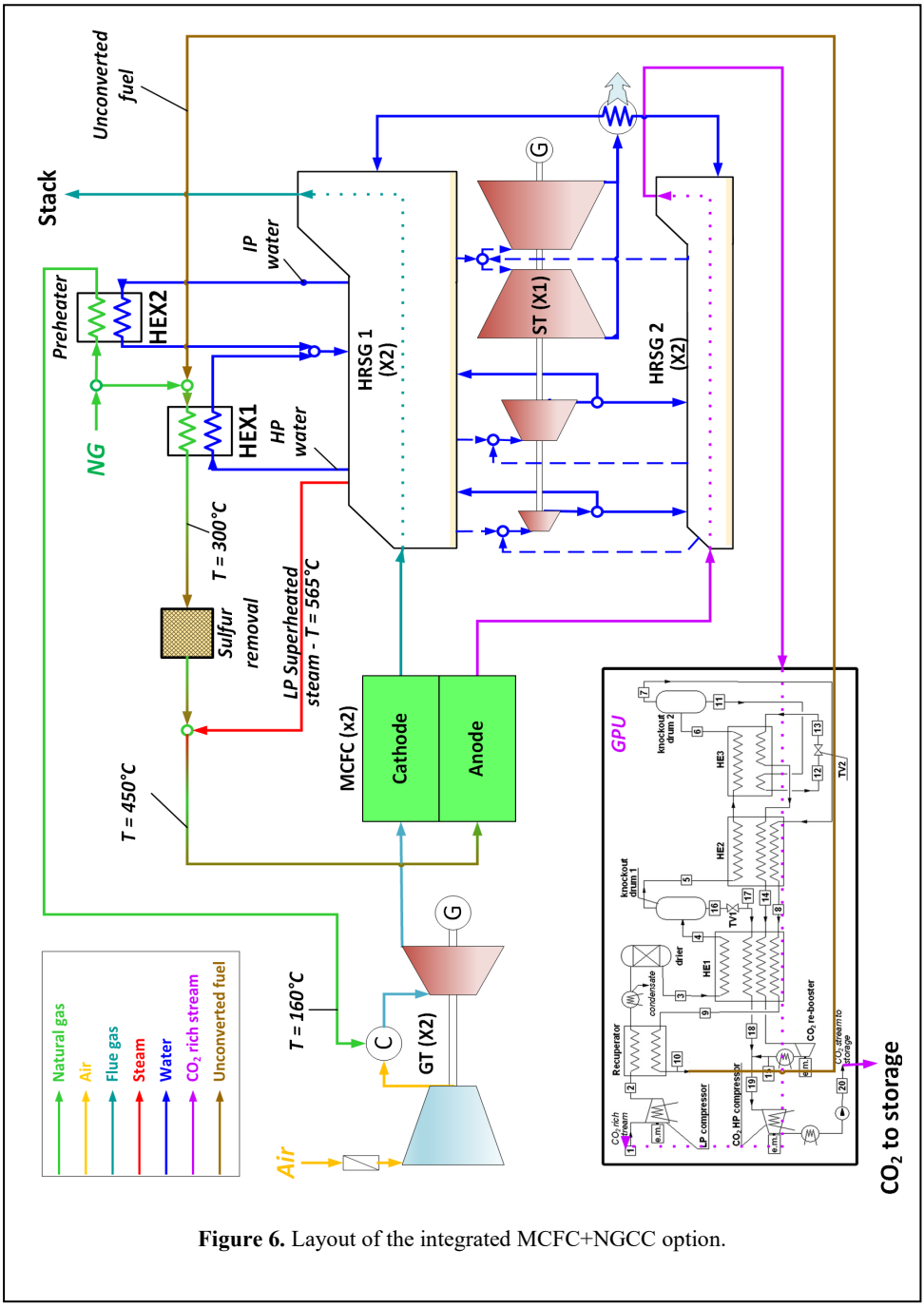

Figure 6. Layout of the integrated MCFC+NGCC option.

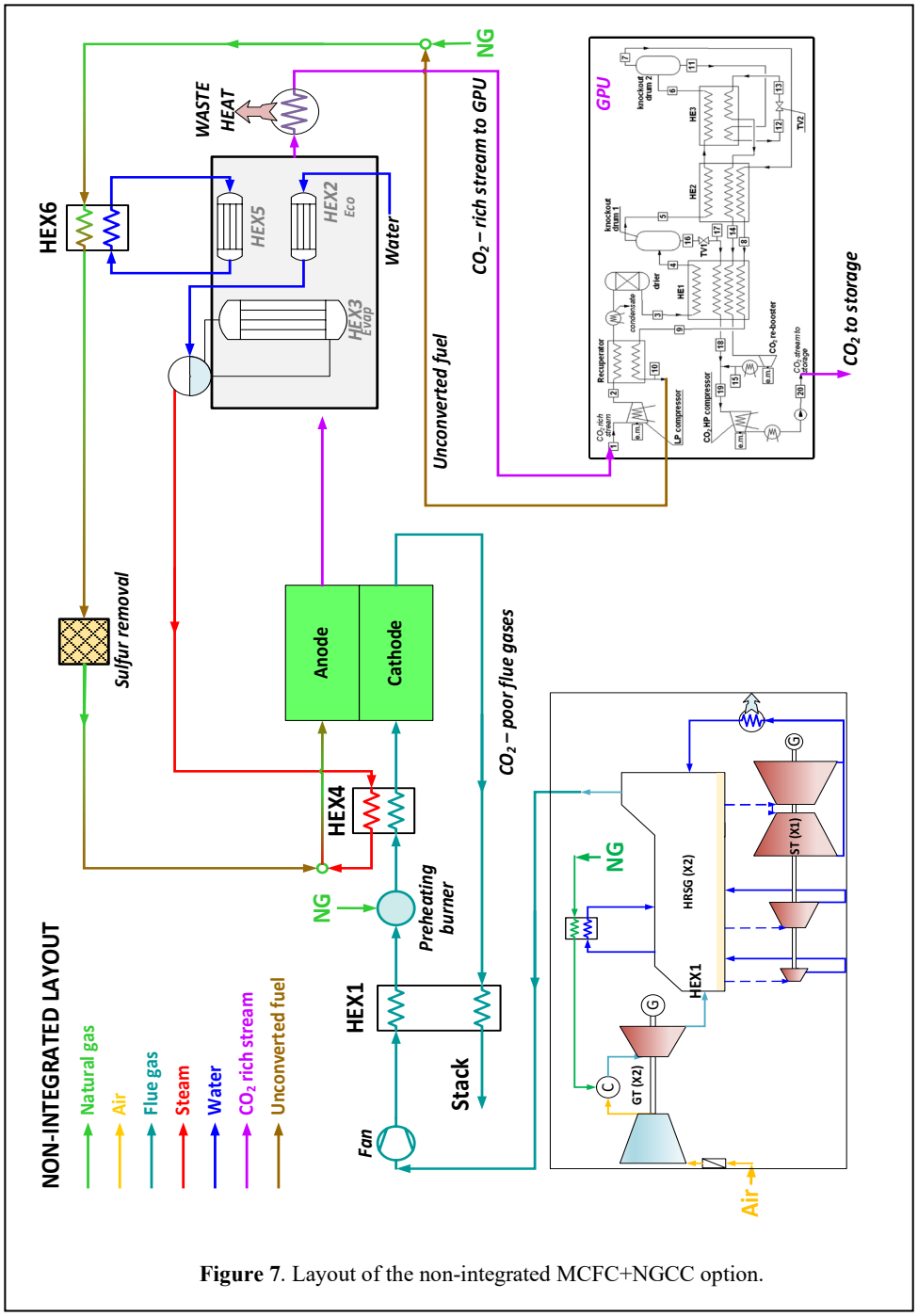

Figure 7. Layout of the non-integrated MCFC+NGCC option.

The initial cathode feed stream preheater (HEX1 in Figure 7), required to increase the NGCC exhaust temperature from the HRSG outlet (87°C) part way to the MCFC operating temperature (580°C), is the most critical component of the heat transfer network because of its size. A rotary regenerative heat exchanger is used to provide a large heat transfer area for the high mass flow rates and low pressure of both the cold and hot streams and the low LMTD (around 70°C) available. HEX1 enables the non-integrated plant to achieve reasonable efficiency by minimizing energy input by the auxiliary, natural gas burner. If the entire preheating duty for the cathode stream, with its large mass flow (1350 kg/s), was provided by the preheat burner, the efficiency would drop by more than 20 percentage points. An alternative to offset the efficiency penalty due to the burner is to raise steam in a dedicated HRSG for the hot cathode exhaust, but this would add additional capital cost and complexity to the "non-integrated" concept. In more detail, cathode feed gas is first preheated to an intermediate temperature using a rotary-type regenerative heat exchanger with MCFC cathode exhaust on the hot side. The cathode feed is further heated to the target MCFC working temperature by the auxiliary NG burner, accepting the efficiency penalty associated with the use of NG for relatively low temperature preheating. The relative share of cathode preheat furnished by the regenerative heat exchanger (HEX1) compared to the auxiliary burner has a significant influence on both power plant capital costs and electric efficiency. For this study, the intermediate temperature of 530°C was determined by minimizing the cost of CO_2 avoided.

Four parallel Ljungström type heat exchangers were designed to supply the preheating duty of the cathode stream (around 670 MWt), using the ε-NTU iterative method described in [31].

The hot anode exhaust, which contains unreacted syngas, cannot be used to preheat the cathode feed in a gas-gas heat exchanger because of metal dusting. Instead, thermal energy is recovered from the anode exhaust by producing the steam required by the fuel cell and preheating the fuel fed to desulfurization prior to the anode inlet. Metal dusting is avoided in HEX3 due to the high heat transfer coefficient on the cold (boiling water) side so the wall temperature is safely below the critical level of metal dusting. HEX5 provides preheat to the fuel preheater, HEX6, using pressurized hot water (175bar/350°C). The steam generated in HEX3 is superheated by HEX4 prior to mixing with preheated fuel for feed to the MCFC anode. For this non-integrated configuration, the cryogenic purification unit uses the same design as the integrated scheme. Almost all the unconverted syngas in the CO_2-rich effluents from the anode outlet is recycled to the anode inlet, approaching complete fuel utilization.

Plant Simulation Methods and Reference Cases

All the power plant simulations have been carried out using GS software [28] and the commercial software programs Aspen Plus [32] and Thermoflex [33]. The NGCC considered as a reference case is documented in the CCS EBTF report [5] and was described in Chapter 7 of the present volume. The power plant without CCS achieves a net efficiency ($\eta_{el,LHV}$) of 58.3% with a power output (P_{el}) of 829.9 MW_{el} and specific emissions of 351.8 g_{CO2}/kWh_{el}. The same NGCC with MEA-based post-combustion CCS achieves a net efficiency of 49.9% with a carbon capture rate (CCR) of 90%. The key assumptions used for the power plant simulations are reported in Table 2.

Table 2. Key assumptions for evaluation of baseline and carbon capture layouts.

Ambient conditions	15°C/1.013 bar/60% humidity
Natural gas conditions	10°C/70 bar
Gas turbine–two F-class machines	
Pressure ratio, β	18.1
Turbine inlet temperature, TIT, °C	1360
Gas turbine efficiency, %LHV	38.25
Heat recovery steam cycle – 3 pressure levels, bar	130/35/4
Superheat temperature, °C	565
Condensing pressure, bar	0.048
Cooling water temperature, °C	18
Temperature at outlet of coolers, °C	28
Electric consumption of auxiliaries for cooling, % of the heat rejected	2
Condensing temperature of refrigerators (where required), °C	32
Polytropic efficiency of flue gas compressors, %	90
Polytropic efficiency of flue gas expanders, %	90
Polytropic efficiency of vacuum pumps, %	85
Polytropic efficiency of CO_2 compressors, %	85
Polytropic efficiency of air blowers, %	85
Hydraulic efficiency of CO_2 pumps, %	75
Electric-mechanical efficiency of motor-drivers, %	95
Minimum temperature difference gas-gas heat exchangers, °C	25
Minimum temperature liquid-gas heat exchangers, °C	10
Relative pressure drop of heat exchangers - gas side, %	2
Relative pressure drop of heat exchangers - liquid side, bar	0.4

GAS PROCESSING UNIT

As highlighted in the MCFC model section, a lower the fuel utilization factor, U_F, enables more stable operation and longer MCFC stack lifetime due to a reduced concentration overpotential. Even though the anode discharge is CO_2-rich - the CO_2 concentration is 80 mol% for the non-integrated case and 83 mol% for the integrated case – it is not suitable for final geological storage or enhanced oil recovery (EOR) applications. The anode exhaust stream requires purification to increase the CO_2 concentration by removing residual inert species (H_2O and N_2) and unconverted fuel (CO and H_2) [15]. Consequently, the CCS plant includes a CO_2 compression and purification unit, designed to achieve the following goals:

- Meet the CO_2 specifications typically envisaged for long range pipeline transport and EOR (Table 3).
- Recover valuable fuel species (CO and H_2) as much as is practical from the MCFC anode exit stream. The anode exhaust contains significant fuel value since about 30% of the MCFC fuel input leaves the anode unreacted. This fuel value must be recovered and recycled to maximize overall fuel utilization and the plant efficiency.

Table 3. CO_2 specifications for the EOR application.

Parameter	Value
Temperature, °C	30
Pressure, bar	110
CO_2, %mol	> 97
H_2O, ppm_v	< 50
N_2 and other non-condensables, %mol	< 3
O_2, ppm_v	< 75

Since the anode exhaust contains a high CO_2 concentration, the required CO_2 purification can be efficiently achieved by a cryogenic, auto-refrigerated, double-stage flash separation process represented in Figure 8.

The GPU uses a multi-stage compression and flash process [15], in which pressurized CO_2 is partly condensed with auto-refrigeration and separated from condensable gases at low temperature via two stages of flash. The auto-refrigeration effect is achieved by using the flashed CO_2-rich liquid streams as cooling sources. The GPU delivers dense-phase CO_2 at 110 bar, and a recovered gaseous stream (containing mostly H_2 and CO) which is preheated and recycled back to the MCFC section. The main advantages of this GPU system are the absence of additional chemical or physical solvents and relatively low energy consumption (531 MJ/t_{CO2} for the integrated scheme and 579 MJ/t_{CO2} for the non-integrated layout) compared to alternative solutions. This system achieves a final purity of 98.9 mol% in the CO_2-rich stream with a CO_2 recovery efficiency of 90%. The balance of the CO_2 leaves the GPU with the recovered syngas (orange stream in Figure 8) and is recycled to the MCFC anode.

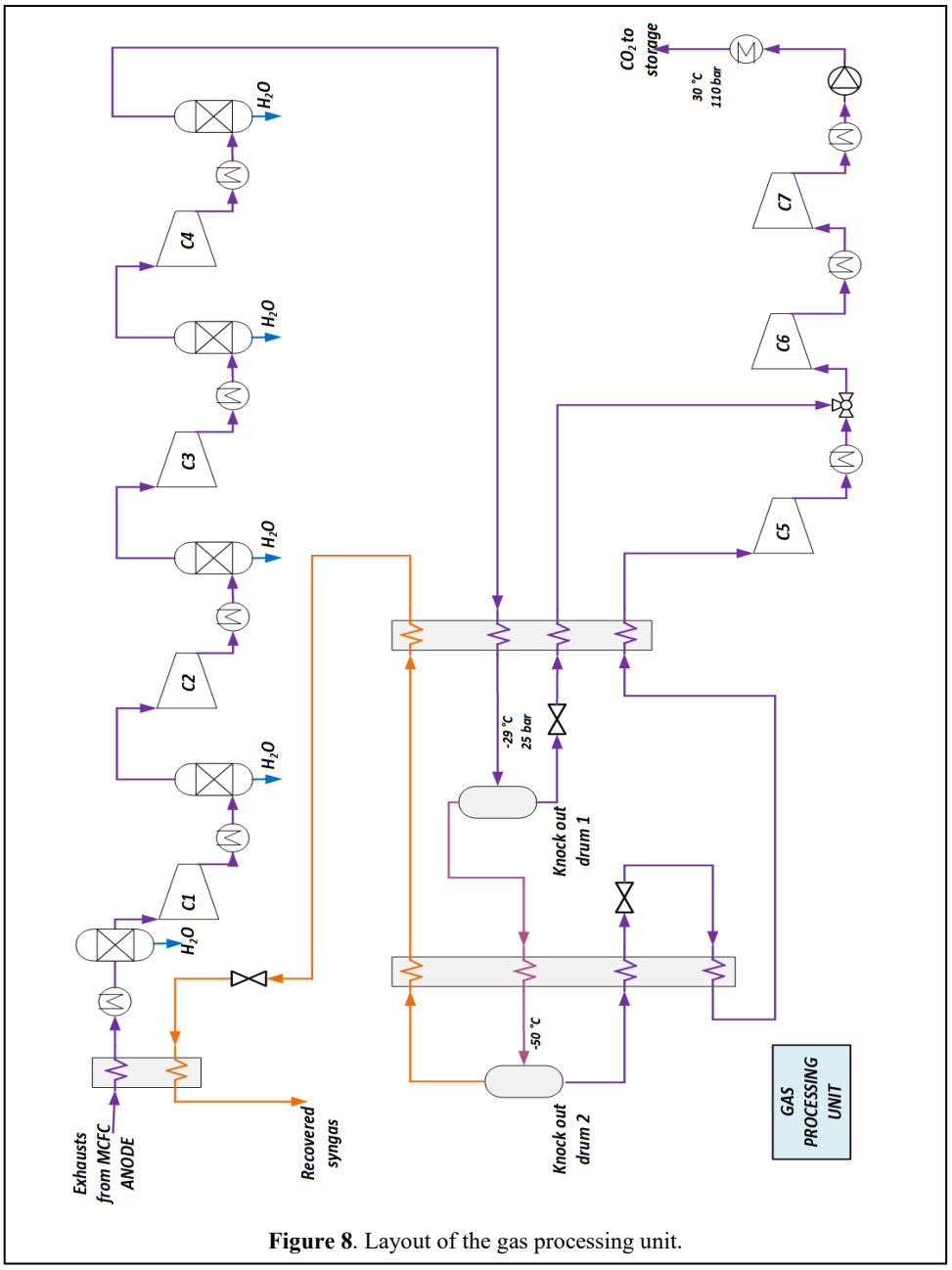

Figure 8. Layout of the gas processing unit.

METHODOLOGY AND MAIN ASSUMPTIONS FOR THE ECONOMIC EVALUATION

The economic analysis methodology is described in Chapter 7 of the present volume. The Total Plant Cost (TPC), along with the Fuel and the Fixed and Variable Operating and Maintenance Costs form the basis for estimating the cost of electricity (COE) and the cost of CO_2 avoided (CCA). The total cost buildup requires the calculation of several intermediate cost values:

- Total Equipment Cost (TEC, Table 4) is the sum of the equipment costs of all the plant sub-units. Each equipment or unit cost was obtained by using a typical power-law function from technical reports or simulation codes (i.e., Aspen plus [32], Thermoflex [33]). For example, the cost of the Ljungström regenerative heat exchangers for the non-integrated option was estimated using the relevant correlation described in [34], which takes into account the effect of gas leakages (evaluated during the Ljungström design) and the effect of high temperature sections, resulting in a total equipment cost of around 30 M$. For the non-integrated option shown in Figure 7, the units HEX2, HEX3, HEX5 and the waste heat recovery boiler have been sized and costed as a unique assembly, using HRSG cost functions as an approximation, even though this assemblage is smaller and has less extreme steam conditions than a typical HRSG for this size power plant. The reference cost for the MCFC (a constant, specific cost of 465 $\$/m^2$) is one of the most uncertain assumptions, because it is based on future mass-production of the stack components at the scale of hundreds of MW per year.

Table 4. Equipment costs for the integrated/non-integrated layouts.

Total Equipment Cost	**Integrated**	**Non-integrated**
GT, M$	134	134
Steam Cycle, M$	136	130
Total Equipment Cost of power section, M$	269	264
Equipment cost of GPU, M$	44	46
MCFC + BOP, M$	99	115
Flue gas blower, M$	2	3
Fuel heaters, M$	7	0.3
Quench boilers, M$	13	11
Cathode stream heaters, M$	-	31
Total Equipment Cost of CO_2 removal section, M$	164	159

- Total Direct Plant Cost (TDPC) is obtained by adding to the TEC all the costs related to equipment installation, expressed as a percentage of the TEC.
- Engineering, Procurement and Construction (EPC) cost is calculated by adding to the TDPC the indirect cost related to engineering, buildings and site improvement.
- Total Plant Cost (TPC), which results from the sum of the EPC cost and the cost associated to all the project planning and contingencies.

As described in Chapter 7, the installation, indirect and project cost contingency are expressed as a fraction of TEC, TDPC and EPC values. The Total Plant Cost is obtained by multiplying the TEC by a series of incremental factors. Since the technology readiness level (TRL) of the specific plant sections reflects the extent of engineering and deployment (if any), the contingency factors are different for each of the plant sections. Some components are classified as mature technologies (e.g., gas turbines), while other components/subsections (CCS equipment) are characterized by more

uncertainty. As an example, the 70% contingency associated with the capture section is much higher than the 35% for the power section because the carbon capture section is characterized by a lower TRL and more limited industrial experience for some key pieces of equipment or plant sections (e.g., MCFC, cryogenic unit, etc.) compared to conventional operations.

Once the TPC is obtained, the economic analysis involves the calculation of the First Year Cost of Electricity (COE), obtained by combining the total capital cost with the cost of fuel, consumables and O&M. These values are calculated according to the technical and financial assumptions documented in Chapter 7 and are consistent with the CCP methodology described in [35]. The cost of CO_2 Avoided (CCA) is calculated according to eq.10. CCA is generally recognized as an important benchmark metric for the techno-economic comparison of CCS systems. The CCA [\$/t_{CO2}] is the ratio of the marginal cost of the electricity for the MCFC+NGCC power plant and the avoided specific CO_2 emissions:

$$CCA \quad \left[\frac{\$2014}{t_{CO2\ avoided}}\right] = \frac{(COE)_{CCS} - (COE)_{REF}}{(e_{CO2})_{REF} - (e_{CO2})_{CCS}} \tag{10}$$

RESULTS AND COSTS FOR THE PROPOSED INTEGRATED AND NON-INTEGRATED SCHEMES

The performance and economic estimates for the integrated and non-integrated layouts are summarized in Table 5. The simulation results show good performance for the integrated system, which avoided nearly 80% of CO_2 emissions with a limited energy penalty. If compared with the baseline NGCC, the net electric efficiency of the MCFC+NGCC power plant is reduced by less than 1%. Compared with the reference NGCC without capture, the power generated by the steam cycle of the integrated case is 7% larger. This is due the supplemental natural gas and water fed to the MCFC anode, which increases the flue gas temperature by 72°C and mass flow. Both the CO_2 and O_2 utilization factors are set (U_{CO2} and U_{O2} are respectively 75.9% and 12.1%) by assuming the outlet concentration of CO_2, which is the limiting reactant for the electrochemical reaction on the cathode side. Since all the CO_2 generated by NG oxidation on the anode side exits with the anode exhaust gas, the CO_2 capture rate (79.7%) is higher than the CO_2 utilization factor. Finally, the limited efficiency penalty and the significant carbon capture rate of the integrated solution are reflected in the value of the SPECCA, which approaches 0 MJ/kg_{CO2}, as observed in previous studies on this CO_2 capture configuration [16]. The proposed integration appears very promising from an economic perspective, achieving a CO_2 avoided cost of about 50 \$/t_{CO2}.

In the non-integrated case, the electric power produced by the MCFC section is 7.5% larger than that produced by the integrated case (up to 193 MW_{el}). The increased MCFC power output is driven by fuel burned in the combustor to heat the cathode feed to the MCFC working temperature. The preheating combustion generates more CO_2 on the cathode-side of the fuel cell, which increases the total current generated by the electrochemical reactions of the MCFC. As a result, the non-integrated layout increases the CO_2 capture rate relative to the integrated system slightly to 81.1% because of the larger size of the MCFC section and consequent larger amount of CO_2 recovered at the anode and fully captured in the MCFC-GPU loop. However, the CO_2 avoided decreases to 79% because the non-integrated system achieves a lower electric efficiency (-4.8% with respect to the integrated scheme) and, consequently, higher specific CO_2 emissions. Nevertheless, the SPECCA index for the non-integrated option i slower than that of the benchmark chemical absorption processes with amine-based solvents (SPECCA=2.5-3.5 MJ/kg_{CO2}). The cost of CO_2 avoided for the non-integrated scheme is about 50% higher than for the integrated case. This is primarily due to the lower electric efficiency of this configuration, mainly due to use of NG for relatively low temperature preheating and the strategic

choice of avoiding any heat integration with the existing NGCC. In addition, the CCA is penalized by the added investment cost of the large Ljungström pre-heater units for the cathode feed stream.

SENSITIVITY ANALYSIS FOR CO_2 UTILIZATION FACTOR

This section presents a sensitivity analysis of performance for both the integrated and non-integrated systems at various levels of the CO_2 utilization factor. This analysis assumes that the fuel cell can achieve safe and stable operation if the minimum molar CO_2 concentration at the cathode outlet is pushed below the recommended value of 1%.

Table 5. General performance and costs of the NGCC+MCFC integrated and non-integrated layouts.

Power balance - NGCC + MCFC	**Reference case**	**Integrated**	**Non-Integrated**
GT - Net electric power, MW_{el}	544.2	542.9	544.2
Steam Cycle - Net electric power, MW_{el}	285.7	305.57	289.9
MCFC - Net electric power (w/o aux), MW_{el}	-	179.08	192.6
Auxiliaries (fan), MW_{el}	-	2.35	8.74
GPU consumption, MW_{el}	-	41.80	48.82
Fuel input, MW_{LHV}	1422.6	1709.4	1839.5
Overall net electric power, MW_{el}	829.9	983.4	969.1
Net electric efficiency	58.3%	57.53%	52.68%
CO_2 Balance			
CO_2 from NGCC, kg/s	81.63	81.63	81.63
CO_2 from MCFC, kg/s	-	16.4	23.76
Carbon capture %	-	79.75%	81.1%
CO_2 specific emissions, g/kWh_{el}	351.8	72.18	73.82
CO_2 avoided, g/kWh_{el}	-	279.62	277.98
CO_2 avoidance rate	-	79.48%	79.0%
SPECCA, MJ/kg_{CO2}	-	0.310	2.382
Economics			
COE , $/MWh	45.0	58.80	66.08
Cost of CO_2 avoided, $/t_{CO2}$	-	49.37	75.85

This assumption needs validation by long-term operational tests. The sensitivity analysis considers three levels of molar CO_2 concentration at the cathode outlet: 2%, 1% (reference value) and 0.5%. The resulting CO_2 utilization factor ranges between 51% and 89%, as shown in Table 6.

Table 6. Results for the sensitivity analysis on CO_2 utilization factor, for the integrated and non-integrated MCFC+NGCC schemes

Power balance - NGCC + MCFC	**Integrated**			**Non-integrated**		
CO_2 concentration at cathode outlet	**2%**	**1%**	**0.5%**	**2%**	**1%**	**0.5%**
CO_2 utilization factor, U_{CO2}	51%	75.9%	88%	54%	77.4%	88.8%
GT - Net electric power, MW_{el}	542.9	542.9	542.9	544.2	544.2	544.2
HRSG - Net electric power, MW_{el}	300.48	305.57	308.27	288.1	289.9	292.1
MCFC - Net electric power, MW_{el}	121.94	179.08	206.26	134.9	192.6	219.3
Auxiliaries, MW_{el}	2.45	2.35	2.33	8.835	8.745	8.722
GPU consumption, MW_{el}	28.07	41.80	48.50	34.02	48.82	56.30
Fuel input, MW_{LHV}	1615.5	1709.4	1755.3	1736.0	1839.5	1886.8
Overall net electric power, MW_{el}	934.8	983.4	1006.6	924.4	969.1	990.5
Net electric efficiency	57.86%	57.53%	57.35%	53.25%	52.68%	52.5%
CO_2 Balance						
CO_2 from NGCC, kg/s	81.63	81.63	81.63	81.63	81.63	81.63
CO_2 from MCFC section, kg/s	11	16.4	19.1	17.85	23.76	26.45
Carbon capture efficiency	56.54%	79.75%	90.24%	59.5%	81.1%	90.6%
CO_2 specific emissions, g/kWh_{el}	154.2	72.18	34.94	157.06	73.82	36.93
CO_2 avoided	56.15%	79.48%	90.07%	55.4%	79.0%	89.5%
SPECCA, MJ/kg_{CO2}	0.256	0.310	0.335	3.029	2.382	2.18
Economics						
COE, $/MWh	55.56	58.80	60.27	63.20	66.08	67.73
Cost of CO_2 avoided, $/t_{CO2}$	53.43	49.37	48.18	93.48	75.85	72.19

Table 6 shows the following effects of increasing U_{CO2}:

- For both the integrated and non-integrated options, an increase of U_{CO2} leads to lower overall efficiency due to a decrease of MCFC voltage. This is caused by the lower average CO_2 concentration in the cathode stream, which decreases the value of Nernst potential (E_{Nernst}, eq.6) and increases the activation losses (ΔV_{act}, eq.5).
- The overall electric power increases with U_{CO2}, because the total current generated by the fuel cell modules is proportional to the flow of CO_2 molecules migrated from the cathode to the anode. This effect overcomes the decrease of MCFC voltage discussed in the previous point. In addition, power output is boosted by: (i) the larger volume of NG and water fed to the MCFC; and (ii) the increased waste heat produced by the higher voltage losses. Both factors contribute to increased steam cycle power output.
- The CO_2 capture efficiency improves with U_{CO2} because of the direct effect of capturing a larger fraction of CO_2 from the cathode feed stream and because the fraction of CO_2 generated from the fuel cell itself by conversion of NG at the anode, which is fully captured, increases with the MCFC power.

Interestingly, the resulting SPECCA values show opposite trends in the integrated and non-integrated schemes. The SPECCA values of the integrated configuration decrease slightly as U_{CO2} decreases. The decrease of SPECCA (from 0.335 to 0.256 MJ/kg$_{CO2}$) is due to the higher voltage (meaning lower concentration polarization) promoted by the higher CO_2 partial pressure at the cathode side of the fuel cell at lower U_{CO2}. On the other hand, the non-integrated option shows a positive effect of high carbon capture designs (the higher the CO_2 utilization factor, the lower the SPECCA). The natural gas used for preheating the cathode feed to the MCFC adds primary energy input to the CO_2 capture section that does not depend on the CO_2 capture rate (which defines the size of the fuel cell stack and its power output) but only on mass flow rate of cathode exhaust.

Contrasting the Integrated and Non-Integrated options:

- For the Integrated case, the fraction of NG sent to the MCFC anode is proportional to the CO_2 permeated from the cathode to the anode of the fuel cell. The higher the CO_2 utilization, the higher the NG demand by the MCFC.
- For the Non-Integrated case, the fraction of NG burned in the preheating section is roughly constant and does not depend on CO_2 utilization, because the entire NGCC exhaust stream must be heated to the MCFC working temperature even with a of low CO_2 capture rate.

As a result, in the Non-Integrated cases with decreasing CO_2 capture (lower U_{CO2}), the constant amount of primary energy used for preheating all the gas mass flow (meaning higher *specific* primary energy for capturing 1 molecule of CO_2) leads to increased SPECCA. This trend also occurs for the cost of CO_2 avoided, which increases much more for the non-integrated case (+30% going from the low capture case to the high capture case) than in the integrated case (+10% going from the low capture case to the high capture case). In conclusion, high carbon capture configurations are essential for high economic performance, especially in the non-integrated case, where a fraction of the primary energy introduced in the capture system doesn't depend on the level of CO_2 capture.

DISCUSSION AND CONCLUSIONS

To assess the potential of the NGCC+MCFC combinations, the analyses reported here are compared with those of a benchmark CO_2 capture process. The benchmark process is post-combustion MEA scrubbing as assessed in the EBTF report [36]. This is a well-proven process, and the technology readiness has been demonstrated by several pilot/demo plants [37]. The comparison of the MCFC-based schemes with the EBTF MEA process and previously assessed in [12] is shown in Table 7.

The integrated case achieves a very low SPECCA of 0.31 MJ/kg$_{CO2}$, which is promising compared to the reference value of 3.34 MJ/kg$_{CO2}$ for MEA and also against the value claimed by the most promising solvents (e.g., [36][38]). The non-integrated case achieves a SPECCA of 2.38 MJ/kg$_{CO2}$, which is promising but much closer to the figures claimed by optimized chemical solvents for post-combustion applications [39]. In terms of CO_2 removal, stand-alone MCFCs are not presently capable of the very high capture rate achievable by chemical solvent plants, due to the constraints on the minimum CO_2 concentration limit at the cathode outlet. When coupled with NGCCs, MCFCs are more suitable for CO_2 removal rates close to 80%, whereas the base MEA case is designed for 90% capture.

Table 7. Techno-economic comparison between MEA and MCFC cases–summary table.

	NGCC + MEA	NGCC + Integrated MCFC	NGCC + Non-integrated MCFC
SPECCA, MJ_{LHV}/kg_{CO2}	3.34	0.31	2.38
Carbon Capture Rate, %	90.5	79.7	81.1
Specific energy penalty, MJ_{el}/kg_{CO2}	1.63	0.18	1.23
Specific cost of the CO_2 capture unit, $/kW	977	820	1043
Specific cost of the overall plant, $/kW	2181	1731	1950
COE, $/MWh	68.6	58.8	66.1
CCA, $/$t_{CO2}$	74.7	49.4	75.9

The economic analysis shows that the integrated case is by far the most promising option. The reference Cost of CO_2 Avoided (CCA) for NGCC+MEA is 75 $/$t_{CO2}$ [12]. The CCA for the NGCC+MCFC non-integrated case is nearly the same (76 $/$t_{CO2}$), while the CCA for the NGCC+MCFC-integrated case is 35% lower (49 $/$t_{CO2}$). The lower CCA for the integrated case is due to 20% lower specific investment cost than for MEA and higher energy efficiency.

Since MCFC and post-combustion scrubbing with MEA are at quite different levels of technical maturity, there is a significant difference in the uncertainty for estimated investment costs, capacity factors, and O&M costs. Since investment cost is expected to be one of the major uncertainties related to the MCFC system, a sensitivity analysis was done to assess the impact of ±50% of the MCFC investment cost on the CO_2 avoidance cost. The results of this analysis are shown in Figure 9 and show that the integrated scheme would achieve a CCA about the same as MEA scrubbing if the MCFC cost is 50% higher than the base assumption.

The major drawback of the integrated scheme is its unsuitability for retrofit applications. For existing NGCCs, the plot space available between the GT outlet and the HRSG inlet typically is not sufficient for the MCFC modules. On the other hand, the non-integrated scheme seems suitable for retrofit applications since no modifications of the existing HRSG are expected. Only modifications of the LP and MP sections of the steam turbine should be necessary to accommodate the additional steam flow rate generated by the external heat exchangers. This issue is similar to that of the MEA process in which about one-third of the LP steam is extracted for solvent regeneration, and the LP turbine is either modified or operated in a throttling mode.

As far as operational flexibility is concerned, since high temperature MCFCs require a long start-up time, neither scheme is likely suitable for frequent on/off (cycling) operation. However, further work is necessary to assess MCFC operational flexibility, start-up sequence, and part-load performance.

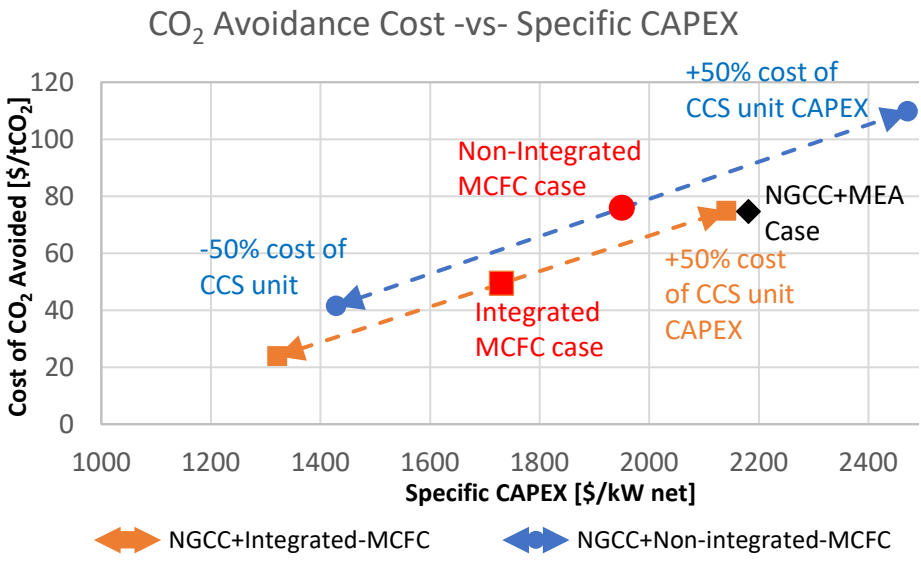

Figure 9. Sensitivity of CCA cost of MCFC cases to specific CAPEX and comparison against MEA estimate.

In summary, the proposed integrated NGCC-MCFC scheme has potential to achieve outstanding energy and economic performance which considerably improves upon the benchmark CO_2 capture technology. A major factor is the proper matching of the MCFC temperature requirements with the similar gas turbine outlet conditions. If the integration is not fully optimized, as is the case in the non-integrated scheme, the efficiency penalty and the increased capital costs associated for the required heat exchangers limit the advantages compared to the benchmark MEA scrubbing process.

NOMENCLATURE

CCA	Cost of CO_2 avoided [$/$t_{CO2}$]
CCR	Carbon Capture Rate
CCS	Carbon Capture & Storage
CHP	Combined Heat and Power
COE	Cost of Electricity [$/$MWh_{el}$]
COP	Conference of Parties
DIR	Direct Internal Reforming
e	Specific Emissions [kg_{CO2}/MWh_{el}]
EBTF	European Benchmarking Task Force
FCE	Fuel Cell Energy Inc.
GHG	Greenhouse gas
GPU	Gas Processing Unit
GT	Gas Turbine
HRSC	Heat Recovery Steam Cycle
HRSG	Heat Recovery Steam Generator

IC	Current density [A/m^2]
IIR	Indirect Internal Reforming
LMTD	Logaritmic Mean Temperature Difference
LP	Low Pressure
MCFC	Molten Carbonate Fuel Cell
MP	Medium Pressure
NG	Natural Gas
NGCC	Natural Gas Combined Cycle
NTU	Number of Transfer Units
p	Partial pressure
P	Power [MW]
Q	Thermal power [MW]
S/C	Steam to carbon ratio
SOFC	Solid Oxide Fuel Cell
SPECCA	Specific Primary Energy Consumption for CO_2 avoided [MJ/kg_{CO2}]
T	Temperature
TIT	Turbine inlet temperature
TRL	Technology Readiness Level
V	Voltage
X	Molar/Volumetric fraction
Greek symbols	
β	Gas turbine pressure ratio
ε	Thermal effectiveness
η	Net efficiency
$\Delta V_{(Act\text{-}Ohm\text{-}Conc)}$	Activation/ Ohmic /Concentration overpotential
Subscripts	
CCS	Carbon Capture & Storage
el	Electric
LHV	Low Heating Value
ref	Reference
spec	Specific

REFERENCES

1. IEA, “Energy, Climate Change & Environment—2016 Insights,” vol. Paris, Fra, 2016.
2. Intergovernmental Panel on Climate Change*, Climate Change 2014 Mitigation of Climate Change*. Cambridge University Press, 2014.
3. IPCC - Intergovernmental Panel on Climate Change*, Climate Change 2014: Impacts, Adaptation and Vulnerability*, 2014.
4. UNFCCC - United Nations Framework Convention on Climate Change, COP23, *United Nations Framework Convention on Climate Change United Nations - Summary for policymakers*, November 2017, pp. 1–33, 2017.
5. CaESAR Consortium*, European best practice guidelines for assessment of CO_2 capture technologies*, pp. 1–112, 2011.
6. J. Milewski, T. Wejrzanowski, Ł. Szabłowski, R. Baron, A. Szczęśniak, and K. Ćwieka, “Development of Molten Carbonate Fuel Cells at Warsaw University of Technology,” *Energy Procedia*, vol. 142, pp. 1496–1501, Dec. 2017.
7. K. Sugiura, K. Takei, K. Tanimoto, and Y. Miyazaki, “The carbon dioxide concentrator by using MCFC*,” J. Power Sources*, vol. 118, no. 1, pp. 218–227, 2003.

8. I. Rexed, M. della Pietra, S. McPhail, G. Lindbergh, and C. Lagergren, “Molten carbonate fuel cells for CO_2 separation and segregation by retrofitting existing plants - An analysis of feasible operating windows and first experimental findings,” *Int. J. Greenh. Gas Control*, vol. 35, pp. 120–130, 2015.
9. G. Discepoli, G. Cinti, U. Desideri, D. Penchini, and S. Proietti, “Carbon capture with molten carbonate fuel cells: Experimental tests and fuel cell performance assessment,” *Int. J. Greenh. Gas Control*, vol. 9, pp. 372–384, Jul. 2012.
10. H. Ghezel-Ayagh, S. Jolly, D. Patel, and W. Steen, “Electrochemical Membrane Technology for Carbon Dioxide Capture from Flue Gas,” *Energy Procedia*, vol. 108, pp. 2–9, Mar. 2017.
11. “ExxonMobil, FuelCell Energy trial MCFCs in carbon capture*,” Fuel Cells Bull.*, vol. 2016, no. 5, pp. 12–13, May 2016.
12. J. Forsyth *et al.*, “Evaluation of Five Alternative CO_2 Capture Technologies with Insights to Inform Further Development,” *Energy Procedia*, vol. 114, pp. 2599–2610, Jul. 2017.
13. E. Audasso, L. Barelli, G. Bidini, B. Bosio, and G. Discepoli, “Molten Carbonate Fuel Cell performance analysis varying cathode operating conditions for carbon capture applications*,” J. Power Sources*, vol. 348, pp. 118–129, Apr. 2017.
14. R. Carapellucci, R. Saia, and L. Giordano, “Study of Gas-steam Combined Cycle Power Plants Integrated with MCFC for Carbon Dioxide Capture,” *Energy Procedia*, vol. 45, pp. 1155–1164, 2014.
15. P. Chiesa, S. Campanari, and G. Manzolini, “CO_2 cryogenic separation from combined cycles integrated with molten carbonate fuel cells,” *Int. J. Hydrogen Energy*, vol. 36, no. 16, pp. 10355–10365, 2011.
16. S. Campanari, G. Manzolini, and P. Chiesa, “Using MCFC for high efficiency CO_2 capture from natural gas combined cycles: Comparison of internal and external reforming,” *Appl. Energy*, vol. 112, pp. 772–783, 2013.
17. S. Campanari, P. Chiesa, G. Manzolini, and S. Bedogni, “Economic analysis of CO_2 capture from natural gas combined cycles using Molten Carbonate Fuel Cells,” *Appl. Energy*, vol. 130, pp. 562–573, 2014.
18. A. Amorelli *et al.*, “An experimental investigation into the use of molten carbonate fuel cells to capture CO_2 from gas turbine exhaust gases,” *Energy*, vol. 29, no. 9, pp. 1279–1284, 2004.
19. V. Spallina, M. C. Romano, S. Campanari, and G. Lozza, “Application of MCFC in Coal Gasification Plants for High Efficiency CO,” in Volume 4: Cycle Innovations; Fans and Blowers; Industrial and Cogeneration; Manufacturing Materials and Metallurgy; Marine; *Oil and Gas Applications*, 2011, vol. 4, pp. 233–242.
20. R. Chacartegui, B. Monje, D. Sánchez, J. A. Becerra, and S. Campanari, “Molten carbonate fuel cell: Towards negative emissions in wastewater treatment CHP plants,” *Int. J. Greenh. Gas Control*, vol. 19, pp. 453–461, 2013.
21. M. Spinelli, M. C. Romano, S. Consonni, S. Campanari, M. Marchi, and G. Cinti, “Application of Molten Carbonate Fuel Cells in Cement Plants for CO_2 Capture and Clean Power Generation,” *Energy Procedia*, vol. 63, pp. 6517–6526, 2014.
22. Berlowitz, P., Barckholz, T., and Lee, A., 2016, “Integration of Molten Carbonate Fuel Cells in Iron and Steel Processing,” US Patent # 10093997, Jan. 2016.
23. R. Hill *et al.*, “Application of molten carbonate fuel cell for CO_2 capture in thermal in situ oil sands facilities,” *Int. J. Greenh. Gas Control*, vol. 41, pp. 276–284, 2015.
24. S. Campanari, “Carbon dioxide separation from high temperature fuel cell power plants*,” J. Power Sources*, vol. 112, no. 1, pp. 273–289, 2002.
25. P. Greppi, B. Bosio, and E. Arato, “Membranes and molten carbonate fuel cells to capture CO_2 and increase energy production in natural gas power plants,” *Ind. Eng. Chem. Res.*, vol. 52, no. 26, pp. 8755–8764, 2013.

26. M. Spinelli *et al.*, “Molten Carbonate Fuel Cells for Retrofitting Postcombustion CO_2 Capture in Coal and Natural Gas Power Plants,” *J. Electrochem. Energy Convers. Storage*, vol. 15, no. 3, 2018.
27. U.S. Department of Energy, *Fuel cell handbook*, 2004.
28. Politecnico di Milano, “Software presentation: GS (Gas-Steam Cycles).” 2012.
29. M. Farooque, J. Daly, and J. Wang, “Contaminants Control for Fuel Cells – FCE Experience,” ANL Conference, Chicago, 2014.
30. H. J. Grabke, “Metal Dusting of Low- and High-Alloy Steels,” *Corrosion,* vol. 51, no. 9, pp. 711–720, 1995.
31. D. Swanepoel and D. Kr, “Rotary Regenerator Design Theory and Optimisation,” *R&D J.*, vol. 12, no. 3, 1996.
32. AspenTech, “Aspen Plus v8.8.” Aspentech, 2016.
33. Thermoflow, “Thermoflex v. 24.” 2014.
34. B. Berkenpas, C. Frey, J. Fry, and E. S. Rubin, “Technical documentation,” Integrated. Environmental. Control Model - https://www.cmu.edu/epp/iecm/iecm_doc.html . May, 2009.
35. Gerdes, K. (ed), *Carbon Dioxide Capture for Storage in Deep Geologic Formations – Results from the CO_2 Capture Project Volume 4: CCS Technology Development and Demonstration; Results (2009-2014),* CPL Press 2015.
36. EBTF - European Benchmark Task Force, “European best practice guidelines for assessment of CO_2 capture technologies,” 2011.
37. “Carbon Capture and Sequestration Technologies @ MIT.” [Online]. Available: http://sequestration.mit.edu/tools/projects/map_projects.html. [Accessed: 03-May-2018].
38. E. Sanchez Fernandez, E. L. V. Goetheer, G. Manzolini, E. Macchi, S. Rezvani, and T. J. H. Vlugt, “Thermodynamic assessment of amine based CO_2 capture technologies in power plants based on European Benchmarking Task Force methodology,” *Fuel*, vol. 129, pp. 318–329, Aug. 2014.
39. D. Sutter, M. Gazzani, and M. Mazzotti, “A low-energy chilled ammonia process exploiting controlled solid formation for post-combustion CO_2 capture,” *Faraday Discuss*., vol. 192, no. 0, pp. 59–83, Oct. 2016.

Carbon Dioxide Capture for Storage in Deep Geological Formations, Volume 5
Karl F. Gerdes (Editor)
© 2022 BP. All rights reserved.

Chapter 9

TECHNO-ECONOMIC ASSESSMENT OF NOVEL VS. STANDARD CCS ABSORPTION PROCESSES USING 5m PIPERAZINE FOR CONVENTIONAL AND HIGH-EFFICIENCY NGCC POWER PLANTS

Antonio Conversano[1,2], Manuele Gatti[2], Roberto Scaccabarozzi[2], Emanuele Martelli[2], Ibrahim Ali[3], Gustavo Moure[4], Stefano Consonni[1,2]

[1]LEAP s.c.a.r.l., Via Nino Bixio 27/C, 29121, Piacenza, Italy
[2] Politecnico di Milano, Dept. of Energy, Via Lambruschini 4, 20156, Milano, Italy
[3] BP International, Chertsey Road, TW16 7BP, Sunbury-on-Thames, UK
[4] Petrobras Research Center, Avenida Horácio Macedo, 950, Rio de Janeiro, RJ, Brazil

ABSTRACT: CO_2 capture and storage (CCS) can mitigate greenhouse gas emissions from natural gas-fired power plants [1,2], although an added challenge is the low CO_2 concentration (i.e., ~4 %mol) in the flue gas. Aqueous amine-based CO_2 capture has been widely studied and demonstrated as a practical solution to decarbonize post-combustion flue gases from natural gas combined cycle power plants (NGCC).

This paper presents the methodology and the results of a techno-economic assessment of a 5 molal (5m) aqueous piperazine (PZ) solution as a new potential baseline solvent for carbon capture from NGCC. Three case studies were defined based on a preliminary literature analysis. The three configurations evaluated are (i) conventional F-class NGCC coupled with the conventional absorber configuration with a direct contact cooler (DCC), (ii) conventional F-class NGCC coupled with an advanced absorber configuration (no DCC – flue gas cooling integrated within the absorber) and (iii) high efficiency, state-of-the-art H-class NGCC, coupled with the advanced absorber configuration. The present work is based on recent findings from University of Texas (UT) research activities.

KEYWORDS: CCS; absorber configuration; piperazine; high efficiency combined cycle

INTRODUCTION

Chemical absorption with aqueous amine-based solvents is a mature technology that has been widely employed to treat post-combustion flue gases Considered effective for carbon dioxide separation from post-combustion gases, MEA (usually 30 wt% monoethanolamine solution in water) has been used as a benchmark by many solvent research initiatives (e.g., CaESAR[3] and CESAR[4] projects). Although MEA has a fast CO_2 reaction rate, which minimizes equipment size, this solvent has several drawbacks–including a high thermal energy requirement to strip CO_2 from the rich solvent (3,9 GJ/tCO_2 [3]). Additionally, the maximum solvent loading in terms of molCO_2/mol Alkalinity and maximum operating temperature are limited to minimize equipment corrosion and degradation of the solvent. These shortcomings have spurred research with the goal of identifying effective alternatives, either in the form of novel solvents or suitable process modifications.

Among the potential alternatives to current amine-based solvents, aqueous piperazine (PZ) has been identified as a promising second generation solvent for CO_2 capture based on extensive experimental activities at the University of Texas at Austin (UT). PZ has several advantages over MEA-it has twice the absorption rate and greater CO_2 capacity (i.e., mol CO_2/kg solution); it is also more oxidatively

and thermally stable, which enables temperatures up to 150°C in the process without significant degradation [6]. The operating conditions for CO_2 capture using 5m PZ covers a temperature range from 40 to 150°C. Although temperatures lower than 40°C can be used, precautions must be taken to avoid solid formation that can occur at low solvent CO_2 loading. Solvent regeneration at higher pressures (6-8 bar) is possible because the solvent can be regenerated at 150°C without significant degradation [7]. This significantly reduces the electric power required for CO_2 compression.

Water-piperazine solutions have been tested at different concentrations by UT, and a 5m solution has been selected for the present investigation. The choice of solvent concentration is based on experimental data, showing that 5m PZ has higher capacity for CO_2 absorption than 7m MEA [8,9] and can be operated at lower lean loading than 8m PZ without solvent precipitation and with better absorber performance. The CO_2 absorption rate for 5m is approximately 30% higher than for 8m PZ, which reduces the size of the absorber. The 5m PZ solution is 50% less viscous than 8m PZ, which enhances mass transfer. However, the L/G ratio for 5m PZ (lean solvent over flue gas flow-rate on a molar basis) must be higher than for 8m to achieve the same capacity [7].

This study is to evaluate the 5m PZ solution performance and costs for CO_2 capture from NGCC flue gas for several NGCC configurations. The work is a collaboration among CCP, LEAP-POLIMI and the group of Professor Gary Rochelle from the University of Texas. Experimental tests were done at the University of Texas to evaluate PZ absorption from flue gases at relevant conditions for NGCC (CO_2 concentration, temperature, loading, L/G, etc.). Details about the pilot tests and results are reported in [10]. The experimental data were used to validate a simulation model of the pilot unit previously developed by UT (Aspen Plus®), which is based on a thermodynamic model suitable for the description of PZ-water and PZ-water-CO_2 interactions [8, 11].

LEAP-POLIMI and CCP have used the UT simulation model to develop three techno-economic case studies:

- **Case 1**: "Conventional Configuration" featuring a standard PZ absorber column with intercooling and a direct contact cooler (DCC). In this scheme, the natural gas combined cycle system (NGCC) is composed of 2 gas turbines (GT) plus 1 steam turbine (ST) and achieves thermal performance typical of established technologies (F-class GT). The flue gases from the heat recovery steam generator (HRSG) are cooled by means of a DCC upstream of the absorber.
- **Case 2**: The "Advanced Configuration," uses an advanced absorber column with pump-around intercooling, and no DCC included [12]. This case assesses the potential for capital and operating cost savings resulting from the DCC removal. The combined cycle system is the same as in Case 1 (2 F-class GT +1ST).
- **Case 3**: Substitutes a high efficiency (62.5%) combined cycle (NGCC, 1GT+1ST) for the standard NGCC used in Cases 1 and 2, coupled with the advanced absorber configuration (Case 2 absorber) to assess the improved performance of the most recent H-class gas turbine (GE 9HA) in an NGCC and its impact on flue gas and the capture unit.

A preliminary version of this work has been previously published by the authors [13].

PROCESS DESCRIPTION

A schematic block flow diagram of the NGCC + CCS concept assessed in this work is shown in Figure 1. There are three major subsystems in the overall plant:

- The Combined Cycle (CC) power system is composed of gas turbines, steam turbines and a heat recovery steam generator (HRSG).

- The flue gases from the CC system flow to the CO_2 capture island, which consists of absorption units for CO_2 capture and stripping units where the CO_2-rich solution is regenerated, and the concentrated CO_2 is released. The CCS Island includes a heat exchanger network (solvent coolers, reboiler and thermal-integration recuperative heat exchangers).
- The low pressure CO_2 from the capture island is processed in the compression and dehydration unit (CCU) for pipeline export.

Depending on the specific case study, the CO_2 capture island may or may not have a direct contact cooler (DCC) which quenches the NGCC flue gases upstream of the CO_2 absorber and partially condenses the water in the flue gas. The CO_2 absorption reaction in the absorber is exothermic, so cooling the flue gases enhances the absorption process. Additionally, the DCC reduces the gas volumetric flow rate, due to higher gas density and lower water content, and it may capture residual emissions (e.g., particulates and NOx), although this last effect has not been assessed in the present study.

The three case studies vary in equipment count and number of trains, depending on the plant size and flue gas flow rate to be processed (Case 1 and 2 have the same flue gas flow rate and composition, while case 3 varies because a different GT is used). Table 1 shows the number of units in the three case studies. In general, a single train has one gas turbine and one HRSG linked to one absorber and stripper with its associated heat-exchanger network. In all cases, there is a single steam turbine and a single CO_2 compression train.

For Case 1 a DCC is used upstream of each of the two absorption trains. The process flow diagram for a single CCS train for Case 1 is shown in Figure 2, and for Cases 2 and 3 in Figure 3. As mentioned previously, Case 1 utilizes the conventional absorber configuration with a DCC similar to the base case using 35 wt% MEA from IEAGHG [14]. The flow configuration for the absorber intercooler of Case 1 is different than that used for Cases 2 and 3. Case 1 utilizes interbed heat removal, in which rich solvent is withdrawn at the bottom of a packed section, cooled, and returned to the absorber at the top of the next lower section. This arrangement was demonstrated at the UT pilot plant. Cases 2 and 3 have a pump-around absorber cooling system, in which warm rich solvent is withdrawn from the bottom of a packed section, cooled, and returned to the top of that same section. The latter configuration has been studied by Zhang *et al.* [12] and identified as the most optimal arrangement in cases without DCC (Case 2 and 3). The choice of intercooling flow configuration affects the packing selection since the pump-around intercooling increases the net liquid flow through the packed sections

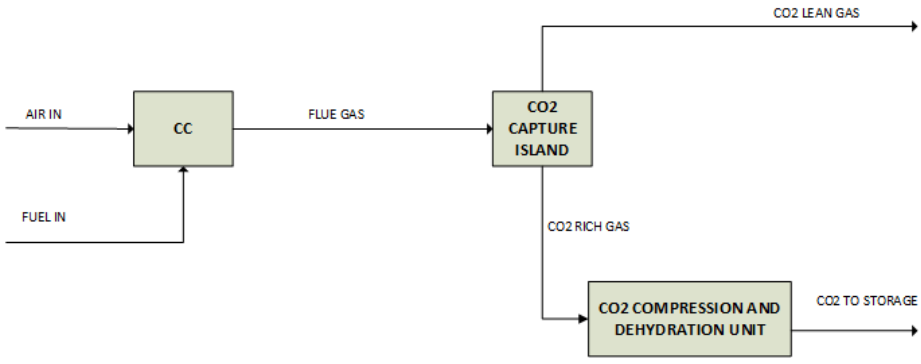

Figure 1. NGCC+CCS unit, simplified block flow diagram with major equipment and streams).

where the system is implemented. The absorber column for all three cases uses three beds of structured packing for the absorption and a water wash section on the exiting flue gas to minimize solvent losses. In all cases, a flue gas fan is used to overcome the pressure drop in the DCC, if present, the absorber and the flue gas ducting.

Table 1. Plant level equipment summary (# unit refers to the pieces of equipment; # train refers to the plant sections).

	CASE 1	**CASE 2**	**CASE 3**
Combined cycle	NGCC	NGCC	High-efficiency NGCC
- GT	2 units	2 units	1 unit
- ST	1 unit	1 unit	1 unit
- HRSG	2 units	2 units	1 unit
- Total Electric Power w/o CCS Island	830 MWe	830 MWe	760 MWe
CCS island			
- DCC	2 units	-	-
- Absorber	2 units	2 units	1 unit
- Advanced Flash Stripper	2 units	2 units	1 unit
CCU	1 train	1 train	1 train

A surge tank is included in the solvent circulation loop that provides the required residence time to smooth flow rate fluctuations from the stripper as well as to provide a mixing volume for the addition of solvent make-up and composition tuning. The lean solvent is pumped to the top of the absorber column, where it flows downward and counter-current to the upward flow of flue gas. The rich solvent is pumped from the bottom of the absorber and heated via heat exchange with other hotter process streams (i.e., regenerated solvent and the hot CO_2 and water vapor mixture exiting the top of the stripper) prior to feeding into the advanced flash stripper (more details in Lin [6]), where it is regenerated in a pressurized stripping column. To regenerate the rich solvent under pressure requires a higher solvent temperature, which is achieved through a combination of rich solvent preheat via heat exchange and use of a once-through steam heater. An advantage of the pressurised regeneration is lower power demand for the CO_2 compression unit, which is has four compression stages with inter-cooling.

More details on the process flow diagram for the CCS unit are reported in Table 2.

Table 2. Equipment description for a single train–Case 1, 2, 3.

	CASE 1	CASE 2	CASE 3
Flue gas Fan	Upstream of DCC, Δp=100 mbar	Δp=50 mbar	Δp=50 mbar
Direct Contact Cooler	3 m packing Structured Mellapak 250 Y	NONE	NONE
Intercooling Mode	n.2 in/out IC	n.2 pump-around IC	n.2 pump-around IC
Absorber Packing			
- Top Bed	Sulzer Mellapak Standard 250Y	Sulzer Mellapak Standard 250X	Sulzer Mellapak Standard 250X
- Intermediate Bed	Sulzer Mellapak Standard 250Y	Sulzer Mellapak Standard 2X	Sulzer Mellapak Standard 2X
- Bottom Bed	Sulzer Mellapak Standard 250Y	Sulzer Mellapak Standard 2X	Sulzer Mellapak Standard 2X
Water-wash	3m, structured packing	3m, structured packing	3m, structured packing
Stripper	2 beds, Raschig Super Ring N. 0.5-Metal 1 train per plant	2 beds, Raschig Super Ring N. 0.5-Metal 1 train per plant	2 beds, Raschig Super Ring N. 0.5-Metal 1 train per plant
CO_2 Compression Unit	4 compression stages	4 compression stages	4 compression stages

TECHNICAL AND ECONOMIC FRAMEWORK

In this section, the modelling approach to analyse the standalone NGCC units and the integrated NGCC-CCS plant is described. The primary tools for this work were Aspen Plus® v.9 and Thermoflex® v. 27.

Case 1 and 2 are based on a NGCC designed to generate 830 MWel of net electric power at full load without capture, with a net electric efficiency of 58.30% on a LHV basis (more details on the combined cycle are reported in the CaESAR project [3]). The NGCC with capture has been simulated to account for extraction of steam from the steam turbine cycle for solvent regeneration (CCS island reboiler). Two different absorber configurations are analysed in Cases 1 and 2, with the most effective one applied to Case 3, which utilizes a high efficiency, H class gas turbine. Although not reported as a separate case study, the high efficiency turbine-based NGCC was analysed without capture to provide base line performance metrics for Case 3. Case 3 illustrates a high-performance, low-emission plant which combines the most recent state-of-the-art combined cycle together with an advanced absorption CCS process.

The design of the Direct Contact Cooler (Case 1) is based on a recent IEAGHG study [14]. Although a sensitivity analysis was used to evaluate the best location for the flue gas fan relative to the DCC (upstream or downstream), the upstream configuration was chosen to avoid sub-atmospheric operation of the DCC.

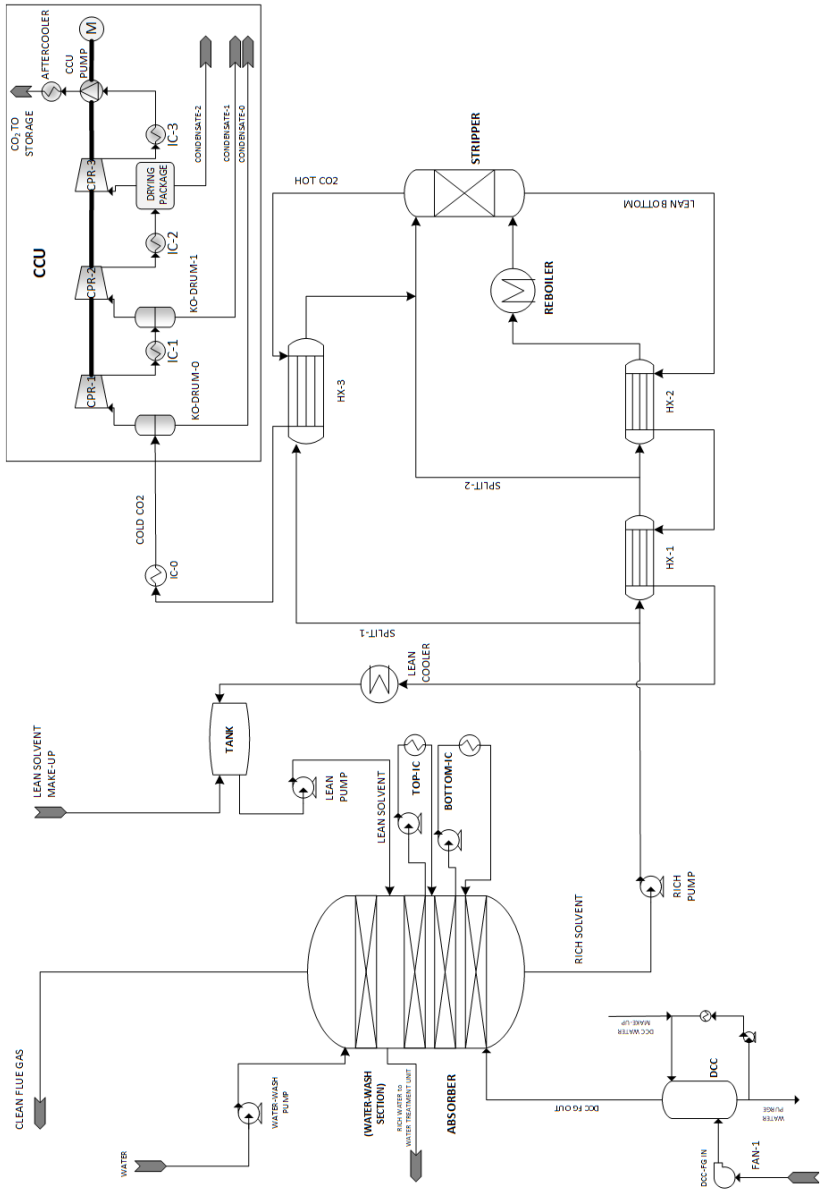

Figure 2. Process flow diagram representing a single train from Case 1.

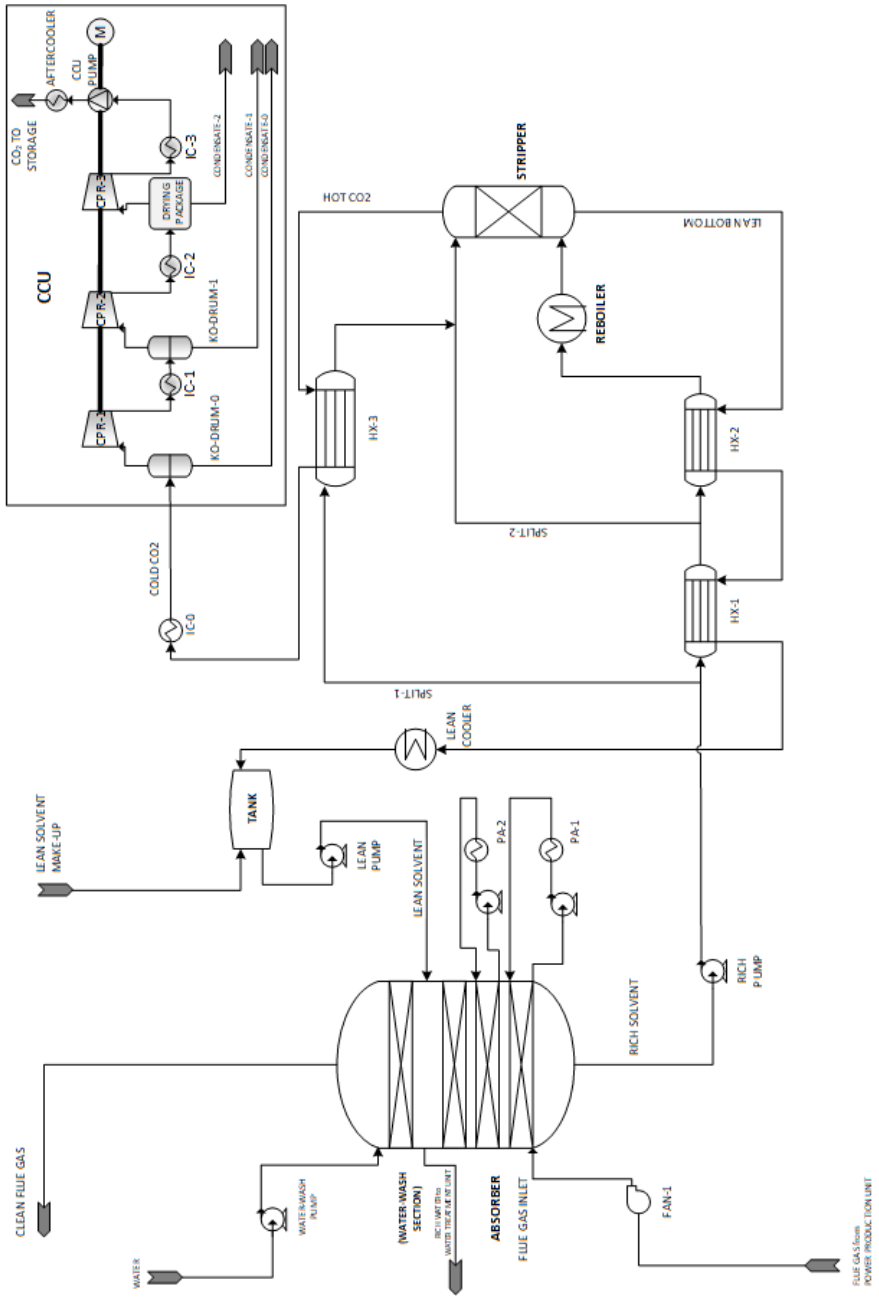

Figure 3. Process flow diagram representing a single train from Case 2 and 3.1.

The same absorber design criteria (e.g., ratio of packing height to minimum solvent flow and % of flood) have been used for all three cases for comparative consistency, as was done in studies by Frailie *et al.* [11] and Sachde and Rochelle [15]. As noted previously, a thermodynamic model developed at UT was calibrated against experimental results from the UT pilot plant [16] and was used as a starting point to predict the performance of a full scale column. Using the absorber model, the relationship between the absorber height and the minimum solvent flow rate to achieve 90% CO_2 capture was determined. The liquid solvent flow rate (L) as a function of packing height asymptotically approaches the minimum solvent rate (Lmin) as the number of separation stages increases, corresponding to infinite absorber height. A practical operating solvent rate was set at 120% of the minimum on a molar basis [12], which sets the absorber height as determined by the simulations. The absorber diameter is set by the liquid and vapor flows and the properties of the particular packing for each case which establishes the gas phase pressure drop and approach to flooding, which was specified to be 80% of flood.

The loading of the lean piperazine solvent entering the absorber can be varied by changing process conditions in the solvent stripper. The optimum value of lean loading was established as 0.226 mol CO_2 /mol Alkalinity based on results from the UT experimental campaign [16]. This lean loading minimizes the overall energy penalty, or equivalent work (W_{eq}) of the capture operation. Weq is the performance index which represents the overall equivalent electricity penalty due to CO_2 capture and compression. The equivalent work consists of the summation of fan work (W_{fan}), pump work (W_{pump}), compression work (W_{comp}) and equivalent work from the reboiler duty (W_{heat}) [6,17].

With the 5m PZ solvent lean loading specified as 0.226 mol CO_2/mol Alkalinity, the process simulation was used to identify the stripper pressure and reboiler temperature which achieve the minimum Weq, while still achieving the specified lean loading. The pressure and temperature meeting these criteria are 5.8 bar and 150 °C. The stripper diameter was specified to operate at 80% of flooding. The packing height was set to 7 m, a value representing a good compromise between packing utilization efficiency (packing costs) and W_{eq} reduction, as reported by UT previous work of Lin [18].

The CO_2-rich gas leaving the stripper is sent to the CCU, which utilizes a 4 stage inter-cooled compressor. The compression ratio at each stage is set to produce equal outlet temperatures. The target pressure for the CO_2-rich gas to storage (stream "CO_2 to storage" in Figure 2, Figure 3) is 110 bar.

Together with the W_{eq}, the Specific Primary Energy Consumption for CO_2 Avoided, or SPECCA index [19] has been adopted as metrics to assess and compare the three cases in a way that focuses on the primary energy consumed for capturing CO_2. The SPECCA Index is generally accepted as a performance indicator of CCS-equipped power plants, since it fairly measures the primary energy penalty of a power plant with CO_2 capture against a reference power plant without CCS.

$$SPECCA = \frac{3600 \times \left(\frac{1}{\eta_{el,CCS}} - \frac{1}{\eta_{el,ref}} \right)}{e_{CO2,el,ref} - e_{CO2,el,CCS}} \quad (1)$$

Where:

- $\eta_{el,CCS}$: power plant net electric efficiency with amine capture
- $\eta_{el,ref}$: power plant net electric efficiency without CCS, i.e. for Case 1,2 ηel, NGCC=58.3%, for Case 3 ηel, NGCC=62.5%
- eCO_2,el,CCS: power plant net specific emission rate with amine capture
- eCO_2,el,ref: power plant net specific emission rate without CCS. For Case 1 and 2 eCO_2,el,ref= 351.8 $kgCO_2/MWh_{el}$, Case 3 eCO_2,el,ref= 330 kg_{CO2}/MWh_{el}

In Case 1 and 2 the reference power plant is the same as in the CaESAR study, while for Case 3, the high efficiency combined cycle without capture (See next section, "Performance Results") has been used to calculate the reference values of power plant electric efficiency and specific emission.

The technical evaluation included a detailed sizing of equipment, which provides the basis for capital cost estimation. Based on sizing information, the total equipment cost (TEC) of the power plant with capture is calculated by adopting a bottom-up approach, where a single piece of equipment is priced according to a power-law relationship. The overall capital expenditure required to build the plant on a green-field basis is the Total Plant Cost (TPC), accounting for TEC, installation costs, indirect costs, escalation, and contingencies. See Chapter 7 of the present volume for details.

The First Year Cost of Electricity (COE) and the Cost of CO_2 avoided (CCA) are derived from the annualized capital costs, operating costs, and fuel costs. A summary of the assumptions related to the economic evaluation are reported in Table 3. The economic framework is described more in detail in Chapter 7.

Table 3. Financial assumptions.

Assumption	Value
Cost and financial	
Plant type	Green-field
Cost year basis	2014
Base currency used, $	US Dollars
Average exchange rate (2014), $/€	1.329
Investment lifetime, years	25
Inflation rate,%	2
Discount rate, %	10
First year capital charge factor, %	9.43
Fuel cost, $/GJ (2014)	4.5
Number of equivalent hours, hours equivalent at full load/year	7880

PERFORMANCE RESULTS

The main results of process simulations with Thermoflex® to define the performance of a high efficiency combined cycle (Case 3- NGCC without capture) are reported in Table 4. The reference NGCC w/o capture for Case 1 and 2 have been taken from CaESAR 2011 [3].

An overview of the absorber simulation results for the three cases, as well as process assumptions and specified conditions, are reported in Table 5 (when more than one train is envisaged by the absorption island, information are related to a single train only).

Table 4. High Efficiency NGCC w/o capture.

Process section	Quantity	Units	Total Value
High Efficiency Combined Cycle (1GT + 1 ST)	Fuel input	MW_{LHV}	1215.8
	Gas turbine model	-	GE9HA.02 (GTPRO)
	Configuration	-	1GT + 1ST
	Gas Turbine Net Power Output	MW_e	528.5
	Steam Cycle Gross Power Output	MW_e	190.4
	Steam Cycle pumps, auxiliaries, cooling tower	MW_e	8.3
	Steam Cycle Net Power Output	MW_e	182.1
	Plant Net Power Output	MW_e	710.6
	Flue gases mass flow rate at HRSG exhaust	kg/s	983.9
	CO_2 in HRSG flue gases	Mol %	4.56%

Table 5. Assumptions and main absorber simulation results per train. In Case 1 solid formation has been excluded after appropriate check of the thermodynamic operating window (temperature vs. loading).

		CASE 1	CASE 2	CASE 3
Flue gas inlet temperature at absorber inlet	[°C]	35	100	114
Flue gas pressure at absorber inlet	[bar]	1.06	1.06	1.06
Flue gas flow-rate	[kmol/s]	22.75	23.51	34.84
Flue gas inlet composition	[%mol]			
- H_2O		5.3	8.38	9.48
- CO_2		4.08	3.96	4.56
- N_2		77.87	75.27	74.84
- O_2		12.75	12.39	11.13
Lean solvent temperature	[°C]	40	40	40
Lean loading	molCO2/mol Alk	0.226	0.226	0.226
Rich loading	molCO2/mol Alk	0.359	0.348	0.354
L/G=1.2×Lmin/G	mol/mol	1.67	1.76	1.94
L/G_{CO2}	Mol solvent/ molCO2	40.85	44.53	42.55
Packing height	[m]	13	11	11

Table 6 shows the performance summary for the three cases. Case 1 utilizes a DCC, unlike Cases 2, so a larger pressure increase across the flue gas fan is required to overcome packing and piping pressure drop relative to Case 2. This results in nearly double the power consumption for the flue gas fan of Case 1 compared to Case 2.

Table 6. Performance Summary of the three Case Studies.

			CASE 1	**CASE 2**	**CASE 3**
Process Section	**Quantity**	**Units**	**Total Value**	**Total Value**	**Total Value**
Natural Gas Combined Cycle	**Fuel input**	**MW_{LHV}**	1422.6	1422.6	1215.8
	Gas Turbine Power Output (2 units)	MWe	544.2	544.2	528.5
	Steam Cycle Net Power Output w/o CCS	MWe	285.7	285.7	231.6
	Net Power Output w/o CCS	MWe	829.9	829.9	760.2
	Steam Cycle Net Power Output with PZ	MWe	225.9	221.5	184.6
	Gross Power Output with PZ	**MWe**	**770.1**	**765.7**	**713.1**
5m PZ Absorption Process	Power consumption DCC (water pumping + heat rejection)	MWe	3.6	0.0	0.0
	Power consumption solvent pumping	MWe	2.8	3.5	2.7
	Power consumption flue gases compression	MWe	17.0	8.6	6.2
	Power consumption for heat rejection	MWe	2.4	6.3	5.0
	Power consumption water wash	MWe	0.6	0.6	0.4
	Total Power CO_2 Capture Auxiliaries	**MWe**	**26.4**	**18.9**	**14.4**
	Captured CO_2	**kg/s**	**73.3**	**73.3**	**63.4**
	Reboiler Thermal duty	**MWth**	**186.9**	**200.5**	**166.9**
	Specific thermal consumption for solvent regeneration	**MJth/ kgCO2**	**2.55**	**2.74**	**2.63**
CO_2 Compression and dehydration Unit (CCU)	**Total Power CO_2 Compression**	**MWe**	**17.5**	**17.4**	**15.1**
Overall Plant Performance	**Net Power Output with CCS**	**MWe**	726.2	729.3	683.5
	Power Plant Net Electric Efficiency with CCS	**%**	51.0%	51.3%	56.2%
	CO_2 specific emissions w/o CCS	**kgCO2/ MWh**	351.8	351.8	330.0
	CO_2 emissions with PZ	**kgCO2/s**	8.4	8.4	6.9
	CO_2 specific emissions with PZ	**kgCO2/ MWh**	41.4	41.3	36.3
	Plant Net Electric Efficiency w/o CCS	**%**	58.3%	58.3%	62.5%
	SPECCA PZ Absorption	**GJ_{LHV}/ t_{CO2}**	**2.83**	**2.73**	**2.20**

It is interesting to note that Case 1 achieves a lower specific thermal consumption for solvent regeneration compared to Case 2, even though Case 2 has a lower SPECCA. This result is not related to the relative amounts of circulating solvent but is due to a higher quantity of CO_2 per unit of solvent (the inverse of L/G_{CO2} [mol solvent/mol CO_2]), which is also related to a greater rich loading attained at the absorber outlet for Case 1. Comparing the three cases, the specific reboiler thermal duty has a trend consistent with L/G_{CO2} at the absorber, hence it shows an opposite trend with respect to the rich loading.

The power required for compression and dehydration (the CCU) is similar for Case 1 and 2 due to the equal amount of CO_2 to be compressed and stored. Case 3 is a smaller plant size, so the overall captured CO_2 flow-rate is lower, requiring less compression power.

The overall plant performance of Case 3, as summarized by the SPECCA index, is superior to the other plant configurations. More specifically, SPECCA from Case 1 is 28% higher and SPECCA from case 2 is 24% higher than SPECCA for Case 3.

TECHNO-ECONOMIC ANALYSIS

Although the performance results shown in Table 6 for Case 1 and 2 indicate that there is minimal advantage for the advanced absorber configuration (without DCC) versus the conventional one, the economic analysis shows a benefit. The SPECCA index is not significantly different, and the net electric efficiency is virtually the same (51.0 % for Case 1 vs 51.3% for Case 2). Since the same volume of CO_2 is captured (73.3 kg/s) in each case, the total compression work at the CCU is the same (around 17 MWe in both cases). The reboiler thermal duty is lower in Case 1 because of a lower amount of circulating solvent, due to a higher rich loading, so there is slightly higher gross power output from the steam cycle (lower steam extracted from the ST). However, this is more than offset by the total power needed by the capture auxiliaries, which is larger for Case 1 compared to Case 2, due mainly to higher power demand for the flue gas fan to overcome DCC and absorber pressure losses.

Case 3 shows the best performance among the three cases for two main reasons; (i) the higher efficiency of the starting NGCC power block, and (ii) the higher CO_2 concentration in the flue gas which enables a lower specific solvent flow rate, L/GCO_2, compared to Case 2. Case 1 also utilizes a lower L/GCO_2 than Case 2 but has a considerably higher power demand for capture auxiliaries.

Although Case 1 and 2 do not show significant differences in terms of performance metrics, the introduction of an additional column (DCC), together with the larger flue gas fan, does have an impact on the economic evaluation and cost of CO_2 avoided. The total equipment cost and the fractional contributions from various process units for the three cases is shown in Table 7.

Comparing the advanced versus conventional absorber cases (Case 1 vs Case 2), the power section capital cost is virtually identical. However, the CCS island is less expensive in the advanced configuration scenario (Case 2, 20% saving in TEC relative to Case 1). The difference in capital cost drives the Cost of CO_2 avoided for the conventional case to be about 14% higher for Case 1 compared to Case 2. (Table 8, Case 1: 77.8 $/t$CO_2$ versus Case 2: 68.3 $/t$CO_2$).

The lowest SPECCA among the cases studied is achieved by Case 3, mainly due to economies of scale from using a single train in both the power and CCS sections, leading to lower specific costs of the major CCS equipment units. Case 3 uses a larger GT (compared to the two in Cases 1 and 2), and a smaller and technologically more advanced (i.e., more expensive materials) steam cycle. This leads to the high-efficiency NGCC without capture having a higher specific cost than the conventional NGCC ($1105/KW versus $1059/KW), although the power cost is lower due to higher efficiency.

For CO_2 capture from an NGCC, the lowest cost option among the three is Case 3, with a CCA of 59.0 \$/tCO_2 (Table 9), compared to 77.77 \$/tCO_2 for Case 1 and 68.77 \$/tCO_2 for Case 2 (Table 8).

Table 7. TEC summary for power and CCS sections (including items break-down for the capture island).

		CASE 1	CASE 2	CASE 3
Power section	M\$2014	258.5	258.3	245.0
Capture section	M\$2014	160.2	133.2	98.5
DCC		10%	-	-
ABSORBER		49%	54%	47%
STRIPPER		2%	3%	2%
FAN AND PUMPS		7%	4%	5%
HEAT EXCHANGERS		15%	19%	21%
CCU		15%	18%	22%
SOLVENT RECLAIMER, TANK		2%	3%	3%

CONCLUSIONS

This chapter presents the methodology and the results of a techno-economic assessment of 5 molal (5m) piperazine (PZ) for carbon capture from NGCC in three different case studies. The energy and cost performance were assessed for two alternative absorber configurations for CO_2 removal from flue gases produced by a conventional F-class NGCC power plant. In addition, the most cost-effective absorber design from the initial comparison was paired with the most recent H-class NGCC technology.

The overall assessment involved both experimental and modelling activities. An experimental pilot plant campaign commissioned by CCP was performed at the University of Texas (UT). The data were used to validate a piperazine absorption simulation, which incorporated a PZ-specific thermodynamic model developed at UT. LEAP-POLIMI, together with CCP, utilized the simulation to scale-up the process and assessed three main configurations: (i) conventional absorber with a direct contact cooler (DCC0, (ii) advanced absorber configuration (no DCC), and (iii) advanced absorber configuration coupled with a high efficiency NGCC based on a state-of-the-art H-class turbine. The process simulations for the CO_2 absorption island have been built in Aspen Plus® (v. 9.0) and the high-efficiency power section has been simulated using Thermoflex® v. 27.

Based on an initial comparison between Case 1 and Case 2, the "advanced absorber configuration" achieved a lower cost of CO_2 avoided (68.27 \$2014/t vs. 77.77 \$2014/t) compared to the conventional absorber. Based on this result, Case 3 was designed to assess the economics of a high-efficiency combined cycle coupled with the advanced absorber set-up.

Table 8. Economic assessment, Case 1 versus Case 2.

		CASE 1									CASE 2								
		EBTF w/o capture		EBTF with capture							EBTF with capture								
		Power section		Power section		CO2 removal section			Total		Power section			CO2 removal section			Total		
		[M$2014]	[$2014/kW]	[M$2014]	[$2014/kW]	[M$2014]	[$2014/kW]	[$2014/tCO2capt]	[M$2014]	[$2014/kW]	[M$2014]	[$2014/kW]		[M$2014]	[$2014/kW]	[$2014/tCO2capt]	[M$2014]	[$2014/kW]	
	TEC	264,18	318,33	258,50	355,97	160,21	220,61	77,07	418,71	576,57	258,28	354,13		133,24	182,68	64,08	391,52	536,81	
	TPC	879,14	1059,33	860,23	1184,56	789,81	1087,60	379,94	1650,04	2272,16	859,50	1178,46		656,85	900,61	315,93	1516,35	2079,08	
Parameter	U. of M.																		
Net Power	[MW]	829,9				726,20							729,34						
Electricity production	[MWh/y]	6539612				5722435							5747199						
Efficiency LHV	[%]	58,3%				51,05%							51,27%						
Fuel consumption	[GJ/h]	5125				5121							5121						
Fuel consumption	[GJ]	40381824				40356317							40356317						
Fuel cost	**[M$]**	**181,72**				**181,60**							**181,60**						
Fixed O&M	**[M$]**	**17,58**		**17,20**			**15,80**		**33,00**		**17,19**				**13,14**		**30,33**		
Variable O&M	**[M$]**	**12,10**		**10,59**			**14,88**		**25,46**		**10,63**				**14,94**		**25,58**		
Capital	**[M$]**	**82,88**				**155,56**							**142,95**						
First year capital charge	**[M$]**	**294,28**				**395,63**							**380,46**						
COE	**[$/MWh]**	**45,00**				**69,14**							**66,20**						
Specific CO2 emissions	[kg/MWh]	351,80				**41,44**							**41,26**						
Specific CO2 avoidance	**[kg/MWh]**	-				310,36							310,54						
Cost of CO2 avoided	**[$/t]**	-				**77,77**							**68,27**						

Table 9. Economic Assessment: Case 3.

CASE 3													
		62.5%NGCC w/o capture		62.5%NGCC with Adv PZ									
		Power section		Power section			CO2 removal section				Total		
		[M$2014]	[$2014/kW]	[M$2014]	[$2014/kW]		[M$2014]	[$2014/kW]	[$2014/tCO2cap]		[M$2014]	[$2014/kW]	
TEC		252,38	332,01	244,99	360,00		98,51	144,76	54,76		343,50	504,76	
TPC		839,85	1104,85	815,27	1197,99		485,66	713,65	269,99		1300,93	1911,64	
Parameter	U. of M.												
Net Power	[MW]	760,15				680,53							
Electricity production	[MWh/y]	5989986				5362577							
Efficiency LHV	[%]	62,52%				55,97%							
Fuel consumption	[GJ/h]	4377				4377							
Fuel consumption	[GJ]	34490779				34490779							
Fuel cost	**[M$]**	**155,21**				**155,21**							
Fixed O&M	**[M$]**	**16,80**		**16,31**			**9,71**				**26,02**		
Variable O&M	**[M$]**	**11,08**		**9,92**			**13,94**				**23,86**		
Capital	**[M$]**	**79,18**				**122,65**							
First year capital charge	**[M$]**	**262,26**				**327,74**							
COE	**[$/MWh]**	**43,78**				**61,12**							
Specific CO2 emissions	[kg/MWh]	330,00				**36,44**							
Specific CO2 avoidance	**[kg/MWh]**	-				293,56							
Cost of CO2 avoided	**[$/t]**	-				**59,04**							

Based on this techno-economic evaluation, Case 3 achieves the lowest cost. It achieves a SPECCA index of 2.20 GJ_{LHV}/tCO_2, which is significantly lower than Case 1 (2.83 GJ_{LHV}/t_{CO2}) and Case 2 (2.74 $GJ_{LHV}/tCO2$). Case 3 is estimated to attain a remarkably high power generation efficiency, even with CCS (56.2%$_{LHV\ basis}$), due to a very low energy penalty due to capture (1.26 $MJ_{ele}/kg_{CO2\ captured}$). The superior energy efficiency and lower TEC of Case 3 leads to the minimum cost of CO_2 avoided of 59 $2014/$t_{CO2}$ among the cases studied here.

ACKNOWLEDGEMENTS

This work was fully funded and supported by Phase 4 of the CO_2 Capture Project (CCP). The authors greatly acknowledge Prof. G. Rochelle and his team for sharing the validated thermodynamic modelling tools and for contributing to the definition of the process configurations.

References

1. EPA United States Environmental Protection agency, “Global Greenhouse Gas Emissions Data.” [Online]. Available: https://www.epa.gov/ghgemissions/global-greenhouse-gas-emissions-data. [Accessed: 01-Aug-2018].
2. IEA, “Global energy-related CO_2 emissions.” www.iea.org.
3. CaESAR, “European best practice guidelines for assessment of CO_2 capture technologies,” https://www.ctc-n.org/resources/european-best-practice-guidelines-assessment-carbon-dioxide-co2-capture-technologies, 2011.
4. “CESAR Project.” http://www.caesar-project.eu/ .
5. CCP, “CO_2 Capture Project.” [Online]. Available: https://www.co2captureproject.org/. [Accessed: 01-Aug-2018].
6. Y. Lin and G. T. Rochelle, “Optimum heat of absorption for CO_2 capture using the advanced flash stripper,” *Int. J. Greenh. Gas Control*, **53**, 169–177, 2016.
7. E. Chen, S. Fulk, D. Sache, Y. Lin, and G. T. Rochelle, “Pilot Plant Activities with Concentrated Piperazine,” *Energy Procedia*, **63**, 1376–1391, 2014.
8. P. T. Frailie, “Modeling of Carbon Dioxide Absorption / Stripping by Aqueous Methyldiethanolamine / Piperazine,” The University of Texas at Austin, 2014.
9. E. Chen, Y. Zhang, Y. Lin, P. Nielsenb, and G. Rochelle, “Review of Recent Pilot Plant Activities with Concentrated Piperazine,” *Energy Procedia*, **114**, 1110–1127, Jul. 2017.
10. Pun,B.,Ibrahim,A.,Raja,J.,Moure,G.,Chen,E.,Selinger,J.,Zhang,Y., and Rochelle,G., “Advancing CO_2 Capture from Natural Gas Combined Cycle Power Plants with Piperazine Scrubbing,” 14th Greenhouse Gas Control Technologies Conference Melbourne 21-26 October 2018.
11. P. T. Frailie, T. Madan, B. J. Sherman, and G. T. Rochelle, “Energy performance of advanced stripper configurations,” *Energy Procedia*, **37**, 1696–1705, 2013.
12. Y. Zhang, B. Freeman, and G. T. Rochelle, “Absorber modeling for NGCC carbon capture with aqueous piperazine,” *Faraday Discuss*., **192**, 459–477, 2016.
13. A. Conversano *et al.*, “Techno-Economic Assessment of Novel vs. Standard 5m Piperazine CCS Absorption Processes for Conventional and High-efficiency NGCC Power Plants,” *SSRN Electron. J.*, 2018.
14. J. Davison, IEAGHG “CO_2 capture at gas fired power plants,” Report 2012/8, July 2012.
15. D. Sachde and G. T. Rochelle, “Absorber Intercooling Configurations using Aqueous Piperazine for Capture from Sources with 4 to 27 % CO_2,” *Energy Procedia*, **63**, 1637–1656, 2014.
16. B. Pun *et al.*, “Advancing CO_2 Capture from Natural Gas Combined Cycle Power Plants with Piperazine Scrubbing,” *SSRN Electron. J.,* pp. 1–2, 2018.
17. Y. Lin and G. T. Rochelle, “Approaching a reversible stripping process for CO_2 capture,” *Chem. Eng. J.,* **283**, 1033–1043, 2016.
18. Y. J. Lin, “Modeling the Advanced Flash Stripper for CO_2 capture using 5 m Piperazine,” The University of Texas at Austin, 2016.
19. P. Chiesa, M. C. Romano, V. Spallina, D. M. Turi, and L. Mancuso, “Efficient low CO_2 emissions power generation by mixed conducting membranes,” *Energy Procedia*, **37**, 905–913, 2013.
20. M. Gatti *et al.*, “Preliminary Performance and Cost Evaluation of Four Alternative Technologies for Post-Combustion CO_2 Capture in Natural Gas-Fired Power Plants,” *Energies*, **13**(3), 543, Jan. 2020.

Carbon Dioxide Capture for Storage in Deep Geological Formations, Volume 5
Karl F. Gerdes (Editor)
© 2022 BP. All rights reserved.

Chapter 10

CO_2 CAPTURE FOR NATURAL GAS COMBINED CYCLES (NGCC) USING PIPERAZINE WITH THE ADVANCED STRIPPER (PZAS™)

Gary T. Rochelle, Tianyu Gao, Athreya Suresh Babu, Ching-Ting Liu, Yuying Wu
McKetta Department of Chemical Engineering, The University of Texas at Austin
Mailcode C0400, 200 E. Dean Keeton St., Austin, TX 78712

ABSTRACT: The natural gas combined cycle (NGCC) continues to be a critical, dispatchable option for power generation, required to supply power when wind and solar energy are unavailable. Piperazine (PZ) with the Advanced Stripper (PZAS™) is a second-generation amine scrubbing process that can capture CO_2 from NGCC. This chapter reports testing of PZAS in two pilot plants on feed gas containing 4% CO_2 typical of NGCC. One week of testing with air/CO_2 in a 0.43 m ID absorber established that the PZAS™ process gives equivalent absorber and stripper performance with 4 to 20% CO_2. Testing at the National Carbon Capture Center (NCCC) demonstrated that the PZAS configuration operated reliably for 2000 hours in a 0.66 m ID absorber on cleaned coal-fired flue gas diluted with air to about 4% CO_2 after SO_2 polishing. The flue gas entered the absorber at 77°C with no direct contact cooler. The Advanced Stripper used 2.4 GJ steam/tonne CO_2 to deliver captured CO_2 at 6.2 bara. Forty feet of M252 packing in two beds provided 90-95% CO_2 removal with a rich loading of 0.40-0.41 mol CO_2/equiv PZ. PZ degraded at a rate of 0.3 kg/tonne CO_2. The cleaned flue gas contained about 1 ppm PZ. Activated carbon treating of the rich solvent in the last 400 hours eliminated the solvent color, reduced ammonia production by as much as 40%, and enhanced both absorber and stripper performance. Corrosion coupon testing established that 304 SS was a suitable material throughout the process.

KEYWORDS: piperazine, carbon dioxide, carbon capture, amine scrubbing, natural gas

INTRODUCTION

The natural gas combined cycle (NGCC) continues to be a workhorse option for producing power even with a large penetration of renewable power. The low cost of natural gas in the U.S and other countries supports the use of NGCC when there is no wind or sun and for baseload operation. However, CO_2 capture and storage (CCS) will be necessary to reduce the carbon footprint of existing and new NGCC facilities.

Figure 1 demonstrates the need for fossil power in the Southwest Power Pool of the central U.S. even when there is ample capacity for renewables. On Nov 1 at 0830 there was 10.1 GW coal, 6.3 GW gas, and 6.5 GW wind. On Nov 5 there was only 2.5 GW of wind, so the bulk of the power was produced by gas- and coal-fired plants. On Nov 8 the projected available wind (22 GW) exceeded the demand for power. This shows the need for dispatchable power to back up renewable sources.

Much of the development work with amine scrubbing for CO_2 capture has focused on the coal application. However, the application to NGCC is equally attractive and avoids many of the issues with the coal application caused by flue gas contaminants. Table 1 compares capture from coal-based power to capture from NGCC. The primary disadvantage of the NGCC application relative to coal-based capture is that the flue gas contains only 4% CO_2, requiring a larger diameter absorber for the

same amount of CO_2 captured. However, for a given power plant capacity, the amount of CO_2 that must be removed and processed is significantly less for NGCC. NGCC is not affected by the impurities of coal and the resulting process issues.

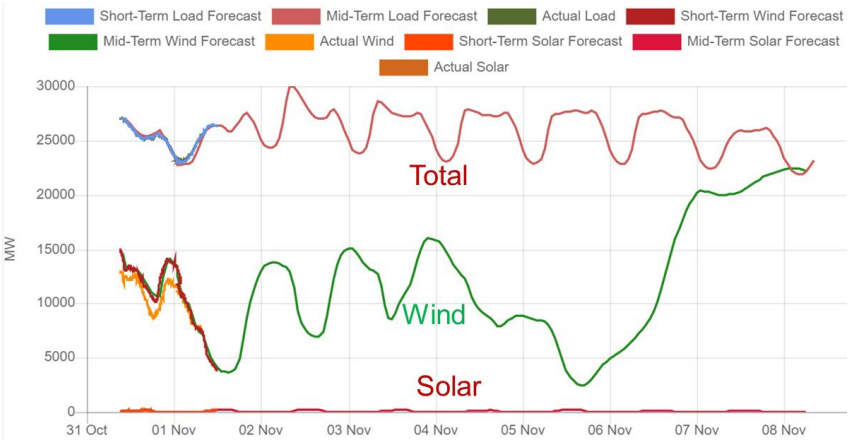

Figure 1. Power generation in the Southwest Power Pool, November 1, 2020 (SPP.ORG).

Table 1. Comparison of capture on NGCC and Coal at 550 Mwe.

	NGCC	Coal	Consequences to NGCC
CO_2 (%)	4.3	12.5	<95% CO_2 removal
Gas (million t/hr)	3.7	3.56	Larger Absorber
CO_2 (t/hr)	110	262	Lower total capture cost /MWe
NO_x (ppm)	10-15	10-50	Less NO_2
SO_2, ash (ppm)	none	1-5 SO_3	No amine aerosol
SO_3, Se, Hg (ppm)	none	50 SO_2	No pre-scrubber needed
H_2O (%)	8	15	No DCC needed for water balance
O_2 (%)	14	7	Greater amine oxidation
T of flue gas (°C)	110	57	Required pump-around Intercooling
Incremental capital cost ($/kw) [1]	796	1507	More attractive with low load factor
Avoided cost ($/t CO_2) [1]	71.	56.	

Note: Costs from NETL study [1] based on CanSolv™ solvent from Shell.

Piperazine with the Advanced Stripper (PZAS™) is a second-generation amine scrubbing technology for CO_2 capture that has been extensively developed since 2000 [2]. Previous research work at the University of Texas at Austin (UT) has been published providing the basis for CO_2 solubility, piperazine volatility, CO_2 absorption rate, thermal and oxidative degradation [6,10,11,17]. The research also includes the development and validation of a rigorous process model (Independence) in Aspen Plus® [3,5,7,8]. PZAS has been extensively tested in pilot plants with synthetic flue gas (Separations Research Program (SRP) at UT) and coal-fired flue gas (National Carbon Capture Center (NCCC)) [14].

The research and pilot-scale testing at the coal-fired conditions established the following features of PZAS:

- Rate of CO_2 absorption 2 times faster than 30% monoethanolamine (MEA) providing 90–95% CO_2 removal with 20 to 30 ft packing
- Intrinsic CO_2 capacity 25% greater than MEA
- Thermal stability permitting stripper operation at 150°C and 7 bar
- Acceptable corrosion with 304 SS in the high temperature stripper
- Oxidation resistance providing <0.3 kg oxidation solvent loss/t CO_2
- PZ emissions from flue gas scrubbing tower <1 ppm with a single stage water wash

At the conditions of NGCC with 4% CO_2 in the flue gas, PZAS should require only 25 ft of packing to get 90% CO_2 removal. A direct contactor cooler is not required to maintain water balance, so the absorber configuration uses pump-around intercooling in the bottom section of packing to deal with the hot flue gas. For sulfur-containing coal, an SO_2 polishing scrubber is required, which is not needed for NGCC.

This chapter reports the results of two pilot plant campaigns with PZAS at NGCC conditions. The pilot plants were used to demonstrate the process performance (CO_2 removal and regeneration energy used) as predicted by the rigorous model in Aspen Plus® and to develop new data on solvent management issues at realistic conditions. One week of operation at 4% CO_2 was performed in 2017 in a four-week campaign at the SRP pilot plant in Austin, Texas to demonstrate the performance of PZAS with 4, 12, and 20% CO_2 in the inlet flue gas. 2000 hours of operation in 2019 at 4% CO_2 was performed at the NCCC pilot plant in Wilsonville, AL. The NCCC test demonstrated long-term operation with a hot inlet flue gas and produced data on solvent degradation, corrosion, and amine emissions at realistic conditions. The NCCC tests results have also been reported by Rochelle *et al.* [18].

PILOT PLANTS AND METHODS

Separations Research Program Pilot Testing

The SRP (Separations Research Program) pilot plant in Austin, Texas, was operated for about one week with 4% CO_2 in air to simulate NGCC conditions (Figure 2). The absorber included three sections of RSP250 structured packing (3 m each). The absorber was operated in two modes, one with two sections of solvent contacting and one section of water wash and one with three sections of solvent contacting. In both modes the solvent was intercooled between the bottom two sections. The Advanced Stripper included two large plate-and-frame exchangers. Cold and warm rich solvent bypasses fed the top of a 0.25 m i.d. stripper with 2.5 m RSR#5 random packing. CO_2 from the stripper was recycled through the cold rich exchanger, condenser, and knockout to the inlet gas of the absorber where it mixed with inlet air and some makeup CO_2.

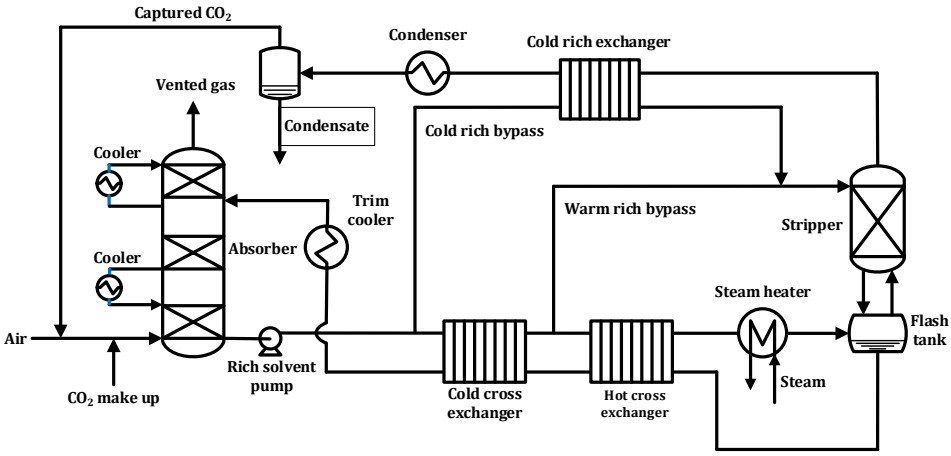

Figure 2. PZAS^{TM} pilot plant at the Separations Research Program [3].

National Carbon Capture Center (NCCC) Testing

The Pilot Solvent Test Unit (PSTU) at the NCCC was modified to test PZAS^{TM} with flue gas containing 4.3 dry mol % CO_2. The flue gas pre-treatment and PZAS process are shown in Figure 3. Coal-fired flue gas containing about 11 mol % CO_2 was fed to a NaOH scrubber to remove SO_2. The gas was then diluted with air to reduce the CO_2 to about 4.3 mol % to simulate NGCC flue gas. The diluted gas could be cooled in the direct contact cooler (DCC) and saturated with water at 40°C or sent directly to the absorber. In bypass mode, the flue gas was heated to 78°C by the blower to partially simulate hot NGCC gas conditions. Three absorber configurations were tested: (A) absorber with in-and-out intercooling and DCC, (B) with pump-around intercooling and DCC, and (C) with pump-around intercooling but no DCC. When the DCC was online, the mixed gas was cooled and saturated with water at 40°C and when it was bypassed, the gas was heated to 78°C by the fan and fed directly to the absorber column.

The absorber column has three beds of packing, but the top bed was not used for solvent contacting. For the in-and-out cooling loop, solvent was removed from the bottom of the middle bed, cooled, and returned to the top of the bottom bed. For the pump-around, solvent was recycled from the bottom of the third bed, cooled, and fed to the top of the third (bottom) bed.

The flue gas counter-currently contacted the solvent in the absorber. The CO_2-scrubbed gas was washed with water to remove entrained solvent and control amine emissions, and then vented. The rich solvent leaving the absorber bottom was pumped to the stripper for regeneration. The solvent was split into cold rich bypass and warm rich bypass for heat recovery. After two cross exchangers, the remaining rich stream was heated to 150–155°C by a steam heater. The bypass streams were fed to the top of the stripper to condense water vapor and recover the latent heat in the stripper overhead. Table 2 summarizes the detailed specifications of the test facilities.

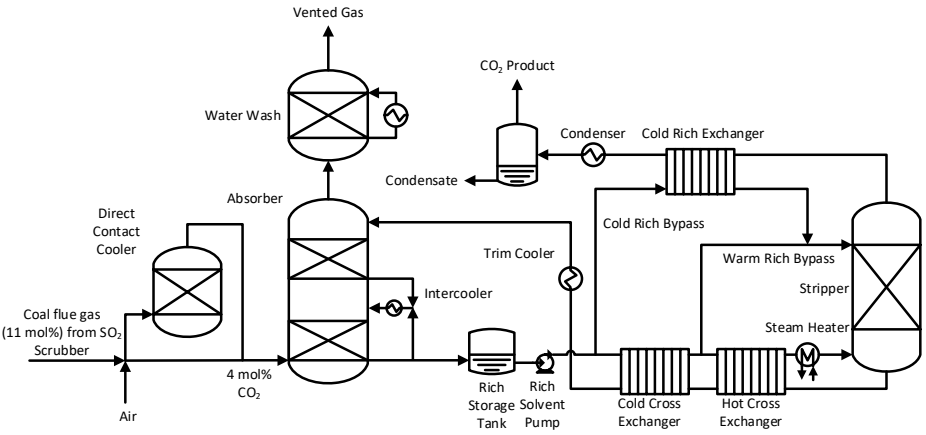

Figure 3. Process flow diagram PZAS^{TM} tested at NCCC, reprinted by with permission from [16] copyright 2020 American Chemical Society.

Table 2. Summary of equipment specifications [16].

Absorber	Column Inner Diameter (*m*)	0.66
	Packing Height (*m*)	2 × 6.10
	Packing type	M252Y
	Material	Stainless Steel
Stripper	Packing Height (*m*)	2 × 2
	Packing Type	RSR #0.5, #0.7
	Material	Stainless Steel
	Cold Cross Exchanger Area (m^2)	114
	Hot Cross Exchanger Area (m^2)	31.9
	Cold Rich Exchanger Area (m^2)	8.5

Aspen Plus® Modeling

The rigorous "Independence" model in Aspen Plus® was used to simulate the absorber and stripper performance. It consists of several sub-models, including solvent properties and packing characterization. Independence includes physical properties, thermodynamics, and kinetics models regressed from bench-scale experiments. The thermodynamics were built in the electrolyte non-random two liquid (e-NRTL) framework [5]. The packing characterization model includes interfacial area, and liquid- and gas-side mass transfer coefficients developed by Song [8] from pilot-scale measurements with various random and structured packings. All the model parameters were regressed independently [8].

PERFORMANCE RESULTS – DEMONSTRATING EXPECTATIONS

Absorber Performance

Limited testing in the SRP pilot plant (Figure 4) showed that the inlet gas CO_2 had little effect on the rich loading achieved in the absorber with a lean loading of 0.24 mol CO_2/mol alkalinity at 90% CO_2 removal. At 98–99% removal, significantly less rich loading was achieved at 4% CO_2. High removal with 4% CO_2 is expected to require a lower rich loading because the temperature bulge is at the top of the absorber, tending to create an equilibrium pinch with the lean loading. Solvent "amine" concentration was determined by acid titration. One mole of PZ provides two moles alkalinity.

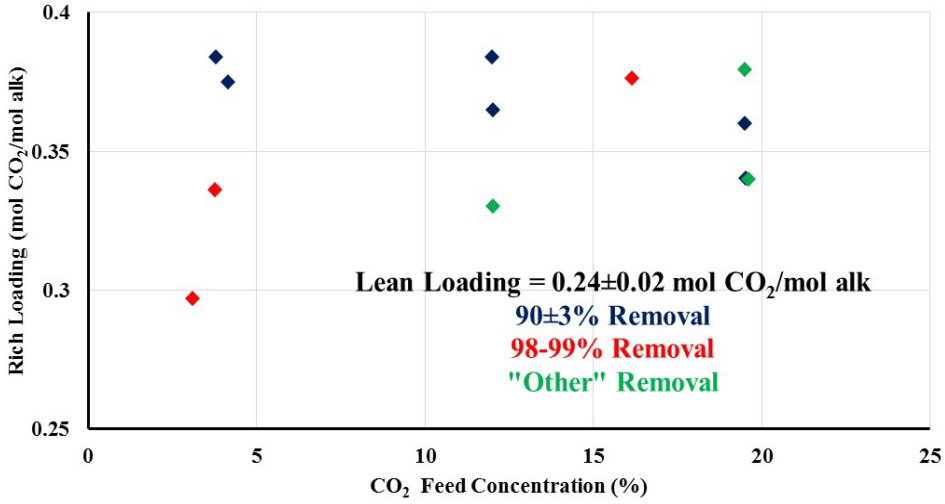

Figure 4. Rich loading in SRP Pilot Plant as a function of CO_2 feed concentration and CO_2 removal rate at a lean loading of 0.24 mol CO_2/mol alkalinity.

Data from 80 absorber steady state runs at NCCC were obtained over 2100 operating hours in 2019. The first 22 runs were parametric tests, which examined the absorber performance over a wide range of conditions, and the rest were from long-term testing designed to study the system stability, solvent oxidation, and other problems. There were four major absorber operating conditions tested during the campaign, as shown in Table 3.

Table 3. NCCC pilot test conditions.

CASE	Absorber Cooling Configuration	Gas Feed Temperature,°C	Intercooler Outlet Temperature,°C
1	In-and-Out	40	40
2	Pump-Around	40	40
3	Pump-Around	78	40
4	Pump-Around	78	35

The CO_2 removal (defined by Equation 1) varied between 85% and 96% with lean loading from 0.19 to 0.25 mol CO_2/mol alkalinity. CO_2 penetration and number of transfer units (NTU) as defined in Equation 2 were used to evaluate absorber performance. The number of transfer units is used to capture the nonlinear increase in the transfer area required to achieve a high CO_2 removal. For example, if the mass transfer is controlled by gas film resistance, it takes twice as much packing area to achieve 99% removal (NTU = 4.6) as for 90% (NTU = 2.3). Usually, the packing height or contacting area of a transfer unit (HTU) is approximately constant.

$$Removal = 1 - \frac{N_{out,CO_2}}{N_{in,CO_2}} \quad (1)$$

$$NTU = -\ln(Penetration) = -\ln(1 - Removal) \quad (2)$$

Figure 5 shows the experimental absorber performance grouped with four operating conditions. The rich loading varied between 0.36 and 0.41, and it is correlated with CO_2 penetration: the rich loading decreases from 0.4 to 0.38 as the removal increases from 90% to 95%. The long-term runs achieved rich loading exceeding 0.4, which is greater than the rich loading from the 2018 PZAS campaign in the same pilot plant at NCCC using coal flue gas [15]. This means that low CO_2 in the NGCC flue gas does not necessarily lead to a lower rich loading, nor to worse energy performance. This is because with pump-around intercooling for the NGCC conditions, the absorber bottoms temperature is lower than it is for coal conditions, which increases the rich loading even at the low CO_2 partial pressure.

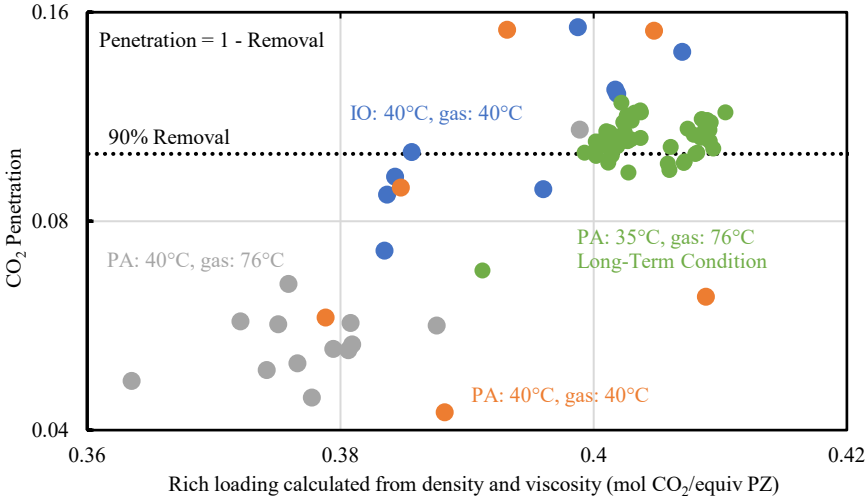

Figure 5. Experimental absorber performance from NCCC 2019 campaign. (IO: in-and-out intercooling, PA: pump-around intercooling, reprinted by with permission from [16] copyright 2020 American Chemical Society.

The absorber performance was modeled rigorously using Aspen Plus®. The CO_2 and PZ concentration for model inputs were estimated from correlation with solvent density and viscosity. The model underpredicts the absorber NTU by 46% and the calculated PZ was increased by a factor of 1.08 to provide a better representation of the pilot plant data. This adjustment could be consistent with systematic analytical error or with systematic degradation of the solvent. Figure 6 compares the measured and modeled absorber NTU in chronological order for the four major absorber conditions. The pump-around data are more scattered because the viscosity measurements showed a greater

variation at these conditions. The relative difference in NTU between the model and the experiments decreases during the long-term testing and reflects the extent of solvent degradation.

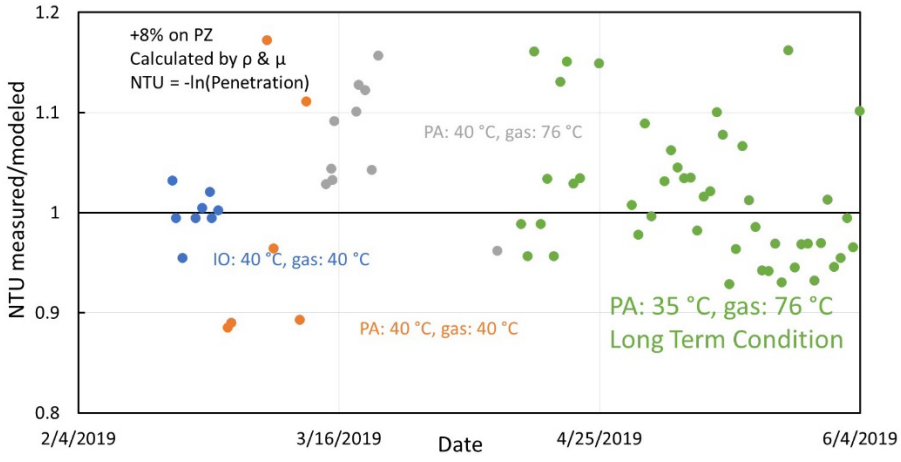

Figure 6. Model prediction of four absorber configurations with 4.3% (dry) CO_2.

Figure 7 shows the agreement of the calculated and measured temperature profile in the absorber for the pump-around intercooling configuration. With 40 feet of packing the CO_2 flux is approaching zero at the bottom of the column, suggesting that less packing could be used with little loss in performance.

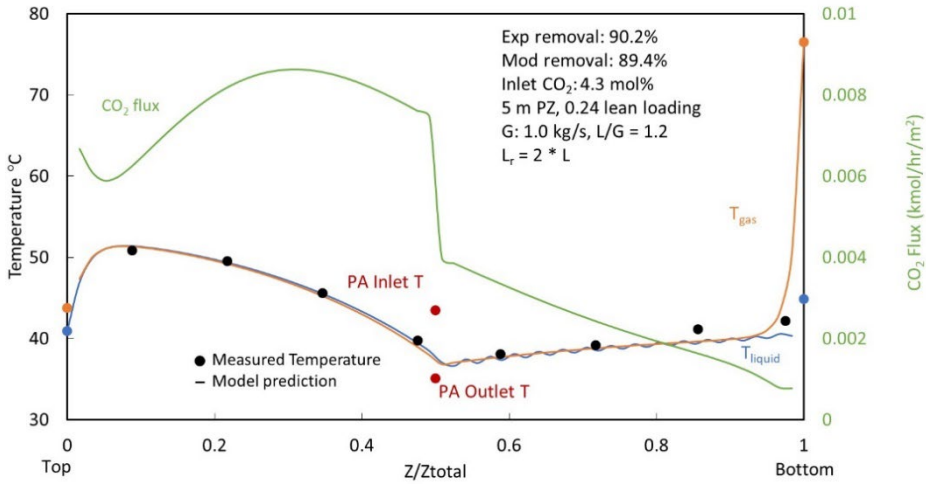

Figure 7. Temperature profile in absorber. Pump-around intercooling with hot flue gas, reprinted by with permission from [16] copyright 2020 American Chemical Society.

Advanced Stripper

The testing of the Advanced Stripper in the SRP pilot plant in 2017 (Figure 8) showed that stripper performance depends on the lean loading, but not on the CO_2 in the inlet flue gas to the absorber. The equivalent work, W_{eq}, is given as the sum of compression work to 150 bar and equivalent work calculated from the steam duty, Q_p, and temperature:

$$W_{eq} = W_{pump} + W_{comp} + W_{heat} \quad (3)$$

$$W_{Heat} = 0.90 Q_p \quad (4)$$

Lower inlet CO_2 concentration will require a lower lean loading in order to achieve the desired removal. A lower lean loading requires greater heat duty resulting in greater required equivalent work. Therefore, the inlet CO_2 concentration affects energy performance indirectly through its effect on rich/lean loadings.

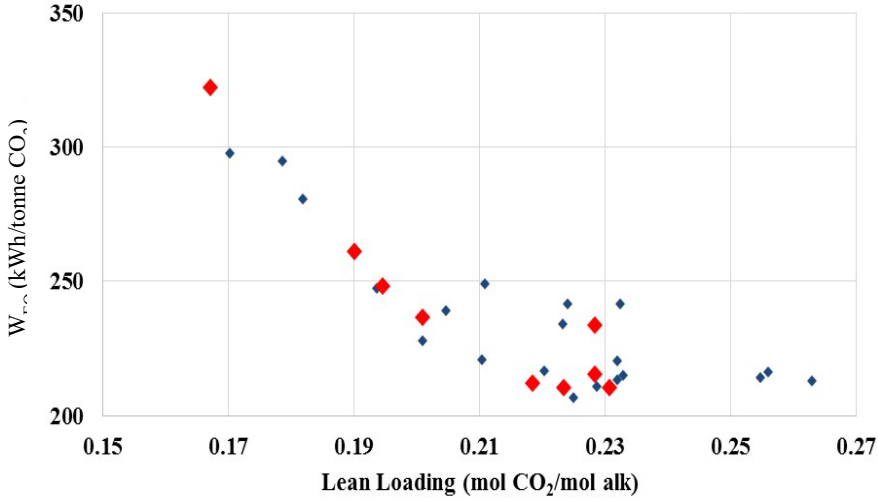

Figure 8. Equivalent work as a function of lean loading for low (red) and high (blue) flue gas CO_2 concentration for PZ with the advanced stripper.

Figure 9 gives the measured energy performance of the Advanced Stripper configuration at coal (11% CO_2) and NGCC (4% CO_2) conditions in the pilot plant at NCCC. The net heat duty has been calculated from the measured steam rate reduced by 70% of the estimated heat loss from measurements in the stripper system with just water.

The net heat duty for coal and gas conditions was practically the same at about 2.5 GJ/tonne CO_2. Three weeks of operation at the end of the NGCC campaign used activated carbon treating to remove impurities from the solvent. The heat duty unexpectedly decreased to 2.3 GJ/tonne and the rich loading increased to 0.41 mol/equiv N. The amine concentration was maintained by adjusting the water balance. With carbon treating, the solvent viscosity was reduced and impurities that might have caused foaming were removed.

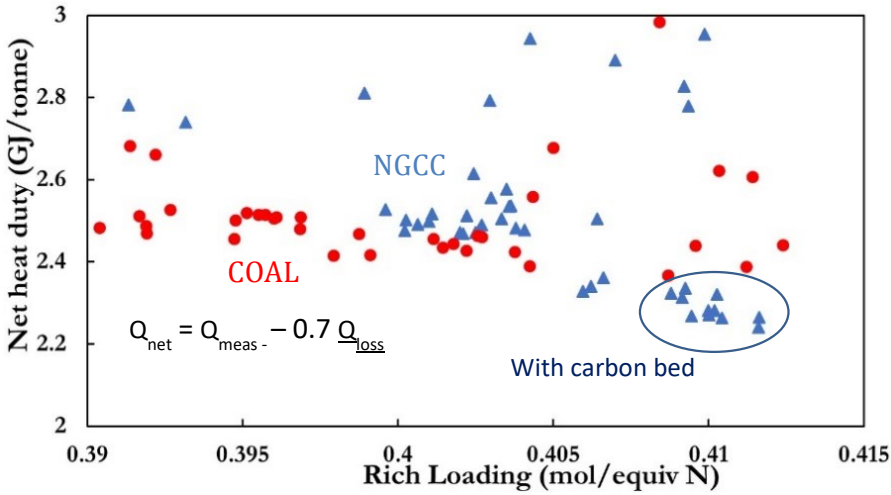

Figure 9. Energy performance of PZAS at NCCC.

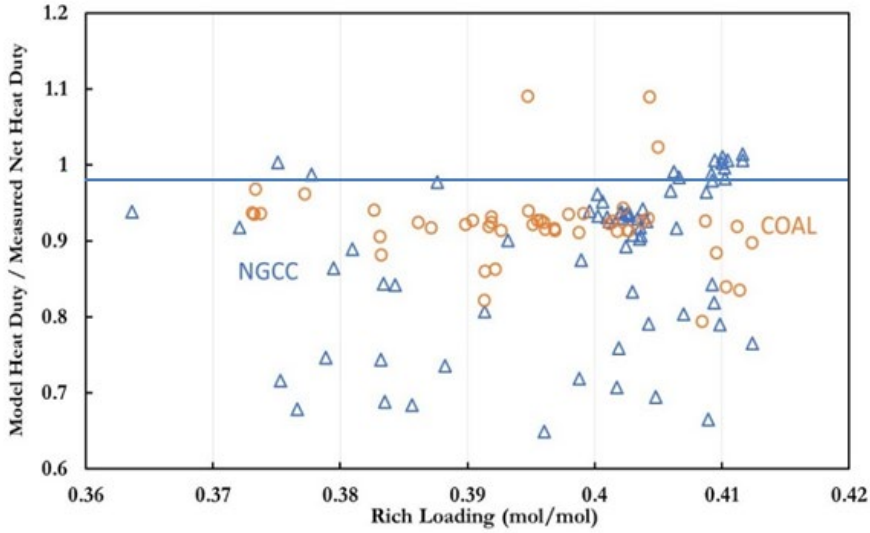

Figure 10. Aspen Plus® model underpredicts heat duty by 10%. Uncertainties in heat loss, measurements, and model thermodynamics. Net heat duty = Measured heat duty – 0.7 x Average heat loss.

Figure 10 shows that the Independence model usually underpredicts the stripper heat duty by 10%. However, the group of points at 0.41 rich loading is predicted quite well. This group corresponds to the period with carbon treating. The wide scatter of other data from the NGCC testing is a consequence

of the wide range and variability of operating conditions associated with the parametric testing at the beginning of the campaign.

Operations

Process Control

Water balance was managed by controlling the temperature of the water wash on the scrubbed flue gas.

Lean loading was maintained constant by controlling the pressure and temperature of the stripper. Pressure was controlled by throttling the CO_2 discharge from the condenser at a typical value of 6.2 bara. Temperature was controlled at a typical value of 150°C by throttling the steam supply. At the somewhat high lean loading in this application, at constant bottoms temperature the stripper pressure depends on the lean loading. In solvents that operate at much lower lean loading the stripper bottoms is basically water, so the P/T cannot be used to set the lean loading.

The pump-around intercooling with hot inlet flue gas was tested without any operational issues. At the typical flue gas rate of 1.00 kg/s, there was no evidence of flooding or other problems in the 26-inch i.d. absorber with flue gas at 76°C entering the bottom section of packing.

Solids Precipitation

Since PZ·$6H_2O$ has a solubility of about 2 molal in water at ambient conditions, there is some concern that solids may form in operations or shutdown. However, no solids should form at CO_2-rich conditions with up to 5 m PZ.

On shutdown, the system was gravity drained to the rich storage tank in the solvent loop exiting the absorber. In the coal and NGCC campaigns there were no issues with solids precipitation over the course of more than eight planned and forced shutdowns.

PZ was originally delivered as 68% solid in a mini-ISO container for testing at coal conditions in 2018. The container was steam heated to melt the PZ. The molten PZ was injected into a circulating stream of hot water/solvent exposed to flue gas to load it with CO_2 as the PZ accumulated. Initial problems with line plugging were addressed by heat tracing all the lines that handled molten PZ.

NEW SOLVENT MANAGEMENT RESULTS AT PILOT PLANT CONDITIONS

Oxidation

The NGCC campaign started with the inventory of used PZ solvent from the coal campaign of 2018. Oxidation of PZ in the pilot plant testing at NCCC was substantially slower than in previous pilot plant testing. Figure 11 compares the production of formate at four pilot plant sites. As much as 60 mM formate was observed at 1500 hours in early campaigns at pilot plant 2 (PP2) and Tarong with a simple stripper and 2–5 ppm NO_2 in the inlet flue gas. Testing with synthetic flue gas (no NO_2) at the Separations Research Program and the extended testing at NCCC with <1 ppm NO_2 produced much less formate.

The use of carbon treating in the last three weeks of the NGCC campaign rapidly eliminated color bodies in the solvent as shown in Figure 12. Figure 13 shows the ammonia concentration in the scrubbed flue gas during the coal and NGCC testing at NCCC in 2018 and 2019. The ammonia production rate increased somewhat with total operating hours, but it seemed to be on a downward trend after carbon treating was initiated. The average calculated PZ oxidation rate based on one mole PZ/mol ammonia was about 0.1 kg/tonne CO_2 at coal conditions and about 0.3 kg/tonne at NGCC

conditions. There is no simple explanation for this difference. At NGCC conditions the oxygen concentration is about twice that at coal conditions, but the solvent rate is three times smaller and there is two times less CO_2 produced with the same solvent inventory in the high temperature stripper. Furthermore, the solvent in the NGCC campaign has more cumulative degradation, and it is known that the oxidation rate increases with the concentration of degradation products.

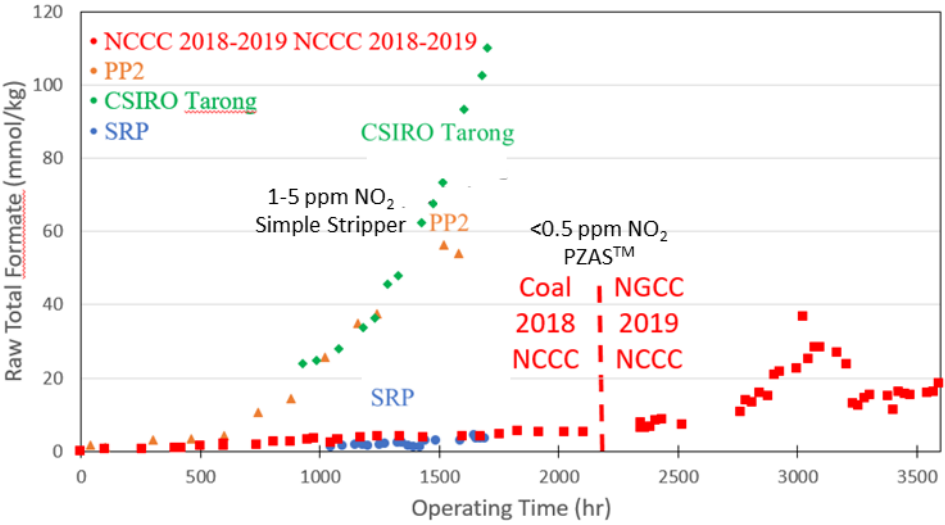

Figure 11. Accumulation of total formate in pilot plant campaigns with piperazine [14].

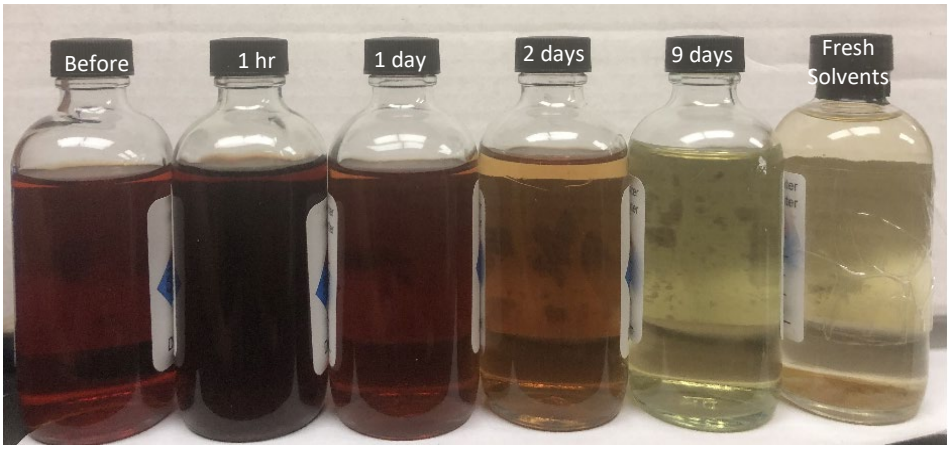

Figure 12. Effect of carbon treating on solvent color.

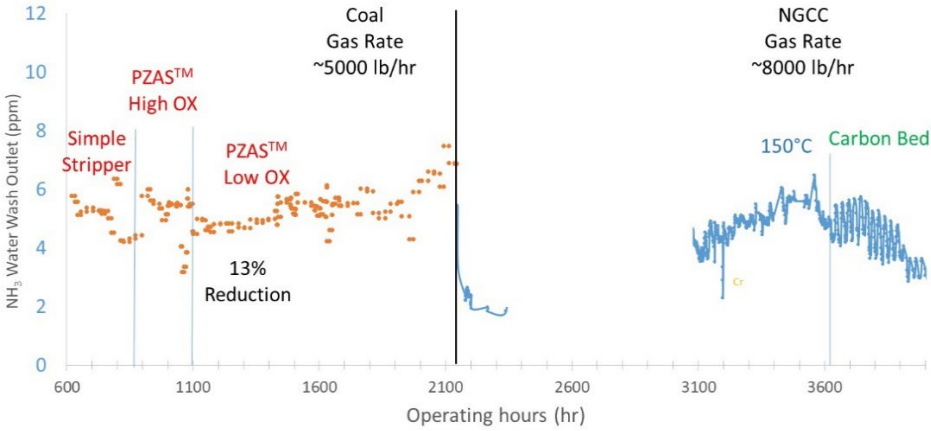

Figure 13. Net ammonia production as ammonia concentration leaving the water wash. In the coal campaign "High Ox" refers to a period with methods used to mitigate oxidation.

Corrosion

304 SS and 220 duplex stainless steel were demonstrated to be acceptable materials at the challenging conditions of the high temperature stripper. Corrosion coupons of carbon steel (CS1010), 304 SS, and 316L SS were placed at various points in the pilot plant at NCCC. They were removed and replaced every 3 to 6 weeks of operation. The corrosion rate was determined by weight loss. Figure 14 summarizes the results for stainless steel. 304 SS had acceptable corrosion (<10 μm/yr) at all points in the system including the extreme condition in the two-phase, high velocity (4–7 m/s), high temperature (154°C) rich solvent pipe between the steam heater and the sump of the stripper. The

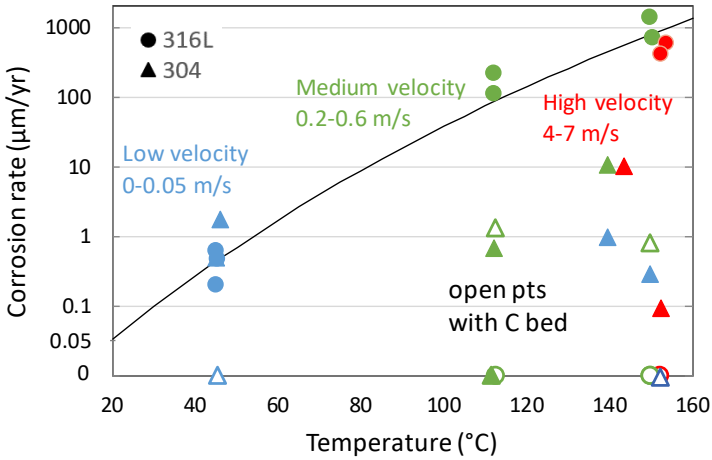

Figure 14. Corrosion of stainless steel with PZAS at NCCC pilot plant in 2019, reprinted by with permission from [18] copyright 2022 Elsevier.

corrosion of 316L was correlated with temperature. It exhibited unacceptable corrosion above 100°C, probably because the protective layer of chromium oxide was dissolved by hot, oxygen-free solvent. It is not known why 304 SS was more resistant, perhaps because it contains less Ni. Two nickel-based alloys (Hastelloy® C276, and Inconel® 625) also failed at high temperature. Limited testing of 2205 duplex stainless showed a corrosion rate less than 1 µm/yr over the full range of temperature.

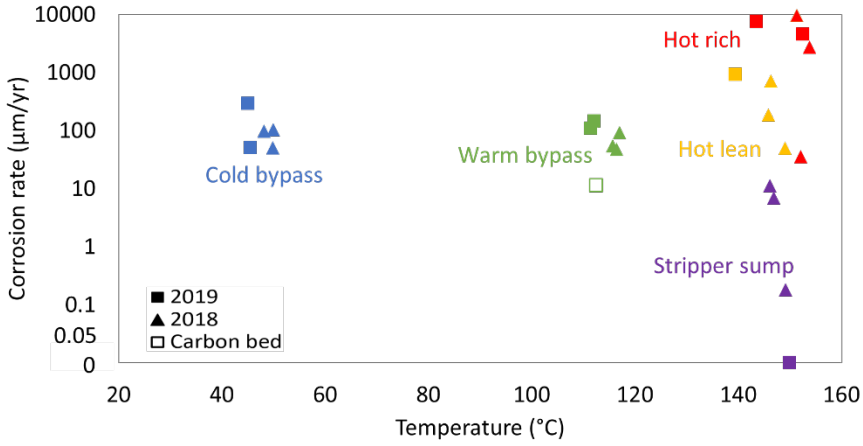

Figure 15. Corrosion of carbon steel (CS 1010) with PZAS at NCCC pilot plant in 2018 and 2019, reprinted by with permission from [15] copyright 2020 American Chemical Society.

PZ Emissions

PZ emissions in the NCCC pilot plant were managed by a water wash column with 10 feet of M252 packing. Excess water and collected PZ were returned to the absorber solvent loop on absorber sump level control. The wash water recycle was cooled and the temperature adjusted between 38 and 44°C to maintain a neutral water balance with the same amount of water leaving in the flue gas from the water wash as enters with the flue gas to the absorber.

Figure 16 shows the PZ concentration leaving the absorber and leaving the water wash during the campaign. The gas concentration was measured by a hot gas FTIR. When data were available from the absorber outlet, the water wash typically removed 90 to 97% (94% average) of the PZ. During much of the NGCC campaign, PZ emission to the atmosphere was 0.5 to 4.0 ppm (< 1.0 ppm average) in the cleaned flue gas. The PZ emission could reflect a small concentration of PZ aerosol generated from residual flyash nuclei from the coal-fired flue gas used to make up the synthetic NGCC flue gas. It could also reflect PZ nuclei created by quenching of the hot (76°C) flue gas in the absorber sump during the latter two thirds of the campaign.

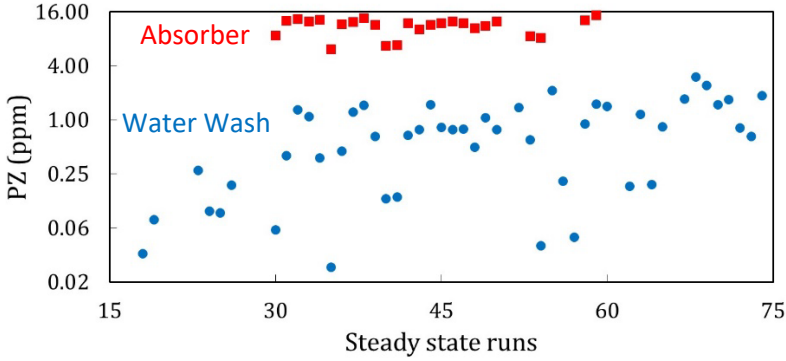

Figure 16. Total PZ in the flue gas measured by hot gas FTIR.[14]

CONCLUSIONS

With only 40 feet of M252 packing PZ provides 90 to 94 % CO_2 removal with a reasonable rich loading of 0.40 to 0.38.

Pump-around intercooling is effective and reliable with flue gas at 76°C.

The heat requirement for PZAS has been demonstrated to be 2.5 GJ/tonne CO_2 with results as low as 2.2 GJ/tonne when using carbon treating on the circulating solvent.

The Independence model represents PZAS performance for the absorber and stripper when the model input is adjusted to increase the measured PZ concentration by 8%.

The specific equipment and liquid hold-up at NCCC demonstrated solvent losses due to oxidation of 0.1 kg PZ/tonne CO_2 at coal conditions and 0.3 kg PZ/tonne CO_2 at NGCC conditions.

PZ emissions are managed by water wash, giving < 1 ppm PZ in the clean flue gas.

304 SS is an acceptable material up to 150°C; CS1010 may be useful at lower temperature; 316 SS should not be used at elevated temperature.

ACKNOWLEDGEMENTS

Funding from CCP4 provided for one week of additional operation with 4% CO_2 at the SRP pilot plant during a longer campaign funded by DOE and MTR to test CO_2 absorption with 12 and 20% CO_2.

Funding from CCP4 provided personnel from the University to supervise and report on 2000 hours of operation at the NCCC pilot plant in 2019. The PZAS configuration at NCCC was previously constructed and operated in 2018 with funding from DOE. The NCCC pilot plant operations were supported by DOE.

REFERENCES

1. James R.E., Kearins D., Turner M., Woods M., Kuehn Norma., and Zoelle A. (2019*) Cost and Performance Baseline for Fossil Energy Plants Volume 1: Bituminous Coal and Natural Gas to Electricity*. NETL-PUB-22638, 9/24/2019.

2. Rochelle G.T., Chen E., Freeman S., Van Wagener D., Xu Q., and Voice A. (2011) Aqueous piperazine as the new standard for CO_2 capture technology. *Chem. Eng. J.* **171** (3), 725−733.
3. Zhang Y. (2018) Absorber and Aerosol Modeling in Amine Scrubbing for Carbon Capture, Ph.D. Dissertation, The University of Texas at Austin.
4. Freeman B. (2020) Bench-Scale development of a hybrid membrane-absorption CO_2 Capture Process, Final report, DE-FE0013118, https://www.osti.gov/servlets/purl/1630534.
5. Frailie P.T. (2014) Modeling of Carbon Dioxide Absorption/Stripping by Aqueous MDEA/PZ, Ph.D. Dissertation, The University of Texas at Austin.
6. Dugas R.E. (2009) CO_2 Absorption, Desorption, and Diffusion in Aqueous PZ and MEA, Ph.D. dissertation, The University of Texas at Austin.
7. Lin Y-J. (20116) Modeling Advanced Flash Stripper for Carbon Dioxide Capture Using Aqueous Amines, Ph.D. Dissertation, The University of Texas at Austin.
8. Song D. (2017) Effect of Liquid Viscosity on Liquid Film Mass Transfer for Packings, Ph.D. Dissertation, The University of Texas at Austin.
9. Sachde D.J. (2016) Absorber Performance and Configurations for CO_2 Capture using Aqueous Piperazine, Ph.D. Dissertation, The University of Texas at Austin.
10. Nielsen P.T. (2018) Oxidation of piperazine in Post-combustion carbon capture, Ph.D. Dissertation, The University of Texas at Austin.
11. Freeman S.A. (2011) Thermal Degradation and Oxidation of Aqueous PZ for CO_2 Capture, Ph.D. Dissertation, The University of Texas at Austin.
12. Chen E. (2007) Carbon Dioxide Absorption into Piperazine Promoted Potassium Carbonate using Structured Packing, Ph.D. Dissertation, The University of Texas at Austin.
13. Hilliard M.D. (2008) A Predictive Thermodynamic Model for an Aqueous Blend of Potassium Carbonate, Piperazine, and Monoethanolamine for Carbon Dioxide Capture from Flue Gas, Ph.D. Dissertation, The University of Texas at Austin.
14. Rochelle G.T., Chen E., Akinpelumi K., Fischer K.B., Gao T., Liu C-T., Selinger J.L., and Wu, Y. (2019) Pilot Plant Demonstration of Piperazine with the Advanced Flash Stripper, *Int.J.GHG Cntrl*, **84**, 72–81. DOI: 10.1016/j.ijggc.2019.03.014
15. Liu C-T., Fischer K.B., and Rochelle G.T., (2020) Corrosion by Aqueous Piperazine at 40–150°C in Pilot Testing of CO_2 Capture. *Ind.Engr.Chem.Res.*, **59**(15), 7189–7197. DOI: 10.1021/acs.iecr.9b05735
16. Gao T., Rochelle G.T., (2020) CO_2 Absorption from Gas Turbine Flue Gas by Aqueous Piperazine with Intercooling, *Ind.Engr.Chem.Res.,* **59**(15), 7174–7181. DOI: 10.1021/acs.iecr.9b05733
17. Voice, A.K. (2013) Amine Oxidation in Carbon Dioxide Capture by Aqueous Scrubbing, Ph.D. Dissertation, The University of Texas at Austin.
18. Rochelle, G.T., Akinpelumi, K., Gao, T., Liu, C-T. Suresh Babu, A., Wu, Y., (2022) Pilot plant results with the piperazine advanced stripper at NGCC Conditions, *IJGCC*, **113**, 103551, DOI: org/10.1016/j.ijggc.2021.103551.

Carbon Dioxide Capture for Storage in Deep Geological Formations, Volume 5
Karl F. Gerdes (Editor)
© 2022 BP. All rights reserved.

Chapter 11

CIRCULAR ABSORBER DESIGN AND COST FOR PZAS™ CAPTURE PROCESS

Gary T. Rochelle[1], Michael Klidas[2], Carey Artrip[2], Miguel Abreu[1]
[1]Department of Chemical Engineering, The University of Texas at Austin, Austin, Texas 78712
[2]Babcock and Wilcox, Akron, OH 44305

ABSTRACT: A Front-End Engineering Design (FEED) of the PZAS™ (Piperazine with the Advanced Stripper™) process for CO_2 capture has been developed with U.S. DOE funding for retrofit application on a 465 MW gas-fired combined cycle power plant. This chapter documents the cost estimate for a circular absorber for this specific application, as an alternative to the rectangular design used in the FEED study. As in the FEED study, the capture system uses two parallel trains – one for each of the gas turbines. Two options for the circular absorbers are developed: one with only structured packing and one with structured packing and dual-flow trays. The dual-flow trays provide good gas distribution, but do not provide the same wetted area per unit volume as structured packing. The estimated cost of materials for two absorbers with the trayed configuration is $20.4 million, compared to $21.5 million with all structured packing. However, the amount of packing specified in costing the trayed configuration is probably not sufficient based on subsequent AspenPlus® modelling. The estimated cost for two erected absorbers with only structured packing is $41.8 million to remove 90% of the CO_2 (1.6 million tonnes captured/year) from 1.6 actual BCFD (1.6 million kg/hr) of flue gas. The cost estimate with comparable scope by AECOM for the DOE FEED project using rectangular absorbers is 8% greater.

KEYWORDS: CO_2 capture, piperazine, absorber, PZAS, structured packing, dual-flow trays

INTRODUCTION

The PZAS™ (Piperazine with the Advanced Stripper™) process for CO_2 capture has been developed by the University of Texas at Austin. Pilot plant testing has been performed at the National Carbon Capture Center at flue gas conditions representative of coal [1] and natural gas combined cycle power generation [2]. A project to develop the Front-End Engineering Design (FEED) of PZAS™ on a 465 MW natural gas combined cycle power plant in Denver City, Texas has been funded by US DOE [3]. The basis for the study includes two trains of the PZAS™ capture operation – one dedicated to each of the two power generation trains, which include a gas turbine and heat recovery steam generation system. The process uses 5 molal (5m, 30 wt%) aqueous piperazine (PZ) as a solvent. The University developed the absorber [4] and stripper concepts. Trimeric has provided the commercial process design and AECOM is providing the engineering, procurement, and construction (EPC) services for the FEED. Figure 1 shows the PZAS process used in the FEED [3].

The system design developed for the FEED by AECOM includes a detailed design and cost estimate for the rectangular absorber used in each train. This geometry has been used on two very large-scale capture demonstrations on coal fired power plants. The absorber has two sections of structured packing for CO_2 absorption and a water wash section at the top of the absorber to minimize solvent loss. The system does not use a lean solvent cooler or a cooler on the flue gas before the absorber.

Instead, it relies on pumparound intercooling in the bottom section of absorber contacting to reduce the inlet flue gas temperature and remove the heat of CO_2 absorption, reducing the temperature in the top section of counter-current contacting and enabling the PZAS^{TM} process to achieve 90% CO_2 capture at a rich loading of 0.4 mol CO_2/mol N.

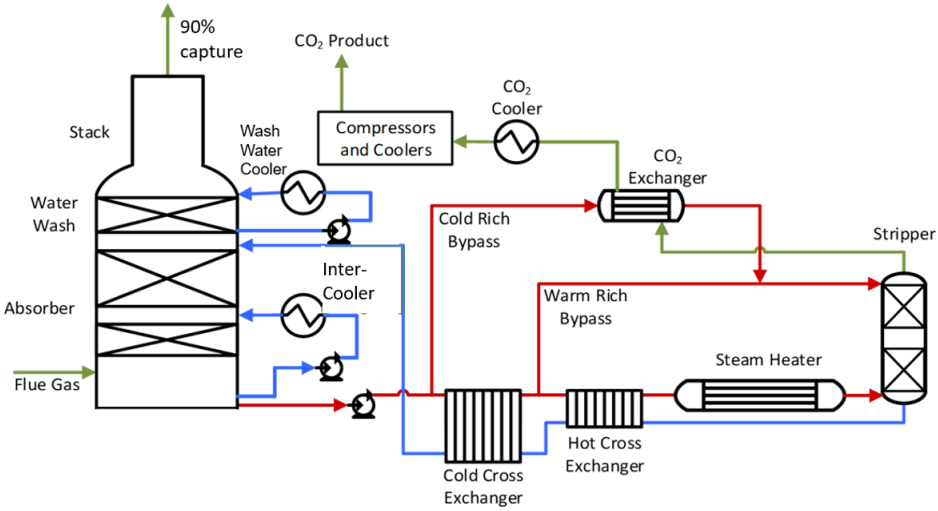

Figure 1. Second-generation amine scrubbing by Piperazine with the Advanced Stripper (PZAS) [3].

The objective of this work is to examine an alternative design concept from that used in the FEED for the CO_2 absorption columns, which represent a large portion of the capital cost of the capture plant. The specific goal is to develop a conceptual design and cost estimate for a circular absorber that uses dual-flow trays in the bottom section of the absorber. Babcock and Wilcox (B&W) has supplied many very large circular absorbers for wet flue gas desulfurization (WFGD) by limestone slurry scrubbing. These absorber systems typically spray limestone slurry onto dual-flow trays to create contacting area between the slurry and the flue gas. The dual-flow trays should provide excellent cooling and gas distribution at reasonable cost.

This work also developed a base case design and estimate for a circular absorber using only structured packing with no dual-flow trays. A circular absorber will use less metal than a rectangular absorber but may be more expensive to erect in the field. The commercial experience of B&W in providing large absorbers will be an asset to commercial deployment of the PZAS^{TM} technology.

The University conducted a critical review of the literature and used Aspen Plus® modelling to predict the performance of the dual-flow trays in the PZAS^{TM} absorber. B&W conducted a feasibility analysis and provided budgetary pricing for two configurations of the circular absorbers: one with all structured packing, as in the AECOM design, and one with two dual-flow trays in the section with pump-around cooling and structured packing in the top section.

DESIGN BASIS–RECTANGULAR COLUMN

The design for retrofit of CO_2 capture to the natural gas combined cycle power plant in Denver City, TX, was prepared by AECOM. The overall design concept utilizes two parallel CO_2 capture trains, with each train having a rectangular absorber with a cross-sectional area of 174 square meters (m^2). Each absorber includes three sections of packing and auxiliaries. The top water wash section contains 3 meters (m) of Mellapak™ 252Y (M252Y) structured packing and is used to cool the exiting flue gas and minimize piperazine emissions. M252Y is a low pressure drop packing with a nominal surface area of 250 m^2/m^3. The top absorber bed has 4.9 m of M252Y packing and is used to contact the lean solvent entering the absorber with the flue gas. The bottom absorber bed has 2.7 m of M252Y packing and is used to contact the incoming flue gas with the solvent flowing down from the middle section plus additional rich solvent being circulated (and cooled) from the absorber bottom surge volume. The rectangular absorber designed by AECOM is shown in Figure 2. The basis for the material balance is given in Table 1.

DESIGN BASIS–CIRCULAR COLUMNS

Tower Design–Packing Only

The circular tower design with packing only is similar to the rectangular absorber design developed by AECOM for the FFED [4]. Each rectangular tower is 12.2 m by 14.3 m and has a cross-sectional area of 174 m^2. A 14.9-m diameter cylindrical tower has the same cross-sectional area. By maintaining almost identical cross-sectional areas, the superficial velocities with packing only and the AECOM absorber design will be the same, which should provide the same mass transfer performance. This also ensures that the liquid storage volumes in the bottom of the absorber are the same as long as the liquid levels stay the same. Both options with the circular tower use the same normal liquid level and maximum liquid level as the AECOM design in Figure 2.

Table 1. Basis for Material Balance.

	Units	Gas Feed Absorber	Lean Solvent to Packing	Rich solvent From intercooler
Temperature	°C	112	46	29.4
Pressure	barg	0.07	3.7	0.83
Mass Flow	kg/s (wet)	432.7	437.8	1400
Volume Flow (Actual)	m^3/s	527	0.416	1.25
H_2O	Mass (%)	7.0	65.0	62.2
CO_2	Mass (%)	6.7	5.9	11.0
N_2	Mass (%)	73.5		
O_2	Mass (%)	13.8		
PZ	Mass (%)		29.1	26.8

The circular tower design with M252Y structured packing used the same depth of packing as the rectangular design: 4.9 m in the top absorber bed and 2.7 m in the bottom absorber bed.

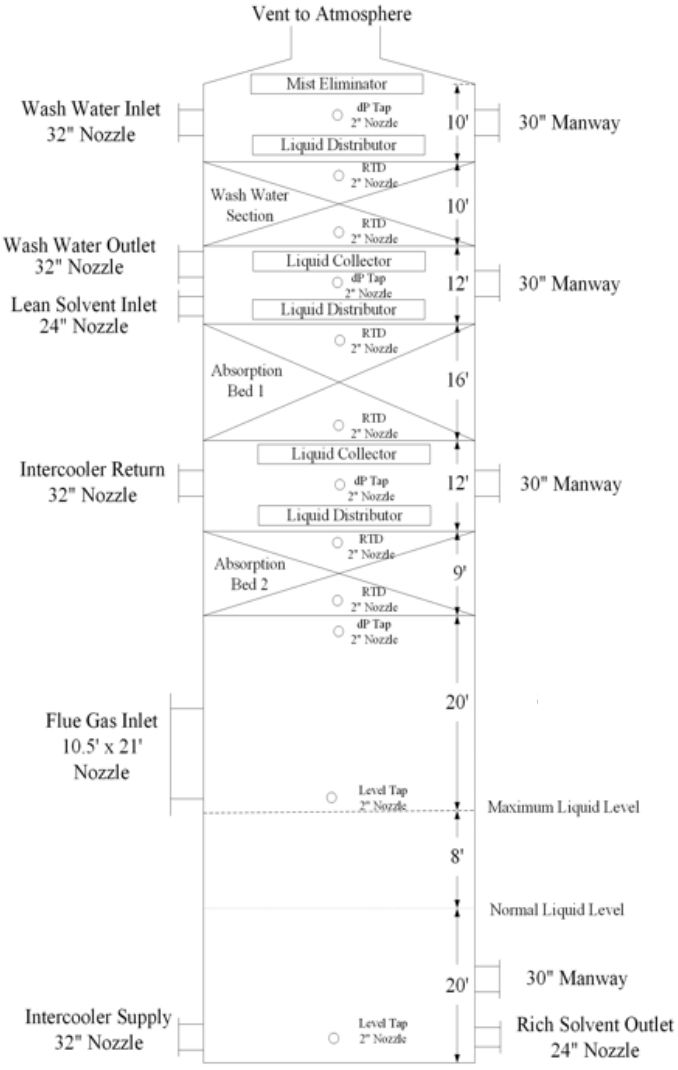

Figure 2. Rectangular Absorber Tower Design by AECOM.

Modelling Results-Two Dual-Flow Trays With One Section of Packing

Since there is no data on the performance of dual flow trays in with CO_2 absorption by amines, an empirical model describing the mass transfer performance of dual-flow trays was implemented in the Aspen Plus® software which was used to estimate the performance of the dual-flow tray absorber. The Independence model for piperazine scrubbing [5] was augmented with a sieve tray model in Aspen Plus®. The sieve tray model used the actual hole size, free area, and plate thickness of the dual-flow tray. The sieve tray active area was matched to the dual-flow tray area using the technique

of Garcia and Fair [6]. The pressure drop of the sieve tray and dual-flow tray were matched by changing the width and height of the sieve tray downcomer. The correlation of Miyahara *et al.* [7] was used to estimate values for the liquid film coefficient (k_l) and the effective wetted area (a_e). The wetted area was corrected for the effect of the spray distributor using B&W data.

The Aspen Plus® simulations showed that the dual-flow trays could not provide the same CO_2 removal as the 2.3 m of structured packing that they replaced. Modelling studies of the entire absorber showed that 7.9 m of higher surface area MellapakPlus™ M302Y packing is required in the main absorber bed to achieve 90% CO_2 removal when two dual-flow trays are used in place of packing in the lower absorber bed. This compares to 4.9 m of M252Y packing used in the original rectangular design. Flooding in these columns is determined by the column loads in the lower absorber bed, therefore it was possible to replace M252Y packing with higher surface area M302Y packing. In this configuration the two dual flow trays were designed with a total pressure drop of 1.25 kPa. Figure 3 shows the calculated column profiles for temperature and CO_2 flux with two dual-flow trays and 7.9 m of M302Y in the packing section. This can be compared to the profiles with all structured packing in Figure 4.

With these changes in the possible design, 7.9 m of M302Y provides 1.25 times more packing area than the total height of M252y in the packing only design (7.9*300/((4.9 +2.7)*(250)). Therefore, it does not appear that the design with dual flow trays will reduce the volume or cost of packing.

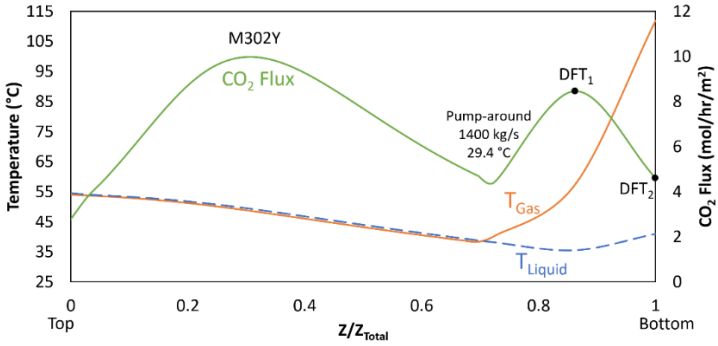

Figure 3. CO_2 Flux and Temperature Profiles using Two Dual Flow Trays (DFT_1 and DFT_2) and 7.9 m of M302Y.

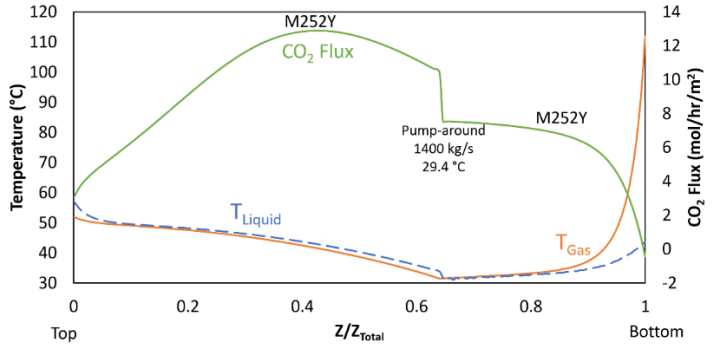

Figure 4. CO_2 Flux and Temperature Profiles with 2.7 m of M252Y in the Bottom Pump-around and 4.9 m of M252Y in the Top Section of Solvent Packing.

Tower Design with Dual Flow Trays

A design and cost estimate were developed for the absorber tower with two dual-flow trays, in combination with a spray header, to replace the packing in the lower absorber bed. The estimate was done for an absorber with 6.9 m of M302Y packing in the main absorber bed. This is the same as the total height of packing in the absorber design with all packing (two beds). It is less than the required packing height of M302Y later determined by Aspen Plus modelling to be 7.9 m.

The total height of the absorber with two dual-flow trays and 6.9 m of M302Y is 1.5 m less than that with all packing. This height includes usual spacing for the dual flow trays and spray and 0.76 m between the top of the spray header and the bottom of the packing.

The height of packing used for the cost estimate (6.9 m) and the height required by the Aspen model (7.9 m) are both greater than usually recommended for a single bed of packing (6.15 m). If this packing was split into two beds to maintain its expected performance, it would significantly increase the column cost by requiring an additional distributor and packing support and adding open space to the height of the absorber.

Above the dual-flow tray or trays, B&W normally uses solvent spray headers both to create droplets for absorption and to distribute solvent evenly to the trays. The spray nozzle quantity, pressure, and layout have been optimized even though the mass and heat transfer performance of the spray headers is small relative to that of the trays. Inclusion of multiple spray headers was evaluated based on B&W experience, but due to the minimal increase in expected performance a single spray level design was selected.

Common Features of the B&W Designs

One difference between the circular absorbers by B&W and the AECOM rectangular design is the inclusion of a of an optional flue gas inlet quench system normally used by B&W in WFGD applications. In WGFD applications with limestone slurry, this inlet design has the advantage of quenching the incoming flue gas to prevent scaling. In this CO_2 application the quench system will be an optional contingency to address possible formation of amine aerosol as some of the solvent may evaporate when the hot gas enters the bottom of the packing.

The AECOM rectangular design includes no additional specific features for quenching the flue gas. Additional quenching may be necessary if the rapid evaporation of the piperazine solvent results in amine aerosol formation. Because this application for amine scrubbing has a lower L/G than wet flue gas desulfurization, B&W has provided pricing of an optional continuous upstream quench in the event that it is deemed necessary for either the rectangular or circular absorber design.

This quench system uses air-water (dual fluid) nozzles capable of achieving small droplet sizes (D_{50}<75 µm depending on compressed air consumption) to ensure rapid gas saturation. Water for this system would be provided as the bleed from the water wash, so it would have no effect on the water balance. B&W has dual-fluid nozzle capabilities and prior experience implementing these types of quench grids as illustrated in Figure 5. Option pricing has been provided for additional quenching with dual-fluid nozzles. The B&W base case designs utilize a modified gas inlet to provide quenching with curtain of water. The AECOM design of the rectangular tower includes no features for quenching.

Both circular column designs by B&W include a stack (6.1 m diameter, 21.95 m height) added to the top of the absorber to comply with EPA method test requirements for fully developed flow to support accurate measurement by the Continuous Emissions Monitoring System (CEMS). The absorber is provided with a 60° transition to provide good mist eliminator performance and to avoid turbulence at the CEMS, resulting in a transition height of 7.44 m. The stack discharge height with packing alone is 64.9 m above grade. The design using dual flow trays has a slightly lower discharge height of 63.4 m resulting from a reduced absorber height.

Weight estimates were prepared for the two tower options. Each tower with packing has an estimated total weight of 609 tonnes. Each tower using dual flow trays has an estimated total weight of 628 tonnes. These weights represent the full tower structure (including stack) and internals in a dry condition. The foundation dead loads are predicted to be less than 2844 tonnes with dual flow trays and 2828 tonnes with all packing.

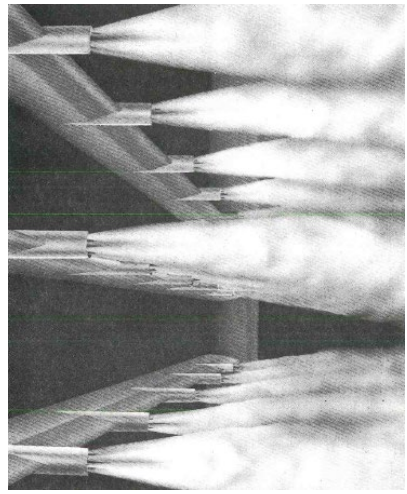

Figure 5. In-Duct Humidification System.

PRICING

Budget Pricing

The budget pricing (±25%) for material supply is given in Table 2. These estimates were prepared in August 2021. Construction and erection costs were estimated for the circular absorbers with all packing and would probably be about the same for the circular absorbers with dual flow trays. The material supply cost is included for the dual-fluid inlet quench which may be considered as an option to add to either circular absorbers or rectangular absorbers.

Table 2. Budget Price for Two Circular Absorbers.

	Material Supply	**Construction & erection**	**Total**
Packing with 2 dual-flow trays (includes M302Y packing in top)	$20,377,000	Not estimated	
All M250Y packing	$21,476,000	$20,350,000	$41,826,000
Dual-Fluid Nozzle Inlet Quench	$2,536,000	Not estimated	

Scope

The materials and equipment cost of the absorber tower was estimated for both circular absorber designs. The capture system includes two absorbers in parallel, each with a water wash, mist eliminator and stack. The cost estimate includes the internals (packing, trays, support, distributor, collector trays, and mist eliminator). It includes the intercooler pumps for recirculating the rich solvent and an absorber access structure.

The cost estimate does not include:

- Primary rich pumps
- Water wash circulation pumps
- Civil work and foundations
- Piping and piping installation
- Insulation and lagging
- Electrical, instrumentation, and controls

Material Supply Pricing

The budget price for materials supply was performed using a bottom-up approach. In addition to the material costs of the various equipment, the prices provided also include engineering and project management costs, transportation to site, and mark-up to simulate the pricing for a firm bid for this project. Historical pricing information was used to estimate the cost of materials for the optional inlet quench system, the recirculation pumps, the tower access structures, and the absorber instruments. Figure 6 shows the distribution of cost in the materials supply. Updated pricing was received from several suppliers on other components including packing, spray nozzles, 304L stainless-steel plate and fabrication, and stack.

The tower internals are the second largest portion of the overall material costs. Both circular tower designs have very similar cost for tower internals (within 1.5% of each other).

Using the weights provided for the packing, internals, and stack, the B&W WFGD absorber structural design program was used to calculate the stiffening requirements and absorber tower shell thicknesses at various elevations. These results were used to estimate the absorber tower material for 304L. Pricing for the various plate materials gave an overall cost of $4.98/kg.

In addition to the cost of raw materials, the pricing also includes fabrication and manufacturing of the modular tower sections which will be delivered to site for construction.

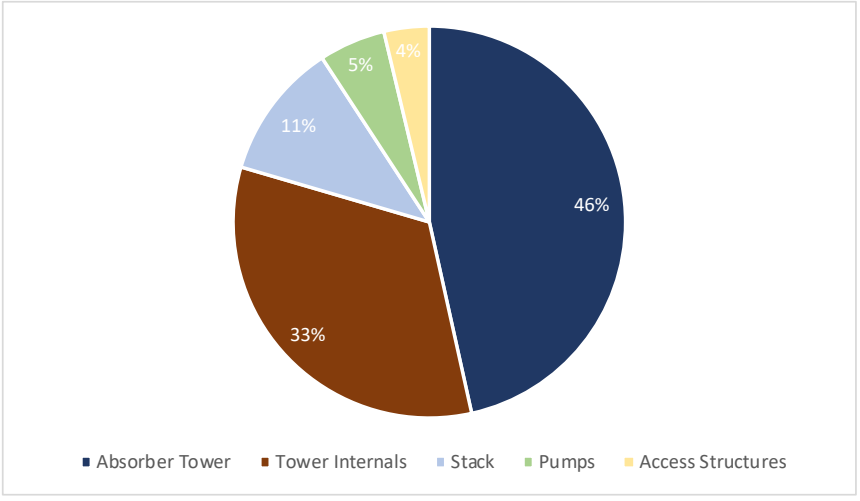

Figure 6. Nominal Material Pricing Breakdown for Various Absorber Components.

Construction Pricing

The construction cost for the circular column using only packing was estimated to be $20,350,000. The construction cost for the column using dual flow trays will be about the same.

The scope for this estimate includes:

- Erect two absorber vessels and install all absorber internals including liquid distributors, structured packing, packing supports, and chimney tray liquid collectors (seal welded).
- Erect an integral chimney stack with single access platform at the top of each absorber.
- Erect absorber access stair towers and platforms.
- Install intercooler pumps and motors and perform required machine alignments.
- Supply and install grout as required on an interface that is the top of concrete.
- Furnish construction equipment, tools, labor, supervision, field verification, layout work, construction supplies, consumables, scaffolding, weather protection, and quality control.

The following tasks are performed by others (not included in construction pricing):

- Civil work and foundations
- Piping and piping installation
- Insulation and lagging
- Electrical, instrumentation, and controls

Milestone Schedule

A detailed schedule was developed for the project. The notable milestones are delivery of the absorber materials in 20 months and complete erection of the absorber in 29 months.

Comparison to Other Absorber Costs

Martorell [8] has prepared a comparison of absorber costs from three different sources for the PZAS FEED (Table 3). In addition to the cost for "all packing" from this effort, he has adjusted costs estimated by AECOM for the rectangular absorber as in Figure 2. He has also scaled costs developed by Bechtel for a smaller circular absorber to the cross-section and packing height of the AECOM estimate. Other adjustments have been made to get the same scope for each of the estimates. The rectangular absorber by AECOM is 8% more expensive than the B&W circular absorber, but the AECOM estimate may be more accurate than the "budget" estimate by B&W. The circular absorber by Bechtel is 18% lower but is probably the least accurate because of uncertainties in the scaling adjustment.

Table 3. Estimated Adjusted Cost for Two Absorbers [8], October 2021-April 2022.

	Geometry	**Total Cost ($million)**
AECOM [9]	Rectangular	39.4
Babcock & Wilcox (this work)	Round	36.4
Bechtel [10]	Round	29.8

Note: Cost adjusted to same tower cross-section and packing height. Cost includes platforms, materials, construction, and erection. Cost does not include pumps, contingency, instruments, piping, foundations, contingency, or overhead.

CONCLUSIONS

The detailed, critical review of the previous literature included in this work suggests that the dual-flow tray will provide much less effective gas/liquid surface area than a comparable volume of structured packing. This work did not include a comprehensive evaluation of pressure drop, but it is also probable that the dual-flow trays will require greater pressure drop, adding to the annual cost of the system. However, the dual-flow trays will provide a positive, effective means of gas distribution. The B&W design also includes an inlet that provides quenching for the hot flue gas.

The budget price of the materials for the dual-flow tray configuration is $20,377,000, about $1,000,000 less than the price for an absorber that uses only structured packing. The dual flow tray configuration appears to be cost competitive with the use of only structured packing. However, the cost estimate for the tray configuration used 6.7 m of packing, which is 1.2 m less than that estimated by the Aspen model as required to meet the CO_2 removal target. A further limitation on these estimates is that whether the packing depth is 6.7 m or 7.9 m, the packing should be split into two beds to maintain mass transfer performance. Therefore, the dual-flow configuration is probably equivalent to or more expensive than the packing only configuration.

The budget, erected price (±25%) for two circular absorbers with the same packing design as the AECOM rectangular absorbers is $41,826,000. These absorbers will provide 90% removal of CO_2 (1.6 million tonnes captured/year) from 1.6 actual BCFD (3.4 million lbs/hr) of flue gas produced by the natural gas combined cycle power plant studied here. The erected price does not include civil work, piping, insulation, and electrical.

The estimated cost of the materials for a flue gas quench with two-fluid nozzles is $2,500,000. This is a contingency option to manage amine aerosol that has not been included in any of the absorber designs.

ACKNOWLEDGEMENTS

The work was supported by the CO_2 Capture Project.

One author of this publication consults for a process supplier on the development of amine scrubbing technology. The terms of this arrangement have been reviewed and approved by the University of Texas at Austin in accordance with its policy on objectivity in research. The authors have financial interests in intellectual property owned by the University of Texas that includes ideas reported in this paper.

REFERENCES

1. G.T. Rochelle, E. Chen, K. Akinpelumi, K.B. Fischer, T. Gao, C-T. Liu, J.L. Selinger, Y. Wu, Pilot Plant Demonstration of Piperazine with the Advanced Flash Stripper, *IJGGC*, **84**, 72–81, 2019. DOI: 10.1016/j.ijggc.2019.03.014.
2. G.T. Rochelle, K. Akinpelumi, T. Gao, C-T. Liu, A. Suresh Babu, Y. Wu, Pilot Plant Results with the Piperazine Advanced Stripper at NGCC Conditions. *IJGCC*, **113**, January 2022, 103551. 10.1016/j.ijggc.2021.103551.
3. F. Closmann, T. Gao, A. Suresh Babu, M. Abreu, B. Drewry, G.T. Rochelle, FEED for Piperazine with the Advanced Stripper on NGCC at Denver City, Texas. *Proceedings* of the 15th International Conference on Greenhouse Gas Control Technologies (GHGT-15), SSRN-id3819272, 2021.
4. T. Gao and G.T. Rochelle, Creative Absorber Design and Optimization for CO_2 Capture with Aqueous Piperazine. *IJGGC* January 2022; **113***, 103534.*

5. P.T. Frailie (2014), *Modeling of carbon dioxide absorption/stripping by aqueous methyldiethanoloamine/piperazine,* Ph.D. dissertation, The University of Texas at Austin.
6. J.A. Garcia, J.R. Fair, Distillation Sieve Trays without Downcomers: Prediction of Performance Characteristics. *Ind Eng Chem Res*. 2002; **41**:1632–1640.
7. T. Miyahara, M. Kurihara, M. Asoda, T. Takahashi, Gas-Liquid Interfacial Area and Liquid-Phase Mass Transfer Coefficient in Sieve Plate Columns without Downcomer Operating at High Gas Velocities. *J. Chem. Eng. Jpn.* 1990; **23**:280–285.
8. J.L. Martorell, G.T. Rochelle, M. Baldea, W.Elliott, C. Bauer, Comparison of Detailed Capital Expense Estimates for Two NGCC Retrofits with Capture by Amine Scrubbing, Presented at GHGT-16, October 23-27, 2022, Lyon, France.
9. G. T. Rochelle, K. Farmer, S. Bryan, M. Bernau, A. Sexton, K. Dombrowski, D. Myers, Marsh M, Piggott B, Jones R. Front-End Engineering Design for Piperazine with the Advanced Stripper, final report for DE-FE0031844, July 29, 2022.
10. Bechtel National, Inc. *Front-End Engineering Design (FEED) Study for a Carbon Capture Plant Retrofit to a Natural Gas-Fired Turbine Combined Cycle Power Plant.* Reston, VA. 2021. DOI: https://doi.org/10.2172/1836563.

Carbon Dioxide Capture for Storage in Deep Geological Formations, Volume 5
Karl F. Gerdes (Editor)
© 2022 BP. All rights reserved.

Chapter 12

PILOT TRIALS OF C-CAPTURE NON-AMINE SOLVENT-BASED CARBON CAPTURE PROCESS ON BIOMASS-FIRED FLUE GAS AT DRAX POWER STATION

Caspar Schoolderman[1*], Duncan Holdsworth[1], Douglas C. Barnes[1], Christopher M. Rayner[1,2], Carl Clayton[3]

[1]C-Capture, Unit 14, Albion Way, Leeds, LS12 2EP, UK
[2]University of Leeds, Leeds, LS2 9DF, UK
[3]Drax Power Station, Selby, YO8 8PH, UK
* Corresponding author

ABSTRACT: Drax Power Station, located near Selby, North Yorkshire, is fully fired by biomass fuel, and represents the UK's biggest renewable electricity generator and the largest decarbonisation project in Europe. C-Capture have developed a non-amine, solvent-based technology for CCS on large scale point source emitters with reduced energy requirements compared to amine-based systems.

The Drax Group are interested in the C-Capture carbon capture process on biomass derived flue gas as an option to achieve Bioenergy with CO_2 Capture and Storage (BECCS). Before conversion to biomass, Drax used coal as the primary fuel source, and thus had Flue Gas Desulphurisation (FGD) absorbers in place. Biomass combustion produces negligible amounts of SO_x and thus FGD is not currently required, and there is potential to re-purpose the FGD absorbers for CO_2 capture. The FGD units are spray absorbers fed by lime water, generating calcium sulphate slurries. The chemical and physical properties of the C-Capture non-amine solvent suggest opportunities for deployment in these absorbers as the solvent has low corrosivity and an attractive toxicity profile. In addition, the higher chemical compatibility of the solvent with the impurities of biomass-derived flue gas, especially metal oxides contained in the flue gas/fly ash, suggested further advantages for this approach compared to conventional solvents.

A C-Capture pilot plant was constructed and operated at Drax on a slipstream from one of the biomass burner flue gas channels downstream of the electrostatic precipitator. The pilot was designed to capture up to 1000 kg/day CO_2. The pilot plant included a conventional packed column and a 10-column spray absorber.

Although the observed capture performance was well below expectations based on laboratory data for both the packed absorber and the spray absorber, the pilot operation provided good information for further research into the absorption mechanism, with the goal of enabling successful scaleup. Operations were cut short by the Covid pandemic. The Drax operation demonstrated high compatibility of the C-Capture solvent with the biomass flue gas–evident from low degradation of the solvent and very low levels of degradation product species emissions in the clean flue gas. Results and experience from the Drax trials were instrumental in preparing for trials at SINTEF and guiding further process and chemistry development.

KEYWORDS: BECCS, non-amine, CCS, carbon capture, biomass, emissions, ageing

INTRODUCTION

The objectives of the work at Drax were:

- To scale up C-Capture's carbon capture mini plant, located in Leeds, to validate and debug the various unit operations and the process as a whole.
- To generate results on solvent flue gas compatibility and solvent ageing.
- To analyse the full spectrum of possible emission products from the carbon capture plant.

To meet the above objectives, a pilot plant operating the C-Capture technology was constructed and operated at Drax on a slipstream from one of the biomass burner flue gas channels, located downstream from the electrostatic precipitator. The pilot was designed to treat between 100 to 250 Nm^3/h flow rate of flue gas and capture up to 1000 kg/day CO_2. The pilot plant included a conventional packed column and a 10-column (series) spray absorber with multiple spray injectors in each column. The spray absorber was designed to assess repurposing the existing FGD scrubbers at the Drax plant and was set up to allow flexibility on input locations for fresh solvent and for recycled loaded solvent.

BIOMASS-DERIVED FLUE GAS CHARACTERISTICS

Table 1 shows the composition of the biomass derived flue gas. Biomass flue gas contains minimal levels of sulphur, hence avoiding the need for a flue gas desulfurisation (FGD) unit. The ash entrained by the flue gas contains a wide spectrum of metal oxides as shown in Figure 1. A number of these metal oxides are known to be potentially powerful oxidation catalysts, particularly copper, iron, manganese, chromium, and vanadium.

Table 1. Drax flue gas composition at 150°C.

Species	Units	Typical	Min	Max
H_2O	vol%	11	10	12.5
CO_2	vol%	12	11	13
O_2	vol%	6	4.5	8
NO_X	ppm	85	50	114
SO_X	ppm	11	0	30
HCl	ppm	1.2	0	3.0
Dust	mg/Nm^3	2.5	1	30

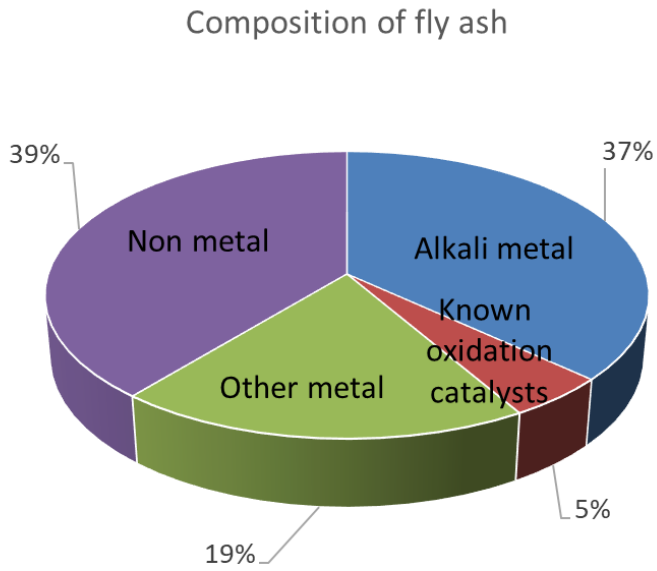

Figure 1. Metals found in biomass derived fly ash from Drax.

PILOT PLANT DESIGN AND LAYOUT

Process Description and Key Operating Conditions

The overall process achieves CO_2 separation by means of chemically reactive solvent absorption. It is conceptually similar to established processes involving amine solvents but utilises C-Capture's proprietary non-amine solvent system.

The incoming flue gas is cooled and condensate is separated prior to feeding to the process. The pressure of the incoming gas stream is slightly boosted with a blower, and it is cooled further with any additional condensates generated at this stage also being removed.

The cooled flue gas is fed to the absorber where the CO_2 selectively reacts with the capture solvent, the degree of CO_2 separation (e.g., 50% to 95% CO_2 removal) being determined by the gas-liquid ratio and the gas residence time in the absorber. When the CO_2 depleted flue gas leaves the absorber, it will contain a small amount of volatile organic compounds (VOCs), which are scrubbed before the flue gas is emitted to the air.

The lean CO_2 capture solvent is pumped from a surge tank to the top of the absorber. As it flows down the absorber, capturing the CO_2, there is a slight temperature increase due to the exothermic capture reaction. The loaded, or rich, solvent is fed from the absorber to the stripper via the lean-rich heat exchanger where the cool, rich solvent incoming to the stripper is heated against the hot, unloaded, or lean, solvent returning from the stripper.

In the stripper, the rich solvent is heated, which reverses the chemical reaction between the solvent and the CO_2, releasing it from solution. The majority of the heating occurs in the lean-rich heat exchanger, with a small amount of "top-up" heat being provided by a reboiler where the solvent is heated against steam to the required temperature.

As in the absorber, the CO_2 gas which leaves the top of the stripper contains a small amount of VOCs, which are scrubbed before the CO_2 leaves the system. The hot, lean solvent leaves the stripper, is cooled initially in the lean-rich heat exchanger against the incoming rich solvent and is further cooled before being returned to the solvent surge tank.

Flue Gas Conditioning and Monitoring

The slip stream of flue gas entering the pilot plant cooled considerably in the long line connecting the flue gas duct to the pilot plant. Condensate is separated from the flue gas before entering the pilot plant. The flue gas is further cooled directly in a gas liquid heat exchanger to the required temperature. No further cooling was required to condition the flue gas prior to entry to the pilot plant.

A PCME QAL 260 particulate monitoring system was installed on the flue gas line to measure the dust loading in the flue gas. The measured fly ash content was found to be approximately 1/5 of the average of the flue gas in the main duct. This is likely due to the flue gas sample point being located at the top of the duct, while most of the fly ash flows along the bottom.

The CO_2 content in the incoming and outgoing flue gas was measured by means of an infrared sensor directly in the gas line. The purity of the CO_2 product was confirmed by a handheld analyser.

Other Analyses

Solvent samples were periodically obtained and analyzed in C-Capture's laboratory to determine the presence, identity, and concentration of degradation products.

Conventional Packed Absorber

A standard packed absorber was used for the pilot plant to remain close to existing unit operation designs. The CO_2 absorption columns were sized to 300 mm diameter and 20 m of packing height split between two columns in series due to height restrictions, as shown in Figure 2.

Spray Absorber

Spray absorbers were trialled in the Leeds facility and at Drax to investigate the feasibility of utilising the existing FGD towers for CO_2 capture. Figure 3 shows the installed spray absorber test rig that consists of 10 spray absorbers in series, potentially capable of achieving high capture fractions.

Figure 2. The C-Capture CCS pilot plant installed at Drax.

Figure 3. Ten column spray absorber installed at Drax.

Heat Integration

Figure 4 shows a number of plate heat exchangers in series, included to achieve good heat integration between lean and rich solvent flows even with the low thermal conductivity of the solvent.

Stripper and Reboiler

An electric steam boiler was used to provide the steam to the pilot as only a small flow was required and there was no nearby steam supply to tap into. The reboiler heat exchanger was a plate heat exchanger as appropriate for the scale, and the setup is shown in Figure 5.

OPERATIONAL CONDITIONS

The process was designed for 110 Nm^3/h of flue gas and operated at close to 20°C flue gas inlet temperature, with absorption near ambient temperature and stripping at elevated temperature and atmospheric pressure (Figure 6). No water or basic solution wash, or particle filtration of the incoming flue gas was used.

It is recognised that the lean solvent and absorber operating temperature is an area for further optimization.

Figure 4. Bank of plate heat exchangers for lean/rich heat integration.

Figure 5. Electric steam generator (at the rear) and reboiler heat exchanger (at the front in an insulated box).

Figure 6. Stripping apparatus.

RESULTS

Operational

The Drax pilot operated for approximately 500 h with Formulation A and 100 h with Formulation M (Figure 7). Formulation M is similar in composition to Formulation A, but the carrier solvent has a lower volatility than that employed in Formulation A to investigate the possibility of reducing VOC emissions.

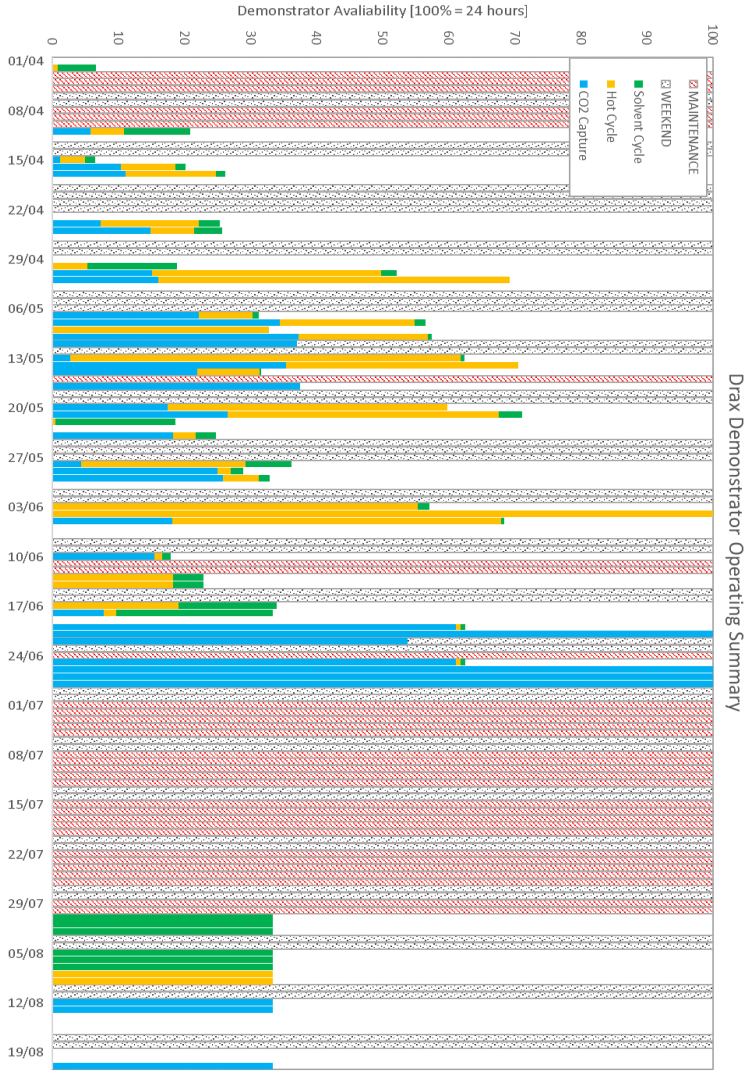

Figure 7. Summary of operational conditions from 2019 test operations.

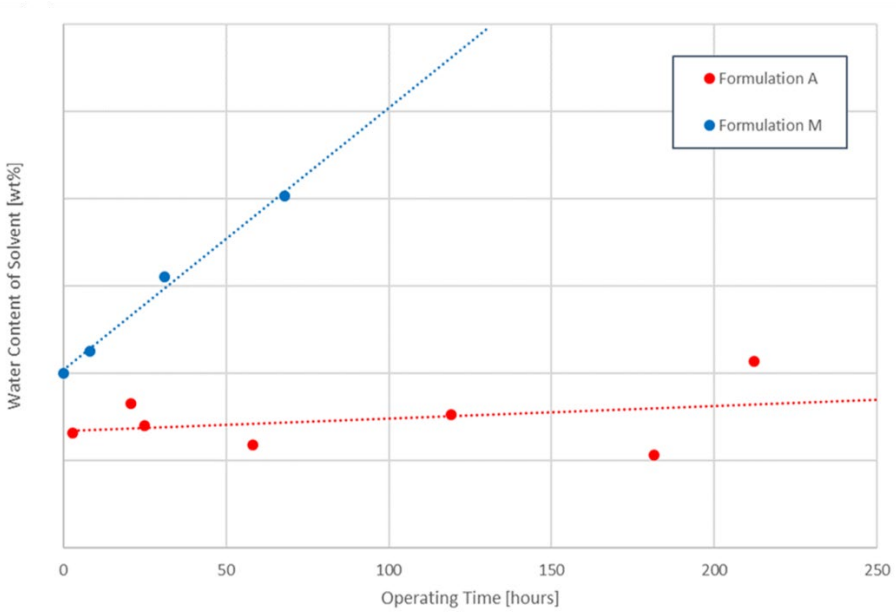

Figure 8. Water content changes in Formulation A and M during operation.

The process captured and released CO_2 in a controlled manner but showed a lower removal capacity than the 90% capture at 0.5 to 1.0 tonne CO_2/day that was expected based on testing a CCS mini plant, which had a limited height packed column.

The Drax pilot testing produced a range of learnings that were employed in follow up trials in Norway at Tiller with BECCS flue gas, absorption testing, VOC abatement, and energy use measurements. The Drax unit was the first CCS pilot to operate with the C-Capture solvents. Design choices had been made based on previous experience from biogas plants (0.2 and 1.0 t/d, Tray column, 45%v/v CO_2 inlet gas, CO_2 removal by air stripping) and translated to the CCS pilot. During commissioning and operation, it was found that equipment needed debugging, which resulted in low availability of the pilot plant.

Issues encountered and addressed with the Drax pilot included:

- The flue gas line to the pilot plant lost sufficient heat to cause condensation in the gas line, which collected in the flexible gas connection to the pilot and caused pressure trips. An additional knock-out pot was installed to avoid the disruptions.
- Single stage centrifugal pumps were used in the biogas pilot plants; however, the CCS plant required multistage centrifugal pumps to generate sufficient head. Unfortunately, the multistage pumps accumulated solids, which resulted in trips. The pumps were replaced by progressive cavity pumps.
- The drain pump of the stripping apparatus did not produce enough head, and gas bubbles got entrained into the pump occasionally. This was resolved by changing the operating conditions of the stripper and modifying the internals.
- The steam boiler water level indicator had frequent issues resulting in over- and underfilling, which caused trips.
- Attempts were made to improve the absorber performance by changing out liquid (re-)distributors in the columns.

Based on learnings from the Drax trials, an improved unit operation design was developed, and changes were made to pumps and liquid lines prior to operation at the Tiller pilot plant in Norway.

Absorption

Packed Bed Absorber

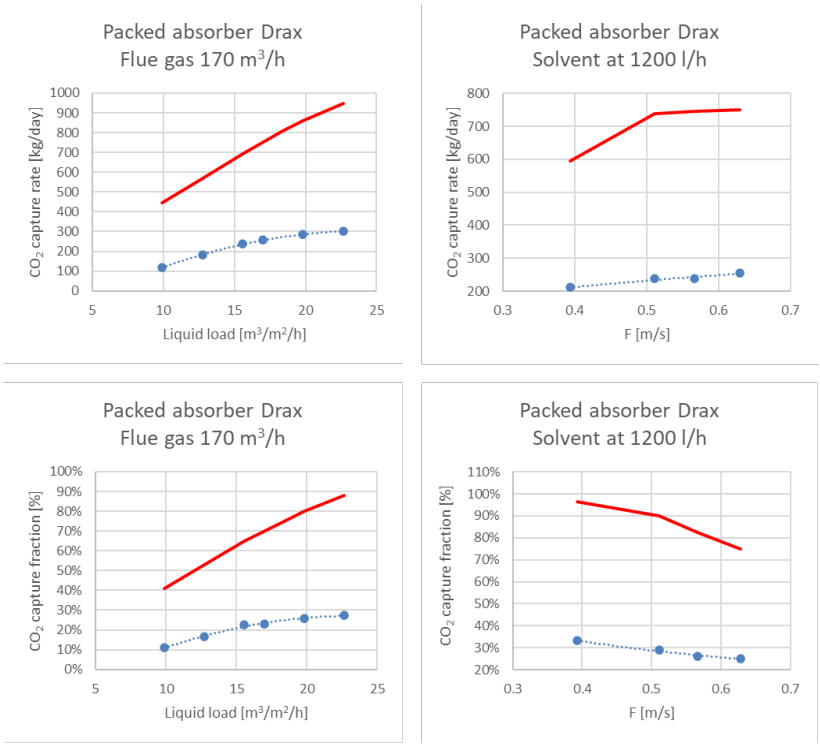

Figure 9. Fraction and amount of CO_2 captured as a function of operational conditions (blue dots = experiment, red line is expected). Liquid load is the liquid flow per cross sectional area of the column. F is gas flow per cross sectional area of the column, which is the effective vertical gas velocity.

The pilot plant packed absorber was scaled up from a 50 mm mini plant column with random packing and the same liquid and gas loads. The CO_2 capture results of the 300 mm pilot columns are shown in Figure 9, and as can be seen, the capture rates are lower than expected. The cause was found to be the mixing history of the fluid, which at the smaller scale worked reliably, but did not scale up as expected. C-Capture has worked with their scale-up partner and have resolved this aspect by choosing an appropriate absorber type with appropriate mixing to give consistent and targeted performance.

Spray Absorber

Spray absorbers were of interest to Drax since the potential existed to re-purpose the existing FGD spray absorber for CO_2 capture. This would potentially be a low-cost option for implementing CCS at scale. C-Capture performed a range of lab experiments to validate the feasibility of using spray absorbers for CO_2 capture.

Within a single spray absorber column, each spray nozzle creates a local absorption zone. Nozzles can be placed quite close together in order to create a mass transfer region with high droplet density

to ensure good contacting between the falling droplets and the rising flue gas. The overall performance can be characterized using the absorption rate per nozzle as a metric.

One pilot test to reproduce a lab experiment involved use of a single spray column with multiple nozzles in series to scrub a slip stream of flue gas flowing up through the falling droplets of solvent. In this test, a fixed volume of solvent was recycled to observe the CO_2 absorption rate versus solvent loading, shown in Figure 10. The performance is below that of the lab trial and much lower considering there are many more nozzles in use.

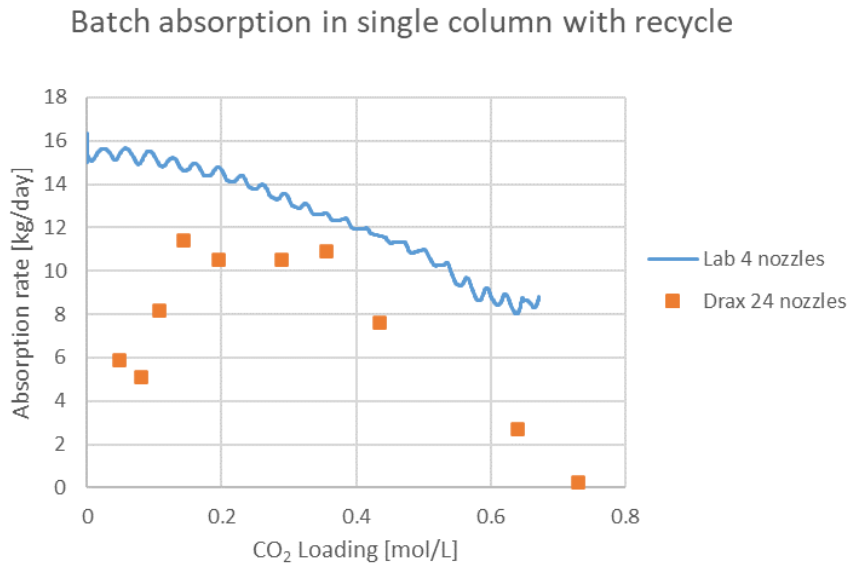

Figure 10. CO_2 absorption rate versus Δ CO_2 Loading (rich-lean) as measured in single column with full solvent recycle.

The 10-column spray absorption system was then operated in continuous mode, where the solvent is fed to each column consecutively, and the flue gas flows in the opposite direction through each column. Figure 11 shows the solvent loading for the 10-column absorber is low, but in line with the full recycle trial when compared on liquid hold-up basis. The loading was well below what was achieved in the lab with same column dimensions and same type of spray nozzles.

The cause of the Drax pilot unit achieving below expectation absorption rates when compared to lab spray tests, is likely due to the spray nozzles not operating as intended. Debugging of the equipment was cut short as the testing had to be stopped on site due to COVID-19.

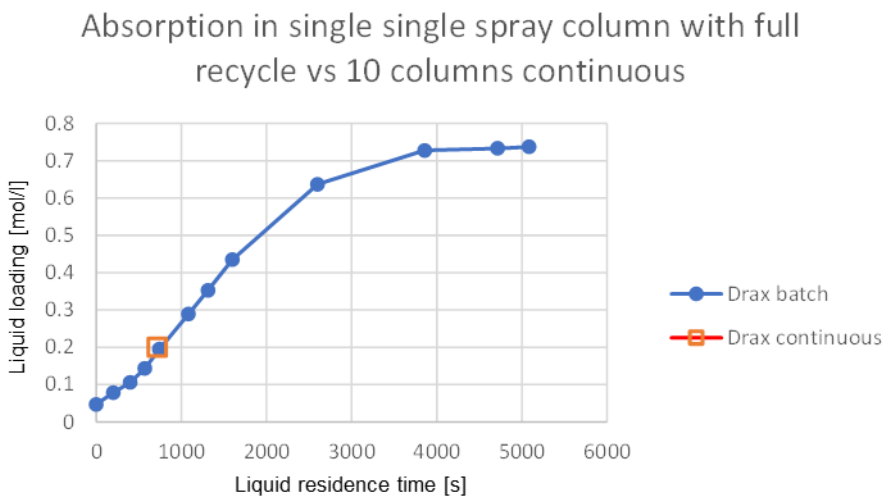

Figure 11. Continuous operation compared to batch operation with columns being fed consecutively.

Heat Integration

The C–Capture solvent has a relatively high organic content, which results in a lower heat transfer coefficient for heat exchange compared to aqueous-based solvents. However, good heat integration can still be achieved at an acceptable pressure drop through suitable design. Figure 12 shows long-term performance of the lean-rich heat exchanger and demonstrates that a minimum approach temperature below 3°C is feasible.

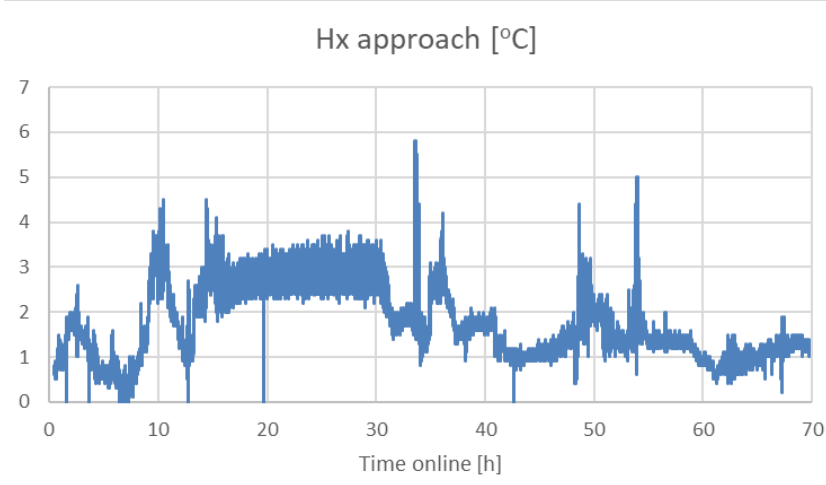

Figure 12. Long-term heat integration performance.

Stripping

The reboiler energy use in the Drax pilot could, in principle, be measured by measuring the power drawn by the electrical steam boiler during operation.

Energy use measurements were impacted by two factors:

- Relatively high heat loss due to scale
- Relatively large errors due to the lower than design throughput

These two factors make the energy use measurements more qualitative than quantitative. Results are shown in Figure 13.

The data shows energy usage going down with cyclic loading. The absolute energy usage was deemed inaccurate due to uncontrolled heat losses.

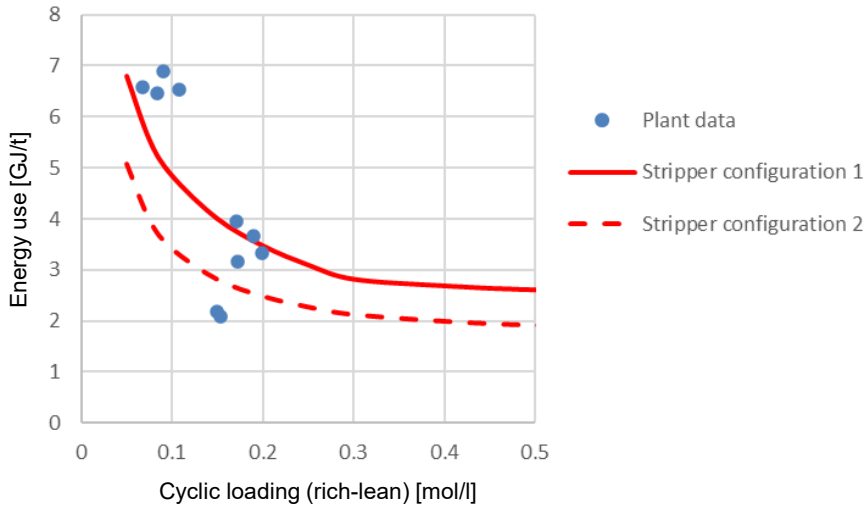

Figure 13. Energy use measurements from the Drax pilot plant.

Solvent Ageing

Establishing the rate of and products from degradation of C-Capture's solvent is essential for estimation of process operating cost and potential VOC emissions. To this end, C-Capture carried out a study of solvent degradation during operations at Drax. Initial analysis showed that the solvent components as supplied contain small amounts (~20 ppm) of volatile impurities, likely left over as byproducts of the production process, which may cause a brief spike in VOC emissions during plant commissioning.

Key impurities in the solvent were studied by gas chromatography. The concentration of the majority of impurities identified did not change significantly over the course of the campaign, indicating either that formation rates of these impurities are very slow, or that a steady state is achieved between impurity formation and vaporization losses. The major degradation product detected is present as a manufacturing impurity in the supplied carrier solvent (~0.1%), and its concentration in the capture

solvent was observed to increase slowly over time at a rate of <50 ppm/day. This compound is less volatile than the capture solvent and is not classified as hazardous according to information from ECHA. The capture solvent contains an antioxidant intended to limit solvent degradation; gas chromatography analysis showed this antioxidant to be steadily consumed at a rate of about 1% per day.

Taken together, the existing data indicates a low rate of degradation under the conditions of the process, with no measurable impact on the performance of the solvent and minimal emission of hazardous byproducts. C-Capture is currently building on this work with a further lab-based study to evaluate exact degradation rates under given conditions, especially with respect to the formation of volatile degradation products, which are difficult to directly assess under process conditions. Together with further pilot-scale trials, the lab data aims to provide a more precise assessment of the lifetime of the capture solvent under different operating conditions.

Emissions

Due to the small-scale nature of the trials, the level of VOC emissions from the Drax pilot plant was not continuously monitored; however, a sampling campaign was undertaken to determine the nature and identity of VOCs in the flue gas, both upstream and downstream of the absorber, and in the CO_2 output from the stripper. The samples were analyzed by SIFT-MS. The samples from downstream of the absorber and the stripper were dominated by the carrier solvent from C-Capture Ltd.'s, (CCL) Formulation A, as might be expected. A panel of some 33 other VOCs were identified in the samples, the majority of which were present in the flue gas prior to the absorber, suggesting that at least in part the source of these compounds is the flue gas itself, perhaps from incomplete lignin or cellulose combustion. Ammonia, nitrosamine, or nitramine emissions, which are of particular concern in relation to amine-based technologies, were all below detection limits.

Due to the manufacturing process for the solvent components, there is an appreciable concentration of small molecule, volatile organic species as impurities in the as-delivered capture solvent. Evidence suggests that these are "blown off" from the fresh solvent when it is first added to the plant, and the levels of emissions quickly settle down after a couple of days of operation.

Further testing by CCL has focused on the control of VOC emissions, and the testing has shown that a cheap and simple solution is possible. Work is ongoing to optimise this unit operation. Work is also continuing on the degradation of CCL's solvent (see above) and how this will impact on the emissions profile.

CONCLUSIONS AND DISCUSSIONS

This chapter gives an overview of the carbon capture pilot campaign performed at Drax power station, with biomass derived flue gas and a novel non-amine based solvent developed by C-Capture Ltd. The main objectives of the work at Drax were met by validating the main components of the plant–the absorber, lean rich heat exchanger, and CO_2 stripper. For the absorption step, both a packed absorber and a spray absorber were tested. Both showed lower than expected absorber performance, which resulted in refocusing around detailed mechanistic studies and developing the appropriate absorber design. The lean-rich heat exchanger approach met design, and approach temperatures were 3°C or lower.

The solvent was found to be compatible with the biomass-derived flue gas, and solvent ageing was found to be minimal at the tested exposure time and fly ash levels, in line with accelerated aging tests with impurity levels simulating gas and coal fired flue gas. The work was used in preparing for solvent aging studies in the SINTEF Tiller 1 t/d pilot plant with BECCS flue gas to set appropriate sampling frequencies and to aim for representative flue gas conditions.

A full spectrum of emission species was characterised in the flue gas from the burner, the scrubbed flue gas after the absorber, and in the CO_2 product. The results showed no nitrogen-based by-products originating from the carbon capture process.

Although it is recognised that many of these aspects require improvement in experimental approach to be definitive, this work was instrumental in preparing for the follow-up work performed with SINTEF at their Tiller plant and ongoing process optimization.

The key result from this study is that a better understanding of the absorption mechanism and precise kinetic rates are required to design an appropriate CO_2 absorber and to achieve performance targets. However, the trials have demonstrated the main benefits of C-Capture's non-amine solvent: low solvent degradation, and no emissions of nitrogen-based degradation products commonly seen with amines apart from what was already present in the flue gas.

ACKNOWLEDGEMENTS

We would like to acknowledge the contributions and support of our partners and shareholders, especially the Department of Business, Energy and Industrial Strategy (BEIS) and the CO_2 Capture Project Phase 4 (CCP4) for funding the BEIS Energy Entrepreneurs Fund grant project, Drax for supporting the pilot plant work financially, technically, and providing the infrastructure. We would also like to acknowledge the on-going support by our investors IPGroup PLC, the North East Technology Fund, BP Ventures, and Drax.

REFERENCES

1. Barnes D. C., Schoolderman C., Jakab G., Lawlor D., Wheatley J. E., Lynham D., Rayner C. M., **2019**, *Transformational Low Energy, Amine-Free Solvents for CO_2 Capture*, 5th Post Combustion Capture Conference, 17th-19th September, Kyoto, Japan.

Carbon Dioxide Capture for Storage in Deep Geological Formations, Volume 5
Karl F. Gerdes (Editor)
© 2022 BP. All rights reserved.

Chapter 13

ASSESSING MCFC FOR CO_2 CAPTURE FROM NATURAL GAS-FIRED INTERNAL COMBUSTION ENGINES

Maurizio Spinelli[1], Martelli Emanuele[2], Manuele Gatti[2], Daniele Di Bona[1], Stefano Consonni[1,2], Raja Jadhav[3], Betty Pun[3], Ibrahim Ali[4], Gustavo Moure[5]

[1] LEAP s.c.a.r.l., Via Nino Bixio 27 C, CAP: 29121, Piacenza
[2] Politecnico di Milano, Via Lambruschini 4, CAP: 20156, Milano
[3] Chevron Energy Technology Co, Richmond CA 94801 USA
[4] BP International, Chertsey Road, TW16 7BP, Sunbury-on-Thames, UK
[5] Petrobras Research Center, Avenida Horácio Macedo, 950, Rio de Janeiro, RJ, Brazil

ABSTRACT: Although many second- and third-generation capture technologies that show potential to lower the cost of CO_2 capture are under development, most CCS technologies are focused on large combustion sources, with CO_2 emission rates of several thousand tonnes per day. When these technologies are applied to smaller CO_2 sources (~ 100 tonnes/day or lower), the cost of CO_2 capture is generally higher since most of these technologies are characterized by a strong economy of scale. Such smaller scale CO_2 sources are prevalent in oil and gas and other process industries. For example, small gas engines and combustion turbines are widely used to provide shaft power in oil and gas production operations. This chapter documents a techno-economic assessment of molten carbonate fuel cells (MCFC) for capturing CO_2 from a cluster of reciprocating gas engines typically used for electric power generation in upstream oil and gas operations. The engine exhaust gas is sent to the cathode of the MCFC, where the CO_2 is transported across the electrolyte to the anode side in a concentrated form, which can be further purified relatively easily. In this process, the MCFC generates additional low-carbon electricity, which can be utilized or sold. Since MCFC systems are modular in nature, they can have an economic advantage when applied to CO_2 capture from smaller sources, as they will not be disadvantaged at small scale, unlike amine systems. This chapter describes the basis of the study, methodology and the different process options considered and presents results from the techno-economic assessment, including the CO_2 capture and avoided costs for small-scale gas engines. Key factors impacting the economics of the process are discussed.

KEYWORDS: molten carbonate fuel cell, carbon capture, internal combustion engine

INTRODUCTION

The efficient use of molten carbonate fuel cells (MCFC) for post-combustion Carbon Capture and Storage (CCS) applications has been studied in several experimental and modelling efforts [1,2]. The application of this CO_2 capture process to NGCC power generation is detailed in Chapters 7 and 8 of this volume. In addition to large-scale fossil fuel-fired systems, small-scale plants and distributed power generation applications are being assessed, since the fuel cell is a modular technology characterized by high efficiency and relatively constant specific investment costs, even at small scale. This is a key advantage compared to alternative post-combustion CO_2 capture systems, like amine scrubbing, which is disadvantaged at small scale.

A recent study assessed the use of MCFC for CO_2 capture in a conventional combined heat and power (CHP) plant [12], where two different integration schemes for Internal Combustion Engine (ICE) with

MCFC are compared. The first configuration utilizes a cryogenic purification process to recover the unconverted fuel from the CO_2-rich anode stream for recycle to maximize the overall energy efficiency, similar to the scheme proposed in [1]. In the second configuration, the CO_2 purity is raised to the level required for pipeline transport using a downstream oxyfired combustor to burn unconverted fuel to provide additional heat for the cogeneration system and avoid the need for a CO_2 purification unit.

The combined use of MCFC and solid oxide fuel cells (SOFC) in small cogeneration systems has been investigated, and excellent electric efficiency and satisfactory carbon capture rates were achieved, while also meeting CO_2 purity requirements without the need of auxiliary purification [13]. The MCFC offers fuel flexibility due to its internal fuel reforming capability, which is a noteworthy advantage of high temperature fuel cells, especially for de-centralized power production. As an example, several attractive CCS concepts are based on synergies between MCFC and biogas-fed power plant systems, based on experimental data [14] and simulations [11]. Rinaldi *et al*. [15], studied the integration of MCFC with a biogas plant to capture the biogenic CO_2 released by a biogas-fed ICE while co-producing electricity, hydrogen and heat. The simulations of this tri-generation system were validated against operating data of an existing MCFC unit. The cases studied cover several plant configurations, including a multi-stack configuration with several MCFCs in series to increase the capture rate, as proposed by Spinelli *et al.* [16].

This study is focused on the use of MCFCs in the oil and gas industry for the decarbonisation of MW-scale power units utilizing ICEs, and included the following major activities:

- Design and simulation of two flowsheets based on CO_2 capture via MCFCs fed by the exhaust gas of a reference internal combustion engine (ICE).
- Generation of material and energy balances of the proposed configurations.
- Comparison of performance of the flowsheets to identify the most cost-effective configuration.
- Evaluation of the cost sensitivity of the MCFC integration.

REFERENCE INTERNAL COMBUSTION ENGINE (ICE) AND PROPOSED MCFC INTEGRATION

Reference ICE

The reference plant without CCS is composed of four identical natural gas-fueled internal combustion engines (ICE) with electric power generators, each capable of producing 1.16 MW_{el} with a net electric efficiency of 40%$_{LHV}$. The Internal Combustion Engine technical performance and engine exhaust gas conditions are reported in Table 1.

The exhaust gas concentrations of CO_2 and O_2 strongly impact the MCFC+ICE process performance because they strongly influence the ideal Nernst voltage and the achievable CO_2 capture rate. Higher CO_2 and O_2 partial pressures increase the theoretical MCFC efficiency. Also, higher exhaust gas CO_2 partial pressure increases the CO_2 capture rate because of the need to maintain a minimum CO_2 concentration at the cathode outlet.

Table 1. Energy balance and exhaust stream properties (single engine).

Internal Combustion Engine Performance	
Fuel Input, kW_{LHV}	2900
Net electric power, kW_{el}	1160
Net electric efficiency, %	40%
Exhaust Gas	
Mass flow rate [Nm^3/h]	4325
Temperature [°C]	484
Pressure [bar]	1.013
xCO_2 [%vol]	7
xO_2 [%vol]	6
xH_2O [%vol]	13
xN_2 [%vol]	74

Proposed MCFC+ICE Process Integration

Two different process flow schemes are compared in this study. In scheme A (Figure 1), the CO_2-rich exhaust gas from the ICE is transferred to the MCFC by a high temperature blower (operating close to 500°C) and preheated to the MCFC working temperature (580°C) in a heat exchanger (HEX1), before entering the fuel cell cathode side. The hot side of this heat exchanger is fed with a fraction of the MCFC cathode outlet stream, from which most of the CO_2 has been removed by the MCFC by the cathode reaction (1) and migration of CO_3^{2-} ions across the cell electrolyte from the cathode to the anode.

$$O_2 + 2CO_2 + 4e^- \rightarrow 2CO_3^{2-} \quad (1)$$

The fraction of CO_2 in the cathode feed consumed in reaction (1) is defined as the CO_2 utilization factor (U_{CO2}) and is limited by the minimum CO_2 concentration required at the cathode outlet. To avoid significant voltage losses due to mass-transfer resistance, the outlet concentration of CO_2, x_{CO2}, is typically limited to a minimum of 1 mol %, which results in a U_{CO2} of 87% in this case. The cathode side hot exit gas not fed to HEX1 is used to superheat low pressure steam required by the MCFC fuel reforming. The conversion is done in two steps – first, in a pre-reforming step (indirect internal reforming, IIR), followed by further reforming catalysed by the anode (direct internal reforming, DIR) in the MCFC [1]. The low-pressure steam is produced using the combined heat-depleted cathode exit streams.

The anode feed is a mixture of preheated natural gas and steam (Steam-to-Carbon = 3) which is reformed and the H_2 produced by the reforming reaction is oxidized by the electro-chemical reaction (2).

$$2H_2 + 2CO_3^{2-} \rightarrow 2CO_2 + 2H_2O + 4e^- \quad (2)$$

The cooled cathode exit (lean in CO_2) is vented. The anode stream (enriched with the CO_2 permeated through the electrolyte in the MCFC) is first cooled by raising additional medium pressure process steam and then by preheating natural gas. The cooled anode stream is sent to the cryogenic Gas Processing Unit (GPU), where CO_2 is further purified and compressed. The heat recovery section on the anode side has been designed to prevent metal dusting [17].

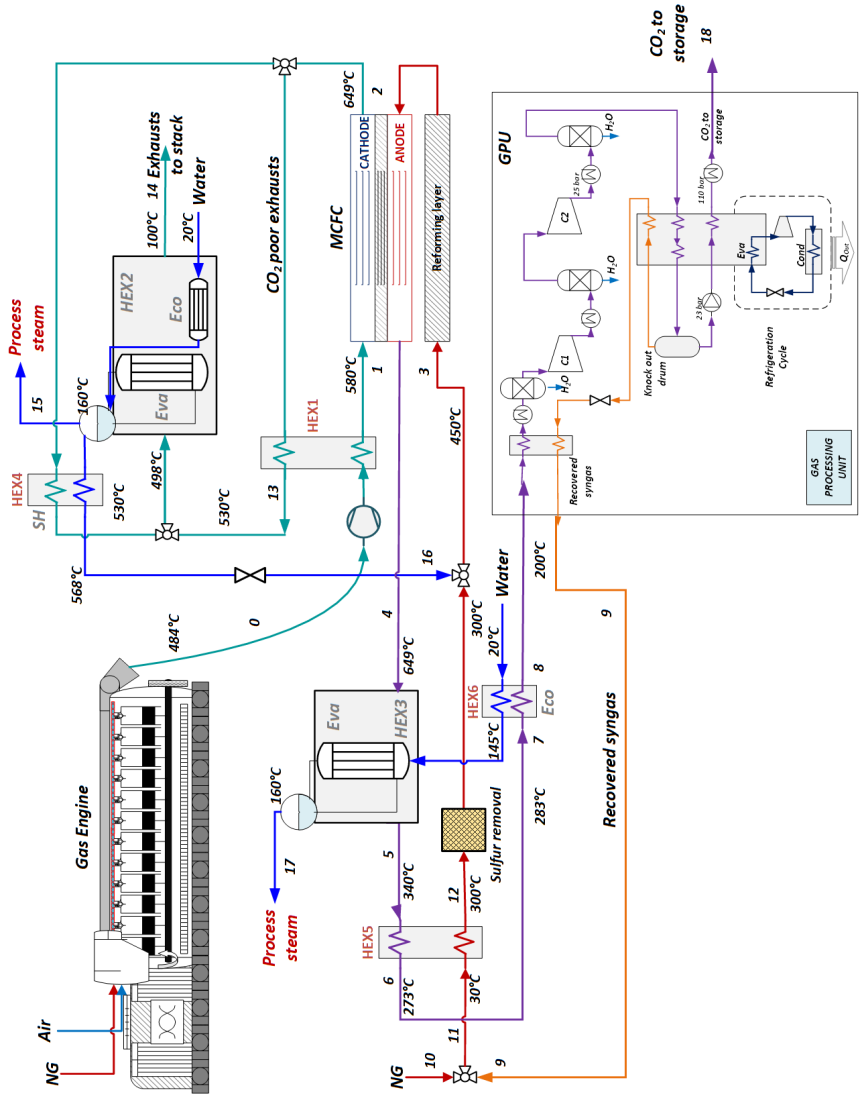

Figure 1. Layout of the ICE+MCFC integrated option: scheme A with unconverted fuel separation and recycle.

Since the fuel conversion at the MCFC anode is limited to achieve reasonable energy efficiency (the fuel utilization factor, U_f, is 75%), the unconverted fuel contained in the anode off-gas is separated in the cryogenic GPU (described in the next section) and recycled to the MCFC anode inlet. In this way nearly complete fuel utilization is achieved.

Scheme B (Figure 2) is similar to Scheme A, with the exception of the anode exhaust processing section. In this configuration, the anode exhaust flows to an oxy-fuel catalytic burner which fully oxidizes the unconverted fuel, theoretically producing a stream containing only CO_2 and H_2O plus small amounts of non-condensable components introduced with the fuel and oxidant. In principle, the CO_2 is purified by water removal, and a GPU is not required–although this will depend on the level of residual O_2. After a preliminary performance assessment, scheme A was selected as the most promising. Scheme B requires about 3 Nm^3/s of oxygen (3% Ar, 2% N_2, 95% O_2) to oxidize the unconverted fuel, which not a large enough volume to consider the installation of an air separation unit. The feasibility of shipping such a volume of oxygen would be site-specific and, in any event, would be costly and entail HES issues. Furthermore, an expensive bottoming cycle (e.g., an Organic

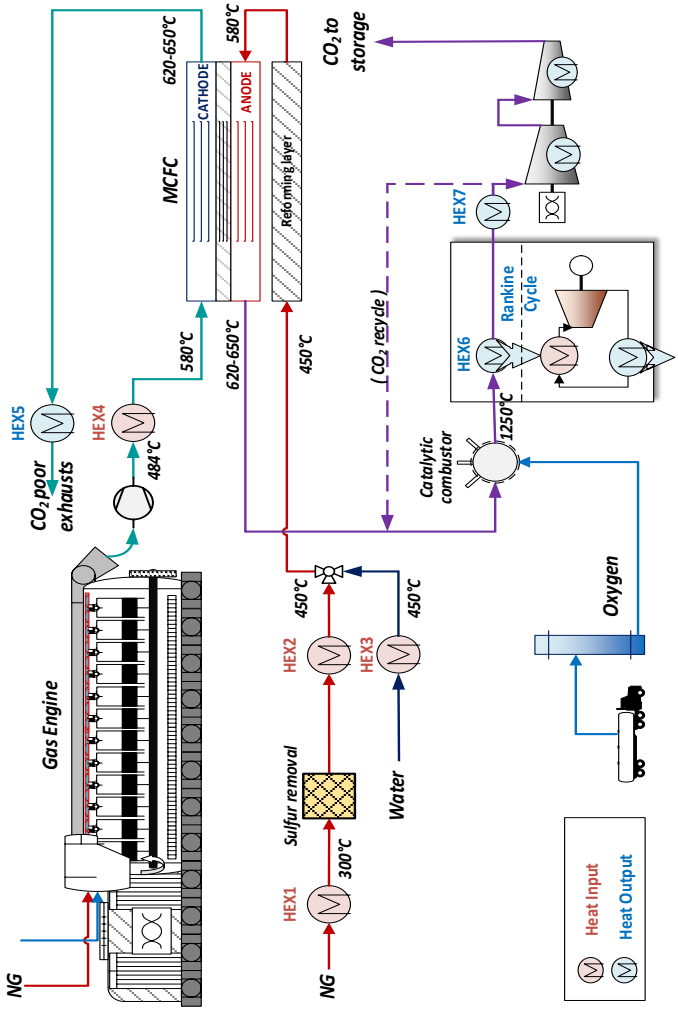

Figure 2. Layout of the ICE+MCFC integrated option: scheme B with catalytic oxidation of the unconverted fuel with oxygen.

Rankine Cycle) would be required to recover the large amount of heat generated by the oxy-combustion process (~2MW_{th}).

Option A therefore appears to be the most suitable for this application. Its main disadvantage is the need for a cryogenic CO_2 separation unit which, due to the small size, is expected to have a lower efficiency and high specific investment cost than larger such units.

Gas Processing Unit (For Integration Scheme A Only)

The anode stream produced by the MCFC is not sequestration-ready and contains unconverted fuel. A dedicated Gas Processing Unit (GPU) compresses and purifies the CO_2 to meet quality standards typically required for geological storage (i.e., CO_2 content higher than 97%mol and total amount of non-condensable gases not higher than 3%mol). Five configurations for the GPU were investigated. The anode stream entering the GPU contains nearly 43 mol % CO_2 diluted with 47 mol % H_2O, 7 mol % H_2, 3 mol % CO, and less than 1 mol % N_2 and Ar. The purpose of the GPU is to recover as much fuel value (hydrogen and carbon monoxide) as possible, while concentrating the CO_2 to be sequestered into a separate dense-phase, purified stream. For large-scale stationary applications of MCFC+CCS, a previous study of this system [4] concluded that the GPU should be a cryogenic separation system in which the anode exhaust is separated into a liquid CO_2-rich stream and a vapour syngas-rich stream by integration of refrigeration and heat recovery along with compression/expansion. According to Chiesa *et al.* [4], the best cryogenic separation and purification scheme, from an energy perspective, is a two-stage isobaric flash, which uses a complex heat exchanger network with three multi-pass cold boxes and auto-refrigeration from Joule-Thomson expansion of liquid CO_2 to minimize the energy penalty of the GPU. Since the size of the GPU for the ICE+MCFC application discussed in this chapter is much smaller than the cases discussed by Chiesa *et al*. (few hundred kW of compression power vs dozens of MW), the main focus of this study was process simplicity rather than performance optimization. The lowest cost configuration for the GPU of the ICE+MCFC could be determined by a full techno-economic optimization. However, the main focus of this work is to assess the technical and cost potential of the overall proposed schemes, rather than fully optimize them. The GPU layout was based on the need to limit complexity and, therefore, the number of equipment items required. We expect that this approach would lead to better operability and lower CAPEX. The GPU here uses a single-stage flash and refrigeration system shown in Figure 3.

The anode exhaust stream (#8 in Figure 1, violet stream (feed inlet) in Figure 3), after cooling in the heat recovery section of the power island, is further cooled to 28°C to condense most of the water. Then, the stream is compressed to 25 bar in two stages with intercooling and knock-out drums to remove more water. Before entering the refrigeration section, the compressed stream is fully dehydrated with a mol sieve dryer (not shown in Figure 3). The dehydrated stream is cooled to -50°C at constant pressure with external refrigeration. At -50°C and 23 bar the mixture enters the 2-phase region and a significant fraction of the CO_2 condenses. The two-phase mixture is separated into gas and liquid streams using a conventional knock out drum. The CO_2-rich liquid stream (violet in Figure 3) is pumped to the sequestration pressure of 110 bar. The vapour stream contains valuable fuel in the form of H_2 (about 43%mol) and CO (about 19 mol %), as well as CO_2 (34 mol %). The liquid and vapour compositions vary with the temperature and pressure conditions chosen for the separation. To increase the energy efficiency of overall system, the vapour stream is recycled to the fuel cell anode. Refrigeration duty is recovered from both the vapor and liquid streams in a multi-stream heat exchanger by precooling the dry compressed anode exhaust. This simple scheme allows recovery of part of the cooling duty without use of a complex HEX network or expansion of the liquid phase.

The refrigeration system uses a reverse Rankine cycle with propane as the working fluid. The refrigeration loop consists of an evaporator operating at -53°C (to cool the dry anode exhaust stream

to -50°C), a refrigerant compressor, a cooler to condense the propane at 21°C (about 9 bar, depending on purity), and a Joule-Thomson valve to produce the refrigeration effect. This refrigeration cycle has a Coefficient of Performance (COP) of 1.5.

The GPU system results in an energy penalty of 829 kJ_{el}/kg of CO_2. CO_2 compression is responsible for around 68% of this energy, and about 26% is attributable to the refrigeration cycle. The remaining auxiliaries account for the remainder. This GPU design can recover as liquid 88% of the CO_2 entering and achieves 98.8%mol CO_2 purity, with a H_2 and CO content of 3500 and 6900 ppmv, respectively.

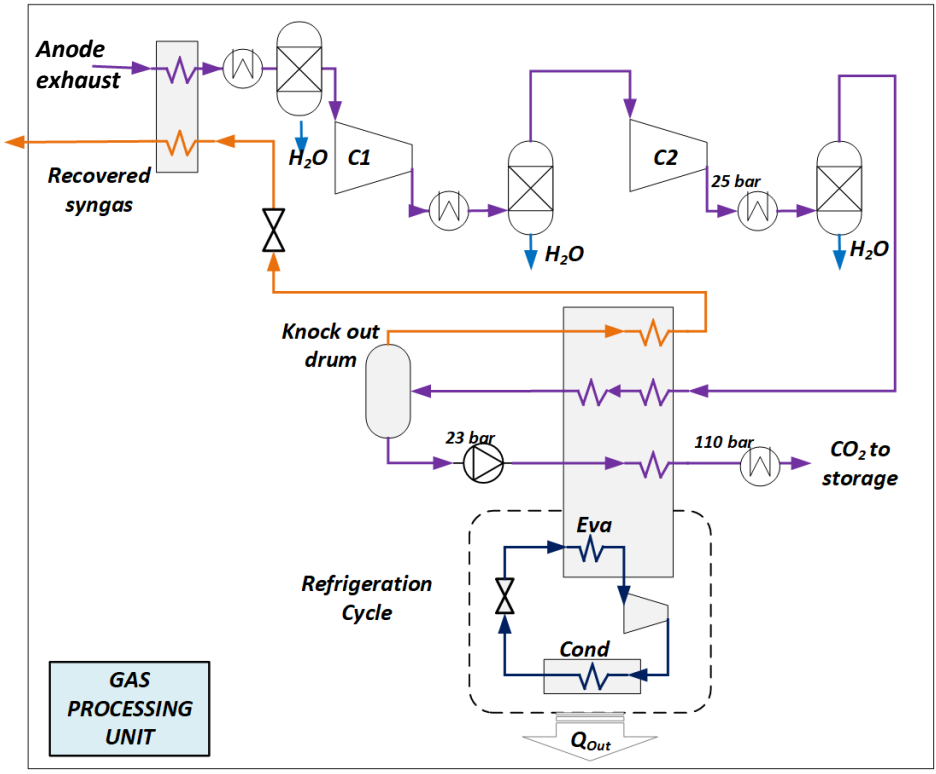

Figure 3. Layout of the cryogenic gas processing unit.

METHODOLOGY, MCFC MODEL AND TECHNO-ECONOMIC ASSUMPTIONS

The proposed plant flowsheets were simulated using an in-house simulation tool based on a lumped parameter approach (GS, [18]). Besides chemical reactors, turbomachines and a relevant set of specific modules, the GS library includes an MCFC model, which has been calibrated using experimental data for advanced MCFCs produced by Fuel Cell Energy Inc. (FCE, USA). The MCFC model in GS predicts the voltage as a function of the relevant parameters involved in the electrochemical process, including current density, and reactant partial pressure and utilization. Input to the model includes reactant properties at the MCFC inlet (temperature, pressure, composition and mass flow rate) and the utilization factor of CO_2 and O_2 (U_{CO2}, or U_{O2}) inside the fuel cell. U_{CO2} is equivalent to the percentage carbon capture and is defined as the ratio of the molar CO_2 flow rate

transferred across the cell to the molar CO_2 flow rate at the cathode inlet. The cell voltage may be either assigned directly as a parametric value or calculated from the reversible Nernst potential and corrected for cell losses, as suggested by Spinelli *et al.* [16], and described in more detail in Chapter 8 of the present volume.

Following the same methodology adopted in previous studies, the performance of the gas processing unit is simulated using ASPEN Plus™ [19]. The main assumptions related to the plant sections are reported in Table 2.

Table 2. Main assumption for the simulation of the MCFC+ICE plant.

Ambient conditions	15°C/1.013 bar/60% humidity
Natural gas conditions	10°C/70 bar
Internal Combustion Engine	**4 Engines**
Exhaust temperature, °C	484°C
Net electric efficiency, %LHV	40%
Molten Carbonate Fuel Cell	**1 single module**
Cathode/anode inlet temperature, °C	580
Pre-reformer inlet temperature, °C	450
Fuel utilization factor (single passage)	75%
Steam to carbon ratio, mol/mol	3
Min÷Max current density (sensitivity performed), A/m^2	1100÷1500
X CO_2 at cathode outlet	1%mol
Pressure losses on anode/cathode, kPa	3/2
Heat losses (% input thermal power)	1%
DC/AC converter efficiency	94%

The total plant cost of the proposed layout is based on the total equipment cost, as described in Chapter 7 of this volume. The cost of each equipment item included in the proposed layout has been estimated using power-law cost functions from relevant cost databases and output from simulation packages [21]. The cost of the MCFC stack, which represent the most expensive component of the carbon capture section, is 465 $\$/m^2$, as estimated in previous work based on future mass-production of the stack components (i.e., hundreds of MW per year) [1]. The additional equipment cost for the Balance Of Plant of the MCFC system is estimated as 25% of the stack cost [1]. The other significant cost center is the refrigeration system, which is estimated to be 3750 \$/kW using the cost function reported in [22]. The Total Equipment Cost (TEC) is the sum of all the equipment costs for the system. The Total Plant Cost (TPC) is estimated by multiplying the TEC by a series of incremental factors to account for the installation, contingency and owner's costs. Typically, the resulting TPC is about three times the TEC. Finally, as in previous CCP studies [20], the annualized investment cost, expressed here as a first year capital charge factor (% of TPC), is based on the project discount rate and inflation. The addition of fuel and O&M costs to first year capital cost gives the cost of electricity (COE).

The cost of CO_2 avoided (CCA) is defined as the ratio between the difference in the cost of the electricity for the MCFC+ICE system and the ICE system alone, and the avoided specific CO_2 emission. CCA is computed using Eq.3.

$$CCA = \frac{(COE_{capture} - COE_{reference})}{(e_{reference} - e_{capture})} \left[\frac{\$}{t_{CO2\ avoided}}\right] \quad (3)$$

Where $COE_{reference}$ is the cost of electricity for the plant without capture (ICE alone) and $COE_{capture}$ is the cost of electricity with CO_2 capture (MCFC+ICE). The CO_2 emission intensity, e, is the amount of CO_2 emitted per unit of power production expressed in $[kg_{CO2}/MWh_{el}]$.

RESULTS

The techno-economic analysis of the ICE+MCFC plant presented here provides a preliminary estimate of the thermodynamic and carbon capture performance of the proposed configuration and a preliminary estimate of the economics of this novel system. The performance and economic results were estimated for a range of MCFC current density (between 1100-1500 A/m^2), which is the most important MCFC parameter affecting the energy and economic performance.

Energy and CO_2 Capture Analysis

The estimated performance of the MCFC-based CCS system is reported in Table 3 as a function of the fuel cell current density assuming constant CO_2 utilization across the range of current density. Low current density (I_c=1100 A/m^2) allows the fuel cell to operate with a higher voltage and a lower temperature increase, resulting in higher energy efficiency and improved materials durability. The temperature increase experienced by the anode and cathode streams is inversely proportional to the MCFC efficiency and should be minimized to reduce material stresses and corrosion and to prevent a premature loss of electrolyte [23]. On the other hand, higher current densities decrease the required fuel cell area with related savings of capital costs.

The MCFC-based CCS system can capture almost 90% of the ICE CO_2 emissions and produces gross electric power output of about 1700-1800 kW_{el}, which is roughly 40% of the reference ICE power output. Almost one-third (600 kW_{el}) of this additional electric power is consumed by the GPU, due mainly to the CO_2 compressors and the external refrigeration. As a result, the net electric export is increased by 20-23% compared to the stand-alone ICE, depending on the current density value. The net electric efficiency decrease associated with the capture process goes from 0.9 percentage points in the case with Ic=1500A/m^2 down to 0% in the case with IC=1100 A/m^2 (ICE electric efficiency is 40%). Consequently, if the MCFC+ICE system is compared to the reference ICE without CCS, the low current density case does not require additional primary energy for CO_2 capture (i.e., SPECCA=0).

Table 3. Summary of energy and carbon capture performance of the proposed MCFC+ICE system.

Molten Carbonate Fuel Cell	I_C=1500 A/m²	I_C=1400 A/m²	I_C=1300 A/m²	I_C=1200 A/m²	I_C=1100 A/m²
Voltage , V	0.684	0.697	0.711	0.725	0.739
ΔT across the fuel cell, °C	84.8	80.8	76.8	72.7	68.7
Energy balance					
MCFC fuel power input, kW_{LHV}	2649.0	2648.7	2648.5	2648.3	2648.0
MCFC gross electric power, kW_{el}	1715.0	1748.8	1783.1	1817.5	1852.5
Inverter consumption, kW_{el}	103.2	104.8	106.8	108.8	111.2
Fan consumption, kW_{el}	85.8	85.8	85.8	85.8	85.8
MCFC net electric power, kW_{el}	1526.0	1558.1	1590.4	1622.9	1655.5
MCFC net electric efficiency, %	57.6%	58.8%	60.1%	61.3%	62.5%
Process steam (5 bar, 160°C), kg/s	0.995	0.983	0.970	0.957	0.944
Process steam thermal power, kW_{th}	2670.5	2636.5	2602.3	2568.0	2533.6
GPU consumption, kW_{el}	595.7	595.7	595.7	595.7	595.7
MCFC+ICE Total Net electric power, kW_{el}	5570.2	5602.4	5634.7	5667.2	5699.8
MCFC+ICE Total electric efficiency, %	39.1%	39.3%	39.5%	39.8%	40.0%
CO_2 capture rate	**89.4%**	**89.4%**	**89.4%**	**89.4%**	**89.4%**
CO_2 emissions, kg/s	0.085	0.085	0.085	0.085	0.085
CO_2 captured, kg/s	0.718	0.718	0.718	0.718	0.718
Specific emission (ICE), g_{CO2}/kWh_{el}	510.1	510.1	510.1	510.1	510.1
Specific emission (ICE+MCFC), g_{CO2}/kWh_{el}	55.2	54.8	54.5	54.2	53.9
CO_2 avoided, %	89.2%	89.2%	89.3%	89.4%	89.4%
SPECCA ($MJ/kg_{CO2,\ avoided}$)	0.46	0.34	0.23	0.11	0.00

Economics

The cost share for the major functional groupings in the proposed MCFC+ICE layout is shown in Figure 5 for the high and low current density cases.

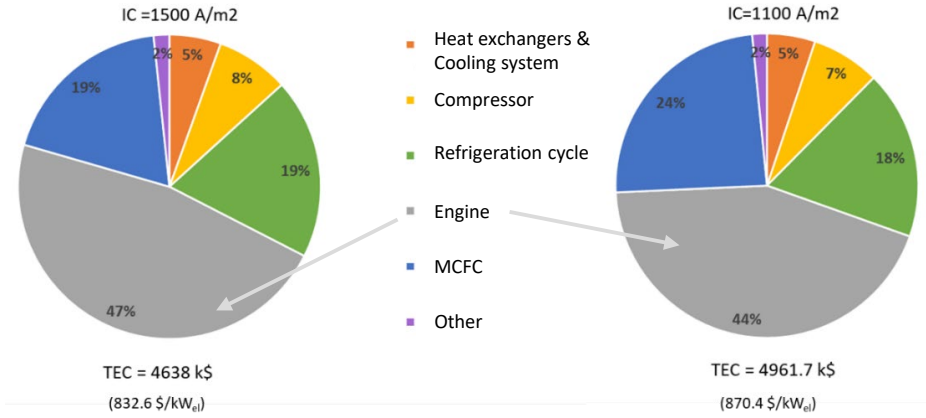

Figure 5. Equipment costs of the proposed MCFC+ICE layout.

In both configurations, almost half of the total equipment cost is associated with the ICE. The gas processing unit (mainly composed of the compressor and refrigeration unit) is estimated to cost more than the MCFC module. The MCFC cost is significantly influenced by the choice of the current density. If I_C is reduced from 1500 to 1100 A/m^2, the fuel cell equipment cost increases by 20%, and the total investment cost increases by 5%. However, higher current density, and the resulting larger temperature increase across the MCFC, could lead to an increase in the maintenance costs, due to more frequent replacement of MCFC stacks. The impact of higher temperature can be characterized only by long-term tests on MCFC systems. Table 4 shows the total plant cost (TPC) and the final economic metrics. The COE and CCA are calculated from the total equipment, fuel and O&M costs as described in Chapter 7. The estimated cost of electricity for the MCFC-based CCS system is significantly higher than the reference COE of the ICE without CCS (+65-75%), and the resulting CO2 avoided cost ranges between 99 and 112 $/tCO2).

Table 4. Summary economic figures of the proposed MCFC+ICE system.

	Reference case (ICE)	1500 A/m^2	1400 A/m^2	1300 A/m^2	1200 A/m^2	1100 A/m^2
Total plant cost (TPC), $/kW$_{el}$	1561.2	3478.7	3515.3	3558.8	3612.7	3679.8
Fuel cost, k$/Y	1480.8	1818.8	1818.9	1818.9	1818.9	1819.4
Fixed O&M, k$/Y	144.88	1036.90	1082.07	1133.34	1193.47	1264.93
Variable O&M, k$/Y	67.64	138.26	139.06	139.86	140.67	141.48
Capital Carrying Charge, k$/Y	682.9	1826.8	1856.6	1890.4	1930.1	1977.3
COE, $/MWh	64.99	109.83	110.92	112.22	113.83	115.85
CCA, $/t$_{CO2}$	-	98.6	100.9	103.7	107.1	111.5

CONCLUSIONS

This study assessed the potential for application of Molten Carbonate Fuel Cells as a CO_2 capture system downstream of stationary Natural Gas-fired Internal Combustion Engines of MW-scale. Two possible integration solutions are described: A) including a GPU for CO_2 purification and unconverted fuel recycle to the MCFC, and B) using purchased O_2 with a catalytic burner to fully oxidize the unconverted fuel before final CO_2 compression. After a preliminary assessment, Scheme B was dropped because of the likely high cost of O_2 import and generation of a considerable of waste heat. Performance metrics for Scheme A estimated by simulation for five different MCFC current densities. The results highlight that the most efficient solution is the one with the lowest current density (1100 A/m^2) which is also preferable to maximize fuel cell reliability and durability. Remarkably, this case achieves the same net electric efficiency as the stand-alone engine (40%$_{LHV}$), but with 90% capture of the CO_2 produced by ICE+MCFC. The higher MCFC efficiency compared to the ICE compensates for the energy burden of the GPU auxiliary energy consumption. From a cost perspective, the best case has the highest MCFC current density (1500 A/m^2), which requires a smaller MCFC and therefore achieves lower CAPEX. The COE for this case is 110 $/MWh (+ 69% compared to the reference case without CCS), and the cost of CO_2 avoided of ~100 $/t$_{CO2}$. Although the integration of MCFC with ICEs for CCS is more costly than for large scale NGCC-CCS plants, the MCFC is fully retrofittable and modular, and process steam/heat is produced which can be utilized on site. The revenues associated with the cogenerated heat are not accounted for in this assessment.

REFERENCES

1. M. Spinelli *et al*., "Molten Carbonate Fuel Cells for Retrofitting Postcombustion CO_2 Capture in Coal and Natural Gas Power Plants," *J. Electrochem. Energy Convers. Storage*, **15**(30), Feb. 2018.
2. S. Campanari, P. Chiesa, and G. Manzolini, "CO_2 capture from combined cycles integrated with Molten Carbonate Fuel Cells," *Int. J. Greenh. Gas Control*, **4**(3), 2010.
3. R. Carapellucci, R. Saia, and L. Giordano, "Study of Gas-steam Combined Cycle Power Plants Integrated with MCFC for Carbon Dioxide Capture," *Energy Procedia*, **45**, 2014.

4. P. Chiesa, S. Campanari, and G. Manzolini, "CO_2 cryogenic separation from combined cycles integrated with molten carbonate fuel cells," *Int. J. Hydrogen Energy*, **36**(16), 2011.
5. S. Campanari, G. Manzolini, and P. Chiesa, "Using MCFC for high efficiency CO_2 capture from natural gas combined cycles: Comparison of internal and external reforming," *Appl. Energy*, **112**, 2013.
6. S. Campanari, P. Chiesa, G. Manzolini, and S. Bedogni, "Economic analysis of CO_2 capture from natural gas combined cycles using Molten Carbonate Fuel Cells," *Appl. Energy*, **130**, 2014.
7. H. Ghezel-Ayagh, S. Jolly, D. Patel, and W. Steen, "Electrochemical Membrane Technology for Carbon Dioxide Capture from Flue Gas," *Energy Procedia*, **108**, Mar. 2017.
8. K. Sugiura, K. Takei, K. Tanimoto, and Y. Miyazaki, "The carbon dioxide concentrator by using MCFC," *J. Power Sources*, **118**(1), 2003.
9. A. Amorelli *et al*., "An experimental investigation into the use of molten carbonate fuel cells to capture CO_2 from gas turbine exhaust gases," *Energy*, **29**(9), 2004.
10. V. Spallina, M. C. Romano, S. Campanari, and G. Lozza, "Application of MCFC in Coal Gasification Plants for High Efficiency CO_2 Capture , *J. Eng. Gas Turbines Power*, **134**(1), Jan. 2011.
11. R. Chacartegui, B. Monje, D. Sánchez, J. A. Becerra, and S. Campanari, "Molten carbonate fuel cell: Towards negative emissions in wastewater treatment CHP plants," *Int. J. Greenh. Gas Control*, **19**, 2013.
12. L. Mastropasqua, M. Spinelli, A. Paganoni, and S. Campanari, "Preliminary design of a MW-class demo system for CO_2 capture with MCFC in a university campus cogeneration plant," in *Energy Procedia*, **126** 2017.
13. L. Mastropasqua, S. Campanari, and J. Brouwer, "Electrochemical Carbon Separation in a SOFC–MCFC Polygeneration Plant With Near-Zero Emissions," *J. Eng. Gas Turbines Power*, **140**(1), Sep. 2017.
14. L. Barelli, G. Bidini, S. Campanari, G. Discepoli, and M. Spinelli, "Performance assessment of natural gas and biogas fueled molten carbonate fuel cells in carbon capture configuration," *J. Power Sources*, **320**, Jul. 2016.
15. G. Rinaldi, D. McLarty, J. Brouwer, A. Lanzini, and M. Santarelli, "Study of CO_2 recovery in a carbonate fuel cell tri-generation plant," *J. Power Sources*, **284**, Jun. 2015.
16. M. Spinelli, M. C. Romano, S. Consonni, S. Campanari, M. Marchi, and G. Cinti, "Application of Molten Carbonate Fuel Cells in Cement Plants for CO_2 Capture and Clean Power Generation," *Energy Procedia*, **63**, 2014.
17. H. J. Grabke, "Metal Dusting of Low- and High-Alloy Steels," *Corrosion*, **51**(9), 1995.
18. "GS process simulation software," www.gecos.polimi.it/software/gs.php. .
19. AspenTech, "Aspen Plus v8.8." Aspentech, 2016.
20. Butler, D., "Financial Study Methodology," in *Carbon Dioxide Capture for Storage in Deep Geologic Formations, - Results from the CO_2 Capture Project Volume 4: CCS Technology Development and Demonstration Results (2009-2014)*. Gerdes, K. (ed). CPL Press:, 2015.
21. Thermoflow, "Thermoflex v. 24." 2014.
22. G. D. Ulrich and P. T. Vasudevan, *Chemical Engineering Process Design and Economics, A Practical Guide.* Process Pub., 2004.
23. U.S. Department of Energy, *Fuel Cell Handbook*, 2004.

Carbon Dioxide Capture for Storage in Deep Geological Formations, Volume 5
Karl F Gerdes (Editor)
© 2022 BP. All rights reserved.

Chapter 14

POTENTIAL IMPROVEMENT IN CO_2 CAPTURE PRODUCTIVITY WITH 3D PRINTED SORBENTS FOR CO_2 CAPTURE FROM REFINERY OFF GASES

Shreenath Krishnamurthy[1], Richard Blom[1], Anna Lind[1], Carlos A. Grande[1], Ibrahim Ali[2]
[1]SINTEF Industry, Forskningsveien 1, Oslo 0373, Norway
[2]BP International Ltd, ICBT Chertsey Road, Sunbury-on-Thames, UK

ABSTRACT: Structured sorbents with better adsorption kinetics and lower pressure drop than packed beds of conventional adsorbents are gaining increasing attention due to the potential advantages of smaller footprint and lower energy consumption in a CO_2 capture process. The aim of this computational study is to examine the potential improvement in productivity of a CO_2 capture process using 3D printed, structured sorbents compared to a conventional packed bed system. The sorbents chosen in this work are silica pellets and 3D printed structures, both grafted with an amino silane. A representative flue gas/FCC regenerator off-gas containing 15 vol % CO_2, 5% H_2O and 80% N_2 and an SMR-off gas containing 21% CO_2, 5% H_2O, and 74% N_2 were considered as feed streams. Detailed genetic algorithm-based optimization of a 6-step vacuum swing adsorption cycle for both adsorbents was carried out to identify the minimum specific energy and maximum productivity for concentrating the CO_2 to 95 vol% purity on a dry basis and capturing 90% of the CO_2. The simulations indicate that use of the 3D printed adsorbent may achieve a 3-fold increase in productivity with about 25-38% reduction in energy consumption relative to the conventional packed bed. Scaling the process to a real system revealed a 1.8 times reduction in the capture footprint for a VSA process using 3D printed sorbents instead of a traditional packed bed.

KEYWORDS: supported amine sorbents, vacuum swing adsorption, structured sorbent, process optimization, genetic algorithm

INTRODUCTION

Structured adsorbents in the form of monoliths, foams, and laminates offer advantages of better mass transfer and lower pressure drop over pelletized adsorbents. This would enable the adsorption process to operate at higher flowrates per unit bed volume and faster cycle times, and thereby reduce the footprint of the capture process [1,2].

The aim of the 3D-CAPS project is to demonstrate an improvement in productivity in a cyclic adsorption process utilizing structured sorbents over a conventional packed bed for carbon capture. In this context, the present work is focused on the simulation and optimization of a vacuum-swing adsorption (VSA) process to capture and concentrate CO_2 from a representative post combustion flue gas. The process uses immobilized amine sorbents, where amine groups are grafted onto a substrate, such as silica. These adsorbents are well known for their tolerance to moisture and high CO_2 capacities at high temperatures.

In the 3D-CAPS project, amino silane was grafted onto commercially available PERLKAT (silica gel) beads. The sorbent was first experimentally characterized to obtain information on adsorption

equilibrium and kinetics. This data was then used to simulate and optimize a 6-step vacuum swing adsorption (VSA) process to obtain specific energy versus productivity Pareto fronts for this adsorbent [3]. The simulations indicate that it is possible to achieve 95% CO_2 purity and 90% capture from a flue gas containing 15% CO_2.

In this chapter, the simulated performance of a 3D printed sorbent for post-combustion carbon capture is documented. The objective of this work is to identify the potential improvement in productivity over traditional packed bed systems for the following applications:

1. FCC Catalyst Regenerator flue gas containing 15%CO_2, 5% H_2O, and 85% N_2 at 363 K and 1 atmosphere.
2. SMR Furnace flue gas containing 21%CO_2, 5% H_2O, and 74% N_2 at 363 K and 1 atmosphere.

In the first step, detailed optimization of the 6-step VSA cycle is performed, and the minimum specific energy and maximum productivity values are compared for the packed bed and the 3D printed sorbent case. Subsequently, the process is scaled up and the footprint of the CO_2 capture process with the two types of adsorbents is evaluated.

The 3D printed sorbent used in this study has been printed by a technique called digital light processing. The adsorbent was lab tested to obtain information on adsorption equilibrium, kinetics, and pressure drop. These data were input for the process simulator used for the rigorous process optimization. Some of the properties of the adsorbents are provided in Table 1. More details about the 3D printed sorbent are available in published literature [4].

Table 1. Physical properties of sorbents.

Parameter	Pellet	3D Printed sorbent
Porosity	0.37	0.38
Adsorbent density (kg/m^3)	1052	669.5
Adsorbent specific heat (J/kg/K)	1700	1700
Channel dimensions (mm)	NA	2.4
Channel wall thickness (mm)	NA	0.7
Pellet diameter (mm)	2.4	Na
Average pore diameter (nm)	15	78
CO_2 capacity at 15 kPa 363 K (mol/kg)	0.76	0.59
CO_2 capacity at 21 kPa 363 K (mol/kg)	0.81	0.63

SIMULATION AND OPTIMIZATION OF THE VACUUM SWING ADSORPTION PROCESS

6-step VSA Process

The schematic of the 6-step VSA process is shown in Figure 1. The cycle has been studied earlier [3,5] and contains the following steps:

1. Adsorption with the feed gas: Preferential adsorption of the heavy component takes place, and the light component is collected at the product end at atmospheric pressure P_H.
2. Rinse: The column is rinsed with a CO_2-rich stream to achieve the CO_2 product at high purity. In this cycle, the rinse step is carried out with the stream from the light reflux step.
3. Co-current evacuation: The feed end is closed, and the column is evacuated to an intermediate pressure P_{INT} to remove most of the light product nitrogen from the column.
4. Counter-current evacuation: The column is evacuated in the counter-current direction to the low pressure P_L to recover the CO_2 product. The column is at a low vacuum pressure although the discharge of the vacuum pump is at ambient conditions.
5. Light reflux: Here the column is purged with a part of the light product from the adsorption step to recover the remaining CO_2 from the bed. The stream from this step is refluxed back to the rinse step. This step is carried out at the low pressure.
6. Light product pressurization (LPP). The column is repressurized using the remaining light product of the adsorption step.

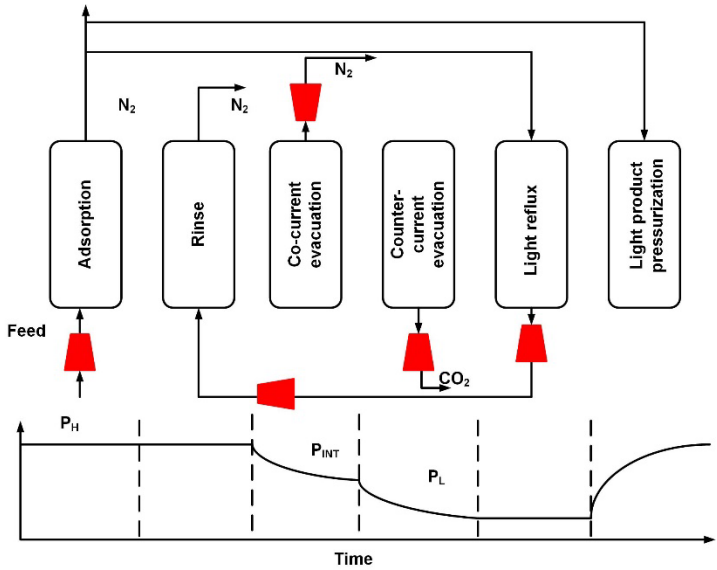

Figure 1. Schematic of the 6-step VSA cycle.

Simulation And Optimization of The VSA Process

A 1D non-isothermal, non-isobaric model assuming ideal gas law and axial dispersion is considered in this study. The model equations contain mass, energy, and momentum balances, and the rate equation uses a linear driving force approximation. The model also assumes instantaneous thermal equilibrium between the gas and the solid phases. The structured adsorbent model equations are

similar to that of the packed bed with differences coming from the correlations used for the pressure drop and the axial dispersion. These differences are listed in Table 2. Details of the model equations for the packed bed are available elsewhere in the literature. [3,5]

The following assumptions are made for simulating the CO_2 capture process:

1. The feed gas is available at 90°C and 1 atmosphere and contains only 5% H_2O. The low value of the H_2O content for these simulations is to allow direct use of measured adsorption equilibrium data, which was limited to low H_2O partial pressure. Oxygen in the flue gas is lumped with nitrogen for the sake of computational efficiency. The adsorption behaviors are similar, and this simulation does not account for potential reactivity of the O_2 with the amine functionality.
2. CO_2 adsorption is considered to be unaffected by the presence of moisture and is described by the dual site Langmuir model, while H_2O adsorption is described by the extended dual site Langmuir model. Nitrogen adsorption was negligible in this sorbent.
3. The height of the packing is 1 m, and the inner diameter of the adsorption column is 20 cm in both the cases. This means that the volume of active adsorbent in the 3D printed case is less than that of the packed bed system.

The model equations are given below.

Component mass balance:

$$\frac{\partial c_i}{\partial t} = -\frac{\partial}{\partial z}\left[cD_L\frac{\partial y_i}{\partial t} + c_i v\right] - \frac{(1-\varepsilon)}{\varepsilon}\frac{\partial \overline{q}_i}{\partial t} \tag{1}$$

By applying ideal gas law $c = {}^{P}/_{RT}$ equation (1) becomes:

$$\frac{\partial y_i}{\partial t} + \frac{y_i}{P}\frac{\partial P}{\partial t} - \frac{y_i}{T}\frac{\partial T}{\partial t} = \frac{T}{P}D_L\frac{\partial(\frac{P\partial y_i}{T\partial z})}{\partial z} - \frac{T}{P}\frac{\partial(\frac{y_i P}{T}v)}{\partial z} - \frac{RT}{P}\frac{(1-\varepsilon)}{\varepsilon}\frac{\partial \overline{q}_i}{\partial t} \tag{2}$$

The overall mass balance equation is given by:

$$\frac{1}{P}\frac{\partial P}{\partial t} - \frac{1}{T}\frac{\partial T}{\partial t} = -\frac{T}{P}\frac{\partial(\frac{P}{T}v)}{\partial z} - \frac{(1-\varepsilon)}{\varepsilon}\frac{RT}{P}\sum_{i=1}^{n}\frac{\partial \overline{q}_i}{\partial t} \tag{3}$$

As mentioned earlier, the mass transfer between the gas and the solid phases was described by a linear driving force approximation which is of the form:

$$\frac{\partial \overline{q}_i}{\partial t} = k_i(q_i{}^* - \overline{q}_i) \tag{4}$$

where, k_i is the mass transfer coefficient and $q_i{}^*$ is the equilibrium solid phase concentration.

The column energy balance and the wall temperature balance equations are as follows:

$$\left[\frac{(1-\varepsilon)}{\varepsilon}\left(\rho_s C_{ps} + C_{pa}\sum_{i=1}^{n}\overline{q}_i\right)\right]\frac{\partial T}{\partial t} = \frac{K_z}{\varepsilon}\frac{\partial^2 T}{\partial z^2} - \frac{C_{pg}}{R}\frac{\partial(vP)}{\partial z} - \frac{C_{pg}}{R}\frac{\partial P}{\partial t}$$
$$+\frac{(1-\varepsilon)}{\varepsilon}\sum_{i=1}^{n}(-\Delta H_i - C_{pa}T)\frac{\partial \overline{q}_i}{\partial t} - \frac{2h_{ins}}{\varepsilon r_{ins}}(T - T_w) \tag{5}$$

$$\rho_w C_{pw}\frac{\partial T_w}{\partial t} = K_w\frac{\partial^2 T_w}{\partial z^2} + \frac{2r_i h_i}{r_o^2 - r_i^2}(T - T_w) - \frac{2r_o h_o}{r_o^2 - r_i^2}(T_w - T_a) \tag{6}$$

In a real capture process, several trains of adsorption columns, containing multiple beds are required to achieve the desired separation. This approach is computationally intensive, and hence we have adopted a one-bed approach for our simulations, in which the equations are solved for one column and the coupled steps are performed by temporarily storing the data.

Process Performance

The performance of the VSA process is defined by the four performance indicators–namely purity, recovery, specific energy, and productivity per unit volume of adsorbent. These are defined in the following manner:

$$\text{Purity} = \frac{\text{Moles } CO_2{}_{\text{COUNTER-CURRENT EVACUATION}}}{(\text{Moles Total} - \text{Moles } H_2O)_{\text{COUNTER-CURRENT EVACUATION}}} \tag{7}$$

$$\text{Recovery} = \frac{\text{Moles } CO_2{}_{\text{COUNTER-CURRENT EVACUATION}}}{\text{Moles } CO_2{}_{\text{FED}}} \tag{8}$$

$$\text{Specific Energy}_{\text{ELECTRIC}} = \frac{\text{Energy}_{\text{VACCUUM}} + \text{Energy}_{\text{COMPRESSION}}}{\text{Moles } CO_2{}_{\text{COUNTER-CURRENT EVACUATION}}} \tag{9}$$

$$\text{Productivity} = \frac{\text{Moles } CO_2{}_{\text{COUNTER-CURRENT EVACUATION}}}{\text{Adsorbent Volume} \times \text{Cycle TIme}} \tag{10}$$

The VSA cycle should achieve at least 90% CO_2 recovery and at least 95% CO_2 purity. The performance indicators are dependent on the durations of the various steps, the feed flow rate (interstitial feed velocity), and the pressures in the vacuum steps. In the 6-step VSA cycle, the performance is affected mainly by the durations of the adsorption, rinse, co-current, counter-current evacuation, and light reflux steps, along with the interstitial velocity and the two evacuation pressures. The light product pressurization (LPP) step duration is dependent on the adsorption step duration, and the step is said to be complete when the pressure of the column reaches the adsorption step pressure. The energy consumption of the vacuum pumps was calculated using equation 11 and assuming 72% isentropic efficiency.

$$Energy_{vacuum} = \frac{1}{\eta} \varepsilon \pi r_i^2 \frac{\gamma}{\gamma - 1_0} \int_{t=0}^{t=t_{vacuum}} vP \left[\left(\frac{P_{atm}}{P(t)_{vacuum}} \right)^{\frac{\gamma}{\gamma-1}} - 1 \right] dt \tag{11}$$

The pressure drop across a packed bed and a column with structured sorbent is shown in Figure 2. As seen from this figure, the structured sorbent exhibits a lower pressure drop in comparison with the packed bed configuration at velocities less than 2m/s.

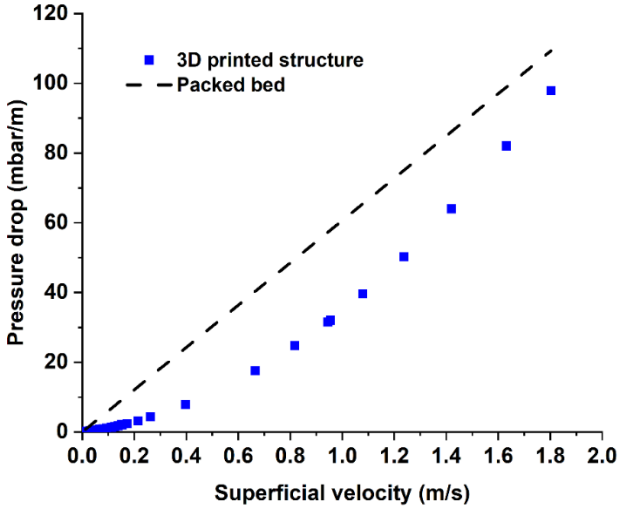

Figure 2. Pressure drop across the column in packed bed containing 2 mm pellets and column containing 3D printed sorbent with 2.4 mm channels. The pressure drop correlation for the packed is given in Table 1, and the values reported for 3D printed sorbent were measured.

Table 2. Parameters and correlations used for the packed bed and structured bed.

Variable	Packed bed	Structured adsorbent
Pressure drop [4,6]	$-\frac{\partial P}{\partial z} = \frac{180}{4r_p^2}\left(\frac{1-\varepsilon_b}{\varepsilon_b}\right)^2 \mu v$	$-\frac{\partial P}{\partial z} = 3191.6\ \varepsilon v_0$ (Adsorption, rinse and LPP) $-\frac{\partial P}{\partial z} = 7748.6\ \varepsilon v_0 - 4390.9$ (Evacuation and LR steps)
Axial dispersion [7,8]	$D_L = 20\ \frac{D_M}{\varepsilon_b} + 0.5\ v_0 d_p$	$D_L = D_M + \frac{(2v_0 a)^2}{192\ D_M}$
$k_{LDF,\ CO_2}$ (s^{-1}) (From lab scale experiments)	$k_{LDF} = 10^6\ e^{-6415/T}$	$k_{LDF} = 2 \times 10^8\ e^{-7255/T}$
$k_{LDF,\ H_2O}$ (s^{-1}) [7,9]	$k_{LDF} = 15\ (\frac{\varepsilon_P}{\tau} D_M)/(\frac{dq}{dc} r_P^2)$	$k_{LDF} = (3D_M)/(\frac{dq}{dc}\ r_{wall,channel}^2)$
Adsorbent dimensions	Spherical Pellet, 2 mm dia, ε_p=0.35, column void fraction=0.37	Hexagonal channel 1.2 mm side, 0.25 mm wall thickness ε_p=0.383

Genetic Algorithm

As discussed above, the performance of a VSA process is dependent on multiple variables. Moreover, it is also necessary to achieve the dual objectives of low energy penalty and smaller footprint. With simple parametric study, it is not possible to identify the optimum performance of a VSA process. On the other hand, evolutionary algorithms, such as genetic algorithms, are gaining increasing attention to perform multi objective optimization of cyclic adsorption processes due to their ability to achieve the global minima and ease of implementation in MATLAB or Python languages. This approach typically requires a fitness function, bounds placed on the decision variables, constraints, the number of simulations to be carried out ([Population size per generation] × [number of generations]), and a genetic representation with parameters for mutation and crossover as inputs. In this work, the objectives are minimization of the specific energy and maximization of the productivity, subject to 95% CO_2 purity and 90% CO_2 recovery targets. Our VSA simulation was developed in MATLAB and the cycle optimization was carried out using MATLAB's function "gamultiobj" for 50 generations and 140 populations per generation. The output from the optimization is plotted as a trade-off plot (Pareto) between the specific energy and the productivity.

RESULTS AND DISCUSSION

Figure 3 shows the Pareto frontier for a packed bed and a column with the structured sorbents. Figure 3(a) represents the Pareto plots for the FCC case, and 3(b) is for the off gas from the SMR process. All these points represent 95% purity on a dry basis and 90% CO_2 recovery. Each point corresponds to a set of operating conditions, and these values are different for different points.

The minimum energy consumption and the maximum productivity for the packed bed system in the FCC case are 1 MJ electrical energy/kg of CO_2 captured and 0.32 mol/m^3 ads s. In comparison, the VSA process with the 3D printed sorbent had a minimum energy of 0.62 MJ electrical energy/kg of CO_2 captured and a maximum productivity value of 0.97 mol/m^3-ads-s. The 3D printed sorbent was able to achieve a 38% reduction in minimum energy compared to the packed bed. Comparing the maximum productivity, a 3-fold increase was observed in the case of the 3D printed sorbent. The minimum energy and maximum productivity are at different operating conditions.

For the SMR off gas scenario, the packed bed had a minimum energy consumption of 0.82 MJ electrical energy/kg of CO_2 captured and a maximum productivity of 0.48 mol/m^3 ads s. The corresponding values for the 3D printed adsorbent are 0.46 MJ electrical energy/kg of CO_2 captured and 1.26 mol/m^3 ads s. This represents a 24% reduction in the minimum specific energy consumption and 2.6 times improvement in the maximum productivity.

The improvement in productivity for the structured sorbent can be attributed to lower pressure drop and faster kinetics. To explain the effect of the kinetics and pressure drop, we revisited the operating conditions corresponding to the points on the Pareto front. In the case of 15% CO_2, the packed bed adsorption step duration and the total cycle time were around 84.5-90.5 seconds and 196-217 seconds, respectively. The comparable durations for the 3D printed sorbents were 34.5-83.7 seconds and 98-201 seconds. For the SMR case, the adsorption step duration for the packed bed was between 64.3-75.5 seconds, and for the 3D printed sorbent the duration was 41-60.6 seconds. The corresponding total cycle times were 159-222 seconds and 86-119 seconds, respectively, for the packed bed and the 3D printed sorbent.

Further, Figure 4 compares the productivity as a function of the feed flowrate and the CO_2 captured per cycle. Between the pellets and the 3D printed sorbent, the latter has a higher feed velocity and consequently a higher amount of CO_2 fed and captured per cycle. This means that the numerator in equation 10 is bigger while the denominator is smaller for the 3D printed sorbent, thereby showing an improvement in productivity. It should also be noted that the volumes of the adsorbent are different,

and the productivity is calculated on an adsorbent basis. One can also see from Figure 4 the velocities are lower for the SMR off gas when compared to the FCC flue gas. This is because the concentration front for higher feed concentrations travels faster than for lower concentrations, leading to a faster breakthrough. The breakthrough of CO_2 would result in losses in recovery and hence the cycle operates at a lower flow rate at feed higher concentrations.

Figure 5 shows the plot comparing the energy consumption against the counter-current evacuation pressure and the amount of CO_2 captured per cycle. The optimizer chose a higher vacuum pressure for the 3D printed sorbent than for the pellet, and this meant that the energy consumed by the vacuum pump is lower for the former. This effect coupled with the larger amount of CO_2 fed resulted in a lower specific energy for the 3D printed sorbent. Comparing Figures 5a and 5c show that at the minimum energy consumption conditions, the SMR off gas required a higher evacuation pressure than the FCC flue gas. This can be explained by the steepness of the isotherm at lower concentrations, which require stronger vacuum for recovering the CO_2 product. Moreover, the less steep the isotherm is, the lower the flowrate to the vacuum pump in the initial duration of the evacuation and this helps in achieving a lower energy consumption at the higher concentrations.

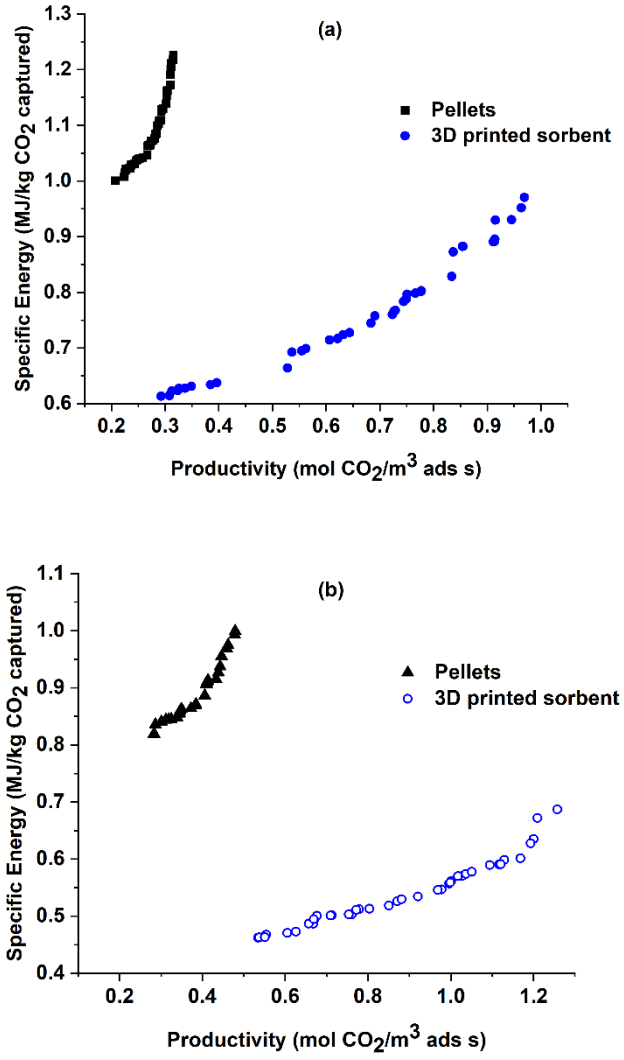

Figure 3. Specific energy vs. productivity pareto for (a) FCC off-gas and (b) SMR off-gas. All points satisfy 95% purity on a dry basis and 90% recovery.

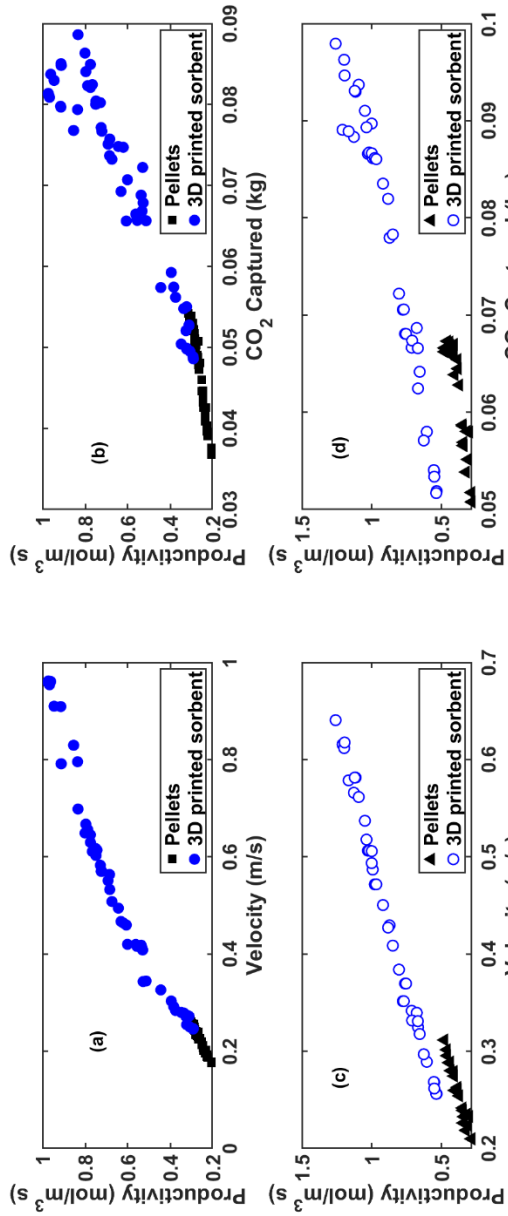

Figure 4. Productivity as a function of the inlet velocity and CO_2 captured per cycle for FCC off gas (Figures a and b) and SMR off-gas stream (Figures c and d).

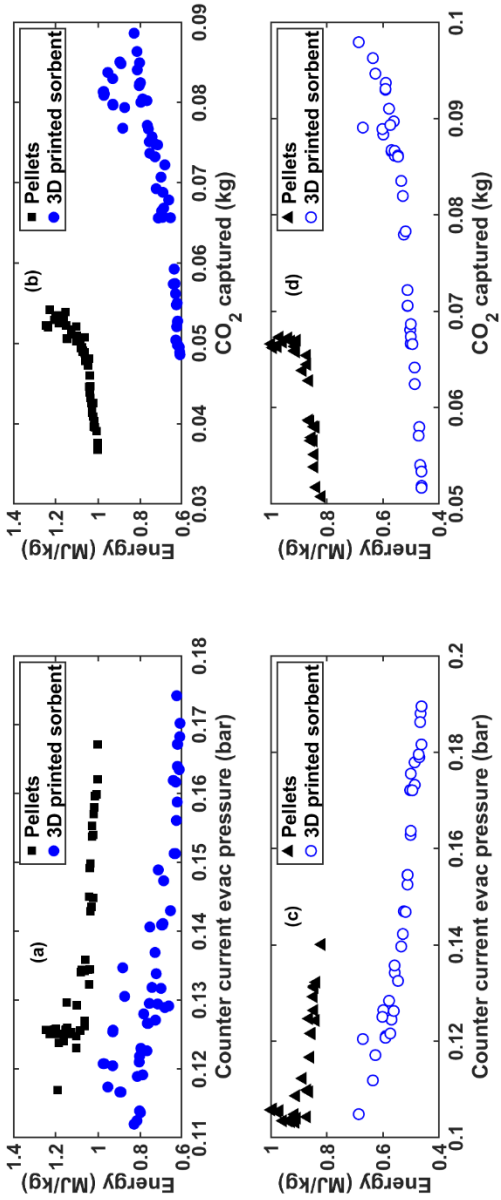

Figure 5. Specific energy as a function of the counter-current evacuation pressure and CO_2 captured per cycle for FCC-off gas (Figures a and b) and SMR off-gas (Figures c and d).

Scale-up

While the productivity is an indication of the footprint, it does not provide explicit information on the size of the unit. To estimate the capture footprint, we have used the following relationship [10]:

$$VSA_{Footprint} = \frac{1}{2}\left\{\left(N_{co-evac\,pump} \times A_{co-evac\,pump} + N_{cn-evac\,pump} \times A_{cn-evac\,pump} + 4D_{column}^2 \times N_{column}\right) \times N_{trains} + N_{compressor} \times A_{compressor}\right\} \quad (8)$$

The area of the co-current evacuation pump is estimated to be 12 m^2, and the area occupied by the compressors is 20 m^2. The 2 in the denominator denotes that the columns would be stacked in 2 tiers. The outer diameter of the column is used.

The first step of scaling up was to define the number and size of the adsorption columns and the number of vacuum pumps necessary for the separation of CO_2 from a specified industrial stream. The SMR unit emits about 600 kton of CO_2/year (1700 kton of off-gas/yr) and the FCC unit emits 240 kton/CO_2 per year (1100 kton of gas/yr)[11]. Based on these feed numbers, the cycle was simulated, and the results are tabulated in Table 3.

The plant footprint for the conventional packed bed system is about 1.8 times larger than that for the 3D printed adsorbent system for both the SMR and FCC cases. This is less than the roughly 3 times increase in productivity observed. This is a clear indication that, while productivity is an useful metric, it is not a strict predictor for the true size of the capture unit.

Table 3. Scale-up results.

Case / Parameter	FCC (Pellet)	FCC (3D printed)	SMR (Pellet)	SMR (3D printed)
Length (m)	2.3	1.8	1.9	1.55
Internal diameter (m)	1	0.55	1.32	0.9
External diameter (m)	1.1	0.61	1.5	1
No. of columns	3	3	3	3
No. of parallel trains	100	100	100	100
No. of co-current evacuation pumps	1	1	1	1
No. of counter-current evacuation pumps	1	1	1	1
Number of compressors	1	1	1	1
VSA footprint (m^2)	4514	2503	7010	4010

CONCLUSIONS

In this work, we have studied the improvement in productivity in a VSA process using 3D printed sorbents relative to conventional packed beds through rigorous process optimization. The case studies chosen were flue gases from a fluidized catalytic cracking unit and steam methane reforming unit. The rigorous process optimization showed that it may be possible to achieve 95% purity and 90% recovery using a supported amine sorbent. An adsorption system using 3D printed sorbent can potentially achieve 3 times higher volumetric productivity relative to a conventional packed bed. The increased productivity of the 3D printed sorbents is estimated to reduce the footprint of the VSA unit by 80% and the amount of adsorbent a factor of 2.5-3 for the two cases assessed. This is a preliminary study to demonstrate an improvement in the process performance with respect to 3D printed sorbents. A recent study by one of the authors [12] has shown that there are other adsorbents like MOFs that can perform better than the silica sorbent used in this study. Furthermore, it is worthwhile to remember that the presence of oxygen and high temperature swings encountered during the cyclic process can have a detrimental effect on the adsorbent stability. Further work is therefore recommended on 3D printed sorbents to evaluate the optimum adsorbent and process configurations.

ACKNOWLEDGEMENTS

This work is a part of the ACT 3D-CAPS project. The ACT 3D-CAPS project # 271503 has received funding from RCN (Norway, 276322), RVO (The Netherlands, 271503) and UEFISCDI, (Romania, 87/2017) and is co-funded by the CO_2 Capture Project (CCP) and the European Commission under the Horizon 2020 programme ACT, Grant Agreement No 691712.

Notations

b_0: Affinity co-efficient of the dual-site Langmuir isotherm for sites 1 and 2

c: Gas phase concentration of component i (mol/m^3)

C_{pg}: Specific heat capacity of the gas mixture (J/kg K)

C_{pa}: Specific heat capacity of the adsorbed phase (J/kg K)

C_{ps}: Specific heat capacity of the adsorbent (J/kg K)

C_{pw}: Specific heat capacity of the column wall (J/kg K)

D_L: Axial dispersion co-efficient (m^2/s)d_p: particle diameter (m)

ΔH: Heat of adsorption (J/mol)

h_i: Internal heat transfer coefficient (W/m^2 K)

h_0: Internal heat transfer coefficient (W/m^2 K)

k_z: Axial thermal conductivity of the gas (W/m K)

k_w: Thermal conductivity of the wall (W/m K)

k_i: Linear driving force coefficient (s^{-1})

P: Total pressure in the system (Pa)

P_H: High pressure in the adsorption step (Pa)

P_L: Vacuum pressure in the counter-current evacuation step (Pa)

P_{INT}: Vacuum pressure in the co-current evacuation step (Pa)

P_{ATM}: Ambient pressure (Pa)

q_i: Solid phase concentration (mol/m^3)

q_s: Solid phase concentration at saturation (mol/m^3)

q_i^*: Equilibrium solid phase concentration at saturation (mol/m^3)

R: Gas constant (J/mol/K)

r_i: Column internal radius (m)

r_0: Column external radius (m)

r_p: Pellet radius (m)

T: Temperature inside the column (K)

T_W: Wall temperature (K)

T_a: Ambient temperature (K)

t: Time (s)

ΔU: Internal energy of adsorption (J/mol)

v: Interstitial velocity (m/s)

y_i: mol fraction of component i

z: Axial dimension (m)

Greek symbols

ε: Bed void fraction

ε_P: Bed void fraction

ρ_s: Density of the adsorbent (kg/m^3)

ρ_g: Density of the gas mixture (kg/m^3)

ρ_w: Density of the wall (kg/m^3)

η: Vacuum pump efficiency

ϒ: Ratio of the specific heats

μ: Viscosity of gas mixture (Pa s)

REFERENCES

1. Rezaei *et al*., Comparison of Traditional and Structured Adsorbents for CO_2 Separation by Vacuum-Swing Adsorption. *Ind Eng. Chem. Res.,* **49**, (2010) 4832–4841.
2. Couck *et al*., 3D-printed SAPO-34 monoliths for gas separation. *Micropor Mesopor Mater,* **255**, (2018) 185-191.

3. Krishnamurthy *et al*., Post combustion carbon capture with supported amine sorbents: from adsorbent characterization to process simulation and optimization. *Chem Eng J* **406**, (2021) 127121.
4. Sluijter *et al*., 3D-printing of adsorbents for increased productivity in carbon capture applications (3D-CAPS), *Int J Greenh Gas Contr* **112**, (2021) 103512.
5. Khurana and Farooq, Simulation and optimization of a 6-step dual-reflux VSA cycle for post-combustion CO_2 capture. *Chem Eng Sci*, (2016) 152, 507-515.
6. Nikolic *et al*., Modelling and optimization of hybrid PSA/membrane separation processes, *Adsorption*, 21, (2015) 283-305.
7. Ruthven, 1984, *Principles of adsorption and adsorption processes*., John Wiley and Sons.
8. Rezaei and Webley, Optimum structured adsorbents for gas separation processes, *Chem Eng Sci*, (2009) 64,5182-5191.
9. Ahn and Brandani, Dynamics of CO_2 breakthrough in a carbon monolith over a wide concentration range, *Adsorption*, 11 (2005) 473-477.
10. Khurana and Farooq, integrated adsorbent process optimization for minimum cost of electricity including carbon capture, *AIChE J*, 65 (2019) 184-195.
11. Onarheim *et al*., (2015) Industrial implementation of carbon capture in Nordic industry sectors, NORDICCS Technical Report D4.2.1501/D18.
12. Krishnamurthy, S., vacuum swing adsorption process for post-combustion carbon capture with 3D printed sorbents: Quantifying the improvement in productivity and specific energy over a packed bed system through process simulation and optimization, Chem Eng Sci, 253, 117585.

Carbon Dioxide Capture for Storage in Deep Geological Formations, Volume 5
Karl F. Gerdes (Editor)
© 2022 BP. All rights reserved.

Chapter 15

TECHNO-ECONOMIC ASSESSMENT OF NEW SOLVENTS FOR CO_2 CAPTURE

Patrick Brandl[1,2], and Ibrahim Ali[3]
[1]Centre for Process Systems Engineering, Imperial College London, London, SW7 2AZ, UK
[2]Centre for Environmental Policy, Imperial College London, London, SW7 1NE, UK
[3]BP International Limited, ICBT Chertsey Road, Sunbury-on-Thames, Surrey, TW16 7LN, UK

ABSTRACT: Gas-fired power plants will likely remain part of the future energy mix, and chemical solvent based post-combustion CO_2 capture offers a way of decarbonizing this type of electricity generation. In this study, we present a techno-economic assessment of chemical and physical solvents, including ionic liquids and two new proprietary solvents, applied in an archetypal capture plant treating a flue gas stream containing either 4 mol% or 8 mol% CO_2, with the higher concentration achieved via flue gas recirculation. Solvent performance is compared using a reduced order modelling technique with partial optimization of process parameters and parametric equipment cost estimation. The CO_2 loading in the lean solvent returned to the absorber is varied in each case to determine the lowest total annualised cost for each solvent. The estimated total annualised costs (which exclude compression, transport, and storage) range from \$100 per tonne of CO_2 down to \$76 per tonne of CO_2. In addition, the impact of exhaust gas recirculation on the capture cost is analysed.

KEYWORDS: CCS, solvents, techno-economic, CO_2 capture, gas power

INTRODUCTION

Carbon capture and storage (CCS) is widely regarded as a vital technology for the cost-effective mitigation of anthropogenic CO_2 emissions and climate change [1,2]. Solvent-based chemical absorption is the most mature technology for CO_2 capture from post-combustion flue gas streams. The technology can be deployed near-term and at large scale. Processes utilizing chemical and physical gas absorption have been successful deployed all over the world dating back to the 1930s [3]. For CO_2 chemical absorption solvents, research effort has so far focused on increasing the solvent equilibrium capacity for absorbing CO_2 and on reducing the inherent energy requirement of regenerating the solvent. This has resulted in thousands of new materials [4] being proposed in recent years. Other critical factors are absorption kinetics, volatility, corrosion, and solvent resistance to degradation.

Transport properties of the solvents, such as viscosity and heat capacity, have an important impact on the total cost of CO_2 capture, which includes the capital expenditure (CAPEX) and operating expenditure (OPEX) [5,6]. These properties can negatively impact mass and heat transfer, which results in an increase in the size of major equipment items like absorbers and heat exchangers. It is widely known that the CAPEX is dominated by the contributions of the absorber and main heat exchangers, while the OPEX is mainly dominated by the solvent regeneration energy and power needed to overcome the pressure drop through the absorber and to compress the captured CO_2. However, multi-dimensional trade-offs between thermodynamic and transport properties (e.g.,

increased equilibrium constant and increased viscosity) are highly non-linear and require a systematic screening approach.

In this study, we present a techno-economic assessment of chemical and physical solvents for CO_2 capture from a conventional gas-fired power plant flue gas. The flue gas CO_2 concentration, y_{CO_2}, is assumed to be 4 mol-%, and the effect of flue gas recycle is studied, for which the flue gas concentration, y_{CO_2}, is assumed to be 8 mol-%. In all cases, a typical post-combustion CO_2 capture flowsheet is specified. The physical solvents analysed in this study are ionic liquids (ILS). The chemical solvents are amine-based, and the benchmark for this study is 30 wt % aqueous monoethanolamine (MEA).

METHODOLOGY

Outline

Previous results indicate that multi-dimensional trade-offs between transport and thermodynamic properties and the rate of reaction of a given solvent influence the cost of capture to different degrees [5, 6]. It is our aim to characterize the impact of solvent thermodynamic and transport properties on the cost associated with an archetypal CO_2 capture plant. This analysis excludes any effects of improvements due to process optimization such as intercooling, or advanced combinations of flashing and stripping [7]. We will focus on two classes of solvents; chemical solvents, being represented by aqueous alkanolamines, and physical solvents, represented by ionic liquids.

Chemical Solvents

Figure 1 shows a typical process topology utilizing a chemical solvent, which includes a reactive component which chemically binds with the dissolved CO_2. Flue gas from a power plant or any other industrial source enters an adiabatic absorber in which CO_2 is removed from the flue gas by the capture solvent.

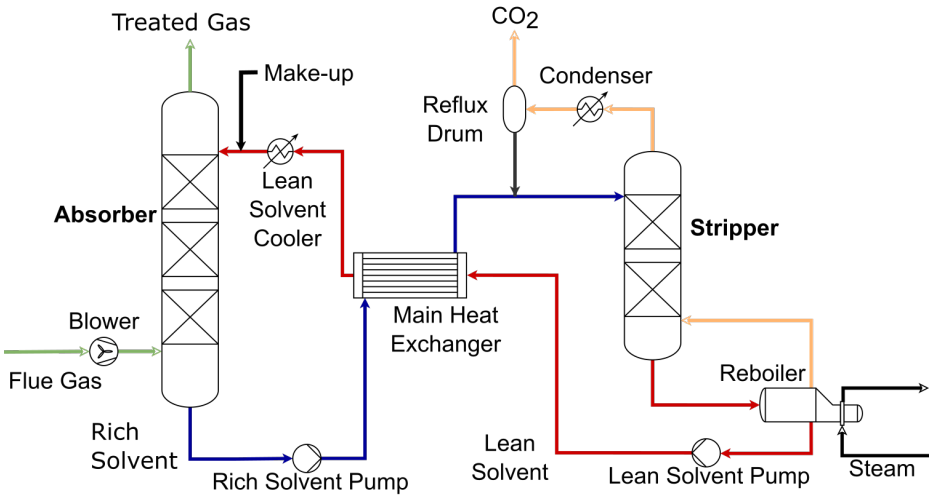

Figure 1. Flowsheet of an archetypal post-combustion CO_2 capture plant comprising an absorber-stripper configuration.

Some solvents benefit from intercooling to remove heat from the absorber, although that configuration is not considered here. The rich solvent is pumped through a heat exchanger prior to entering the stripper in which the CO_2 is released from the solvent. The CO_2 is stripped out of the solvent by vapour that is generated in a reboiler, in which predominantly water from the aqueous solvent is vaporized. The water- and CO_2-rich gaseous stream from the top of the stripper passes subsequently through an overhead condenser, resulting in a high-purity CO_2 stream, which is further dried (dehydrated) and compressed for transport and storage. The recycled lean solvent is cooled prior to being returned to the absorber.

Process Topology

The CO_2 absorption rate by a chemical solvent depends on mass transfer (transport of the CO_2 molecules from the gas to the liquid interface and dissolution and mixing in the liquid phase) and the kinetics of the chemical reaction between the solvent and the CO_2. Aqueous MEA solutions are often cited in the literature as the benchmark for comparing CO_2 capture solvents and were proposed for gas separations by R. R. Bottoms in 1930 [8]. The total thermal energy requirements for stripping CO_2 from 30wt% aqueous MEA is estimated to be in the range of 3.5 to 4 GJ per tonne of CO_2, depending on the process configuration [1,2]. Secondary amines (e.g., diethanolamine [DEA]), and tertiary amines (e.g., triethanolamine or N-methyl-diethanolamine [MDEA]), tend to have both a reduced rate of reaction and lower energy of regeneration compared to MEA. Heterocyclic amines such as piperidine and piperazine (PZ) have also been extensively assessed [9–11]. Commercially deployed solvents such as Shell's Cansolv® [12], Fluor's Econamine FG+® and MHI's proprietary hindered amine KS-1 [13] claim a total heat requirement as low as 2.3 GJ per tonne of CO_2.

In this study, we assessed five chemical solvents: three aqueous amines–30wt% MEA, 30wt% DEA, and 5m PZ, and two proprietary solvents designated S1 and S2. MEA, DEA, and PZ are respectively primary, secondary, and heterocyclic alkanolamine-based solvents, for which data are publicly available. S1 is an aqueous blend of alkanolamines; S2 is an organic solvent with lower water content compared to the other solvents.

An overview of the thermo-physical properties of the three solvents with publicly available data at lean conditions (40℃, optimal lean loading) is listed in Table 1 with data from the DIPPR[1] database and [6,26,27,30–40]. The viscosity of DEA based solvents is higher than those based on MEA. It is known that solvent viscosity has a direct influence on the heat and mass transfer. However, the similar viscosities of aqueous solvents led to this parameter being often neglected [5]. In this study, we endeavour to see if viscosities of other solvent classes are of the same significance.

Table 1. Overview of thermo-physical properties at lean conditions, entering the absorber at 40℃.

Solvent	Density g/L	Viscosity Pa·s	Heat Capacity J/mol/K	Surface Tension kg/s^2
30wt-% *aq.* MEA	1170	0.002	89.7	0.069
30wt-% *aq.* DEA	1390	0.003	102	0.058
5m *aq.* PZ	1100	0.004	85.1	0.068

[1] Design Institute for Physical Property Data (DIPPR) 801 database

PZ solvents have shown good performance in process configurations with absorber intercooling or an advanced flash stripper configuration which achieves improved energy efficiency compared to the simple stripper shown in Figure 1 by utilizing cold and warm rich solvent bypass to recover latent heat from the excess stripping steam leaving the top of the stripper [7]. This indicates that further cost savings exist beyond optimizing operating parameter as carried out within this study. PZ is solid at ambient conditions and dissolves in water to form the CO_2 capture solvent. Our model assumes a pseudo-single phase (e.g., liquid) and does not describe the precipitation of PZ, which can occur at higher solvent concentrations or certain process conditions. CO_2 absorption in PZ is about 1.5 to 2 times faster than in MEA [21]. The viscosity of a 5 molal (5m) PZ solvent is slightly higher than 30 wt% aq. MEA and has a higher working capacity (difference between rich and lean loading) than MEA. PZ shows a faster rate of reaction and mass transfer compared to MEA and DEA [15,25]. The selected amine concentrations reflect widely assumed values and are not optimized within the context of this study.

Physical Solvents/Ionic Liquids (ILs)

The first published mention of an ionic liquid (IL) was in 1888 [26]. The synthesis of the low melting ethylammonium nitrate ionic liquid in 1914 [27] is widely cited as a first ground-breaking paper about ILs. ILs have gained recent attention due to reports highlighting their potential as CO_2 capture solvents. The relatively high costs of ILs have limited their application so far.

Table 2. List of Ionic Liquids ILs analysed in this study.

Name	Abbreviation
1-ethyl-3-methylimidazolium dicyanamide	[C2C1im][DCA]
1-ethyl-3-methylimidazolium bis[(trifluoromethyl)sulfonyl]imide	[C2C1im][NTf2]
1-ethyl-3-methylimidazolium Tetrafluoroborate	[C2C1im][BF4]
1-ethyl-3-methylimidazolium Ethyl sulfate	[C2C1im][EtSO4]
1-butyl-3-methylimidazolium tricyanomethanide	[C4C1im][C(CN)3]
1-butyl-3-methylimidazolium bis[(trifluoromethyl)sulfonyl]imide	[C4C1im][NTf2]
1-butyl-3-methylimidazolium trifluoromethanesulfonate	[C4C1im][TfO]
1-butyl-3-methylimidazolium Tetrafluoroborate	[C4C1im][BF4]
1-pentyl-3-methylimidazolium bis[(trifluoromethyl)sulfonyl]imide	[C5C1im][NTf2]
1-hexyl-3-methylimidazolium Tetracyanoborate	[C6C1im][B(CN)4]
1-hexyl-3-methylimidazolium bis[(trifluoromethyl)sulfonyl]imide	[C6C1im][NTf2]
1-hexyl-3-methylimidazolium Tetrafluoroborate	[C6C1im][BF4]
1-Butyl-1-methylpyrrolidinium bis[(trifluoromethyl)sulfonyl]imide	[bmpyr][NTf2]
1-butyl-3-methylpyridinium bis[(trifluoromethyl)sulfonyl]imide	[bmpy][NTf2]
1-octyl-3-methylimidazolium bis[(trifluoromethyl)sulfonyl]imide	[C8C1im][NTf2]

However, with thousands of known ILs, including relatively inexpensive ones, and their "tuneable" thermo-physical properties, it is of interest to assess the performance of a range of ILs for CO_2 capture.

ILs have very low vapour pressures, which would result in lower solvent losses compared to e.g., alkanolamines, and are reported to be thermally and chemically stable. They dissolve significant amounts of CO_2 (low Henry's coefficient) and have a higher viscosity compared to alkanolamines. Despite numerous recent publications, the full range of data required to calculate capture performance, is not publicly available for the majority of ILs. Table 2 lists the ILs analysed in this study by their IUPAC name along with the abbreviation in the form: [cation][anion]. The selection is based on the availability of data and relations in molecular structure e.g., potential trends by changing cation or anion, or alkyl chain.

Physical solvents do not show a significant chemical reaction and thus their absorption capacity is solely dictated by their Henry's constant. Most ILs show a relatively low Henry's constant (high solubility of CO_2); however, the low partial pressures of CO_2 in atmospheric flue gases makes flue

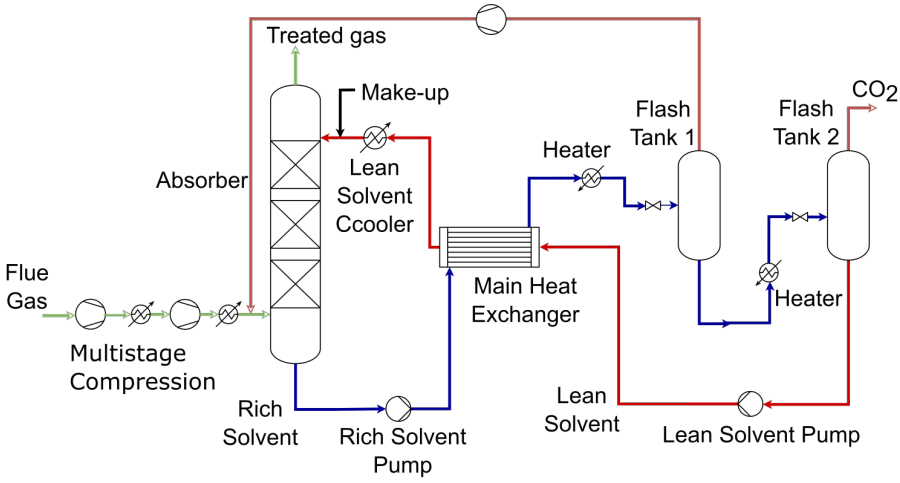

Figure 2. Process topology for a physical solvent (Ionic Liquid) CO_2 capture process.

gas compression necessary (see Figure 2). The flue gas enters a multi-stage compression train with intercooling before being contacted with the IL inside a pressurized (>10 bara) absorber. The solvent is regenerated by staged lower pressure flashes. The absorber pressure, regeneration pressure (lowest flash pressure), and number of flash stages are adjusted to achieve the minimum capture cost while producing a minimum of 95% CO_2 purity in the product stream. This optimization includes the CAPEX and OPEX of the flue gas compression train and the recycle compressor. We found that the additional CAPEX was outweighed by the OPEX savings by re-compressing the flash-gas. Typical absorber operating pressures are around 20 bara. The gaseous recycle stream contains a significant amount of CO_2 which needs to be recycled to the absorber.

The flue gas compression required by ILs is an obvious disadvantage compared to chemical solvents that mainly impacts the CAPEX. However, operating at higher pressures reduces the diameter of the

absorber (although the pressure rating of the absorber is now higher) and enables the steam-free regeneration of the solvent, which leads to a significant OPEX reduction. This opens a trade-off between higher investment costs (flue gas compressors) and potentially lower operating expenditure (if the elimination of steam outweighs the electricity requirement for flue gas compression).

Thermodynamics and Capture Costs

We have previously developed a model for screening potential chemical solvents [5,6] which estimates the process performance for a particular solvent and, subsequently, the costs based on the size of the process units and their energy requirements. The model computes both process performance indices, such as the solvent flowrate, height of the absorption column, and area of the heat exchangers, as well as financial indices, such as annualised capital expenditure (CAPEX), operating expenditure (OPEX), and total annual cost (TAC).

The columns are modelled as adiabatic packed beds, and mass transfer is treated using a rate-based approach. The model comprises the mass and energy balances, the equilibrium relations, and the rate equations required to describe mass transfer. Non-equilibrium rate-based models, some of which discretize film layers during the mass transfer, are mathematically stiff and solvent specific, which makes these approaches unsuitable for screening a large number of solvents (in the order of hundreds) [28]. However, our model includes a physically based description of heat and mass transfer and is sufficiently computationally tractable for our purposes. The mass transfer has been modelled following the two-film theory [29] as reviewed for CO_2 capture by Wilcox *et al.* [30]. Non-reactive thermodynamic equilibrium is assumed to be attained at the gas–liquid interface, with reactions assumed to occur in the liquid film. Finally, it is assumed that the concentration of molecular CO_2 in the bulk liquid is negligible for the chemical solvents [31]. For more details on the model, the reader is referred to the supporting information. A summary of the thermo-physical property models deployed in the tool is shown in Table 3.

Table 3. Correlations used in the solvent screening model.

Correlation	Reference
Reaction rate constant	Arrhenius equation
Effective surface area	Onda *et al.* (random packing)
Mass transfer coefficient	Onda *et al.* (random packing)
Enhancement factor	Wellek *et al.*
Gas phase diffusivities	Fuller *et al.*
Binary liquid phase diffusivities	Wilke and Chang
Liquid phase diffusivities	CO_2: Takahashi *et al.* Wilke and Chang as modified by Perkins and Geankoplis
Pressure drop and holdup	Billet and Schultes
Single phase heat transfer coefficient	Nusselt corelations
Multiphase heat transfer coefficient	Chen's method with Lockhart-Martinelli correction

A key objective of this work is to calculate the total annualised cost (TAC) associated with a capture plant utilizing each of the solvents. This number gives an indication how much money must be spent per year, to capture one tonne of CO_2 at the plant boundary before the compression equipment. It should be noted that this is a short-cut approach, and the TAC is not equivalent to the cost of CO_2

captured or cost of CO_2 avoided calculated based on discounted cash flow analyses. It is not intended to give either the cost of CO_2 captured or avoided, rather, it provides a means of discriminating between solvents based on economic indicators. The TAC is defined as:

$$\mathrm{TAC} = CRF \cdot \sum_k^{\mathrm{units}} CAPEX_k + \sum_l OPEX_l \quad (1)$$

where the CRF is the capital recovery factor and is given by:

$$CRF = \frac{i(1+i)^n}{(1+i)^n - 1} \quad (2)$$

Which is a function of the discount rate i and the annuity period n (i.e., the time period over which the capital is amortised). A discount rate of 8% and an annuity period of 25 years have been assumed [40]. The costs reported in this study are per captured tonne of CO_2 and not avoided costs given that no specific reference power plant has been assigned. Main inputs for the model are flue gas flowrate and composition, which are directly linked to the size and type of the power plant, as well as process KPIs such as solvent circulation rate.

The CAPEX for each process unit is correlated to key parameters such as size and material of construction [41]. In the following, widely used academic equations/correlations describing the investment costs for equipment used within a capture unit are represented. This is to provide the reader an overview of the approach taken and remind that these correlations are solely used to compare the relative costs of the different cases/solvents within this study. For example, the installed cost of an absorption column is given by:

$$C_{abs} = 1.281[f_1 C_b + V_p C_p + C_{p1}]C_I \quad (3)$$

Where f_1 refers to the material of construction, V_p is the volume of packing, and C_b is a function of the weight of the shell, given by:

$$C_{b,abs} = 1.218\, e^{6.629 + 0.1826 \ln W + 0.02297 (\ln W)^2} \quad (4)$$

Where W is the weight of the shell. C_{p1} is given by:

$$C_{p1} = 300 D^{0.7396} Z_T^{0.7396} \quad (5)$$

Where D and Z_T are the column diameter and height, respectively. The CAPEX of heat exchangers is calculated by [41] based on a similar principle:

$$C_{HX} = 1.218(f_d f_m f_p C_b)C_I \quad (6)$$

Where f_d, f_m, and f_p are functions of the heat exchanger type, material of construction and pressure range, respectively. C_I is a cost multiplier to account for the cost of installation. C_b is an explicit function of the heat transfer area, A, and is given by:

$$C_{b,HX} = \exp[8.821 - 0.30863(\ln A) + 0.0681(\ln A)^2] \quad (7)$$

The cost for electricity consumption and heat requirements is calculated via the short-run marginal cost assuming an on-site generator/boiler burning a fuel (e.g., natural gas). The cost of steam is calculated assuming that the efficiency of the boiler is 90%. The costs of compression of the CO_2 for transport and storage have not been included in this work (as it is assumed that this cost will be similar

for all solvents). Any CO_2 emissions associated with an auxiliary boiler are not included in the overall capture rate. A previous study shows that the cost of cooling, CO_2 compression and dehydration is on the order of \$20–25 per t_{CO2} [42,43]. The key economic assumptions are summarized in Table 4.

Table 4. Summary of key economic parameters adapted from [40].

Parameter	Value
discount rate	8%
annuity period	25 years
Lang-Factor	3.7
Short-run marginal costs	70 \$/MWh_{elec}
	25 \$/t_{steam}
Water costs	0.025 \$/$m^3_{H_2O}$

The model does not take second order effects such as corrosion, degradation, and foaming into account, as these effects are not fully understood yet and describing them quantitatively in a screening approach is left for future work. The size of the equipment is a function of the solvent properties and operating conditions. In contrast to operating an existing plant with differing conditions and solvents, in this study, the equipment is resized using the model for each solvent and operating condition to achieve a cost-optimal plant. For example, changing the lean loading in an existing plant would be achieved by controlling the heat supply to the reboiler, while changing other operating parameters in a trade-off to find the minimal energy requirements. This is also implemented in our model, however, the model re-sizes the whole plant to the new operating conditions so that the equipment is optimally designed leading to minimal costs.

An evaluation of the sensitivity of key process design variables and TAC to solvent properties is presented in [5,6]. The accuracy of the cost estimates is expected to be ± 30% [44]. Uncertainty associated with the thermo-physical data (e.g., uncertainty in the experimental data itself e.g., ± 6.5% for heat capacity) was found to have a maximal impact on the TAC of 10% via propagation of error.

The main challenge of this study was defining the extent of optimisation for each solvent. This was a trade-off between varying process conditions to determine the lowest TAC for each case with the amount of time and computational effort required. It is probable that every solvent will have a unique set of optimal operating parameters. If a particular set of parameters is used to screen all solvents, then this could systematically disadvantage all but one solvent from which the parameter set was taken. It is therefore essential to identify which parameters have a first order impact on process performance and subsequently optimize them. This balances accuracy and fairness against computational effort. We identified the following operating parameters which have a major impact in the process performance and costs:

- Absorber and stripper temperatures
- Stripper pressure
- Lean loading
- Temperature of lean solvent leaving lean-rich cross heat exchanger
- CO_2 fraction in flue gas
- Capture rate

In this study, we fixed the capture rate at 90% of the CO_2 in the flue gas and specified the purity at >95 mol-% CO_2. The absorber and stripper operating conditions are set based on the solvent's VLE

properties. The temperature profile in the lean-rich cross heat exchanger is adapted to the solvent flowrate. The model is capable of screening the solvents for any flue gas conditions. For this study, the CO_2 fraction in the flue gas is set to y_{CO_2}= 4 mol-% for the gas-fired power case and to y_{CO_2}= 8 mol-% to analyse the impact of exhaust gas recirculation. Thus, the main study parameter are the solvent properties, operating conditions such as lean loading, flue gas CO_2 concentration, and main heat exchanger approach temperature.

The model assumes equilibrium between the CO_2 in inlet flue gas entering the absorber and the solvent leaving the absorber. This assumption is valid for pseudo-first order solvents with sufficient column heights but deteriorates with decreasing CO_2 concentration. This is illustrated in Figure 3. The equilibrium loading is solvent specific and depends on the temperature, pressure, and CO_2 concentration in the flue gas. The lean loading is constrained between a lower limit of zero and an upper limit in equilibrium with the exiting flue gas. A lean loading close to zero imposes a high enthalpy demand within the reboiler, because nearly all CO_2 must be stripped out of the solvent. A lean loading close to the equilibrium loading results in a small cyclic solvent capacity, which requires higher solvent volume per captured unit of CO_2 to maintain constant capture rate. In both cases, the energy demand (regeneration and cooling) and/or CAPEX contribution driven by the solvent flowrate increase the costs relative to an operating point further away from those boundaries.

Therefore, an optimum loading $\theta_{\text{lean}}^{\text{opt}}$ resulting in minimal total annualised costs, will be in the range $[0; \theta_{\text{equi}}]$. Using the specific optimal lean loading $\theta_{\text{lean}}^{\text{opt}}$ for both the low concentration flue gas (4%) and for the high concentration (8%) is essential for a fair comparison, because the solvents will be compared at their individual best operating conditions.

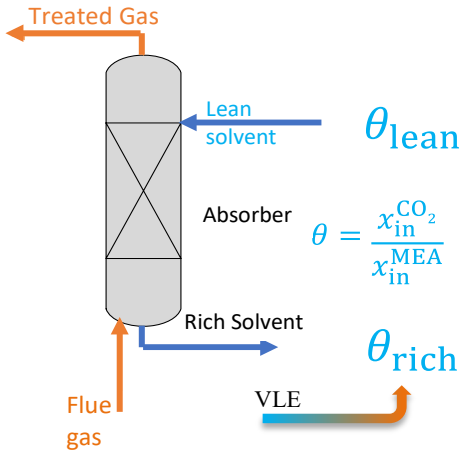

Figure 3. Definition of lean and rich loading around the absorber; lean loading is to be optimized and rich loading is calculated based on equilibrium with inlet flue gas.

RESULTS AND DISCUSSION

Amine Solvent Assessment for Gas-Fired Power

Table 5 summarizes the optimal lean loading and the equilibrium loading for the three solvents with publicly available data for a gas-fired power plant with the flue gas CO_2 concentration equal to 4 mol-%. Our model shows that the cyclic capacity of 5m *aq.* PZ is higher than the capacities of 30 wt-% *aq.* MEA or 30 wt-% *aq.* DEA. This is driven by the solvents' vapour-liquid equilibrium (VLE).

Table 5. Result of the lean loading optimization for minimal total annualised costs.

Solvent	θ_{lean}^{opt} $\mathbf{mol_{CO_2}}/\mathbf{mol_{Amine}}$	θ_{equi} $\mathbf{mol_{CO_2}}/\mathbf{mol_{Amine}}$
30wt-% *aq.* MEA	0.34	0.46
30wt-% *aq.* DEA	0.32	0.41
5m *aq.* PZ	0.34	0.80

Figure 4 compares the Total Annualised Cost (TAC) for 30 wt-% *aq.* MEA, 30 wt-% *aq.* DEA, 5 m *aq.* PZ and the two proprietary solvents S1 and S2 at their optimal lean loading (see Table 5). The sum of the CAPEX (blue) and OPEX (green) contributions defines the TAC.

The DEA-based solvent requires a more expensive process than MEA, which is mainly driven by its relatively higher OPEX. The DEA-based solvent's viscosity is about 17% higher than that of MEA, and Mota-Martinez *et al.* [5], having identified the negative impact of high viscosity on the process costs, an increase in TAC of 9.5% seems reasonable. The cyclic capacity of 30wt-% *aq.* DEA is also lower than that of MEA, which requires more solvent and thus, larger equipment, to capture the same amount of CO_2. This, coupled with the lower absorption rate of DEA, explains the CAPEX increase relative to MEA.

In contrast to DEA, 5m *aq.* PZ shows a 15% lower TAC than MEA and requires the lowest CAPEX spending of all the solvents evaluated in this work. Although its viscosity is about 44% higher than MEA, PZ can offset this with a 2.8 times higher cyclic capacity and a higher absorption rate. This means that less solvent is needed to capture the same amount of CO_2 and the equipment size decreases leading to CAPEX savings compared to MEA. This is driven by PZ's VLE, its higher rate of reaction and faster mass transfer compared to MEA. Therefore, our model shows that the positive impacts of higher absorption capacity and higher absorption rate can offset the negative impact of higher viscosity. The key driver behind the capture cost is the overall solvent circulation rate, which in turn is a function of cyclic capacity (VLE), viscosity, and density.

The proprietary S1 solvent requires approximately the same OPEX as MEA and a much lower CAPEX. The solvent's VLE is advantageous compared to MEA; it has a higher cyclic capacity at similar viscosity as MEA. S1's TAC is almost identical to that of 5m *aq.* PZ. However, secondary effects such as degradation, foaming, precipitation, and corrosion, which are not assessed here, may further distinguish the two solvents.

The proprietary S2 solvent has the lowest TAC of all screened solvents. Its cost advantage compared to 30wt-% *aq.* MEA is 18% and 3% relative to 5m *aq.* PZ. Like PZ, S2 can trade off disadvantageous transport properties compared to MEA with an increased cyclic capacity resulting in a lower solvent flowrate. This is indicated by a slightly increased OPEX and strongly decreased CAPEX relative to 30wt-% *aq.* MEA.

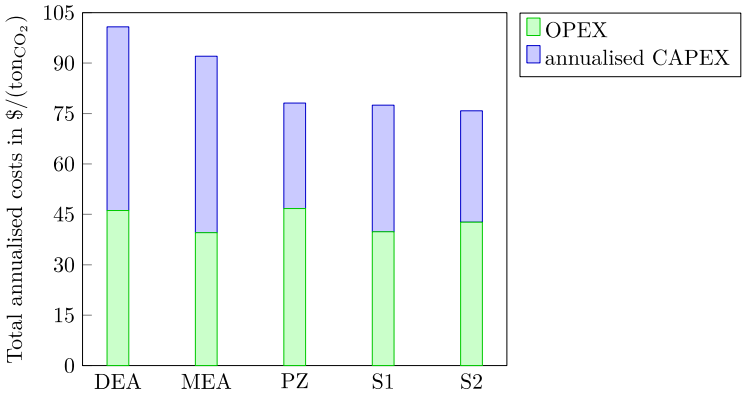

Figure 4. Comparing the total annualised costs of 30wt-% *aq.* MEA, 30wt-% aq. DEA, 5m *aq.* PZ and two proprietary solvents for a gas-fired power plant's flue gas y_{CO_2}=4%.

The estimated TAC of a capture plant utilizing S2 is \$76 per t_{CO2}. The TAC of all solvents can be further decreased with process intensification and optimization, although these might improve specific processes/solvents more than others [45].

Impact of Exhaust Gas Recirculation (EGR)

Exhaust gas recirculation (EGR) significantly decreases the volume flow rate of the flue gas to the CO_2 capture plant while increasing its CO_2 concentration. In this study, we have assumed a recycling of 50% of the flue gas to the inlet of the gas turbines of the power plant, which is in line with IEAGHG assumptions in their assessment of EGR [46]. Choi *et al*. had shown, based on simulations, that recycle of up to 50% maintains enough O_2 to sustain the turbine combustor operation [46]. This results in a CO_2 concentration in the flue gas to the CO_2 capture plant of 8 vol%. The actual level of recycle that is doable depends on the design details of the combustion turbine [47].

For this assessment of EGR, only the effect of flue gas flow rate and CO_2 concentration on the capture plant costs is considered. The power loss due to back-pressure on the gas turbine is not considered as the actual power plant is outside the battery limit of this study. The target electrical output is 500 MW assumed to be driven by two gas turbines with approximately 190 MW_g output.

Figure 5 summarizes the impact of EGR on the five solvents: The TACs are reduced by 34% for *DEA*, 48% for *MEA*, 44% for *PZ* and *S1,* and 46% for *S2*. The CAPEX reduction is larger than is the OPEX reduction for all solvents. This is due to the solvents reaching a much higher equilibrium loading and working capacity, thereby lowering solvent circulation rate, and the lower flue gas flow rate leading to lower footprint (diameter) for the absorber. The lower solvent rate reduces equipment size all through the process. Theoretically, the cost ranking *DEA* > *MEA* > *PZ* > *S1* > *S2* could change depending on the slope of the equilibrium line of CO_2 partial pressure versus solvent loading. However, the solvents in this study exhibit similar equilibrium behaviour, so no significant changes in cost ranking are observed. In fact, the relative difference between PZ and S1 decreases to practically zero and within the error of the input data. It must be noted that the saving due to EGR represents an upper limit due to scope of the plant considered for the analysis (the absorbers, strippers, and main heat exchangers). Other equipment like CO_2 compressors (which are out of scope of our analyses) are unlikely to be impacted by EGR and therefore, when these costs are included, we expect the decrease in total cost to be much lower (possibly of the order of 15–20%). It should also be noted that this work

does not consider any impact (e.g., decreased power output) of EGR on the combined cycle. While this preliminary work shows that EGR has the potential to decrease the cost of CO_2 capture, we recommend that further evaluation including the NGCC, the CO_2 capture plant and the CO_2 compression and dehydration system be carried out to understand the full impact of EGR.

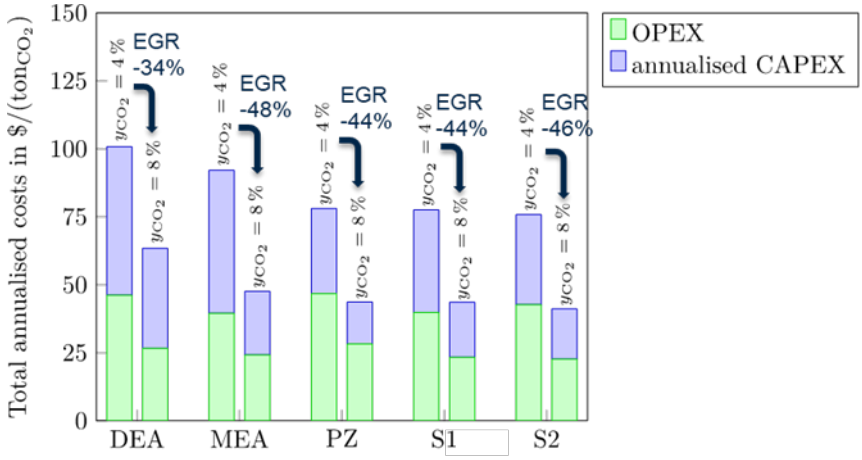

Figure 5. Comparing the impact of exhaust gas recirculation (EGR) on the total annualised costs.

Ionic Liquids for CO_2 Capture

Previous results [5,6] indicate that the impact of viscosity dominates the installed costs for solvent-based CO_2 capture. This might limit the practical application of ionic liquids as post-combustion capture solvents since they mostly have high viscosity.

Figure 6 compares the calculated height of the absorber utilizing various ILs while capturing 90% of the feed CO_2. The lowest height is for the IL with the lowest viscosity. All other ILs require an absorber taller than the current highest chemical tower. Some ILs even require an absorber as tall as the tallest buildings in the world, which means those ILs are highly unlikely to be deployed on industrial scale. This representative selection of ILs also indicates that even with flue gas compression, the driving force for the CO_2 absorption is too small to obtain smaller equipment compared to alkanolamines.

Figure 7 shows a sensitivity analysis between solvent viscosity, CO_2 solubility, and the TAC. The TAC for the selected IL's ranges from \$100/tonne CO_2 up to \$260/tonne CO_2. Comparing ILs solely by viscosity and solubility neglects the other thermo-physical properties and hence does not show a full comparison. ILs' viscosities are at least an order of magnitude higher than those of alkanolamines (see Table 1), which negatively impacts mass transfer and CO_2 absorption rates, resulting in higher capture costs for ILs compared to the benchmark 30 wt-% *aq.* MEA. A common strategy for improving IL performance is to increase the CO_2 solubility by functionalizing the IL with CO_2-philic atoms or groups such as Fluorine (F) or cyano (CN). The downside of this approach is an increase in viscosity due to the added polar inter- and intra-molecular interactions, which decreases the freedom

of movement of the ion pairs. A sole focus on increasing the CO_2 solubility and viscosity will therefore not lead to a cost-efficient solvent.

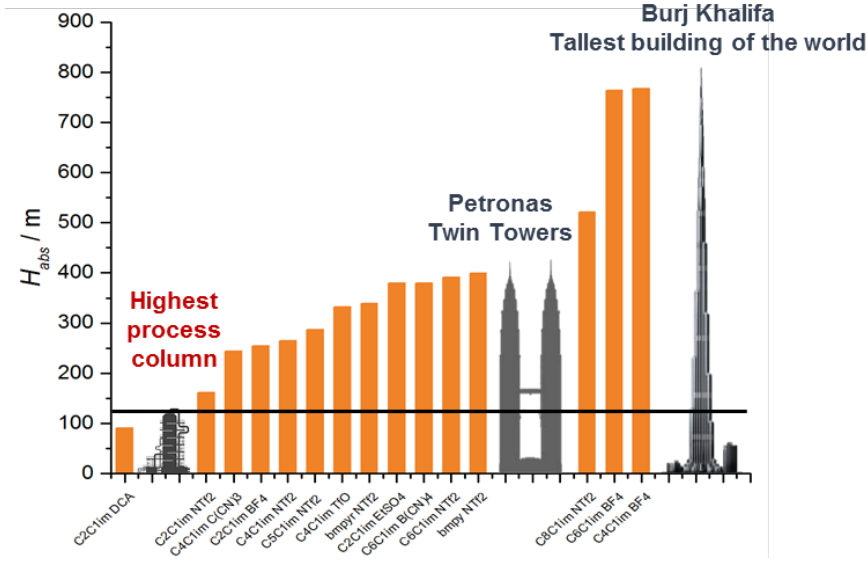

Figure 6. Height of absorber column utilizing ionic liquids.

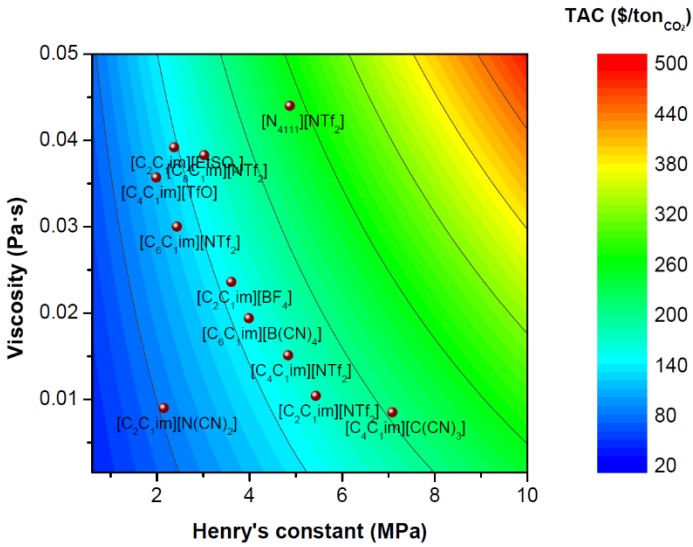

Figure 7. Sensitivity of the total annualised costs to CO_2 solubility and viscosity (note that the lower values of the Henry's constant represent higher solubility of CO_2 in the solvent).

CONCLUSIONS

We have developed a high-level approach for rapidly screening CO_2 capture physical and chemical solvents and understanding their potential for cost savings. For physical absorption solvents like ionic liquids (ILs), a quick evaluation of the potential of the solvent can be performed, based on non-monetized performance indicators such as absorber height, which is significantly affected by the impact of transport properties such as viscosity on mass transfer. There is a large number of ILs reported in the public domain but the majority of those cannot be screened using our method due to lack of data for key properties. The ILs that we screened show higher capture cost compared to 30wt-% *aq.* MEA. Reducing viscosity while maintaining high CO_2 solubility is key in developing new ILs that are more cost effective.

We optimized the lean loading for a number of chemical absorption solvents to capture CO_2 from gas-fired power plant flue gas for a conventional configuration and with exhaust gas recirculation (EGR) to reduce volume and increase CO_2 concentration. Using the total annualised costs to rank the screened solvents, reveals the order in descending order of cost as 30wt-% *aq.* DEA > 30wt-% *aq.* MEA > 5m *aq.* PZ > S1 > S2 for an archetypal post-combustion CO_2 capture plant utilizing the solvents. A proprietary solvent, S2, required the lowest costs with \$76 per t_{CO2} for a gas-fired power plant with flue gas $y_{CO_2} = 4\%$. A power plant with EGR shows potential for reducing capture costs. Further work is required to understand the full impact of EGR.

ACKNOWLEDGEMENTS

The authors gratefully acknowledge the financial support from the CO_2 Capture Project (CCP), Parts of this project have been presented at 14th Greenhouse Gas Control Technologies Conference in Melbourne.

NOMENCLATURE

Abbreviation	Explanation
A	Area
aMDEA	Activated MDEA
c	Concentration
C	Cost
CAPEX	Annualised Capital Expenditure
CapRate	Capture Rate
C_b	weight function for costing
CCS	Carbon Capture and Storage
CEPCI	Chemical Engineering Plant Cost Index
C_I	Cost factor installation (Lang type)
C_{p1}	Cost function based on weight size
CRF	Capital Recovery Factor
D	Diffusivity Coefficient
DEA	Diethanolamine
DIPPR	Design Institute for Physical Properties
E	Enhancement Factor
ETS	Emissions Trading Scheme
f	Fugacity
f_I	Material factor for costing
f_d, f_m, and f_p	cost function parameter for heat exchanger

G	Gibbs Free Energy
GHG	Greenhouse Gas
H	Enthalpy
H	Height absorber physical solvents
Ha	Hatta Number
He	Henry's Law Constant
i	interest rates
IEAGHG	IEA Greenhouse Gas R&D Programme
IL	Ionic Liquid
K	Equilibrium Constant
k	Mass Transfer Coefficient
k_2	Second Order Reaction Rate Constant
KPI	Key Performance Indicator
LMTD	Logarithmic Mean Temperature Approach
MEA	Monoethanolamine
MHEX	Main Heat Exchanger
Mtpa	Mega ton per annum
n	Moles
n	annuity period
NGCC	Natural Gas Combined Cycle
OPEX	Operating Expenditure
p	Pressure
ppm	parts per million
PZ	Piperazine
R	Universal Gas Constant
R&D	Research and Development
S	Entropy
S1	Proprietary solvent designated S1
S2	Proprietary solvent designated S2
SS	Stainless Steel
T	Temperature
TAC	Total Annualised Cost
TEAA	Tetraethylammonium acetate tetrahydrate
TEGDME	Tetraethylene glycol dimethyl ether
TMAF	Tetramethylammonium fluoride tetrahydrate
TMAM	Tetramethylammonium malonate monohydrate
VLE	Vapour Liquid Equilibrium
V_p	Volume packing
W	weight
WACC	Weighted Average Cost of Capital
z	Stoichiometric Factor
Z_T	Column Height
Θ	Loading

SUPPORTING MATERIAL

The following section contains supporting information about the process topology and design, thermodynamic modelling, and economic evaluation.

Figure 2 of the main paper shows the process topology of an archetypal absorption-based post-combustion CO_2 capture plant. The underlying model does not design a capture plant rigorously. Model complexity is reduced to provide greater flexibility and quick convergence times. That means auxiliaries such as valves, control loops, storage tanks, analytical equipment, and filters are not explicitly modelled but included in the costing. Table S1 outlines the key equipment modelled and S2 summarizes key operating conditions.

Equipment size (e.g., columns, heat exchangers, pumps) is variable and re-calculated for every change in operating conditions and solvent; that means e.g., height, diameter, surface area, wall thickness, and number of units constantly re-adjust for minimal capture cost. This enables a cost-optimal comparison of different solvents utilized in the same process topology but not in a physically identical plant. Absorber and stripper columns diameter is estimated using a 70% flooding approach and the pressure drop is calculated using the Billet and Schultes method. Heat exchangers are designed as shell and tube (horizontal and vertical depending on purpose). Table S2 lists more details on the equipment including its type, design limits, sizing, and material. If the design limit of a certain equipment item is reached, then multiple units are added (unless this feature is deactivated as shown with the ionic liquid absorber sizes).

Table S1. Equipment design including limits, sizing method, material, and costing method. SS = stainless steel.

Equipment	Type	Design Limit	Sizing	Material
Absorber, Stripper	Packed column	< 450 t	rate based short-cut	SS304
Main heat exchanger, Lean solvent cooler	Shell and tube	< 1115 m^2	Kern's method	SS316
Reboiler, Condenser	Vertical shell and tube	< 1115 m^2	(48)	SS316
Pump	Centrifugal pump	< 800 m^3/h	(48)	SS304

Table S2. Summary of key default operating conditions.

Parameter	Value
Absorber operating pressure	110 kPa_a
Absorber solvent inlet temperature	40°C
Flooding factor	70%
Flue gas flowrate	17.7 kmol/s (500kg/s at y_{CO_2}=4 mol%)
CO_2 fraction in flue gas, y_{CO_2}	1-30 mol%
Flue gas temperature after pre-treatment	40°C
Capture rate	90% and 95%
CO_2 purity	95%
Reboiler pressure	159 kPa
Steam	420K and 250 kPa
Main heat exchanger temperature approach	20°C (LMTD)

The following section describes the thermodynamic modelling:

The mass transfer resistance is considered to occur exclusively in the liquid film. The liquid mass transfer coefficient (k_L) has been estimated using Onda's correlations for randomly packed columns [32,33]:

$$k_L^0 \left(\frac{\rho_t^L}{\mu_L g}\right)^{1/3} = 0.0051 \frac{Re_L'^{2/3} (a_p d_p)^{0.4}}{Sc_L^{0.5}} \quad \text{(S1)}$$

Where ρ_t^L = mass density, μ_L = viscosity of the liquid, g = acceleration due to gravity–9.81 $m \cdot s^{-2}$, Sc = Schmidt number, a_p = specific area of packing, d_p = size of packing and Re_L' = Reynolds number using the wet interfacial specific area calculated as a correction of the packing specific area (a_p) via Onda's correlation:

$$a' = a_p \left(1 - \exp\left(-1.45 \left(\frac{\sigma_c}{\sigma}\right)^{0.75} Re_L^{0.1} Fr_L^{-0.05} We_L^{0.2}\right)\right) \quad \text{(S2)}$$

Where σ is the surface tension of the liquid and σ_c is the critical surface tension of the packing. Fr_L and We_L are, respectively, the Froude and Weber dimensionless numbers for the liquid phase.

Avoiding the computationally intensive calculation of the rate of diffusion via Maxwell-Stefan formulations, we include a description of the limiting diffusivity (i.e., the diffusion of the unreacted base to the reaction plane):

$$D_L = x_B D_{B,H2O}^0 + x_{H2O} D_{H2O,B}^0 \quad \text{(S3)}$$

where the diffusivity coefficients at infinite dilution were estimated with the Wilke–Chang correlation:

$$D_{l,j}^{0} = 7.4\ 10^{-8}\frac{(\phi M_i)^{1/2}T}{\mu_i V_j^{0.6}} \tag{S4}$$

where M_j is the molecular weight of solvent j, V_i is the molecular volume of the solute i, and Φ is the association factor of the solvent [34].

The enhancement factor, E, depends on the Hatta number $Ha = \frac{\sqrt{D_B^L k_2 C_B^I}}{k_i^L}$ and it can be estimated for instantaneous reactions:

$$E_i = 1 + \frac{D_B c_B}{z D_L C_{CO2}^I} \tag{S5}$$

where D_B is the diffusivity coefficient of the amine (reactive) component in the aqueous phase, c_{CO2}^I is the molar concentration of CO_2 at the liquid interface, c_B is the molar concentration of the amine component, and D_L is the diffusion coefficient of component i in the liquid phase. For a fast pseudo-first order reaction, the enhancement factor can be estimated as [35]:

$$E \approx \frac{\sqrt{D_B^L k_2 C_B^I}}{k_i^L} = Ha \tag{S6}$$

where k_2 is the pseudo-first order reaction constant. The molar flux of CO_2 at the interface J_{CO2} can be calculated using:

$$J_{CO2} = k_{L,CO2}^{0} E\left(c_{CO2}^{0,I} - c_{CO2}^{B}\right) \tag{S7}$$

The solubility of CO_2 in the solvents (vapour liquid equilibrium, VLE) is calculated using either an equilibrium model, such as Gabrielsen *et al.* [36] for MEA and DEA, or using experimental data and fits for all other solvents. Both approaches lead to an equation that links the CO_2 loading ($\theta = x_{CO_2}/x_{Amine}$) with the CO_2 partial pressure in the flue gas, expressed as mole fraction y_{CO_2} for a given temperature. The minimum data requirement is a VLE for each operating temperature in the absorber and stripper. The losses/vaporization of solvent (amine and water) is calculated using the solvents' vapour pressure (Antoine equation).

The simplified approach described above captures the influence of the reaction kinetics, the mass transfer across the gas–liquid interface, the thermodynamic equilibrium and the hydrodynamics of the packing while reducing the numerical complexity of the model.

All heat exchangers are modelled as shell and tube exchangers, with Nusselt correlations for laminar and turbulent flow, depending on the Reynolds and Prandtl numbers for single-phase heat transfer:

$$Nu_t = \begin{cases} 1.86\ (Re_t Pr_t)^{\frac{1}{3}} \left(\frac{d_{\text{in}}}{L_{\text{tube}}}\right)^{\frac{1}{3}} \left(\frac{\mu}{\mu_w}\right)^{0.14} \\ C\ Re_t^{0.8} Pr_t^{1/3} \left(\frac{\mu}{\mu_w}\right)^{0.14} \end{cases} \quad (S8)$$

$$Nu_S = j_h RePr^{\frac{1}{3}} \left(\frac{\mu}{\mu_w}\right)^{0.14} \quad (S9)$$

Where $\mu_w =$ viscosity at wall temperature, $j_h =$ shell-side factor, $d_{\text{in}} =$ internal diameter of the tube, and $L_{\text{tube}} =$ length of tube.

The condenser is modelled as a horizontal shell and tube heat exchanger with condensation in the shell. The reboiler has been modelled as a thermosiphon using the model proposed by Chen for forced-convective boiling [37]. This method considers that the heat transfer of the boiling stream is the sum of the contribution of convective and nucleate boiling. The convective boiling coefficient h_{cb} can be estimated via a convective effective model:

$$h_{cb} = h'_{l_{in}} + h'_{nb} \quad (S10)$$

The first summand $h'_{l_{in}}$ is calculated based the Nusselt correlations (see equations 8) and corrected by a two-phase flow factor based on the Lockhart–Martinelli two-phase flow parameter [38]. The second summand h'_{nb} (nucleate boiling, nb) is described with the Foster and Zuber effective model [39].

$$h_{nb} = 0.00122 \left[\frac{k_l^{0.79} Cp_l^{0.45} \rho_l^{0.49}}{\sigma^{0.5} \mu_l^{0.29} \Delta H_{vap}^{0.24} \rho_v^{0.24}}\right] \left(T_{\text{wall}} - T_{\text{vap}}\right)^{0.24} \left(p_{\text{wall}} - p_{\text{vap}}\right)^{0.75} \quad (S11)$$

Where $k_l =$ thermal conductivity of the liquid, and ΔH_{vap} the enthalpy of vaporization.

REFERENCES

1. M. E. Boot-Handford *et al.*, "Carbon capture and storage update," *Energy Environ. Sci.*, vol. 7, no. 1, pp. 130–189, 2014.
2. M. Bui *et al.*, "Carbon capture and storage (CCS): the way forward," *Energy Environ. Sci.*, vol. 11, no. 5, pp. 1062–1176, 2018.
3. R. R. Bottoms, "Organic Bases for Gas Purification," *Ind. Eng. Chem.*, vol. 23, no. 5, pp. 501–504, May 1931.
4. C. Altintas *et al.*, "Database for CO_2 Separation Performances of MOFs Based on Computational Materials Screening," *ACS Appl. Mater. Interfaces*, vol. 10, no. 20, pp. 17257–17268, May 2018.
5. M. T. Mota-Martinez, J. P. Hallett, and N. Mac Dowell, "Solvent selection and design for CO_2 capture–how we might have been missing the point," *Sustain. Energy Fuels*, vol. 1, no. 10, pp.

2078–2090, 2017.
6. M. T. Mota-Martinez, P. Brandl, J. P. Hallett, and N. Mac Dowell, “Challenges and opportunities for the utilisation of ionic liquids as solvents for CO_2 capture,” *Mol. Syst. Des. Eng.*, vol. 3, no. 3, 2018.
7. Y.-J. Lin and G. T. Rochelle, “Optimization of Advanced Flash Stripper for CO_2 Capture using Piperazine,” *Energy Procedia*, vol. 63, pp. 1504–1513, Jan. 2014.
8. R. R. Bottoms, “Process for Separating Acid Gases,” *United States Patent, Appl. 1783901*, no. 1783901, 1930.
9. G. Puxty *et al.*, “Carbon Dioxide Postcombustion Capture: A Novel Screening Study of the Carbon Dioxide Absorption Performance of 76 Amines,” *Environ. Sci. Technol.*, vol. 43, no. 16, pp. 6427–6433, Aug. 2009.
10. S. Bishnoi and G. T. Rochelle, “Absorption of carbon dioxide into aqueous piperazine: reaction kinetics, mass transfer and solubility,” *Chem. Eng. Sci.*, vol. 55, no. 22, pp. 5531–5543, 2000.
11. S. Bishnoi and G. T. Rochelle, “Absorption of carbon dioxide in aqueous piperazine/methyldiethanolamine,” *AIChE J.*, vol. 48, no. 12, pp. 2788–2799, 2002.
12. D. Shaw, “Cansolv CO_2 capture: The value of integration,” *Energy Procedia*, vol. 1, no. 1, pp. 237–246, 2009.
13. D. G. Chapel, C. L. Mariz, and J. Ernest, “Recovery of CO_2 from Flue Gases : Commercial Trends,” *Can. Soc. Chem. Eng. Annu. Meet.*, p. 17, 1999.
14. Y.-J. Lin and G. T. Rochelle, “Optimum heat of absorption for CO2 capture using the advanced flash stripper,” *Int. J. Greenh. Gas Control*, vol. 53, pp. 169–177, 2016.
15. R. Dugas and G. Rochelle, “Absorption and desorption rates of carbon dioxide with monoethanolamine and piperazine,” *Energy Procedia*, vol. 1, no. 1, pp. 1163–1169, Feb. 2009.
16. S. A. Freeman, R. Dugas, D. Van Wagener, T. Nguyen, and G. T. Rochelle, “Carbon dioxide capture with concentrated, aqueous piperazine,” *Energy Procedia*, vol. 1, no. 1, pp. 1489–1496, 2009.
17. G. Rochelle, E. Chen, S. Freeman, D. Van Wagener, Q. Xu, and A. Voice, “Aqueous piperazine as the new standard for CO_2 capture technology,” *Chem. Eng. J.*, vol. 171, no. 3, pp. 725–733, 2011.
18. S. A. Freeman and G. T. Rochelle, “Density and Viscosity of Aqueous (Piperazine + Carbon Dioxide) Solutions,” *J. Chem. Eng. Data*, vol. 56, no. 3, pp. 574–581, Mar. 2011.
19. S. A. Freeman, R. Dugas, D. H. Van Wagener, T. Nguyen, and G. T. Rochelle, “Carbon dioxide capture with concentrated, aqueous piperazine,” *Int. J. Greenh. Gas Control*, vol. 4, no. 2, pp. 119–124, 2010.
20. P. T. Frailie, J. M. Plaza, and G. T. Rochelle, “Thermodynamics of Aqueous Methyldiethanolamine/Piperazine for CO_2 Capture,” in *Process Systems and Materials for CO_2 Capture: Modelling, Design, Control and Integration* (Papadopoulos and Seferlis, editors). Wiley, 2017.
21. X. Chen, F. Closmann, and G. T. Rochelle, “Accurate screening of amines by the Wetted Wall Column,” *Energy Procedia*, vol. 4, pp. 101–108, Jan. 2011.
22. T. T. Teng, Y. Maham, L. G. Hepler, and A. E. Mather, “Viscosity of Aqueous Solutions of N-Methyldiethanolamine and of Diethanolamine,” *J. Chem. Eng. Data*, vol. 39, no. 2, pp. 290–293, Apr. 1994.
23. E. I. Concepción, Á. Gómez-Hernández, M. C. Martín, and J. J. Segovia, “Density and viscosity measurements of aqueous amines at high pressures: DEA-water, DMAE-water and TEA-water mixtures,” *J. Chem. Thermodyn.*, vol. 112, pp. 227–239, 2017.
24. A. Muhammad, M. Abdul Mutalib, M. Thanapalan, and A. Shafeeq, *Thermophysical Properties of Aqueous Piperazine and Aqueous (N-Methyldiethanolamine + Piperazine) Solutions at Temperatures (298.15 to 338.15) K*, vol. 54. 2009.

25. H. Kierzkowska-Pawlak, “Carbon Dioxide Removal from Flue Gases by Absorption/Desorption in Aqueous Diethanolamine Solutions,” *J. Air Waste Manage. Assoc.*, vol. 60, no. 8, pp. 925–931, Aug. 2010.
26. S. Gabriel and J. Weiner, “Ueber einige Abkömmlinge des Propylamins,” *Berichte der Dtsch. Chem. Gesellschaft*, vol. 21, no. 2, pp. 2669–2679, 1888.
27. Walden P., “Molecular weights and electrical conductivity of several fused salts,” *Bull. Acad. Imper. Sci. (St. Petersburg)*, vol. 1800, 1914.
28. E. Y. Y. Kenig, R. Schneider, and A. Górak, “Reactive absorption: Optimal process design via optimal modelling,” *Chem. Eng. Sci.*, vol. 56, no. 2, pp. 343–350, 2001.
29. W. K. Lewis and W. G. Whitman, “Principles of Gas Absorption,” *Ind. Eng. Chem.*, vol. 16, no. 12, pp. 1215–1220, 1924.
30. J. Wilcox, P. Rochana, A. Kirchofer, G. Glatz, and J. He, “Revisiting film theory to consider approaches for enhanced solvent-process design for carbon capture,” *Energy Environ. Sci.*, vol. 7, no. 5, p. 1769, 2014.
31. E. Y. Kenig, R. Schneider, and A. Górak, “Rigorous dynamic modelling of complex reactive absorption processes,” *Chem. Eng. Sci.*, vol. 54, no. 21, pp. 5195–5203, 1999.
32. K. Onda, E. Sada, and H. Takeuchi, “Gas absorption with chemical reaction in packed column,” *J. Chem. Eng. Japan*, no. 1963, pp. 62–66, 1967.
33. K. Onda, H. Takeuchi, and Y. Okumoto, “Mass Transfer Coefficients Between Gas and Liquid Phases in Packed Columns,” *J. Chem. Eng. Jpn.*, vol. 1, no. 1, pp. 56–62, 1968.
34. C. R. Wilke and P. Chang, “Correlation of diffusion coefficients in dilute solutions,” *AIChE J.*, vol. 1, no. 2, pp. 264–270, Jun. 1955.
35. D. W. van Krevelen and P. J. Hoftijzer, “Kinetics of simultaneous absorption and chemical reaction.,” *Chem. Eng. Prog.*, vol. 44, pp. 529–536, 1948.
36. J. Gabrielsen, M. L. Michelsen, E. H. Stenby, and G. M. Kontogeorgis, “A Model for Estimating CO_2 Solubility in Aqueous Alkanolamines,” *Ind. Eng. Chem. Res.*, vol. 44, no. 9, pp. 3348–3354, 2005.
37. J. C. Chen, “Correlation for Boiling Heat Transfer to Saturated Fluids in Convective Flow,” *Ind. Eng. Chem. Process Des. Dev.*, vol. 5, no. 3, pp. 322–329, Jul. 1966.
38. R. W. Lockhart and R. C. Martinelli, “Proposed correlation of data for isothermal two-phase, two-component flow in pipes,” *Chem. Eng. Prog., Symp. Ser.*, vol. 45, pp. 39–48, 1949.
39. H. K. Forster and N. Zuber, “Dynamics of vapor bubbles and boiling heat transfer,” *AIChE J.*, vol. 1, no. 4, pp. 531–535, 1955.
40. IEAGHG Report 2012/08, CO_2 Capture at Gas Fired Power Plants, July 2012.
41. J. R. Couper, “Chemical Process Equipment Selection and Design,” in *Chemical Process Equipment Selection and Design*, 2nd ed., J. R. Couper, Ed. Butterworth-Heinemann, 1990, pp. 663–690.
42. C. Kolster, E. Mechleri, S. Krevor, and N. Mac Dowell, “The role of CO_2 purification and transport networks in carbon capture and storage cost reduction,” *Int. J. Greenh. Gas Control*, vol. 58, pp. 127–141, Mar. 2017.
43. P. Brandl, S. M. Soltani, P. S. Fennell, and N. M. Dowell, “Evaluation of cooling requirements of post-combustion CO_2 capture applied to coal-fired power plants,” *Chem. Eng. Res. Des.*, vol. 122, 2017.
44. R. K. Sinnott, “Chapter 6-Costing and Project Evaluation,” in *Chemical Engineering Technical Series:Volume 6 Chemical Engineering Design*, Second Edition, Pergamon, 1993, pp. 209–244.
45. B. Smit *et al.*, “CCS–A technology for the future: general discussion,” *Faraday Discuss.*, vol. 192, no. 0, pp. 303–335, 2016.

46. Choi, G., Chu, R., Degen, B., Wen, H., Richen, P., and Chinn, D., "CO_2 Removal from Power Plant Flue Gas – Cost Efficient Design and Integration Study," in Carbon Dioxide Capture for Storage in Deep Geologic Formations–Results from the CO_2 Capture Project, Vol 1; D.C.Thomas (editor); Elsevier, 2005.
47. Elkady, A., Evulet, A., Brand, A., "Application of Exhaust Gas Recirculation for Post Combustion CO_2 Capture: Effect on Lean Premixed Combustion," in *Carbon Dioxide Capture for Storage in Deep Geologic Formations – Results from the CO_2 Capture Project, Vol 3*; L.I.Eide (editor); CPL Press, 2009.
48. Couper JR. Chemical Process Equipment Selection and Design. In: Couper JR, editor. *Chemical Process Equipment Selection and Design*. 2nd ed. Butterworth-Heinemann; 1990. p. 663–90.

Carbon Dioxide Capture for Storage in Deep Geological Formations, Volume 5
Karl F. Gerdes (Editor)
© 2022 BP. All rights reserved.

Chapter 16

DEVELOPMENT OF GRAPHENE OXIDE-BASED MEMBRANES FOR CO_2 CAPTURE

Shenxiang Zhang[1], Huanghe Li[1], Fan Wang[1], Miao Yu[1], Weiwei Xu[2], Howard Meyer[2], Shiguang Li[2]

[1]Rensselaer Polytechnic Institute (RPI), Troy, NY 12180, USA
[2]Gas Technology Institute (GTI), Des Plaines, IL 60018, USA

ABSTRACT: Ultrathin graphene oxide (GO)-based membranes with grafted, brush-like CO_2-philic agents are prepared by a facile coating process onto a porous polymeric substrate for highly efficient CO_2/N_2 separation under wet condition. Amine-containing molecules, such as piperazine and diethylenetriamine (DETA), as an effective CO_2-philic agent, are introduced as a carrier-brush into the GO nanochannels with physical/chemical bonding. Both hollow fiber support and flat sheet support are used for depositing GO-based membranes. These membranes exhibit excellent separation performance under simulated flue gas conditions with CO_2 permeance >1,000 GPU and CO_2/N_2 selectivity of 300, demonstrating great potential for post-combustion CO_2 capture.

KEYWORDS: CO_2 capture, graphene oxide, membrane separation, CO_2-philic agent, facilitated transport

INTRODUCTION

CO_2 emissions from the combustion of fossil fuels is considered a primary reason for human-induced climate change, which has raised a widespread environmental concern [1]. The 2020 Carbon Capture Program, administered by the US Department of Energy (DOE), announced the post-combustion capture goal of achieving 90% CO_2 capture with <35% increase in the levelized cost of energy [2]. To achieve this goal, various carbon capture technologies, such as adsorption, absorption, and membrane separation, have been widely investigated [3].

Membrane separation is based on the difference of gas permeation rates through membrane barriers. It has been considered a very promising technology because of the potential to achieve high energy efficiency, low capital investments, operational simplicity, and flexibility to scale up [4–7]. Polymer membranes were first proposed for CO_2 separation in the late 1970s due to their superior film-forming ability and processability [4,8]. Many following studies have been conducted to explore the potential of polymer membranes for CO_2 separation. In particular, Membrane Technology and Research, Inc. (MTR) reported their Polaris™ membrane with a CO_2 permeance of 1,000 to 2,000 GPU (Gas Permeance Unit; 1 GPU = 1×10^{-6} cm^3(STP) cm^{-2} s^{-1} cm Hg^{-1} = 3.348×10^{-10} mol m^{-2} s^{-1} Pa^{-1}) and a CO_2/N_2 mixture separation selectivity of 50 – 60 [9]. This membrane has been scaled up to a 2,000 m^2 pilot scale system and tested for coal-fired flue gas CO_2 capture at the National Carbon Capture Center [10]. Polymer membranes, however, due to the intrinsic mobility of polymer chains, suffer the trade-off between permeability and selectivity, and thus are usually constrained by an upper bound limit [11]. Thus, it remains a big challenge to produce highly permeable and selective membranes for CO_2 capture.

Graphene-based materials, such as graphene and graphene oxide (GO) (Figure 1), have been studied as promising next-generation membrane materials. They are only sub-nanometer thick and thus may form ultrathin separation membranes to minimize transport resistance and maximize flux. Initial research efforts by this group aimed at developing ultrathin, graphene-based membranes demonstrated the feasibility of using a vacuum filtration process to fabricate ultrathin GO membranes (thickness of ~ 1.8 nm) on a porous substrate [12]. The structural defects on GO flakes provide molecular-sized pores that can serve as a transport pathway for selective gas separations.

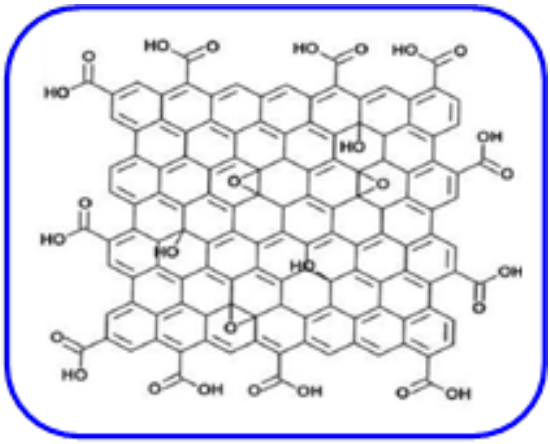

Figure 1. Chemical structural model of GO.

This development of GO-based membranes for CO_2 capture from flue gases is being done under support by DOE (DE-FE0026383). The high-selectivity membranes showed CO_2 permeances as high as 1,020 GPU with a CO_2/N_2 selectivity of 680, much higher than the state-of-the-art membranes [13].

After extensive material and structure optimization, we have also developed high-flux membranes using GO quantum dots (GOQD), which are graphene nanoparticles less than 100 nm in diameter, as a membrane building block. Until this work, GOQD materials have not been employed as building blocks to form new membrane structures, due to the intrinsic difficulty in assembling GOQD on porous ultrafiltration membranes, which have pores much larger than the GOQD. We report a method of depositing single-walled carbon nanotubes (SWCNT) as an ultrathin (50 nm) "skeleton" layer on a commercially available polyether sulfone (PES) porous membrane to support the assembly or "growth" of a layer of nitrogen-doped GOQDs to form a densely packed GOQD-based membrane [14]. Nitrogen-doped GOQD (N-GOQD)/SWCNT membrane transport interstices can be functionalized by crosslinking CO_2-philic agents, such as amine molecules, to boost gas permeance and selectivity. This amine/N-GOQD/SWCNT/PES membrane achieves CO_2 permeance of 1,450 GPU and 520 CO_2/N_2 selectivity at 80°C using a sweep gas on the permeate side.

For CO_2 capture from flue gas with membranes, especially under moderate-temperature and high-humidity conditions, membrane stability – mainly due to loss of the amine – is a challenge [15]. We developed a facile and generic strategy to fabricate a stable and highly CO_2 permeable membrane in nanowire network where amine-carriers are confined/stabilized by electrostatic forces [15]. In this work, a SWCNT network with high porosity and sub-10-nm pore size was prepared on a porous PES substrate to form a strong "skeleton" for the infiltrated CO_2-selective layer. Then, a coating solution containing GOQD, negatively charged poly(sodium-p-styrenesulfonate) (PSS) and protonated amine-

carrier was cast onto the SWCNT network to form an amine/N-GOQD/PSS/SWCNT/PES membrane. In this structure, the mechanically strong, interconnected nanowires act as the frame for the selective layer and provide numerous nanochannels for gas transport. Negatively charged PSS can wrap around SWCNT firmly to provide stable anchoring points for amine-carriers within the nanochannels of SWCNT network. By virtue of the carrier-facilitated transport in which there is a fast reaction between CO_2 and the amine groups ($CO_2 + R - NH_2 + H_2O \leftrightarrow HCO_3^- + R - NH_3^+$) [16], simultaneous high CO_2 permeance (up to 3,300 GPU) and high CO_2/N_2 selectivity (400) were achieved at 90 °C with 0.3 bar (absolute pressure) on the permeate side, which is the best reported separation performance for facilitated transport membranes.

We tested the stability of GO-based membranes at near-realistic flue gas conditions (saturated with water vapor and containing O_2, SO_2 and NO_x). Our results indicate membrane performance is not affected by SO_2 and NO_x. We scaled-up the GO-based membranes to modules with effective areas of 500-1,000 cm^2. A GO-based membrane with surface area of 1,000 cm^2 was fabricated on a hollow fiber substrate. The membrane showed CO_2 permeance of 984 GPU with CO_2/N_2 selectivity of 330 at 80°C. at a 40.3 % CO_2 capture rate. The CO_2 purity on the permeate side was as high as 96.6 %.

EXPERIMENTAL METHODS

Chemicals and Materials

Chemicals: Citric acid (ACS reagent, ≥99.5%), ammonia (28.0–30.0% NH_3 solution), sodium sulfate (ACSreagent, ≥99.0%), dopamine hydrochloride (99%), poly(sodium 4-styenesulfonate) (average MW: ~1,000,000) and Diethylenetriamine (DETA, 99%) were purchased from Sigma-Aldrich and used without further purification. Single wall carbon nanotubes (SWCNT) (diameter: < 3 nm, length: > 5 μm, purity: > 85%) and sodium dodecylbenzenesulfonate (> 95.0%) were purchased from TCI, US, and used as received.

Polymeric substrates: PES hollow fiber membrane (pore size: 25 nm; inside diameter: 0.8 mm; outside diameter: 1.2 mm) was purchased from Hydronautics, CA. The PES flat sheet membrane with effective pore size of 0.45 μm was commercially available from Sterlitech (WA, USA). "Minikros Sampler" PES hollow fiber membrane module was purchased from Repligen company with effective surface area of 1,000 cm^2 and molecular weight cut-off of 500 Kilodalton (KDa).

Preparation of N-GOQD

N-GOQD was synthesized by carbonization of citric acid (CA) with ammonia by hydrothermal treatment, as described previously with some modification [17,18]. In brief, 80 ml of a CA aqueous solution (100 mg/mL) and 20 mL ammonia aqueous solution (30%) were transferred into a Teflon®-lined autoclave and heated at 180 °C for 24 h. After cooling to room temperature, the pH of the light yellow GOQD suspension was adjusted to 8 by adding NaOH solution (1 mg/mL) dropwise. The resultant dark-yellow N-GOQD solution was dialyzed in dialysis tubing (3,000 Da, Spectrum Lab. Inc.) against DI water for 4 h to remove impurities and excess ammonia. After dialysis, an aqueous suspension of N-GOQD was centrifuged at 10,000 rpm to remove any aggregates.

Preparation of Polydopamine Modified SWCNTs

A dispersion of SWCNT was prepared by adding 10 mg SWCNT and 100 mg sodium dodecylbenzene sulfonate to 100 mL DI water, followed by sonication for 10 hours under a power of 2 kW (ultrasonic bath, Branson Ultrasonics™). The dispersion was then centrifuged at 10,000 rpm for 45 min to remove any undispersed SWCNTs. The concentration of the final SWCNTs dispersion was 0.02 mg mL^{-1}. Then 10 mg dopamine hydrochloride was added followed by stirring for 1 hour at 40°C, and 10 ml

0.1 M HCl–Tris (pH = 7.5) was added with a further stirring for 36 h at 40°C. The final solution was centrifuged at 10,000 rpm for 30 min to obtain the polydopamine/SWCNT dispersion. The bulk dispersion was diluted into 0.005 mg/mL^{-1} prior to deposition on the membrane substrate. This method of making a polydopamine/SWCNT dispersion is not optimized for commercial use but serves as a proof of concept.

Preparation of GOQD-Based Membranes On Hollow Fiber Support

N-GOQD/SWCNT/PES Membrane

Two coating solutions were prepared by diluting the SWCNT suspension to 0.005 mg/mL and N-GOQD dispersion to 0.1 mg/mL, respectively, and then sonicating for 10 mins. Ultrathin N-GOQD/SWCNT membranes were fabricated using a vacuum assisted coating method by sequential application of SWCNT and then N-GOQD to the polymer substrate. First, the coating solution (SWCNT or N-GOQD) was pumped into the tube side of a PES hollow fiber membrane by a syringe pump with a constant flow rate of 0.5 mL/min until the solution continuously flowed through the coating solution exit channel without any air bubbles. Subsequently, a vacuum was applied on the outside of the fibers to draw suspended particles into the substrate. The process was stopped after a specific time interval of vacuum filtration (20 or 40 mins for SWCNT coating, and 20 mins for N-GOQD coating in this work). To protect the as-seeded SWCNT framework or N-GOQD/SWCNT membrane layers, we sealed the two ends (the tube-side inlet and outlet) of the hollow fiber supports with an impulse sealer (PFS-100) and disconnected the coating module from the solution tubes. A further vacuum and drying step of 30 minutes was used to remove all the water from the inside of hollow fiber and to consolidate a high quality and uniform coating layer. Overall, each layer (SWCNT and NGOQD layers) was deposited by this two-step vacuum assisted coating method. A heat drying step (60°C for 2 hours) was conducted after SWCNT coating and before N-GOQD coating to stabilize the carbon skeleton structure, and a heat treatment at 80°C was conducted after N-GOQD coating.

DETA/N-GOQD/PSS/SWCNT/PES Membrane

An amine-carrier solution containing GOQD (1 mg/mL), Poly(sodium 4-styenesulfonate) PSS (30 mg/mL) and Diethylenetriamine (DETA) (100 mg/mL) was coated onto the inside surface of PES hollow fibers previously coated with a CNT layer. The amine-carrier coating solution was pumped through the tube side of the hollow fibers at a constant rate of 5 mL/min until the solution continuously exited the hollow fibers without any air bubbles and was further maintained for 2 minutes. The residual amine-carrier coating solution was purged with nitrogen. The membrane module was dried in an oven at 60°C for 1 hour. Before separation performance testing, the membrane module was heated at 80°C and 100% humidity for 2 hours.

Preparation of GOQD-Based Membranes on Flat Sheet Support

DETA/N-GOQD/PSS/SWCNT/PES Flat Sheet Membrane

A flat sheet PES support (450 nm average pore size) was first coated with SWCNT suspension by vacuum filtration. The resulting SWCNT/PES substrate typically had a SWCNT framework layer of 100 - 200 nm thickness depending on the extent of loading. The CNT-loaded substrate was dried before a secondary coating. An amine-carrier coating solution containing 0.5 mg/mL GOQD, 30 mg/mL PSS and 100 mg/mL DETA was coated on the surface of the prepared CNT network by either casting or inkjet printing. For the casting method, a glass rod is used to spread drops of DETA/GOQD/PSS solution onto the CNT-covered surface of the SWCNT/PES substrate to make a relatively uniform, thin coating layer. For the inkjet printing method, the DETA/GOQD/PSS ink solution is printed onto the SWCNT/PES substrate with a modified inkjet printer. The resulting DETA/GOQD/PSS/SWCNT/PES flat sheet membrane was dried for 30 min at room temperature

before being assembled into the flat sheet membrane module. Before separation performance testing, the membrane module was heated at 80℃ and fed with $CO_2/N_2/H_2O$ simulated flue gas at 100% relative humidity for 2 hours.

Membrane Characterization Methods

Scanning Electron Microscopy and Transmission Electron Microscopy

The membrane surface and cross-sectional morphology were observed by Field Emission Scanning Electron Microscope (Carl Zeiss SUPRA 55 FESEM). For cross-sectional analysis, the sample was cryogenically fractured in liquid nitrogen. All the samples were sputtered for 60 seconds to obtain a thin gold layer before SEM tests. Particle size and distribution of N-GOQD was observed with transmission electron microscopy (TEM, JEM-2100F, JEOL Ltd. Japan).

X-Ray Photoelectron Spectroscopy

The N-GOQD and N-GOQD/SWCNT/PES membrane chemical compositions were analysed by X-ray photoelectron spectroscopy (Kratos Axis Ultra DLD XPS system).

Attenuated Total Reflectance-Fourier Transform Infrared Spectroscopy (ATR-FTIR)

The material and membrane chemical properties were characterized by attenuated total reflectance-Fourier transform infrared spectroscopy (PerkinElmer Spectrum 100 FT-IR). Spectra were recorded from 500 to 4000 cm^{-1}.

Membrane Separation Performance Testing

Two testing configurations on the permeate side were employed for the membranes: sweep and vacuum.

Hollow Fiber Membrane Sweep Testing Procedure

For sweep testing, the measurements of membrane transport properties were conducted by using the gas permeation system shown in Figure 2. The membrane module with one hollow fiber (active membrane area: 0.5024 cm^2) was contained in a cylindrical stainless steel cell inside a temperature-controlled oven (Forced Convention Oven, JeioTech Co., Ltd. US). The feed gas was a mixture of CO_2 (99.999%, Airgas, US) and N_2 (99.999%, Airgas, US), and the composition was controlled using mass flow controllers (MFC) on each gas. The sweep gas for the permeate was Helium (99.999%, Airgas, US). Before contacting the hollow fiber membranes, the feed gas and the sweep gas (He) were saturated with water vapor by bubbling through humidifiers followed by a vessel with glass beads to remove condensed or entrained water. The relative humidity (RH) on the feed side was measured at >99%.

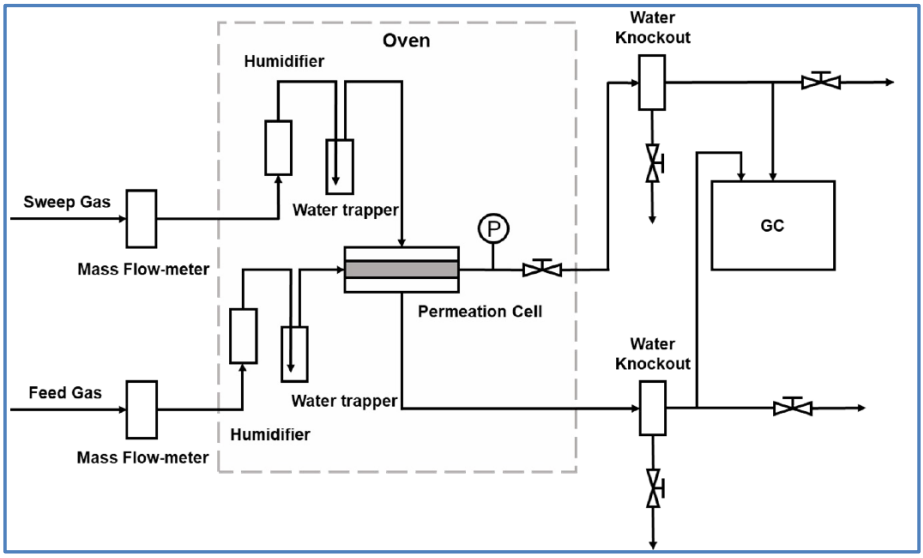

Figure 2. Schematic diagram of sweep testing mode for hollow fiber membrane module.

The retentate and permeate streams leaving the oven were cooled to ambient temperature and condensed water was removed in knockout vessels before the streams entered an Agilent HP-5890-II gas chromatograph (GC) (Agilent Technologies) for gas composition analyses. Helium was used as the carrier gas. The GC used a RESTEK Rt-UBOND 19750 (Restek, Bellefonte, PA) column and thermal conductivity detector (TCD). The membrane system was operated under specific conditions (temperature and pressure) and feed gas composition until the GC showed constant composition for at least 30 minutes to ensure steady state. The feed rate was high enough to avoid concentration polarization. The permeance of CO_2 and N_2 was calculated from the sweep gas flow rate and composition. The permeate pressure in the system was maintained at atmosphere pressure.

The permeation temperature was maintained by the oven. The gas flow rate was measured with a gas flowmeter (ADM2000, Agilent Tech., DE, US.). The pressure was adjusted by a needle valve and measured by a pressure gauge at the retentate exit as shown in Figure 2. The feed pressure was set at 1-2 psig to avoid back-flow of sweep gas, and the sweep pressure was set close to atmospheric pressure. Gas flow rates were accurately set by flow meters (Brooks Instrument, Hatfield, PA) at 80 cm^3 (STP)/min (sccm) for the feed side and 20 sccm for the sweep side. Depending on the particular test, the feed and sweep gases directly entered the cell as dry gas or passed through the humidifier as wet gas with >99% humidity (measured by SRH77A Temperature/Humidity Instrument, Cooper-Atkins, CT, US.).

Flat Sheet Membrane Vacuum Testing Procedure

For the vacuum testing mode, a flat sheet membrane was installed in a stainless steel permeation cell inside a temperature-controlled oven (Figure 3). Simulated flue gas containing 85 vol% N_2 and 15 vol% CO_2 to represent coal flue gas was maintained at 1 bar absolute. The flow rate was controlled by a mass flow controller (MFC). Before entering the permeation cell, feed gas was saturated with water vapor by bubbling through a humidifier inside the oven. A vacuum is drawn on the permeate side of the cell with a scroll pump (Edwards nXDS). To avoid water condensation in the vacuum pump, dry He controlled by MFC 2 was used to dilute the permeate gas before leaving the oven. The

permeate pressure was controlled at 0.3 bar (absolute pressure) by a needle valve (Swagelok, OH) and a digital vacuum pressure gauge (Dwyer DPGA-00), which was workable for this short term testing. The diluted permeate gas was fed directly to a GC (Agilent 6890) for composition analysis.

The permeance, $\mathbf{P}_i$, of gas species '*i*' was calculated by equation (1):

$$\mathbf{P}_i = X_i / (A \bullet \Delta P) \quad (1)$$

where X_i is the molar flow rate of component *i* through the membrane (mol s^{-1}), A is the membrane area (m^2), and ΔP is the transmembrane pressure difference for the component *i* (Pa). The selectivity of CO_2 over N_2 was calculated by equation (2):

$$\alpha = \mathbf{P}_{CO2} / \mathbf{P}_{N2} \quad (2)$$

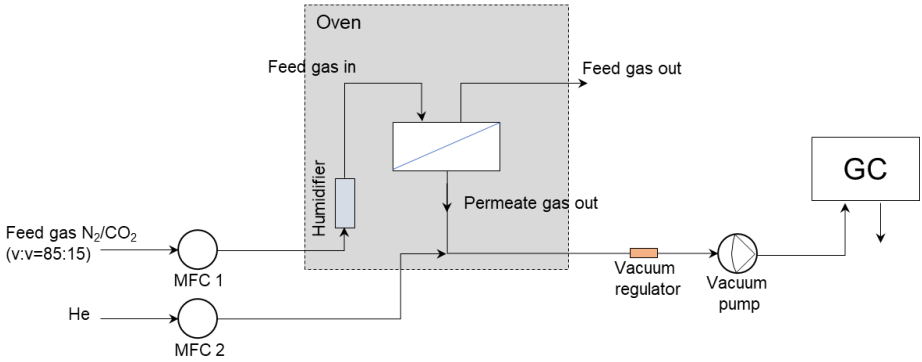

Figure 3. Schematic diagram of vacuum testing rig for both hollow fiber and flat sheet membranes.

Commercial Hollow Fiber Substrates for Membrane Scaleup

Membrane scaleup was inititated with commercial hollow fiber substrates with an effective area of 55 cm^2 shown in Figue 4(a). The detailed structure and morphology of PES hollow fiber membrane were charaterized by SEM. As shown in Figure 4 (b), the inner diameter is around 1 mm. The wall thickness is about 100 μm. The inner surface of the PES hollow fiber is very smooth and has pores in the range of 50-200 nm (Figure 4 (c)). The porosity in the porous Polyethersulfone (PES) substrate layer is about 10 %. Figure 4 (d) and (e) show that under the skin layer is a porous support layer with a porous strcture, which allows high permeance for gas separation.

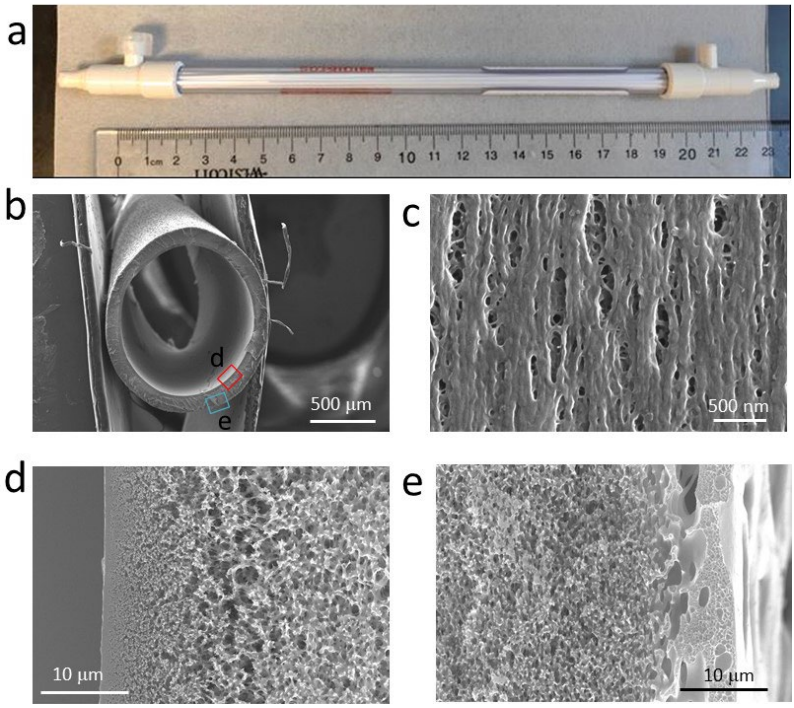

Figure 4. (a) Images of a PES hollow fiber membrane module. (b) Cross-sectional SEM image of PES hollow fiber membrane. (c) Inner surface SEM image of PES hollow fiber membrane. (d) and (e) Enlarged cross-sectional SEM images of PES hollow fiber membrane.

Stability Testing of GO-Based Membranes in The Presence of Flue Gas Contaminants

The stability of GO-based membranes in the presence of flue gas contaminants was tested in a unit (Figure 5) located in a walk-in hood with negative pressure relative to the laboratory. Figure 6 shows a process flow diagram of the gas permeation system. A pre-mixed simulated flue gas containing 46 ppmv SO_2, 3.0 vol.% O_2, 11.0 vol% CO_2, and balance N_2 was used in the test. A syringe pump was used to add water to the loop to regulate the water vapor concentration. The liquid water is pumped in and mixed with the $SO_2/O_2/CO_2/N_2$ mixture inside the oven so that the water is vaporized prior to entering the membrane cell.

Figure 5. Photograph of a gas permeation system.

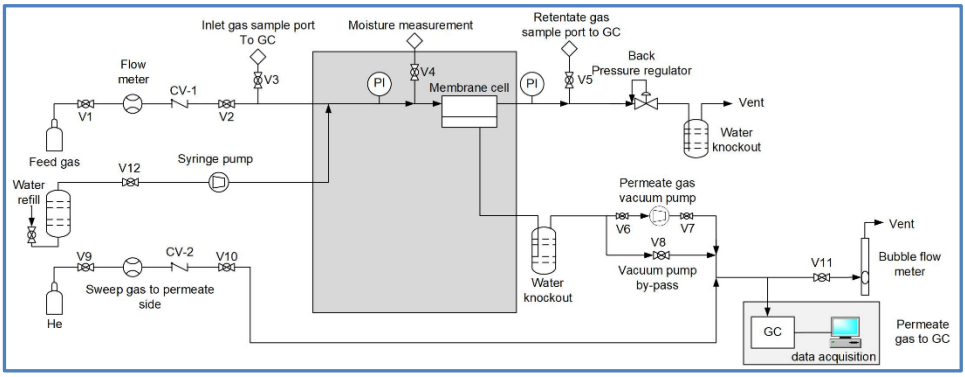

Figure 6. Process flow diagram (PFD) of the gas permeation system.

RESULTS AND DISCUSSION

Characterization of N-GOQDS

Figure 7 (a) shows the dark-yellow N-GOQD powder after drying. Figure 7 (b) compares N-GOQDs in DI water (0.6 mg/mL) in the freshly prepared state (left) and after one month (right), respectively. The super hydrophilic nature of N-GOQDs maintains a well-dispersed, stable suspension. The as-synthesized N-GOQDs were further characterized to determine particle size and composition. The TEM image in Figure 7 (c) shows that the N-GOQD particles are around 3 to 8 nm. The lattice fringes of a N-GOQD with a *d*-spacing of 0.215 nm (Figure 7 (d)) are consistent with the (100) facet of graphene and its crystalline structure. The corresponding fast Fourier transform (FFT) pattern (Figure 7 (e)) confirms the hexagonal carbon network of N-GOQDs.

An XPS full scan of N-GOQDs shows a predominant graphitic C 1s peak at around 285 eV, a N 1s peak at 400 eV, and a O 1s peak at 532 eV. The O/C atomic ratio for as-synthesized N-GOQDs is 0.316. The N peak confirms the incorporation of N atoms into GOQDs by the hydrothermal reaction.

The N/C ratio reaches 0.139, which is higher than that in reported nitrogen-doped graphene quantum dots [20]. This demonstrates improved N atom conjugation by the synthesis method developed in this work. Figure 7(f) shows the deconvoluted C 1s spectrum of the N-GOQDs ranging from 280 to 292 eV. Five characteristic peaks emerge at 284.5, 285.6, 286.5, 287.8, and 288.7 eV, which are attributed to C-C, C-N, C-O, C=O, and O-C=O bonds, respectively. The high-resolution N 1s spectrum is deconvoluted in Figure 7(g), which shows the presence of the pyridinic (399.4 eV), pyrrolic (400.5 eV), and graphitic (401.5 eV) nitrogen atoms, respectively. The high percentages of pyridinic and pyrrolic nitrogen suggest that most of the N atoms were located at the graphene panel edge.

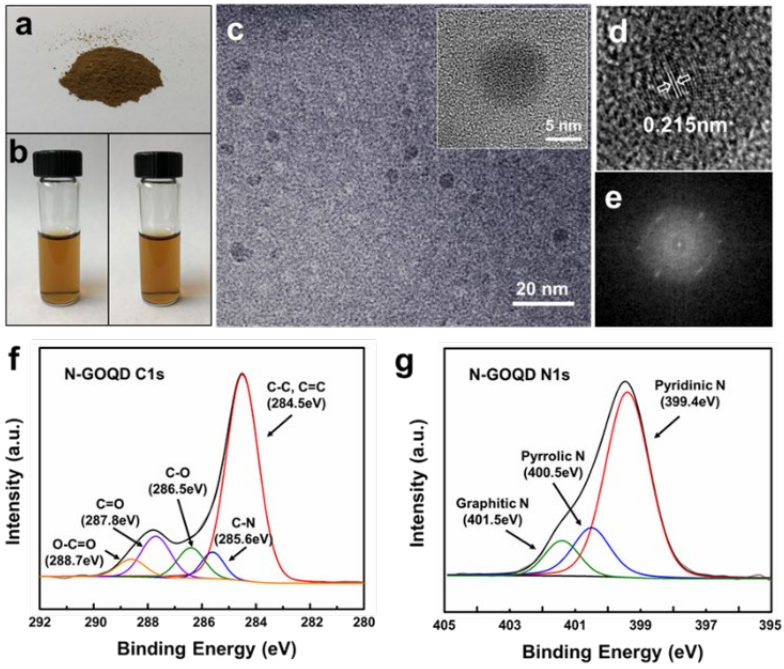

Figure 7. Digital photos of (a) N-GOQD powder and (b) N-GOQDs dispersed in DI water in the freshly-prepared state (left) and after a month (right), respectively. (c) High-resolution TEM image of N-GOQDs; the inset is the image at higher resolution. (d) TEM image showing the d1 spacing (0.215 nm) between the lattice fringes. (e) Fast Fourier transform (FFT) pattern of N-GOQDs. Deconvoluted XPS spectra of (f) C 1s and (g) N 1s of N-GOQDs.

Characterization of N-GOQD/SWCNT/PES Membrane

In this work, we used 30 nm-pore PES substrates in both hollow fiber and flat sheet form as supports. The method used to fabricate ultrathin, compact membranes composed of GOQD is illustrated in Figure 8. First, an ultrathin SWCNT-based “skeleton” layer with pores smaller than or comparable to GOQD is deposited on the substrate. N-GOQDs are then infiltrated into the SWCNT “skeleton” as “flesh”, followed by a heat treatment to form a dense layer.

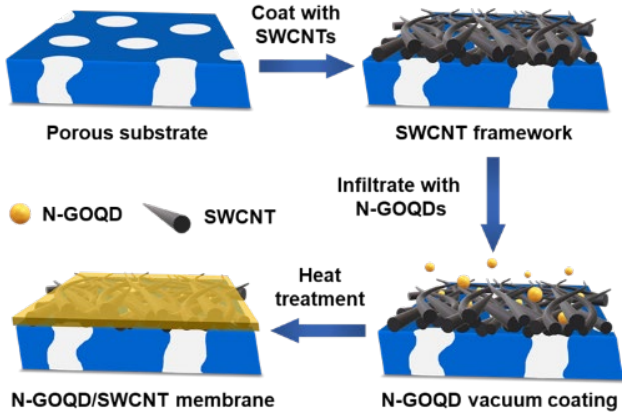

Figure 8. Schematic illustration of N-GOQD/SWCNT membrane preparation.

SWCNTs have been extensively investigated for membrane fabrication as either free-standing membranes or as inorganic fillers for mixed matrix membranes due to the porous structure and strong mechanical properties [21]. In this work, SWCNTs were pre-treated with polydopamine to produce a hydrophilic surface to maintain a stable dispersion in water. A vacuum-assisted coating process is used to deposit an ultrathin polydopamine-SWCNT coating several tens of nanometers thick with a net-like structure as the carbon skeleton. As shown in Figure 9 (a), the SWCNT support layer exhibits a highly interconnected net-like structure with high surface porosity, and the effective pore size is reduced to a few nanometers. The cross-sectional SEM image in Figure 9 (b) shows that the thickness of SWCNT layers is ~50 nm.

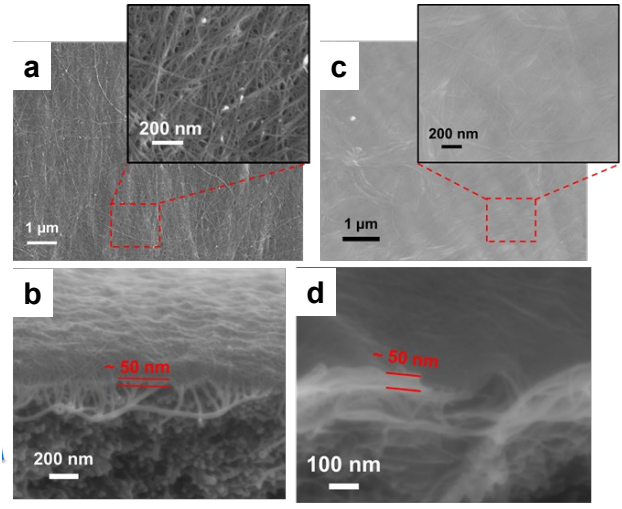

Figure 9. (a) Surface and (b) cross-sectional SEM images of the SWCNT framework layer. (c) Surface and (d) cross-sectional SEM images of the N-GOQD/SWCNT membrane.

N-GOQDs are infiltrated into the SWCNT ultrathin mesh layer by vacuum-assisted deposition, followed by a heat treatment at 80°C for 2 hours to crosslink N-GOQDs with polydopamine coated SWCNTs and to produce a dense N-GOQD/SWCNT composite membrane. The SWCNT supported N-GOQD membranes were characterized by FESEM. The membrane surface morphology is shown in Figure 9 (c); a uniform, dense and high-quality membrane layer was formed by completely filling SWCNT mesh pores with N-GOQDs. The SWCNT backbone under the coating layer can still be seen, demonstrating that the membrane structure consists of the carbon skeleton and carbon quantum dot filling units. The ultrathin thickness is revealed by the cross-sectional SEM image (Figure 9 (d)), which shows an approximately 50 nm thick membrane layer on the polymer support.

The chemical composition of the as-prepared N-GOQD/SWCNT membrane was examined by XPS and FTIR spectroscopy. Figure 10 (a) shows the XPS elemental surveys of the 1D SWCNT framework and the N-GOQD/SWCNT composite membrane, respectively. After incorporating N-GOQDs into the SWCNT framework, the oxygen and nitrogen content increased from 7.0 and 2.7% to 14.5 and 6.5%, respectively, suggesting the successful loading of N-GOQDs in the SWCNT skeleton. The deconvoluted C1s spectrum (Figure 10 (b)) clearly exhibits C=O and O-C=O peaks, resulting from the carboxyl groups at the edge of N-GOQDs. Compared to the C1s spectrum of N-GOQDs (Figure 7 (f)) and SWCNT mesh, the slightly enhanced C-N peak could be evidence of the crosslinking between the N-GOQDs and the polydopamine coating on SWCNTs. The FTIR spectrum (Figure 10

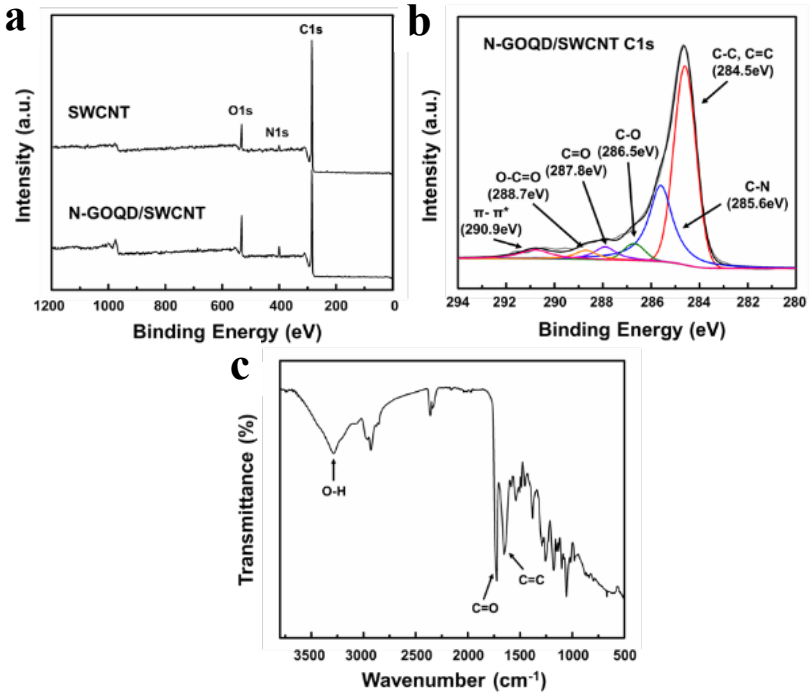

Figure 10. (a) XPS full surveys of the SWCNT mesh and N-GOQD/SWCNT membrane. (b) Deconvoluted C 1s XPS spectrum of the N-GOQD/SWCNT membrane. (c) ATR-FTIR spectrum of the N-GOQD/SWCNT membrane.

(c)) further verified the N-GOQD/SWCNT membrane chemical composition. As compared to the SWCNT skeleton, new peaks at 1,651 and 1,753 cm^{-1} emerged because of the C=C and C=O stretching vibrations from N-GOQD. The peak at 3,297 cm^{-1} corresponds to the -OH groups on the surface of N-GOQDs.

Characterization of DETA/N-GOQD/SWCNT/PES Membrane

An image of the coated Diethylenetriamine (DETA)/N-GOQD/SWCNT hollow fiber membrane is shown in Figure 11 (a). Compared to PES blank substrate, a uniform grey colour on the inner surface of hollow fiber was observed.

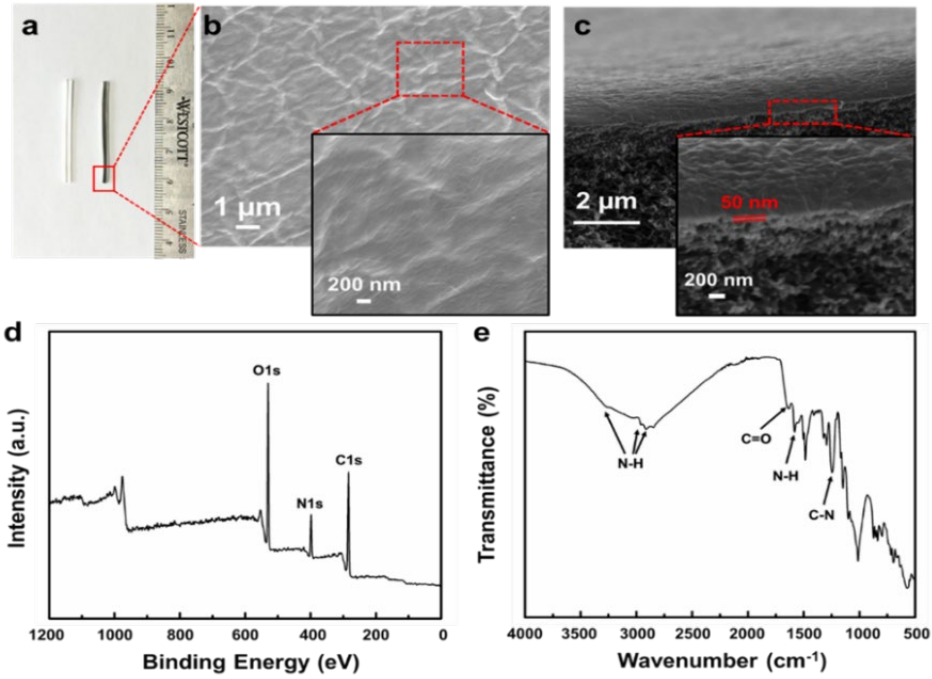

Figure 11. DETA functionalized N-GOQD hollow fiber membrane. (a) Image of the PES blank substrate and as-coated N-GOQD membrane. (b) Surface SEM images of DETA/N-GOQD hollow fiber membrane, (c) Cross-sectional SEM images of DETA/N-GOQD membrane. The thickness of N-GOQD selective layer is around 50 nm. (d) and (e) XPS and ATR-FTIR spectra of DETA/N-GOQD membrane.

In addition to the facilitated transport of CO_2 enabled by the amine functionalization on the N-GOQD membrane, DETA could also possibly act as a crosslinker to bond N-GOQD material with SWCNT mesh, and thus strengthen the carbon-based composite membrane structure [14]. As shown in the surface SEM image (Figure 11 (b)), the backbone of SWCNT mesh can still be seen, while all the pores and gaps have been fully filled with DETA functionalized N-GOQDs. With a further heat treatment, amine groups on DETA could react with the functional groups at the surface of polydopamine wrapped SWCNTs and crosslink more N-GOQDs on SWCNTs to form a rigid carbon matrix structure. The carbon-based membrane layer possesses relatively large oxygen and amine functional groups (relative to the GODQ without N doping), which significantly favors CO_2 and water

transport. The cross-sectional SEM image (Figure 11 (c)) of one membrane prepared on 50-nm SWCNT mesh shows that the effective membrane thickness is still around 50 nm, indicating that the selective separation layer is ultra-thin and may allow high gas permeance. The XPS spectrum of the DETA functionalized N-GOQD/SWCNT membrane is shown in Figure 11 (d). The nitrogen peak intensity increased significantly, owing to the incorporated amine molecules in the transport interstices. The ATR-FTIR spectrum (Figure 11 (e)) further verified the amine functionalization, as N-H stretching and bending vibrations at 2,851, 2,917, and 1,580 cm^{-1}, and C-N stretching at 1,245 cm^{-1} were clearly observed.

CO_2 Separation Performance of DETA/N-GOQD/SWCNT/PES Hollow Fiber Membrane

Gas permeation tests were conducted on N-GOQD/SWCNT composite hollow fiber membranes using mixed gas feed (15% CO_2/85% N_2) and sweep gas on the permeate side to explore the base transport resistance and selectivity. The N-GOQD/SWCNT membrane had a CO_2/N_2 selectivity of 29 with CO_2 permeance of 96 GPU. The gas transport in the hydrated N-GOQD/SWCNT membrane followed the well-known solution-diffusion mechanism. Similar in behavior to glassy and rubbery polymer membranes, the hydrated N-GOQD/SWCNT membrane can be represented as a "poly-0D quantum dot" matrix. The free volume, which is the Angstrom-sized interstices, is expected to be located between the nano-meter sized zero-dimensional quantum dots and carbon nanotube skeleton. Gas molecules dissolve into the hydrated "poly-0D quantum dot" matrix and diffuse to the low chemical potential side as shown in the inset diagram of Figure 12(a).

The low CO_2 performance of N-GOQD/SWCNT can be enhanced, as discussed in our previous studies on GO-amine hollow fiber membranes for CO_2 capture [13], by functionalizing by crosslinking CO_2-philic agents, such as amine molecules, to boost gas permeance and selectivity. In previous work, we have successfully functionalized GO hollow fiber membranes by adding piperazine and ethylenediamine, and improved CO_2 capture performance was observed. Here, we pre-functionalized our N-GOQDs with another amine, DETA, which has three amine functionalities and thus is expected to have very high capacity for binding CO_2 and to exhibit a high absorption rate.

The CO_2 permeance of the DETA functionalized N-GOQD membrane was evaluated at different temperatures under sweep testing. We found the CO_2 permeance and CO_2/N_2 selectivity increased exponentially with increasing temperature, and the membrane performance was stable in the temperature range tested. The permeance and selectivity were 1,450 GPU and 520 at 75°C (Figure 12 (a)). Instead of the solution-diffusion mechanism, the facilitated transport mechanism dominates the CO_2 molecular transport, as reflected by the high activation energy for CO_2 permeation (48.42 kJ/mol) which suggests activated diffusion of CO_2 in the membrane due to the chemical bonding. We postulate that the bonded amine molecules act as CO_2 carriers to reversibly react with CO_2 molecules at the high concentration side (feed side) and generate bicarbonate ions which could rapidly transport in the membrane interstices and dissociate to CO_2 again at the low concentration side (permeate side).

Two different thicknesses of the DETA/N-GOQD/SWCNT/PES membrane were tested for CO_2/N_2 separation for 80-hours continuous operation, as shown in Figure 12 (b). For the 85-nm membrane, the CO_2 permeance maintained at about 600 GPU with CO_2/N_2 selectivity at around 500. For the thinner N-GOQD/SWCNT membrane (50 nm), the CO_2 permeance increased to 1,450 GPU with 520 CO_2/N_2 selectivity, mainly due to the thinner selective membrane layer and thus a shorter transport pathway for gas molecules. This membrane performance is compared with other published data on a Robeson upper bound plot [11] in Figure 12 (c), where the CO_2 permeability is replaced by the CO_2 permeance by assuming 100 nm thickness for polymeric membranes. The DETA functionalized N-GOQD membrane shows superior performance as compared to others.

DETA/N-GOQD/SWCNT/PES hollow fiber membrane modules with 10 cm^2 area were fabricated with N-GOQD composite fibers. Results of the separation testing are shown in Figure 12(d). At 5 and 10 sccm feed rates, the feed concentration of 15% was reduced to 2.8% and 5.0%, respectively, in the retentate, which corresponds to approximately 81% and 67% CO_2 removal. At a feed rate of 15 sccm, about 50% CO_2 removal was achieved with the 10 cm^2 module. This module showed stable CO_2 capture performance for a 134 hour run at 75°C.

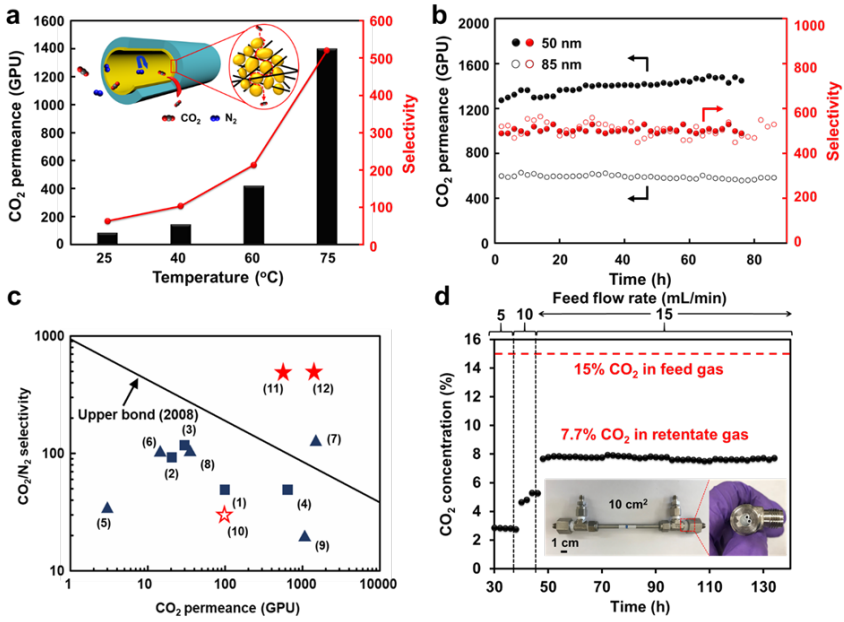

Figure 12. CO_2 separation performance of DETA functionalized N-GOQD/SWCNT/PES hollow fiber membranes. (a) Temperature effect on membrane (50 nm thickness) separation performance. The inset figure shows the CO_2 molecule transport path in the N-GOQD/SWCNT matrix. (b) Short term stability of DETA functionalized N-GOQD/SWCNT hollow fiber membranes with two different thicknesses (85 nm and 50 nm). (c) Membrane performance comparison on a 2008 Robeson upper bound plot. (1) GO. (2) GO-Pebax. (3) GO-DETA-Pebax. (4) GO-borate. (5) Pebax-PEG-POSS. (6) DETA-silica-Pebax. (7) PDMS.57 (8) PVAm. (9) PEG-based. (10) Base N-GOQD/SWCNT hollow fiber membrane in this work. (11 and 12) DETA functionalized N-GOQD/SWCNT hollow fiber membranes with 85 and 50 nm thickness, respectively, in this work. (d) Impact of feed flow rate on 10 cm^2 DETA functionalized N-GOQD/SWCNT hollow fiber membrane (50 nm thickness). The retentate CO_2 concentration was monitored and the flow rate varied from 5 to 10 to 15 mL (STP) per min on the feed side.

Characterization Results for DETA/N-GOQD/PSS/SWCNT/PES Membrane

As mentioned above, a mobile amine carrier, DETA, was assessed for enhanced CO_2 removal in the GO-based membrane. Loss of amine carrier was observed, especially under moderate-temperature,

high-humidity conditions, with vacuum on the permeate side. Under vacuum testing, the separation performance of DETA/N-GOQD/SWCNT/PES hollow fiber membrane decreased significantly with time, because of the loss of mobile amine-containing carrier. The membrane makeup was modified to include a "Negative Charge Confined" membrane structure, where the positively charged amine carriers for CO_2 are confined within the negatively charged poly(sodium-p-styrenesulfonate (PSS)-modified SWCNT network. This approach mitigated the DETA loss [15].

To form an ultrathin, defect-free selective layer, a thin, porous SWCNT network layer was coated on the inner surface of the PES hollow fiber substrate by vacuum filtration. As shown in Figures 13 (a) and (b), the thickness of the interconnected SWCNT layer is ~220 nm. Then, a suspension of 10 mg/mL GOQD in a solution containing 30 mg/mL PSS (to mitigate DETA loss) and 100 mg/mL DETA was applied to the surface of the SWCNT layer with vacuum on the outside of the fiber. A continuous selective layer was obtained after drying at 60°C for 3 h. After coating with the DETA/PSS/GOQD solution, the SWCNT layer was fully covered and the thickness increased to 300 nm (Figures 13 (c) and (d)).

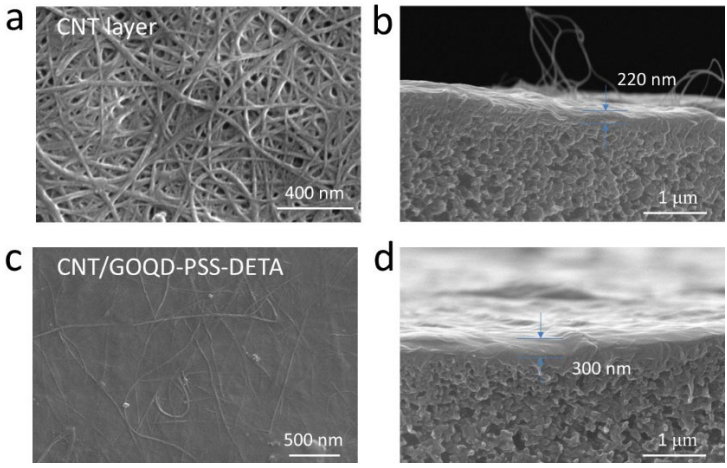

Figure 13. The surface (a) and cross-sectional (b) SEM images of SWCNT layer. The surface (c) and cross-sectional (d) SEM image of DETA/GOQD/PSS/ SWCNT/PES membrane.

CO_2 Separation Performance of DETA/N-GOQD/PSS/SWCNT/PES Membranes

As mentioned above, DETA, confined in the SWCNT network, served as an effective CO_2 carrier to promote CO_2 separation performance. The separation performance of the membranes for simulated flue gas (containing CO_2, N_2 and water vapor) was evaluated using a gas permeation unit under vacuum operation mode. The permeate side was connected to a vacuum pump, and the permeate stream, containing CO_2, N_2, and water vapor, was routed to the GC for composition analysis using heliumas a carrier gas.

Mixed gas (CO_2 : N_2 = 15% : 85% in vol%) separation performance of the DETA/N-GOQD/ PSS/ SWCNT/PES membranes was measured at 80°C under vacuum mode. The feed gas is water saturated. The permeate pressure was controlled at 44 KPa absolute pressure. The CO_2 and N_2 concentrations in feed, retentate and permeate streams were measured by GC. The water vapor in the permeate was

largely removed with a chilled condenser (-20°C). The results are shown in Table 1. The CO_2 permeance was 1,150 GPU and CO_2/N_2 selectivity is 370.

Table 1. Separation performance of DETA/N-GOQD/PSS/SWCNT/PES hollow fiber membrane using vacuum mode at 80°C.

Membrane area (cm^2)	CO_2 permeance (GPU)	N_2 permeance (GPU)	CO_2/N_2 selectivity
55	1,150	3.1	370

To evaluate membrane stability, a 100-hour run on a CO_2/N_2 mixture was conducted. The DETA/N-GOQD/PSS/SWCNT/PES hollow fiber membrane demonstrated stable separation performance (fluctuation less than 10%) for at least 100 h with average CO_2 permeance of 100 GPU and CO_2/N_2 selectivity of 370 at 80°C and 0.3 bara on the permeate side (Figure 14).

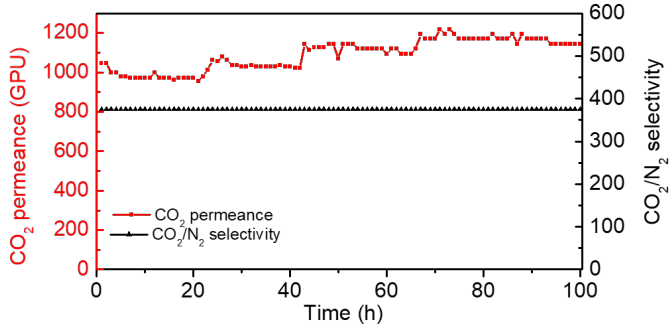

Figure 14. Stability of DETA/N-GOQD/PSS/SWCNT/PES membrane.

Stability of GO-Based Membranes in The Presence Of SO_2 and O_2

Two DETA/N-GOQD/PSS/SWCNT/PES membranes were tested at 80°C and a feed pressure of 1 bara and permeate pressure of 0.44 bar. The feed gas composition was nominal CO_2:N_2:O_2:H_2O of vol % 12.8%: 38.9%:1.6%:46.7%, for both membranes, with one having added 46 ppmv SO_2.

Figure 15 shows similar transient permeation behavior for tests with and without SO_2 as the membranes reached steady state in 2 hours after a vacuum was applied on the permeate side. Considering the testing precision (±10%), the CO_2 permeance and CO_2/N_2 selectivity calculated for each test (with and without SO_2) were identical. The precision estimate is based on 3 repeated measurements. This shows that the membrane performance is not affected by SO_2, at least in a short test. Testing with NO_2 in the feed (66 ppmv) also indicated that the membrane performance was not affected. It should be noted that these are preliminary test results. In the current project, the membrane will be tested at the National Carbon Capture Center (NCCC) with actual flue gas.

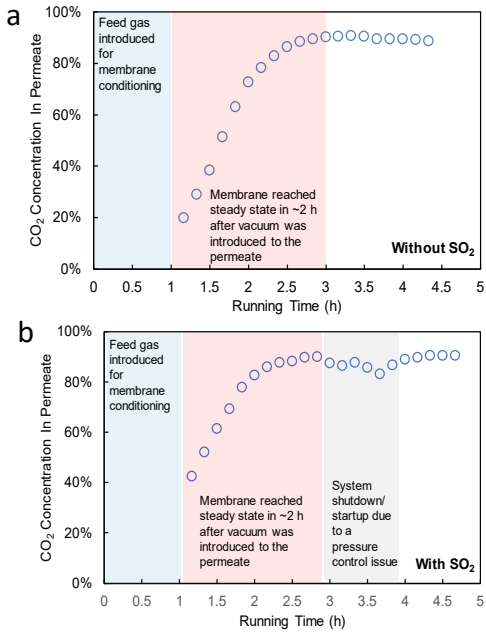

Figure 15. Transient permeation behavior and steady-state performance of PES hollow-fiber supported GOQD-PSS-DETA membranes: (a) without SO_2 and (b) with SO_2.

MEMBRANE SCALE-UP

Scale-Up of GO-Based Flat Sheet Membrane To 50 Cm^2

A DETA/GOQD/PSS/SWCNT/PES membrane with a permeation area of about 50 cm^2 was fabricated using the same vacuum filtration and casting method described previously. An image of the cast membrane is shown in Figure 16. The membrane was tested with feed and permeate pressures of 1.0

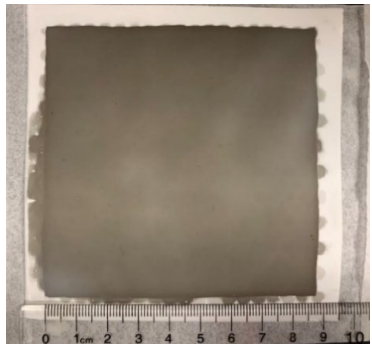

Figure 16. Photograph of a GO-based flat sheet membrane with area of 72 cm^2

bar and 0.37 bara, respectively. The permeation temperature was controlled at 85 ºC. The CO_2/N_2 separation performance is summarized in Table 2.

Table 2. Separation performance of a GO-based flat sheet membrane with testing area of 54 cm^2 under vacuum test at 85ºC.

Effective testing area (cm^2)	CO_2 permeance (GPU)	N_2 permeance (GPU)	CO_2/N_2 selectivity
54	1,050	4.1	260

Scale-Up of GO-Based Hollow Fiber Membrane Modules to Effective Areas Of 1,000 Cm^2

A DETA/GOQD/PSS/SWCNT membrane with surface area of 1,000 cm^2 was fabricated on a commercial PES hollow fiber substrate. Figure 17 shows the commercially available PES membrane module.

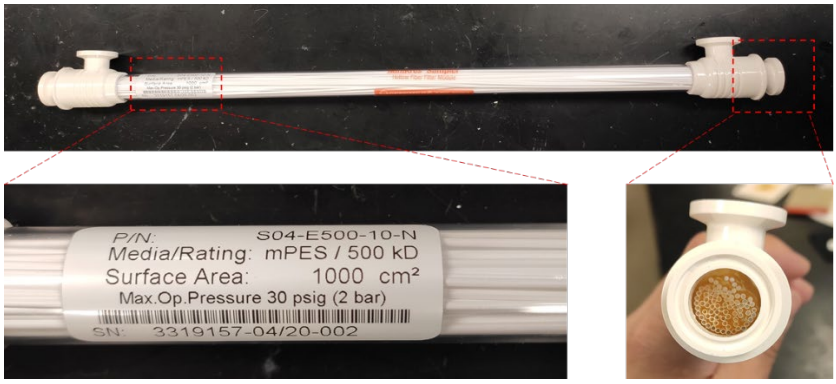

Figure 17. Photograph of PES hollow fiber membrane module with effective membrane area of 1,000 cm^2.

The 1,000 cm^2 DETA/GOQD/PSS/SWCNT membrane module was tested at 80ºC with a feed rate of 768 sccm of simulated flue gas (composition: CO_2 9.1%; N_2 50.8 %; H_2O 40.1 %, or 15 CO_2 /85 N_2 on a dry basis). The feed pressure was 1.0 bara and the permeate pressure was 0.40 bar. The separation performance of the membrane is summarised in Table 3. The CO_2 permeance is 984 GPU and the CO_2/N_2 selectivity is 330. The CO_2 capture rate and CO_2 purity at permeate side were 40.3% and 96.6 % (dry basis), respectively.

Table 3. Separation performance of DETA/GOQD/PSS/CNT membrane module with effective membrane area of 1,000 cm^2 under permeate vacuum at 80ºC.

Membrane area (cm^2)	CO_2 permeance (GPU)	CO_2 flux (mol m^{-2} s^{-1})	CO_2/N_2 selectivity	CO_2 purity at permeate side	CO_2 capture rate
1000	984	1.62E-4	330	96.6%	40.3%

FUTURE WORK

Further development is needed to mature the GO-based membrane technology. These developments include the following:

- Test the membrane at broader range of temperature and feed composition
- Test at high stage-cut to better define optimal process configurations for application
- Test the membrane with actual flue gas to identity if any pretreatments are needed
- Further scale up the membrane to commercial sized modules and verify performance on actual flue gas

CONCLUSIONS

In summary, a facile and scalable method to prepare GO-based membranes has been developed which is applicable to producing flat sheet or hollow fiber membranes. The support layer is formed from SWCNTs which are deposited on a porous polymer substrate (PES). GO is then incorporated into the membrane in the form of nitrogen-doped GOQD. Finally, a CO_2-philic functionality can be added in the form of amine moieties, such as DETA. With the facilitated transport of CO_2, the GO-amine-based hollow fiber membranes showed high CO_2 permeance and superior CO_2/N_2 mixture selectivity at 80 °C under simulated flue gas feed conditions. The membranes achieved CO_2 permeance above 1,000 GPU and CO_2/N_2 selectivity greater than 200, demonstrating potential for CO_2 capture from flue gas. In addition, membrane was scaled up to 1,000 cm^2. Construction of a bench-scale GO-based membrane system was completed. The next step is to perform field testing with actual flue gas at the National Carbon Capture Center (NCCC).

ACKNOWLEDGEMENTS

We gratefully acknowledge support by the CCP4 and the US Department of Energy (Contract Numbers DE-FE-0004787). We thank Dr. Betty Pun and Dr. Raja Jadhav at Chevron, Dr. Ibrahim Ali at BP, Paulo Frederico Prunzel at Petrobras, and DOE/NETL Project Manager Dustin Brown for their assistance and many valuable discussions. We also acknowledge the permission from the Journal of Materials Chemistry A for allowing us to use figures from reference 14.

REFERENCES

1. S.I. Seneviratne, M.G. Donat, A.J. Pitman, R. Knutti, R.L. Wilby, Allowable CO_2 emissions based on regional and impact-related climate targets, Nature. 529 (2016) 477–483. https://doi.org/10.1038/nature16542.
2. D. (National E.T.L. Hancu, Carbon Capture Program Overview, in: DOE-NETL'S 2020 Integr. Proj. Rev. Meet. - CARBON CAPTURE, 2020. https://netl.doe.gov/sites/default/files/netl-file/20VPRCC_Hancu.pdf.
3. D. (National E.T.L. Hancu, Carbon Capture Program CDR Annual Meeting, in: CARBON Manag. OIL GAS Res. Proj. Rev. Meet. - CARBON DIOXIDE Remov. Res., 2021. https://netl.doe.gov/sites/default/files/netl-file/21CMOG_CDRR_Hancu.pdf.
4. P. Bernardo, E. Drioli, G. Golemme, Membrane Gas Separation: A Review/State of the Art, Ind. Eng. Chem. Res. 48 (2009) 4638–4663. https://doi.org/10.1021/ie8019032.
5. Y. Chen, L. Zhao, B. Wang, P. Dutta, W.S. Winston Ho, Amine-containing polymer/zeolite Y composite membranes for CO2/N2 separation, J. Memb. Sci. 497 (2016) 21–28. https://doi.org/https://doi.org/10.1016/j.memsci.2015.09.036.
6. M. Karunakaran, R. Shevate, M. Kumar, K.-V. Peinemann, CO 2-selective PEO–PBT (PolyActive^{TM})/graphene oxide composite membranes, Chem. Commun. 51 (2015) 14187–14190.

7. L. Huang, J. Liu, H. Lin, Thermally stable, homogeneous blends of cross-linked poly (ethylene oxide) and crown ethers with enhanced CO2 permeability, J. Memb. Sci. 610 (2020) 118253.
8. R.W. Baker, B.T. Low, Gas separation membrane materials: a perspective, Macromolecules. 47 (2014) 6999–7013.
9. L.S. White, X. Wei, S. Pande, T. Wu, T.C. Merkel, Extended flue gas trials with a membrane-based pilot plant at a one-ton-per-day carbon capture rate, J. Memb. Sci. 496 (2015) 48–57. https://doi.org/https://doi.org/10.1016/j.memsci.2015.08.003.
10. R.W. Baker, T.C. Merkel, B.C. Freeman, Large Pilot Testing of the MTR Membrane Post-Combustion CO_2 Capture Process, 2018. https://www.netl.doe.gov/sites/default/files/netl-file/R-Baker-MTR-Membrane-Large-Pilot-Testing.pdf.
11. L.M. Robeson, The upper bound revisited, J. Memb. Sci. 320 (2008) 390–400.
12. H. Li, Z. Song, X. Zhang, Y. Huang, S. Li, Y. Mao, H.J. Ploehn, Y. Bao, M. Yu, Ultrathin, molecular-sieving graphene oxide membranes for selective hydrogen separation, Science (80-.). 342 (2013) 95–98.
13. F. Zhou, H.N. Tien, W.L. Xu, J.-T. Chen, Q. Liu, E. Hicks, M. Fathizadeh, S. Li, M. Yu, Ultrathin graphene oxide-based hollow fiber membranes with brush-like CO 2-philic agent for highly efficient CO 2 capture, Nat. Commun. 8 (2017) 1–8.
14. F. Zhou, H.N. Tien, Q. Dong, W.L. Xu, B. Sengupta, S. Zha, J. Jiang, D. Behera, S. Li, M. Yu, Novel carbon-based separation membranes composed of integrated zero-and one-dimensional nanomaterials, J. Mater. Chem. A. 8 (2020) 1084–1090.
15. S. Zhang, H. Li, H. Li, B. Sengupta, S. Zha, S. Li, M. Yu, Negative Charge Confined Amine Carriers within the Nanowire Network for Stable and Efficient Membrane Carbon Capture, Adv. Funct. Mater. 30 (2020) 2002804.
16. Y. Han, W.S.W. Ho, Recent advances in polymeric facilitated transport membranes for carbon dioxide separation and hydrogen purification, J. Polym. Sci. 58 (2020) 2435–2449. https://doi.org/https://doi.org/10.1002/pol.20200187.
17. M. Fathizadeh, H.N. Tien, K. Khivantsev, Z. Song, F. Zhou, M. Yu, Polyamide/nitrogen-doped graphene oxide quantum dots (N-GOQD) thin film nanocomposite reverse osmosis membranes for high flux desalination, Desalination. 451 (2019) 125–132.
18. N.T. Ho, H.N. Tien, S.-J. Jang, V. Senthilkumar, Y.C. Park, S. Cho, Y.S. Kim, Enhancement of recombination process using silver and graphene quantum dot embedded intermediate layer for efficient organic tandem cells, Sci. Rep. 6 (2016) 1–8.
19. R.E. James III, D. Kearins, M. Turner, M. Woods, N. Kuehn, A. Zoelle, Cost and performance baseline for fossil energy plants volume 1: bituminous coal and natural gas to electricity, NETL, 2019. https://doi.org/https://doi.org/10.2172/1569246.
20. Y. Li, Y. Zhao, H. Cheng, Y. Hu, G. Shi, L. Dai, L. Qu, Nitrogen-Doped Graphene Quantum Dots with Oxygen-Rich Functional Groups, J. Am. Chem. Soc. 134 (2012) 15–18. https://doi.org/10.1021/ja206030c.
21. Z. Shi, W. Zhang, F. Zhang, X. Liu, D. Wang, J. Jin, L. Jiang, Ultrafast Separation of Emulsified Oil/Water Mixtures by Ultrathin Free-Standing Single-Walled Carbon Nanotube Network Films, Adv. Mater. 25 (2013) 2422–2427. https://doi.org/https://doi.org/10.1002/adma.201204873.

Carbon Dioxide Capture for Storage in Deep Geological Formations, Volume 5
Karl F. Gerdes (Editor)
© 2022 BP. All rights reserved.

Chapter 17

TECHNO-ECONOMIC ASSESSMENT OF CO_2 CAPTURE FROM AN NGCC POWER PLANT USING MHI'S KM CDR PROCESS™

Raja Jadhav[1], Ibrahim Ali[2], Betty Pun[1], Paulo Prunzel [3]

[1]Chevron Technical Center, 100 Chevron Way, Richmond, CA, USA
[2]BP International, Chertsey Road, TW16 7BP, Sunbury-on-Thames, UK
[3]Petrobras Research Center, Avenida Horácio Macedo, 950, Rio de Janeiro, RJ, Brazil

ABSTRACT: The objective of this study is to provide a techno-economic assessment (TEA) of CO_2 capture from a Natural Gas Combined Cycle (NGCC) Power Plant based on state-of-the-art commercially available post-combustion solvent technology. The CO_2 Capture Project (CCP) team contracted with Mitsubishi Heavy Industry (MHI) to develop an Engineering, Procurement and Construction (EPC) cost estimate for their KM CDR Process™. Based on the NGCC reference case costs and the economic methodology developed in Chapter 7 of the present volume, the Total Plant Cost (TPC) was estimated. The costs of CO_2 captured and avoided were estimated to be $65 and $76/tonne of CO_2, respectively. Key economic parameters and assumptions affecting these costs are briefly described.

KEYWORDS: NGCC; CO_2 capture; KM CDR Process™; MHI; post-combustion

INTRODUCTION

The focus of this study is to estimate the cost of CO_2 capture from NGCC power plants using current state-of-the-art technology. Based on learnings from CCP2 and CCP3, post-combustion solvent capture of CO_2 provides the most cost-effective solution for NGCC power plants in the near-to-medium term [1, 2]. In Chapter 7, the outcome of a preliminary study aimed at assessing the potential techno-economic advantages of four novel post-combustion technologies was presented and benchmarked against conventional technology, namely post-combustion capture by monoethanolamine (MEA) solvent. MHI's KM CDR Process™ was chosen for this study to represent the current commercial benchmark of post-combustion solvent capture.

MHI'S KM CDR PROCESS™

MHI and Kansai Electric Power Co. began developing the Kansai-Mitsubishi Carbon Dioxide Recovery process (KM CDR Process™) in 1991. The process has been commercially operating since 1999 with the construction of the first plant in Malaysia. MHI has continued to apply lessons learned from each project to improve the technology. The process utilizes the patented KS-1™ solvent, which is based on advanced hindered amines. The carbon dioxide capture process consists of three main sections: flue gas cooling, CO_2 absorption and solvent regeneration, as shown schematically in Figure 1.

Flue Gas Cooling

The flue gas temperature from an NGCC power plant is usually in the range of 80 to 120°C, depending on the design of the Heat Recovery Steam Generator (HRSG). Since this temperature is much higher than what the amine solvent can tolerate, the flue gas is cooled in a Direct Contact Cooler (DCC) to an optimum temperature of around 35 to 45°C before entering the CO_2 absorber. Lowering the flue gas temperature increases the efficiency of the exothermic CO_2 absorption reaction and minimizes the solvent losses. In addition to cooling the flue gas, the DCC is designed to partly remove other impurities such as NOx, SOx (if present), dust and suspended particulate matter (PM). In many amine-based post-combustion CO_2 capture technologies, the DCC cooling medium is not pure water, but a solution of NaOH in water is used to remove acidic species. For this study, a blower is provided downstream of the DCC to overcome the pressure drop in the absorber (Not as shown in the generic schematic of Figure 1).

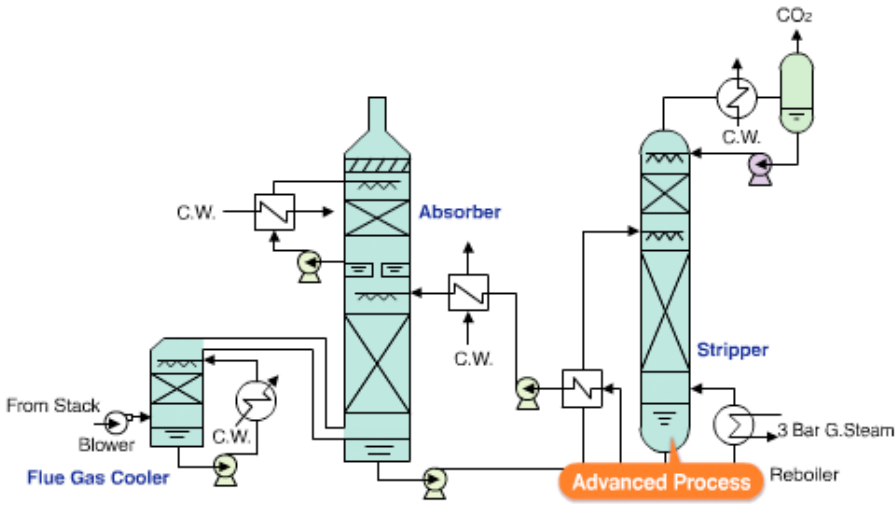

Figure 1. MHI's KM CDR Process™ generic schematic (courtesy MHI).

Absorber

The cooled and clean flue gas, water saturated at 35–45°C, is sent to the absorber and flows upward through structured metal packing countercurrent to CO_2-lean KS-1™ solvent, which is distributed evenly at the top of the absorption section onto the packing. The CO_2 is absorbed from the flue gas into the solvent upon direct contact. The CO_2 rich solvent is sent to the stripper column for regeneration, and the scrubbed flue gas flows upwards into a washing section utilizing circulating water to absorb vaporized solvent for recycle back into the CO_2 absorption section. The wash section also serves to condense water from the exiting flue gas, so a water balance can be maintained within the system.

Regenerator

The rich solvent from the absorber is heated in a lean/rich cross heat exchanger using the heat in the lean solvent leaving the bottom of the CO_2 regenerator.

The heated rich solvent is then introduced to the top section of the CO_2 regenerator (or stripper) where the CO_2 in the rich solvent is stripped off in the regenerator at about 120°C. The CO_2 stream leaving the top of the regenerator is at very high purity (>99.9 vol%, dry) and is further compressed and dehydrated for transport and sequestration or use. The lean amine with the reduced CO_2 content exchanges heat with the rich solvent in the cross-heat exchanger, is further cooled to ~40°C, and is recycled back to the CO_2 absorber, completing the closed loop solvent cycle.

POST-COMBUSTION CO_2 CAPTURE FROM NGCC POWER PLANTS

Reference Case NGCC Power Plant Without Capture

The baseline system of this study is the Natural Gas Combined Cycle described in the CCS European Benchmarking Task Force report [3], which is thought to be representative of the state-of-the-art of this power generation technology. Table 1 reports the main characteristics of the reference NGCC power plant.

The reference NGCC power plant in this study is a greenfield application designed to produce 830 MWe net electric power at full load and features a net electric efficiency of 58.3% on a LHV basis. The NGCC plant employs two F-Class gas turbines (GE 9FA) paired with two heat recovery steam generators and a single steam turbine. Figure 2 shows a simplified schematic of the NGCC power plant. Further details of the performance of the reference NGCC power plant can be found in Chapter 7 of this volume [4].

Table 1: Reference NGCC power plant characteristics.

	Unit	**Value**
Natural gas input	MW_{LHV}	1422.6
Gas turbine output (2 units)	MW_e	544.2
Steam turbine output	MW_e	285.7
Total output	MW_e	829.9
Net electric efficiency	%	58.3
Flue gas temperature	°C	94
Flue gas pressure	bar	1.01
Flue gas flow rate	kmol/s	47.02
	kg/s	1330.6
CO_2 flow rate	tonnes/day	7080
Flue gas composition (before the DCC)	Mol %	
H_2O		8.38
CO_2		3.96
N_2		74.38
O_2		12.39
Ar		0.89
NOx		$1.04x10_{-3}$

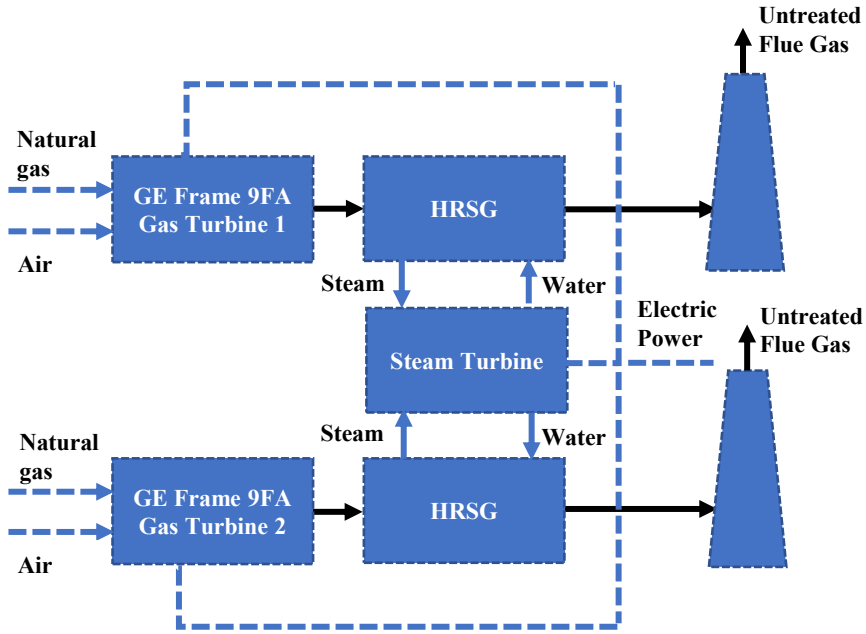

Figure 2. Simplified block flow diagram of an NGCC power plant without CO_2 capture.

NGCC Power Plant with Post-Combustion Capture

A simplified block flow diagram of the CO_2 capture plant is shown in Figure 3. Two absorber trains, one for each gas turbine/HRSG, and a single regenerator is employed. The hot flue gas exiting each HRSG is around 94°C and is sent to a DCC, bypassing the stack. A blower increases the pressure of the cooled flue gas before it is routed to the absorber. 90% of the CO_2 in the flue gas, which is 6,372 tonnes/day of CO_2, is removed in the absorber by countercurrent contact with the lean KS-1™ solvent, and the scrubbed flue gas is released to the atmosphere at the top of the absorber. Rich solvent from each absorber is heated individually against the hot lean solvent returning from the combined regenerator. The hot rich solvent is combined and sent to the common regenerator, where low pressure steam is used to release the CO_2. The product CO_2 stream is dehydrated and compressed in a single multi-state intercooled compression train to the pipeline pressure of 110 bar, ready for transportation.

As described in Chapter 7 [4], the main utilities required for the capture plant–regeneration steam and power–are taken from the host NGCC plant. The steam (~5 bara at 160°C) is extracted from the steam turbine between the intermediate- and low-pressure sections. Because of the steam extraction for solvent regeneration, there is a reduction in the gross power generated by the steam turbine. In addition to the power requirement for the various equipment in the capture plant, an electric-drive compressor is used to deliver CO_2 at high pressure. The combined effect of steam extraction and power demand is a reduction in the net output of the Base Case by ~95 MW_{el} compared to the reference plant, and the overall impact is to reduce the net efficiency of the plant from 58.3% to 51.6% on a Lower Heating Value (LHV) basis. This is summarised in Table 2.

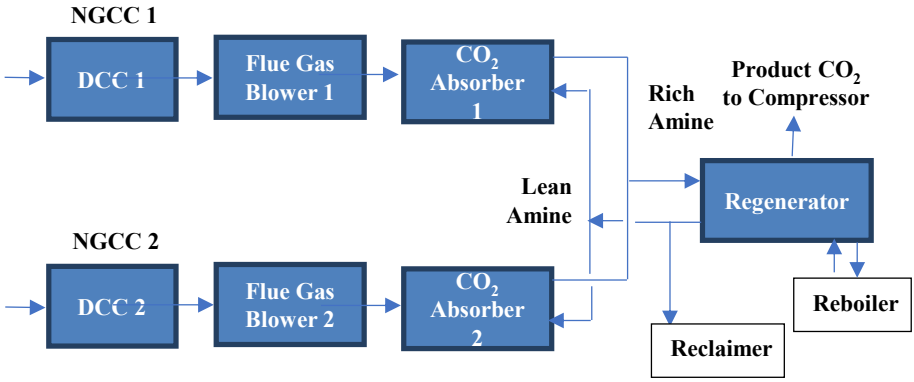

Figure 3. Simplified block flow diagram of the CO_2 capture process.

Table 2: Performance of the NGCC power plant without (w/o) and with (w/) capture.

	NGCC plant w/o CO_2 capture (Reference plant)	NGCC plant w/ KM CDR Process® (Base plant)
Fuel input, MW_{LHV}	1422.6	1422.6
Gas turbine net power (2 units), MW_e	544.2	544.2
Steam cycle net power, MW_e	285.7	*
Overall net power, MW_e	829.9	734.7**
Net electric efficiency, $\%_{LHV}$	58.3	51.6
CO_2 captured, %	-	90
CO_2 emissions, kg_{CO2}/MWh_e	351.8	40

* The amount of steam required for the regeneration process is not disclosed.
**The overall net power includes the derate on the steam turbine and the power requirement for the capture and compression process.

Indicative Cost Estimate

MHI provided a conceptual design and indicative cost estimate of the CO_2 capture plant for this CCP-sponsored study. The CO_2 capture plant design concept used by MHI was based on their experience with thirteen (13) operating commercial KM CDR Process™ projects worldwide. This includes the Petra Nova coal-fired power plant near Houston, Texas, which is the world's largest CDR installation with a design capture capacity of 1.6 million tonnes per year of CO_2.

The design process utilized proprietary MHI tools for optimization and integration of the absorber, regenerator, heat exchangers, and other systems, which was then used to develop equipment sizing, heat and material balances, and utility requirements. Chemical consumption was estimated based on operating experience, specific flue gas characteristics, and detailed knowledge of the KM CDR Process™ chemistry.

MHI's scope included the CO_2 capture unit and all associated equipment inside the battery limits (ISBL) (shown in Figure 3). MHI assumed that flue gas, steam, power, cooling water, and other utility waters would be provided to the CO_2 capture system battery limit.

The capital cost estimate by MHI assumed turn-key delivery of MHI's scope (ISBL) in conjunction with a third-party constructor and included the following:

1. KM CDR Process™ license
2. Engineering
3. Procurement
   a. Mechanical Equipment
   b. Piping
   c. Instrumentation
   d. Electric
   e. Structural Assemblies
   f. Process
      i. KS-1™ Solvent (initial fill through end of commissioning)
      ii. Catalyst/Chemicals
      iii. Laboratory Equipment
4. Logistics and Transportation
5. Site Construction
6. Start-up Spares
7. Commissioning Support
8. EPC Indirect Costs

Based on previous project experience, MHI provided an EPC cost estimate (overnight 2020$, US Gulf Coast basis), utility requirements, and the operating costs for the capture plant, which are not reported here individually because of confidentiality.

Economic Assessment

Starting with the EPC cost estimate, the contingency and Owner's costs were estimated using certain factors. To these costs, the compression and dehydration capital costs (estimated by LEAP for the MEA case in Chapter 7 [4]) were added to arrive at the Total Plant Cost (TPC) of 785M$ (overnight 2020$, US Gulf Coast basis).

The capital cost estimate excludes any atypical site preparation (e.g., removal of existing obstructions and foundations) and owner's (e.g., land, FEED studies, delivery of utilities to the CO_2 capture plant boundary, permitting, etc.). The accuracy of the cost estimate is expected to be in the range -15% to +20%.

Once the TPC is calculated, the First Year Cost of Electricity (COE) is calculated, in line with the CCP methodology described in the 4_{th} volume of CCP results [2] Chapter 4, and according to the financial assumptions of Table 3. The overall assessment results are in Table 4.

The costs of the reference NGCC from Chapter 7 [4] were escalated from 2014 to 2020 basis using Chemical Engineering Plant Cost Index (CEPCI) [5].

The Cost of CO_2 Captured (CCC) is the ratio of the increase in the COE to the specific CO_2 capture rate:

$$CCC\left[\frac{\$}{t_{CO2\ captured}}\right] = \frac{(COE)_{CCS} - (COE)_{REF}}{(t_{CO2}/MWh)_{Captured}}$$

Table 3 - Financial assumptions.

Financial Parameter	Value
Location basis	US Gulf Coast
Plant type	Greenfield
Cost year basis	2020
Base currency used, $	US Dollars
Investment lifetime, years	25
Discount rate, %	10
First year capital charge factor, %	9.43
Fuel cost, $/GJ	4.5
Number of equivalent hours, hours equivalent at full load / year	7880

The Cost of CO_2 Avoided (CCA) is the ratio of the increase in the COE to the specific CO_2 avoidance rate:

$$CCA\left[\frac{\$}{t_{CO2\ avoided}}\right] = \frac{(COE)_{CCS} - (COE)_{REF}}{(t_{CO2}MWh^{-1})_{REF} - (tMWh^{-1})_{CCS}}$$

Table 4. Economic evaluation of KM CDR Process™.

Parameter	Units	NGCC plant w/o CO_2 capture (Reference plant)	NGCC plant w/ KM CDR Process™ (Base plant)
Power Section TEC	[M$2020]	273	273
Power Section TPC	[M$2020]	909	909
CO_2 Removal Section TPC	[M$2020]	-	785
Total TPC	[M$2020]	909	1694
Net Power	[MW]	829.9	734.7
Efficiency LHV	[%]	58.3	51.6
Fuel cost	[M$]	182	182
Fixed O&M (2% of TPC)	[M$]	18	34
Variable O&M*	[M$]	12	25
First year capital charge	[M$]	86	160
COE	[$/$MWh_{el}$]	45.5	69.2
CO_2 captured	[kg/s]	-	73.8
CO_2 emissions	[kg/s]	-	8.2
Specific CO_2 emissions	[kg/MWh_{el}]	351.8	40
Specific CO_2 avoidance	[kg/MWh_{el}]	-	312
CCC	[$/t]	-	65
CCA	[$/t]	-	76

*For consistency, Variable O&M is assumed to be the same as reported in Chapter 7 [4].

The capital cost increase of the "Base" relative to the "Reference" plant is nearly 86% (TPC increases from 909 M$ to 1694 M$), and the Cost of CO_2 avoided is 76 $/t$CO_2$ at a CO_2 capture rate of 90%. These results exclude CO_2 transport and storage costs. See Table 4.

In comparison, the TPC estimated by LEAP for the MEA case in Chapter 7 [4], escalated to 2020$, was 909 M$ for the Reference NGCC plant without Capture and 1,602 M$ for the Reference plus Capture plant (overnight 2020$, US Gulf Coast basis). Although the TPCs of the two studies are similar considering the range of accuracy, it should be noted that these costs were developed by different groups, during different time periods. More importantly, the configurations of the CO_2 capture systems were also different–the LEAP study considered two separate absorption and regeneration trains, where this study considered two absorbers and a single combined regenerator.

The cost estimate in this study is based on a methodology that is meant to reflect industry standards. However, the performance and cost estimates do not include any first-of-a-kind costs or exceptional-case risk premiums or contingencies that might be needed for demonstration or first commercial CCS projects. Other exclusions in the capital cost estimate are noted earlier. It should be noted that the costs reported here for the MHI KM CDR Process™ are indicative and actual project costs will be based on several factors not considered in this preliminary study.

CONCLUSIONS

This study was undertaken to provide a techno-economic assessment (TEA) of capture CO_2 from a Natural Gas Combined Cycle (NGCC) Power Plant based on MHI's KM CDR Process™. Based on the NGCC reference case costs and the economic methodology developed in Chapter 7 [4], the indicative costs of CO_2 captured and avoided were estimated to be $65 and $76/tonne of CO_2, respectively. These results exclude CO_2 transport and storage costs.

ACKNOWLEDGEMENTS

CCP would like to thank MHI for undertaking this study and providing the cost of a CO_2 capture system for an NGCC power plant.

REFERENCES

1. CCP, 2009, *Carbon Dioxide Capture for Storage in Deep Geologic Formations–Results from the CO_2 Capture Project–Volume 3: Advances in CO_2 Capture and Storage Technology Results (2004-2009),* (Ed. Lars Ingolf Eide), CPL Press.
2. CCP, 2015, *Carbon Dioxide Capture for Storage in Deep Geologic Formations–Results from the CO_2 Capture Project–Volume 4*: *CCS Technology Development and Demonstration; Results (2009-2014)*, (Ed. Karl F. Gerdes), CPL Press.
3. CAESAR, 2011. European best practice guidelines for assessment of CO_2 capture technologies, EU project 213206 Deliverable D4.9, Feb 2011.
4. Gatti, M., Martelli, E., Capra, F., Di Bona, D., Gabba, M., Magli, F.,Scaccabaro, R., Spinell, M., Vignao, F., and Consonni, S., 2022, Preliminary Performance and Cost Evaluation of Four Alternative Technologies for Post-Combustion CO_2 Capture in Natural Gas Fired Power Plants, in *Carbon Dioxide Capture for Storage in Deep Geologic Formations–Results from the CO_2 Capture Project–Volume 5* (Ed. Karl F. Gerdes).
5. Chemical Engineering, The Chemical Engineering Plant Cost Index - Chemical Engineering (chemengonline.com).

Carbon Dioxide Capture for Storage in Deep Geological Formations, Volume 5
Karl F. Gerdes (Editor)
© 2022 BP. All rights reserved.

Chapter 18

TECHNOLOGY SCREENING STUDY FOR CO_2 REMOVAL IN OFFSHORE NATURAL GAS TREATING

Ray McKaskle and Austyn Vance
Trimeric Corporation
100 S. Main St, Buda, TX

ABSTRACT: This chapter summarizes a comparison of the state-of-the-art technologies for the offshore removal of CO_2 from natural gas and provides guidance on the suitability of the various technologies at varying CO_2 and hydrocarbon compositions.

KEYWORDS: CO_2 removal, natural gas, offshore

INTRODUCTION

This assessment of current state-of-the-art and emerging technologies for offshore removal of CO_2 from natural gas was initiated in 2015. The overall goals of the assessment were as follows:

- Inform and align CCP4 on the state of the art in offshore CO_2 removal.
- Identify emerging and breakthrough technologies.
- Provide expert informed opinion on the various technologies.
- Identify potential technology development projects and provide a basis for deciding whether to invest in one or more of them.

CCP and Trimeric worked together to establish the design basis for the project. To gain understanding of the range of applicability for the various CO_2 removal technologies, six hypothetical reference cases were defined covering CO_2 feed concentrations of 6, 20, and 60 mol. %, combined with both rich (less than 80% C_1) and lean (more than 98% C_1) natural gas mixtures. The project was executed in two main stages. Stage 1 utilized a literature review to identify as many potentially applicable technologies as possible, followed by qualitative rankings of these processes. The Stage 1 evaluation identified 15 established technologies, 20 emerging technologies, and over 50 literature references. Established technologies were subjectively ranked by a team of experienced Trimeric engineers. Stage 2 developed a quantitative ranking of technologies that advanced from Stage 1. The Stage 2 evaluation was based on vendor input for each of the specific cases of interest to CCP.

INITIAL SCREENING

Stage 1 objectives were as follows:

- Identify a wide range of potentially applicable technologies for offshore CO_2 removal.
- Summarize the results of literature searches and other efforts to identify potentially viable technologies.
- Provide process descriptions for each technology considered and evaluate the preliminary pros and cons of each technology including typical applications, known design

limitations, and current Technology Readiness Level (TRL) based on the U.S. Department of Energy's Technology Readiness Assessment Guide, DOE G 413.3-4A.
- Propose a list of viable technologies for further evaluation in Stage 2 and subsequent stages of the project.

An initial list of potentially applicable technologies was compiled based on previous experience with CO_2 removal from natural gas in onshore and offshore applications. A literature search was also conducted including supplier websites, internet publications, and conference proceedings. Many of the potentially applicable emerging technologies had been identified by Trimeric's work supporting U.S. Department of Energy (DOE) funded research on technologies for carbon capture from flue gas applications. Some examples are as follows:

- ION Advanced Solvent CO_2 Capture Pilot Project – DE-FE0013303
- Pilot Test of a Nanoporous, Super-hydrophobic Membrane Contactor Process for Post-combustion CO_2 Capture – DE-FE0012829
- Post-Combustion CO_2 Capture using Rapid Temperature Swing Adsorption with Polymer/Supported Amine Composite Hollow Fibers – DE-FE0007804
- Ionic Liquids: Breakthrough Absorption Technology for Post-combustion CO_2 Capture – DE-FC26-07NT43091
- Development of a Novel Biphasic CO_2 Absorption Process – DE-FE0026434

The following types of established technologies were considered:

- Absorption processes using chemical solvents including alkanolamines and alkaline salts, physical solvents, and mixed solvents (combinations of alkanolamine and physical solvents)
- Membranes
- Adsorption coupled with temperature and pressure swing regeneration
- Low temperature separation processes including conventional distillation, extractive distillation, and separation by freezing point utilizing cryogenic distillation
- Combinations of the above processes

The following types of emerging technologies were considered:

- Novel solvent approaches including ionic liquid solvents, high pressure water, chilled ammonia, phase changing solvents, catalyst activated solvents, and enzyme activated solvents. While Stage 1 of this screening study was primarily focused on screening separation technologies, novel equipment designs such as frothing contactors, rotating packed bed absorbers, and some specific novel solvents were also included
- Emerging membrane technologies including inorganic, thermally rearranged, mixed matrix/metal oxide framework, and facilitated transport membranes
- Cryogenic processes that separate CO_2 from natural gas by freezing the CO_2 as a solid or by condensing the CO_2 as a liquid
- A combination process that uses a membrane to facilitate contact with a chemical solvent

Ranking of Technologies

A series of weighted criteria for ranking existing technologies was defined. Since the performance of the various CO_2 removal technologies may depend on the inlet concentration of CO_2, a separate ranking was performed for each inlet concentration. These rankings are summarized in Tables 1 – 3 at the end of this section considering the following weighted parameters:

- Capital Expenses (CAPEX), 30%

- Offshore Suitability, 20%
- Inherently Safer Design, 15%
- Hydrocarbon Recovery, 10%
- Energy Required, 10%
- Operating Expenses (OPEX) (Excluding Energy), 5%
- Technology Maturity, 5%
- Operability/Complexity, 5%

This ranking process was a subjective evaluation, based on the experience of the experts making the assessment. For each of the criteria, the process with the best expected performance was given a 5 and the process with the worst expected performance was given a 1. Others were ranked in accordance with their expected performance with respect to those expected to be the best and the worst for each of the criteria. The evaluation was performed separately for each of the inlet CO_2 concentrations. The expert panel determined that combinations of processes in series would not be the favored approach for offshore applications if the product specifications can be met with a single process. The accuracy of this subjective ranking process is estimated to be between 0.25 and 0.50 on the 5.00 scale.

The results of the initial ranking exercise are summarized in Tables 1 – 3 below.

A broad range of technologies for offshore CO_2 removal from natural gas was identified during this project. Based on the subjective ranking process described above, the following established technologies were carried forward to Stage 2:

- 6 mol. % CO_2 in feed: membranes and chemical solvents
- 20 mol. % CO_2 in feed: membranes, chemical solvents, and physical solvents
- 60 mol. % CO_2 in feed: membranes and physical solvents

While emerging technologies were also considered as part of this study, the detailed information about emerging technologies is not included in this chapter due to confidentiality constraints. Suppliers of two emerging technologies that showed promise in Stage 1 provided enough information to be evaluated in Stage 2. One technology is a novel gas-liquid contactor for chemical solvent treating which utilizes hollow fiber membranes, with the gas on one side of the membrane and solvent on the other side. The other one is a novel cryogenic process which freezes out the CO_2 contained in the feed gas (anti-sublimation) and separates the solid CO_2 which can be subsequently melted and pumped to the required pressure. These two technologies were only assessed for 6% CO_2 rich gas case in Stage 2, because the vendors only supplied information for that case. However, these technologies might also be applicable for some other cases. Other promising technologies identified in Stage 1, including an enzyme-enhanced solvent and a high-pressure water absorption process were not evaluated in Stage 2 because the suppliers declined to respond, or the technology did not meet the minimum Technology Readiness Level that CCP specified for the project (TRL 3 or higher).

Table 1. CO_2 Removal in Offshore Natural Gas Technology Ranking Table - 6% Inlet CO_2.

Technology/Name or Example	CAPEX	Inherently Safer Design	Hydrocarbon Recovery	Energy Required	OPEX (Excl. Energy)	Tech Maturity	Operability/ Complexity	Offshore[1] Suitability	Composite Score
	Ranking weight, %			Qualitative ranking criteria: 1 = worst, 5 = best					
↓	30	15	10	10	5	5	5	20	
Alkanolamine chemical solvent	5	4	5	3	4	5	4	3	4.2
Potassium carbonate chemical solvent	3	4	5	3	2	5	4	3	3.5
Physical solvent	3	4	4	3	3	5	4	3	3.4
Mixed chemical and physical solvent	5	4	4	3	3	5	4	3	4.0
Membranes	4	5	4	5	5	5	5	5	4.6
Physical adsorbent w/ Temperature Swing Regeneration	N/A	N/A	N/A	N/A	N/A	N/A	N/A	N/A	
Physical adsorbent w/ Pressure Swing Regen.	2	5	1	4	3	1	3	4	3.0
Conventional refrigerated distillation	N/A	N/A	N/A	N/A	N/A	N/A	N/A	N/A	
Extractive distillation	1	1	4	1	1	5	1	1	1.5
Separation by Freezing Point, CFZ	3	3	4	3	3	1	3	3	3.0
Membranes and chemical solvent in series	N/A	N/A	N/A	N/A	N/A	N/A	N/A	N/A	
Membranes and physical solvent in series	N/A	N/A	N/A	N/A	N/A	N/A	N/A	N/A	
Distillation and membranes in series	N/A	N/A	N/A	N/A	N/A	N/A	N/A	N/A	
Distillation and chemical solvent in series	N/A	N/A	N/A	N/A	N/A	N/A	N/A	N/A	
Distillation and physical solvent in series	N/A	N/A	N/A	N/A	N/A	N/A	N/A	N/A	

Notes: (1) Combined impacts of motion, weight, and footprint

Table 2. CO_2 Removal in Offshore Natural Gas Technology Ranking Table - 20% Inlet CO_2.

Technology/Name or Example	CAPEX	Inherently Safer Design	Hydrocarbon Recovery	Energy Required	OPEX (Excl. Energy)	Technology Maturity	Operability/ Complexity	Offshore[1] Suitability	Composite Score
	Ranking weight, %				Qualitative ranking criteria: 1 = worst, 5 = best				
	30	15	10	10	5	5	5	20	
Alkanolamine chemical solvent	3	4	5	3	4	5	4	3	3.6
Potassium carbonate chemical solvent	3	4	5	4	2	5	4	3	3.6
Physical solvent	4	4	4	5	3	5	4	3	3.9
Mixed chemical and physical solvent	3	4	4	3	3	5	4	3	3.4
Membranes	5	5	4	5	5	5	5	5	4.9
Physical adsorbent w/ Temperature Swing Regeneration	N/A	N/A	N/A	N/A	N/A	N/A	N/A	N/A	
Physical adsorbent w/ Pressure Swing Regen.	2	5	1	4	3	1	3	4	3.0
Conventional refrigerated distillation	N/A	N/A	N/A	N/A	N/A	N/A	N/A	N/A	
Extractive distillation	1	1	4	1	1	5	1	1	1.5
Separation by Freezing Point, CFZ	4	3	4	3	3	1	3	3	3.3
Membranes and chemical solvent in series	3	4	4	4	4	4	3	2	3.3
Membranes and physical solvent in series	2	4	3	5	4	4	3	2	3.0
Distillation and membranes in series	2	4	4	4	4	4	3	2	3.0
Distillation and chemical solvent in series	2	3	4	3	4	4	2	2	2.7
Distillation and physical solvent in series	2	3	4	3	4	4	2	2	2.7

Table 3. CO_2 Removal in Offshore Natural Gas Technology Ranking Table - 60% Inlet CO_2.

Technology/ Name or Example	CAPEX	Inherently Safer Design	Hydrocarbon Recovery	Energy Required	OPEX (Excl. Energy)	Technology Maturity	Operability/ Complexity	Offshore[1] Suitability	Composite Score
	30	15	10	10	5	5	5	20	
	Ranking weight, %		Qualitative ranking criteria: 1 = worst, 5 = best						
Alkanolamine chemical solvent	2	4	5	2	4	5	4	3	3.2
Potassium carbonate chemical solvent	3	4	5	4	2	5	4	3	3.6
Physical solvent	5	4	4	5	3	5	4	3	4.2
Mixed chemical and physical solvent	2	4	4	2	3	5	4	3	3.0
Membranes	3	5	4	4	5	5	5	5	4.2
Physical adsorbent w/ Temperature Swing Regeneration	N/A	N/A	N/A	N/A	N/A	N/A	N/A	N/A	
Physical adsorbent w/ Pressure Swing Regen.	2	5	1	4	3	1	3	4	3.0
Conventional refrigerated distillation	N/A	N/A	N/A	N/A	N/A	N/A	N/A	N/A	
Extractive distillation	1	1	4	1	1	5	1	1	1.5
Separation by Freezing Point, CFZ	4	3	4	3	3	1	3	3	3.3
Membranes and chemical solvent in series	4	4	4	4	4	4	3	2	3.6
Membranes and physical solvent in series	4	4	3	4	4	4	3	2	3.5
Distillation and membranes in series	3	4	4	3	4	4	3	2	3.2
Distillation and chemical solvent in series	3	3	4	2	4	4	2	2	2.9
Distillation and physical solvent in series	4	3	4	4	4	4	2	2	3.4

Notes: (1) Combined impacts of motion, weight, and footprint.

QUANTITATIVE TECHNOLOGY RANKING

Stage 2 objectives were as follows:

- Obtain more data and, where possible, vendor data specific to this project, for the established and emerging technologies selected in Stage 1 for further evaluation.
- Identify important factors including data sources and availability, cost estimate methodologies, product specifications, and selected product values and energy costs, which have bearing on the conclusions in the Stage 2 evaluation. Key limitations of the study are also addressed.
- Provide a more quantitative comparison of the established and emerging technologies that moved forward from the Stage 1 evaluation.
- Discuss possible activities for further evaluation and optimization.

The Stage 2 evaluation was based on vendor input for each of the six cases of interest to CCP as shown in Table 4. Important information for these cases, including budgetary capital costs, major operating costs, equipment weight and footprint, pre-treatment requirements, and the like was requested from 14 technology and equipment suppliers. Sufficient responses for inclusion in the Stage 2 evaluation were received from three established technology providers and from two emerging technology providers. Some vendors declined to respond due to concerns with protecting intellectual property or confidential information. Other vendors declined to participate without financial compensation for their input, which CCP did not provide to any technology supplier as part of this project.

Vendors were asked to provide input on as many as six cases of varying feed composition. For each case, the following conditions applied: flow rate 500 MMscfd, pressure 1,015 psig, maximum temperature 122 °F, water saturation 100%, and the gas contained no H_2S. Vendors were asked to comment on the implications of up to 1 mol. % H_2S content in the feed gas. In order to limit the number of cases, the flow rate, pressure, temperature, water content, and H_2S content were held constant. However, vendors were asked to comment on any limitations regarding upper and lower limits and on impacts of variations in these parameters.

Table 4. Summary of Cases for Stage 2 Evaluation.

Case	CO_2 Feed Content (% mol.)	Rich or Lean Natural Gas
1	6	Lean
2	20	Lean
3	60	Lean
4	6	Rich
5	20	Rich
6	60	Rich

The reference location for the project was the U.S. Gulf Coast. The desired product specifications for the natural gas stream were a maximum of 3% mol. CO_2 and a maximum of 4 ppmv H_2S. Although there was no specification for natural gas product pressure, compression of the treated natural gas back to the feed pressure of 1,015 psig was included for CO_2 separation processes for which the treated gas pressure was significantly lower than the feed pressure. The study defined two different target specifications for CO_2 removed from the natural gas. The first was pipeline quality CO_2 with a

minimum CO_2 content of 95 mol. % and a maximum of 200 ppmv H_2S. The second was for a CO_2 stream suitable for reinjection in a nearby oil field with a minimum content of 70 mol. % CO_2 and no limit on H_2S content. The target pressure for the CO_2 product streams was 2,175 psig. Vendors were asked not to include product compression in their responses, so that the compression costs and energy requirements could be estimated in a uniform manner for each of the vendor responses.

This was an early-phase, conceptual evaluation with a very broad scope. As such, there were several important limitations that impact the level of detail possible. The following list highlights the key limitations that must be taken into consideration when interpreting or using the results of this study.

- The number of vendors that responded was limited.
- Only non-confidential information is included in the reports.
- There are different data sources for equipment cost and weight, since not all vendors provided this information. According to CCP experts, the total offshore cost of a process is highly dependent on the space and weight, which is not accounted for quantitatively in the results of the study.
- The results provided by the vendors may not have been optimized due to the nature of this project and a limited amount of time.
- The product specifications selected for this project were more stringent than typical offshore projects. The natural gas and CO_2 purity specifications that were used on Stage 2 of this project are typical onshore purity specifications. These specifications and the product values and utility costs selected also have significant bearing on the Stage 2 technology comparisons and conclusions.

Evaluation Approach

In all, 18 different vendor responses were evaluated. Vendor responses provided limited details. However, vendors did provide sufficient process data for all the established chemical solvent, membrane, and physical solvent technologies that advanced from Stage 1 to be evaluated in all cases. These process data typically included process flow diagrams, heat and material balances, major energy requirements, and sizing for major equipment required for natural gas/CO_2 separation. In some cases, vendors also provided data for purchased equipment cost and weight. When such data was not provided, the process data from the vendor were used as inputs for Aspen In-Plant Cost Estimator 34.0.0 Build 3438 (Aspen) to estimate the purchased equipment cost and weight for the natural gas/CO_2 separation equipment. A key difference in the data sources used in this evaluation is that membrane module cost and weight information were based on vendor provided data, whereas equipment cost and weight for chemical and physical solvent processes were estimated using Aspen. Vendors also provided recommendations for pre-treatment requirements, but did not provide any process, cost, or weight information for the pre-treatment equipment.

Pretreatment Equipment

A mix of vendor input, Aspen, and in-house data were used to estimate equipment cost, energy requirements, and equipment weight for pre-treatment requirements for the various CO_2 removal options. An inlet coalescing filter separator was included to remove any entrained liquid droplets in the feed for all natural gas/CO_2 separation processes. A molecular sieve dehydration system was included upstream of all membrane and cryogenic processes. Figure 1 shows the process flow diagram for the molecular sieve dehydration system. The use of mole sieve dehydration for all cases allowed the development of estimated equipment and operating costs and weight for one representative set of dehydration pre-treatment equipment that was judged to be sufficient in all of the cases requiring dehydration. This approach may result in overestimation of the pre-treatment requirements in some cases depending on the process conditions and the type of natural gas/CO_2 separation equipment

selected. Hydrocarbon dew point reduction was included for all membrane cases with rich feed. This may also be an overly conservative assumption depending on a particular set of operating conditions and the type of membrane technology selected. Figure 2 shows the process flow diagram for the refrigeration-based hydrocarbon dew point reduction equipment.

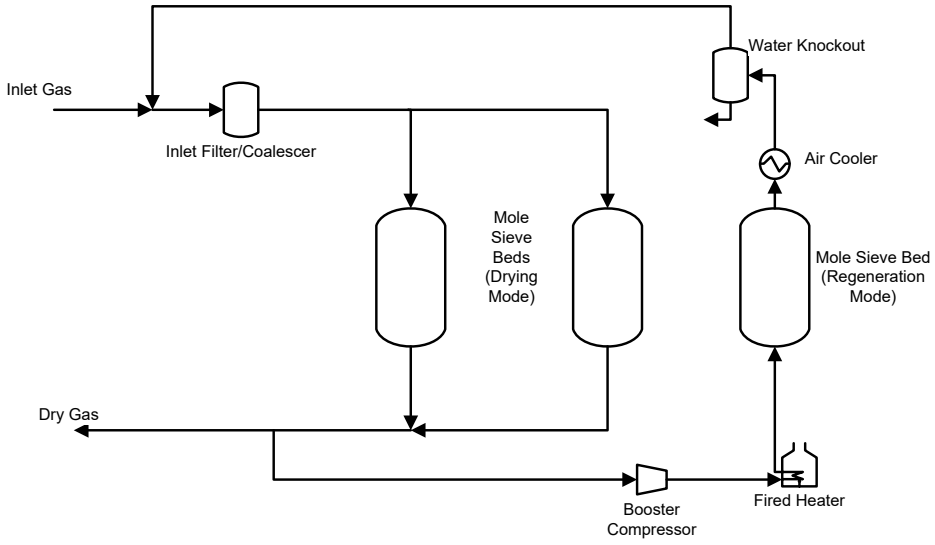

Figure 1. Inlet Gas Dehydration Process Flow Diagram.

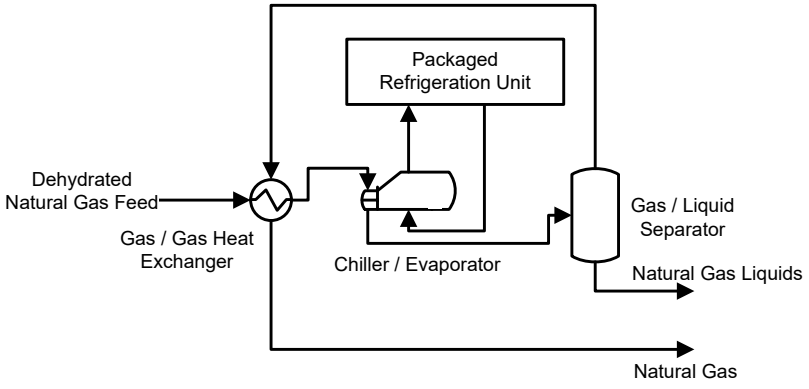

Figure 2. Hydrocarbon Dew Point Reduction Process Flow Diagram.

Compression Equipment

Aspen was used to estimate equipment costs, operating costs, and weight for all compression requirements. These include compression requirements internal to the natural gas/CO_2 separation process as well as any required compression to meet the natural gas and CO_2 product specifications. Centrifugal compressors were selected for all compression requirements.

Natural Gas and CO_2 Product Dehydration

Natural gas triethylene glycol (TEG) dehydration equipment costs were estimated using a reference from the literature (Tannehill, 2009). Equipment costs for CO_2 dehydration using TEG were estimated using Trimeric in-house data from similar projects. The TEG dehydration operating costs were judged to be negligible relative to the major energy requirements for these facilities and were not estimated for this project. The process flow diagrams for TEG dehydration for natural gas and CO_2 are essentially the same. However, there are some differences such as materials of construction. Specifically, corrosion resistant materials such as stainless steel are typically needed for some parts of the CO_2 dehydration system, whereas carbon steel is generally acceptable for natural gas dehydration. Figure 3 shows the TEG dehydration process flow diagram.

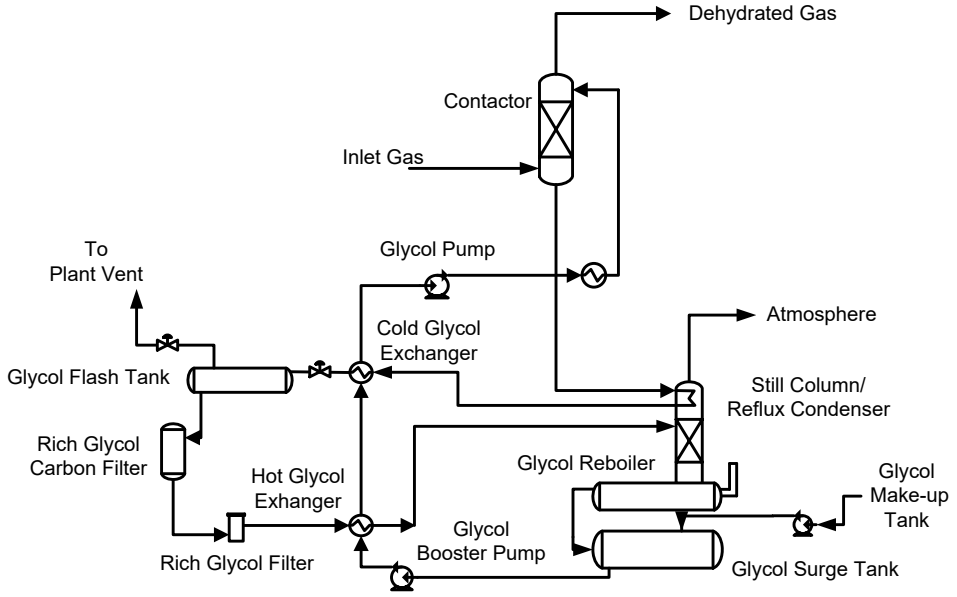

Figure 3. TEG Dehydration Process Flow Diagram.

Natural Gas/CO_2 Separation Technologies

The details of the natural gas/CO_2 separation processes used in the Stage 2 evaluation are confidential. However, the processes are well represented by the conceptual descriptions and process flow diagrams provided below.

Chemical Solvents

Figure 4 provides a conceptual process flow diagram for a chemical solvent absorption process. In these processes, CO_2 is removed from natural gas typically using counter current flow of CO_2-lean solution that enters the top of a contactor and flows downward while CO_2-laden natural gas enters the bottom of the contactor and travels upward through the vessel. Packing, trays, or other contactor internals provide surface area for mass transfer and ensure proper gas and liquid distribution so that the CO_2 is removed from the natural gas and absorbed into the solvent via a reversible chemical reaction. The most widely used solvents are aqueous solutions of alkanolamines. There is a huge volume of literature on the best solvent to use depending on feed gas composition, process conditions, and treated gas specification (Kohl and Nielsen, 1997). Natural gas with a reduced CO_2 content leaves the top of the contactor and CO_2-rich solvent is flashed to a lower pressure in a flash vessel and then heated in a stripping column to remove the CO_2 from the solvent, providing a CO_2 product stream leaving the top of the stripper and lean solvent leaving the bottom of the stripper for reuse in the contactor. Heat exchange between rich and lean solvent streams improves the energy efficiency of the process.

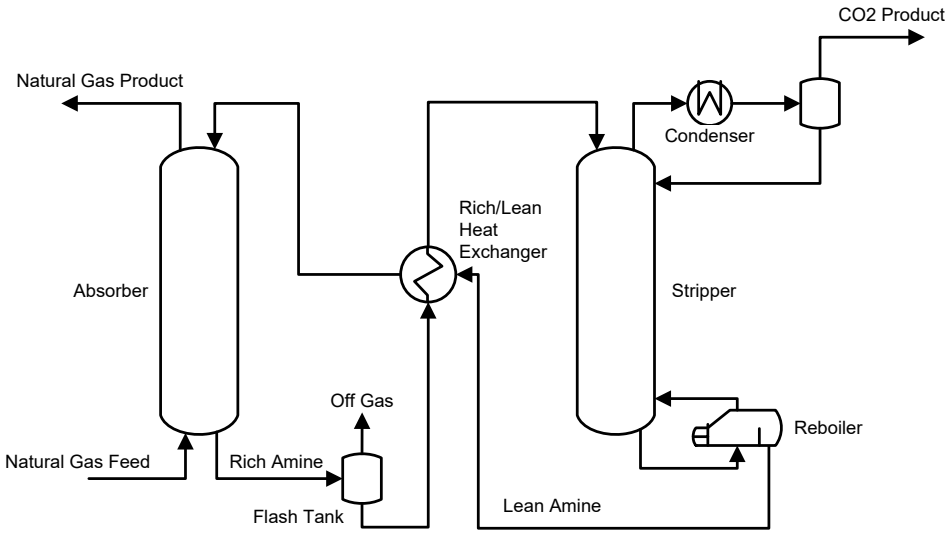

Figure 4. Conceptual Process Flow Diagram for Absorption Using a Chemical Solvent.

Membranes

Figure 5 provides conceptual process flow diagrams for three typical membrane separation approaches. Individual molecular species in a gas stream pass through the membrane at different rates based on differences in selectivity and permeability. The selectivity and permeability are properties of the membrane material. Pre-treatment requirements are an important part of a membrane process and will vary depending on the process conditions and the type of membrane selected. Pretreatment requirements may include inlet filter coalescing separation, and varying levels of dehydration and hydrocarbon dew point reduction, as well as removal of heavy hydrocarbons (C_{10}-C_{15}), which can damage certain types of membranes. Vendors should be contacted in order to determine specific pre-

treatment requirements for a given feed composition and set of process conditions. The pre-treatment equipment cost is not trivial and, in some cases, may be comparable to the cost of the balance of the membrane separation system.

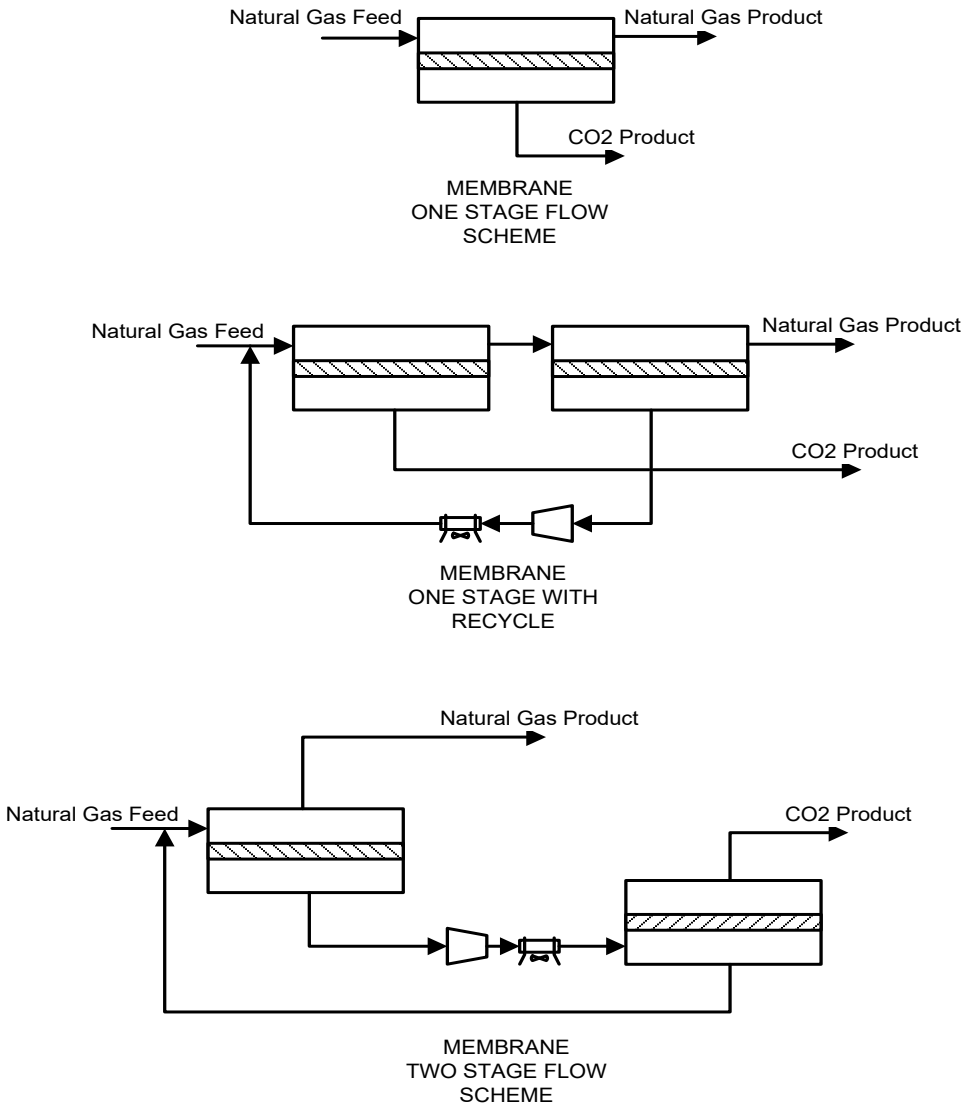

Figure 5. Conceptual Process Flow Diagrams for Membrane Separation Systems.

Physical Solvents

Figure 6 provides a conceptual process flow diagram for a physical absorption process. This process is similar to the chemical absorption process. The main difference is that the CO_2 is absorbed into a physical solvent by physical attraction of the CO_2 and solvent molecules as opposed to a chemical reaction. The physical solvent is often regenerated only by pressure change, whereas both heat input and pressure reduction are mechanisms for solvent regeneration in chemical processes. Lower CO_2 concentrations in the feed favor the stronger CO_2-solvent interaction in the chemical absorption processes. Physical absorption is favored at higher CO_2 partial pressures–a combination of higher CO_2 concentration and higher pressure in the gas stream to be treated–due to lower energy requirements than for chemical solvents.

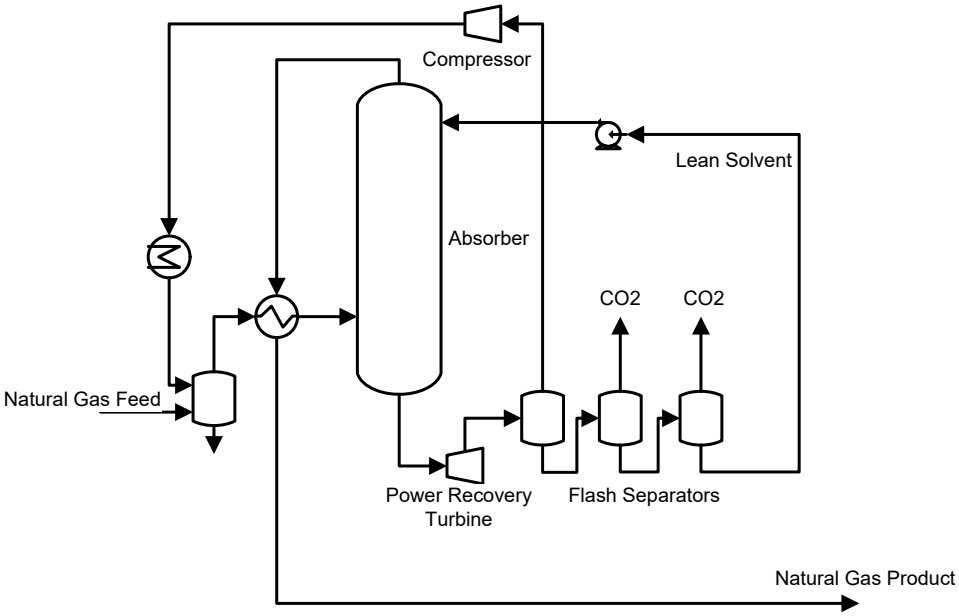

Figure 6. Conceptual Process Flow Diagram for Absorption Using a Physical Solvent.

Distillation/Low Temperature Separation Processes

Figure 7 shows a conceptual process flow diagram for a distillation process to separate CO_2 from natural gas. Distillation relies on the difference in relative volatilities (boiling points) of the compounds to be separated. Packing, trays, or other distillation column internals provide gas-liquid contact area and ensure proper gas and liquid distribution within the column. Heat is applied at the bottom of the column to generate stripping gas that travels up the column while cooling is applied to the overhead stream to condense some of the less volatile components (CO_2 in this instance) and to return a reflux liquid stream to travel back down the column. Low temperatures are required for distillation of CO_2 from natural gas, so refrigeration and heat integration are critical components that significantly impact the performance and capital and operating costs of this process. Distillation alone is not sufficient to produce a natural gas stream that meets the CCP product specifications in this project. In order to reach the required natural gas purity, temperatures in the upper portion of the distillation column would be so low that CO_2 would solidify in the distillation column.

Therefore, other approaches beyond conventional distillation such as extractive distillation (e.g., Ryan-Holmes) or conventional distillation in combination with another treatment method like a physical solvent or other processes that intentionally form solid CO_2 during the cryogenic separation process are required to further purify the overhead natural gas stream leaving the distillation column to meet natural gas product specifications. One such emerging technology was included in the Stage 2 evaluation; however, the details are not included in this chapter due to confidentiality concerns.

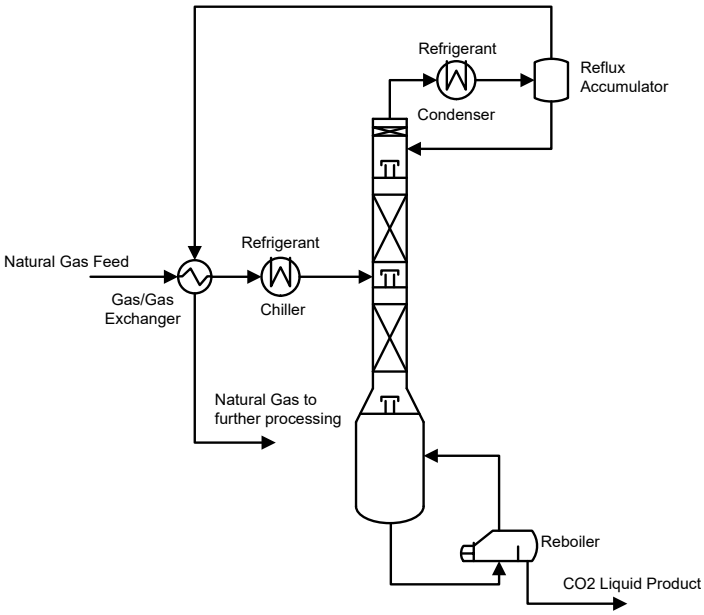

Figure 7. Conceptual Process Flow Diagram for Distillation.

Product Values and Utility Costs

Product values and utility costs for fuel gas and electricity have significant influence on the quantitative comparisons. Table 5 summarizes these values used for this study. CCP specified that the value for natural gas should be consistent with other studies coordinated by CCP. Fuel gas requirements were assumed to reduce the net amount of product natural gas on a heating value basis and therefore, the cost of fuel gas was assumed equal to the value of the product natural gas. The design basis for this study includes no offshore facilities for fractionation, storage, and transportation of NGL products, and therefore the value of NGL products was based on the heating value and the same price per Btu as that of the product natural gas. The offshore facility is specified to generate power for all operations including natural gas/CO_2 separation. The power cost used in this study, $ 0.05/kWh, is lower than that for a typical residential customer which might be closer to $ 0.10/kWh in the U.S, reflecting the absence of distribution losses and costs.

The value of CO_2 product was based on typical pipeline values in West Texas for Enhanced Oil Recovery (EOR) applications. The study basis is $40/bbl of oil and a rough correlation between the price of purchased CO_2 and the price of oil is CO_2 price in $/Mscf equal to 2% of the price of oil in $/bbl. To account for the different purities of CO_2 produced by the separation processes, the price of high purity CO_2, at $ 0.80/Mscf, was multiplied by the vol. % of CO_2 to estimate the value of CO_2

streams with differing purity. This gives some advantage to 99%+ purity chemical solvent processes, some penalty to 70% purity membrane cases, and a basis for differentiation of the cases that fall somewhere in the middle.

Table 5. Summary of Selected Product Values and Utility Costs.

Product/Utility	Units	Value
Natural Gas	$/MMBtu (HHV)	4.5
Fuel Gas	$/MMBtu (HHV)	4.5
NGL	$/MMBtu (HHV)	4.5
Electricity	$/kWh	0.05
CO_2	$/Mscf ($/tonne)	0.80 (15.19)

QUANTITATIVE SCREENING RESULTS

This section provides the results of the quantitative Stage 2 comparisons for each of the six selected cases. The inlet CO_2 content in the feed had a stronger impact on the technology rankings than whether the gas was lean or rich. While membrane systems are generally regarded as having lighter weight than solvent processes, membrane processes require internal and product compression. The compression equipment adds to the total estimated weight for the membrane processes. A subtlety for the 6% CO_2 cases (without H_2S) is that the chemical solvent process can be sized to treat half of the feed gas flow rate and still meet the treated natural gas specification of 3% CO_2. This significantly reduces the chemical solvent system weight for these cases. Other factors such as shorter equipment height, possibly smaller footprint, and a simpler process with membranes compared to solvent-based processes, can strongly influence costs for offshore operations, and would have to be taken into consideration by the end user in a project specific application.

6% CO_2

Physical solvent vendors acknowledged that physical solvent processes would not be competitive at the low CO_2 partial pressures associated with the 6% lean and rich gas composition cases, so no assessment was done for these cases. One key factor in the technology comparison for the 6% lean and rich cases is that about half of the 500 MMscfd feed flow rate needs to be treated in the chemical solvent process to meet the natural gas CO_2 content specification. In contrast, the entire feed flow rate is treated in the other processes.

Established technologies considered for the 6% cases, both lean and rich gas, were chemical solvent and membrane processes. Table 6 provides the results summary for the lean gas case and Table 7 for the rich gas case.

Emerging technologies were also considered for the 6% rich case; however, the detailed results are not included here due to confidentiality. A novel gas-liquid contactor which utilizes hollow fiber membranes for chemical solvent treating may show promise where space and weight constraints impose high costs – a factor which was not assessed quantitatively in this study. Also considered was a cryogenic process which freezes out the CO_2 contained in the feed gas (anti-sublimation) and separates the solid CO_2, which can be subsequently melted and pumped to the required pressure. Too little information was provided to perform a detailed assessment, but the cryogenic approach appeared uncompetitive in terms of estimated capital costs and weight at the low CO_2 concentration for this

case. It is possible that the anti-sublimation technology is more competitive at higher CO_2 concentrations, but emerging technology supplier only provided input for the 6% rich case.

Table 6. Results Summary for 6% CO_2, Lean Gas Composition.

Parameter	Units	Chemical Solvent	Membrane
Purchased Equipment Costs	$ MM	14	31
Installed Equipment Costs	$ MM	45	78
Gross Revenue	$ MM/yr	750	741
Major Operating Costs	$ MM/yr	11	9
Net Revenue	$ MM/yr	739	732
Natural Gas Product Rate	MMscfd	484	478
Estimated Weight	tonne	3,392	5,293
CO_2 Product Purity	mol. %	99.8	70.7

Table 7. Results Summary for 6% CO_2, Rich Gas Composition.

Parameter	Units	Chemical Solvent	Membrane
Purchased Equipment Costs	$ MM	14	39
Installed Equipment Costs	$ MM	45	99
Gross Revenue	$ MM/yr	964	953
Major Operating Costs	$ MM/yr	11	8
Net Revenue	$ MM/yr	953	945
Natural Gas Product Rate	MMscfd	484	457
Estimated Weight	tonne	3,392	4,981
CO_2 Product Purity	mol. %	99.7	71.9

20% CO_2

Established technologies considered for the 20% cases, both lean and rich gas, were chemical solvent, membrane, and physical solvent processes. Table 8 provides the results summary for the lean gas case, and Table 9 for the rich gas case.

Table 8. Results Summary for 20% CO_2, Lean Gas Composition.

Parameter	Units	Chemical Solvent	Membrane	Physical Solvent
Purchased Equipment Costs	$ MM	53	70	40
Installed Equipment Costs	$ MM	151	155	124
Gross Revenue	$ MM/yr	661	602	652
Major Operating Costs	$ MM/yr	59	27	19
Net Revenue	$ MM/yr	602	576	633
Natural Gas Product Rate	MMscfd	410	375	408
Estimated Weight	tonne	9,641	6,128	5,057
CO_2 Product Purity	mol. %	99.8	71.0	95.5

Table 9. Results Summary for 20% CO_2, Rich Gas Composition.

Parameter	Units	Chemical Solvent	Membrane	Physical Solvent
Purchased Equipment Costs	$ MM	53	70	42
Installed Equipment Costs	$ MM	151	160	161
Gross Revenue	$ MM/yr	841	787	770
Major Operating Costs	$ MM/yr	59	21	19
Net Revenue	$ MM/yr	781	765	751
Natural Gas Product Rate	MMscfd	410	353	376
Estimated Weight	tonne	9,641	6,716	6,178
CO_2 Product Purity	mol. %	99.8	70.8	78.4

60% CO_2

Vendor data were obtained for chemical solvent processes for the 60% lean and rich cases, but operating costs including reboiler heat input and pump power were not competitive with the other options considered, so an economic evaluation for the chemical solvent process was not performed for these cases. Two membrane configurations were evaluated for the 60% lean and rich cases. The first used only a primary membrane configuration, which had less equipment with attendant lower capital and operating costs. However, it achieved significantly lower natural gas recovery and could not meet the 95% CO_2 product specification. The second membrane option used both primary and secondary membrane modules, which requires additional compression and has higher capital and operating costs than the single-stage scheme. However, the second option achieves higher natural gas product recovery, and it was able to meet the 95% CO_2 specification. For the membrane cases, the feed gas pressure (1,015 psig) is let down for optimal functioning of the membranes. Although use of a power recovery turbine or heat integration may enhance the economics of the membrane systems, budget and time constraints precluded such an evaluation in this case.

Established technologies considered for the 60% lean and rich cases were membrane and physical solvent processes. Tables 10 and 11 provide the results summary for these cases.

Table 10. Results Summary for 60% CO_2, Lean Gas Composition.

Parameter	Units	Membrane Option 1	Membrane Option 2	Physical Solvent
Purchased Equipment Costs	$ MM	67	93	66
Installed Equipment Costs	$ MM	149	202	178
Gross Revenue	$ MM/yr	253	377	382
Major Operating Costs	$ MM/yr	47	55	44
Net Revenue	$ MM/yr	206	322	339
Natural Gas Product Rate	MMscfd	110	191	195
Estimated Weight	tonne	6,051	10,305	7,481
CO_2 Product Purity	mol. %	76.1	95.0	96.3

Table 11. Results Summary for 60% CO_2, Rich Gas Composition.

Parameter	Units	Membrane Option 1	Membrane Option 2	Physical Solvent
Purchased Equipment Costs	$ MM	76	96	57
Installed Equipment Costs	$ MM	173	213	165
Gross Revenue	$ MM/yr	342	469	377
Major Operating Costs	$ MM/yr	45	53	43
Net Revenue	$ MM/yr	297	416	334
Natural Gas Product Rate	MMscfd	115	187	173
Estimated Weight	tonne	7,115	8,760	7,162
CO_2 Product Purity	mol. %	79.0	95.3	89.9

CONCLUSIONS

Key findings from the cases evaluated in Stage 2 were as follows:

- Chemical solvents have higher hydrocarbon recovery percentages than membrane and physical solvent processes.
- Chemical solvent approaches appear to be the favored option over membranes for lower inlet CO_2 concentrations (up to 6 mol. % CO_2 in the feed) in both lean and rich natural gas cases. One key reason for this is that only half of the feed needs to be treated with chemical solvents in order to meet the product specifications in the absence of H_2S.

- Physical solvents are not practical for 6 mol. % CO_2 in the feed due to prohibitively high solvent circulation rates and resulting equipment sizes and operating costs at these low CO_2 partial pressure feed conditions.
- At 20 mol. % CO_2 in the feed, system weight, and operating costs of chemical solvents are very likely to be high enough to offset the revenue advantages that they provide with higher hydrocarbon recovery.
- Physical solvent and membrane processes appear competitive at 20 mol. % CO_2 in the feed. At this CO_2 concentration in the feed, physical solvents may have a slight advantage over membranes with lean natural gas in the feed due to lower estimated installed equipment costs and higher net revenue. Membranes are favored over physical solvents with 20 mol. % CO_2 and rich natural gas in the feed as hydrocarbon losses into the physical solvent increase.
- Chemical solvents are not practical for 60 mol. % CO_2 in the feed due prohibitively high solvent circulation rates and resulting equipment sizes and operating costs at these high CO_2 content feed conditions.
- Physical solvents had a slight advantage over membranes with 60 mol. % CO_2 and lean natural gas in the feed. Membranes had a clear advantage over physical solvents with 60 mol. % CO_2 and rich natural gas in the feed due to higher hydrocarbon losses into the physical solvent.
- In some cases, certain technologies were not able to achieve 95% CO_2 purity (at least, not cost-effectively). For example, the membranes were able to achieve 95% CO_2 purity only in the 60% CO_2 feed cases, and the physical solvent could achieve 95% CO_2 purity in the 20% and 60% CO_2 lean feed cases, but not in the corresponding rich feed cases. If 95% CO_2 purity is desired, then in some cases chemical solvents (or hybrid processes) may be the only viable option out of the established processes considered.
- The most promising emerging technology identified was a novel gas-liquid contactor utilizing hollow fiber membranes for solvent scrubbing. This technology may be a good candidate for applications where weight and space constraints impose high costs, particularly with lower CO_2-content feed streams and/or lower limits for CO_2 in product natural gas that are not suitable for a membrane-only approach.

A technology landscape map (Figure 8) based on results of this study has been developed, which illustrates where chemical solvents, membranes, and physical solvents appear to be favored.

Chemical solvents appear to be more competitive for ≤ 6 mol. % CO_2 in the feed. As the CO_2 feed content increases, the size, weight, and energy consumption of chemical solvent processes increase, and the membrane domain is entered. In the region around 15 – 20 mol. % CO_2, chemical solvents and membranes are both competitive. Physical solvents are most suitable for lean natural gas applications when CO_2 concentrations are high enough, but at lower CO_2 feed concentrations, physical solvents can accommodate richer natural gas because the circulation rate is lower, which reduces hydrocarbon losses, hence the slope of the application boundary between physical solvents and membranes in Figure 8.

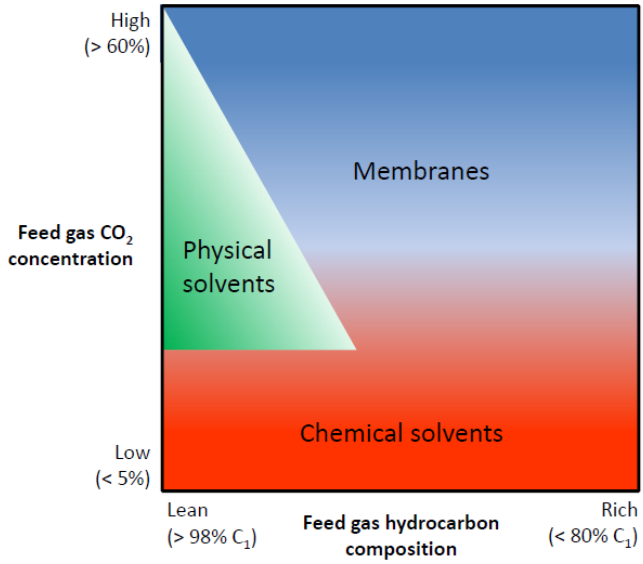

Figure 8. Technology Landscape Map.

SUMMARY

Vendor input for the Stage 2 quantitative evaluation confirmed some of the Stage 1 findings, but in other cases, the detailed assessment led to different results than anticipated during the qualitative Stage 1 evaluation. The quantitative results confirmed Stage 1 expectations that membrane technology is a leading, established technology for offshore natural gas/CO_2 separation applications. They also confirmed that chemical solvent approaches would be prohibitively expensive at high CO_2 feed concentrations, and that physical solvent processes are similarly impractical at low CO_2 feed concentrations. Although higher natural gas recovery with chemical solvents tends to favor this technology over membranes and physical solvents, this does not hold in all cases. For low CO_2 feed concentrations (e.g., around 6 mol. % CO_2 in the feed), only about half of the total gas feed stream needs to be treated using chemical solvents to meet the project specifications for natural gas and CO_2 products (in the absence of H_2S). This partial stream treatment approach reduces equipment cost, weight, and footprint in these cases, making solvent-based approaches economically attractive for these offshore applications.

The product specifications selected for the Stage 2 evaluation were more stringent than those in typical offshore projects. In effect, the natural gas and CO_2 purity specifications used on Stage 2 of this project are similar to typical onshore purity specifications. Technology comparisons and conclusions are highly sensitive to product specifications for natural gas and CO_2, values for natural gas and NGL products, utility costs, and system weight.

The most promising emerging technology identified was a novel gas-liquid contactor utilizing hollow fiber membranes for solvent scrubbing. This technology may be a good candidate for applications where weight and space constraints impose high costs, particularly with lower CO_2-content feed streams and/or lower limits for CO_2 in product natural gas that are not suitable for a membrane-only approach. The emerging cryogenic process evaluated in Stage 2 appeared uncompetitive in terms of estimated capital costs and weight with 6% CO_2 in the feed, but this was the only case that the supplier

provided data for assessment. Cryogenic approaches may be a better fit at high CO_2 feed concentrations (e.g., 60 mol. % CO_2). A novel high pressure water absorption process may be of interest, but it did not meet the Technology Readiness Level requirements that CCP specified at the time of this study. A handful of emerging solvents evaluated in Stage 1 such as enzyme enhanced solvents may hold promise, but suppliers cited resource limitations and declined to provide input for evaluation in Stage 2.

REFERENCES

General Reference

Shimekit, B., and Mukhtar, H. (2012). *Natural Gas Purification Technologies - Major Advances for CO_2 Separation and Future Directions*. In *Advances in Natural Gas Technology* Hamid A. Al-Megren, IntechOpen, DOI: 10.5772/38656. Available from: https://www.intechopen.com/books/advances-in-natural-gas-technology/natural-gas-purification-technologies-major-advances-for-co2-separation-and-future-directions

Tannehill, Carter (2009). *Budget Estimate Capital Cost Curves for Gas Conditioning and Processing – Updated.* Gas Processors Association. Available from: https://gpamidstream.org/publications/item/?id=4315

Established Technologies

Chemical Solvents

Chitnis, G., *et al*., (2015) *FLEXSORB™ Technology and FLEXSORB SE Hybrid Technology Suite*, Selective Gas Treating to Enhance Upstream and Refining Projects, at 6th IGTC Conference Dubai, February 19-20, 2015, https://docplayer.net/59984993-Flexsorb-technology-and-flexsorb-se-hybrid-technology-suite.html

Kohl, A. L., and R. B. Nielsen, 1997, *Gas Purification*, 5th Ed. Gulf Publishing Co.

UOP Offshore Gas Processing, Brochure: "Proven gas treating solutions for offshore floating or fixed platforms," at http://www.uop.com/?document=uop-offshore-gas-processing-brochure&download=1 .

Jain, P., J.C. Kuo, M. Hernandez, G. Garza, and Dr. T.L. Hernandez, 2000, "Offshore Gas Sweetening and Acid Gas Injection: An Overview," (Cantarell field offshore Mexico, fixed platform, MDEA treater to remove H_2S and CO_2 at 1,100 psia), *Proceedings of 50th Laurance Reid Gas Conditioning Conference,* Norman OK.

Carroll, J., and Maddocks, D., 1999, Design Considerations for Acid Gas Injection, *Proceedings of 49th Laurance Reid Gas Conditioning Conference*, Norman, OK.

Lidal, H., J.I. Nilsen, H. Isaksen, and V. Hoang-Dinh, 1998, "CO_2 Removal at Sleipner," (Statoil, N. Sea field offshore Norway, fixed platform, activated MDEA treatment of 850 MMSCFD of 9.2% CO_2 natural gas at 1,508 psia, CO_2 acid gas reinjected), *Proceedings of 48th Laurance Reid Gas Conditioning Conference,* Norman OK.

Epps, R., 1990, "UCARSOL Solvents State of the Art Amine Technology," (Excessive H_2S levels in sales gas containing 2,000 ppm H_2S and 4.8% CO_2 from an offshore California crude oil production platform were solved by using UCARSOL HS-102), *Proceedings of 40th Laurance Reid Gas Conditioning Conference,* Norman OK.

Minkkinen, A., and J. Levier, 1992, "IFP, IFPEXOL: Complete Gas Treatment with a Basic Single Solvent," (The IFPEX-2 CO_2 removal part of the process is compared with MDEA, notes applicability to offshore and cold locations), *Proceedings of 42nd Laurance Reid Gas Conditioning Conference,* Norman OK.

Seagraves, J., and R. Weiland, 2007, Ineos, "Troubleshooting Amine Plants Using Mas Transfer Rate-Based Simulation Tools", (Case 2 study refers to offshore MDEA process treating 450 MMSCFD of natural gas containing 3.25% CO_2 and 1.35% H_2S), *Proceedings of 57th Laurance Reid Gas Conditioning Conference,* Norman OK.

UOP, Brochure: "UOP Benfield Process - Low Cost Removal of CO_2 and H_2S from Natural and Synthesis Gas,"at http://www.uop.com/?document=benfield-process-datasheet&download=1

Shell, web link Sulfinol, http://www.shell.com/business-customers/global-solutions/gas-processing-licensing/gas-processing-technolgies-portfolio.html

Physical Solvents

Mak, *et al.*, 2003, "New Physical Solvent Treating Configurations for Offshore High Pressure CO_2 Removal," Offshore Technology Conference, https://www.onepetro.org/conference-paper/OTC-15354-MS

Mak, *et al.*, 2010, "Fluor Solvent – A Flexible CO_2 Removal Process," *Proceedings of 60th Laurance Reid Gas Conditioning Conference,* Norman OK.

Mak, *et al.*, 2015, "Coping Under Pressure," *LNG Industry*, Jul/Aug 2015

Lima, *et al.*, 2014, "Technical, Economic and Environmental Viability of Offshore CO_2 Reuse from Natural Gas By Dry Reforming," American Institute of Chemical Engineers Annual Meeting, https://aiche.confex.com/aiche/2014/webprogram/Paper369173.html

Adsorption

Molecular Gate Brochure, http://www.moleculargate.com/carbon-dioxide-removal-adsorption-system.html

Extractive Distillation

Chart Energy and Chemicals, http://files.chartindustries.com/Integrated-Process-Systems.pdf

Finn, *et al.*, 2014, "Processing of Carbon Dioxide Rich Gas," GPA Annual Convention, Sep. 17, 2014, http://costain.com/media/13020/gpa-conference-sept-2014-1mb.pdf

Controlled Freeze Zone

ExxonMobil, http://corporate.exxonmobil.com/en/engineering/energy-efficiency/controlled-freeze-zone/technology

Kelley, *et al.*, 2011, "Controlled Freeze Zone Commercial Demonstration Plant Advances Technology for the Commercialization of Sour Gas Reserves," GHGT-10, Amsterdam, http://www.sciencedirect.com/science/article/pii/S1876610211001275 .

Finn, *et al.*, 2014, "Processing of Carbon Dioxide Rich Gas," GPA Annual Convention, Sep. 17, 2014, http://costain.com/media/13020/gpa-conference-sept-2014-1mb.pdf .

Membranes (Established)

Echt, *et al.*, 2002, "Fundamentals of Membrane Technology for CO_2 Removal from Natural Gas," *Proceedings of 52nd Laurance Reid Gas Conditioning Conference,* Norman OK.

Munoz, *et al.*, 2007, "Successful Commissioning of CO_2 Removal Facility in Gulf of Thailand," (Cynara membrane for Carigali Hess to process 700 MMSCFD of 37% CO_2 to produce 425 MMSCFD of sales gas with 23% CO_2 spec, membrane design basis was 15% CO_2 in sales, (2) x 50% pretreatment trains each feeding 4 membrane clusters each, (8 total) configured in parallel), *Proceedings of 57th Laurance Reid Gas Conditioning Conference,* Norman OK.

Oil & Gas Journal, May 28, 2007, "Offshore processing plant uses membranes for CO_2 removal," http://www.ogj.com/articles/print/volume-105/issue-20/processing/offshore-processing-plant-uses-membranes-for-cosub2-sub-removal.html

UOP Offshore Gas Processing, Brochure: "Proven gas treating solutions for offshore floating or fixed platforms," at http://www.uop.com/?document=uop-offshore-gas-processing-brochure&download=1 .

Echt, *et al.*, 2009, "Design, Fabrication and Startup of an Offshore Membrane CO_2 Removal System," (Offshore, Asia, feed 590-680 MMscfd, 44.5% CO_2 in feed, treat to 8% CO_2), Gas Processors Association Annual Convention, http://www.uop.com/?document=design-fabrication-startup-of-an-offshore-separex-membrane-system&download=1,

UOP, 2009, Presentation: "UOP Separex Membrane Technology," (Slide 31 of 44: Offshore membranes 2 off Thailand, 1 in Malaysia, in construction 1 in Thailand, 1 in S. America, 1 in Tunisia), https://www.honeywell-uop.cn/wp-content/uploads/2011/02/UOP-Separex-Membrane-Technologytech-presentation.pdf

Gulf Publishing, 2013, "Cameron awarded FPSO process equipment from SBM Offshore," *Gas Processing News*, http://gasprocessingnews.com/news/cameron-awarded-fpso-process-equipment-from-sbm-offshore.aspx

RIGZONE.COM, 2008, "NATCO to Provide Membrane Technology Offshore Libya," http://www.rigzone.com/news/oil_gas/a/64290/NATCO_to_Provide_Membrane_Technology_Offshore_Libya

Bikson, *et al.*, 2013, "PoroGen, Advances in Membrane Technology Open New Options for Natural Gas Treating," *Proceedings of 53rd Laurance Reid Gas Conditioning Conference,* Norman OK.

Distillation–Physical Solvent in Series

Ross, *et al.*, 2009, "Economical Option for CO_2/Methane Separation in Produced Gas Containing a High CO_2 Fraction," *Proceedings of 49th Laurance Reid Gas Conditioning Conference,* Norman OK.

Membranes–Chemical Solvent in Series

Leppin, 2013, "Acid Gas and Trace Contaminant Removal from Synthesis Gas produced by fluidized bed gasification of wood using the Morphysorb® Process in the GTI Flex Fuel Pilot Plant," Gas Technology Institute tcbiomass Conference, 3-6 Sept 2013, Chicago.

Anderson, 2005, "Case Study: Membrane CO_2 Removal from Natural Gas, Grissik Gas Plant, Sumatra, Indonesia," *Proceedings of 45th Laurance Reid Gas Conditioning Conference,* Norman OK.

Blizzard, *et al.*, 2005, "CO_2 Separation Membranes – A Critical Part of the Mallet CO_2 Removal Facility," (portion of plant is membrane followed by MDEA), *Proceedings of 45th Laurance Reid Gas Conditioning Conference,* Norman OK.

Membranes – Physical Solvent in Series

Blizzard, *et al.*, 2005, NATCO, CO_2 Separation Membranes – A Critical Part of the Mallet CO_2 Removal Facility, (portion of plant is membrane followed by Selexol), *Proceedings of 45th Laurance Reid Gas Conditioning Conference,* Norman OK.

Emerging Technologies

Ionic Liquids

Vlugt, *et al.*, 2012, 'State of the Art of CO_2 Capture with Ionic Liquids,' *Industrial & Engineering Chemistry Research*, http://pubs.acs.org/doi/pdf/10.1021/ie3003705

Ionic Liquid – Membrane Combination

Lennert, *et al.*, 2015, 'Highly Efficient Materials for Enhanced Natural Gas Sweetening,' *Proceedings of 55th Laurance Reid Gas Conditioning Conference,* Norman OK.

High Pressure Water

Partnering-in-Innovation, http://www.pi-innovation.com/#/pi-co2-technology-index/

Chilled Ammonia

Askander, *et al.*, 2013, "Chilled Ammonia Process at Technology Center Mongstad - First Results," *Energy Procedia* **51** (31-19) http://www.sciencedirect.com/science/article/pii/S1876610214008662 .

Phase Changing Solvents

Westendorf, 2015, "Bench-Scale Process for Low-Cost Carbon Dioxide (CO_2) Capture Using a Phase Changing Absorbent," NETL CO_2 Capture Technology Meeting, http://www.netl.doe.gov/File%20Library/Events/2015/co2captureproceedings/T-Westendorf-GE-Phase-Changing-Absorbent.pdf

Catalyst Activated Solvents

Lippert, *et al.*, 2015, "An Advanced Catalytic Solvent for Lower Cost Post-combustion CO_2 Capture in a Coal-fired Power Plant," NETL CO_2 Capture Technology Meeting, http://www.netl.doe.gov/File%20Library/Events/2015/co2captureproceedings/C-Lippert-CAER-UK-Advanced-Catalytic-Solvent.pdf

Enzyme Activated Absorption

Zaks, 2015, "Low Energy CO_2 Capture Enabled by Biocatalyst Delivery System," NETL CO_2 Capture Technology Meeting, http://www.netl.doe.gov/File%20Library/Events/2015/co2captureproceedings/A-Zaks-Akermin-Biocatalyst-Delivery-System.pdf

Akermin, 2014, Akermin Announces Commercial-Scale, International Demonstration Project, http://akermin.com/akermin-announces-commercial-scale-international-demonstration-project/

Hardcastle, 2015, "CO_2 Solutions Completes Carbon Capture Pilot Testing," Environmental Leader, http://www.environmentalleader.com/2015/04/27/co2-solutions-completes-carbon-capture-pilot-testing/

Other Solvents

Kumagai, *et al.*, 2011, "HiPACT – Advanced CO_2 Capture Technology for Green Natural Gas Exploration," GHGT-10, http://www.sciencedirect.com/science/article/pii/S1876610211000336

Tanaka, *et al.*, 2013, "Demonstration Test Result of High Pressure Acid gas Capture Technology (HiPACT)," GHGT-11, http://www.sciencedirect.com/science/article/pii/S1876610213001422

Pek, *et al.*, 2013, "A High Capacity Floating LNG Design, Shell Projects and Technology," (ADIP-X), LNG 17, Houston, http://www.gastechnology.org/Training/Documents/LNG17-proceedings/12-1-Barend_Pek.pdf

Carbon Clean Solutions, CDRMax: http://www.carboncleansolutions.com/technology/process-technology

Adsorbents

ECN Immo-Ammo:http://www.ispt.eu/media/7418-A4-ISPT-Posterboek-2016-webv3.pdf

Novel Contactors

Westec Environmental Solutions: http://wes-worldwide.com/ (Novel absorption contactor using transitory froth formation in co-current process)

Wang, *et al.*, 2011, "Progress on HiGee distillation—Introduction to a New Device and Its Industrial Applications," *Chemical Engineering Research and Design*, **89** (8) http://www.sciencedirect.com/science/article/pii/S0263876211000712 ,

Hardcastle, 2015, CO_2 Solutions, GasTran Systems Aim to Lower Carbon Capture Costs, Environmental Leader, https://www.environmentalleader.com/2015/06/co2-solutions-gastran-systems-aim-to-lower-carbon-capture-costs/ .

Membranes–Electrochemical Cell

Ghezel-Ayagh, 2015, "Electrochemical Membranes for CO_2 Capture and Power Generation," NETL CO_2 Capture Technology Meeting, Pittsburgh, https://www.netl.doe.gov/File%20Library/Events/2015/co2captureproceedings/H-Ghezel-Ayagh-FCE-Electrochemical-Membranes.pdf .

Membranes–Graphene Oxide

Xin, *et al.*, 2015, "Enhancing the CO_2 Separation Performance of Composite Membranes by the Incorporation of Amino Acid-functionalized Graphene Oxide," *Journal of Materials Chemistry A*, https://pubs.rsc.org/en/Content/ArticleLanding/2015/TA/C5TA00506J#!divAbstract

Li, *et al.*, Energy Efficient GO-PEEK Hybrid Membrane Process for Post-combustion CO_2 Capture, December 7, 2015, https://www.netl.doe.gov/File%20Library/Research/Coal/carbon%20capture/post-combustion/FE0026383-Kickoff-Presentation.pdf .

Membranes–Inorganic

Zhang, *et al.*, 2012, "Current Status and Development of Membranes for CO_2/CH_4 separation: A Review," https://www.sciencedirect.com/science/article/abs/pii/S1750583612002423 .

Membranes–Thermally Rearranged

Zhang, *et al.*, 2012, "Current Status and Development of Membranes for CO_2/CH_4 separation: A Review," http://www.sciencedirect.com/science/article/pii/S1750583612002423

Membranes–Mixed Matrix/Metal Oxide Framework

Zhang, *et al.*, 2012, "Current Status and Development of Membranes for CO_2/CH_4 separation: A Review," https://www.sciencedirect.com/science/article/abs/pii/S1750583612002423 .

Hupp, *et al.*, 2008, "Separation of CO_2 from CH_4 Using Mixed-Ligand Metal-Organic Frameworks," http://chemgroups.northwestern.edu/hupp/Publications/251.pdf .

Cryogenic Processes

Baxter, 2015, "Cryogenic Carbon Capture," Poster at NETL CO_2 Capture Technology Meeting, https://www.netl.doe.gov/File%20Library/Events/2015/co2captureproceedings/L-Baxter-SES-Cryogenic-Carbon-Capture.pdf .

Air Liquide, 2015, Press Release: Cryocap Process, https://www.airliquide.com/media/world-premiere-air-liquide-inaugurates-its-co2-cold-capture-system-cryocap

Hollow Fiber Contactor/Chemical Solvent Hybrid Process

Leppin, *et al.*, 2014, "Development of Porous PEEK Hollow Fiber-Based Gas/Liquid Membrane Contactors for Sour Gas Treating," *Proceedings of 54th Laurance Reid Gas Conditioning Conference,* Norman OK.

Carbon Dioxide Capture for Storage in Deep Geological Formations, Volume 5
Karl F. Gerdes (Editor)
© 2022 BP. All rights reserved.

Chapter 19

DEVELOPMENT OF MEMBRANE-BASED CO_2 SEPARATION FOR SUBSEA PROCESSING

Pål Helge Nøkleby[1], Taek-Joong Kim[2], Rune Gaarder[2], He Zhao[3]
[1]Aker Carbon Capture, Lysaker, Norway
[2]Sintef Industry, Trondheim/Oslo, Norway
[3]Aker Solutions, Lysaker, Norway

ABSTRACT: The COMPMEM project is a joint industry project to validate the concept of using membrane-based CO_2 separation on the sea floor, with subsequent reinjection of the CO_2 into an oil reservoir undergoing CO_2 enhanced oil recovery (EOR). This concept seeks to exploit the qualification for commercial use in recent years of critical elements for subsea processing, such as pumps, separators, and compressors. The chapter provides an overview of CO_2 EOR and the challenges of offshore EOR which incentivize use of subsea facilities to avoid building costly offshore surface facilities (platforms or floaters). The use of EOR enables maximum recovery of oil from existing reservoirs, while also geologically storing meaningful quantities of CO_2. Reported here are results from testing several membrane materials at lab scale at the conditions relevant to subsea gas separation–within a broad range of temperature, pressure and CO_2 content in the feed gas. The compatibility of the materials constituting the membrane module with exposure to acidic water (carbonic acid), hydrocarbon condensate, methanol and monoethylene glycol was also tested. Out of four membranes tested, two were found satisfactory to be applied in a subsea processing train.

KEYWORDS: subsea CO_2 separation, membranes, EOR, CO_2 storage

INTRODUCTION

The issue of climate change has prompted interest in how oil and gas (O&G) operations can be done in a more sustainable manner. One way to reduce the impact of the O&G industry that may seem contradictory is using captured CO_2 for enhancing the oil recovery from existing oilfields. Maximizing production from existing fields could reduce the need to develop new oilfields, while at the same time contribute to meeting energy demand during the transition to fully sustainable energy sources. Most of the CO_2 that is injected in an oil reservoir for EOR becomes permanently stored, and as such, this concept does contribute to reduced emissions. The reservoir can be converted to a dedicated storage site when commercial EOR operation ends.

The incremental production from CO_2-flooding oil reservoirs has been estimated for major oil producing offshore regions such as the Gulf of Mexico, and the Danish, British and Norwegian sector of the North Sea. For the biggest offshore basins in the world, an estimated 114 billion barrels of oil can be produced by CO_2 flooding with a simultaneous storage of CO_2 on the order of 40 billion tonnes (Gt).

Using CO_2 for EOR has been applied for decades onshore, especially in the US. There are various reasons discussed in this report why this technology has not been widely applied offshore. A main

challenge with implementing CO_2 for EOR on existing offshore fields is the need for handling large incremental gas volumes with high CO_2 content, for which the original facility was not designed. Existing surface facilities (platforms or floating structures) may not be suitable for sour gas and may have limited space available for the additional equipment to separate and recycle CO_2. Introducing high CO_2 levels to existing process facilities may require very expensive retrofits and extensive facility shutdowns to perform the retrofit.

The latest developments and qualification of subsea technology for commercial use have shown that subsea solutions to mitigate some of the challenges for topside CO_2 handling may be technically and economically feasible. The COMPMEM project seeks to further develop a subsea processing concept, which is based on subsea separation and injection of CO_2 utilizing state-of-the-art subsea processing technology. Specifically, the successful deployment of subsea compression in 2015 represents a key enabler for subsea gas treatment.

The concept being developed by the COMPMEM project is applicable both for processing CO_2-rich associated gas from a CO_2-flooded oilfield and for offshore fields that are naturally rich in CO_2. The unique element in this subsea concept is CO_2 separation from natural gas using selective membranes. Membranes offer a simpler alternative to other commercial methods for CO_2 removal, such as solvent absorption and solid adsorption which are not well-suited to subsea implementation.

BACKGROUND

Brief Review of CO_2 EOR

The technical basis for the use of CO_2 injection for enhanced oil recovery (EOR) is well documented [1] and only a short summary is given here. When CO_2 is injected to a depth of about 800m or deeper, it can be pressurized to a supercritical state characterized by a liquid-like density and a gas-like viscosity. The supercritical CO_2 gas will, under certain conditions, develop miscibility with the reservoir oil leading to improved sweep efficiency and increased recovery of oil. The minimum miscibility pressure at which the injected gas behaves as a solvent depends on the composition of the injectant and the temperature of the reservoir. The presence of non-condensable gases, such as methane, or higher temperature increases the minimum miscibility pressure. To carry out a miscible flood, the minimum miscibility pressure must be less than the rupture pressure of the sealing cap on the reservoir. To minimize the pressure required to achieve miscibility, the injected CO_2 purity is typically greater than 95 mol %.

Primary recovery refers to oil production from the reservoir by virtue of the pressure energy in the reservoir. Over time, as the reservoir pressure drops, so-called secondary recovery may be implemented by injection of either or both water and natural gas to maintain the reservoir pressure and enable more oil recovery than primary production. Finally, tertiary recovery refers to use of CO_2 injection to produce further incremental oil.

When hydrocarbon (HC) gas or CO_2 is injected into an oil reservoir, the injected gas and reservoir oil will exchange components. Under favourable conditions, the injected gas will pick up components from the contacted reservoir oil until it becomes fully miscible with the reservoir oil (i.e., it behaves like a solvent for the oil). Miscibility is defined as when the gas and oil phases may be mixed in any proportion forming one phase. Historically, CO_2 has been favoured over HC gases for tertiary EOR because it was lower cost [1]. To achieve miscibility with natural gas, typically it must be enriched with heavier HC, such as propane.

When CO_2 is injected into an oil reservoir for EOR, there will be an increase in oil and gas production from the producing wells. Eventually, the injected CO_2 will break through, and the CO_2 content and volume of the associated gas will increase. Because CO_2 is imported to an EOR operation at a cost,

the CO_2 that is produced with the oil is recovered and recycled to the EOR operation for reinjection. A challenge in the design of the gas handling facilities for EOR is that the production volume grows over time and the CO_2 content increases, reaching 70% or more.

The CO_2 used for EOR is ultimately stored, since produced CO_2 is recycled and re-injected. The figures vary somewhat based on project-specific factors, but in a report from 2014, Scottish Carbon Capture and Storage estimated that 89-94% of the externally supplied CO_2 will remain in the reservoir when oil production ends [10]. In World Energy Outlook 2018, the IEA estimated that over 95% of externally supplied CO_2 could remain in the reservoir.

Benefits of Offshore CO_2 EOR & CCS

There is potential environmental benefit related to CO_2-based EOR in offshore reservoirs. The sustainable nature of extracting additional oil that cannot be produced by conventional methods in combination with simultaneous and permanent storage of CO_2, is an attractive concept. The depleted oil reservoir can be converted to permanent CO_2 storage after the hydrocarbon production ceases.

For the Norwegian Continental Shelf (NCS), the incremental oil from CO_2 EOR has been estimated in various studies, such as Holt *et al.* [2] and the Norwegian Government report about increased recovery on the NCS by the Åm Committee [3]. An estimated 300 million Sm^3 (~1.9 B bbl) oil, corresponding to about 10% of the accumulated oil production on the NCS, can be obtained as incremental production by CO_2 flooding. The incremental volume corresponds to increased reservoir recovery factors in the range 4–9 percentage points.

An extensive study done by Kuuskraa [4] mapped the technically and economically recoverable oil resources in the Gulf of Mexico (GoM) at various oil and CO_2 prices. At US$100/barrel and a CO_2 price of US$50/tonne, the incremental oil is estimated at about 100 million Sm^3 (0.6 B bbl).

The incremental oil volumes by CO_2 flooding on the UK Continental Shelf (UKCS) has recently been estimated by Scottish Carbon Capture and Storage (SCCS) [5]. SCCS estimates a volume in the UK and Norwegian sector of the North Sea in the range from 3 to 6 billion barrels recoverable by CO_2 flooding. In the study, the value of CO_2 EOR and its impact on the society compared to other investments in alternative energy sources were also assessed. The estimated return of investment to society was 7.2 times the investment in CO_2 EOR.

Data from Eide *et al.* [6] provides a global estimate of recoverable volumes of oil and the corresponding storage amounts of CO_2. The total incremental oil is 114 billion barrels, and the associated estimate of stored CO_2 is 40.2 Gtonne in offshore reservoirs globally.

This brief overview of the extensive potential of incremental oil production by CO_2 flooding in offshore reservoirs motivates development of the COMPMEM concept to help the expected gap between demand and supply of oil in the future, in combination with greenhouse gas (GHG) abatement.

History of Offshore CO_2 EOR

Very few offshore CO_2 EOR projects exist. In 2011, Petrobras carried out a first CO_2 EOR pilot project offshore Brazil. The pilot at the supergiant Tupi oilfield used CO_2 separated from associated gas for EOR. The reservoir lies in deep water (more than 2,000 m), below a thick salt formation, at a total depth between 5,000 and 7,000 m. For the pilot, CO_2 was separated from the associated gas produced from the field and re-injected to test the feasibility of CO_2 EOR early in the lifetime of the field. Two years later, Petrobras implemented commercial operation. By 2019, Petrobras had eight

floating production systems which incorporated CO_2 capture and injection facilities. As of December 2019, more than 14 million tonnes of CO_2 have been injected [7].

In Southeast Asia, there have been a couple of offshore CO_2 EOR projects. In Vietnam, a small-scale pilot test was conducted at the Rang Dong Oilfield, located 135 km off the coast of Vung Tau, in 2011. About 111 tons of CO_2 were injected through an existing production well, followed by a four-day oil recovery test from the same well two days later. The test was successful, but according to Kawahara *et al.* [8], the CO_2 injection alternative has been abandoned and replaced by hydrocarbon gas injection for oil recovery.

CO_2 EOR has not yet been commercially implemented in the Gulf of Mexico due to economic (offshore drilling and pipeline costs) and facility limitations (i.e., offshore installation of large gas processing kit). Five CO_2 EOR pilots were carried out in Louisiana's shallow near-shore and bay waters in the 1980s. In all the pilots, the CO_2 was delivered to the injection site by barges where the CO_2 was injected followed by either nitrogen or HC gas. All pilots were successful.

Table 1 Estimated volumes of oil to be recovered by CO_2 flooding and associated storage amount of CO_2.

BASIN	Incremental Oil Million BBL	Stored CO_2 Gtonne
Rub Al Khali	28000	8.8
North Sea	14400	4.0
Maracaibo	14300	4.5
Gulf of Mexico	23500	12.6
Niger Delta	10400	3.1
Offshore Caspian	8700	2.6
West-Central Coastal Gabon	4000	1.3
Campos	3100	1.1
Red Sea	3100	1.0
Baran Delta/Brunei	1900	0.6
Gippsland	1300	0.3
Malay	1300	0.3
TOTAL	114000	40.2

In Europe, the potential for large-scale offshore CO_2 EOR projects is substantial. In the North Sea, HC gas is used on a large scale for enhanced recovery by pressure maintenance, with total gas volumes in the order of 35 billion m^3/y. A Norwegian sector study identified potential demand for 12-16 million tonnes CO_2 annually for at least 25 years [9]. Several technical feasibility studies for CO_2 EOR, for example at the giant Gullfaks (sandstone) and Ekofisk (chalk) fields, have confirmed the technical feasibility of large-scale CO_2 injection for EOR offshore. Similar technical potential for CO_2 EOR in

the UK offshore sector has also been identified. However, no projects have progressed past the feasibility stage due to economic factors and lack of sufficient available volumes of CO_2. In general, initiatives for CO_2 capture and supply infrastructure are needed to enable large-scale CO_2 EOR in the offshore sector.

Barriers to Large Scale Offshore CO_2 EOR

Despite the huge reserves and potential for increasing the value of offshore oil production by CO_2 flooding, there are significant barriers to commercial-scale deployment of the technology. Some of these are briefly described below:

- Availability of CO_2
- Cost of CO_2 at injection wellhead
- Cost of retrofitting existing topside facilities

The estimated amount of CO_2 needed to flood a representative North Sea oil reservoir is about 5 million tonnes/y according to the Norwegian Ministry of Oil and Energy. Estimates of CO_2 demand to recover as much as 300 MSm^3 or 1.9 B BBL are prepared for the NCS. At present, the CO_2 costs at the wellhead are estimated to be too high for economic EOR.

A major barrier to offshore CO_2 EOR projects is the cost to convert existing offshore platform facilities from water or gas injection to CO_2 injection. The main cost challenges are related to the need to handle increased volume of gas, material corrosion, and added facilities to remove CO_2.

Opportunities and Recommendations for Overcoming Barriers

A major barrier to the development of offshore CO_2 storage or EOR is the lack of progress with large-scale CO_2 capture projects which have the potential to supply large volumes of CO_2 at reasonable cost. The following sections highlight opportunities and recommendations that apply to transport and storage (or EOR).

Offshore CO_2 Storage

There are no technical barriers to offshore CO_2 storage. The barriers identified are in the areas of access to storage capacity and national regulations. In Norway, Equinor has injected CO_2 for permanent storage at the Sleipner field since 1996 and at Snøhvit since 2008.

There are risks and long lead times involved in qualifying virgin storage capacity (saline aquifers), especially in sedimentary basins that have not seen significant mineral exploration. Such risks may need incentives or government programs to support the development of first-wave or even second-wave CCS projects. The long lead time (in the range of 7-10 years) means that storage qualification defines the start-up time of a CCS project. Although the unit cost of storage is lower than that of capture [11], a 'dry' hole (a formation that proves not to be acceptable for storage) would significantly increase the cost of storage. The CO_2 emission tax in Norway and the contract-for-difference in the UK are examples of funding mechanisms that provide certainty of funding during the lifetime of a CCS project, whether it is a demonstration or full-scale project.

Offshore CO_2 EOR

Current CO_2 EOR practice, such as that used in Texas, seeks to minimize the volume of CO_2 stored in the oil field and maximize the volume of CO_2 that is circulated to minimize the purchased volume of CO_2. The EOR process may be modified to maximize the stored CO_2 volume, while still enhancing

oil production. If there is an economic benefit via emission credits in storing the CO_2 it would significantly improve the value of CO_2 EOR operations as part of a capture-transport-storage project.

A major barrier for offshore CO_2 EOR projects is the investment required for the modification of existing platforms and installations. In addition, there is the lost revenue during modification. Recent advances in subsea separation and processing may enable moving equipment required to separate and condition the CO_2 to the seabed and avoid major modifications to the platform.

Although there are exceptions, most of the current CO_2 capture projects are of modest size–on the order of 1 mmtpa of CO_2. The Petra Nova capture project in Texas was designed to capture 1.6 mmtpa, which was piped to the West Ranch oil field for onshore EOR [12]. As mentioned above, the CO_2 requirement is large for full-field EOR at large oilfields in the North Sea. The CO_2 demand curve of a typical EOR operation decreases after a peak at the start, which makes the economics of a dedicated pipeline to the field unattractive. Ship transport may provide the flexibility that is required in such cases. A small number of ships could link emerging capture projects to pilot and demonstration-scale offshore CO_2 EOR operations. This may trigger larger EOR operations, in turn seeding the first elements of offshore CO_2 transport pipelines.

Onshore EOR Processing

Typical Onshore EOR Processing Facility

The specific elements of the facility for the well stream processing depends on the nature and composition of the well fluids, but generally includes gas/liquid separation and a further gas treatment process. A general block diagram for an EOR facility is shown in Figure 1 [13].

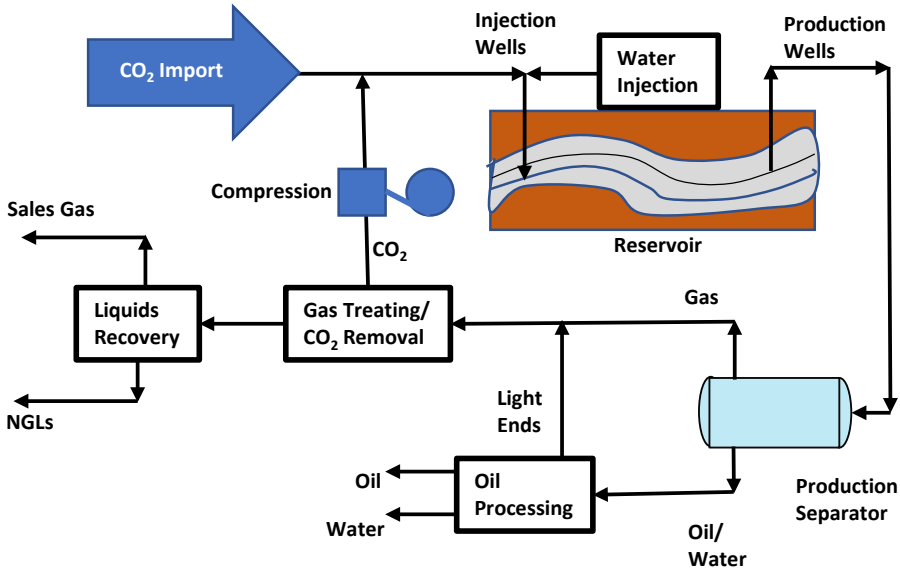

Figure 1. CO_2 EOR Process Flow (after [13]).

The EOR processing facility includes separation systems for oil/water/gas and a treatment plant for the CO_2-rich associated gas. The performance of the gas treatment plant is very important in typical onshore applications to recycle as much CO_2 as possible, while maintaining the required purity of the CO_2, to minimize external acquisition of CO_2, which is a major operating cost for EOR. At the same time valuable hydrocarbons like residue gas (pipeline gas) and natural gas liquids (NGLs) are recovered for sale. The gas processing is further complicated if the associated gas contains H_2S. Aside from stringent specifications in sales gas (typically 4 ppmv H_2S), CO_2 for reinjection may have H_2S specifications to avoid hazardous conditions in the event of a leak in the distribution system, with limits typically in the range of 10-100 ppmv. H_2S is not detrimental to the efficiency of CO_2 in EOR service [14]. A comprehensive description of an EOR facility is given by Jarrell [15].

CO_2 Separation

The associated gas produced from the reservoir during CO_2 EOR increases in volume and CO_2 content steadily as the injected gas breaks through to producing wells in the flooded reservoir. The timing of gas breakthrough is uncertain, and this presents a challenge in planning for the facilities needed to process the produced gas. The first large scale CO_2 EOR project was at the SACROC field in the Permian Basin of Texas and commenced operation in 1972 [13]. Early experience from the SACROC project showed that the CO_2 content in the associated gas increased after CO_2 injection started and additional gas separation capacity and technologies had to be installed in stages. Recent US onshore CO_2 EOR projects have been designed for CO_2 content in the range 80-90 vol%.

Kohl and Nielsen [16] provide a thorough evaluation of various CO_2 separation methodologies for onshore CO_2 EOR operations based on various amine processes, cryogenic and membrane-based separation principles. The main treatment options are:

- Conventional amine based on diethanolamine (DEA)
- Cryogenic fractionation processes
- Triethanolamine (TEA) bulk CO_2 removal
- Membrane permeation

A variety of factors such as impurities in the gas, requirements for hydrocarbon-rich gas and purity of CO_2 for reinjection govern the technology to be used. Liu *et al*. [36] have made a survey of technologies for separating CO_2 from CO_2–EOR associated gas. They state that the membrane-based separation process is the most appropriate method.

A hybrid approach, with bulk removal of CO_2 achieving acceptable purity in the recovered CO_2 using membranes, coupled with further removal from the HC-rich gas using amines to meet export specifications has been used on several projects. A benefit of the hybrid approach is that the front-end bulk removal of CO_2 by membranes can be increased in stages as the EOR flood matures. A schematic of a hybrid system in Figure 2 [17].

Topside Processing Solutions

There are no fundamental differences in well stream properties for an offshore CO_2 EOR flood compared to a typical onshore case, so the basic requirements for treatment and separation in an offshore application are the same as for onshore application. There are special challenges for offshore treatment of well streams from an EOR flood–mainly related to the high cost of adding separation equipment and gas treatment processes like amine contactors offshore. In most cases, there are very limited space and weight reserves on existing facilities since they were not designed for late life EOR service. Accordingly, studies for implementing offshore CO_2 EOR have concluded that the costs are

too high. An added factor may include replacement of low-grade steel with steel that can withstand the corrosive nature of wet CO_2.

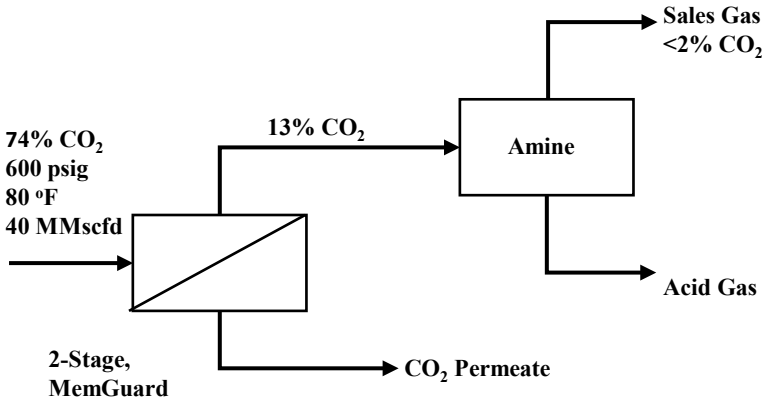

Figure 2. Schematic of a hybrid CO_2 removal system [17].

There is little public literature on the impact of implementing offshore CO_2 EOR. However, some studies have analysed the impact on the well separation train, gas injection system, safety issues, material concerns, and other related topics arising from handling well streams from a CO_2-flooded reservoir.

A study by Goodyear *et al.* [18] noted that well streams that typically result from CO_2 flooding are characterized by high water cuts and high CO_2 concentrations, up to 90 vol%, in the gas phase. The gas treatment facility, which includes gas dehydration (TEG contactors) and NGL recovery is very large, with the weight of equipment in the range of 6,000-16,000 tonnes. This drives the need for very efficient and compact solutions for the gas treatment equipment. Gas dehydration is needed to avoid corrosion and hydrates in the reinjection pipeline. There are various options for processing the recycled gas to produce a CO_2-rich stream for re-injection. The recycled gas may have different composition compared to the pure CO_2 from external sources. This change in composition may have an impact on the performance of the EOR flooding efficiency since various impurities, especially CH_4, will affect the minimum miscibility pressure (MMP).

Goodyear *et al.* [18] observed that offshore CO_2 concept selections have concluded that methane recovery with current technology used onshore is not attractive. The extractive distillation approach used in a number of US-based onshore projects has high CAPEX and power requirements. New technology concepts based on cryogenic principles and membrane separation are said to provide solutions for more favourable offshore CO_2 EOR projects.

Salim *et al.* [19] documented a variety of implications of bringing CO_2 EOR offshore and using existing topsides facilities. Areas that require assessment include:

- Behaviour of dense phase CO_2 (e.g., good solvent, difficult sealing issues, hydrate behaviour).
- Process design (e.g., impact of changing mol weight on compression, dehydration).
- Safety (e.g., handling asphyxiant).
- Flare, vent, and relief system assessment (e.g., heavier than air, assist gas for flammability).

- Impact of CO_2 on platform risk profile (e.g., CO_2 release and dispersion).
- Impact on HC process systems (e.g., changing volume and composition, corrosion).
- Reservoir and subsurface issues (e.g., changing GOR, sand production).

The Salim study [19] is based on a typical topside facility in the North Sea. The study concluded that a new CO_2 EOR module on a separate structure was needed. This arrangement was chosen due to the impact of the corrosive nature of CO_2 on the existing facilities. No recovery of NGLs or hydrocarbon gas was considered for this case. The dehydration system for the CO_2 rich gas stream was analysed in detail. The water content in the dried gas to avoid condensation in the downstream high pressure (HP) compressor and CO_2 pump was about 105 ppmv. The final HP compressor lifts the pressure from about 40 bar to 145 bar, and the CO_2 injection pump increases the pressure further to 240 bar. The external CO_2 supply is brought in by ship via a buoy and delivered at the EOR module at 150 bar and 4°C.

The Energy Institute [20] assessed the implications for offshore treating of a well stream from a CO_2 flooded oil reservoir and emphasized the complexity and costs for retrofitting existing facilities. Options for the treatment were assessed, including a complete treatment process with recovery of HC gases and a simpler system involving only liquid separation and reinjection of the complete gas phase. For the HC recovery option, the production fluids are let down in stages and water is separated. The gases are compressed to 55 bar (800 psi), dehydrated, and processed with membranes to produce an export gas containing 15% CO_2 and a recycle CO_2 stream containing 2-3% HC. An H_2S scavenger step can be added prior to the dehydration step. An alternative to the membrane system is an amine treater. For the simplified system, all gas flashed from the oil is recycled for reinjection.

Subsea Processing Options

Public information about subsea processing for offshore CO_2 EOR is very limited. However, a US DOE report states; "*…there is need for continued sponsorship of research for improving subsea technologies essential for deep water CO_2-EOR. Statoil's recent development of subsea gas compression is an example of technology that would be beneficial to deep water CO_2-EOR*" [21].

A recent joint study funded by Aker Solutions, Statoil (now Equinor) and CIPR, assessed a concept for subsea processing of a CO_2-rich well stream resulting from a CO_2-flooded oil reservoir [35]. This concept is based on recent developments in subsea processing systems and has identified some areas that need further qualification. Accordingly, an overview of relevant technologies is given below.

A subsea processing concept is described in the report by Eide *et al.* [6] as shown in Figure 3. The system is also described in the patent application by Nøkleby *et al.* [23].

Available Subsea Building Blocks

There have been several subsea processing projects installed in the past decade. Even though technology qualification will be required for a subsea CO_2 processing system, several elements are available and may be considered partially or fully qualified. When dealing with CO_2 processing applications, selection of materials for equipment will need to be reviewed.

A subsea separation train can typically consist of all or some of these main processing building blocks:

- Gas/liquid separators: Several gas/liquid separators have been installed subsea, including scrubbers.
- Liquid/liquid separators and water de-oiling equipment: De-oiling hydro cyclones have been qualified and installed subsea (Marlim Project, Petrobras).

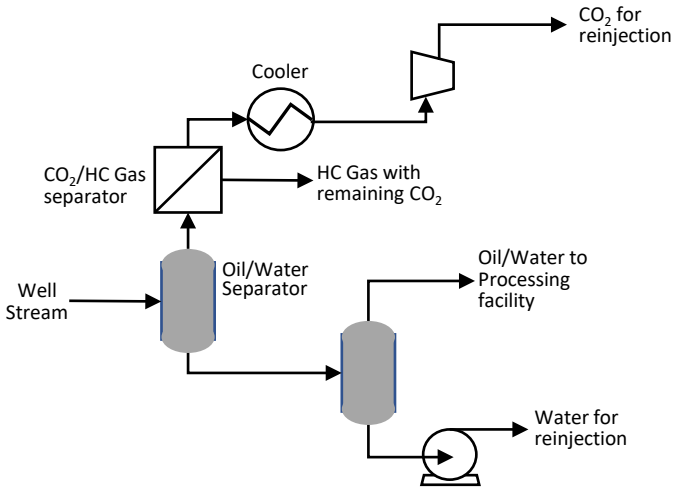

Figure 3. Subsea processing concept for EOR [6].

- Coolers: Passive subsea coolers (no temperature control) are qualified, installed, and in operation as part of Equinor's Åsgard subsea compression project. Active coolers with temperature control would need further qualification.
- Compressors: A subsea compressor system for HC gas is qualified, installed, and in operation since 2015 as part of the Åsgard subsea compression project. No fundamental showstoppers have been identified for extending the Åsgard technology to CO_2 applications. However, material selection for CO_2 applications may need to be further examined.
- Pumps: Multiphase and single-phase pumps are qualified technology for subsea use. However, the required duty and impeller/diffuser selection may need to be evaluated for specific cases.
- Subsea de-sanding equipment: Cyclonic de-sanders are considered qualified technology for subsea use.
- Control system: The control system in general is available for subsea use. A technology assessment for the exact configuration and instrument selection is needed for each project.
- Power system: Several power system solutions have been qualified for subsea use and are available. A technology assessment for the exact configuration and equipment selection is needed for each project.

Based on this status, many major technology elements are available for subsea processing of the well stream from a CO_2 flooded oil reservoir. However, the CO_2 gas separation has not been implemented or qualified for commercial use. The relevance for using membranes for this operation and a brief status of membrane technology is given in the following section.

Traditional CO_2 removal systems using solvent systems or solid sorbents require more unit operations that contain rotating machinery. This adds complexity, difficult energy supply, and costs. Such systems are not considered suitable for subsea use.

Membrane Technology

The use of membranes is an alternative to the use of solvents for CO_2 removal and has been in commercial use for decades. Conventional gas separation membranes are made from polymers, such as cellulose acetate, polyimides, or perfluoro polymers [24]. Membrane systems are simpler than solvent absorption systems, but this is partly offset by the requirements for pre-treatment that traditional membrane systems require to prevent degradation of membrane performance due to various constituents in the feed gas. A pre-treatment system may contain a coalescing filter, particle filter and heater, but may also include dehydration, adsorbent guard bed, and refrigeration [25].

The configuration of membrane systems consists of many parallel containment vessels which hold the membrane separation elements. Various flow configurations are used, but at least three flow streams (feed, permeate, and retentate) require piping and manifolding. Overall, these systems are usually large, making them difficult and expensive to install subsea and the number of connection points increases the risk of leaks. Alternative vessel designs that minimize connections by consolidating membrane elements may be more suitable for subsea use.

Principles of Membrane Gas Separation

Gas separation membranes separate individual species based on differences in their permeation rate through the membrane. Individual species permeation rates depend both on molecular properties of the species and on the membrane material. The driving force for permeation is provided by the partial pressure differential for each component across the membrane. Since the separation depends on relative rates of permeation and on the presence of a finite driving force, the permeate is never 100% pure and recovery is never 100% [16]. This is a defining characteristic of gas separation membranes. The maximum separation in a single membrane stage is the absolute pressure ratio across the membrane [26].

$$\left(\frac{y_{i,permeate}}{y_{i,feed}}\right) \leq \left(\frac{p_{feed}}{p_{permeate}}\right)$$

Where y_i is the gas phase mole fraction of component *i*, and *p* is the absolute pressure.

The rate of mass transfer in a dense polymeric membrane is described based on Fick's Law:

$$Ji = \frac{D_i * K_i * (p_{if} - p_{ip})}{l} = \frac{\boldsymbol{P_i}}{l} * (p_{if} - p_{ip}) \quad (1)$$

Where:

J_i	Molar flux of component i
D_i	Diffusion coefficient of component i (indicates the degree of mobility of the gas)
K_i	Gas sorption coefficient of component i (indicates the degree of solubility in the membrane material)
p_{if}	Partial pressure of component i on the feed side
p_{ip}	Partial pressure of component i on the permeate side
l	Membrane thickness
P_i	Permeability of component i

The product of the constants D_i and K_i is called the membrane permeability for species 'i', P_i. The selectivity of the membrane, α_{ij}, is an important measure of a membrane's ability to separate two gasses *i* and *j*, and is defined as the ratio of the permeabilities:

$$\alpha_{ij} = \frac{\boldsymbol{P_i}}{\boldsymbol{P_j}} = \frac{D_i/D_j}{K_j/K_i} \quad (2)$$

In polymeric membranes, the diffusion coefficients decrease with increasing molecular size, while the solubility tends to increase [26].

A fundamental aspect of membrane gas separation is the trade-off between the percentage removal of CO_2 from the feed gas and the purity of the CO_2 in the permeate. For a single stage membrane, the stage cut is the fraction of feed gas that permeates the membrane. The higher the stage cut, the higher will be the recovery of the permeating CO_2, but the purity will be lower. For a given feed flow rate and pressure ratio, the stage cut is increased by using more membrane area. For a fixed membrane area, the stage cut increases with increased pressure ratio or decreased feed flow rate. The effect of changing temperature depends on the properties of membrane material because both selectivity and diffusion rate change for all species.

As CO_2 selectively transfers across the membrane, the CO_2 concentration adjacent to the membrane on the feed side is reduced while the concentration of the other species in the feed gas mixture is increased. The result is a reduction in the driving force for transfer of the CO_2 and a reduced flux. This effect can be mitigated by, for example, introducing turbulence into the flow of gas on the feed side to mix the boundary layer.

Membrane performance can also be affected by plasticization, where the structure of the membrane swells due to sorption of constituents in the gas. Among species known to plasticize some membrane materials are CO_2 and aromatics. To avoid the membrane plasticization, pre-treatment to remove aromatics and other heavy hydrocarbons can be done. In addition, control of temperature can minimize such effects. Membrane materials with a higher degree of cross-linking may have a higher glass transition temperature and are more robust to plasticization.

New polymer materials that are compatible with aromatics and water condensation will require less pre-treatment of the gas upstream of the membrane separator. Since extensive pre-treatment systems for subsea applications will require costly and complex arrangements, the use of new and robust membrane materials is attractive for this application. Accordingly, such new membrane systems are tested in this project.

Gas Stream Pre-treatment

Pre-treatment of the feed gas is important in conventional membrane separation processes to avoid or minimize fouling, plasticization, and condensation of hydrocarbons within the membrane system. Condensation of liquid hydrocarbons on the surface of the membrane material can occur as the retentate stream changes composition (increasing HC content as CO_2 is removed) at the same time as temperature drops due to the Joule-Thomson effect, which can take place on the permeate side. Accordingly, a typical pre-treatment train for CO_2 EOR operations includes dehydration, coalescing filter, adsorbent bed and refrigeration (to knock out HC liquids), and reheating to move away from the dew point [25].

Developments in Membrane Technology

In recent years, new membrane materials, membrane configurations and packing arrangements have been developed specifically for the treatment of highly sour gases. Good summaries of membrane separation technology are provided by Baker and Lokhandwala [25] and Dai *et al.* [27]. A recent overview of membranes for CO_2/CH_4 separation has been provided by Oyama [28].

Virtually all commercial membranes are made with a layered structure–a very thin separating layer (0.1-0.5 μm) to maximize the mass transfer rate, supported on a porous supporting layer to provide structural strength. The two layers may be the same material (asymmetric) or different (composite). Composites are typically used when the material in the separating layer is costly.

SUBSEA CO_2 SEPARATION CONCEPT

The subsea processing concept is shown in Figure 3 [6, 23]. A subsea processing system must be designed using robust and simple solutions to reduce cost and complexity. For a membrane system, this includes minimizing the need for pre-treatment through use of mechanically and chemically stable membranes.

The well stream is initially separated in a 2-phase scrubber. The gas phase is fed to the membranes and is separated into a CO_2-rich permeate stream and a hydrocarbon-rich retentate stream. The membrane retentate stream is combined with the oil stream from the liquid-liquid separator before being pressurized via a centrifugal multiphase pump and sent to the topside facility. The liquid phase from the scrubber is further separated in a bulk liquid-liquid separator. The produced water is pumped and reinjected to the same reservoir, another reservoir nearby or a suitable aquifer for permanent disposal.

The pressure of the CO_2-rich permeate stream from the membranes is boosted for reinjection into the reservoir using a centrifugal compressor, followed by cooling and boosting of dense phase CO_2 in a centrifugal pump. Cooling is included to further increase fluid density. The higher density provides a higher fluid static head in the well injection tubing. This reduces the pressure to which the fluid must be boosted because the pressure required at the wellhead for the injected fluid to flow into the reservoir is reduced.

If the host facility has sufficient capacity for handling the produced water, a simplified system that eliminates the oil-water separation can be used.

Design Constraints and Trade-offs

Enhanced oil recovery through CO_2 injection offshore is typically characterized by the following competing objectives:

- Maximize hydrocarbon recovery in both gas and oil streams.
- Minimize CO_2 routed to topside facility due to: (1) sour gas tolerance of existing facilities, (2) limited topside gas handling capacity, (3) constraints on permissible export gas CO_2 content, (4) benefits of maximizing recirculation of CO_2 for EOR (to minimize external and costly CO_2 import).
- Achieve required purity CO_2 for reinjection to meet CO_2 flooding scheme.
- Achieve sufficient separated water quality for reinjection (or water can be sent to host facility for further treatment).
- Minimize cost, complexity, and risk.

The process design therefore represents a balance among these objectives. The amount of CO_2 going to the host facility depends on the amount of CO_2 that is dissolved in the liquid and the amount of CO_2 remaining in the retentate stream.

A lower inlet separator pressure in the subsea system allows more CO_2 gas to flash from the liquid phase. This results in less CO_2 being carried with the liquid going to the host facility (oil and/or water). CO_2 dissolved in the liquid will be released during the topside stabilization process. However, lowering the subsea separator pressure also lowers the membrane inlet pressure, and if the permeate pressure is unchanged, the differential pressure across the membranes will be lower, which reduces the membrane separation performance.

The pressure differential across the membranes can be increased, thereby improving CO_2 separation from the hydrocarbon gas, by lowering the permeate pressure (compressor suction). However, this is limited by the maximum compression ratio and maximum actual volume flow through the

compressor, which increases greatly with decreasing suction pressure. The compression ratio may be increased by using two or more compressors in series; however, this significantly increases the cost and complexity of the system.

Another important parameter is the separator temperature. A high temperature in the inlet separator at the subsea processing station allows more CO_2 to flash from the liquid phase. On the other hand, traditional membranes are operated at a lower temperature than a typical well stream due to material limitations and typically improved performance at lower temperature. Operating the membrane separation stage outside the conventional temperature range may be critical for practical subsea systems, which would require development of more robust materials.

The operating temperature of the membrane is an important parameter since it affects whether condensation of liquid on the feed side of the membrane can occur and impact separation efficiency. The composition of the gas on the feed side of the membrane changes as the CO_2 selectively permeates through the membrane. In addition, the Joule-Thompson effect will cause cooling of the gas. With unfavourable temperature and pressure conditions, some liquid may be formed by condensation as dew point conditions are reached on the feed side. If the membrane surface is covered by liquid film, the gas transfer rate will be greatly reduced. The membrane design must take this into account by increasing the total membrane surface area, or conditions must be controlled to avoid condensation during normal operation. Potential for liquid condensation is mitigated by cooling the gas, removing liquid in a demister vessel, then reheating the demisted gas upstream of both membrane separators.

Membrane CO_2 separation is improved by using two membrane stages in series operation. The retentate stream from the first stage then becomes the feed stream to the second stage membrane. In this case, the complexity of the system is increased by the requirement to add another compressor.

Flow Assurance

Low fluid temperature must be avoided throughout the subsea process system to prevent hydrate formation in all the process streams–both gas and liquid. A 15°C margin above the maximum hydrate formation temperature is considered adequate for all streams. The cooler design must hence ensure that the gas is not cooled below 30°C. The oil/water stream must also be assessed for the hydrate forming temperature and the system designed to avoid that condition.

The subsea system should be designed with insulated piping and pressure vessels so that hydrates do not form during a brief shut-in situation. In addition, the equipment is designed so that liquid can drain by gravity to a low point where hydrates may be inhibited by injection of monoethylene glycol (MEG). Wherever possible, liquid in pipes and coolers should drain into vessels such as the gravity separator and/or the demisters. Valves in liquid filled parts of the process system should be located at low points such that hydrate-inhibitor fluid is covering the valve inlet and outlet surfaces when closed.

The system should be designed so that the subsea processing modules can be isolated and hydrate formation mitigated by MEG injection prior to displacement of the flowline and riser system. The process module is maintained in a safe state by injecting MEG into the piping system at locations that will ensure collected liquid is mixed with enough MEG to prevent hydrate formation at seawater temperature. The system design must allow for restart without physical intervention after being out of service for an extended time.

SUBSEA TECHNOLOGY

Subsea Design and Modularization

In general, subsea processing facilities are considered for fields with water depths that are not accessible for divers. This means that any access is by use of a remotely operated vehicle (ROV). The ROV is a subsea robot controlled by an operator, with a camera and two arms that can lift/handle items up to about 50 kg. It has one very dexterous hand and one that is less dexterous, but stronger, that is often used to keep the ROV steady while working. The main purpose of the ROV is to aid during installation and retrieval, as well as to perform inspections and replace smaller items on the subsea equipment. The ROV cannot fix items that have failed, so all items that fail must be replaced. So, if the item that fails is designed for replacement by the ROV, this is a rather standard procedure. If the item that fails is either heavier than the ROV can handle, or the item is not designed for replacement by the ROV (e.g., items that are bolted cannot be loosened by the ROV) the whole unit will need to be retrieved.

If a complete subsea system was grouped on a single module, the resultant module would be so heavy that a heavy-lift vessel would be required. This is very expensive and would need to be contracted far in advance. Conversely, placing each process item on a separate module would be very expensive. The intramodular piping connections are both costly and represent a potential leak path and should therefore be minimized.

The installation depth is taken into consideration during design, by grouping the various process items together in retrievable modules. These modules will range in weight from about 50 to 250 tonnes and are retrievable by use of a construction vessel with a suitable crane and the assistance of one or two ROVs.

Typically, when it is necessary to retrieve a module, the ROV will prepare it by loosening piping connections and electrical connections, and the crane can pick up the module to the vessel deck. Often, depending on the spare parts philosophy, the retrieved module is immediately replaced by a spare, identical module. It is important to consider ROV access in the design of the process station and leave room for the ROV to manoeuvre where it needs to do work.

Subsea Equipment

Gas/Liquid Separation

Two- and three-phase gravity separators are in use in subsea applications today and are considered fully qualified for commercial use. More compact options can also be evaluated (e.g., cyclonic separators.)

Membrane Separation

A subsea membrane separator must be designed so that the membranes are accessible for replacement. Figure 4 shows a concept for assembly and manifolding to allow extraction of the membranes via a body flange lock in the containment pressure vessel. The lowest level assembly is shown on the left in Figure 4. The membrane cartridges are assembled into a string with feed and permeate streams from each membrane cartridge connected. Several strings of membranes are brought together into an insert fitted into a pressure vessel. This concept design is based on standard 6-inch diameter cartridges [29]. This arrangement is based on a subsea vessel height of no more than 6 meters to suit modularization, a vessel diameter limited to what is considered feasible to manufacture, and use of a body flange connection.

As seen in the cartridge flow illustration, Figure 5, the feed flows radially into the membrane, a permeate stream exits at the top and the retentate stream including any condensate exits at the bottom.

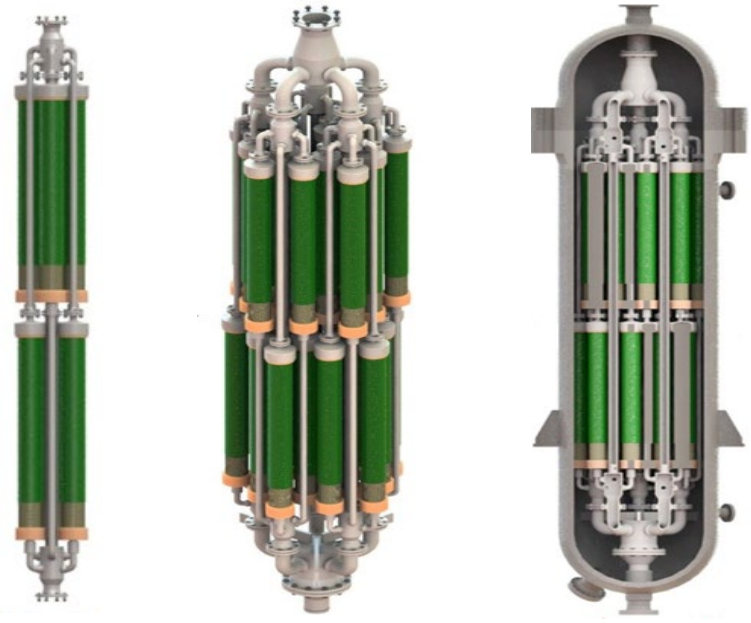

Figure 4. Subsea membrane deployment concept. From left to right: membrane cartridges assembled into a string; the strings are arranged into an insert to a pressure vessel; assembled subsea membrane separator.

The feed enters the vessel shell via nozzle connections. The permeate and retentate streams are connected to manifold and header systems.

The membrane cartridges and membrane strings have parallel conductivity. Feed flow is distributed to all membrane strings and further to each membrane cartridge. The permeate stream is merged from all membrane cartridges and from all strings into one top outlet. Feed to the assembly is from the vessel side nozzle, while the retentate stream is removed from the bottom outlet on the vessel.

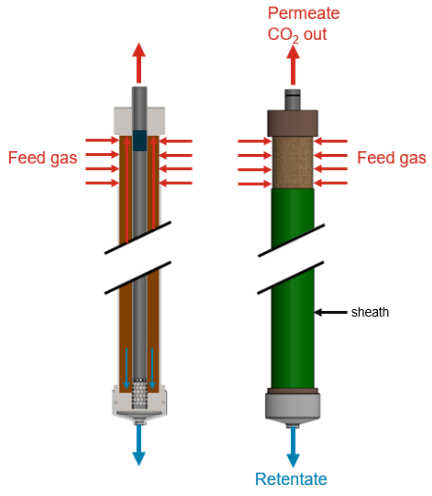

Figure 5. Membrane cartridge flow pattern.

Estimation of specific membrane module capacities is based on assuming a single 8-inch (~200 mm) diameter membrane separator has a feed flow capacity in the order of 1 million SCFD. The capacity of a different sized membrane is adjusted by ratioing based on the reduced cylinder outer surface area for a smaller diameter membrane element. The 8-inch cartridge would not fit efficiently in the subsea pressure shell. There are 8 membrane cartridges in each string. Each membrane cartridge is 170 mm (~6.7 inches) in outer diameter and is 1,520 mm long.

Subsea Coolers

A passive subsea cooler consists of an inlet and outlet header connected by smaller tubes in parallel. The small tubes can be configured in multiple serpentine passes to provide the necessary heat transfer area, as shown in Figure 6.

All coolers in the gas processing system are passive. Heat is dissipated from the tubes to the surrounding seawater by natural convection. Liquid condensation will occur in the cooler. A constraint is that the fluid temperature must be above the hydrate formation temperature during normal operation. Hydrates form at low temperature and high-pressure conditions when hydrocarbon and/or CO_2 gas, and free water are present. MEG can be injected into the coolers for hydrate mitigation during start-up if required.

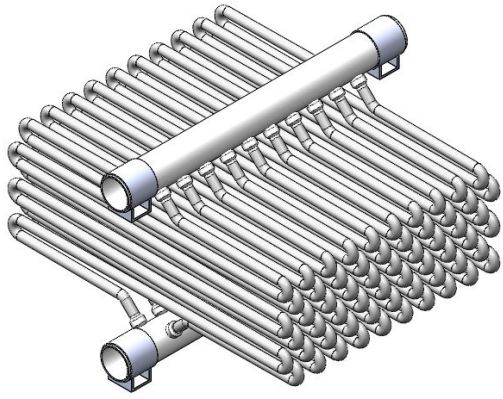

Figure 6. Passive subsea cooler.

Since subsea coolers are passive coolers with no control of the cooling medium, accurate and robust cooler design is very important. Detailed engineering, including heat transfer assessment with CFD, and multiple scenarios are considered when sizing the passive subsea coolers. The temperature distribution along the tubes and the response of the surrounding water plume are evaluated.

If necessary, alternative cooler designs could be assessed, such as a cooler with several sections to enable more control of the discharge temperature. There are also active coolers that can give better temperature control, but these concepts require further qualification (field testing at suitable scale).

Subsea Compression

The compressor specified for this subsea CO_2 processing module is based on the qualification, development testing and operational experience [30] for the HOFIM™ type compressor from MAN Energy Solutions. For subsea application, the HOFIM™ machine is available with two motor sizes. The M43 with a nominal power of 11.5 MW is fully qualified for subsea use. The smaller M33 with a nominal power of 6 MW has undergone pilot testing for subsea application.

The MAN HOFIM™ compressor and motor have been in operation on the two subsea compression trains since 2015 at the Åsgard field in the Norwegian sector of the North Sea [30].

Subsea Pumping

Subsea pumping will be required to boost the pressure of the produced fluids to reach the surface facility and of the CO_2 rich fluid for injection if the liquid head is not sufficient to overcome reservoir pressure and injection pressure. For liquid or dense phase pumping, a LiquidBooster™ pump is proposed. For multiphase pumping, a MultiBooster™ pump is proposed [30]. Both pumps have a similar configuration, but there are some differences with regards to the bearing and sealing systems.

The pump is vertically arranged where back-to-back mounted radial impellers ensure axial force balancing. The axial split of the inner casing enables balancing of the complete pump rotor in its final assembled condition. This provides excellent rotor-dynamic behaviour and balance, and there is no need for a vulnerable balance piston. The pump can be driven by electrical motors in the range of 1.6 MW to 6 MW. The motor is designed with a robust shaft and bearing arrangement to ensure rotor-dynamic stability and safe operation up to 6,000 revolutions per minute (RPM).

Control System

The design of a subsea processing control system is based on standard, proven designs that have been implemented previously in various subsea projects. Control and monitoring of the subsea system will be executed by control equipment located both topside and subsea. The control system is all electric, which means that no traditional standard electro-hydraulic valve actuators are incorporated in the design. Low voltage power is supplied via an umbilical, along with the fibre optical cables for communication between the topside and subsea control equipment. Chemicals and barrier fluid lines to the pump are fed through dedicated lines in the same umbilical.

Topside and subsea control systems are fully redundant for all electrical and communication services. The system is designed for easy fault diagnosis without system retrieval. A dedicated condition monitoring system will cover both subsea and topside equipment.

Design of equipment and interfaces are standardized wherever possible. The subsea control system is designed for diver-less and guideline-less installation and intervention. The subsea control system is modularized in such a way that functional components requiring maintenance or replacement can be disconnected and retrieved to surface.

HV Power System

High voltage (HV) power systems have been deployed at several subsea processing projects. Each project will require an evaluation of required step out, power levels, and equipment ratings to ensure compatibility with already qualified equipment or to identify any gaps. There are no major gaps expected related to the power system. However, material compatibility will always need to be verified for project-specific conditions regarding the penetrators (the specialized couplings that provide a waterproof seal between a power cable and a pressure vessel).

MEMBRANE PERFORMANCE TESTING

The CH_4/CO_2 separation performance was tested in micro-scale for four candidate membranes, which vary by manufacturer, material, and configuration. The objective with the micro scale tests was to get qualitative information about the impact of the expected subsea separation process conditions on the performance of the separation. Key performance metrics measured were permeance and selectivity of CO_2 versus CH_4. Accordingly, the tests have been conducted over the expected operational space of the main external variables. The test samples of the membranes were provided as either flat sheet or hollow fibre membrane configuration. Due to confidentiality clauses with the various membrane suppliers, the vendor names and membrane trade names are not disclosed in this report. They are labelled as Membrane A, B, C, and D. A and D are flat sheet arrangements while B and C are hollow fibre configuration. A, B, and C are from commercial suppliers while D is under development.

In addition to parametric testing of the membranes for CO_2 separation, they were tested for the effect of some of the contaminants typically found in gas mixtures.

Testing Methodology

Micro-scale modules (total membrane area 10–20 cm^2) were prepared for the performance screening as shown in Figure 7. The membranes were aged prior to the testing as per recommendations from the suppliers. No change in performance was observed even after 2 months.

The test arrangement provides consistent gas supply to the test modules, where the total inlet gas flow, feed composition, temperature and pressure are accurately controlled. The permeate stream flow rate and composition are accurately measured, while the retentate flow and composition are calculated from the mass balance. This applies to both the hollow fibre and flat sheet membrane arrangements.

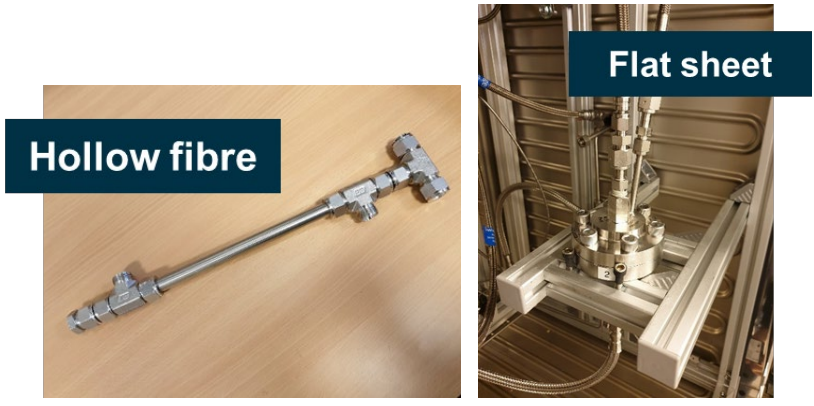

Figure 7. Test configuration of micro-scale membrane modules.

Ensuring that the performance measurements not were influenced by varying degree of plasticisation at different conditions, the membranes were conditioned in the order of 3–6 hours to reach steady state before actual separation tests were done. The conditioning time was advised by the respective suppliers.

Principles of Statistically Designed Experiments

Gas separation processes with membranes are influenced by many variables–the five most important of which are: specific gas flow (gas flow per membrane area), temperature, feed CO_2 concentration, feed pressure, and permeate pressure. The intrinsic properties and structure of the membrane material is critical, but this study did not investigate varying the material properties. Given the number of process variables, use of the traditional experimental methodology, which changes one factor at a time, would make it difficult to identify two-factor interactions without a massive number of experiments.

Statistical Design of Experiments (DoE) enables extraction of as much information as possible with a minimum number of experiments. DoE allows identification of significant variable(s) and quantification of major effects and two-factor interactions. Features of DoE that maximize the quality of the analysis include randomizing tests, planning replicates, and adding centre points. These methods are further explained by Rencher and Christensen [32] and Box *et al.* [33]. Below is a brief description of the test plan and the differences between the traditional experimental approach and DoE approach.

The DoE approach explores the full parameter-space more efficiently by changing multiple variables at a time. Nonlinear effects of variables are difficult to elucidate with the traditional approach as it can only find curvature effects for each of the variables along their axes but not inside the parameter-space, which again requires changing of multiple variables at the same time.

Accordingly, an initial test matrix was developed, and some constraints had to be considered as a part of the plan, since not all combinations of the independent variables are practically possible. Such constraints include the requirement for a positive driving force for the CO_2 to permeate the membrane (higher partial pressure on the feed side) and the need for a minimum pressure difference across the membrane. See the discussion in the section “Principles of membrane gas separation” of this chapter.

To visualize the scattered design of the various test conditions, see Figure 8, which shows that the various test conditions are relatively well scattered. An ideal pattern requires a randomly scattered pattern across the entire window. The upper left corner is completely missing tests due to constraints on low feed pressure and high permeate pressure which represent low or no driving force for separation.

Experimental Test Matrix for CO_2/CH_4 Separation

The process parameters that were varied to determine the impact on CO_2 separation performance and the respective ranges are given in Table 2. The value of the variables was selected from conditions that were assumed to represent extreme conditions in the subsea operating window.

The variables in Table 2 are not completely independent since there are combinations that are not physically possible, such as having the permeate side CO_2 partial pressure higher than the inlet side.

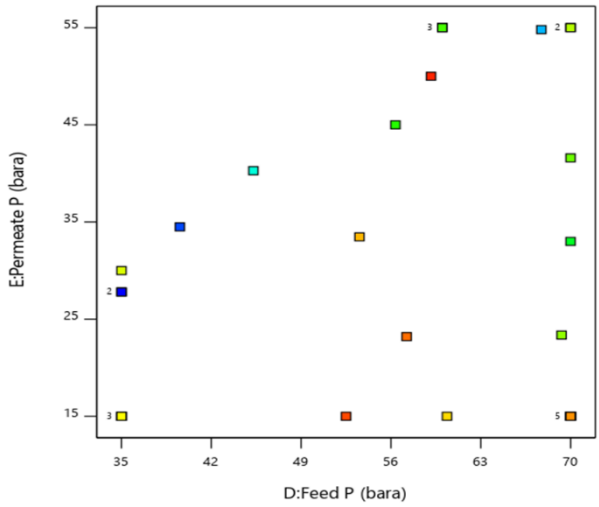

Figure 8. Illustration of data points for DoE.

The test matrix was designed to avoid such conditions, resulting in an unsymmetrical test matrix.

Examples of the test matrix is shown in Tables 3 and 4. The flows and compositions resulting from these conditions were used to calculate membrane permeance and selectivity. The tests in the first block were carried out to ensure that the extreme conditions specified for testing were workable and to tune parameters for the Block 2 if necessary. Having complete test results from both blocks enabled development of empirical models utilizing single- and second-degree parameter interactions to predict permeance and selectivity.

Table 2. Range of process parameters tested.

Variable	Unit	Low value	High value	Comment
Gas feed rate	ml/(min* cm^2)	37	70	Standard conditions
Feed gas composition	% CO_2	10	90	Balancing gas CH_4
Feed gas temperature	°C	40	90	
Feed gas pressure	bara	35	90	
Permeate pressure	bara	2	35	

Table 3. Block 1 data points.

Test Condition Number	Data Point Type	Gas Feed ml/(min cm^2)	Temp, °C	Feed, % CO_2	Feed P, bara	Permeate P, bara
1	Center	50	56	50	67	17
2	Model	37	40	70	35	2
3	Model	37	40	10	90	2
4	Model	63	71	10	35	2
5	Lack of Fit	37	53	10	35	2
6	Lack of Fit	63	46	10	90	2
7	Replicate	37	71	70	90	60
8	Model	63	40	70	90	60
9	Replicate	63	71	10	35	2
10	Model	37	71	70	90	60
11	Model	63	71	70	90	2

Contaminant Testing

Some constituents in a gas mixture fed to a membrane separator may impact the performance of the membrane with respect to the desired separation–CO_2/CH_4 in this case. The impact of water and H_2S were tested to a limited degree in this project.

Effect of Contaminants on Membrane Performance

Tests with Humidified Gas

The purpose of the tests with humidified gas was to measure the impact of presence of water in the gas to the CO_2/CH_4 separation, not to measure the permeation of water as such. The gas mixture was bubbled through liquid water to saturate the gas at the same temperature and pressure as the test conditions. The humidity readings confirmed that the feed gas was fully saturated.

The results are given as CO_2 flux and CO_2/CH_4 selectivity. Water flux was estimated based on humidity measurements of the permeate flow.

The impact of wet gas is critical since the subsea separation train will process feed gas with a high-water content. Two sets of process conditions were tested using a feed gas with 30% CO_2 and 70% CH_4 with and without humidification of the feed gas and compared:

- Condition 1: 40°C and Feed pressure/Permeate pressure equal to 35/9 bara.
- Conditions 2: 65°C and Feed pressure/Permeate pressure equal to 53.8/16 bara.

The conditions 1 and 2 are referred to as the low and high temperature conditions, respectively, in Figures 14 and 15.

Table 4. Block 2 data points for each membrane tested.

Test Condition Number	Data Point Type	Gas Feed ml/(min cm^2)	Temp, °C	Feed, % CO_2	Feed P, bara	Permeate P, bara
12	Model	37	59	30	83	24
13	Model	37	71	50	56	2
14	Model	37	84	70	90	31
15	Model	47	90	70	63	2
16	Replicate	53	59	30	90	24
17	Model	63	40	70	49	2
18	Model	53	90	10	56	2
19	Model	50	40	70	90	31
20	Model	47	90	70	35	24
21	Model	53	59	30	90	24
22	Model	40	90	30	90	2
23	Model	63	90	50	35	2
24	Model	57	90	70	90	60
25	Model	37	90	50	63	31
26	Model	47	53	70	90	2
27	Model	63	90	70	90	31
28	Model	57	40	30	56	17
29	Model	63	59	70	56	39
30	Model	37	40	50	63	31
31	Replicate	50	40	70	90	31

Tests with H_2S

Possible effect of H_2S on the membrane separation performance was tested at 60 bar with a mixture of CO_2:CH_4=10:90 vol % with 1000 ppm H_2S at two temperatures (40 and 70°C). Prior to the tests, performance of the virgin membrane materials was measured at the same conditions without H_2S. The separation performance of the membrane was again tested after exposure to H_2S for up to 355 hrs. to check if irreversible damage to the membrane material occurred after exposure to H_2S.

EXPERIMENTAL RESULTS

Microscale CO_2 Separation Tests

This section provides the CO_2 separation performance test results and an assessment of the results.

Stage Cuts

Typically, at the microscale, permeation tests are performed with a low stage cut to reveal intrinsic properties of the membrane material. To carry out experiments at the same stage cut (e.g., 5%)

adjustment of the feed flow rate and the resulting permeate flow rate has to be done. This is possible when membrane performance within the wide range of operation conditions is known in advance, as in the case for one of the candidate membranes (C) which was tested at an external laboratory.

For the other three candidate membranes tested by SINTEF, no information on membrane performance was provided before the tests. For these membrane tests, the stage cut or percentage of the feed flow volume that permeates, is a result of the process variables that are set for the specific test. The feed rate and the pressure differential would have the biggest impact on stage cut.

The candidate membrane with a high stage cut (or high permeance) produced a wide range of 5–50% stage cut over the range of variables tested, while the candidate membrane with a low stage cut (or low permeance) produced a narrower 1–17% stage cut range.

Low stage cuts are linked to the membrane characteristics, which lead to lower permeation of the gas components than for the other candidate membranes. Low stage cuts are usually coupled with higher selectivities and hence, less hydrocarbon loss. Additionally, with low stage-cuts, the inherent performance of a membrane can be measured in the absence of concentration polarization and depletion effects, which would otherwise have to be included in the flux modelling to extract the true permeance and selectivity of the material.

All test conditions with the membrane tested at the external laboratory were adjusted to keep a low stage-cut intentionally at about 5%. As a result, the feed flow rates for these tests were different from, and in many cases higher than those used in other candidate membranes tests by SINTEF, which made it difficult to compare directly with the other candidate membranes. However, in accordance with the objectives of the test program, the focus was to characterize the capability of each individual membrane to perform under the extreme conditions of interest. As described in sections below, comparisons between the various membranes are made despite differences in stage cut ranges. To compare the performance of the individual membranes, they will be tested at equal conditions, including stage cuts, in phase 2 of the project.

Permeance and Selectivity

The results from the performance tests are presented as permeance and selectivity values for membranes A, B, and C. The initial material compatibility tests of membrane D showed that this membrane could not withstand the exposure to hydrocarbons and acidic water. Hence, membrane D was not tested in the performance experiments. The results are shown in the following figures.

The permeance and selectivity values are plotted against experimental order, not reflecting the test condition number given in Tables 3 and 4. How the various test conditions are connected and hence the comparison between the membranes are discussed in the following section.

The results shown in Figures 9 and 10 can be perceived as randomly distributed, but in fact, contain a lot of underlying information. For all membranes, both the permeance and selectivity vary from test to test due to the variations in the control variables. The wide variations observed are not random and can be explained to a high degree. This is further discussed in the following section. Some general conclusions can however be drawn as follows:

- The high permeance membranes (A and C) have approximately 3 times higher permeances than the low permeance membrane (B) at similar process conditions. This can be an important factor for selecting a CO_2 membrane in situations where the hydrocarbon recovery is a lower priority. A permeance threshold located at about 65 GPU separates between the high and low permeance membranes.

- The high selectivity membrane (B) has a selectivity about 2.5 times higher than the selectivities achieved by the other membranes at similar conditions. A selectivity threshold of about 11 separates the two classes of membranes.

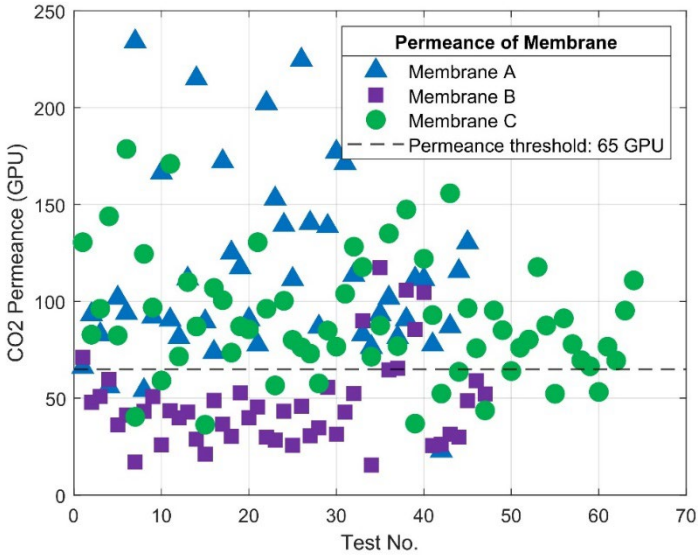

Figure 9. Resulting measurements of CO_2 permeance at the various test runs. The test run number does not correspond to the test condition number in Tables 3 and 4.

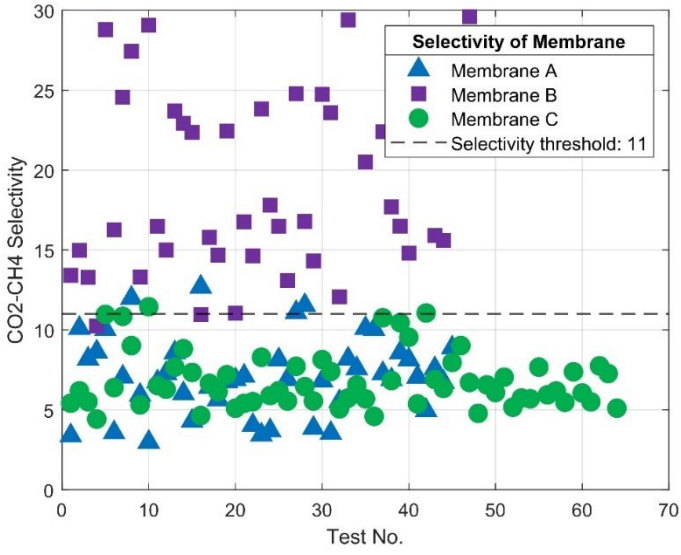

Figure 10. Selectivity measurements for membranes A, B, and C. The test run number does not correspond to the test condition number in Tables 3 and 4.

Significant Separation Process Effects

An ideal CO_2 membrane separation process would provide a combination of a high permeance of CO_2 (for high CO_2 removal) and a high CO_2/CH_4 selectivity (for hydrocarbon recovery). However, tuning the operational variables to maximize both the permeance and selectivity at the same time is not usually possible, and the optimization requires taking both goals into consideration. A discussion of how the main process variables explain variations in the measured permeance and selectivity values follows. Empirical models were developed from the micro scale test results for the respective membranes. These model relationships capture the underlying variations in the observed results for permeance and selectivity. The details of the model coefficients are not disclosed.

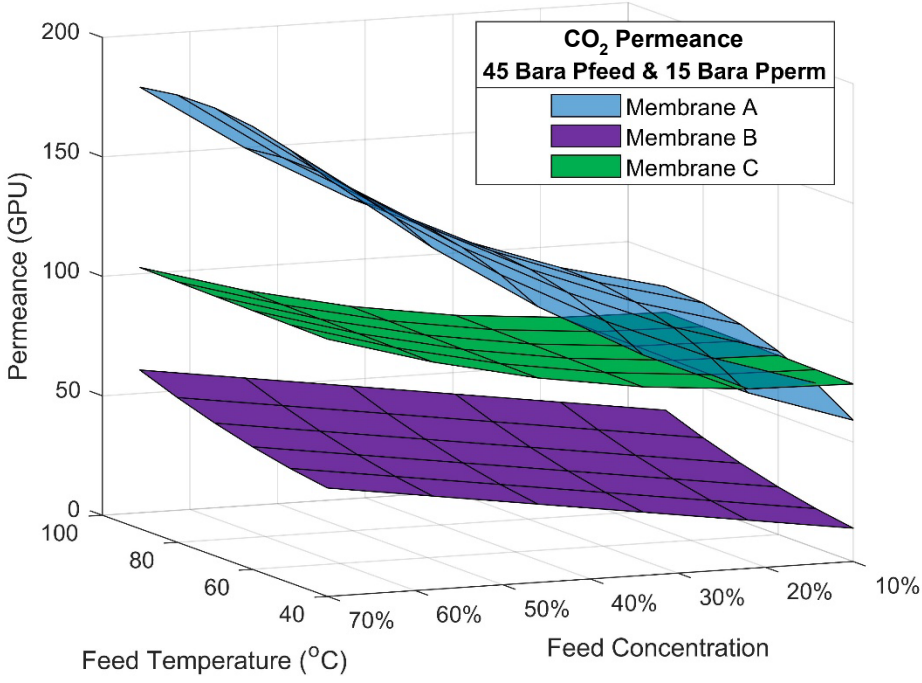

Figure 11. 3D model showing permeance for membranes A, B, and C as a function of temperature and CO_2 concentration. Feed pressure, feed flow rate and permeate pressure are held at equal, fixed values for these tests.

Figure 11 displays the membrane permeance at varying temperatures and CO_2 inlet concentrations for fixed feed rate and pressure conditions. All the membranes show relatively low sensitivity to inlet CO_2 concentration and increasing permeance with increasing temperature. However, Membrane A is exponentially more responsive to increased feed CO_2 concentration.

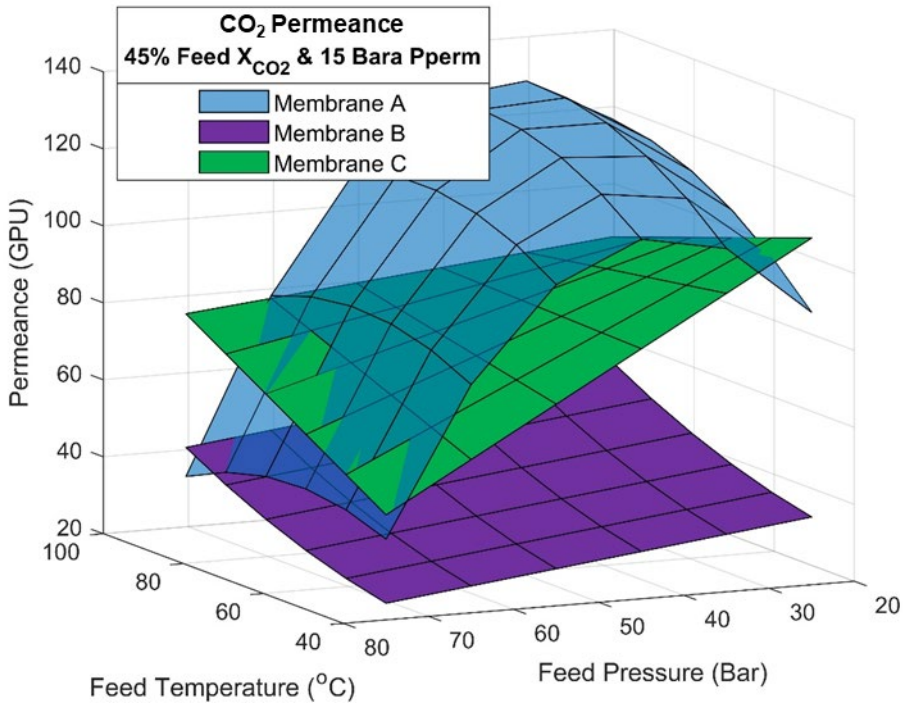

Figure 12. 3D model showing permeance for membranes A, B, and C as a function of feed pressure and temperature. Feed flow rate, CO_2 content, and permeate pressure are kept at fixed values.

The respective empirical model for each membrane contains different significant terms and coefficients, and these models will not be applicable for designing a membrane separation step. However, for preliminary assessment of the membrane responses to critical process conditions these models and figures are very useful.

The selectivity response surfaces in Figure 13 indicate that, for the given set of fixed conditions, the selectivity for membrane A and C are relatively insensitive to variations in the CO_2 feed concentration and temperature. Membrane B shows an increased selectivity at increasing feed concentration.

Temperature

Temperature is the most influential factor for selectivity for all the membranes tested. For conventional membrane materials, the selectivity is mostly negatively correlated with temperature. Temperature also has significant effect on CO_2 permeance of membranes with higher selectivity but has a less significant effect for the membranes that exhibit high permeance.

The good membrane performance observed in these tests with respect to impact of higher temperature is very promising, since the conditions expected for subsea wellhead separation will likely have higher temperatures than typically recommended for conventional sweetening operations.

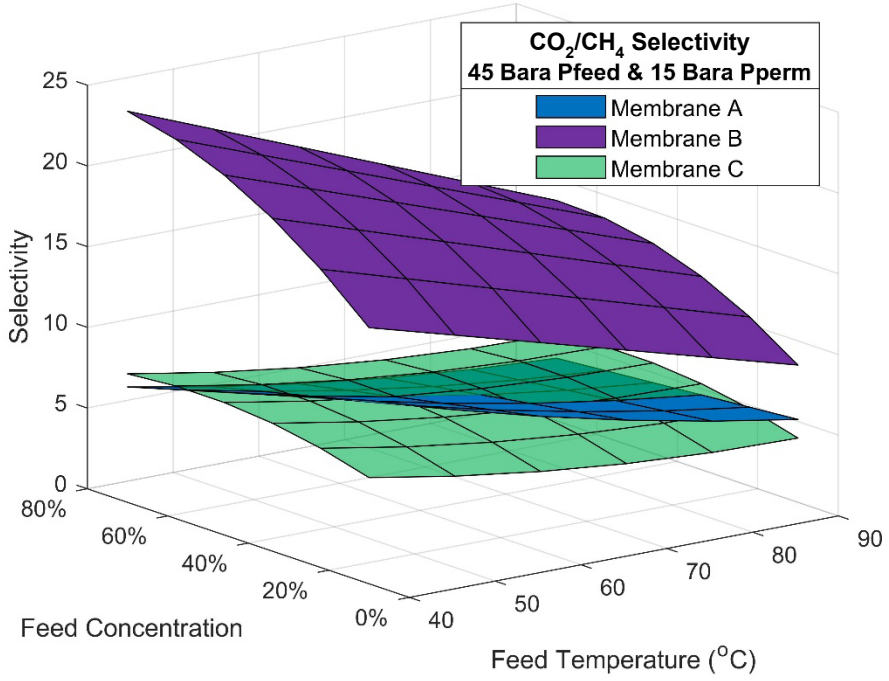

Figure 13. 3D plot of modelled selectivity for membranes A, B, and C as a function of temperature and CO_2 concentration. Feed pressure, feed flow rate, and permeate pressure were fixed values for the various membrane tests.

Feed Pressure

Feed pressure was found to have very significant impact for the higher permeance membranes. Both permeance and selectivity decline as feed pressure increases. However, for membranes with high selectivity, the effect is minor. This is possibly due to dense membrane material structure associated with high selectivity exhibiting a higher resistance to structural change under pressure.

Feed Flow Rate

It was found that the feed flow rate does not have a significant effect on either apparent permeance or selectivity if the rate is high enough to avoid depletion and concentration polarization. This was more obvious for the low permeability membrane at low stage-cuts.

Contaminant Effects

Effect of Water (Humidified Gas)

Humidification of the feed gas affects the gas separation behaviour of all the membranes tested significantly, with variations ranging from ± 5 to ± 40% for permeance and from ±3 to ±20% in selectivity compared with the dry gas feed conditions. The conditions for the two series of tests are

designated as “low” and “high” temperature. In more detail, the low temperature tests are at 40°C and Feed pressure/Permeate pressure equal to 35/9 bara, and the high temperature tests are at 65°C and Feed pressure/Permeate pressure equal to 53.8/16 bara.

The results are presented in Figures 14 and 15. The reference point is the individual permeance and selectivity values for each of the membrane materials as measured in dry condition.

Figure 14 illustrates clearly that the permeance of the membrane materials react very differently to the presence of water and to temperature. Membrane materials A and C generally showed increased permeance under humid conditions, while B showed the opposite. The temperature at which exposure occurred had varied impact on A and C, with permeance returning to base value upon drying for A after low temperature exposure but not for high and C returning to base permeance after high but not low temperature exposure. The permeance of C returned to the base value for both conditions.

Selectivity behavior of the membrane materials was more consistent (Figure 15), compared to permeance, with all three materials returning to base selectivity after exposure. Membrane C showed the least selectivity variation. Both membranes A and C showed significant loss of selectivity at low temperature.

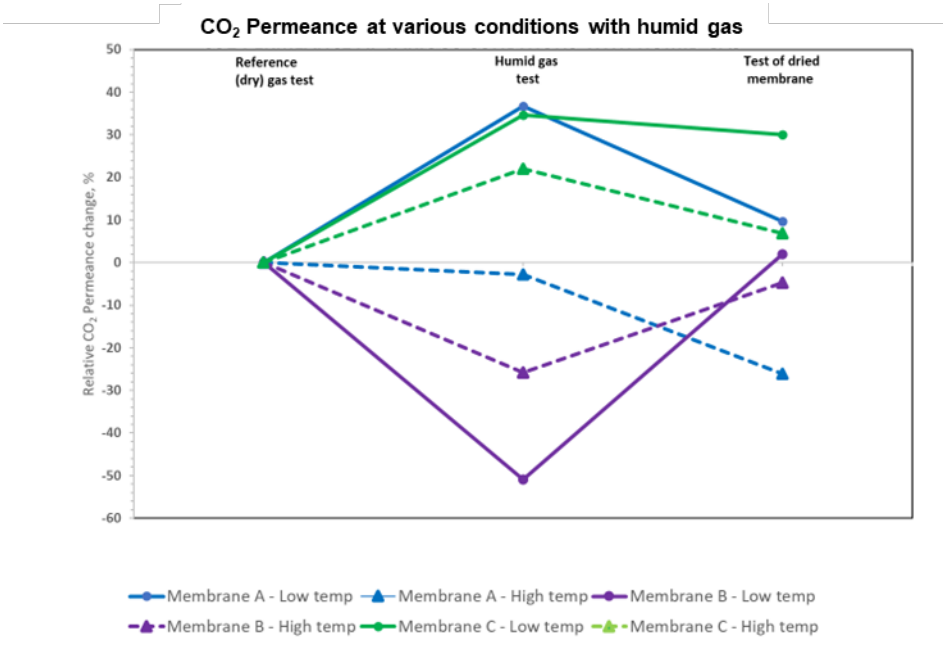

Figure 14. Relative variations in CO_2 permeance between the membrane materials at two test conditions.

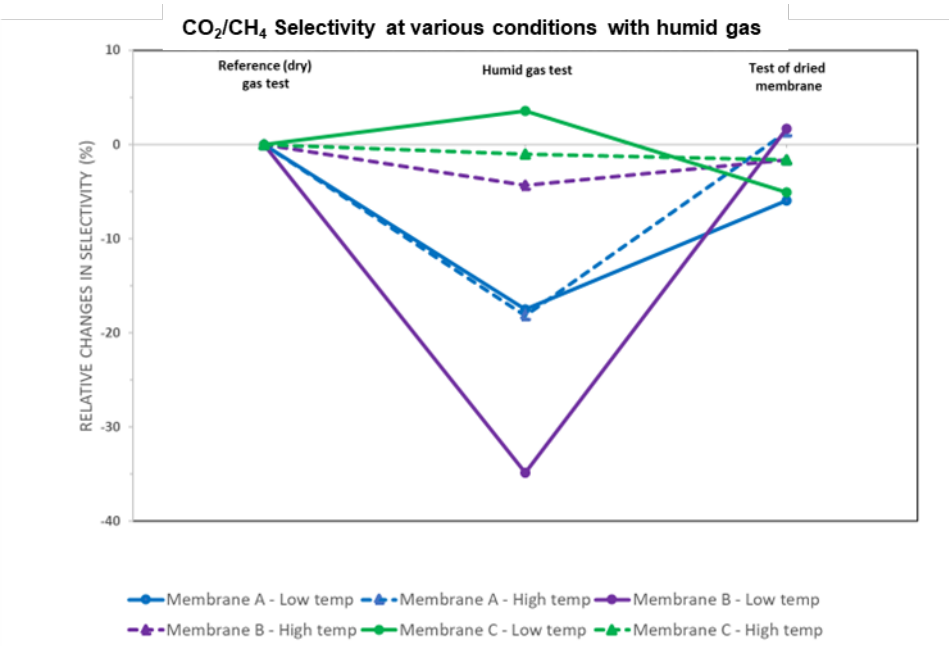

Figure 15. Relative variations in CO_2/CH_4 selectivity between the membranes at two test conditions.

It should be noted that water-saturated feed gas did not deteriorate the membrane gas permeation performance completely even at the harsh conditions prevalent in the subsea separation. Furthermore, tests indicate that the membrane performance generally returned to the base value when dry gas was supplied after the exposure to humidified gas in the same test.

The observed contradictory trend among the different membranes is related to the quite different membrane polymer systems. Details of the properties and characteristics were not disclosed to this project. The tests were conducted from the perspective of observing the potential impact of the presence of water in the feed gas. In general, H_2O is a fast molecule in polymeric membrane separations and is assumed to permeate faster than CO_2.

No general conclusions can be drawn regarding the impact of water vapor since tests were only made at two different conditions and for short time exposure. Since the associated gas will contain water to some degree, more systematic testing of wet gas at various conditions for long exposure time is required to obtain the actual separation performance.

Effect of H_2S

Two of the tested membranes were found to be selective towards H_2S. Even though the separation factor is, in general, lower compared to CO_2, it was clear that these membranes would remove both CO_2 and H_2S from natural gas.

An example of CO_2 separation measurements in the presence of H_2S for membrane B is shown in Figure 16. The inlet pressure was equal to 60 bara and the temperature 40°C. The big variations in permeance and selectivity are due to lowering of flow rate in the test cell during night-time.

The figure shows that the membrane performance is stable at steady state conditions, indicating that the H_2S content does not influence the separation performance of CO_2 and CH_4. Tests of membranes not exposed to H_2S show no or insignificant variation in performance in the presence of H_2S.

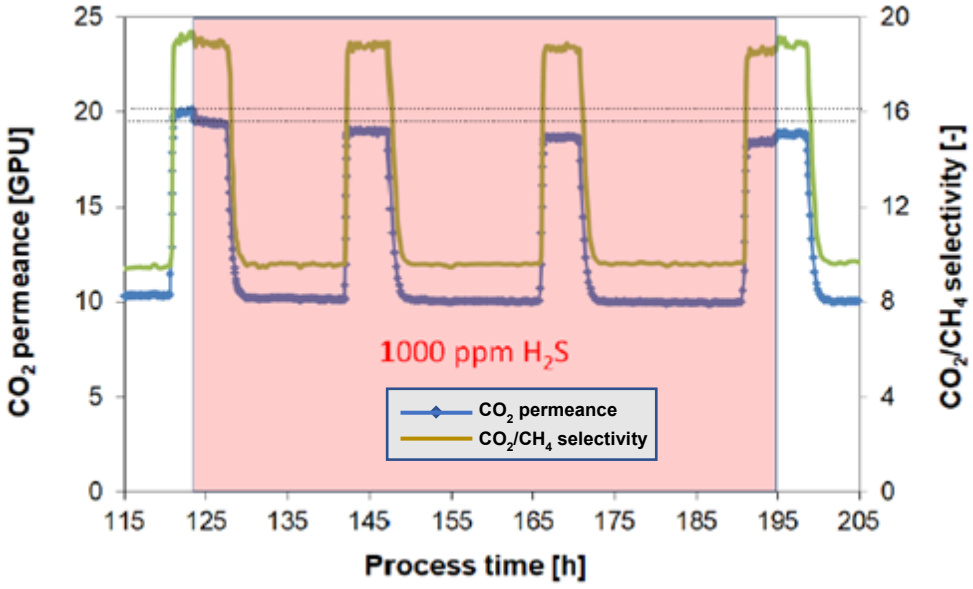

Figure 16. Measurement of CO_2 and CH_4 separation in presence of H_2S. Membrane B at 40°C and 60 bara.

Figures 17 and 18 compare the performance of all membrane materials in the presence of H_2S at various testing conditions. In addition to the membranes A, B, and C, one special version of membrane A was also tested. Reference CO_2/CH_4 selectivities in the absence of H_2S were measured and are almost identical to the ones with H_2S present and hence are not plotted in the figure.

The figures shows that all membranes show a decline in selectivity towards both CO_2 and H_2S as temperature increases, however, to varying degree. Membrane B is relatively more stable than C and D. The regular membrane C is not selective towards H_2S as the figure shows, but a special version of membrane C was tested and showed good selectivity towards H_2S.

All membranes tested were found to be stable over the period investigated in the presence of 1,000 ppm H_2S. Although a slight reduction in CO_2 permeance was observed upon introduction of H_2S, the membrane performance was stable over time. The presence of H_2S at the tested conditions seems to cause reversible competitive sorption.

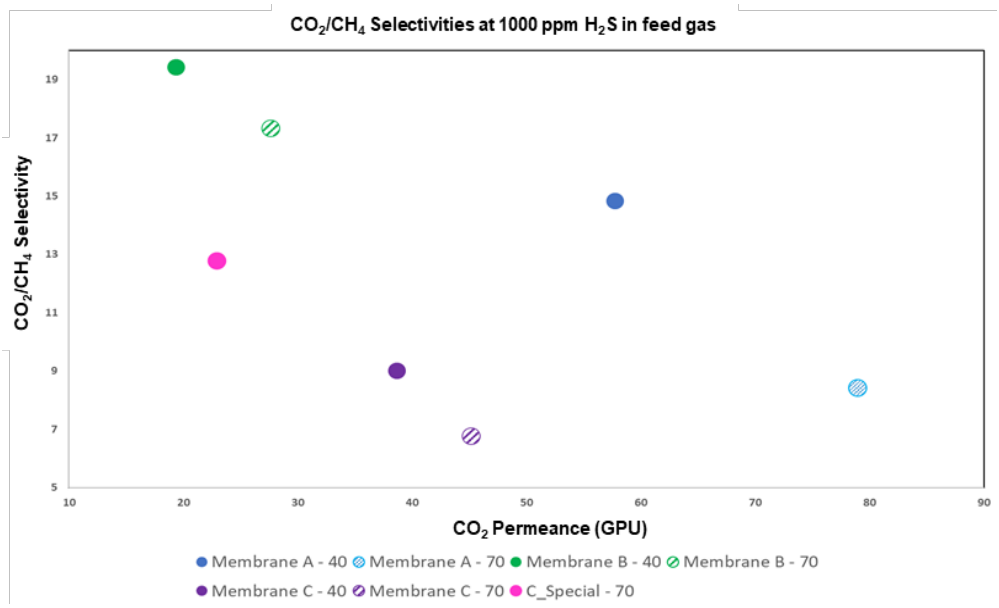

Figure 17. Complete overview of measured CO_2/CH_4 selectivities. The number in the legend indicates test temperature in °C.

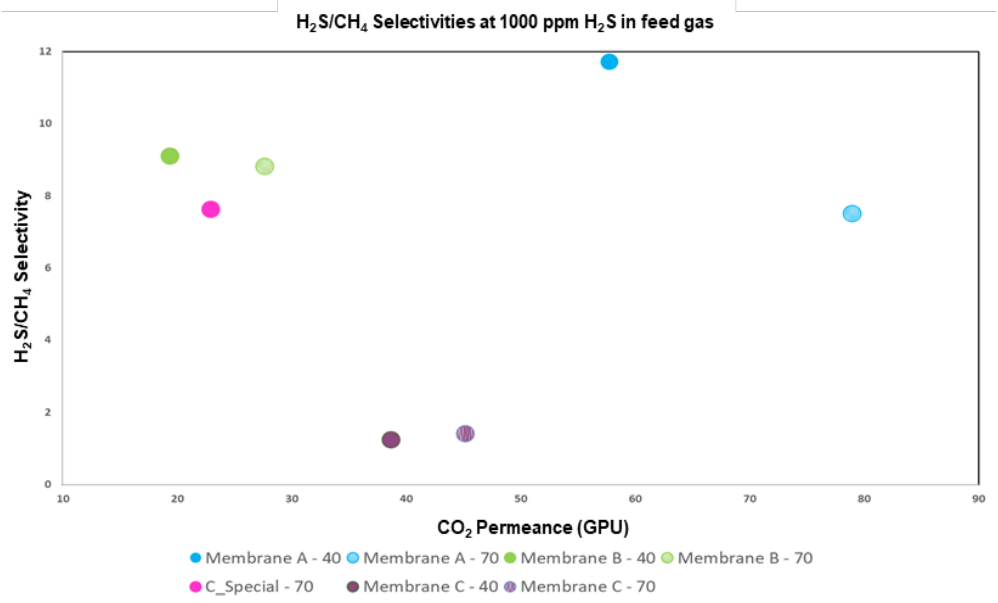

Figure 18. Complete overview of measured H_2S/CH_4 selectivities. The number in the legend indicates test temperature in °C.

Performance Prediction and Process Optimization

As discussed above, the performance of a membrane is dependent on multiple variables and the interaction between these variables. In this section, an example of the prediction of membrane performance by the empirical model based on the experimental results is shown. The optimization of the membrane separation process is also discussed. The empirical equations express how the external testing conditions impact the membrane performance, measured as permeance, selectivity, or degree of CO_2 removal. Hence, such empirical models are not applicable for designing a membrane separation process where dynamic behaviour of gas flow and driving forces must be accounted for.

It is emphasized that the simulation models are based on the external mass balances on inlet and outlet streams and accordingly, do not consider changes along the fibre length or cross flow path. Such mechanistic models will be developed in phase 2 of the project when representative industrial scale membrane modules will be tested, and the models will account for the gas flow patterns in the modules.

It should also be noted that the current models and hence mass balances are based on dry gas and without considering the effect of higher molecular weight hydrocarbons than methane, which would be present in real associated gas.

Performance Prediction

An example of the predicted versus measured membrane performance is shown for CO_2/CH_4 selectivity in Figure 19. As shown in the figure, the points are distributed close to the benchmark line which indicates that the regression models give satisfactory predictions.

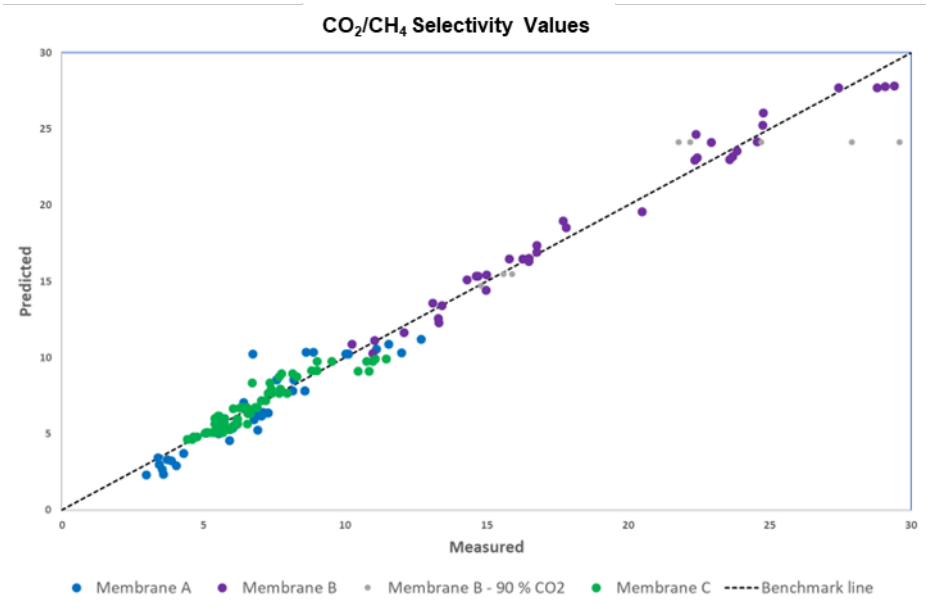

Figure 19. Predicted selectivity vs measured.

The figure shows that 97-98% of the variation of measured selectivity is explained by the regression models for the various membranes. The empirical models for each membrane are different. The figure also shows results for each membrane tend to cluster, indicating that there are quite different characteristics. The high degree of model agreement with the data indicates that the membrane performance can be predicted by relatively simple empirical models that contain statistically valid terms. These models are only valid within the experimental space used in the tests.

A few tests were done with membrane B at various conditions using 90% CO_2 in the inlet gas. The model for membrane B was used to predict these results (grey circles in Figure 19). The figure shows that these points were reasonably well predicted by the model tuned with no data above 70% CO_2.

CO_2 Separation Process Optimization

The results from membrane performance measurements expressed as permeance and selectivity provide information about individual membranes at specific conditions. These two properties, as estimated by the empirical relationships noted above, are combined with the membrane area to estimate CO_2 removal. CO_2 removal is defined as the fraction of CO_2 that permeates through the membrane relative to the CO_2 in the feed.

Figure 20 shows the degree of CO_2 removal by membranes A, B, and C as a function of feed temperature and pressure for a feed CO_2 concentration of 40%. For this scenario, the area of each membrane is fixed and equal, the permeate pressure is 10 bar, and the feed flow rate is constant.

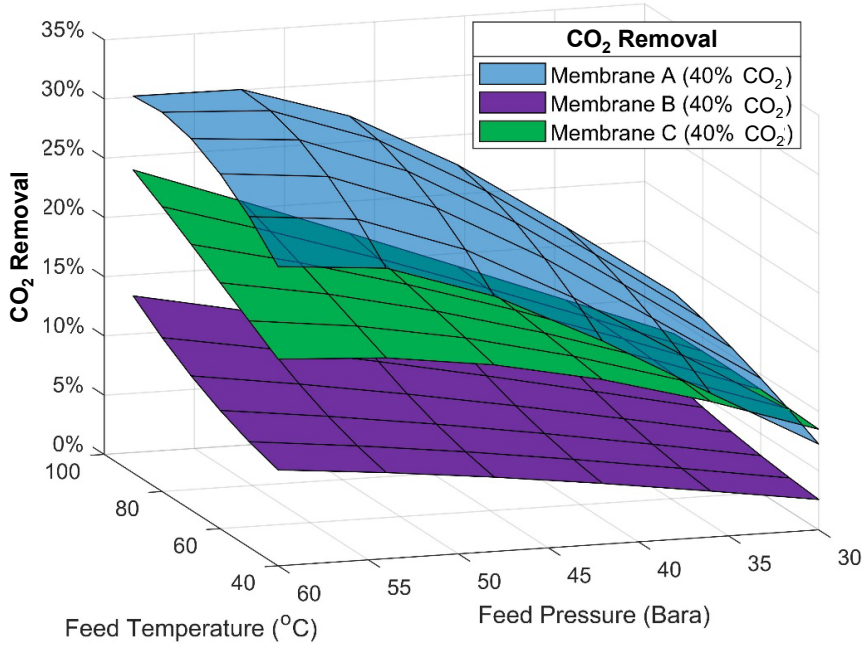

Figure 20. The response surface for degree of CO_2 removal at specific conditions for membranes A, B, and C with the same feed and membrane area.

The fraction of CO_2 removed is a non-linear function of both feed temperature and pressure, particularly when the temperature is above 65°C and the pressure is higher than 45 bar. For membrane B, the permeance and selectivity are relatively less sensitive to temperature, so the surface is flatter. All three membranes achieve low removal fractions at low temperatures, mainly due to reduced permeance. The overall performance, or CO_2 removal, is a result of the combined influence of permeance, selectivity, and the mass transfer driving force (CO_2 partial pressure difference). It should be noted that Figure 20 shows the performance for a specific membrane area at specific conditions. A larger membrane area achieves higher CO_2 removal, although the CO_2-rich permeate will have lower purity. In addition, the assessment of optimum process conditions must usually consider CH_4 loss. The trend shown in Figure 20 shows that the overall degree of removal increases as temperature increases (valid for the selected conditions). The increased CO_2 removal at higher temperature is driven by increased CO_2 permeance, while declining selectivity leads to lower purity.

The highest CO_2 removals for the tested membrane qualities are measured at about 60%. These data points are linked to high driving forces. When similar membrane areas and driving forces are used, the final CO_2 removal will be governed by the permeance.

The empirical models and response surface plots are very useful to investigate which conditions are most suitable for the subsea processing train, both to define the optimal process conditions with respect to CO_2 removal and the necessary membrane area. A process response surface with sharp curvature means that a small change in operating conditions can cause a big impact on the performance, which is undesirable.

Conclusions from Membrane Performance Testing

Microscale CO_2 Permeation Tests

Four membranes were proposed for testing that was planned according to statistical design of experiments to explore performance across the limits of the conditions set in the project. Membrane D did not perform well in compatibility tests compared to A, B, and C, so this membrane was not subject to the complete performance test program, and the results of testing membrane D that was completed are not reported.

The test conditions cover a wide range of temperature, pressure, and flow rates with several compositions of CO_2 and methane. The measurements of permeance and selectivity were used to tune empirical models that explain the variations of the measurements to a high degree of statistical confidence. The low standard deviations from replicates and the low standard deviations from the frequent sampling of process parameters during each experimental condition indicate that the measurements were of good quality with only small randomly distributed deviations between the predicted and measured values.

The empirical models of membrane performance for CO_2/CH_4 selectivity and permeance provide information about membrane performance at conditions beyond the typical recommended range for which there is application experience. These extreme conditions are relevant for the subsea processing concept considered in this project. The empirical models are not applicable for designing membrane modules, but they are useful for assessing the impact of the various process conditions on membrane performance. The models are useful in making comparisons between the membrane materials.

The results also show that the various membranes tested have different characteristics with respect to permeance and selectivity at changing conditions. An important observation for the materials tested is that the selectivity is inversely proportional to temperature, although not exponentially as is typical for polymeric membranes.

Exposure to Humid Gas

All membranes were tested at two different conditions with water-saturated gas. Although only a limited number of tests with the humidified gas were done, the results indicate that the separation performance is affected by the presence of vapor-phase water to very varying degrees for the different membrane materials. The original performance at dry conditions were recovered when the samples were dried and tested again with dry feed gas. As such, the water doesn't seem to have an irreversible damaging effect on the performance.

Satisfactory CO_2 separation in the presence of water vapor will be critical for this subsea processing concept since it will be challenging to implement typical dehydration operations on the gas stream in the subsea environment. Understanding the impact of water and critical concentrations will be important topics for further assessment.

Exposure to H_2S

All membranes showed quite good electivity to both CO_2 and H_2S relative to CH_4 and followed a general pattern of reduced H_2S selectivity at increasing temperature. Membrane CO_2 removal performance did not show any deterioration from H_2S exposure at the conditions and test duration of these experiments.

MATERIALS COMPATIBILITY TESTING

The robustness of materials used to fabricate membrane modules for subsea gas processing was evaluated for three candidate membranes (A, B, and C) by testing compatibility with liquids that are expected to be present in the subsea processing system. The liquids used were carbonic acid (water saturated with CO_2), a hydrocarbon mixture as specified in NORSOK M710, methanol, and monoethylene glycol (MEG).

The tests of the membrane cartridge components were conducted on isolated samples, such as the gluing system, spacer material, O-rings, and the like. Also, the adhesion between the embedded polymeric membrane fibres and the cured epoxy potting system was assessed for membrane modules where such fabrication is a part of the module design. Compatibility of the potting/glue material was given the highest attention since this was considered to represent the most vulnerable part of the membrane cartridge.

Compatibility of membrane materials with acidic water (AW) and the hydrocarbon mixture (HC) was evaluated by testing membrane separation performance before and after exposure the entire membrane unit to the liquids.

Due to limited relevant test standards for this application (subsea gas processing), the focus was to compare the component properties before and after the exposure and not to consider absolute figures. Only a high-level summary is given in this chapter.

Test Methods

Exposure to the acidic water and HC liquids was performed in an autoclave at 55 bar CO_2 partial pressure at three different temperatures (60, 75, 90°C) with a duration of three to five weeks with weekly retrievals of samples. Exposure to MEG and methanol was done at 20 bar CO_2 pressure at room temperature. Depressurization of the autoclaves after cooling to room temperature took place at less than 1 bar/minute.

The fluids used in the experiments:

- Acidic water: Ultraclean (i.e., filtered tap water), saturated at ambient temperature with approximately 55 bar of CO_2. Oxygen content in the water was less than 0.01 ppm.
- Hydrocarbon mixture: Simulated aromatic production fluid for sweet aging tests consisting of 70% heptane, 20% cyclohexane, and 10% toluene by volume. The fluid was purged with N_2 and CO_2 before the autoclave was pressurized with CO_2 to 55 bar.
- Methanol: pure methanol, analytical grade, purged with N_2. Purging was stopped when the oxygen concentration was less than 0.1 ppm. After the autoclave was filled with the liquid, it was pressurized to 20 bar with CO_2.
- MEG: A mixture of 90% MEG and 10% purified water purged with N_2. Oxygen was removed using the same purging procedure as for the other liquids. After the autoclave was filled with the liquid, it was pressurized with CO_2 to 20 bar.

A range of tests were carried out before and after exposure to evaluate the degree of compatibility:

1. Visual inspection of the material after exposure to the different test liquids.
2. Dynamic Mechanical Thermal Analysis (DMTA). Specimens with a geometry that suited a rheometer using the torsion bar principle were cut and tested.
3. Swelling and weight gain.
4. Mechanical testing. Tensile test of dried and reconditioned rectangular specimens identical to those used for DMTA with reduced waist, was performed.
5. Hardness. The hardness (indentation hardness) was measured according to ISO 868:2003 in the wet and dried state.
6. Other tests, when this was necessary to complement results from the test above, included:
    - DSC (Differential Scanning Calorimetry) to check cure and membrane glass transition temperature, Tg.
    - TGA–thermogravimetric analysis of the material in the dried state.

For testing compatibility to liquid exposure of the membrane materials, the micro-modules (shown in Figure 7) were filled up with a liquid (acidic water or hydrocarbon condensate) and pressurized with CO_2 up to 55 bara at 60°C for 10 hours. The liquid was then drained and the membranes thoroughly dried. Separation performance of the membranes before and after the exposure was tested with a gas mixture of CO_2:CH_4=30:70 vol % at 40°C, 35 bara feed gas pressure and 9 bara permeate pressure.

For the MeOH and MEG exposure tests, the membrane materials were soaked in the liquids for two weeks and samples retrieved and tested during this time interval.

For the acidic water and hydrocarbon liquid exposure, the membrane modules were soaked in the liquids at the specified elevated temperature and pressure for six hours.

After exposing the membranes to the liquids, they were dried overnight until no change in weight was observed. Then they were flushed with N_2 and subsequently heated.

EXPERIMENTAL RESULTS

Effect of Exposure to Liquids on Membrane Cartridge Components

Exposure to Acidic Water

The adhesive or potting material used by the suppliers to fabricate the membrane modules must meet different requirements due to differences in module design. For the membrane A design, a flat sheet fabricated into a spiral wound configuration, the polymer must adhere strongly to adjacent polymer

layers and be quite flexible. The relatively low glass transition temperature, T_g, adhesive used in this design was not resistant to acidic water exposure at elevated temperatures (DMTA results in Figure 21). Some other polymeric materials used in this module design also showed limited compatibility with acidic water at the highest exposure temperatures. Based on the T_g test results, the recommended maximum operating temperature for the adhesive is 60°C in the absence of acidic water changes. However, due to the absence of resistance to acidic water, this membrane was not considered applicable for use in the challenging subsea operating conditions, even though the membrane itself provides overall good performance with respect to CO_2 separation.

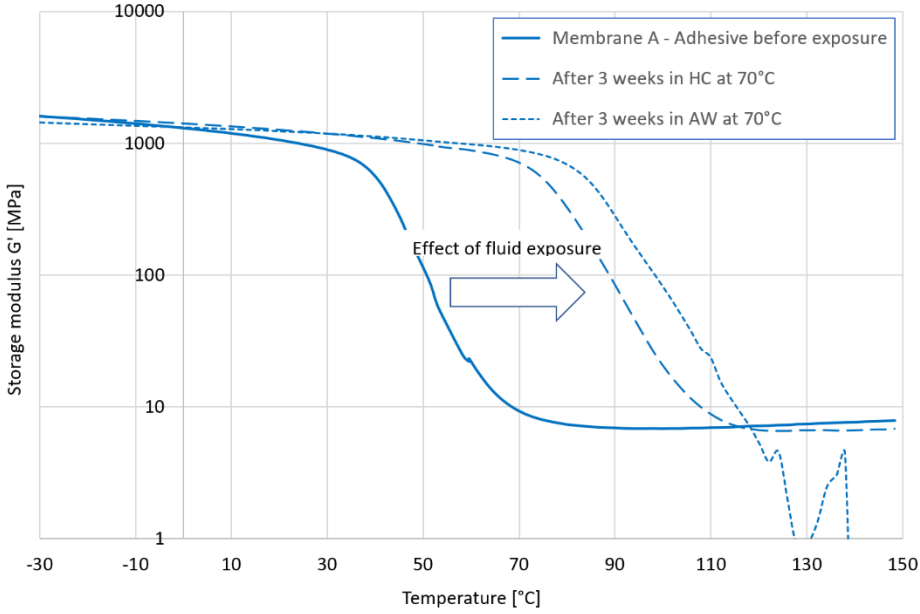

Figure 21. The effect of exposure in acidic water and hydrocarbon fluid at 70°C for 3 weeks of a relatively soft adhesive used in Membrane A, as expressed by the storage modulus G' from DMTA.

For membranes B and C, which use a hollow fibre configuration, the fibres are embedded in a potting matrix. The potting material is a high T_g thermoset polymer with high stiffness and strength. The initial properties of the two potting materials were almost identical. After exposure to acidic water, the potting for both membranes showed moderate weight uptake, swelling, and change in hardness. After drying and reconditioning, the initial properties were recovered, as shown in Figure 22. The mechanical properties changed little, with the potting system used in Membrane C showing less sensitivity to exposure at 90°C, as depicted in Figure 22. However, the DMTA showed that the thermo-mechanical response was influenced by the exposure and a relatively large increase in the T_g was observed for one of the potting materials. This resulted in a slightly reduced ductility expressed by the tensile strain-to-failure. The tests indicated that both B and C potting materials should be stable at temperatures up to 90°C. However, specific long-term ageing tests need to be performed to confirm the initial observations.

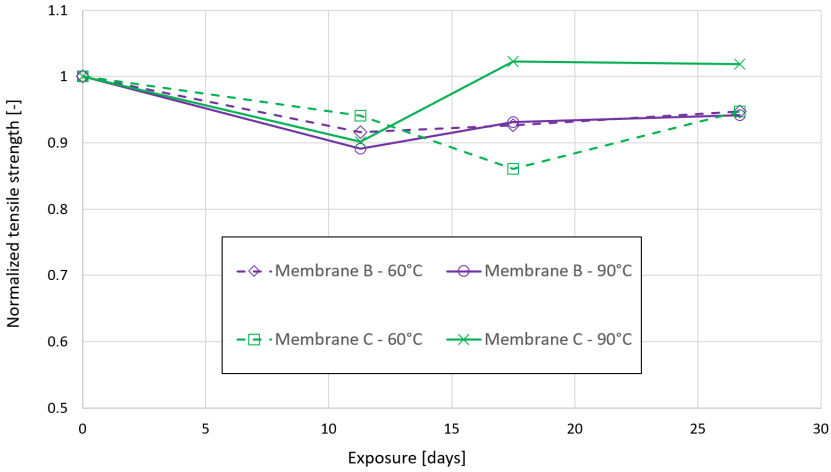

Figure 22. Normalized tensile strength of epoxy potting used in Membrane B and C, as a function of exposure duration in AW. Specimens dried and reconditioned after exposure.

The acidic water exposure at 90°C for three weeks did not cause debonding of the hollow fibres from the potting resin when the fibre/potting materials were tensile tested perpendicular to the fibre longitudinal direction. However, acidic water exposure resulted in a pronounced loss of membrane fibre strength, as shown in Figure 23. Hence, the operational temperature should be kept well below 90°C. Similar experiments should be carried out at lower temperatures to determine the maximum operational temperature with better precision, when exposed to harsh acidic conditions.

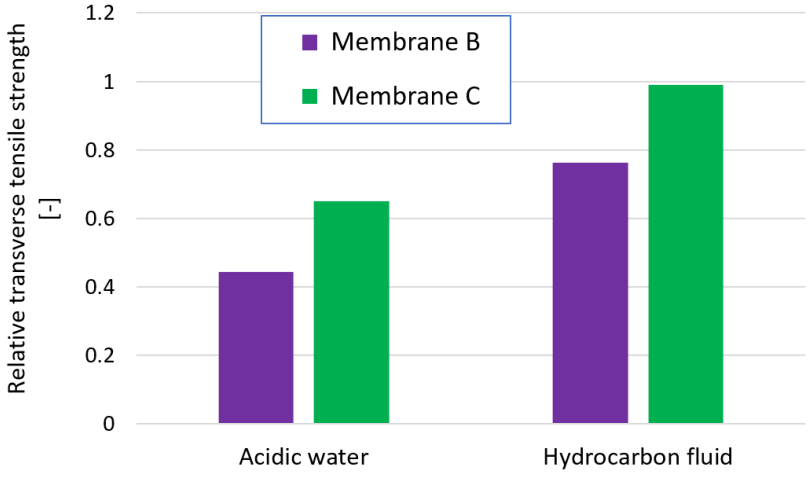

Figure 23. Relative transverse tensile strength of bespoke circular flat disc specimens of the hollow fibre polymer material embedded in epoxy potting from membrane B and C, after exposure in AW and HC for three weeks at 90°C.

Membrane C utilized O-rings in the design, and these were subjected to acidic water exposure, and the limited analysis of the post-test O-rings showed that they swelled and absorbed liquid. A quick investigation of the outer surface and the cross-section of some rings did not reveal any cracks at moderate magnification levels.

Exposure to Hydrocarbon Liquid

The relatively soft adhesive with low T_g used in the membrane A flat sheet module designs was compatible with the hydrocarbon mixture at all test temperatures in that no degradation was noted. However, the material did swell. The adhesive was on the boundary of being acceptable according to the NORSOK M-710 standard requirement for an elastomeric sealing material (swelling < 25%).[1] One of the thermoplastic materials used in this membrane module was also affected by exposure to hydrocarbon mixture.

The high-temperature resistant potting used in the hollow fibre designs was only minimally affected by exposure in the HC-mixture. This was the case for swelling, weight gain, and change in thermo-mechanical properties assessed by the DMTA analysis. A small increase in the T_g was observed, which indicated a post-cure effect. However, the change did not affect the apparent stiffness nor the strain-at-failure of the tensile specimens. The potting materials coped well with the hydrocarbon exposure at 90°C.

The effect of exposure of the potting/discs of fibre material to the hydrocarbon mixture was different for the two different membranes (B and C). The membrane C potting/fibre material was not affected at all, whereas the other (C) showed a reduction in transverse strength. The comparison is not straightforward, however, because the B and C specimens were quite different with respect to fibre volume fraction and fibre orientation. The main conclusion is that the hollow fibre materials are more sensitive to acidic water exposure than to the HC exposure.

The hollow fibre module O-rings were affected by exposure to the aromatic-containing hydrocarbon mixture. This was as expected, as oil is the most used plasticiser for these elastomer types. The result was a 10% permanent loss in weight and a subsequent increase in hardness.

The test conditions were harsh and provide guidance on the limits of operating conditions to maintain the membrane performance and stability. The changes that do occur seem to depend on exposure time. This suggests that emptying a temporarily flooded vessel (membrane separator) relatively quickly would minimize detrimental changes to the membrane system performance.

Exposure to Methanol and MEG/Water

The adhesive in the flat sheet membrane (A) was not compatible with pure methanol exposure at room temperature. Some of the other polymers used in this design also showed limited resistance to methanol. This was confirmed by tensile testing, which determined that there was a clear loss of ductility.

The potting materials in the hollow fibre designs were not found to be any better. They were permanently degraded by exposure to pure methanol.

The MEG/water exposure at room temperature did not have any effect on the studied materials. This is useful information with respect to which chemical to use for hydrate mitigation.

[1] The general assessment of compatibility of sealing materials used in the industry categorizes a material according to swelling as poor if 20-40%, good if 10-20%, and excellent if less than 10%.

The exposure of the membranes to MeOH and MEG was done to test the material compatibility, not for measuring any potential impact on separation performance.

Effect of Exposure to Liquids on Membrane Performance

Exposure to Acidic Water

Both the permeance and selectivity of all the membranes tested were noticeably affected by exposure to acidic water at the selected test conditions. However, behaviour of each of the membranes due to the exposure was different from the other membranes. The results from these exposure tests are shown in Figures 24 and 25.

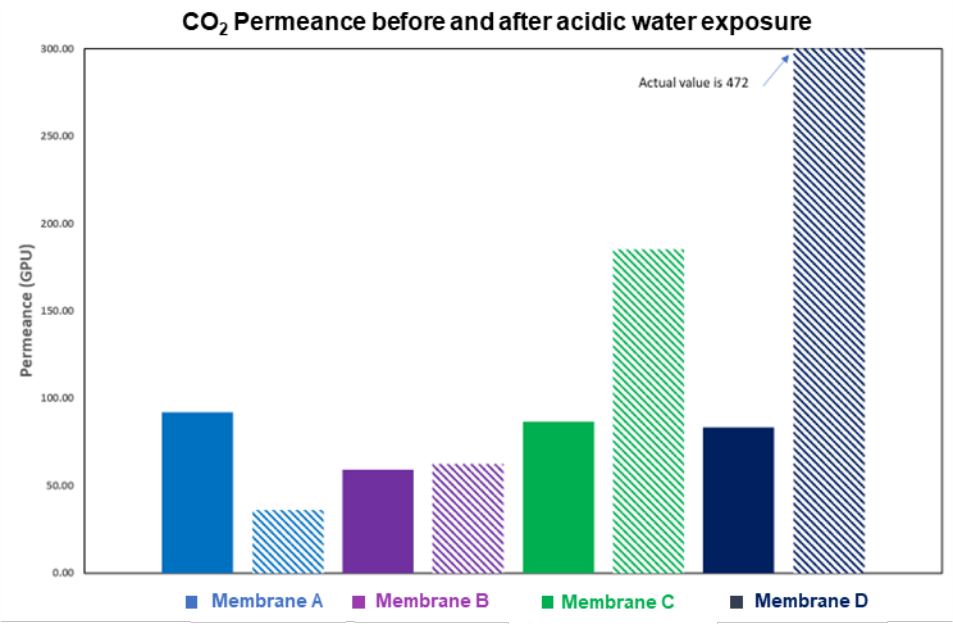

Figure 24. CO_2 permeance before and after exposure of membrane module to acidic water. The filled bars show permeance before and shaded bars after AW exposure.

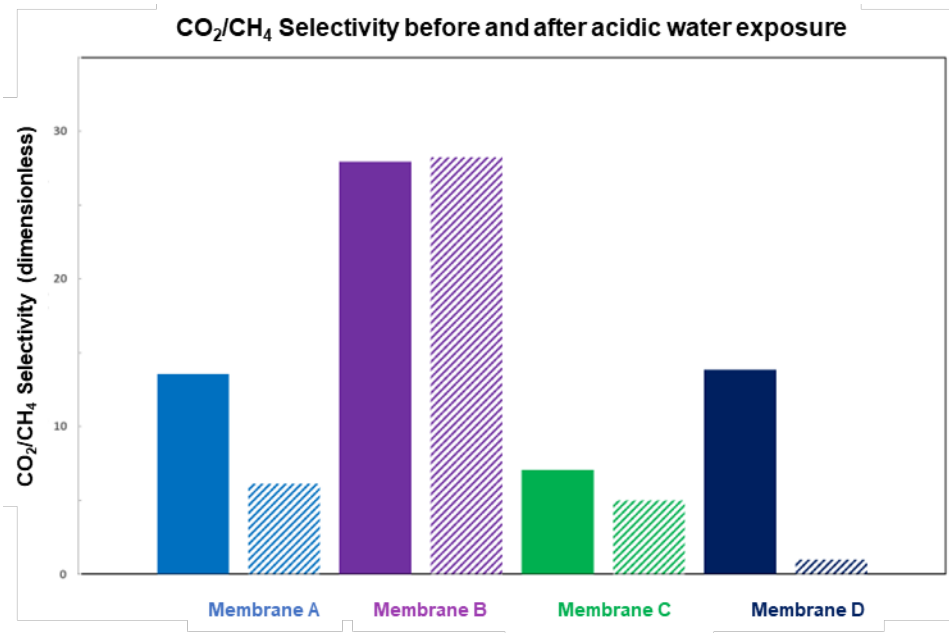

Figure 25. Selectivity before and after AW exposure. Filled bars show selectivity before exposure and shaded bars after exposure.

The membrane least affected by the acidic water exposure (B) showed slightly increased permeance and selectivity by about +6% and about +1%, respectively. The other membranes showed significant changes to permeance or selectivity or both. Performance of membrane D deteriorated significantly after exposure to acidic water. Although permeance was high, most of the CO_2 separation capacity was lost due to severe loss of selectivity. Membrane D was ruled out for subsea processing, and no further testing was done.

Exposure to Hydrocarbon Liquid

The impact on membrane permeance and selectivity due to liquid HC exposure was not as significant as changes from acidic water exposure, except for membrane D. Membrane D showed a manifold increase in permeance for both CO_2 and CH_4, resulting in a net loss of selectivity of about 70%. This result, combined with the sensitivity to acidic water, makes this membrane unsuitable for subsea processing. Such application would require water and HC dewpoint control and avoidance of condensing conditions.

The least affected membrane material, (B), showed about 5% increase in CO_2 permeance and about 4% decrease in selectivity. The other membranes showed more significant effects of about -15 to +20% variations in permeance and selectivity.

Hydrocarbon liquid in direct contact with the membrane may swell the membrane, although the degree of swelling will depend on the membrane material and structure. Sweeping the membrane with dry gas after such exposure would slowly remove the hydrocarbons remaining on the surface of the membrane and within the membrane. Retained hydrocarbons would affect the membrane performance

either by keeping the membrane material swollen (increasing gas transport) and/or hindering the transport of the other gases.

Further investigation is required to understand if and how the membrane will recover and what the gas permeation will be during and after hydrocarbon exposure.

OVERALL CONCEPT ASSESSMENT

There are several prerequisites needed to make the subsea concept feasible for well stream separation of CO_2-containing gas and the subsequent compression and reinjection of the CO_2-rich gas. A few main issues are referred to here:

- The membrane must provide good, stable CO_2 separation performance at the process conditions of interest when processing water-containing associated gas.
- Pre-treatment requirements should be minimal–preferably limited to removal of entrained liquids.
- The membrane material and the materials used to fabricate the membrane modules must be stable with respect to exposure to normal process fluids (high CO_2 gas) and to fluids in upset conditions–such as carbonic acid, liquid HC, and hydrate suppression liquids (methanol or glycols).
- The fraction of CO_2 removal from the associated gas must be high enough to avoid the need for huge gas processing equipment on the topside.

The subsea CO_2 removal system must meet the above objectives, while subject to several constraints:

- Limited pressure ratio across the membrane is available.
- Compression of permeate stream becomes energy intensive and costly as the permeate pressure decreases.
- Compression required for recycle would be very costly and complex.
- Limited opportunity for gas pre-treatment (e.g., dew point control).

An important objective with the project has been to screen membrane systems that would be suitable for subsea processing conditions. The results from the compatibility tests showed that membranes B and C were found to be suitably robust for this application. However, this does not exclude membranes not tested in the COMPMEM project from being qualified for subsea service.

The CO_2 separation tests of membrane B and C have demonstrated suitable performance within the expected operating window for a subsea system. This means that it should be possible to design a membrane-based separation step as a part of a complete subsea separation system to carry out the steps described in this report. To verify this, a detailed assessment and design of the modules and subsea technology elements in the system is needed. Water handling is expected to be a critical topic, which entails mitigating formation of hydrates, minimizing water routed to the permeate side, and avoiding water and HC condensation on either side of the membrane.

The results from this project and the overall assessment support this concept of subsea CO_2 separation, compression, and reinjection as a technically feasible option for further development.

CCS Perspective

The sustainable aspect of the subsea CO_2 gas separation and reinjection concept is that most of the CO_2 injected into the oil reservoir for flooding (in the EOR case) will ultimately be stored in the reservoir. To obtain a qualified estimate of the total amount of CO_2 that will be stored in the reservoir

over the project lifetime, a mass balance of externally purchased CO_2, back produced and reinjected CO_2 must be prepared. This topic has not been the focus of the COMPMEM project. However, mass balances prepared for the preliminary subsea study estimated the degree of removal of CO_2 from the well stream to be in the range of 85% to 95%. These estimates are based on preliminary assessments of membrane performance before the membrane testing for this project.

Implicit to the subsea processing concept, the CO_2 that does not get removed from the associated gas and reinjected is produced with the gas and liquids routed to the surface facility. The need for further treatment of the gas, including dissolved gas removed from the oil in the oil stabilization process, will depend on the concentration of CO_2 in the HC gas and gas export requirements.

In previous studies the assumption has been made that the subsea processing modules can be utilized to inject CO_2 for permanent storage after the EOR phase. This enables more CO_2 to be stored over the project lifetime than the CO_2 that is emitted from the incremental oil produced.

This concept is a sustainable opportunity that combines incremental oil production to meet increased energy demand while permanently storing CO_2.

FUTURE WORK

A high priority for future work is to test membranes B and C at pilot scale using membrane modules that provide representative industrial design and size. The microscale testing, while indicative of expected performance at conditions expected in the subsea application, did not provide representative flow distribution and module performance. Such tests would provide a more robust basis for upscaling the performance and costs for the system.

Further testing to evaluate the impact of water in the feed gas stream is also important. For applications with H_2S-containing gas, further testing to verify compatibility and H_2S separation performance is needed. Further tests of relevant membrane systems for material compatibility must be done as a part of the technology qualification.

SUMMARY

Initial analyses of the subsea CO_2 gas separation and reinjection processing concept indicate that operating conditions for a membrane separation will lie outside the conventional operating window and qualified conditions for commercially available membranes.

Processing constraints imposed by the subsea environment (remote, low temperature, and need for simplicity) have dictated the need for performance tests covering the expected subsea operating conditions. The impact of H_2S and humidity in the inlet gas stream has also been tested.

The design of a subsea processing system must account for the fact that shutdowns and operational upsets will happen. During a shutdown, cooling by the cold ambient water will expose the membrane components to condensing liquids. The robustness of subsea components is an important part of the technical feasibility of such a concept since retrieval of subsea components is very costly. Accordingly, a part of the scope in the COMPMEM project has been to perform a comprehensive test program to verify the compatibility of the membrane systems by exposing the various membrane components to carbonic acid and a liquid hydrocarbon mixture. The membrane system may also be exposed to hydrate inhibitors that are introduced during a shutdown, so exposure tests were conducted with methanol and monoethylene glycol.

The performance (permeance and selectivity) of the various membrane materials varies considerably over the range of conditions in the subsea operational window. Since there are multiple process variables, performance tests were planned according to principles of statistically designed

experiments. Based on these results, empirical models were developed to describe the variations in performance metrics and to identify the relative importance of the various variables.

Four membranes have been tested in the program, labelled as A, B, C, and D. The tests of membrane A revealed that the membrane material is very susceptible towards exposure to water and the components used to glue the components together easily deteriorated by the exposure to acidic water.

Membrane D lost its integrity when exposed to acidic water and the hydrocarbon mixture. Hence, membranes A and D were excluded as applicable for the subsea processing concept. This doesn't exclude these membranes for other applications when proper pre-treatment can be applied.

Membrane B and C have both achieved good CO_2 separation performance, even at the extreme conditions. These membranes have quite different characteristics. Membrane B generally achieved a higher degree of selectivity, while membrane C delivered higher permeance. Both membranes show good robustness versus exposure to acidic water and liquid hydrocarbon mixtures used in the tests. These membranes are feasible candidates for this challenging subsea application, although extended performance and compatibility tests are needed to qualify these membranes for the subsea processing concept.

This preliminary assessment of membrane feasibility in subsea processing is based on the results from the laboratory scale tests. System requirements for mitigating or coping with abrasion from solid particles, for example, will be made in phase 2 of this project.

The project has further developed the subsea processing concept based on the membrane testing. This project did not focus on overall system qualification, but from the description of and TRL of the main subsea processing building blocks, processing units and systems, the subsea gas processing concept is feasible. The technology concept might accordingly unlock the potential for the sustainable exploitation of the huge oil reserves in offshore basins. The technology is also applicable to offshore gas fields with high sour gas content.

ACKNOWLEDGMENTS

The project is funded by the Norwegian CLIMIT programme and the industry partners Equinor, CCP4 Consortium, TotalEnergies, Pertamina, and Aker Solutions/Aker Carbon Capture. Sintef was a research partner in the project.

REFERENCES

1. US DOE (2010) *Carbon Dioxide Enhanced Oil Recovery,* https://www.netl.doe.gov/sites/default/files/netl-file/CO_2_EOR_Primer.pdf.
2. Holt, T., Lindeberg, E., Vassenden, F. and Wessel-Berg, D. (2004) "A large-scale infrastructure model for CO_2 disposal and EOR–Economic and capacity potential in the North Sea". Proceedings from *7th Int. Conf. on Greenhouse Gas Control*, 5-9 Sept., Vancouver.
3. Energy (2010, September 22). *regjeringen.* Retrieved from Global assets/OED-oktutvinning.pdf (regjeringen.no) [Note: in Norwegian].
4. Kuuskraa, V., Malone, T., & DiPietro, P. (2014, June 5). *US Department of Energy-NETL.* Retrieved from CO_2-EOR Offshore Resource Assessment: www.netl.doe.gov.
5. SCCS. (2015). *CO_2 Storage and Enhanced Recovery in the North Sea.* Edinburgh: University of Edinburgh, ISBN 978 - 0 -9927483-2-6.
6. Eide, L. I., *et al.* (2019) Enabling Large-Scale Carbon Capture, Utilisation, and Storage (CCUS) Using Offshore Carbon Dioxide (CO_2) Infrastructure Developments-A Review. *Energies* (**12**) *1945*, pp. 2-21.

7. OGCI, “PETROBRAS Applying carbon dioxide capture and EOR at scale in ultra-deep waters.” OGCI Member Case Study | Petrobras - Applying carbon capture and EOR at scale in ultra-deep waters case study.
8. Kawahara, Y., & Hatakeyama, A. (2016, October 5). *cslforum.org*. Retrieved July 08, 2021, from https://www.cslforum.org/cslf/sites/default/files/documents/tokyo2016/Kawahara-VietnamEORProject-Workshop-Session1-Tokyo1016.pdf.
9. Norwegian Ministry of Oil and Energy (2004). Økt utvinning på norsk kontinentalsokkel». En rapport fra utvinningsutvalget. 2004. Publikasjonskode: Y-0115 B.
10. SCCS (2014) Stewart, R., and Haszeldine, S., (2014*) Carbon Accounting for CO_2 Enhanced Oil Recovery.*
11. National Energy Technology Laboratory, *Quality Guidelines for Energy System Studies: Carbon Dioxide Transport and Storage Costs in NETL Studies*, U.S. Department of Energy, Pittsburgh, PA, 2019.
12. Shimokata, N. (2018), Petra Nova CCUS Project in USA, https://pronto-core-cdn.prontomarketing.com/2/wp-content/uploads/sites/837/2018/06/Noriaki-Shimokata-Petra-Nova-CCUS-Project-in-USA.pdf.
13. Melzer, S. L. (2012). Carbon Dioxide Enhanced Oil Recovery (CO_2 EOR): Factors Involved in Adding Carbon Capture, Utilization and Storage (CCUS) to Enhanced Oil Recovery. prepared for the National Enhanced Oil Recovery Initiative, Center for Climate and Energy Solutions.
14. Guvelioglu, G., *et al.* (2015), H_2S Removal from CO_2 by Distillation. Laurance Reid Gas Conditioning Conference.
15. Jarrell, P. *et al*. (2002) *Practical Aspects of CO_2 Flooding*. SPE Monograph Series.
16. Kohl, A. and Nielsen, R. (1997). *Gas Purification 5th Edition.* Gulf Publishing Company.
17. Echt, W. (2002). Hybrid Systems: Combining Technologies Leads to More Efficient Gas Conditioning. Laurence Reid Gas Conditioning Conference.
18. Goodyear, S., *et al.* (2011, July 19-21). Moving CO_2 EOR Offshore. SPE Enhanced Oil Recovery Conf, Kuala Lumpur. *SPE 144939*.
19. Salim, M. *et al.* (2012). Process Design Aspects for Taking CO_2 Enhanced Oil Recovery Offshore. SPE EOR Conf at Oil and Gas West Asia, *SPE 155527*.
20. Energy Institute. (2013). Research report*: Hazard Analysis for offshore Carbon Capture platforms and offshore pipelines.* Prepared by the Energy Institute (London).
21. Malone, T. *et al.* (2014). *CO_2-EOR Offshore Resource Assessment.* US Department of Energy, Report NETL/DOE 2014-1631.
22. CLIMIT. (n.d.). Retrieved June 2021, from http://www.climit.no/no/havbunnsanlegg-kan-åpne-for-økt-oljeutvinning-og-CO_2-håndtering-til-havs : https://climit.no/en/.
23. Nøkleby, P., *et al.* (2015). *International Patent No. WO/2016/108697.*
24. Scholes, C., Stevens, G.,and Kentish, S. (2012). Membrane gas separation applications in natural gas processing. *Fuel*, **96**(1).
25. Baker, R., and Lokhandwala, K. (2008). Natural gas processing with membranes: an overview. *Ind. Eng. Chem. Res.*, **47**(7), 2109-2121.
26. Kidnay,A., Parrish,W., and McCartney, D., (2020) *Fundamentals of Natural Gas Processing* 3rd Ed, CRC Press.
27. Dai, Z. *et al.* (2016), Recent advances in multi-layer composite polymeric membranes for CO_2 separation: A review. *Green Energy & Enviro.* **1**(2), 102-128.
28. Oyama, T. And Stagg-Williams (editors) (2011). *Inorganic Polymeric and Composite Membranes Structure, Functions and Other Correlations.* Membrance Science & Technology Book Series, Vol 14., Elsevier.
29. Nøkleby, P. H. (2020, June 4*). International Patent No. WO/2020/111949*.

30. *Offshore* (Sept 23, 2020), Åsgard subsea compressors deliver high availability. The Petroleum Group.
31. Aker, https://www.akersolutions.com/what-we-do/subsea-production-systems-and-lifecycle-services/subsea-pump-systems/.
32. Rencher, A. and Christensen, W. (2012). Methods of Multivariate Analysis, 3rd Edition. New York: John Wiley & Sons.
33. Box, G., Hunter, W., and Hunter, J. (1978). Statistics for Experimenters-An Introduction to Design, Data Analysis and Model Building. New York: John Wiley & Sons Inc.
34. Robeson, L.M. (1991). Correlation of separation factor versus permeability for polymeric membranes. J Membr Sci. 62(165).
35. CLIMIT: https://climit.no/en/project/mulighetsstudie-for-et-havbunnssystem-for-separasjon-og-reinjeksjon-av-CO2/.
36. Bingcheng Liu, Yishu Qiao, Qiang Li, Wenguang Jia and Ting Wang: "CO_2 separation from CO_2–EOR associated gas using hollow fiber membranes: A process design and simulation study". Journal of Natural Gas Science and Engineering 100 (2022) 104451.

Carbon Dioxide Capture for Storage in Deep Geological Formations, Volume 5
Karl F. Gerdes (Editor)
© 2022 BP. All rights reserved.

Chapter 20

CO_2 CAPTURE–KEY FINDINGS IN CCP4 AND FUTURE WORK

Raja Jadhav[1], Ibrahim Ali[2], Betty Pun[1], Paulo Prunzel[3]

[1]Chevron Technical Center, 100 Chevron Way, Richmond, CA, USA
[2]BP International, Chertsey Road, TW16 7BP, Sunbury-on-Thames, UK
[3]Petrobras Research Center, Avenida Horácio Macedo, 950, Rio de Janeiro, RJ, Brazil

ABSTRACT: The main conclusions from the various capture projects/studies in CCP4 are summarized here. In addition, potential research needs and areas for future work are discussed.

KEYWORDS: CO_2 capture; NGCC; SMR; hydrogen; gas treating; post-combustion; pre-combustion; oxy-combustion; solvents; membranes; adsorbents; techno-economic assessment (TEA)

MAIN LESSONS LEARNED

It has been widely recognized that CCS will be needed to reach the climate goals of the Paris Agreement [1]. Since the launch of the CCP4 program in 2015, there has been a flurry of activity in the area of CO_2 capture technology development. Novel technologies continue to be developed and new breakthrough technologies continue to be proposed and evaluated. Several commercial CCS projects at the scale of more than 1 million tonnes per year (TPY) of CO_2 capture rate have been developed, improving our understanding of CAPEX and OPEX requirements for large-scale CCS projects and providing real-world project experience. New commercial CCS projects continue to be proposed and developed around the world. To support these deployments, numerous front-end engineering design (FEED) studies have been completed in recent years for both conventional and novel capture technologies. Providers of commercial CO_2 capture technology also continue to optimize solvent formulations and develop novel process schemes to reduce the CAPEX and OPEX of capture technologies.

Notwithstanding the progress made in developing novel, lower-cost CO_2 capture technologies over the last two decades and the recent commercial deployments, the current cost of CCS for many industries is still higher than the carbon price in many regions. Projects supported in CCP4 have resulted in improved understanding of the economics of CO_2 capture technologies and progressed their technology readiness level (TRL) by supporting work at lab, bench, and pilot scale.

A considerable amount of effort in CCP4 was focused on assessing and developing post-combustion capture technologies, based on novel solvents, adsorbents, and membranes. These technologies have shown potential to have a lower cost of CO_2 avoided compared to the state-of-the-art capture technologies. However, it needs to be stressed that these novel technologies are still at a lower TRL, and much work needs to be done to progress their readiness and validate the anticipated cost savings.

Although the main focus in CCP4 was on large scale NGCC power plants, capture of CO_2 from smaller reciprocating engines was also evaluated in a study. For the smaller scale CO_2 sources, the costs of conventional solvent-based capture technologies are disproportionately higher, as the

economy of scale cannot be realized. For these smaller sources, the work in CCP4 has shown that modular capture technologies, such as the molten carbonate fuel cell (MCFC) or membranes could provide lower capture costs and could be an alternative to the conventional capture technologies.

Similar to CCP3, techno-economic studies in CCP4 confirmed that the capital cost of a capture plant is the dominant factor contributing to overall CO_2 avoided costs, especially for smaller-scale CO_2 sources. There is a need to develop capture technologies with simpler process schemes and modular equipment to reduce the capital investment. The regeneration energy demand is also an important economic metric; however, many of the technology providers currently offer capture technologies with >30% reduction in energy demand compared to conventional MEA-based process. In addition, due to the lower price of natural gas, especially in North America, regeneration energy demand (and OPEX) is not as important as the CAPEX in the overall economics of CCS.

In addition, techno-economic studies carried out in CCP4 highlighted that when a technology is deployed in a project setting, many engineering details and site-specific considerations will affect the specific process design. This results in sometimes significant deviations from the expected cost of carbon captured and avoided that are derived from standard scenarios such as those used in the technology evaluations in this book.

In the following section, key findings from the various projects in CCP4 are described briefly. More details have been provided in various chapters in this book. In addition, recommendations on the research needs and future work are provided. The projects supported in CCP4 included a wide range of capture technologies, encompassing three different scenarios – Oil Refinery, Post-combustion, and Natural Gas Treating.

OIL REFINERY SCENARIO

The third phase of the CO_2 Capture Project (CCP3) had identified CO_2 capture from steam methane reformer (SMR) hydrogen plants as one of the lowest cost CO_2 capture opportunities for oil refineries [2]. Therefore, the Oil Refinery Scenario in CCP4 focused on SMR, which can also be the single largest emitter of CO_2 in a typical refinery, compromising up to 40% of total refinery emissions. The CCP4 projects in this scenario consisted of lab/bench scale experimental studies as well as techno-economic assessments.

In a study carried out in collaboration with IEA Greenhouse Gas R&D program (IEAGHG), CCP4 performed a techno-economic assessment of CO_2 capture from various locations in an SMR plant:

- From the shifted syngas stream upstream of the hydrogen purification unit.
- From the tail-gas exiting the hydrogen purification unit.
- From the reformer furnace flue gas (which includes the purification unit tail gas).

Each of the three locations has its advantages and disadvantages. Capturing before the hydrogen purification unit has the advantage of a higher pressure (and CO_2 partial pressure) and consequently, more compact CO_2 capture equipment. However, CO_2 emissions from the reformer flue gases are not addressed. Hence, the total CO_2 capture rate is around 55%. Capturing from the reformer flue gases offers the opportunity to achieve a high rate of capture (90% or greater) but it entails handling a higher volumetric flow rate of gases due to the near-atmospheric pressure with higher demands for both CAPEX and OPEX. The IEAGHG study showed that an MDEA solvent-based process implemented upstream of the hydrogen purification unit had the lowest CO_2 avoided cost while an MEA solvent-based process implemented on the reformer flue gas had the highest cost of CO_2 avoided.

In the 3D-CAPS project, 3D-printing of hydrotalcite (HTC) sorbent for use in the sorption-enhanced water–gas shift (SEWGS) process was carried out. Relevant properties of the structured adsorbent necessary to obtain a significant productivity increase, as characterized by kg CO_2/m^3h, were defined.

Several structured hydrotalcite sorbents in the form of monoliths and foam structures were prepared by 3D-printing using DLP (digital light processing) for the first time. Experimental results showed that the printing and post-processing methods developed for the preparation of 3D-structured HTC sorbents did not negatively affect the CO_2 capture capacity of the material at the relevant SEWGS conditions. Overall, the combined results in the preparation of 3D-printed HTC and modelling of structured SEWGS indicated that a marked productivity increase compared to conventional packed beds was possible. Compared to a conventional packed bed, a structured adsorbent maintained a sharp breakthrough curve at higher flowrates and achieved more efficient regeneration in combination with lower pressure drop.

As part of the 3D-CAPS project, a preliminary techno-economic assessment of the SEWGS process for CO_2 capture from SMR plants was carried out. The configuration of the 3D-SEWGS process was optimized to achieve high productivity. Although this led to a lower CAPEX due to a more compact process, this approach significantly reduced the steam export (and electricity production) from the SMR unit. Based on the assumed capital cost savings in the 3D-SEWGS process, a 15% lower CO_2 avoided cost over that of an MDEA-based process was estimated. The SEWGS process also resulted in a higher CO_2 avoidance rate.

In another adsorption-based project in CCP4, a Metal Organic Framework (MOF)-based structured adsorbent deployed in a rotating bed to implement a rapid cycle TSA process was evaluated for CO_2 capture from the flue gas of a cement plant at a pilot scale of 1 tonne per day (TPD). The concentration of CO_2 in cement plant emissions is about 18-20 mol %, similar to modern SMR plants. The pilot project achieved steady state performance with high purity CO_2 product (> 95%) and met the key performance indicators (KPIs), including productivity and steam ratio.

CCP4 sponsored laboratory-scale development of a new type of membrane based on graphene oxide (GO) and an associated process for post-combustion CO_2 capture. The project included testing on synthetic NGCC and other flue gases; however, the novel membrane is expected to be even more advantageous for higher concentration flue gases. Therefore, as part of the project, a techno-economic assessment (TEA) of CO_2 capture from the flue gas of an SMR plant was carried out. The preliminary economic results, based on the assumed cost of the novel membranes, indicated that the levelized cost of hydrogen (LCOH) and CO_2 avoided cost of an SMR plant employing the GO-based membrane process were lower than that for a conventional MEA solvent-based process.

Research Needs and Future Work

Because SMRs are major contributors to a refinery's total CO_2 emissions and the CO_2 is found at higher pressures and/or concentrations, they will likely be the main targets for early deployment of CCS at refineries. In addition, the market for low-carbon intensity hydrogen for new uses such as fuel for transportation, heating, and power generation is expected to sharply increase in the coming years. Considering the lower carbon ambitions of many countries and specific strategies, hydrogen with reduced carbon footprint (or Blue H_2) is slated to be an increasingly important fuel source in the near future. Low-carbon hydrogen production is also attractive for the production of biofuels, which is being incorporated into many refinery operations.

Although the current costs of CO_2 avoided for hydrogen plants are the lowest of other operations at a refinery, these are still higher than the market price of carbon in many jurisdictions around the world. California might be a notable exception with the current high price of Low Carbon Fuel Standard (LCFS) credit. Thus, there is a need to further decrease the cost of CO_2 avoided for hydrogen plants, while also increasing the overall CO_2 avoidance rate. This would imply the need to capture of CO_2 from the reformer furnace, which is at atmospheric pressure. Adsorption, membrane, and cryogenic technologies offer a potential to reduce the costs compared to conventional solvent-based technologies because of their improved applicability for higher concentration CO_2 streams. In addition, considering

the space constraints in a refinery, modular technologies with smaller footprint will need to be developed.

In CCP3, CO_2 capture from refinery heaters & boilers (H&Bs) was evaluated in detail, including the option of pre-combustion capture by using low-carbon hydrogen fuel for H&Bs [2]. Although this particular CO_2 source in a refinery was not studied further in CCP4, production of low-carbon, low-cost hydrogen is an enabler for pre-combustion capture for H&Bs. There is a continuing research need to develop pilot/demo projects with hydrogen-fired H&Bs and assess an integrated process scheme with a large SMR or autothermal reformer (ATR) supplying low-carbon hydrogen fuel to the H&Bs.

POST-COMBUSTION SCENARIO

Work in CCP3 highlighted that post-combustion solvent-based capture technology offered the lowest CO_2 avoided cost for the applications considered in CCP3. Therefore, the work in CCP4 continued to further evaluate novel post-combustion capture technologies by implementing techno-economic assessments as well as lab, bench, and pilot studies. Although an array of applications with CO_2 concentration in the range of 4-20 vol% was considered, the focus in CCP4 was on the CO_2 capture from NGCC power plants.

Because of the low CO_2 concentration (~4 vol%) in the flue gas at atmospheric pressure, capture of CO_2 for NGCC power plants is not an easy application. Extensive studies in CCP2 [3] and CCP3 [2] concluded that post-combustion capture from NGCC power plants was a better alternative than pre-combustion capture, where low-carbon hydrogen is used as a fuel in NGCC power plants. CCP4 focused on further reducing the cost of CO_2 capture from the flue gas of NGCC power plants by conducting techno-economic assessments (TEA) of several novel technologies as well as supporting development of solvent-based capture technologies at bench and pilot scales.

A consistent TEA comparison of novel technologies that included molten carbonate fuel cell (MCFC), membrane, pressurized CO_2 absorption, and supersonic anti-sublimation concluded that MCFC technology integrated with NGCC power plant would have the lowest CO_2 avoided costs. Another TEA study in collaboration with Mitsubishi Heavy Industries (MHI) was also carried out to estimate the cost of CO_2 avoided for a state-of-the-art solvent-based capture technology, which can be used as a benchmark to compare the performance of novel capture technologies.

In another study, a techno-economic assessment of chemical and physical solvents, including ionic liquids (ILs) and two new proprietary solvents, was carried out. Performance of solvents was compared using a reduced order modelling technique with partial optimization of process parameters for each solvent and cost estimation of equipment. The ILs that were screened showed higher capture cost compared to 30 wt-% aq. MEA. It was determined that reducing viscosity while maintaining high CO_2 solubility was key in developing new ILs that were more cost effective.

CCP4 supported development of two novel solvent-based technologies at the pilot scale: a non-amine solvent from C-Capture and concentrated piperazine (PZ) solvent from the University of Texas. Results from the C-Capture pilot work demonstrated the main benefits of the non-amine solvent: low solvent degradation, and no emissions of nitrogen-based degradation products commonly seen with amines. It was also learned that a better understanding of the absorption mechanism and precise kinetic rates were required to design an appropriate CO_2 absorber and to achieve performance targets. Pilot testing of PZ solvent with an Advanced Stripper (PZAS) at 4% CO_2 concentration showed that the PZ provided excellent absorption with faster kinetics than MEA, required as low as 2.3 GJ/tonne of regeneration duty, emitted < 1 ppmv of PZ in the flue gas, and potentially enabled the use of carbon steel as a material of construction in parts of the plant.

Research Needs and Future Work

Even with the ever-increasing contribution from renewable energy to the power grid, reliable and low-carbon power generation from NGCC power plants will remain an important contributor to the power supply for a long time.

With continued improvement, conventional post-combustion capture technologies will be the best option in the near- to mid-term for NGCC power plants. As concluded in CCP3, work should continue identifying and supporting the development of novel solvents, adsorbents/adsorption cycles, and membranes. For solvents, the focus should be on reducing the CAPEX, by developing novel solvents that are resistant to SOx and NOx, and are non-corrosive to eliminate the need for expensive materials of construction. Although energy use for solvent regeneration has come down from the MEA-based benchmark, lower energy solvents are still of interest to reduce OPEX. Adsorbents and membranes offer an advantage as potentially being modular and lower-cost, and potentially lower energy use than solvents; however, current technologies struggle economically at lower CO_2 concentrations. Thus, there is a need for development of novel adsorbents and membranes that can handle low CO_2 concentration streams effectively. Novel process schemes, such as exhaust gas recycle (EGR) or selective EGR (e.g., using membranes) should be further evaluated and demonstrated to increase the CO_2 concentration in the flue gas, which can reduce the CO_2 capture costs of solvent-based technologies and potentially enable application of adsorbent- and membrane- based capture technologies.

In the long-term, pre-combustion capture on NGCC can be a viable option, although the cost of low-carbon hydrogen will need to come down further. Many of the original equipment manufacturers (OEMs) of gas turbines are currently developing or certifying machines that can burn up to 100% hydrogen fuel. There is a research need to demonstrate these hydrogen-fired technologies for larger gas turbines, while keeping the NOx levels in the exhaust gas at low levels.

In addition to the post- and pre-combustion capture technologies, technologies based on novel power cycles can be a viable option. An example is the oxy-combustion technology based on Allam cycle, which is currently being developed as a new-built option to produce power at a higher efficiency while capturing the CO_2 [4].

Although the focus in CCP4 was on larger NGCC power plants, smaller gas turbines and cogeneration plants are widely used in refineries and upstream oil production operations to provide power and steam. Because of their smaller size, the per tonne avoided cost of CO_2 is high compared to the larger NGCC power plants. There is a need to develop modular and lower-cost capture technologies that are applicable for CO_2 emission rate in the range of 100-1,000 tonnes per day (TPD).

NATURAL GAS TREATING SCENARIO

In CCP4, a new scenario was added to support the development of technologies for offshore removal of CO_2 from natural gas during its production. Two projects were carried out – evaluation of current state-of-the-art and emerging technologies for removal of CO_2; and an experimental program to qualify membranes for subsea removal of CO_2 from offshore natural gas production.

To understand technology development needs for CO_2 removal, a detailed evaluation study of current state-of-the-art and emerging technologies for removal of CO_2 was carried out. The study concluded that membrane technology was a leading, established technology for offshore natural gas/ CO_2 separation applications, whereas chemical solvent was prohibitively expensive at high CO_2 feed concentrations. Of the emerging technologies evaluated, a novel gas-liquid contactor utilizing hollow fibre membranes for solvent scrubbing was the most promising, based on the assessment that this technology would be a good candidate for applications where weight and space constraints imposed

high costs, particularly with lower CO_2-content feed streams and/or lower limits for CO_2 in product natural gas that are not suitable for a membrane-only approach.

In a joint industry project, validation of the concept of using membrane for CO_2 separation on the sea floor was carried out. Several membranes were evaluated at lab scale at the conditions relevant to subsea gas separation – within a broad range of temperature, pressure and CO_2 content in the feed gas. The compatibility of the polymeric membrane and potting materials with exposure to acidic water, hydrocarbon condensate, methanol, monoethylene glycol and H_2S was also tested. Based on the results of the experimental programs, two membranes were qualified for further testing at a pilot scale.

Research Needs and Future Work

With respect to CO_2 removal from natural gas, membrane separation technology can be considered as benchmark with chemical absorption competitive in low-CO_2-content natural gas streams. Nevertheless, research efforts aim to improve performance of the membranes with a higher methane recovery factor, a lower pressure drop on the retentate side and better stability. New materials like ceramics or advanced polymers may address these issues. Novel gas-liquid contactors combining absorption and membrane technologies could offer performance advantages, and developments in this area should be monitored.

Removing CO_2 from natural gas in a subsea environment offers huge challenges like performance and compatibility of membrane materials in the presence of liquids and hydrate prevention chemicals. On the other hand, this technology may allow debottlenecking in brownfield scenarios such as increasing oil and gas production where topsides improvements are constricted. Membranes from different manufacturers may differ in performance (permeance and selectivity). This can be challenging when considering subsea environment but also offers an opportunity to combine different performance characteristics in a two-stage membrane separation process. This alternative should be investigated in future work.

REFERENCES

1. Al Amer, N., *CCS in the latest IPCC report "Mitigation of Climate Change,"* Global CCS Institute, April 2022.
2. Gerdes, K. (Ed.), (2015) *Carbon Dioxide Capture for Storage in Deep Geologic Formations – Results from the CO_2 Capture Project, Vol.4 - CCS Technology Development and Demonstration Results (2009-2014)*, CPL Press, UK.
3. Eide, L.I. (editor), (2009) *Carbon Dioxide Capture for Storage in Deep Geologic Formations – Results from the CO_2 Capture Project, Vol 3 Advances in CO2 Capture and Storage Technology - Results (2004-2009)*; ISBN 0-08-044570-5, CPL Press, UK.
4. Baker Hughes press release, "Baker Hughes partners with NET Power to Advance Development and Global Deployment of Zero-Emissions Power Plants," Feb 22, 2022.

Carbon Dioxide Capture for Storage in Deep Geological Formations, Volume 5
Karl F. Gerdes (Editor)
© 2022 BP. All rights reserved.

Chapter 21

CO_2 STORAGE, MONITORING & VERIFICATION IN CCP4 INTRODUCTION & OVERVIEW

Scott Imbus
Chevron CCP SMV Team Lead 2003-19, Houston TX

ABSTRACT: The CCP4 Storage Monitoring and Verification program (CCP4-SMV) developed and executed a portfolio of projects aimed at closing technical gaps and providing reassurance to stakeholders that a range of real, but unlikely, untoward scenarios can be detected and mitigated. The technical development portfolio tended towards early to mid-phases of technology maturity, but the team identified opportunities to apply several technologies to realistic settings such as the meso-scale (underground lab) or field scale (third party pilots and demonstrations).

INTRODUCTION

The CO_2 Capture Project (CCP) was established in 2000 by eight international energy companies along with co-funding from the US, EU, and Norwegian governments to deliver major cost reduction for capture and demonstrate that geological storage is safe, measurable, and verifiable. From the start, there was the opportunity to leverage the century-old experience of the oil and gas industry in exploration and production. Over the four phases of CCP, the SMV program has developed and managed a portfolio of projects that address key gaps in CO_2 storage reliability and assurance while seeking opportunities for synergistic operations and cost reduction.

In CCP phase 4, the focus of the SMV program was to demonstrate the viability of monitoring tools in the field and to develop robust leakage detection, characterization, and if needed, intervention protocols. The latter was pioneered late in Phase 3. Projects across the range of technical development stages (TDS) were maintained to balance risk and reward. The program has largely maintained its general themes: “Assurance”, “Surveillance”, “Optimization”, and “Risk Assessment”, which evolved to include “Field Trialing” and “Contingencies”. In the present chapter, individual project work, organized by themes, is outlined in terms of purpose, methods, findings, and implications. Implications for the broader “CCUS World” and its techno-economic prospects as a key GHG mitigation contributor are outlined in Chapter 34.

OVERVIEW

Subsurface Assurance

The CCP4 Subsurface Assurance theme aimed at understanding risks associated with brownfield oil and gas reservoir and facilities redevelopment for CO_2 storage.

A coupled reservoir (flow) and geomechanical simulation parametric study by Nassir and Walters (Chapter 22) aimed to assess impacts of past oil development phases on containment integrity for a prospective future CO_2 injection, first for EOR and then for permanent storage. For the Pembina Oil Field (central Alberta) clastic Cardium formation it was shown that future operational safety factors could be maintained by taking into account prior cumulative stresses (in this case the “initial state” is

after primary and secondary production and notably, a calibration with a recent CO_2 injection pilot) and avoiding exceedances of key geomechanical constraints in the operational model. Among the parameters tested are Young's modulus, off-planar leakage factor, curvature of relative permeability curve (water versus CO_2) and for the top seal specifically, effective cohesion. The modelling indicates that a 15% increase in the injection unit's magnitude of minimum total stress endangers caprock sealing performance by impacting the stress contrast between the reservoir and caprock. An operational focus on minimizing this stress contrast while achieving required injectivity would therefore be critical should the Pembina Cardium formation become a storage target.

In Chapter 23, Zhang *et al.* developed a scenario for detecting and locating leaking CO_2 coincident with an injected plume intersecting degraded plugged and abandoned (P&A) wells. "Early and deep" indications of leakage are few and may be too subtle to detect. "Shallow and later" indications are more likely to be detected but after significant damage to a water resource or surface amenity may have occurred. Detection limits for given volume/saturations at various depths using electromagnetic (EM) or seismic are fairly straightforward, but a resolution level that localizes the plume (particularly its origin and path) would require their joint inversion and would still rely on some reasonable models of well versus aquifer/aquitard geometry. Nevertheless, such attempts would be essential to design and deploy an intervention attempt and should be carried as a pre-injection contingency.

Contingencies

CCP pioneered the concept of "contingencies" (untoward event detection, characterization, and intervention) as an additional confidence builder for CO_2 storage late in the CCP3 program (~2013). Related studies have progressed from early parametric simulations to bench experimental scale and semi-field scale (see also Mont Terri studies below) in CCP4.

In Chapter 24, Moneke *et al.* investigate permeability modification approaches to CO_2 leakage remediation, seal enhancement and flood conformance. Simulations conducted with experimental calibration of a silica gel agent were used to assess the efficacy of sealant injection as a preventative (in cases where seal integrity is marginal) or to intervene in an active leakage case. More generally, such sealants could be applied to conformance control to optimize storage capacity (based on well-established EOR sweep techniques). Reservoir-condition micromodel (P and T) and coreflood experiments (using acetic acid as a proxy for CO_2 pH reduction) showed two orders of magnitude (2 OM) reduction in permeability. Applying calibrated data to a reservoir simulation model of a fracture sealing case showed a three orders of magnitude permeability reduction. Successful application of permeability modifiers in the field would rely on properly assessing the specifics of reservoir permeability distribution, fluid chemistry, and operating parameters.

Although injected or displaced fluid migration through natural systems could be very difficult to detect and mitigate and potentially highly impactful, such events are expected to be very rare. Fluid migration through well systems, in contrast, are more common and in principle, considerably easier to detect and mitigate, and mostly avoidable if proper plug and abandonment (P&A) procedures were completed. CCP4 engaged in development of the "SMART" Tool (Suncor Micro-Annulus Remediation Tool), a novel alternative approach to well P&A, designed to target an operation subject to well leakage that is loosely analogous to CCUS–Canadian oil sands steam assisted gravity drainage, SAGD. The study is not included in this volume but is available through the Society of Petroleum Engineers (SPE-201253-MS). The tool was designed to expand radially against the casing, resulting in mechanically closing micro-annuli and thus, fluid flow through damaged or missing cement. Bench scale tests using the casing-cement formulation used in typical SAGD wells did not reduce behind casing flow as much as expected. The problem may be more complicated than initially anticipated (e.g., influence of geometries of micro-annuli and the placement, in terms of position and extent in the well, of the tool).

Optimization

Critical to launching safe, effective, and economic storage projects is a focus on design and operation optimization whether it's maximizing storage capacity (effectively controlled by conformance and pressure) or jointly conducted with EOR to realize a return. CCP4 conducted modelling studies using a range of field and operational designs and history-matched to a large, well-monitored EOR operation.

Chapter 25 (Hosseini *et al.*) used the Cranfield Oil Field in Mississippi (USA) to demonstrate that CO_2 EOR is *de facto* storage of CO_2. The Cranfield oil field was the subject of a large CO_2 EOR pilot conducted with considerable surveillance data. An opportunity was presented to apply a reservoir simulation to quantify the type and extent of CO_2 trapping mechanisms for several different modes of EOR (continuous gas injection, water-alternating-gas or WAG, gas curtain and combinations thereof). Simulations showed that operational methods have a profound effect on CO_2 utilization (each with variances in the proportion of specific storage mechanisms) and thus the desired balance between CO_2 disposal and oil recovery. WAG (most widely used today) provides the best balance between storage and recovery.

In Chapter 26, Godec outlines the start-up/early operations experience of pilots, demonstrations, and commercial projects. Such projects have generated a wealth of data that could be used to learn from incidents or inefficiencies. Underestimating geological complexities (via characterization) was a key reason for project setbacks or unexpected results. Unanticipated variances between predicted and actual performance can be compensated for by more intense operational monitoring early, while there is still time to change operational parameters to avoid more serious problems. The most serious instance entailed abandoning the injection reservoir for an alternative one due to excessive pressure build up in an under-characterized reservoir.

Godec and Williams conducted an analysis of the anticipated cost reduction from FOAK ("First of a kind") towards NOAK ("Nth of a kind") in Chapter 27. Cases considered included storage only (saline), EOR and conversion (EOR to storage). Costs of CO_2 storage, like any other technology, are expected to go down with increasing experience, including better characterization and operational planning and monitoring. Since the lead time is long for a storage project, changes in stakeholder expectations or technology evolution/integration should be a consideration. Three representative storage cases in different settings are assessed for how FOAK to NOAK might change. In the analysis, capital costs were dominated by wells and operational costs by seismic surveys. Substantially limiting these costs by other means (better characterization, optimizing injection capacity, alternative operational surveillance, and management techniques) would considerably improve economic viability of all three types of project cases, with some local variations.

Surveillance & Field Trials

CCP4-SMV participated in two distinct experiments at the Mont Terri Underground Laboratory (MT-UGL) 300m deep in the Jura Mountains of NE Switzerland. This locale affords an opportunity to test natural and induced phenomena in a controlled setting at the meso-scale (here, the depth and dimensions lie between laboratory-bench and reservoir scale).

Mont Terri Scale Well (CS-A)

CCP4 installed a scale well (~14m length) that was used to test the performance of novel sealants in mitigating fluid flow through deliberately induced damage to the well (particularly micro-laminae between the casing and cement sheath or fracturing within the cement sheath). The well was plumbed to allow injection and sampling of fluids and instrumented to monitor pressure isolation and temperature.

Goodman *et al.* (Chapter 28) outline the construction, testing, and operations of the Mont Terri CS-A well, which were aimed at testing the efficacy of novel sealants to mitigate induced defects. Initial problems with cementing and heat cycling (to induce damage) complicated the experiment and there were difficult-to-interpret pressure and chemical data from each of the injections (and expectedly the cumulative effects thereof) but through selective repeat injections and tests, the relative performance of each sealant was adequately characterized. The sealant results:

- **Smart-gel (Los Alamos National Lab)–**This is a hydrogel that massively expands upon encountering a low pH-triggering environment such as would be expected in a subsurface system that experienced CO_2 injection. The sealant succeeded in reducing interval permeability soon after injection, although some degradation of sealant utility was noted at higher pressure differential (up to 35 bar), perhaps due to the high permeability of the original pathway and thus higher volume injection needed. The test was considered a success.
- **Polymer (University of Texas)–**This is a polyacrylic acid that polymerizes upon encountering higher pH. Such a situation might be expected where carbonic acid is altering well cement. The sealant successfully reduced permeability up to the pressure differential at which the smart-gel sealant (above) showed signs of breaking down. Sealing appears durable at a lower pressure differential for the period monitored (~3 months). There is indication that silica oil present in the well system may have impacted the sealant's effectiveness. It is unclear if this would be impactful in settings where hydrocarbon oil is present.
- **Silicate gel solution (IFP-Energies Nouvelles)–**Once preparation errors were overcome, the sealant was shown to be effective up to the established test pressure differential. With time, however, sealing capability declined, probably because of the well-known syneresis phenomenon associated with silica gel curing (i.e., accelerated dewatering in the high pH cement environment).
- **Polymer-based nano-sealant (University of New Mexico)–**After initially plugging injection lines in one interval, the sealant was successfully injected into a second where it showed immediate sealing function. A noticeable decrease in sealing capacity was noted after a week, however, which was attributed to shrinkage during hardening (with possible debonding).

In Chapter 29, Goodman *et al.* detail and interpret observations from the exhumed portions of the post-experimental well, thus lending further insight into well damage types, sealant performance, and explanations for hydrogeologic testing observations. The original plan was to overcore and remove the completion, cement, and some of the formation. In the end, two lateral bore holes were drilled to intersect and sample the test well. Although only two of the sealant-exposed intervals were encountered in the well sampling, the most prevalent type of induced defects seen was micro-annulus formation between the cement and host rock. Possible mechanisms include shrinkage during cement curing or artifacts of thermal cycling or hydraulic testing pressure testing. There is no indication of induced damage during the over-coring process. Detected sealant remnants appeared to be confined to the highest permeability channels.

In Chapter 30, Zhang *et al.* link available data from the mesoscale CS-A experiment and new bench-scale cement bond characterization to develop a finite element analysis (FEA) model to explain the origin of well defects. Observation from a previously over-cored Mont Terri well (CS) and experimental observations indicate (1) shear failure of the casing/cement interface from excessive wellbore pressure and (2) tensile failure at the cement/rock interface due to shrinkage during cement curing. This information, combined with the new laboratory tests of cements and their bonding, was used to calibrate the FEA model to be applicable at a well depth of 1000m (as opposed to 300m deep

at MT-UGL). From this, it is inferred that the geometry of the injection system and cement sheath influence cement degradation and that increased temperature during cement curing reduces shrinkage and thus cement/rock tensile failure.

Mont Terri Fault Slip Experiment (FS-B)

CCP4 was a primary designer and sponsor of this complex experiment, which aimed to test at the meso-scale possible impacts of injection-induced faulting on the seal integrity of a CO_2 storage project.

Guglielmi *et al.* detail the aims, results, and implications of the FS-B experiment in Chapter 31. Multiple, constant rate water injections into a fault zone were monitored by three wells equipped with sensors for pore pressure, displacement, and seismic response. Fault slip and its seismic and fluid migration response were documented. Among the observations:

- The response was complex and varied by distance and hydraulic connectivity to the fault system–this fault deformation complexity was reflected in the fluid leakage patterns. The response was described as a "rupture" front preceding a "fluid pressure" front.
- After the induced pressure was released, there were indications of instantaneous decrease in p-wave velocity with injection pressure and hysteretic effects in p-wave travel times.
- There were overall indications that significant leakage can occur in full scale analog cap rocks. More detailed analysis may help to develop a predictive capability of magnitude/pattern of deformation and fluid migration.
- The observed p-wave hysteresis may be useful in determining restoration of integrity to sealing system post mitigation.

The experiment is a critical link between simulations and real systems at scale in qualifying the risk to CO_2 storage integrity due to top-seal fault slip.

Aquistore

Aquistore is a "commercial" scale, relatively deep (~3km) saline storage project in Saskatchewan that benefited from extensive characterization and operational surveillance. CCP saw the opportunity soon after Aquistore's first major injection period to test novel surveillance sensors and take advantage of baseline and ongoing project monitoring. Two techniques that CCP deployed were time lapse borehole gravity (BHG) logging and borehole to surface electromagnetics (BSEM).

In Chapter 32, Niel *et al.* outline the theory and abbreviated field results of the Aquistore BHG program. The CCP4 team had identified BHG logging as potentially capable of detection of density changes due to fluid replacement of brine with CO_2. Successful deployment would introduce a potentially cost-effective tool for repeat monitoring of CO_2 injection. Forward modelling showed the potential for threshold detection at Aquistore relative to the mass of CO_2 injected. A field deployment was launched in late 2019, but equipment failures (namely lack of instrumental temperature stability) required abandonment of the survey without useful data acquisition. Repairs were attempted, but funding ceased before a second deployment could take place. The chapter therefore focuses on the numerical model for detection at given thresholds and the potential for complementing 3D seismic data. This model shows that the CO_2 fluid saturation replacement expected at the given injection volume/rate should be detectable at ~0.5km from the leading edge of the plume. BHG determinations could reduce uncertainty in seismic models (presumably by constraining density assumptions). While not ready for field application (at this depth) at the time of the first attempt, the potential resolution of BHG and its promise to enhance the more expensive repeat seismic interpretations should encourage continued development and testing.

In Chapter 33, Belliveau *et al.* outline the limitations on repeat EM surveys at Aquistore. BSEM (Borehole to Surface EM) forward modelling showed potential for plume detection and resolution using various configurations and subsurface physics and conductivity models. No pre-injection baseline was available, but a survey after two years of injection was carried out in 2019. It was evident that this single survey could not detect, much less resolve the plume, primarily due to natural near surface water saturation variations and error introduced by slight variation in positioning of sensors from one survey to its repeat. A repeated attempt is unlikely to be successful due to lack of permanent sensor locations and unknown variations in near surface conductivity profiles (e.g., seasonal or post rainfall).

SUMMARY & CONCLUSIONS

Please refer to Chapter 34 Key Findings, Conclusions & Recommendations for a perspective on the significance of the CCP4-SMV program results in context of CCUS assurance and cost at the scale needed.

Carbon Dioxide Capture for Storage in Deep Geological Formations, Volume 5
Karl F. Gerdes (Editor)
© 2022 BP. All rights reserved.

Chapter 22

OPERATIONAL AND PARAMETRIC ANALYSIS OF THE LONG-TERM CO_2 INJECTION INTO PEMBINA OIL FIELD

Mohammad Nassir and Dale Walters
CGG Geo-consulting Calgary, AB, Canada

ABSTRACT: A coupled reservoir and geomechanics study was completed to evaluate the geomechanical effects of the full operational history of a selected EOR well pattern on CO_2 storage in the Pembina Cardium zone. The modelled operational history and loading/unloading of the Cardium sand provided the starting point to model long-term CCS forecasts to investigate the dynamically induced fracture length and the long-term integrity of the caprock for various ranges of flow and stress models' parameters. The study demonstrates the significance of the Cardium sand Young's modulus, the off-planar leak-off factor, the curvature of the relative permeability curves, the initial stress in the Cardium sand and the caprock effective cohesion on both the induced fracture length and a safe, leakage-free CO_2 sequestration process.

KEYWORDS: cardium, geomechanics, reservoir, caprock integrity, dynamic fracture, sensitivity analysis

INTRODUCTION

The Pembina oil field is located near the town of Drayton Valley, west of Edmonton. The oil field is extensive, covering an area of about 140,000 km^2 (140 townships) and is composed of several producing zones from Devonian to Tertiary in age, with the Upper Cretaceous Cardium Formation being by far the most prolific. The four reservoir units comprising the Cardium Formation reach a maximum cumulative thickness of about 20 m and occur at depths ranging from 1600 m in the northeast to 1650 m in the southwest of the pilot site area. The upper sandstone is the most productive reservoir and CO_2 was injected into this unit to enhance the oil recovery as well as for carbon storage. At the injection site each of the sandstone units is 3 m thick and the intervening shale units are 1 m (between the upper and middle sandstone units) and 5 m (between the middle and lower sandstones) in thickness. The geological study indicates average core porosity and permeability range from 8% and 31 md in the conglomerate to 16% and 21 md in the middle and upper sandstone units, respectively [1]. Permeability may exceed 1000 md in individual beds of the conglomerate. Average permeability in the lower sandstone is 10 md, half that of the upper and middle sandstone units. The history matching in this study based on the field data and the previous experiences regarding the Cardium formation suggest that the Cardium sand and the conglomerate permeabilities should be smaller in magnitudes than what is shown in the geological report. The reservoir temperature is 50°C and current pressure of the water-flooded reservoir is approximately 19 MPa, similar to the original reservoir pressure of 18 to 19 MPa.

The objectives of the scope of work were to evaluate the geomechanical effects of the full operational history of a typical clastic (sandstone/shale) oil reservoir subjected to primary, secondary and EOR processes, and specifically, the effects related to CCS or EOR- CO_2 opportunities and their impact on the seal integrity of that reservoir. This modelling of the operational history and loading/unloading of the Cardium sand was then followed by modelling long-term CCS forecasts to investigate the long-term integrity of the caprock and the risk of leakage.

The study focused on a typical disposal zone (Pembina Cardium) appropriate for CCS (depth > 800 m, T > 30ºC), (Figure 1) such that the CO_2 is miscible with the oil, in a dense liquid phase. The Cardium is a prolific zone and has been operated with waterflooding at pressures higher than the CO_2 miscible pressure. Composite models based on good quality public data were constructed to investigate the caprock integrity during the historical operations and followed by long-term CCS.

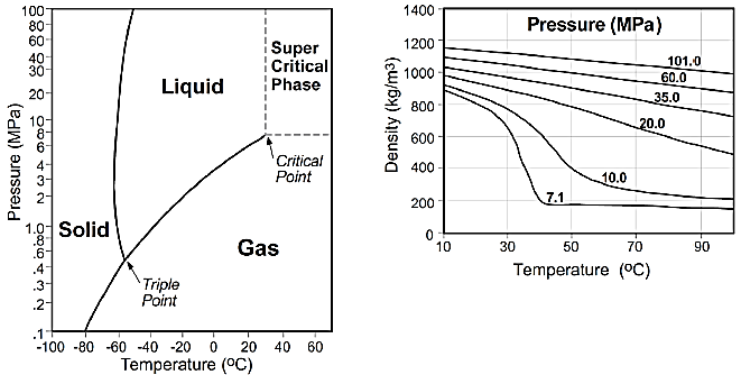

(a) (b)

Figure 1. Relevant CO_2 characteristics (a) phase diagram (b) density variations.

RESERVOIR & GEOMECHANICAL COUPLING METHOD

The geomechanical modelling completed in this study used a commercially available coupled reservoir/geomechanics simulator called GEOSIM™. GEOSIM™ is a modular software system combining a 3D, 3-phase thermal reservoir simulator with a general 3D finite element stress-strain simulator.

The GEOSIM™ model uses two grid systems, one for the flow solution (reservoir simulator TRS) and another for the finite element (FEM) stress solution (finite element code FEM3D). In this study an identical Cartesian grid is used for both geomechanical and reservoir models. A generic picture showing the typical set-up of the two grid systems is shown in Figure 2. For all grid modifications such as extension, lumping, cutting a window and refinement, the CGG Taurus proprietary software called CPG-GRID-MODIF is used in this project.

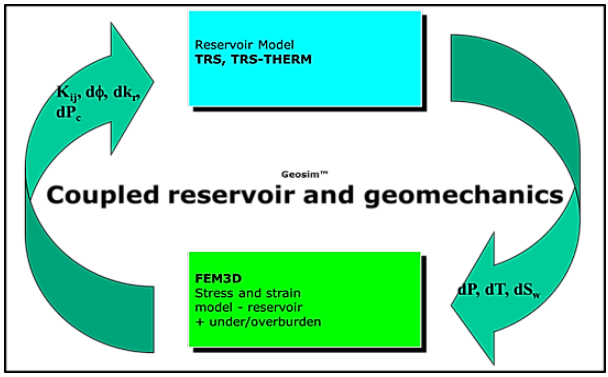

Figure 2. A generic picture showing the typical set-up of the two grid systems [2].

An explicit coupling method was employed in this study to couple flow and geomechanics. Pressure and temperature variations resulting from the flow solution are passed to the geomechanical and fracture module to calculate the variations in stress and displacements and the fracture initiation and propagation in order to update the coupling parameter, which in this study is permeability. The updated permeability is used in the subsequent time step according to the "explicit" coupling technique. The simulation timestep is controlled by the reservoir module; the dynamic fracture propagation and sudden permeability enhancement of the fractured blocks result in relatively small timesteps to ascertain the controlling norms of fluid flow solution (i.e., PNORM and SNORM) are honored. These types of models have been practiced extensively by CGG-Taurus for various geomechanical simulations of compaction drive reservoirs, CO_2 injection, waterflood and PWRI fracturing, tight gas fracturing [3, 4, 5, 6].

Dynamic Fracture Propagation Modelling

The fracturing option in GEOSIM™ simulates either a stationary or dynamic hydraulic fracture. Dynamic tensile (for rigorous length and height growth) and shear fracture propagations (volumetric growth) are modelled by a newly implemented robust method, the so called "pseudo-continuum" approach. The fracture is combined with the grid blocks by an averaging technique ("pseudo-continuum") where the non-linear Barton-Bandis material model is used to describe the relatively larger nonlinear deformation in the fractured block. The blocks are initially assumed to be non-fractured linear elastic material and are switched to pseudo-continuum fractured block as soon as the following tensile fracturing criterion is met:

$$S'_{min} < \textit{Tensile strength of the rock.} \quad (1)$$

Within the simulator, a cubic function is used to accurately calculate the induced fracture permeability and the subsequent change in the fractured block transmissibility as a function of the fracture width obtained from geomechanical calculations.

The Barton-Bandis hyperbolic model describing the stress strain behavior of a single fracture is shown in Figure 3.

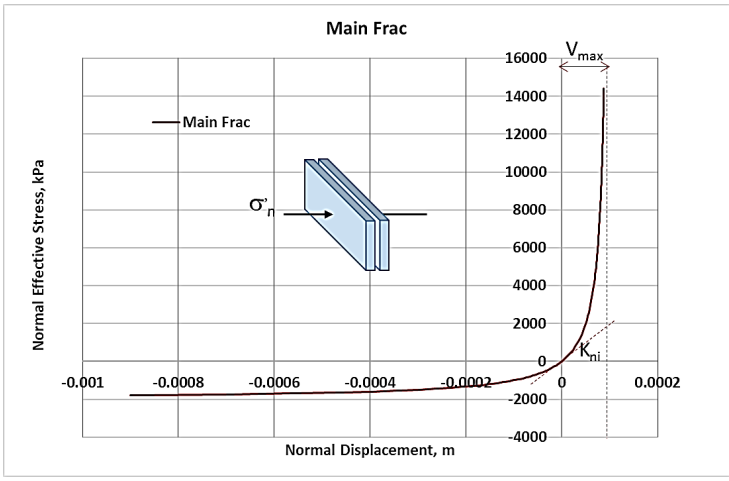

Figure 3. Stress-displacement behavior of the fracture used in the simulation model.

The stiffness of the fracture approaches zero when the confining normal effective stress goes into tension, in contrast to infinite stiffness when the fracture is subjected to a large normal effective stress, which represents a closed fracture. The hyperbolic model describing the stress-displacement of the fracture is:

$$\sigma_n' = \frac{k_{ni}\Delta v}{1-\frac{\Delta v}{\Delta v_{max}}} \quad and \quad k_n = \frac{d\sigma_n'}{d\Delta v} = \frac{k_{ni}}{\left(1-\frac{\Delta v}{\Delta v_{max}}\right)^2} = k_{ni}\left[1-\frac{\sigma_n'}{\Delta v_{max}k_{ni}+\sigma_n'}\right]^{-2} \tag{2}$$

where Δv_{max} is the maximum fracture closure from zero effective stress and k_{ni} is the fracture stiffness at zero effective stress as shown in Figure 3.

The "pseudo-continuum" approach used in GEOSIM numerically embeds the discrete fracture in the block containing the fracture. The overall Young's modulus (a measure of the stiffness of a material) of a fractured block is calculated by the following equation:

$$\frac{1}{E_{avg}} = \frac{1}{E} + \frac{1}{S_f K_n} \tag{3}$$

where E is the intact rock Young's modulus, S_f is the block width and K_n is the fracture stiffness, the slope of the hyperbolic curve at a certain normal effective stress.

The shear fracture modeling in GEOSIM uses the approach based on Mohr Coulomb shear failure criterion where stress level is calculated following Equation 4. Changes in stress level are due to changes in effective stress, which is computed by the coupled reservoir model.

$$Stress\ level = \frac{(\sigma'_{max}-\sigma'_{min})}{(\sigma'_{max}-\sigma'_{min})|_{failure}} \tag{4}$$

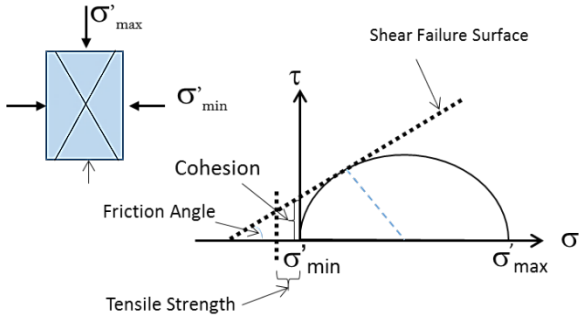

Figure 4. Shear fracturing mechanism in Mohr-Coulomb diagram.

A stress level of one and above indicates shear fracturing. Assuming Mohr-Coulomb shear failure criterion at a certain σ'_3, the σ'_1 should reach the following magnitude until the block fails in shear:

$$\sigma_1' \geq \sigma_3' + \frac{2c\cos\phi + 2\sigma_3' \sin\phi}{1-\sin\phi} \tag{5}$$

The angle of internal friction, or friction angle (ϕ), is an intrinsic property of the material. As soon as a certain block fails in shear, hypothetical shear fractures are embedded in the block based on minimum and maximum principal stress directions as shown in Figure 4. The Young's modulus of the fractured block will be a function of the normal effective stress acting on the hypothetical fracture plane, and the Young's modulus of the equivalent block is calculated using Eq. (3).

The contribution of a single fracture set to the total fractured block permeability tensor, $\overline{\overline{K}}_{f,ij}$, is calculated from the following equation [16]:

$$\overline{\overline{K}}_{f,ij} = \frac{\eta}{S_{fs}} \frac{w_f^3}{12} \left(\delta_{ij} - n_i n_j\right) \tag{6}$$

where n is the unit normal vector of the fracture set and δ_{ij} is the Kronecker delta (δ_{ij} = 1 for i=j and δ_{ij} = 0, i≠j). S_{fs} is the fracture spacing, w_f is the fracture width, and η is the permeability correction factor due to tortuosity. The total fractured block permeability tensor, $\overline{\overline{K}}$, is a combination of the intact block and the induced fracture permeabilities:

$$\overline{\overline{K}} = \overline{\overline{K}}_{blk} + \overline{\overline{K}}_{f,ij} \tag{7}$$

DATA REVIEW, ANALYSIS AND MODEL BUILDING

The first step of the project was to review and analyze the existing data, and to build the required coupled models for the fracturing study. In this section, the data are reviewed, analyzed and the base model construction is summarized.

The Reservoir Model for History Match

The original PennWest Waterflooding reservoir model was shifted to the northeast by Δx= 569 m and Δy= 230 m so that the model would exactly overlay the well pattern used for the CO_2 pilot study. Figure 5 shows the original PennWest Waterflooding reservoir model (red solid line diamond), the new shifted section (red dashed line diamond) and the generated model in GEOSIM for history matching from 1962 and 2005.

The grid system from the PennWest model was extended vertically from top and bottom in the coupled reservoir and geomechanics analysis. However, no extension in the sides was needed for the model since there were repeated well patterns during the primary production and the waterflooding from 1962 and 2005. Laterally fixed boundary conditions were assumed to honour the repeated patterns.

Figure 5 also presents a vertical (X-Z) cross-section as well as the grid extension above and below the original reservoir model. In total, 8 layers were used to construct the coupled model for the history matching period–6 reservoir layers plus an overburden and an underburden layer. The main goal is to obtain the stress hysteresis in the reservoir layers where the fluid pressure variation is substantial. Overburden and underburden are very tight and impermeable such that their stress magnitudes are barely influenced by the reservoir pressure changes during the history matching period, but the slight change predicted is also taken into consideration.

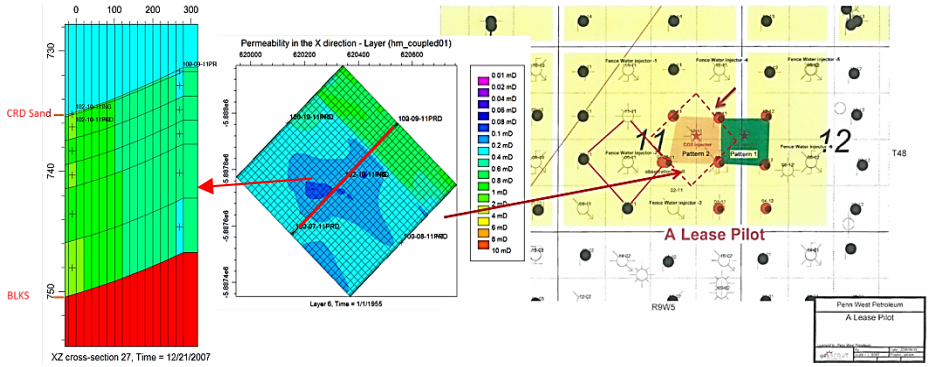

Figure 5. The original PennWest Waterflooding reservoir model (red solid diamond), the new selected section (red dashed diamond) and a SW-NE vertical cross-section built for history matching from 1962 and 2005.

The Reservoir Model for CO_2 Pilot Injection from 2005 to 2016

In the CO_2 Pilot EOR period the model was substantially extended in the lateral directions as shown in Figure 6. The model accounts for both CO_2 injectors (102-10-11ING & and 102-12-12ING) and all the producers. The layering in the model is assumed to be the same as used in the waterflooding history match model, as explained in the previous section, except one more layer was added to both the overburden and the underburden. The primary production and waterflooding history match output results were used to initialize the CO_2 Pilot reservoir model. Average layer properties were used for the lateral extended grid blocks.

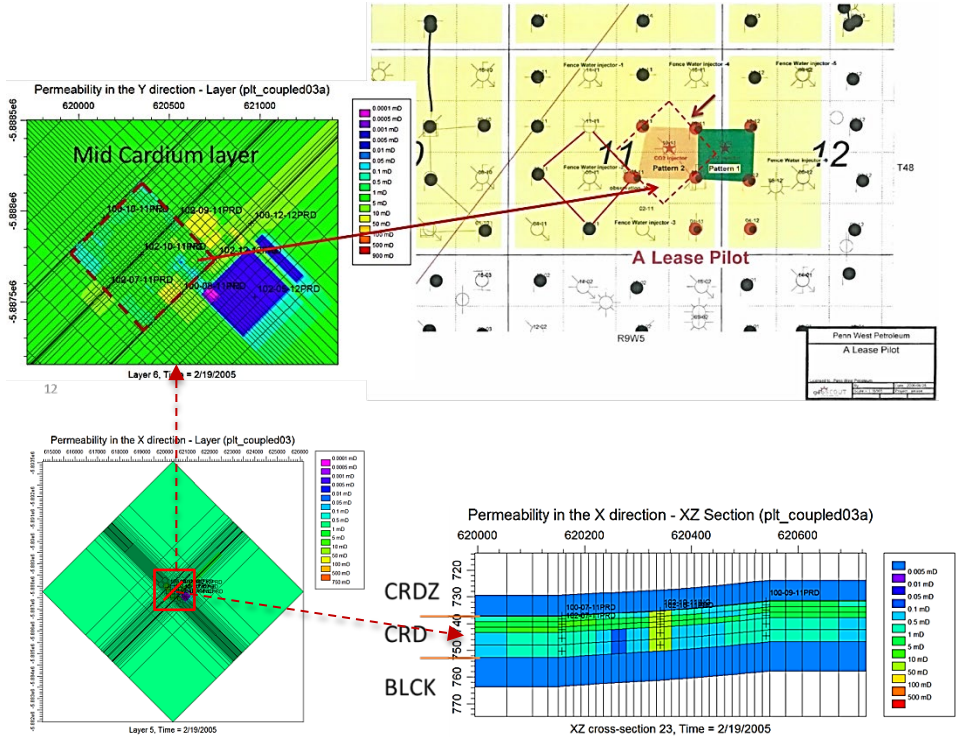

Figure 6. The original PennWest Waterflooding reservoir model (red solid diamond), the new extended section, and a SW-NE vertical cross-section built for CO2 Pilot history matching from 2005 and 2016.

The Reservoir Model for Forecast

To alleviate the long run-time required for a full coupled reservoir and geomechanical model, horizontal symmetry was assumed and a quarter model from the pilot phase was extracted for the whole range of sensitivity analysis as shown in Figure 7. Using a quarter of the model enabled refining the reservoir and the caprock grids to obtain a better resolution for the dynamic fracture propagation and a more accurate analysis of the caprock integrity. The forecast model contains 19 layers, 7 in overburden, 9 in reservoir and 3 in underburden as shown in Figure 7. The quarter of symmetry assumption inherits lack of considering the rock heterogeneities in other quarters which is a drawback of this simplification.

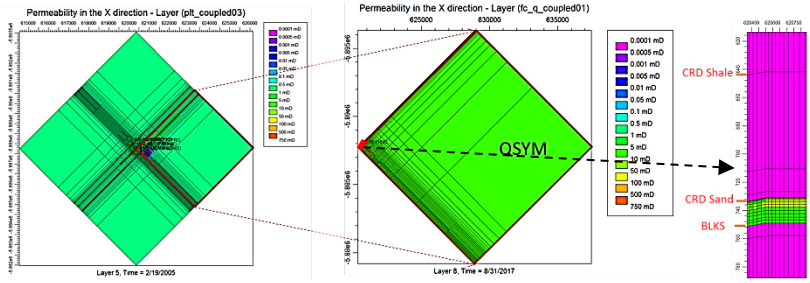

Figure 7. Quarter of symmetry model used for forecast sensitivity analysis and the respective x-z cross-section.

The Reservoir Model Input Data

The porosity, permeability and net-to-gross data are imported from the ECLIPSE industry reference reservoir model developed for the original field analysis. However, to better match the model to field data during the CO_2 EOR Pilot period, local modification of the permeability data was necessary. There is virtually a channel between 102-12-12ING and 102-05-12PRD in the conglomerate, based on the observation that almost all of the CO_2 injected into 102-12-12ING (12.5 MM m^3) was produced from the 102-05-12PRD well (cumulative gas production = 13.3 MM m^3).

Small water and oil productions from 102-05-12PRD indicate that there is an impermeable Cardium layer under the conglomerate around this well, which causes gas override. It also demonstrates limited vertical connection between the conglomerate and Cardium formations, since all the gas injected into the 102-12-12ING can easily flow towards 102-05-12PRD, but the water injected into 102-12-12ING does not impact 102-05-12PRD (It appears the conglomerate has poor injectivity to water compared to gas or CO_2, which is typical of water damage effects in waterflood operations). Low cumulative gas production (no gas breakthrough) and high water production in wells 102-07-11PRD, and 102-09-11PRD indicate fracture growth and containment in the Cardium sand layers.

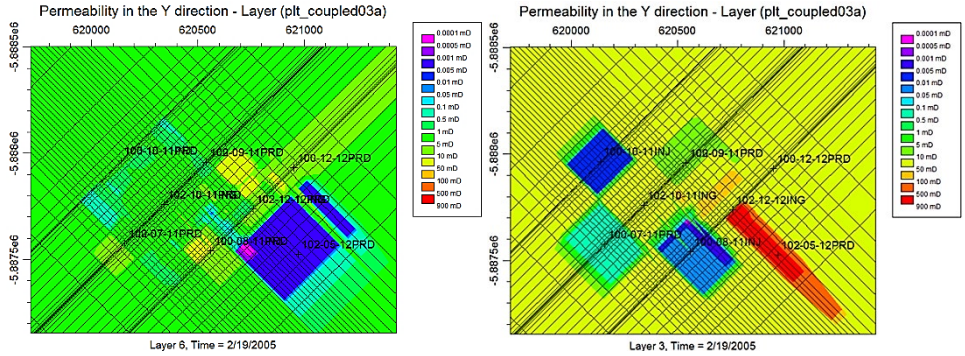

Figure 8. Permeability maps used to obtain history match during the Pilot CO_2 EOR process; left the mid Cardium sand and the right the conglomerate layer.

The available swelling test data [10] was used to tune the black-oil PVT data for pressures above 17 MPa, the first entry pressure data in the swelling test. The Vasquez and Beggs correlation [7] was used for predicting the oil formation volume factor and solution gas oil ratio input. We assumed that only CO_2 will be dissolved in the reservoir oil at this pressure and above during the CO_2 injection, so the gas phase composition is treated as pure CO_2, which simplifies the modelling. Figure 9 summarizes the tuned pvt table used to account for CO_2 swelling effects.

P	Rs	Bo	Eg	Vo	Vg
KPa	g/o	rb/STB	STB/rb	cp	cp
100	0	1.01	1	3	0.01
1379	6.58	1.0434	12.4	2.298	0.01196
2050.7	10.62	1.0526	18.71	2.0452	0.01208
2722.5	14.94	1.0625	25.19	1.8365	0.01221
3394.3	19.49	1.0732	31.86	1.664	0.01236
4066.1	24.22	1.0845	38.71	1.5201	0.01253
4737.9	29.12	1.0964	45.74	1.3989	0.01271
5409.7	34.17	1.1088	52.95	1.2957	0.01291
6081.5	39.34	1.1217	60.34	1.207	0.01314
6753.3	44.64	1.135	67.9	1.13	0.01337
7425.1	50.04	1.1488	75.61	1.0626	0.01363
8096.9	55.55	1.1631	83.48	1.0032	0.01391
8768.7	61.14	1.1777	91.47	0.9505	0.0142
9440.5	66.83	1.1927	99.58	0.9034	0.01452
10112.3	72.6	1.2082	107.77	0.861	0.01486
10784.1	78.45	1.2239	116.02	0.8228	0.01521
11455.9	84.38	1.2401	124.31	0.788	0.01558
12127.7	90.37	1.2566	132.6	0.7564	0.01597
12799.5	96.44	1.2734	140.86	0.7274	0.01638
13471.3	102.57	1.2905	149.06	0.7007	0.0168
14059.5	107.99	1.3058	156.16	0.6741	0.01718
14814.9	113.41	1.321	163.93	0.65	0.01757
15486.7	118.83	1.3363	169.49	0.625	0.01795
16158.5	124.25	1.3516	175.44	0.605	0.01833
16830.3	129.67	1.3668	181.82	0.585	0.01871
17502.1	150.6309	1.406013	186.92	0.553455	0.01909
18000	166.1659	1.435075	192.31	0.530075	0.01947
18845.7	204.71	1.522997	198.02	0.486419	0.01985
19517.5	235.3284	1.59284	204.08	0.451759	0.02023
20189.3	265.9467	1.662683	209.42	0.41706	0.02061
20861.1	296.5651	1.732526	215.05	0.38238	0.021
21532.9	322.0515	1.785065	220.99	0.368329	0.02138
22204.7	347.538	1.837605	227.27	0.354277	0.02176
22876.5	373.0245	1.890144	233.92	0.340226	0.02214
23548.2	398.5072	1.942675	239.52	0.326176	0.02252
24220	423.9937	1.995214	245.4	0.312125	0.0229
24891.8	449.4802	2.047754	251.57	0.298073	0.02328
25563.6	474.9667	2.100293	258.06	0.284022	0.02366
26235.4	497.5327	2.138079	264.9	0.27879	0.02404
26907.2	520.0987	2.175865	270.27	0.273558	0.02442
27579	542.6647	2.213651	275.86	0.268326	0.02481
28250.8	565.2307	2.251437	281.69	0.263094	0.02519
28922.6	587.7967	2.289224	287.77	0.257862	0.02557
29594.4	610.3627	2.32701	291.97	0.252629	0.02595
30266.2	632.9287	2.364796	296.3	0.247397	0.02633
30938	655.4947	2.402582	300.75	0.242165	0.02671
31609.8	678.0607	2.440368	305.34	0.236933	0.02709
32281.6	700.6266	2.478154	310.08	0.231701	0.02747

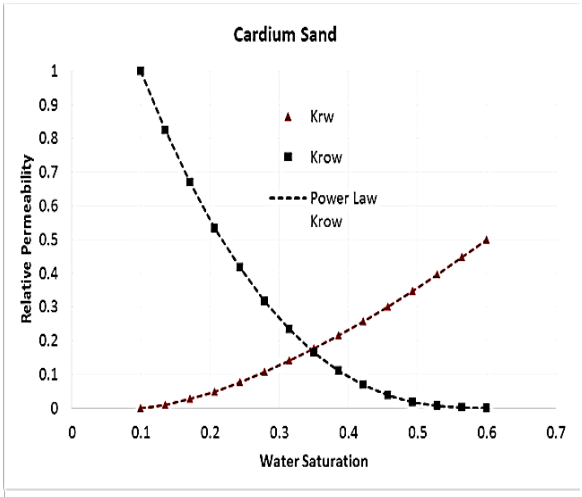

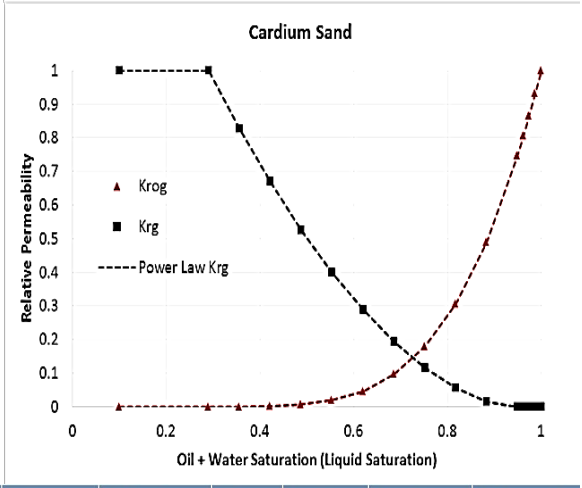

Oil Density	Gas Density, kg/m3	Water Density, kg/m3	Oil Compressibility, 1/kPa	Water Compressibility, 1/kPa	Oil Viscosity pressure variance above Pb, cp/kPa	Water Viscosity, cp	Inj water Viscosity, cp	Formation compressibility, 1/kPa	Ref Pressure, kPa
824.26	0.7	1000	2E-7	4.24E-7	2E-5	0.45	1	4.44E-06	18000

Figure 9. PVT, relative permeability, and other input data used in the CO_2 pilot EOR model [8].

The default end points in the relative permeability tables were S_{WC}=0.1, S_{OR}=0.4, S_{LOC}=0.29; but were modified to S_{WC}=0.2, S_{GC}=0.14, and RPOSWC = 0.86 (Oil Relative Permeability @ Swc) to obtain a reasonable match with the field data from the Pilot CO_2 injection period [10].

The Geomechanical Model Input Data: Initial Stress

The geomechanical grid used for the history matching and the forecast periods was the same as that used for the reservoir models. Figure 10 presents the results of the stress initiation analysis for the well 102/09-11-048-09W5/0. To initialize the model stress, the P and S velocities were used to calculate the dynamic Young's moduli and Poisson's ratios. The existing geomechanical laboratory data were used to obtain the static-to-dynamic stress ratios (0.2 for both Cardium sand and shale). Minifrac data from the Cardium shale zone was used to estimate the necessary tectonic and glacial loads such that the log-interpreted stress matches the minifrac result. Top depths of various formations including Lea Park, Colorado (CLRD), Cardium Group Shale (CRDZ), Cardium Sand (CRDM) and Blackstone (BLCK) were also available. The log interpreted stresses indicate a stress barrier may exist above and below the upper Cardium sand providing contained vertical fracture growth if the injection pressure exceeds the fracturing pressure. The calibrated stress log used an applied tectonic strain in the x direction of 0.002 and a glacial loading effect of 15 MPa with hysteresis in the Poisson's ratio factor of 0.95. The above parameters describing the tectonic and glacial loads are the results of minimum stress calibration against the known caprock (Cardium Shale) minimum horizontal stress. The intermediate stress was not calibrated against field data such as borehole breakouts; the failure criteria used in this study require minimum and maximum stress terms. The gamma ray shows relatively clean sand at the top of the upper Cardium sand which may represent the conglomerate sand (Figure 11).

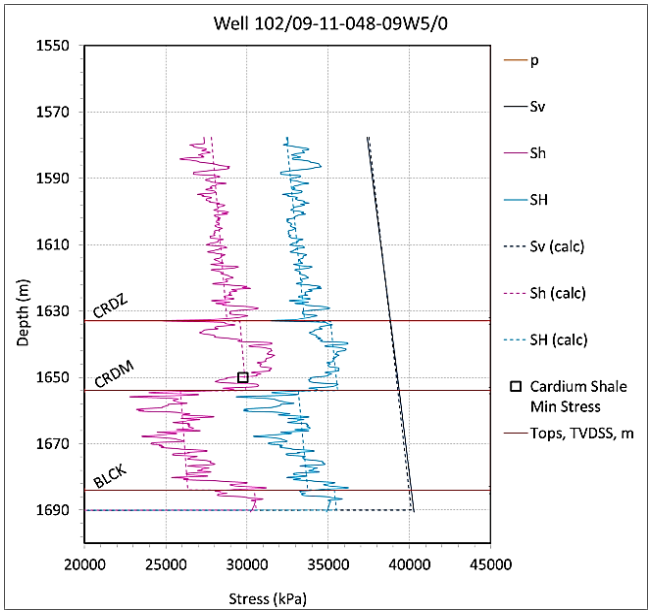

Figure 10. Stress initialization results from available data of the well 102/09-11-048-09W5/0.

A significant drop in Poisson's ratio is seen at the Cardium shale and Cardium sand interface as shown in Figure 11. Based on the final report of Pembina Cardium CO_2 Monitoring Pilot Project, the average minimum horizontal stress gradient in the PennWest field is 18.5 kPa/m in the caprock [9]. Based on this study and the reported mini-frac test result [11], the caprock fracture gradient was assumed to be around 18.5 kPa/m as shown in Figure 10 under the "Cardium Shale Min Stress" legend. Table 1 contains the stress gradients used for various formations in this simulation study.

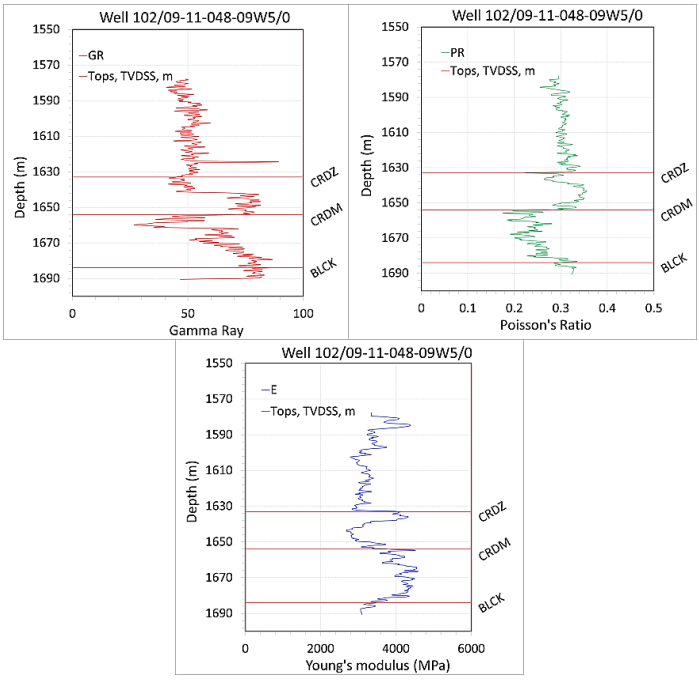

Figure 11. Gama ray, static Young's modulus and Poisson ratio from well 102/09-11-048-09W5/0 log analysis.

Table 1. Summary of the calculated initial stress gradients based on the well 102/09-11-048-09W5/0.

Formation		Tops, TVDSS, m	Bottom, m	γ_{Sh}, kPa/m	γ_{SH}, kPa/m	γ_{SV}, kPa/m
Lea Park	LPRK	1319	1490	18	19	24.3
Colorado Shale	CLRD	1490	1633	18	21	24.3
Cardium Shale	CRDZ	1633	1654	18.5	22	24.3
Cardium Sand	CRDM	1654	1684	16	20.5	24.3
Blackstone	BLCK	1684	1690	18.5	21.5	24.3

The Geomechanical Model Input Data: Constitutive Models

Data from two full geomechanical lab test programs were available for the reservoir and caprock materials, both conducted at the University of Alberta [11, 12]. The second program was conducted on core from a well from the pilot study area. The core samples were from the Cardium shale, Lea

Park shale, and Middle and Lower Cardium sandstone. These laboratory tests were used to calibrate nonlinear elastic (NLE) material models and shear strength envelopes as shown in Figure 12. For the initial history matching between 1962 and 2005, these NLE constitutive models were used to represent the material behaviour in loading and unloading (accounting for hysteresis effects on the induced stress state). However, for the detailed modelling focused on the CO_2 Pilot history match and the sensitivity analysis conducted for CCS forecasts, equivalent linear elastic materials were assumed for Cardium shale and Cardium sand in order to improve numerical efficiency of the sensitivity analysis

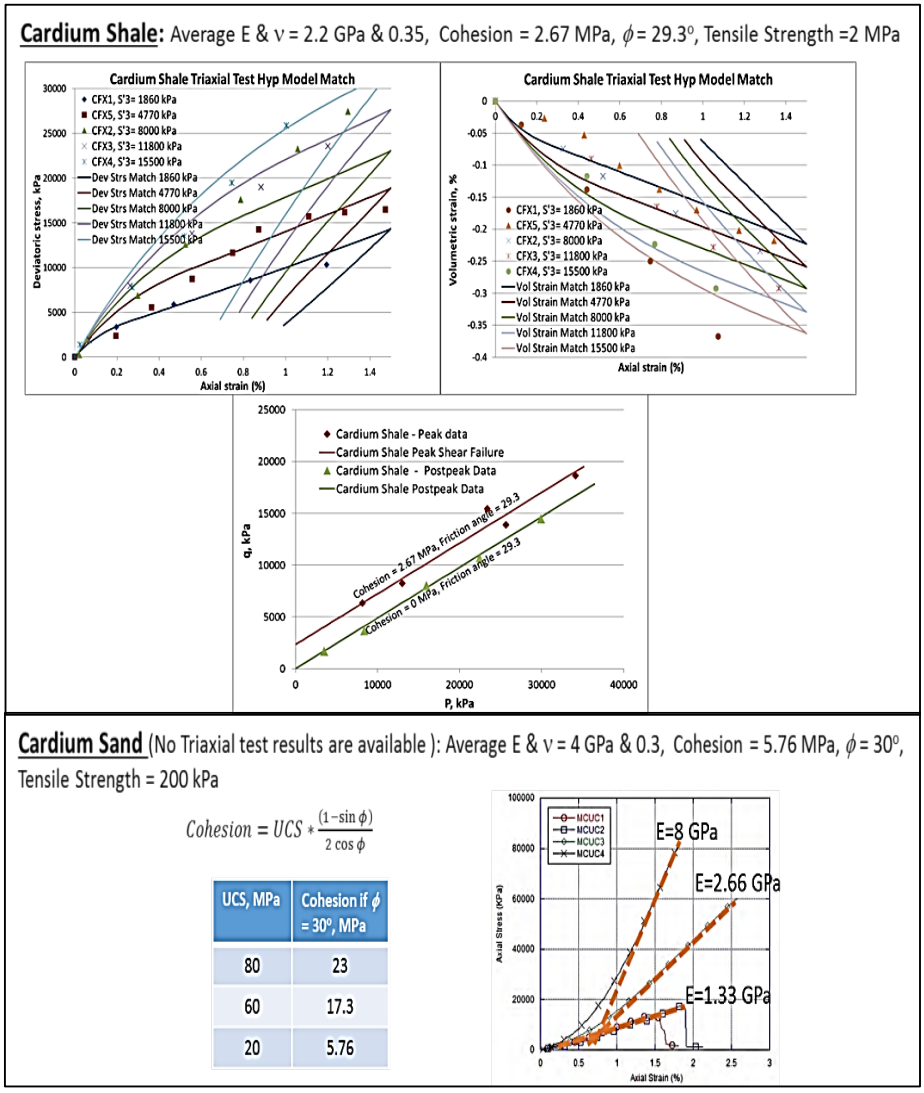

Figure 12. Average linear elastic material properties for Cardium shale and Cardium sand, data from [10, 11].

and allow the use of the highly non-linear (and more rigorous) fracture model to dynamically propagate during the injection periods. Figure 12 illustrates the NLE material models that were calibrated to the lab data and the plots used to find the equivalent linear elastic material properties for the Cardium shale and sand. For Cardium sand the highest E (E = 8 GPa) obtained from the UCS tests was used to represent this material, since in real reservoir conditions, the Cardium sand is confined under a much higher stress magnitude than the atmospheric used in the UCS test and therefore the upper bound of the E from the UCS results would be a more realistic selection.

Dynamic propagation of fracture follows the principals described in the theoretical section of this chapter. For the main tensile fracture, the calibrated maximum fracture closure is 1e-4 m, the fracture initial stiffness is 2e7 kPa/m and the fracture spacing is 0.05 m, the same as the width of blocks containing the fracture. The respective values for the shear fracture propagation in the Cardium shale and sand are 4e-5 m, 1e7 kPa/m and 0.2 m.

HISTORY MATCHING RESULTS

Figure 13 shows the history match results for the primary production and waterflooding from 1962 to 2005. The lack of wellhead pressure data for various wells was a major problem in this study; however, as a basis for the study, the typical operating practice for this field was followed, which is to operate producer wells pumped off and the injector wells at the fracturing pressure if possible. The permeability maps in the PennWest ECLIPSE model were relatively high in magnitude, and already reduced by 0.25 in the simulation input file. The history match required a multiplier of 0.08 for the Cardium sands permeability and an average permeability of 14 md for the conglomerate layer. Figure 14 also shows the history matching results for the individual wells in the pattern modelled.

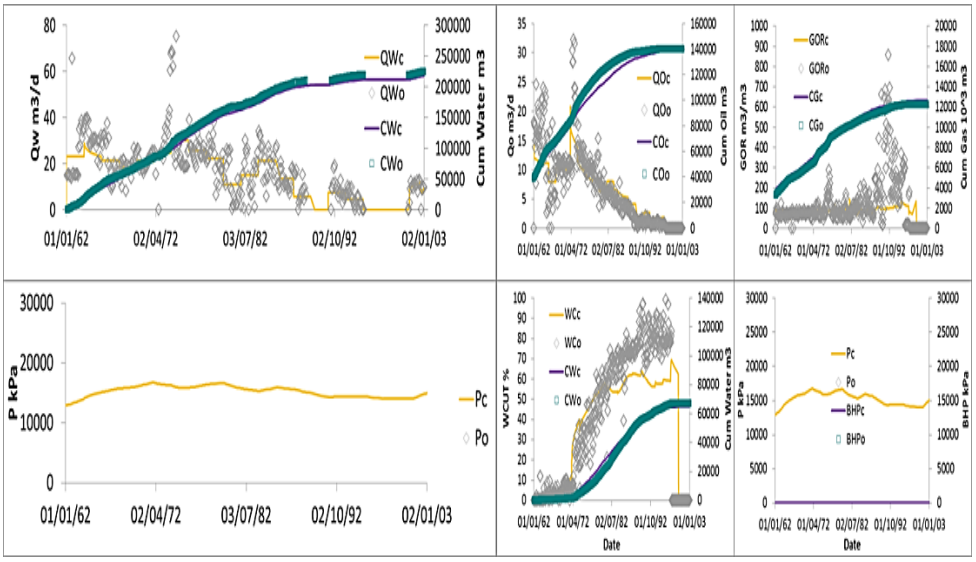

Figure 13. History match results for field injections and productions from 1962 to 2005.

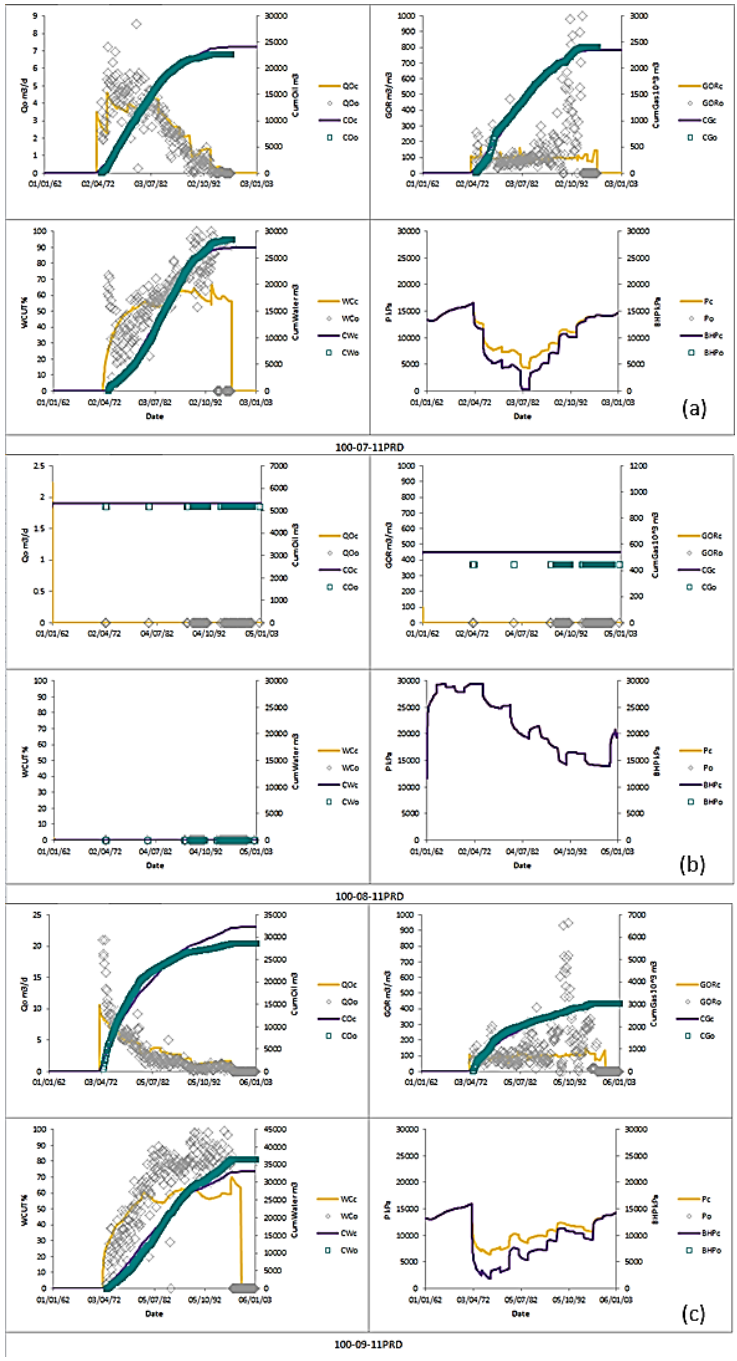

Figure 14 (a,b,c). History math results for 1962-2005.

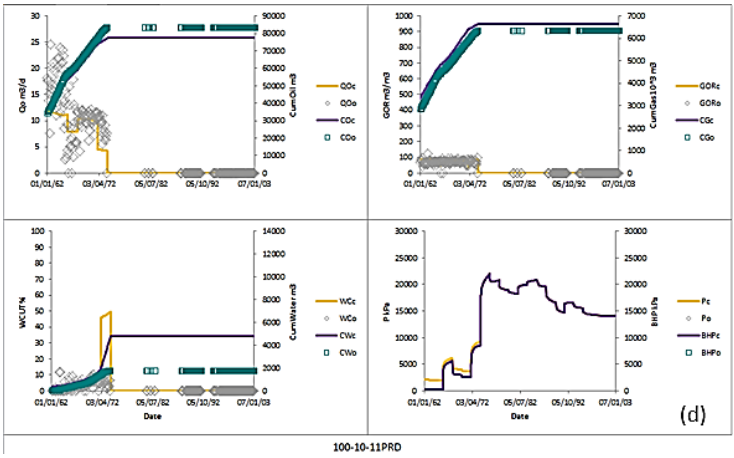

Figure 14 (d). History match results for different injections and productions from 1962 to 2005.

Figure 15 plots the history matching results for the CO_2 EOR period from 2005 to 2016. A reasonable match was obtained for the overall field injection operations and production. To match the individual well field data, some local modifications of permeability were implemented, but in general the reservoir and fluid properties obtained from earlier history matching were used. The permeability modifications are shown in "The Reservoir Model Input Data" section. Figure 16 indicates the maximum fracture growth during the CO_2/water injections into the injectors of 102-10-11ING/W and 102-12-12ING/W. The total stress build-up due to long time injection periods in the well 102-10-11ING/W causes the fracture to open more at the top and bottom of the Cardium sand as shown in the figure. On the other hand, the fracture opening in the 102-12-12ING/W is more like conventional fracture opening, with the maximum in the middle Cardium sand, due to the fact that a non-permeable zone exists south of the fracture. Furthermore, the initial stress in the conglomerate is as high as in the caprock, such that the fracture barely protrudes into the conglomerate layer. All history match modifications described above were retained when attempting to match the injection and production processes between the two 102-12-12ING/W and 102-05-12PROD as explained in "The Reservoir Model Input Data" section. The pressure distribution around 102-12-12ING/W shown in Figure 17 confirms the low permeable zone in the Cardium sand (below the induced fracture plane) despite the high permeability channel in the conglomerate.

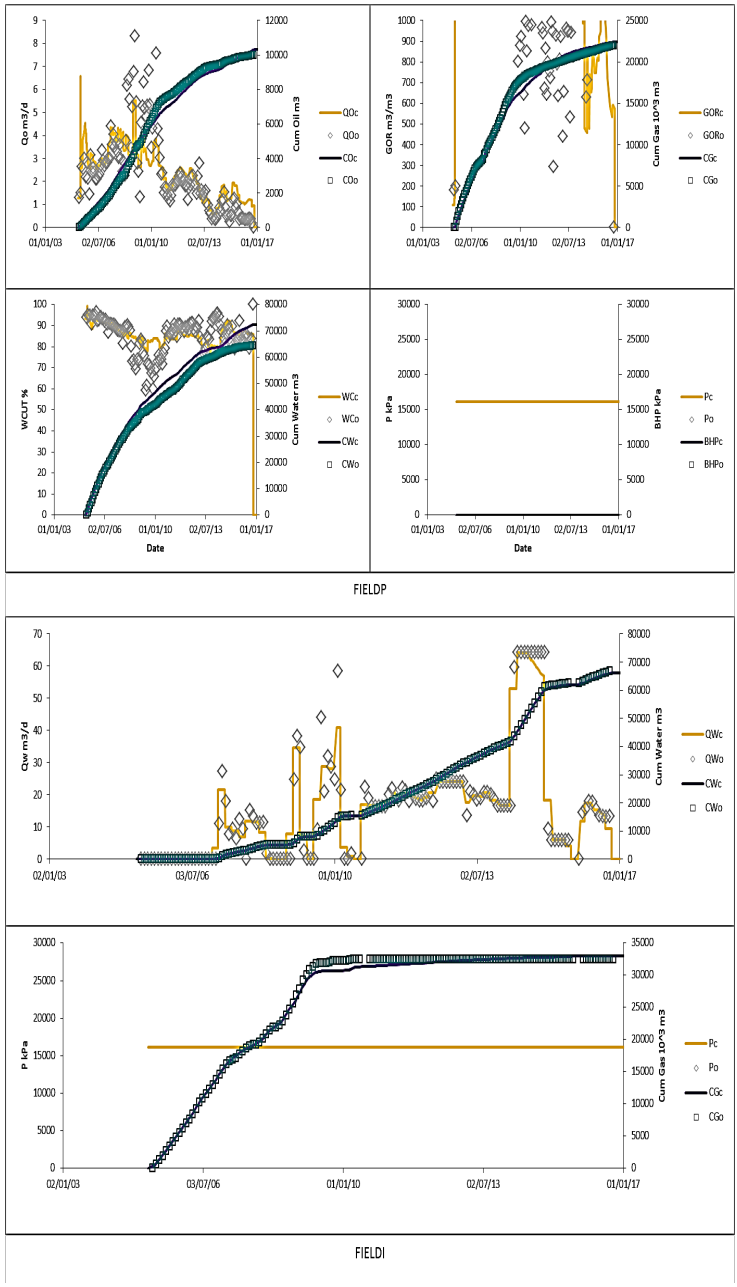

Figure 15. History match results for field injections and productions from 2005 to 2016.

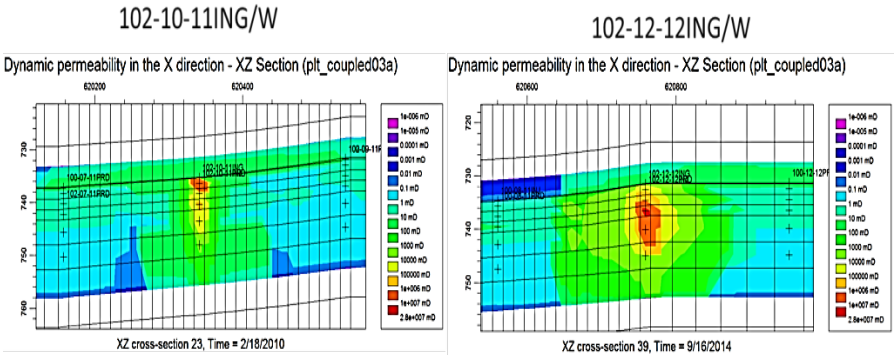

Figure 16. Maximum fracture propagation in the two CO2/Water injectors of 102-10-11ING/W and 102-12-12ING/W.

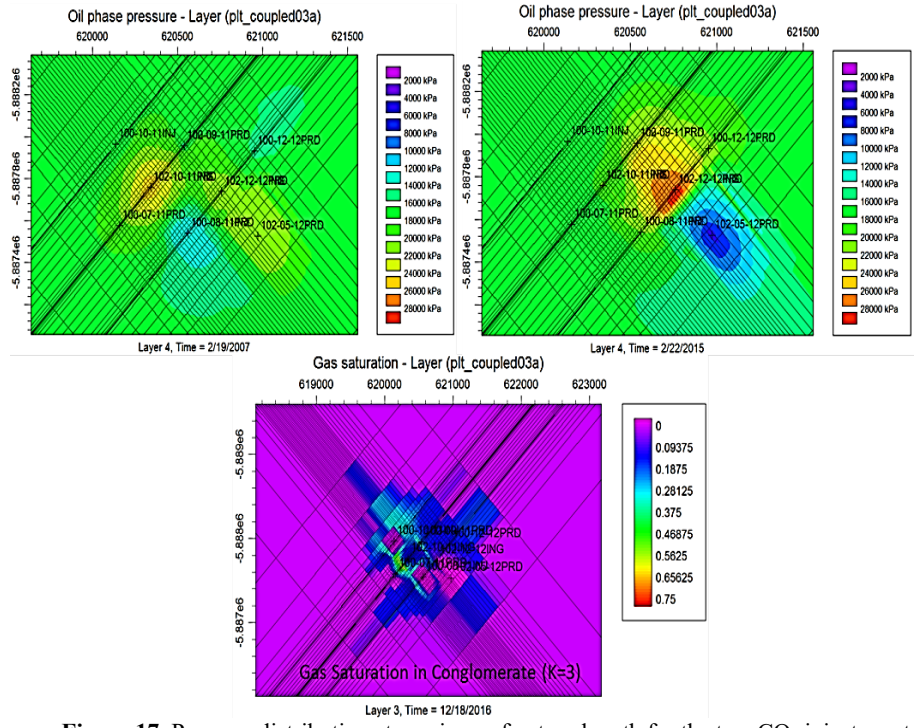

Figure 17. Pressure distribution at maximum fracture length for the two CO_2 injectors at top of Cardium and the gas saturation distribution at the end of EOR at conglomerate layer.

Figure 17 presents the pressure distribution at the time of maximum fracture length for the two CO_2 injectors at top of Cardium sand and the gas saturation distribution at the end of EOR in the conglomerate layer.

FORECAST CO_2 INJECTION FROM 2017-2066

As explained in "The Reservoir Model for Forecast" section, a quarter of the full model from the pilot phase was used for the sensitivity analysis, allowing use of a refined representation of the reservoir rock and caprock, which yields a better resolution for the fracture propagation and characterization of the caprock integrity, and, in turn, a better prediction of injection bottomhole pressure (BHP).

Base Case Scenario (fc_q_coupled01, 7c2)

For the base case scenario, the CO_2 injection rate was assumed to be 25000 STD m^3/day (6250 STD m^3/day for the quarter model). The simulation results (Figure 18) show a maximum fracture half-length of 600 m (average) after about 49 years of CO_2 injection. The fracture length can be distinguished from the dynamic permeability plots as a zone of enhance permeability due to fracture width. The injection (BHP) increases to a maximum of 27 MPa. The caprock does not show any sign of breach, although due to shear fracturing the first bottom layer is affected (as will be shown in the "Caprock Cohesion Sensitivity" section), but it is constrained and controlled. A total volume of about 448 MM m^3 for the full field model will be injected during the 49 years of CO_2 injection period.

A key feature of this formation which affects the movement of CO_2 injected is the presence of the thief conglomerate layer, which takes most of the injected CO_2. Geological analysis does not show permeable conglomerate across the entire the reservoir. Some impermeable conglomerate sections were also reported [1]. To better analyse the distribution of the diffused CO_2 in the reservoir, a more accurate permeability map of conglomerate is essential. Figure 19 shows the vertical fracture connection to the conglomerate during high pressure injection and the resulting CO_2 plume associated with the high permeability (high leak-off) layer.

Table 2. Table of selected variable ranges for the sensitivity analysis during the future forecast period.

Scenario	Cardium Young's Modulus, GPa	Cardium sand Cohesion, kPa	Caprock Young's Modulus, GPa	Caprock Tensile Strength, kPa	Caprock Cohesion, kPa	Caprock Vert perm, md	Cardium Sand Thermal Exp Coef, 1/°C	Cardium Shale Therm Exp Coef, 1/°C	Stress Dependent Leak-off	CO_2 Solution in Water	Rel perm modification	Initial Stress in Cardium	Caprock Stress
Fc_q_coupled01, Base Case Scenario	8.0	5760	3.0	2000	2670	1E-6	1E-5	1.5E-5	No	No	No	100 %	100 %
Fc_q_coupled01_IsoT	Injection temperature is 50 °C , the same as the reservoir temperature												
Fc_q_coupled01a, 01b	In 01a the CO_2 injection rate is half and in 01b the injection rate is double												
Fc_q_coupled02a, 02b	4, 12												
Fc_q_coupled03a, 03b		3000, 4000											
Fc_q_coupled04a, 04b			4, 6										
Fc_q_coupled05a, 05b				500, 1000									
Fc_q_coupled06a, 06b					500, 1000								
Fc_q_coupled07a, 07b,						1E-4, 1E-5							
Fc_q_coupled08a, 08b							0.5E-5, 2E-5						
Fc_q_coupled09a, 09b								1E-5, 2E-5					
Fc_q_coupled10a, 10b									2 & 4 times				
Fc_q_coupled11b										14% more CO_2 solution in Water			
Fc_q_coupled12a, 12b, 12c, 12d, 12e, 12f	12a: Sgc = 0.04 (0.14 - 0.1); 12b: Sgc = 0.24 (0.14 + 0.1); 12c: Sor = 0.3 (0.4 - 0.1) & Sloc = 0.19 (0.29 - 0.1); 12d: Sor = 0.5 (0.4 + 0.1) & Sloc = 0.39 (0.29 + 0.1); 12e: Powers + 1 ; 12f: Powers - 1												
Fc_q_coupled13a, 13b												95, 115 %	
Fc_q_coupled14a, 14b, 14c													90%, 80%, 70%

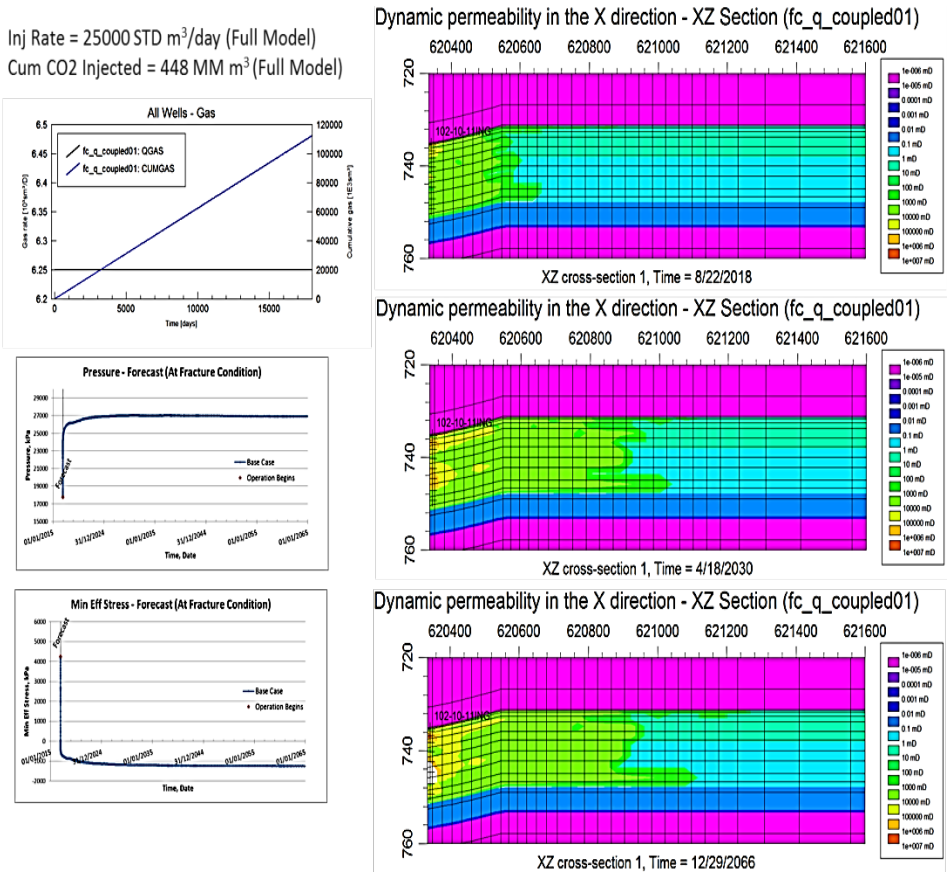

Figure 18. Dynamic permeability evolution with time, total CO_2 injection, BHP and minimum effective stress perpendicular to the fracture plane at the wellbore for the base case scenario.

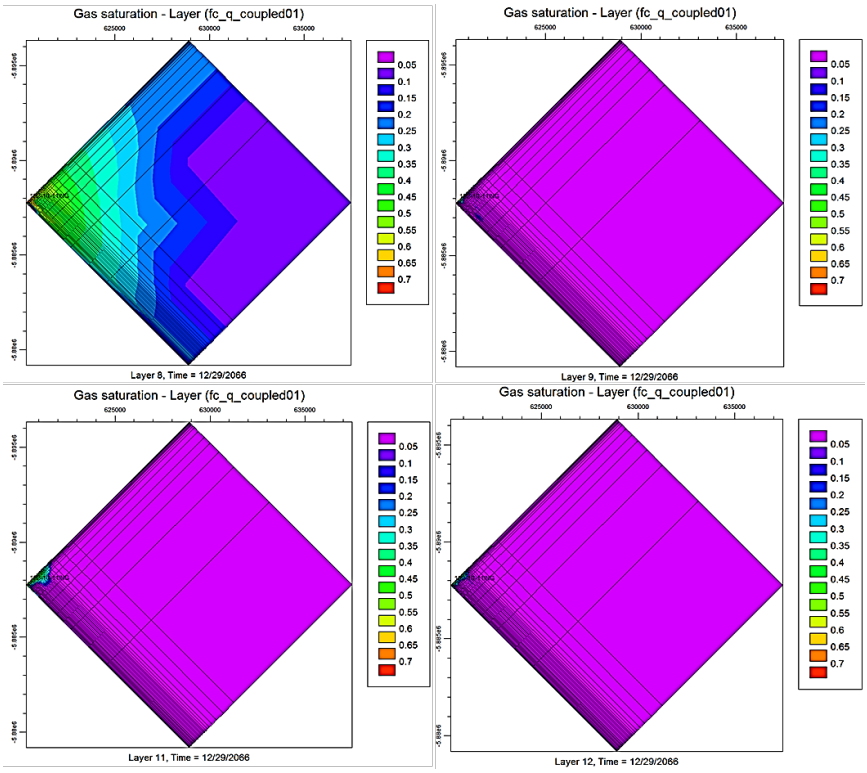

Figure 19. CO_2 saturation maps at different layers, with the maximum propagation in the conglomerate layer (left-top).

Temperature Effect (fc_q_coupled01_isot)

Figure 20 presents the simulation results for the effect of temperature on the fracture half-length and the injection BHPs as well as the minimum effective stress perpendicular to the fracture plane of the injector grid block. In general, the thermal cooling effect lowers the required injection pressure as shown in the figure. Fracture permeability increases in regions where the cooling is maximum due to the thermal cooling contraction of the formation allowing more opening of the induced fracture. An important benefit of the applied fracture model is the stiffness softening in the fractured blocks which allows for free opening of the fracture plane when contraction in the adjacent blocks occur due to the thermal cooling effect. Figure 20 also shows the softening in the fractured block Young's modulus when the fracture opens in tensile mode.

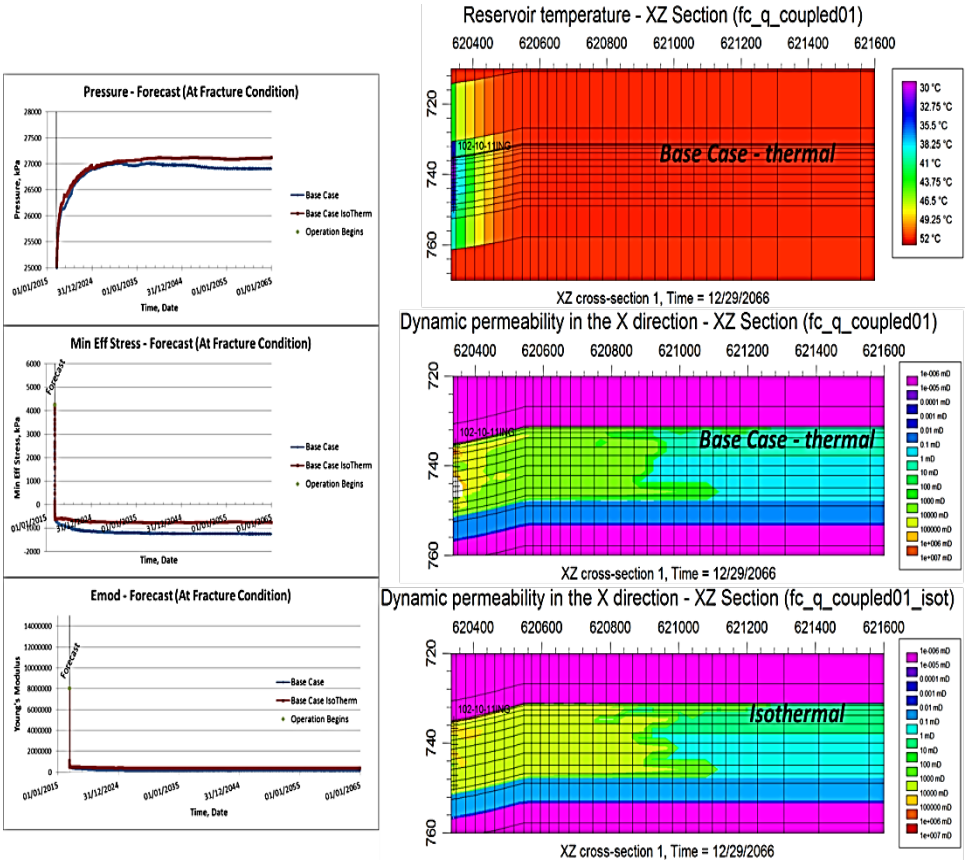

Figure 20. Temperature effect on the fracture propagation and the injection BHPs.

CO_2 Gas Injection Rate Effect (fc_q_coupled01a, 1b)

Reducing the CO_2 injection rate by half results in a much smaller fracture half-length as shown in Figure 21. In contrast, the fracture half-length will eventually be much longer for the case with double the injection rate. After 3 years the fracture length with double the injection rate is the same as the end of base case. As one may expect, due to friction in the fracture the injection pressure in the double rate case is higher and in the half rate case is smaller than the base case. These results illustrate that the fracture growth rate is strongly a function of leak-off. Depending on the far field pressure boundary conditions of the drainage area, eventually the fracture may stabilize as the injection rate is balanced by the leak-off. This result would have an impact on spacing of injection wells and/or placement of wells to efficiently perform CCS.

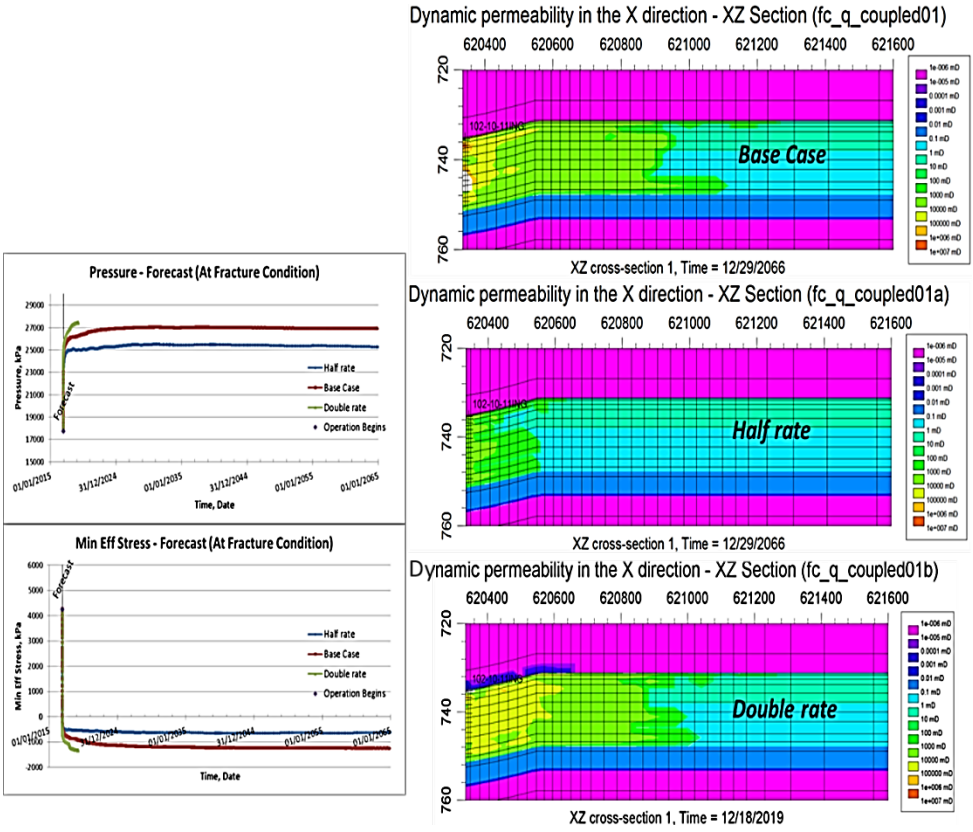

Figure 21. CO_2 injection rate effect on the fracture propagation and the injection BHPs.

Young's Modulus Effect (fc_q_coupled02a, 2b)

The Biot's constant varies with the bulk modulus or at a constant Poisson's ratio, it is a direct function of the block's Young's modulus. The Biot's constant is simply defined as,

$$\alpha = 1 - \frac{K_b}{K_{gr}}$$

where K_b and K_{gr} are the bulk and grain moduli respectively. A higher Cardium sand bulk modulus results in lower Biot's constant and in smaller total stress built-up. Consequently, the required BHP during the long-term injection process becomes smaller in magnitude as shown in Figure 22. The fracture length at higher Young's modulus values is longer than facture lengths for smaller magnitudes of Young's modulus for the same injection scenario.

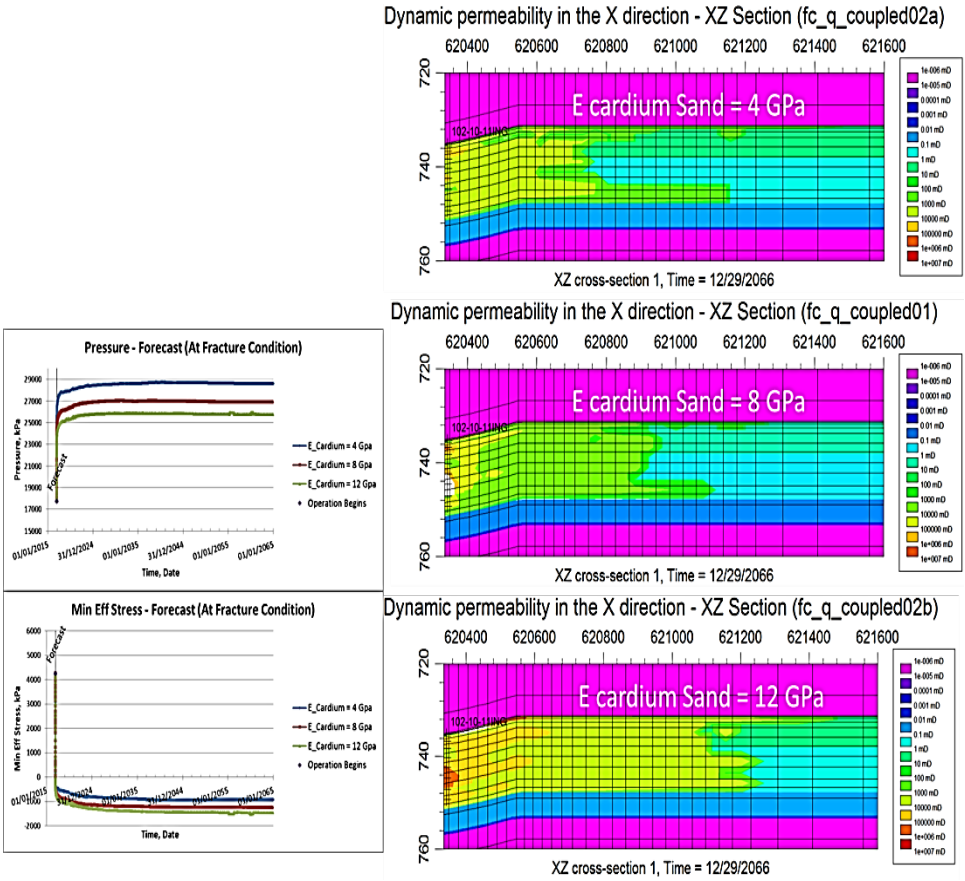

Figure 22. Young's modulus magnitude effect on the fracture propagation and the injection BHP.

Cardium Sand Cohesion Effect (fc_q_coupled03a, 3b)

The Cardium sand cohesion was varied from 5760 kPa down to 1000 kPa, and no shear fracturing was predicted by the fracture model in the Cardium sand. The results were the same as the base case with cohesion of 5760 kPa as plotted in Figure 23.

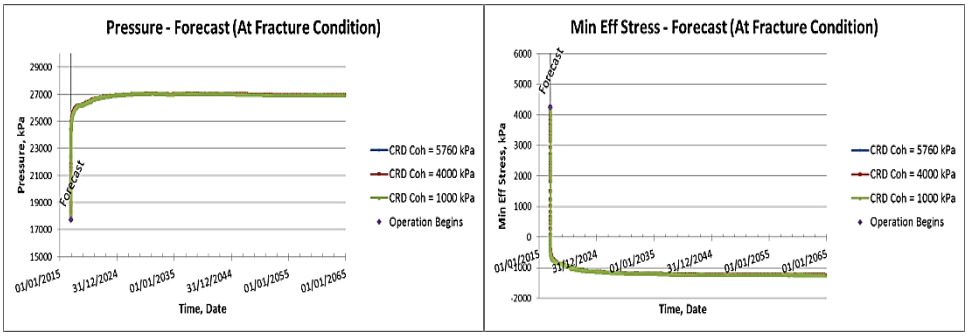

Figure 23. Cardium sand cohesion effect on the fracture propagation and injection BHP.

Cardium Shale Young's Modulus (E) Effect (fc_q_coupled04a, 4b)

A softer caprock E makes it easier for the fracture in Cardium Sand to prop open. In that case, lower injection BHP is required for the same fracture to propagate in the Cardium sand as shown in Figure 24. The effect of variation in the caprock Young's modulus is opposite to the effect of varying the reservoir Young's modulus on fracture propagation and injection BHP.

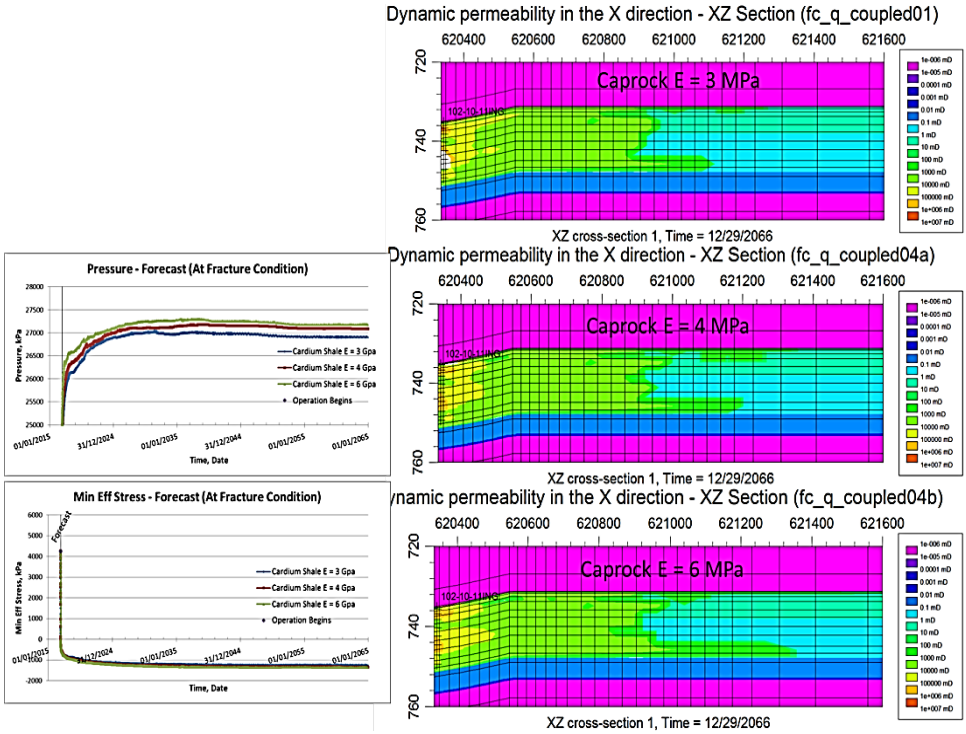

Figure 24. Cardium shale Young's modulus effect on the fracture propagation and injection BHPs.

Cardium Shale Tensile Strength Effect (fc_q_coupled05a, 5b)

The effect of the caprock tensile strength on fracture propagation in the caprock was studied by varying it from 2 MPa (base case) down to 0.5 MPa. There is a sufficient stress contrast between the Cardium sand and shale (caprock) such that even by lowering the tensile strength of the caprock, the fracture is still contained, as shown in Figure 25.

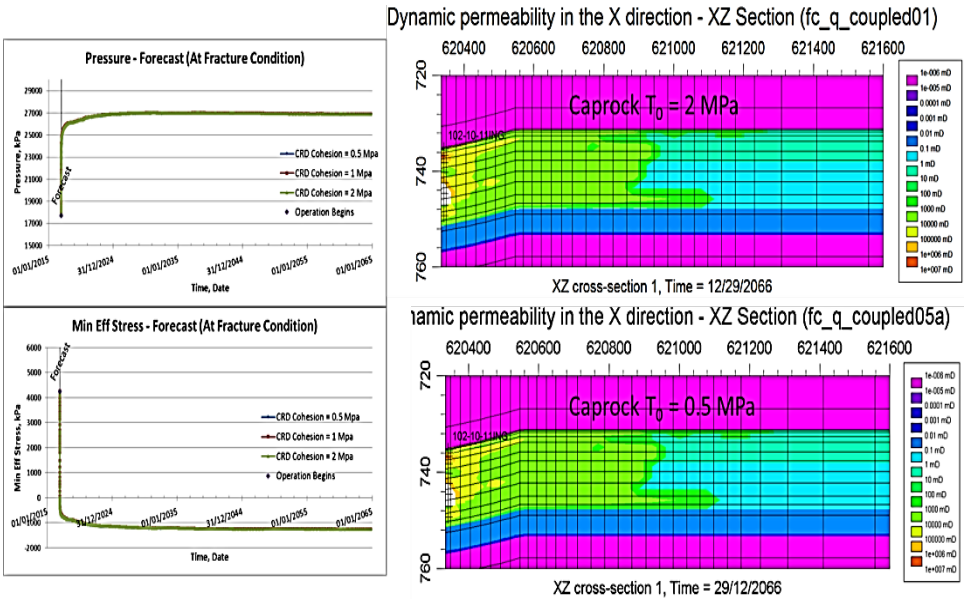

Figure 25. Cardium shale tensile strength effect on the fracture propagation and injection BHPs.

Cardium Shale Cohesion Effect (fc_q_coupled06a, 6b)

In this sensitivity, a relatively high tensile strength is given to the caprock to merely sensitize the shear failure in Cardium Shale. The base case caprock cohesion is 2.67 MPa. Shear fracturing occurs when the caprock cohesion is 0.5 Mpa; but the fracture remains contained within the Cardium sand. Minor shear fracturing is also observed when the caprock cohesion is 1 Mpa; however, it's not a major issue. No caprock breach was seen for the base case with a caprock cohesion of 2.67 Mpa, as shown in Figure 26.

GEOSIM uses an upstream transmissibility formulation for the fracture propagation. Therefore, the first layer of the caprock will observe a pressure increase if the fracture has propagated to the base of the caprock. If there is fracture propagation into layers above this lowest caprock layer and the fractures continue to grow, then the situation would be considered risky with regard to leakage through the caprock. Further fracture propagation into the caprock is highly dependent on the magnitudes of the Barton-Bandis parameters assumed for the induced shear fracture. Further sensitivity models for the enhanced shear fractured block permeability of 10 md or more indicated the caprock to be compromised for the cases with smaller cohesion. However, from Authors' experience, the permeability enhancement from shear fracturing is limited and it is less likely for the caprock to totally be breached.

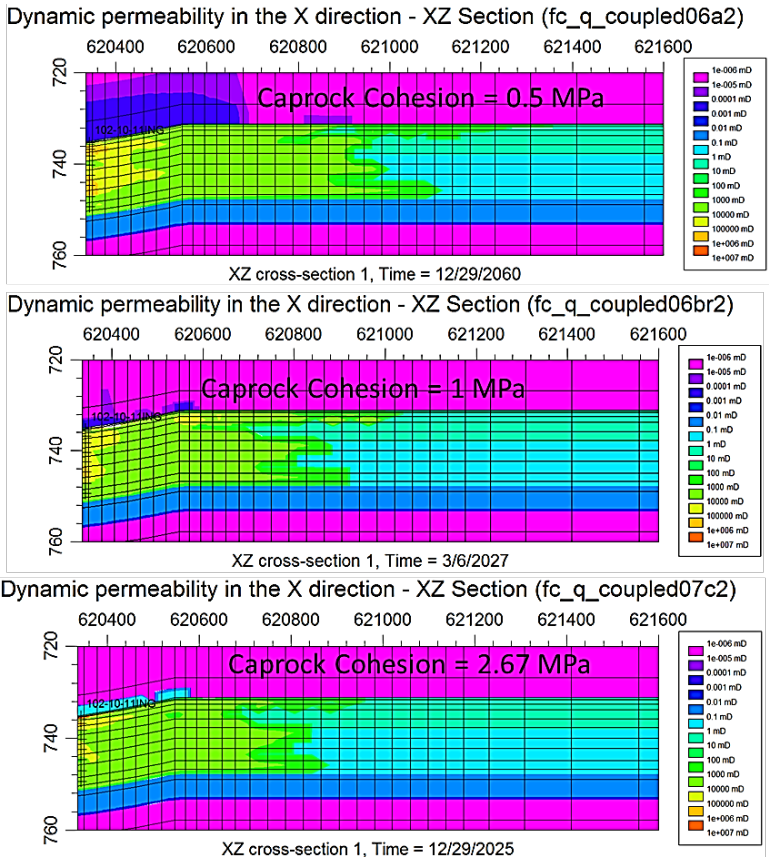

Figure 26. Cardium shale tensile strength effect on the fracture propagation. Injection BHPs are note shown since all are the same.

Cardium Shale Initial Permeability Effect (fc_q_coupled07a 7b)

For the range of caprock permeabilities studied, no variation in caprock integrity was observed, as shown in Figure 27. The relatively higher minimum stress in the caprock (compared with Cardium sand) is the dominant factor preventing the fracture growth into the caprock. The slight fracture propagation into the first caprock layer, which is in shear mode is due to the upstream transmissibility treatment in GEOSIM as described above. The caprock is only considered to be breached if the fractures continue further into upper caprock layers. The last case is also the base case with shear fracturing mode in the caprock layers activated in the input data. Although a slight growth of fracture tip into caprock is seen; since it did not grow further up into the caprock, the operating situation is considered to be safe. The sensitized caprock permeability values have shown the same BHPs with time.

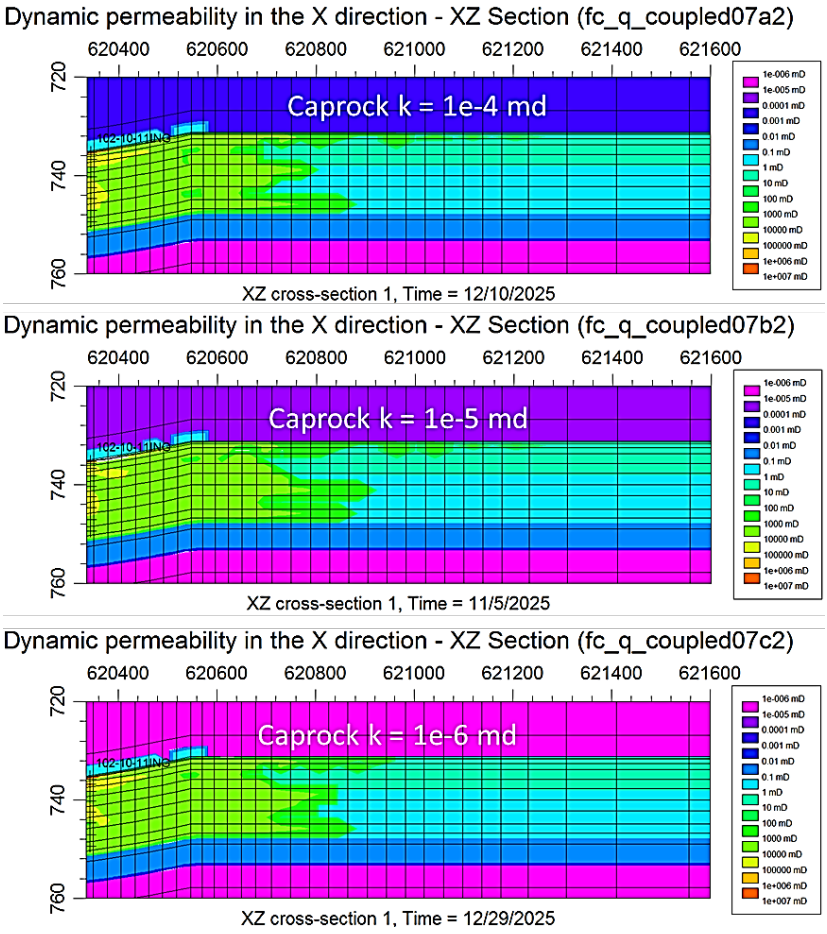

Figure 27. Cardium shale initial permeability effect on the fracture propagation. Injection BHPs not shown since all are the same.

Cardium Sand Thermal Expansion Coefficient Effect (fc_q_coupled08a, 8b)

A higher Cardium sand thermal expansion coefficient causes more reduction in the effective stress due to the thermal cooling effect. This consequently increases the overall fracture permeability and reduces the injector's bottomhole pressure as shown in Figure 28.

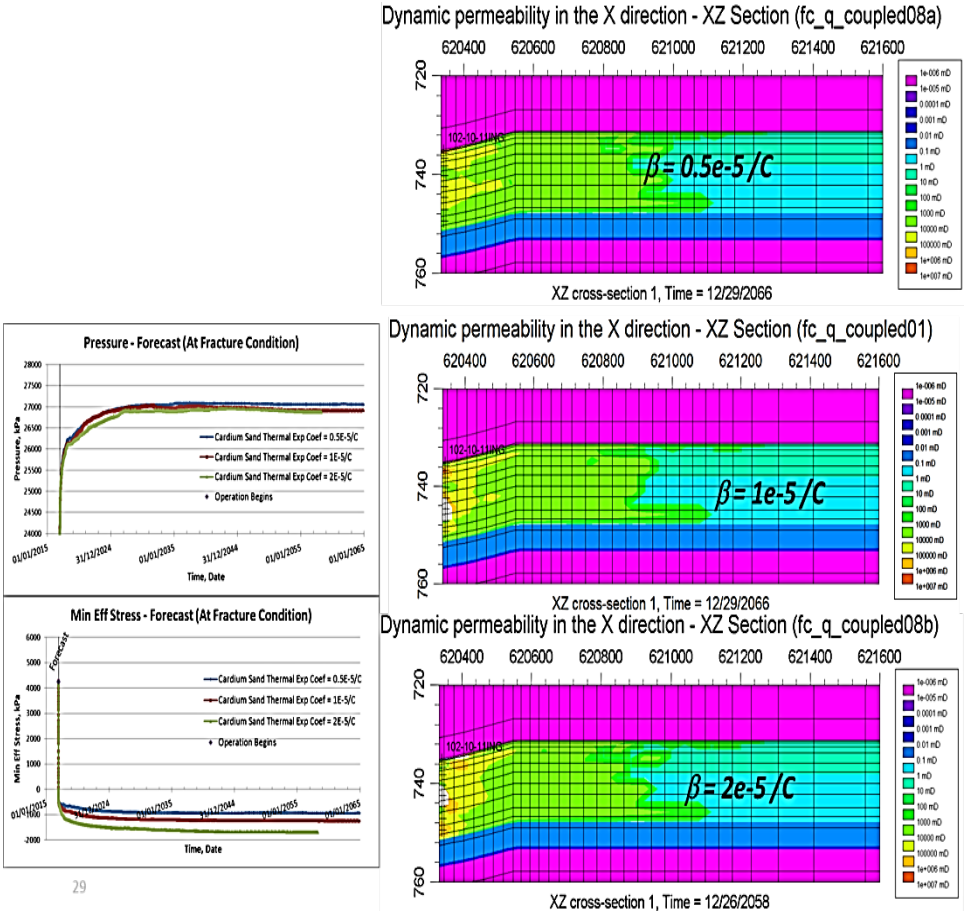

Figure 28. Cardium sand thermal expansion coefficient effect on the fracture propagation and injection BHPs.

Cardium Shale Thermal Expansion Coefficient Effect

Higher Cardium shale thermal expansion coefficient increases the possibility of shear fracturing in the caprock. As shown in Figure 29, in the case with β = 2e-5/°C there is some fracturing in the first shale layer. However, even for this high value of β, the caprock integrity is intact.

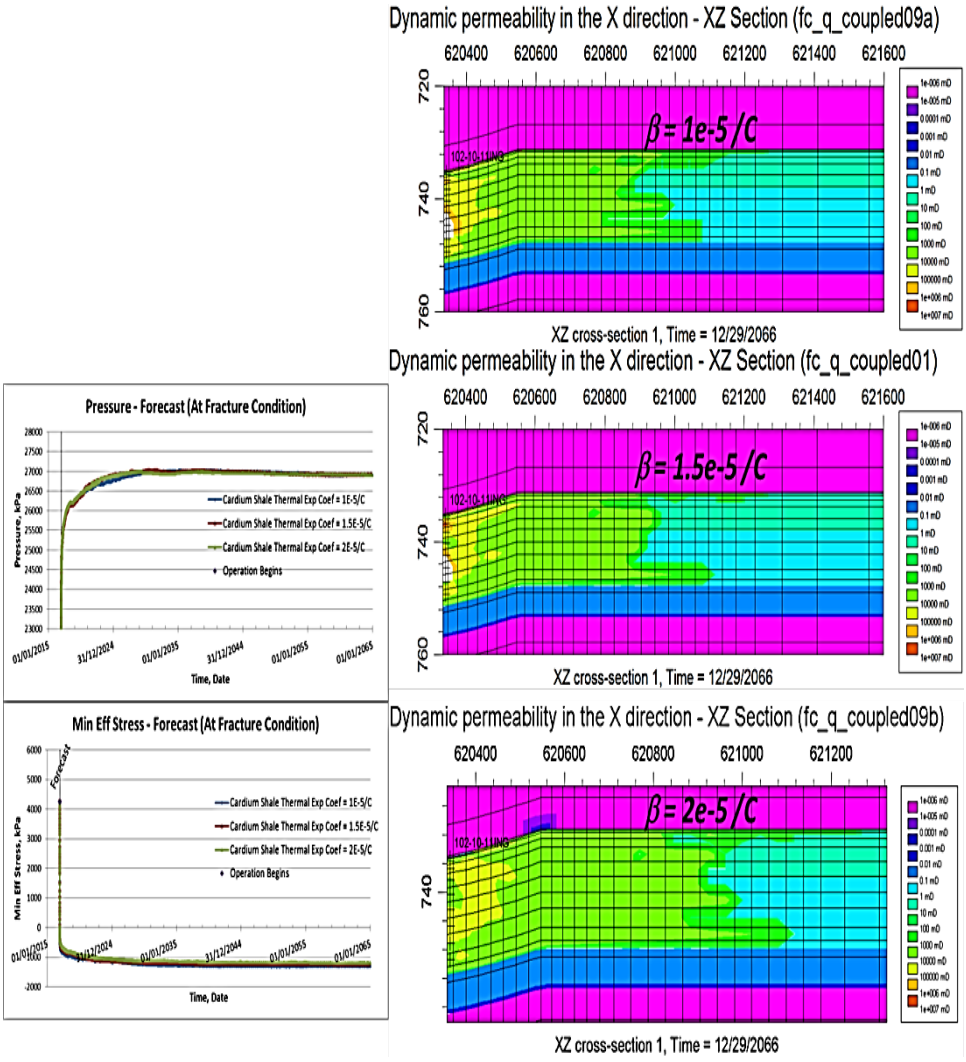

Figure 29. Cardium shale thermal expansion coefficient effect on the fracture propagation and injection BHPs.

Off-Planar Fluid Leak-off Effect (fc_q_coupled10a, 10b)

Higher leak-off from a fracture controls fracture growth as a higher permeability provides higher leak-off and increased injectivity for a given fracture area. Likewise, smaller injection BHP is also required as the fracture length is shorter in magnitude when fluid leak-off is higher and, therefore, the friction effect from the well to the fracture tip is less (Figure 30).

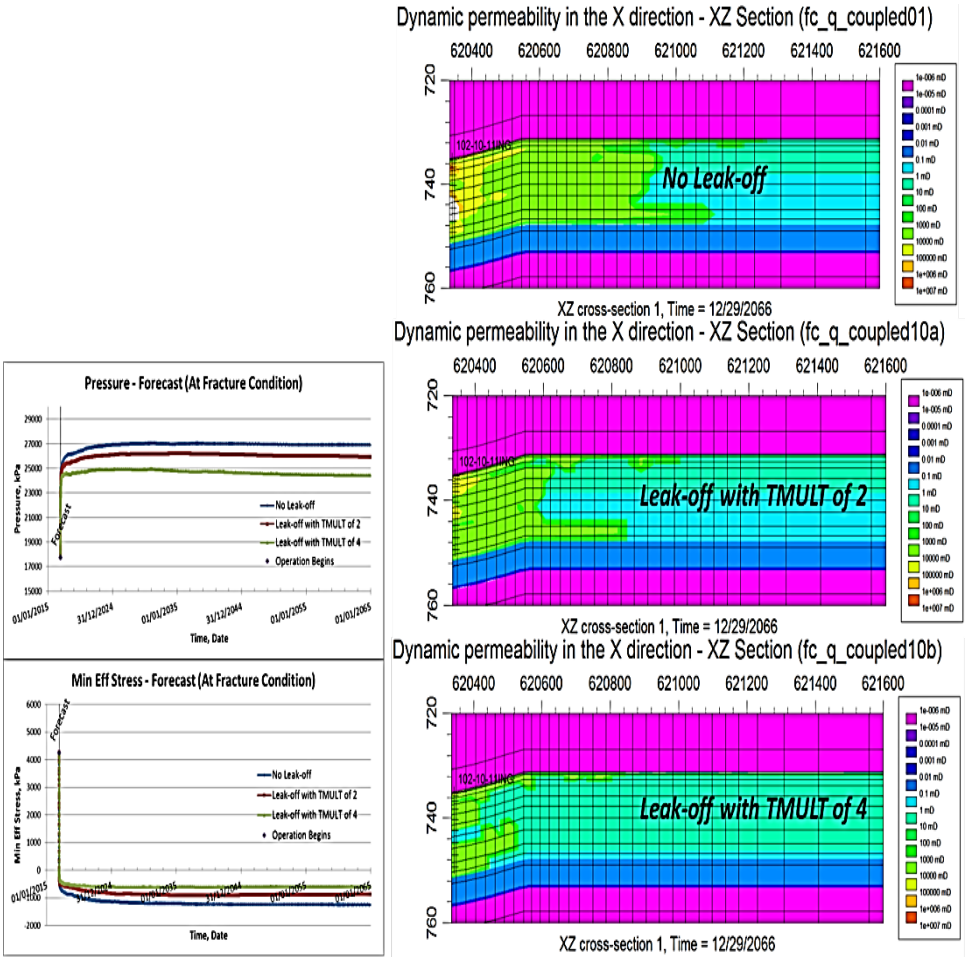

Figure 30. Fluid leak-off from fracture walls effect on the fracture propagation and injection BHPs.

CO_2 Solution in Water Effect (fc_q_coupled11b)

At the reservoir conditions, the solubility of CO_2 in brine and oil are 1.25 mol/L and 8.5 mol/L respectively [14]. In GEOSIM there is no option to account for gas dissolved into the water. The water to oil saturation ratio in the beginning of CO_2 injection is close to one. To approximate the effect of CO_2 solubility, the GOR was increased by about 14% to account for more CO_2 injection into the reservoir. Figure 31 shows the free gas saturation for the cases with and without solubility in the water. It is hard to differentiate the excessive CO_2 dissolution from the gas saturation maps in the conglomerate. But the BHP shows lower injection pressure for the specified base injection rate when CO_2 dissolution in water is considered.

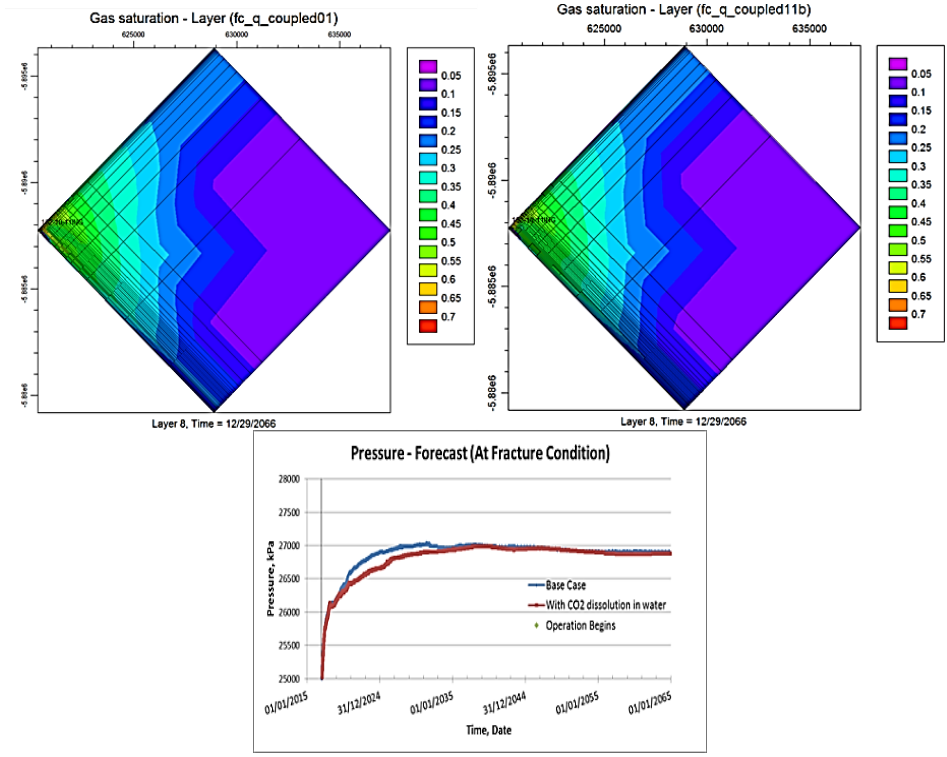

Figure 31. CO_2 solution in water effect on the gas saturation and injection BHPs.

Permeability End Points Effect (fc_q_coupled12a, 12b, 12c, 12d, 12e, 12f)

This section describes the sensitivity of the CO_2 injection process and the length of the induced fracture to changes in the parameters which impact the injection formation relative permeability. The analysis is conducted for 6 scenarios; the first assumes Sgc-0.1 (fc_q_coupled12a), the second Sgc+0.1 (fc_q_coupled12b), the third Sor-0.1 and Sloc-0.1 (fc_q_coupled12c), the forth Sor+0.1 and Sloc+0.1 (fc_q_coupled12d), the fifth Power-1 (fc_q_coupled12e), and the last Power+1 (fc_q_coupled12f).

When the critical gas saturation (Sgc) is increased, the injection BHP and the fracture length marginally increase, as opposed to the case with smaller Sgc. Lower Sor and Sloc slightly increases the BHP and the fracture length, whereas increasing the respective values decreases the BHP and the length of the induced fracture. Changing the relative permeability exponents has the largest impact on the fracture length and the BHPs (Figures 32 and 33). A unit reduction of the power exponent (reduce the interference of phases and essentially increase effective permeability of gas) reduces the BHP by up to 1500 kPa and the power increase (increase the interference of phases and essentially decrease effective permeability of gas) increases the required BHP by up to 500 kPa. This effect of effective permeability on the leak-off can also be seen in the fracture lengths shown in Figure 33 (b), where the Power-1 case has a much smaller fracture length than the Power+1 case.

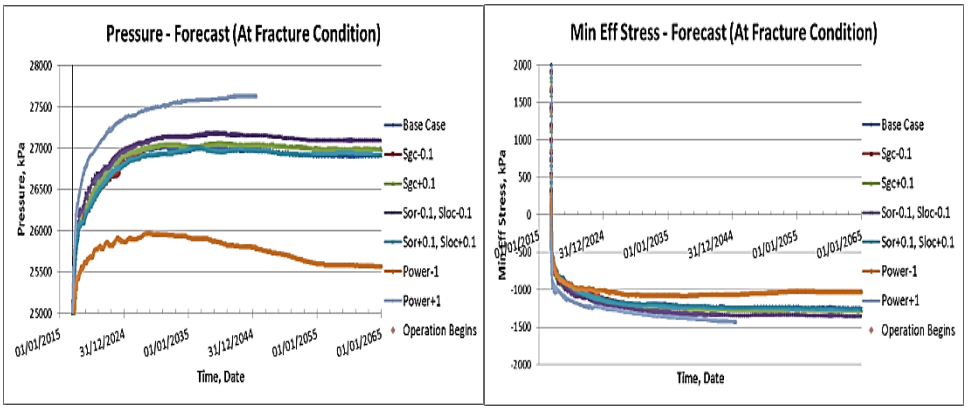

Figure 32. Relative permeability end points effect on the injection BHPs.

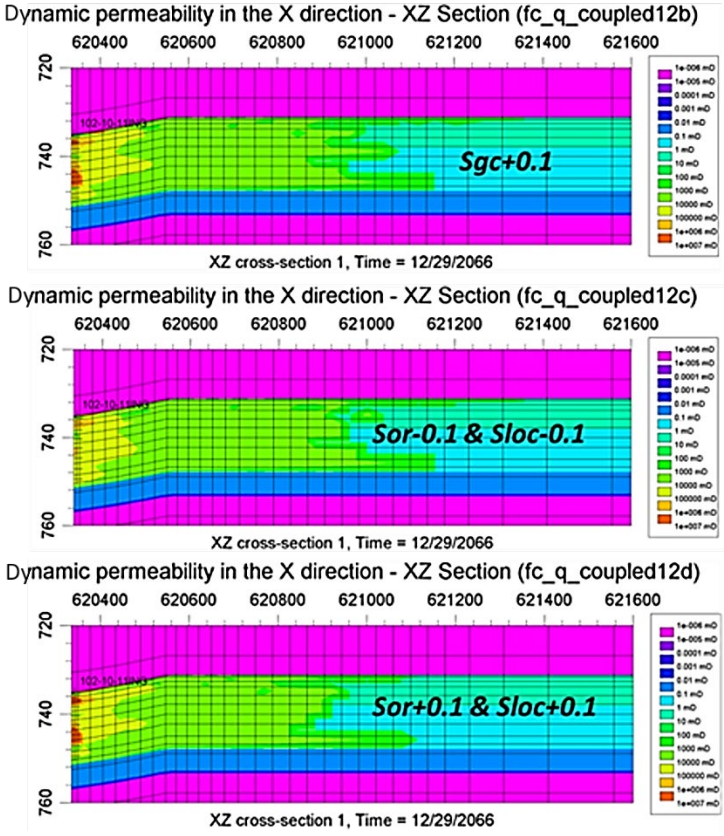

Figure 33(a). The ultimate dynamic fracture propagation for various relative permeability end points.

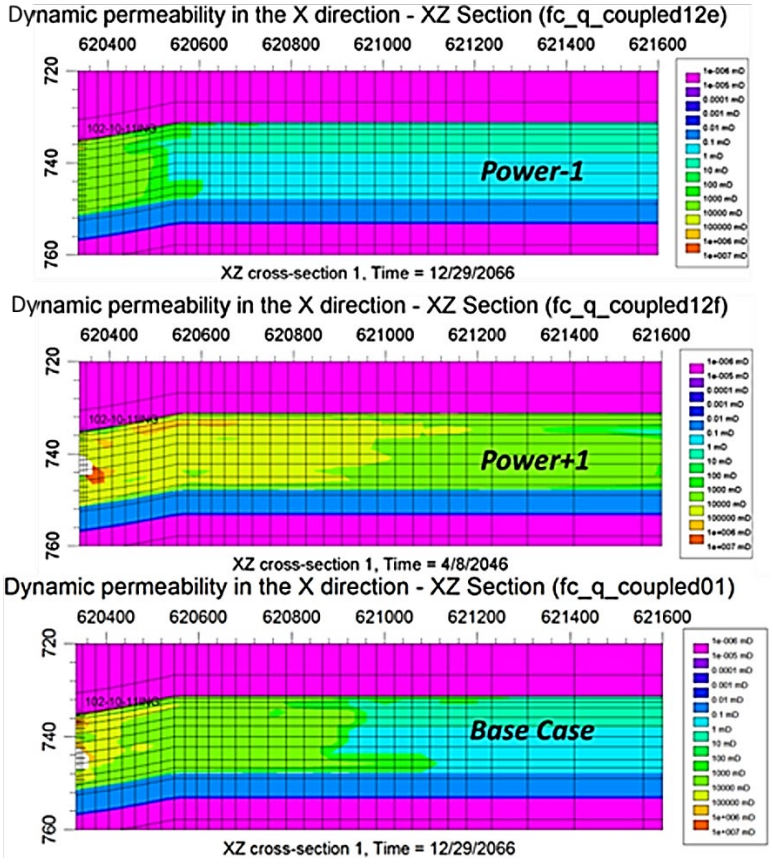

Figure 33(b). The ultimate dynamic fracture propagation for various relative permeability end points.

Cardium Sand Initial Minimum Stress Effect (fc_q_coupled13a, 13b)

Decreasing the initial minimum total stress in Cardium sand by 5% does not affect the caprock integrity during injection, similar to the base case. However, the required injection BHP is decreased, and the induced fracture length is increased as shown in Figure 34. Increasing the initial total minimum stress by 15% however shows an adverse effect. The caprock integrity is compromised as the required injection BHP increases substantially proportional to the increase in the minimum total stress. The caprock breach is clearly shown in Figure 34. Imposition of 15% higher initial stress in Caridum Sand (reservoir) compared to the base case causes the initial stress in Caridum Sand to become almost the same as in Cardium Shale. Unless there exists a higher initial stress in the caprock, for the same reservoir and caprock tensile strengths, the fracture has no reason to grow laterally when it reaches to the reservoir top. The shallower the depth, the smaller the minimum horizontal stress (based on its gradient). Going upward, fluid loses its pressure by its hydrostatic gradient (~10 kPa/m); whereas the minimum stress declines faster with an 18.5 kPa/m gradient.

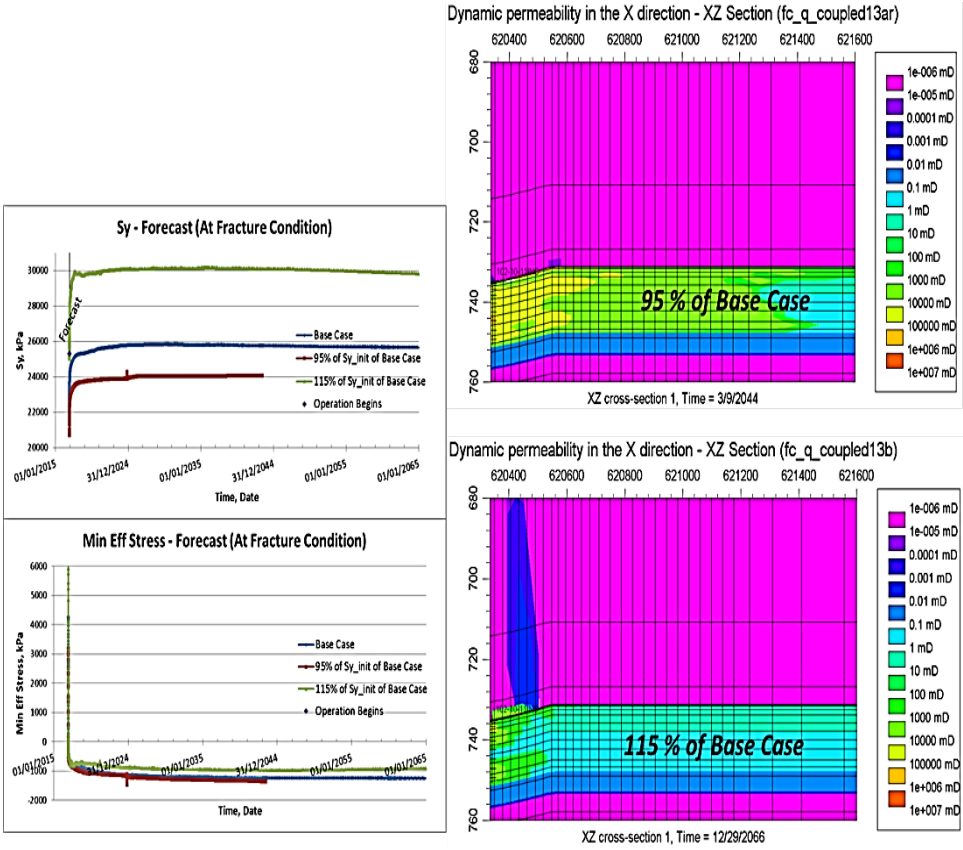

Figure 34. BHP and the ultimate dynamic fracture propagation for different initial total Cardium sand stress.

Cardium Shale Initial Stress Effect (fc_q_coupled14a, 14b, 14c)

Lowering the Cardium shale initial total stress increases the risk of caprock breach to a great extent as it directly impacts the stress contrast between the caprock and reservoir and a fracture containment mechanism. Figure 35 shows a total caprock breach when the second and the third (80 and 70% of the base case) scenarios prevail, while no breach is observed for the 90% case. In the third case (70%), the caprock breaks in both shear and tensile mode.

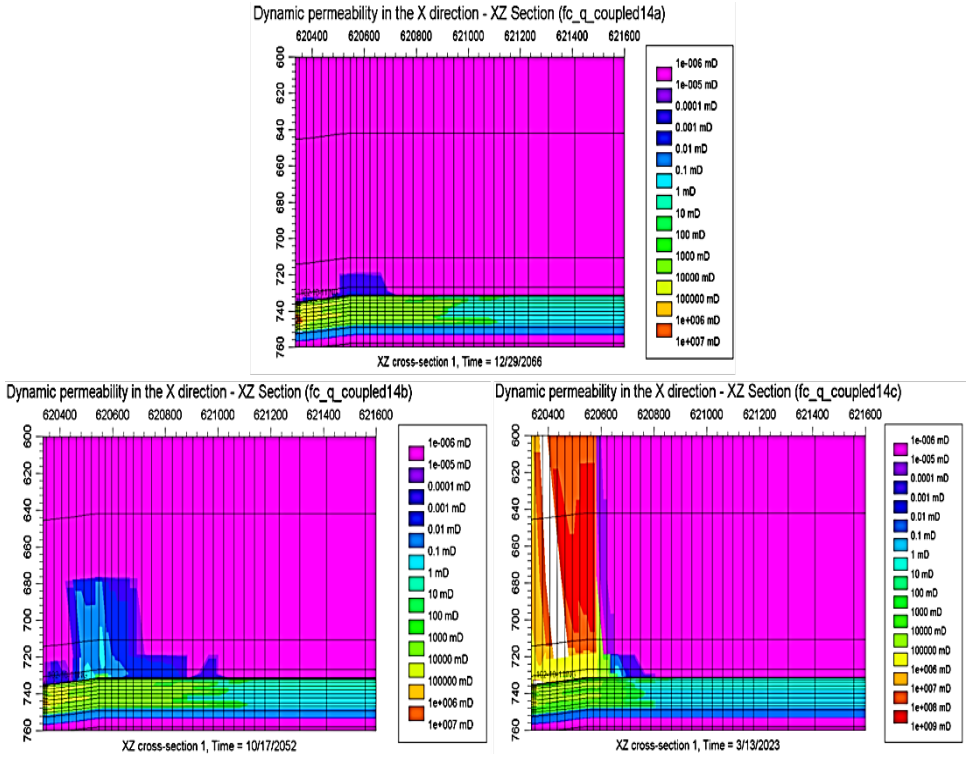

Figure 35. The ultimate dynamic fracture propagation for different initial total Cardium shale stress.

CONCLUSION

A simulation study of reservoir operations and follow-up CCS was completed for a clastic reservoir, the Cardium formation. The historical operations included primary production, waterflooding and CO_2 pilot injection. Overall, a good history match of the field data was obtained.

History matching of the CO_2 pilot period was important as it allowed some calibration of the reservoir to CO_2 injection, which increases the confidence of forecasting of CCS. An important feature of this study is the application of a new fracture constitutive model, which allows a more rigorous treatment of fracture opening by softening the fractured block stiffness and automatically calculating the enhanced permeability as a function of the opened fracture width.

A sensitivity analysis conducted in this study reveals interesting results related to the use of the Cardium reservoir for CO_2 sequestration and illustrates the sensitivity of caprock integrity to reservoir and geomechanical characteristics and to operational parameters. Figure 36 provides the tornado plots indicating the significance of the various parameters on the injector BHPs and the length of the induced fracture. Leak-off from the fracture plane, the exponents of the equations describing the relative permeability curves (impacting effective permeability of the system) and the Young's modulus of the Cardium sand have respectively the highest impacts on the fracture half length. The parameters showing the strongest influence on the injection BHPs was the Cardium sand Young's modulus, followed by the leak-off and relative permeability exponents. The thermal cooling effect

was found to have minor impact on the CO_2 injection process and fracture propagation. Other parameters have relatively smaller effect on the induced fracture propagation as shown in the Tornado plots.

The analysis indicates that a 15% increase in the magnitude of the minimum total stress in the Cardium sand endangers the caprock sealing performance. Likewise, assuming smaller magnitudes of the total minimum stress in the Cardium shale caprock will lead to an uncontrolled CO_2 leakage from a caprock breach. Both changes directly impact the stress contrast between the reservoir and caprock and the main fracture containment mechanism. This result confirms that a reservoir with a good fracture containment mechanism is critical to a safe CCS operation especially when injecting at fracturing conditions to attain the required injectivity.

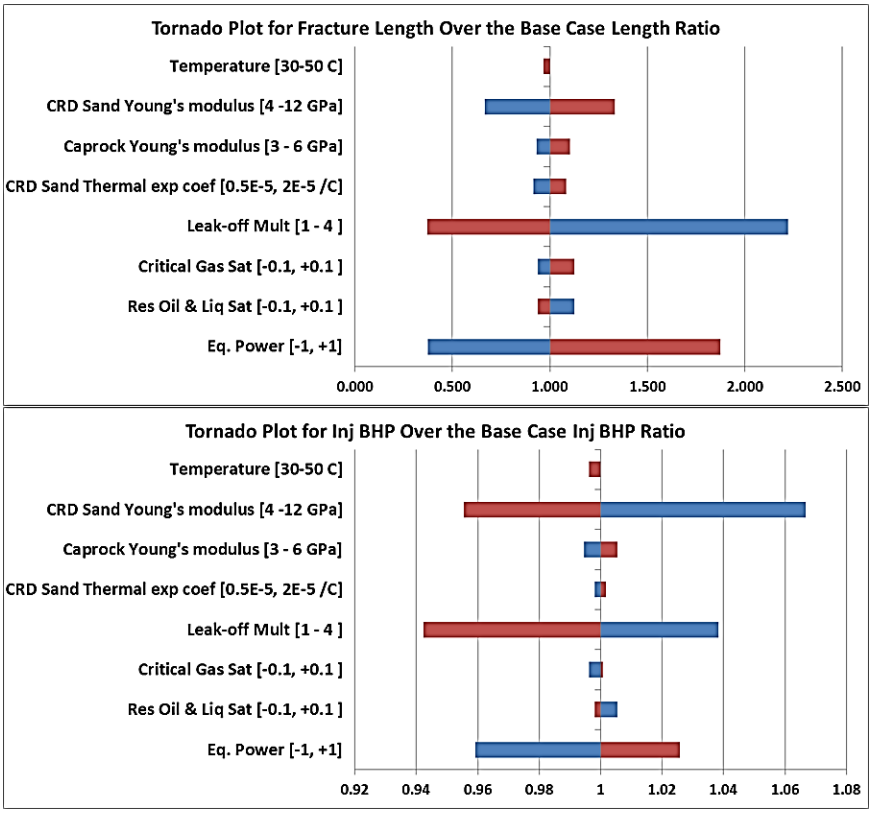

Figure 36. The tornado plots indicating the significance of the various sensitized parameters on the injector BHPs and the length of the induced fracture.

ACKNOWLEDGEMENTS

The authors would like to acknowledge Mark Chan for his contributions to the development of the study topic and management of the technical work and Jenny Gao for her thorough review of the project work and valuable comments.

REFERENCES

1. R. Coats (2003) “Application For Enhanced Recovery Pilot Scheme With CO_2 Injection in Pembina Cardium Pool-Geology of Pembina”A “Lease CO_2 Pilot Area,” PennWest, Calgary.
2. A. Settari (2017) GEOSIM Coupled Multiphase Flow Thermal And Geomechanics Simulator Manual, Calgary, AB.
3. A. Settari, K. Al-Ruwaili and V. Sen (2013) “Upscaling of Geomechanics in Heterogeneous Compacting Reservoirs,” *presented at the 2013 SPE Reservoir Simulation Symposium*, The Woodlands, TX, USA, SPE 163641., Feb 18-20, 2013.
4. A. Settari, R. Sullivan and R. Bachman (2002) “The Modeling of the Effect of Water Blockage and Geomechanics in Waterfracs,” in *SPE Annual Technical Conference*, San Antonio, TX, Sept. 29-Oct. 2, 2002.
5. D. Walters, J. C. Chavez, M. Nassir, Q. Riyami and B. Roure (2017) “Induced Fracture Monitoring and Characterization for a Thermal Fracturing Process,” in *American Rock Mechanics Association*, San Francisco, 25 to 28 June 2017.
6. S. Goodarzi, A. Settari, M. Zobak and D. Keith (2010) “Thermal Aspects of Geomechanics and Induced Fracturing in CO_2 Injection With Application to CO_2 Sequestration in Ohio River Valley,” in *SPE International Conference on CO_2 Capture, Storage, and Utilization*, New Orleans, Louisiana, SPE 139706, 10-12 November 2010.
7. M. VAZQUEZ and H. BEGGS, “Correlations for Fluid Physical Property Prediction,” *Journal of Petroleum Technology,* pp. June, pp. 968-970, 1980.
8. H. E. R. Laboratories (2006) “Reservoir Condition CO_2-Brine Drainage and Imbibition Relative Permeability Displacement Characteristics in the Pembina Area, Cardium Sandstone and Colorado Shale Formations,” Calgary.
9. M. Liu (2013) Behavior of Shale Rock Under Exposure To Supercritical CO_2, MSc Thesis, University of Alberta, AB, Canada.
10. B. Hitchon (2009) “Pembina Cardium CO_2 Monitoring Pilot: A CO_2-EOR PROJECT, Final Report,” ALBERTA, CANADA.
11. Ming Liu (2011) Reservoir Geomechanics Group, Dept. of Civil & Environmental Eng., “Pembina Cardium CO_2 Monitoring Project, Geomechanics Laboratory Program Lea Park Shale, Cardium Shale and Sandstone,” University of Alberta, Edmonton.
12. Reservoir Geomechanics Research Group (2011) Department of Civil & Environmental Eng., “Geomechanics Laboratory Program on Lea Park Caprock for ARC Resources Ltd.,” University of Alberta, Edmonton.
13. S. Goodarzi, M. Nassir and D. Walters, “Caprock Integrity Analysis Associated With CCS After EOR Processes In Oil Reservoirs,” Calgary, AB, Canada, 2017.
14. P. Olden, E. Mackay, G. Pickup, J. Stewart and G. Johnson (2015) “CO_2-EOR: Security of Storage,” Edinburgh, UK.
15. Reservoir Geomechanics Research Group, Department of Civil & Environmental Eng., “Geomechanics Laboratory Program on Lea Park Caprock, ARC Resources Ltd.,” University of Alberta, Edmonton, July 2011.
16. M. Bagheri (2006), Modeling geomechanical effects on the flow properties of fractured reservoirs (doctoral thesis). University of Calgary, Calgary, AB.

NOMENCLATURE

Bo–formation volume factor of oil
c–rock cohesion
E–Young’s modulus
Eg–gas expansion coefficient

K–permeability
Kn–fracture normal stiffness
P–pressure
Rs–solution gas-oil ratio
Sf–fracture spacing
Sgc–relative permeability end point-Residual gas saturation
Sloc–relative permeability end point-Liquid saturation at which oil ceases to flow in the liquid-gas system with connate water
Sor–relative permeability end point-Irreducible oil saturation
Swc–relative permeability endpoint-Irreducible (conate) water saturation
T–rock tensile strength
UCS–Unconfined compressive strength test
v–fracture displacement
Vg–gas viscosity
Vo–oil viscosity
Wf–fracture width
φ–rock friction angle
σ–total stress
σ'–effective stress

Carbon Dioxide Capture for Storage in Deep Geological Formations, Volume 5
Karl F. Gerdes (Editor)
© 2022 BP. All rights reserved.

Chapter 23

SCENARIO DEVELOPMENT FOR DETECTING AND LOCATING CO_2 FROM LEAKING PLUGGED & ABANDONED (P&A) WELLS

Yingqi Zhang[1], Anshul Agarwal[2], Erika Gasperikova[1], Thomas M. Daley[1], Curtis M. Oldenburg[1]

[1]Energy Geosciences Division, Lawrence Berkeley National Laboratory
[2]Energy Resources Engineering Department, Stanford University

ABSTRACT: Plugged and abandoned (P&A) wells are recognized as a key vulnerability for long-term containment of CO_2 at geologic carbon sequestration sites developed in depleted hydrocarbon reservoir areas. To address this potential containment risk, practical monitoring approaches such as geophysical surveys and the Modular Borehole Monitoring (MBM) tool have been developed to improve storage monitoring and to detect and characterize leakage. In addition, research has been carried out on how to address contingencies such as well leakage by subsurface or downhole interventions to reduce leakage impacts. The present study is a first step to fill the gap in understanding between intervention approaches in general and intervention for various leakage scenarios, particularly those involving inaccessible wells. Specifically, before a particular intervention approach can be designed and applied, the operator needs to know the character and location of the plume. In fact, to refine characterization, monitoring should be carried out as close to the source of an indicated plume as possible (e.g., as indicated by near-surface anomalies). In this study, we carried out numerical simulations of coupled deep and shallow leakage of CO_2 up a prototypical P&A well with degraded cement. The results provide synthetic data on plume configurations, saturations, and leakage rates that serve to characterize what a shallow CO_2 plume arising from P&A well leakage might look like. Based on the same model setup and plume configuration, we consider basic electrical monitoring approaches to constrain the limits of detectability and inform how to design more targeted electrical surveys. The results suggest that cross-well and surface electrical resistance tomography (ERT) have the potential to detect and characterize free-phase (high resistivity) and dissolved-phase (low resistivity) plumes, with particularly good ability to constrain the areal extent (footprint) of a shallow plume and much more limited ability to constrain the thickness of the plume. We also consider seismic monitoring detectability for the scenarios. Our initial assessment of seismic monitoring assumes a detection threshold of 5% CO_2 saturation and forecasts the detectable plume over time. At various times either surface seismic or vertical seismic profile acquisition geometries are indicated for the detectable plumes. Future work should be aimed at developing full forward models of seismic and electromagnetic (EM) monitoring for the leakage scenarios, which can then be used to assess the potential of improved quantitative assessment using joint seismic-EM inversion. Subsequently, there should be a focus on development of various intervention scenarios to understand mitigation effectiveness and to design the monitoring schemes needed to confirm effectiveness.

KEYWORDS: CO_2 storage, well integrity, leakage scenario, modular borehole monitoring, electrical monitoring, ERT, seismic detection

INTRODUCTION

The CCP3 Contingencies program identified and modeled potential solutions to breaches in geologic barriers [1], and recent events continue to remind us of the importance of preventing well failures (e.g., [2,3]). Plugged and abandoned (P&A) wells, particularly conducted before modern regulations (e.g., US EPA UIC) were in place, continue to be the most probable and in some cases most impactful threats to fluid containment during CO_2 storage. In addition to impacting underground sources of drinking water (USDW), the protection of which forms the basis for the U.S. EPA's Class VI well permits for geologic carbon sequestration, CO_2 leakage pathways formed in these wells can potentially bypass the low-permeability sealing layers of cap rock and go all the way to shallow formations, and potentially beyond to the ground surface. In addition, many prospective CO_2 storage projects will be situated in mature sedimentary basins, which usually have a large number of previously drilled and abandoned wells. If the cement or casing steel of these wells is exposed to the pH-lowering effects of CO_2 dissolved in water, corrosive processes may degrade well materials over time allowing CO_2 and other formation fluids to leak upward.

The project under which this study was conducted is aimed at filling the gap between work on modular borehole monitoring (MBM) [4], which seeks to develop practical well-based monitoring approaches, and on leakage contingency [5], which seeks to develop ways to address containment failures of CO_2 storage projects. The gap between these two projects is methods to identify (detect and locate) and characterize leakage incidents in the subsurface. In short, operators need information about leakage processes to develop approaches to detect and, if necessary, intervene to mitigate leakage and its impacts. The objective of this study is to address the leakage identification and characterization problem so that mitigation measures can be designed and implemented. Specifically, we have simulated CO_2 leakage from a prototypical P&A well to provide a synthetic dataset for understanding expected characteristics of CO_2 leakage and the potential for identifying and characterizing such leakage by remote geophysical monitoring methods. We constructed a leakage scenario and carried out forward modelling to investigate leakage plume characteristics and the potential for detectability of the CO_2 leakage. Next, potential monitoring strategies were analyzed for the simulated scenarios using generalized proxy modelling of electrical resistivity in subsurface systems. Intervention options were considered informally in the project to set the stage for future simulation and analysis of mitigation strategies.

BACKGROUND AND MOTIVATION

Whereas there is some degree of concern about integrity for any P&A well, CO_2 storage creates some specific and unique threats to P&A wells (e.g., [6,7]), including:

1. Mechanical deformation of wellbore cement generally caused by operational activities and changes in temperature and pressure cycles.
2. Chemical degradation of wellbore cement caused by dissolution of CO_2 into formation water and resulting corrosion of the cement.
3. Corrosion of the wellbore casing steel caused by the corrosion of steel components under the influence of dissolved hydrogen ions.

Figure 1 reproduces the iconic figure illustrating the potential leakage pathways through an abandoned well [8]:

(a) Along the casing-cement interface;
(b) Along the cement plug-casing interface;
(c) Through the cement pore space as a result of cement degradation or fracturing;
(d) Through casing as a result of steel deformation or corrosion;
(e) Through fractures in cement; and

(f) Slong the cement-rock interface. A given leakage pathway could also be a combination of these.

Although well integrity is one of the most recognized potential causes of CO_2 storage failure, failure events are generally manageable in accessible (pre-P&A) wells. For wells that are not accessible, it may be possible to carry out intervention procedures following the detection and characterization of leakage which will inform decisions about intervention approach. The workflow activities of leakage intervention, as shown in Benson *et al*. [1], are:

1. Detect leakage,
2. Characterize leakage,
3. Evaluate intervention options,
4. Intervene,
5. Assess containment, and
6. Complete intervention.

This study focuses on the first three parts in this workflow. The goal of the study presented here is to understand what kind of shallow leakage signals P&A well leakage can produce, how large the leakage rate can be, how the leak rate is related to the well and formation characteristics (e.g., permeability), how fast the plume can grow in the shallow formation, what are the possible monitoring methods for certain leakage rates, and to briefly comment on some potential intervention methods.

This paper is organized to explore these questions in sequence.

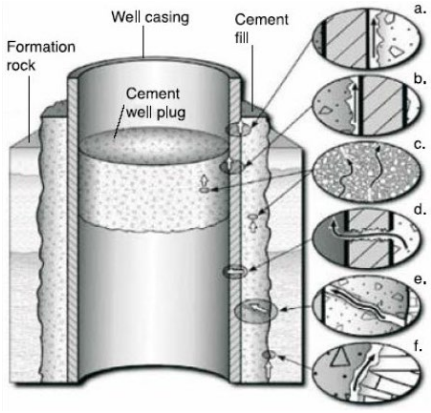

Figure 1. Illustration of potential leakage pathways of a P&A well [6,8].

DETECTABILITY OF CO_2 LEAKAGE FROM WELLS

Overview of Approach

Before interventions can be designed and targeted, the first step is to understand the detectability of CO_2 leakage, a challenging proposition because very low leakage fluxes may not be detectable unless occurring over an extended period of time. We carried out numerical simulations for a prototypical leaking well scenario to generate synthetic leakage signals (changes in pressure, temperature, saturation) and to assess generally the feasibility of intervention. Based on the simulation results of this scenario, we evaluated the effectiveness of seismic and electrical monitoring methods.

Simulations are performed using the ECO2N module of TOUGH2/iTOUGH2. TOUGH2 is a non-isothermal multiphase, multi-component flow and transport simulator [9]. The ECO2N fluid property module was designed for applications involving geologic storage of supercritical CO_2 in saline aquifers. iTOUGH2 [10] provides inverse analysis for TOUGH2 models. In addition, iTOUGH2 has some functional enhancements relative to TOUGH2 forward models.

Scenario Description

The scenario we consider includes a storage reservoir, a leaky well and a shallow formation. The storage reservoir is assumed to be located at 1480 meters (m) below ground surface. The scenario assumes that the CO_2 injection project ceased operation many years prior, and the reservoir is at 40% CO_2 saturation. Within the P&A well penetrating the (deep) storage reservoir, a vertical leakage pathway develops over time through a cement well plug (Scenario c in Figure 1). This leakage pathway does not encounter a thief zone until it reaches a shallow formation at 260 m depth, where the damaged cement is connected to the shallow aquifer establishing a lower pressure sink for upward leakage flow. As a result, reservoir fluids (CO_2 and brine) travel upward through the leakage pathway by buoyancy and overpressure forces and leak into the shallow formation.

Simulations for the scenario are conducted in two parts: (1) leakage from the deep reservoir, and (2) leakage into shallow formation via the degraded well. The first part provides an understanding of the relationship between leak rate and well permeability, and the second part provides an understanding of CO_2 plume growth in the shallow formation as a foundation for analysis and development of potential monitoring and intervention methods.

Signal of CO_2 Leakage from Deep Reservoir

The model domain for simulating leakage from the deep reservoir includes the leaky well and the shallow formation that is connected to the leaky well (Figure 2). The storage reservoir is modeled as a boundary condition that provides a constant overpressure of 5 bars (0.5 MPa) (above hydrostatic pressure), with a fluid mixture consisting of 40% of free-phase CO_2 and 60% of reservoir native fluid assuming no salinity. The well is modelled as a one-dimensional (1D) column. The simulation is done under non-isothermal conditions as the temperature difference between the reservoir and shallow formation is substantial and CO_2 fluid properties will change as pressure and temperature change during upward migration. The thermal conduction between the wellbore and the formation is modelled using a semi-analytical solution implemented in iTOUGH2.

At present, the ranges of permeability of actual degraded well cements are poorly constrained, and it is uncertain how the permeability will evolve over longer time scales [11,12]. As a simplification, a constant relatively high permeability is used in the simulation to represent degraded cement, with different permeabilities used to understand how cement permeability affects leakage rate.

The leak is assumed to occur for five years. Simulation results at the end of five years are summarized in Table 1. Note that these results will be affected by the capillary pressure and relative permeability characteristic curves used. For the van Genuchten curves used in this study, the time it takes for CO_2 to arrive at the shallow formation is very sensitive to the “n” parameter (n is related to pore-size distribution).

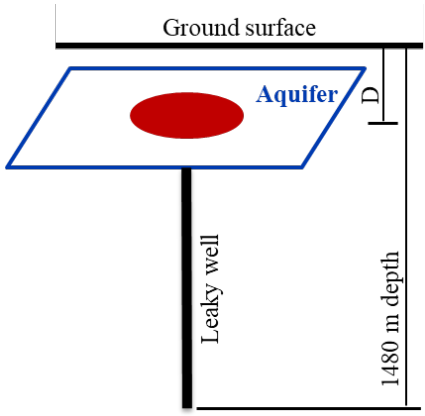

Figure 2. A schematic figure of the model for leakage from the deep reservoir.

Simulations indicate that cement permeability is the dominant factor controlling leakage rate, as expected. CO_2 arrives at the shallow formation in the gas phase with a density of about 55 kg/m^3. The leakage rate is about 0.08 kg/s for the largest well permeability used, which is comparable to some of the leak rates from the literature (e.g., [13]). The brine leak rate is 4.5e-4 kg/s for this scenario. These leak rates are passed on as input generation rate conditions to the shallow formation simulation.

The fluid temperature arriving at the shallow formation is very close to the shallow formation temperature, after the fluid experiences a number of non-isothermal processes (heat conduction with formation, cooling caused by gas expansion, etc.). Anomalous temperature is unlikely to be an effective indicator of upward leakage unless the leakage is very fast such as occurs in an open-well blowout scenario in which case expansion cooling has a large effect. For the scenario considered here, pressure and free-gas saturation in the plume provide effective signals of leakage in the shallow formation for potential detection.

Table 1. Simulation results for leakage rate from deep reservoir.

Scenario (results are shown for the point where CO_2 enters the aquifer)	k = 100 D	k = 10 D	k = 1 D
CO_2 arrival time at the shallow aquifer (day)	1	10	97
CO_2 leakage rate (kg/s)	0.08	0.008	8.e-4
Liquid (water) leak rate (kg/s)	4.5e-4	4.8e-5	4.7e-6
Highest overpressure (bar) [MPa]	0.6 [0.06]	0.1 [0.01]	0.08 [0.008]
CO_2 saturation	0.74	0.76	0.21
CO_2 extend (radius) at 5 years at the shallow aquifer (m)	191	77	23

CO_2 Leakage Into Shallow Aquifer

In this section, we describe the fate of the leaked CO_2 from the deeper reservoir under various scenarios. The primary goal of this activity is to constrain the various plume characteristics expected in the shallower overburden as a result of migration of CO_2 from a deep leakage source. For the purpose of modelling, we assume a homogeneous overburden with layers of low-permeability rock forming barriers or baffles. While idealized, this configuration is broadly representative of low-permeability barriers encountered in the path of leakage due to the heterogeneity in the Earth's subsurface. As a general rather than site-specific study, we formulate three different scenarios for the shallow subsurface permeability structure. The worst case for leakage upward from a shallow aquifer where CO_2 has accumulated following leakage up a well is the case where there is no barrier at all in the shallow overburden, and CO_2 is allowed to move upward freely, eventually reaching the ground surface. The results of this scenario are not only important as a worst-case analysis, but also gives an indication that the worst-case situation is not all that serious. The other two scenarios are cases in which we consider a single sealing layer in one scenario and two sealing layers in the shallow overburden in the other. Due to the existence of these barriers to flow, the upward migration of the CO_2 plume is slowed down because of lateral diversion, and the leakage flow rates are reduced considerably relative to the no-barrier case. The second goal for doing this analysis is to understand the effects of various uncertain parameters used in the simulations. We assume saturated overburden with associated dissolution of CO_2 occurring, without the existence of a vadose (unsaturated) zone. Also, the salinity at shallow depths is held at zero, and the simulations are isothermal. While the latter two assumptions are reasonable for the depths considered in the simulation, there is considerable learning to be achieved from simulations with a vadose zone [14]. Finally, the ongoing goal of this work is to use knowledge from the simulation study to formulate intervention scenarios for stopping the leakage or reducing the effects of leakage. Some of the subsurface intervention techniques such as hydraulic intervention [15] can be studied using simulations tailored to our model. However, without the knowledge of the leakage location or any surface or borehole seismic or electromagnetic (EM) data indicating the plume pathway, the location, depth, and optimal rate of water injection to mitigate plume impacts, not to mention uncertainty among parameters, add to the complexity of the system.

Figure 3 shows the reservoir model used for evaluating the three different scenarios discussed above. The simulations were performed with TOUGH2/ECO2N in a 2D radial- (r-z) coordinate system. The CO_2 and brine leakage rates obtained from the deeper reservoir are input as source terms in the bottom left-hand-side grid block, and simulated for the next 30 years. The reservoir extends to infinity in the radial direction, and is open to atmosphere at the top ground surface boundary. The vertical permeability is one order of magnitude smaller (1.e-13 m^2) than the horizontal permeability (1.e-12 m^2). When the sealing layer is modelled, the permeability is further reduced by a factor of 100 to model a cap rock effect. We incorporate a gap in this sealing layer which allows the plume to go through it and travel towards the ground surface.

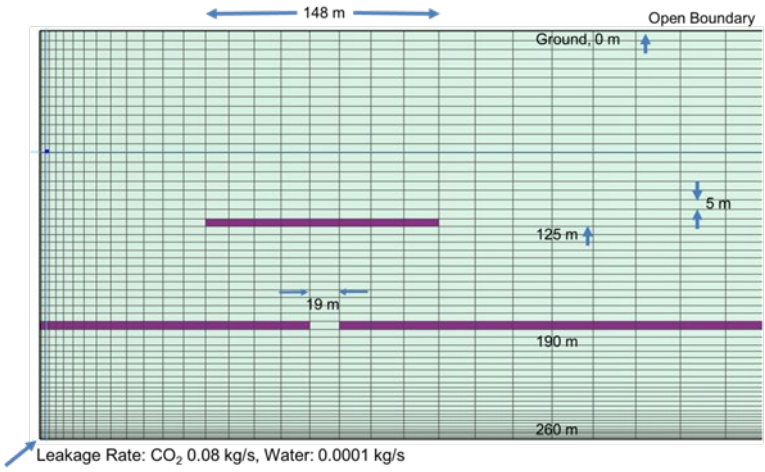

Figure 3. Reservoir simulation model showing the presence of two low-permeability layers. The bottom left-hand-side grid block is the leakage source at a depth of 260 m. There is no vadose zone in the current model. The right-hand side boundary conditions are fixed creating an effective infinitely acting radial boundary.

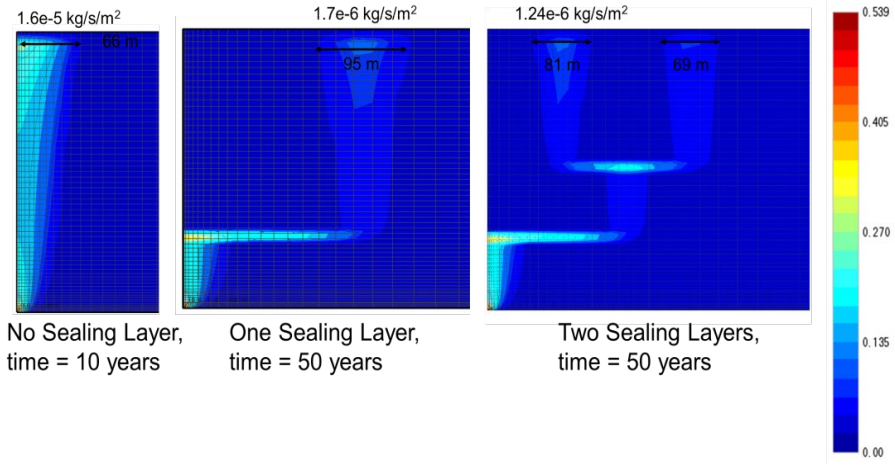

Figure 4. Plume movement for scenarios with no barriers, a single barrier and two barriers. The maximum z direction flux values are given for each case. The color bar shows the gas (CO_2) saturation. The saturation can vary between 0 and 1.

The initial conditions are set at 100% water saturation. We use the van Genuchten model for capillary pressure and monitor the rate of growth of the CO_2 plume for the three cases. Figure 4 shows the comparison of the three scenarios. We observe that when there is no sealing layer at all, CO_2 reaches the ground within 10 years. When a single barrier is introduced, we observe a reduction in the flux value by an order of magnitude, and the time taken to reach the ground increases by a factor of five. The plume extent is similar compared to the no-barrier case, but the CO_2 saturations are smaller. The

maximum flux value reduces only slightly in the scenario with the two-sealing-layers, but the plume splits into multiple (in this case, two) bodies, and remediation of each of these would require different hydraulic injection parameters. We also noticed during the simulation that the plume branch on the right-hand side grows much more slowly compared to the left branch which is closer to the leakage location. This behavior occurs for at least two reasons: (1) there is a larger effective driving force for the plume on the left-hand side because it is closer to the leakage source; (2) the grid is radial, meaning that CO_2 spreading radially distributes itself with higher saturations at smaller radii and lower saturations at larger radii. The relative permeability of CO_2 is higher at higher saturations, therefore plume rise will be faster closer to the center of the radial system. This phenomenon mimics the situation of multiple leakage plumes of differing intensity in real reservoirs. This is an important factor for an intervention, because curbing the larger plume might be more critical or even sufficient in some cases for stopping the leakage. The maximum CO_2 fluxes in the vertical direction are given on top of each case in Figure 4. These simulated average CO_2 fluxes at the ground surface are small and would be hard to detect. We note that in the context of leakage signal detection within a natural ecosystem, it was reported that a typical net ecosystem exchange (NEE) of CO_2 (CO_2 flux arising from plant respiration and soil/biomass processes) is on the order of 4.4×10^{-7} kg/s/m^2 [16] making the anomalous fluxes found here ~3-40 times larger than NEE, difficult to detect for unknown leakage locations and due to spatial and temporal variability.

So far, we have discussed the ideal reservoir simulation parameters and analysed the results based on that model. However, cement deterioration and associated effects on permeability over time might further impact the plume by constraining the gas movement due to reduced permeability resulting from carbonate deposition (e.g., in formations with reactive Fe/Mg-containing minerals) [17]. Our results presented here might be too conservative due to the constant leakage location and constant permeability assumption. Studies incorporating site-specific details of the subsurface will be needed for monitoring and remediation design at specific sites.

Comments on Intervention

Figure 5 shows the growth of the plume at different times during the 50 years of simulation for the scenario with two sealing layers. We observe that for the first 15 years, there is no trace of the plume in the upper 125 m below ground surface meaning surface observational approaches to monitoring for leakage would be ineffective. This implies that in order to detect leakage early, geophysical methods applied to the deep subsurface are likely needed. In addition, the evolution of the plume shown in Figure 5 suggests that it would be easier to control the plume by hydraulic methods if the leak were caught early when the plume was smaller and more localized. A comparison study of the cases when water injection for hydraulic control starts earlier than 15 years after leakage begins, as opposed to a later time, would be useful in analysing the cost and efficiency of remediation.

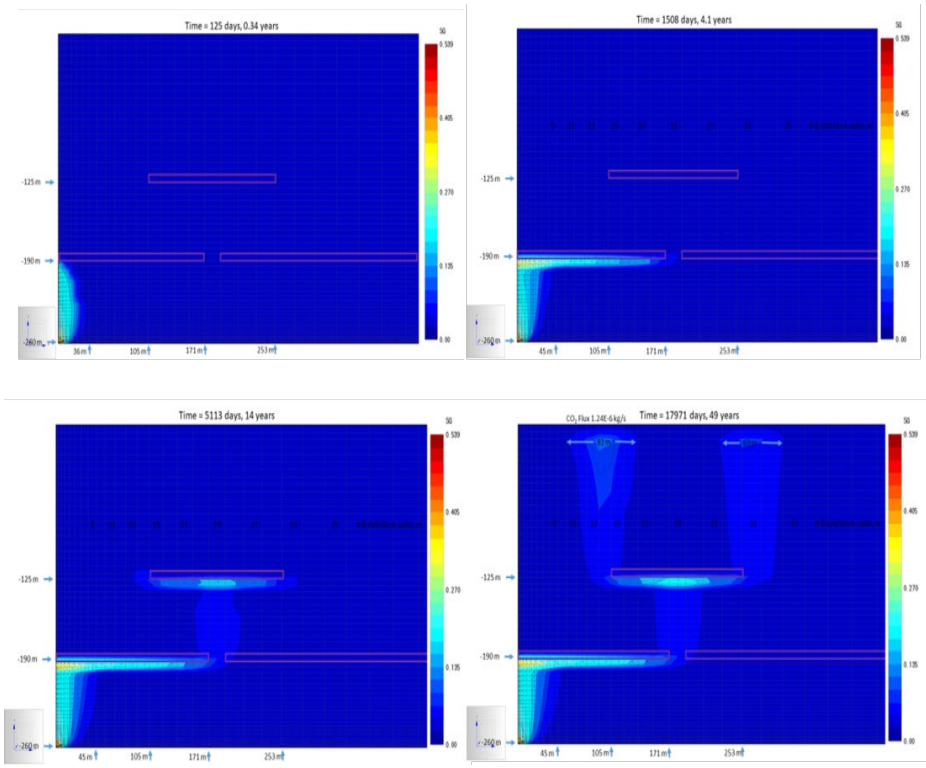

Figure 5. CO_2 saturation at different times from the start of simulation over 50 years. The color bar shows the gas (CO_2) saturation. The saturation can vary between 0 and 1.

The changes in pressure and saturation values in the simulation are potential signals for detecting leakage by geophysical monitoring techniques, as discussed in the next section. The insights provided by monitoring are extremely important for designing an effective intervention and remediation system. First, monitoring is needed to locate to the extent possible the leakage source; direct remediation methods involving gel injection and well-plugging cannot be used if the leakage location is not known. For plumes with less-well-defined sources but that can be located with some certainty,

intervention using water injection is one of the best studied and potentially most cost-effective methods.

Figure 6 shows the locations of some potential water injector wells that might be useful in arresting the plume movement at early and late times for the leakage scenario we simulated. It is important to note that during water injection, the leaking well will continue to supply CO_2 to the overburden because the leak location is most likely to remain unknown and therefore not amenable to well-plugging (e.g., with methods such as gel technology). In general, the most important factor for any kind of intervention is the ability to locate the leakage source. If that is not possible, then the plumes can potentially be addressed through hydraulic controls (e.g., plume steering by strategic injection/withdrawal of water at certain locations, which will require site-specific characterization, modeling and engineering to design and evaluate for technical feasibility).

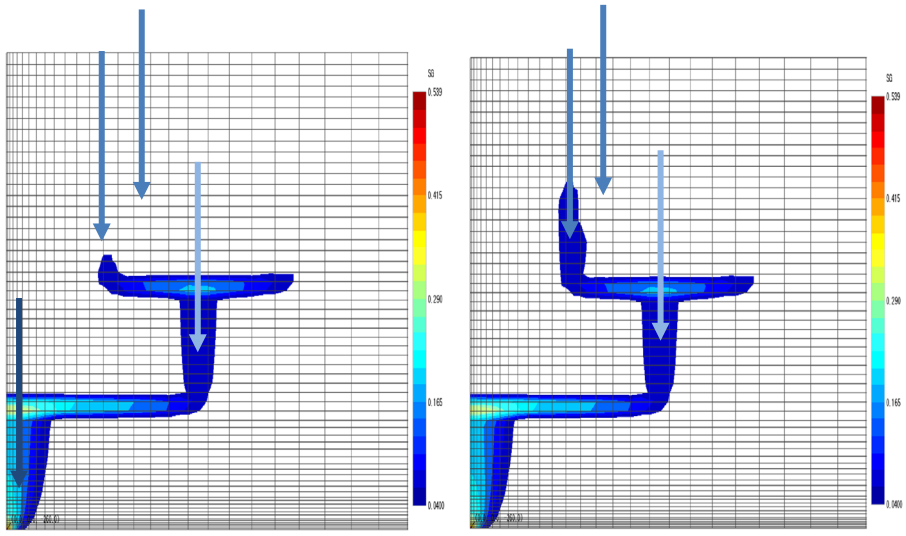

Figure 6. CO_2 leakage plumes with arrows showing the locations of the injection wells at 15 years and 20 years.

So far, we discussed the ideal reservoir simulation parameters and analysed the results based on that.

Monitoring and Detection

Depending on the injected CO_2 plume size and saturation, and the location and characteristics of the CO_2 leakage plume of interest (e.g., deep vs. shallow, dispersed vs. confined to a narrow flow channel), different monitoring methods may be applicable. In this project, we focus on the applicability of electrical and seismic methods through sensitivity analysis of systems analogous to the simulated leakage plumes. Seismic monitoring is initially assessed by assuming a minimum CO_2 saturation necessary for detection (5%), and plotting the extent of this saturation threshold at various times for the simulated leakage scenarios. Surface and borehole electrical methods are evaluated for applicability to monitoring of CO_2 leakage using simplified models with a focus on leakage detection in shallow aquifers, assuming that deeper leakage plumes have been identified.

Monitoring Using Electrical Methods

When CO_2 leaks from a well in the subsurface at a high enough rate that free-phase CO_2 persists, it forms partially saturated CO_2 plumes of a finite size that change the subsurface resistivity resulting in a resistivity contrast relative to the baseline formation resistivity. The goal of monitoring using electrical methods is to identify a local variation in resistivity relative to the background response, and if an anomalous signal is present, to locate a possible CO_2 plume.

The resistivity of CO_2 is high, similar to other gases such as air. The resistivity of brine decreases with increased total dissolved solids (TDS). In brine-bearing formations that are below and hydrologically separated from drinking water reservoirs, TDS is in general high (10,000 parts per million (ppm) and up, where for reference, 1 ppm = 1 mg of salt in 1 litre of water), which results in a low fluid resistivity, while in drinking water aquifers TDS is low (600 ppm or less), and the fluid resistivity is higher.

The electrical resistivity of the subsurface is highly sensitive to changes in formation porosity, pore fluid resistivity, and fluid saturation. A wide range of empirical relations exists for linking formation and electrical properties. Commonly used is Archie's Law [18], which describes the electrical resistivity (ρ_b) of sedimentary rocks as a function of water saturation (S_w), porosity (φ), and pore-fluid resistivity (ρ_w),

$$\rho_b = a\phi^{-m}\left[{}^{\rho_w}/_{S_w^n}\right]$$

where a is tortuosity, and m and n are constants with $1.8 < m < 2$ and $n \cong 2$.

As CO_2 leaks into the formation at a sufficiently high rate, the brine is replaced by free-phase CO_2, which results in a non-zero CO_2 saturation. Figure 7 shows the rock bulk resistivity (ρ_{rock}) as a function of CO_2 saturation (S_{CO2}) for the formation with brine resistivity (ρ_{brine}) of 0.33 Ohm-m and 25% porosity. If there are no chemical reactions between the CO_2, brine and rock, CO_2 presence results in resistivity increase. If subsurface conditions support dissolution of CO_2, this causes an increase in TDS which results in a decrease in resistivity.

As seen from Figure 7 the detectability of saturation changes below 0.2 using resistivity methods decreases, and would be possible only with very high-quality (low-noise) acquired data.

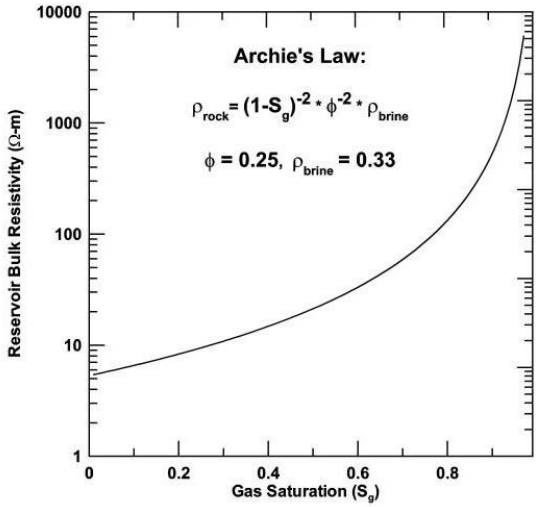

Figure 7. Reservoir bulk resistivity (ρ_{rock}) as a function of gas saturation ($S_g = 1 - S_w$) for a reservoir with brine resistivity equivalent to sea water (ρ_{brine} = 0.33 Ω-m) with 25% porosity [19].

Electrical resistance tomography (ERT) is an indirect method for visualizing the movement of fluids in porous media that requires the use of an inversion algorithm to convert raw measurements of electrical resistance to a tomographic image (resistivity or concentration) of a fluid plume. ERT spatial resolution is a complex function of numerous factors (e.g., electrode layout, measurement schedule, data quality, imaging algorithm, resistivity distribution). Uncertainty in ERT tomographic images and ERT-derived CO_2 saturation may come from many sources, such as data noise, electrode degradation, electrode location errors, regularization parameters, numerical and model errors, pre-processing procedures, assumptions in Archie's equation, and choice of inversion constraints.

For borehole arrays, if long-term monitoring is required, electrodes need to be permanently installed in the boreholes within a depth interval at least as great as the distance between boreholes. The image resolution also depends on the distance between boreholes. Electrode configurations and intervals between repeated measurements should be selected based on forward modelling and analysis of models that capture complexity of the geology at the monitoring site. The advantage of cross-hole ERT is that the subsurface can be monitored in detail because of measurements proximity to the source or target of interest. The disadvantage of this array is its very limited areal coverage, and thus it is not suitable for monitoring leakage over large areas. For this purpose, borehole-to-surface or surface measurements are more appropriate.

In this study, we assume a model based on the CO_2 plume at 125 m depth as in the flow simulations described in the previous section (Figure 5). A CO_2 saturation plume is modelled as a resistive body, and a dissolved CO_2 plume is modelled as a conductive body. A background resistivity of 100 Ohm-m was used in all models. Resistivity contrasts between the background and the anomalous bodies used as proxies for CO_2 plumes were based on flow and geophysical simulations done for another project [20]. Example values of bulk resistivity for different saturation values vary depending on whether the saturation creates a conductive or resistive anomaly as shown in Table 2.

Table 2. CO_2 saturation and resistivity values for conductive and resistive bodies with 100 Ohm-m background.

CO_2 saturation	Resistivity (Ohm-m)
Conductive body	
0.5	25
0.2	50
0.1	80
0.05	90
Resistive body	
0.5	400
0.2	155
0.1	125
0.05	110

Modeling results described below illustrate resolution levels and capability of borehole and surface ERT techniques for relatively shallow leaks, and identify parameters that are important in a design of an effective monitoring array. An actual plume characterization and monitoring strategy would be a multi-step process developed based on available site information, and how it was determined that there is a leak. It is very likely that if the leaky well location were unknown, a 3D surface geophysical survey would be done first to localize the plume, and then based on the depth and size of the plume and the desired resolution, an appropriate monitoring array would be implemented.

Figures 8 and 9 show simulation results for 2D borehole ERT for conductive and resistivity bodies, respectively, serving as proxies for CO_2 plumes at a depth of 125 m. Three boreholes with a separation of 110 m, and electrodes from surface to the depth of 300 m every 10 m (black symbols) are used for these simulations. A maximum decrease in an apparent resistivity that would be calculated from measured potential and current as a response to conductive targets shown in Figures 8a-8d was 80%, 60%, 20%, and 8% respectively. A maximum increase in the apparent resistivity for resistive targets shown in Figures 9a-9d was 60%, 25%, 13%, and 6%, respectively. All these changes are considered to be above the noise in typical field measurements, and therefore detectable with borehole ERT measurements. The lateral extent of the anomalous zone is resolved better than the depth extent, but overall the anomaly location and shape are well characterized. Similar results would be obtained for a deeper target if the borehole electrode array were extended deeper.

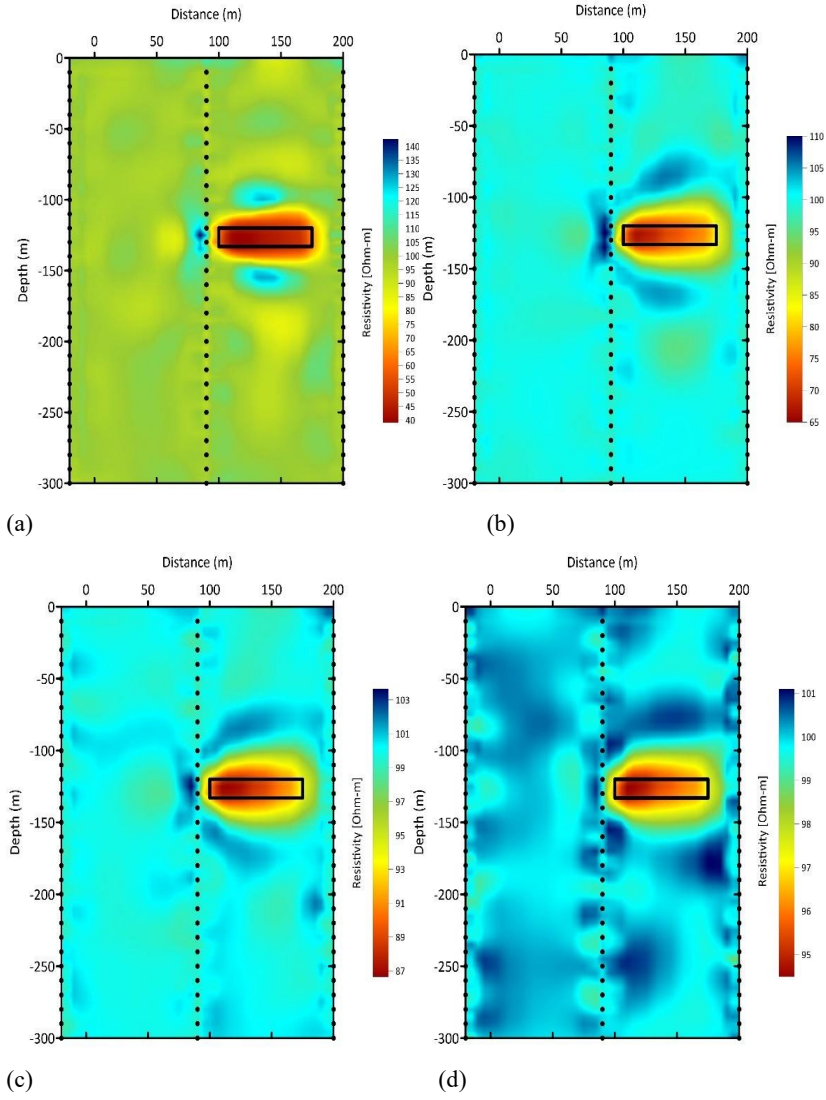

Figure 8. 2D ERT inversion for anomalous conductive bodies representing dissolved CO_2 plumes with CO_2 saturations of (a) 0.5, (b) 0.2, (c) 0.1, and (d) 0.01. Black symbols indicate electrode positions in three boreholes.

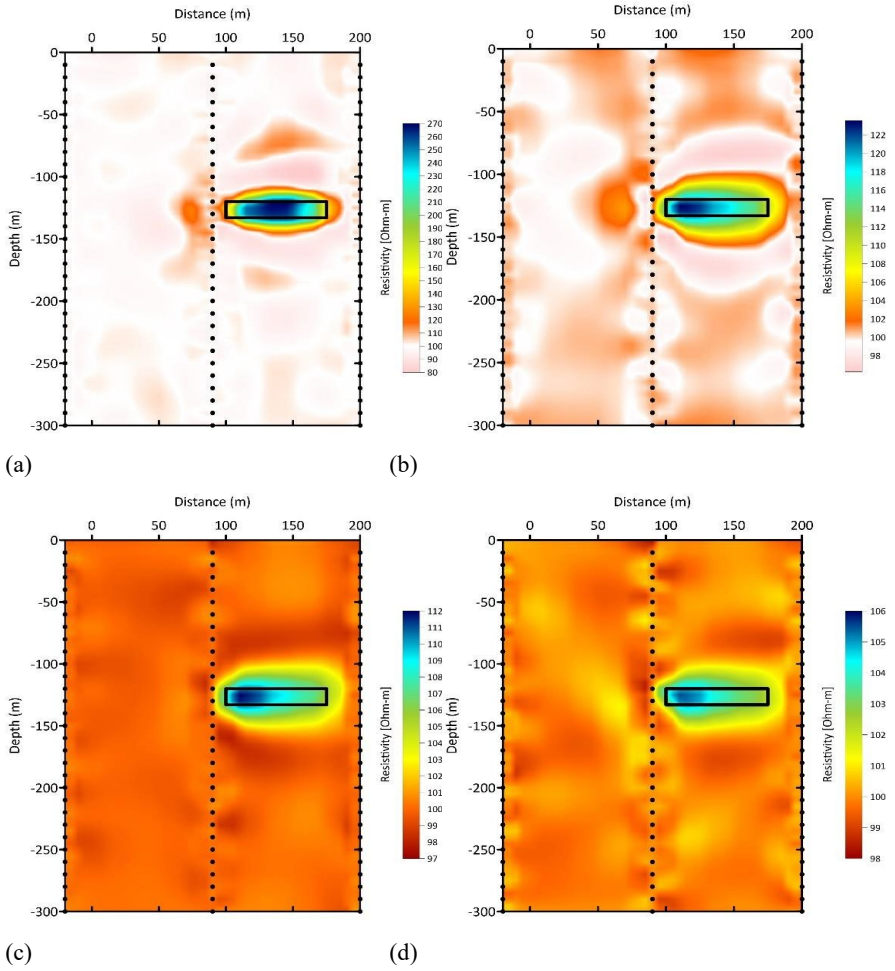

Figure 9. 2D ERT inversion for anomalous resistive body (CO_2 saturation plume) with CO_2 saturation of (a) 0.5, (b) 0.2, (c) 0.1, and (d) 0.01. Black symbols indicate electrode positions in three boreholes.

Figure 10 shows results for anomalies with more complicated shapes with 0.2 CO_2 saturation again for both CO_2 saturation plumes and dissolved CO_2 plumes. These bodies produce 30% apparent resistivity changes. The inversion locates the anomalies reasonably well in both cases. The results also show that a distance of an anomaly to a monitoring well plays a role in resolving the properties of the anomaly.

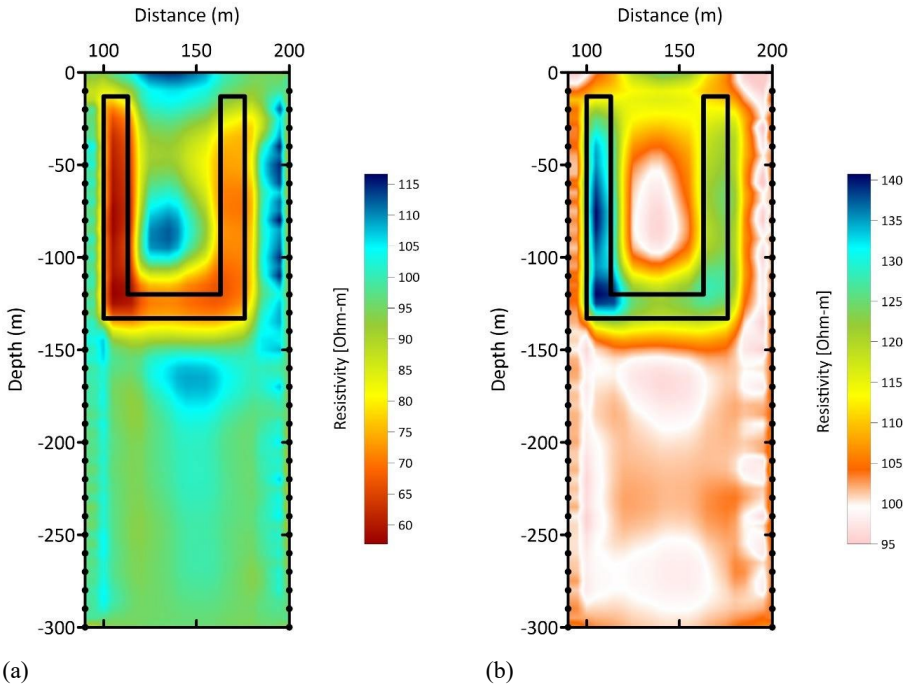

Figure 10. 2D borehole ERT inversion for (a) conductive and (b) resistivity anomalies caused by 0.2 CO_2 saturation. Black symbols indicate electrode positions in two boreholes.

Figure 11 illustrates the importance of an optimal borehole array to resolve a structure of interest. The boreholes are 220 m apart in this model. The resistive body represents CO_2 saturation of 0.5. As the distance between the anomaly and the monitoring array increases the resolution decreases. Figure 11a illustrates the highest sensitivity to the anomaly, while Figure 11c shows that the anomalous signal is so small that the inversion is unable to resolve the location of the anomaly. The results for a conductive body with the same saturation (not shown) are worse, as only the configuration of Figure 11a is able to locate the body.

Surface ERT offers more flexibility and an ability to monitor larger areas, but with a decreased resolution or sensitivity to deep targets. In short, deeper targets must be larger in order to be detected using surface monitoring arrays. Figures 12 and 13 show results from surface ERT for conductive and resistivity bodies, respectively, at the depth of 125 m. The maximum changes in apparent resistivity for Figures 12a and 12b and Figures 13a and 13b models were 10% and 5%, and 11% and 4%, respectively. The lower values are at the detection limit; therefore, a plume of the same size and at the same depth with CO_2 saturation smaller than 0.2 would produce changes that would be within

expected noise variations or numerical errors associated with inversion and would not be detectable with surface measurements. As with well-based arrays, the lateral extent of both bodies was resolved very well, while there was a high uncertainty in the thickness of the bodies.

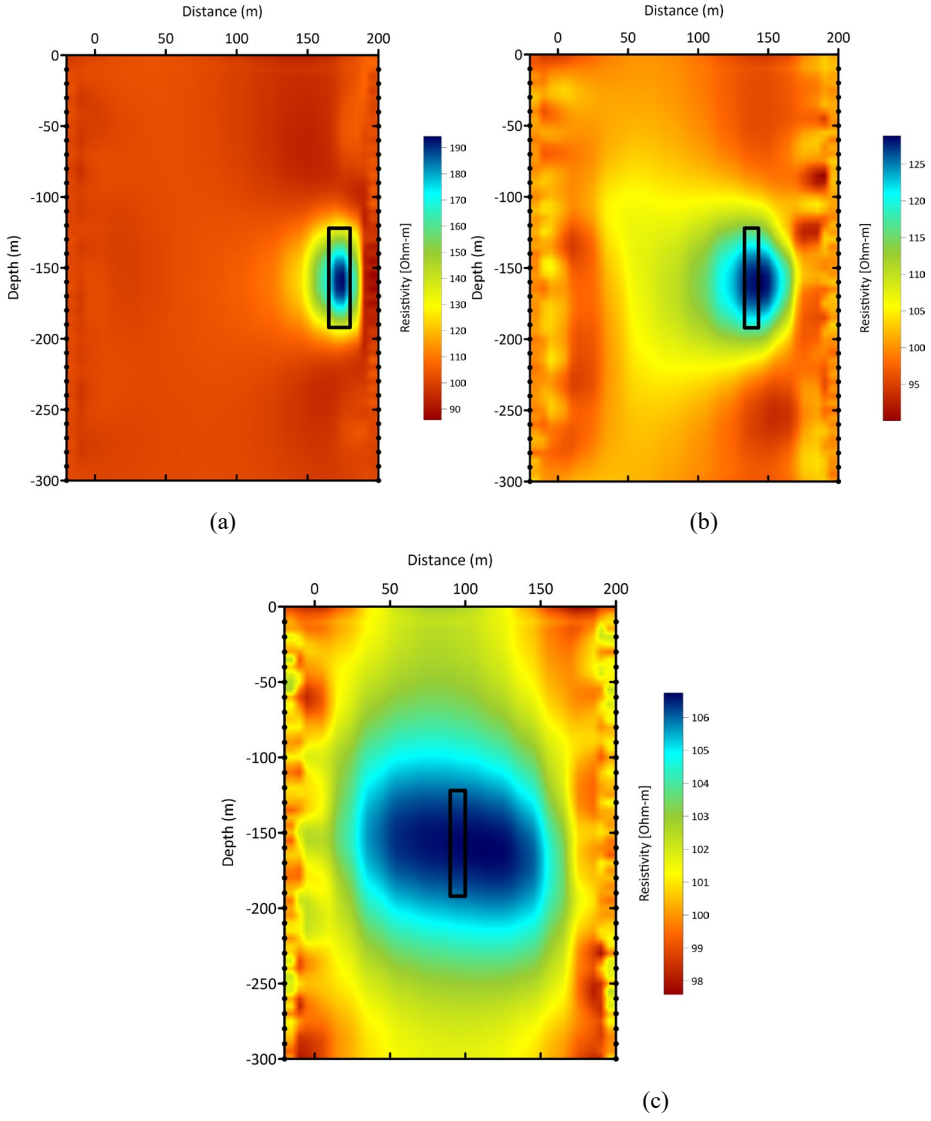

Figure 11. Structure resolution of resistive body as a function of the distance to the monitoring array depicted by the black symbols along two wells on the left and right-hand sides of the figures.

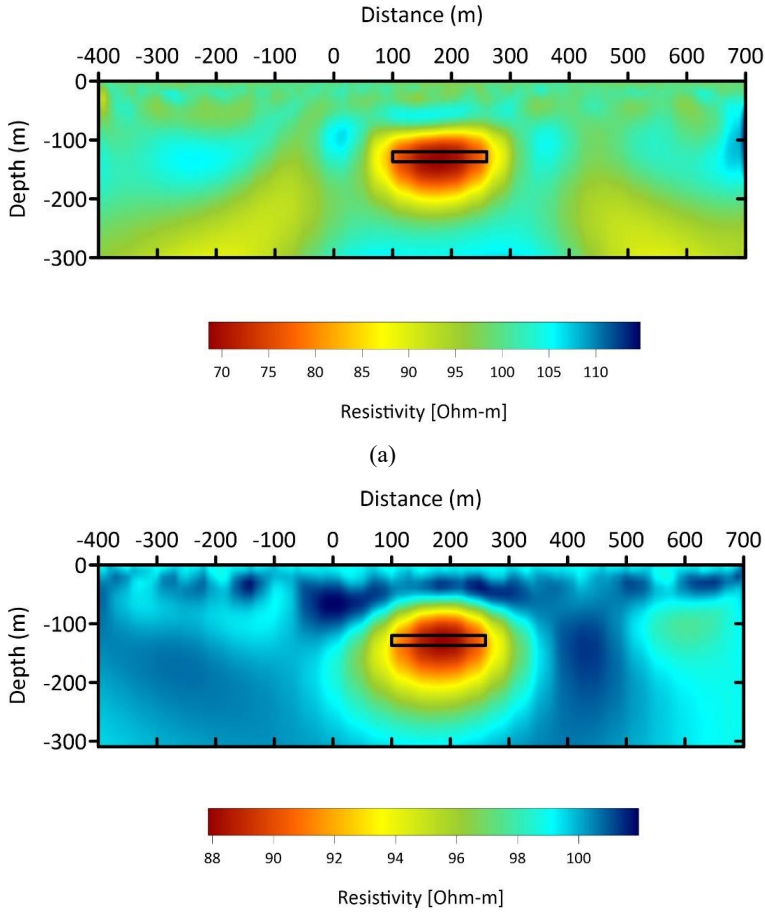

Figure 12. 2D surface ERT inversion results for a conductive horizontal structure at the depth of 125 m for (a) 0.5 and (b) 0.2 CO_2 saturations.

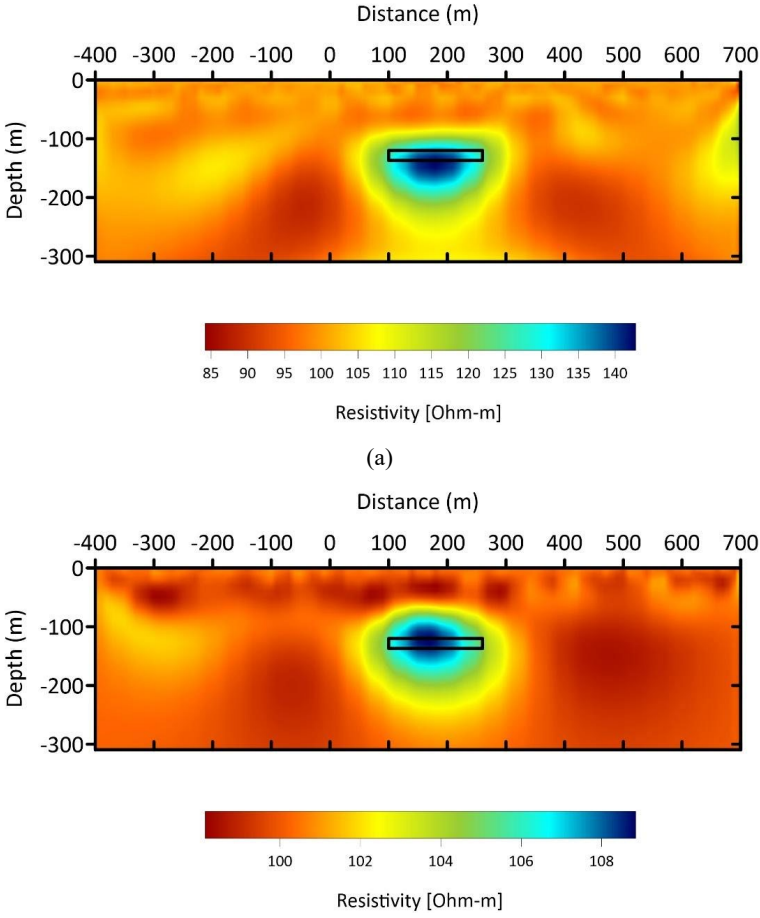

Figure 13. 2D surface ERT inversion results for a resistive structure at the depth of 125 m for (a) 0.5 and (b) 0.2 CO_2 saturations.

Figures 14 and 15 show results for more complicated structures with CO_2 saturation of 0.2 and 0.1 for both conductive and resistive bodies. Changes in apparent resistivity for Figures 14a and 14b, and Figures 15a and 15b models were up to 35% and 10%, respectively. Surface measurements were able to identify shallow portion of the leaks reliably, while the depth extent was not resolved very well.

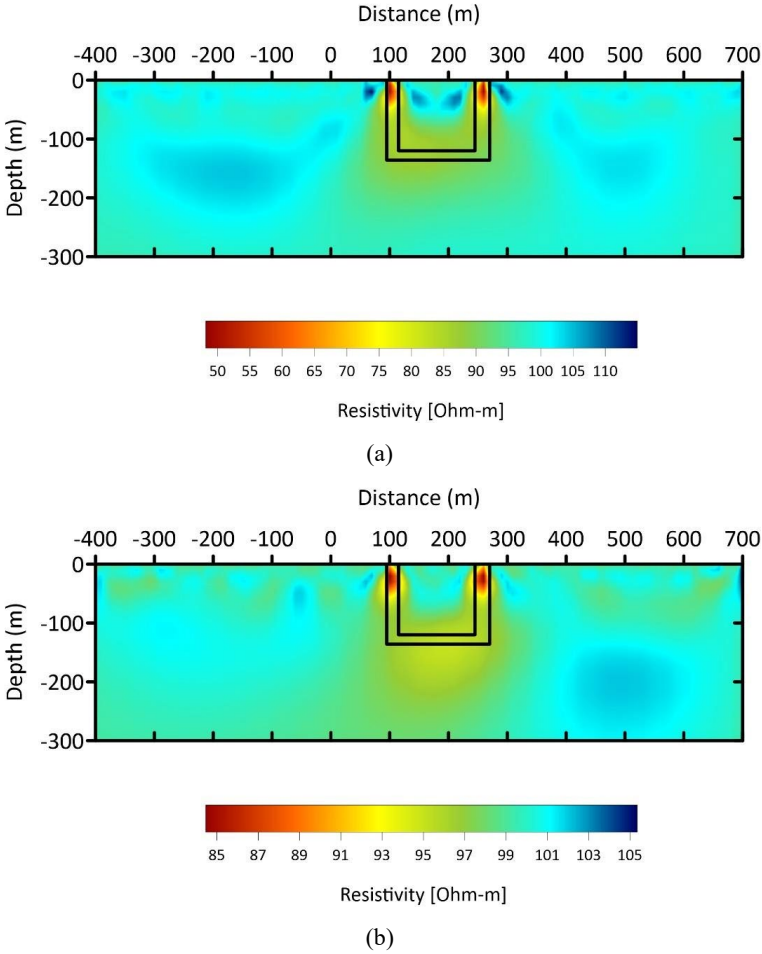

Figure 14. 2D surface ERT inversion results for a conductive structure for (a) 0.2 and (b) 0.1 CO_2 saturation.

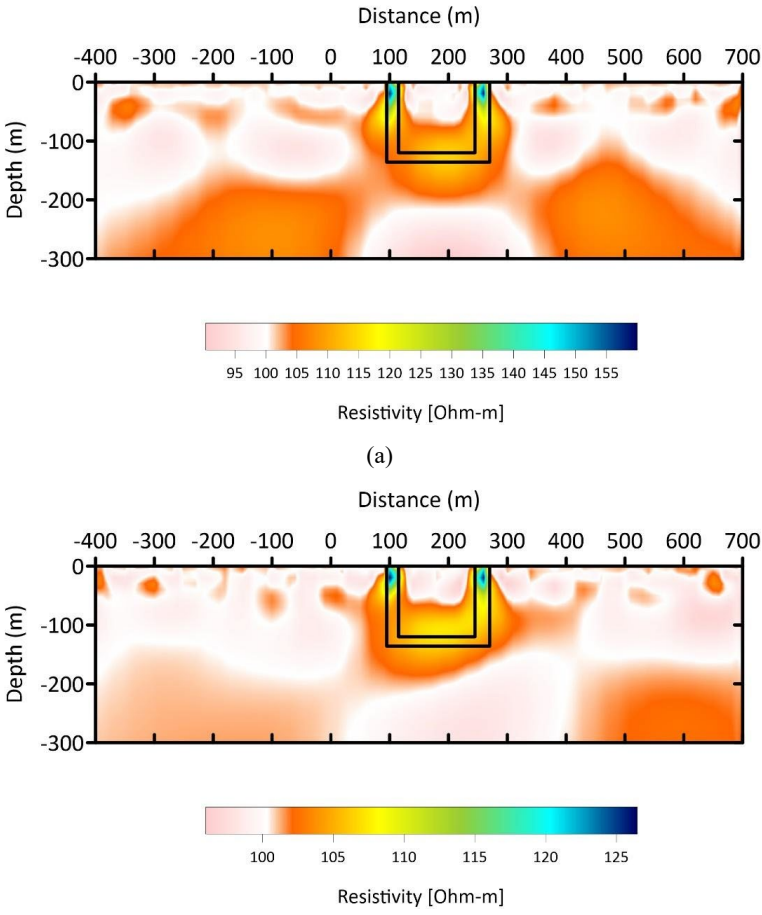

Figure 15. 2D surface ERT inversion results for a resistive structure for (a) 0.2 and (b) 0.1 CO_2 saturations.

Detection capabilities, limitations, and parameters that are important in designing borehole and surface ERT monitoring arrays were demonstrated using simplified models. For complex scenarios presented in the previous section, a monitoring network would be designed based on 3D simulations, and would most likely also include borehole-to-surface configurations that would provide more lateral and vertical resolution.

Seismic Monitoring Assessment

For seismic monitoring of CO_2, the bulk modulus, K, is perhaps the most important elastic modulus because of its sensitivity to pore fluid. The P-wave seismic velocity (Vp) of an isotropic rock volume is a function of K, and for fluid saturated rocks the bulk modulus K_{sat} is modified by the saturating fluids in the rock pore space, including CO_2. Understanding changes in Vp due to CO_2 saturation typically follows the work of Gassmann, as summarized, for example, by Smith, *et al* [21]. The

fundamental relationship in Gassmann fluid substitution expresses the bulk modulus of a saturated rock, K_{sat}, in terms of the 'dry frame' bulk modulus, K*, the bulk modulus of the minerals making up the rock frame, K_0, the bulk modulus of the pore fluid, K_{fl}, and the rock porosity, ϕ. The result of this formulation is a relationship between Vp and CO_2 saturation of the form shown in Figure 16 for the Gassman+Reuss (blue) curve. While other petrophysical models shown in Figure 16 are appropriate in specific cases, a standard porous aquifer monitored at typical seismic wavelengths is expected to follow Gassman+Reuss.

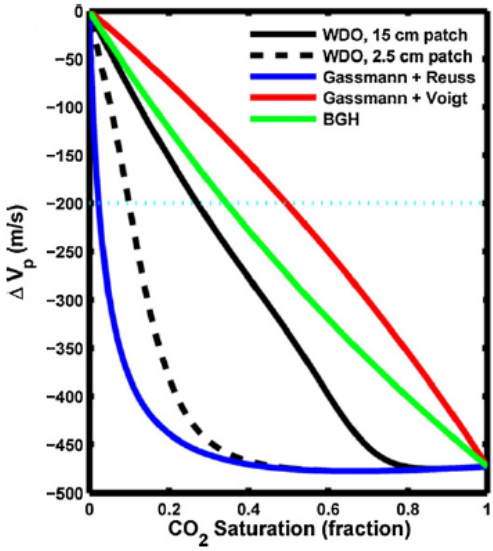

Figure 16. Change in P-wave velocity (Vp) as a function of CO_2 saturation in a typical high porosity brine aquifer for a range of petrophysical models. The Gassmann+Reuss (blue) curve is the conventional assumption for long wavelength seismic data. WDO is the White-Dutta-Ode model, and BGH is the Biot-Gassmann-Hill model. Data using reservoir properties from the Frio formation. Taken from Figure 8 [22].

The specific values of Vp are dependent on the matrix and brine properties, along with P-T conditions, however the shape of the Gassmann-Reuss curve is typical and demonstrates that the major change in Vp is for 5-10% CO_2 saturation. Since full-physics modeling of seismic wave propagation is beyond the scope of this study, we use a simple "cutoff" saturation to consider seismic detection of the scenarios in our study. We use a value of 5% saturation to delineate the volumes of CO_2 which could be detected by seismic monitoring at various time steps in our scenarios. If different rock properties or different rock physics are impacting the response, then the size of the detectable plume will vary. We consider the response of the single and double sealing layer scenarios. Figure 17 (a through f) shows the evolution of detectable leakage for the single sealing layer scenario from 0 through 20 years.

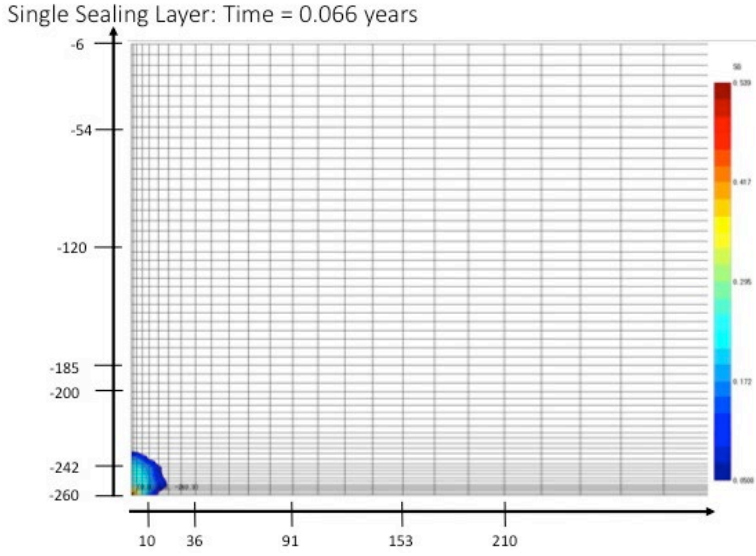

(a)

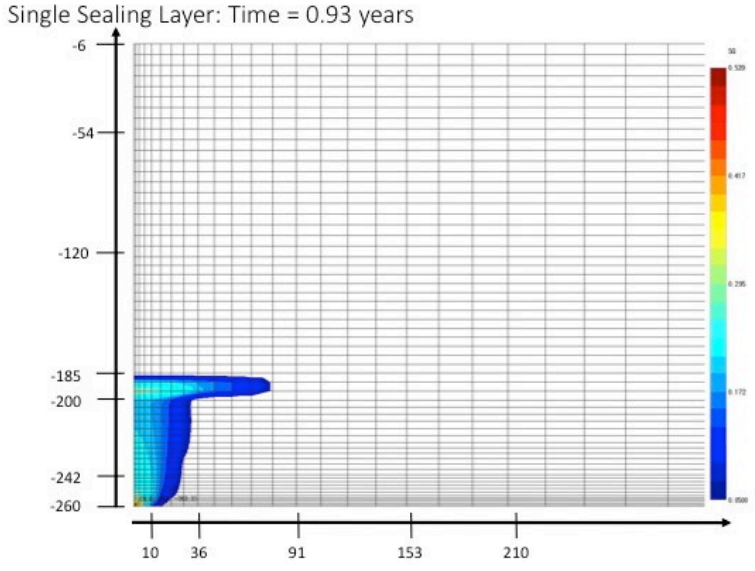

(b)

Figure 17 a and b

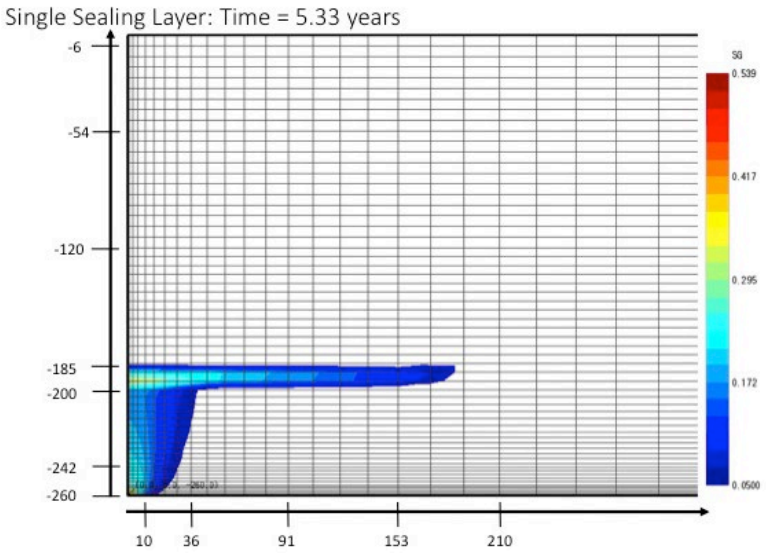

(**c**)

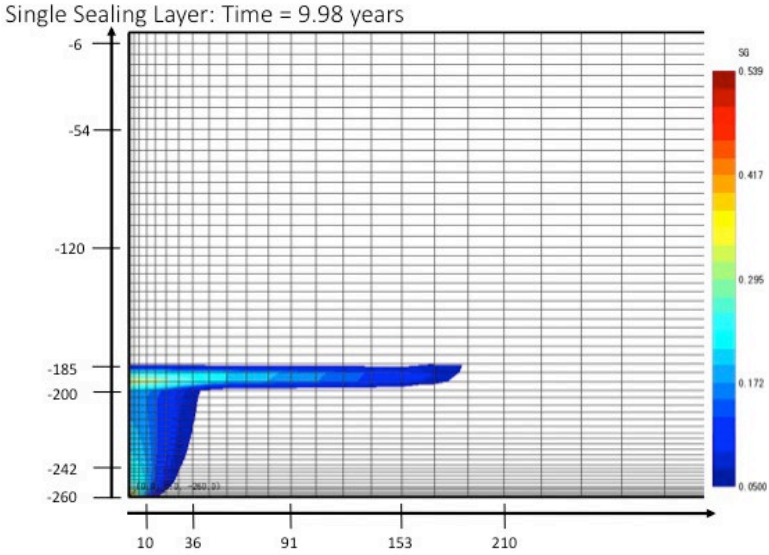

(**d**)

Figure 17 c and d

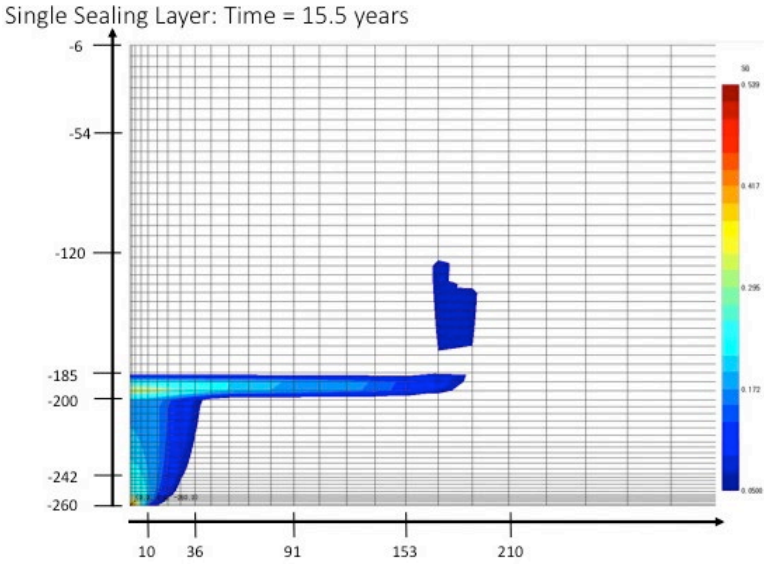

(**e**)

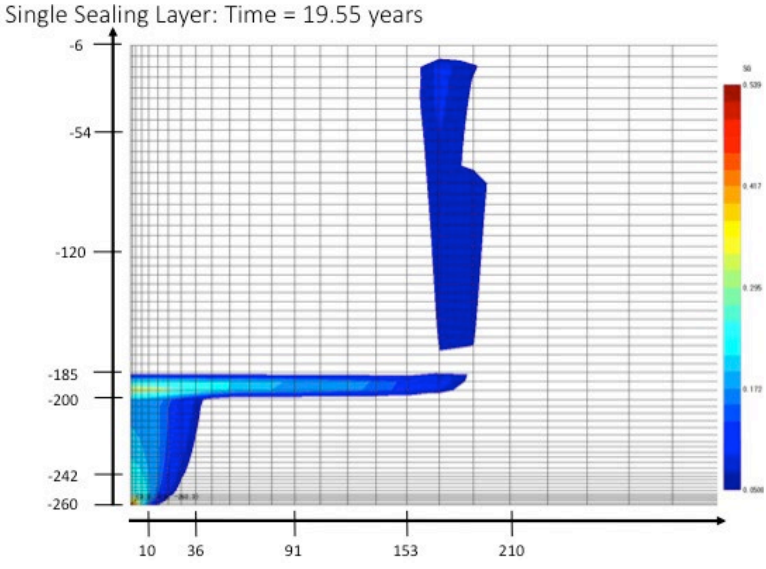

(**f**)

Figure 17. CO_2 plume with saturations greater than 5% for specific times of a) 0.07 years; b) 0.93 years; c) 5.3 years; d) 9.98 years; e) 15.5 years; and f) 19.55 years. Horizontal and vertical distance labels are in meters and are not linear due to varying cell width.

We consider time-to-detection, defined as the time at which the smallest-size plume is detected. However, with the complex plumes in these scenarios we can also consider the time-to-detection of various components of the plumes. For the single sealing layer, seismic detection is interpreted as possible after 1 year (Figure 17b) and likely after 5 years (Figure 17c). The secondary vertical plume detection is possible after 15.5 years (Figure 17e) and likely after 19.5 years (Figure 17f).

Figure 18 (a through f) shows the evolution of detectable leakage from 0 through 50 years for the two-sealing layers scenario. We interpret these results as detection is possible after 2 years for the first layer (horizontal plume), 11 years for the second layer, 20 years for the closer secondary vertical plume and 50 years for the farther secondary vertical plume. In general, vertical plumes will be best detected by vertical seismic profile (VSP) data using borehole sensors and offset sources; while the horizontal plumes could be detected by either VSP or surface seismic acquisition geometries. The relatively small horizontal extent of the vertical plumes is what limits their detection with surface seismic acquisition. Horizontal plumes are generally better imaged by surface seismic if they have enough lateral extent (e.g., greater than 100 m). In general, any seismic detection is most likely using time-lapse data with a baseline survey before leakage.

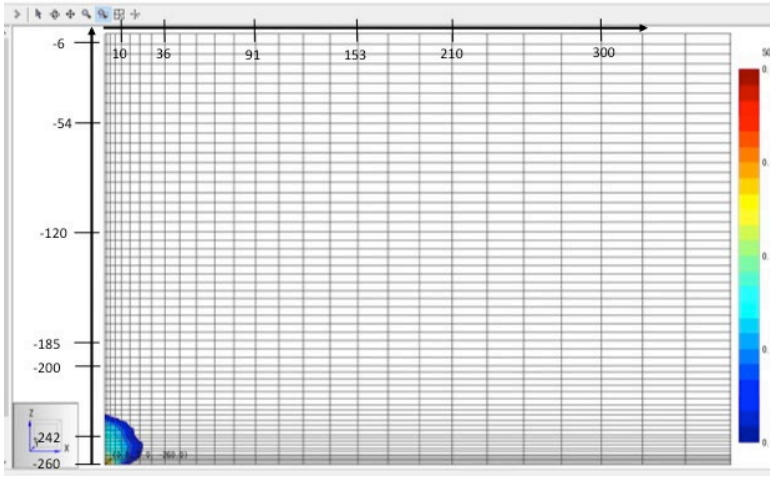

(**a**)

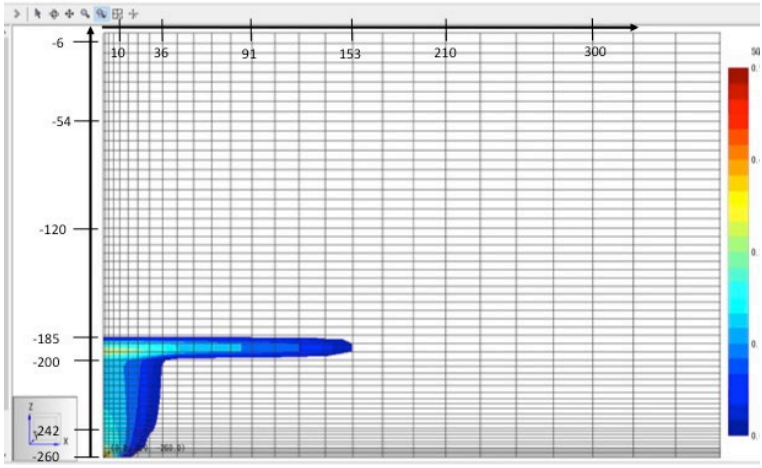

(b)

Figure 18 a and b

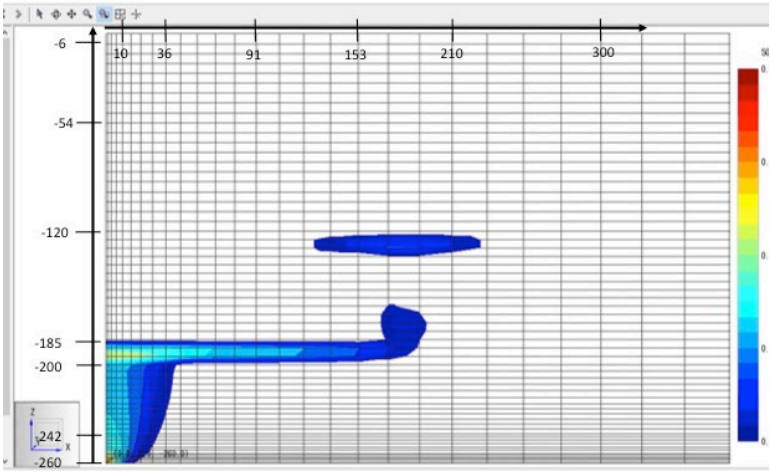

(c)

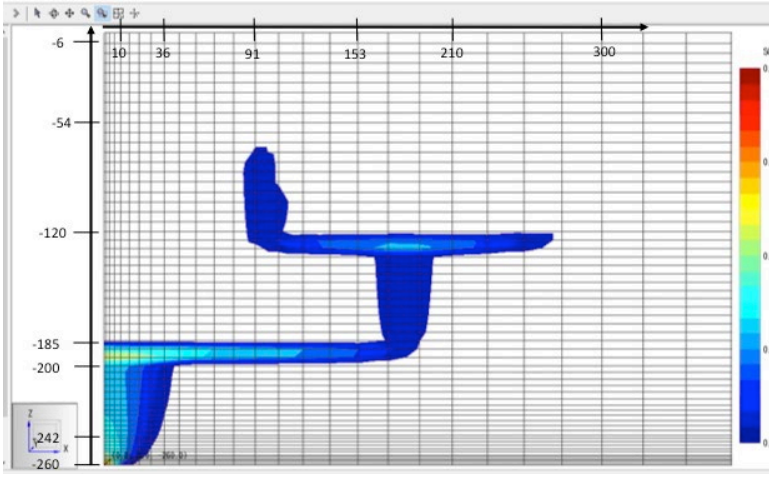

(d)

Figure 18 c and d

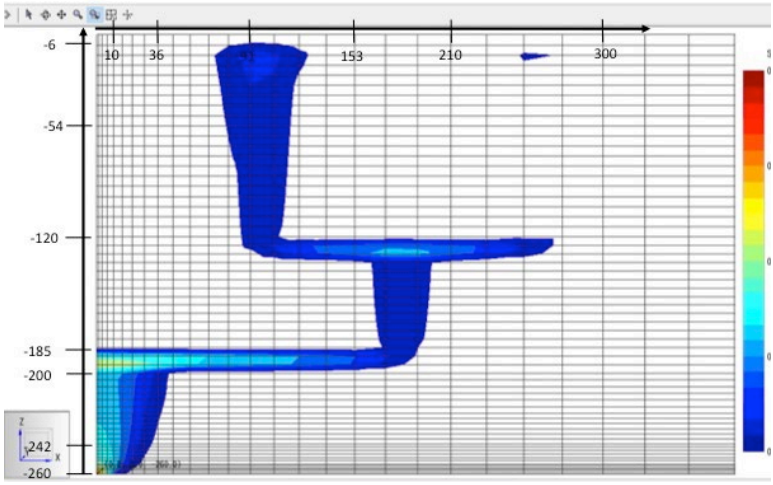

(e)

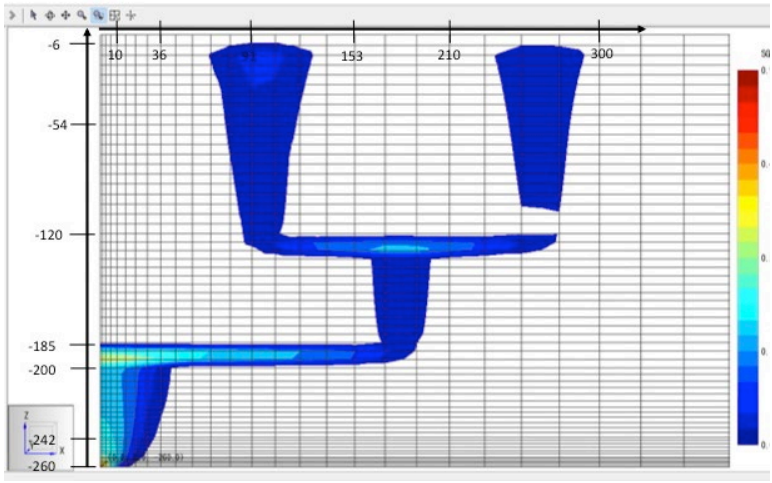

(f)

Figure 18. CO_2 plume with saturations greater than 5% for specific times of a) 0.09 years; b) 2.09 years; c) 11.3 years; d) 20.3 years; e) 32.0 years; and f) 49.1 years. Horizontal and vertical distance labels are in meters and are not linear due to varying cell width.

CONCLUSIONS

In this study, we developed a scenario for a prototypical plugged and abandoned (P&A) well with degraded cement, in which reservoir fluids including CO_2 and brine travel upward from the deep storage reservoir, through a leakage pathway within a well cement plug, and leak into the shallow formation. We performed numerical simulations of coupled deep and shallow leakage of CO_2. The characterized CO_2 plume in the shallow aquifer was used as the basis for a discussion of potential monitoring approaches. Assuming an initial detection of a CO_2 plume in the shallow aquifer, we demonstrated the effectiveness of electrical monitoring at different CO_2 saturations, which serves as the basis for future work. For seismic detection we used a somewhat arbitrary plume saturation of 5%, guided by petrophysical theory and conventional aquifer properties, to estimate the time to detection for seismic methods for the single and double sealing layer scenarios, and for the various component plumes in these scenarios. These times range from 0.1 to 50 years for components of the complex leakage plumes. At various times either surface seismic or vertical seismic profile acquisition geometries are indicated for imaging the detectable plumes. Recognizing that seismic methods are sensitive to small changes in CO_2 saturation which are difficult to detect by electrical methods, while the electrical methods are sensitive to larger CO_2 saturation changes when seismic methods lose the sensitivity suggests that an optimal monitoring approach would include a combination of both techniques. Future work should be aimed at developing full forward models of seismic and electromagnetic (EM) monitoring for the leakage scenarios, which can then be used to assess the potential of improved quantitative assessment using joint seismic-EM inversion.

ACKNOWLEDGEMENTS

This work was supported the CO_2 Capture Project Joint Industry Program. Work at Lawrence Berkeley National Laboratory was also supported by the U.S. Department of Energy under Contract No. DE-AC02-05CH11231, and work at Stanford University was also supported by Stanford University.

REFERENCES

1. Agarwal *et al*, (2015) Overview of Assessment of Leakage Detection and Intervention Scenarios for CO_2 Sequestration, in *Carbon Dioxide Capture for Storage in Deep Geologic Formations – Results from the CO_2 Capture Project, Vol 4 CCS Technology Development and Demonstration Results (2009-2014)*, Gerdes, K. (ed), CPL Press, 2015.
2. Conley, S., Franco, G., Faloona, I., Blake, D.R., Peischl, J. and Ryerson, T.B., (2016) Methane emissions from the 2015 Aliso Canyon blowout in Los Angeles, CA. *Science*, p.aaf2348.
3. Pan, L., Oldenburg, C.M., Freifeld, B.M., and Jordan, P.D., (2018) Modelling the Aliso Canyon underground gas storage well blowout and kill operations using the coupled well-reservoir simulator T2Well, *J. Petrol. Sci. and Eng.*, *161*, p. 158-174.
4. Freifeld, B., Daley, T., and Cook, P., Modular Borehole Monitoring an Integrated Deployment Package Development, in *Carbon Dioxide Capture for Storage in Deep Geologic Formations – Results from the CO_2 Capture Project, Vol 4 CCS Technology Development and Demonstration Results (2009-2014)*, Gerdes, K. (ed), CPL Press, 2015.
5. Agarwal, A., Aird, T., Benson, S., Cameron, D., Druhan, J., Harris, J., Maher, K., Reece, J., Vialle, S., and Zahasky, C., Overview of Assessment of Leakage Detection and Intervention Scenarios for CO_2 Sequestration, in *Carbon Dioxide Capture for Storage in Deep Geologic Formations – Results from the CO_2 Capture Project, Vol 4 CCS Technology Development and Demonstration Results (2009-2014)*, Gerdes, K. (ed), CPL Press, 2015.

6. IEA Greenhouse Gas R&D Programme Report, (2009) "Long Term Integrity of CO_2 Storage – Well Abandonment," https://hub.globalccsinstitute.com/sites/default/files/publications/98891/long-term-integrity-co2-storage-well-abandonment.pdf
7. International Energy Agency Greenhouse Gas R&D Programme (IEAGHG), (2012) "Wellbore Integrity Network Summary Report," 14 pp. https://ieaghg.org/docs/General_Docs/Reports/2012-01.pdf
6. Gasda, S.E., S. Bachu, and M.A. Celia., (2004). The Potential for CO_2 Leakage from Storage Sites in Geological Media: Analysis of Well Distribution in Mature Sedimentary Basins. *Environ. Geol*., 46 (6-7), 707-720.
8. Pruess K., C. Oldenburg, and G. Moridis, (1999) TOUGH2 User's Guide, Version 2.0.
9. Finsterle, S., M. Commer, J. K. Edmiston, Y. Jung, M. B. Kowalsky, G. S. H. Pau, H. M. Wainwright, Y. Zhang, (2017) iTOUGH2: A multiphysics simulation-optimization framework for analyzing subsurface systems, *Computers & Geosciences*, 108, https://doi.org/10.1016/j.cageo.2016.09.005
10. Carey, J. W., R. Svec, R. Grigg, J. Zhang, W. Crow., (2010) Experimental investigation of wellbore integrity and CO_2–brine flow along the casing–cement microannulus. Int. J. Greenhouse Gas Control, 4 (2), pp. 272-282
11. Huerta,v N. J., S.L. Bryant, B.R. Strazisar, M. Hesse, (2011) Dynamic alteration along a fractured cement/cement interface: implications for long term leakage risk along a well with an annulus defect. Energy Proc., 4, pp. 5398-5405
12. Jordan, A., P. H. Stauffer, D. Harp, W. Carey, and R. J. Pawar, (2015) A response surface model to predict CO_2 and brine leakage along cemented wellbores, *International Journal of Greenhouse Gas Control*, 33 (2015) 27–39.
13. Oldenburg, C. M., and A. J. A. Unger, (2003) On Leakage and Seepage from Geologic Carbon Sequestration Sites. Vadose Zone J. 2:287-296. doi:10.2136/vzj2003.2870.
14. Zahasky, C. and Benson, S.M., (2016) Evaluation of hydraulic controls for leakage intervention in carbon storage reservoirs. International Journal of Greenhouse Gas Control, 47, pp.86-100.
15. Oldenburg, C.M. and Unger, A.J., 2004. Coupled vadose zone and atmospheric surface-layer transport of carbon dioxide from geologic carbon sequestration sites. *Vadose Zone Journal*, *3*(3), pp.848-857.
16. Gawel K., Todorovic J., Liebscher A., Wiese B, and Opedal N., (2017) Study of Materials Retrieved from a Ketzin CO_2 Monitoring Well, Energy Procedia, Volume 114, Pages 5799-5815.
17. Archie, G. E., (1942) The electrical resistivity log as an aid in determining some reservoir characteristics: Trans., AIME 146, pp. 54-62.
18. Gasperikova, E., Hoversten, G.M., (2006) A feasibility study of nonseismic geophysical methods for monitoring geologic CO2 sequestration, The Leading Edge, 25, 1282-1288.
19. Gasperikova, E., T. Daley, Z. Wang, R. Dilmore, W. Harbert, L. Huang, K. Gao, T. Chen, M. Zhang, D. Appriou, X. Yang, T. Buscheck, K. Mansoor, S. Carroll, C. Yonkofski, T. Johnson, J. Burghardt, C. Strickland, C. Brown, (2017) Geophysical Techniques for CO_2 Plume Monitoring. Technical report.
20. Smith, T. M., Sondergeld, C.H., and Rai, C. S., (2003) Gassmann fluid substitutions: A Tutorial, Geophysics, 68, p. 430-440.
21. Daley, T. M., Ajo-Franklin, J. B., Doughty, C., (2011) Constraining the reservoir model of an injected CO_2 plume with crosswell CASSM at the Frio-II brine pilot, IJGGC 5.https://doi.org/10.1016/j.ijggc.2011.03.002

Carbon Dioxide Capture for Storage in Deep Geological Formations, Volume 5
Karl F. Gerdes (Editor)
© 2022 BP. All rights reserved.

Chapter 24

PERMEABILITY MODIFICATION FOR CO_2 LEAKAGE REMEDIATION

Kene Moneke, Yujing Du, Peixi Zhu, Shayan Tavassoli, Jenny Ryu,
David DiCarlo, Matthew Balhoff
Hildebrand Department of Petroleum and Geosystems Engineering and the Center for Subsurface Energy and the Environment, The University of Texas at Austin, Austin, TX 78712, USA

ABSTRACT: Long-term geologic storage of CO_2 requires that migration and leakage are minimized. We investigate the use of a permeability modifier (silica gel) as a conformance control agent and cap rock sealant. We measured the gel time at different silicate content, acid concentrations, salinities, and temperatures. The results were fit to an existing model for gelation time and then used as a predictive tool. Micromodel and core flood experiments were performed to investigate the reactive transport of silicate gel in porous media, to compare to bulk experiments and to investigate the capability of the gel in permeability reduction and sealing of the core. Experiments were conducted under both ambient conditions with an acetic acid solution as a CO_2 substitute and at high-pressure (1500 psi), high-temperature (60°C) with CO_2-saturated brine. The results of gel injection in both the micromodels and core floods showed that the permeability was reduced by approximately two orders of magnitude.

A numerical reservoir simulation study was performed to investigate the injection of silica gels as a treatment method for fracture sealing and leakage remediation in a CO_2 storage reservoir. An adsorption and permeability reduction approach was adopted to model the fracture sealing by the gel. The results show that a successful treatment can reduce CO_2 leakage by a factor of 1000 over 25 years of post-treatment CO_2 injection.

KEYWORDS: gel treatment, CO_2 storage, leakage remediation, silica gel, conformance control

INTRODUCTION

Carbon Capture and Storage (CCS) is a long-term process proposed to mitigate emissions of greenhouse gases. Migration and leakage of CO_2 from the storage reservoir is likely to occur if the reservoir caprock loses its integrity and creates a leakage pathway [1]. To ensure the CO_2 storage effectiveness and minimize the environmental and economic risk, it is important to monitor the subsurface CO_2 migration and apply a treatment method if leakage is detected. A gel system approach relies on the gel to arrive at the fracture location of the caprock and seal the leakage pathway. Two gel systems, crosslinked polymer and silica, have been used for decades to improve the relative permeability of the oil phase during water or CO_2 flooding enhanced recovery. The success of these gel systems as conformance control agents in improving oil recovery has inspired researchers to investigate their use as a treatment method for leakage remediation in CCS [1–3].

Silica gel is environmentally friendly because no heavy metal is required for the gelation process. The starting composition is a stable solution of sodium silicate ($(SiO_2)_n$:Na_2O, $n<4$) monomers at pH > 11. The gelation process can be triggered by a change of pH, salinity or temperature. The silicate molecules react with each other at pH < 10 and form oligomer, and then small particles. The particles

will continue to grow into larger sizes through polymerization. When pH < 7 or salt is present, colloidal aggregation can simultaneously occur between particles and lead to a 3D gel network [4–6]. Rheological measurements show that the triggered silica solution is a low-viscosity, Newtonian fluid at early time, which is advantageous for reservoir injection. However, the continuing reaction causes the apparent viscosity to increase by several orders of magnitude at the "gel time" [7,8]. Since the gel time is dependent on the gelation kinetics, it is also known be affected by pH, temperature, salinity, silica concentration [9] and morphology of silica [10]. Prediction of gel time in bulk solution is challenging; however, an empirical equation has been proposed to estimate the gel time [11].

It has been shown in core flood experiments that silica gel can reduce permeability in conventional core samples (typical permeability > 10 md) by 100-1000 times, and the produced gel can withstand 1000-4000 psi/ft of pressure gradient before failure [9,12]. Jurinak *et al.* [9] also measured the permeability of CO_2 before and after gel treatment. They showed that CO_2 accelerated the gelation process and the gel could achieve a 99.5% permeability reduction. For field injection, the gelation process can be triggered in either a pre-injection [13] or post-injection manner by reservoir fluid pH, e.g., during CO_2 flooding [14]. A pre-flush with brine may be necessary to remove Mg^{2+} or Ca^{2+}, in addition to iron. Silica solution produces a basic (high pH) environment, which can cause those metals to precipitate and lead to early plugging [13]. Silica gel treatments have been shown to be successful for flow diversion in oil recovery by reducing water-cut, gas-oil ratio and improving oil production [7,8,14]. The application for leakage remediation to ensure CO_2 storage has only been conceptually proposed [15]. Compared to oil field injection, the main goal in CO_2 leakage remediation is to seal the fractured rocks, although flow diversion can be an additional benefit of the treatment [1]. Reservoir conditions such as pH, temperature and salinity must be considered at the design of a silica injection, because these factors are critical to the gel kinetics and gel time, especially for leakage remediation. Unfortunately, the gel time is difficult to control due to the complexity of the gelation process as well as the presence of dispersion in porous media.

Numerical simulations can be a useful tool to study the gel transport in porous media and aid the design of silica gel treatment. Most of these simulations simplify the gelation process as one simple chemical reaction. Kim *et al*. [16] performed simulations of silica injection for gel barrier construction to control ground water flow. The gel plugging was modelled by specifying the produced gel as a very high viscosity (low mobility) fluid. Concentration of silica and salinity were included in the kinetics of gel reaction. Effects of pH and temperature were not considered in the simulations. Amiri *et al.* [17] performed 2D simulations to match experimental observations of silica injection into an unconsolidated core containing oil and water. To do so, they assume very slow silica gelation at early time of the simulation, and switch to fast gelation reaction at the gel time observed from coreflood experiments. This approach makes upscaling of the simulations challenging, since the gel time must be input to the model. A similar approach that relies on experimental observation to determine gel time was adopted by Hatzignatiou *et al.* [15]. In their work, the gel plugging was modelled as permeability reduction caused by gel adsorption on to the rock surface. Omekeh *et al.* [18] developed a population model that incorporates nucleation, polymerization and colloidal aggregation into the gelation process. While assumptions were made to simplify the model, the model includes all the important aspects of the gel reaction. For the prediction of bulk gel time, the model matches well with experimental data. They also demonstrated large scale simulation and showed that silica gel can reach over 3000 ft from the wellbore if a pre-flush is applied to remove high valent metals. However, Omekeh *et al.* [18] did not match their model with core flood experiments and did not study permeability reduction of gel in porous media.

EXPERIMENTAL APPROACH

Fluid Preparation

Brine solutions were prepared using laboratory-grade sodium chloride (NaCl) dissolved in deionized water. Deionized (DI) water and the appropriate salts were mixed using a magnetic stir plate and magnetic stirrer bars. Before injecting the brines (or any fluids) into a core, micromodel chips or batch samples, the brines were filtered with a 0.45-micron cellulose filter. Ethylenediamine-tetraacetic acid (EDTA), sodium bicarbonate ($NaHCO_3$), and sodium hydrosulfate ($NaHSO_4$) salts were dissolved in deionized water to form the desired EDTA solution. The resulting solution was mixed using a magnetic stir plate and magnetic stirrer bars.

The acid solutions were prepared with the acid reagents (either acetic (HAc) or hydrochloric (HCl) acid), sodium chloride (NaCl) and deionized water. The acids were used as ambient temperature and pressure surrogates for CO_2. HCl was used by Stavland [11] and was the initial choice of acid surrogate, but it was shown to be too strong an acid; weaker acetic acid was chosen as an alternative. The desired solutions were made up by adding specified weights of solids to measured volumes of liquid reagents of known concentration. The acetic acid had an assay of 99.7% and a density of 1.05 g/cm^3. The required acid concentration was calculated using the density and the assay of the acid reagent. Deionized (DI) water, acid solution and NaCl were thoroughly mixed using a magnetic stir plate and magnetic stirrer bars. CO_2-saturated brine solutions were created by bubbling CO_2 through brine at the appropriate pressure and temperature.

The stock silicate solution used is a 28.7 wt% potassium silicate solution (Betol K28T) purchased from Woellner. It has a density of 1.25 g/cm^3 and viscosity of 28 mPa s (cP). The chemical formula of potassium silicate is $(SiO_2)_n$: K_2O with n = 3.92. Therefore, the SiO_2 and K_2O content is 20.5 wt.% and 8.2 wt.%, respectively. The pH of the stock solution is 11.62. Potassium silicate is stable at this pH and no gelation occurs. The silicate solutions used for experimental core flood injections were diluted from this stock solution with deionized water to the desired concentrations. Betol K28T has been used at a field test in Serbia to induce the formation of a barrier through the reaction of a potassium silicate solution with leaking CO_2 – either in the form of dissolved CO_2 or supercritical CO_2 [19].

Bulk Gelation Experiments

The gelation process and gel time of the silicate solution were investigated in bulk. The gel times at different silicate content, acid type, acid content, salinity, and temperature were measured and analysed. Acetic (HAc) and hydrochloric (HCl) acid were used as two different gelation initiators, and these were used as surrogates for CO_2. The CO_2 concentration that resulted in the same pH as the acetic/HCl acid solutions was used for determining the equivalent gel time.

Preparation of Sealant and Gelling System

Aqueous solutions with measured acid and NaCl concentration were prepared in test tubes. NaCl was chosen for the salinity study because we assume that the formation will be preflushed with NaCl brine to remove calcium and magnesium. A predetermined amount of stock potassium silicate solution (Betol K28T) was added into the test tubes to form a gelling system that has desired concentration of each species. The test tubes were well shaken to ensure a homogeneous mixture and quickly transferred into an oven that was set at a target temperature. The gelation time was determined by visual inspection of the sample and tilting the test tube until a significant loss of sample fluidity was observed. The sample was inspected every 5-15 minutes at early times. For samples with long gelation, the time interval for inspection was gradually increased. Figure 1 shows the gelation change

of the gel system from clear fluid to white gel during the gelation process. After the gel is formed, water is slowly expelled from the gel phase.

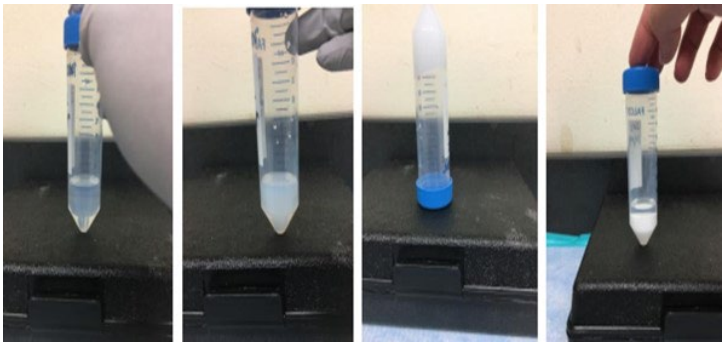

Figure 1. Photos showing phase change of a gel system. From left to right: a clear fluid; cloudy fluid; solid gel; expelled water separated from the solid gel.

Gelation Activated by Acetic Acid (HAc)

Gelation of diluted Betol K28T and acetic acid (1M) was studied by varying the acid concentration, silicate concentration, salinity, and temperature. Gelation was observed at 40°C for various fractions silicate solution (6.12 wt%, 8.11 wt%, 10.1 wt% and 12.1 wt%) and acetic acid concentrations (0.6 wt%, 0.7 wt%, 0.8 wt% and 0.9 wt%). The effect of salinity and temperature on the gel time was then determined at a constant silicate content of 8.64 wt% and acetic acid (HAc) content of 0.94 wt%. at varying salinities (500, 1000, 2500 and 5000 ppm) and temperatures (22.2°C, 40°C, 45°C, 55°C, 62.5°C, and 78°C).

Additional experiments were performed at higher salinities and acid concentrations. The samples in this set of experiments have fixed silicate content of 9 wt% and varying HAc concentration from 0.001 to 1 wt% and salinity from 5000 to 50,000 ppm. The gelation time was measured at 60°C.

Gelation Activated by Hydrochloric Acid (HCl)

Several mixtures of diluted Betol K28T and hydrochloric acid (1M) were prepared with varying salinities and tested at different temperatures. The effect of acid and silicate concentrations on gel time was determined at 40°C for various fractions of the diluted stock potassium silicate solution (6.12 wt%, 8.11 wt%, 10.1 wt% and 12.1 wt%) and hydrochloric acid concentrations (0.6 wt%, 0.7 wt%, 0.8 wt%, 0.9 wt% and 1 wt%). The effect of salinity on gel time was then determined using a constant silicate content of 8.11 wt% and hydrochloric acid (HCl) content of 0.7 wt% at 40°C with varying salinities (500, 1000, 2500 and 5000 ppm, respectively). The effect of temperature was studied for various fractions of the diluted stock potassium silicate solution (6.57 wt%, 8.57 wt%, and 10.36 wt%) and hydrochloric acid concentrations (0.6 wt% and 0.7 wt%) at temperatures of 40°C to 78°C.

Micromodel Experiments

Fabrication

The experiments were conducted in two types of micromodels–both designed and fabricated in-house using the protocols developed in previous work [20,21]. The first micromodel (denoted as M1) is a 2.5 cm × 1.5 cm planar wafer with a homogeneous pore-network and three-dimensional features (2.5D) (Figure 2a-b). The pore bodies are about 200 µm in width and 20 µm in depth, and the pore throats are about 30 µm in width and 5 µm in depth. The second micromodel (denoted as M2) is a planar, serpentine structure with a 1.0-foot flow path with a 2.5D, heterogenous porous matrix (Figure

2c-e). The M2 pore bodies are about 13.5 µm in depth and the pore throats are 3–4 µm in depth. For both micromodels, the geometrical patterns were designed with CAD software, and then a photomask was generated for photolithography. Photolithography and wet-etching using hydrofluoric acid were used to engrave the designed geometry patterns onto a soda-lime glass substrate with a thickness of 2 mm. A smooth soda lime glass was used as the cover glass to enclose the flow channels. The etched substrate and the cover glass were bonded together using the thermal bonding method at temperature of 690°C.

2.5D micromodels (adding a variation in depth to 2D flow channel configurations) are more realistic than 2D micromodels in that pore-scale 3D (2.5D) features are included by etching the pore throats shallower than the pore bodies. Therefore, both the pore bodies and pore throats are connected, allowing the continuity of the wetting phase and the capillary snap-off of the non-wetting phase, while capillary snap-off generally won't occur in the 2D system [21, 22]. In addition to the 2.5D features, M2 better mimics the real cores by having a heterogenous porous matrix and a length scale of up to 1.0 ft. Capillary end effects and any impacts due to the small geometry of traditional micromodels are ameliorated.

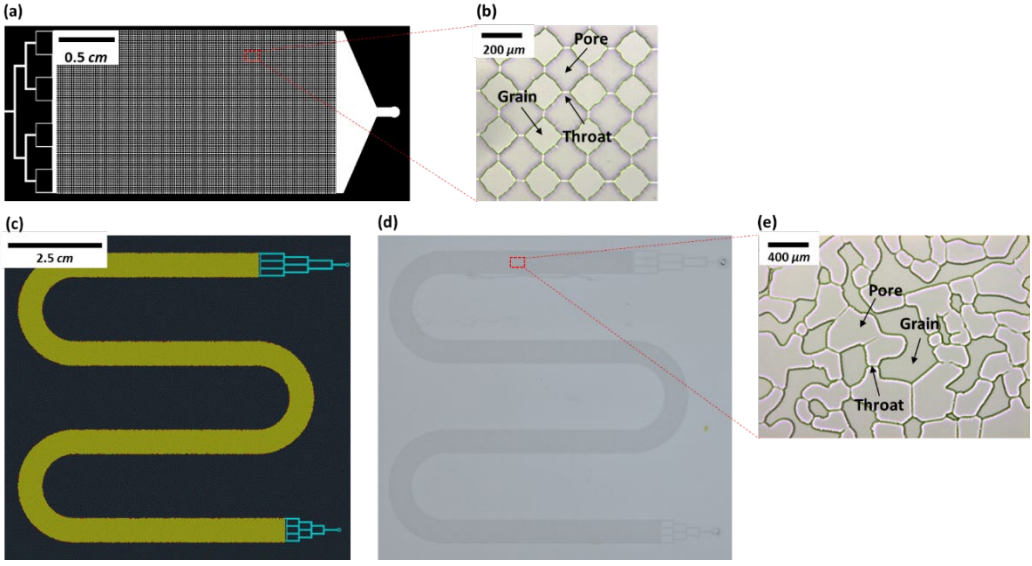

Figure 2. (a) Photomask design and (b) microscopic image of M1. (c) Photomask design, (d) actual image by a digital camera, and (e) microscopic image of M2.

Experimental Procedure

In the experiments, the micromodels were placed horizontally on the microscope platform (Accu-Scope, EXI-310) (Figure 3). A syringe pump (PHD 2000, Harvard Apparatus) was used to inject the flooding fluid into the micromodels at ambient temperature and pressure. The pressure drop across the micromodel was monitored using the pressure sensor (LabSmith, uPS0250-T116-10) connected to inlet of the micromodel (the outlet was at ambient). In each experiment, the micromodel was first saturated with 1 wt% acetic acid (HAc) with 1000 ppm NaCl. After fully saturation, the 8.64wt% potassium silicate solution was injected at a constant flow rate of 1ft/day, or 4 µl/hour for M1 and 0.96 µl/hour for M2. After the experiments, the pore-scale images were captured by the microscope camera (INFINITY 2, Lumenera).

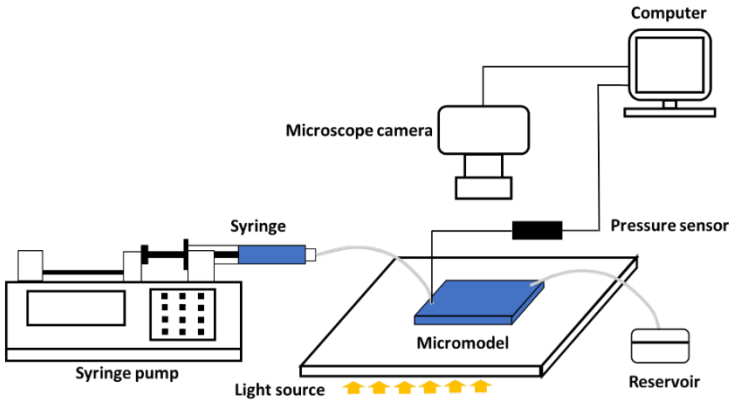

Figure 3. Schematic sketch of the experimental setup.

Core Flood Experiments

Core flood experiments were performed to illustrate the reactive transport of silicate gel in porous media, to compare the gelation results obtained from the porous medium to the gelation results from the earlier bulk experiments, and finally, to investigate the capability of the gel for permeability reduction and sealing of the core. These core flood experiments were performed under two conditions: (1) ambient with an acetic acid solution as a CO_2 substitute and (2) High-Pressure High-Temperature (HPHT) condition with CO_2 saturated brine.

Equipment and Experimental Setup

All cores used in these experiments were Bentheimer sandstone cylinders ~1.5 inches in diameter and ~12 inches in length. Cores were drilled out from the original Benthemier sandstone blocks and dried in a high-temperature oven (at least 90°C) for at least 36 hrs. The sandstone cores were taken from the oven after being dried and left to cool to room temperature. The length and mass of the core, as well as the diameter at three different locations, were measured. The bulk volume (V_B) of the core was determined using the core length and cross-sectional area. The bulk density of the core was determined using the measured mass and bulk volume.

Figure 4 shows the experimental setup and apparatus. For experiments at ambient temperature and pressure, two end caps were glued on the ends of the core with quick 5-minute curing epoxy (Grainger). The end caps were custom made from polycarbonate or ULTEM (for corrosive chemicals that react with polycarbonate such as silanes or acetone). Additional 5-minute epoxy was then coated along the length of the core to seal the core surface face. The core was then secured along the center line of a larger polycarbonate tube (2.0-inch diameter and 15-inch length) using a slow curing, 24-hour epoxy. The epoxy was prepared by mixing the epoxy base (EPON Resin 828) with the curing agent (Versamid 125) in a 2:1 ratio by weight. This slow curing epoxy was poured into the annular space between the core and the polycarbonate tube. The core was left to cure overnight, at minimum. Three evenly spaced holes for pressure taps were drilled into the core. The taps were secured with more epoxy and connected to 3-way Swagelok valves and pressure tested.

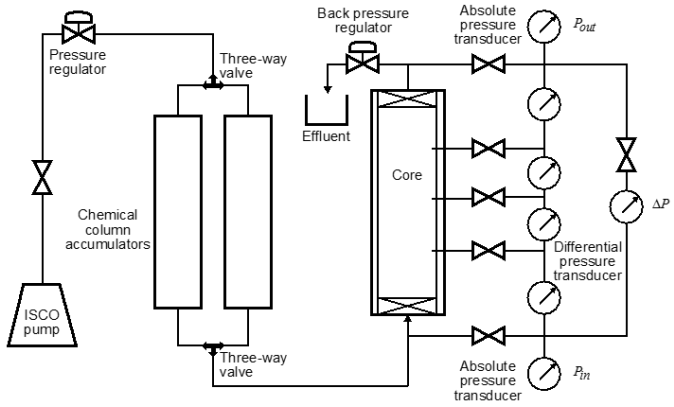

(a)

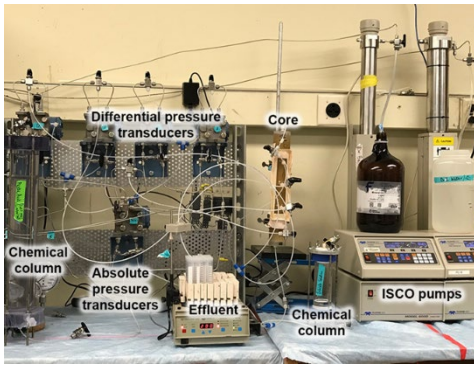

(b)

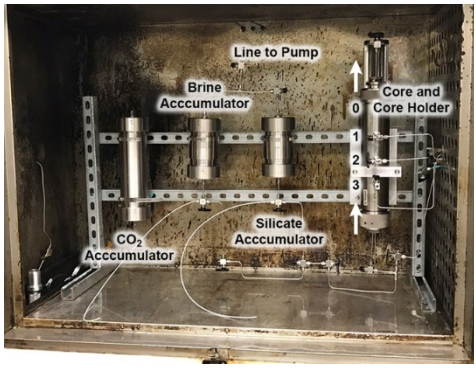

(c)

Figure 4. Coreflood apparatus: (a) general schematic, (b) ambient apparatus, and (c) oven including accumulators and coreholders for HPHT experiment (pumps and transducers remain outside oven).

For high pressure, high temperature CO_2 experiments, the core was encased in 2" heat-shrink Teflon tubing (Geophysical Supply Company). The Teflon tubing was shrunk onto the core using a Steinel HL 1810 S professional heat gun or kept in the oven at 100°C for 48hrs. Three layers of aluminium foil were then wrapped on the Teflon layer. The aluminium layers prevent CO_2 from damaging the rubber sleeve inside the core holder, and the Teflon layer prevents the brine from damaging the aluminium. The Teflon-aluminium wrapped core was inserted into the core holder and secured from both ends. The layers were drilled at each pressure tap to allow pressure communication. All the connections were completed as described in Fig. 4a. A confining pressure was applied to the core of 10.34 MPa (1,500 psi) using DI water, and the core was evacuated to -29 inches of Hg for three hours.

For all of the core flood tests, pressure transducers with a range of 0-30 psi (Rosemount 3051T) were used to measure the differential pressure along segments of the sample. Two additional transducers with a range of 0-2000 psia were used to record absolute pressures. During each experiment, all the pressures were recorded by a data acquisition software (National Instruments LabViewTM).

For low pressure tests, custom polycarbonate tubes held the acetic acid (HAc), brine, EDTA and potassium silicate (Betol K28T) solutions injected into the core. The test solutions were displaced into the core holder by pumping mineral oil into the fluid reservoirs. Glass cylinders (Kontes

Chromaflex®) with a pressure rating of 50 psi, 0.5 to 2 feet in length, and 2 inches in outer diameter were used for brine solution injection. For the HPHT experiments, the injection fluids (sodium chloride brine, silica gel solution, and liquid CO_2) were fed to the core holder from stainless steel piston accumulators (Phoenix Instruments).

All core flood experiments were performed at constant flow rates. An ISCO pump (Teledyne Instrument Specialties Company) was used to inject fluid at the desired flow rate. Mineral oil was pumped to displace fluids into the core sample. The pump was refilled immediately when emptied to avoid periods of no flow in the sample during chemical floods. Depending on the experiment, the effluent either went to a fractional collector (Teledyne ISCO Retriever 500), or the mass of the effluent was recorded using a digital balance scale (Sartorius).

Procedure

To begin a test, the core was initially saturated with high salinity brine by connecting the core inlet to a graduated cylinder and letting the fluid imbibe into core as the core holder was subject to vacuum. The pore volume was estimated from the volume of fluid imbibed. Porosity was then estimated as the ratio of the pore volume to bulk volume. A salinity tracer test was performed to determine the heterogeneity of the core and to provide a second estimate of the aqueous pore volume. The test was conducted by injecting a lower salinity fluid (1000 ppm NaCl aqueous solution) at 5 ml/min to displace the higher salinity fluid (5000 ppm NaCl aqueous solution) until the effluent concentration is observed to have the same salinity as the injected brine. Waterflood brine (i.e., 5000 ppm NaCl) was used to measure single phase brine permeability by injecting the brine into the core at different flow rates. Permeabilities were calculated from the pressure gradients and flow rates at steady state. The brine permeability was then back-calculated using Darcy's law.

The Bentheimer sandstones used in these experiments contain significant amounts of iron ions, which can degrade the silicate solution chemically. Ferric ions can crosslink silicate solution to form microgels, which increases the retention of the silicate solution, prevents good transport, and degrades the silicate solution in the presence of oxygen. To avoid these issues, the cores are reduced before injecting silicate solutions following the procedure described by Lee [23]. The core was flooded with an aqueous solution of 4% $NaHCO_3$, 1% EDTA- Na4+, and 1% Na_2S2O_4, at 23°C and 0.5 ml/min (4.74 ft/D) to reduce the core and to remove amorphous oxidized iron from the core. Flooding was continued until the steady-state iron concentration reached 3 ppm in the effluent as measured by MQuant Iron Test Strips (0, 3, 10, 25, 50, 100, 250, 500 mg/l Fe2+). Once the effluent iron content was less than 3 ppm, the core was flushed with brine (4% $NaHCO_3$ + 1% $Na_2S_2O_4$) to clear the core of EDTA, and the iron concentration measured by the test strip was 0 ppm.

Acetic acid solutions were transferred into the accumulator vessels by pulling a vacuum to prevent additional gasses from being dissolved in the solution. The filtered acetic acid was injected at a constant flow rate of 0.5 ml/min until steady-state pressure is observed for all four sections of the core and effluents were collected in the fractional collector. Once steady state is reached, the acetic acid (HAc) flood is continued for an additional 2-3 pore volumes.

For high pressure, high temperature CO_2 experiments, the core was saturated with CO_2-saturated brine to mimic the initial reservoir conditions before applying the gelling solution. The procedure is to first, saturate the brine with CO_2 by filling the stainless-steel accumulator with 30,000 ppm brine and pressurizing to 1500 psia. The CO_2 tank line was connected to the base of the accumulator and the amount of CO_2 needed to saturated the brine was slowly "bubbled" into the brine while maintaining pressure with a back pressure regulator, thus forming the CO_2 saturated brine needed for the HPHT experiment. This solution was then injected at a rate of 1.0 ml/min into the core that was previously filled with unsaturated brine at 1500psia. Pressure drops were measured to acquire a baseline permeability. The core was then depressurized and this process was repeated with identical results.

For the gel floods, the silicate solutions were injected into the core at a constant flow rate, and pressure drops were measured for steady flow, after which the pump was turned off. To see how the gel performed over time, at certain time intervals the injection was restarted, and the pressure drops were again measured once steady state was reached. Effluents from the experiments were collected and analysed similar to the brine flood effluent samples. The changes in pressure drop in sections and across the core were monitored and used to determine permeability reduction.

MODELING APPROACH

Reservoir Model and Numerical Simulation

Figure 5a shows the reservoir model domain. The model domain dimensions are 410 ft (length) × 410 ft (width) × 65 ft (height) and is divided into uniform cells, 10 ft ×10 ft × 5 ft. A sensitivity study showed that further grid refinement does not significantly change the simulation result enough to justify the additional computational time. The model includes reservoir and caprock regions with associated porosity and permeability property spatial models. The caprock is the top layer and the reservoir is represented by the remaining 14 layers. Porosity within the model is assumed to be constant and homogeneous with a value of 18%. The reservoir permeability is modelled with sequential Gaussian simulation [24] to allow for control of the permeability distribution, well conditioning and spatial continuity informed by a variogram model for design of experiment. A Dykstra-Parson's coefficient of 0.6, and horizontal and vertical correlation lengths of 500 and 20 ft were specified.

The caprock is assumed to have zero permeability as shown by the gray layer in Figure 5a. The top view of the caprock is provided in Figure 5b. A fractured grid cell (shown in red) is placed in the caprock at 57 ft from the center of the model providing a potential leakage pathway for stored CO_2. This fractured grid cell is assumed to have a permeability of 2 Darcy. The reservoir has two existing vertical wells, one for CO_2 injection and the other for gel injection, respectively. The injection well for gel treatment intersects the center of the caprock layer in Figure 5b, while the CO_2 injector intersects the caprock 141 ft from the model center.

An example of the reservoir permeability heterogeneity is also shown in Figure 5a [24]. The heterogeneous permeability, which has a log-normal distribution, is calculated with the Stanford Geostatistical Modeling Software [26]. The average permeability, Dykstra-Parsons coefficient and horizontal correlation length of the reservoir region of the model are provided in Table 1. These parameters were also applied for one-at-a-time sensitivity analysis.

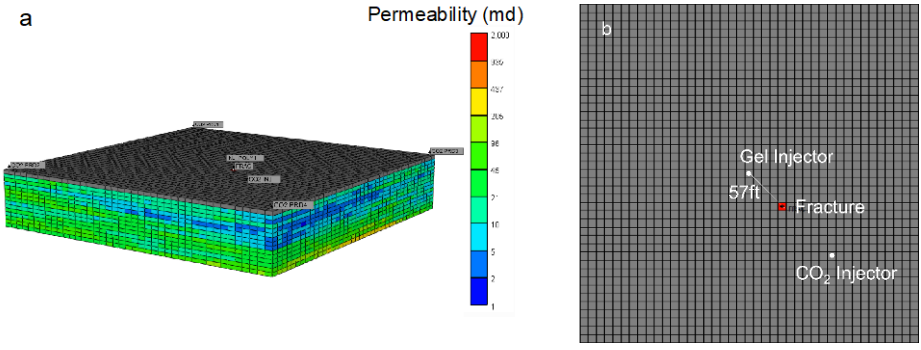

Figure 5. (a) Permeability of the reservoir model. (b) Top view of the caprock layer. Figure taken from [25].

Table 1. Reservoir properties and operating conditions.

Property and Operating Conditions	Value	Units
Reservoir porosity ϕ	0.18	N/A
Reservoir average permeability k_{mean}	50	Md
Dykstra-Parsons coefficient V_{dp}	0.6	N/A
Horizontal correlation length γ_h	500	Ft
Vertical correlation length γ_v	20	Ft
Reservoir temperature	122	°F
Silica		
Injection rate	200	bbl/day
Injection time	10	Day
Maximum bottom hole pressure	5000	Psi
Silica concentration	4	wt%
Silica viscosity	0.35	Cp

The reservoir has an initial uniform pressure of 3550 psi. CO_2 is initially injected into the reservoir at 1 MMscf/day for 5 years. A maximum bottom hole pressure of 5000 psi is used as the secondary constraint. The CO_2 injection well is perforated at the bottom three grids. Four pseudo producer wells with 3550 psi constant bottom-hole pressure are placed at the bottom corner grids for pressure balance. This approach is adopted to represent a realistic case where the 410 ft × 410 ft × 65 ft computational domain is only a small section of a much larger reservoir as typically employed in a sector model study. Another pseudo constant pressure producer well is placed at the fracture grid cell (only completed at the top grid of the formation) in the seal region to simulate CO_2 flowing along the leakage pathway and escaping to rock units above the caprock. The amount of leakage can therefore be monitored from the produced CO_2 in this pseudo well. The producing pressure was set to 3530 psi, slightly lower than the initial reservoir pressure. It is assumed that leakage is detected after five years of CO_2 injection.

At the start of year six, CO_2 injection is paused, and silica gel treatment is applied to mitigate the caprock fracture. The operating conditions of gel treatment are provided in Table 1. Injection of gel system was 30 days in all cases. After treatment, the well was shut in to allow sufficient time for gel reaction. The treatment period including the gel injection time is fixed to one year. CO_2 injection started again at year seven and lasted for 25 more years. The entire simulation time length is 31 years, within which one year was used for gel injection and reaction, and the balance of time for CO_2 injection. To demonstrate the impact of the treatment, control cases were simulated over 31 years in which there is no gel treatment and CO_2 injection is shut in during the time that corresponds to the gel treatment period. All simulations were calculated with CMG STARS software [27].

Silica Gelation and Permeability Reduction

Silica gel treatment would be applied when CO_2 leakage is detected from a storage formation. The concept is that unreacted silica gel which has been injected into the reservoir is activated in place by the low pH of the reservoir due to CO_2 dissolution. For a simple model, we assume no gel generation prior to the gel time, and instantaneous gel reaction once the gel time is reached [17]. The gel time is a function of silica concentration, salinity, temperature, and overall acid concentration. We assume conditions such that t_{gel} = 55 days.

In our simulations, we continuously inject silica gel for no more than 30 days, then shut-in the treatment well and allow silica to convert to gel, which is assumed to 100% convert instantaneously at the gel time. The gel blockage to seal fractures is also modelled as permeability reduction (Eq. 1) due to gel adsorption,

$$R_f = 1.0 + (RRF - 1.0)(A_D/A_{Dmax}) \quad (1)$$

Where R_f is the permeability reduction, RRF is the residual resistance factor (= 5000), A_D is the amount of gel adsorption determined as a function mass fraction of gel in the aqueous phase [25] and A_{Dmax} is the maximum amount of adsorption (0.45 lb_m/ft^3) [15,28].

RESULTS AND DISCUSSION

Bulk Gelation Experiments

Acetic Acid (HAC)

Figure 6a shows gelation time versus acetic acid (HAc) concentration at varying silicate levels. These gelation times were all measured at 40°C. The results clearly show a shorter gelation time with increasing acetic acid content regardless of the silicate concentration. Figure 6b shows the data plotted as gelation time versus silicate content. The gelation time shows a minimum with increasing silicate in the solution.

Figure 6c shows the effect of salinity at different gelation temperatures for a fixed, intermediate silicate level and high acid concentration. The gelation time is shorter at higher salinity. This can be explained by the classical DLVO theory [29] which describes the aggregations of aqueous dispersions quantitatively. According to the theory, the stability of colloids in suspension at high salinity is due to stronger electrostatic attraction around silicate particles, which induces the silicate particles to agglomerate and form a gel phase. Figure 6d shows that the log of gelation time is linear with inverse temperature, showing that the gel reaction follows an Arrhenius law.

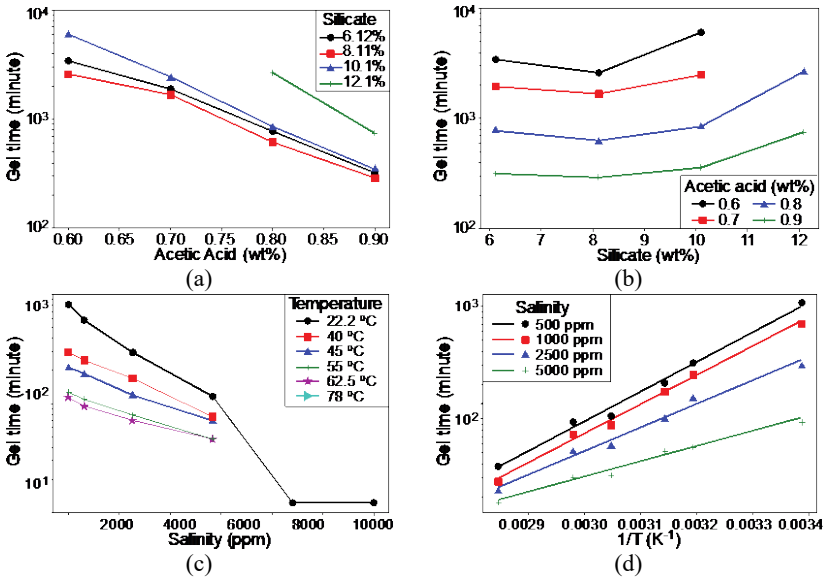

Figure 6. Gelation time, for experiments with acetic acid, versus (a) acetic acid content at 1000 ppm salinity and silicate concentration from 6.12 to 12.1 wt.%, (b) silicate solution content at 1000 ppm salinity and acetic concentration from 0.6 to 0.9 wt.%, (c) salinity at constant silicate content 8.64 wt.% and HAc content 0.94 wt.%, (d) temperature at constant silicate content 8.64 wt.% and HAc content 0.94 wt.%.

Hydrochloric Acid (HCl)

The plot of gelation time versus HCl concentration (Figure 7a) is more complicated compared to the results for acetic acid. At high silicate content (10.1 wt.% and 12.1 wt.%), the gelation time is shorter with higher HCl concentration. However, at low K-silicate content (6.12 wt.% and 8.11 wt.%) the gelation time first decreases then increases with HCl.

The gelation behavior at low silicate content is driven by the gelation mechanism. During the gelation process, the silicate first forms oligomers, which aggregate and form covalent bonds to produce a 3D-network of gel. At low acid concentration, the oligomers are mostly negatively charged on the surface, due to the presence of the Si-O group. With increasing acid content (more H^+), some of the negative-charge sites are neutralized to Si-OH, which results in less repulsive force between oligomers and a faster gelation process (shorter gelation time). When the acid content is high enough, all the Si-O group on the oligomer surface will be neutralized, and the gelation should have the fastest kinetics at this point. Further increases in acid content can produce $Si\text{-}OH_2^+$ groups and flip the oligomer surface charge from negative to positive. The oligomers become repulsive again beyond this point, so the gelation process slows. Since HCl is a much stronger acid than HAc, it can alter the surface charge of silicate oligomers at high enough concentration (about 0.7 wt% for 6.12 and 8.11 wt.% silicate content in these experiments). As the HCl concentration increases, the gel changes from white and opaque to transparent, indicating a transition of gelation mechanism from negative-charged aggregation to positive-charged aggregation as explained above.

The effect of salinity on gelation time in an HCl environment was measured at a constant silicate concentration of 8.11 wt.% and HCl concentration of 0.7% (Figure 7b). Gelation time increases then decreases with salinity. As discussed previously, the chosen silicate and HCl composition may lead

to positive-charged oligomers. Although the gel time behavior shown in Figure 7b can be explained in terms of a hydration effect and steric effect of the silicate-oxyl group [30], the silicate gelation mechanism is still not fully understood.

Figure 7c shows a linear relationship in a semi-log plot of gelation time versus 1/T for selected K-silicate and HCl concentration, indicating that the gelation kinetics follows an Arrhenius law.

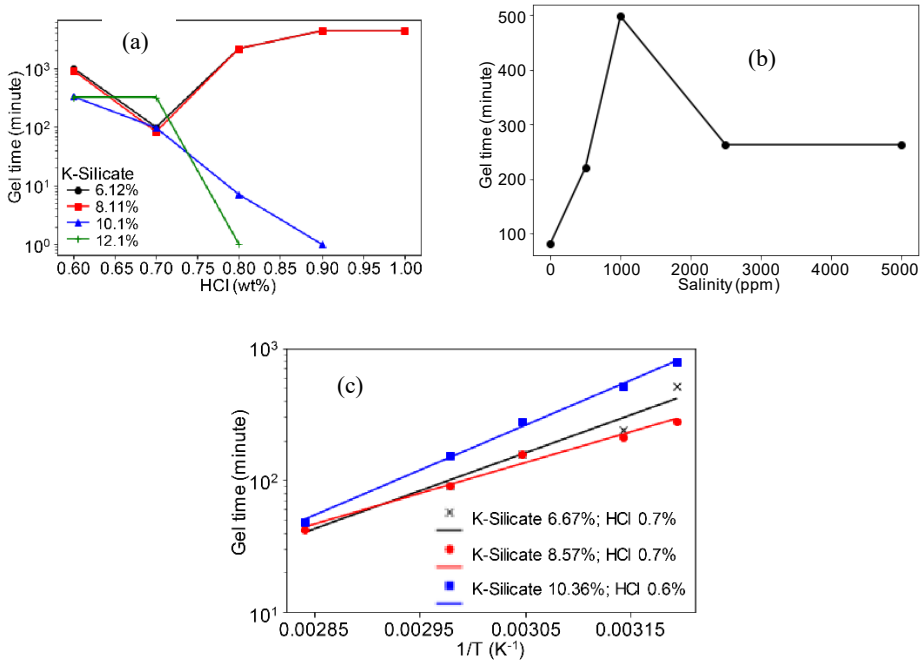

Figure 7. Gelation time, for experiments with hydrochloric acid, versus (a) HCl content at silicate concentrations from 6.12 to 12.1 wt.%, (b) salinity at constant silicate content 8.11 wt.% and HCl concentration of 0.7 wt.%, (c) temperature at various silicate and HCl concentrations.

Gel Model and Application to Carbon Dioxide (CO_2)

A gel model was proposed by Stavland *et al.* [11] to predict gelation time as a function of silicate content, acid concentration, salinity, and temperature.

$$\ln t_{gel} = M + a[Si] + b[HAc] + c[NaCl] + E_a/\mathrm{RT} \quad (2)$$

where, t_{gel} is the gelation time in minutes
[Si], [HAc], [NaCl] are silicate, acetic acid and NaCl concentration in wt.%
T is the temperature in Kelvin
M, a, b, c, and E_a (activation energy) are fitting parameters
R = 8.314 J·mol^{-1}·K^{-1}.

By fitting our bulk gelation data, we found M = 598, a = 30.9, b = -954, c = -263 and E_a = 41.3 kJ/mol.

Application of Equation 2 to the High-Pressure High Temperature (HPHT) experiments with CO_2 requires determination of the acetic acid concentration [HAc] that has the same pH as the

CO_2-saturation brine solution. Acetic acid and CO_2-saturated brine are both weak acids that undergo dissociation with equilibrium constants, K_{Ac} and K_{CO2}, respectively.

$$HAc + H_2O \underset{\rightleftarrows}{K_{Ac}} H_3O^+ + Ac^- \tag{3a}$$

$$CO_2 + H_2O \underset{\rightleftarrows}{K_{CO2}} H^+ + HCO_3^- \tag{3b}$$

where K_{Ac} is temperature dependent (8.71E-6 at 20°C; 1.51E-4 at 60°C) and K_{CO2} is a function of salinity and temperature [31]. The equivalent acetic concentration, c_{HAc} (mol/L), that has the same pH as carbon dioxide concentration can be found as,

$$c_{HAc} = \frac{-K_{AC}^2 + \left[(K_{AC} - K_{CO2}) + \sqrt{K_{CO2}^2 + 4K_{CO2}\, c_{CO2}}\right]^2}{4K_{AC}} \tag{4}$$

Equation 4 gives the equivalent acetic concentration in mol/L and can be converted to wt% for use in Equation 2 using the molecular weight of acetic acid (60 g/mol) and density of water.

Micromodel Experiments

Permeability Reduction

Pressure drop across both the M1 and M2 micromodels increased during the silicate solution injection. The permeability reduction (K_i/K) was calculated according to the pressure increase and plotted in Figure 8. For M1, there was a delay of ~1.1 pore volumes (~3800 s) before the permeability started to decrease (Figure 8a). For M2, the delay was ~100 s which was insignificant in terms of pore volumes (Figure 8b). In the experiments, a permeability reduction of 180 (M1) and over 900 (M2) was observed. The plateau behavior shown in Figure 8a and 8b is due to the limits of the pressure transducer.

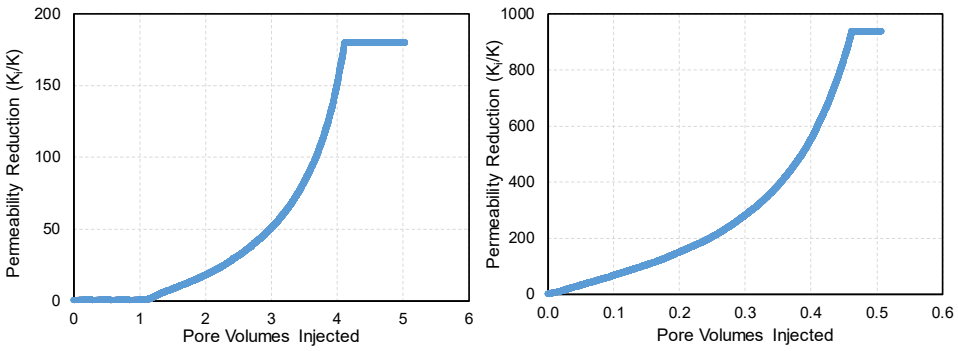

Figure 8. Permeability reduction versus pore volumes injected during silicate solution injection in (a) M1 and (b) M2.

Gelation in Pores

The pore-scale visualizations after the flood experiments are shown Figure 9. Gelation was observed throughout the micromodels in both cases. It is noted that the images in M1 were captured after the micromodel was dried by heating, and the images in M2 were captured right after the injection. From

the images captured from different sections in the micromodels, gelation occurred throughout the micromodel, which explains the continuous decrease of the permeability (Figure 8).

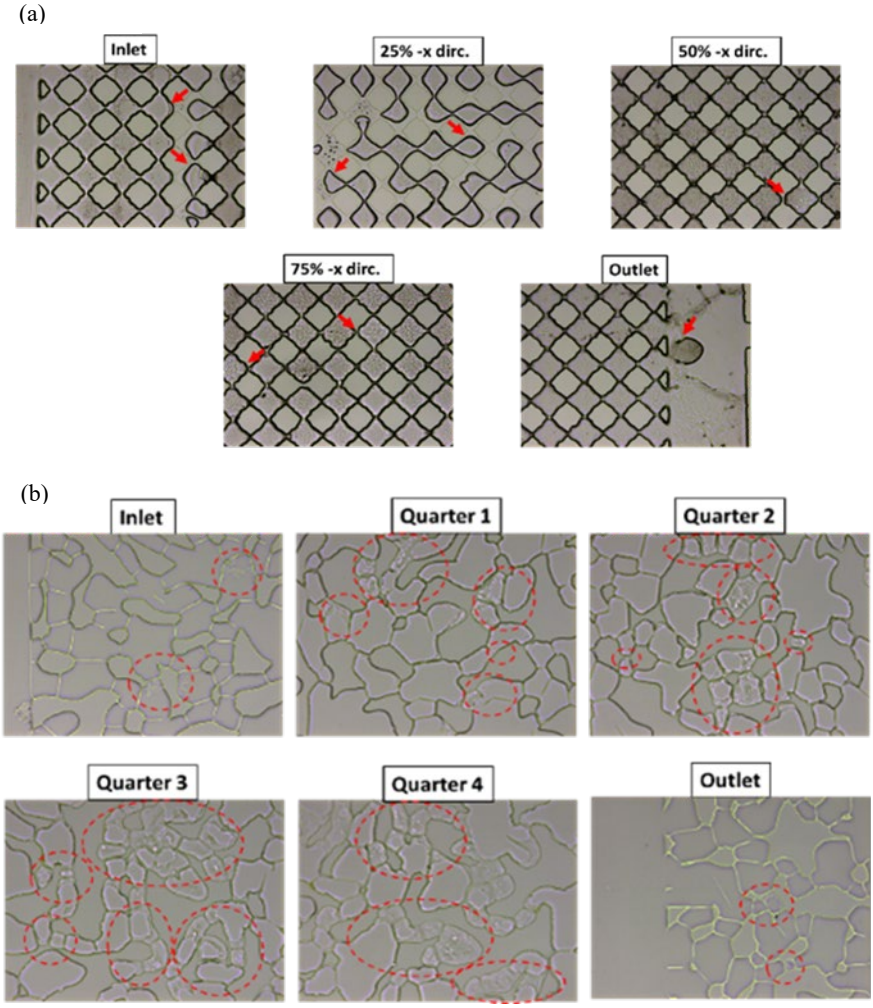

Figure 9. Gelation in (a) M1 and (b) M2. The red arrows in (a) point out the interface of the gel, and the red circles in (b) highlight the occurrence of the gels.

Coreflood Experiments

Table 2 summarizes the rock and fluid properties for all coreflood experiments. The first two experiments were conducted at ambient (14.7 psi, 20°C) conditions with acetic acid. The third and fourth experiments were performed with CO_2-saturated brine at 1500 psi and 60°C and were identical except different core samples were used. The third and fourth experiment also had a higher salinity (30000 ppm NaCl) than the first two experiments (1000 ppm and 2500 ppm, respectively) to better mimic reservoir conditions. The silicate concentration was increased to 15 wt% in the third and fourth

experiment (compared to 8.64% in the first two experiments) to delay the gelation time (Equation 2). The permeability (1400-2600 mD) and porosity (23-25%) were typical of Bentheimer sandstones.

Table 2. Properties of rock and fluids for coreflood experiments.

Exp	PV(ml)	ϕ	Whole section, K (mD)	Acid	Acid Conc (wt%)	Salinity (ppm)	Silicate Conc (wt%)	μ Silicate (cp)
1	82	23.68	1469	Acetic	1.00	1000	8.64	3.00
2	83.13	23.92	2566	Acetic	1.00	2500	8.64	3.00
3	83.23	24.53	1605	CO_2	saturated	30000	15	3.00
4	82.95	23.78	1707	CO_2	saturated	30000	15	3.00

Experiment #1

In ambient experiment #1, the Benthemier (1469 mD) sandstone was initially saturated with 1 wt% acetic acid and 1000 ppm NaCl brine. The gelation time duration was expected to be ~12 hrs at a frontal velocity of 1.0 ft/day of silicate solution based on data from the aforementioned bulk gelation experiments. The silicate residence time was ~24 hrs. The pressure build-up was expected to occur mostly at the bottom (inlet) section.

Figure 10a and 10b show the pressure drop across the core (ΔP) and permeability reduction ($\Delta P/ \Delta P_i$), respectively, versus pore volumes injected (PVI) for experiment #1. We refer to the permeability reduction here as the pressure drop across the core divided by the baseline pressure drop. Using Darcy's law, a baseline pressure drop (ΔP) for a 1.0 cp Newtonian fluid (brine solution) at a frontal velocity of 1.0 ft/day was calculated as 0.025 psi. An 8.64 wt.% silicate solution (3 cp) was injected (t=0) into the core at 1.0 ft/day for 16.0 hrs (~ 0.67 PVI). No permeability reduction was observed for the first 0.4 PVs, but then permeability reduced monotonically between 0.4 and 0.67 PVs to ~30. After 0.6 PV, the frontal velocity was reduced to 0.5 ft/day (which corresponded to a baseline pressure drop of 0.0125 psi) to increase the silicate residence time for gelation. After an initial transition period, permeability reduction continued to increase to over 80. After 0.81 total PV (22 hours of injection), the experiment was shut-in for five days to determine if the system would re-seal while at rest.

After the shut-in period, additional silicate was injected at frontal velocities of 0.5 ft/day to investigate the strength of the gel and its corresponding maximum pressure drop. Injection continued for a short duration (0.03 PV). Pressure data was inaccurate during the start-up period, but data suggest the gel strength was retained. The experiment was shut in again for 20 hours and injection continued at 0.5 ft/day for 0.47 PV. Pressure drops continued to increase, and the final permeability reduction factor was approximately 240. Although not shown, pressure data across sections indicated that permeability reduction occurred mostly in the inlet portion of the core.

Experiment #2

In ambient experiment #2, the Benthemier (2566 mD) sandstone was initially saturated with 1 wt% acetic acid and 2500 ppm NaCl brine (compared to 1000 ppm in the first experiment). The gelation time duration was estimated to be between 5 and 6 hrs using the aforementioned bulk gelation experiments. The silicate residence time was estimated to be 24 hrs at a frontal velocity of 1 ft/day. The pressure build-up was expected to occur mostly at the inlet section of the core.

Figure 11 shows the results of experiment #2. The total injection time was 14 hours at a constant frontal velocity of 1.0 ft/day. The baseline pressure drop (ΔP) for 1 cp Newtonian fluid (brine solution) in this core and velocity of 1.0 ft/day was calculated using Darcy's law as 0.015 psi. Pressure drop in the whole core and each section increased monotonically for ~0.55 PVs. The pressure drop across the

whole core was 2.4 psi at the end of the experiment which corresponded to a permeability reduction of ~150. The inlet section of the core had the largest permeability reduction.

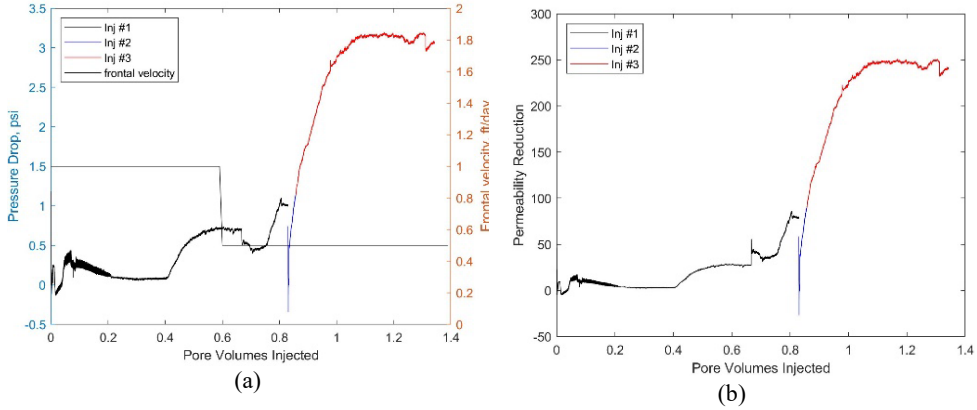

Figure 10. (a) Pressure drop and (b) permeability reduction versus pore volumes injected for ambient phase experiment #1.

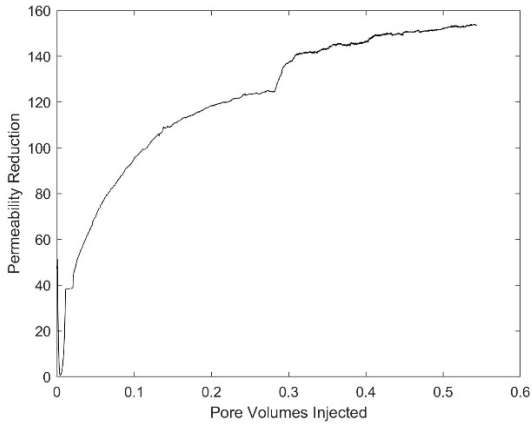

Figure 11. Permeability reduction versus pore volumes injected for ambient phase experiment #2.

Experiment #3

Experiment #3 was a High-Pressure High Temperature (HPHT) core flood with dissolved CO_2 at 1500 psi and 60°C. CO_2 was bubbled through brine (30,000 ppm salinity) to create a CO_2-Saturated brine solution (0.755 mol/kg). Prior to silicate injection, CO_2 saturated brine was injected at 1.0 ml/min (17 ft/day) into the Benthemier sandstone (1605 mD). The gelation time duration was estimated to be ~40 minutes using the aforementioned bulk gelation experiments and the procedure described in Equation 2. The silicate residence time was estimated to be at least 1.2 -1.5 times the bulk gelation time (i.e., 48 -60 mins). The pressure build-up was expected to occur mostly at the inlet section of the core.

Figure 12 shows the permeability reduction versus pore volumes injected for the whole core. The baseline pressure drop for the whole core was estimated as 0.225 psi using Darcy's law and the viscosity of CO_2-saturated brine at 60°C (~ 0.55 cp). A 15 wt.% silicate solution (in DI water without CO_2) was injected (t=0) into the core at a flow rate of 1.0 ml/min (17 ft/day) to initiate the gelation process with the CO_2 saturated brine core. A rapid and continuous increase in the pressure drop was observed as more silicate solution is injected. After 8.0 PV, the pressure drop across the whole core was ~18psi which corresponded to a permeability reduction of ~80 and most of the permeability reduction was in the inlet portion of the core.

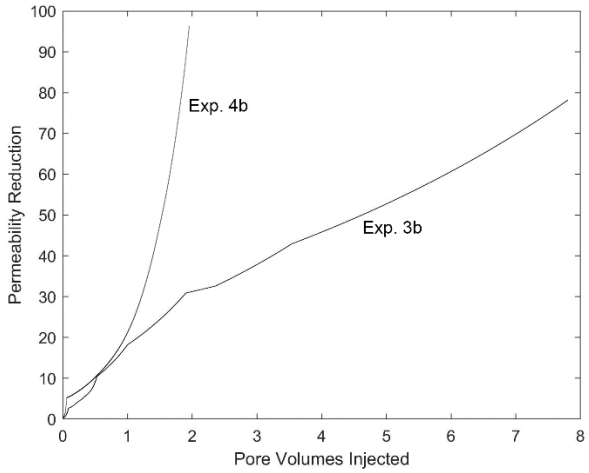

Figure 12. Permeability reduction versus pore volumes injected HPHT, CO_2-saturated brine experiments #3 and #4.

Experiment #4

In experiment #4, the procedure from the previous CO_2 HTTP experiment was repeated using the same solutions but with a different Bentheimer core. The baseline pressure drop and individual section pressure drops were measured with flowing CO_2 saturated brine. The baseline pressure drop was 0.21 psi for the whole core. Figure 12 shows the increase in permeability reduction which reaches nearly 100 after ~2 pore volumes. As was the case in the other experiments, permeability reduction was mostly in the inlet section of the core.

NUMERICAL SIMULATIONS

The reservoir simulation of gel treatment for the base case is illustrated in Figure 13 and Table 3. The CO_2 injection rate is 1 MMSCFD (19.1 kt/year). The silica concentration was 4% and injection time is 10 days. The selected silica concentration in the base model is typical for most silica gel applications [15,17,28]. The post-treatment CO_2 leakage over 25 years is 0.04 kilotons (Table 3). However, the leakage is 800 times lower than the case without gel treatment, which is still a negligible amount and suggests a satisfactory remediation.

Table 3. CO_2 leakage data for the base cases.

Cumulative CO_2	Initial period (0-5 years) kt	Post-Treatment (6-31 years) kt	All time kt	Leakage ratio %		
				Initial period	Post treatment	All time
Injected	95.27	476.73	572.0	N/A	N/A	N/A
Leakage without treatment	0.185	35.17	35.35	0.19	7.4	6.2
Leakage (Silica)	0.185	0.044	0.229	0.19	0.009	0.04

Figure 13 shows that remediation distance (distance from the injection well to the edge of the gel plume) increases with longer silica injection time. Treatment is successful if silica is injected for ≥ 10 days.

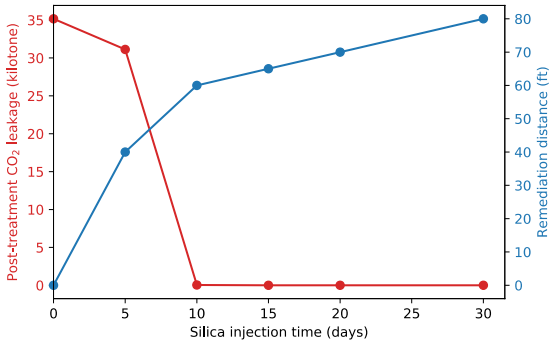

Figure 13. Post-treatment CO_2 leakage (red) and the corresponding remediation distance (blue) vs. silica injection time. Parameters other than injection time are the same as the base case model. The results for zero injection time corresponds to the case without gel treatment. Figure taken from [25].

Remediation distance also increases monotonically with silica concentration (Figure 14). Figure 14 shows that silica concentration ≥ 3% is needed for satisfactory CO_2 leakage remediation.

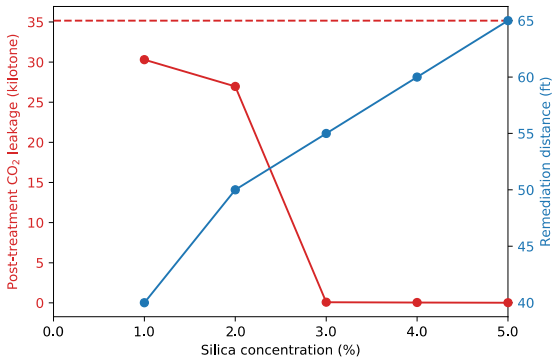

Figure 14. Post-treatment CO_2 leakage (red) and the corresponding remediation distance (blue) vs. silica concentration. The red dash line indicates leakage amount corresponding to the post-treatment period for the case without gel treatment. Figure taken from [25].

CONCLUSIONS

To investigate the use of silica gel for leak remediation in geologic storage formations, experimental work included bulk gelation experiments, micromodel floods and core floods. Bulk gelation experiments were initially performed to measure the gel time at different silicate content, acid concentrations, salinities, and temperatures. Gel formation in the silicate system is triggered by acidic pH conditions. The bulk experiments used acetic acid as a proxy for the carbonic acid that is formed by high pressure CO_2 injection into a brine-containing formation. The results were used to fit an existing model for gelation time. The fitted model was used as a predictive tool to establish conditions for the micromodel and core flood experiments. Micromodel and core flood experiments (using acetic acid at ambient conditions and CO_2-saturated brine at HPHT conditions) were then performed to investigate the reactive transport of silicate gel in porous media, to compare the results obtained from gelation in porous media to the gelation results from the earlier bulk experiments and finally, to investigate the capability of the gel in permeability reduction and sealing of the core.

The main conclusions from the experiments are summarized below:

- When the gelation was initiated by acetic acid, bulk experiment results show that increasing acid content consistently accelerates the gelation kinetics (shorter gelation time) regardless of silicate content, while adding more silicate to the gelation system initially retards, then accelerates the gelation. Higher salinity in the system and higher temperature both lead to faster gelation time. The effect of acid content and salinity on gelation kinetics is much more complicated when a strong acid (HCl) was used as the initiator. In particular, more strong acid accelerates gelation at high silicate content. However, at low silicate content, increasing strong acid in the solution first accelerates then deaccelerates gelation. Increasing salinity inhibits gelation at low salt concentration but increases kinetics at high salt concentration. These observations suggest the controlling kinetic processes differ between weak acid initiated and strong acid-initiated gelation.
- A literature model for gelation time prediction was adopted and the parameters were tuned to match the bulk gelation experimental results. The fitted model was used as a predictive tool for the core flood experiments.
- Two micromodels of porous media were fabricated with flow lengths of 2.5 cm and 1 foot, heterogeneous properties, and three-dimensional features. Gel injection induced

permeability reduction of 2-3 orders of magnitude. Visualization of gelation by a microscope showed that gelation occurred relatively uniformly throughout the 1 ft micromodel.

- Two sets of gel injection experiments were conducted using sandstone cores at ambient conditions (with acetic acid). The first experiment was performed using 1000 ppm NaCl brine and the second experiment used 2500 ppm NaCl to investigate the gel's capability at sealing and permeability reduction. Permeability was reduced by up to a factor of 100-250 in the experiments. Permeability reduction was found to occur mainly in the first part of the core. The downstream sections of the core showed permeability reduction only after multiple pore volume injections of silicate solution.
- Two gel injection experiments in sandstone cores were conducted at High-Pressure High Temperature (1500 psi, 60°C). The CO_2-saturated brine had a salinity of 30,000 ppm. Both experiments showed permeability reduction by approximately two orders of magnitude.

The key observations from the reservoir simulations are:

- The base case models in reservoir-scale numerical simulations show that with appropriate operating conditions, silica gel systems can successfully seal the fracture and significantly reduce CO_2 leakage by a factor of 1000.
- Reservoir simulation predicts that longer injection times lead to larger treatment area and, therefore, to a more likely successful treatment. At 200 bbl/day of silica injection rate, a fracture 57 ft from the gel injection well can be sealed if silica is injected for ≥ 10 days for the permeability distribution tested. A higher injection rate also leads to larger treatment area because a larger amount of gel was injected. To obtain satisfactory leakage remediation, silica gel treatment requires a high injection concentration (≥ 3%) because it has a relatively low residual resistance factor (weak gel strength).
- Gel treatment can be unsuccessful at low average permeability because low injectivity does not allow the gel to reach the fracture. However, extremely low permeability can help to prevent CO_2 leakage to a certain extent. A higher Dykstra-Parsons (V_{dp}) coefficient (more heterogeneity) leads to a preferential flow path for gel to reach the fracture. At very high V_{dp} (V_{dp}≥0.8), the low permeability around the injection well can cause low injectivity and insufficient treatment area, but also help to somewhat prevent CO_2 leakage. When the horizontal correlation length is ≥ 750 ft, the gel cannot reach the fracture, which leads to treatment failure.

ACKNOWLEDGEMENTS

The authors would like to acknowledge the CO_2 Capture Project (CCP) for the financial and technical support of this project.

REFERENCES

1. Tongwa, P., Nygaard, R., Blue, A., and Bai, B., 2013, "Evaluation of Potential Fracture-Sealing Materials for Remediating CO_2 Leakage Pathways during CO2 Sequestration," *International Journal of Greenhouse Gas Control*, 18, pp. 128–138.
2. Hadi Mosleh, M., Govindan, R., Shi, J.-Q., Durucan, S., and Korre, A., 2016, "Application of Polymer-Gel Solutions in Remediating Leakage in CO_2 Storage Reservoirs," SPE 180135, SPE Europec featured at 78th EAGE Conference and Exhibition, Vienna, Austria.
3. Manceau, J.-C., Hatzignatiou, D. G., de Lary, L., Jensen, N. B., and Réveillère, A., 2014, "Mitigation and Remediation Technologies and Practices in Case of Undesired Migration of

CO_2 from a Geological Storage Unit—Current Status," *International Journal of Greenhouse Gas Control*, **22**, pp. 272–290.
4. Axford, S. D. T., 1997, "Aggregation of Colloidal Silica: Reaction-Limited Kernel, Stability Ratio and Distribution Moments," *J. Chem. Soc., Faraday Trans*., 93(2), pp. 303–311.
5. Iler, R. K., 1979, The Chemistry of Silica: Solubility, Polymerization, Colloid and Surface Properties, and Biochemistry, Wiley, New York.
6. McIntosh, G. J., 2012, "A Theoretical Kinetic Model of the Temperature and PH Dependent Dimerization of Orthosilicic Acid in Aqueous Solution," *Phys. Chem. Chem. Phys*., 14(2), pp. 996–1013.
7. Jurinak, J. J., and Summers, L. E., 1991, "Oilfield Applications of Colloidal Silica Gel," SPE 18505-PA, *SPE Journal*, 6(04), pp. 406–412.
8. Lakatos, I., and Lakatos-Szabo, J., 2012, "Reservoir Conformance Control in Oilfields Using of Silicates: State-of-the-Arts and Perspectives," SPE 159640-MS, SPE Annual Technical Conference and Exhibition, San Antonio, Texas, USA.
9. Jurinak, J. J., Summers, L. E., and Bennett, K. E., 1991, "Laboratory Testing of Colloidal Silica Gel for Oilfield Applications (Supplement to SPE 18505)."
10. Huang, J., Al-Mohsin, A., Bataweel, M., Karadkar, P., Li, W., and Shaikh, A., 2017, "Systematic Approach to Develop a Colloidal Silica Based Gel System for Water Shut-Off," Society of Petroleum Engineers.
11. Stavland, A., Jonsbråten, H., Vikane, O., Skrettingland, K., and Fischer, H., 2011, "In-Depth Water Diversion Using Sodium Silicate – Preparation for Single Well Field Pilot on Snorre," SPE European Formation Damage Conference, Noordwijk, 7-10 June 2011.
12. Nasr-El-Din, H. A., and Taylor, K. C., 2005, "Evaluation of Sodium Silicate/Urea Gels Used for Water Shut-off Treatments*," Journal of Petroleum Science and Engineering*, **48**(3–4), pp. 141–160.
13. Skrettingland, K., Giske, N. H., Johnsen, J.-H., and Stavland, A., 2012, "Snorre In-Depth Water Diversion Using Sodium Silicate - Single Well Injection Pilot," SPE 154004-MS, SPE Improved Oil Recovery Symposium, Tulsa, Oklahoma, USA.
14. Oglesby, K. D., D'Souza, D., Roller, C., Logsdon, R., Burns, L. D., and Felber, B. J., 2016, "Field Test Results of a New Silicate Gel System That Is Effective in Carbon Dioxide Enhanced Recovery and Waterfloods," SPE 179615-MS, SPE Improved Oil Recovery Conference, Tulsa, Oklahoma, USA.
15. Hatzignatiou, D. G., Helleren, J., and Stavland, A., 2014, "Numerical Evaluation of Dynamic Core-Scale Experiments of Silicate Gels for Fluid Diversion and Flow-Zone Isolation," SPE 170240-PA*, SPE Production & Operations*, **29**(02), pp. 122–138.
16. Kim, M., Corapcioglu, M. Y., and Park, J.-W., 2007, "Numerical Investigation of the Gel Barrier Formation with Vertical Injection Pipe," *Environ Geo*l, **53**(3), pp. 635–642.
17. Akhlaghi Amiri, H. A., Hamouda, A. A., and Roostaei, A., 2014, "Sodium Silicate Behavior in Porous Media Applied for In-Depth Profile Modifications," *Energies*, **7**(4), pp. 2004–2026.
18. Omekeh, A., Hiorth, A., Stavland, A., and Lohne, A., 2017, "Silicate Gel for In-Depth Placement - Gelation Kinetics and Pre-Flush Design," 19th European Symposium on Improved Oil Recovery, Apr 2017,Stavanger, Norway.
19. Castañeda-Herrera, C. A., Black, J. R., Llanos, E. M., Stevens, G. W., and Haese, R. R., 2018, "Formation of an Amorphous Silica Gel Barrier under CO2 Storage Conditions," *International Journal of Greenhouse Gas Control*, 78, pp. 27–36.
20. Mejia, L., Zhu, P., Hyman, J. D., Mohanty, K. K., and Balhoff, M. T., 2020, "Coreflood on a Chip: Core-Scale Micromodels for Subsurface Applications," *Fuel*, 281, p. 118716.
21. Xu, K., Liang, T., Zhu, P., Qi, P., Lu, J., Huh, C., and Balhoff, M., 2017, "A 2.5-D Glass Micromodel for Investigation of Multi-Phase Flow in Porous Media," Lab Chip, 17(4), pp. 640–646.

22. Cha, Luming, Chiyu Xie, Qihong Feng, and Matthew Balhoff. “Geometric criteria for the snap-off of a non-wetting droplet in pore-throat channels with rectangular cross-sections.” *Water Resources Research* **57**, no. 7 (2021): e2020WR029476.
23. Lee, V. B., 2015, “The Development and Evaluation of Polymers for Enhanced Oil Recovery,” Thesis, University of Texas at Austin.
24. Pyrcz, M. J., and Deutsch, C. V., 2014, *Geostatistical Reservoir Modeling*, Oxford University Press, Oxford, New York.
25. Zhu, P., Tavassoli, S., Ryu, J., Pyrcz, M., and Balhoff, M. T., in review, “Injection of Gel Systems for CO2 Leakage Remediation,” *International Journal of Oil, Gas, and Coal Technology.*
26. Remy, N., Boucher, A., and Wu, J., 2011, Applied Geostatistics with SGeMS: A User’s Guide, Cambridge Univ. Press, Cambridge.
27. CMG STARS (Computer Software), 2018 CMG.
28. Hiorth, A., Sagen, J., Lohne, A., Nossen, J., Vinningland, J. L., Jettestuen, E., and Sira, T., 2016, “IORSim-A Simulator for Fast and Accurate Simulation of Multi-Phase Geochemical Interactions at the Field Scale,” ECMOR XV - 15th European Conference on the Mathematics of Oil Recovery.
29. Derjaguin, B., and Landau, L., 1941, “Theory of the Stability of Strongly Charged Lyophobic Sols and of the Adhesion of Strongly Charged Particles in Solutions of Electrolytes*,” Acta Physicochimica*, 14, pp. 633–662.
30. Gorrepati, E. A., Wongthahan, P., Raha, S., and Fogler, H. S., 2010, “Silica Precipitation in Acidic Solutions: Mechanism, PH Effect, and Salt Effect,” *Langmuir*, **26**(13), pp. 10467–10474.
31. Mao, S., Zhang, D., Li, Y., and Liu, N., 2013, “An Improved Model for Calculating CO_2 Solubility in Aqueous NaCl Solutions and the Application to CO_2–H_2O–NaCl Fluid Inclusions,” *Chemical Geology*, 347, pp. 43–58.

Carbon Dioxide Capture for Storage in Deep Geological Formations, Volume 5
Karl F. Gerdes (Editor)
© 2022 BP. All rights reserved.

Chapter 25

DEMONSTRATION OF DE-FACTO CO_2 STORAGE AT A CO_2-EOR SITE, CRANFIELD, MS

Seyyed A. Hosseini[1], Masoud Alfi[2], Jean-Philippe Nicot[1], and Vanessa Nunez-Lopez[1]
[1]Bureau of Economic Geology, The University of Texas at Austin, Austin, TX, USA
[2]Petroleum Engineering Department, Texas A&M University, College Station, TX, USA

ABSTRACT: Carbon dioxide injected for enhanced oil recovery will distribute into several phases in the target geological formation. This distribution in oil, gas (either free or residually trapped) and brine phase depends on many factors including reservoir temperature and pressure, initial fluid saturations, brine salinity, relative permeability parameters, etc. In post-injection periods, as the CO_2 mass evolves and stabilizes, this distribution will change. Our numerical simulations, based on Cranfield CO_2-EOR project data, demonstrate these variations are significant and mostly depend on the operator's selected field development strategy: continuous gas (CO_2) injection, water alternating gas, water curtain injection, or combinations of these.

KEYWORDS: CO_2 defacto storage, Cranfield, trapping mechanism, CO_2-EOR

INTRODUCTION

The increasing pressure to combat climate change has brought carbon capture and storage (CCS) to the fore as a fossil fuel emission mitigation tool and greater attention is being paid to the potential for CO_2 enhanced oil recovery (CO_2-EOR) to support geological CO_2 storage. CO_2-EOR offers commercial opportunities to improve oil recovery from mature oil fields while offering a permanent storage option for large CO_2 volumes. Normally only 25-35% of the oil in a reservoir can be extracted from pressure depletion methods during the primary production stage. Primary recovery generally uses just the original reservoir pressure to facilitate production whereas, in EOR, CO_2 is injected into an oil-bearing stratum under high pressure to push additional oil to a production wellbore. Oil displacement by CO_2 injection relies on phase behaviour of mixtures of gas and oil, which are strongly dependent on reservoir temperature, pressure, and oil composition. There are two main types of CO_2-EOR processes: miscible and immiscible CO_2-EOR. During the passage of CO_2 from injection well to production well, to increase oil production some of the CO_2 will be permanently trapped in the injection interval. Such a dual-nature process represents a technically attractive and potentially economic way to spur greater CCS action. In other words, by performing additional site characterization and risk assessment tasks, employing reliable monitoring techniques, and revisiting the field abandonment practices, CO_2-EOR practices can be modified at a minimal cost and tied to CCS projects to deliver significant capacity for long-term CO_2 storage.

Although mature oil fields are considered potential candidates for carbon storage sites, the fact that such underground structures have held hydrocarbons for millions of years does not rule out the possibility of CO_2 leakage. EOR sites provide a great amount of information about the formation quality and performance (data available from initial characterization, primary and secondary recovery); however, there are some unwanted issues as well. Mature oil and gas fields include many

legacy and plugged and abandoned wells (P&A wells), about which there is little or no information on the current sealing quality of some of them. This can add to the overall risk of the project. These wells should be considered as possible leakage pathway(s) from deep subsurface to shallower formations (possibly including ground water resources or the surface). The long timescales associated with CO_2 storage require operators to demonstrate safe storage during injection and after the site closure. This demands a detailed risk assessment plan. Better understanding of CO_2 storage in oil reservoirs is essential for reliable assessment of storage performance and related risks. A considerable source of uncertainty is driven by the lack of knowledge of the relative importance of the diverse CO_2 trapping mechanisms and of the CO_2 distribution between the different phases over time. The main trapping mechanisms include stratigraphic trapping (CO_2 is trapped in the gaseous or supercritical phase under low permeability cap rocks), capillary trapping (CO_2 retention due to capillary forces), dissolution trapping (CO_2 is dissolved in oil and brine), and mineral trapping (conversion of CO_2 into mineral precipitants) [1]. Stratigraphic trapping of CO_2 usually constitutes a considerable portion of the stored CO_2; however, this trapping mechanism corresponds to the highest leakage risk because the CO_2 is still potentially mobile. The lower density and viscosity of the supercritical phase could drive lateral or vertical CO_2 plume migration as a result of pressure difference or buoyancy forces. On the other hand, dissolved CO_2 is considered less prone to leakage due to the higher density and viscosity of the liquid hydrocarbon and brine. Small-scale experiments and simulations [2,3] have shown that CO_2 dissolved in brine can increase convective forces in the brine and create convective mixing, but it has not been proven to occur in large scale systems, such as at the Bravo Dome natural CO_2 deposit [4]. CO_2 dissolved in residual oil is also stored permanently unless, thanks to newer technologies, those resources are produced in the future. Mineral trapping is the safest mechanism to trap CO_2 for long time periods, but this mechanism typically takes effect later after the abandonment of the site (hundreds of years time scale).

A better understanding of CO_2 trapping mechanisms and, in particular, of their relative importance, would help not only to set our storage goals but also to optimize the project risks and rewards. An additional important motive to study this topic is related to the U.S. Department of Energy (USDOE) requirements to provide accurate mass balance and accounting for CO_2-EOR projects. This can potentially impact how storage is defined for any future tax credit claim.

Guided by these overarching needs to assess risks and do mass accounting, the current study discusses CO_2 distribution among different phases during a typical CO_2-EOR and storage operation. This study uses Cranfield, Mississippi data to constrain the results and to address the uncertainty related to CO_2 distribution. We restricted our simulations to a 75-year time period and, based on Cranfield field observations reporting low to non-existent level of geochemical rock-fluid interaction [5], we have ignored CO_2 mineral trapping within this timeframe.

One important point is related to the definition of the CO_2 retention for a commercial project. If we define any movement of CO_2 out of the area of review as leakage (for example, area of review could be limited vertically by top and bottom seals and horizontally by lease boundaries or area covered by monitoring, verification, and accounting-MVA-program), then any CO_2 present beyond these boundaries should not be considered as stored. This does not necessarily mean that CO_2 has migrated back to the atmosphere but simply that it cannot be counted as stored CO_2.

This study includes an uncertainty quantification for the effect of various geologic and flow parameters during CO_2-EOR and storage processes. Simulation results from this part of study provide a clear picture of CO_2 distribution and trapping mechanisms and the uncertainty associated with different reservoir parameters. The uncertainty quantification study used a simple synthetic model instead of the actual Cranfield model to enable quick execution of thousands of simulations to estimate CO_2 partitioning with varying reservoir, rock, and fluid parameters.

This study relies on public-domain data related to the Denbury Onshore, LLC-operated EOR site of Cranfield, MS, where The University of Texas Bureau of Economic Geology (UT-BEG) has been conducting a research program for almost a decade [6]. The site is ideal for the study because it provides an optimal mass accounting data set–this was required by its comprehensive MVA program–which is used to constrain the reservoir simulations. UT-BEG used up-to-date geomodels developed for the Cranfield reservoir to simulate multi-physics scenarios that help to better understand the partitioning of CO_2 between the different trapping mechanisms.

One of the uncertain parameters in the study was the relative permeability of the Cranfield reservoir rocks. UT-BEG sent core plug samples to external labs to measure reservoir condition flow parameters. Appendix A in this paper specifically discusses material related to the experimental work on Cranfield core plugs. However, the rest of the study used flow parameters from the original Cranfield flow model.

The paper is organized as follows: first, we introduce our models and methods. Second, we discuss CO_2 distribution between the different phases during CO_2-EOR for four different injection scenarios. To account for the uncertainty related to the input parameters, an uncertainty quantification study on a wide range of parameters is also carried out. The document concludes with a summary of important findings and recommendations.

MODELING METHOD AND DESCRIPTION

Cranfield Background

Cranfield, MS has been the subject of several field experiments described in 16 papers grouped in a special issue of the *International Journal of Greenhouse Gas Control* (including [6,7,8]). The Cranfield site is located on the Adams-Franklin county line in Mississippi, east of the town of Natchez [9]. The original productive area of the reservoir was estimated to be 31.3 km^2 with a producing depth range of 3,060 to 3,193 m, a clastic reservoir located at the apex of a 4-way anticline in the Tuscaloosa Formation of Cretaceous age. Downdip an active aquifer provided pressure support. The initial reservoir temperature was reported to be 125°C with an initial reservoir pressure of 32.4 MPa at 3,040 m. A sealing fault divides the productive zone into two compartments (the dashed NW-SE line in Figure 1a). To see more regional and local cross sections, refer to [6,15].

The first oil producing well was drilled in 1944. Since then, a productive area of about 7,750 acres has been defined by 93 producing wells. The oil wells were drilled based on a 40 acre spacing, whereas the spacing for the gas wells was 320 acres. The dome-shaped reservoir consists of an oil ring overlain by a large gas cap. A cycling and extraction gas plant was used to reinject the produced gas from the Cranfield and deeper Paluxy reservoirs into the Tuscaloosa Formation. By 1951, the injected gas had reached many of the oil zone wells. The gas cycling continued until 1960 with dry gas sweeping the gas cap and the oil zone. Although the gas injection plans were meant to avoid, or slow down, the pressure depletion in the reservoir, reservoir pressure gradually fell below 27.6 MPa (4,000 psi) causing water to encroach into the oil zone as the oil was produced. By the beginning of 1960, most of the wells had either a ~100% water cut or a gas-oil ratio (GOR) greater than 100,000 standard cubic feet per stock tank barrel (scf/STB) with an average field water cut equal to 88% and GOR equal to 85,000 scf/STB. The blowdown of the gas cap started then. At the same time, water was produced in large volumes and reinjected into other overlying formations to prevent the aquifer from pushing the remaining oil into the gas space. Gas injection stopped in 1964 when the project was near its economic limit. Production from the field was halted in 1966 and the reservoir was abandoned. This time period, from 1944 to 1966, corresponds to the conventional historical production interval. Over the next several decades, a strong water drive restored pressure to near-initial levels.

In 2007, CO_2-EOR was initiated by Denbury Onshore, LLC to sweep the bypassed residual oil. Between 2008 and 2015, more than half of the oil ring (Figure 1a) was developed using a semi five-spot injection pattern with continuous CO_2 injection. Initial patterns started in the northern part of the field and continued clockwise around the oil ring. This time period corresponds to the historical CO_2-EOR injection period. More details about reservoir specifications, production history, simulation projects, and monitoring efforts can be found in other works [6,7,9-12].

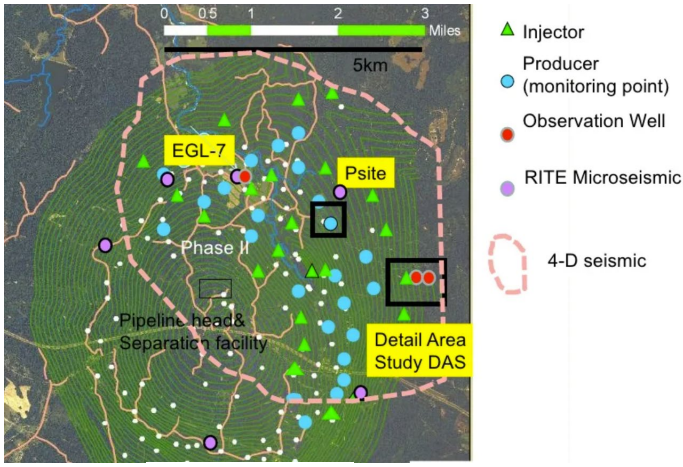

(a) Cranfield Site

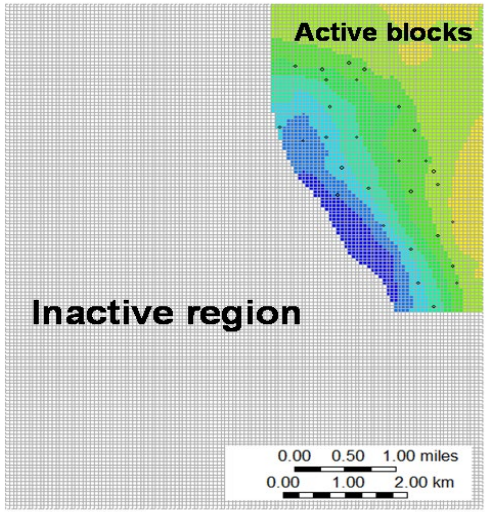

(b) Simulation gridding

Figure 1. Structural contour map at Cranfield (a) the black dashed line represents the sealing fault that separates the northeastern section of the reservoir from the rest and reservoir simulation model to simulate the CO_2 injection process (b) Simulation effort is focused on the northeastern side of the reservoir, so the rest of the model is inactive to reduce the computational cost.

Model Description

The current work takes advantage of the minimum interaction between the two productive zones at Cranfield, which are separated by a sealing fault. Historical production data and monitoring wells across faults during the development of the project has shown no signal of fluid communication across the fault. Because of this fact, the operator of the field decided to develop one side of the fault first and then years later moved to the other side of fault with no concerns regarding the pressure (miscibility) and fluid loss across the fault. Using a well-defined compartment allowed us to run faster simulation scenarios with an emphasis on the physics of the problem without loss of generality. The work focuses on the smaller zone, the northeastern part of the reservoir, with no concern about the fluid movement between this northeast compartment and the rest of the reservoir, as the balanced field development plan minimizes such interactions. Results obtained from the study are easily scalable to other parts of reservoir as pattern geometry and operations repeated systematically around the field. This approach substantially decreased the number of active grid blocks in the model, reducing the computational cost.

A 3-D model with a 124×149×20 (X×Y×Z) cartesian grid encompasses the entire reservoir area of 7.5×9.1 km^2 with a maximum reservoir thickness of 24.4 m. The total number of grid blocks is 369,520, out of which 82,559 grid blocks located in the northeastern compartment of the reservoir are active (Figure 1b). All grid blocks have a uniform size of 61×61×1.2 m^3.

This smaller zone of the reservoir currently includes 11 injection wells and 10 production wells. We have access to conventional historical production and injection data (1943-1966) as well as to recent historical CO_2-EOR production and injection volumes (including recycle stream) since 2007 when CO_2 injection started [13]. Additional available data in this area include well logs (e.g., resistivity, RST), 4D seismic[10], geochemical samples of brine before and during injection period, extensive pressure and temperature data [6-7,14], detailed analysis of injected and produced gas including the methane content (time series; continuous gas composition is available from the UT-BEG monitoring wells), some oil phase PVT and CO_2-oil minimum miscibility pressure data (MMP), relative permeability, and pressure transient tests. Extensive petrographic studies of the formation rocks (Lower Tuscaloosa conglomerates and sandstones) have also been performed with detailed analyses of core samples [5,15]. Aqueous chemistry from autoclave reaction experiments using the reservoir rock and brine is also available [5].

The miscibility process achieved during the CO_2-EOR process is one of the main driving mechanisms that helps achieve high efficiency in sweeping the residual oil. CO_2 dissolves into the oil phase, facilitating its movement and reducing the amount of oil trapped in the reservoir. However, such a process exhibits complicated physics compared to regular immiscible water flooding processes. An accurate simulation of such processes requires a physics-based model that takes into account the thermodynamics of CO_2/hydrocarbon interactions. Failure of black oil models, although very efficient in less complicated cases, to correctly address such complexities have historically led to the introduction of the more thermodynamically robust compositional models as a more reliable alternative to simulate miscible processes. CO_2 injection processes in this study are simulated using a GEM module from the Computer Modelling Group (CMG). GEM is an advanced general equation-of-state compositional simulator, which includes equation of state, CO_2 miscible flood, CO_2/brine interactions, and complex phase behavior. The simulator is set up to model three fluid phases including water, oil, and gas. Compositional models inherit a heavy computational load because of the large number of chemical components in the system.

The Peng Robinson equation of state [16] is used in this study to model reservoir fluid properties. Our fluid model is composed of seven different components, including CO_2. The actual oil has more components, but to improve computational efficiency, several components, in particular heavy ones, have been lumped into a single component. The thermodynamic model and component properties

were tuned based on Cranfield fluid data published by Weaver and Anderson [9]. The fluid data used for this purpose included bubble point pressure, solution gas-oil-ratio, formation volume factor, and oil and gas viscosities. One important factor during modelling of CO_2-EOR and storage processes in reservoirs with aquifers is to correctly generate the CO_2/brine solubility data. CO_2/water solubility in the current model is modelled using Henry's Law. Henry's Law assumes a linear relationship between CO_2 partial pressure/fugacity and solubility in water.

$$f = x * H$$

where *f* is the fugacity of the component, *x* is the composition of the component in the aqueous phase; and *H* is the Henry's Law constant.

The Henry's Law constants, *H*, at any pressures, *p*, in the range of validity, are calculated as follows:

$$\ln (H) = \ln (hens) + v_\infty * (p\text{-}refp)/RT$$

where *ln* is the natural log operation, *T* is temperature, *R* is ideal gas constant, *refp* is the reference pressure, v_∞ is partial molar volume of CO_2 in water at infinite dilution and *hens* is the reference Henry's Law constant at reference pressure and temperature.

The CO_2/brine solubility data at different pressures, temperatures, and salinities are from Duan and Sun [17]. Figure 2 displays the CO_2 solubility at 120°C and 30 MPa [17,18], which are close to Cranfield pressure and temperature, for different salinity values. The salinity of the brine at Cranfield is categorized as a highly saline formation water, with a salinity of 150,000 ppm or 2.8 molality (NaCl).

We obtained the reference Henry's Law constant (*hens*) based on data plotted in Figure 2. Formation brine can dissolve 0.76 mole of CO_2 per kilogram of solution, which is equivalent to a maximum mole fraction of 0.013 CO_2 dissolved in brine at ~30 MPa and 120°C. The reference Henry's Law constant based on the CMG-GEM definition has a value of 670 MPa at the reference pressure of 6.9 MPa and 125°C (it is extrapolated for other pressures). CMG-GEM computes the Henry's Law constant as a function of temperature and pressure. For more details, refer to CMG-GEM user manual.

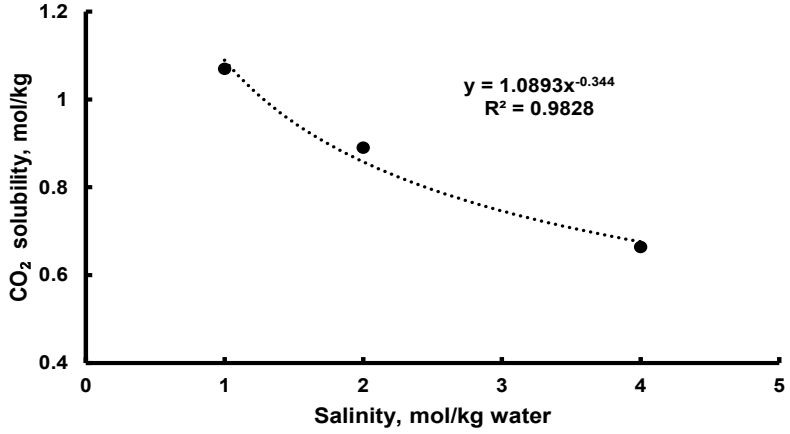

Figure 2. CO_2 solubility in brine for different salinity values at 120°C and 30 MPa. Data points plotted from [17].

The original permeability and porosity distribution is from Hosseini *et al.* [7]. They used a purely mechanistic approach to recognize eight different facies (flow zones) in the reservoir based on combined permeability and porosity sets. Each flow zone has a porosity and permeability specified, which is constant for the entire zone. These flow zones, which make up the entire reservoir model, are categorized under two main groups of low permeability ("*shale*") and high permeability ("*sand*") zones. High permeability channels in the lower Tuscaloosa Formation at Cranfield have been mapped and confirmed by various fluid-flow responses [15,19]. However, the geometry of high permeability channels throughout the field presented by Hosseini *et al.* [7] are based on a facies-based geostatistical extrapolation of the available data in the Petrel software. In this study, the permeability contrast between the sand and shale facies and the shape and location of high permeability flow paths was examined as a history matching parameter to match field data by using an ensemble of the realizations. During the history matching process in each individual realization, the shape and location of channels remain constant. Table 1 provides the reservoir properties used in this work.

Table 1. Reservoir-related parameters used in numerical modeling of Cranfield.

Parameter	**Value**
Kh/Kv (permeability anisotropy)	0.05
Brine salinity	150,000 ppm
Initial bubble point pressure	31.7 MPa
Original water oil contact depth	3,064 m
Original gas oil contact depth	3,008 m

Relative permeability curves used in this study are originally obtained from the data published by Weaver and Anderson [9]. The relative permeability endpoints and residual saturations were slightly modified to match the field production data. Although quite helpful in obtaining an acceptable match between the field data and simulation results, the slight modifications of relative permeability data (Figure 3) have not significantly affected the agreement between the relative permeability set used in this study and the one originally published by Weaver and Anderson [9].

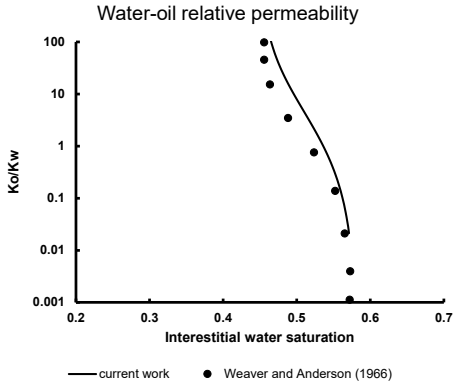

(a) Water-oil relative permeability.

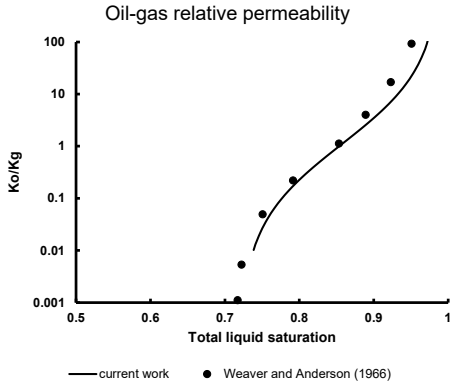

(b) Oil-gas relative permeability.

Figure 3. Water-oil (a) and oil-gas (b) relative permeability curves used in the current study are slightly modified from the original Weaver and Anderson [9] values to match oil, gas, and water production data during the CO_2 injection period.

As mentioned in the introduction, experiments to obtain a new set of relative permeabilities from Cranfield core plugs were still being performed at the completion of the simulations and their results were not used. The experiments were specifically designed for the CO_2-brine system at reservoir pressure and temperature (see Appendix A).

To perform our numerical studies, the Cranfield reservoir model was first calibrated to the available conventional historical data (1944-1966). Our past history matching studies were done using a black oil simulator but, in this study, we performed the history matching using a compositional model, although the same static model was used. Some of the calibration data are shown in Figure 4, including injection and production rates and changes in average reservoir pressure.

We executed an extensive set of simulations to history match the conventional historical data related to the northeastern compartment of Cranfield. The main uncertain parameters used in this history matching were field-wide porosity and permeability multipliers, perforated interval for wells, water-oil contact and gas-oil contact depth, as well as the locations of high-permeability channels. More details about the history matching process is in [7]. In addition, history matching helped to select the best facies model (best location of channels and their distribution). Overall oil production data were used as hard constraints to history match other field observations. Aquifer parameters such as permeability, porosity, and thickness were calibrated to ensure that at the end of the historical shut-in period (to 2007), the average reservoir pressure was back up to its original initial value. Input and output data of the model at the end of the conventional historical production, including the historical shut-in period, were then saved and used to restart the model with the additional parameters needed to accurately represent the CO_2-EOR operations.

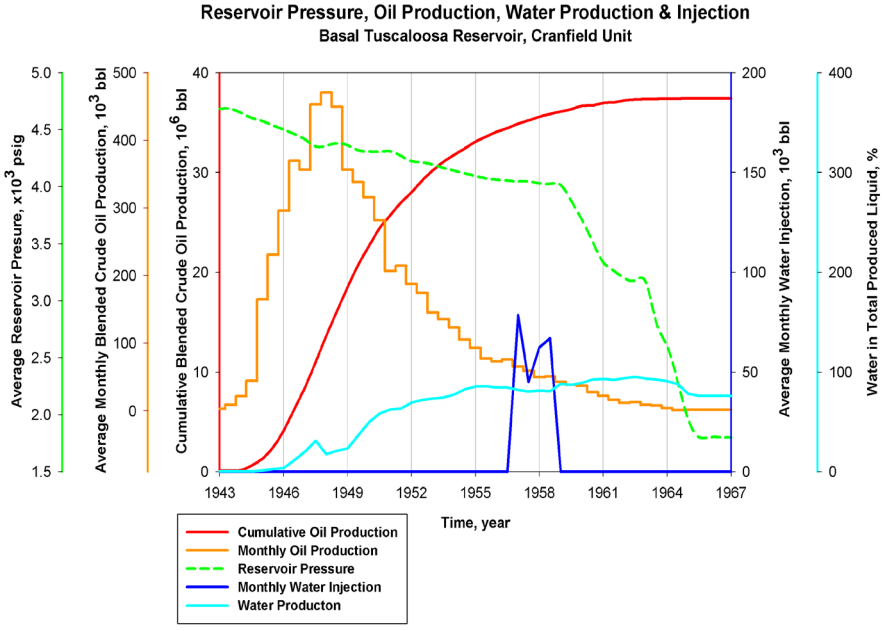

Figure 4. Historical injection production data at Cranfield for history matching and initializing the reservoir model prior to CO_2-EOR operations.

A total number of 12 injection wells and 10 production wells were used in the course of the CO_2-EOR period. Injection wells were modelled based on the known injected CO_2 volumes available for the historical CO_2-EOR injection period at each well location. To account for the amount of CO_2 entering the study area, one injection well operating at the edge of the area of interest was set at half of its actual injection rate. The other half is assumed to enter the other compartment of the reservoir. Oil, water, and gas production rates were available for all the producing wells during the historical CO_2-EOR injection period (July 2008 to October 2012). Monthly oil production rates were used as the operational constraint for the production wells and water and gas production were history matched. This second round of history matching was based on observing/matching reservoir response by adjusting the relative permeability parameters and the CO_2 miscibility in oil. These parameters are specifically used for calibrating the model for CO_2-EOR so that our prior history matching efforts are not lost. As discussed before, the presence of high permeability channels at Cranfield has been previously reported [7]. Analysis of CO_2 breakthrough times (the time it takes for CO_2 to reach the production wells) confirmed the presence of such high permeability channels as CO_2 reaches some of the producing wells in a relatively short time after injection starts, despite the noticeable distance between the injection and production wells.

Methods

The Cranfield Model

We assumed four different scenarios, starting from continuous gas (CO_2) injection (CGI) which is the actual production scenario in this field followed by the operator. This is not a typical CO_2-EOR strategy for many operators, but depending on the availability of the CO_2, one may choose this type of strategy. Additional scenarios include water alternating gas (WAG) and CGI along with water curtain injection (WCI). WCI consists in injecting water at the periphery of the reservoir and below the water oil contact (WOC) to keep the CO_2 within the patterns and limit its downward movement. The water curtain can have other benefits; for example, for reservoirs with low pressure, it can help to increase the reservoir pressure to miscibility pressure. In some reservoirs with high permeability where increasing and maintaining the pressure inside patterns is difficult, a water curtain may be deployed around the patterns (not necessarily at WOC). The last scenario combines the WAG and WCI. In all these scenarios, injection was active for 25 years. At the end of 25 years, all wells are shut in and the simulations keep running for another 50 years (post-injection period). In the CGI scenario, we used average injection and production rates from 2008 to 2012 to model the remainder of the active CO_2-EOR period (to 2033).

We then calculated the amount of CO_2 in the oil, brine, and gas (mobile and immobile) phases. Mobile CO_2 here is defined as any gas saturation that is above the residual gas saturation and can potentially move (due to gravity or other external forces). Please note that if relative permeability hysteresis is included in the simulation model, this estimation of the residual gas saturation may not be accurate as residual gas saturation changes during subsequent drainage and imbibition processes. These calculations are based on exported cell by cell saturation and mole fractions. For example, if a grid block gas saturation is at 35% and residual gas saturation is set at 5%, 30% of the gas saturation is assumed to be mobile for that grid block. This mobile gas is assumed to be trapped by the structure of formation.

In addition, to further our study, we split the amount of CO_2 in the reservoir into two parts: CO_2 stored above the WOC, and CO_2 stored below the WOC. Some of the injected CO_2 at the edge of WOC will move down dip into the aquifer because of the strong viscous forces exerted by the injection well. This excursion out of the bounds of the reservoir will be limited and, at some point, will be counter balanced by gravity forces. The fluvial nature of the depositional system at Cranfield exaggerates this

down dip movement because its high permeability channels create opportunities for CO_2 downdip movement.

Based on available data and published results [12], pressure at some of the production and observation wells during the CO_2 injection process will go up to about 38 MPa but no higher, so in all of the scenarios discussed here, the overall reservoir pressure is kept under 38 MPa. This pressure criterion has helped us to adjust the injection rates for CO_2 and water in each scenario. For example, when WCI scenarios are tested, the CO_2 injection rates must be reduced (roughly the rate is based on equal reservoir volume basis) and add the water injection wells, so that average reservoir pressure is still below the selected threshold. On the other hand, if we keep the CO_2 injection rates as in the CGI scenario and just add water curtain injection, then the average reservoir pressure will exceed the acceptable limit. We have used this criteria so our simulations under various scenarios are comparable. Obviously if the reservoir pressure is allowed to reach much higher values in some scenarios, then higher production will result.

Simple Uncertainty Analysis

Some of the parameters used in numerical simulations of Cranfield are uncertain. We decided to perform uncertainty quantification simulations to evaluate the effect of these uncertain parameters on CO_2 distribution in different phases. We also expanded the analysis by varying some well-known parameters (see Table 2), in addition to varying the uncertain parameters, to create a picture that not only applies to Cranfield but also is applicable to other similar formations.

Table 2. Range of the parameters used in uncertainty quantification simulations. For definition of parameters, refer to Figure 5.

Parameter	Min	Max	Parameter	Min	Max
Swcon	0.05	0.35	Sgcrit	0.00	0.10
1-Swcrit	0.00	0.20	Krgcl	0.60	1.00
Soirw	0.05	0.30	Liquid relative permeability exponent	1.00	3.00
1-Sorw	0.00	0.20	Gas relative permeability exponent	1.00	3.00
Krocw	0.20	1.00	Solubility pressure (kPa)	3E4	1E5
Krwiro	0.10	0.60	Pore compressibility (1/kPa)	2E-6	1E-5
Water relative permeability exponent	1.00	3.00	Mole fraction of C21	0.06	0.14
Oil relative permeability exponent	2.00	4.50	Mole fraction of C7	0.26	0.30
Soirg	0.05	0.25	Permeability multiplier	0.01	0.50
1-Sorg	0.00	0.20	Porosity multiplier	0.7	1.5
Initial salinity (g NaCl/kg brine).	50	250			

Parameters considered in our uncertainty quantification analysis include all the parameters relevant to oil-water and gas-liquid relative permeability models, permeability and porosity multipliers, brine salinity, solubility pressure, pore space compressibility, and heavy component mole fractions (uncertain miscibility pressure). The model we are using here considers the interactions between

parameters and uses linear and quadratic form of the polynomial function to fit the response surface for production data (oil, water, and gas).

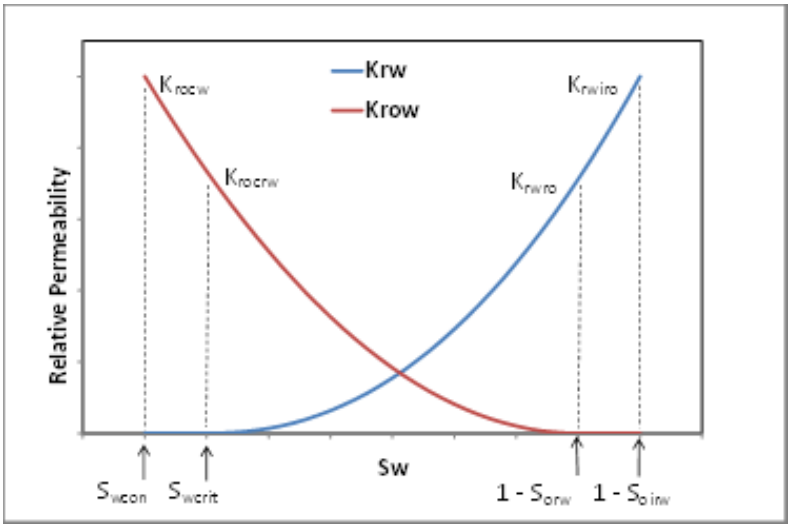

(a) Oil-water relative permeability.

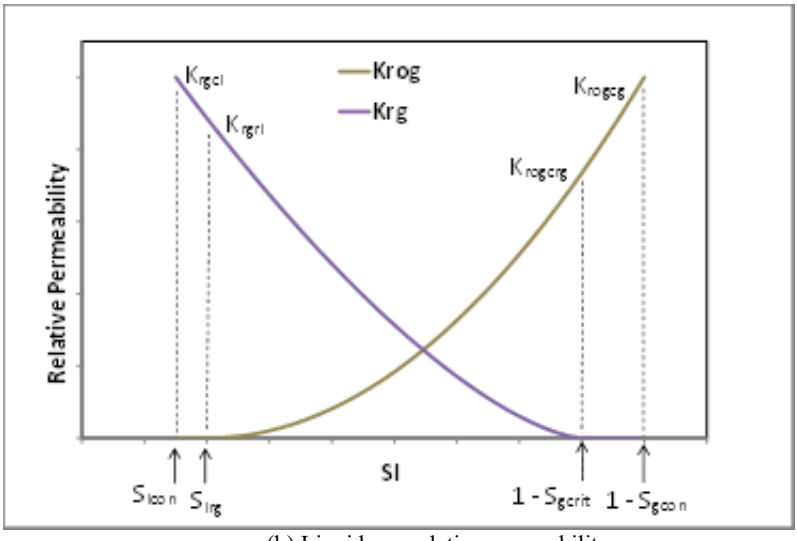

(b) Liquid-gas relative permeability.

Figure 5. Oil-Water relative permeability and liquid-gas relative permeability parameters used for uncertainty quantification study.

Table 2 provides a list of the parameters used in the study along with the minimum and maximum ranges. For this part of study, we used CMG-CMOST to run the numerical simulations. CMOST program designs a set of experiments using Latin Hyper Cube method and chooses the values for

each parameter within the provided range assuming a uniform probability distribution. Selection of the parameters is designed to enable the CMOST program to create a response surface.

To perform numerous numerical simulations required for uncertainty analysis, only a quarter of a five-spot injection/production pattern model is considered to decrease the run time of the simulations without loss of generality for the results (Figure 6). Before performing the uncertainty quantification on different parameters, several preliminary runs were completed to determine the optimum grid size for the simulations and to minimize the effect of grid size on simulation results. For example, if extra-large grid blocks are used, then as soon as enough CO_2 enters that grid block, the brine will be saturated with CO_2, following the local equilibrium assumption, which potentially can overestimate the amount of CO_2 in brine. On the other hand, having fine grid blocks may increase the computational cost unnecessarily.

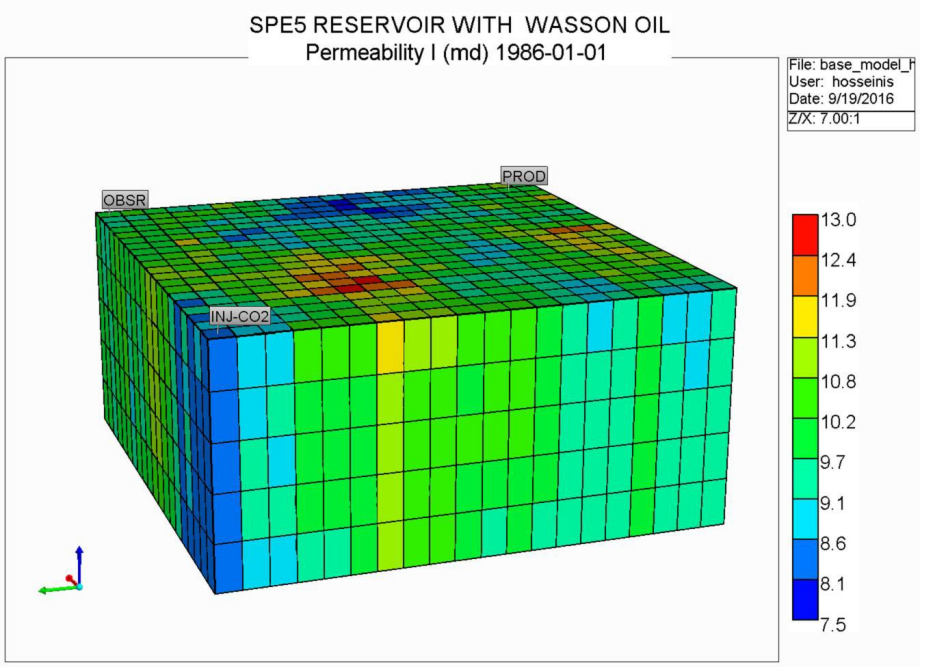

Figure 6. One Quarter of a five-spot pattern is used to perform the uncertainty quantification simulations to minimize the simulation time.

While high-resolution models provide more accurate results, the overall time to complete all required runs dramatically increases. Hence, the optimum grid size should be fine enough to honor the physics of the process while keeping the run-time in a reasonable range.

For both the Cranfield model and uncertainty quantification model, the Stone II model [20] is used to estimate three phase relative permeability. Furthermore, the "HYSTERESIS" keyword is used in CMG-GEM to activate the hysteresis model. No experimental data for hysteresis existed, so default values are used. Both models have very similar residual oil saturations and initial conditions where no History matching is done for this model.

CO_2 Dissolution into Brine and of Mineralization

Several geochemical datasets were available to us to assess mineralization and dissolution into brine. Mineralization, in which CO_2 is incorporated into the structure of carbonate minerals, is generally understood as a slow mechanism acting only on a millennium timescale but which might not be effective at Cranfield. Precipitation or building of carbonate minerals depend on the presence of metals such as calcium and magnesium in rock-building minerals and on their ability to be leached, dissolved, or somehow degraded. At Cranfield, thin section count and bulk XRD mineral compositions of core samples show abundance of quartz (~80% on average) and chlorite (a type of clay mineral), more specifically chamosite, (~12% on average), with minor kaolinite (3.1%), illite (1.3%), calcite (1.1%), dolomite (0.4%), and albite, a plagioclase feldspar (0.2%), metamorphic and igneous rock fragment making up the balance [5]. Quartz and chlorite are not reactive to CO_2. Common minerals more reactive to CO_2 include K-feldspar, absent at Cranfield, and carbonate minerals, uncommon at Cranfield. Most chlorite occurs as coatings surrounding detrital grains and, in effect, limiting their interaction with the pore fluid. Calcite and dolomite, sometimes iron-rich, mostly occur as locally more abundant as patchy cement.

Dissolution in brine is a well-known trapping mechanism that is well documented in the laboratory but is of unclear extent in the subsurface due to the uncertainty in the amount of interfacial contact between water and CO_2 resulting from fingering, typically enhanced in high-permeability media, and from channelling favored by the strong local fluvial heterogeneity.

In the course of the multi-year Cranfield project, more than 100+ downhole fluid samples from 10+ wells, including 5 wells with 8+ repeat samples, have been collected using the U-tube technology. An analysis of the time evolution of the geochemical samples could provide some insight on the time dependence of CO_2 dissolution into brine. Unfortunately, no exsolving gas phase was captured during the sampling, which limited the reach of our interpretation. In terms of assessing mineralization, no coring was done after CO_2 injection had begun and after CO_2 started to interact with the resident fluids and rocks. However, autoclave experiments on Cranfield cores that were exposed to CO_2 at reservoir conditions for several weeks [5] provided some dynamic insight on early rock-water interactions, confirming the conclusions obtained through the static analysis of thin sections and cores and geochemical observations of produced water.

The results of this analysis of autoclave experiments led to the assumption that no mineralization trapping needed to be modelled. Examination of various scanning electron microscopy (SEM) imaging of the CO_2-reacted samples showed no evidence of mineral dissolution or precipitation. The CO_2-reacted samples still exhibit intact quartz grains and intact chlorite platelets. The reacted brine solution showed limited release of Ca (from carbonate dissolution) and, more surprisingly, of K, likely from undetected K-feldspar, rather than from illite clay. Because CO_2 is minimally consumed and retarded by mineral reaction, CO_2 and brine were assumed to be instantaneously at equilibrium within a grid block. It is worth mentioning that in a different geological setting, and depending on the rock and fluid chemical compositions, mineral trapping could play a larger role in long term storage of CO_2.

RESULTS AND DISCUSSION

Successful History Matching of Conventional Primary and Secondary Production

The main purpose of history matching the conventional historical data and historical shut-in period was to ensure that the CO_2-EOR simulations can be started on a sound basis and with confidence. This is particularly important when initializing our CO_2-EOR model in which we know that the initial oil saturation distribution is heterogeneous. Without loss of generality, we focused on a permeability field realization with a particularly good history match. Other suboptimal realizations were addressed in the study. Results of our final historical history matching studies are given in Figure 7. After matching the conventional historical data until the 1970s, all wells in the model were shut in until the initiation of the CO_2-EOR operations in 2008. (CO_2-EOR started in 2007 in other parts of Cranfield but not until 2008 in our modelled section.) Residual oil saturations are different throughout the formation not only because of formation heterogeneity but also because of the field operations (e.g., gas injection [at top of the formation] and aquifer water influx from below the water oil contact).

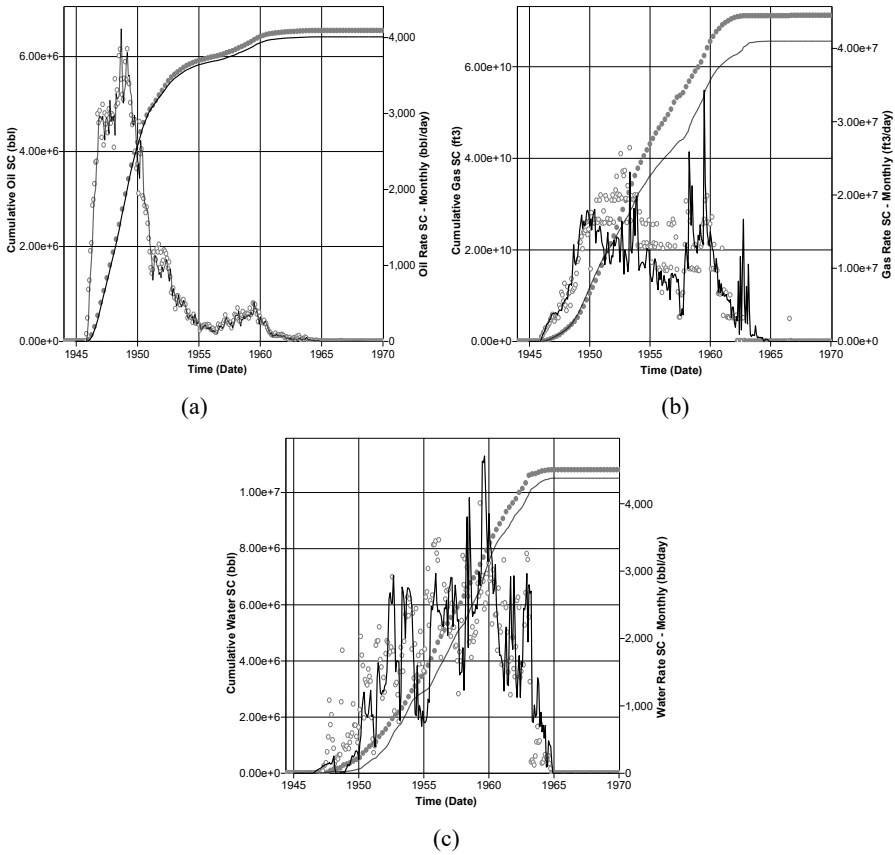

Figure 7. History matching of oil (a), gas (b), and water (c) during the conventional primary and secondary production at Cranfield.

Some of the major parameters we used to obtain the conventional history match included aquifer parameters (thickness, radius, porosity, and permeability), slight modifications to relative permeability parameters (end points and residual saturations) and field-wide porosity and permeability multipliers. The results show a reasonably good agreement between the field data and simulation results, which increases the reliability of the numerical model to be used for the next steps. Results show that our numerical simulations are slightly underestimating the cumulative oil, water, and gas production. History matching can always be improved, but we decided that the current level of match was sufficient to move forward and start the history matching of CO_2-EOR operations.

Please note that in our next subsection (modelling the CO_2-EOR period), we tune some other model parameters. We have rerun the numerical simulation results for conventional history matching simulation described in this section, and Figure 7 shows the final match obtained after both steps of the history matching.

Successful History Matching of the Historical CO_2-EOR Data

We then history matched the CO_2-EOR historical period with 2008 to 2012 field data. In this second round of history matching, we mostly tuned the oil MMP and CO_2 properties to minimize the impacts on previously history matched results. CO_2 injection rates, and bottom hole pressures at injection and production wells were used as hard constraints (i.e., as inputs to simulator). We history matched the gas, water, and oil production rates (i.e., as outputs from simulator). Figure 8 shows the reasonable agreement of the model results and data after the CO_2-EOR operations history matching. During history matching, we simulated the field development strategy used by the field operator (which is CGI, or continuous gas (CO_2) injection).

We used CO_2 breakthrough times in production wells as another measure to confirm the history matching results. Figure 9 compares the simulated breakthrough times with that of the field data. The numerical model was able to predict the breakthrough times with an acceptable accuracy. A good match of the breakthrough times is especially important to confirm the level of heterogeneity assumed in the model. If model heterogeneity were substantially underestimated or overestimated (with respect to actual field heterogeneity), simulation results would show either late or early breakthrough times, respectively. This twice history matched model is then used to run the forecast scenarios (i.e., to extend the simulation beyond 2012, to 2033). Because we did not want to change the parameters that are fixed in conventional primary and secondary production history matching, creating much better matches for breakthrough times is very difficult (because they are mostly controlled by shape and distribution of the channels). Since the overall performance of the model is reasonable, we accepted the final history matched parameters for the EOR period. At this point, the overall goal of history matching is to ensure volume balance and reservoir heterogeneity are reasonably modelled.

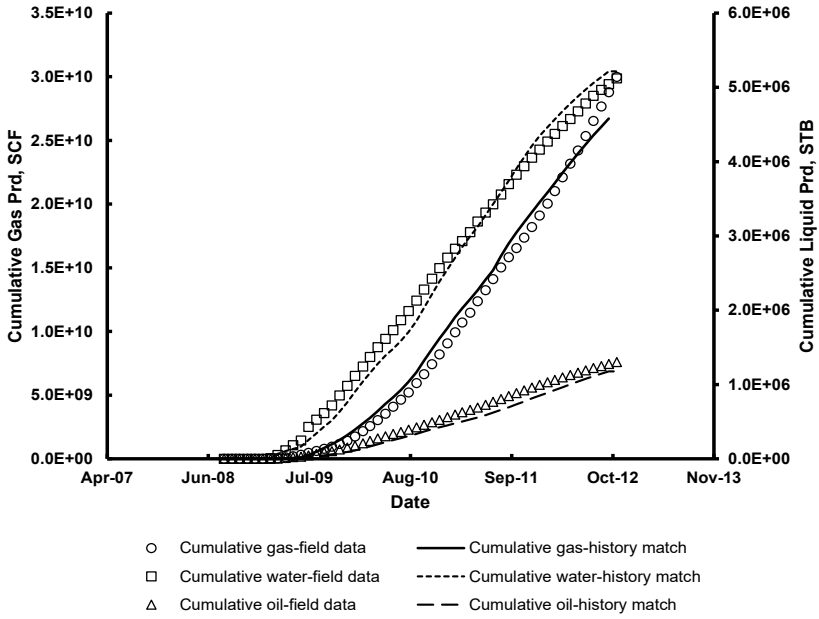

Figure 8. History matching results of 4 years of CO_2-EOR production data shows an agreement between cumulative field production data and simulation results.

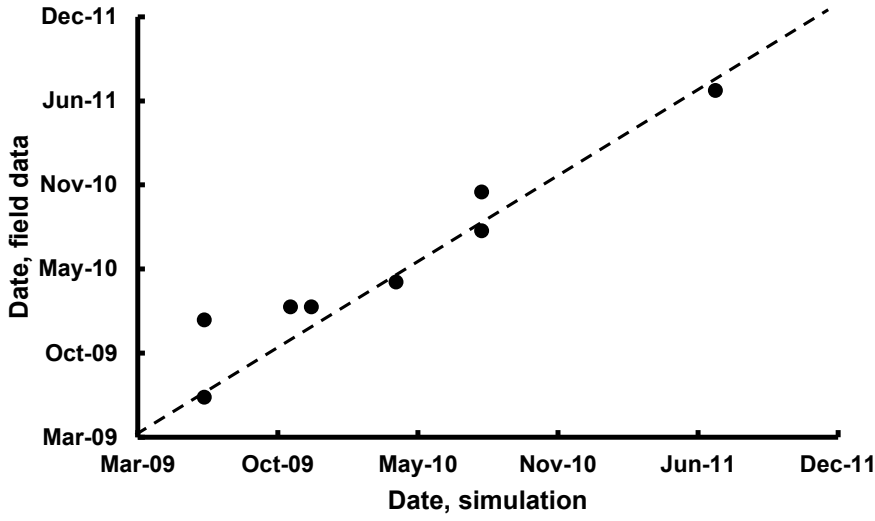

Figure 9. Breakthrough times for the producing wells show an agreement between the simulation results and field data (x-axis shows the breakthrough times from simulation and y-axis shows that of real field data).

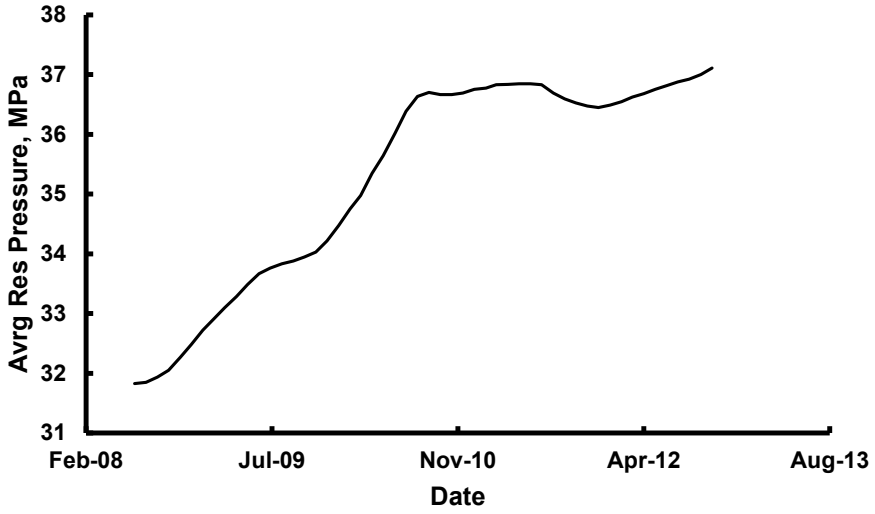

Figure 10. Reservoir pressure increases after CO_2 injection commences in 2008, pushing CO_2 outside the reservoir boundaries.

Figure 10 shows the simulated average reservoir pressure during historical EOR operation. Looking at the average reservoir pressure from the current simulation, one can notice that reservoir pressure will rise to as high as 37 MPa because of CO_2 injection. Such a high pressure in the reservoir can direct the CO_2 to move below the WOC, since initial reservoir pressure was 32 MPa.

Continuous Gas Injection (CGI) Scenario

CGI scenario final results are shown in Table 3 for both the end of the injection period and at the end of the post-injection period. Our calculations show that at the end of the injection period in the CGI scenario, 58% of the CO_2 in the reservoir is in the supercritical phase (51% mobile and 7% immobile), whereas 32% is dissolved in brine and only 11% is dissolved in the oil phase. In general, CO_2 solubility in brine is expected to be considerably smaller than its solubility in the oil phase (since CO_2 is miscible in the oil at the reservoir pressure and temperature). However, for this CGI scenario, the CO_2 amount in brine is larger than that in oil, given that injection of CO_2 occurs at the edge of WOC (CO_2 encroachment is towards the aquifer), and we leave only small amounts of the residual oil in the reservoir at the end of the scenario.

If the objective is to maximize oil recovery from the CO_2-EOR operation, we would prefer that all the injected CO_2 be used to mobilize and produce oil, with minimum loss of CO_2 to the aquifer. However, if the goal is to increase CO_2 storage in the subsurface, having some CO_2 migrate to below the WOC achieves this by increasing the overall amount of stored CO_2.

In our CGI scenario at the end of the injection period, 55% of the total stored CO_2 is located above the WOC (35% in gas, 10% in oil, and 9% in brine) whereas 45% of the total stored CO_2 can be found below the WOC (22% in gas, 1% in oil, and 23% in brine). The small amount of oil below the initial WOC is due to the downward movement of CO_2.

The same type of analysis is repeated at the end of the post-injection period. All the results for the CGI scenario are provided in Table 3.

Table 3. Fraction of CO_2 in different phases for CGI scenario at the end of 25 year CO_2-EOR phase (2033), and at the end of the post-injection period (2083).

CGI	**2033**			**2083**		
	Above WOC	**Below WOC**	**Total**	**Above WOC**	**Below WOC**	**Total**
Oil	0.103	0.005	**0.107**	0.128	0.006	**0.135**
Brine	0.088	0.228	**0.315**	0.098	0.250	**0.348**
Gas (mobile)	0.332	0.176	**0.508**	0.307	0.140	**0.447**
Gas (immobile)	0.026	0.043	**0.069**	0.025	0.045	**0.070**
Total	**0.548**	**0.452**	**1.000**	**0.559**	**0.441**	**1.000**

Figure 11 illustrates the average CO_2 thickness in the reservoir in feet, which represents the vertically averaged thickness of CO_2 adjusted to average vertical porosity at the same location. By the end of the 50-year post-injection period, high CO_2 saturations around the injection wells at the end of the injection period are rearranged into a more homogeneous distribution. At the end of the post-injection period in the CGI scenario, 52% of the CO_2 in the reservoir is in the gas phase (mobile + immobile) whereas 13% is dissolved in the oil phase and 35% in the brine. This shows that over the post-injection period, about 5% gaseous CO_2 has been dissolved into oil and brine. In addition, within the same time frame the total amount of CO_2 below the WOC has only been reduced by 1%.

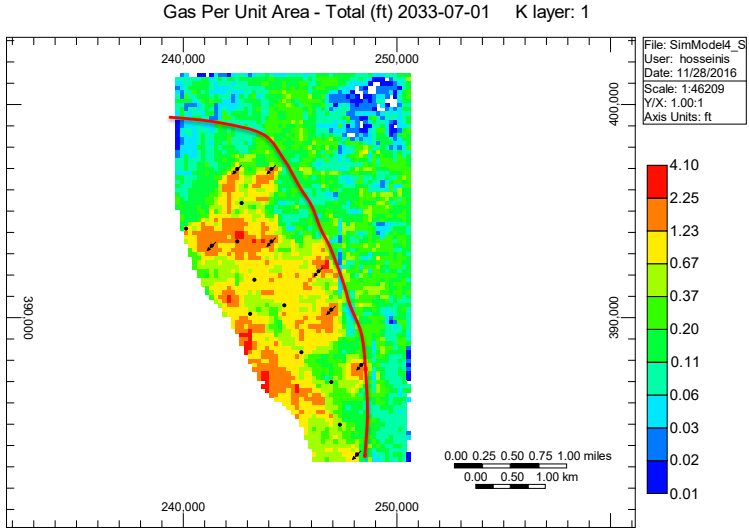

(a)

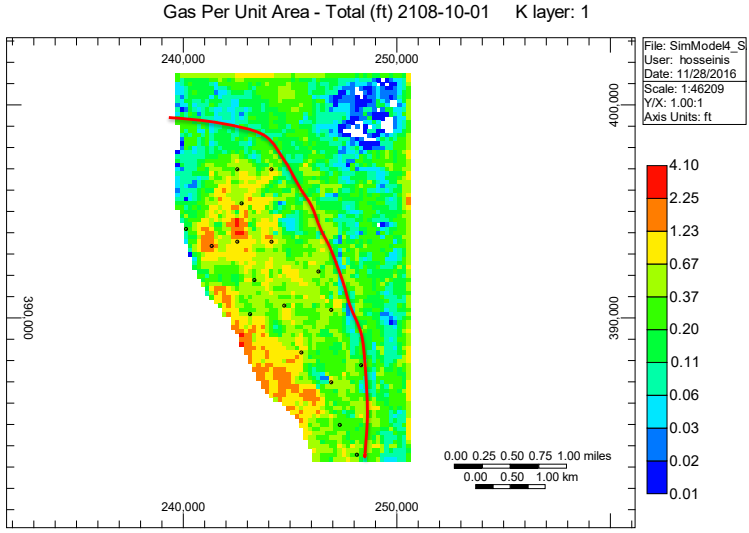

(b)

Figure 11. CO_2 distribution at the end of 25 years of CGI (a) followed by (b) 50 years shut in period.

It is clear that CGI is a very aggressive approach in flooding the residual oil zone, and after just 4 years of CO_2 injection, some of the CO_2 is moving below the WOC (Figure 12b). This potentially can be useful for CO_2 storage but is not optimal for maximizing oil production.

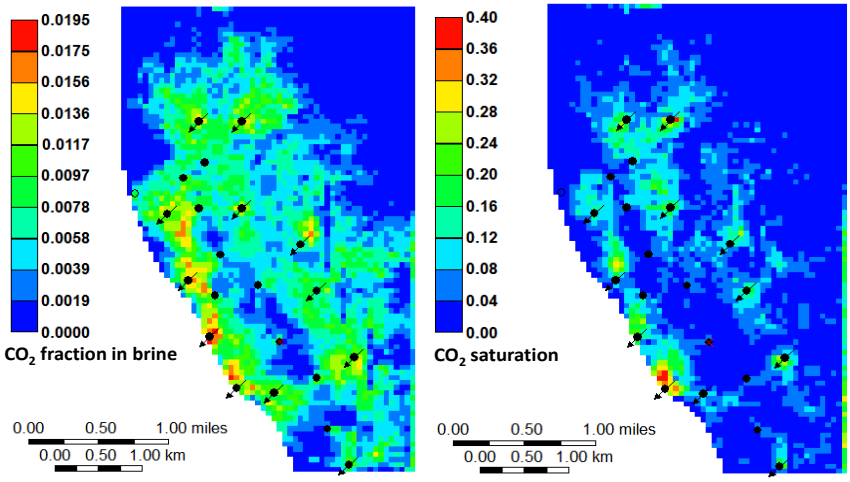

(a) (b)

Figure 12. (a) CO_2-brine solubility map (CO_2 mole fraction in the aqueous phase in October 2012) shows that CO_2 moves from the high-pressure injection zones into the low-pressure areas at the edge of the reservoir. (b) CO_2 saturation distribution map in October 2012 shows CO_2 accumulated around the injection wells (black dots with arrows).

Figure 12a shows the CO_2 mole fraction in brine in October 2012. Because of the low solubility of CO_2 in brine, the brine can reach its maximum aqueous solution capacity even in the presence of small amount of CO_2. In addition, the CO_2 and brine reaching equilibrium is a relatively fast process, so it would not take a long time for CO_2 to saturate the brine when they come in contact [21]. In numerical simulations, as soon as CO_2 enters a grid block, it is assumed the CO_2 is in contact with all the brine in that grid block. Given the small size of the grid blocks, we believe this is a reasonable assumption.

As illustrated in Figure 11, injected CO_2 accumulates around the injection wells. CO_2 is also observed to leave the model boundaries through the eastern and northern limits. The presence of high permeability sandy zones at Cranfield provides the pathway for the injected CO_2 to find its way out of the reservoir. Part of the injected CO_2 moves towards the center of the reservoir where production wells are located. However, portions of the injected CO_2 will move into the low-pressure zones below the WOC.

Some operators may prefer a storage mode that does not merely focus on maximizing oil production. In the next sections, we will describe other potential operational strategies and their impact on the CO_2 distribution in the different phases.

Water Alternating Gas (WAG) Scenario

In a second injection scenario, we assumed that the operator undertook WAG injection instead of CGI from the very beginning of the CO_2-EOR period. We assumed a WAG ratio of 1 (6 months of CO_2

injection followed by 6 months of water injection). Table 4 shows the amount of the CO_2 below and above the WOC.

Table 4. Fraction of CO_2 in different phases for WAG scenario at the end of CO_2-EOR (2033) and at the end of the post-injection period (2083).

WAG	Year 2033			Year 2083		
	Above WOC	**Below WOC**	**Total**	**Above WOC**	**Below WOC**	**Total**
Oil	0.221	0.007	**0.228**	0.245	0.008	**0.253**
Brine	0.110	0.211	**0.321**	0.115	0.232	**0.346**
Gas (mobile)	0.174	0.206	**0.379**	0.155	0.175	**0.330**
Gas (immobile)	0.031	0.041	**0.072**	0.028	0.043	**0.071**
Total	**0.535**	**0.465**	**1.000**	**0.542**	**0.458**	**1.000**

A major difference between the CGI and WAG scenarios is in the amount of CO_2 in the oil and gas phases. The amount of CO_2 dissolved in oil in the CGI scenario is less than in the WAG scenario. There could be several reasons for this, including the possibility of having a more stable WAG process, such that during water injection oil banks are formed that are more accessible to CO_2. Alternatively, during CGI most of the injected CO_2 follows the high perm channels and bypasses oil to reach low-perm areas. In addition, although the amount of immobile gas and CO_2 in brine in both scenarios is almost identical, the amount of the mobile CO_2 is higher for the CGI scenario relative to WAG. This potentially can have implications on the risk profile of each strategy.

Another difference between these two scenarios is visible by comparing Figure 13 to Figure 11. The figures show that, compared to CGI, WAG CO_2 is more homogeneously distributed through the reservoir and that areas with very high gas saturations are generally absent. This is consistent with operational expectations, as each batch of CO_2 is followed by a batch of brine. Post-injection trends for WAG are similar to CGI in that percentages of CO_2 in the gas phase are decreasing as more CO_2 gets dissolved in oil and brine. The amount of immobile gas in both scenarios is almost identical. In part, this could be because of the way we are calculating the mobile and immobile gas fractions, as explained in the methods section.

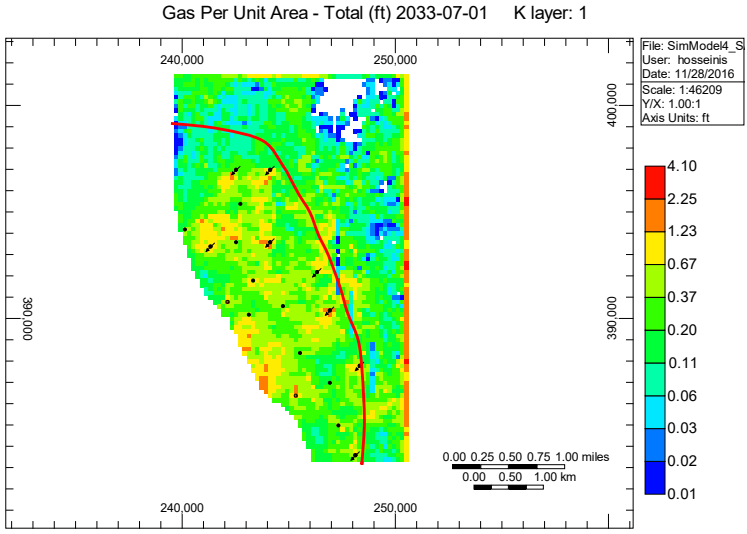

(a)

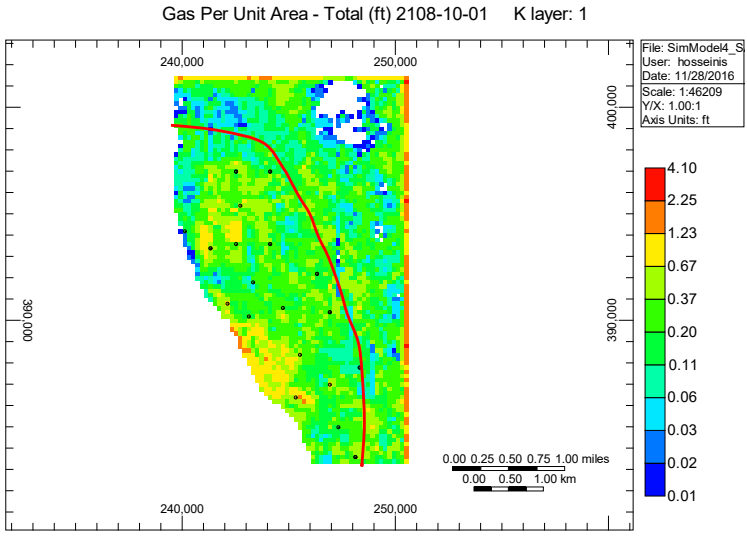

(b)

Figure 13. (a) CO_2 distribution at the end of 25 years of WAG followed by (b) 50 years shut in period.

Combined Water Curtain and CGI Scenario

In the third injection scenario, we assume that the operator conducted water curtain injection (WCI) from the very beginning of CO_2-EOR. In this scenario, continuous gas injection is implemented in all wells as was the case in the CGI scenario. However, this scenario also includes a new line of injection wells drilled slightly below the WOC to provide a water curtain barrier, limiting the downward movement of CO_2. Table 5 shows the amount of CO_2 stored below and above the WOC differentiated based on various mechanisms.

Table 5. Fraction of CO_2 in different phases for WCI scenario at the end of CO_2-EOR (2033) and at the end of the post-injection period (2083).

WCI	**Year 2033**			**Year 2083**		
	Above WOC	**Below WOC**	**Total**	**Above WOC**	**Below WOC**	**Total**
Oil	0.288	0.002	**0.289**	0.352	0.002	**0.354**
Brine	0.156	0.058	**0.214**	0.179	0.069	**0.248**
Gas (mobile)	0.410	0.035	**0.445**	0.336	0.014	**0.350**
Gas (immobile)	0.042	0.010	**0.052**	0.039	0.010	**0.048**
Total	**0.896**	**0.104**	**1.000**	**0.905**	**0.095**	**1.000**

The major difference between the water curtain scenario and CGI is the large impact of the water curtain in curtailing CO_2 movement from the reservoir to below the WOC. In this scenario, only 10% of CO_2 moves below the WOC compared to 45% in the CGI and WAG scenarios. However, this comes at the cost of producing less oil (less CO_2 injection, less CO_2-oil contact). In this scenario, less CO_2 is dissolved in brine compared to the CGI and WAG scenario, which is mainly due to the limited CO_2-brine contact.

The effectiveness of the water curtain is evident from an examination of Figure 14. The figure shows that compared to CGI and WAG scenarios, CO_2 flood conformance to the pattern is improved with the addition of WCI. Because the CGI is still applied within the oil zone, high gas saturations and zonal thicknesses (red cells) are observed toward the dome of the formation, similar to observations from the CGI scenario without WCI. In effect, small volumes of CO_2 still manage to get through the water curtain barrier to reach model boundaries.

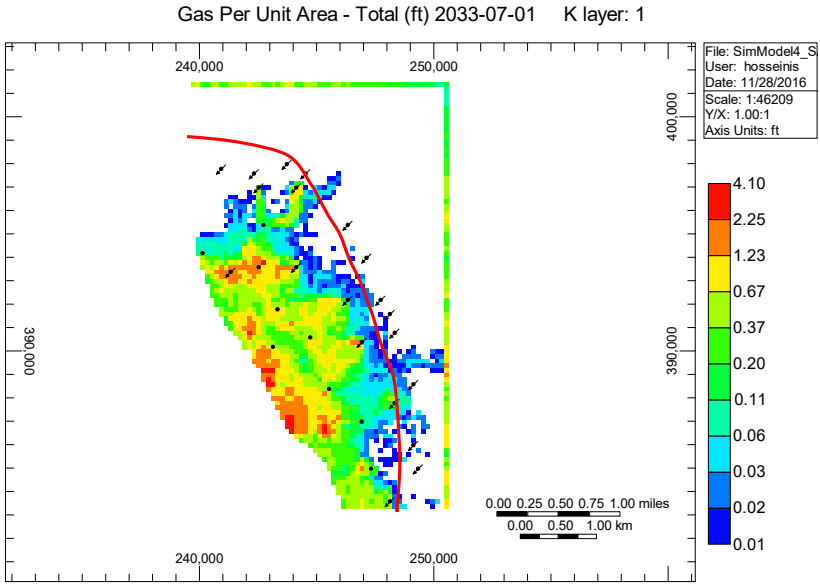

(a)

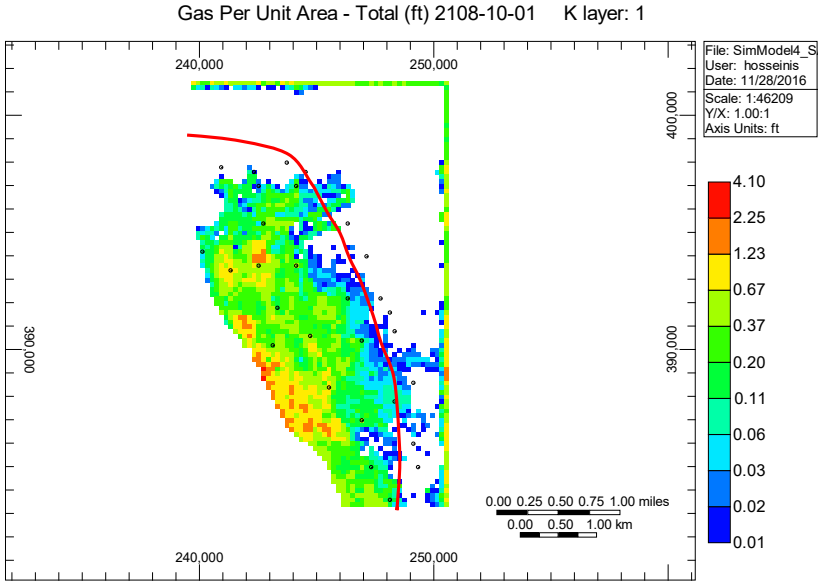

(b)

Figure 14. CO_2 distribution at the end of 25 years of WCI (a) and at the end of an additional 50 years (shut-in period (b).

Combined Water Curtain and WAG Scenario

In a fourth injection scenario, we combined WAG injection with water curtain injection from the beginning of CO_2-EOR (2008). Table 6 shows the amount of the CO_2 above and below the WOC.

Table 6. Fraction of CO_2 in different phases for WCI scenario at the end of CO_2-EOR (2033) and at the end of the post-injection period (2083).

WAG+WCI	Year 2033			Year 2083		
	Above WOC	**Below WOC**	**Total**	**Above WOC**	**Below WOC**	**Total**
Oil	0.372	0.004	**0.376**	0.404	0.005	**0.409**
Brine	0.165	0.113	**0.278**	0.172	0.126	**0.298**
Gas (mobile)	0.223	0.059	**0.282**	0.199	0.031	**0.230**
Gas (immobile)	0.045	0.019	**0.064**	0.044	0.020	**0.064**
Total	**0.805**	**0.195**	**1.000**	**0.819**	**0.181**	**1.000**

Again, the major difference between this scenario and CGI-only or WAG-only is the success of the water curtain in limiting CO_2 movement to below the WOC. In this scenario, only 20% of CO_2 moves below the WOC compared to. ~45% in both the CGI and WAG scenarios. This scenario also has the largest amount of the CO_2 remaining within the oil phase (40%) at the end of post-injection period.

The effectiveness of the water curtain is shown in Figure 15. A WAG approach is used within the oil zone; the high gas zone thicknesses (red colors) are reduced compared to that observed for the WCI scenario. Small amounts of CO_2 still manage to get through the water curtain barrier to reach model boundaries.

Evolution of CO_2 Trapping

CO_2 trapping by different mechanisms evolves quite substantially with time. For the CGI and WAG scenarios, the predicted evolution in CO_2 trapping with time is shown in Figure 16. Specifically, for Cranfield, 75 years of simulation time was modelled (again for 25 years injection and 50 years post-injection). During this period, the amount of CO_2 trapped via solubility (CO_2 dissolved in both oil and brine) consistently increased with time, while the amount of CO_2 trapped structurally (CO_2 in the mobile gas phase) correspondingly decreased with time. The amount of CO_2 trapped via residual trapping (CO_2 in the immobile gas phase) remained relatively stable with time after CO_2 injection stopped. These observations are in general agreement with expectations, including those published by IPCC [22]. For these Cranfield cases, solubility trapping plays an increasingly more important role over time than does residual trapping. In particular, the amount of CO_2 residually trapped is predicted to be low because the relatively permeability curves used in these simulations result in low residual gas saturations.

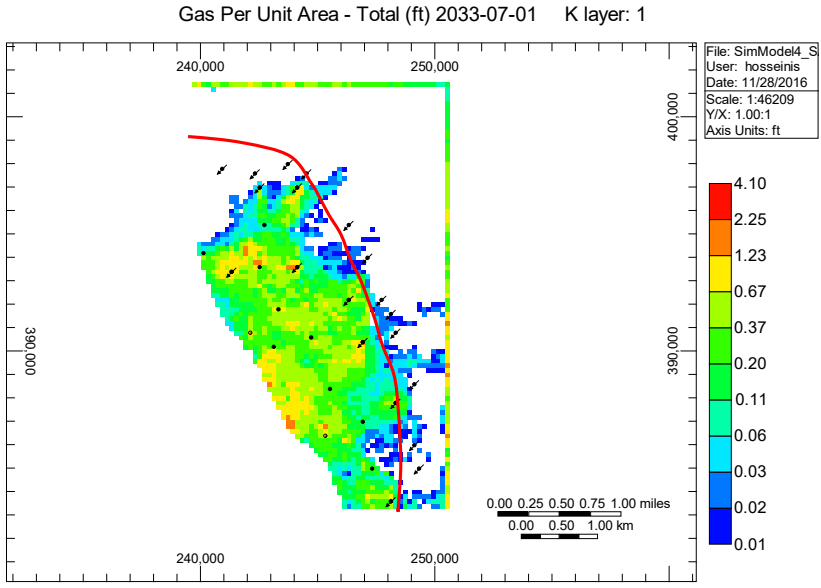

(a)

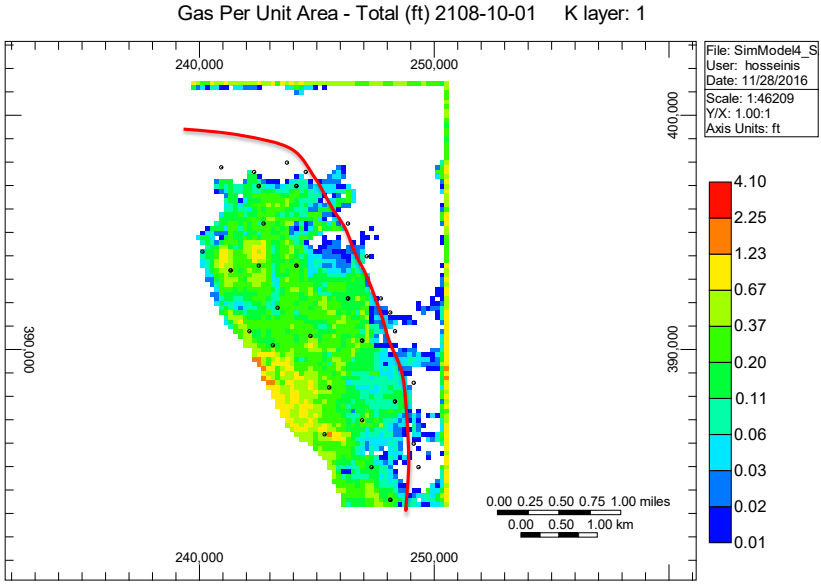

(b)

Figure 15. CO_2 distribution at the end of 25 years of hybrid WAG+WCI (a) and at the end of the subsequent 50 years shut in period (b).

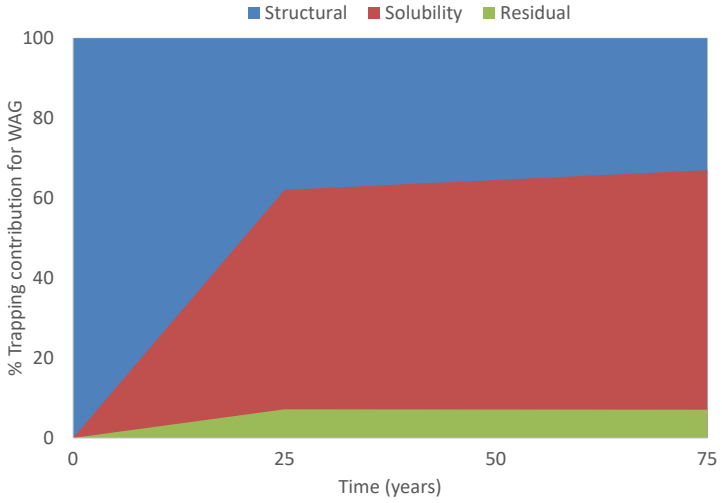

(a) WAG

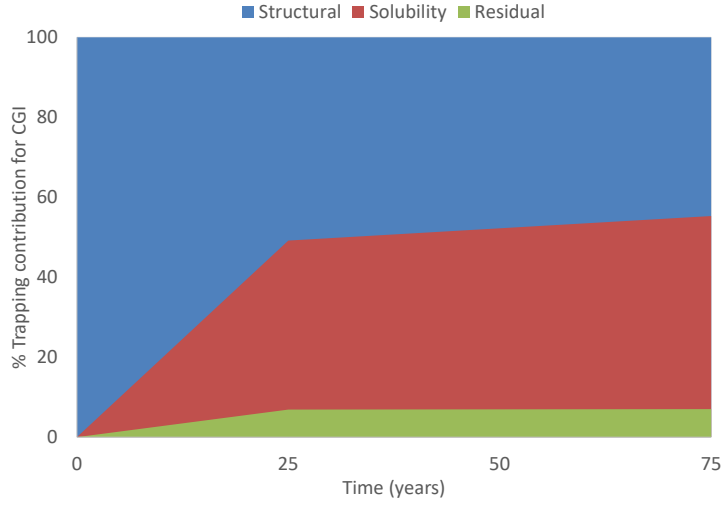

(b) CGI

Figure 16. Trapping contribution evolution over time for CGI and WAG scenarios.

Uncertainty Quantification for CGI Scenario

Results of the uncertainty quantification analysis show that for a wide range of parameters a large spread of CO_2 distribution in different phases can be obtained. Please note that there is no aquifer in this model as it is assumed that the pattern modelled sits completely above the WOC and is entirely filled with residual oil (representing oil saturation after a water flood). Moreover, in uncertainty quantification we have only examined the CGI scenario. To adjust our Cranfield simulation results for a CGI scenario so it would represent the same set of assumptions, we have only considered the distribution of CO_2 above the WOC. For this purpose, fractions above the WOC are normalized to one (by removing the CO_2 volumes below the WOC), as is shown in Table 7.

Table 7. Normalized fraction of CO_2 in different phases for CGI scenario at the end of CO_2-EOR as well as post-injection period for Cranfield simulations.

CGI	**2033**		**2083**	
	Above WOC	**Normalized above WOC**	**Above WOC**	**Normalized above WOC**
Oil	0.103	0.187	0.128	0.229
Brine	0.088	0.161	0.098	0.176
Gas (mobile)	0.332	0.605	0.307	0.549
Gas (immobile)	0.026	0.047	0.025	0.046
Total	**0.548**	**1.000**	**0.559**	**1.000**

Results of the uncertainty quantification are presented in a box plot (Figure 17) for year 2033 (end of injection) and 2083 (end of simulation). In addition, we have also shown the results for two intermediate dates (2010 and 2063). Note that CO_2-EOR starts in 2008 in the northeastern compartment of the reservoir. Superimposing the normalized results of Cranfield CGI scenario on the results of the uncertainty quantification, the amount of CO_2 in the oil phase and immobile CO_2 are within the 25-75th percentile. The amount of CO_2 in brine is above the 75th percentile, whereas the amount of mobile CO_2 falls below the 25th percentile. All the results are bounded by expected minimum and maximum values.

Based on the current study, we cannot state the relative sensitivity of the results to each individual parameter (e.g., provide tornado charts) unless we define a base case and specific objective function to measure the sensitivity. This could have been done, if, for example, we had chosen the cumulative oil production as a parameter in a base case, and then study how sensitive cumulative oil production is with respect to input variables. Among other parameters, amount of CO_2 in oil/brine/gas, cumulative volume of injected CO_2, cumulative amount of recycled CO_2, and total amount of CO_2 stored can be selected for such a study.

In a more recent study at SACROC (Scurry Area Canyon Reef Operators Committee) unit in the Permian Basin of Texas, various field development strategies similar to this study have been evaluated. Results show the same type of conclusions in carbonate formations, which could have behaved differently from the clastic formation considered in this study. Based on SACROC simulation model results, WAG shows a good balance between maximizing oil production and CO_2 storage with a lower utilization ratio compared to CGI. In addition, WAG improves the storage security by decreasing the amount of mobile CO_2 in the reservoir [26,27,28]. In the SACROC study, WAG shows

much higher residual CO_2 in comparison to that of CGI, which is ultimately due to the frequently reinforced hysteresis effect during WAG injection. (Figure 18).

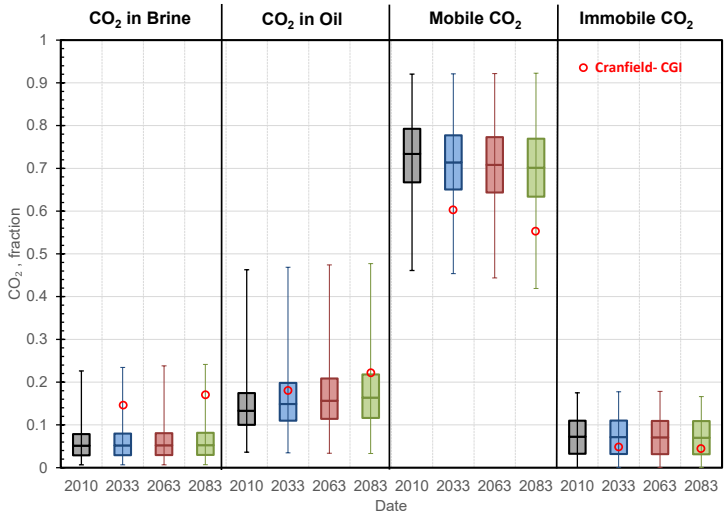

Figure 17. The uncertainty quantification shows that results of the Cranfield study fall between the expected maximum and minimum values for both end of EOR and end of post-injection simulations.

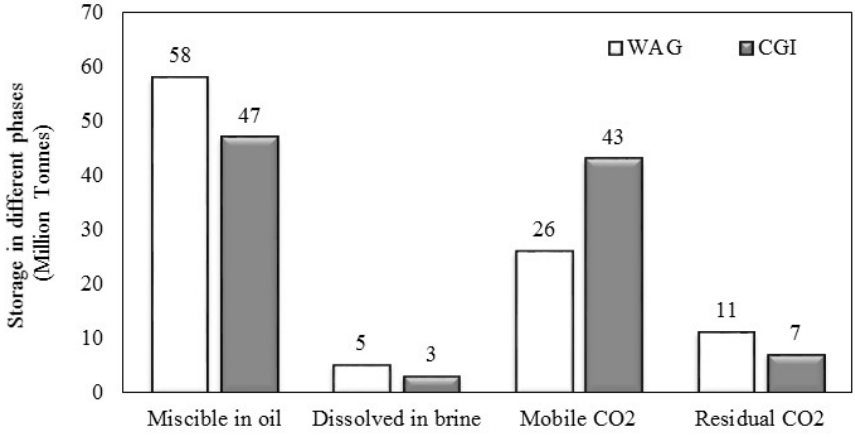

Figure 18. CO_2 stored by different trapping mechanisms at the end of the CO2–EOR operation in SACROC unit, Permian basin.

Extent of CO_2 Dissolution into Brine and of Mineralization

Solubility trapping is the hardest mechanism to quantify. CO_2 dissolution could occur quickly but is also a strong function of the geometry and dynamics of the system. In this study, we assumed that CO_2 dissolution into brine occurs fast enough to have local equilibrium at the scale of a grid block. Our intent was to use the numerous brine geochemical samples taken in the course of the project to demonstrate the validity of the assumption. In particular, samples taken ahead of the CO_2 front before breakthrough could shed light on the extent of the diffusion and mixing mechanisms that would saturate the brine with CO_2. Analysis of the monitoring well response to injection showed that the CO_2 breakthrough was always clearly identified by pH drop and bicarbonate increase along with a pressure increase in the tubing. However, it turns out that the breakthrough was not preceded by a slow build-up in cations from dissolved minerals (we know that Cranfield rocks are little reactive) or a progressive drop in pH that would be expected in the dissolved CO_2 halo ahead of the free-phase plume (likely because of fingering).

The following reactions describe CO_2 dissolution. The dominant dissolved species is a strong function of the pH of the solution.

$$CO_2(aq) + H_2O = H_2CO_3$$

$$H_2CO_3 = H^+ + HCO_3^-$$

$$HCO_3^- = H^+ + CO_3^{-2}$$

$$CaCO_3 + CO_2(aq) + H_2O = Ca^{2+} + 2HCO_3^-$$

The total dissolved CO_2 amount is given by $CO_2(aq) + H_2CO_3 + HCO_3^- + CO_3^{-2}$ with $CO_2(aq)$ likely the most abundant at Cranfield. Bicarbonate and carbonate were measured (via alkalinity); however, $CO_2(aq)$, which exsolves as soon as the sample is brought to the surface, was not captured during the sampling. In addition, aqueous concentrations of bicarbonate and carbonate species do not result from CO_2 dissolution only; they are impacted by the presence of carbonate minerals. The petrographic analyses presented earlier also led us to understand that variations in bicarbonate concentrations, in particular its increase, were more representative of the spotty calcite distribution rather than of CO_2 dissolution kinetics. It follows that it is difficult to tell apart increase in bicarbonate concentrations due to CO_2 dissolution and due to carbonate dissolution. To summarize, the geochemical data, although abundant, were not sufficient to formally confirm the assumption of local equilibrium at the scale of a grid block. Nevertheless, we could use the reverse argument stating that because CO_2 does not react, it can diffuse faster to areas not contacted by free-phase CO_2.

An assumption of no mineralization seems valid for the (short) time scale of this study. Examination of autoclave results and other field observations suggest that calcite and carbonates are being dissolved rather than precipitated at these early stages of CO_2 injection. In the much longer term, chlorite, dissolving at a very slow rate, might release significant amount of Mg and Fe cations [5].

DISCUSSION

The large spread of results illustrates that ***the CO_2 distribution in the various phases is a strong function of the field development strategy***. In Figure 19-Figure 23, we compare some other relevant model outputs for the injection scenarios to emphasize the variability in the results. For example, we would prefer to have a lower net utilization ratio for a CO_2-EOR project (so that a smaller amount of injected CO_2 produces more oil). For the calculation of the net utilization ratio, the amount of the recycled CO_2 is subtracted from the total amount of injected CO_2. ***Because the rate and total volume of CO_2 injection must be reduced to control the reservoir pressure in scenarios in which WCI is used, scenarios where WAG is incorporated have the best performance*** (Figure 20).

Scenarios that use WCI have the lowest net utilization ratios, but they may not necessarily produce the maximum amount of oil or store the maximum net amount of CO_2 (Figure 21 and Figure 22). In addition, the total amount of the injected CO_2 will not be the same in all the scenarios (Figure 23).

Overall, it seems that ***WAG offers the best compromise between oil produced and CO_2 stored, and it has a better potential to be optimized for the optimal performance in the field, especially when the performance is analyzed based on hydrocarbon pore volume (HCPV) injected***. For example, less CO_2 is injected in WAG compared to WCI, yet WAG produces more oil than does WCI (Figure 22).

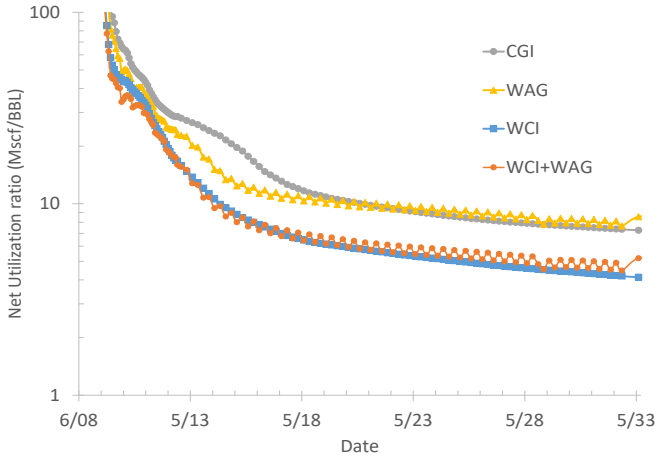

Figure 19. Net utilization ratio for various field development strategies. Date is month/year.

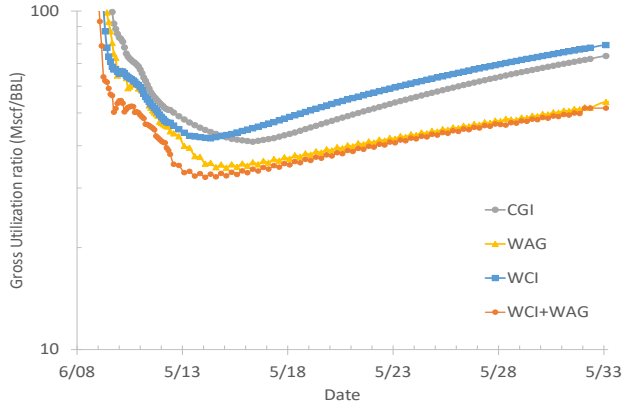

Figure 20. Gross utilization ratio for various field development strategies. Date is month/year.

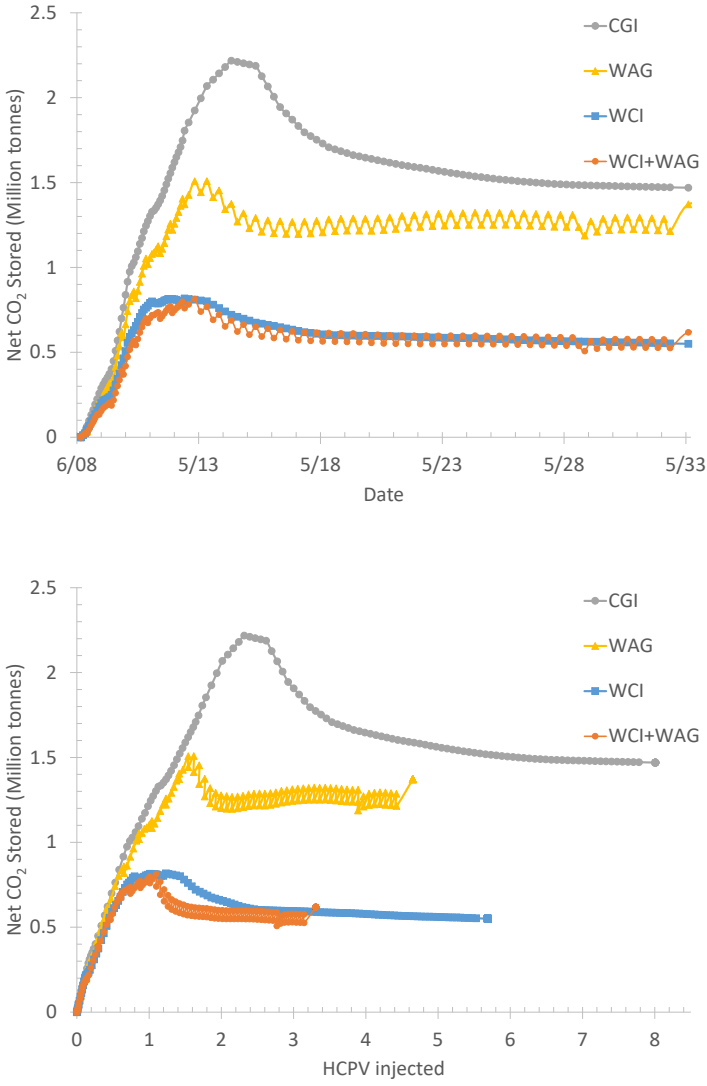

Figure 21. Net amount of CO_2 stored by end of CO_2-EOR operations (2033) plotted both against the date and CO_2 HCPV injected. Date is month/year.

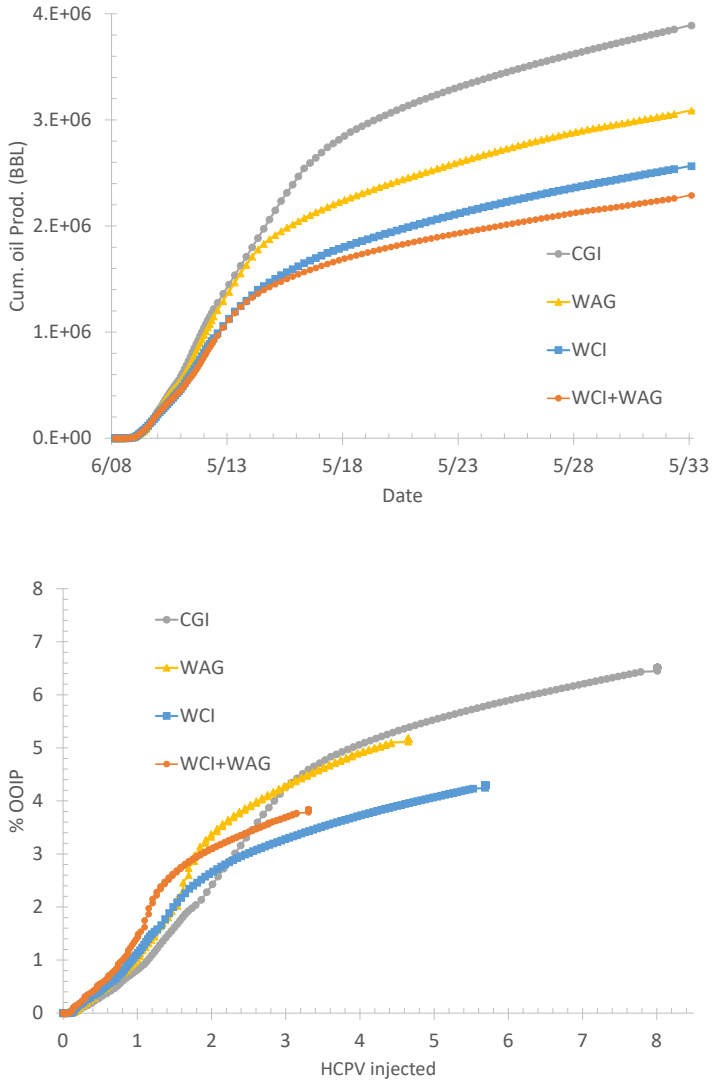

Figure 22. Cumulative oil produced plotted against the date and cumulated oil produced in terms of percentage of original oil in place plotted against CO_2 HCPV injected. Date is month/year.

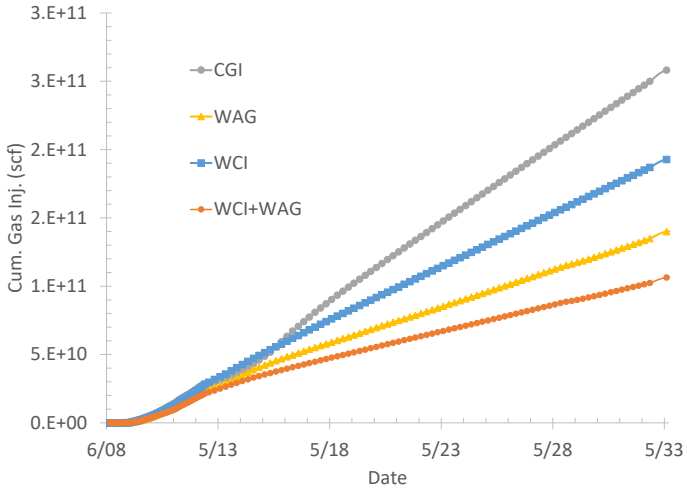

Figure 23. Cumulative volume of injected CO_2 under various field development scenarios. Date is month/year.

SUMMARY

In summary, our work shows that the field development strategy selected by the operator has a very significant impact on the relative importance of the different trapping mechanisms for a reservoir. In our simulations, while CGI maximizes oil recovery and CO_2 storage in absolute volume terms, WAG appears to offer a more balanced approach. WAG can produce large amounts of oil and store large volumes of CO_2 with the lowest gross utilization ratio. Also compared to CGI, WAG improves the storage security by reducing the amount of mobile CO_2. However, it is important to note that the final decision on effectiveness of these strategies should consider economics of the project. The cost of water injection and handling, cost of CO_2 compression and injection, number of required injection wells, and the possibility of having any tax credit for storing CO_2 are factors that eventually guide the operator to choose the best strategy.

Another factor that can be considered in optimizing the field development strategy is to minimize the project risks by controlling how the stored CO_2 is being eventually trapped in the subsurface. This factor is sometimes overlooked in risk assessment analysis. For example, from a risk assessment standpoint, CO_2 in the mobile gas phase poses the most risk as it has the greatest potential to move in the subsurface.

FUTURE WORK

Among the various scenarios explored, WAG seems to be a promising operational approach to balance both storage and oil production and is actually one of the major CO_2-EOR methods used by industry. A similar uncertainty quantification study can be done to find the limits of WAG in storing CO_2 through the various mechanisms discussed here. Another complementary work could be a sensitivity analysis defined around a specific target, to find the sensitivity of each storage mechanism to input

parameters. This would let us create tornado charts that can be very informative on understanding the importance of each individual parameter.

Analysis of various WAG ratios is another important study. This would improve our understanding of how we can increase or decrease the role of a specific storage mechanism by changing the WAG ratio. This can be potentially extended to economics of the project by assuming dollar values for different components of the system.

Another point to mention is that in the study, we assumed that, for different scenarios, we were limited to a specific 25-year duration for CO_2 injection. Because of this time constraint assumption, we ended up injecting different amounts of CO_2 in the various scenarios. This study could be repeated, but with the amount of the injected CO_2 being the same for all scenarios as projects are allowed to run for different time intervals (e.g., 50 years of WAG injects the same amount of CO_2 as 25 years of CGI).

In addition, CO_2 dissolution in brine and convective movement of the heavy brine are documented experimentally and have been simulated in small scale models. Effectiveness of such a mechanism in large-scale models with strong aquifers needs more detailed work.

From relative permeability experiments, it is clear that depending on the injection rate of CO_2, we would have different limiting regimes (capillary limited, viscous limited, or transition in-between) that can impact relative permeability parameters. Velocity-dependent relative permeability models can be used for future studies to study this behavior. In addition, a more critical review of the horizontal relative permeability data is needed. Comparison of the relative permeability curves from vertical sample and horizontal samples could potentially yield interesting insights as well. Relative Permeability hysteresis effects and uncertainty might also have a significant impact on the trapping mechanism warranting a closer look in future sensitivity studies.

Another interesting study can focus on transitional scenarios. This means field development strategies would be changing during the life of project to maximize oil production and CO_2 storage while keeping the utilization ratios low. For example, based on Figure 22, we could have started with WCI+WAG first up to 1.8 HCPV, then switch to WAG up to 3 HCPV, and finally finish the project with CGI.

ACKNOWLEDGMENT

We would like to thank Subhash C. Thakur (BP, Houston, Texas) and D. Brian Williams (Caeli Associates LLC) for their valuable comments throughout the study. This work was supported by the CO_2 Capture Project (CCP), Gulf Coast Carbon Center (GCCC) at the Bureau of Economic Geology and the National Energy Technology Laboratory (NETL) under contract DE-FE0024433. We also thank the Computer Modelling Group (CMG), Calgary for providing the software for the numerical simulations.

REFERENCES

1. Han, W.S., McPherson, B.J., Lichtner, P.C., Wang, F.P. (2010) Evaluation of trapping mechanisms in geologic CO_2 sequestration: Case study of SACROC northern platform, a 35-year CO_2 injection site. *Am. J. Sci*. 310, 282–324.
2. Soltanian, M.R., Amooie, M.A.,Dai, A., Moortgat, C.D. (2016) Critical Dynamics of Gravito-Convective Mixing in Geological Carbon Sequestration. Nature Scientific Reports 6, 35921.
3. Moghaddam, R.N., Rostami, B., Pourafshary, P. (2015) Scaling analysis of the convective mixing in porous media for geological storage of CO_2: an experimental approach. *Chemical Engineering Communications* 202 (6), 815–822.

4. Sathaye, K.J., Hesse, M.A., Cassidy, M., Stockli, D.F. (2014) Constraints on the magnitude and rate of CO_2 dissolution at Bravo Dome natural gas field. *Proc Natl Acad Sci USA.* 111(43), 15332–15337.
5. Lu, J., Kharaka, Y.K., Thordsen, J.J., Horita, J., Karamalidis, A., Griffith, C., Hakala, J.A., Ambats, G., Cole, D.R., Phelps, T.J., Manning, M.A., Cook, P.J., Hovorka, S.D. (2012) CO_2–rock–brine interactions in Lower Tuscaloosa Formation at Cranfield CO_2 sequestration site, Mississippi, USA. *Chemical Geology* 291, 269-277.
6. Hovorka, S.D., Meckel, T.A., Treviño, R.H. (2013) Monitoring a large-volume injection at Cranfield, Mississippi—Project design and recommendations. *Int. J. Greenh. Gas Control* 18, 345–360.
7. Hosseini, S.A., Lashgari, H., Choi, J.W., Nicot, J.-P., Lu, J., Hovorka, S.D. (2013) Static and dynamic reservoir modeling for geological CO_2 sequestration at Cranfield, Mississippi, U.S.A. *Int. J. Greenh. Gas Control* 18, 449–462.
8. Nicot, J.P., Hovorka, S.D., and Meckel, L.D., III (2013) Editorial: Midproject assessment of the SECARB Early Test at Cranfield, Mississippi, *Int. J. Greenh. Gas Control* 18, 343-344.
9. Weaver, L., Anderson, K., (1966) Cranfield field, Cranfield unit, Basal Tuscaloosa Reservoir, Adams and Franklin counties, Mississippi. Oil Recover. From Gas-cap Reserv. an Eng. Eval. Conserv. Pract. Six reservoirs. Interstate Oil Compact Comm., Oklahoma City 42–58.
10. Alfi, M., Hosseini, S.A. (2016) Integration of reservoir simulation, history matching, and 4D seismic for CO_2-EOR and storage at Cranfield, Mississippi, USA. *Fuel* 175, 116–128.
11. Alfi, M., Hosseini, S.A., Alfi, M., Shakiba, M. (2015) Effectiveness of 4D Seismic Data to Monitor CO_2 Plume in Cranfield CO_2-EOR Project, in: Proceedings 2015 Carbon Management Technology Conference, Nov 17-19, Sugarland, TX.
12. Choi, J.W., Nicot, J.P., Meckel, T.A., Hovorka, S.D. (2011) Numerical modeling of CO_2 injection into a typical US Gulf Coast anticline structure. *Energy Procedia* 4, 3486–3493.
13. Choi, J-W., Nicot, J.P., Hosseini, S. A., Clift, S. J., and Hovorka, S. D. (2013) CO_2 recycling accounting and EOR operation scheduling to assist in storage capacity assessment at a U.S. gulf coast depleted reservoir, *Int. J. Greenh. Gas Contro*l 18, 474-484.
14. Kim, S., Hosseini, S.A. (2014) Above-zone pressure monitoring and geomechanical analyses for a field-scale CO_2 injection project in Cranfield, MS, *Greenhouse Gases: Science & Technology* 4 (1), 81-98.
15. Lu, J., Kordi, M., Hovorka, S.D., Meckel, T.A., Christopher, C.A. (2013) Reservoir characterization and complications for trapping mechanisms at Cranfield CO_2 injection site. *Int. J. Greenh. Gas Control* 18, 361–374.
16. Peng, D.-Y., Robinson, D.B. (1976) A New Two-Constant Equation of State. *Ind. Eng. Chem., Fundam.* **15**, 59–64.
17. Duan, Z., Sun, R. (2003) An improved model calculating CO_2 solubility in pure water and aqueous NaCl solutions from 273 to 533 K and from 0 to 2000 bar. *Chem. Geol*. **193**, 257–271.
18. Yan, W., Huang, S., Stenly, E. (2011) Measurement and modeling of CO_2 solubility in NaCl brine and CO_2–saturated NaCl brine density. *International Journal of Greenhouse Gas Control* **5**(6),1460–1477.
19. Mukhopadhyay, S., Doughty, C., Bacon, D., Li, J., Wei, L., Yamamoto, H., Gasda, S., Hosseini, S.A., Nicot, J.-P., Birkholzer, J.T. (2015) The Sim-SEQ Project: Comparison of Selected Flow Models for the S-3 Site. *Transp. Porous Media* **108**, 207–231.
20. Stone, H.L. (1973) Estimation of three-phase relative permeability and residual oil data. *J Can Pet Technol* **12** (4), 53–61.
21. Mitchell, M.J., Jensen, O.E., Cliffe, K.A., Maroto-Valer, M.M. (2010) A model of carbon dioxide dissolution and mineral carbonation kinetics. *Proc. R. Soc. A* **466**, 1265–1290.

22. Metz B, Davidson O, de Coninck HC, Loos M, Meyer LA (2005) IPCC special report on carbon dioxide capture and storage. Prepared by Working Group III of the Intergovernmental Panel on Climate Change; Cambridge, UK/New York, USA: Cambridge University Press.
23. Huppler, J.D. (1969) Waterflood relative permeabilities in composite cores, *JPT* **21**, 539-540.
24. Virnovsky, G. A., Friis, H. A., Lohne, A. (2004) A steady-state upscaling approach for immiscible two-phase flow, *Transp. Porous Media*, **54**(2), 167–192.
25. Reynolds, C. A., and Krevor S. (2015) Characterizing flow behavior for gas injection: Relative permeability of CO_2-brine and N_2-water in heterogeneous rocks, *Water Resour. Res.* **51**, 9464–9489.
26. Hosseininoosheri, P., Hosseini, S.A., Nunez-Lopez, V., Lake, L.W., Impact of field development strategies on CO2 trapping mechanisms in a CO_2–EOR field: A case study in the Permian basin (SACROC unit), *Int. J. Greenh. Gas Contro*l 72, 92-104.
27. Hosseininoosheri, P., Hosseini, S.A., Nunez-Lopez, V. and Lake, L.W., 2018 (a), April. Modeling CO_2 Partitioning at a Carbonate CO_2-EOR Site: Permian Basin Field SACROC Unit. In *SPE Improved Oil Recovery Conference*. Society of Petroleum Engineers.
28. Hosseininoosheri, P., Hosseini, S.A., Nunez-Lopez, V. and Lake, L.W., 2018 (b), April. Evolution of CO_2 Utilization Ratio and CO_2 Storage under Different CO_2-EOR Operating Strategies: A Case Study on SACROC Unit Permian Basin. In *SPE Western Regional Meeting*. Society of Petroleum Engineers.

APPENDIX A: RELATIVE PERMEABILITY EXPERIMENTS

Introduction

Multiple core plugs from a UT-BEG monitoring well at the Cranfield, MS site were collected and sent to a commercial laboratory to measure the basic petrophysical properties of the rock samples, including porosity, permeability, relative permeability, and capillary pressure. Because of the intrusive nature of capillary pressure experiments, these were done following the relative permeability experiments using the same plugs. Two sets of core plug composites were prepared: one horizontal and the other vertical. These core plugs were assembled to create composites (using Huppler's method [23]) prior to running the experiment sequentially on each assembled composite. Figure A-1 shows a few of the core plugs with an indication of the sample depth.

Basic properties of these core plugs are tabulated in Table A-1. Horizontal and vertical core plugs are clearly marked in the table. The average Klinkenberg permeability of horizontal samples is around 250 md, while the permeability of vertical samples is only 6.6 md. For all the samples, the average porosity and density is around 0.28 and 2.7 gr/cc, respectively.

Vertical core plugs were drilled perpendicular to the rock bedding plane. For this reason, individual vertical plugs are typically longer (~2-5 inches) than horizontal plugs (~2 inches). As shown in Figure A-3, the ratio of vertical to horizontal permeability for the samples averages around ~0.05, reflecting very high anisotropy in the cored formation. In addition to these static measurements, helical CT scans of the core plugs were carried out to investigate bedding and morphology of the core plugs (Figure A-2). The length of each of the two composites built from these core plugs (one composite built from vertical and another from horizontal plugs) is ~1ft. Relative permeability experiments made use of gamma-ray monitoring, which allows saturations to be measured directly.

As of the end of May 2017, relative permeability experiments were completed for the horizontal and vertical composites. Table A-2 shows the final experiment timeline as provided by the vendor.

Data presented in the following sections are our preliminary understanding of the first batch of results, and a more critical evaluation of the results is needed to define a clear pathway for future studies.

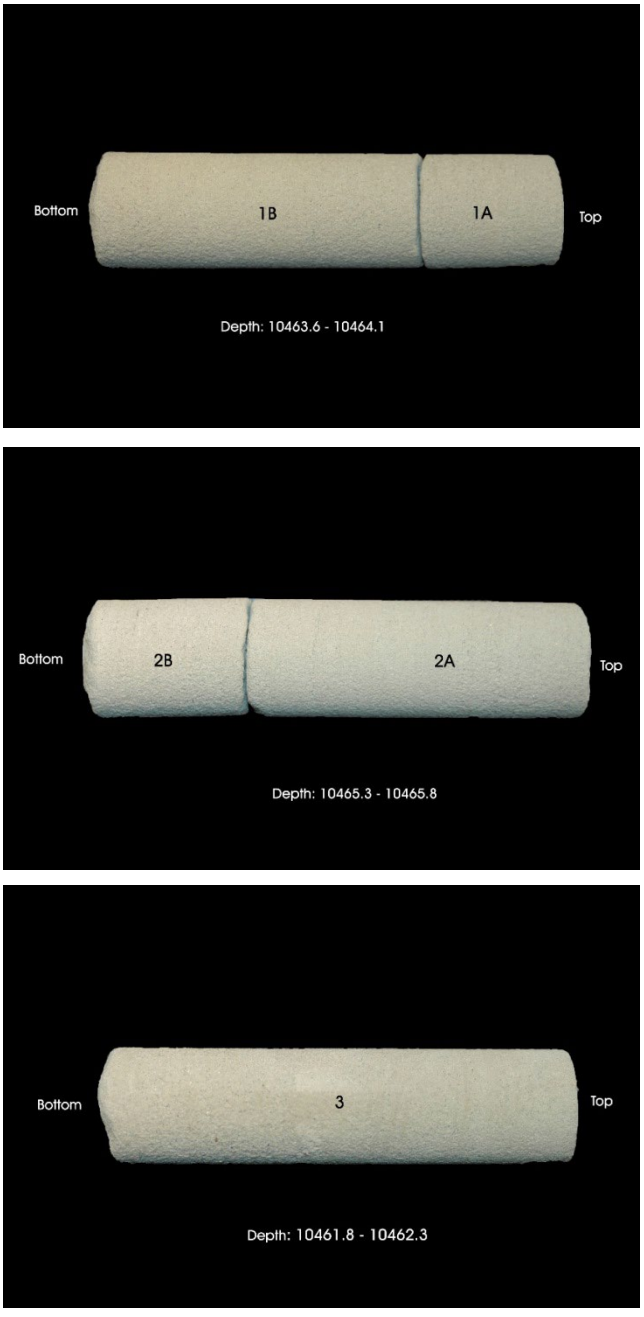

Figure A-1. Cranfield core plugs selected for experiments.

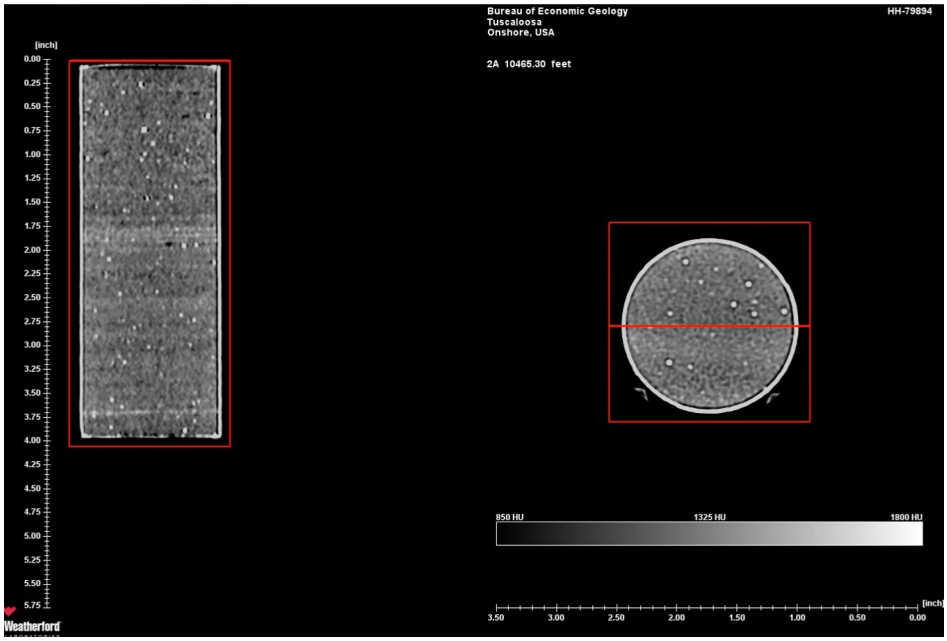

Figure A-2. Helical CT scan of vertical sample 2A.

Table A-1. Basic petrophysical properties of the Cranfield core plugs.

		Sample	Permeability		Net Confining Stress	Grain
Sample	**Sample**	**Depth**	**millidarcies**		**Porosity**	**Density**
Number	**Type**	**feet**	**to Air**	**Klinkenberg**	**percent**	**gm/cc**
22	Horizontal	10462.66	312	288	27.7	2.68
23	Horizontal	10462.83	483	452	28.3	2.69
24	Horizontal	10463.00	278	256	27.8	2.69
26	Horizontal	10463.45	107	95.2	25.9	2.69
29	Horizontal	10464.04	207	189	28.3	2.69
30	Horizontal	10464.20	286	264	28.9	2.69
31	Horizontal	10464.45	237	217	28.2	2.69
3	Vertical	10461.80 - 10462.30	6.79	5.61	28.3	2.69
1A	Vertical	10463.60 - 10464.10	10.3	8.05	28.7	2.69
1B	Vertical	10463.60 - 10464.10	11.2	9.17	28.9	2.70
2A	Vertical	10465.30 - 10465.80	3.71	2.97	28.2	2.70
2B	Vertical	10465.30 - 10465.80	9.40	7.39	28.2	2.69

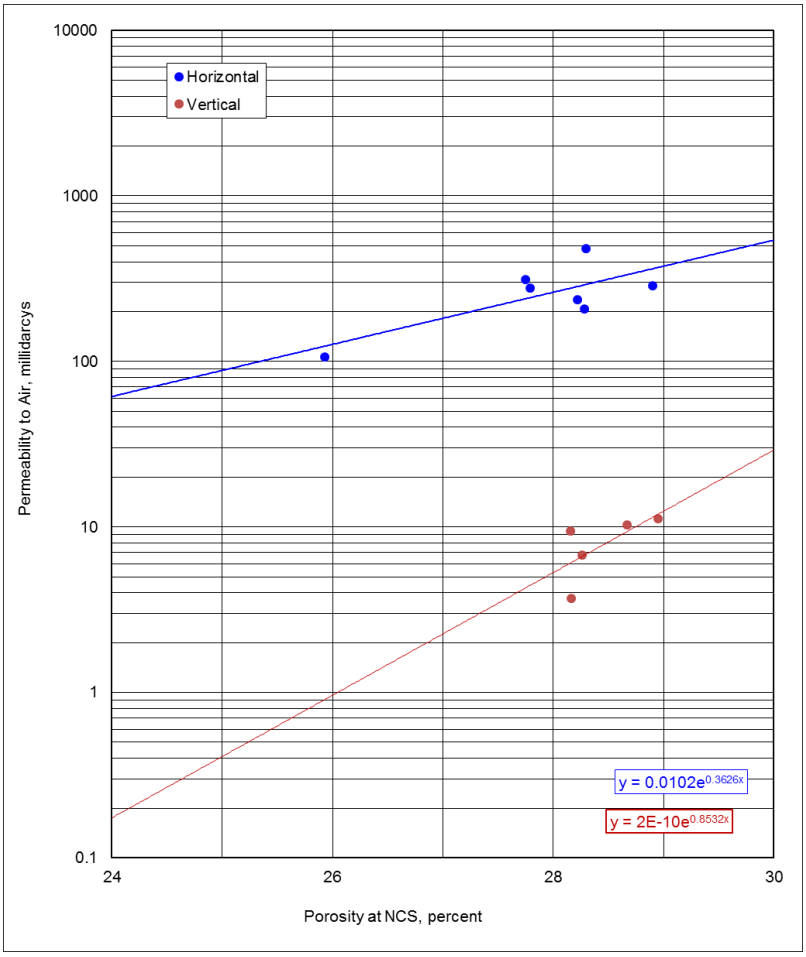

Figure A-3. Horizontal and vertical permeability of Cranfield core plugs differ by over one order of magnitude.

Table A-2. Relative permeability experiment final timeline.

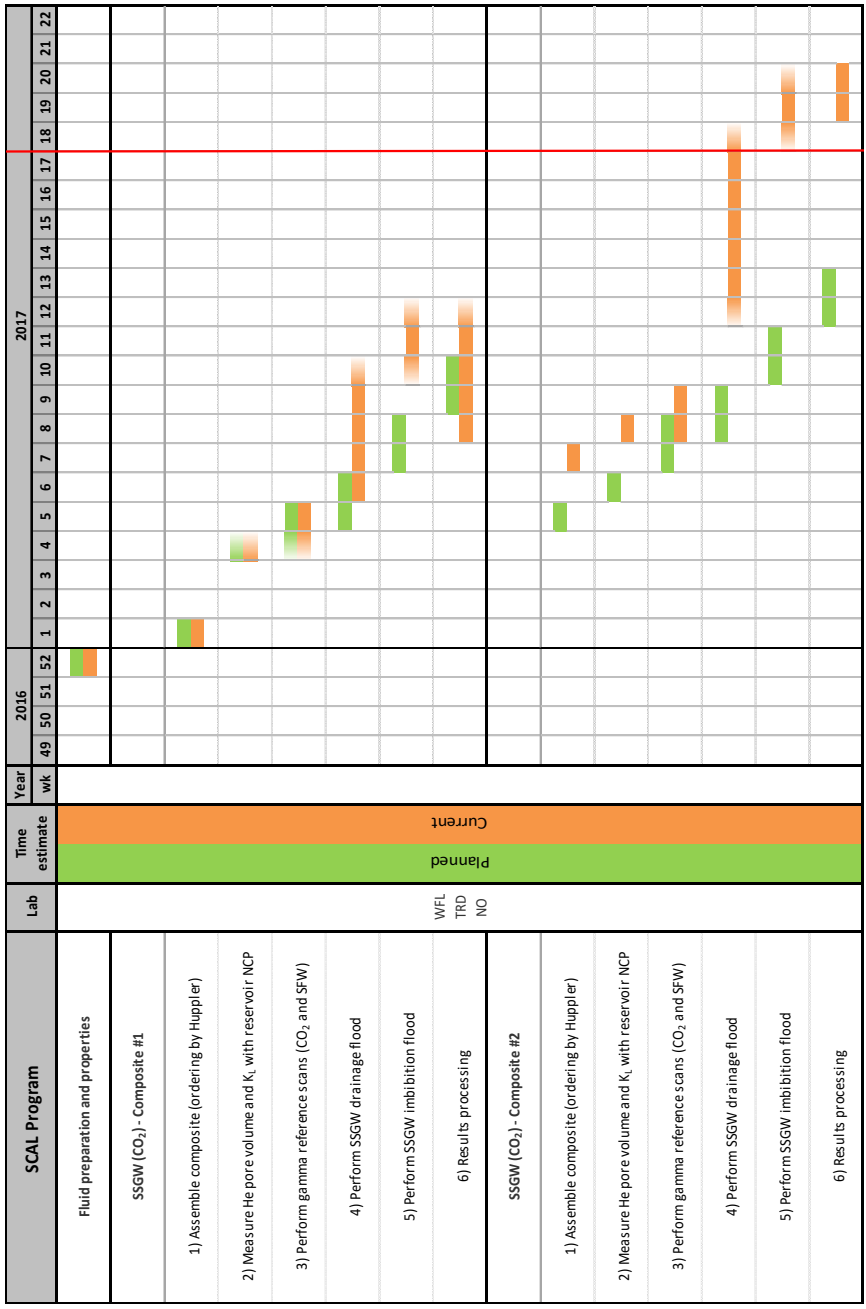

The vendor was asked to measure steady-state relative permeability at reservoir pressure and temperature. Capillary pressure curves were measured both by porous plate and MICP methods.

Details of the relative permeability experimental procedure are as follows (as described by the vendor):

- Plug samples are cleaned and dried to a constant weight. Air permeability and porosity are measured on the cleaned and dried samples at net confining stress (NCS).
- CO_2 is compressed to the designated test pressure ahead of the inlet. The synthetic brine is saturated with CO_2 at designated test pressure and temperature.
- Composite samples are prepared according to Huppler's method, and the samples are marked to allow for the samples to be reconfigured if it becomes necessary. For example, the design for vertical composite is given in Table A-3. (Based on the vendor's suggestion, we removed one of the plug samples (plug 2A) from the vertical composite, as it appears to exhibit slightly different porosity-permeability properties, relative to the other four samples.)

Table A-3. Arrangement of the core plugs for vertical composite, based on Huppler's method.

		Gas inlet (top) →			outlet (btm)
WFTLab ID		B15759	B15762	B15758	B15760
ID		1A	2B	3	1B
Depth	(ft)	10463.60-10464.10	10465.30-10465.80	10461.80-10462.30	10463.60-10464.11
Lengh	(cm)	3.52	4.53	13.81	9.72
Diameter	(cm)	3.67	3.74	3.73	3.72
Grain density (Houston)		2.69	2.69	2.69	2.70
Porosity, ϕ_{He} (Houston)	(frac.)	0.287	0.282	0.283	0.289
Klinkenberg corrected gas permeability, K_L	(frac.)	8.85	9.21	6.89	10.6

Arranged by Huppler ordering (K_L)

- The composite sample is loaded in the specially designed Hassler-type core holder constructed of a special alloy that allows penetration by the x-rays used to monitor saturation changes during steady-state testing.
- The composite sample and system are brought to test conditions. The sample is then x-ray scanned at the 100% CO_2 saturation while determining specific permeability to CO_2 at three flow rates.
- The system is returned to ambient conditions, and the composite is then unloaded. The composite sample is placed under vacuum and then pressure saturated with a laboratory brine of the desired salinity, containing 73 gm/l sodium iodide as the x-ray blocker.
- The sample is x-ray scanned at the 100% brine saturation while determining brine permeability at three flow rates.
- The system is elevated to reservoir conditions. 100% brine is then displaced by 100% CO_2 saturated brine in the composite sample.
- The sample is then x-ray scanned at the 100% CO_2 saturated brine saturation while determining brine permeability at three flow rates.
- Humidified CO_2 and CO_2 saturated brine is injected simultaneously at several increasing gas-water injection ratios to allow the gas saturation within the sample to increase. Saturation changes are monitored by x-ray scan.
- Injection is continued at each ratio until an equilibrium, steady-state condition is established within the core plug, based on the consistency of the saturation profile and

differential pressure. Flow rates and differential pressures are monitored throughout the test process. Finally, gas alone is injected while scanning the sample every injected pore volume, and effective permeability to gas at residual water saturation is determined at two injection rates.

- The system is cooled to ambient temperature and depressurized, and then a final x-ray scan is taken. The composite is unloaded and submitted to Dean-Stark, leached of salts with methanol, and dried to a constant weight in a vacuum oven.
- Measured flow rates and differential pressures at equilibrium conditions for each water-gas injection ratio are used to calculate the steady-state relative permeability data for each sample. Saturations are determined by the x-ray attenuation method, where x-ray scans measured at each saturation are combined with base scans at 100% saturations.

Horizontal Composite Results

Horizontal core plugs are arranged in the order presented in Table A-4 to create the composite for the relative permeability experiment. Average composite properties at reservoir conditions are given in Table A-5. The main purpose of increasing the core length is to ensure that the differential pressure signal is sufficiently high throughout the experiment, which is mainly an issue with very permeable core material. Increasing the length will also increase the pore volume, which may reduce the uncertainty in material balance calculations (e.g., correction for system dead volumes). For these experiments, we are using gamma-ray monitoring, which allows saturation to be measured directly (no corrections required).

Table A-4. Arrangement of the core plugs for horizontal composite based on Huppler's method.

Individual Plug Sample Properties		Flow direction: btm ← top						
Sample ID		31	29	30	24	22	26	23	
Depth	(ft)	10464.45	10464.04	10464.20	10463.00	10462.66	10463.45	10462.83	
Length	(cm)	4.02	4.03	4.02	4.24	5.14	3.72	4.44	
Length (trimmed)	(cm)	4.02	4.03	4.04	4.24	5.10	3.72	2.91	
Diameter	(cm)	3.69	3.67	3.69	3.66	3.68	3.68	3.58	
Petrophysical measurements - 0 / 25 bar NCP, ambient temp									
Pore volume	(ml)	12.23	12.05	11.98	12.30	14.72	10.20	12.95	without NCP
Klinkenberg gas permeability, K_L	(mD)	244	183	251	210	371	136	260	

Table A-5. Horizontal composite average properties.

Average composite properties at reservoir conditions		
Length	(cm)	28.06
Diameter	(cm)	3.66
Pore volume, He @ reservoir NCP	(ml)	77.08
Porosity, φ from bulk @ reservoir NCP	(frac.)	0.261
Klinkenberg gas permeability, K_L	(mD)	141
K_g (CO_2) - multi-rate	(mD)	103
K_w multi-rate - base permeability	(mD)	28.8
K_w/K_L		0.20

Experiments were carried out at reservoir pressure and temperature. The pore pressure was set at 4,656 psi, with overburden pressure of 8,049 psi. Net confining pressure (NCP) of the system was kept at 3,394 psi, and all experiments were carried out at a constant temperature of 252 degrees Fahrenheit. Water density was estimated to be around 1.043 gr/ml and its viscosity is 0.323 centipoise. CO_2 density and viscosity are 0.606 gr/ml and 0.049 centipoise, respectively. Porosity along the composite was more or less homogeneous, averaging around 26% (Figure A-4).

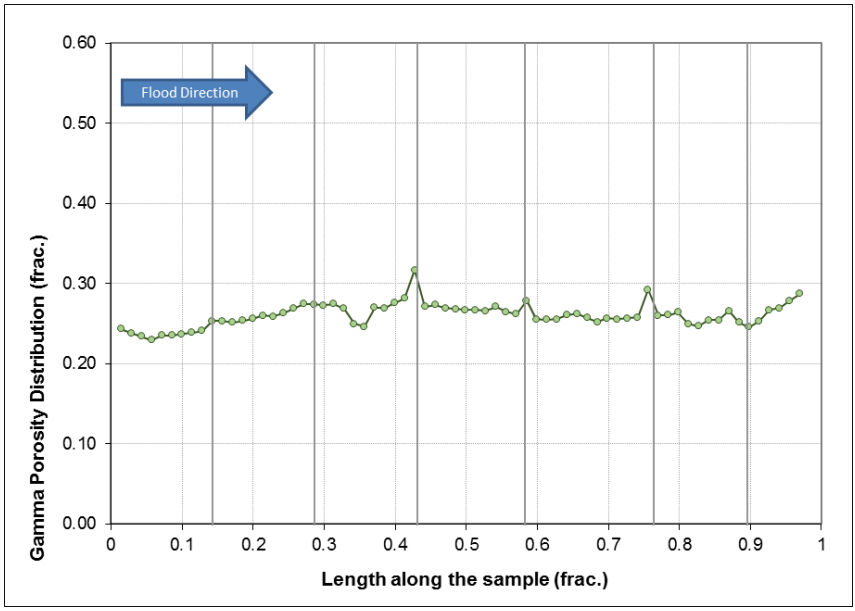

Figure A-4. Gamma ray porosity distribution along the length of horizontal composite shows a homogeneous distribution.

During the experiments, the vendor had some issues with sudden leakages, probably related to gaskets reacting to CO_2/brine, but they were able to resolve the issues. Based on the pressure differentials (Figure A-5) and water saturation profiles (Figure A-6), the vendor does not believe that the leakages affected results. The differential pressure remained more or less constant throughout the test, by varying the gas and water rates at each fractional flow. Initially, a differential pressure of approximately 600 mbar was targeted, which for the early fractions resulted in gas rates between 0.03–0.20 ml/min (Figure A-5). However, this relatively low gas injection rate does not seem to provide a sufficient displacement pressure, due to the strong wettability of samples. Recovery was improved by increasing the gas rate. Drainage experiments were followed by imbibition experiments (Figure A-7 and Figure A-8). The resulting relative permeability curves obtained from drainage and imbibition experiments are shown by Figure A-9.

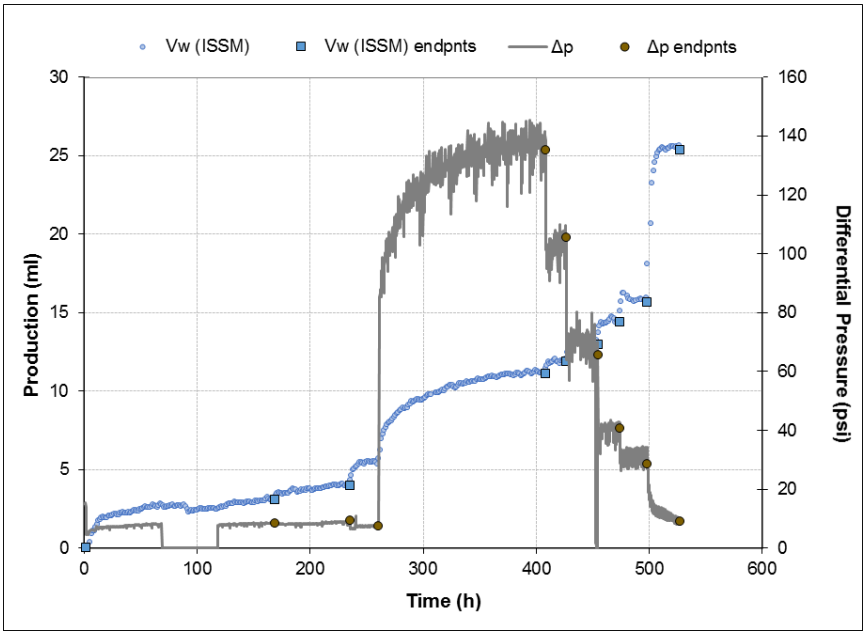

Figure A-5. Drainage production data and pressure differentials for horizontal composite. (Vw=water volumetric rate; Δp=pressure differential)

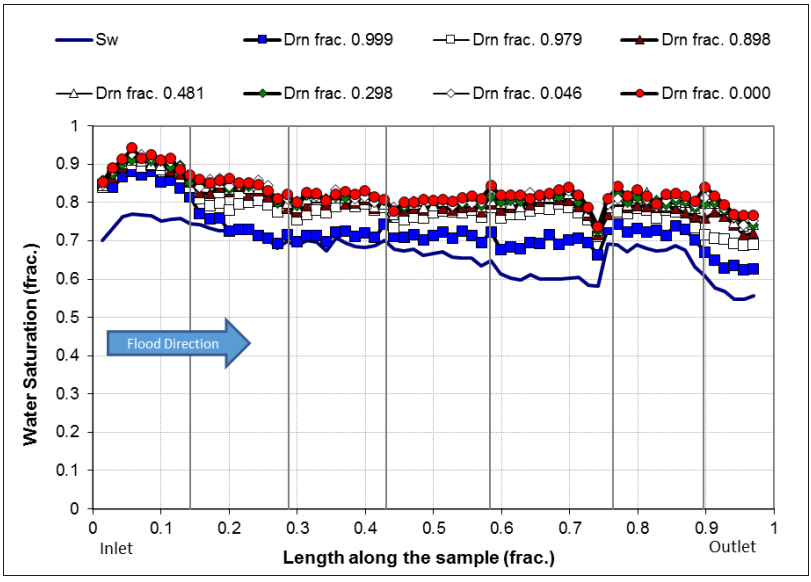

Figure A-6. Drainage saturation profiles for horizontal composite. (Sw=water saturation; Drn=drainage)

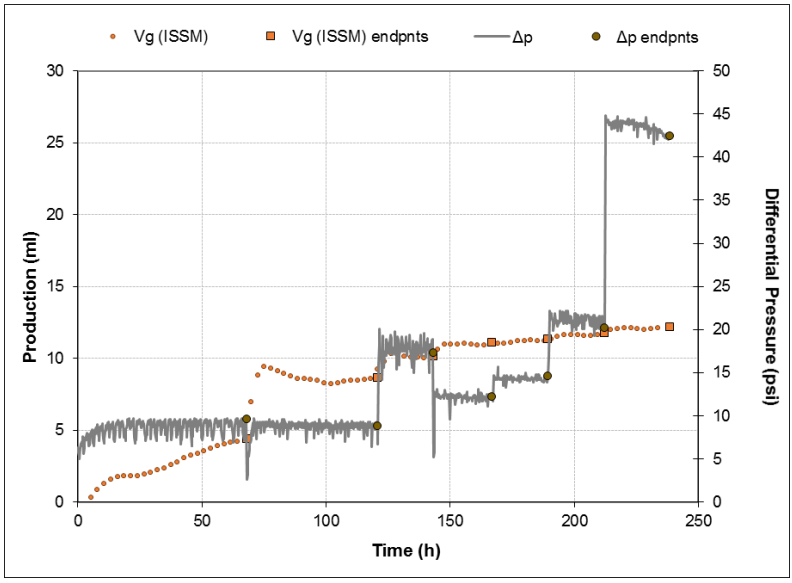

Figure A-7. Imbibition production data and pressure differentials for horizontal composite. (Vg=gas volumetric rate; ISSM=In-situ saturation monitoring)

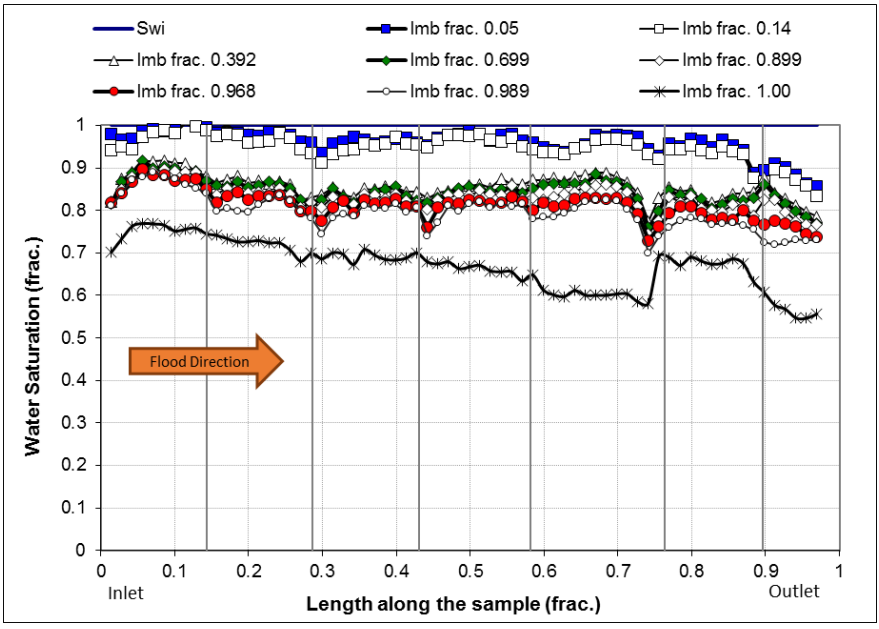

Figure A-8. Imbibition saturation profiles for horizontal composite. (Imb=imbibition)

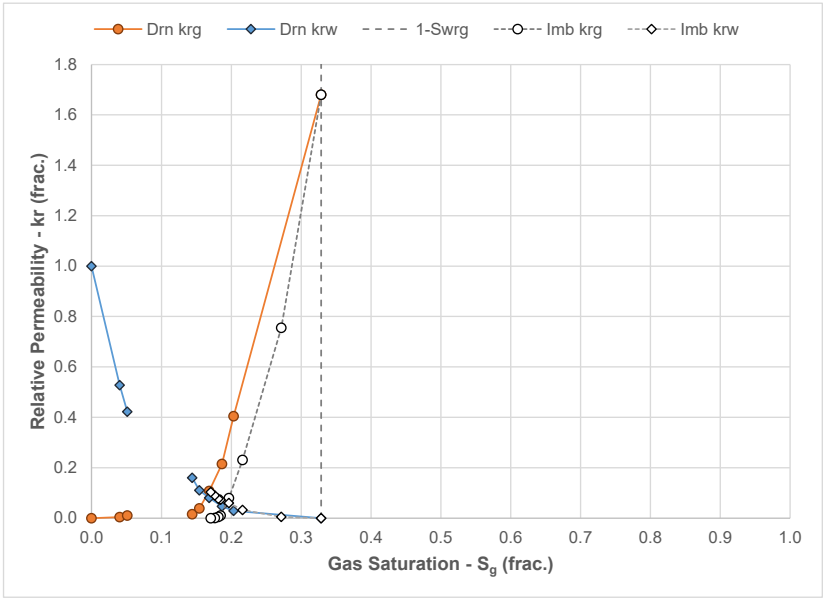

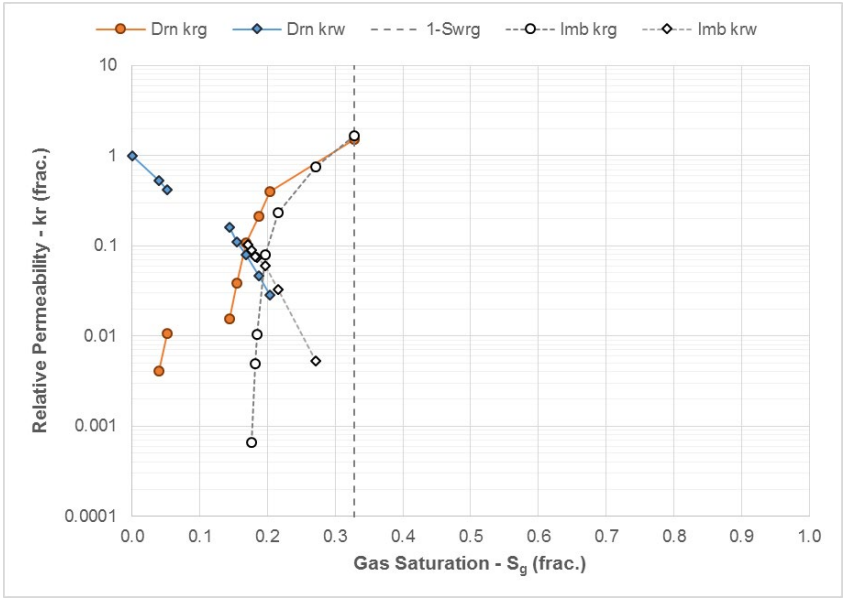

Figure A-9. Relative permeability curves obtained from drainage and imbibition experiments in normal and log scale.

Figure A-10 shows the comparison between the relative permeability curves used in our numerical simulations versus those obtained from the lab experiment on the horizontal composite. The respective curves are generally similar in shape, but there are some differences. Residual water saturation is slightly higher for the relative permeability curves used in the numerical simulations. The residual gas saturation is lower in our numerical simulations (~1-5%) than for the experimental results (~10-20%). The residual water saturation after gas flooding is quite high (approx. 67%). The gas relative permeability exceeds 1.0 (krg ~1.7) (Figure A-9).

From these results, it looks like CO_2 behaves quite similar to what may be expected of other gas/water systems, where strong water wetting preferences result in high Swrg. Because Kw was used as the base permeability, then krg > 1.0 (Kw < KL because of the strong water wetting preferences).

Fractional flow for drainage and imbibition experiments are plotted in Figure A-11. The discontinuity in the drainage curve relates to the point at which the vendor decided to increase the injection rate of CO_2 to increase the displacement pressure. Those experimental points at lower gas fractional flows probably fall in the capillary limited regime. It is interesting that under the capillary limited regime, the residual gas saturation is lower than that in the transition zone. This is most probably because to reach the transitional or viscous limited regimes, we need to inject larger rates of the CO_2. Because of the higher rates, more pores are invaded by CO_2 and potentially more CO_2 will be residually trapped.

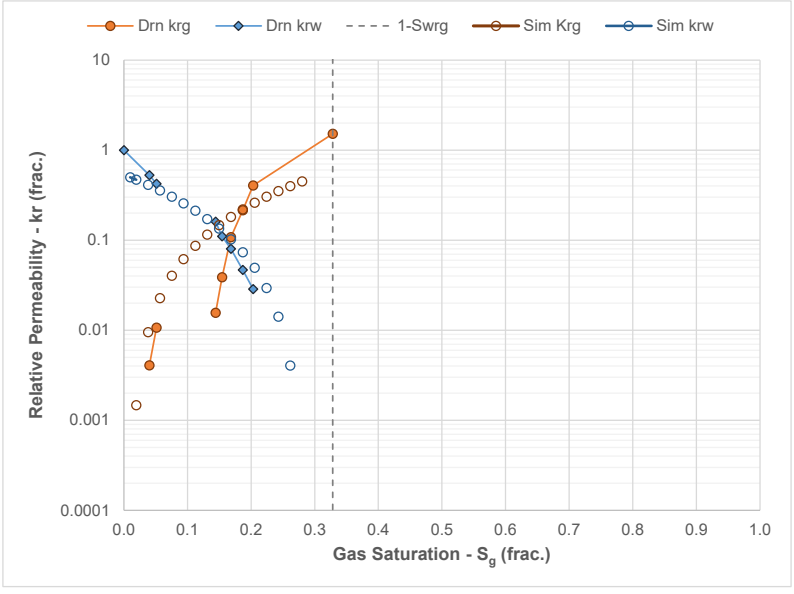

Figure A-10. Comparison of experimental relative permeability curves with curves used in numerical simulations.

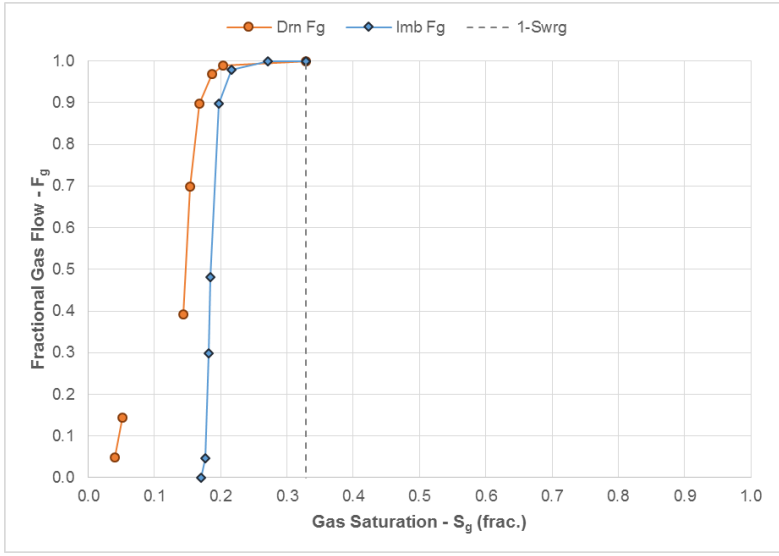

Figure A-11. Fractional flow curve for drainage and imbibition curves.

We have made an attempt to calculate the capillary number using the method of Virnovsky [24] for the various injection rates; although, at this point the capillary pressure is unknown (Figure A-12). Capillary pressure experiments are planned on the same core plugs. Based on assumed capillary pressure of 1000 mbar, all the data points of this experiments fall in the transition zone. The values observed with this assumption appear to be in general agreement with observations by others [25].

For the vertical composite, we will plan to use displacement rates that keep conditions within the mid-range of the capillary transition zone, applying the same methodology as presented in this report.

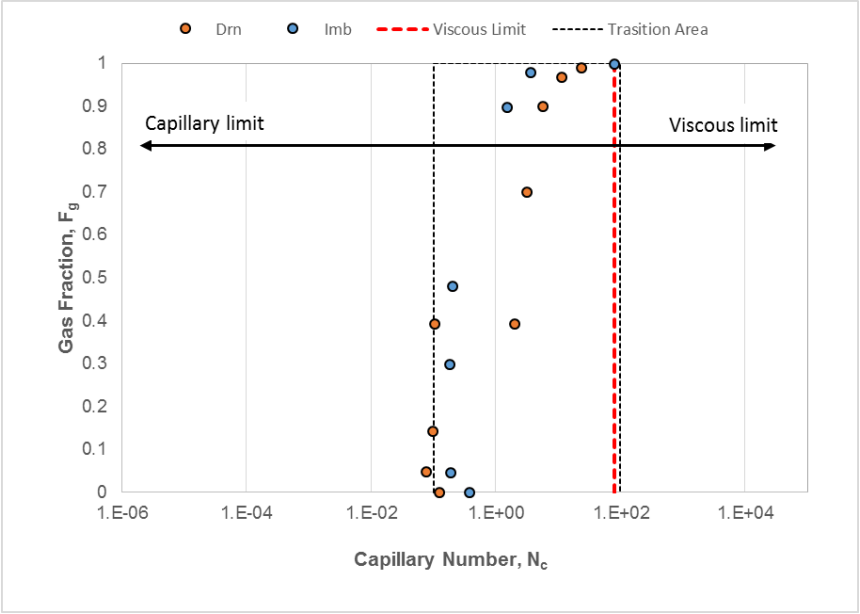

Figure A-12. Capillary number estimated for drainage and imbibition curves.

Carbon Dioxide Capture for Storage in Deep Geological Formations, Volume 5
Karl F. Gerdes (Editor)
© 2022 BP. All rights reserved.

Chapter 26

REVIEW OF CO_2 INJECTION START-UP/EARLY OPERATIONS FOR CCS DEMOS

Michael L. Godec[1]
[1]Advanced Resources International, 4501 Fairfax Drive, Suite 910, Arlington, VA 22203 USA

ABSTRACT: In carbon dioxide (CO_2) capture and storage (CCS) projects targeting storage in deep saline aquifers, the early stages of injection are when initial, pre-injection characterization and dynamic modelling efforts that were used to design the project are first put to the test. Injection and operational monitoring activities during these early stages of a CO_2 injection and storage project are of high value in determining that the reservoir is accepting CO_2 as planned, or critically, in detecting that a deviance from expectations is occurring that may require timely modification of operations so that the project can continue without straying into unacceptably risky conditions.

As more commercial CCS projects are deployed, it will be important that they take advantage of the lessons learned from the early CCS research and demonstration (R&D) projects. Taking advantage of these lessons should serve to improve operations, reduce risks, and allow for greater cost effectiveness for later commercial projects.

KEYWORDS: carbon dioxide (CO_2), capture and storage (CCS), CO_2 injection, saline storage, demonstration projects

OBJECTIVE

The objective of this project was to assess the experience of the saline CO_2 storage R&D projects pursued to date, which have been through start-up and early injection stages. For some projects, this is based on experience derived from R&D programs attached to "commercial" projects or projects pursued for purposes other than strictly R&D. Where possible, the outcome of injection operations and monitoring activities was compared to that anticipated as the result of initial, pre-injection characterization and dynamic modelling efforts that were used to design the project. This assessment can provide the basis for developing an experience base applicable for proposing successful strategies to guide the next generation of CO_2 storage projects through preparation for and successful execution of start-up and early injection operations.

OVERVIEW OF APPROACH

The effort involved assembling a data base of experiences derived from the results to-date of previous or ongoing small and larger scale CO_2 injection R&D projects. This data base was assembled from published, accessible literature, and was augmented to some extent by interviews with selected project developers and performers. In addition, for several of the selected projects, the effort took advantage of direct project experience.

Fourteen (14) CCS R&D projects targeting CO_2 storage in deep saline aquifers were reviewed. These projects are listed in Table 1, in approximately chronological order when they were initiated.

Table 1. Saline R&D Projects Investigated that have Conducted Start-Up and Early Injection Operations.

Name	Location	Relative Project Duration/Scale
Sleipner	North Sea	Large
Nagaoka	Japan	Moderate
Frio 1&2	Texas	Small
Mountaineer	West Virginia	Small
Plant Daniel	Mississippi	Small
MRCSP–Bass Islands Dolomite	Michigan	Moderate
MRCSP–Plant Burger	Ohio	Small
MRCSP–Rabbit Hash	Kentucky	Small
Snøhvit	Barents Sea	Large
Illinois Basin Decatur	Illinois	Moderate
Citronelle	Alabama	Small
Aquistore	Saskatchewan	Moderate
Quest	Alberta	Large
Tomakomai	Japan	Moderate

Information was collected for each of these projects that documented their start-up and early injection experience. This information was gathered, for the most part, from documented reports, papers, and articles accessible in the public domain (See Reference section). This compiled experience data included as much relevant information as possible, though the extent of documentation of project experiences varies considerably from project-to-project. Since all the information contained in this report was obtained from public domain literature, it is not subject to confidentiality or other restrictions on data usage.

For each of the 14 R&D projects reviewed, information on the following was collected (as available in the public domain literature):

- An overall summary of the project, including information on its key performing entities, location, objective, rationale, scale, source of CO_2, target formation, and planned timeline.
- The planned CO_2 injectivity and storage capacity, which was compared to the injectivity and storage capacity achieved to date.
- The monitoring/surveillance activities planned for the project, and how these activities may have evolved over the course of the project.
- The original characterization and reservoir simulation/modelling activities associated with the planned injection, based on the reservoir information and assumptions established at project initiation. Where assumptions were changed as project activities proceeded, modifications to the characterization and reservoir modelling are also documented.
- The original volume (rate), pressure, and temperature (PVT) assumptions at the initiation of the project, and any anomalies from these original assumptions that were realized after CO_2 injection had taken place.
- The initial predictions of CO_2 and pressure front movement compared to that realized during and after (if applicable) CO_2 injection. This includes information on any out-of-zone migration that may have occurred that was most likely not anticipated.
- Any well integrity and/or operational equipment issues that may have been encountered over the course of the project.
- Any seismicity or micro-seismic experiences that may have occurred over the course of CO_2 injection.

- Documentation of the references and communications that serve as the basis for the information collected.

Finally, this information was reviewed for common trends and findings that occurred across multiple projects, to serve as a basis for providing lessons learned for future CO_2 storage projects targeting deep saline aquifers. In addition, these lessons were considered in terms of their additional potential applicability to other types of CO_2 storage situations, such as storage in association with CO_2-EOR, conversion from CO_2-EOR to CO_2 storage, and storage in both brownfield and greenfield residual oil zone (ROZ) projects deploying CO_2-EOR.

SUMMARY OF FINDINGS FOR THE SALINE R&D PROJECTS

One important consideration when reviewing these 14 R&D projects is that some were very small injection tests, often injecting for less than a year, and in some cases for just a day or two. In most of these projects, injected CO_2 volumes were constrained by the availability and/or the costs of CO_2 and the constraints of project budgets. These small tests included Nagaoka, Frio 1&2, Mountaineer, Plant Daniel, MRCSP Bass Islands, MRCSP Ohio Plant Burger, and MRCSP Rabbit Hash. In many cases, injected CO_2 volumes were so small that it was difficult to ascertain the extent to which pre-injection expectations were realized.

In contrast, several R&D projects were larger tests, where 100,000 tonnes or more of CO_2 were ultimately injected and stored, or where volumes of this size or larger are planned to be injected. These projects include Sleipner, Snøhvit, Illinois Basin Decatur, SECARB Phase III Anthropogenic Test (Citronelle), Aquistore, and Quest. When summarizing commonalities and differences among the various saline storage projects, if is often necessary to differentiate between the smaller and larger R&D projects in terms of the volume of CO_2 injected.

CO_2 Injectivity/Capacity

In nearly all the projects, initial understanding of reservoir characteristics was revised once injection operations were underway. However, for some of the small projects, the small CO_2 injection volumes often made it difficult to fully ascertain initial expectations relative to ultimate results. In a few cases, like Plant Daniel, reservoir permeability was better than anticipated, resulting in better injectivity than planned. In others, like Plant Burger, injectivity was less than expected due to less favorable reservoir characteristics and unanticipated heterogeneity.

For the larger projects, in some cases injection activities played out according to plan, such as for Sleipner. For some, like Quest, injectivity was better than planned. For others, like Snøhvit, initial reservoir understanding was erroneous, with much greater reservoir complexity encountered, requiring evolving injection strategies as greater understanding was acquired. In the case of Decatur, the initial understanding was different than what was encountered, but injection rates were not affected. Injectivity was constrained at Citronelle due to operational issues, where moisture accumulation may have led to some pipeline corrosion. Injection rates were lower at Aquistore due intermittent CO_2 availability and possible channeling that may have occurred that limited the injectivity during early operations.

Perhaps the most important lesson learned from this as applied to future projects is to “plan for the unexpected.” In deep saline aquifers, reservoir understanding is limited over the areal (and often vertical) extent of the target reservoir, especially relative to that which may exist for producing oil and gas fields. Surprises may likely be in store relative to reservoir heterogeneity and complexity, and near wellbore characterizations may not extend further into the reservoir. Reservoir models and simulation results should take this uncertainty into account.

Monitoring/Surveillance

Monitoring activities varied considerably from site to site, as summarized in Table 2. Of course, different monitoring requirements will be associated with volume of CO_2 injected, settings (e.g., offshore vs. onshore, heavily wooded vs. arid terrain, etc.), and in most cases, the project budget. Most projects conducted a survey of various possible monitoring activities and determined what could be the "best bang for the buck" for the monitoring options considered, given project budget constraints and determinations of what is essential based on a risk assessment of stakeholder expectations as opposed to what would be "nice to have".

Moreover, given the fact that most of these were primarily R&D projects, with costs subsidized by government research support, more monitoring/surveillance was conducted that may have been necessary, or justified, for a commercial CO_2 storage project.

Most of the projects monitored subsurface temperatures and pressures in the targeted injection zone, and in most cases, also in geologic formations above the injection zone. Most also conducted some sampling of reservoir fluids, before, during, and after injection (when the project was completed). Most onshore projects conducted some type of ground water monitoring, and most conducted either soil gas/soil flux monitoring, some type of atmospheric monitoring, or both.

Most also performed some type of seismic monitoring, either surface 2-D or 3-D, or cross-well seismic or vertical seismic profiling (VSP). Where the use of 2-D seismic is noted, that generally implies that previously existing 2-D seismic data were used.

Some general conclusions can be drawn from a review of the monitoring activities for these projects:

- Repeated 3-D seismic surveys have proven to be an effective monitoring approach for following the CO_2 plume, provided a sufficient volume of CO_2 has been injected. To be most effective and conclusive, 3-D seismic data should be confirmed/ calibrated with other collected data, such as gravimetric surveys (Sleipner), temperature measurements, etc. The same can be true for the application of interferometric synthetic aperture radar (InSAR) for onshore projects, if the extent of vegetation is such that minor land deformations can be observed.
- Monitoring for CO_2 leakage at the surface or near surface has generally proven to be not effective. This is due to high levels of natural variability, along with both natural and induced "noise" associated with field operations. Recently developed laser-based systems for surface leak detection hold promise but have not yet been thoroughly tested.[1]

[1] However, though not one of the projects assessed in this effort, background soil gas measurements were used at the Weyburn project to disprove an unwarranted claim of leakage to surface.

Table 2. Monitoring Activities Conducted at Saline Projects Investigated.

	3D Seismic	2D Seismic	Crosswell Seismic	VSP	EM/ Gravity Surveys	Continuous Downhole P & T	Wireline Logging
Sleipner	x	x			x		x
Nagaoka			x			x	x
Frio 1&2			x	x	x	x	x
Mountaineer				x		x	x
Plant Daniel		x		x		x	x
MRCSP Bass Islands			x			x	
MRCSP Ohio Plant Burger		x				x	x
MRCSP Rabbit Hash						x	
Snøhvit	x				x	x*	x
Illinois Basin Decatur	x		x	x		x	x
SECARB Anthropogenic		x	x	x		x	x
Aquistore	x			x		x	x
Quest	x			x		x	x
Tomakomai	x	x				x	x

Table 3. Monitoring Activities Conducted at Saline Projects Investigated.

	Fluid Sampling (formation & above zone)	Micro-Seismic	Tracers	Soil Gas/ Flux	Ground Water Monitor-ing	Atmos-pheric Monitor-ing	InSar/ GPS/ Tilt-meters
Sleipner	x						
Nagaoka	x	x					
Frio 1&2	x	x	x	x	x	x	
Mountaineer					x		
Plant Daniel			x	x	x		
MRCSP Bass Islands	x	x		x			
MRCSP Ohio Plant Burger							
MRCSP Rabbit Hash							
Snøhvit							
Illinois Basin Decatur	x	x	x	x	x	x	x
SECARB Anthropogenic				x	x	x	
Aquistore	x	x		x	x	x	x
Quest	x	x		x	x	x	x
Tomakomai		x		x	x		

- Tracers can be effective, if care is taken not to accidentally release them. In at least one case, the accidental release of tracer to the atmosphere during sampling made the use of atmospheric detection of tracers inconclusive.
- In a few longer-term, higher volume tests (e.g., Quest, Decatur), monitoring activities and regulatory requirements evolved over time as more information was gained, the relative effectiveness of various monitoring activities was better established, greater understanding of the reservoir and its setting was acquired, and duplicative monitoring activities could be identified, with some eliminated.
- Some sophisticated and relatively complex monitoring systems (e.g., the modular borehole monitoring (MBM) system employed at the SECARB Phase III test), especially when deployed for the first time, can became more of a hindrance than an aid. Such complicated systems are difficult to maintain and keep operational, often do not perform as planned, and are thus costlier. Until problems associated with earlier versions of such systems are sorted out, for commercial-scale projects, simpler may often be better.
- For several of the projects (e.g., Frio 1&2, SECARB Anthropogenic Test), it was concluded that baseline monitoring prior to injection (especially ground water monitoring) was insufficient to provide useful information, and more baseline monitoring should have been conducted.
- The more recent projects, like Quest and the Illinois Industrial CCS Project (IL-ICCS) (the follow-on to the Illinois Basin Decatur Project (IBDP), are beginning to take advantage of the lessons learned from the previously-conducted projects and are implementing comprehensive risk assessment processes to develop more optimized monitoring programs that evolve over time as risks are better understood and/or reduced.

In fact, most relevant to this point, the IL-ICCS Project which started injection on April 7, 2017 and plans to inject up to 5 million tonnes over 3 years (or longer), took advantage of the lessons learned in the initial IBDP to dramatically refine its monitoring/surveillance program in the second project relative to the first. Specifically, while the IBDP conducted a comprehensive R&D, risk-based program, the IL-ICCS is being pursued as a targeted, regulatory-focused project, based on the lessons learned from IBDP. This has justified a substantial decrease in monitoring density and frequency, as illustrated in Figure 1.

Modeling

Often, initial project monitoring activities proved that initial assumptions about the reservoir, as incorporated in reservoir and simulation models, were erroneous. This has often required major changes to the modelling assumptions. In at least one case (Snøhvit), this necessitated a major change in reservoir injection strategy.

Use of sophisticated, multiphase compositional simulators often proved to be time consuming and costly–especially when “real time” comparison of actual to simulated results were desired. In some cases, simpler models were used that were calibrated to the more sophisticated simulation tools.

In almost all settings, monitoring results and the comparison of simulated to actual results indicated that the target reservoir for injection was much more heterogenous than originally assumed. Major adjustments to the heterogeneity assumptions in the reservoir models and simulator input were required to achieve acceptable matches of model predictions compared to actual results.

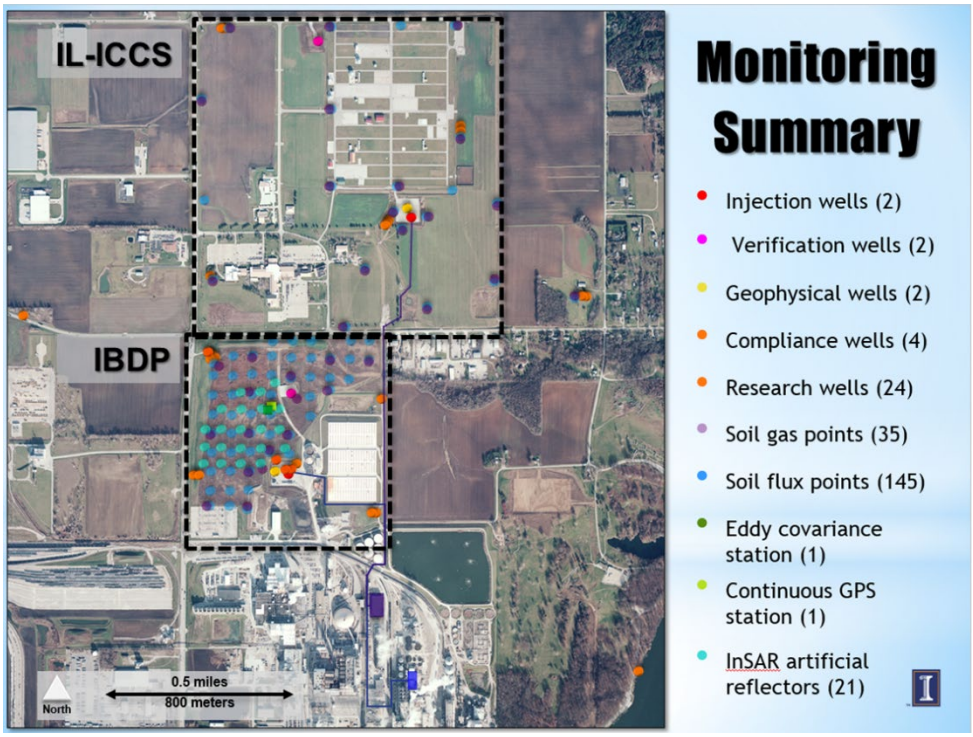

Figure 1. Comparison of Monitoring Station Density between IBDP and IL-ICCS.
©2017 University of Illinois Board of Trustees. Used with permission of the Illinois State Geological Survey.

PVT Anomalies

Higher than expected wellbore pressures were usually the result of lower-than-expected permeability, or greater reservoir heterogeneity than expected. In a few cases, more extensive reservoir compartmentalization or internal baffling also contributed (Snøhvit, Decatur). Initial PVT anomalies were usually resolved once such initial reservoir characterization inaccuracies were understood operationally and incorporated into revised predictive tools.

In some cases, problems occurred when injection pressures and temperatures approached the liquid/gas phase boundary. For example, this was the case at Snøhvit, where it was determined that injection was occurring in a previously unidentified fault block, resulting in unsustainably high wellbore pressures, necessitating an alternative reservoir injection strategy.

In a few of the large tests (e.g., SECARB Phase III, Quest, Aquistore), better-than expected reservoir quality resulted in less wellbore pressure build-up than anticipated.

Pressure and Fluid Front Movement/Out of Zone Migration

Greater reservoir heterogeneity than expected can also result in the fluid front extending over a larger areal extent, and often more rapidly, than anticipated, as the CO_2 front quickly rose to the top of the formation or migrated along previously undetected higher permeability streaks. Moreover, the plume

front was often more asymmetrical than anticipated based on modelling. For example, this was the case at Sliepner, Frio 1&2, Mountaineer, Plant Daniel, and Decatur.)

Seismic data could often be used to determine the presence of the CO_2 plume, but quantitative estimates of saturation were challenging at best. Seismic data usually needed to be used in conjunction with other data, like geophysical logs, fluid samples, pressure and temperature data, etc., to achieve quantitative estimates. However, when applied, such methods could be used to quantify saturations, or to identify where solubility and residual trapping could be occurring.

Detected CO_2 leakage to the surface was not reported for any of the projects, though in some cases, the monitoring activities conducted–such as soil flux or surface atmospheric monitoring–may not have seen leakage had it occurred due to problems with implementation or insufficient availability of quality background characterizations. In addition, though perhaps more difficult to detect, no CO_2 leakage to aquifers was reported either.

In the smaller tests, insufficient volumes of CO_2 were injected to provide much information on plume and pressure front migration – the focus of success was based purely on injectivity, and whether the front migrated to one or more nearby monitoring wells. This is also true for the larger scale projects that are just getting started.

Well Integrity and Equipment Issues

Issues associated with well integrity or equipment consideration were minimal, or at least generally not reported. However, this may have been because most wells were new builds or existing wells in good condition.

No concerns about well bore, casing, pipeline, or equipment corrosion were reported; though, in most cases, the short periods of testing should not have resulted in serious corrosion issues. (The SECARB Phase III test was one minor exception, where pipeline corrosion occurred when moisture collected in low spots, leading to build-up of magnetite, and clogged up pump the filter when operations started up again.)

A few projects had well bore completion issues, or had clogged perforations, that required remedies.

Seismicity Issues

Some of the projects were conducted in areas of very low seismicity concerns, so problems with induced seismicity were not anticipated or experienced. Even the longest running project (Sleipner) has experienced little pore pressure increase after 15 years of injection.

The Japanese projects could demonstrate that CO_2 injection did not correlate to any induced micro-seismic activity, even though these projects were conducted in an earth-quake prone area that experienced natural (not induced) earthquakes during and after CO_2 injection.

APPLICABILTY TO OTHER STORAGE SITUATIONS

These findings and lessons learned from CO_2 injection and storage in deep saline aquifers have potential applicability to other types of CO_2 storage situations, such as storage in association with CO_2-EOR, conversion from CO_2-EOR to CO_2 storage, and storage in both brownfield and greenfield residual oil zone (ROZ) projects deploying CO_2-EOR.

Issues and considerations associated with the extension or modification of the findings and “lessons learned” for the 14 R&D CO_2 storage projects to other storage situations are highlighted below:

- Regarding issues related to CO_2 injectivity and storage capacity; with EOR projects, operators are much more likely to have a better understanding of overall reservoir characteristics and heterogeneity (both areal and vertical) that would likely exist for most deep saline settings. The density of well drilling in an EOR project provides better understanding and less uncertainty of the distribution of characteristics within the reservoir. While true for storage in association with CO_2-EOR and conversion from CO_2-EOR to CO_2 storage; storage in greenfield and brownfield ROZ projects deploying CO_2-EOR may lean towards considerations more akin to saline storage projects.
- Regarding issues related to monitoring/surveillance activities, many of the most commonly applied monitoring activities summarized in Table 2 are also often applied at some CO_2-EOR projects. However, for the 14 projects surveyed, concerns about current and previously drilled wells (both producers and injectors) were not present, unlike that in CO_2-EOR projects. These wells – often referred to as legacy wells – provide the most likely conduit for leakage in projects in which CO_2-EOR has previously been conducted. Thus, substantially greater pre-injection integrity assessment and operational monitoring focus will need to be applied to these legacy wells. In addition, and related to this fact, greater attention will likely need to be paid to above zone and ground water monitoring than may have been applied during CO_2-EOR operations.
- Regarding the original characterization and reservoir simulation, CO_2-EOR operations are likely to have been subject to a long history of development of detailed reservoir models and associated simulations, providing a solid understanding of subsurface reservoir performance that can provide the basis for understanding the potential for CO_2 storage in the same setting. In these cases, deviations between simulated and actual performance are a lot less likely. Again, while true for storage in association with CO_2-EOR and conversion from CO_2-EOR to CO_2 storage, this may less true for storage in association with both greenfield and brownfield ROZ projects deploying CO_2-EOR.

ACKNOWLEDGEMENTS

Special thanks should go to the CO_2 Capture Project (CCP4) for their support in this assessment.

BIBLIOGRAPHY

Sleipner

Boait, F. C., N. J. White, M. J. Bickle, R. A. Chadwick, J. A. Neufeld, and H. E. Huppert, "Spatial and temporal evolution of injected CO_2 at the Sleipner Field, North Sea," *Journal of Geophysical Research*, **117** (2012) B03309-.

Eiken, Ola, Philip Ringrose, Christian Hermanrud, Bamshad Nazarian, Tore A. Torp and Lars Høier, "Lessons Learned from 14 years of CCS Operations: Sleipner, In Salah and Snøhvit," *Energy Procedia* **4** (2011) 5541–5548.

Furre, Anne-Kari, Ola Eiken, Håvard Alnes, Jonas Nesland Vevatne, and Anders Fredrik Kiær, "20 years monitoring CO_2-injection at Sleipner," *Energy Procedia*, **114**, (2017) 3916-3926.

Singh, V. P., Cavanagh, A., Hansen, H., Nazarian, B., Iding, M., & Ringrose, P. S. (2010, January 1)," Reservoir Modeling of CO_2 Plume Behavior Calibrated Against Monitoring Data from Sleipner, Norway," Society of Petroleum Engineers Paper No. 134891-MS presented at the *SPE Annual Technical Conference and Exhibition*, 19-22 September, 2010, Florence, Italy.

Verdon, James P., J.-Michael Kendall, Anna L. Stork, R. Andy Chadwick, Don J. White, and Rob C. Bissell, "Comparison of geomechanical deformation induced by megatonne-scale CO_2 storage at Sleipner, Weyburn, and In Salah," *Proc Natl Acad Sci U S A*. (2013) July 23**; 110**(30): E2762–E2771.

Chen Zhu, Guanru Zhang, Peng Lu, Lifeng Meng, and Xiaoyan Ji, "Benchmark modeling of the Sleipner CO_2 plume: Calibration to seismic data for the uppermost layer and model sensitivity analysis," *International Journal of Greenhouse Gas Control*, **43** (2015) 233–246.

Nagaoka

Mito, Saeko and Ziqiu Xue, "Post-Injection Monitoring of Stored CO_2 at the Nagaoka Pilot Site: 5 Years Time-Lapse Well Logging Results," *Energy Procedia* **4** (2011) 3284-3289.

Nakajima, Takahiro, Ziqiu Xue, Jiro Watanabe, Yoshinori Ito, and Susumu Sakashita, "Assessment of Well Integrity at Nagaoka CO_2 Injection Site Using Ultrasonic Logging and Cement Bond Log Data," *Energy Procedia* **37** (2013) 5746–5753.

Nakajima, Takahiro, Takuma Ito, and Ziqiu Xue, "Numerical simulation of the CO_2 behaviour to obtain a detailed site characterization: A case study at Nagaoka pilot-scale injection site," *Energy Procedia,* **114** (2017 2819-2826 .

Mito, Saeko and Ziqiu Xue, "Geochemical trapping of CO_2 in saline aquifer storage: Results of repeated formation fluid sampling at the Nagaoka site," *Energy Procedia* **37** (2013) 5449–5455.

Frio 1&2

Hovorka, S. D. (2006) Frio Brine Storage Experiment—lessons learned, in *8th International Conference on Greenhouse Gas Control Technologies*, Trondheim, Norway, June 19–22, CD-ROM [6 p.]. GCCC Digital Publication Series #06-13. (http://www.beg.utexas.edu/gccc/forum/codexdownloadpdf.php?ID=64)

Hovorka, S., (2009) Frio Brine Pilot: the First U.S. Sequestration Test, September/October 2009, *Southwest Hydrology*, pages 26-31. (http://www.swhydro.arizona.edu/archive/V8_N5/feature5.pdf)

C. Doughty, Site Characterization for CO_2 Geologic Storage and Vice Versa – The Frio Brine Pilot as a Case Study, Proceedings, *CO_2SC Symposium 2006*, Lawrence Berkeley National Laboratory, Berkeley, California, March 20-22, 2006. (http://www.osti.gov/scitech/servlets/purl/900649/)

Mountaineer

Bacon DH, MD White, N Gupta, JR Sminchak, and ME Kelley. (2009) CO_2 Sequestration Potential in the Rose Run Formation at the Mountaineer Power Plant, New Haven, West Virginia. *Carbon dioxide sequestration in geological media- State of the science: AAPG Studies in Geology* **59**, pp. 553-570. American Association of Petroleum Geologists, Tulsa, OK.

McNeil, C, I Bhattacharya, T Lohner, H J Holley Ii, M Kennedy, S Mawalkar, N Gupta, S Mishra, R Osborne, M Kelley, Lessons Learned from the Post-Injection Site Care Program at the American Electric Power Mountaineer Product Validation Facility, *Energy Procedia*, **63** (2014) 6141-6155.

Mishra S, Orugnati Y, Gupta N, Ravi Ganesh P, McNeil C, Bhattacharya I, Spitznogel G., "Modeling CO_2 plume migration based on calibration of injection and post-injection pressure response at the AEP Mountaineer Project," *Greenhouse Gases: Science and Technology,* **4**(3) (2014) 331-56.

Plant Daniel

Plant Daniel Project Closure Report Volume 1. Final Report. DOE-NETL. September 30, 2009.

MRCSP - Bass Islands Dolomite

Final Report, Michigan Basin Phase II Geologic CO_2 Sequestration Field Test, Report Prepared for: U.S. Department of Energy, National Energy Technology Laboratory, April 28, 2011.

Midwest Regional Carbon Sequestration Partnership, PHASE II FINAL REPORT, DOE-NETL Cooperative Agreement DE-FC26-05NT42589, April 29, 2011

MRCSP –Plant Burger/ MRCSP – Rabbit Hash

Battelle (2011) Final Report: Appalachian Basin – R.E. Burger Plant Geologic CO_2 Sequestration Field Test. DOE-NETL Cooperative Agreement DE-FC26-05NT42589. January 4,2011.

Midwest Regional Carbon Sequestration Partnership (MRCSP), PHASE II FINAL REPORT, DOE-NETL Cooperative Agreement DE-FC26-05NT42589, April 29, 2011.

Wickstrom, L., Slucher, E., Baranoski, M.T. (2006) Preliminary Geologic Assessment of the Burger Power Plant and Surrounding Vicinity for Potential Injection of Carbon Dioxide. Ohio Department of Natural Resources: Geological Survey. June 2006.

Snøhvit

https://www.netl.doe.gov/File%20Library/events/2013/carbon%20storage/12-45-Snohvit_LLNL_final.pdf

Eiken O, Gilding D, Hansen H, Hansen O, Nazarian B, Osdal, B, Ringrose P. Snøhvit: "The history of injecting and storing 1 Mt CO_2 in the fluvial Tubåen Fm." *Energy Procedia* **37** (2013) 3565 – 3573.

Eigen, Ola, Philip Ringrose, Christian Hermanrud, Bamshad Nazarian, Tore A. Torp and Lars Høier, "Lessons Learned from 14 years of CCS Operations: Sleipner, In Salah and Snøhvit," *Energy Procedia* **4** (2011) 5541–5548.

Ji-Quan Shi, Claire Imrie, Caglar Sinayuc, Sevket Durucan, Anna Korre, and Ola Eiken, "Snøhvit CO_2 storage project: Assessment of CO_2 injection performance through history matching of the injection well pressure over a 32-months period," *Energy Procedia* **37** (2013) 3267 – 3274.

Illinois Basin Decatur

Finley, R.J. 2014, An overview of the Illinois Basin – Decatur Project, *Greenhouse Gases Science and Technology*, **4**, 571-579.

Archer Daniels Midland Company Class VI UIC Permit Applications, April 2014. Available from http://www.epa.gov/region5/water/uic/adm/index.htm

Larrick, D. and Brauer, D. (2014) CCUS Education and Outreach at the National Sequestration Education Center, Decatur, Illinois, *International workshop on public education, training, and community outreach for carbon capture, utilization, and storage*, National Sequestration Education Center, Decatur, Illinois, July 30 – 31, 2014.

Finley, R. (2014) A Successful Demonstration of Carbon Dioxide Storage at a Biofuel Facility in Decatur, Illinois USA: The Illinois Basin – Decatur Project (IBDP), *Thirteenth Annual Carbon Capture, Utilization & Storage Conference*, Pittsburgh, PA, April 28 - May 1, 2014.

Hickman, S. *et al.* (2014) USGS Monitoring of Injection-Induced Seismicity for the Decatur, IL, Carbon Dioxide Sequestration Project, *Thirteenth Annual Carbon Capture, Utilization & Storage Conference*, Pittsburgh, PA, April 28 - May 1, 2014.

Locke II, R.A., Greenberg, S.E., Jagucki, P., Krapac, I.G., Shao, H. (2016) Regulatory uncertainty and its effects on monitoring activities of a major demonstration project: The Illinois Basin – Decatur Project case, *Energy Procedia*, **114** (2017) 5570-5579.

Sallie E. Greenberg (2017) Successful Storage of One Million Tonnes of Carbon Dioxide at the Illinois Basin – Decatur Project, Presentation at the *Exchange Monitor CCUS Conference*, Chicago, IL, 12 April 2017

R.A. Locke II, S.E. Greenberg, P. Jagucki, I.G. Krapac, and H. Shao (2017) "Permitting Experiences from the IBDP Injection Well, CCS#1," Presentation at the *Exchange Monitor CCUS Conference*, Chicago, IL, 12 April 2017

Citronelle

UIC Report (2011) Supplement to Denbury onshore, LLC Class V Experimental Injection Well Permit applications for proposed injection wells 1 and 2.

Pashin, J. C., McIntyre, M. R., Grace, R. L. B., and Hills, D. J. (2008) Southeastern Regional Carbon Sequestration Partnership (SECARB) Phase III Final Report. Geological Survey of Alabama. Tuscaloosa, Alabama. September 30, 2008

Koperna, G., Riestenberg, D., Kuuskraa, V., Rhudy, R., Trautz, R., Hill, G., and Esposito, R., The SECARB Anthropogenic Test: A US Integrated CO_2 Capture, Transportation and Storage Test. *International Journal of Clean Coal and Energy* **1** (2012) 13-26.

Aquistore

https://www.undeerc.org/pcor/technicalpublications/accordion%20pdf/TP-2014-Model-Development-Aquistore-CO2-Storage-Project.pdf

Jiang, T., L. Pekot, W.D. Peck, J. A. Sorensen, and C.D. Gorecki (2016) A Numerical Simulation Update of the Aquistore CO_2 Storage Project, presentation at the *2016 AIChE Annual Meeting*, San Francisco, CA November 17, 2016. https://www.aiche.org/conferences/aiche-annual-meeting/2016/proceeding/paper/638d-numerical-simulation-update-aquistore-co2-storage-project

White, Don, Kyle Harris, Lisa Roach, Brian Roberts, Kyle Worth, Anna Stork, Christopher Nixon, Douglas Schmitt, Tom Daley, and Claire Samson, Monitoring results after 36 ktonnes of deep CO_2 injection at the Aquistore CO_2 Storage Site, Saskatchewan, Canada, *Energy Procedia* **114** (2017) 4056-4061.

Worth, Kyle, Don White, Rick Chalaturnyk, Jim Sorensen, Chris Hawkes, Ben Rostron, and Aleana Young, Aquistore: Year One – Injection, Data, Results, *Energy Procedia,* **114** (2017) 5624-5635.

Quest

Global CCS Institute, *Global Status of CCS: 2016. Saline Aquifer Storage Performance at the Quest CCS Projec*t, webinar presented November 22, 2016 (http://www.globalccsinstitute.com/events/webinar/2016-11-21-230000-2016-11-22-000000/global-status-ccs-2016-saline-aquifer-storage-performance-quest-ccs-project)

https://www.energy.alberta.ca/AU/CCS/KnowledgeSP/Documents/2016/QuestMMVPlan_2016.pdf

O'Brien, Simon, and Owen Tucker (2016), "Quest-MMV Overview," presentation at the California Air Resources Board, Technical Discussion Series on Monitoring, August 2016

Shell Canada Limited. Application for the Quest Carbon Capture and Storage Project; Radway Field. Shell Canada Limited. [Online] July 10, 2012. [Cited: February 22, 2017] https://www.aer.ca/documents/decisions/2012/2012-ABERCB-008.pdf

http://ieaghg.org/docs/General_Docs/2modmon_pres/3.4%20Simon%20O'Brien%20-%20Quest%20Lightsource.pdf

Tomakomai

Tanaka, Yutaka, Masanori Abe, Yoshihiro Sawada, Daiji Tanase, Toshikazu Ito, and Tetsuo Kasukawa, "Tomakomai CCS Demonstration Project in Japan, 2014 Update," *Energy Procedia* **63** (2014) 6111 – 6119.

Tanase, Daiji, Takashi Sasaki, Toru Yoshii, Satoshi Motohashi, Yoshihiro Sawada, Satoshi Aramaki, Yoshinori Yamanouchi, Tomoyuki Tanaka, Shiro Ohkawa, and Ryuichi Inowaki, "Tomakomai CCS Demonstration Project in Japan," *Energy Procedia* **37** (2013) 6571 – 6578.

Japan CCS Co., Ltd. (JCCS), "Progress of the Tomakomai CCS Demonstration Project," presentation at the Combined Meeting of the IEAGHG Modelling and Monitoring Networks, 7 July 2016.

Japan CCS Co., Ltd. (JCCS), "Tomakomai CCS Demonstration Project," presentation at the CSLF Technical Group Meeting, October 4, 2016.

Carbon Dioxide Capture for Storage in Deep Geological Formations, Volume 5
Karl F. Gerdes (Editor)
© 2022 BP. All rights reserved.

Chapter 27

POTENTIAL FOR CO_2 STORAGE COST REDUCTIONS WITH GREATER COMMERCIAL DEPLOYMENT

Michael Godec[1] and Brian Williams[2]
[1]Advanced Resources International, Incorporated
[2] CO_2 Capture Project

ABSTRACT: The costs associated with conducting CO_2 storage today are estimated for current regulatory requirements and using existing technologies and practices. Particular attention is paid to the costs associated with storage, monitoring, and verification (SMV), and their contribution to the overall costs of CO_2 storage (i.e., as first-of-a-kind, or FOAK, costs). Then, the paper characterizes how evolving regulatory requirements and expectations, technology applications and performance, operator and regulator experience, proper attention to risk characterization and assessment, and knowledge of best practices, can potentially lead to cost reductions in various SMV activities as more CCS projects get deployed (i.e., as nth-of-a-kind, or NOAK, costs).

The potential issues and estimated costs associated with FOAK to NOAK evolution for three "representative" CO_2 storage cases are assessed, based on an application of a risk-based approach to facilitate evolution from FOAK to NOAK SMV approaches and technologies and their associated costs.

KEYWORDS: carbon dioxide (CO_2), CO_2 capture and storage (CCS), CO_2 storage costs, demonstration projects, risk assessment

BACKGROUND AND OBJECTIVE

Many believe that the costs incurred in carbon capture and storage (CCS) research and demonstration (R&D) projects need to be substantially reduced for large-scale deployment of CCS to be realizable. This is traditionally thought to be true for the costs of CO_2 *capture*. Such costs are discussed in terms of the cost reductions that can be realized going from first-of-a-kind (FOAK) capture facilities to facilities that take advantage of more mature technologies, practices, and experience, the so-called nth-of-a-kind (NOAK) facilities. This same situation exists for CO_2 *storage* as well, though perhaps not in quite the same way.

The objective of this study was to develop and characterize the costs associated with conducting CO_2 storage today (FOAK costs), under current regulatory requirements and using existing technologies and practices, with focus on the costs associated with SMV, and their contribution to the overall costs of CO_2 storage. In addition, this study identified and evaluated how evolving regulatory requirements and expectations, technology applications and performance, operator and regulator experience, proper attention to risk characterization and assessment, and knowledge of best practices, can potentially lead to cost reductions as more CCS projects get deployed (NOAK costs).

`

ESTIMATING SMV COSTS

For this effort, the U.S. Department of Energy, Office of Fossil Energy/National Energy Technology Laboratory's (FE/NETL) CO_2 Saline Storage Cost Model [1] (2014 version) was used as the integrated costing and financial analysis framework for the development of estimated life-cycle CO_2 storage costs. Using U.S. onshore settings as a starting point, the analysis assumed compliance with U.S. Environmental Protection Agency (USEPA) requirements for Class VI CO_2 storage wells [2] or Class II CO_2 injection wells for enhanced recovery [3] (where applicable) for geologic storage of CO_2, along with US EPA reporting requirements under its Greenhouse Gas Reporting Program (GHGRP) [4] for facilities that inject CO_2 underground -- Subpart UU applies to CO_2 injected to enhance hydrocarbon recovery [5] and Subpart RR to CO_2 injected for storage [6].

Cost estimates were developed for three representative case studies:

- A CO_2 storage project in an onshore saline aquifer in the U.S. Gulf Coast area.
- A CO_2-EOR project converting to a CO_2 storage project in the (onshore) U.S. Permian Basin.
- CO_2 storage in association with CO_2-EOR, for four onshore U.S. project settings.

Characteristics of the first two case studies are summarized in Table 1. The characteristics and assumptions associated with the four onshore CO_2-EOR project settings are summarized in Table 2. Key characteristics differentiating these cases are highlighted in yellow.

CO_2 storage cost estimates for all the cases considered include incremental costs associated with well and facility construction (or rehabilitation), abandonment, operations, SMV activities, post-injection site care, and site closure. These are based on the technical requirements in EPA Class VI and GHGRP rules and regulations, along with associated published guidance documents.

The SMV activities and associated cost elements considered in this assessment are listed in Table 3.

Table 1. Key Characteristics of "Representative" Onshore Saline Storage and CO_2-EOR Conversion to Storage Prospects.

	CO_2 Storage Project Deep Saline Formation in U.S. Gulf Coast	**CO_2-EOR Project Converted to CO_2 Storage in the U.S. Permian Basin**
Maximum Monitoring Area	30,080 acres	10,240 acres
Well Depth	8,705 feet	5,045 feet
Assumed Field-Wide CO_2 Injection Rate	6 million metric tonnes per year	2 million metric tonnes per year
Assumed CO_2 Injection Rate per Well	500 tonnes per day	50 tonnes per day
Project Life, Total Capacity	30 years; 180 million tons of total capacity	20 years; 40 million tons of total capacity
Years for Post Injection Site Care (PISC)	50	10

`

Table 2. Key Characteristics of "Representative" Onshore CO_2-EOR Storage Projects with Associated CO_2 Storage.

	Permian Basin	Gulf Coast	Mid-Continent	Rocky Mountains
Field Area (acres)	28,000	7,200	20,000	2,600
Well Depth (feet)	5,500	6,200	6,000	5,000
Field-Wide CO_2 Injection Rate				
MMcf/year	211,000	86,000	28,000	58,000
Million tonnes/year	4.0	1.6	0.5	1.1
CO_2 Injection Rate per Well (tonnes per day)	25	186	39	66
# of injection wells	594	24	50	63
Project Life (years)	28	29	16	20
Stored/Total Injected CO_2	0.44	0.62	0.55	0.47
Field-wide CO_2 Storage Rate (million tonnes per year)	1.8	1.0	0.3	0.5
Total Injected (million tonnes)	112	47	8	22
Total Stored (million tonnes)	50	29	5	10
Years for Post Injection Site Care (PISC)	10	10	10	10

`

Table 3. SMV Cost Elements Considered in this Assessment.

Data Acquisition, Planning, and Permitting	**Electrical/Other**	**Well Costs (one time, except Mechanical Integrity Tests [MITs])**
Regional Evaluation	Electrical Resistivity Tomography	New Class VI Injection Wells
Site Characterization	Gravity Survey	New Deep Monitoring Wells
Data Preparation and Analysis	Micro-seismic (Initial)	New Stratigraphic Wells
Initial and Periodic Modeling	Micro-seismic (Annual O&M)	EOR Well Convert to Monitor Wells
Corrective Action Planning	**Atmospheric Surveys**	EOR Wells Converted to Injectors
FEED	Eddy Covariance–Initial	Well Testing
Class VI Permitting	Eddy Covariance–O&M	MITs (annual)
Leasing	Color Infrared Orthoimaging (CIR) monitoring	**Plugging and Abandonment (one time)**
Public Outreach	Laser System and LIDAR - O&M	Existing EOR wells
Other Permitting	Surface Leak Detection–Initial	CO_2 Injection Wells
Subpart RR Requirements	Surface Leak Detection–Annual	Stratigraphic Wells
Aerial /Satellite Survey	Cased Hole Logging (Annual)	Deep Monitoring Wells
Aerial Survey	Coring (initial)	Groundwater Monitoring Wells
Air Magnetic Survey	**Subsurface Monitoring**	Vadose Monitoring Wells
Interferometric synthetic aperture radar (InSAR)	Vadose Zone Monitoring (initial)	**Operations Monitoring**
Geophysical Surveys (Seismic)	Vadose Zone Monitoring (Annual)	Monitor Surface P, T, and Rates
Seismic Planning Q&A	Soil Flux Monitoring (initial)	Gas Composition Sampling
3-D Seismic	Soil Flux Monitoring (Annual)	Corrosion Monitoring
2-D Seismic	Groundwater Monitoring (initial)	Monitor Subsurface P, T, and Fluids
Crosswell	Groundwater Monitoring (Annual)	Tracers
Vertical Seismic Profile		**Post Injection Site Care (PISC) and Closure (One Time)**
Tiltmeters		Site Closure Report

`

The FE/NETL CO_2 Saline Storage Cost Model can address costs associated with 500 distinct activities. This study focused on the costs for more than 60 SMV activities. For many activities, the cost estimates and logic in the FE/NETL Model were used. For others, alternative estimates and logic, based primarily on ARI's experience in managing CO_2 storage demonstration projects, were recommended and used.

Recommendations for costs included preferred units, frequency, etc. for which the costs would apply, and their applicability (i.e., saline storage, CO_2-EOR conversion to CO_2 storage, and/or CO_2 storage with CO_2-EOR). For activities not unique to storage, the assumed costs in the FE/NETL model were used. These included, for example, the costs associated with surface equipment and facilities, distribution pipelines, compression, wells and associated equipment.

Certain costs potentially associated with CO_2 storage projects were not considered in this assessment. These included potential costs associated with bonding, long-term stewardship trust fund or operational oversight fund contributions, pore space rights, land use permits, water discharge permits, air emission permits, taxes, mitigation, reservoir pressure control/brine production, and any location-specific cost adjustment factors.

Financial analyses were performed over their assumed project life, including, where appropriate, the time for post-injection site care (PISC). Defaults included in the 2014 version of the FE/NETL CO_2 Saline Storage Cost Model were used for these financial parameters.

Importantly, SMV costs represent only a portion of overall storage costs, with a larger proportion of the total associated with operating wells, equipment, and surface facilities. Even when substantial existing infrastructure is usable for CO_2 storage, the costs of operating these wells, equipment, and facilities are larger than the costs associated with SMV activities. For example, for the saline storage case, from 30% to 50% of total costs are associated with non-SMV activities, depending on the scenario considered. For the case of converting from a CO_2-EOR project to a CO_2 storage project, more than 70% of the overall project costs are associated with non-SMV activities. For a project storing CO_2 in association with CO_2-EOR, however, most of the costs related to wells, equipment, and surface facilities are borne by the CO_2-EOR project, and thus are *NOT* considered incremental costs associated with CO_2 storage.

APPLICATION OF A RISK-BASED APPROACH TO FACILITATE EVOLUTION FROM FOAK TO NOAK SMV COSTS

A risk-based approach was pursued for characterizing the evolution from FOAK to NOAK SMV costs. The sequential approach to assessing potential, low probability material impact (LPMI) events consisted of: (1) quantitative project goal setting (identification of potential material impacts), (2) characterization of risks and uncertainties, and (3) a procedure that is called "assessment of low probability material impacts (ALPMI)." Following this work flow allows a design for an SMV program that is "fit-for-purpose," in that monitoring can be designed and deployed to test for the presence or absence of "low probability material impacts." This is based on a methodology outlined in Reference 7.

The approach involves engaging with stakeholders in defining thresholds of measured quantities of potential CO_2 leakage at the selected storage site. These threshold levels are modelled, establishing detection capability and potential attribution. This information is then used to develop realistic SMV strategies that can both reduce risk and be more cost effective.

The results of undertaking an ALPMI process will be different for specific types of CO_2 storage projects and settings. For example, given their different initial risk profiles, risks (and associated SMV approaches appropriate for risk evaluation, and thus associated costs) will likely be quite different for

`

CO_2-EOR versus saline aquifer settings. The process explicitly considers the primary factors contributing to potential leakage pathways for a specific setting.

A CO_2 Capture Project workshop was conducted with the objective of applying this risk-based approach to the three generalized categories of CO_2 storage settings, with the focus devoted to characterizing risk pathways for each of the three settings. The workshop participants concluded that the risks associated with CO_2-EOR projects (either conversion or storage with CO_2-EOR) are substantially smaller than for saline storage projects. Further, SMV schemes to ascertain "material impacts" can be better defined and focused for CO_2-EOR projects relative to saline aquifer projects, since greater knowledge usually exists of the characteristics of the target storage horizon.

For saline storage projects, all risk pathways are considered "important" until proven otherwise. For saline aquifers, evolution from FOAK to NOAK occurs as knowledge is gained within a storage horizon. Hence, all "early" projects in a saline storage target are likely to deploy FOAK technologies and processes.

Moreover, FOAK CO_2-EOR conversion projects probably can be characterized more like NOAK saline storage projects, as there will typically be substantial historical knowledge and experience gained with the previous CO_2-EOR project. FOAK to NOAK evolves over time as greater knowledge is obtained, storage performance matures, and experience is gained. Along with importance, risks for all settings also have temporal components within the life-cycle of a project.

NOAK and FOAK characterizations and associated costs were developed based on these insights. The application of and results from this approach for the three storage settings considered are discussed in the following sections.

CO_2 STORAGE PROJECT IN A SALINE AQUIFER IN THE U.S. GULF COAST

Regarding CO_2 storage projects in deep saline aquifers, the workshop concluded that initial data acquisition, planning, and permitting activities for the first/early project(s) can inform and be utilized for advantage in later/nth project(s), thus reducing costs in the future. Based on potential risks, some monitoring activities were determined as more likely to yield minimal benefits; these include, for example, eddy covariance monitoring, vadose zone monitoring, and soil flux monitoring. Moreover, it was determined that multiple, redundant monitoring approaches, such as those utilizing seismic techniques, should be able to be reduced to a core set. As knowledge and experience is gained, participants concluded that frequency and/or density of monitoring technologies/approaches can also be reduced. This could include 3-D seismic, vertical seismic profiling (VSP), logging, and mechanical integrity testing (MITs). Over time and with experience, it was believed that the process for developing monitoring, reporting, and verification (MRV) plans and submitting annual reports under Subpart RR of the GHGRP should also become more routine and efficient.

Based on these conclusions, the following four scenarios were defined for CO_2 storage projects in deep saline aquifers:

- A FOAK case, for "first" or "early" projects in a target storage formation (play) assumes an extensive set of SMV activities, defined as an "All in Case."
- A NOAK case, based on a later/nth project in the target storage formation/play, assumes insights and experience gained that allows a move from FOAK to NOAK over time.
- For both FOAK and NOAK cases, initial concerns and associated monitoring requirements can evolve over time as experience and knowledge is gained *at a specific site*.

This results in several theoretical cases. The first set of SMV strategies applies to cases where operators are learning with experience *within a play*. Also, in theory, learning can occur over time

even within an individual project, as more is learned about the site-specific geologic and operational setting. Here, both FOAK/early storage project(s) and NOAK storage project(s), costs are reduced over time as knowledge and experience is gained at the project site. However, while this case was conceptualized, it was not explicitly evaluated due to limitations with the FE/NETL CO_2 Saline Storage Cost Model.

The SMV activities assumed in these cases are illustrated in Table 4, where **red** indicates activities not included in the scenario/case, **green** indicates those included in the scenario/case, and **blue/NA** represents only an initial activity that does not continue over the course of the project.

Only the cases corresponding to the first two columns of Table 4 were evaluated for the onshore Gulf Coast saline aquifer storage project, for two levels of assumed per-well injectivity. These are summarized in Table 5. As shown, depending on injection rate, overall storage costs can be reduced by an estimated 37% to 49%. For a per-well injectivity of 500 tonnes per day per well, estimated costs drop from $9.03 per tonne for the FOAK case to $5.60 per tonne for the NOAK case. For a per-well injectivity of 2,000 tonnes per day per well, storage costs drop from $6.71 per tonne for the FOAK case to $3.39 per tonne for the NOAK case.

CONVERTING CO_2-EOR TO A CO_2 STORAGE PROJECT

For this assessment of conversion of a CO_2 EOR project to a CO_2 storage project, it was assumed that a thorough and accurate assessment of risks would allow the "grandfathering" of existing Class II wells for CO_2 storage for both the NOAK and FOAK cases, and that new wells constructed to Class VI standards would not be necessary. Moreover, as for the saline storage case, several monitoring activities are assumed to yield minimal benefits based on anticipated risks and would therefore not be necessary (e.g., eddy covariance, vadose zone, and soil flux). Also, multiple redundant monitoring approaches, such as some utilizing seismic techniques, can be reduced to a core set. As knowledge and experience is gained, frequency and/or density of some monitoring technologies and approaches can be reduced, and the process for developing MRV plans and submitting annual reports becomes more routine and efficient, with reduced costs. Finally, it was assumed that some "blowdown" of the CO_2-EOR project would be undertaken to allow for higher per-well injection rates than would take place during CO_2-EOR operations.

Unlike in storage projects in saline aquifers, experience and knowledge should have already been gained, and potential risks would already be well characterized, for a CO_2-EOR project that has operated for several years. However, issues associated with operations in a higher-pressure regime may be an exception. For this case, the costs associated with initial site characterization should be reduced, though some characterizations unique to CO_2 storage would need to be conducted. The greater existing well density, compared to a saline aquifer storage project, should allow both better reservoir characterization and multiple points for reservoir monitoring.

However, for an existing project, legacy wells could be a concern, since their potential for leakage, and their ability to withstand corrosion when exposed to CO_2 and water under conditions different than for CO_2-EOR would need to be assessed and considered.

Based on this characterization, three cases were considered:

- A FOAK case that assumes an extensive set of SMV activities; defined as an "All in Case."
- A "risk-based FOAK case" that applies a risk-based approach for SMV program planning.
- A "risk-based NOAK case" that applies a risk-based approach for SMV program planning, but also assumes cost reductions will occur as knowledge and experience is gained over time.

Table 4(a). SMV Cost Elements Considered in the Saline Storage Cases.

Cost Element	FOAK "All in" Case-1st in Play	NOAK-"All in" Case-nth in Play	FOAK-1st in Play later in life-cycle	NOAK-nth in Play later in life-cycle
Data Acquisition, Planning, and Permitting				
Regional Evaluation			Not Applicable	Not Applicable
Initial Site Characterization		No initial data costs	Not Applicable	Not Applicable
Data Preparation & Analysis		1/2 of "1st in Play"	Not Applicable	Not Applicable
Initial & Periodic Modeling		1/3 of "1st in Play"		1/3 of "1st in Play"
Corrective Action Planning		1/2 of "1st in Play"	Not Applicable	Not Applicable
FEED			Not Applicable	Not Applicable
Class VI Permitting		1/2 of "1st in Play"	Not Applicable	Not Applicable
Leasing			Not Applicable	Not Applicable
Public Outreach				
Other Permitting			Not Applicable	Not Applicable
Subpart RR Requirements		3/4 of "1st in Play"	3/4 of "early in LC"	3/4 of "1st in Play"
Aerial/Satellite Survey				
Aerial Survey				
Air Magnetic Survey				
SAR & InSAR				
Geophysical Surveys (Seismic)				
Seismic Planning Q&A				
3-D Seismic				
2-D Seismic				
Crosswell			1/2 freq of early in LC	1/2 freq of early in LC
Vertical Seismic Profile			1/2 freq of early in LC	
Tiltmeters				

Table 4(b). SMV Cost Elements Considered in the Saline Storage Cases.

Cost Element	FOAK-"All in" Case-1st in Play	NOAK-"All in" Case-1st in Play	FOAK-1st in Play later in life-cycle	NOAK-nth in Play later in life-cycle
Electrical/Other				
Electrical Resistivity Tomography				
Gravity Survey				
Micro-seismic (Initial)				
Micro-seismic (Annual O&M)				
Atmospheric Surveys				
Eddy Covariance–Initial				
Eddy Covariance - O&M				
CIR				
Laser System & LIDAR-O&M				
Surface Leak Detection-Initial				
Surface Leak Detection-Annual				
Cased Hole Logging-Annual			1/2 freq of early in LC	1/2 freq of early in LC
Coring–Initial			Not Applicable	Not Applicable
Subsurface Monitoring				
Vadose Zone Monitoring–Initial				
Vadose Zone Monitoring–Annual				
Soil Flux Monitoring–Initial				
Soil Flux Monitoring–Annual				
Groundwater Monitoring–Initial				
Groundwater Monitoring–Annual				

Table 4(c). SMV Cost Elements Considered in the Saline Storage Cases.

Cost Element	FOAK-"All in" Case-1st in Play	NOAK-"All in" Case-1st in Play	FOAK-1st in Play later in life-cycle	NOAK-nth in Play later in life-cycle
Well Costs (one time, except MITs)				
New Class VI Injection Wells			Not Applicable	Not Applicable
New Deep Monitoring Wells			Not Applicable	Not Applicable
New Stratigraphic Wells			Not Applicable	Not Applicable
EOR Wells Convert to Monitor Wells				
EOR Wells Convert to Injection				
Well Testing			Not Applicable	Not Applicable
MITs (annual)			5-yr MIT sched.	5-yr MIT sched.
Plugging and Abandonment (one time)				
Existing EOR Wells				
CO_2 Injection Wells			Not Applicable	Not Applicable
Stratigraphic Wells			Not Applicable	Not Applicable
Deep Monitoring Wells			Not Applicable	Not Applicable
Groundwater Monitoring Wells			Not Applicable	Not Applicable
Vadose Monitoring Wells			Not Applicable	Not Applicable
Operations Monitoring				
Monitor Surface P, T, and Rates				
Gas Composition Sampling				
Corrosion Monitoring				
Monitor Subsurface P, T, and Fluids				
Tracers				
PISC and Closure (One Time)				
Site Closure Report			Not Applicable	Not Applicable

Table 5. Comparison of Estimated FOAK and NOAK Costs for the Onshore Gulf Coast Saline Storage Project for Two Assumed Levels of Well Injectivity.

Cases	Total Life-Cycle Costs ($/tonne)	Difference from 500 t/d/well FOAK case ($/t)	% Change
"All In", 500 tonnes/day/well (FOAK)	$9.03		
"All In", 2000 tonnes/day/well (FOAK)	$6.71	($2.32)	-26%
Saline NOAK, 500 tonnes/day/well	$5.69	($3.34)	-37%
Saline NOAK, 2000 tonnes/day/well	$3.39	($5.64)	-62%

The SMV activities assumed in these cases for conversion of a CO_2-EOR project to a CO_2 storage project are illustrated in Table 6, where **red** indicates activities not included in the scenario/case, and **green** indicates those included in the scenario/case. The results associated with the assessment of these cases are summarized in Table 7. As shown, for a per-well injectivity of 50 tonnes per day per well, estimated costs drop from $12.66 per tonne for the FOAK case to $11.50 per tonne for the NOAK case. For a per-well injectivity of 200 tonnes per day per well, costs drop from $5.15 per tonne for the FOAK case to $3.99 per tonne for the NOAK case.

Table 6(a). SMV Cost Elements Considered in the CO_2-EOR Conversion to a CO_2 Storage Project Case.

Cost Element	"All in" Case	Risk-Based FOAK	Risk-Based NOAK
Data Acquisition, Planning, and Permitting			
Regional Evaluation			
Initial Site Characterization			
Data Preparation & Analysis			
Initial & Periodic Modeling			1/3 of FOAK
Corrective Action Planning			1/2 of FOAK
FEED			
Class VI Permitting	Class II wells not grandfathered		
Leasing			
Public Outreach			
Other Permitting			
Subpart RR Requirements			3/4 of FOAK initially
Aerial/Satellite Survey			
Aerial Survey			
Air Magnetic Survey			
SAR & InSAR			
Geophysical Surveys (Seismic)			
Seismic Planning Q&A			
3-D Seismic			
2-D Seismic			
Crosswell			
Vertica Seismic Profile			
Tiltmeters			

Table 6(b). SMV Cost Elements Considered in the CO_2-EOR Conversion to a CO_2 Storage Project Case.

Cost Element	"All in" Case	Risk-Based FOAK	Risk-Based NOAK
Electrical/Other			
Electrical Resistivity Tomography			
Gravity Survey			
Micro-seismic (Initial)			1/2 of FOAK
Micro-seismic (Annual O&M)			1/2 of FOAK
Atmospheric Surveys			
Eddy Covariance–Initial			
Eddy Covariance–O&M			
CIR			
Laser System & LIDAR-O&M			
Surface Leak Detection–Initial			
Surface Leak Detection–Annual			
Cased Hole Logging–Annual			
Coring–Initial			
Subsurface Monitoring			
Vadose Zone Monitoring–Initial			
Vadose Zone Monitoring–Annual			
Soil Flux Monitoring–Initial			
Soil Flux Monitoring–Annual			
Groundwater Monitoring–Initial			
Groundwater Monitoring–Annual			

Table 6(c). SMV Cost Elements Considered in the CO_2-EOR Conversion to a CO_2 Storage Project Case.

Cost Element	"All in" Case	Risk-Based FOAK	Risk-Based NOAK
Well Costs (one time, except MITs)			
New Class VI Injection Wells	Class II wells not grandfathered		
New Deep Monitoring Wells			
New Stratigraphic Wells			
EOR Wells Convert to Monitor Wells			
EOR Wells Convert to Injection			
Well Testing			
MITs (annual)	1-yr MIT sched.	5-yr MIT sched.	5-yr MIT sched.
Plugging and Abandonment (one time)			
Existing EOR Wells			
CO_2 Injection Wells			
Stratigraphic Wells			
Deep Monitoring Wells			
Groundwater Monitoring Wells			
Vadose Monitoring Wells			
Operations Monitoring			
Monitor Surface P, T, and Rates			
Gas Composition Sampling			
Corrosion Monitoring			
Monitor Subsurface P, T, and Fluids			
Tracers			
PISC and Closure (One Time)			
Site Closure Report			

Table 7. Comparison of FOAK and NOAK Life-Cycle Costs for the CO_2-EOR Project Converted to Storage Case, for the Permian Basin, for Two Assumed Levels of Well Injectivity.

	Total Cost ($/t)
"All In" Case	
50 tonnes/day/well	$25.71
200 tonnes/day/well	$8.98
FOAK Case	
50 tonnes/day/well	$12.66
200 tonnes/day/well	$5.15
NOAK Case	
50 tonnes/day/well	$11.50
200 tonnes/day/well	$3.99

CO_2 STORAGE IN ASSOCIATION WITH CO_2-EOR

The assumptions for the case of CO_2 storage in association with onshore CO_2-EOR are analogous to those associated with the conversion of a CO_2-EOR project to a CO_2 storage, with a few exceptions. Specifically, monitoring activities already associated with CO_2-EOR can also be utilized for the monitoring of storage. Thus, the incremental costs of monitoring can be minimal, especially for a sophisticated, well-monitored existing CO_2-EOR operation. Special concerns associated with elevated operating pressures do not exist for CO_2 storage in association with CO_2-EOR operations, though existing legacy wells remain a concern.

Taking account for these considerations results in three cases:

- A FOAK case that assumes an extensive set of SMV activities; defined as an "All in Case."
- A "risk-based FOAK case" that applies a risk-based approach for SMV program planning.
- A "risk-based NOAK case" that applies a risk-based approach for SMV program planning, but also assumes cost reductions will occur as knowledge and experience is gained over time.
- An "In-Between" Case, that assumes costs associated with a scenario are in between the "All in Case" and the "risk-based" NOAK case.
- A "Minimal Additions" case, which assumes incremental costs over and above what would already be taking place in a sophisticated, well-monitored existing CO_2-EOR operation. This represents a case comparable to recently approved MRV plans submitted to the USEPA GHGRP.

The SMV activities assumed in these cases are illustrated in Table 8, where **blue** corresponds to activities that are already part of EOR operations (and so have no incremental cost for storage), **red** indicates activities not included in the scenario/case, and **green** indicates those included in the scenario/case.

Table 8(a). SMV Cost Elements Considered in the CO_2 Storage in Association with CO_2-EOR Project Case.

Cost Element	"All in" Case	Risk-Based FOAK	Risk-Based NOAK
Data Acquisition, Planning, and Permitting			
Regional Evaluation			
Initial Site Characterization			
Data Preparation & Analysis			
Initial & Periodic Modeling		1/3 of "All in"	1/3 of FOAK
Corrective Action Planning			1/2 of FOAK
FEED			
Class VI Permitting	Class II wells allowed	Class II wells allowed	Class II wells allowed
Leasing			
Public Outreach			
Other Permitting			
Subpart RR Requirements			3/4 of FOAK initially
Aerial/Satellite Survey			
Aerial Survey			
Air Magnetic Survey			
SAR & InSAR			
Geophysical Surveys (Seismic)			
Seismic Planning Q&A			
3-D Seismic			
2-D Seismic			
Crosswell			
Vertica Seismic Profile			
Tiltmeters			

Table 8(b). SMV Cost Elements Considered in the CO_2 Storage in Association with CO_2-EOR Project Case.

Cost Element	"All in" Case	Risk-Based FOAK	Risk-Based NOAK
Electrical/Other			
Electrical Resistivity Tomography			
Gravity Survey			
Micro-seismic (Initial)			1/2 of FOAK
Micro-seismic (Annual O&M)			1/2 of FOAK
Atmospheric Surveys			
Eddy Covariance–Initial			
Eddy Covariance–O&M			
CIR			
Laser System & LIDAR–O&M			
Surface Leak Detection-Initial			
Surface Leak Detection–Annual			
Cased Hole Logging–Annual			
Coring–Initial			
Subsurface Monitoring			
Vadose Zone Monitoring–Initial			
Vadose Zone Monitoring–Annual			
Soil Flux Monitoring–Initial			
Soil Flux Monitoring–Annual			
Groundwater Monitoring–Initial			1/2 of FOAK
Groundwater Monitoring–Annual			1/2 of FOAK

Table 8(c). SMV Cost Elements Considered in the CO_2 Storage in Association with CO_2-EOR Project Case.

Cost Element	"All in" Case	Risk-Based FOAK	Risk-Based NOAK
Well Costs (one time, except MITs)			
New Class VI Injection Wells			
New Deep Monitoring Wells			
New Stratigraphic Wells			
EOR Wells Convert to Monitor Wells			
EOR Wells Convert to Injection			
Well Testing			
MITs (annual)	1-yr MIT sched.	5-yr MIT sched.	5-yr MIT sched.
Plugging and Abandonment (one time)			
Existing EOR Wells			
CO_2 Injection Wells			
Stratigraphic Wells			
Deep Monitoring Wells			
Groundwater Monitoring Wells			
Vadose Monitoring Wells			
Operations Monitoring			
Monitor Surface P, T, and Rates			
Gas Composition Sampling			
Corrosion Monitoring			
Monitor Subsurface P, T, and Fluids			
Tracers			
PISC and Closure (One Time)			
Site Closure Report			1/2 of FOAK

`

Table 9. Comparison of Estimated FOAK and NOAK Life-Cycle Costs for CO_2 Storage in Association with an Onshore CO_2-EOR Project, for Four Regions.

	Permian Basin		Gulf Coast		Mid-Continent		Rocky Mountains	
Stored/Total Injected CO_2	0.44		0.62		0.55		0.47	
	$/tonne injected	**$/tonne stored**	**$/tonne injected**	**$/tonne stored**	**$/tonne injected**	**$/tonne stored**	**$/tonne injected**	**$/tonne stored**
Storage with EOR Cases								
"All in" Case	$7.54	$16.98	$3.21	$5.19	$11.30	$20.63	$5.66	$12.15
Risk-Based FOAK	$2.90	$6.53	$1.00	$1.62	$4.45	$8.12	$2.03	$4.36
Risk-Based NOAK	$2.77	$6.24	$0.90	$1.46	$4.03	$7.36	$1.85	$3.97
"In-Between Case"	$4.25	$9.57	$1.39	$2.25	$5.70	$10.41	$2.63	$5.65
"Minimal Additions Case"	$0.99	$2.23	$0.29	$0.47	$1.28	$2.34	$0.63	$1.35

Overall life-cycle project costs are shown in Table 9 for the CO_2 storage in association with CO_2-EOR case. The impact is shown for each of the scenarios, for all four regions. As shown, only monitoring scenarios comparable to the "Risk-Based NOAK" and "Minimal Additions Case" would likely be commercially viable for storage in association with CO_2-EOR.

CONCLUSIONS

The paper concludes that in general, although costs are highly variable, overall life-cycle CO_2 storage costs can be roughly ranked as follows by project type (Figure 1):

- Storage in association with CO_2-EOR is the lowest cost.
- Conversion of CO_2-EOR may be the most expensive.
- CO_2 storage in relatively high permeability deep saline aquifers generally falls in between.

This is shown graphically on an apples-to-apples basis for the "All-In" Cases in Figure 1, for the different assumptions of per-well injectivity considered.

Figure 1. Estimated Overall Project Costs for "All In" Cases for the Three Types of CO_2 Storage Projects.

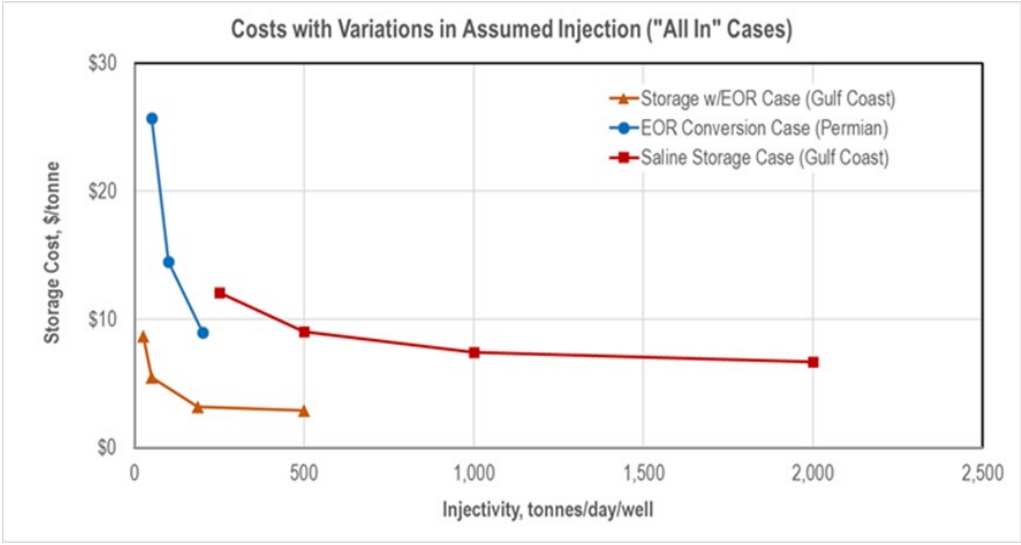

It is important to note that the results will likely be very different for specific types of CO_2 storage projects and settings.

This study also concludes that risk-based approaches for SMV strategies can have a substantial impact on life-cycle storage costs. For example:

- For saline storage case, costs can be reduced as much as 37% to 49%, depending on injection rate per well.
- For EOR conversion case, costs can be reduced from 43% to 56%, depending on injection rate.
- For storage with EOR case, costs can be reduced from 61% to 91%, depending on regional setting, and monitoring scenario considered.

The study shows that the application of risk-based approaches may be how SMV strategies evolve from FOAK to NOAK, and that the outcomes of risk-based analyses appear to align with historical expectations for more cost-effective SMV strategies.

REFERENCES

1. http://www.netl.doe.gov/research/energy-analysis/analytical-tools-and-data/co2-saline-storage
2. https://www.epa.gov/uic/class-vi-wells-used-geologic-sequestration-co2
3. https://www.epa.gov/uic/class-ii-oil-and-gas-related-injection-wells
4. https://www.epa.gov/ghgreporting
5. https://www.epa.gov/ghgreporting/subpart-uu-injection-carbon-dioxide
6. https://www.epa.gov/ghgreporting/subpart-rr-geologic-sequestration-carbon-dioxide
7. Hovorka, Susan, "Optimizing Deep Subsurface Monitoring Methods: Principles," Presented to California ARB Carbon Capture and Sequestration Technical Discussion Series: Monitoring, August 5, 2016 (https://www.arb.ca.gov/cc/ccs/meetings/Univ_of_Texas_Austin_Hovorka_Presentation_8-5-16.pdf)

Carbon Dioxide Capture for Storage in Deep Geological Formations, Volume 5
Karl F. Gerdes (Editor)
© 2022 BP. All rights reserved.

Chapter 28

CS-A EXPERIMENT–WELL LEAKAGE AND REMEDIATION EXPERIMENT

Ursula Rösli[1], Jocelyn Gisiger[1], Christian Minnig[2], and Harvey Goodman[3,4]
[1]Solexperts AG, Mettlenbachstrasse 25, 8617 Mönchaltorf, Switzerland
[2]SWISSTOPO, Seftigenstrasse 264, 3048 Wabern, Switzerland
[3]Chevron Emeritus Fellow, Houston TX, USA
[4]Los Alamos National Laboratory, Los Alamos, NM 87545, USA

ABSTRACT: The Mont Terri "Well-Sealing" experiment was designed to characterize the efficacy of novel sealants in a scale well with induced defects. Four sealants were injected to assess capability to restore pressure containment in the cased and cemented interval after exposure to repetitive heating-cooling cycles. The sealants were: (1) a nanoparticle hydrogel sealant, (2) a polymer gel, (3) a silicate-based sealant, and (4) an epoxy-based sealant.

The test data obtained over the 5-year course of investigation consists of 3 types of information: 1) an extensive hydraulic data set with detailed hydrogeological analytics, 2) an extensive post-injection core examination program consisting of high-resolution CT, geochemical and geomechanical analytics, and 3) numerical modelling trained to experimental test site conditions intended to relate the hydraulic and core-based data sets over the entire cased hole injection interval.

This chapter summarizes the test well design, installation, sealant testing program and hydraulic based sealant performance outcomes. The following Chapter 29 summarizes the complete post sealant program performance outcome based on the complete analytical assessment program employed.

KEYWORDS: CO_2 geological storage; containment assurance; CO_2 breach mitigation; underground rock laboratory

INTRODUCTION

Aim of Experimental Program and Site Location

The aim of the CS-A experiment (carbon storage program) is to develop long-term sealant solutions to damaged well systems used for CO_2 injection. The focus is on potential leakage pathways associated with micro-annuli along casing-cement interfaces and fractures that develop within the cement sheath and country rock (Figure 1). The experimental test well site was designed to provide sufficient quantitative data under simulated CO_2 injection well conditions to enable up-scaling to deep field storage site operations. The work was performed under the auspices of an international energy company partnership of researchers composed of BP (UK), Chevron (US), Petrobras (BR) and TOTAL (FR).

The principal research facility that made this project possible is the Mont Terri Underground Research Laboratory (MT-URL) located in NW Switzerland near the village of St Ursanne shown in Figure 2. SWISSTOPO (Swiss Office of Topography) manages MT-URL logistics that includes on-site principal investigator (PI) support. The laboratory provides the experimentalist an intermediate scale

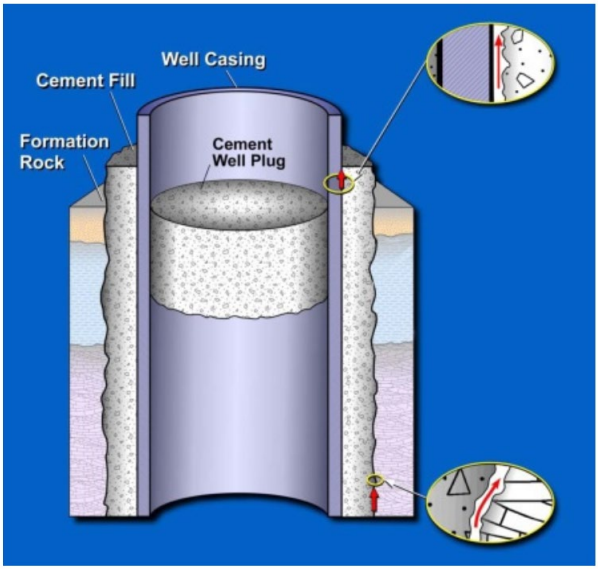

Figure 1. Well system leakage mechanisms at casing/cement and cement/rock formation boundaries. Modified after Bourgoyne [1, 2, 3].

test site at a depth of 300 m that can bridge the gap between the laboratory bench and full field conditions (e.g., 2400 m depth injection sites).

Test Well Design Concept

According to the special report on CO_2 storage submitted to the IPCC [2], active injection wells, along with inactive wells that have been abandoned, are the most probable sources of leakage pathways for CO_2 escape to the surface. The origin of the pressure-driven leakage common to injection well architecture and field operations described by Bourgoyne [1] were used to guide the design and experimental protocols for the CS-A program.

The experimental plan included:

- Creation of flow paths in the cemented annulus along a casing by cyclic heating/cooling
- Characterization of these micro-annular interfaces
- Injection of 4 novel sealants
- Estimation of the long-term sealing performance

The preparation for the project began in 2013 with the design of the downhole and surface instrumentation. In 2015, the on-site work started with borehole drilling and the installation of the equipment.

A summary of the first steps leading to the creation of the micro-annuli and their characterization prior to sealant injection was published at GHGT13 by Goodman *et al.* [3]. The following sections give an overview of the sealant injection program and sealant performance results from the hydraulic testing program and prior to the overcoring program. Concluding remarks address operational difficulties encountered during site installation and questions raised which should be addressed in future experiments.

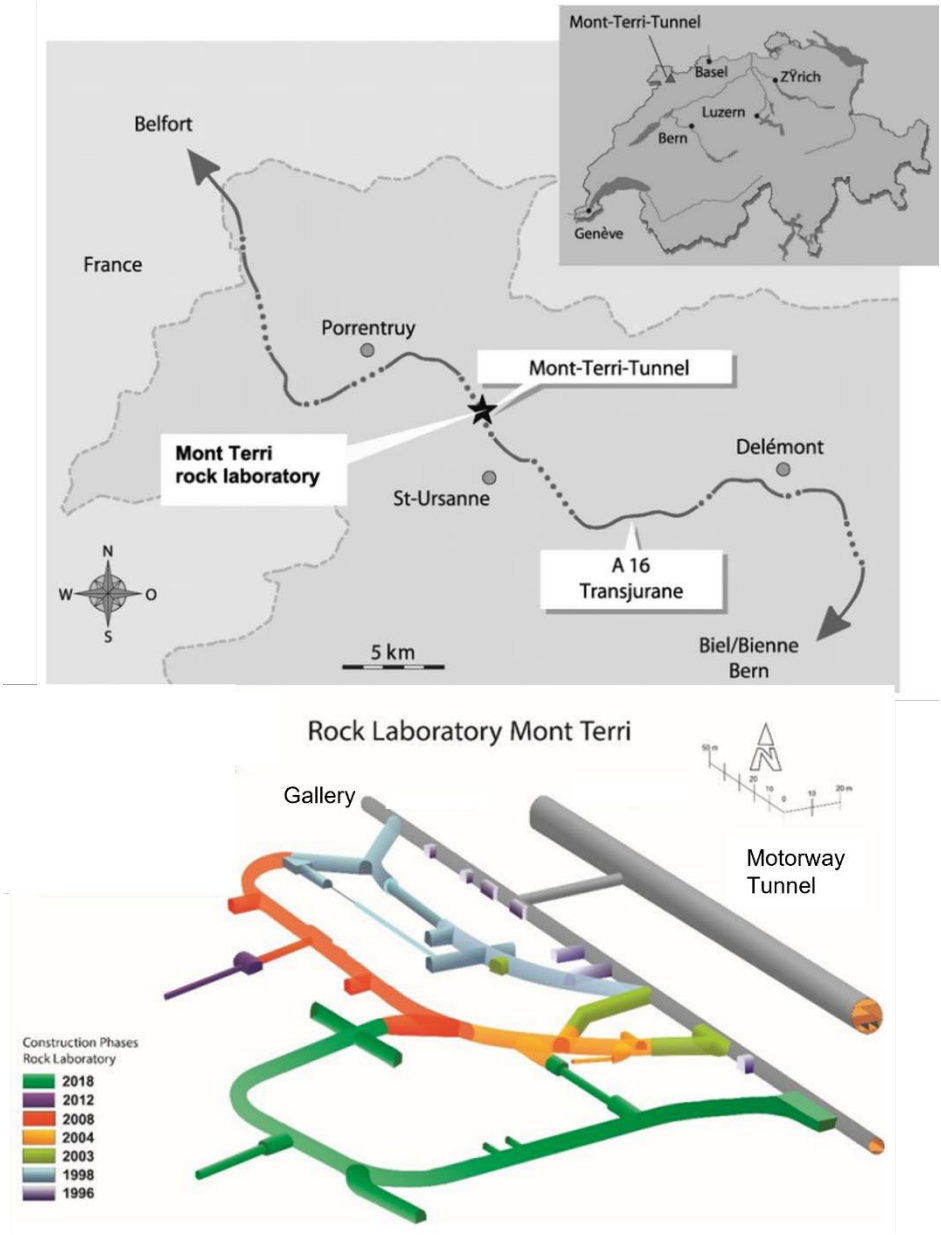

Figure 2. Mont Terri Underground Research Laboratory location.

OVERVIEW OF PROJECT PHASE ACTIVITIES

Test Well Architecture

The experimental borehole BCS-A layout consists of a 400 mm diameter pilot borehole to a depth of 4.26 m in the upper part and a borehole of 200 mm diameter drilled to the final depth of approx. 14.40 m. The layout of the borehole and accompanying interval volumes are shown in Figure 3. Pressure compartments are comprised of Intervals 1-8. Interval 1 is the lower open hole injection interval, while Intervals 2-7 comprise the cased and cemented intervals with injection-extraction ports (I/P modules) and Interval 8 is the uppermost open hole observation section. A total of 30 stainless steel flow lines connect the I/P intervals with the injection pump located topside within the gallery. Three cables for the temperature sensors are routed through the inner part of the casing to the gallery.

The borehole packer system consists of a top packer with a length of 2.5 m. Two grout packers are present, isolating the top interval 8 and the bottom interval 1 during cement injection. The section between both grout packers consists of a 6.0 m long casing section with the six I/P modules for injection/extraction and pressure measurements.

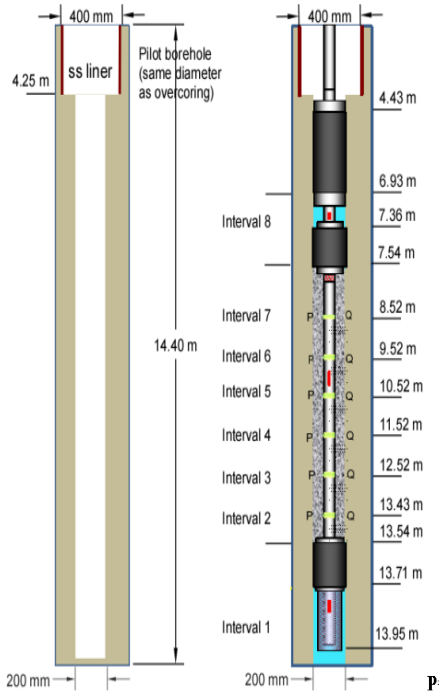

Section	From [m]	To [m]	Length [m]	Volume [L]*	Comments
Interval 1	13.54	14.40	0.86	18.514	Temperature sensor
(Grout packer 1)	13.54	13.71	0.18	-	Deflated after cement injection
Interval 2	13.43	-	-	0.152	I/P module 1
Interval 3	12.52	-	-	0.169	I/P module 2
Interval 4	11.52	-	-	0.180	I/P module 3
Interval 5	10.52	-	-	0.236	I/P module 4
					Temperature sensor
Interval 6	9.52	-	-	0.161	I/P module 5
Interval 7	8.52	-	-	0.293	I/P module 6
(Grout packer 2)	7.36	7.54	0.18	-	Deflated after cement injection
Interval 8	6.93	7.54	0.61	13.256	Temperature sensor
Packer	4.43	6.93	2.50	-	

P=Pressure, Q= flow

Figure 3. Setup of borehole after drilling (left), with instrumentation (center) and interval locations and volumes right).

Project Phase Activity

Referring to Table 1, the experimental site work started April 2015 with the drilling of borehole BCS-A1 to a depth of 14.45 m and the installation of the 3-fold packer system with a customized test section consisting of 6 access injection/extraction ports and lower and upper observation intervals. The

annulus between the upper and lower observation intervals was then cemented. After saturation of the intervals using water made compatible to the Opalinus Clay host rock chemistry, a test campaign was performed to define the initial hydraulic connectivity condition along the borehole completion before temperature cycling (task No 3).

The test well was conditioned by circulating hot water inside the casing. The design temperature increase threshold of 60°C above ambient was not achieved until the 3rd heating cycle (task No 7). The temperature was increased to a maximum 78.4°C (about 65°C increase above ambient), after which sufficient hydraulic connectivity between borehole test intervals was achieved for sealant testing. Flow connectivity between intervals was measured via diploe flow injection/extraction (task No. 9).

The preparation of the sealant injection in the appropriate dipoles included dead volume tests, tracer testing, water sampling and flushing of the dipoles (tasks No. 11, 12, 14).

Four different sealants were injected in six different intervals. Sealant 1 is a nanoparticle hydrogel sealant developed by Los Alamos National Laboratories (LANL). Sealant 2 is a polymer gel developed by University of Texas (UT), Sealant 3 is a silicate-based sealant developed by IFP Energies Nouvelles (IFPEN) and Sealant 4 is an epoxy-based sealant developed by University of New Mexico (UNM). Sealant injections were carried out over a two-year period (tasks No. 15, 16, 17, 18). Sealant performance was regularly tested after each sealant injection. The hydraulic parameters after completion of the sealant injections were determined during a final hydraulic test campaign (task No 19).

In preparation for overcoring to extract the test well along with immediately adjacent rock, the intervals were filled with resin sealant. Overcoring and associated analyses of sealant performance work concluded in 2022 and is reported in Chapter 29.

EXPERIMENTAL EQUIPMENT FABRICATION & INSTALLATION DETAIL

Phase 0-1:

Borehole Instrumentation

Referring to Figure 3 and Table 1, the borehole was instrumented with a customized triple packer system and a cased and cemented 6 m test length section. Six intervals within the cased and cemented section can be independently injected and/or fluid extracted from via access ports spaced one meter apart. These injection flow / pressure lines are termed I/P modules. Figure 4a shows various flow-stream lines between I/P modules and Figure 4b shows one of the six perforated stainless flow access rings.

Three temperature sensors are included to measure the borehole temperature during heating. A total of 30 lines and three cables for the temperature sensors are routed through the inner part of the casing to the gallery. The main parts of the borehole completion are described in references [3] and [4] and in the following sub-sections.

Table 1. Overview of CS-A project phases and associated activities.

Date	Phase	No.	Activity
13.04.2015 – 21.04.2015	Drilling	0	Ø 400 mm down to 4.25 m, Ø 203 mm to 14.40 m
22.04.2015 – 23.04.2015	Installation	1	Installation of borehole completion and grouting of annulus
06.05.2015 – 29.07.2015	Saturation	2	Saturation of all intervals at pressures up to 6 bar
26.08.2015 – 07.12.2015	Hydraulic testing 1	3	Initial hydraulic testing
17.12.2015 – 31.12.2015	Heating cycle 1	4	Heating to max. 31.6°C
12.01.2016 – 15.01.2016	Heating cycle 2	5	Heating to max. 37.7°C
19.01.2016 – 01.03.2016	Hydraulic testing 2	6	Hydraulic testing
06.04.2016 – 11.05.2016	Heating cycle 3	7	Heating to max. 78.4°C
18.05.2016 – 24.05.2016	Hydraulic testing 3	8	Hydraulic testing
07.06.2016 – 29.09.2016	Dipole testing	9	
05.10.2016 – 06.10.2016	Dead volume tests	10	
07.10.2016 – 07.02.2017	Tracer testing	11	
18.01.2017 – 03.02.2017	Water sampling	12	
13.07.2017 – 14.09.2017	Mg-Anode	13	Installation in observation borehole to delay expected casing corrosion
11.09.2017 – 14.09.2017	Flushing	14	
21.09.017 – 21.11.2017	Sealant 1 - nanoparticle hydrogel	15	Interval 6 & 7 injection sites. Interval 7 corrosion from reduced cement coverage at top of cased hole interval. Large voids expected.
15.02.2018 – 27.08.2018	Sealant 2 - polymer gel	16	Interval 5 injection site
18.03.2019 – 30.08.2019	Sealant 3 – silicate based sealant	17	Interval 4 injection site
21.08.2019 – 23.09.2019	Sealant 4 – epoxy-based sealant	18	Interval 3 & 2 injection site
26.08.2019 – 16.10.2019	Hydraulic testing 4	19	Final hydraulic testing
16.10.2019 – 17.10.2019	Final resin injection	20	Site stabilization for overcoring
	Overcoring	21	

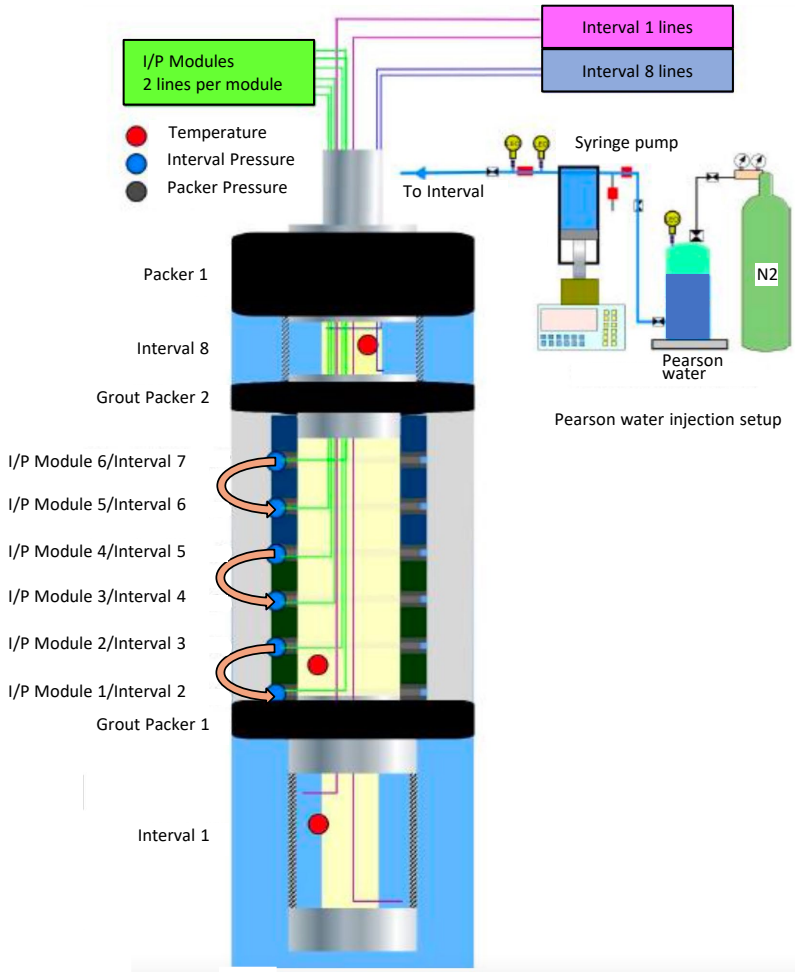

Figure 4a. Well equipment design with flow directions.

Figure 4b. I/P module detail. One of the six I/P module access ports controlling dipole flow every meter starting at 8.7 m below the underground site floor. Note the I/P modules surround the cased section, i.e., the schematic cutaway side view for inside casing view of flow lines and heating elements.

Interval 1 (13.54 m–14.40 m)

The 0.86 m long bottom interval is equipped with a 0.24 m long and 0.19 m diameter stainless steel tube with a slotted filter section (Figure 5) and two lines – one 4 mm flow line for injection or withdrawal and one 2.4 mm pressure line with the port at the lower end of the tube. Above the slotted tube section, a 0.18 m long hydro-mechanical packer made of natural rubber is mounted on the casing, which is inflated before cement is injected into the annulus between the upper and lower grout packers to prevent the cement flowing into interval 1. In addition, a temperature sensor measures the temperature during heating.

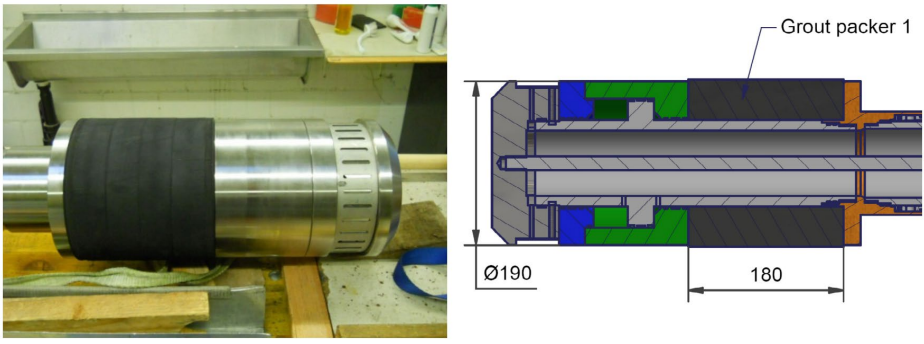

Figure 5. Detail of the injection interval (Interval 1) and grout packer 1.

Cemented borehole section with I/P modules (7.54 m–13.54 m)

The cemented borehole section has a casing with an outer diameter of 120 mm and an inner diameter of 100 mm. The annulus between the borehole wall and the casing is 40 mm thick. The lower 3 m section of casing is made of stainless steel; the upper 3.0 m section is made of carbon steel. The stainless steel casing was used because of the greater thermal expansion coefficient compared to the more basic carbon steel used in field operations. There was some uncertainty that thermal cycling

would not cause enough contraction after cooling to produce the desired microannuli at the casing–cement boundary. Integrated in the casing are six I/P modules, which are numbered from bottom to top as interval 1 to interval 7. During installation and cement injection, the I/P module access ports were closed until the cement hardened, then individually opened by a hydraulic actuator. Now each I/P module provides a narrow cavity access to the cement–casing interface that enables injection/extraction and pressure measurement (Figure 6). A temperature sensor is installed between interval 5 and interval 6.

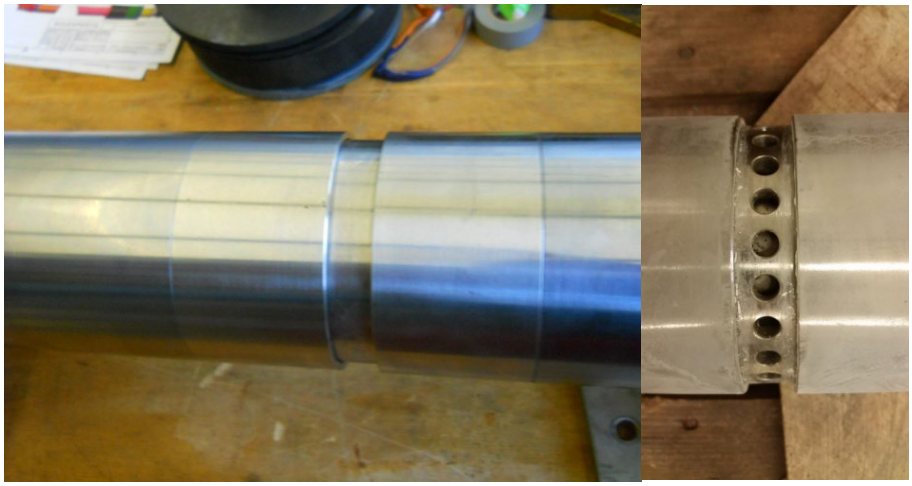

Figure 6. I/P module in closed position to enable cement circulation (left) and after opening after cement set (right).

Additional lines inside the casing include two lines for grouting – a 12 mm injection line at the top of the lower grout packer and a 10 mm overflow line at the bottom of the upper grout packer. Furthermore, a stainless steel loop (6-1/4 mm) for hot water circulation during heating runs the length of the casing to the lower grout packer. In addition, there is a hot water injection line in interval 1 and a return line in interval 8.

Below the port of the grout overflow line, a central pull rod was implemented in the casing to retrieve the completion parts above the cemented borehole section before overcoring (Figure 7).

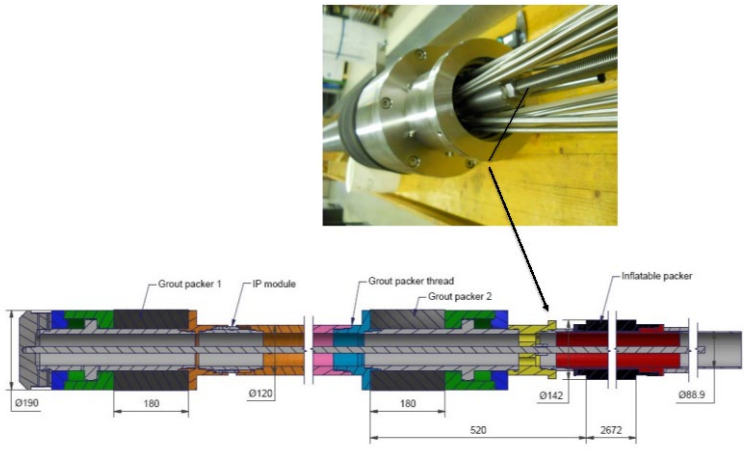

Figure 7. Threaded central pull rod.

Interval 8 (6.93 m–7.54 m)

The 0.61 m long top interval is equipped with two lines – one 4 mm flow line for injection or withdrawal and one 2.4 mm pressure line. At the lower end of the interval, a 0.18 m long hydro-mechanical packer made of natural rubber is integrated, which is inflated before cement injection to prevent the cement flowing into interval 8. In addition, a temperature sensor measures the temperature during heating. Interval 8 is isolated from the upper 4.43 m borehole section and from the gallery by a 2.5 m long hydraulically inflated packer made of natural rubber.

Surface Equipment

All lines inside the casing from packers and the intervals were connected to control systems at the surface. The packer lines were equipped with a manometer and the interval pressure lines with a manometer and a pressure sensor which is connected to the Data Acquisition System (DAS).

In addition, the surface equipment consisted of an injection module with a pressure vessel and a syringe pump for controlled injection (Figure 8). The heater module included a tank with heating elements, a pump, and a temperature controller. The surface equipment was installed in cabinets for protection (Figure 9).

All sensors were connected to the DAS for continuous monitoring.

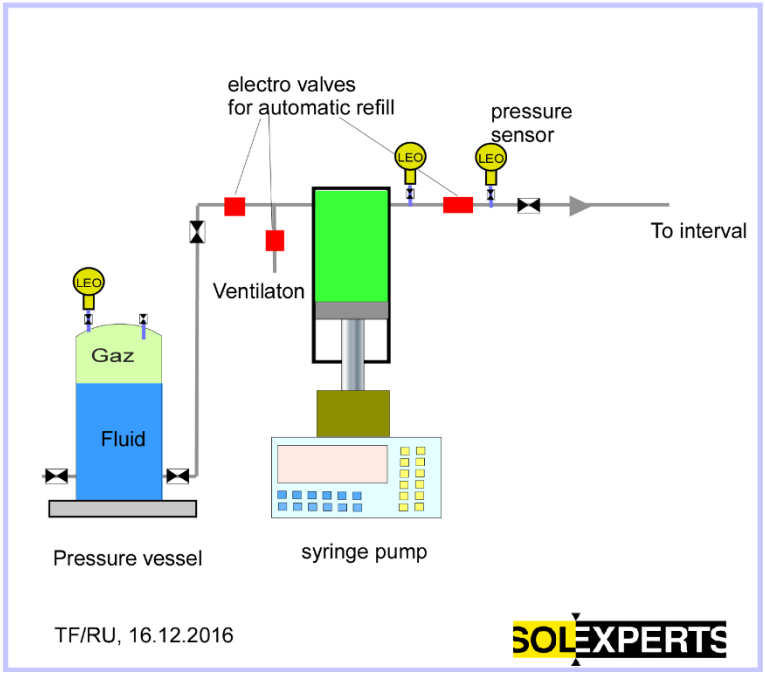

Figure 8. Schematic layout of surface equipment for injection.

Figure 9. Overview of experimental site with surface equipment (small cabinets are the control boards).

System Verification and Installation

Preliminary tests were performed in the workshop to help ensure proper functioning of the borehole completion kit prior to installation. A test series was conducted on the cement composition and injection and the opening of the I/P module by the hydraulic system. In addition, a bench test was conducted to test the fracturing of the cement by temperature cycling. The installation procedure was adjusted based on the test results.

The borehole system was successfully installed on 22 April 2015. The system was pressure tested and the packers were inflated to 40 bar to isolate appropriate sections of the bore hole. Then, cement was injected through the lower grout line into the annulus between the casing and the borehole wall and extracted from the upper grout line. Cement Class G from Lafarge was used. Unfortunately, the grout mixture showed pronounced sedimentation. Therefore, up to 60 weight % cement was added to the mixture. The grout was circulated through the annulus for about 15 minutes. Then, the circulation was stopped, and the cement was allowed to cure for about 2 weeks.

The valves to the I/P modules were hydraulically opened and the grout packers were deflated. The intervals were flushed with CO_2 and the interval volume was determined by saturation of the intervals with water (see Figure 3 - right). Interval 8 took up a large volume of injected water during saturation, and it was concluded that the uppermost part of the cement had not properly cured due to the sedimentation of the cement during injection and due to an increased amount of water in the cement mixture in the upper part of the annulus.

Summary

The borehole completion was successfully installed in the borehole BCS-A1. Then, the annulus between casing and borehole wall was grouted. Despite the successful testing of the cement in the workshop, the mixture used in the field sedimented quickly. Therefore, it was concluded that the upper part of the annulus might have been only partly grouted. The ports through the casing in the I/P modules could be successfully opened and this was confirmed by interval saturation testing.

WELL SYSTEM PREPARATION ACTIVITIES PRIOR TO SEALANT INJECTION CAMPAIGN

Phases 2-14:

Phase 2: Saturation

Initially, all intervals were water saturated without backpressure and with open outflow lines using water compatible with the Opalinus Clay rock chemistry. On 19 May 2015, a backpressure of 1.8 bar was applied and type A1 Pearson water was injected (Table 2). This experimental water formulation was developed for laboratory experiments associated with the Opalinus Clay host rock exposure [5].

Table 2. Two formulations developed by Pearson in are given, with salinities corresponding to the highest Cl (A1 type) and lowest Cl (A3 type) waters from the Mont Terri field Laboratory [5].

	A1 Type Version 980318	A3 Type Version 9806
NaCl	**12.38**	**6.13**
KCl	**0.12**	**0.06**
$MgCl_2$	**1.61**	**0.47**
$CaCl_2$	**2.86**	**0.77**
$SrCl_2$	**0.08**	**0.05**
Na_2SO_4	**2.00**	**1.63**
$NaHCO_3$	**0.04**	**0.05**
Final pH	**7.6**	**7.9**

In a first step, injection was performed in all intervals, in a second step, intervals 1 and 8 were saturated and, finally, constant rate injection tests were performed in interval 1 and 8 [3,4].

The following observations were made during the saturation phase:

- Intervals 8 and 1 were well connected.
- Intervals 6 and 7 immediately reacted to the injection in intervals 1 and 8.
- Intervals 5, 4 and 3 reacted to injection in intervals 1 and 8 with a small delay.
- Interval 2 only slightly reacted to the pressure increase in the other intervals and mostly stayed at atmospheric pressure.
- After shut-in of the injection, the measured pressures decreased to near or even below atmospheric, indicating suction from the formation around the borehole (undersaturation in the formation).

Phase 3: Hydraulic Testing 1

A first hydraulic test campaign was conducted between September and December 2015 to characterize the borehole before the temperature cycling to create flow channels.

Testing and Analysis Methods

Nine pulse injection tests (PI) were conducted in the I/P module intervals to characterize the near-field around the modules and the quality of the cement injection. For the pulse injection tests, type A1 Pearson water was injected with the syringe pump for less than one minute with a differential pressure between 1 and 3.5 bar. Then, the pressure recovery was recorded and analysed. Because of the short injection time for the pressure pulse, the radius of investigation for the pulse tests is small and the calculated transmissivities refer to the interval surroundings.

In the observation intervals 1 and 8, constant head injection tests (HI) were performed (Figure 10a). Type A1 Pearson water was injected in these intervals with an injection pressure of about 3 bar for a period of 5 and 7 days, respectively. Afterwards, the pressure recovery was recorded. From these tests, the cross-hole reactions in the other intervals could be analysed. In addition, the pressure recovery yielded some information on the possible flow model (Figure 10b and 10c).

The pulse injection tests were analysed with the type-curve matching procedure after [6] and [7]. The constant head injection tests were analysed plotting the flow rate normalised drawdown data (ΔP/q) versus log time. The transmissivity was estimated applying the straight-line analysis (SLA) of [8]. The pressure recovery periods of the HI tests (HIS) were analysed based on the straight-line analysis method [9] using the Agarwal equivalent time [10]. Because of uncertainties in the interval length and volume of the I/P modules (intervals 2 to 7), transmissivities are used to describe the permeability distribution along the borehole completion, as discussed in the next section (Figure 11), along with the estimated hydraulic conductivities.

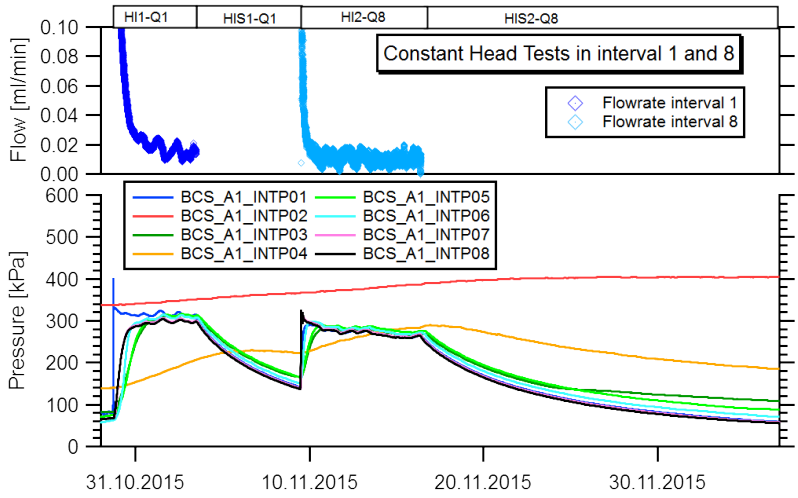

Figure 10a. Pressures and flow rates measured during the HI tests in interval 1 and interval 8.

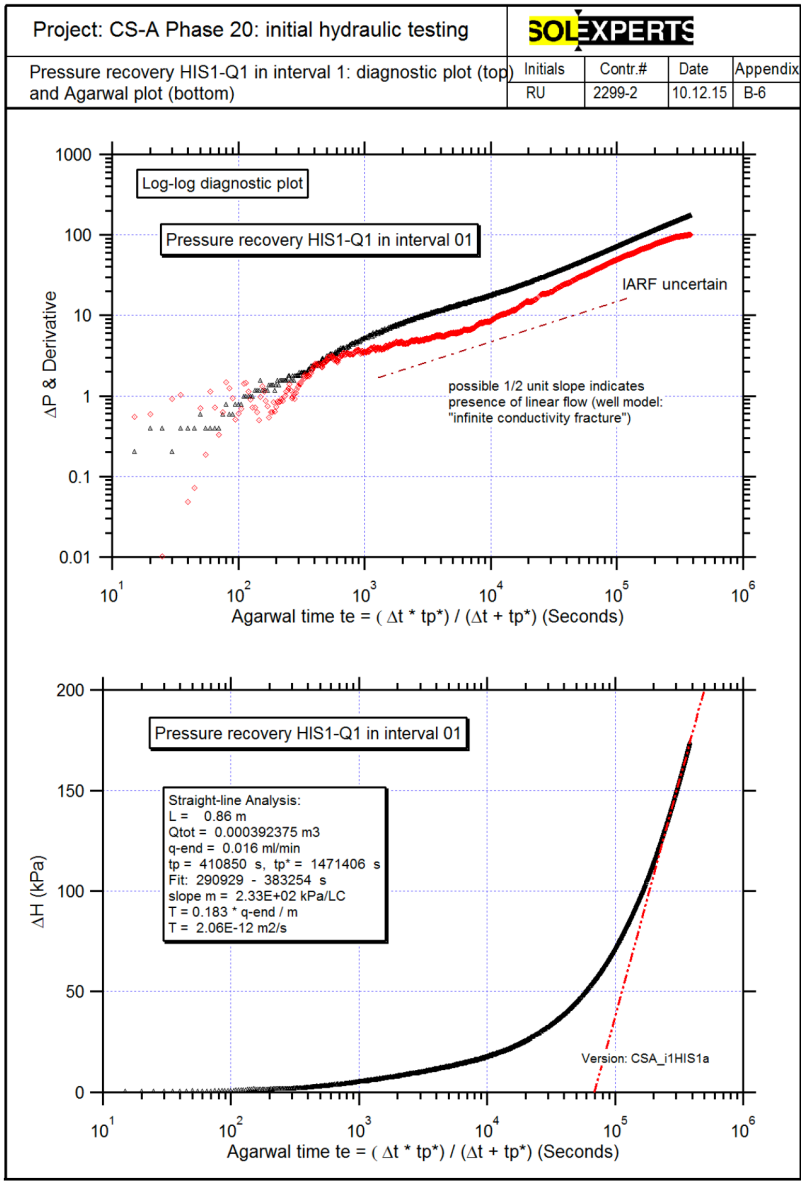

Figure 10b. Pressures recovery diagnostic plot indicating linear flow per ½ slope pressure recovery for interval 1 initial hydraulic testing.

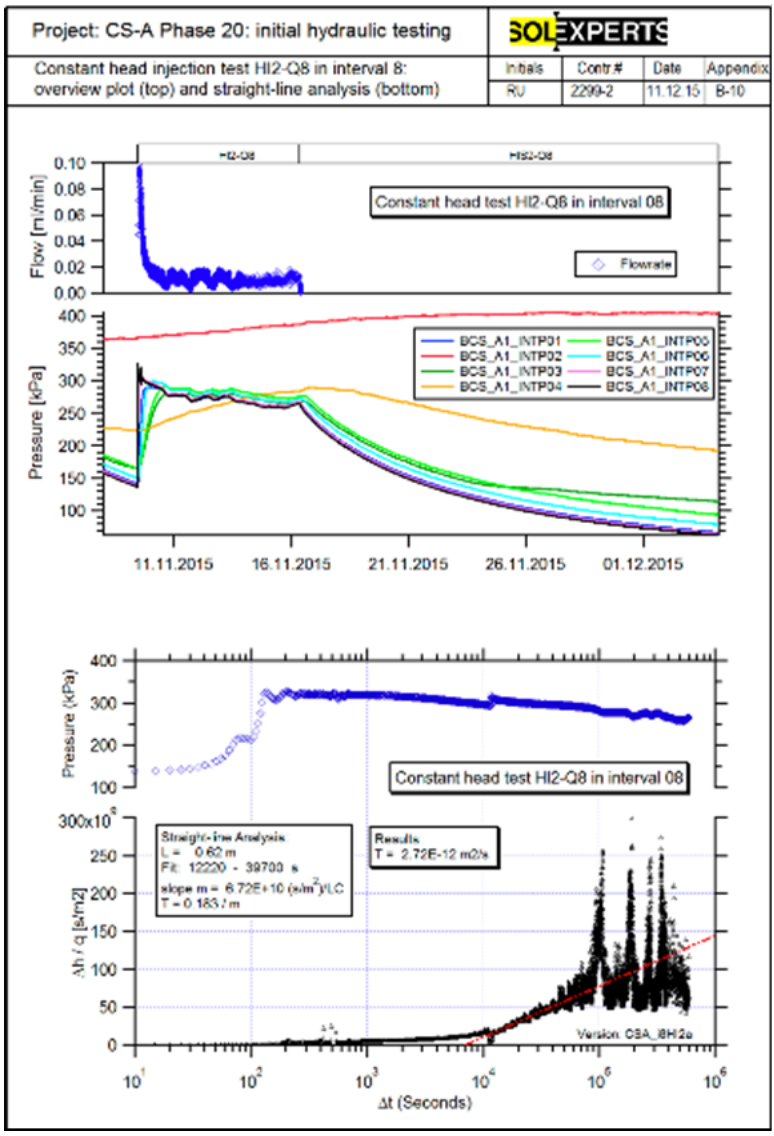

Figure 10c. Pressures recovery diagnostic plot showing radial flow regime per unit slope pressure recovery for interval 8 initial hydraulic testing.

Transmissivity Distribution Along the Borehole

The calculated transmissivities vary between 2E-14 and 5E-11 m^2/s, (Figure 11) which corresponds to an approximate hydraulic conductivity between 2E-13 and 2E-10 m/s (2E-05 and 2E-08 Darcy).

The transmissivity determined for interval 1 and interval 8 is 2E-12 m^2/s, which is similar to the transmissivity of the surrounding Opalinus clay. The diagnostic plot of the pressure recovery for interval 1 shows a possible ½ unit slope of both the pressure and the derivative curve indicating linear flow possibly along fractures or detachments along the cement / OPA boundary (Figure 10b). In contrast, the pressure recovery curves after the test in interval 8 show a near-unit initial slope indicative of radial flow (Figure 10c).

The pulse tests performed in the I/P modules (intervals 2 to 6) mostly yield very low transmissivities down to 3E-14 m^2/s. Generally, the connectivity between the intervals is rather pronounced, as indicated from the pressure recovery discussed above and might be related to fractures or fissures behind along the cement / OPA boundary. However, this connectivity cannot be observed during the pulse tests due to small radius of influence related to the short injection time (typical for pulse tests) and relatively low applied injection pressure.

The normalized pressure curves from the tests in intervals 2 and 3 show a decrease of the transmissivity at a certain distance from the injection point. The pulse test in interval 7 yields the highest transmissivity value of 5E-11 m^2/s.

Figure 11 shows the cross-hole reactions to the injection tests in interval 1 and interval 8. Interval 2 and interval 4 are almost isolated from the other intervals and only slightly react to the tests. In addition, the pressure in both intervals increases to pressures higher than in the injection intervals with only a minor reaction on the shut-in phases. The other intervals react rather fast and to pressures similar to the injection pressure. The interval response time delay to the head injection testing is shown in Figure 12. Interval 8 immediately reacts to the injection in interval 1, followed by interval 5, 7, 3 and 6. The first reaction on the test in interval 8 is found in interval 7, followed by interval 6, 1, 5 and 3.

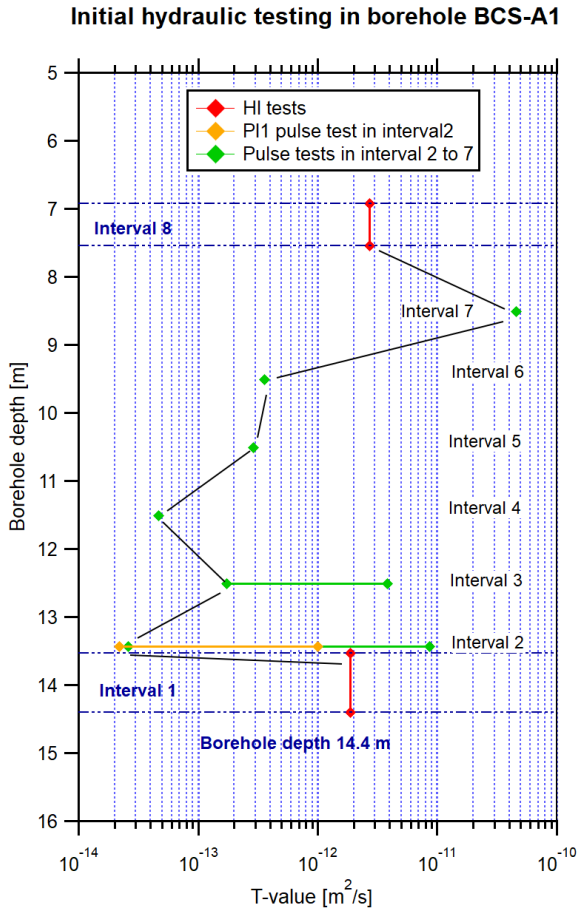

Figure 11. Transmissivity vs. borehole depth during hydraulic testing 1.

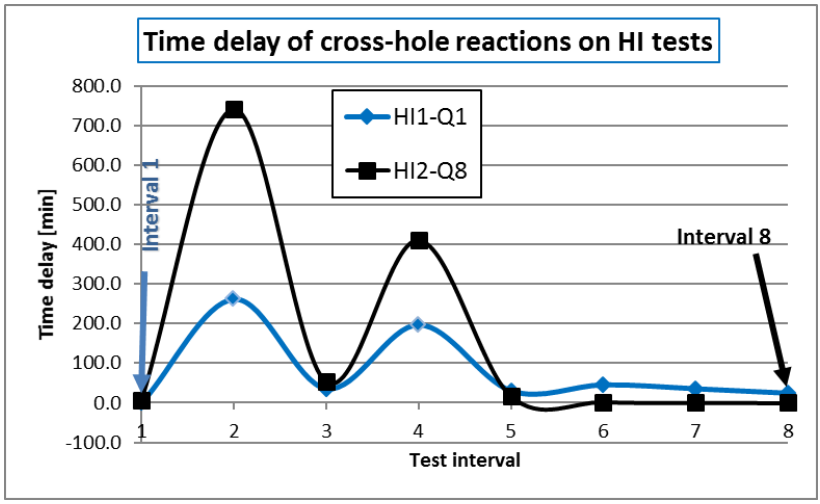

Figure 12. Time delay of cross-hole reactions on tests in intervals 1 and 8 during hydraulic testing 1.

Summary

The measurements in intervals 1 and 8 yield transmissivities similar to the surrounding Opalinus clay. The results from hydraulic testing 1 prove the successful isolation of the intervals 2 to 6, as reflected by the low permeability. For intervals 2 and 3, a slightly increased transmissivity was determined in the vicinity of the ports, possibly due to small fractures or open cavities. The high transmissivity determined for interval 7 might be related to open spaces due to the sedimentation of the cement and consequently, the bad sealing of the uppermost part of the annulus. This hypothesis is supported by the immediate and similar response of interval 7 to the test in interval 8. The good cross-hole connection between interval 1 and interval 8 might be explained by a small but directly connected flow path, possibly along the cement/Opalinus clay interface.

The ½ unit slope observed in the diagnostic plot of the pressure recovery after the HI test in interval 1 indicates the presence of linear flow in the well model "infinite conductivity fracture" and might confirm the presence of an open fracture-like flow path. Intervals 5, 6, and 3 show fast cross-hole reactions on both HI tests, possibly also related to rather good connections along the cement-Opalinus clay interface. The horizontal distance between the ports and the cement-Opalinus clay interface is only 0.04 m.

At the end of the tests, all measured pressures, except those in interval 2 and interval 4, decreased below atmospheric pressure, indicating suction from the formation around the borehole.

Phase 4 and 5: Heating Cycle 1 and 2

The heat cycling of the borehole completion for cement fracture stimulation started on 17 December 2015 with a first heating cycle and continued with a second heating cycle on 12 January 2016. The measured pressures and temperatures are displayed in Figure 13.

Heating Cycle 1

For the heating of the borehole completion, water from a heater is circulated in a 6-1/4 mm OD stainless steel tube which runs inside the casing down to interval 1 (bottom interval) and loops back inside the casing to return to the heater. Heating cycle 1 circulated water with a maximum temperature of 65°C. The packer pressure was controlled and readjusted, which caused a sudden increase of interval pressures. Temperatures between 32°C and 24°C were achieved in the borehole together with a maximum interval pressure of 13 bar. After 14 days, the heat controller failed, which stopped the heating.

Heating Cycle 2

After repair of the heat controller, heating cycle 2 circulated water with a maximum temperature of 90°C. Temperatures between 37°C and 27°C were achieved in the borehole together with a maximum interval pressure of 22 bar. After 3 days, the heat controller failed, and heating stopped. The borehole temperature dropped back to ambient after each cycle.

Summary

The first two heating cycles experienced failures with the heater controller and the heating module. In addition, the heat loss along the borehole was high, which limited the temperature rise in the borehole completion to 33 to 63°C lower than the temperature of the circulated hot water. A further limitation on the heating process was the small volume of water that could be circulated through the 4 mm ID stainless steel line (12.6 ml/min).

The tight intervals 2 and partly 4 showed some sudden pressure decreases which might be due to the opening of fractures around the intervals. At the end of the heating, all measured pressures, except the ones of interval 2 and interval 4, decreased below atmospheric pressure, indicating suction from the formation around the borehole.

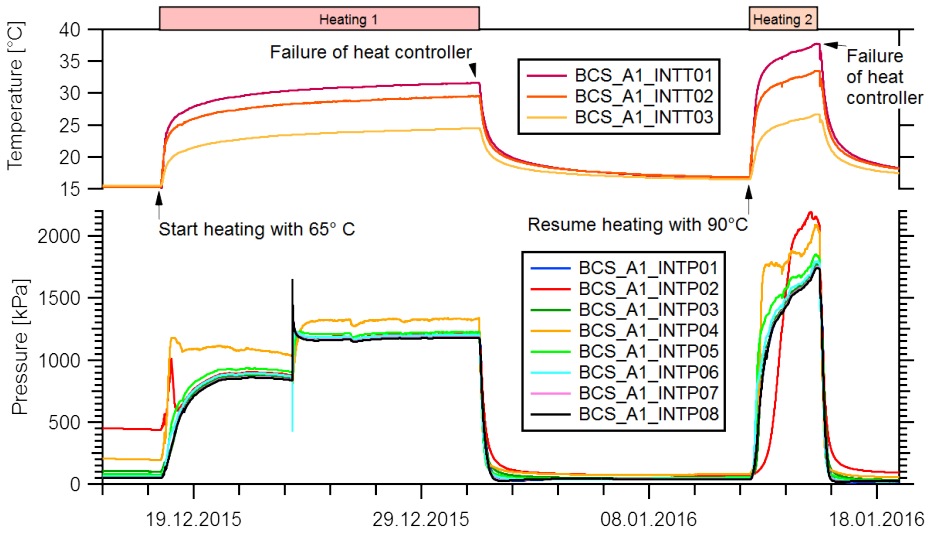

Figure 13. Pressures and temperatures measured during heating cycles 1 and 2.

Phase 6: Hydraulic Testing 2

A second hydraulic test campaign was conducted between January and March 2017 to characterize the borehole after the stimulation by the heating cycles 1 and 2.

Testing and Analysis Methods

Eight pulse injection tests (PI) were conducted in the I/P module intervals to characterize the near-field around the modules. For the pulse injection tests, type A1 Pearson water was injected with the syringe pump for less than one minute with a differential pressure between 0.5 and 5.1 bar. Then, the pressure recovery was recorded and analyzed. In the observation intervals 1 and 8, constant head injection tests (HI) were performed (Figure 14). Type A1 Pearson water was injected in these intervals with an injection pressure of about 1.9 bar for a period of 6 and 7 days, respectively. Afterwards, the pressure recovery was recorded. From these tests, the cross-hole reactions in the other intervals could be analyzed. In addition, the pressure recovery yielded some information on the possible flow model.

The analysis methods are the same as described for Phase 3.

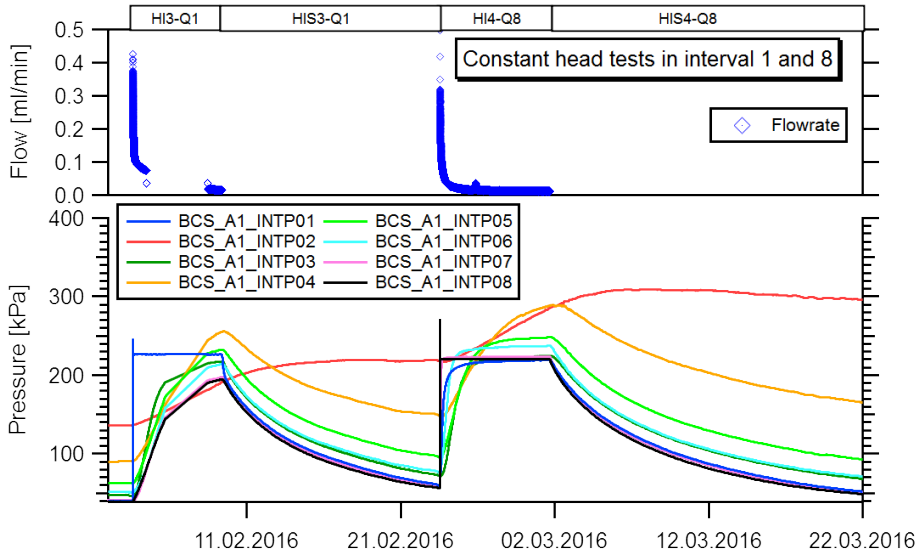

Figure 14. Pressures and flow rates measured during the HI tests in interval 1 and interval 8.

Transmissivity Distribution Along the Borehole

The calculated transmissivities vary between 2E-13 and 3E-11 m^2/s, (Figure 15) which corresponds to an approximate hydraulic conductivity between 2E-12 and 1E-10 m/s (2.2E-08 and 2.2E-05 Darcy).

The transmissivity determined for both intervals 1 and 8 is 2E-12 and 3E-12 m^2/s, respectively, which is similar to the transmissivity determined during the hydraulic testing 1. After shut-in of the test in interval 1, the pressure immediately decreases to the pressure in interval 7 and 8 and follows these curves, which match very well. The diagnostic plot of the pressure recovery for interval 1 shows a possible first Infinite-acting radial flow (IARF) phase which gives a high transmissivity of 2E-11 m^2/s

followed by a ½ unit slope of both the pressure and the derivative curve, similar to hydraulic testing 1. The curves for the pressure recovery after the test in interval 8 show a unit slope.

The I/P modules intervals 4 to 6 exhibited higher transmissivities compared to the hydraulic testing 1. The results from intervals 2, 3 and 7 are similar to those obtained in test 1. The pulse test in interval 7 continued to show a high conductivity of 3E-11 m^2/s.

Figure 16 shows the time delay of the cross-hole reactions on the injection tests in interval 1 and interval 8. Interval 2 is still rather isolated from the other intervals and shows only a slight pressure increase (Figure 14). Interval 4 shows a more pronounced pressure reaction. Again, the pressure in both intervals increases to pressures higher than in the injection intervals. The other intervals react rather fast and reach pressures similar to the injection pressure, especially on the test in interval 8. Interval 1 immediately reacts to the injection test in interval 8, followed by interval 6, 5 and 3. The first reaction on the test in interval 1 is found in interval 2, however with a reduced pressure increase, followed by the other intervals.

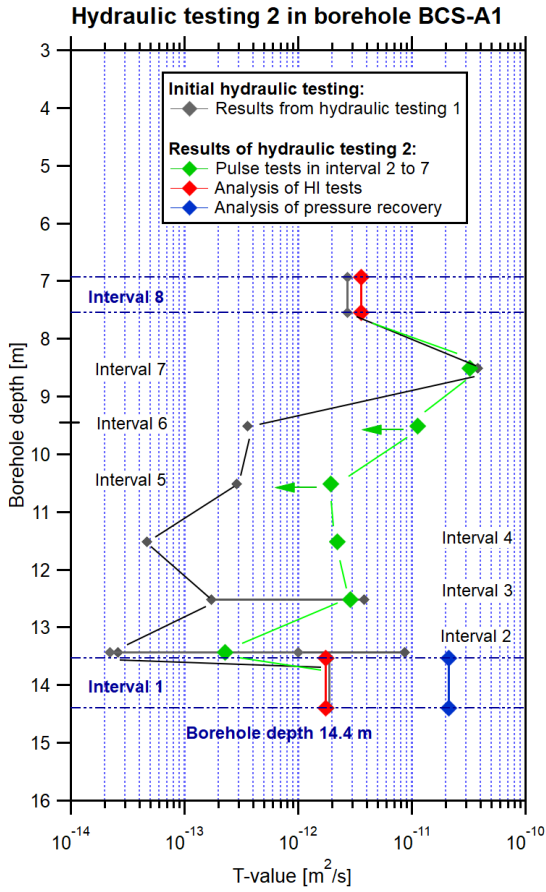

Figure 15. Transmissivity vs. borehole depth during hydraulic testing 2.

Summary

The constant head injection tests in intervals 1 and 8 are similar to the tests performed during hydraulic test 1 with similar transmissivities. From the pressure recovery of the test in interval 1, a first high borehole-near transmissivity could be estimated together with a ½ unit slope phase, confirming the model of a fracture flow along the cement-Opalinus clay interface (model: truncated channel). The pulse tests yield transmissivities which are up to one order of magnitude higher than before the temperature cycling, especially in the near-field of the ports. In the far field, the transmissivities, especially for intervals 5 and 6, seems to decrease indicating that small fractures might have opened only around the ports. The transmissivity of interval 7 is as high as in hydraulic test 1.

The cross-hole reactions on the constant head injection test in the intervals 1 and 8 are similar to the previous results, indicating that the connections between the intervals, possibly along the cement-Opalinus clay interface, did not change. Only the time delay of the reaction in interval 2 and 4 decreased (see Figure 16) probably due to the small breakthroughs, which could be observed during the heating, and creating a slightly better connection from the casing to the outer interface.

At the end of the pressure recoveries, the measured pressures, except for the intervals 2 and 4, decreased below atmosphere, indicating suction from the formation around the borehole.

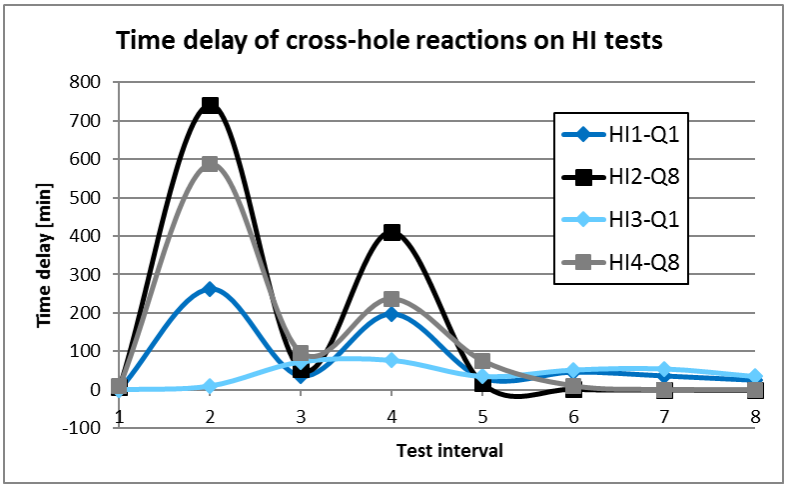

Figure 16. Time delay of cross-hole reactions on tests in intervals 1 and 8 after hydraulic testing 2.

Phase 7: Heating Cycle 3

Because the first two heating cycles resulted in lower transmissivities and reduced fracture openings between the intervals than desired, a third heating cycle was performed with an enhanced heating system [3,4]. A second heater was added which circulated hot water directly into the casing.

The first step of heating cycle 3 started on 06 April 2016 with the injected water temperature at 80°C. The maximum temperature reached in the completion was 40°C: The surface equipment was modified to achieve better heating. A second heating system was installed, with a separate heater, larger circulation lines, and the hot water was circulated directly inside the casing. Finally, during the fifth

heating step of cycle 3 with a heated water temperature of 85°C, the temperature in the borehole completion reached a maximum of 78.4°C.

During the heating steps, breakthroughs with a sudden pressure decrease could be observed. especially in the intervals 2, 3 and 4, indicating the opening of fractures. During step 5, the pressures in all intervals aligned with each other, confirming a good connection between all intervals. The measured pressures and temperatures are displayed in Figure 17.

At the end of the pressure recovery, the measured pressures of all intervals decreased far below atmosphere, indicating suction from the formation around the borehole.

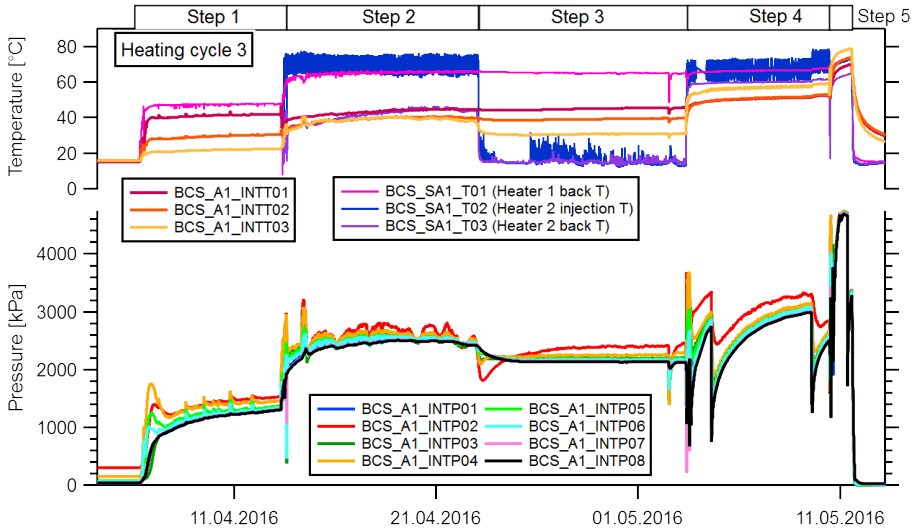

Figure 17. Pressures and temperatures measured during heating cycle 3.

Summary

The original heating system could not achieve borehole temperatures to achieve large fracturing in the cement. The heat loss along the lines and in the casing was the main problem. The problem was solved by increasing the heat input with larger hot water flows.

Phase 8: Hydraulic Testing 3

A third hydraulic test campaign was conducted April/May 2016 to characterize the borehole completion after the stimulation by heating cycle 3.

Testing and Analysis Methods

Eleven pulse injection tests (PI) were conducted in the I/P module intervals to characterize the near-field around the modules. For the pulse injection tests, type A1 Pearson water was injected with the syringe pump for less than one minute with a differential pressure between 1 and 7 bar. In the observation intervals 1 and 8, constant head injection tests (HI) were performed (Figure 18). Type A1

Pearson water was injected in these intervals with an injection pressure of about 1.4 and 2.4 bar for a period of 1 and 2 days, respectively. Afterwards, the pressure recovery was recorded. From these tests, the cross-hole reactions in the other intervals was analyzed. In addition, the pressure recovery yielded information on the possible flow model.

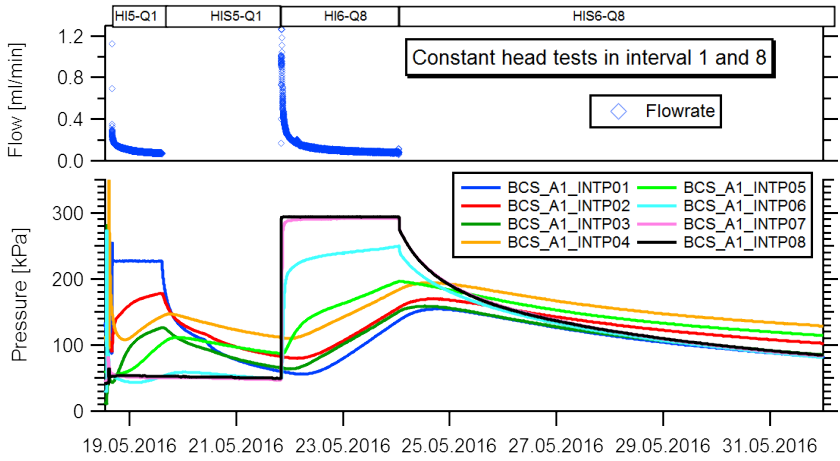

Figure 18. Pressures and flow rates measured during the HI tests in interval 1 and interval 8.

Transmissivity Distribution along the Borehole

The calculated transmissivities vary between 2E-11 and 2E-09 m^2/s, (Figure 19) which corresponds to an approximate hydraulic conductivity between 2E-11 and 1E-08 m/s (2.7E-06 and 1.8E-03 Darcy).

The transmissivity determined for both intervals 1 and 8 is between 2E-11 and 7E-11 m^2/s, which is about one order of magnitude higher than the transmissivity determined during hydraulic tests 1 and 2. Both tests show a decrease of the transmissivity at late time with increasing distance from the interval, for both the HI test and the pressure recovery phase.

The pulse test in intervals 2 to 6 yielded transmissivities which are one and three order of magnitudes higher than those determined by hydraulic tests 1 and 2.

Figure 20 shows the cross-hole reactions to the injection tests in interval 1 and interval 8. The cross-hole reactions considerably changed compared to the previous tests.

The reaction to the test in interval 1 is rather heterogeneous along the borehole. Intervals 2, 3, and 5 immediately reacted to the test in interval 1, whereas almost no reaction could be observed in intervals 6, 7, and 8.

All intervals show a cross-hole reaction on the test in interval 8 with increasing delay related to increasing distance. Interval 7 measures almost the same pressure trend as interval 8 and interval 6 also shows a good connection to interval 8.

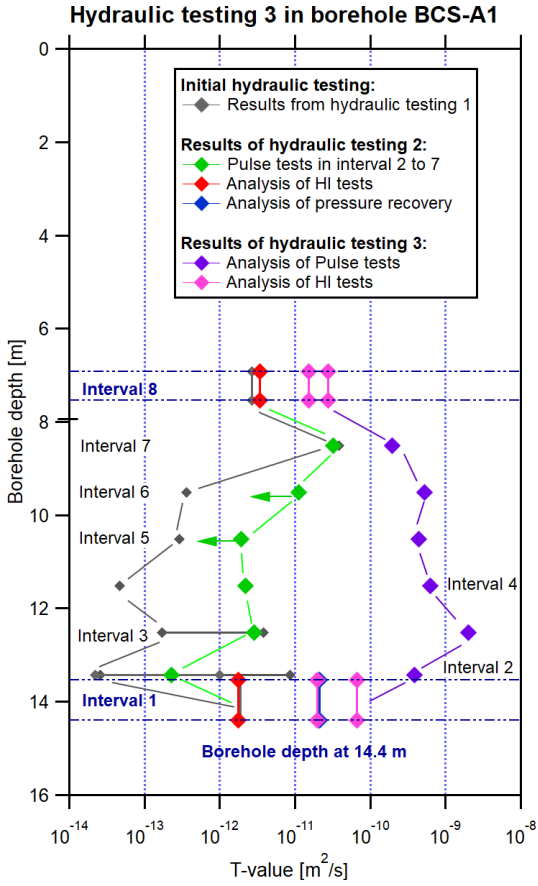

Figure 19. Transmissivity vs. borehole depth after hydraulic testing 3.

Summary

Heating cycle 3 considerably changed the behaviour of all I/P modules. The transmissivities in all intervals increased by one to three orders of magnitude, both adjacent to the intervals and further away from the intervals. Generally, the intervals seem to have a good connectivity. All intervals reacted on the HI test in interval 8, with decreasing connectivity at increasing distance. However, no connectivity could be observed for intervals 7 and 8 to the HI test in interval 1.

The diagnostic plot of the pressure recoveries, especially for interval 8, might be explained by the model of a truncated channel describing the intervals located in the rather tight Opalinus clay with enhanced transmissivity along the borehole towards the neighbouring intervals.

At the end of the pressure recoveries, the measured pressures, except for the intervals 4 and 5, decreased below atmosphere, indicating suction from the formation around the borehole.

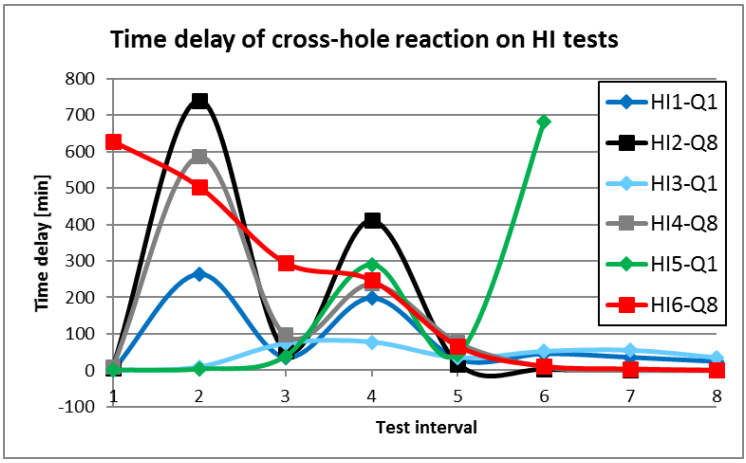

Figure 20. Time delay of cross-hole reactions on tests in intervals 1 and 8.

Phase 9 /10 /11: Dipole Testing/Dead Volume Test/Tracer Tests

The behaviour of the borehole completion after the stimulation was difficult to understand and the extent of fracture opening could not be easily calculated in preparation for the planned sealant injection. The connectivity between the individual intervals (I/P modules) was further evaluated during several testing campaigns. Three campaigns were conducted with dipole testing between the intervals. During one campaign, the dead volume around the intervals was estimated by tracer injection. Finally, three dipole tracer tests and two push-pull tracer tests were conducted. The tests were performed between June 2016 and February 2017.

Dipole Testing 1

Seventeen dipole tests were conducted during the first dipole test campaign, with different injection and extraction intervals and injection pressures between 12 bar and 50 bar. The tests were performed by injection of type A1 Pearson water in the Q or P line of one interval and extraction from one, two or three adjoining intervals. The following observations were made:

- For most interval pairs, the injection flow rates were higher than the extraction flow rates. The highest injection flow rates were measured for interval 5 (12 ml/min) and interval 6 (Figure 21). Maximum extraction flow rates were 2.5 ml/min for all intervals.
- Higher injection flow rates were observed with increasing injection pressure (up to 50 bar). This was most pronounced above 30 bar injection pressure, with no or only a small increase in the extraction flow. The high injection pressures seem to have caused fracture opening, leading to higher injection flowrates, even at subsequent lower pressure injection.
- Interval 2, 3, and 4 show low injection flow rates and bad connectivity to the other intervals (Figure 22).
- The main water storage volume was supposed to be intervals 1 and 8.
- The entire system seems to have been saturated and pressurized towards the end of the dipole test campaign 1 which caused slightly higher flow rates.
- Promising dipole connections were found for the following pairs: Q7 → Q8, Q5 → Q6, Q6 → Q5, P5 → P4.

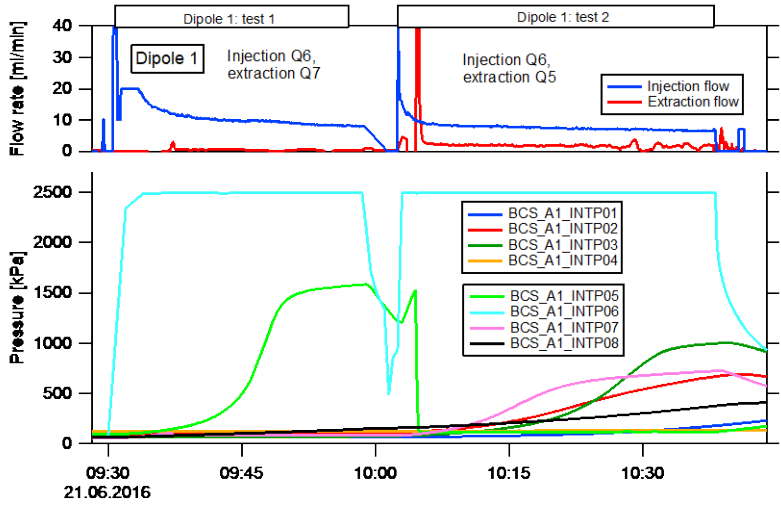

Figure 21. Injection at interval 6 with extraction from the neighbouring intervals.

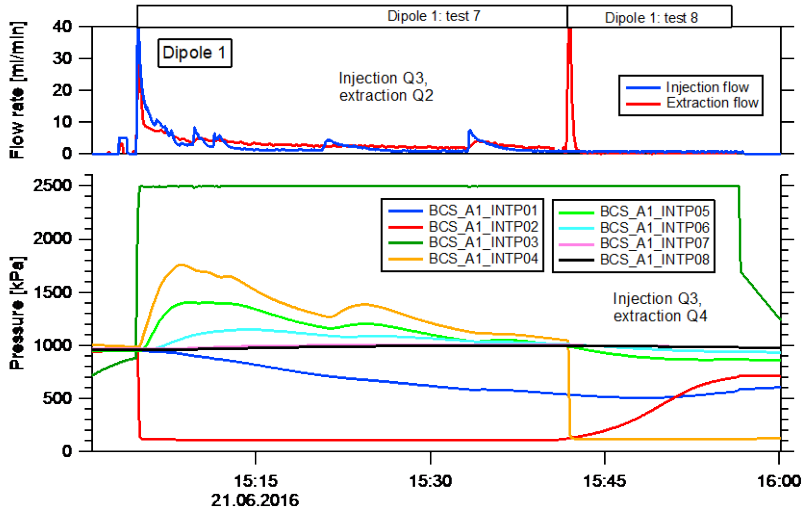

Figure 22. Injection at interval 3 with extraction from the neighbouring intervals.

Dipole Testing 2

The results of the first dipole test series suggested an enhanced influence of the open volumes of the intervals 1 and 8 on the performance of the dipole tests. Therefore, a second test series was proposed with closed and open grout packers, to understand the influence of the intervals 1 and 2 on the dipole tests. Also, injection tests were done in each interval with extraction from all the other intervals to better understand the flow paths in the borehole completion.

The following observations were made:

- Interval 1 was not fully isolated by the inflation of the grout packer and showed a pressure increase for injection in all intervals.
- Intervals 7 and 8 are closely connected.
- Interval 7 and 8 only showed a reaction on the injection in interval 6 so that the influence of the grout packer could not be evaluated.
- For most interval pairs, the injection flow rates were much higher than the extraction flow rates. The best connection was observed from interval 6 to 7 and minor reactions from interval 5 to 6 and from 4 to 6.
- Intervals 2, 3 and to a minor extent 4 show only minor dipole connections.
- All pressures returned to atmosphere pressure or even suction after pressure recovery.

Dipole Testing 3

In preparation for tracer tests, a third dipole test series was conducted between the uppermost intervals 6, 7 and 8. The injection interval was interval 7.

The following observations were made:

- Low extraction flow rates from interval 6 were observed at an injection pressure of 20 bar, higher flow rates could be achieved with 25 bar injection pressure.
- A good connection was found between interval 7 and 8 with only slightly lower flow rates from interval 8 after saturation of interval 8.

Dead Volume Estimation

As preparation for the tracer tests, the dead volume of the grouted intervals was estimated by tracer circulation through the intervals. The tracer was injected through the Q line and extracted from the P line. From the dilution of the tracer in the circuit, including the volume of the surface equipment and the lines, the interval volume was calculated. The results of the dead volume tests only slightly differ from the initial volume estimation (Table 3).

Table 3. Interval volumes.

Section	Position [m]	Volume [L]*	Volume [L]**	Comments
Interval 2	13.43	0.152	0.158	I/P module 1
Interval 3	12.52	0.169	0.176	I/P module 2
Interval 4	11.52	0.180	0.139	I/P module 3
Interval 5	10.52	0.236	0.316	I/P module 4
Interval 6	9.52	0.161	0.127	I/P module 5
Interval 7	8.52	0.293	0.293	I/P module 6

* Including line volume, determined by water injection, used for hydrotests.
** Estimated from dead volume tests, used for tracer tests.

Tracer Testing

Three dipole tracer tests and two push-pull tracer tests were performed in the borehole completion:

- Tracer test 1 with injection at 3 bar in interval 7 (500’000 ppb Uranine) and extraction from interval 8.

- Tracer test 2 with injection at 18 bar in interval 6 (1000 ppb Uranine) and extraction from interval 7.
- Tracer test 3 with injection at 20 bar in interval 6 (500'000 ppb Uranine) and extraction from interval 7.
- Push-pull tracer test 1 with injection in interval 6 (1000 ppb Uranine) and extraction from interval 7 and vice versa.
- Push-pull tracer test 2 with injection in interval 7 (1000 ppb Uranine) and extraction from interval 8 and vice versa.

The results of the tracer test series are summarized in the following sections.

Tracer Test 1 – Interval 7 → Interval 8

Constant injection and extraction flow rates of 8 ml/min were obtained (Figure 23). Tracer arrived at the interval 8 extraction port 6.1 hours after start of tracer injection. The peak of 10.6 ppb at interval 8 was reached after 13.2 hours. For the analysis of the tracer test, the flow volume between interval 7 and interval 8 was assumed to be ~3500 ml with a Peclet number of 25 in this flow pathway. A recovery of 2 % was calculated at the end of the test. An extrapolation of the incomplete tracer recovery curve yields a maximum 10 % tracer recovery.

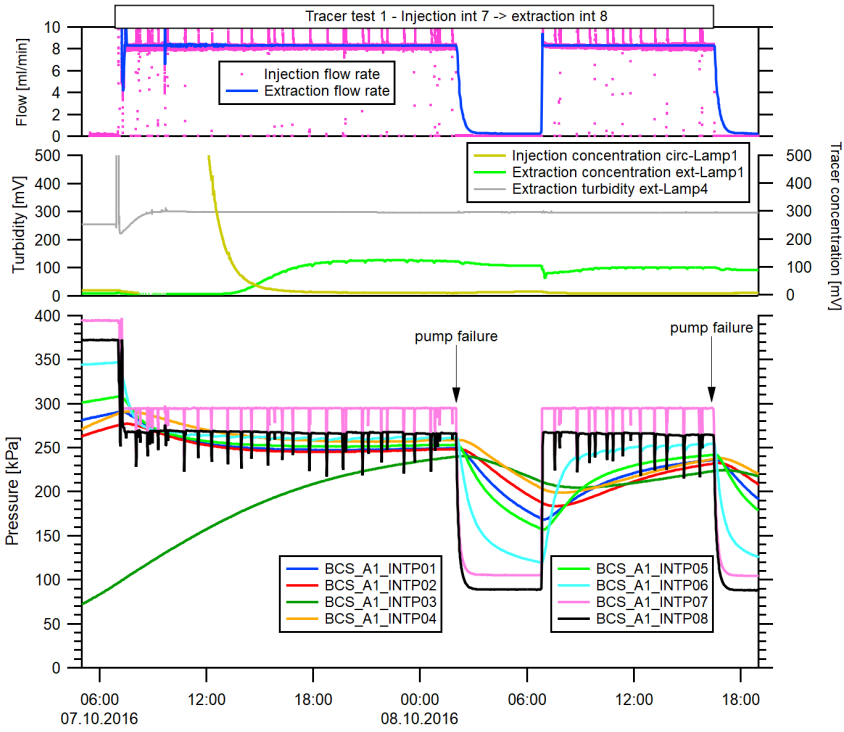

Figure 23. Tracer test 1 with injection in Q7 and extraction from Q8.

Tracer Test 2 – Interval 6 → Interval 7

No tracer concentration was observed at the extraction point at interval 7 despite the fact that the extraction flow rate of about 2 ml/min was similar to the injection flow rate. Therefore, the test could not be evaluated and was repeated with a higher injection concentration.

Tracer Test 3 – Interval 6 → Interval 7

A maximum 2 ml/min injection flow rate and similar extraction flow rate were obtained during tracer test 3 (Figure 24). Tracer arrival at the extraction port of interval 7 occurred 21.6 hours after start of tracer injection. The peak of 3.2 ppb at interval 7 was reached after 72.6 hours. For the analysis of the tracer test, the assumption of a direct flow from interval 6 to interval 7 requires a flow volume of ~11'000 ml and a Peclet number of 3. An alternative model, assuming the flow from interval 6 to interval 8 and then to interval 7 was also used to interpret the tracer results, which resulted in an estimated flow volume of 3000 ml and a Peclet number of 15. A recovery of 0.6 % was calculated at the end of the test. An extrapolation of the incomplete tracer recovery curve yields maximum 10 % of tracer recovery.

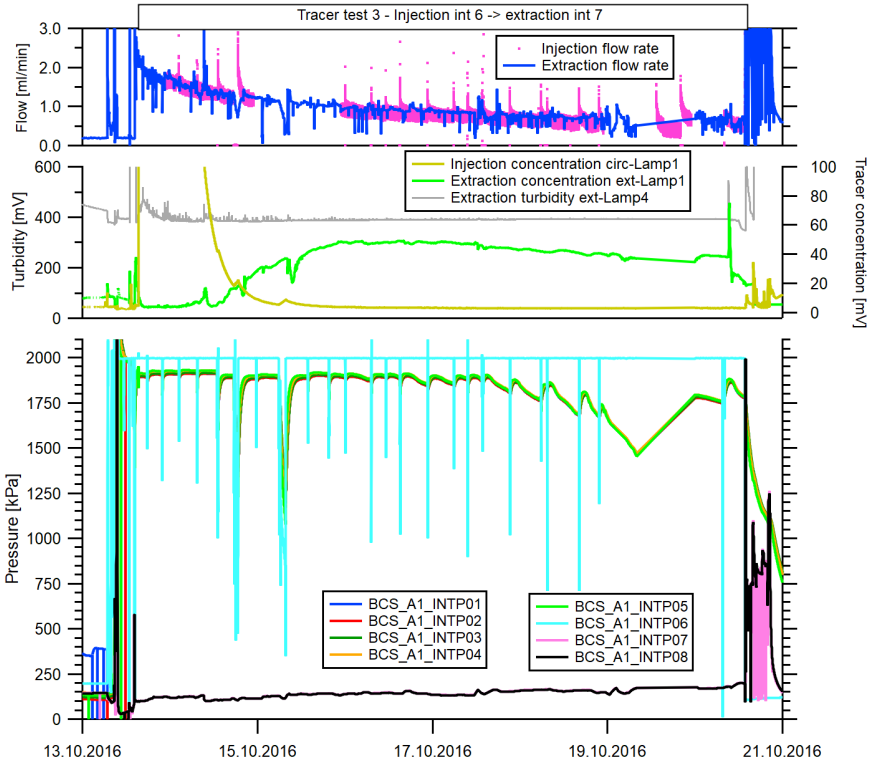

Figure 24. Tracer test 3 with injection in Q6 and extraction from Q7.

Push-pull Tracer Test 1 – Interval 6 ←→ Interval 7

In preparation of the first push-pull tracer test, 30 ml of 1000 ppb Uranine tracer were circulated in the surface equipment. The injection in interval 6 and extraction from interval 7 lasted about 16 hours. The flow was then reversed (Figure 25).

The injection volume estimated from the mean of the injection function to the push-pull transition was about 100.5 ml, and the extraction volume from the transition to the mean of the extraction function was about 121 ml. These volumes are considered to be in relatively good agreement. The integrated area under the extraction curve was about 88% of the area under the injection curve, which implies a tracer recovery of 88%. This recovery may not be statistically distinguishable from 100% because of flowmeter noise and the use of different flowmeters.

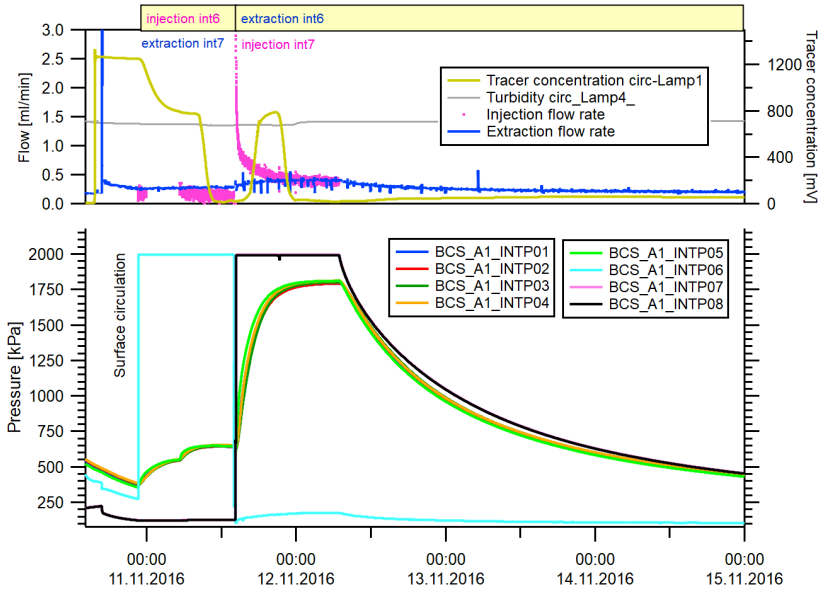

Figure 25. Push-pull tracer test 1 between Q6 and Q7.

Push-pull tracer test 2 – interval 7 ←→ interval 8

A push-pull tracer test 2 was performed between interval 7 and interval 8. The injection with 35 ml of 1000 ppb Uranine in interval 7 lasted about 0.5 hours, followed by a waiting period of 0.25 hours. Then, the extraction from interval 7 started. Only a small amount of tracer could be recovered from interval 7. In addition, during both the push and the pull phases, sudden decreases of the pressure in interval 7 were observed.

Summary of Dipole and Tracer Testing

The dipole tracer tests only showed a very low tracer recovery at the extraction side (max. 10 %) with a long tailing indicating that the intervals might not be directly connected to each other, but the flow

paths might be more difficult (e.g., from interval 6 to interval 8 and back to interval 7). There might be voids in the system or even in the host rock where the tracer is not recovered.

The push-pull test 1 results suggest that at least 150 ml of flow pathways in the immediate vicinity of the interval 6 injection port are well behaved in the sense that tracer is almost completely recovered in only slightly more volume than the injection volume and with little apparent dispersion or tailing. These results suggest that the flow pathways near the injection port are likely rather 'tight" and do not have significant void spaces within them.

Phase 12: Water Sampling

During the dead volume tests, high turbidity water was extracted from several intervals, indicating a high concentration of small particles in the extracted water. Brown water was extracted from interval 6 before the start of the push-pull test 1. High turbidity was also found during the flushing of interval 7 in preparation of the push-pull test 2.

Porewater chemistry

Up to this phase of the experimental work, type A1 Pearson water was used for water injection. However, an issue with calcium carbonate precipitation was observed that was resolved by a new Pearson water "A3" formulation (Table 4). The A3 Pearson water removed divalent cations and lowered the pH that resolved the precipitation issue. The MES-buffer (2-ethanesulfonic acid) was added to the new-A3 Type Pearson water for flushing purposes to adjust the pH to about 4 and to overcome the cement buffering capacity. Both new Pearson water types were used starting from Phase 14.

Table 4. Pearson water formulations * [11].

		A1 Type*	**A3 Type***	**New-A3**	**MES-new-A3**
Salt quantities [mg/kg]	NaCl	12'380	6'130	6'130	6'130
	KCI	120	60	1800	1800
	$MgCl_2$	1'610	470	0	0
	$CaCl_2$	2'860	770	0	0
	$SrCl_2$	80	50	0	0
	Na_2SO_4	2'000	1'630	1'630	1'630
	$NaHC0_3$	40	50	50	50
MES buffer					0.1 M
Final pH		7.6	7.9	7.9	6.5
Conductivity [mS/cm]		28.9	14.5		

XRD Analysis of Solid Phase in Samples

The solid phases in a sample from interval 7 (collected on the 16 August 2016) were analysed by XRD analysis. The analysis showed an increased content of calcite with secondary phases of ettringite, brucite and Fe-oxychloride. The main elements were Fe and Ca, with secondary peaks for Cl, Mn, S, Mg, Al and Si.

The high calcite content was due to precipitation from Pearson water or by leaching from cement and a subsequent precipitation. The Mn content was attributed to corrosion processes, whereas the high iron content might be either a casing corrosion product or a result of oxidation of pyrite in the Opalinus Clay.

Analysis of Borehole Water

To better understand the origin of solids in the water, samples from each interval were analysed to examine the compositional variation of the residual pore water along the borehole completion. Four distinct water types were found along the borehole (Figure 26):

- Low pH, intermediate to high conductivity – intervals 1 and 8 → similar to Pearson water and representative for the Opalinus Clay.
- Intermediate pH, high conductivity – intervals 2, 3, 4 → clear water and minimal precipitation due to slightly increased pH compared to Pearson water. These intervals had poor connectivity to other intervals and therefore reduced flow-through.
- High pH, intermediate conductivity – intervals 6 and 7 → typical for water-cement interaction and precipitation cycles.
- Low pH, low conductivity – interval 5 → clear water, precipitation and removal of nearly all elements. Interval 5 is located at the transition from stainless steel (below) to carbon steel (above). Did this affect the chemical composition of the water?

Further Injection Tests

A series of further injection tests was performed between 18 January and 02 February 2017 with the goal of reducing and stabilizing the pH in the grouted intervals. However, monitoring the pH of the fluid in interval 7 showed that the interval 7 water quickly equilibrated to a high value. The fluid extraction from the other intervals was rather small. Repeatedly, solids were observed in the samples, which occasionally re-dissolved after sampling.

Summary

The analyses performed during this phase gave some insight into the behaviour of type A1 Pearson water during injection. Flushing with type A1 Pearson water to control pH was only possible for a limited time in interval 7, as the Pearson water immediately reacts with cement and buffers up to a pH of 12-13. At elevated pH, minerals like calcite, brucite and others are precipitated from the fluid. This process is temporarily reversed by the injection of fresh type A1 Pearson water. Precipitation, transport, and dissolution of minerals was thought to be responsible for the observed inconsistent reaction of the system during the previous testing campaigns.

Phase 13: Installation of a Mg-Anode

In a previous experiment at Mont Terri URL, well sealing integrity was studied in a test well bore in the presence of pressure and temperature stresses and CO_2-rich brine [12]. Corrosion leading to penetration of the carbon steel casing and loss of containment to the adjoining interval was observed. The corrosion occurred at a cement-free section of the carbon-steel casing in an interval containing multiple metallic materials, which may have led to galvanic-based corrosion. In the present study, the uppermost part of interval 7 contains a transition from carbon steel to stainless steel and was determined to be incompletely cemented, based on the increased volumes in this part of the borehole and the good connection between interval 7 and interval 8. This situation raised the possibility that the CS-A casing might be subject to corrosion. To mitigate the potential for corrosion a sacrificial Mg-Anode was installed.

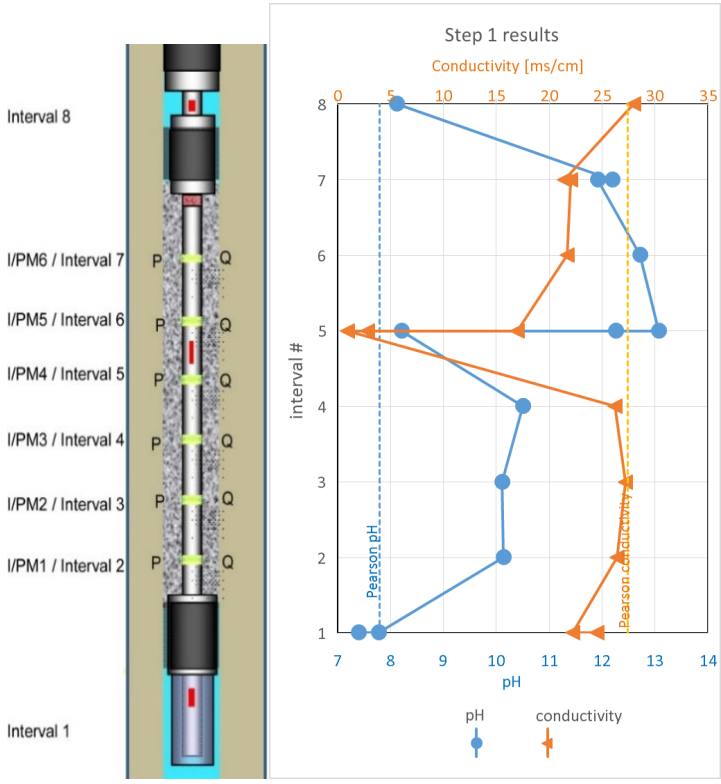

Figure 26. pH and conductivity measured in samples along the borehole.

On 13 July 2017, a sacrificial magnesium anode was emplaced in a new borehole (BCS-A2) to mitigate corrosion at the carbon steel interface to stainless steel. The borehole was backfilled with a mixture of 75% gypsum, 20% bentonite and 5% sodium sulphate. The anode was connected to the borehole completion by copper wires. The pressures in the intervals immediately started to increase (Figure 27) to maximum pressures between 20 and 25 bar in September 2017.

On 11 September 2017, gas was extracted from all intervals after an initial extraction of water. The gas contained 95.2 Vol % Hydrogen. The hydrogen formation at the cathode during the cathodic protection process according to the reaction $2H_2O + 2e^- \rightarrow H_2 + 2OH^-$ under neutral or alkaline conditions is know from the literature [13]. Because of the explosion risk of hydrogen, the sacrificial Mg-Anode was disconnected from the borehole completion on 14 September 2017.

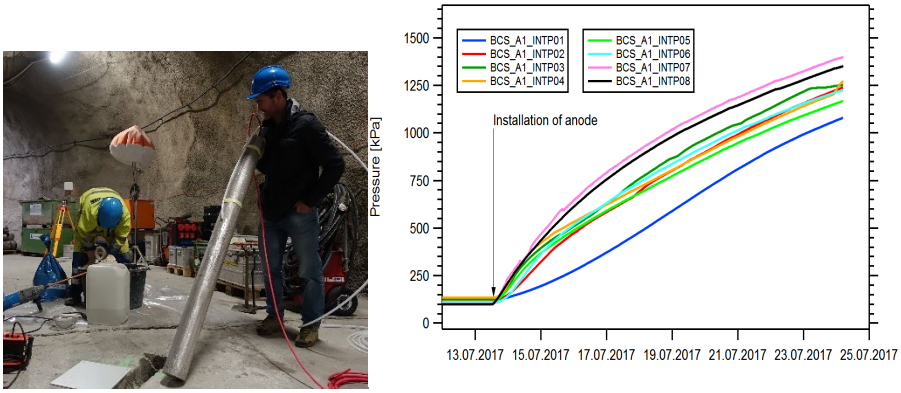

Figure 27. Mg-Anode (left) and initial pressure increase related to its installation (right).

Phase 14: Flushing of all Intervals

As noted previously, turbid water was extracted from the intervals and decreased connectivity between the intervals was observed during the tests using A1 type Pearson water. A flushing of all intervals was done using the type new-A3 Pearson water with all the Ca, Mg, and Sr replaced by an equivalent amount of charge of K to reduce the interaction with cement and the subsequent formation of Ca and Mg carbonate or hydroxide precipitates which were thought to be responsible for the clogging of the flow paths. The goal of the flush was to clean the flow paths between the intervals and prepare for the sealant injection in the designated intervals. To clear accumulated precipitates out of the system, an MES buffer of 0.1 M was added to the type new-A3 Pearson water to adjust the pH to about 4 to balance the cement buffering capacity. The specifications of the type new-A3 Pearson water without and with MES-buffer are shown in Table 3.

During the first step of the flushing procedure, the water in all intervals was displaced with the type MES-new-A3 Pearson water, which was left in place to dissolve the precipitates. In addition, type MES-new-A3 Pearson water was circulated between interval 7 and interval 8, which increased the connectivity between interval 7 and 8. The flush apparently dissolved the precipitates from the system.

For the final step of the flushing, type new-A3 Pearson water was circulated until the extracted water showed the same composition as the injected water.

Summary

The flushing produced an observable increase in the connectivity between the intervals.

SEALANT INJECTION CAMPAIGN

Phases 15-18:

Four different sealants were injected in six different intervals. Sealants were developed by the following organizations, Sealant 1) nanoparticle hydrogel sealant developed by Los Alamos National Laboratories (LANL), Sealant 2) polymer gel developed by University of Texas (UT), Sealant 3) silicate-based sealant developed by IFP Energies Nouvelles (IFPEN) and Sealant 4) an epoxy-based

sealant developed by University of New Mexico (UNM). An overview of sealant formulations will not be presented in this chapter, while full details are documented by earlier published work [14, 15, 17, 18].

Phase 15: Sealant 1

The goal of the CS-A experiment is to test sealants for mitigation of outside-casing seepage of CO_2. In September 2017, 2.5 years after the installation of the borehole completion, the first sealant was injected into a dipole between two intervals. Sealant 1 was produced at the Los Alamos National Laboratories [14]. This phase of the project was conducted by Hakim Boukhalfa with the support of Robert Roback and Paul Reimus, all from LANL.

HI Step Tests

A test procedure with HI step tests was developed, which provides quick, comparable tests for characterizing permeability in each interval at different injection pressure levels. The test involved injection of type new-A3 Pearson water at 20, 25, 30 and 35 bar for 4 minutes at each step. The flow rates at the end of each step are compared. These tests have limitations:

- The initial flow rate is mostly dominated by wellbore storage, especially at higher flow rates.
- The final flow rate after 4 minutes is not in equilibrium with the formation around the interval and cannot be used for permeability estimation.
- This is confirmed by the observation that the flow rates vary considerably for repeated tests and that especially the flow rates at 35 bar decrease over a repeated test series, indicating the initial wellbore storage of the interval being reduced by the ongoing filling with fluid.

Nevertheless, the results provide a quick hydraulic characterization of the intervals during and after the different activities and to assess the long-term performance of the sealants in the intervals. An example of the first series of three HI step tests in interval 6 is given in Figure 28.

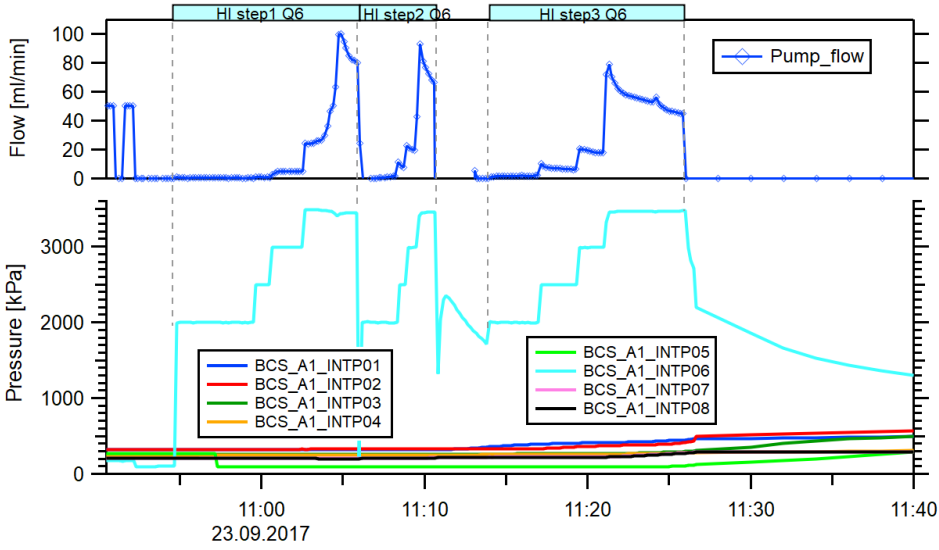

Figure 28. Example of the first HI step tests performed in interval 6.

Sealant 1 Description

The first sealant was a low pH-triggered hydrogel with different particle sizes. The smart gel particles were prepared at Los Alamos National Laboratory by using emulsion polymerization techniques. The particles were composed of a 1:1 mol ratio of methyl acrylate to 2-(dimethylamino)ethyl methacrylate with 1 mol % diethyleneglycol dimethacrylate as a crosslinking agent. Particle size was controlled through the combination of surfactant and monomer concentrations, with high surfactant and lower monomer concentrations producing smaller particles. Six batches were produced for the sealant injection at BCS-A1 borehole by varying the surfactant and monomer concentrations slightly. Interval 6 and interval 7 were chosen for the sealant 1 injection. The concept was to flow the smart gel suspension into the interval to fill flow channels with the gel particles, which form a gel upon exposure to low pH caused by subsequent injection of CO_2. A photo of the expanded gel after a bench test is shown in Figure 30.

Site Preparation

In a first step, the remaining water and non-soluble gas (hydrogen), which might reduce the permeability, were removed from the intervals by extraction of water and gas from the interval and sweeping with CO_2. Then, the intervals were saturated with type new-A3 Pearson water until free outflow was observed. A series of HI step tests were performed.

Tracer Tests

Initial tracer tests were performed in interval 6 and interval 7 by injection of a solution with bromide tracer and Amino-G acid as an additional fluorescent tracer.

Tracer test 1 with injection in interval 6 → interval 7 and interval 8

A tracer solution with 500 ppm Amino-G acid and 1000 ppm bromide was injected in interval 6 with a backpressure of 20 bar. No tracer was detected at interval 7. The injection pressure was increased to 31 bar and no tracer was detected in either interval 7 or 8.

Tracer test 2 with injection in interval 7 → interval 8 and interval 6

A tracer solution with 780 ppm Amino-G acid was injected in interval 7 with a flow rate of 12 ml/min and a maximum pressure of 1.5 bar. The tracer concentration at both extraction points interval 6 and interval 8 started to increase after about 1.5 hours to 31.2 mV at interval 8 and 1980 mV at interval 6. The extraction tracer concentration stayed at or near these levels until the end of the tracer test.

The tracer tests revealed reduced connectivity between interval 7 and interval 8. There was no connection verified between interval 7 and interval 6. In light of this lack of connectivity identified in tracer test 1, the high tracer concentration at the extraction from interval 6 during the tracer test 2 likely was a result of residual tracer from tracer test 1.

Interval Permeability Assessment

Two series of HI step tests were performed before and after the tracer tests. The 4 min flow rates after each step are displayed in Figure 28. The graph shows that the flow rate at injection pressures between 20 and 30 bar does not exhibit a regular progression from step to step – sometimes increasing and sometimes decreasing at the same pressure. At 35 bar, the flow rate decreases from step to step during each series. The last HI step test (HI_step6) seems to represent the most stabilized flow rates with near-steady-state conditions (see yellow curve in Figure 29). In addition, at pressure of 35 bar, a cross-hole reaction can be observed in interval 7 and interval 8 confirming a connection to these intervals at higher pressures.

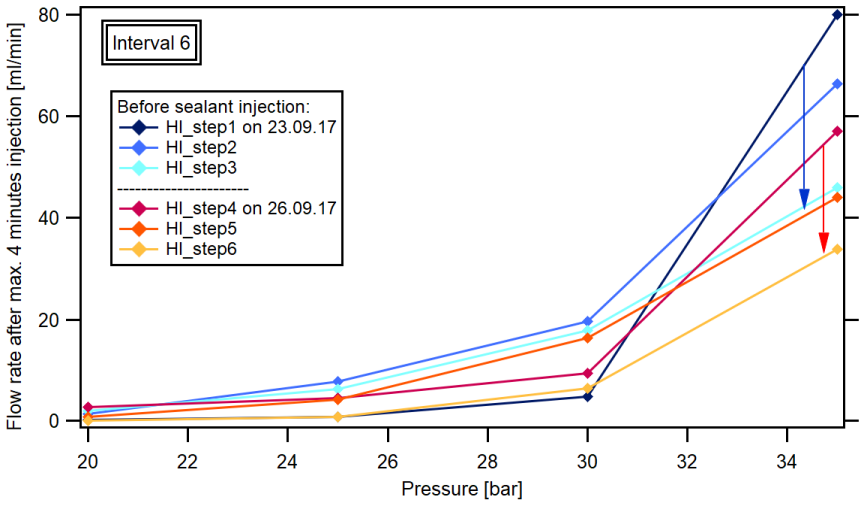

Figure 29. Flow rates vs. injection pressure for HI tests before sealant 1 injection in interval 6.

Sealant 1 Preparation

Before the injection, the batches of sealant 1 were mixed with type new-A3 Pearson water. The homogeneous suspension was injected into the interval by displacement with water using a syringe pump (Figure 30).

For the injection in interval 7, the initial plan was to mix multiple batches of sealant. However, this caused coagulation. Each batch was injected separately.

Sealant 1 Injection in Interval 6

On 26 September 2017, sealant 1 was injected into interval 6 by applying an injection pressure of 50 to 70 bar. A total of 736 ml of sealant was injected during the first batch. CO_2 was then injected for about 3 hours to reduce the pH and activate the sealant. HI tests following the gel activation yielded lower injection flow rates compared to tests before the sealant 1 injection. At 50 bar injection pressure a higher flow rate was obtained, indicating failure of the sealant at this high pressure.

A second batch of sealant 1 with smaller particles was injected in interval 6 immediately following the HI test. A total volume of 577 ml was injected at a maximum pressure of 60 bar. After the activation and pressurization of the interval with CO_2 to 20 bar, a pressure decrease of 2.6 bar was observed over a period of 15 hours, confirming the improved tightness of the interval.

Sealant 1 Performance in Interval 6

After the sealant 1 injection in interval 6, HI step tests were repeatedly performed until the end of the experiment to assess the long-term sealing performance of sealant 1. The 4 minutes flow rate vs. injection pressure results of the HI step tests are displayed in Figure 31. If multiple tests were performed in series, the medium flow rates are given for each test series. The major changes in the injection flowrates are indicated with arrows and the corresponding numbers.

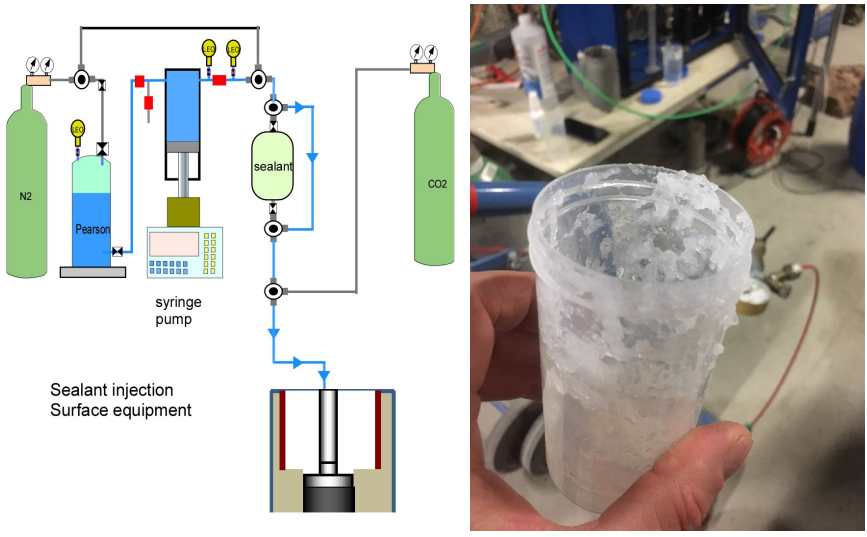

Figure 30. Layout of surface equipment for sealant injection (left) and bench test result (right).

1. Decrease of flow rates after the sealant 1 injection in interval 6 (Figure 32)
2. Increase in flow rates during long-term observation
3. Decrease of flow rates after sealant 2 injection in interval 5
4. Stable and low flow rates until the final resin injection

A first major decrease in flow rates in interval 6 occurred after the first sealant 1 injection in interval 6. After the second sealant 1 injection in interval 6, various injection tests were performed, including a long-term step performance test between 25 October and 10 November 2017. The first two steps at 20 and 30 bar injection pressures showed very low injection flow rates below 0.2 ml/min with only minor cross-hole reactions in the other intervals. During the last injection step at 40 bar, the injection flow rates immediately increased and the pressures in all other intervals also increased to about 36 bar, indicating partial failure of the sealant or possibly the creation of new flow paths. Even with the failure, the injection flow rates remained lower than before the sealant 1 injection and a residual sealing capacity remained.

After the sealant 2 injection in interval 5, the injection flow rates during the HI step test in interval 6 decreased considerably and remained at a low level until the final resin injection in December 2019.

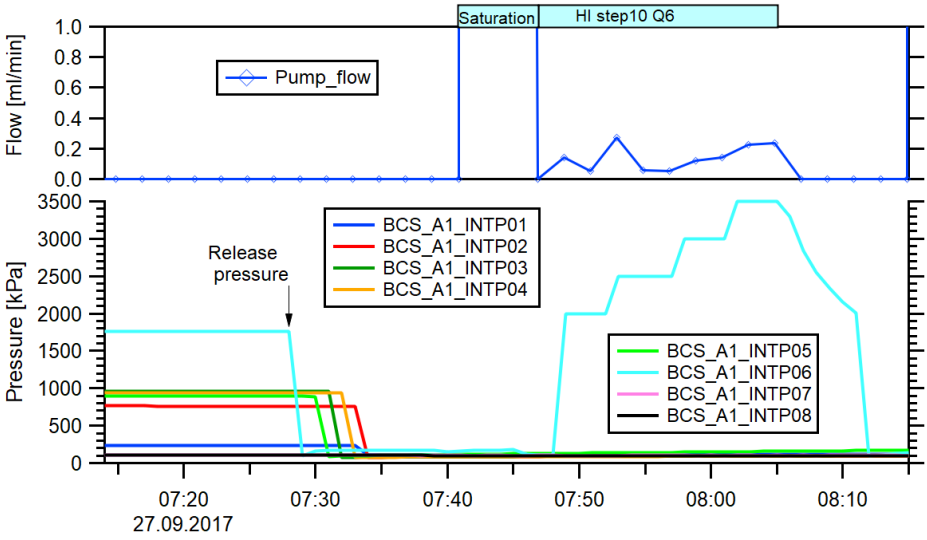

Figure 31. Example of HI step test performed on 27.09.2017 in interval 6.

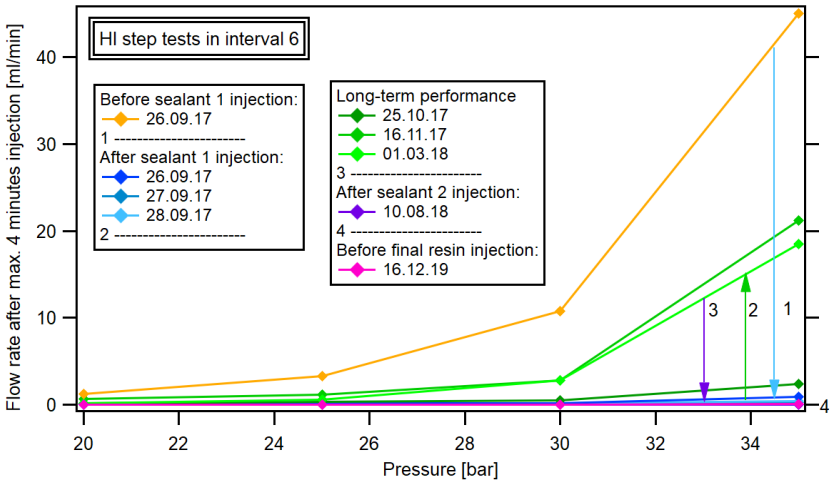

Figure 32. Flow rates vs. injection pressure for HI tests before and after sealant 1 injection in interval 6.

Sealant 1 Injection in Interval 7

Injection tests in interval 7 always yielded high injection flow rates and showed a good connection to interval 8. Before the injection of sealant 1, constant head injection tests were performed in interval 7, which required high flow rates of up to 200 ml/min at 4 bar injection pressure. The injection of sealant 1 in interval 7 started on 27 September 2017. A total of 4.25 l of sealant 1 were injected in 6 batches with a maximum injection pressure of 15.9 bar. Uranine was added to the first batch which was detected in interval 8 after 0.5 hours. Because of the stiffness of the sealant, the last four injections were made with a backpressure from the pressure vessel. After each batch, CO_2 was injected to activate the sealant.

Sealant 1 Performance in Interval 7

After the sealant 1 injection in interval 7, several HI tests were performed to assess the long-term performance of the sealant 1 in interval 7. The 4 minutes flow rate vs. injection pressure results of the HI tests are displayed in Figure 33. The flow rates before sealant 1 injection are not displayed as flow rates up to 200 ml/min were measured. On 29 September 2017, a long-term injection test was started in interval 7 with an injection of 7 bar. Flow rates as low as 0.5 ml/min were recorded at steady-state conditions. After about 3 days of injection, the flow rate started to increase to about 2.5 ml/min indicating a partial failure of the sealant in interval 7. However, the permeability at this point was considerably lower than before the sealant 1 injection.

The injection flow rates in interval 7 displayed in Figure 33 do not show a clear trend during and after sealant 1 injection. The last test yields higher flow rates at all injection pressures. As the permeability of interval 7 is generally higher compared to the other intervals, the HI step test protocol might not be adequate for this interval to estimate sealant performance, and the high flow rates might still be related to wellbore storage effects.

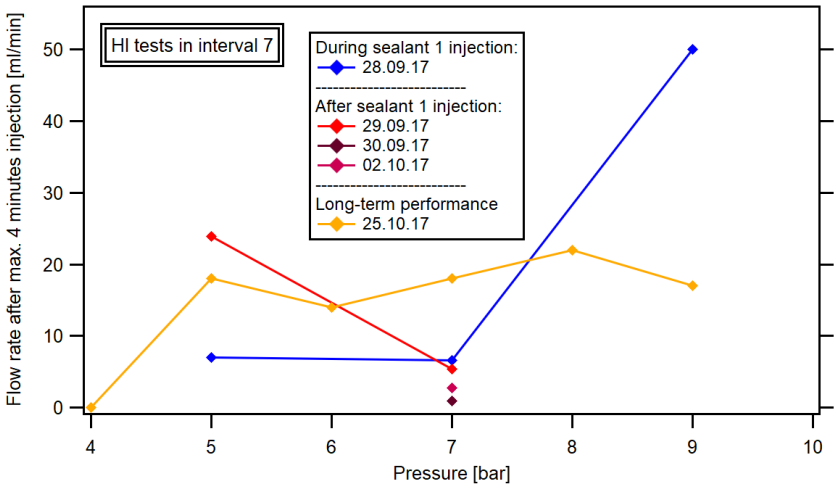

Figure 33. Flow rates vs. injection pressure for HI tests during and after sealant 1 injection in interval 7.

Summary

The sealant 1 injection in interval 6 reduced the permeability of the interval up to injection pressures of about 35 bar [14]. At higher pressures, the sealing partially failed, but still reduced flow rates into interval 6.

High injection flow rates were measured during the initial injection tests in interval 7. Because the flow paths in interval 7 created a high open volume, a large amount of sealant had to be injected. The permeability of the interval was considerably reduced up to injection pressures of about 7 bar. During the long-term injection test at 7 bar injection pressure, a partial failure of the sealant was observed.

Phase 16: Sealant 2

Sealant 2 was produced at the University of Texas at Austin for injection into interval 5. This phase of testing was conducted by Shayan Tavassoli with the support of Matthew Balhoff, both from the University of Texas at Austin. The details are described in [15].

Sealant 2 Description

Carbopol® 934, a polyacrylic acid polymer is supplied as a solid powder. The candidate sealant was an aqueous solution of 3 wt % Carbopol 934 in deionized (DI) water prepared on site.

A saturated aqueous solution of sodium triphosphate was used as a preflush to the sealant. The solution was prepared by adding powder to deionized (DI) water. Sodium triphosphate or chelating agent was injected prior to the sealant to prepare the environment for the sealant. The chelating agent was used to improve the tolerance of the sealant to hardness and salinity.

Site Preparation

The site preparation started on 15 February 2018. First, the remaining water and non-soluble gas (hydrogen), which might have remained in the system from the Mg-anode emplacement, were

removed from the intervals by vacuum extraction and injection of CO_2. Gas was extracted from all intervals except intervals 1 and 8. Interval 8 contained some foam, probably a remnant of sealant 1 injection in interval 7.

The site preparation included extended testing of all intervals in two test campaigns to evaluate the best interval for the injection of sealant 2. The following tests were performed between 15 February and 22 May 2018 in the intervals 2-6:

- HI step tests in all intervals: Four minutes of high injection flow rates (>15 ml/min) above 30 bar for interval 2 and 5 and above 35 bar for all intervals
- Interval 4: second test shows a breakthrough and a long-term injection flow rate of 10 ml/min at 30 bar
- Interval 3: long-term injection flow rate of 5 ml/min at 35 bar
- Interval 5: long-term injection flow rate of 17 ml/min at 35 bar
- Interval 2: Steady-state conditions with injection flow rate of 180 ml/min at 35 bar and same extraction flow rate from interval 1
- Interval 2: Steady-state conditions with injection flow rate of 26 ml/min at 20 bar and same extraction flow rate from interval 1

After this test series, MES-buffer was injected into interval 2 and interval 5 and left in the system overnight. On 23 May 2018, the following tests were performed:

- HI tests in interval 2 with constant injection flow rates at all pressure steps and a maximum flow rate of 113 ml/min at 30 bar
- HI step test in interval 5, medium flow rate of 30 ml/min at 35 bar

No change in the permeability was observed after MES-buffer injection in interval 2 and interval 5. Because of the immediate reaction of interval 1 on the injection in interval 2, interval 5 was considered to be better suited for the test of sealant 2.

Sealant 2 Preparation

Saturated aqueous solution of sodium triphosphate was prepared as the pre-flush chelating agent and 3 wt % aqueous solution of Carbopol® 934 as the sealant. Polymer powder was gradually mixed with distilled water and mixing was continued for 24 hours before polymer injection. A bench test was performed to test for the rheological behaviour (see Figure 34).

For the injection of sealant 2, the surface setup had to be modified. In addition to the syringe pump and the sealant vial, two piston tanks were used for the injection – one for the chelating agent and one for the sealant. An example layout for the sealant injection is given in Figure 35. The piston tank has a high-pressure limit of 38 bar. Therefore, a high-pressure tank, filled with 4.5 l silicone oil, was used to pressurize the Swagelok vial with the sealant at higher pressures.

Figure 34 Polymer gel samples: test sample (left in both images) and sample taken at the outlet (right in both images).

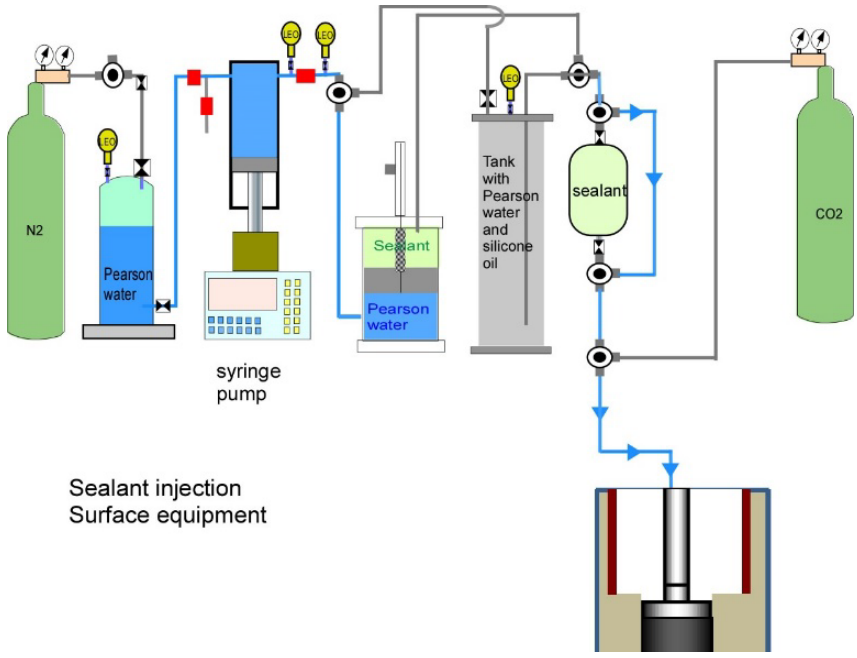

Figure 35. Layout of surface equipment for sealant 2 injection.

Sealant 2 Injection in Interval 5

On 28 May 2018, the injection of sealant 2 was started. The following procedure was applied:

- Saturation of interval 5 with chelating agent with injection in the Q line and extraction from the P-line, controlled based on decreasing pH.
- Injection of a total volume of 3.319 l of chelating agent in interval 5 up to pressures of 50 bar on 28 May 2018
- Saturation of the interval with sealant with injection in the Q line and extraction from the P-line, controlled based on pH and viscosity.
- Injection of a total volume of 1.100 l of sealant 2 in interval 5 up to pressures of 60 bar on 29 May 2018. The final injection flow rate was 25 ml/min. A breakthrough occurred at 60 bar followed by a slight pressure decrease.

Sealant 2 Performance in Interval 5

Eight injection tests were conducted in interval 5 between 30 May and 10 August 2018 to test the performance of sealant 2. Figure 36 is a plot of the 4-minute flow rate versus injection pressure for the HI tests. If multiple tests were performed in series on the same date, the median flow rate is used for each test series. The major changes in the injection flowrates are indicated with arrows and the corresponding numbers.

1. Decrease of flow rates after the sealant 2 injection in interval 5
2. Increase of flow rates during long-term observation
3. Reduced flow rates before the final resin injection

For the initial HI step tests, the maximum flow rates were about 4.2 ml/min at 35 bar. No cross-hole reactions were observed in the other intervals. Long-term injection tests were successfully conducted at 35 bar with a final steady-state flow rate of 3.2 ml/min and at 30 bar with a final steady-state flow rate of 0.11 ml/min. This long-term HI test at 30 bar, which lasted for 11 days, showed considerable cross-hole reactions in all intervals, most pronounced in the intervals 6, 7 and 8.

A CO_2 injection test on 30 May 2018 showed a slow pressure decrease of 3 bar in 16 hours. After two months on 27 August 2018, the CO_2 test was repeated and showed a faster pressure decrease of 21.4 bar in 10 hours.

During the baseline test campaign before the sealant 3 injection in interval 4, a further HI step test was performed in interval 5 which produced slightly higher flow rates of 15 ml/min at 35 bar injection pressure. These flow rates are lower than the initial flow rates before sealant injection.

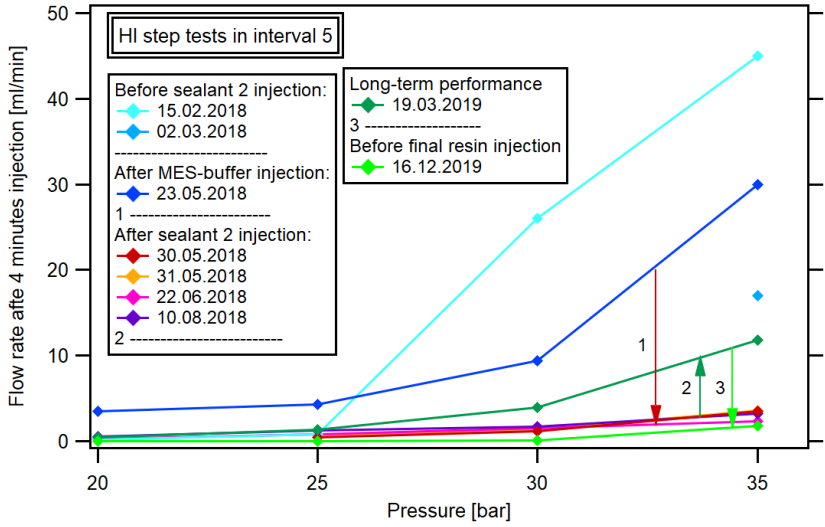

Figure 36. Flow rates vs. injection pressure for HI tests during and after sealant 2 injection in interval 5.

Post-sealant 2 Bench Test with Silicone Oil

A post-sealant bench test at higher pressures than the injection tests was conducted with the surface equipment used for the injection of sealant 2 using a high-pressure vessel filled with silicone oil. The aim was to test the fluid interaction, especially regarding possible mixing processes, of the silicone oil and the sealant during injection into a glass jar. The same injection pressure steps were applied as had been used for the formation injection tests. After the injection of about 740 ml of sealant 2, single bubbles of silicone oil could be observed at the extraction side. Finally, only silicone oil was extracted. The cleaning of the Swagelok vial revealed substantial remnants of sealant 2, indicating that silicone oil by-passed the sealant in the vial towards the end of the sealant injection. See Figure 37 illustration of the Sealant 2 injection cycle. Sealant injection was performed using a 1-2-4-s-w configuration, where polymer was pushed from the top by viscous silicon oil (100 cp) in the Swagelok accumulator, which fed into the wellbore [20].

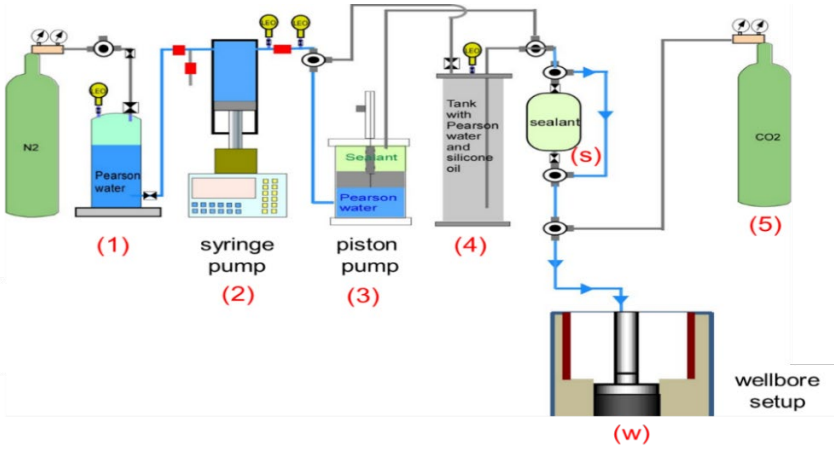

Figure 37. Fluid injection setup including a refill tank (1), syringe pump (2), piston pump (3), high-pressure tank (4), Swagelok vial (4), CO_2 tank (s), and connection to wellbore setup (w) [20].

Summary

The sealant 2 injection in interval 5 was successfully performed and the permeability of the interval was reduced up to injection pressures of about 35 bar. No tests were performed at higher pressures to avoid failure of the sealant as observed for the interval 6 post-injection testing.

We conclude that the sealant performed well in the fracture environment of interval 5 up to a fluid pressure of 35 bar for a short period and up to a pressure of 30 bar for a longer period [15]. For a period of at least 3 months, no changes in the interval behaviour could be observed, and the same low injection flow rates were measured. After about 10 months, the injection flow rates at 30 and 35 bar were higher and might indicate a slightly reduced sealing capacity of sealant 2.

However. the degree to which the sealant performance was negatively affected by silicone oil pumped together with the sealant into the interval cannot be assessed at this stage. The analysis of the drill core after the overcoring of the experiment might reveal further details.

Phase 17: Sealant 3

Sealant 3 for injection in interval 4 was developed at IFPEN in the framework of the MiReCOL project. This phase was conducted by Marc Fleury from the IFPEN.

Sealant 3 Description

The MiReCOL project [16], is aimed at developing corrective measures for leakage from CO_2 storage. Within the scope of the project, IFPEN developed a sealant using alkaline silicate solutions which form a gel after addition of an acid in appropriate strength and quantity [17].

The challenge for the Mont Terri application was to find a formulation for which the gelling time was tuneable so that the solution could be prepared at the surface and injected into the formation before gelling. This class of product compared to polymers and suspensions has several fundamental advantages:

- The initial solution before gelling does not contain any particles and has a viscosity close to water.
- After gelling, it is inherently stable for pH < 9 and this is obviously of interest for CO_2 application; silica particles are formed, sticking to solid surfaces (including metal) and plugging the porous media.
- An external activation inside the formation is not needed.

If CO_2 is in contact with the sealant, it will react rapidly and possibly reinforce the plugging, since it will lower the pH and might form solid carbonates within the gel by reacting with the cations of the injected sealant solution.

The initial silicate solution has a pH of about 12, which is then lowered to about 11.5 by adding acid. The acid addition triggers a further decrease of pH down to about 11. However, since the interstitial water of the cement has a pH greater than 13, a back-dissolution of the sealant cannot be excluded for the CS-A completion.

Site Preparation

The site preparation started on 18 March 2019. In a first step, water was extracted, and samples were obtained from intervals 2, 3, and 4 and type MES-new-A3 Pearson water was injected in these intervals. In a second step, the MES-buffer was extracted from the same intervals, followed by flushing with type new-A3 Pearson water. Then, the intervals were characterized by performing HI step tests with interval 1 open. The following tests were performed between 19 and 26 March 2019 in the intervals 2, 3, and 4 (See Figure 38):

- Four HI step tests in interval 4
- CO_2 injection test in interval 4 with a pressure of 24 bar
- One HI step test in interval 3 and interval 2

The HI step tests in interval 4 gave similar injection flow rates for the steps up to 35 bar. At 40 bar injection pressure, the flow rates suddenly increased starting from the third test because of a probable opening of flow paths. Interval 4 was chosen for the injection of sealant 3.

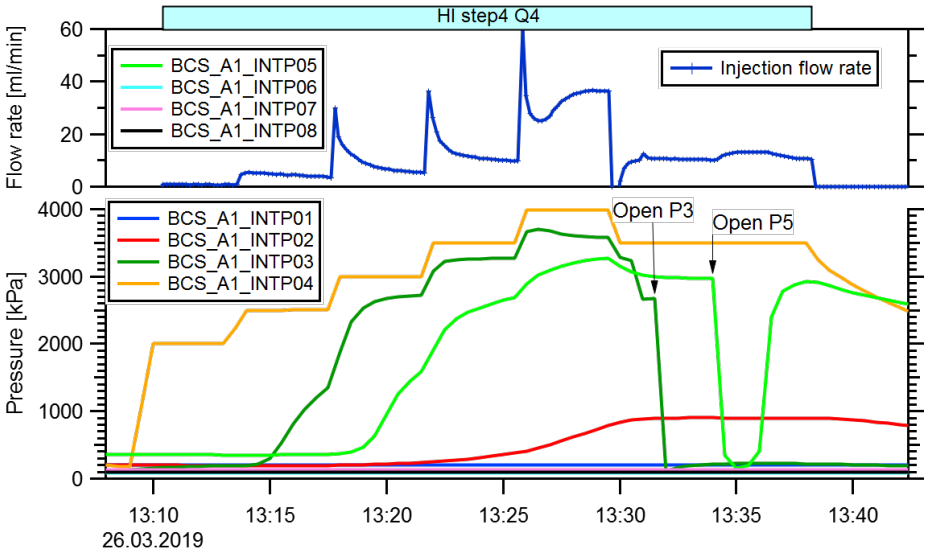

Figure 38. HI step test on 26.03.2019 before sealant 3 injection in interval 4.

Sealant 3 Preparation

An ISCO pump from IFPEN was used for the injection of the sealant 3. Preparation of sealant 3 entailed mixing potassium silicate solution appropriately diluted with water and a small amount of acetic acid using an electromagnetic stirrer.

Before gelling, the solution behaves as a simple liquid with a viscosity close to water; after gelling it cannot be pumped and can plug the injection lines. The composition of the mixture was adjusted so that the gelling time was a minimum of 4 hours after mixing was completed. Immediately after mixing, the pump was filled with the reactive solution and injection into the interval was started.

For all batches, a reference sample was taken from the pump and placed in a plastic container to observe the effective gelling of the injected solution.

Figure 39 shows the behaviour over an extended time of the second batch of sealant 3 in a plastic container. A gradual increase of a supernatant fluid expulsed from the initial uniform nanoporous structure can be observed. This syneresis effect is due to slow chemical substitutions transforming the relatively soft gel with good sealing capacity into a harder gel with potentially weaker performance. Figure 40 shows the same batch of sealant 3 placed in a glass container. There, the gel sticks to the surface of the container and the syneresis effect cannot easily be observed. These observations indicate that the exact behaviour of the gel in the borehole completion is not well known.

For the third injection, the formulation was modified to limit the syneresis effect. The amount of acid was changed to maintain a large enough gelling time.

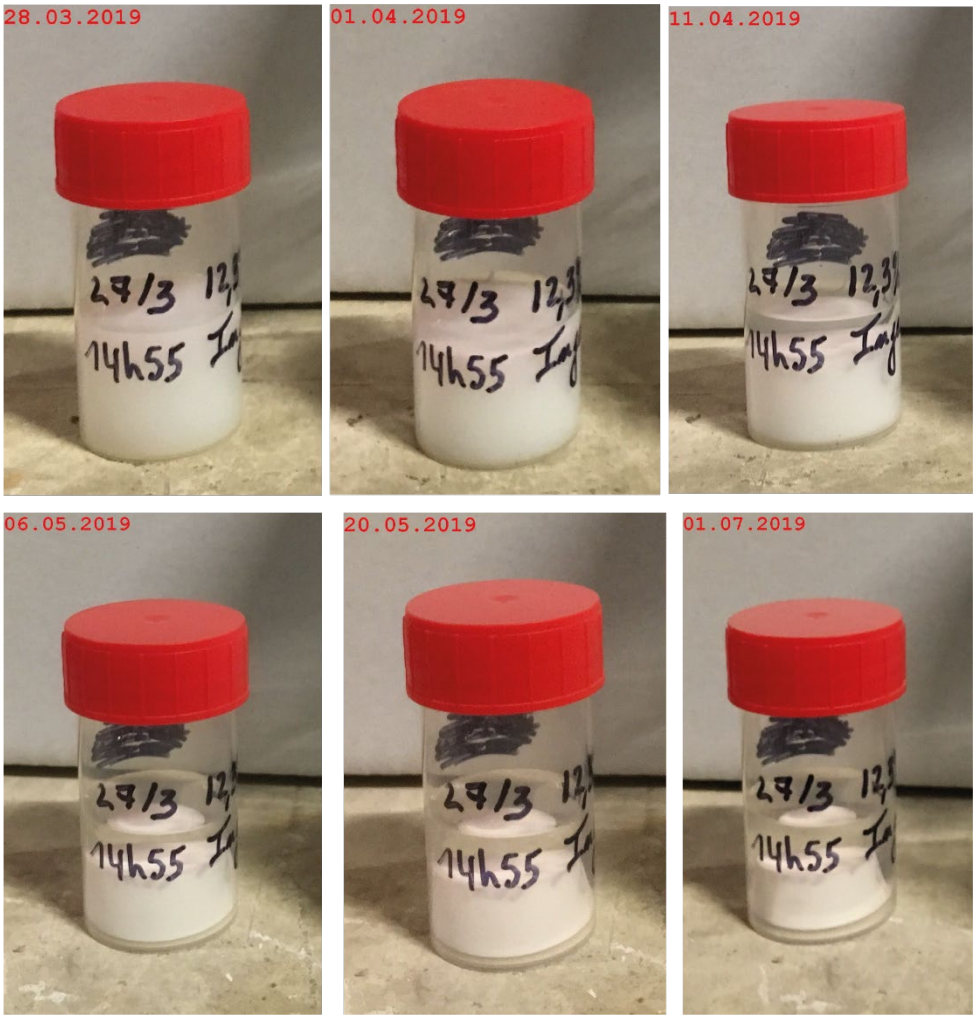

Figure 39. Development of reference sample over time in a plastic container.

Figure 40. Development of reference sample over time in a glass container.

First Sealant 3 Injection in Interval 4

On 26 March 2019, a first batch of sealant 3 was injected into interval 4 by applying a back pressure of maximum 45 bar. A total of 842 ml of sealant 3 was injected. Immediately after the injection of sealant 3, interval 3 and interval 4 were flushed by circulating type new-A3 Pearson water through the P and Q lines until the dead volume was exchanged two to three times.

Performance Test after First Injection of Sealant 3 in Interval 4

Two HI step tests were conducted in interval 4 which produced flow rates similar to those observed prior to the sealant 3 injection. A good cross-hole reaction was observed for interval 5, but no cross-hole reaction was observed for interval 3. As the reference sample did not show any gelling, it was assumed that the sealant 3 preparation was affected by an error and that the batch of sealant 3 did not gel after injection.

Second Sealant 3 Injection in Interval 4

On 27 March 2019, a second batch of sealant 3 was injected into interval 4 by applying a back pressure of maximum 55 bar. A total of 535 ml of sealant 3 was injected. Immediately after the injection of sealant 3, interval 4 was thoroughly flushed and a HI step test was performed in interval 3 to remove any sealant.

Performance Test after Second Injection of Sealant 3 in Interval 4

Six HI step tests were conducted in interval 4 over a period of one month and one additional test after three months. The tests initially showed very low flow rates and no cross-hole reaction. Then the flow rate continuously increased and cross-hole reactions started at the 35 bar pressure step – first only in interval 3 and then also in interval 5 and to a minor extent in interval 2.

The 4 minutes flow rate versus injection pressure results of the HI step tests are displayed in Figure 41. The major changes in the injection flowrates are indicated with arrows and described by the following numbered points:

1. Decrease of flow rates after the second sealant 3 injection in interval 4
2. Continuous increase in flow rates during long-term observation

The normalized ΔP/q values of the final long-term 35 bar pressure steps versus the elapsed time after the second injection are displayed in Figure 42. The decreasing slope of the curves with time indicate increasing permeability around interval 4 with time.

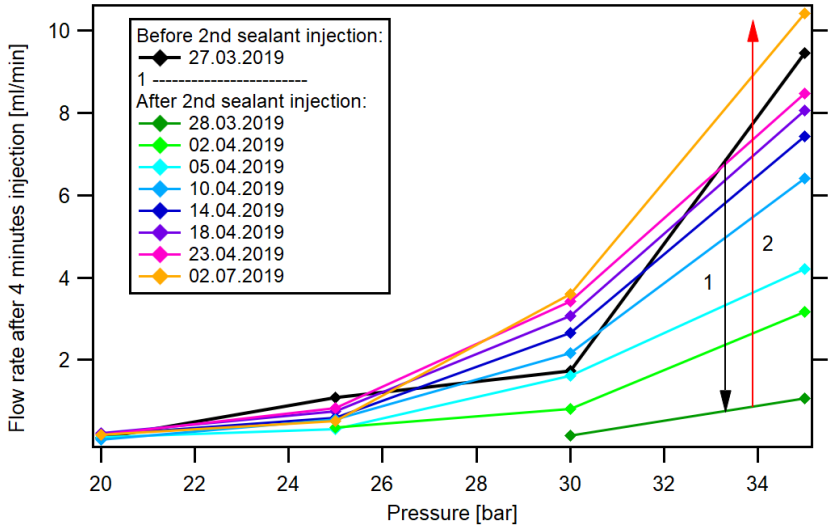

Figure 41. Flow rates vs. injection pressure for HI tests before and after second sealant 3 injection in interval 4.

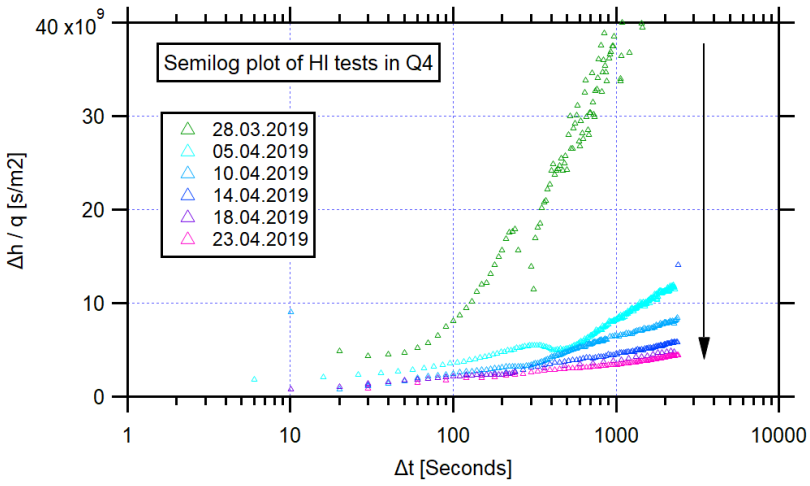

Figure 42. ΔP/q vs. elapsed time in a semilog plot for 35 bar HI steps after second sealant 3 injection in interval 4.

Third Sealant 3 Injection in Interval 4

Due to the decreased extent of sealing observed after the second sealant 3 injection between 28 March and 2 July 2019, a third injection of a modified formulation of sealant 3 was performed in interval 4 on 2 July 2019. A total of 340 ml of sealant 3 was injected at a maximum backpressure of 50 bar. Immediately after the injection of sealant 3, interval 4 was thoroughly flushed and a HI step test was performed in interval 3 to remove any sealant.

Performance Tests after Third Injection of Sealant 3 in Interval 4

Four HI step tests were conducted in interval 4 over a period of two months and one additional test after five months. The tests initially showed very low flow rates of 0.16 ml/min at 35 bar injection pressure and no cross-hole reaction (Figure 43). Then the flow rates increased, and cross-hole reactions were observed at the 35 bar pressure step, first only in interval 5 and then also in interval 3 and to a minor extent in interval 2.

The major changes in the injection flowrates in Figure 44 are indicated with arrows and described by the following corresponding numbered points:

1. Decrease of flow rates after the third sealant 3 injection in interval 4
2. Increase of flow rates during long-term observation
3. Reduced flow rates before the final resin injection

For some of the HI step tests, longer 35 bar steps were recorded which could be evaluated as HI tests to estimate an approximate transmissivity. For two tests, the pressure recovery could be displayed in a diagnostic plot.

Figure 45 shows the increase of the transmissivity after the second and third sealant 3 injection, determined from the long-term pressure steps of the HI step tests at 35 bar. Figure 46 displays a log-log diagnostic plot of the pressure recovery, where 1/2 unit slope can be observed for both the pressure and the derivative curve, indicating linear flow (flow model: infinite conductivity fracture).

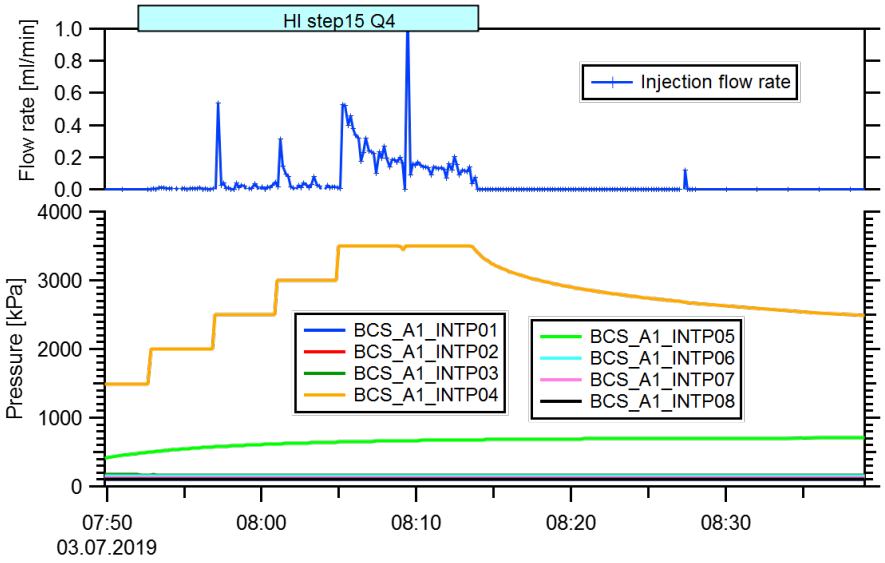

Figure 43. HI step test after third sealant 3 injection in interval 4.

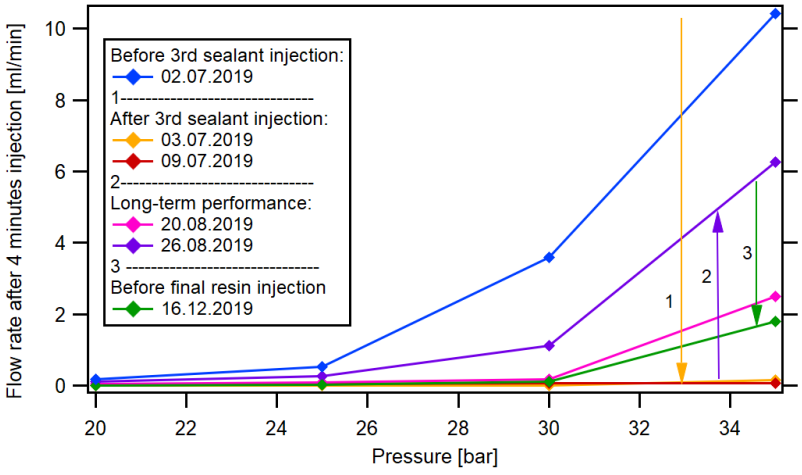

Figure 44. Flow rates vs. injection pressure for HI tests before and after third sealant 3 injection in interval 4.

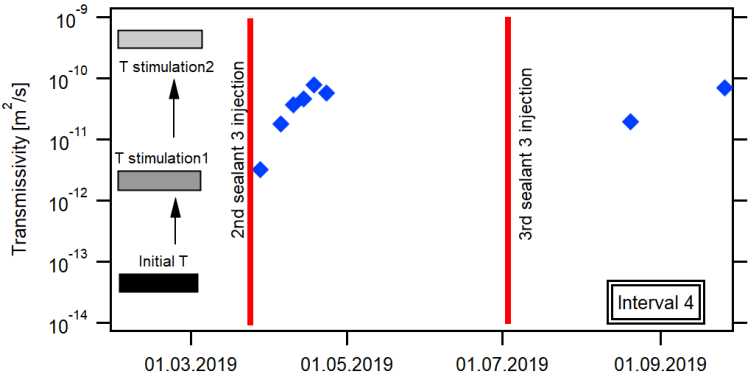

Figure 45. Changes in transmissivity of interval 4 after the second and third sealant 3 injection. In grey: transmissivities determined in 2016/2017 before and after stimulation.

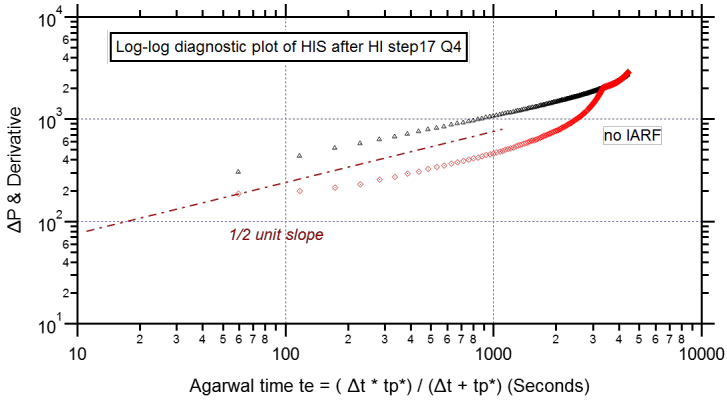

Figure 46. Diagnostic plot of recovery phase after a HI step test on 20.08.2019 in interval 4.

Performance Tests in Interval 3

Before and after each sealant 3 injection in interval 4, interval 3 was tested by a HI step test. This was also necessary to remove remnants of sealant 3 after each sealant injection because of the increased cross-hole reaction and the good connectivity between interval 4 and interval 3. The HI step tests show a continuous decrease of the injection flow rates up to an injection pressure of 35 bar, as shown in Figure 47. The two test steps of 40 bar indicate a fracture opening at this pressure step.

The major changes in the injection flowrates in Figure 47 are indicated with arrows and described by the following corresponding numbered points:

1. Decrease of flow rates after first sealant 3 injection in interval 4
2. Decrease of flow rates after second sealant 3 injection in interval 4
3. Decrease of flow rates after third sealant 3 injection in interval 4

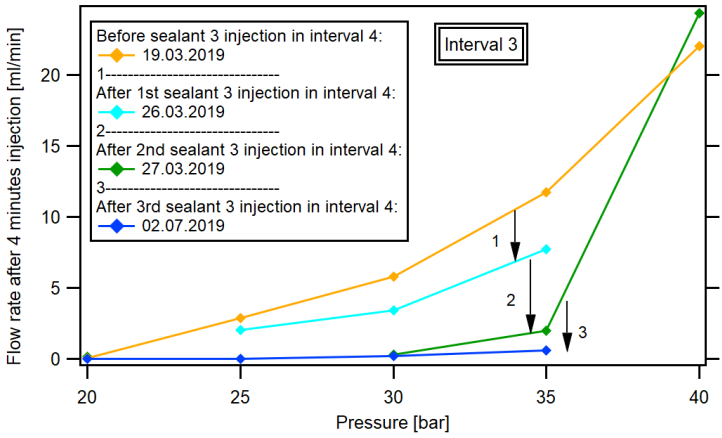

Figure 47. Flow rates vs. injection pressure for HI tests in interval 3 before and after sealant 3 injection in interval 4.

Summary

The sealant 3 injection testing in interval 4 included three sealant injections. No sealing could be observed after the first sealant 3 injection, which was attributed a lack of gelling by the sealant due to a possible preparation error. After the second sealant injection, the initial tests showed a good sealing performance of sealant 3. However, increasing flow rates with increasing time span from the sealant injection were observed, together with increasing transmissivities determined from the last 35 bar long-term HI injection step. This indicates possible ongoing decrease of the sealing capability with time. The reduction of sealant performance over time is suspected to be the result of syneresis effects with a potentially unknown contribution from sealant destabilization due to high pH cement water. The syneresis effect was unambiguously observed in the reference samples.

After a third sealant injection with a modified formula, an even better sealing could be observed with very low initial flow rates, but also with a slow increase of the injection flow rates and the transmissivities. The log-log diagnostic plots of the pressure recoveries after the HI step tests in interval 4 indicate a flow model with the main flow paths along fractures (well model: infinite conductivity fracture).

Generally, we concluded that the modified sealant composition performed rather well in the fracture environment of interval 4 up to a fluid pressure of 35 bar.

The low injection flow rates in interval 4 before the final resin injection are probably related to the reduction of the permeability in the borehole completion because of sealant 4 injection in the intervals 3 and 2.

A connectivity from interval 4 seems to exist with interval 3 and interval 5. Interval 5 each time showed a continuous pressure increase followed by a slow pressure decrease, which was much slower than that observed in the injection interval 4. This could be related to the opening of fractures at the 35 bar pressure step, which closed again during the pressure decrease in interval 4, such that the pressure in interval 5 could not be released.

The following observations relate to the connection between interval 4 and interval 3:

- Mostly good cross-hole reaction in interval 3 during the 35 bar injection steps after the second sealant 3 injection
- Decrease of injection flow rates in interval 3 after each sealant 3 injection in interval 4

Phase 18: Sealant 4

Sealant 4 is a polymer-based sealant engineered using nanotechnology developed at the University of New Mexico [18]. The sealant is designed to be applied at a wide range of temperatures (10-110°C) and is designed to penetrate, flow and seal very thin microcracks (below 30 micrometers).

Site Preparation

The site preparation started on 21 August 2019. First, water was extracted, and samples were obtained from intervals 2 and 3, and type MES-new-A3 Pearson water was injected into these intervals. Next, the MES-buffer was extracted from the same intervals by CO_2 injection, and the intervals were saturated with type new-A3 Pearson water. Then, the intervals were characterized by performing HI step tests with interval 1 open. The following tests were performed between 22 and 26 August 2019 in the intervals 2 and 3:

- Two HI step tests in interval 3 with injection pressures up to 40 bar
- One HI step test in interval 2 up to 35 bar

The HI step tests in interval 3 resulted in high injection flow rates up to 84 ml/min at 40 bar injection pressure and immediate cross-hole reactions in interval 4 at 35 bar. The flow rates in interval 2 at 35 bar reached the upper limit for the injection flow rate (150 ml/min).

Sealant 4 Preparation

Sealant 4 consists of a two-part liquid (Part A & Part C) and one-part powder (Part B). Part A was cooled to design temperature to slow down the polymerization process, and then weighed. Part C was also cooled and weighed. Part C was added to Part A and mixed for one minute with a handheld mixer at medium speed. Part B (powder) was weighed and added to the liquid mix of A & C, followed by mixing for one additional minute at high speed. The sealant was then injected. The same procedure was followed for all the injections.

Sealant 4 Injection in Interval 3

Sealant 4 was injected using a piston tank with a water back-pressure from the syringe pump (Figure 48). Sealant 4 injection was started on 28 August 2019 by circulating the sealant through interval 3. The extraction line was then closed, and a stepwise increase in injection pressure was imposed. A total volume of 1367.88 ml was injected at a maximum back pressure of 65 bar. Immediately after the injection of sealant 4, interval 3 was thoroughly flushed. On 28 August 2019, an attempt was made to test interval 3 with an HI step test. However, no water could be injected into or extracted from both P and Q lines. To mitigate the blockage, toluene was injected at 95 bar for several hours. No reaction was observed in interval 3 upon this injection and the sealant in the lines could not be removed.

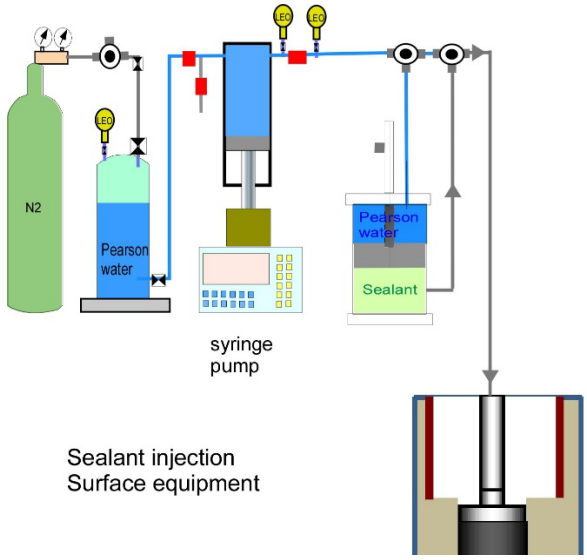

Figure 48. Schematic layout of surface equipment for sealant 4 injection in intervals 3 and 2.

Performance Tests in Interval 3

Because of the clogged lines, no performance tests could be performed in interval 3 after sealant 4 injection. The flow rates of the HI step tests during sealant 3 injection (see also Figure 47) and after MES-buffer injection are displayed in Figure 49. The major changes in the injection flowrates are indicated with arrows and described by the following corresponding numbered points.

1. Decrease of flow rates during sealant 3 injection in interval 4
2. Increase of flow rates after MES-buffer injection in interval 3

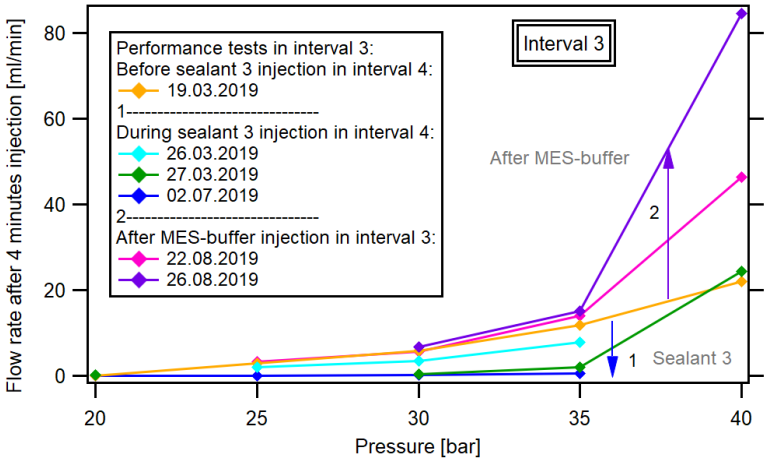

Figure 49. Flow rates vs. injection pressure for HI tests in interval 3 before and after MES-buffer injection.

Sealant 4 Injection in Interval 2

After the complete clogging of the lines to interval 3 by sealant 4, the decision was made to test this sealant by injecting it into interval 2. Previously, a very good connection between interval 2 and interval 1 was observed because of the short distance between the two intervals of 0.105 m.

Sealant 4 injection in interval 2 started on 28 August 2019 with stepwise increases of the injection pressure. A total volume of 648.8 ml was injected at a maximum backpressure of 55 bar. After the injection of about 75 ml, interval 1 started to react and the injection volume flow increased. Finally, the same pressure was measured in both intervals.

Immediately after the injection of sealant 4, interval 3 was thoroughly flushed and a small amount of solvent was circulated in the lines to prevent clogging of the interval access lines.

Performance Tests after Injection of Sealant 4 in Interval 2

Three HI step tests were conducted in interval 2 with interval 1 port open over a period of about one month. The tests initially showed reduced flow rates during step-rate testing of 9.35 ml/min at 35 bar injection pressure and no cross-hole reactions. Afterwards, the step-rate flow rates increased, without any cross-hole reaction because of interval 1 connectivity.

The major changes in the injection flowrates in Figure 50 are indicated with the arrows and the corresponding numbers:

1. Decrease of permeability after the sealant 4 injection in interval 2
2. Increase in permeability during long-term observation

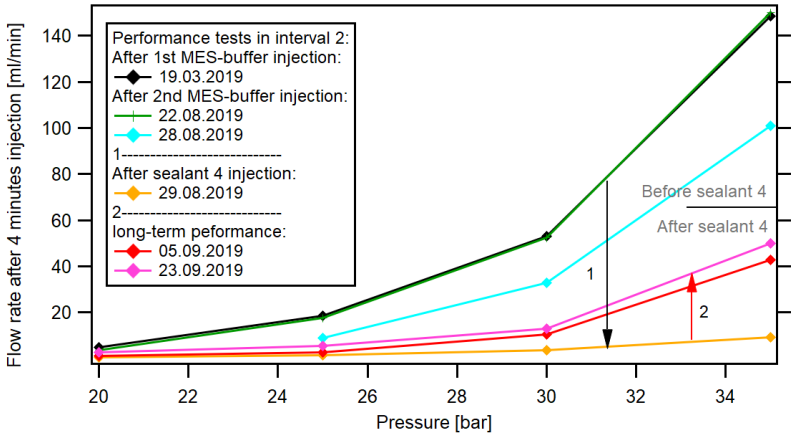

Figure 50. Flow rates vs. injection pressure for HI tests in interval 2 before and after sealant 4 injection.

Summary

Although sealant 4 was successfully injected into interval 3 [19], the interval 3 lines became clogged despite extensive water flushing. Efforts to dislodge the sealant from the lines were not successful, so no further testing on interval 3 could be performed.

To obtain data on sealant 4, the decision was made to inject into interval 2. In preparation, interval 2 was thoroughly flushed with MES-buffer. This considerably increased the flow rates into interval 2 and the connection towards interval 1, as the distance between these two intervals is only 0.105 m.

Sealant 4 injection into interval 2 showed good sealing capability immediately after sealant injection. However, after about one week, pulse testing showed an increase of the injection flow rates, and a noticeable decrease of the sealing capacity was observed. Potential reasons might be:

- Gradual hardening of the sealant increased the material stiffness, which cracked to open flow paths at a high injection pressure.
- A gradual minimal shrinkage of the sealant after emplacement during solidification could compromise sealing.
- Opening of new flow paths at pressures of 35 bar due to the sealing of the pre-existent ones.

Generally, similar to interval 7 connectivity to interval 8, the sealing of interval 2 seems to be a challenge due to the short flow path to interval 1.

POST-SEALANT INJECTION HYDRAULIC CONNECTIVITY–PRELIMINARY VIEW

Phase 19:

A final test campaign was conducted between 26 September and 16 December 2019 to assess the hydraulic parameters in the borehole completion after injection of sealant. One pulse injection test and seven constant head injection tests were conducted.

Testing and Analysis Methods

One pulse injection test (PI) and seven constant head injection tests (HI) were conducted to characterize the near-field around intervals and I/P modules. For the pulse injection test, type new-A3 Pearson water was injected in interval 5 with the syringe pump for less than one minute with a differential pressure of about 5 bar. Then, the pressure recovery was recorded and analysed. Constant head injection tests (HI) could be performed in all intervals except for interval 3 and interval 7. Type new-A3 Pearson water was injected in these intervals with an injection pressure of between 10 and 20 bar for a period of 1 and 11 days, respectively (Figure 51). Afterwards, the pressure recovery was recorded. From these tests, the cross-hole reactions in the other intervals could be analyzed. In addition, the pressure recovery yielded some information on the possible flow model.

The analysis methods are the same as described for Phase 3.

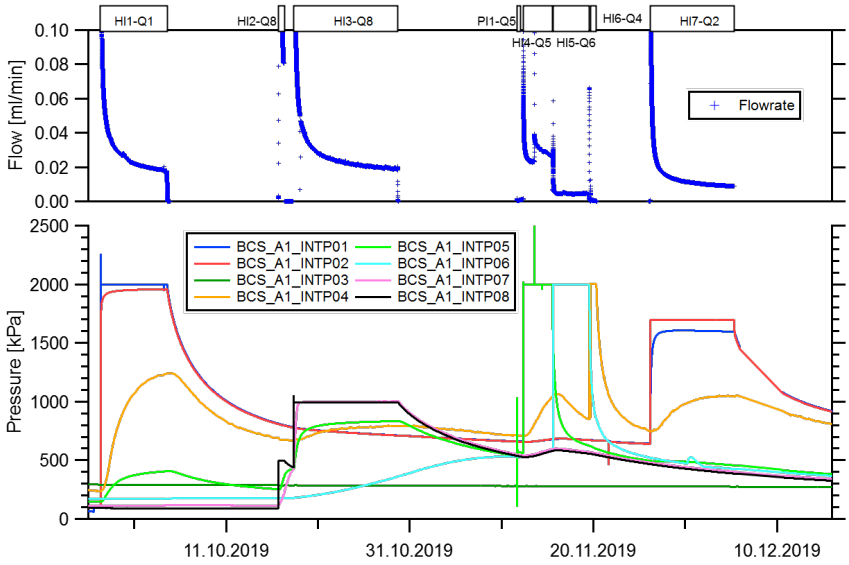

Figure 51. Pressures and flow rates measured during the HI/PI tests during the final hydraulic tests.

Transmissivity Distribution along the Borehole

The transmissivities determined by the hydraulic testing vary between 1E-12 and 4E-14 m^2/s (Figure 52), which correspond to approximate hydraulic conductivity values between 5E-12 and 3E-13 m/s (6.3E-07 and 3.0E-08 Darcy). The highest transmissivities are determined for interval 8 and 5, and the lowest for interval 4. The pulse injection test PI1-Q5 in interval 5 gives an even higher transmissivity of 1.5E-11 m^2/s, which might represent interval-near conductivity from cement sheath fracturing during heat cycling.

The final transmissivity determined for intervals 1 and 8 is 5E-13 and 1E-12 m^2/s, which is about two times lower than the transmissivity determined during the hydraulic testing 1 before the stimulation of the borehole completion. A first HI injection test in interval 8 yielded much higher flow rates and indicated a possible linear no-flow boundary. This might be related to decreasing transmissivities with increasing distance from interval 8 along the borehole completion.

The result for interval 2 is similar to interval 1 confirming the good connection between both intervals.

The pressure recoveries after the HI tests normally show an initial unit slope for both the pressure curve and the derivative, indicating wellbore storage. The pressure recoveries from the test in interval 4 and the second test in interval 8 are wellbore storage dominated and do not show an infinite-acting radial flow (IARF) phase. The pressure recovery after the test in interval 5 shows a ½ unit slope for both the pressure curve and the derivative, which might indicate the presence of linear flow (well model: “infinite conductivity fracture”). This might be related to a linear flow path at a certain distance from interval 5. The late-time transmissivity is similar to the one determined for interval 8.

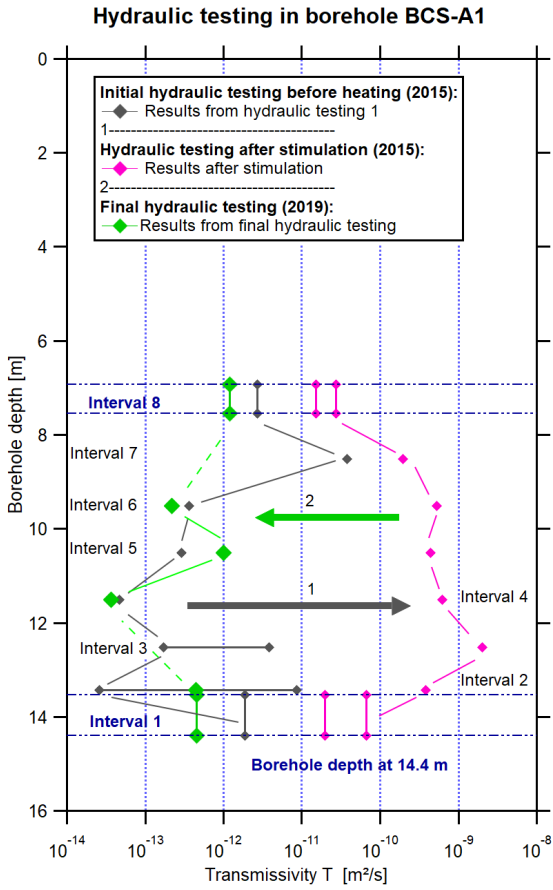

Figure 52. Transmissivity vs. borehole depth after hydraulic testing 4 compared to the previous hydraulic test campaigns.

The pressure recovery for the interval 2 test shows two possible IARF phase with an initial higher transmissivity of 6.9E-12 m^2/s and a late-time transmissivity of 3.5E-13 m^2/s. The later corresponds to the transmissivity determined for interval 1. The higher early-time transmissivity might describe the zone between interval 2 and interval 1.

Figure 51 shows the major changes since the hydraulic testing 1 in the borehole completion, marked with arrows and the corresponding numbers:

1. Increase of transmissivity due to the stimulation by heating
2. Decrease of transmissivity due to sealant injection in all intervals (I/P modules)

Additional Performance Tests in the Intervals

Before the final resin injection [19], five HI step tests were conducted in the intervals 1, 4, 5, 6, and 8. Interval 1 interestingly showed an unusual behaviour, with a slow pressure increase together with a steadily decreasing flow rate (Figure 53). This was attributed to remnants of different sealants,

accumulated in interval 1 during the sealant 4 injections, which considerably increased the compressibility of this part of the system, which reacts elastically on an injection test. Note sealant 4 was injected as a sealant and also as for use as a well system consolidation polymer prior to overcoring.

The 4-minute flow rates are displayed in Figure 53. Interval 6 was found to be rather tight whereas intervals 4 and 5 showed increased flow rates at 35 bar injection pressure. The 4-minute flow rates in intervals 1 and 8 are not representative because of the high interval volume compared to other intervals and which is reflected by correspondingly high wellbore storage. Interval 8 injection flowrates in the first minute were as high as 200 ml/min.

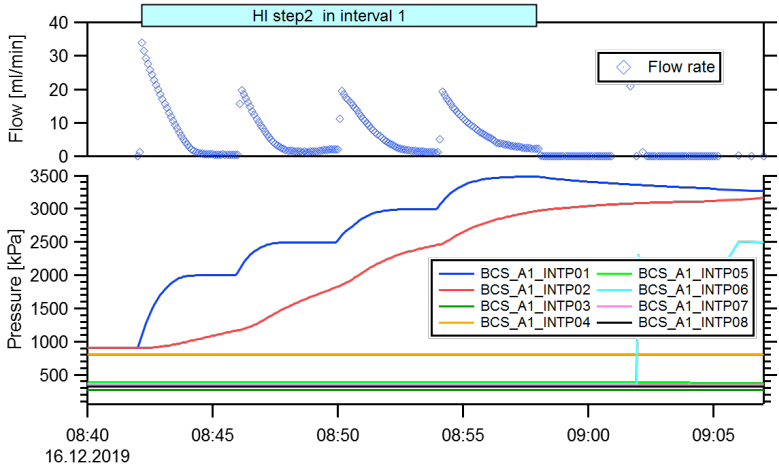

Figure 53. Final HI step test in interval 1.

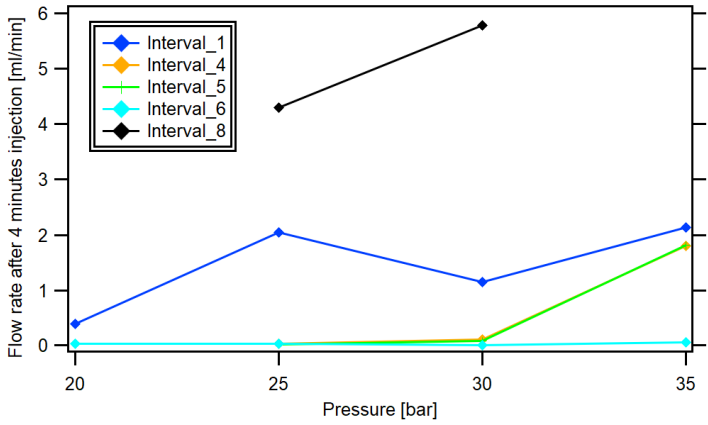

Figure 54. Flow rates vs. injection pressure for final HI step tests in the given intervals.

Summary

The final hydraulic testing showed that the transmissivities in all intervals decreased by one to four orders of magnitude since the stimulation of the borehole completion. The transmissivities observed for the lowermost and uppermost intervals 1 and 8 were below the initial transmissivities determined directly after system installation and saturation. The transmissivities in the other intervals were mostly similar to the initial ones. Unfortunately, no tests were performed in interval 3 and 7, due to clogging. Only minor cross-hole reactions were observed.

The hydraulic testing 4 revealed good sealing of the entire borehole completion after the injection of sealants 1 to 4. All intervals yield transmissivities similar to the ones for the Opalinus Clay. Possibly the sealant injection into the cement closed all the flow paths and the flow in the host rock dominated the hydraulic tests. No fracture flow was observed in the analysis of the pressure recoveries and only interval 8 and interval 2 showed two distinct transmissivities. In interval 8, this is related to the reduced sealing and high transmissivity towards interval 7. Interval 2 showed an excellent connection to interval 1.

SITE PREPARATION FOR OVERCORING

Phase 20:

The final resin injection was conducted with sealant 4 with the desire of consolidating the entire wellbore site before overcore drilling. Prior to resin injection, a very flowable cement slurry was injected into Interval 1 on 16 December 2019, with the aim of consolidating the lower uncased interval. A cement bentonite mixture was used. On 17 December, the final resin injection was initiated. Sealant 4 was injected in intervals 1, 2, 4, 5 and 6 with a backpressure of 40 bar. Interval 7 was not filled with resin between interval 7 and interval 8 for the later attempt to remove packer 1 from the borehole completion.

OPEN QUESTIONS AFTER SEALANT PLACEMENT AND HYDRAULIC TESTING

Open questions remain regarding the complexity of the damaged near-wellbore system and exactly where the sealants were placed during injection. To help answer these questions, the well system will be overcored. This is documented in the following chapter. After retrieval, the overcore will be analyzed by several research laboratories based in Switzerland, France and Norway.

The successful capture of the overcore should help to bridge the gap in understanding wellbore damage complexity by connecting purely hydraulic information to directly measurable damage mapping of the composite cased and cemented system with associated intact and coupled host rock. This ground truthing of the hydraulic testing damage methodology should prove useful to aiding formulation of field storage site breach solutions. This is important because, in the field, caprock seal performance and injection well system integrity analysis is based only on hydraulic flow testing methods.

ACKNOWLEDGEMENTS

We are greatly thankful to the CCP Project crew, which always were interested in the results of the different phases and always supported all of us despite the difficult and unforeseen behaviour of the borehole completion especially during the first phases. We would especially thank Tony Espie for his interest and his steadiness, and Thomas Fierz for his great ideas and solutions and the Mont Terri crew for their onsite support.

REFERENCES

1. Bourgoyne, A.T., Scott, S.L. and Manowski, W. (1999) *A Review of Sustained Casing Pressure Occurring on the Outer Continental Shelf*, available at: https://www.bsee.gov/sites/bsee.gov/files/tap-technical-assessment-program//008de.pdf
2. IPCC Special Report on Carbon dioxide Capture and Storage (September 2005), section 5.7.2 *Processes and pathways for release of CO_2 from geological storage sites*, page 244.
3. Goodman, H.E., Imbus, S.W., Espie, T., Minnig, C., Rösli, U., Fierz, T. and Lettry, Y. (2016): Large rock mass experimentation at Mont Terri underground research laboratory - CO_2 containment assurance experiments. 13th International Conference on Greenhouse Gas Control Technologies, Lausanne, Switzerland, 14-18 November 2016 (GHGT-13). *Energy Procedia*, **114**, pp. 5239-5250.
4. Goodman, H., Espie, T., Minnig, C., Rösli, U., Gisiger, J. and Roback, R. (2018): Testing Advanced Sealants to Address Wellbore Seepage of Co2 Behind Casing at the Mont Terri Underground Research Laboratory. 14th Greenhouse Gas Control Technologies Conference Melbourne 21-26 October 2018 (GHGT-14). Available at SSRN: https://ssrn.com/abstract=3365937
5. F. J. Pearson, "WS-A Experiment: Artificial Waters for Use in Laboratory and Field Experiments with Opalinus Clay", TECHNICAL NOTE 99-31, January 1999, Paul Scherrer Institut.
6. Cooper, H.H. Jr., Bredehoeft, J.D. and Papadopulos, S.S. (1967). Response of a Finite-Diameter Well to an Instantaneous Charge of Water, *Water Resources Research*, First Quarter 1967, pp. 263-269.
7. Bredehoeft, J.D. and Papadopulos, S.S. (1967): A Method for determing the Hydraulic Properties of Tight Formations, *Water Resources Research*, **3**(2), pp. 233-238.
8. Jacob, C.E. and Lohman S.W. (1952): Non-steady flow to a well of constant drawdown in an extensive aquifer. *Trans Amer. Geophys. Union*, **33**, pp. 556-569.
9. Cooper, H.H. and Jacob, C.E. (1946): A generalized graphical method for evaluating formation constants and summarizing well-field history, *Transactions of the American Geophysical Union*, **27**(IV), pp 526-532.
10. Agarwal, R.G. (1980): A New Method to Account for Producing Time Effects When Drawdown Type Curves Are Used to Analyze Pressure Buildup and Other Test Data, Soc. of Petroleum Engineers, SPE Paper 9289, presented at SPE-AIME Meeting, Dallas, Texas, Sept. 21-24.
11. Pearson, F. J., Arcos, D., Bath, A., Boisson, J.-Y., Fernández, A. M., Gäbler, H.-E., Gaucher, E., Gautschi, A., Griffault, L., Hernán, P., Waber, H. N., (2003). *Mont Terri Project – Geochemistry of water in the Opalinus Clay Formation at the Mont Terri Rock Laboratory*. Swiss Federal Office for Water and Geology Series No. 5. Bern.
12. Manceau, J.C., Tremosa, J., Lerouge, C., Gherardi, F., Nussbaum, C., Wasch, L.J., Aberic, P., Audigane, P. and Claret, F. (.2016): Well integrity assessment by a 1:1 scale wellbore experiment: Exposition to dissolved CO_2 and overcoring. *International Journal of Greenhouse Gas Control*, **54**, pp. 258–271.
13. Zainalabedin, K.A., Al-Habib N.S. & Ahmad, G. (2002): Safety Practices for Servicing Wells with Hydrogen Gas Generated in the Wells Annuli. Society of Petroleum Engineers. doi:10.2118/73929-MS. SPE International Conference on Health, Safety and Environment in Oil and Gas Exploration and Production, 20-22 March, Kuala Lumpur, Malaysia.
14. Welch N., Gilbertson, R., Boukhalfa, H., Robak, R., Carey, J.W., Goodman, H., Rösli, U., Gisiger, J., Espie, T. and Minnig, C. (2020): Effectiveness of a "Smart" Hydrogel in Well Leakage Remediation. *Proceedings SPE ATCE 2020*, SPE Paper 201682.
15. Tavassoli, S., Shafiei, M., Minnig, C., Gisiger, J., Rösli, U., Petterson, J., Theurillat, T., Mejia, L., Goodman, H., Epie, T. and Balhoff, M. (2019), Pilot Case Study of Wellbore Leakage

Mitigation using pH-Triggered Polymer Gelant. Society of Petroleum Engineers. doi.org/10.2118/194251-MS, SPE/ICoTA Well Intervention Conference and Exhibition, 26-27 March, The Woodlands, Texas, USA.
16. Neele, F., Grimstad A.-A., Fleury M., Liebscher A., Korre A., and Wilkinson M. (2014): *MiReCOL:* Developing Corrective Measures for CO_2 Storage, *Energy Procedia*, 63, 4658–4665, doi:10.1016/j.egypro.2014.11.499.
17. Fleury, M., Sissmann O., Brosse E., and Chardin M. (2017): A Silicate Based Process for Plugging the Near Well Bore Formation, *Energy Procedia*, 114, 4172–4187, doi:10.1016/j.egypro.2017.03.1558.
18. Genedy, M., Matteo, E. N., Stenko, M., Stormont, J. C., Taha, M. R. (2019): Nanomodified Methyl Methacrylate Polymer for Sealing of Microscale Defects in Wellbore Systems. *J. Mater. Civ. Eng*., 2019, **31**(7): 04019118.
19. Murcia, D.H., Minnig, C., Gisiger, J., Stormont, J. and Taha, M.R. (2021), Nano Sealant for CO_2 Seal Integrity and Overcoring at Mont Terri, 15th Greenhouse Gas Control Technologies Conference Abu Dhabi, 15-18 March 2021 (GHGT-15).
20. Shayan Tavassoli, Lucas Mejia, Mohammadreza Shafiei, Christian Minnig, Jocelyn Gisiger, Ursula Rösli, James Patterson, Thierry Theurillat, Harvey Goodman, Tony Espie, Matthew Balhoff. (2021): Pilot test of pH triggered polymer sealant for CO_2 storage*,* 15th Greenhouse Gas Control Technologies Conference Abu Dhabi, 15-18 March 2021 (GHGT-15).

Carbon Dioxide Capture for Storage in Deep Geological Formations, Volume 5
Karl F. Gerdes (Editor)
© 2022 BP. All rights reserved.

Chapter 29

SEALANT TESTS AT THE MONT TERRI CS-A EXPERIMENT THAT ADDRESS SEEPAGE OF CO_2 BEHIND CASING

Harvey Goodman[1,2], Ursula Rösli[3], Jocelyn Gisiger[3], David Jaeggi[4], Christian Minnig[4]

[1]Chevron Emeritus Fellow, Houston TX, USA
[2]Los Alamos National Laboratory, Los Alamos, NM 87545, USA
[3]Solexperts AG, Mettlenbachstrasse 25, 8617 Mönchaltorf, Switzerland
[4]SWISSTOPO, Seftigenstrasse 264, 3048 Wabern, Switzerland

ABSTRACT: The Mont Terri "Well-Sealing" experiment was designed to characterize efficacy of novel sealants in a scale well with induced defects. Four sealants were injected to assess capability to restore pressure containment in the cased and cemented intervals after exposure to repetitive heating-cooling cycles. The test data obtained over the 5 year course of investigation consists of three types of information: (1) an extensive hydraulic data set with detailed hydrogeological analytics; (2) an extensive post-injection core examination program consisting of high-resolution computed tomography (CT), geochemical, and geomechanical analytics; and (3) numerical modelling tuned to experimental test site conditions intended to relate the hydraulic and core based data sets over the entire cased hole injection interval.

This chapter presents the complete post-sealant program performance results based on the complete analytical assessment program employed.

KEYWORDS: CO_2 geological storage; containment assurance; CO_2 breach mitigation; underground rock laboratory

INTRODUCTION

Long-term sealant solutions for damaged well systems used for CO_2 injection were investigated using an experimental test well installed at the Mont Terri Rock Laboratory (MTRL) located in NW Switzerland (see Chapter 28). The Mont Terri URL facility provides the experimentalist an in-situ scale test site at a depth of 300 m that may serve as ground-truth for upscaling to CO_2 injection field conditions (e.g., 2,400 m depth saltwater aquifer with overlying shale caprock).

The test well was designed to replicate cased and cemented injection site conditions. The well casing size and accompanying cement sheath thickness placed in the cased hole annulus are similar to deep field conditions. Here, we provide a very basic description of the test well design, installation, and instrumentation, while a more detailed description is found in Chapter 28.

Four sealants were tested to assess the capability to restore pressure containment in the cased and cemented interval after exposure to heating-cooling cycles meant to damage the well seal. Data collected during the 5-year course of investigation is dominated by hydraulic fluid injection information consisting of flow rates and pressures at specific recorded time increments. Injection protocols resulted in pressure increase/decrease episodes that may also have affected damage growth in the cased and cemented test interval.

`

Upon conclusion of the sealant injection program, the well site was cored by two lateral boreholes designed to intersect the cased hole interval, intended to obtain intact formation/cement/casing samples. Extensive analytics were applied on the recovered core that included high-resolution CT, geochemical, and geomechanical measurements.

Data analytics consisting of extensive numerical modeling that had been successfully benchmarked to account for cement rheology properties during the entire curing phase of the cased hole installation were then applied. The numerical model was tuned to the MTRL experimental test site conditions to relate the hydraulic and core-based data measurements over the entire cased hole injection interval.

Test well protocols used to induce cased wellbore damage for the casing/cement/formation coupled system, and the diagnostic schemes employed to assess that damage and to implement the sealant treatments include:

- Creation of flow paths in the cemented annulus along a casing by cyclic heating/cooling.
- Characterization of the permeability of these micro-annular interfaces pre-treatment.
- Injection 4 novel sealants.
- Characterization of the micro-annular interface permeability post-treatment.

The post-treatment characterization of the cased hole section is the focus of this chapter.

Test Well Installation

The layout consists of a 400 mm diameter pilot borehole to a depth of 4.26 m in the upper part and a borehole of 200 mm diameter to the final depth of approximately 14.40 m (Figure 1). Pressure compartments are comprised of Intervals 1-8. Interval 1 is the lower open hole injection interval, while Intervals 2-7 comprise the cased and cemented interval injection-extraction ports (I/P modules), and Interval 8 is the uppermost open hole observation section. Note the six IP modules are located at Intervals 2–7 (i.e., IP module 1–Interval 2 to IP module 6–Interval 7). Table 1 summarizes the downhole instrumentation and compartment interval volumes. The precise locations of the injection/extraction flow lines are indicated by the letters P and Q.

The borehole packer system consists of a top packer with a length of 2.5 m. Two grout packers are included, isolating the top interval 8 and the bottom interval 1 during cement injection. The section between both grout packers consists of a 6.0 m long casing section with the six I/P modules for injection/extraction and for pressure measurements. Three temperature sensors are included to measure the borehole temperature during heating. A total of 30 lines and three cables for the temperature sensors are routed through the inner part of the casing to the gallery. Refer to Chapter 28 for a detailed description of the equipment fabrication and installation components.

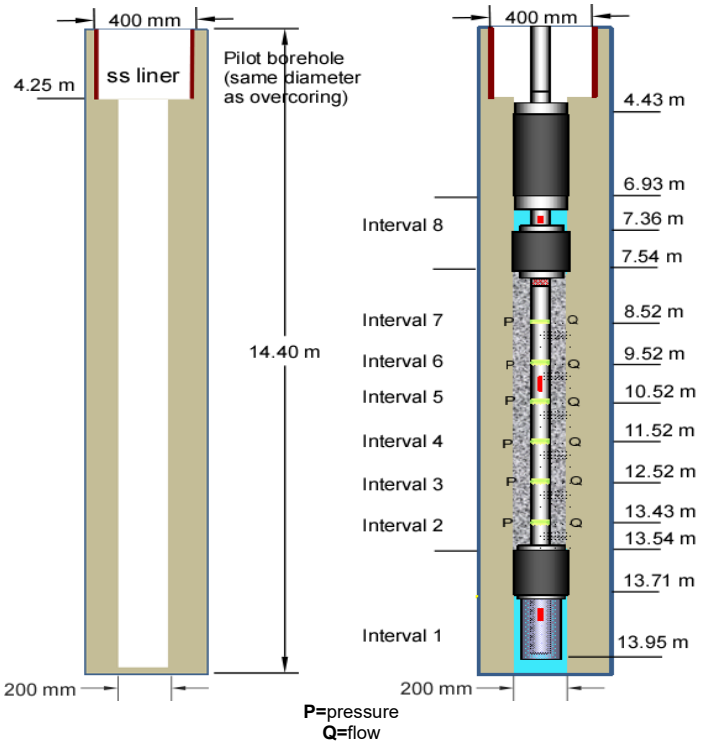

Figure 1. Setup of borehole BCS-A1 after drilling (left) and with instrumentation (right).

Table 1. Instrumentation of borehole BCS-A1.

Section	From [m]	To [m]	Length [m]	Volume [L]*	Comments
Interval 1	13.54	14.40	0.86	18.514	Temperature sensor
(Grout packer 1)	13.54	13.71	0.18	-	Deflated after cement injection
Interval 2	13.43	-	-	0.152	I/P module 1
Interval 3	12.52	-	-	0.169	I/P module 2
Interval 4	11.52	-	-	0.180	I/P module 3
Interval 5	10.52	-	-	0.236	I/P module 4 Temperature sensor
Interval 6	9.52	-	-	0.161	I/P module 5
Interval 7	8.52	-	-	0.293	I/P module 6
(Grout packer 2)	7.36	7.54	0.18	-	Deflated after cement injection
Interval 8	6.93	7.54	0.61	13.256	Temperature sensor
Packer	4.43	6.93	2.50	-	

`

Project Phase Activity Post-Sealant Injection

Referring to Table 2, the experimental site work commenced in April 2015 with the drilling of borehole BCS-A1 to a depth of 14.40 m. Project phases through No. 18 after the sealants were injected are discussed in Chapter 28. The following discussion begins with the final hydraulic test result (phase 19) before introducing the overcoring operation and post sealant analytical program that supports project outcome conclusions (No. 21–27).

Table 2. Overview of CS-A project phases.

Date	Phase	No	Activity
13.04.2015 – 21.04.2015	Drilling	0	Ø 400 mm down to 4.25 m, Ø 203 mm to 14.45 m
22.04.2015 – 23.04.2015	Installation	1	Installation of borehole completion and grouting of annulus. Note poor cement coverage for top several cm near Interval 7 - I/P module 6
06.05.2015 – 29.07.2015	Saturation	2	Saturation of all interval at pressures up to 6 bar
26.08.2015 – 07.12.2015	Hydraulic testing 1	3	Initial hydraulic testing
17.12.2015 – 31.12.2015	Heating cycle 1	4	Heating to max. 31.6°C
12.01.2016 – 15.01.2016	Heating cycle 2	5	Heating to max. 37.7°C
19.01.2016 – 01.03.2016	Hydraulic testing 2	6	Hydraulic testing
06.04.2016 – 11.05.2016	Heating cycle 3	7	Heating to max. 78.4°C
18.05.2016 – 24.05.2016	Hydraulic testing 3	8	Hydraulic testing
07.06.2016 – 29.09.2016	Dipole testing	9	
05.10.2016 – 06.10.2016	Dead volume tests	10	
07.10.2016 – 07.02.2017	Tracer testing	11	
18.01.2017 – 03.02.2017	Water sampling	12	
13.07.2017 – 14.09.2017	Mg-Anode	13	Installation in observation borehole to delay expected casing corrosion
11.09.2017 – 14.09.2017	Flushing	14	
21.09.017 – 21.11.2017	Sealant 1	15	Interval 6 & injection sites with post sealant performance assessment (LANL sealant). Interval 7 corrosion from reduced cement coverage at top of cased hole interval. Large voids expected.
15.02.2018 – 27.08.2018	Sealant 2	16	Interval 5 injection site with post sealant performance assessment.

Date	Phase	No	Activity
			(UT sealant)
18.03.2019 – 30.08.2019	Sealant 3	17	Interval 4 injection site with post sealant performance assessment. (IFPEN sealant)
21.08.2019 – 23.09.2019	Sealant 4	18	Interval 2 site injection and post sealant performance accessed; Interval 3 sealant injection, but clogged flow line prevented performance assessment. (UNM sealant)
26.08.2019 – 16.10.2019	Hydraulic testing 4	19	Final hydraulic testing & preliminary results
16.10.2019 – 17.10.2019	Final resin injection	20	Site stabilization for overcore
15.08.2020 – 15.12.2020	Overcore rig build	21	Design & build overcore rig at SCHÜTZEICHEL GmbH & Co. KG, 53577 Neustadt (Wied), Germany
01.03.2021 – 09.03.2021	Overcoring 454/367 mm	22	Coring operation experienced rock damage compromising recovery; elected to drill lateral borehole for 102.5 mm core along the cement/formation interface
17.03.2021 – 18.03.2021	Sampling borehole BCS-A3	23a	Lateral borehole drilled for 102.5 mm cores; 100% core recovery
22.03.2021 – 25.03.2021	Sampling borehole BCS-A4	23b	Lateral borehole drilled for 102.5 mm cores; 100% core recovery
29.01.2020 – 25.02.2022	Core/cement/sealant analytics BRGM (French Geological Survey)	24	Macro-microscopic (optical, SEM), chemical data mapping, XRD, phase chemistry
27.04.2021 – 17.11.2021	CT core scan; EMPA (Swiss Fed Laboratories)	25	X-ray computed tomography (CT) and data analysis of CS-A experiment core samples (diameter 105 mm, length 400 mm).
01.09.2021 – 02.01.2022	Core fragments mechanical/ petrophysical properties; SINTEF (Foundation for Industrial and Technical Research - NGO), Trondheim Norway	26	Illustrate possible workflow for commercial CCS operations with less costly core taking and laboratory testing procedures; steps to “rehabilitate” old or non-preserved caprock samples with aim to develop correlations to be used when no reference plugs are available
01.01.2020 – 02.23.2022	Test site numerical modelling; Missouri S&T	27	CS-A experiment site modelling to predict cement failure and micro-annuli development

`

Hydraulic Testing

The hydraulic test campaign consisted of pulse injection tests, constant head injection (HI), and dipole crossflow injection testing between individual intervals (I/P modules). Figure 2 illustrates the large changes in the test well interval connectivity from the initial state to after the final heating cycle 3 (Phase No 7) prior to sealant testing. Results show two to three orders of magnitude increase in permeability in the cased and cemented completion interval designated by Intervals 2–7. Note Interval 7 initial transmissivity is relatively high, which was attributed to poor cement coverage near the top of cased hole interval. However, this corrosive damage has not been directly observed, being inferred from corrosive by-products in our water analyses and apparent larger than expected fluid storage volumes near Interval 7 - I/P module 6.

Although described in Chapter 28, an abbreviated description of the first dipole test campaign is provided to introduce the pressure test protocol used to compare sealant performance. Seventeen dipole tests were conducted with different injection and extraction intervals. Refer to Figure 1 for I/P module location and flow direction profiles. The tests were performed by injection in the Q or P line of one interval and extraction from one or two or three adjoining intervals.

The test protocol provided a quick method to assess the permeability around each interval at different pressure levels. The test included injection of treated water developed by A. F. Pearson [1]. See Table 3 below. The injection protocol consists of 4-minute pressure increments each at 20, 25, 30 and 35 bar.

Table 3. Two formulations developed by Pearson are given, with salinities corresponding to the highest Cl (A1 type) and lowest Cl (A3 type) waters from the Mont Terri field laboratory.

	A1 Type Version 980318	A3 Type Version 9806
NaCl	**12.38**	**6.13**
KCl	**0.12**	**0.06**
$MgCl_2$	**1.61**	**0.47**
$CaCl_2$	**2.86**	**0.77**
$SrCl_2$	**0.08**	**0.05**
Na_2SO_4	**2.00**	**1.63**
$NaHCO_3$	**0.04**	**0.05**
Final pH	**7.6**	**7.9**

These tests should be considered with the following qualifications:

- The initial flow rate is mostly dominated by wellbore storage, especially at higher flow rates experienced in the specific interval tested.
- The final flow rate after 4 minutes is not in equilibrium with the cement around the interval and cannot be used for permeability estimation.
- The flow rates considerably vary for repeated tests, and especially the flow rates at 35 bar decrease over a repeated test series, indicating the initial wellbore storage of the interval being reduced by the ongoing filling with fluid.

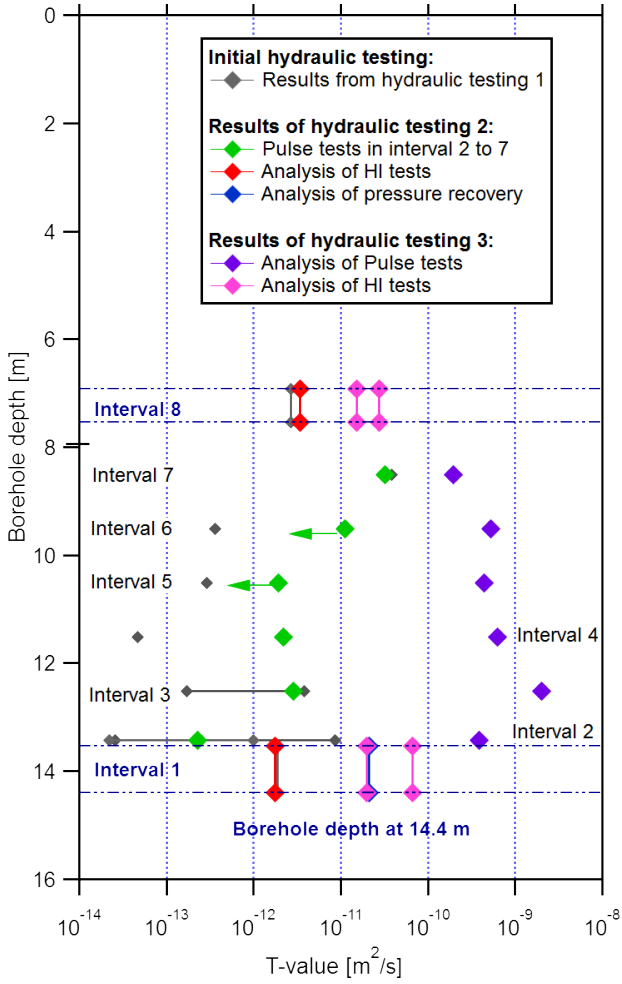

Figure 2. Pre-sealant injection transmissivity vs. borehole depth from hydraulic testing program 1-3.

Nevertheless, the results can be used for a quick characterization of the intervals during and after the different activities and to assess the long-term performance of the sealants in the intervals. The flow rate was measured manually by timed sample captures.

The complexity of hydraulic connectivity was noted. The following observations were made:

- For most interval pairs, the injection flow rates were higher than the extraction flow rates. The highest injection flow rates were obtained for interval 5 (12 ml/min) and interval 6 (8 ml/min, Figure 3). Maximum extraction flow rate was 2.5 ml/min for all intervals.
- Higher injection flow rates were observed with increasing injection pressure (up to 50 bar) and most pronounced above 30 bar injection pressure, with no or only a small increase at the extraction side. High injection pressure seems to have caused a fracture opening since higher injection flowrates were subsequently observed at lower pressures.
- Intervals 2, 3, and 4 show low injection flow rates and a bad connectivity to the other intervals (Figure 4).
- The main water storage volume was considered to be intervals 1 and 8, although wellbore storage is influenced by apparent connectivity to the host rock observed during tracer testing [2].
- The entire system seems to have been saturated and pressurized towards the end of the first dipole testing, which caused slightly higher flow rates.
- Sufficient flow connectivity for injection tests was established for dipole pairs: Q7 → Q8, Q5 → Q6, Q6 → Q5, P5 → P4.

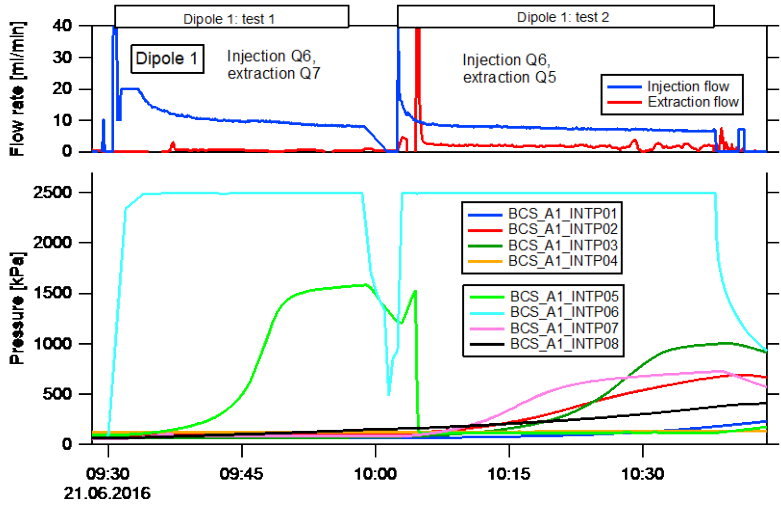

Figure 3. Injection at interval 6 with extraction from the neighbouring intervals.

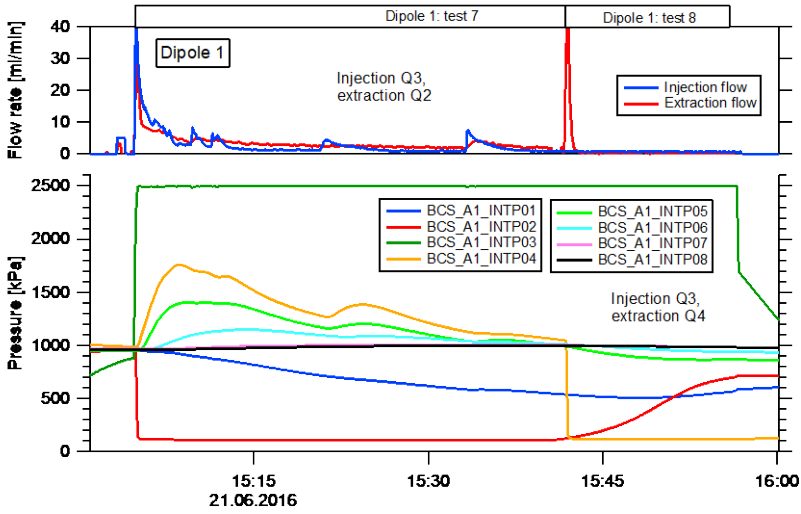

Figure 4. Injection at interval 3 with extraction from the neighbouring intervals.

OVERVIEW OF SEALANT PERFORMANCE–HYDRAULICS PERSPECTIVE

Four different sealants were injected in six different intervals. The sealants and their developers are:

- Sealant (1) is a nanoparticle hydrogel sealant developed by Los Alamos National Laboratories (LANL).
- Sealant (2) is a polymer gel developed by University of Texas (UT).
- Sealant (3) is a silicate-based sealant developed by IFP Energies Nouvelles (IFPEN).
- Sealant (4) is an epoxy-based sealant developed by University of New Mexico (UNM).

The hydraulic injection test procedure step was developed to provide quick, comparable tests for characterizing permeability in each interval at different injection pressure levels. The test involved injection of type new-A3 Pearson water at 20, 25, 30 and 35 bar for 4 minutes at each step. The flow rates at the end of each step are compared. Pearson Type A3 was newly developed after calcium precipitation was observed in water samples taken in Phase 12 prior to starting the sealant testing campaign. See Table 4 below. The A3 Pearson water removed divalent cations and lowered the pH that resolved the precipitation issue. The MES-buffer (2-ethanesulfonic acid) was added to the new-A3 Type Pearson water for flushing purposes to adjust the pH to about 4 and to overcome the cement buffering capacity. Both new Pearson water types were used starting from Phase 14.

Details of the sealant formulations are not presented in this chapter. The specifics are documented separately by the developers [3, 4, 5, 6, 7, 8].

Table 4. New Pearson water formulations.

		A1 Type*	A3 Type*	New-A3	MES-new-A3
Salt quantities [mg/kg]	NaCl	12'380	6'130	6'130	6'130
	KCI	120	60	1800	1800
	$MgCl_2$	1'610	470	0	0
	$CaCl_2$	2'860	770	0	0
	$SrCl_2$	80	50	0	0
	Na_2SO_4	2'000	1'630	1'630	1'630
	$NaHC0_3$	40	50	50	50
MES buffer					0.1 M
Final pH		7.6	7.9	7.9	6.5
Conductivity [mS/cm]		28.9	14.5		

Sealant 1 Performance

Sealant 1 achieved good sealing up to 35 bar in the low permeability interval 6, but provided only temporary sealing in the (much) higher permeability interval 7. The success in the low permeability interval shows promise for providing a successful caprock seal in a CO_2 storage aquifer environment.

Interval 6 Injection

The 4 minutes flow rate vs. injection pressure results of the HI step tests are displayed in Figure 5. Multiple tests were performed in series, and the median flow rates are given for each test series. The major changes in the injection flowrates are indicated in Figure 5 with the arrows and the corresponding numbers:

1. Decrease of permeability after the first Sealant 1 injection in interval 6.
2. Increase in permeability during long-term observation.
3. Decrease of permeability after Sealant 2 injection in the adjoining interval 5.
4. Stable permeability until the final resin injection (lower right corner).

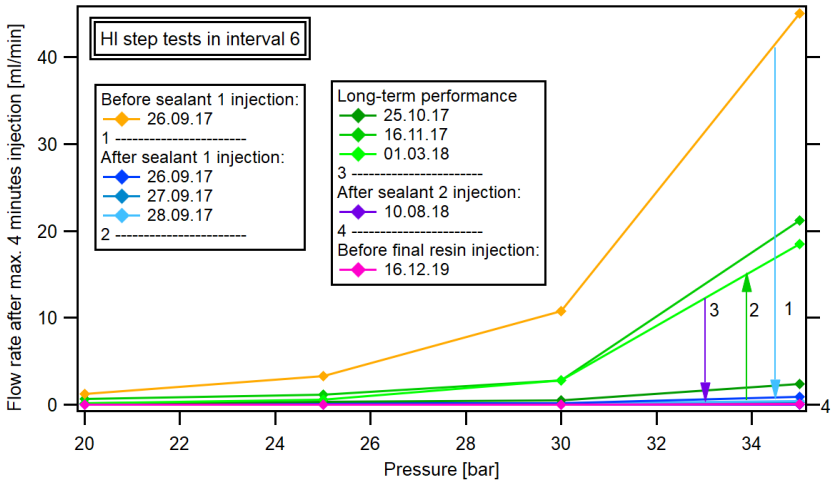

Figure 5. Flow rates vs. injection pressure for HI tests before and after Sealant 1 injection in interval 6.

A major decrease in permeability of interval 6 occurred after Sealant 1 injection into that interval. Different injection tests were performed–amongst others, a long-term step performance test between 25 October and 10 November 2017. The first two steps at 20 and 30 bar injection pressures showed very low injection flow rates below 0.2 ml/min with only minor cross-hole reactions in the other intervals. During the last injection step at 40 bar, the injection flow rate immediately increased and the pressures in all other intervals also increased to about 36 bar, indicating partial failure of the sealing capacity or the creation of new flow paths. However, despite the apparent failure, the injection flow rates at a given pressure after the failure were still lower than before the Sealant 1 injection and a residual sealing capacity remained.

Interval 7 Injection

The 4 minutes flow rate vs. injection pressure results of the HI tests in interval 7 are displayed in Figure 6. The flow rates before Sealant 1 injection are not displayed, since flow rates up to 200 ml/min were measured (far off scale in the figure). On 29 September 2017, a long-term injection test was started in interval 7 with a backpressure of 7 bar. Flow rates as low as 0.5 ml/min were recorded at steady-state conditions. After about 3.1 days of injection, the flow rate started to increase to about 2.5 ml/min, indicating a possible higher permeability due to a partial failure of the sealant in interval 7. However, the permeability was still considerably lower than prior to the Sealant 1 injection.

The flow rates displayed in Figure 6 do not show a clear trend during and after Sealant 1 injection. In particular, the last test yielded higher flow rates at all injection pressures. As the permeability of interval 7 is generally higher compared to the other intervals and the interval volume might be larger due to poor cement coverage, the HI step test might not be adequate for this interval to estimate sealant performance and the high flow rates might still be related to wellbore storage effects.

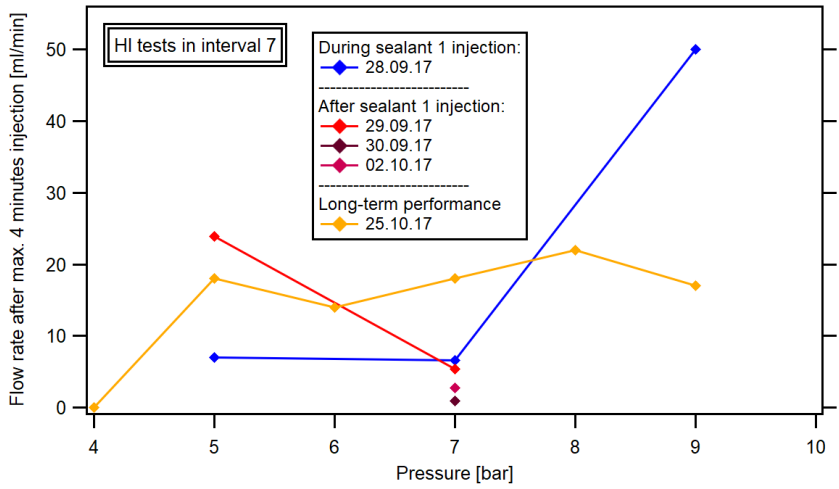

Figure 6. Flow rates vs. injection pressure for HI tests during and after Sealant 1 injection in interval 7.

Sealant 2 Performance

Sealant 2 significantly reduced leakage rates, although not to zero, with flow reduced to 3 ml/min at applied differential pressures of less than 30 bar in the long term.

Interval 5 Injection

Eight HI step tests were conducted in interval 5 between 30 May and 10 August 2018 to test the performance of Sealant 2. The 4 minutes flow rate vs. injection pressure results of the HI tests are displayed in Figure 7. If multiple tests were performed in series on the same date, the median flow rate for the series is given. The major changes in the injection flowrates are indicated with the arrows and the corresponding numbers.

1. Decrease of permeability after the Sealant 2 injection in interval 5.
2. Increase in permeability during long-term observation–possible sealant degradation.
3. Reduced permeability before the final resin injection possible well storage effects.

The initial HI step tests after Sealant 2 injection gave maximum flow rates of about 4.2 ml/min at 35 bar. No cross-hole reactions were observed in the other intervals. Long-term injection tests were successfully conducted at 35 bar with a final steady-state flow rate of 3.8 ml/min and at 30 bar with a final steady-state flow rate of 0.11 ml/min. The later test, which lasted 11 days, showed cross-hole reactions in all intervals, most pronounced in the intervals 6, 7, and 8.

A CO_2 injection test on 30 May 2018 showed a slow pressure decrease of 3 bar in 16 hours. After three months, the CO_2 test was repeated and showed a faster pressure decrease of 21.4 bar in 10 hours. Referring to Table 5, the injection tests after the sealant injections starting with HI step 4, yielded much lower flow rates with a maximum of 4.2 ml/min at 35 bar. The long-term injection test HI7 was successfully conducted for 35 minutes at 35 bar with a final steady-state flow rate of 3.8 ml/min, and the test HI9 was conducted for 11 days at 30 bar and with a final steady-state flow rate of 0.11 ml/min.

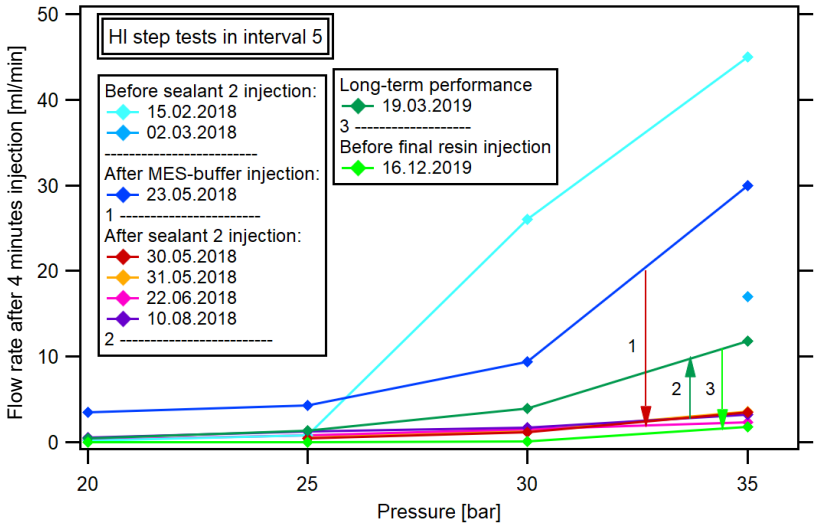

Figure 7. Flow rates vs. injection pressure for HI tests during and after Sealant 2 injection in interval 5.

Table 5. Results of performance tests between 30 May and 10 August 2018.

Interval	Test No.	Date	20 bar	25 bar	30 bar	35 bar
			[ml/min] [1]	[ml/min] [1]	[ml/min][1]	[ml/min][1]
Int. 5	HI step4	30.05.2018	--	0.55	1.4	4.2
	HI step5	30.05.2018	--	0.3	1.0	2.8
	HI6	30.05.2018	Steady-state flow rate after 14 minutes		0.4[2]	--
	HI7	30.05.2018	Steady-state flow rate after 35 minutes		--	3.8 → 3.2
	HI step8	31.05.2018	--	0.7	1.3	3.6
	HI9	31.05.2018	Long-term injection, steady-state flow rate after 11 days with other intervals open		0.5 → 0.11	--
	HI step10	22.06.2018	0.31	0.80	1.55→ 0.26 [3]	2.33
	HI step11	10.08.2018	0.54	1.28	1.67	3.21

The pressure reaction of all intervals during the long-term test HI9 in interval 5 might be related to the reduced fracture volume in the system and the tight Opalinus clay boundary, which causes a fast pressurization of the entire borehole.

During the baseline test campaign on 19 March 2019 before the Sealant 3 injection in interval 4, a further HI step test was performed in interval 5, which gave slightly higher flow rates at 30 and 35 bar injection pressure of maximum 12 ml/min. This flow rate, however, is still below the initial flow rates before sealant injection.

Sealant 3 Performance

Sealant 3 showed initial sealing but degraded after several days.

Interval 4 Injection

Four HI step tests were conducted in interval 4 over a period of two months after the third Sealant 3 injection and one additional test after five months. The tests initially showed very low flow rates of 0.16 ml/min at 35 bar injection pressure and no cross-hole reaction. Then the flow rates increased, and cross-hole reactions started at the 35 bar pressure step, first only in interval 5 and then also in interval 3 and to a minor extent in interval 2.

The major changes in the injection flowrates in Figure 8 are indicated with the arrows and the corresponding numbers.

1. Decrease of permeability after the third Sealant 3 injection in interval 4.
2. Increase in permeability during long-term observation–possible sealant degradation.
3. Reduced permeability before the final resin injection–possible well storage effects.

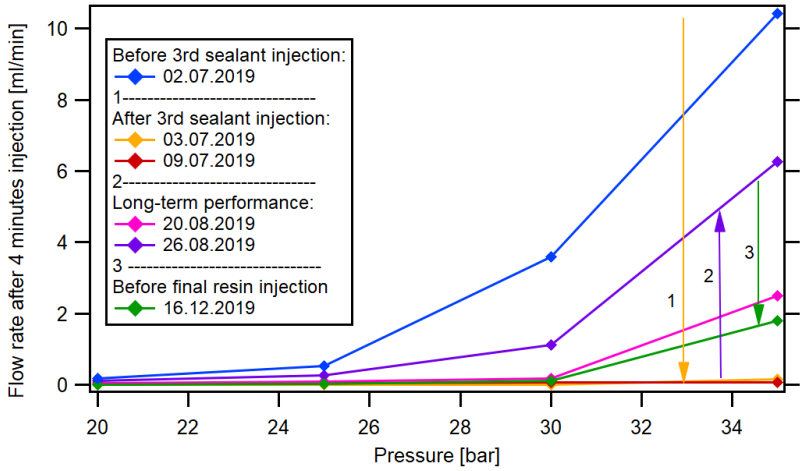

Figure 8. Flow rates vs. injection pressure for HI tests before and after third Sealant 3 injection in interval 4.

Sealant 4 Performance

Sealant 4 showed excellent sealing performance directly after injection, but a noticeable decrease of sealing capacity after several days because of a good and short-distance connection of interval 2 to the observation interval 1.

Interval 3 Injection

Sealant 4 injection was started on 28 August 2019 by circulating the sealant in interval 3 and then by closure of the extraction line and stepwise increase of the injection pressure. Because of clogging in the access lines, no performance tests could be performed in interval 3 after sealant injection.

Therefore, it was decided to additionally inject Sealant 4 in interval 2. Previously, a very good connection between interval 2 and interval 1 was observed because of the short distance between the two intervals of 0.105 m.

Interval 2 Injection

The observations after Sealant 4 injection in interval 2 indicate a good sealing performance directly after Sealant 4 injection and a noticeable decrease of sealing capacity after about one week, mainly at 35 bar injection pressure. Note Interval 2 is separated from the bottom open hole interval 1 by only a 105 mm long cemented section. With regard to measured transmissivity reported in an internal Technical Notes document (TN2018-83, made available by permission), and referring to Table 6 below, the following was observed:

Table 6. Results of Interval 2 performance tests between 29 August and 23 September 2019.

Test No.	**Date**	**20 bar [ml/min][1)]**	**25 bar [ml/min][1)]**	**30 bar [ml/min][1)]**	**35 bar [ml/min][1)]**	**40 bar [ml/min][1)]**	**Comments**
HI step3	*29.08.19*	*0.50*	*1.42*	*3.47*	*9.35*	--	*10 min: 4.43 ml/min No cross-hole*
HI step4	*05.09.19*	*1.06*	*2.81*	*10.58*	*42.73*	--	*10 min: 46.3 ml/min No cross-hole*
HI step5	*23.09.19*	*2.73*	*5.42*	*12.99*	*50.02*	--	*No cross-hole reaction*

Note 1. Flow rate after 4 min of HI injection at the corresponding pressure, if not otherwise stated

A transmissivity of 3.7E-10 m^2/s was determined for HI step3 at 35 bar, together with a fracture-dominated flow model. HI step4, performed after seven days, showed an increase in flow rates at 35 bar, together with an increase of the transmissivity to 1.2E-09 m^2/s. The pressure recovery was too fast to give indications of the flow model. It should be noted that these transmissivities were determined at a pressure of 35 bar and, due to potential opening of new, unsealed flow paths at high pressure, might not reflect the system permeability after injection of Sealant 4.

The major changes in the injection flowrates in Figure 9 are indicated with the arrows and the corresponding numbers.

1. Decrease of permeability after the Sealant 4 injection in interval 2.
2. Increase in permeability during long-term observation – additional sealant injection was not conducted as the interval 2 site was deemed unsuitable due to proximity to interval 1.

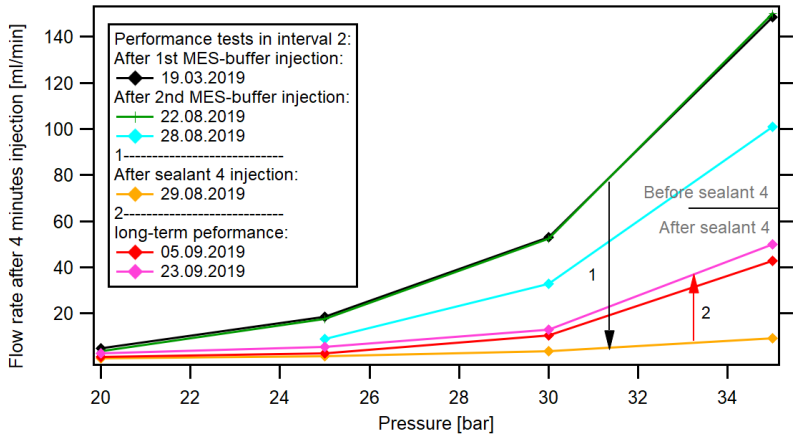

Figure 9. Flow rates vs. injection pressure for HI tests before and after Sealant 4 injection in interval 2.

Summary of Sealant Performance–Hydraulics Perspective

A final hydraulic test campaign was conducted between 26 September and 16 December 2019 to assess the hydraulic parameters in the borehole completion after injection of four different sealants in all intervals. One pulse injection test and seven constant head injection tests were conducted.

For the pulse injection test, water was injected in interval 5 with the syringe pump for less than one minute with a differential pressure of about 5 bar. Then, the pressure recovery was recorded and analysed. Constant head injection tests (HI) could be performed in all intervals except for interval 3 and interval 7. Water was injected in these intervals with an injection pressure of between 10 and 20 bar for a period of 1 and 11 days, respectively. Afterwards, the pressure recovery was recorded (see Figure 10). From these tests, the cross-hole reactions in the other intervals could be analyzed. In addition, the pressure recovery yielded some information on the possible flow model.

Additional performance testing with five HI step tests was conducted in the interval 1, 4, 5, 6, and 8. Interval 3 was not tested due to flow line damage. Interval 1 interestingly showed a special behavior with a slow pressure increase together with steadily decreasing flow rates. This was attributed to remnants of different sealants, accumulated in interval 1 during the sealant injections, which could considerably increase the compressibility of this part of the system and elastically react on a pressure increase.

The 4 minutes flow rates are displayed in Figure 11. Interval 6 proved to be tight, whereas intervals 4 and 5 showed slightly increased flow rates at 35 bar injection pressure. The flow rates in intervals 4, 5, and 6 are much reduced compared to the previous HI step tests, probably because of the additional sealing of the adjoining intervals by the following sealant tests. The 4 minutes flow rates in intervals 1 and 8 are not representative because of the high interval volume and correspondingly of the high wellbore storage. Interval 8 injection flow rates in the first minute were as high as 200 ml/min.

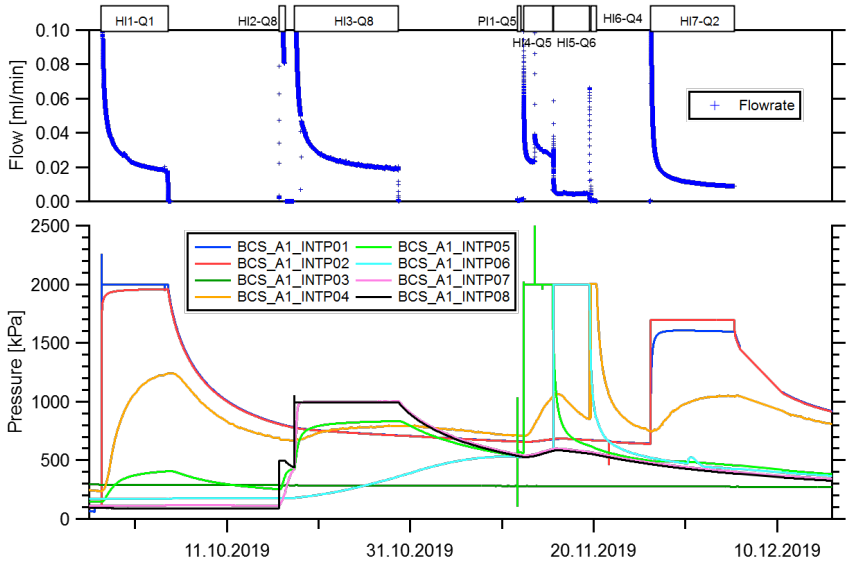

Figure 10. Pressures and flow rates measured during the HI/PI tests during the final hydraulic tests.

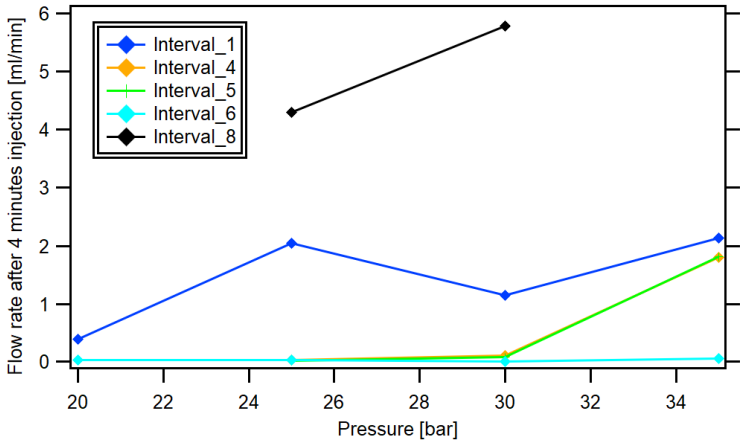

Figure 11. Flow rates vs. injection pressure for final HI step tests in the given intervals.

Figure 12 gives an overview of the transmissivities measured before and after the stimulation and at the end of the test after sealant injection. The major changes are indicated with arrows:

1. Increase of permeability after stimulation.
2. Decrease of permeability after injection of Sealants 1 to 4.

The final hydraulic testing revealed a good sealing of the entire borehole completion after the injection of Sealants 1 to 4. All intervals yield permeabilities similar to that of the Opalinus Clay host rock (See Figure 12). Possibly, the flow paths along the borehole that opened during stimulation are entirely sealed and no longer active, and the flow in the host rock is dominating the hydraulic tests. Supposed fracture flow was only observed for interval 5, showing the highest permeability, and interval 8 and interval 2 showed two distinct transmissivities in the analysis of the pressure recoveries. In interval 8, this is related to the reduced sealing and increased permeability towards interval 7. Interval 2 still shows a higher-permeability connection towards interval 1.

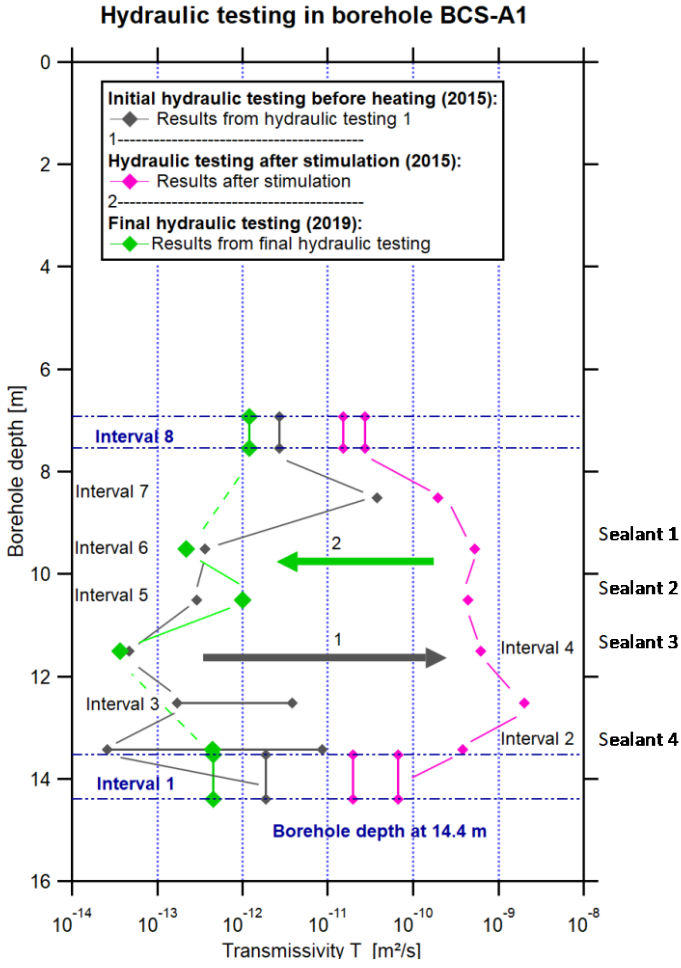

Figure 12. Transmissivity vs. borehole depth.

Open Questions After Hydraulic Testing

Induced damage after cyclic heating-cooling and repeated pressure pumping protocols have resulted in great complexity in the permeability distribution of the experimental well system. Questions remain that include sealant flow path geometry and characteristics, penetration depth of sealants, interaction of sealants with cement, casing and host formation, and degradation of sealants, cement, and casing.

To help answer these questions, the entire well system was planned to be overcored to observe the borehole damage network and subsequent sealant placement and performance.

OVERCORE OPERATION, CORE ANALYSES, AND NUMERICAL MODELLING

Coring (Phase 21–23)

The objective of the overcore program was to capture the entire CS-A experimental well down to 14.5 m depth, including completion, cement, and some of the formation. The focus was to retrieve the 6.5 m long test section (7.4–13.9 m depth). The overcoring rig was designed and built by Schutzeichel GmbH & Co. (53577 Neustad (Wied) Germany). Due to the size and weight of the overcore, and the fragility of the Opalinus clay host rock, intact core recovery was deemed risky but manageable. Figure 13 shows the overcoring concept. After capture, the overcore was to be analyzed by research laboratories based in France, Switzerland and Norway. See Table 2, phase 24–26. Figure 14 shows the overcoring rig.

The successful capture of this overcore would help to gain understanding of the wellbore damage complexity by connecting purely hydraulics information with directly measurable damage mapping of the composite cased and cement system, including associated intact and coupled host rock. This ground truthing of the hydraulic testing damage methodology would be useful in formulating field storage site breach solutions. That is because information on caprock seal performance and injection well system integrity analytics are limited to data from hydraulic flow testing methods.

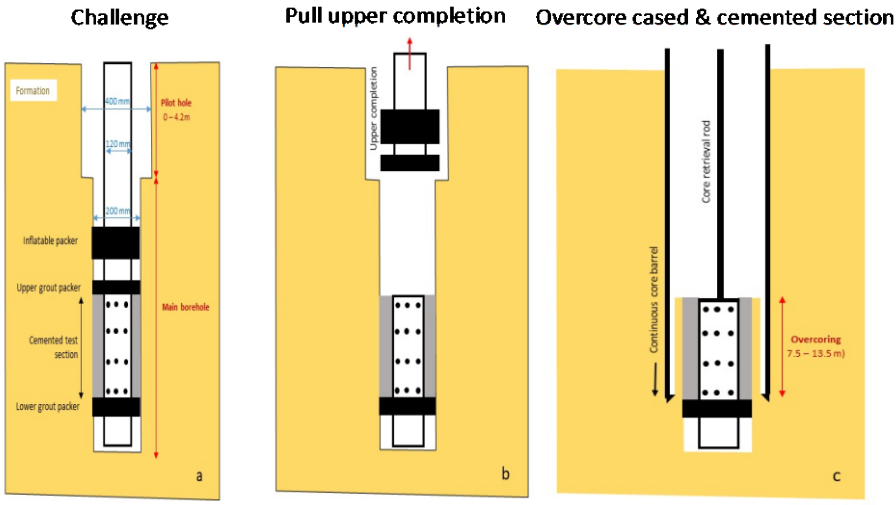

Figure 13. Overcoring strategy–cased & cemented interval focus.

Figure 14. Overcoring drill rig custom-made by SCHÜTZEICHEL GmbH & Co. KG delivered to Mont Terri Rock Laboratory (left) and deployed (right) in Niche EZ-A (Photo: D. Jaeggi, swisstopo).

Coring Operations

The drill rig was mobilized and set up March 2, 2021, and drilling commenced the next day. Refer to Table 2, phase No. 22. Figure 15 schematically shows reaming below the end of the 400 mm pre-shaft at 4.50 m.

In Figure 16, the upper right inset (6.04 m) shows the borehole inspection photo referenced near 6.0 m. The hydraulic isolation packer, Opalinus (OPA) clay formation ring and the inner core barrel surface is depicted inside the 200 mm wellbore. The lower Inset (7.15m) shows the top of the grout packer within the 200 mm borehole. At this depth, the borehole appears intact and clear of cuttings and debris. However, as drilling progressed, some broken fragments of the OPA ring began to be observed with cuttings size becoming increasingly smaller. The broken and fragmented OPA material caused growing concerns that OPA below the grout packer disintegrates and falls down inside the inner barrel and is milled away as drilling progresses.

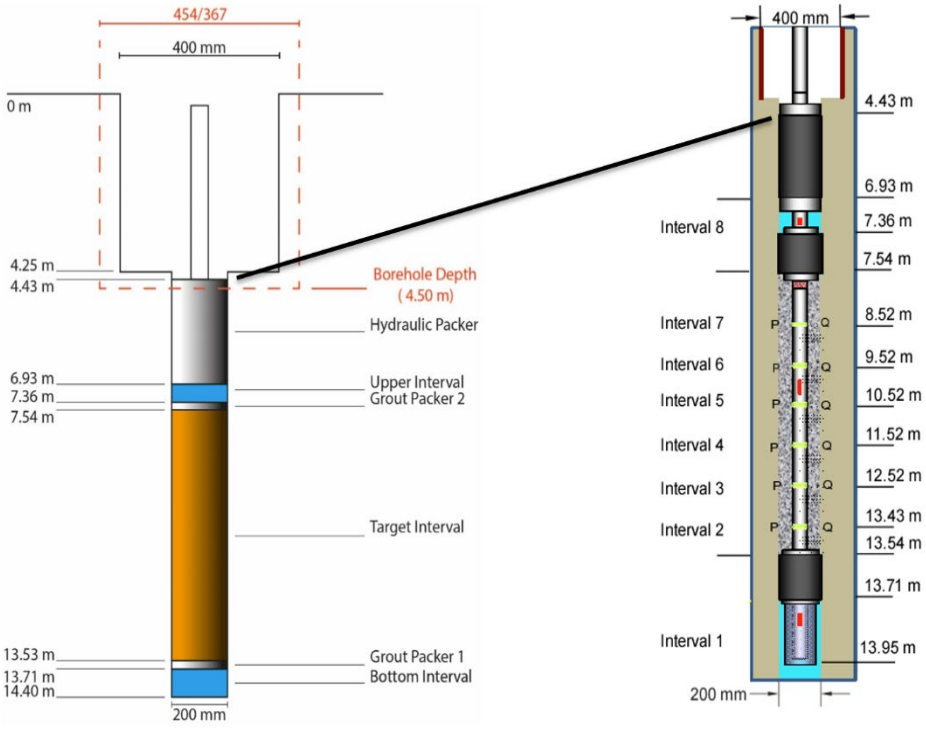

Figure 15. Reaming depth 4.5 m near top of hydraulic pressure isolation packer.

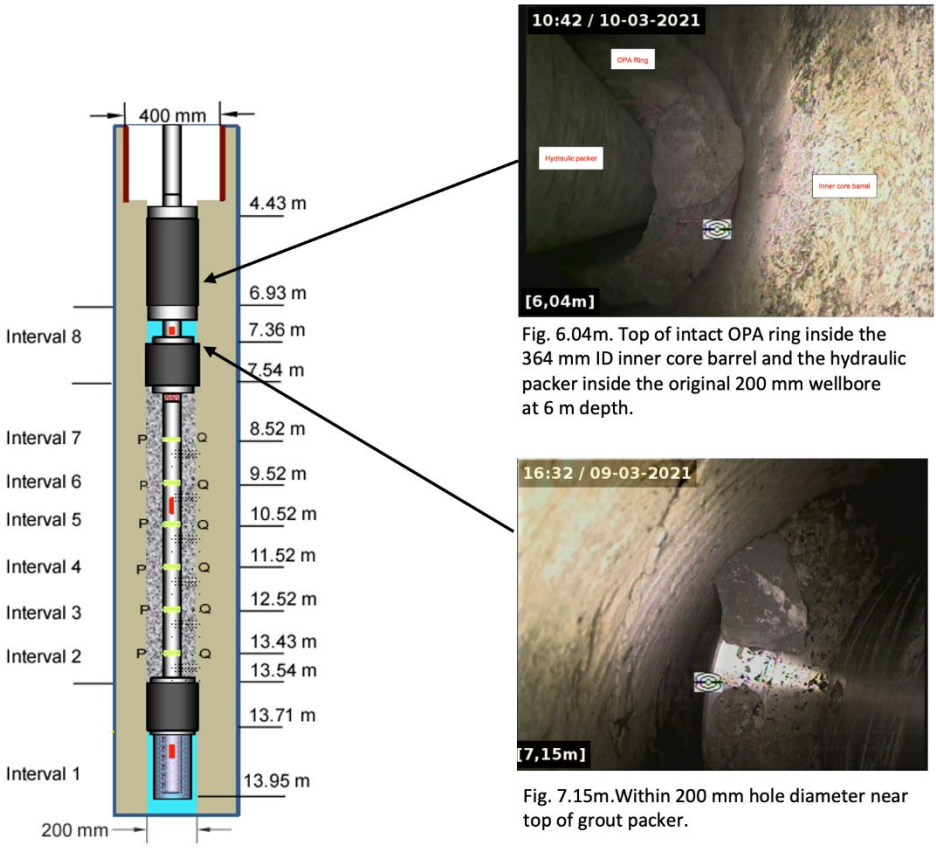

Figure 16. Camera inspection of hole during overcoring operation.

In Figure 17, the upper right inset (7.5m) shows OPA fragments near the top of the cased and cemented hole interval. The lower inset (8.65m) shows ground up OPA ring and cement material near the bare 120 mm steel casing. At this point, it became apparent that an intact cement and OPA overcore could not be obtained and the decision was taken to drill two lateral boreholes to intersect the cased and cemented 200 mm hole. Lateral boreholes BCS-A3 and BCS-A4 were drilled nearly parallel to BCS-A1 to intersect Interval 5 near IP Module 4 and Interval 3 near IP Module 2, respectively. Figure 18 shows the trajectories for these laterals and corresponding BCS-A1 intersections.

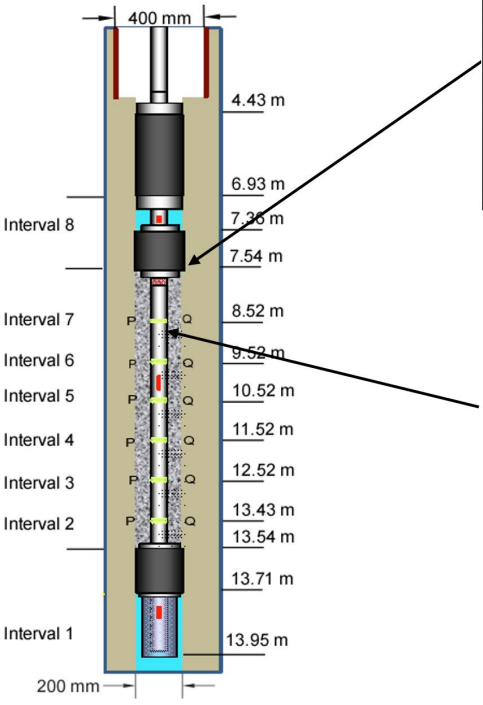

Fig. 7.5m. Broken OPA ring fragments at 7.5 depth at bottom of grout packer. Growing concerns that OPA below grout packer disintegrates and falls down inside inner barrel and is milled away as drilling progresses.

Fig. 8.65m. OPA and cement both have gone at 8.65 m depth (in target section and well below grout packer). Bare 120 mm steel casing of completion is visible on the right-hand side.

Figure 17. Camera hole inspection near base of upper grout packer and within the cased and cemented target interval.

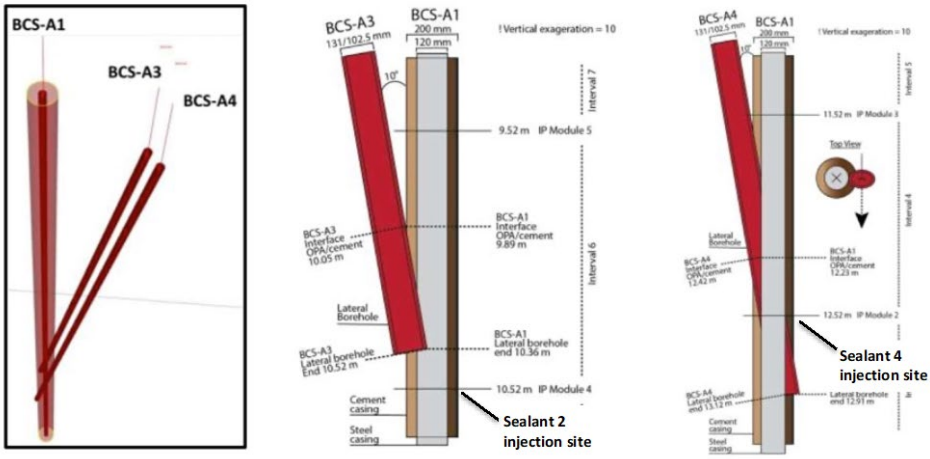

Figure 18. Borehole trajectories designed to intersect the original 200 mm cased and cemented borehole BCS-A1 by lateral boreholes BCS-A3 and BCS-A4.

Lateral borehole BCS-A3 was drilled at an angle of -80° from horizontal, almost parallel to the completion (Figure 18). The hole was drilled from 7.30 m to final depth of 10.60 m, which is equal to 10.43 m BCS-A1 depth. The core drilling hole diameter is 131 mm core diameter, designed to capture a 102.5 mm core. The interface of OPA/cement was encountered at 10.05 m, which is equal to 9.89 m BCS-A1 depth. The Sealant 2 injection point is shown relative to the A3 borehole.

The BCS-A3 lateral captured a very good quality undamaged 1.5 m core (9.10 to 10.60 m). Figure 19 shows the last few centimeters could be preserved in liner and is of very good quality.

Referring to Figure 18, lateral borehole BCS-A4 was drilled from 6.20 m to final depth of 13.10 m, which is equal to 12.93 m BCS-A1 depth. The OPA/cement interface was encountered at 12.42 m, which is equal to 12.23 m BCS-A1 depth. Approximately 70 cm of well-preserved OPA/cement interface of Interval 3 could be retrieved. The Sealant 4 injection point is shown relative to the A4 borehole.

Referring to Figure 20, the BCS-A4 retrieved core preserved in the plastic liner (top photo) and equivalent depths relative to the main test borehole BCS-A1 (bottom photo). Core photo shows the cement (top side of core) and OPA (bottom side).

Figure 19. Lateral borehole BCS-A3 (left) last centimeters of sample with OPA/cement interface and parts of the steel casing of the completion.

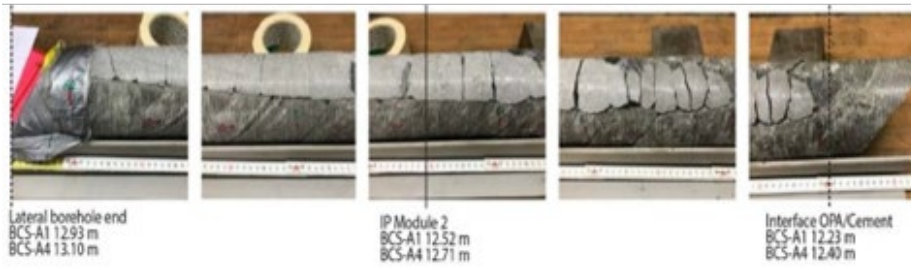

Figure 20. BCS-A4 retrieved core preserved in plastic liner; view of cement patch (top) near 13.10m depth and (bottom photo) with depth interpretation relative to BCS-A1 borehole. The cement (top side)/OPA (bottom side) contact is clearly seen.

`

Summary of Core Sample Analysis

The analysis campaign on the core samples began in January 2020 with the overcore planning session held by CCP and SWISSTOPO partners. The BRGM (French Geological Survey) group also participated and ultimately provided the principal core analytics for the project.

Supporting laboratory work groups include EMPA (Swiss Federal Laboratories), SINTEF (Trondheim Norway based NGO), and Missouri S&T (US engineering school). Technical work provided by these groups is summarized below in Table 7.

Table 7. Analytic Groups and Activities.

Laboratory/University	**Activity**
EMPA (Swiss Fed Laboratories), Zurich, CH	X-ray computed tomography (CT) and data analysis of CS-A experiment core samples (diameter 105 mm, length 400 mm).
BRGM (French Geological Survey), Orleans, France	Core/cement/sealant analytics: Macro-microscopic (optical, SEM), chemical data mapping, XRD, phase chemistry
SINTEF (Foundation for Industrial and Technical Research - NGO), Trondheim, Norway	Illustrate possible workflow for commercial CCS operations with less costly core taking and laboratory testing procedures; steps to “rehabilitate” old or non-preserved caprock samples with aim to develop correlations to be used when no reference plugs are available
Missouri S&T, Rolla, Missouri, USA	CS-A experiment site modelling to predict cement failure and micro-annuli development

Core X-ray Tomography (CT) by EMPA

The work performed by EMPA is documented in an internal project report delivered to CCP partners [10]. The document release requires permission from CCP.

Two 105 mm diameter cores from boreholes BCS-A3 (depth 9.10–10.60 m) and BCS-A4 (depth 11.50–13.05 m) were delivered to EMPA for X-ray tomography (CT) scans in April 2021. From each well, 400-mm core sections of interest that contained cement and OPA were dry-cut to match CT scanner sample length requirements. These 105 mm diameter cores were scanned by the RayScan500 CT scanner (Figure 21-left) using RayWare software for data acquisition (version 4.10.0) and data reconstruction (version 4.9.4).

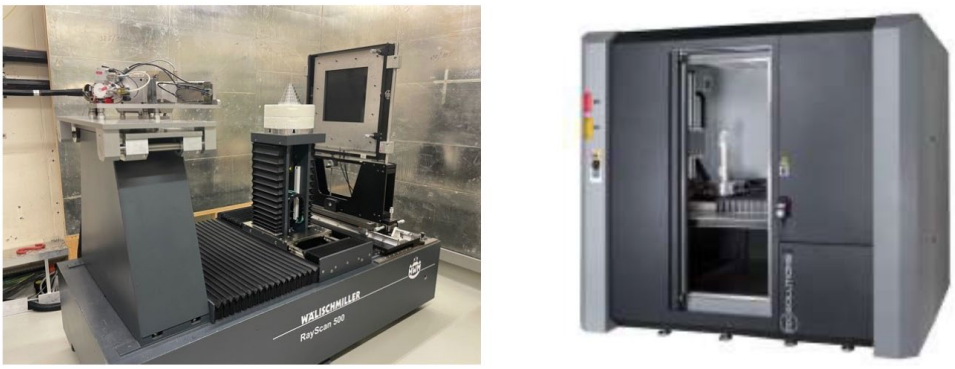

Figure 21. RayScan 500 scanner for 105 mm whole core (left) and RX Solutions EasyTom XL Ultra for 16 mm^3 subsamples (right).

Two additional subsamples for the BCS-A3 core were also scanned at higher resolution to support the work by BRGM. The higher resolution scan dimensions are 16 x 16 x 16 mm from depths 10.27 m and 10.50 m. The subsamples were scanned on the RX Solutions EasyTom XL Ultra (Figure 21-right) with the software XACT (version 21.04.2). Samples were contained in Styrofoam before rolling into the CT scanner. See Figure 22.

To achieve good spatial resolution for the two 400 mm cores, sample scans were overlapped with a vertical offset of 100 mm producing 4 individual scans. Consequently, 16 scans were made. Voxel size is approximately 68 μm^3. See Figure 23 for sample location mapping.

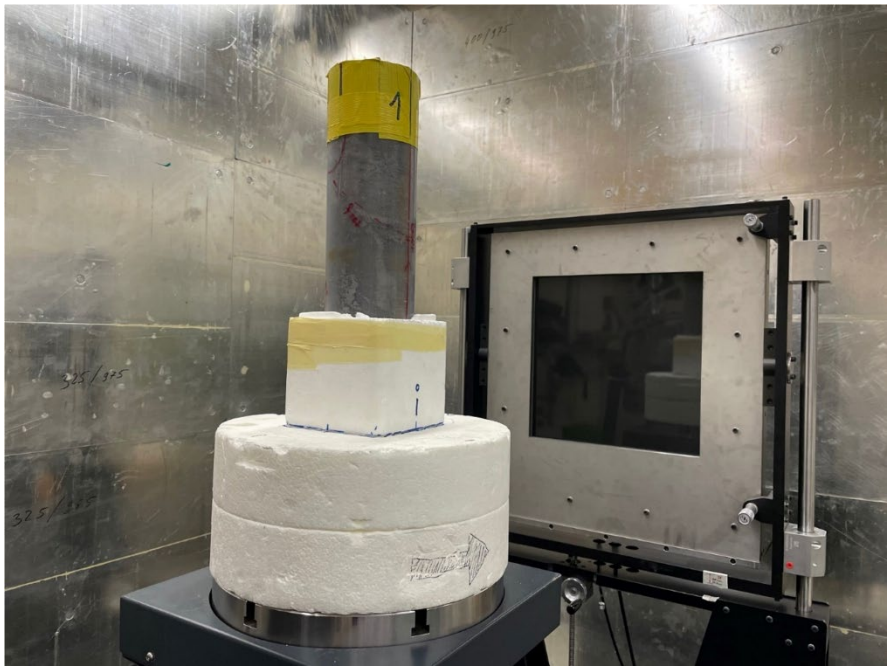

Figure 22. The 105 mm diameter core samples were fixed in a Styrofoam box and mounted vertically on the manipulator of the CT scanner.

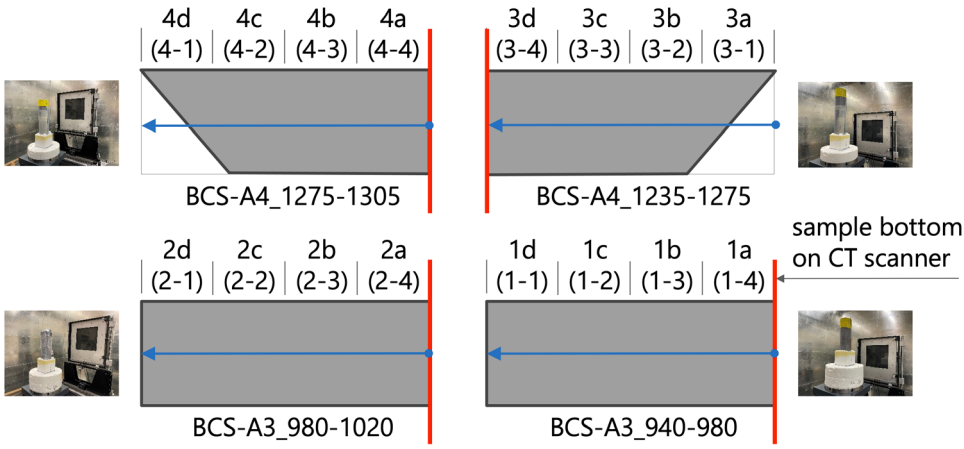

Figure 23. Identification of the individual scans, starting with scan number 1a and ending with number 4d in sequence of the depth of the drill cores. The red line indicates the bottom of the sample during scanning.

CT Scan Outcomes Brief

The EMPA CT scans provided exceptional detail that proved useful in mapping the retrieved core damage and fracture content. Of particular interest was the nature of the outer cement sheath contact with the OPA host rock. Samples were chosen for CT scanning that contained cement material. Fracturing in the cement sheath and OPA formation are of interest in mapping sealant presence and any alteration of the host materials due to sealant chemistry.

Figures 24 and 25 show the BCS-A3 CT scan for the 105 mm core. Some hairline fractures can be seen in the OPA while the cement is relatively intact. The boundary between the cement sheath and the OPA formation is detached. Several technical aspects of this study support the notion that the cement/OPA contact has been compromised from the onset of the cased and cemented borehole installation. This will be discussed in the next section after the remaining core analytics results have been summarized.

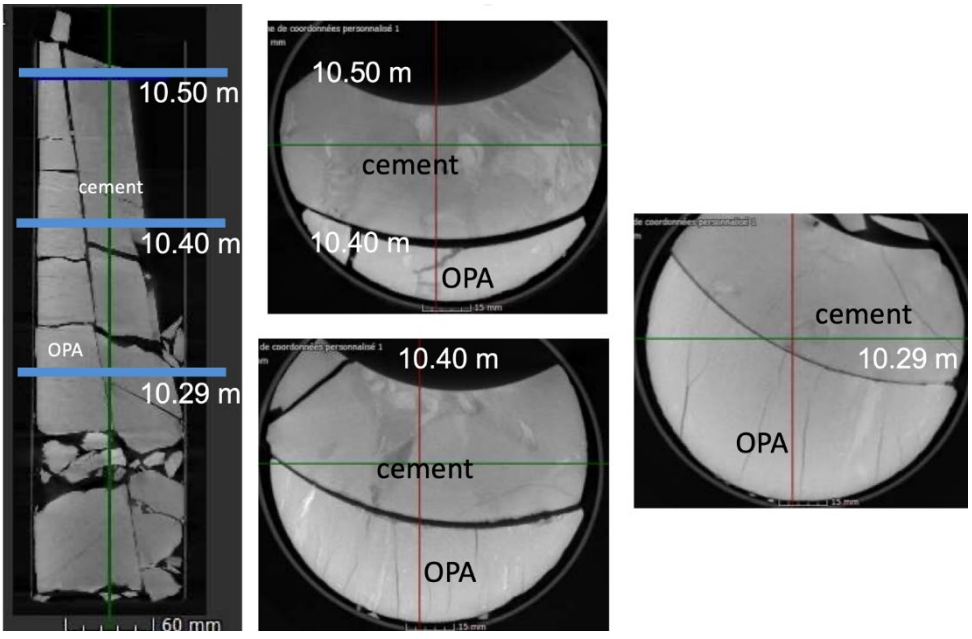

Figure 24. BCS-A3 CT scans performed by EMPA. Modified after EMPA test report No. 5214027275-made available by permission [10].

`

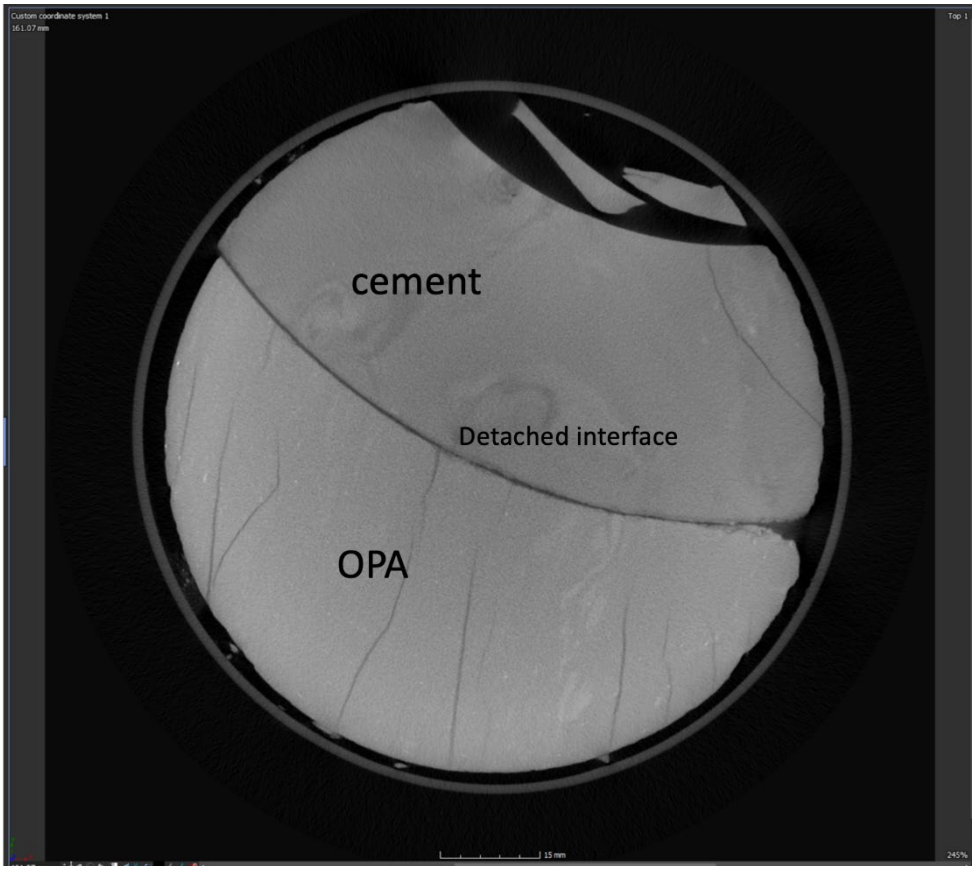

Figure 25. BCS-A3 scan sample 2b showing separation or gap at the cement/OPA boundary.

BRGM Analytics

Subsamples of the BCS-A3 core were extracted at BRGM after review of the 105 mm diameter core. The subsamples had the following dimensions: depth 10.27 m–16 x 16 x 16 mm and depth 10.50 m–12 x 12 x 12 mm. Results and conclusions from this work will be highlighted in this subsection. For a detailed account, please refer to the technical report delivered to CCP by C. Lerouge, *et al.*, BRGM [11]. The BRGM analytical program is described by Table 8.

To assess the impact of the sealant injection and, in particular, its ability to seal the system, different techniques of observation (optical microscope, scanning electron microscope [SEM]) have been combined with mineral determination and chemistry techniques. This work includes macroscopic observations to examine cement texture, fractures, and color contrasts. X-ray diffraction on bulk cement identified crystalline phase, SEM elemental mapping size, and distribution of phases and electron microprobe analytics for bulk chemistry, mineral mapping, and porosity and sealant distribution identification. Infrared and Raman spectroscopy was used to identify cement phase and distribution of sealant as well [11].

Table 8. BRGM analytical program.

TECHNIQUES	OBJECTIVES
CT-scan of the cores(EMPA) Optical microscope, SEM	Macroscopic and microscopic observations →OPA/cement and cement/steel interfaces →General aspect of the cement: texture, fracture network, grain size
X-ray diffraction on bulk cement	Identification and quantification of the cement phases
Electron microprobe: elemental mapping	Mineral map and cement phase chemistry →size and distribution of cement phases →Bulk cement chemistry → Porosity/resin distribution
Infrared spectroscopy	Detection of the resin in the bulk cement
Raman spectroscopy	Detection of the resin at the µm-scale

A focus of the BRGM work was to understand sealant performance at 1:1 scale provided by the Mont Terri Underground Research Laboratory facility. The mineralogical analysis aims to relate changes in borehole effective transmissivity to changes such as fracture opening, sealant clogging, and mineralogical transformations. This detail provides insight to hydraulic injection pressure and flowrate-based performance assessment techniques available to the CO_2 injection well engineering community of practice.

Four sealants were injected at the CS-A experimental well site per Table 2 Phase No. 15–18. However, only Sealants 2 and 4 injection sites could be accessed by core. The following summary of core derived findings can be made regarding the consequences of sealant injection.

Sealant 2 Injection Interval 5/IP Module 4

Referring to Figure 18, the cement/OPA interface in BCS-A3 was intersected at 10.05 m in this deviated hole. The corresponding BCS-A1 depth is 9.89 m. The total depth for the BCS-A3 lateral borehole is 10.52 m corresponding to 10.36 m in BCS-A1. The Sealant 2 injection site depth in BCS-A1 is 10.52 m in Interval 5 via the IP 4 module, which is 16 cm below the lateral intercepting BCS-A3 borehole termination. In other words, the bottom of the core is close (< 20 cm) to IP Module 4, where Sealant 2 was injected.

Figure 26 displays BCS-A3 core subsamples consisting of three 1 cm-thick sections cut perpendicular to the core axis. The nearest sample to the Sealant 2 injection point is the far-right 10.49-50 m sample, about 19 cm above the injection zone. The middle sample at 10.39-10.40 m is 29 cm above the zone of injection, and the third (far-left) sample at 10.28-10.29 cm is approximately 41 cm above the zone of injection.

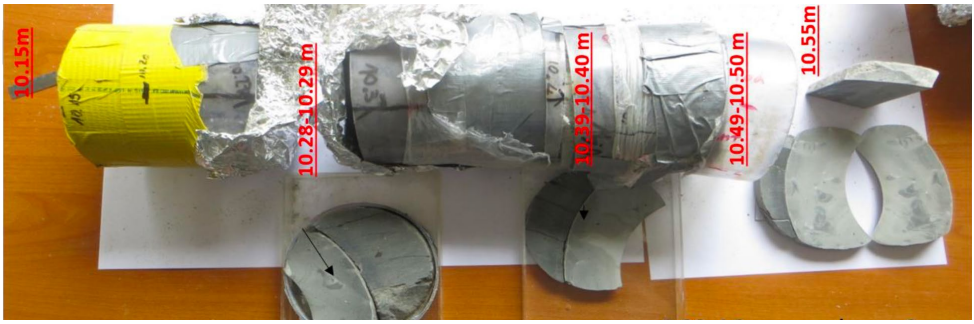

Figure 26. Lateral borehole BCS-A3 core subsamples (10.29 m, 10.40 m, 10.50 m).

Figure 27 shows the BCS-A3 subsamples side by side in order of depth. The deeper (c) far-right sample is closest to the Sealant 2 injection site (19 cm away), and the far-left sample (a) is 41 cm away. The interpretation of these images follows.

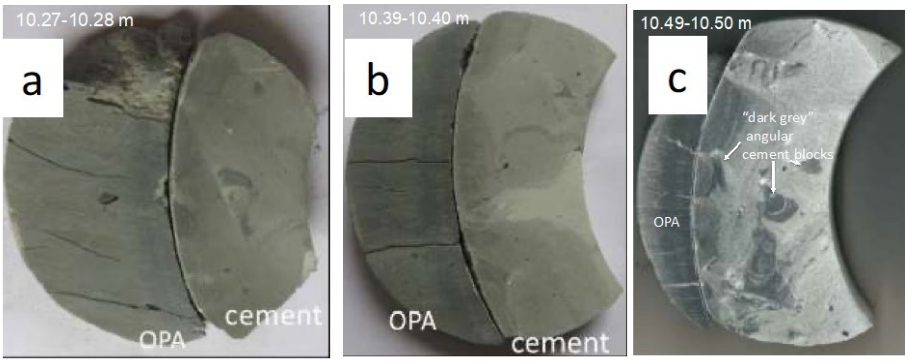

Figure 27. Core subsample zone of injection of the IP module 4 in Interval 5–Photographs of the 1 cm-thick sections perpendicular to the core BCS-A3-figure modified after C. Lerouge, *et al.* [11].

The section depicted by Figure 27c from 10.49-10.50 m is the most heterogeneous in term of grey contrast and texture. The cement in contact with the steel casing is homogeneously light grey and of fine-grained aspect. Further in the cement sheath, some blocks, more or less angular, are present in the light grey fine-grained cement. The cement in contact with OPA is dark grey with some small light grey bands that are perpendicular to the cement/OPA interface. This macroscopic texture might be interpreted as a progressive front of the resin from the zone of injection at the cement/steel interface toward the OPA/cement interface. The more or less angular elements of dark grey cement might be part of the cement that was fractured before the resin injection. Few micro-fractures observed in the cement go through the interface with OPA. Most of the fractures (small openings) in OPA are sub-parallel and are perpendicular to the cement/OPA interface. These small fractures/openings correspond to the bedding of the clay.

The section depicted by Figure 27b from 10.39-10.40 m at 10 cm from the sealant injection point is slightly less contrasted in term of grey color. The cement in contact with the steel casing remains slightly lighter grey than the cement in contact with OPA. A whitish cm-large zone beginning from the cement/steel interface crosscut the cement sheath. By looking at the CT-scan of the core volume,

this zone is connected to a large fracture, and might be interpreted as an important fracture zone filled with sealant.

The section depicted by Figure 27a from 10.27-10.28 m, 20 cm from the sealant injection point, remains slightly contrasted in terms of grey color: light grey color on the side of cement/steel interface and dark grey color on the side of cement/OPA interface. An element of dark grey cement with a straight edge is observed in the middle of the cement sheath, whereas a small whitish zone is present on a corner of the section.

Interpretation

Before Sealant 2 injection, the cement sheath was fractured, and the "dark grey" angular cement blocks are likely the remaining signs of that fracturing (Figure 27c 10.49-10.50 m). The sealant sealed those fractures, but the sealing process was accompanied by a significant sealant/cement reactivity leading to carbonation and high texture modifications. Electron microprobe elemental mapping allowed detailing the chemistry of the cement phases along with sealant distribution characterized as porosity/resin.

The elemental maps (Si, Al, Fe, K, Na, Ca, Mg, and S) were recorded by stage rastering using a stationary beam, with a spatial resolution of 1 µm per pixel and containing 256 by 256 pixels. Each pixel corresponds to a chemical analysis reported in wt% of element and in wt% of oxides. The sum of the oxides of each analysis was compared to 100% to determine a possible contribution of micronic porosity/resin or elements that were not analyzed (CO_2, H_2O). Table 9 lists cement phase oxides summations.

Table 9. List of the cement phases, the structural formula, and their corresponding sum of oxides at electron microprobe, taking into account that CO_2 and H_2O are not measured.

		Sum of Oxides (wt %)
Calcium Carbonate	$CaCO_3$	~55
Portlandite	$Ca(OH)_2$	~76
Brownmillerite	$Ca_2(Al,Fe^{+++})_2O_5$	~97
Katoite	$Ca_3Al_2(SiO_4)_{3-x}(OH)_4$	~87
C4AF	$Ca_4Al_2Fe_2O_{10}$	100
C3A	$Ca_3Al_2O_6$	100
Silice, quartz	SiO_2	100
Hydrotalcite	$Mg_6Al_2(CO_3)(OH)_{16} \bullet 4(H_2O)$	~57
Hydrocalumite	$Ca_2Al(OH)_6[Cl_{1-x}(OH)_x] \bullet 3(H_2O)$	~56

The analyses were then reported in a Ca-Si-(Al+Fe+Mg) triangular diagram wt % of element, classically used to identify major cement phases. The position of analyses in the triangular diagram allowed identifying the major cement phases present in the cement. From this identification, populations of analyses for each cement phase were defined and allowed reconstructing a mineral map. The different steps of treatment of the analyses are summarized in Table 10 and Figure 28.

Table 10. Different steps of treatment of the chemical analyses, modified after C. Lerouge *et al.* [11]

Step	Field Limits	Cement Phases
0	Sum of oxides < minimal value (stat histogram)	⟪ porosity ⟫ / resin
1	Ca/(Ca+Si+AFM)×100 >75	Calcite/portlandite
2	Si/(Ca+Si+AFM))×100 >70	Silice/quartz
3	AFM/(Ca+Si+AFM)<10	CS/CSH
4	AFM/(Ca+Si+AFM)>70	Hydrotalcite
10	Si<70-AFM<70-Ca<30	⟪ clay ⟫
5	AFM/(Ca+Si+AFM)>25 and Si/(Ca+Si+AFM)×100 <10	C4AF, C3A, Afm and AFt
6	AFM/(Ca+Si+AFM)>25 and Si/(Ca+Si+AFM)×100 >10	Stratingite, katoite…
7	AFM/(Ca+Si+AFM)>25	CASH – mix CSH/AF

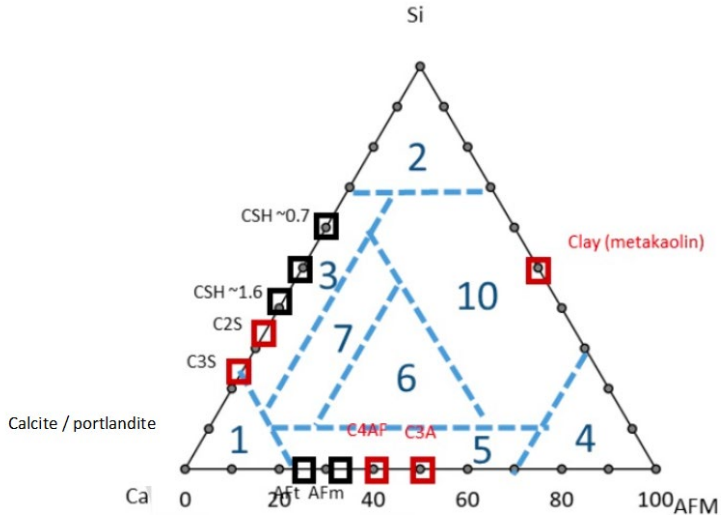

Figure 28. Fields of the chemical compositions of the different cement phases in a Ca-Si-(A+F+M) tertiary [11].

Referring to Table 9, the distribution of Sealant 2 in the 10.50 m sample (Figure 27c) is characterized as porosity/resin (i.e., sealant inference associated with Step 0). Step 0 was performed to sort electron microprobe analyses in which the sum of oxides is very low compared to the sum of oxides of the cement phases possibly present in the cement (e.g., ~55 wt.% for calcium carbonates). No value was equal to zero. The analyses correspond to a mixing between porosity/resin and a cement phase, giving information on micron-sized cement porosity. Figure 29 displays the porosity/resin map distribution of Sealant 2 as well as the mineral content signatures associated with portlandite in the tertiary diagram.

Note Step 10 (Si<70, AFM<70 and Ca<30) is a step applied between Step 4 and Step 5 to separate spot analyses that are close to the clay (metakaolin) endmember in the cement triangular diagram and corresponds in this study to analyses of clay particles present at interface between the cement sheath and OPA.

Based on the portlandite content, the cement sheath generally shows a low carbonation process except in contact with Sealant 2. The textural changes of the cement close to the injection of that resin suggests a reactivity of the cement. This reactivity seems to decrease rapidly with the distance from the resin injection zone. The carbonation process associated with the presence of Sealant 2 is a process that remains unknown. The photomicrograph shown in Figure 29 shows the relatively wide distribution of sealant-resin filled porosity in black.

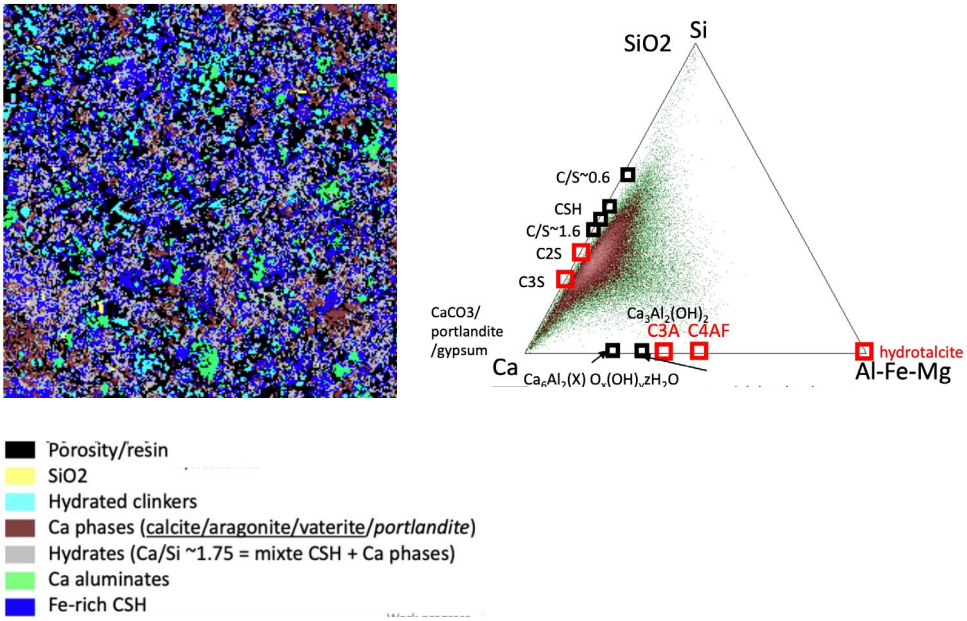

Figure 29. BCS-A3 10.50 m mineral mapping of light grey cement in the Sealant 2 injection interval (elemental mapping (left) & electron microprobe quantification-right).

Although alteration of the cement occurred, re-healing of the damage is observed, and sealing restored. This conclusion is supported by the final hydraulic transmissivity T of 1E-12 m^2/s, two orders of magnitude less than the transmissivity T of 4E-10 m^2/s after heat/cool cycling. See Figure 12.

The cohesion between the cement/casing and cement/OPA has been lost, but the textures of both materials are preserved.

Sealant 4 Injection Interval 3/IP Module 2

Referring to Figure 18, BCS-A4 encountered the cement/OPA interface at depth 12.23 m until depth 12.91 m. This borehole did not encounter any cement casing interface, but part of this core was located

directly in front of IP Module 2, where Sealant 4 has been injected. Figure 20 (bottom photo) shows the BCS-A4 core laid out with the cement (top-light gray)/OPA (bottom-dark gray) contacts.

Referring to Figure 30, to characterize the cement of this interval, three samples were studied. A 1 cm-thick section was cut perpendicular to the core axis at 12.71 m, which was the Sealant 4 injection depth. A 1 cm-thick section was also cut perpendicular to the core axis at 12.90 m, about 20 cm from the sealant injection, and a 1 cm-thick section of cement perpendicular to the core axis at 12.82 m (Figure 29).

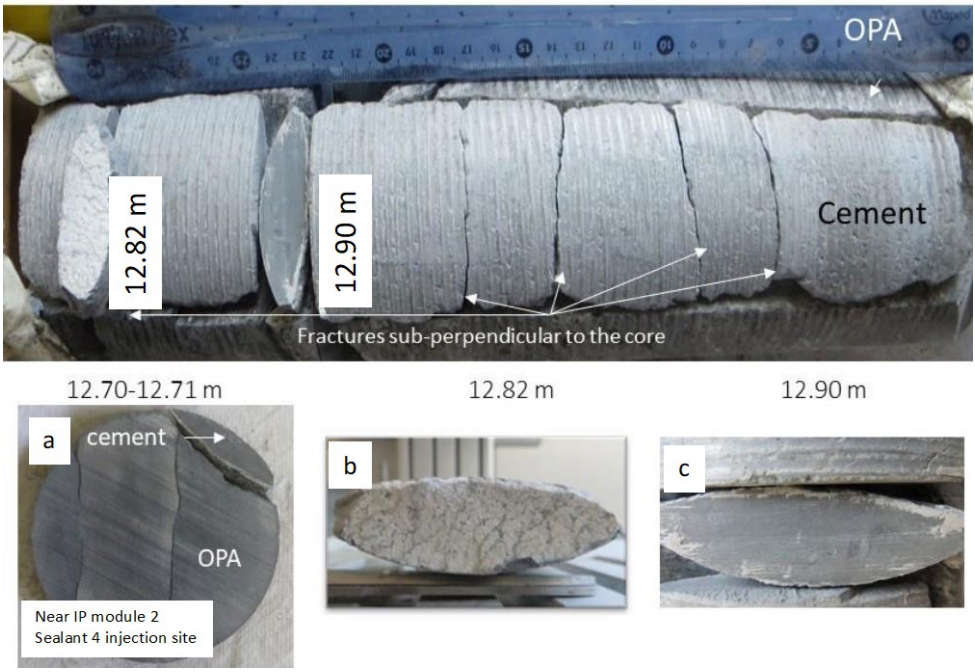

Figure 30. Photographs of the BCS-A4 taken from C. Lerouge, *et al.* [11] - three 1 cm-thick sections perpendicular to the core 12.70-12.71 m (a), 12.82 m (b) and 12.90 m (c). Sealant 4 injection site at IP module 2 is located near 12.71 m.

Interpretation

All the subsample sections taken from the BCS-A4 core (at 12.71 - IP Module 2 sealant injection site, at 12.82 and at 12.90 m) sampled approximately 2 cm of cement at the contact with OPA. All samples have a homogeneous dark grey color. No microfractures were observed.

Sealant 4 was observed to reach and seal (at least) some of the fractures. This view is also supported by the hydraulic injection testing campaign shown in Figure 12. The Sealant 4 injection following the induced permeability heating cycles reduced hydraulic transmissivity by three orders of magnitude from 5E-10 m^2/s to 4E-13 m^2/s.

The sealing appears to be limited to the zones where the sealant could flow (high permeability pathways). In that sense, the effectiveness of Sealant 4 is more "limited" than that of Sealant 2 as no reactivity with the surrounding cement was observed.

SINTEF Analytics

The original project plan needed to be modified due to overcoring abandonment and a method devised to extract meaningful well integrity and sealant performance information from limited core material. Details for the SINTEF work were taken from a report delivered to CCP and a recent publication [12, 13] summarizing the SINTEF geomechanics work.

The original analytical program included the following:

- Test the intact cement/formation core for reference strength and permeability.
- Analyze core samples with good remediation fluid in fracture using CT imaging before and after sealant treatment.
- Expose core samples with good remediation to temperature cycles.
- Test core samples with cracked remediation for leakage risk (stress path program)
- Compare CT image scan to borehole sonic logging.

It should be noted that there is a distinction between mechanical strength of the test well system, which is characterized by the geomechanical property values sought by the SINTEF work, and the "strength" of a sealant injected and deemed successful to restoring CO_2 storage containment. For example, sealant strength is often quantified in terms of pressure holding differentials in terms of kPa/m [14].

The new focus for the SINTEF work was to develop a workflow for commercial CCS operations with less costly core acquisition and laboratory testing procedures than utilized in this study. This workflow includes steps to "rehabilitate" old or non-preserved caprock samples with aim to develop correlations to be used when no reference plugs are available.

Two cores from the Opalinus clay formation (OPA) were investigated in this study. One was an unpreserved "as received" core from the BCS-A3 and A4 lateral boreholes, the other was a well-preserved core from an adjacent borehole near the test site supplied by Mont Terri consortia member Nagra (National Cooperative Disposal of Radioactive Waste located in Wettingen, CH). For this geomechanical properties work, only small sample sizes were available. Refer to the Stroisz *et al.* [13] for core sample preparation and testing detail.

Summary of Results–Geomechanical Perspective

All samples were cylindrical, and the measurements were performed in the axial direction. Results show that obtaining valuable data on the damaged cores, such as unpreserved shale, is possible by utilizing adequate testing methods. For example, tests on the small-size samples provide reliable information regarding the acoustic and mechanical properties of the material. It is, however, disputable to what extent one can recover the original properties from the unpreserved material.

Referring to Figure 31a, a strong dependence on moisture content dominates these results. This is common to argillaceous rocks such as the OPA and can also be observed for the preserved core data set in Figure 31b. The rock property trends are relevant to addressing in situ properties. However, the absolute values are still questionable as restoration to in situ moisture conditions for the OPA sample sets is uncertain**.**

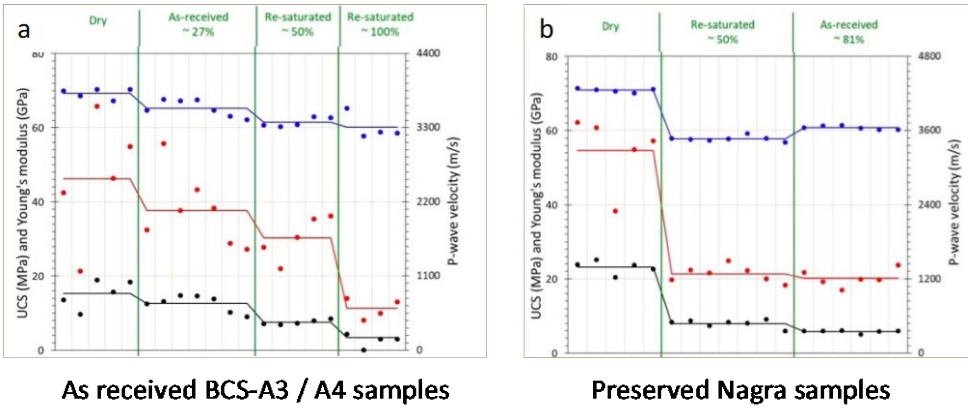

Figure 31. UCS results for unpreserved "as received" OPA samples (left plot - a) compared to preserved samples (right plot - b) strength (red), Young's modulus (black), P- wave velocity (blue). Solid lines refer to average values, (±std) denotes standard deviation - modified after Stroisz *et al.* [13]

As far as was possible with limited intact cement samples, no strength anomaly was detected although some distinct differences appear between casing and shale cement boundaries. Since no coupled cement/OPA core was recovered in the BCS-A3/A4 boreholes, (i.e., the cement-OPA interface was decoupled) nothing definitive could be determined regarding strength at sealant healed contacts.

Missouri S&T–Comprehensive Experimental Site Modelling

The simulation results predict that the integrity of the Mont Terri pilot injection well was compromised early in the life of the well installation by the cement hardening process that caused decoupling or detachment at the cement/OPA interface [15]. That is, tensile debonding failure initiates at the cement-formation interface due to excessive cement shrinkage during hardening. This conclusion is supported by the initial hydraulics testing program results that showed an extremely short duration time delay of injection pressure response between bottom open hole interval 1 and top open hole interval 8. See Figure 12 in Chapter 28 of this volume for details. Furthermore, this decoupled interface between the cement-formation interface could help explain the poor overcore drilling performance. See Figures 17 and 18.

Modelling also predicts that cement shear failure initiates at the casing-cement interface during pressure testing (excessive wellbore pressure). This result may be evidenced in the hydraulic cross-flow data between IP Modules during the dipole testing campaign. Refer to Table 2 phase No 9. However, since the overcoring program was compromised by rubblizing and grinding of the cement sheath and OPA ring during drilling, shearing at the casing cement interface could not be verified.

Furthermore, modelling of the CS-A experiment site conditions taking into account the pressure and thermal cycling protocols implemented, predict shear failure of the cement sheath at the injection nozzles (i.e., IP Modules). The hydraulics data support this prediction. However, the core samples that included cement sections did not find fracture damage that could be determined to be non-drilling induced. Note the cement CT scans (Figures 25 & 26) and polished sections (Figures 27, 28, & 31) find cement to be undamaged.

CONCLUDING REMARKS

The goal of this project is to determine the long-term sealing integrity of well systems, focusing on potential leakage pathways associated with micro annuli interfaces, and to develop a sealants-based approach to restore pressure containment. This was achieved.

The final hydraulic testing campaign revealed a good sealing of the entire borehole completion after the injection of four sealants. All intervals yield permeabilities after damage restoration similar to the original OPA host rock condition.

The experimental test site at Mont Terri is located roughly 300 m below ground surface, providing subsurface conditions of stress and interactions of a relatively large rock mass, to enable realistic well damage processes that are thought to occur at deep carbon storage sites. Even though the test site subsurface conditions planned for this multiyear project were achieved, more work is required to move to real field conditions.

It is hoped that the four novel sealants tested will be further developed for introduction to deep carbon storage site operations.

ACKNOWLEDGEMENTS

We thank the CCP4 Project Partners and SWISSTOPO for their technical and financial support. Especially thanks to Thomas Fierz, managing partner with Solexperts for his test site design collaboration efforts that have made this project possible.

REFERENCES

1. Pearson,F.J., "WS-A Experiment: Artificial Waters for Use in Laboratory and Field Experiments with Opalinus Clay", TECHNICAL NOTE 99-31, January 1999, Paul Scherrer Institut.
2. TECHNICAL NOTE 2016-45 July 2017, CS-A Experiment: Tracer Test campaign 1: Check of potential dipole flow fields, Rösli, U., Gisiger, J., Minnig,c., Reimus, P., and Roback. R.
3. Goodman, H.E., Imbus, S.W., Espie, T., Minnig, C., Rösli, U., Fierz, T. and Lettry, Y. (2016): *Large rock mass experimentation @ Mont Terri underground research laboratory - CO_2 containment assurance experiments*. 13th International Conference on Greenhouse Gas Control Technologies, Lausanne, Switzerland, 14-18 November 2016 (GHGT-13). *Energy Procedia*, Vol. 114, pp 5239-5250. Available at: https://www.sciencedirect.com/science/article/pii/S1876610217318696.
4. Goodman, H., Espie, T., Minnig, C., Rösli, U., Gisiger, J. and Roback, R. (2018): *Testing Advanced Sealants to Address Wellbore Seepage of Co2 Behind Casing at the Mont Terri Underground Research Laboratory*. 14th Greenhouse Gas Control Technologies Conference Melbourne 21-26 October 2018 (GHGT-14). Available at SSRN: https://ssrn.com/abstract=3365937.
5. Welch N., Gilbertson, R., Boukhalfa, H., Robak, R., Carey, J.W., Goodman, H., Rösli, U., Gisiger, J., Espie, T. and Minnig, C. (2020): *Effectiveness Of A "Smart" Hydrogel In Well Leakage Remediation*. Proceedings SPE ACTE 2020. In prep.
6. Tavassoli, S., Shafiei, M., Minnig, C., Gisiger, J., Rösli, U., Petterson, J., Theurillat, T., Mejia, L., Goodman, H., Espie, T. and Balhoff, M. (2019): *Pilot Case Study of Wellbore Leakage Mitigation using pH-Triggered Polymer Gelant*. Society of Petroleum Engineers. doi.org/10.2118/194251-MS, SPE/ICoTA Well Intervention Conference and Exhibition, 26-27 March, The Woodlands, Texas, USA.
7. Fleury, M., Sissmann, O., Brosse, E., and Chardin, M., A Silicate Based Process for Plugging the Near Well Bore Formation, *Energy Procedia* 114 (2017) 4172–4187.

8. Wiese, B., Fleury M., Basic I., Abdollahi, J., Patrnogic, A., Hofstee C., Carlsen I., Wollenweber J., Schmidt-Hattenberger C., Drysdale R., and Karas D. (2019): Near well-bore sealing in the Becej CO_2 reservoir: field test of a silicate based sealant. *International Journal of Greenhouse Gas Control*, **83**, pp. 156-165.
9. Pearson, F. J., Arcos, D., Bath, A., Boisson, J.-Y., Fernández, A. M., Gäbler, H.-E., Gaucher, E., Gautschi, A., Griffault, L., Hernán, P., Waber, H. N., (2003). *Mont Terri Project – Geochemistry of water in the Opalinus Clay Formation at the Mont Terri Rock Laboratory*. Swiss Federal Office for Water and Geology Series No. 5. Bern.
10. Empa test report No. 5214027275, Eidg. Materialprüfungs- und Forschungsanstalt Dübendorf, 3rd December 2021.
11. Lerouge, C., Tremosa, J., Manceau, JC, Duee, C., Maubec, N., Wille, G., and Lahfid, A., TECHNICAL NOTE TN-2021-87 February 2022, CS-A Experiment: Post-Mortem analysis and interpretation of the Mont-Terri CS-A experiment, BRGM.
12. SINTEF - SNOWPACCS - Swiss Norwegian Post-Mortem Analysis of Mont Terri CCS well project at SINTEF, sponsored by Gassnova through the CLIMIT-Demo program, project #618176.
13. Stroisz, A.M., Bhuiyan, M.H., Agofack, N., Edvardsen, L., Cerasi, P., "The hidden value of insufficiently preserved shale material", American Rock Mechanics Association, ARMA 22–683, 56th US Rock Mechanics/Geomechanics Symposium, Santa Fe, New Mexico, USA, 26-29 June 2022.
14. Ho, J., Tavassoli, S., Patterson, J., Shafiei, M., Huh, C., Bommer, P., Bryant, S., and Balhoff, M., "The Use of a pH-Triggered Polymer Gelant to Seal Cement Fractures in Wells", SPE-174940 (2016).
15. Zhang, W., Eckert, A., and Goodman, H., "INTEGRATED INVESTIGATION OF WELLBORE INTEGRITY OF THE MONT TERRI EXPERIMENTAL CO_2 INJECTION WELL", Chapter 30*, Carbon Dioxide Capture for Storage in Deep Geological Formations, Volume 5*, Karl F. Gerdes (Editor) 2022.

Carbon Dioxide Capture for Storage in Deep Geological Formations, Volume 5
Karl F. Gerdes (Editor)
© 2022 BP. All rights reserved.

Chapter 30

INTEGRATED INVESTIGATION OF WELLBORE INTEGRITY OF THE MONT TERRI EXPERIMENTAL CO_2 INJECTION WELL

Weicheng Zhang[1], Andreas Eckert[1], Harvey Goodman[2]
[1] Department of Geosciences and Geological and Petroleum Engineering, Missouri University of Science and Technology, Rolla, Missouri, USA
[2]Chevron ETC, Houston, TX, USA

ABSTRACT: The Mont Terri project is an international research project that performs hydrogeological, geochemical, and geotechnical characterization of the Opalinus Clay formation and investigates the feasibility for geological wastewater disposal and carbon dioxide sequestration in such a formation, with a particular focus on injection well integrity. The integrity of the cement sheath for the Mont Terri Underground Research Laboratory (MT-URL) test site pilot CO_2 injection well is critical to maintain zonal isolation and prevent inter-zonal communication. Loads arising from changes during multiple stages of the wellbore life span may induce various modes of cement failure within the cement (shear failure and tensile cracks) and at the cement-casing and the cement-formation interfaces (debonding fractures). This project utilizes an integrated laboratory and numerical approach to investigate the cement hardening process, and to predict cement failure for the Mont Terri CO_2 injection well under various loading conditions. An innovative experimental setup was established to measure the cement pore pressure variation during the hardening process under downhole conditions, and a staged 3D finite element analysis approach including loads from various operations is used to model in-situ downhole conditions and predict failure occurrence. For the Mont Terri CO_2 injection well, the modelling results predict that cement shear failure initiates at the casing-cement interface during pressure testing (excessive wellbore pressure). Tensile debonding failure initiates at the cement-formation interface due to excessive cement shrinkage during hardening. The location, initiation conditions, and severity of cement failure are largely affected by the geometry of the injection string and the cement sheath. Increasing the temperature of the injected fluid can mitigate micro-annulus (MA) occurrence caused by cement shrinkage during hardening to a certain degree. The enhanced understanding of the cement hardening process and cement failure occurrence can provide insights and guidance for future construction of CO_2 injection wells and optimize the operation of CO_2 injection operations.

KEYWORDS: wellbore integrity, cement failure, micro-annulus, cement hardening, staged finite element analysis, integrity analysis, cement shrinkage

INTRODUCTION

Micro-Annulus as an Important Hazard to Compromise Wellbore Integrity

Ensuring and maintaining wellbore integrity over the life cycle of a well is one of the primary goals for successful and sustainable geologic CO_2 sequestration. The integrity of the cement sheath is crucial

to maintain zonal isolation and to prevent the unwanted leakage of injected CO_2. During the lifespan of an injection well, loads arising from multiple processes can affect the state of stress in the wellbore system and, under severe conditions, may induce failure in the cement sheath. As shown in Figure 1, different types of failure, including debonding (micro-annulus, MA, Figure 1a, 1b, and 1d), radial cracking (Figure 1c), and shear failure (Figure 1c), can occur throughout the life of the well, causing severe leakage problems, which in turn can dramatically reduce the injection efficiency. The systematic and inter-connecting debonding fractures at the casing-cement and the cement-formation interfaces (Figure 1a, 1b) are defined as micro-annuli (MA), which initiate when the radial stress exceeds the tensile strength [1]. For certain loading conditions, the debonding fractures at the cement-casing and the cement-formation interfaces may have apertures large enough (10-100μm) to act as a fluid flow channel [2] and may propagate far enough to connect different zones. There are three major factors that can lead to a decrease of the radial stress in the wellbore system and promote the generation of MA:

- Mechanical loads due to drastic pressure decrease on the inside of the casing. The radial stress of the wellbore system may become tensile when the inner casing pressure unloads rapidly [3].
- Cement shrinkage during hardening. The cement volume during hardening can change as much as 5% [4,5]. The amount of shrinkage that occurs after the cement slurry becomes immobile (~0.1-2%) and establishes elastic properties can lead to the development of tensile radial stress and the generation of MA [3,6]. The volumetric shrinkage of cement slurry is a centripetal process that tends to compress the casing-cement interface, reducing the likelihood of generating MA, and to extend the cement-formation interface, thus increasing the likelihood to generate MA [4,7].
- Thermal stresses arising from temperature differences between a cold injection fluid and the formation (e.g., rapid cooling during injection) can significantly decrease the radial stress and thus lead to the generation of MA [6,8]. In addition, thermal cycling resulting from alternating fluid injection applications [9], as well as seasonal variations of the ground temperature, and different wellbore sections are important factors that need to be considered [10,11].

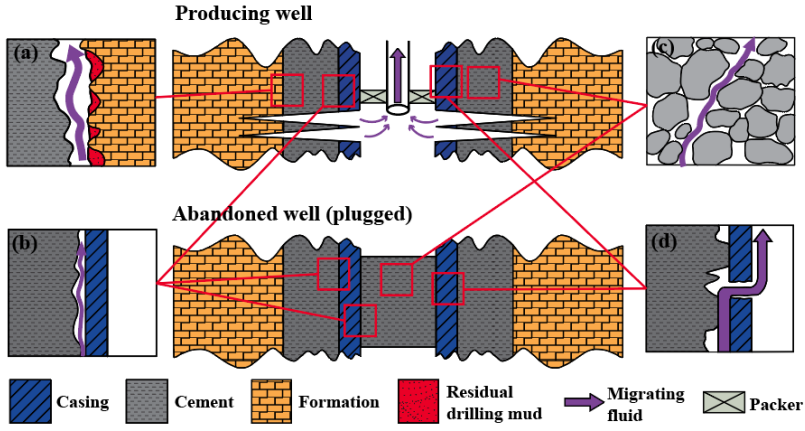

Figure 1. Leakage pathways in a damaged wellbore system. Cased wellbore (upper) and abandoned/plugged wellbore (lower).

The prediction of the conditions and the location of MA occurrence has been addressed by various laboratory experiments and numerical modelling studies [9,10,11,12]. However, the state of stress developing in the cement during hardening is not well-understood and well-quantified. The chemical, mechanical, and thermal processes during the cement hardening process are largely driven by the downhole conditions, which in turn affect the resulting mechanical properties and the state of stress in the cement. Previous numerical studies are commonly based on limiting and generalized assumptions regarding the process of cement hardening and the resulting state of stress [9,10,11]. An isotropic compressional stress equal to the cement slurry pressure minus the mud pressure is commonly assumed for the hardened cement by most numerical studies; this assumption ignores the influence of cement bulk shrinkage and pore pressure variation during hardening. These assumptions largely affect the accuracy, representation, and value of the modelling results. A new approach that systematically considers downhole conditions and represents the cement hardening process is needed for the prediction of MA occurrence and severity, and the evaluation of wellbore integrity.

Cement Integrity Damage Due to CO_2 Injection

For CO_2 injection wells, the carbonation reaction between Portland cement and CO_2 is a complicated process controlled by CO_2 concentration, presence of water, age of the cement, pressure, temperature, and the level of intactness of the cement matrix [13,14]. Oilwell cement and CO_2 reactions have been extensively investigated by various laboratory studies, including the influence of pressure and temperature [15,16], reaction period [15], and presence of various additives [15]. Silica-based additives and pozzolanic additives are widely used to increase the resistivity of cement against the carbonation reaction [15]. The major chemical reactions between CO_2 and different compositions in the cement are presented in Figure 2 and Equation 1 to 5 [17].

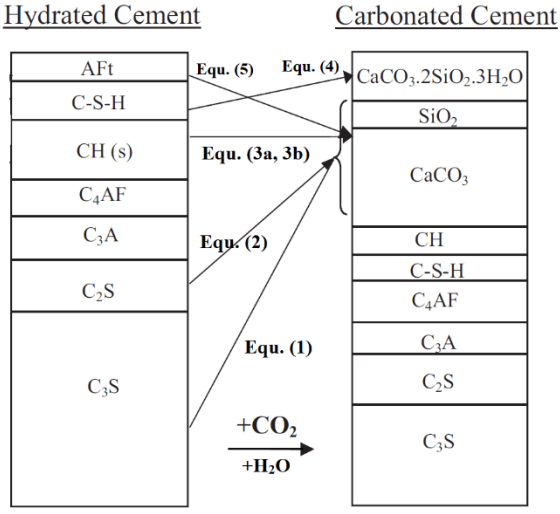

Figure 2. Carbonation reactions of Portland cement, figure adjusted from Kashef-Haghighi *et al.* [17]. Numbers refer to reaction equations 1 to 5 on the following page.

The carbonation reactions listed in Equation (1) to (5) are aqueous phase reactions and involve both dissolution of solid cement compositions and reaction with the dissolved CO_2:

$$3CaO \cdot SiO_2(s) + 3CO_2(aq) + nH_2O \rightarrow SiO_2 \cdot H_2O(s) + 3CaCO_3(s) \quad (1)$$

$$2CaO \cdot SiO_2(s) + 2CO_2(aq) + nH_2O \rightarrow SiO_2 \cdot H_2O(s) + 2CaCO_3(s) \quad (2)$$

$$3CaO \cdot 2SiO_2 \cdot 3H_2O(s) + 3CO_2(aq) \rightarrow 3CaCO_3 \cdot 2SiO_2(s) \cdot 3H_2O(s) \quad (3)$$

$$Ca(OH)_2(s) \rightarrow Ca(OH)_2(aq) \quad (4a)$$

$$Ca(OH)_2(aq) + CO_2(aq) \rightarrow CaCO_3(s) + H_2O \quad (4b)$$

$$3CaO \cdot Al_2O_3 \cdot 3CaSO_4 \cdot 32H_2O(s) + 3CO_2(aq) \rightarrow 3CaCO_3(s) + 3CaSO_4 \cdot 2H_2O(s) + 2Al(OH)_3(s) + 9H_2O \quad (5)$$

Based on the reaction products and porosity distributions in cement samples reacted with CO_2 (with an initial porosity of 10%), Barlet-Gouedard [15] divided the cement into four zones along the direction of CO_2 invasion (Figure 3):

- Zone I is the sample skin, consisting of calcium carbonate precipitations and a highly corroded cement matrix. A balance is achieved between the calcium carbonate dissolving into calcium and carbonate ions and the calcium and carbonate ions in the surrounding water precipitating into calcium carbonate. This zone is very loose and features a very high porosity up to 35% (Figure 3c).
- Zone II is the carbonated zone. Carbonation reaction products (mostly calcium carbonate, Equation 1 to 6) develop a consolidated and low porosity (5-8%; Figure 3c) carbonate matrix. The developed carbonate matrix has a positive influence on increasing the cement strength and reducing the cement permeability [17]. However, due to the relatively high dissolution rate of the calcium carbonate, Zone II would lose calcium and carbonate ions in the long-term and finally becomes Zone I.
- Zone III is the dissolution zone. A large quantity of CO_2 (saturated in water) invades the cement, and the carbonation reactions occur systematically. As a result, the cement matrix developed by the hydration reaction starts to dissolve, which features a significant porosity increase (up to 30%; Figure 3c).
- Zone IV is the diffusion zone. A relatively small amount of CO_2 diffuses into the cement matrix through seepage and reacts with the cement components, but most of the cement components have not yet reacted and the matrix skeleton remains intact.

Various cement characteristics developed during the hardening process have significant influence on the cement-CO_2 reaction. Li *et al*. [18] reported that a more compact cement matrix can better resist the invasion of the CO_2 and delay the carbonation reaction. Omosebi *et al.* [16] pointed out that a more intact and consolidated cement matrix has better integrity against CO_2 invasion under high temperatures (up to 200°C). Wolterbeek *et al.* [19] observed that the presence of pre-existing fracture can significantly accelerate the carbonation reactions.

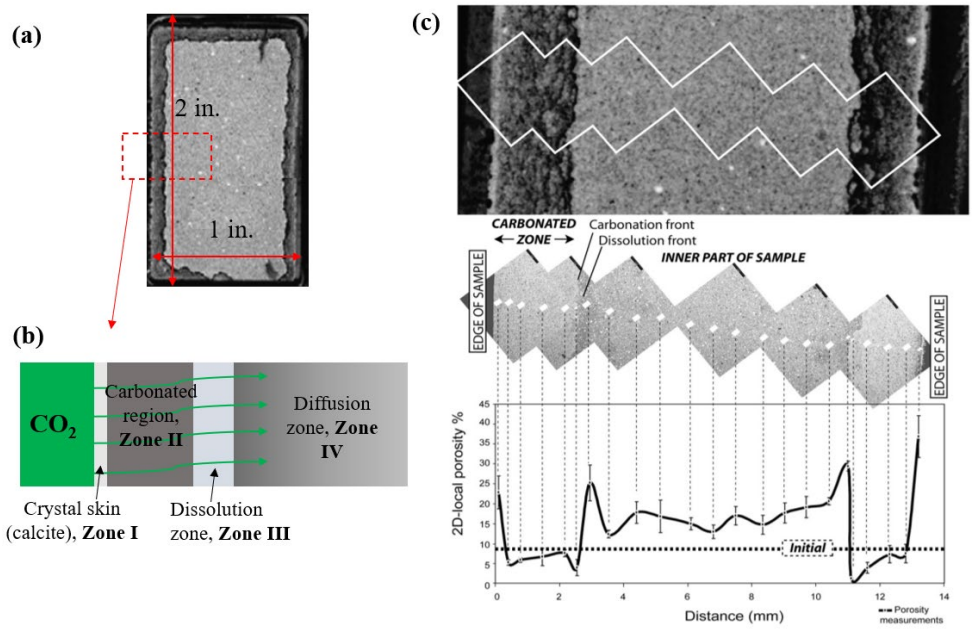

Figure 3. Four representative zones in a CO_2 degraded cement (adjusted from [15]). (a) a Class G cement intersection after reacting with CO_2 under 10 MPa and 80°C for 60 days. (b) four zones along the invasion direction of CO_2. (c) Porosity can be used to distinguish the four zones.

Mont Terri CO_2 Injection Well

An experimental injection well was drilled at the Mont Terri Rock Laboratory in April 2015 to obtain a better understanding of CO_2 injection efficiency, migration, and potential leakage problems during long-term CO_2 injection. The structure of the wellbore is shown in Figure 4. The pilot hole has a diameter of 400 mm and a depth of 4.26 m. The diameter of the second stage is 200 mm, and the well has a depth of 14.4 m. An injection string with injection and monitor modules (I/P modules), packers, and hydraulically controlled valves has been installed in the well (Figure 5). Neat Portland class G cement was used to cement the surface liner and the injection string to the borehole wall, as well as the section of the string between grout packer 1 and grout packer 2. The cement slurry was grouted into the annulus only by gravity and without any additional pressure. Supercritical CO_2 was the main injection fluid for injection activities of this well. Injection fluid leakage and reduction of injection efficiency were observed after pressure and temperature cycles (see Chapter 28). After completion of all injection tests, the wellbore section outlined by the dashed purple box (Figure 4) was over-cored to evaluate the damage of the cement sheath [20].

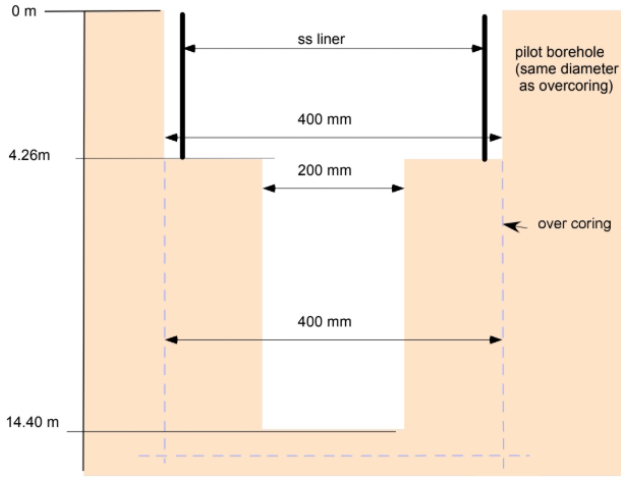

Figure 4. Wellbore structure of the Mont Terri CO_2 injection well.

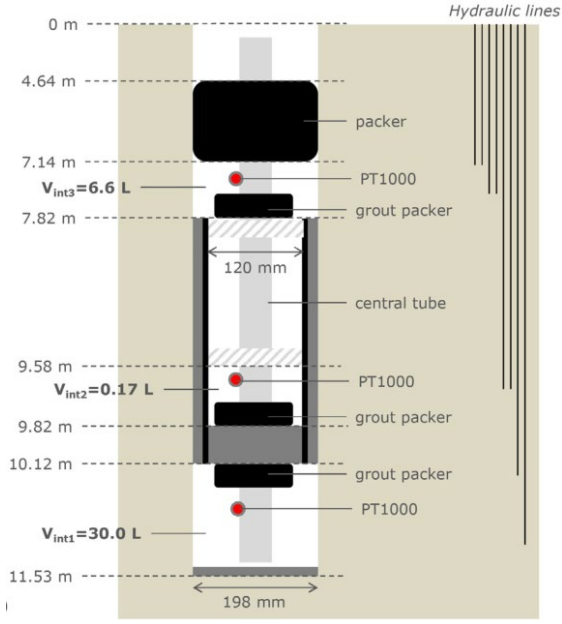

Figure 5. Completion design of the Mont Terri CO_2 injection well. Figure adapted from Manceau *et al*. [20].

Study Objective

The objective of this study is to develop an integrated approach to investigate the wellbore integrity of the Mont Terri CO_2 injection well and to upscale the approach to a general field-scale CO_2 injection well. Figure 6 illustrates the structured workflow of this study. The approach integrates a staged Finite Element Analysis (FEA) [14,21], various laboratory tests, and geochemical analyses to simulate loads arising during the lifespan of the Mont Terri CO_2 injection well and to predict the initiation, evolution, and severity of cement failure. Particular emphasis is placed on the cement hardening process due to its significant influence on failure occurrence in the cement seal. Results from the integrated approach are compared with the field observations of the Mont Terri CO_2 injection well to validate and calibrate the analysis. Based on the findings of the Mont Terri injection well, the approach is upscaled to a generalized field-scale CO_2 injection well at 1000 m depth. To account for the differences in downhole conditions, an additional experimental cement pore pressure measurement setup is introduced to better simulate the cement hardening process, the cement-formation interaction, and the resulting state of stress. Finally, this study combines results from both Mont Terri and the generalized field-scale CO_2 injection wells and summarizes factors which promote or inhibit cement failure, requirements for cement properties, and suggestions for field operations. A limitation on this study is that modelling of cement degradation due to CO_2 is omitted in the upscaling process due to the limited degradation test data available for the targeted downhole conditions.

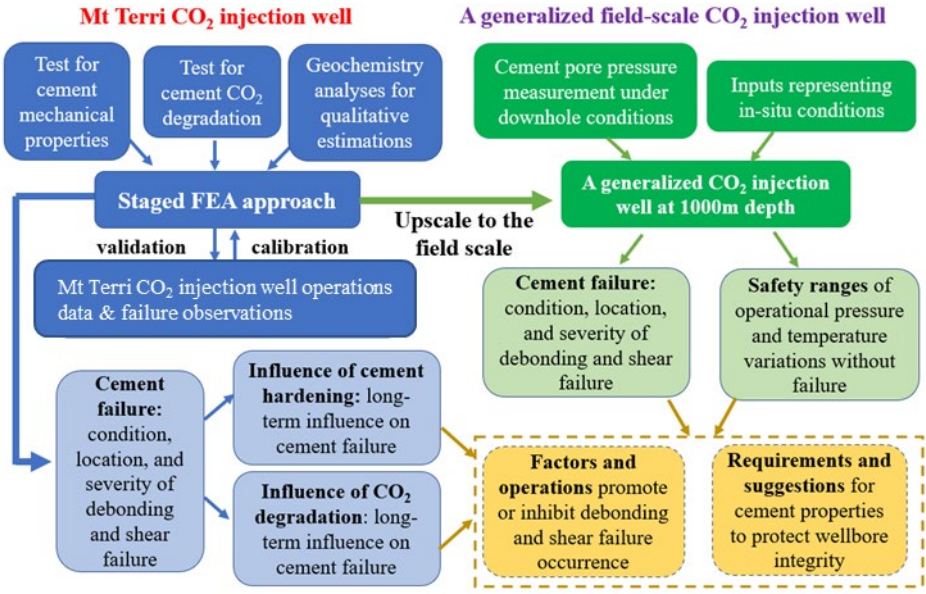

Figure 6. Flowchart of the integrated approach of this study. Content in blue represents the investigation of the Mont Terri CO_2 injection well; Content in green represents the upscaling to a generalized field-scale CO_2 injection well; Content in yellow shows generalized implications for field operations.

INTEGRATED INVESTIGATION OF THE MONT TERRI PILOT WELL

As shown in the blue content in Figure 6, the integrated approach for investigating wellbore integrity for the Mont Terri CO_2 injection well has three main components to acquire accurate input parameters for the staged FEA models:

1. Ultrasonic measurement of cement elastic parameters.
2. Cement CO_2 degradation experiments and subsequent mechanical tests to quantify the influence on the cement mechanical properties.
3. Macro-meso-micro scale geochemical analyses to qualitatively estimate the long-term variations of the cement microstructure and mechanical properties.

Cement properties obtained for the Mont Terri CO_2 injection well are input to the cement hardening model embedded in the staged FEA approach. Discussion of the cement state of stress developed after hardening, failure occurrence during pressure and thermal cycling, and the failure likelihood after long-term CO_2 degradation are presented in this section.

Ultrasonic Measurement of Cement Elastic Parameters

Ultrasonic testing was performed during curing of cement samples to determine the elastic parameters of Poisson's ratio and Young's modulus to be used as input parameters for the subsequent modelling process. After calibration, a GCTS ULT-100 ultrasonic interface was used for the test (Figure 7). Cement samples were prepared to represent the cement cured under Mont Terri downhole conditions:

- Portland Class G cement with a water:cement ratio of 0.44 was used.
- The excessive water from the cement slurry was removed every 10 minutes.
- Four samples were tested after 20 hours, 30 hours, 40 hours, and 50 hours. Due to the drastic material property change, shrinkage occurrence, and state of stress development [3,13,14], 20-50 hours is the critical period and are compared to Bourissai's results [20].

The test results are plotted in Figure 8 and compared to the laboratory measurements of Bourissai *et al.* [20], which were performed under similar conditions. As shown in Figure 8, the test results of the two studies are in agreement. The results from Bourissai *et al.* are used for our modelling process as they extend over a longer time period.

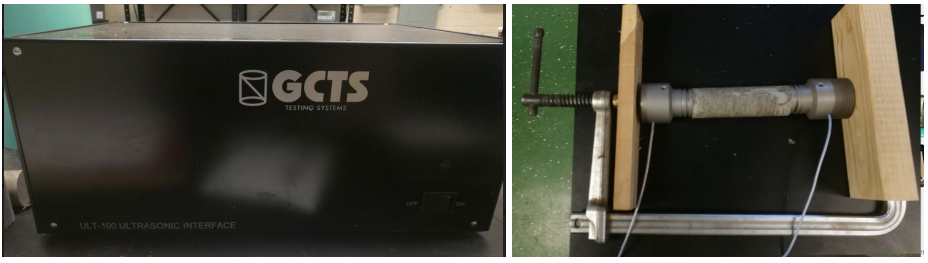

Figure 7. The ultrasonic test interface and setup for testing elastic parameters during cement hardening.

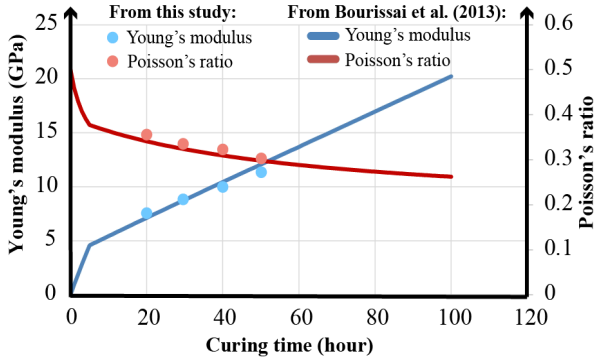

Figure 8. The measurements from the test plotted with the elastic parameter tested under the same conditions from Bourissai *et al.* [20].

Cement Degradation under CO_2-rich Conditions

Two types of experimental setup can be used to study oilwell-cement CO_2-degradation based on how the CO_2 interacts with the cement matrix–static soaking and dynamic flow. For the static test [15,16,18], cement samples are placed into a pressure vessel, which is fully or partially filled with water and CO_2 at specified pressure and temperature conditions. For the dynamic test [19], the cement sample is placed in a Hassler core holder and held at a specified pressure, back pressure, and temperature, and CO_2 is injected from one end at the designated pressure.

In this study, a static reaction setup is adopted to simulate the Class G Portland cement degradation since the Mont Terri pilot well data was obtained for similar conditions. As shown in Figure 9a, b, and c, the experimental setup consists of a pressure vessel to contain the cement samples for reacting with the CO_2, a gas accumulator, a CO_2 gas tank to provide the CO_2, and a syringe pump that directly provides the fluid pressure to the accumulator. After the cement samples are placed, the pressure vessel is filled to 2/3 of its total volume with distilled water. The supercritical CO_2 is injected at the top of the vessel, and the pressure and temperature are maintained at 2000 psi (13.8 MPa) and 80°C (Figure 10) for 40 days, which exposes the cement samples placed at the top 1/3 volume to wet supercritical CO_2, and the samples at the bottom 2/3 to CO_2 saturated water. After 40 days, the pressure and temperature are both gradually reduced to ambient conditions in 5 days. After the test, the pH value of the water in the pressure vessel was 5, which assures that the water is saturated by CO_2. The pressure and temperature tested is in the same range of the Mont Terri CO_2 injection well, and the testing period represent a normal injection cycle [20].

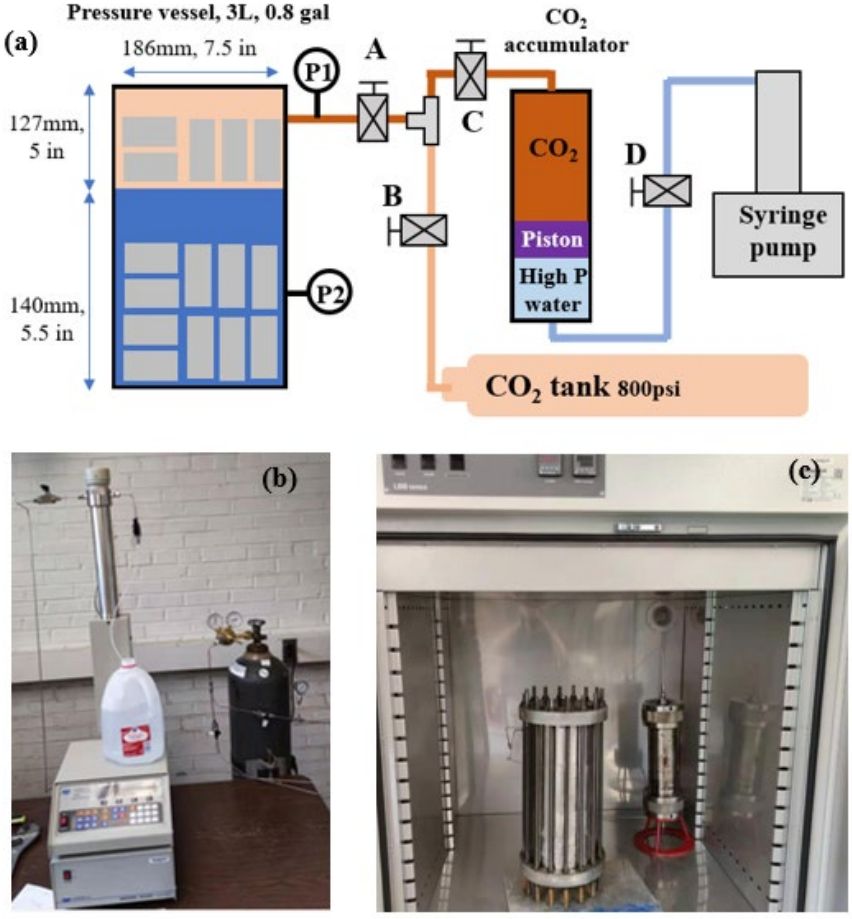

Figure 9. Experimental setup for cement CO_2 degradation. (a) Schematic illustration of the setup. (b) The control station, including the syringe pump, CO_2 tank, pressure gauges, and valves. (c) Pressure vessel and accumulator are placed in an oven under a controlled temperature.

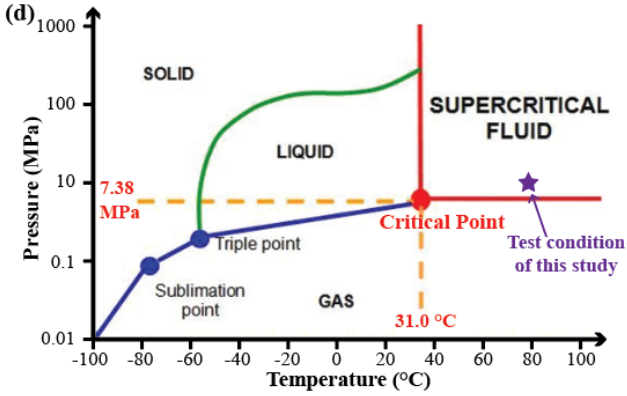

Figure 10. The phase diagram of CO_2; the purple star labels the test conditions of this study.

Two sample sizes are used in this study: 1-in diameter and 2-in length cylinder for the uniaxial compression test and the 2-in diameter and 1-in length cylinder for the Brazilian tensile test (API-10A). The samples were cast using Portland Class G cement mixed with a water-cement ratio of 0.44, which is the same as for the cement used in the Mont Terri CO_2 injection well. The cement samples were cured under four different conditions for 14 days before the reaction with CO_2. The field scenarios these conditions represent are listed in Table 1. To obtain a quantitative comparison, as listed in Table 2, three cases are designed for the CO_2 degradation test, and samples prepared under four different conditions different conditions (Table 1) are tested for each degradation condition.

Table 1. Different curing conditions for cement samples.

Cement curing condition	Case code	Description	Field scenarios represented
Ambient condition	Case-Amb	Samples are cured under 20°C and 40% humidity for 14 days	Mont Terri CO_2 injection well
Convection oven, ambient temperature	Case-CO	Samples are cured under 20°C and 10% humidity for 14 days	Mont Terri CO_2 injection well
Moisture room with ambient P and T	Case-MR	Samples are cured under 20°C and 100% humidity for 14 days	Shallow CO_2 injection well
10MPa confining pressure	Case-10P	Samples are cured under 20°C and 10MPa water pressure for 14 days	Regular CO_2 injection well

Table 2. Various degradation conditions tested in this study.

Degradation conditions	Case code	Field scenarios represented
In distilled water at 80 °C and 13.8 MPa for 40 days	Case-PT	Regular injection well
In CO_2 saturated water at 80 °C and 13.8 MPa for 40 days	Case-CO2SatW	Mont Terri CO_2 injection well
In supercritical CO_2 at 80 °C and 13.8 MPa for 40 days	Case-ScCO2	Mont Terri CO_2 injection well

After the degradation reaction, the uniaxial compression test and Brazilian tensile test are performed with a Humboldt HM-5150 load frame (Figure 11) following the ASTM D7012 and ASTM D 3967-86 standards. To minimize the error and increase the accuracy, five samples are tested for each scenario for both mechanical properties tests. Before the test, all sample faces are ground until the surface roughness is below 0.1 mm.

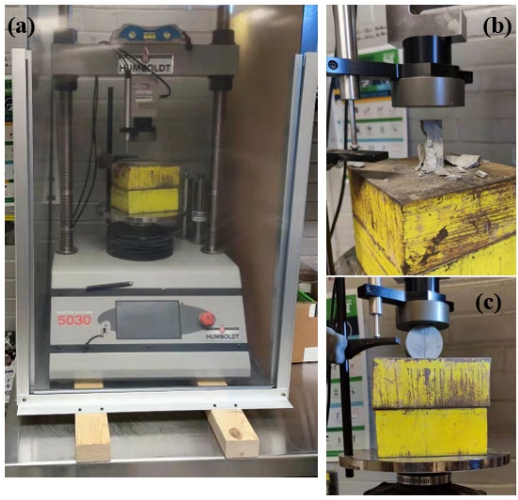

Figure 11. Utilization of Humboldt HM-5150 load frame to test the Uniaxial Compressive Strength (UCS) and tensile strength of cement samples. (a) setup of the test system, (b) implementation of a uniaxial compressive test, (c) implementation of a Brazilian tensile test.

Mechanical Test Results for Cement Strength

The cement strength results are shown in Figure 12. Samples cured under four different conditions (Table 1) were degraded under three different scenarios (Table 2). For degradation scenarios, the pressure, temperature, and reaction time are kept the same. For each case, the distribution of measured strength value is plotted as blue bars, and the averaged value of the five values is plotted as red dots. The uniaxial compressive strength obtained from the uniaxial compressive test is shown in Figure 12a, and the tensile strength measured by Brazilian tensile test is illustrated in Figure 12b.

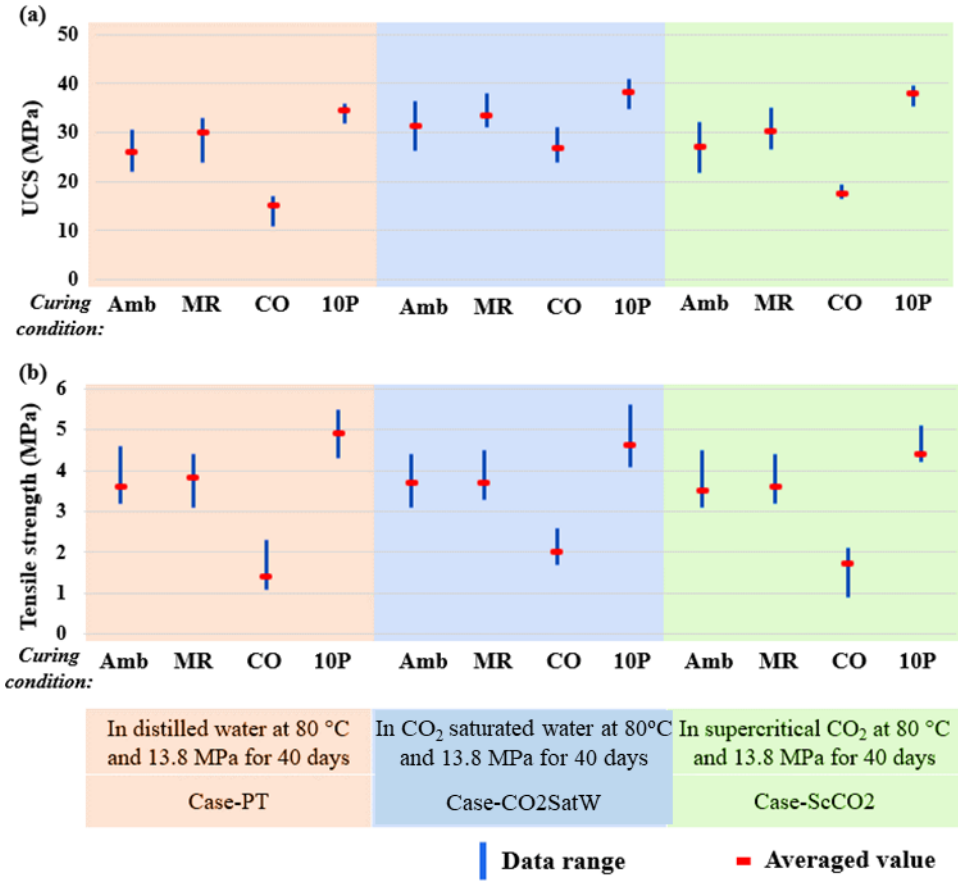

Figure 12. The strength test results for scenarios listed in Table 1 and 2. (a) Unconfined compressive strength results. (b) Tensile strength results.

Geochemical Macro-meso-micro-scale Analyses

To understand the microstructures and pore size distribution, a mercury intrusion test was performed with a Poremaster porosimeter, and combined Scanning Electron Microscopy (SEM) with Energy Dispersive X-Ray Spectroscopy (EDS) observation was implemented with a Helios Hydra CX. The porosity, pore size distribution, microstructures, and element abundancy for samples with or without CO_2 degradation were investigated both qualitatively and quantitatively.

After reaction with CO_2-saturated water at 80°C and 13.8 MPa for 40 days, several cement samples were cut and polished into pellets (Figure 13a and b) for optical microscope and SEM observations. EDS (energy dispersive X-ray spectroscopy) was set to scan a 100 by 100 μm area to obtain an averaged element distribution. The pellet sample from Case-10P-CO2SatW (cured under 10 MPa and reacted with CO_2-saturated water) had both the best surface quality and the best imaging quality, hence, results of this sample are illustrated in this section. Region (1) to (5) in Figure 13a along the radius of the sample were chosen for SEM observations (Figure 13), which represent the invasion path of the CO_2 from the surrounding water. These regions comprise: (1) the surface of the sample,

(2) the region adjacent to the skin, (3) in the middle of the dark carbonated zone, (4) the region beyond the margin of the dark zone towards the center, and (5) the center of the sample.

As shown in Figure 14a, mineral crystals precipitate on the skin, and their EDS result (Figure 14b) indicate almost 100% calcium carbonate. For Region (2) to (5), ~2 mm by 2 mm by 4 mm flakes are cut from the sample for the mercury intrusion porosity test. The average porosities are 0.38, 0.13, 0.29, and 0.16, respectively. Figure 15 shows the SEM images for the various zones at 10k (first row in Figure 15) and 15k magnification (second row in Figure 15), as well as the elemental compositions (third row). According to the zones defined by Barlet-Gouedard *et al.* ([15], Figure 3), Region (2) has a scaly-textured and highly porous matrix (Figure 15, column 1) and can be distinguished as Zone I (loose surface zone). Region (3) has a compact and dark carbonate matrix (Figure 15, column 2) and can be distinguished as Zone II (the carbonated zone). Region (4) has a relatively high porosity, but the microstructure is predominately cement matrix with some carbonate crystals (Figure 15, column 3), thus can be designated as Zone III (the dissolution zone). Region (5) has a similar porosity magnitude, microstructure, and element compositions as the unreacted cement; thus, it can be distinguished as Zone IV (the diffusion zone) or unreacted cement.

The element concentrations measured by the EDS (Figure 15, row 3) shows that the Calcium content decreases drastically from Region (5) to (2); the Carbon content increases moderately from Region (5) to (2); the Oxygen content increases drastically from Region (5) to (4), but the increase slows down from Region (4) to (2); the Silicon content remains constant from Region (5) to (4) and decreases slightly from (4) to (2). These variations are in agreement with the observation of Li *et al*. [18] and Wolterbeek *et al*. [19]. The element abundances of Calcium, Oxygen, Carbon, and Silicon have the potential to be used as indicators for the degree of carbonation. More tests are needed to obtain their quantitative relationships.

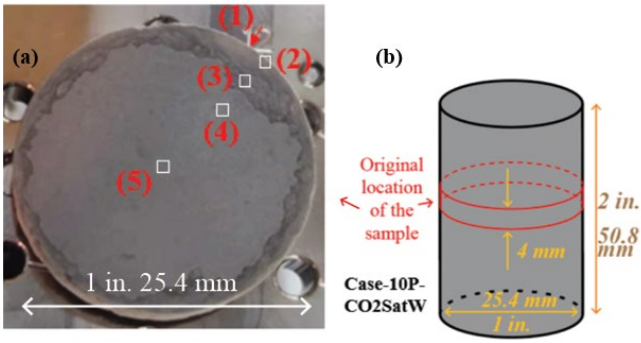

Figure 13. The pellet sample from Case-10P-CO2SatW for the SEM+EDS observations. (a) Five regions (in white boxes) are chosen along the radius of the intersection and labelled as Region (1) to (5). (b) The pellet sample is acquired from the central section of the original cylinder sample.

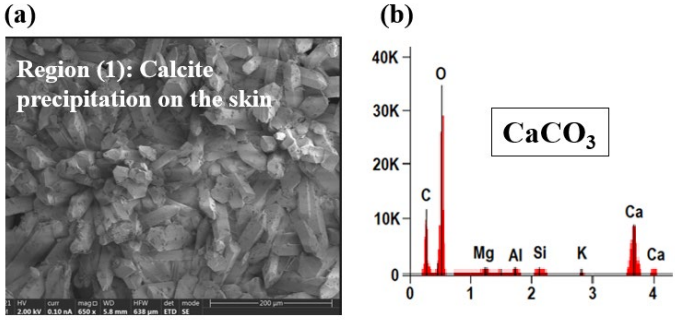

Figure 14. The SEM image of Region (1) in Figure 13 (on the sample skin). (a) Crystal mineral precipitates can be observed from SEM, and (b) EDS results indicate these mineral precipitates are calcium carbonate.

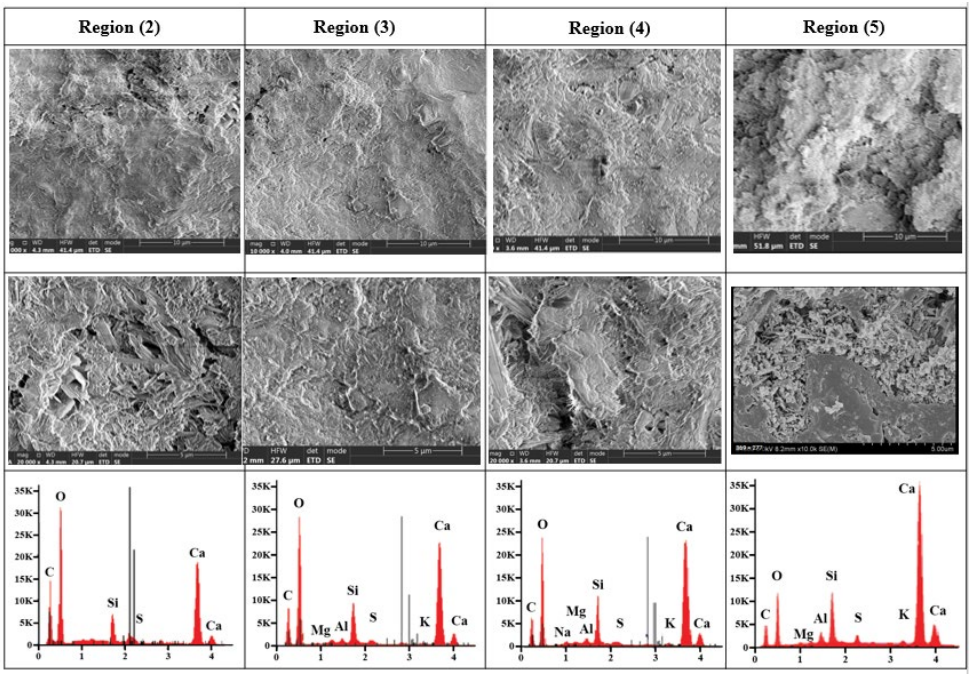

Figure 15. SEM and EDS observation results of the Region (2)-(5) in Figure 13. The first to fourth column shows the results for Regions (2) to (5). The first row shows the 10k magnification SEM images, the second row shows the 15k images, and the third row shows the EDS results.

The Presence of Pre-existing Fractures

Before the degradation test, Case-CO (cured under drying conditions) and Case-10P (cured under 10 MPa pressure) samples were processed into pellet samples for the SEM observation. As shown in Figure 16a, a systematic fracture network can be observed across the Case-CO sample at 500 times

magnification, and the fracture aperture is ~5 µm. As shown in Figure 16b, no fracture is observed on Case-10P at 500 times magnification, and the cement matrix is relatively compact and homogenous.

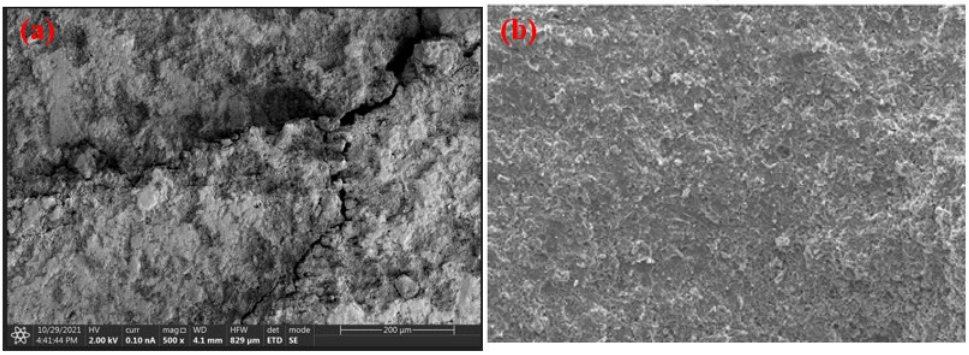

Figure 16. Comparison of the cement cured under drying condition (Case-CO) and under a 10 MPa confining pressure (Case-10P). Both SEM images are at 500 times magnification.

After degradation in CO_2 saturated water, Case-CO-CO2SatW was processed into a large pellet (~28mm by 40mm by 4mm, Figure 17a and b), which showed several fractures. Figure 17 c, d, and e show the optical microscope images at the skin, of a large fracture adjacent to the skin, and of a large fracture at the inner side of the sample, respectively. Dark carbonated zones are developed at both sides of the pre-existing fractures (Figure 17a). In contrast to the homogeneous sample shown in Figure 13a, where the carbonated zone (Region 3) is confined to a small region near the edge of the sample, the fractures in Case-CO-CO2SatW promote carbonation systematically throughout the sample. Figure 17c, d, and e show that the pre-existing fractures are filled with mineral crystals, and no void space or aperture is left. This suggests that the carbonation reaction product (calcium carbonate) fills the fracture gaps, adheres to the fracture surfaces, and increases the level of integrity of the sample. Hence, the strength of the fractured cement sample is expected to be significantly increased after the CO_2 degradation. This strength increase was observed in this study and is in agreement with Wolterbeek *et al.* [19].

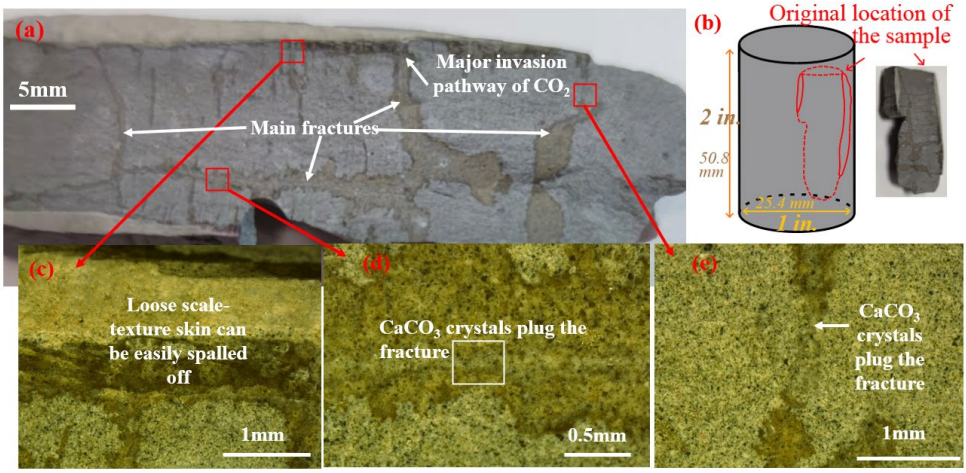

Figure 17. Carbonation reaction of the cement sample with pre-existing fractures. (a) The large pellet for Case-CO-CO2SatW. (b) The original location of the sample. Optic microscope observations of (c) a large fracture inside the cement sample, (d) adjacent to the skin of the sample, and (e) a large fracture close to the skin. The testing pressure was depressurized evenly for 24 hours, avoiding creating any artificial fractures.

Cement Integrity during Degradation: Influence of the Hardening Process

As illustrated in Figure 12, the cement samples cured under different conditions have significant variations in strength. For Case-PT samples (pink block in Figure 12), the Uniaxial (or Unconfined) Compressive Stress (UCS) and tensile strength of the sample cured under a drying condition (Case-CO-PT) are only 44% and 27% of the sample cured under a compressive condition (Case-10P-PT), respectively. The excessive shrinkage due to the absence of external water supply induces tension throughout the sample. As a result, a fracture network (similar to Figure 16) would develop in the not yet fully hardened cement matrix and thus reduce the strength significantly.

In contrast, once samples are exposed to CO_2, both in CO_2 saturated water and supercritical CO_2 (blue and green blocks in Figure 12), the matrix strength of Case-CO-CO2SatW and Case-CO-ScCO2 significantly increases. Compared to Case-CO-PT, the UCS and tensile strength of Case-CO-CO2SatW increased 86% and 54%, respectively, and the UCS and tensile strength of Case-CO-ScCO2 increased 32% and 31%, respectively. The fractures developed during hardening serve as pathways for CO_2 to enter the sample (Figure 16). CO_2 saturated water or supercritical CO_2 flows into the sample through the fractures and seeps into the cement matrix adjacent to the fracture. Then, the calcium and carbonate ions combine and precipitate (Equation 1-4) on the fracture surface, fill the fracture space, and plug the fractures. The cohesion of the cement sample is increased by the fractures plugged by the calcium carbonate crystal (Figure 17b and d). As a result, the UCS and tensile strengths of the sample are enhanced significantly.

For samples without pre-existing fractures, the reaction with CO_2 saturated water and supercritical CO_2 also increases the strength. UCS and tensile strength for Case-Amb (cured under ambient condition) increased by 24% and 8%; for Case-MR (cured under water-abundant condition) increased by 11% and 3%; and for Case-10P (cured under 10 MPa confining pressure) increased by 5% and 0.8% for degradation with CO_2 saturated water and supercritical CO_2. The difference between the three cases is that different curing conditions induce different levels of cement matrix compactness.

The abundant supply of water and a high confining pressure promote the development of a compact matrix, increases the strength, reduces permeability, and prevents the onset of fractures [23,13]. Hence, it is more difficult for CO_2 to invade Case-MR and Case-10P samples, and thus the strength improvement due to the carbonation effect is less evident than Case-Amb.

Implications for the Long-term Degradation

The CO_2 degradation test data from this study is obtained after 40 days of CO_2 exposure and only represents the effect of short-term CO_2 injection (~months). However, for the long-term impact (~years for operatable wells, decades for abandoned wells), these test results can only provide qualitative implications. As illustrated in Figure 13a and Figure 14, a weak and loose zone (Zone I) is developed adjacent to the skin of the sample after 40 days of degradation. This zone is 0.5-1 mm thick and approximately occupies 8% of the entire volume of the sample. The first column in Figure 15 shows that the matrix of this zone is highly porous (porosity =0.38), and calcium carbonate crystals are loosely embedded in the pore space. Although the carbonated zone temporarily increases during the early-to-middle period of CO_2 exposure, in the long-term period, the calcium carbonate would dissolve into the surrounding fluid due to the continuous supply of the acidic CO_2-contained fluid, and the carbonated zone would finally become the loose skin zone. Hence, as illustrated in Table 3, we assume that over time, this loose skin zone would enlarge, and the compact/condensed cement matrix would diminish with longer exposure to CO_2 degradation action. More research is necessary for a complete quantification of these reactions.

Table 3. A qualitative summary of the temporal variation of cement properties under the CO_2 degradation.

	Hours to days	Days to weeks	Months	Years
Major process	Surface dissolution and precipitation	Carbonation close to the skin	Thorough carbonation	Matrix degradation, carbonate dissolve
Reaction volume %	<1%	30%	>80%	100%
Material property variation	Not affected	Slight increase in strength and stiffness, reduction in porosity and permeability		Strength and stiffness decrease, increase in porosity and permeability

Staged Finite Element Approach

In this study, the wellbore region is simulated using the commercial finite element software package Abaqus™ [24]. Only a quarter representation of the wellbore is simulated, since symmetry conditions are assumed, and improved numerical efficiency is achieved. The model domain includes casing, cement sheath, and a formation component. Cement and formation components are simulated as poro-elasto-plastic materials with thermal and pore pressure properties. The casing is modelled as a linear elastic material. Interface bonds using cohesive contact behaviour governed by a quadratic traction-separation law [24] are inserted between casing-cement and cement-formation components.

The staged FEA modelling covers six steps, which are based on the general stages during the life span of an injection well (Figure 18). A static pre-stressing load step to establish an equilibrated gravitational-loaded state of stress in the rock is applied before drilling [13,14,25]. The steps are:

- Step 1: Pre-stressing. In this step, the in-situ state of stress and the pore pressure are applied to the model domain (intact formation).

- Step 2: Drilling. In this step, a cylindrical volume of rock is removed from the borehole location and a uniform mud pressure is applied on the surface of the borehole wall.
- Step 3-1: Casing. Casing elements are introduced in this step. Equal mud pressures are applied on the inner and outer casing walls.
- Step 3-2: Cementing. A cement slurry pressure is applied on the inner wall of the formation and outer wall of the casing to represent the fluid pressure from the cement slurry column. The cement elements are added to the model. The inner surface of the casing is still loaded with the mud pressure.
- Step 4: Cement hardening. An initial state of stress equal to the hydrostatic pressure of the cement slurry minus pore pressure is applied to the cement. Then the cement bulk shrinkage, poro-elastic property development, strength development, and pore pressure variation are simulated. See Zhang and Eckert [21] and Zhang [26] for details.
- Step 5: Well test. A well test process is simulated using FEM to obtain the maximum inner casing pressure when the cement failure occurs, and to investigate the maximum temperature increase and decrease the wellbore system can tolerate. This process includes the pressure and temperature variations at the inner casing during pressure tests (i.e., leak-off test and hydraulic fracturing test), heating test, and thermal cycling associated with injection or production [27]. The pressure is increased at a rate of 1 MPa/s for pressure testing simulation, and the temperature is either increased or decreased at 1°C/s until any type of failure occurs [28].
- Step 6: Cement degradation due to Injection. This step is assumed to occur after a certain period of CO_2 injection (i.e., six months) and simulates the degradation of cement sheath mechanical properties and strength. Well tests (Step 5) are also performed after this step, and occurrence of failure is predicted.

A more in-depth description of the numerical modelling procedure is given in Zhang and Eckert [21].

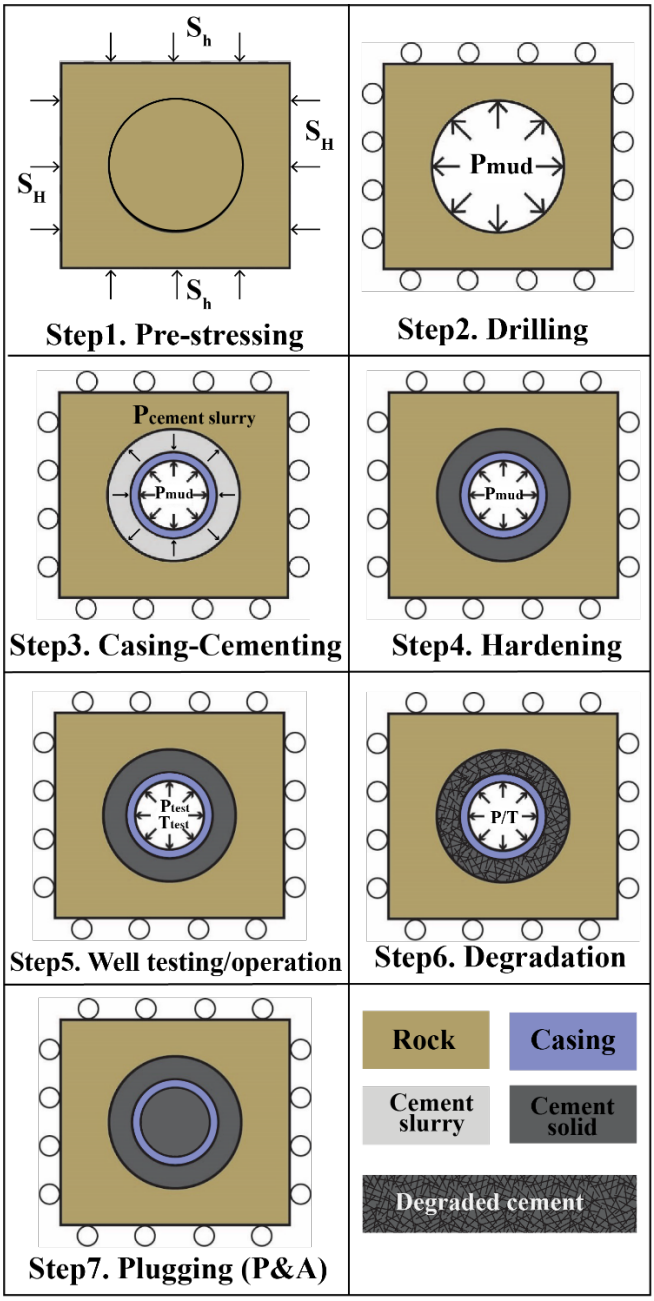

Figure 18. Load steps of the multi-staged FEA approach to simulate downhole conditions.

Integration of the Laboratory Measurements and Numerical Modelling

Two separate sections of the Mont Terri CO_2 injection well are modelled: the wellbore section with I/P (Injection/Pressure measurement) modules and the section between two adjacent I/P modules (Figure 19). The staged finite element approach is used to simulate the drilling, casing, cementing, cement hardening, pressure testing (pulse testing; see Chapter 28), and thermal cycling (heat testing; see Chapter 28) processes as detailed in the previous section. Scenarios tested are listed in Table 4. The pressure and temperature variations are applied at the inner side of the casing during the pressure testing and the thermal cycling steps. Figure 20 shows the measured pressure and temperature variations for the pulse testing and heat testing experiments, respectively. The applied pressure (blue line in Figure 20a) and temperature (red line in Figure 20b) are input parameters to the numerical model.

The in-situ stress in the formation is taken from the measurement of Bossart and Wermeille [29]: vertical stress S_V=6.5 MPa, maximum horizontal stress S_H=4.5 MPa, and minimum horizontal stress S_h=2.5 MPa. Since the Mont Terri injection well is very close to the surface (from 7.12 m to 10.12 m) and above the local water table, the pore pressure and the cement slurry pressure are neglected in this simulation. Material properties for the formation rock are taken from the core analysis of Amann *et al*. [30] for the Mont Terri rock laboratory (Table 5). Because the cement slurry was cured under ambient conditions (i.e., without applying additional pressure to the cement), input parameters for the cement hardening and the cement mechanical properties are taken from the ultrasonic measurements for this study and Justnes *et al.* [31]–both measured under ambient conditions (Figure 21). The staged finite element framework adapts the elastic proportion of the bulk shrinkage (represented by the coefficient *s*, detailed assumptions and validation process see Zhang *et al.* [13] and Zhang and Eckert [21]). Previous analyses indicate that *s*=25% under ambient conditions without sufficient water supply [13,26].

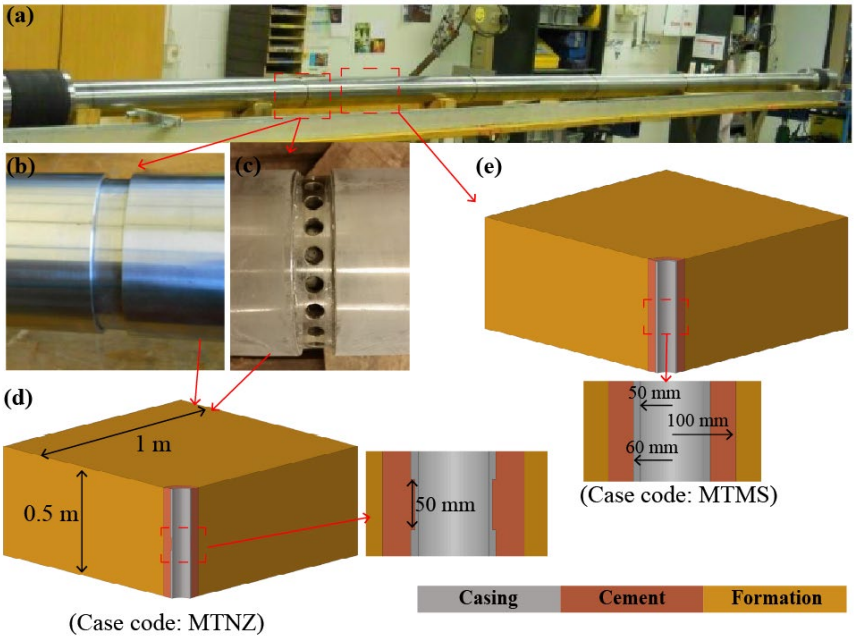

Figure 19. Numerical adaptation of the Mont Terri Injection well into numerical models. (a) The injection string of the injection well before installation. (b) The injection nozzle in the turned-off mode. (c) The injection nozzles in the turned-on mode. (d) Model geometry to represent the section with injection nozzles. (e) Model geometry to represent the section without injection nozzles.

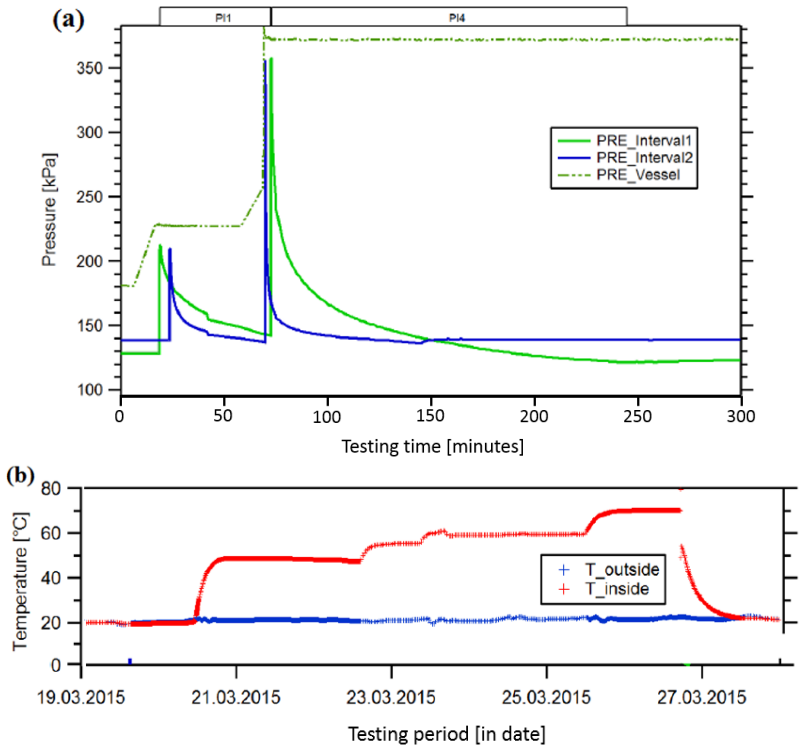

Figure 20. Well testing data from Mont Terri CO_2 Injection well. Figures are from the Mont Terri injection well drilling and testing report. (a) The pressure records during the pulse test. (b) The temperature records during the heating test.

Table 4. Simulation scenarios for the Mont Terri CO_2 injection well.

Simulated wellbore section	Cement hardening step	Pressure testing (pulse testing)*	Thermal cycling step**
The section with injection nozzles. (case code: MTNZ)	Case code: MTNZ-Hardening	Case code: MTNZ-PressureTesting	Case code: MTNZ-ThermalCycling
Middle section between two injection nozzle sets. (case code: MTMS)	Case code: MTMS-Hardening	Case code: MTMS-PressureTesting	Case code: MTMS-ThermalCycling

*Pressure inputs are based on the pressure measurement of the pulse test, which is illustrated in Figure 20a.
**Temperature inputs are based on the temperature measurement of the heating test, which is illustrated in Figure 20b.

Table 5. Mechanical properties of Opalinus clay [30].

Young's Modulus, E	Poisson's Ratio, ν	Tensile Strength, T_o	Shear Strength, τ_o	Compressive Strength, σ_c
GPa		MPa	MPa	MPa
8.205	0.3	2.38	8	13.79

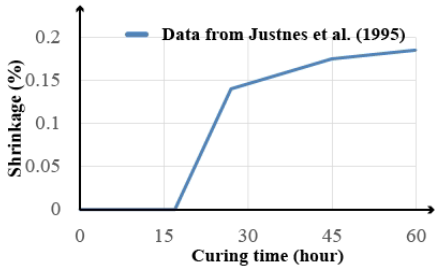

Figure 21. Input parameter for the Mont Terri injection well models. Data are measured under conditions similar to the curing condition of cement in the injection well.

For the cement degradation simulation, since the cement failure condition is unknown, two extreme scenarios are simulated: the cement is compact and intact, and the cement has pre-existing fracture networks. Based on the quantitative measurement, qualitative analysis, and data collected from similar studies [15,18,19], the variation of the cement Unconfined Compressive Stress (UCS) during the CO_2 degradation is shown in Figure 22. The strength of the intact cement increases about 5% from 0-3 months and then decreases 25% from 3-6 months (the red line in Figure 22). The strength of the

fractured cement increases about 80% from 0-3 month and then decreases to 70% of the initial value from 3-6 months (the blue line in Figure 22). For adaptation into the numerical model, two assumptions are made (due to the lack of quantitative measurements): (1) the Young's modulus of the cement matrix varies in the same degree as the strength (Figure 21); and (2) the remaining cement properties (friction angle, Poisson's ratio) are unchanged after degradation.

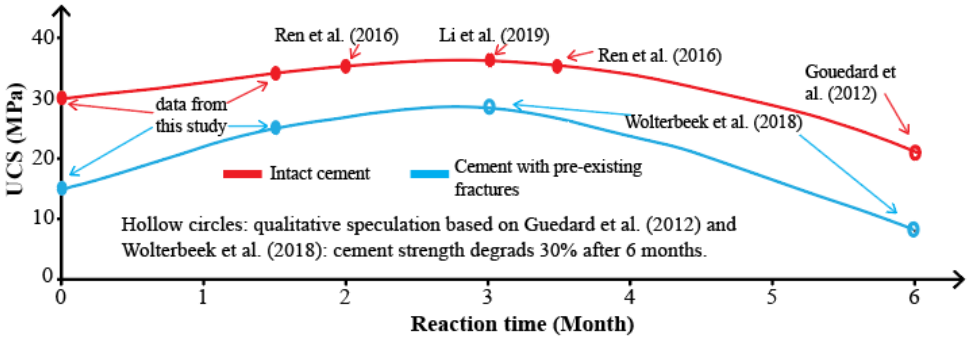

Figure 22. Model inputs for the cement degradation simulation.

NUMERICAL RESULTS

Based on previous studies, the casing-cement interface (inner part of the cement sheath) and the cement-formation interface (outer part of the cement sheath) are the two critical zones that most likely feature failure during the cement hardening process [8,9,11,13].

Hence, to illustrate the state of stress at the casing-cement interface (inner cement sheath), as is shown in the highlighted elements in Figure 23a and b, the hoop and radial stresses at the edge of the nozzle locations are plotted for MTNZ scenarios; for MTMS cases (without injection nozzles), hoop and radial stresses are plotted at the inner side of the cement in the center of the model. To illustrate the state of stress at the cement-formation interface (outer cement sheath), the contact pressure and the resulting debonding fracture aperture at the cement-formation interface (acquired at the middle section of the outer cement sheath, Figure 23c) are plotted for both MTNZ and MTMS scenarios.

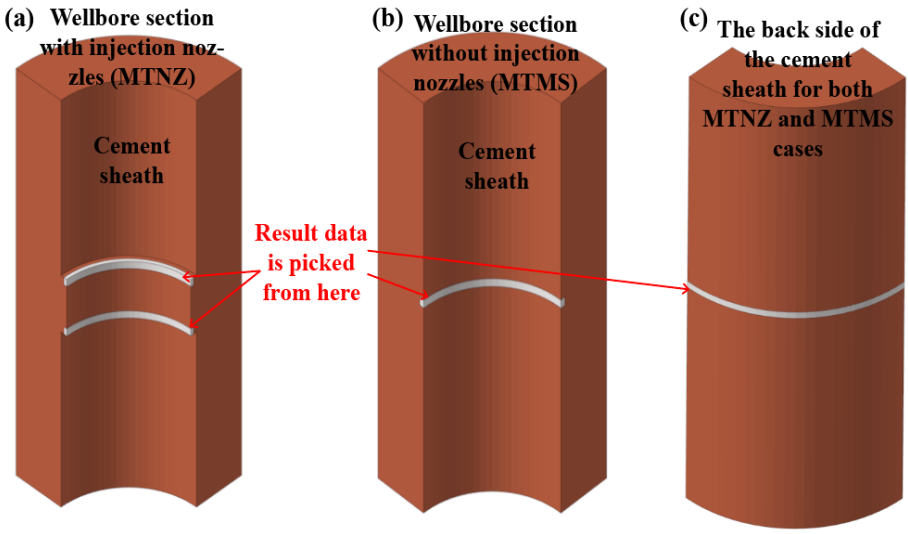

Figure 23. Simulation result locations highlighted for MTNZ and MTMS scenarios, for (a) the inner side of the cement for the wellbore section with injection nozzles, (b) the inner side of the cement for the wellbore section without nozzles, (c) the outer side of cement for both cases.

Simulated Cement Hardening

Figure 24 shows the variation of the radial and hoop stresses for MTNZ-Hardening and MTMS-Hardening scenarios during cement hardening. The cement is approximately at a stress-free state at the beginning of hardening. Hardening begins after 18 hours of curing time. Then, during the 48 hours of the hardening process, the radial stress reaches -3.8 MPa and -0.7 MPa for MTNZ-Hardening and MTMS-Hardening, respectively. The hoop stress decreases to -5.65 MPa and -3.2 MPa for MTNZ-Hardening and MTMS-Hardening, respectively (Figure 24a). These negative stress magnitudes are the direct result of shrinkage during hardening, and debonding at the cement-formation interface occurs 12 hours after hardening has started for both scenarios. The contact pressure at the cement-formation interface decreases to -1.75 MPa and -1.62 MPa for MTNZ-Hardening and MTMS-Hardening, respectively. The final resulting MA aperture is 20.6 µm and 19 µm (Figure 24b) for MTNZ-Hardening and MTMS-Hardening, respectively.

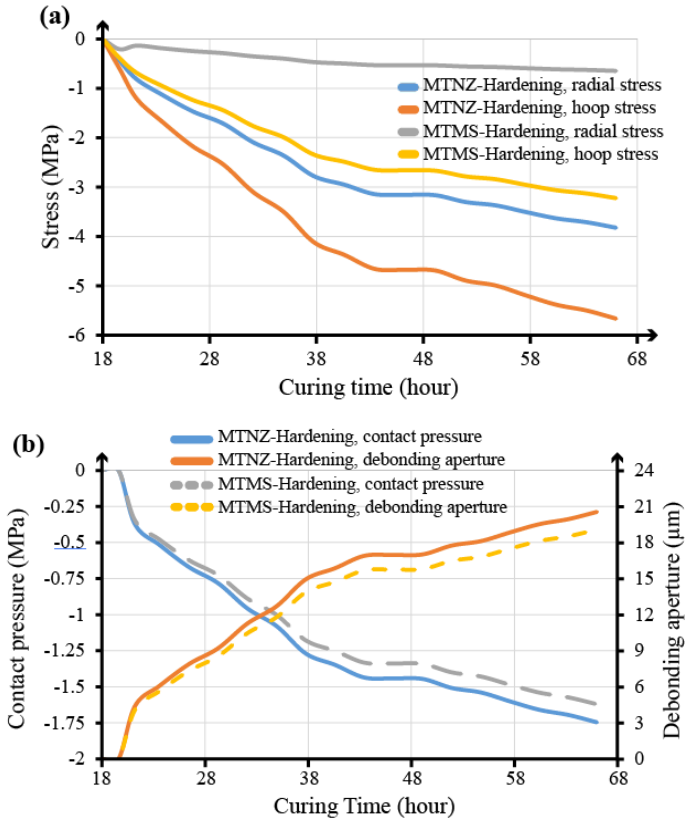

Figure 24. Simulation results after cement hardening. (a) Radial and hoop stress for MTNZ and MTMS scenarios. (b) Resulting contact pressure and debonding aperture at the cement-formation interface for MTNZ and MTMS scenarios.

Simulated Pressure Testing

To illustrate cement failure, Figure 25a shows the Von Mises stress and the resulting equivalent plastic strain (PEEQ) with respect to the inner casing pressure for pressure testing scenarios (pulse testing). Shear failure initiates for the MTNZ-Pressure Testing model for an inner casing pressure of 20 MPa, when PEEQ > 0 (orange line in Figure 25a). Shear failure does not initiate for the MTMS-Pressure Testing model as PEEQ remains 0. During pressurization, the Von Mises stress reaches a maximum of 8.9 MPa and 6 MPa for MTNZ-Hardening and MTMS-Hardening, respectively. At the maximum inner casing pressure, the equivalent plastic strain reaches 12.7×10^{-5}, and the damaged region is illustrated in Figure 25b. The entire area in the immediate vicinity of the injection nozzles experiences failure induced by the excessive inner casing pressure during the pulse testing.

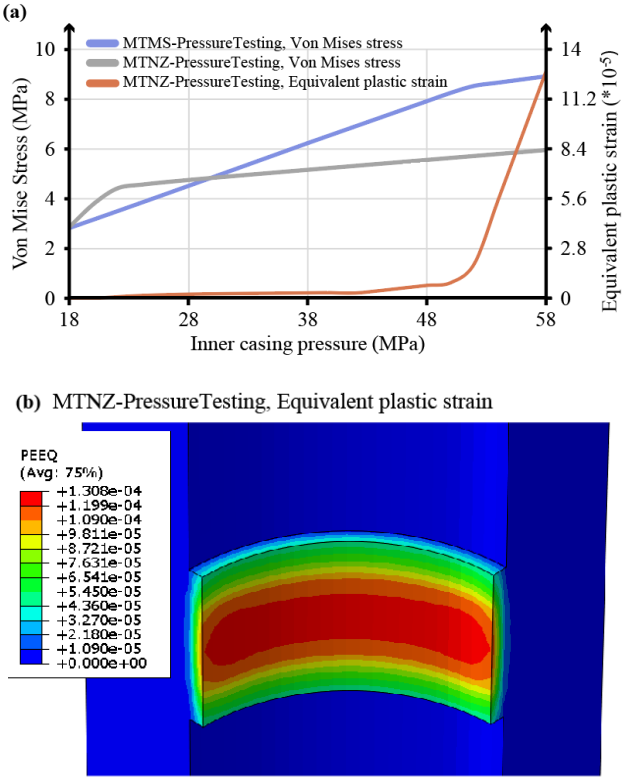

Figure 25. Simulation results for the pressure testing (pulse testing) step. (a) Von Mises stress variation with inner casing pressure for MTNZ-PressureTesting and MTMS-PressureTesting, and the equivalent plastic strain (PEEQ) varying with inner casing pressure for MTNZ-PressureTesting. (b) Illustration of the damaged region at the cement

Simulated Thermal Cycling

Figure 26 shows the variation of contact pressure (a) and debonding aperture (b) for the MTNZ-PressureTesting model during the thermal cycling (heating test). As shown by the red line in Figure 26, the inner casing is heated in three stages from 20°C to 50°C, from 50°C to 60°C, and from 60°C to 70°C. For both the MTNZ-ThermalCycling model and the MTMS-ThermalCycling model, the contact pressure variations induced by the three heating stages are 21.5 MPa, 6 MPa, and 4 MPa. Also, for both cases, the micro-annuli (MA) initially developed during the cement hardening are closed by the compressional thermal stress induced by heating during the first heating stage (yellow and orange lines in Figure 26b). Moreover, the MA at the cement-formation interface remain closed during the entire heating test for both cases. The variation of both contact pressure and MA aperture show the same trend for both cases, both in magnitude and in temporal variation, after the large step changes in the applied temperature. These observations agree with the experimental studies by DeAndrade *et al.* [12] and Therond *et al*. [32].

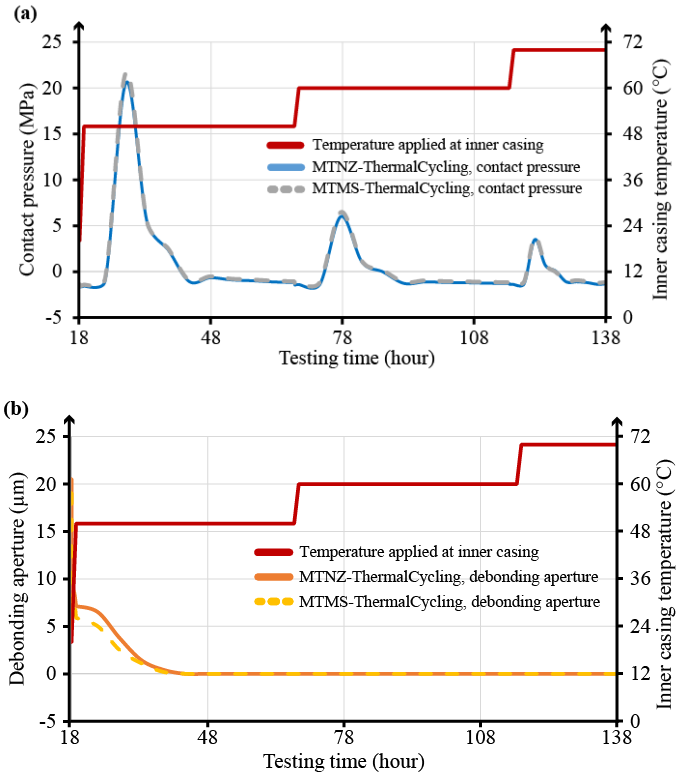

Figure 26. Simulation results of the thermal cycling (heating test) step. (a) The variation of contact pressure at the cement-formation interface for MTNZ-ThermalCycling and MTMS-ThermalCycling. (b) The variation of debonding aperture at the cement-formation interface for MTNZ-ThermalCycling and MTMS-ThermalCycling.

Numerical Investigation of Impact of Degradation Results

To quantify the influence of cement degradation on wellbore integrity, the degradation test results from this study and other similar studies were quantitatively and qualitatively incorporated into the finite element framework discussed previously. The central section of the injection string of the Mont Terri injection well (scenario MTMS) was simulated, and it was assumed that no external pressure or temperature variations occur during the degradation process.

A Mohr-Coulomb shear failure index, η, is introduced to quantify the likelihood of shear failure occurrence. Cement shear failure occurs for $\eta \geq 1$ (detailed derivation and explanation are presented in Appendix A):

$$\eta = \frac{(\sigma_1 - \sigma_3)}{cos\phi sin\phi(\sigma_1 + \sigma_3) + 2cos^2\phi S_0} \quad \text{Equation (6)}$$

$$S_0 = \frac{UCS}{2}\frac{1-sin\phi}{cos\phi} \qquad \text{Equation (7)}$$

Where, σ_1 and σ_3 denote the effective maximum and minimum principal stresses; ϕ is the internal friction angle; UCS is the Unconfined Compressive Strength, and S_0 is the cohesion and can be calculated by the equation (6).

Figure 27 shows the modeling results of the η variation due to CO_2 degradation over time, incorporating the varying UCS values shown in Figure 22. η values at the outer and inner side of the intact (red line in Figure 22) and fractured (blue line in Figure 22) cement sheath are plotted in Figure 27a and b, respectively. From 0 to 3 months, η values decrease 0.04 and 0.03 at the inner and outer cement sheath for the intact cement, respectively; and η values decrease 0.16 and 0.15 at the inner and outer cement sheath for the fractured cement, respectively. The decrease of η values indicates a decreasing shear failure likelihood due to the cement strength improvement by the short-term CO_2 invasion and the early-stage carbonation reactions. From 3 to 6 months, η values increase 0.14 and 0.13 at the inner and outer cement sheath for the intact cement, respectively; and η values increase 0.32 and 0.3 at the inner and outer cement sheath for the intact cement, respectively.

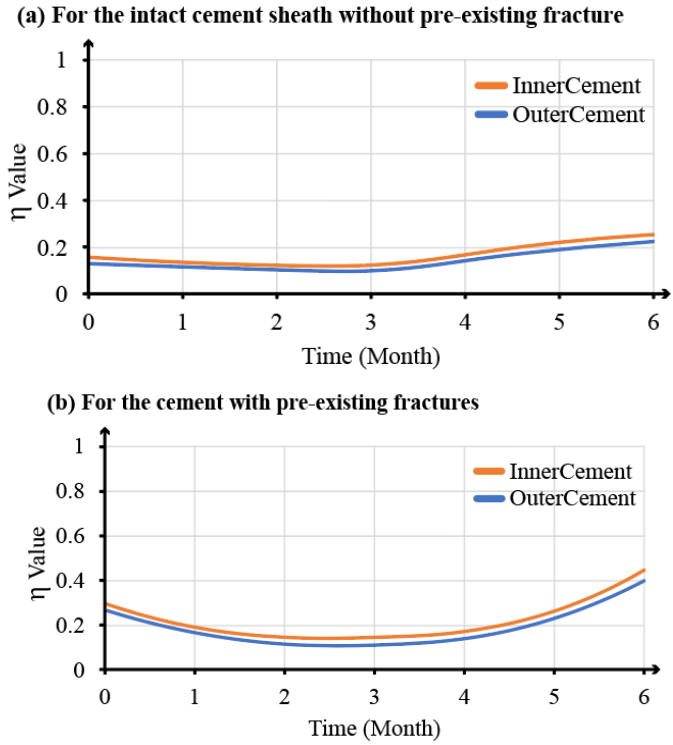

Figure 27. The temporal variation of the η value at the outer and inner cement sheath for the middle of the injection string of the Mont Terri injection well (MTMS) after 0 to 6 months of CO_2 injection. (a) The variation of η values for the intact cement without fractures. (b) The variation of η values for the cement with pre-existing fractures.

These increased η values indicate a drastic increase of shear failure likelihood because of the strength deterioration due to the long-term carbonation reaction.

Although the shear failure likelihood has increased after a 6-month period of CO_2 degradation, no failure would occur without external loads (e.g., cyclic injection, injection hot/cold fluids, salt creep), and the wellbore still maintains integrity. However, the simulation period of this study ends after 6 months due to degradation data availability. It is possible that the η value for the wellbore would further increase after longer CO_2 exposure. For abandoned wells, which are exposed to CO_2 for several years to decades, the long-term integrity of the cement seal requires further investigation.

To evaluate the impact of an external load on degraded cement, a pressure testing step is simulated for the wellbore system after 0, 3, and 6 months of CO_2 degradation. During the pressure test, the inner casing pressure is increased from 0 MPa to 30 MPa (an extreme range of pressure for quantifying and comparing the likelihood of cement sheath failure [21,28]). This process could represent an increase in injection pressure or subsequent operations in old wells. For both intact and fractured cement, the variation of η values at the inner side of the cement, where shear failure is most likely to occur, is shown in Figure 28. For the intact cement, the numerical results indicate that the cement sheath maintains mechanical integrity during the pressure test prior to CO_2 degradation (purple line

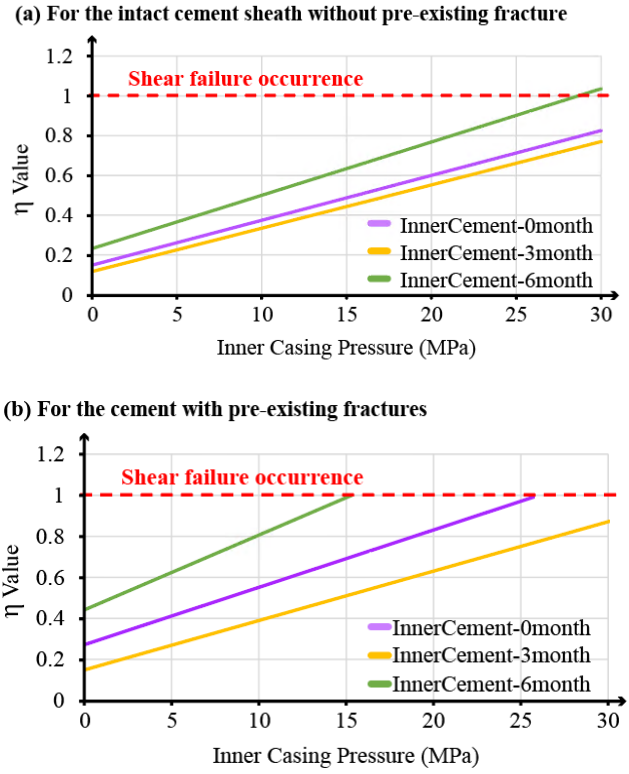

Figure 28. The variation of η values at the inner side of cement during the pressure testing performed after 0, 3, and 6 months of CO_2 exposure. (a) The variation of η values for the intact cement without fractures. (b) The variation of η values for the cement with pre-existing fractures.

in Figure 28a) and after 3 months of CO_2 degradation (yellow line in Figure 28a). As shown in Figure 28a, the short-term exposure to CO_2 slightly promotes cement integrity. However, after CO_2 exposure for 6 months, shear failure occurs when the testing pressure exceeds 28.5 MPa. For the fractured cement, shear failure occurs at 26 MPa without CO_2 degradation (purple line in Figure 28b) and at 15.5 MPa after 6 months of CO_2 degradation (green line in Figure 28b). No failure occurs during the pressure test after 3 months of CO_2 degradation (yellow line in Figure 28b).

As a direct consequence, the maximum allowable pressure and temperature (inducing thermal stress which has a similar effect as the excessive inner casing pressure) should be adjusted according to the severity of CO_2 and cement reaction. Drastic pressure and temperature variations should be avoided after long-term CO_2 injection. To maintain long-term sealing for CO_2 injection wells, including wells in service, inactive wells, and abandoned and plugged wells, regular leakage assessment should be performed, and the amount of CO_2 escaping should be monitored. For leaking wells, remediation operations should be implemented to mitigate CO_2-induced damage and strengthen the cement matrix.

For fractured cement, the predicted reduction in η value and shear failure likelihood at 0-3 months of CO_2 exposure is due to the CO_2 invasion and carbonation reactions promoted by the pre-existing fractures and the plugging/adhering in these fractures by the reaction products, which corresponds with our mesoscale observations (Figure 17). The significant increase of the η value and the shear failure likelihood for the fractured cement after 3-6 months of CO_2 exposure can be explained by enhanced strength deterioration due to the long-term CO_2 exposure. This result agrees with the qualitative observation of Nygaard *et al*. [33] and Wolterbeek *et al.* [19] that the cement integrity loss would be accelerated by fractures after extended exposure to CO_2.

An important detail of this study is that the cement CO_2 degradation data used in the numerical models represent static exposure to CO_2 (see Figure 9a). These static experimental conditions represent a well without active injection operations (i.e., a non-injecting well for which the wellbore and formation pressures are in balance or a plugged and abandoned well). For an active injection well, the CO_2-cement interaction should be represented by a dynamic environment, with the CO_2 flowing through the cement in conjunction with the corresponding reactions. Injection tubing and related components also need to be taken into consideration. Hence, further investigation is needed to extend the understanding of CO_2-driven cement degradation for more general applications.

Wellbore Integrity Damage in the Mont Terri CO_2 Pilot Injection Well

The simulation results predict that the integrity of the Mont Terri pilot injection well may be compromised by the cement hardening, pressure testing, and thermal cycling processes. The simulations indicate that cement cured at the conditions of the Mont Terri injection well may not act as a stable barrier to prevent leakage of the injection fluid. Several major conclusions about the failure occurrence can be drawn from the numerical results:

- The major failure type occurring during cement hardening is debonding failure at the cement-formation interface. The lack of an initial compressional stress and excessive shrinkage of the neat Portland Class G cement are the main contributors to the failure occurrence. The well samples obtained at Mont Terri by overcoring [20] shown in Figure 29a support the numerical prediction. Severe and systematic debonding can be seen at the cement-formation interface.
- Shear failure of the cement sheath was predicted to occur at the injection nozzles during the pressure test by the modelling results. Excessive inner casing pressure induces stress concentrations here, which can damage the cement sheath and contribute to long-term casing erosion. The overcoring sample shown in Figure 29b supports the numerical

predictions. Severe cement damage and casing erosion occurred at the region adjacent to the injection nozzles.

- Injecting a high-temperature fluid was predicted to contribute to the closure of the MA at the cement-formation interface. Reduction of annular permeability after injecting a high-temperature fluid into the wellbore was observed during the Mont Terri field tests, which is also in agreement with the numerical predictions.
- Long-term CO_2 exposure (e.g., >6 months) may compromise the wellbore integrity and promote cement failure. The strength deterioration due to long-term cement CO_2 degradation likely played a critical role to the catastrophic cement failure observed in Figure 29.
- The combined consequence of multiple rounds of pressure and temperature cycling and the long-term cement CO_2 degradation (indicated by the Mont Terri injection well report) needs further investigation. Data from overcoring observations, geochemical measurements, and mechanical tests are needed.
- A more detailed quantitative calibration and comparison between models and data need to be performed once the overcoring operation in the Mont Terri site is fully completed and CT scan results for the MA aperture magnitudes are obtained.

To further understand the factors leading to the observed and predicted cement damage, a standard ASTM bleeding test (ASTM C232) was performed for the same cement slurry recipe used in the Mont Terri CO_2 injection well to quantify the fluid loss during the hardening process. After the mixing process, the free water at the top of the cement slurry is removed every 5 minutes for 2 hours.

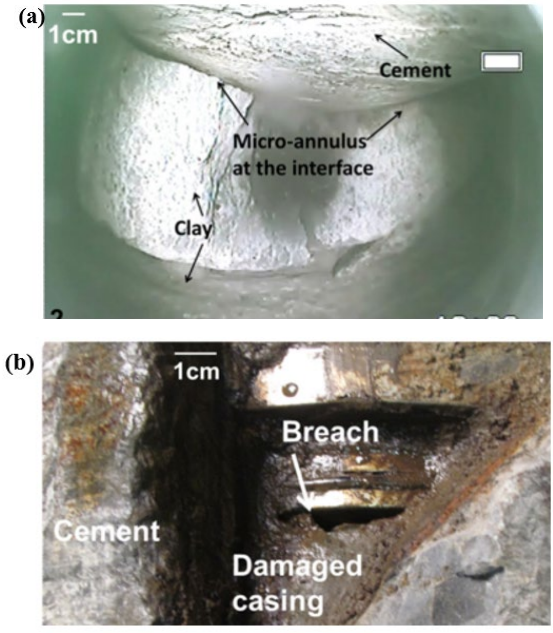

Figure 29. Observation from the overcored wellbore system [20]. a) The interface between the cement sheath and the formation rock (Opalinus Clay); b) The interface between the casing (the injection string) and the cement sheath.

The bleeding test results (Figure 30) indicate that the neat Class G Portland experiences significant fluid loss during the early stage of hardening. Under the downhole conditions of the Mont Terri well, the free water escaping from the cement slurry is likely to be absorbed by the Opalinus clay as the entire injection well is above the local water table.

During the first 120 minutes, the fluid loss of the cement slurry reached as much as 8% by volume, resulting in a decrease of the water cement ratio (w/c) from 0.44 to 0.375. A lower w/c results in a high Young's modulus, a low Poission's ratio, and accelerated shrinkage [28], which would significantly reduce the level of compression in the cement, promote the occurrence of cement failure, and reduce the long-term endurance of the hardened cement [21]. This is in agreement with all Mont Terri observations of the long-term well integrity (~16 months, see Manceau *et al*. [20].

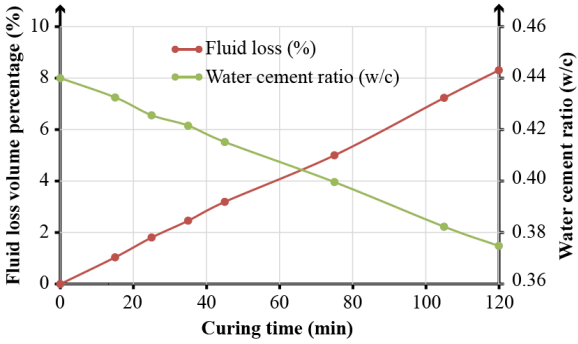

Figure 30. The bleeding test result of the cement paste.

UPSCALING TO FIELD-SCALE INJECTION WELLS

To gain insight for field applications, the integrated simulation is upscaled to an example injection well of 1000 m depth. To better account for detailed in situ conditions, cement pore pressure measurements were performed during the cement hardening process (Zhang *et al.*, [33]). The cement pore pressure, mechanical properties, and other inputs are all measured/collected for the 1000 m downhole conditions. The upscaling efforts at this stage do not include the CO_2 degradation results, as the degradation data were obtained for the specific case of the Mont Terri well.

Laboratory Measurements of Cement Pore Pressure

The experimental setup for this study is designed to cure the cement slurry under representative downhole conditions, which include high confining pressure, high temperature, and sufficient supply of external water. In contrast to previous studies (e.g., Appleby and Wilson [34]; Amziane and Andriamanantsilavo [35]), which measure the cement pore pressure evolution over a period of 72 hours, the study reported here gathered data on the variation of cement pore pressure for up to several weeks, which is sufficient time for the cement pore pressure to decrease and fully equilibrate with the formation pressure. The pore pressure in the cement of the Mont Terri injection well is not relevant for this study due to the shallow depth (14 m). However, the cement pore pressure is a significant, even predominant factor that determines the state of stress in the cement of field-scale deep injection wells. The pore pressure data measured in this work are analyzed for inclusion in the simulated assessment of field-scale CO_2 injection wells.

The overview and top view of the setup are presented in Figure 31a and b and the schematic diagram of the device is illustrated in Figure 31c. The pressure vessel consists of a 7-inch diameter cylindrical body with top and end caps secured using 16 high-strength steel rods. Four holes were drilled and threaded on the pressure vessel: one on the top cap for a thermocouple; one on the bottom cap for the fluid pressure sensor; one on the lower sleeve connected to a pump, to enable pressurization and provide water; and one on the upper sleeve with a valve to release the pressure and water. The mold for the cement has permeable material to hold the cement slurry in place and allow the cement to be

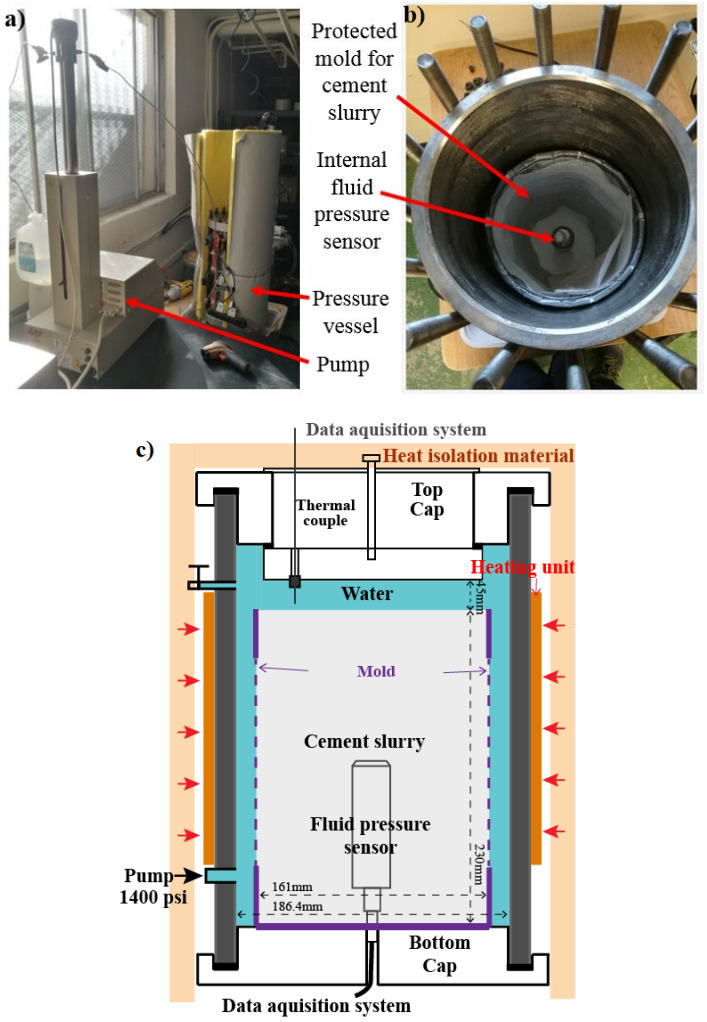

Figure 31. The laboratory setup. (a) Overview of the entire experimental setup. Data acquisition system is not shown in the image. (b) Top view of the pressure vessel with the top cap removed. (c) Schematic of the cement pore pressure setup.

exposed to water. There is a 0.5 in annulus between the cement mold (with an external diameter of 6 inches) and the chamber containment wall to ensure that the outer side and the top of the cement sample contact water and are exposed to uniform pressure.

The fluid pressure sensor is enclosed within an impermeable rubber protection sheath to prevent exposure of the sensor to cement slurry. The space between the sheath and the sensor body is filled with water, and any air bubbles are eliminated, so that the external fluid pressure is sensed by the pressure sensor. The pressure measurement by the sensor represents the fluid pressure in the cement around the sensor [36]. After the slurry solidifies, this pressure represents the pore pressure [4,34,35,37]. After the testing, the rubber protection sheath was still intact after the sensor was removed from the set cement sample. A data acquisition system collected fluid pressure temperature data. Benchmarking tests were performed with only water in the vessel to verify experimental safety, to check seal integrity, and to calibrate pressure and temperature measurements. The equipment can hold 2000 psi (13.7 MPa) without leakage for 12 hours, and the pressure measurements are +/- 0.5 psi and temperature measurements are +/-0.1°C.

Three pore pressure experiments were conducted in this study:

- Case 1 applied a confining pressure of 1400 psi (9.65 MPa) at room temperature (15°C).
- Case 2 applied a confining pressure of 1400 psi (9.65 MPa) at 35°C, which represents typical downhole conditions at a depth of 1000 m.
- Case 3 starts with the same conditions as Case 2 during the first 48 hours, followed by a temperature increase from 35°C to 55°C in 15 minutes and maintained for the remainder of the test. Case 3 is a heating test aiming to evaluate cement strength and calibrate the FEA model.

The intent of the sudden temperature increase in Case 3 was to induce fractures in the cement. The initiation conditions for these fractures are used to calibrate the numerical simulation for the cement hardening process using the same boundary conditions. For all cases, tests are terminated when the pore pressure data becomes steady (i.e., changes are less than 0.1 MPa per day).

Figure 32a shows the cement pore pressure measurements during the entire curing process for Cases 1-3. Figure 32b shows the pore pressure during the first 48 hours for Case 1 and 2 (Case 3 is omitted due to its similarity during that time frame with Case 2). For Case 1, the pore pressure starts to decrease from the 1400 psi (9.65 MPa) confining pressure after ~15 hours, drops to 1350 psi (9.3 MPa) by 48 hours, and stabilizes at 48 psi (0.33 MPa) after 19-20 days. For Case 2, the pore pressure starts to drop after 4 hours, reaches 1095 psi (7.55 MPa) by 48 hours, and stabilizes at 40 psi (0.28 MPa) at 12 days. For reference, 7.55 MPa (22% pore pressure drop) represents the cement pore pressure by the end of the typical wait time after injecting cement (i.e., 48 hours) at 1000 m depth in a permeable formation with hydrostatic pore pressure. The pore pressure evolution of Case 3 during the first 48 hours is almost the same as for Case 2 (identical curing conditions). The heating test is performed from 48 hours to 50 hours as a validation case for the numerical simulation, during which the pore pressure increases back to the confining pressure and then starts to drop until it stabilizes at 238 psi (1.64 MPa) after 15-16 days. Detailed information for the validation process is illustrated in Zhang *et al.* [13] and Zhang [26].

Unlike the test protocol used here, Appleby and Wilson's experiment did not supply external water to the cement [34]. The observation of gradual pore pressure decline when external water is supplied (as in this study) is similar to the study of Reddy *et al*. [37] where the cement pore pressure decreased gradually from 1000 to 200 psi after 208 hours.

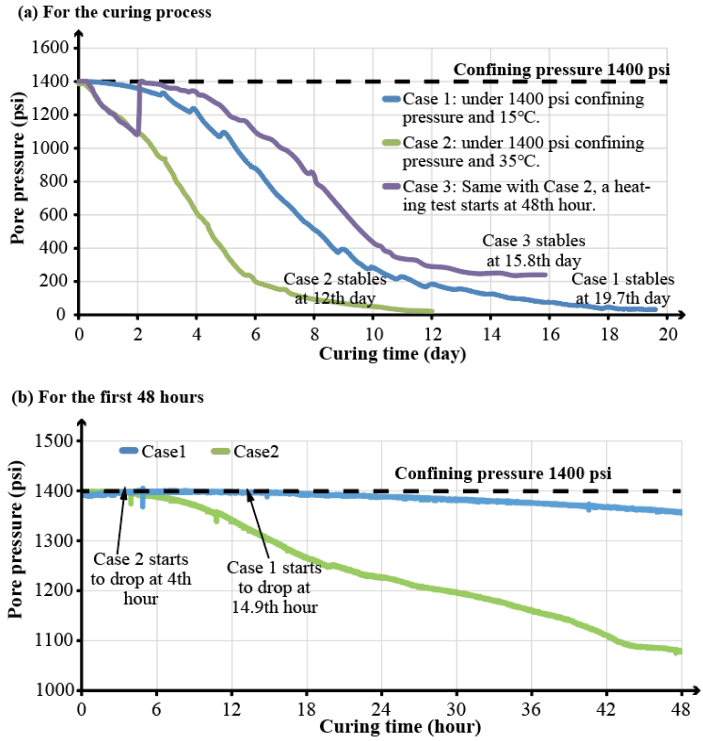

Figure 32. Cement pore pressure measurements from this study. (a) Case 1, 2, and 3 for the entire curing processes; (b) Case 1 and 2 for the first 48 hours.

Modelling a Field-Scale Injection Well

A typical field scale injection well is modelled for this study. The well model consists of a 5-½ inch casing and cement sheath in a 7-⅞ inch borehole, embedded in a formation component. An idealized extensional stress regime is defined in the formation with isotropic horizontal stresses ($S_H'=S_h'$) and an effective horizontal (S_H') to vertical (S_V') stress relationship of $S_H'=0.75\ S_V'$. The formation pore pressure in the model domain is specified to be uniform and hydrostatic at 1000 m depth. The major input parameters which define the operational stages of the well are listed in Table 6. The poro-elastic parameters and bulk shrinkage data came from laboratory tests representing downhole conditions at different depths [38]. The cement pore pressure laboratory measurements from the present study are inputs for the base case scenario (SDCS-BaseCase). These data characterize the cement pore pressure variations during hardening under downhole conditions of 1000 m depth in a permeable formation with hydrostatic pore pressure (see Case 2 from the pore pressure measurements above). A cement pore pressure drop scenario of 100% was simulated to investigate downhole conditions for an impermeable formation or without hydrostatic pore pressure gradient [16]. The cement hardening process was simulated using the staged finite element framework, which provides a representative state of stress of the wellbore system developed after cement hardening. Several scenarios for different load processes and different key parameters are listed in Table 7.

Table 6. Input parameters for the staged FEA approach of this study. The in-situ stresses are given in effective stresses.

	S_V'	S_H'	S_h'	Pore pressure	Mud pressure	Cement slurry pressure	Fluid injection pressure
500m	7MPa	5.25MPa	5.25MPa	4.9MPa	6MPa	7MPa	6.4MPa
1000m (BaseCase)	14MPa	10.5MPa	10.5MPa	9.8MPa	12MPa	14MPa	12.8MPa
1500m	21MPa	15.75MPa	15.75MPa	14.7MPa	18MPa	21MPa	19.2MPa

Table 7. Staged Downhole Condition Scenarios (SDCS) investigated in this study.

	Case codes	Sensitivity analysis (introduction)		Pressure testing	Injection related cooling
Step 4. Cement hardening process	SDCS-BaseCase	Establishes downhole conditions of 1000m	Step 5a, 6: operations after cement hardening process	SDCS-BaseCase-PTesting	SDCS-BaseCase-Cooling
	SDCS-Shrinkage	Various degrees of poro-elastic bulk shrinkage in cement		SDCS-Shrinkage-PTesing	SDCS-Shrinkage-Cooling
	SDCS-TempFluc	Addition of temperature fluctuation in cement		SDCS-TempFluc-PTesting	SDCS-TempFluc-Cooling

The context of the various cases is:

- For cases associated with pressure or temperature/heat tests (i.e., BaseCase-PTesting, and BaseCase-Cooling), the inner casing pressure is increased at a rate of 1 MPa/s, and the inner casing temperature is increased or decreased at 1°C/s until any type of failure occurs [28].
- Models SDCS-BaseCase, BaseCase-PTesting, and BaseCase-Cooling illustrate a typical scenario of an injection well section at 1000 m depth. These scenarios serve as the base case for comparison with other sensitivity analyses.
- Models SDCS-Shrinkage, Shrinkage-PTesting, and Shrinkage-Cooling predict the influence of different degrees of cement shrinkage during hardening on the occurrence of debonding and shear failure under various loads. The staged finite element framework adapts the poro-elastic proportion of the bulk shrinkage via the input shrinkage coefficient (s). Previous analyses indicate that s=50% in typical for in situ conditions at 1000 m depth [21,26].
- Models SDCS-TempFluc, TempFluc-PTesting, and TempFluc-Cooling illustrate the effects of temperature fluctuation during hardening due to the heat released by the cement hydration reaction. A significant amount of heat is released by the cement during the early stage of hardening, and the system gradually cools down during the later stage. This temperature fluctuation is prominent for the cement hardening process under downhole conditions (Nelson and Guillot 2004) and should be analyzed jointly with the cement shrinkage and poro-elastic property development. The influence of the temperature

changes on the onset of cement failure during subsequent load steps was investigated. The detailed explanation and input data are presented in Zhang and Eckert [21].

Occurrence of Shear Failure During Pressure Testing

For the SDCS-BaseCase-PTesting model (Figure 33a, b), the pressure applied to the inner casing (testing pressure) increases from the mud pressure (12 MPa) to a maximum pressure of 40 MPa (a representative value during a pressure test [29]). While the contact pressures remain compressive throughout pressure testing (i.e., no debonding failure occurs), the equivalent plastic strain (PEEQ) in the cement is monitored as an indicator of shear failure (Figure 33b). The PEEQ at the outer cement elements is zero and not shown in Figure 33b. A non-zero PEEQ develops in the inner cement at a testing pressure of 30 MPa. The pressure at which PEEQ develops is referred to as $P_{tolerance}$ (30 MPa, in this case) and represents the pressure marking the onset of plastic failure. PEEQ reaches a magnitude of 1.03×10^{-4} at an inner casing pressure of 40MPa.

For SDCS-TempFluc-PTesting, which imposes the temperature fluctuation during hardening, PEEQ at the inner cement initiates at a testing pressure of 23.4 MPa. The PEEQ reaches a magnitude of 2.26×10^{-4} at an inner casing pressure of 40 MPa. For case of a pore pressure drop of 100% (impermeable formation rock), $P_{tolerance}$ = 37.2 MPa. For SDCS-Shrinkage-PTesting, for s=0 and 0.25, the $P_{tolerance}$ = 68 MPa and 47.5 MPa (Figure 33c).

Occurrence of Debonding Failure During Injection-Induced Cooling

For the SDCS-BaseCase-Cooling model (Figure 34), the contact pressure at the casing-cement interface decreases from 12 MPa to 11.4 MPa during the completion step (red area), to 9.9 MPa by the end of the Charging process (the cooling process with inner casing pressure temperature decrease, blue area) and stabilizes at 10.3 MPa (grey area). The contact pressure at the cement-formation interface drops from 0.8 MPa to 0.3 MPa during the completion step, then to zero after 3 minutes of the Charging process and reaches -0.5 MPa by the end of the Charging process and stabilizes at -0.5 MPa. The resulting MA reaches 20 μm of aperture by the end of the Plateau process. The influence of cement pore pressure decrease, shrinkage and temperature fluctuations are presented in detail in next section.

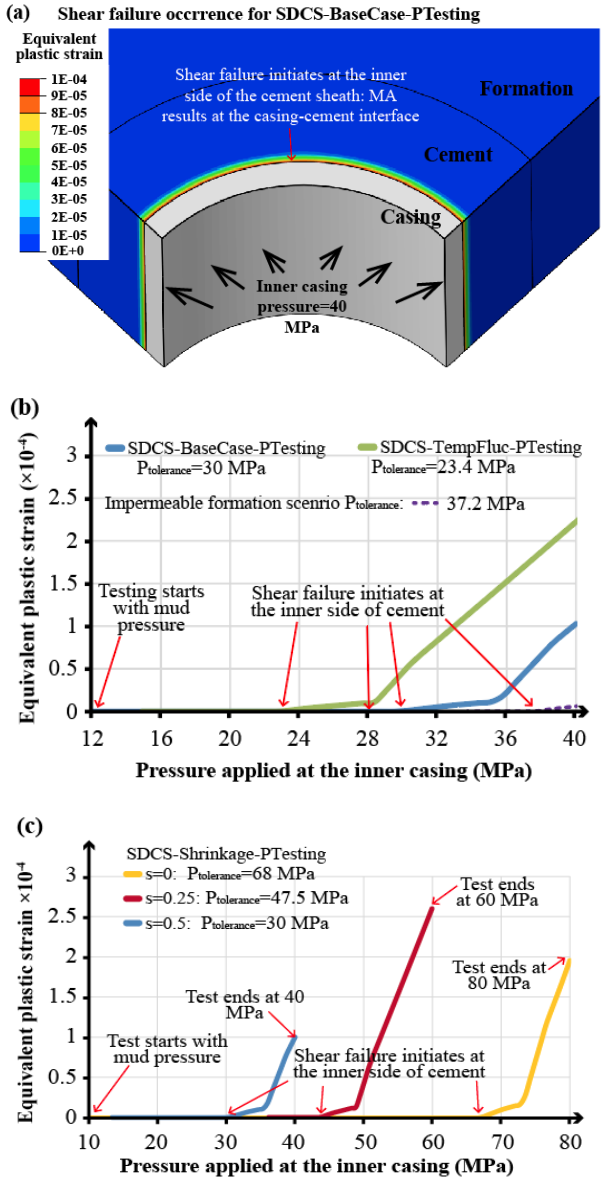

Figure 33. (a) Illustration of the equivalent plastic strain (PEEQ) distribution when the inner casing pressure is 40 MPa. (b) The resulting equivalent plastic strain (PEEQ) change with the applied inner casing pressure during the pressure testing for SDCS-BaseCase-PTesting (blue line) and SDCS-BaseCase-TempFluc (green line). (c) The resulting PEEQ variation during pressure testing for SDCS-Shrinkage-PTesting.

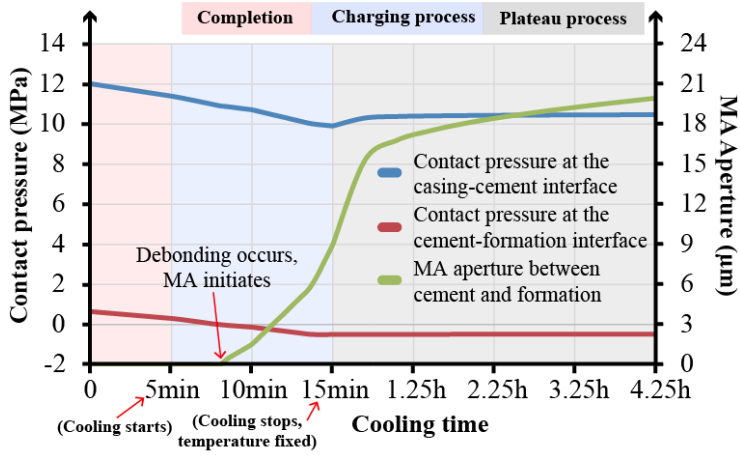

Figure 34. Contact pressure at the casing-cement (blue line) and cement-formation (red line) interfaces, and the resulting MA at the cement-formation interface (green line) change with time during completion and injection steps for SDCS-BaseCase-Cooling scenario.

Discussion of the Influence of Various Factors on Cement Failure Occurrence

To evaluate mechanisms and factors contributing to MA occurrence for real-scale injection wells, the various downhole scenarios presented in Table 7 are compared and evaluated with respect to the maximum inner casing pressure, $P_{tolerance}$, which induces shear failure (Figure 35a), and the temperature drop which initiates debonding during injection related cooling (Figure 35b).

Observations regarding $P_{tolerance}$, (Figure 35a) show that:

- The poro-elastic bulk shrinkage coefficient, *s*, is a measure of the degree of cement bulk shrinkage during hardening. Smaller magnitudes of *s*, indicating less poro-elastic volumetric shrinkage, result in less differential stress and thus a higher $P_{tolerance}$ can be sustained. Hence, the less the cement shrinks, the better the cement integrity. Shrinkage control or expansive additives need to be appropriately used to ensure wellbore integrity.
- Cement pore pressure decrease during hardening has a moderate influence on $P_{tolerance}$. For the SDCS-BaseCase, which has 22% pore pressure decrease, the $P_{tolerance}$ is 30 Mpa, while the case with a 100% pore pressure decrease, $P_{tolerance}$ increases to 37.2 MPa.
- Temperature decrease during the hardening process decreases $P_{tolerance}$ from 30 MPa (SDCS-BaseCase-PTesting) to 23.4 MPa, as the cooling effect during the later stage of the hardening step increases the differential stress, which weakens the cement. Since the numerical simulation of this process is based on a qualitative adaptation, representative quantitative measurements under downhole conditions are recommended.
- Cement integrity increases with increasing depth. Elevated confining pressure at a higher depth increases the initial state of stress in the cement and thus promotes cement integrity.

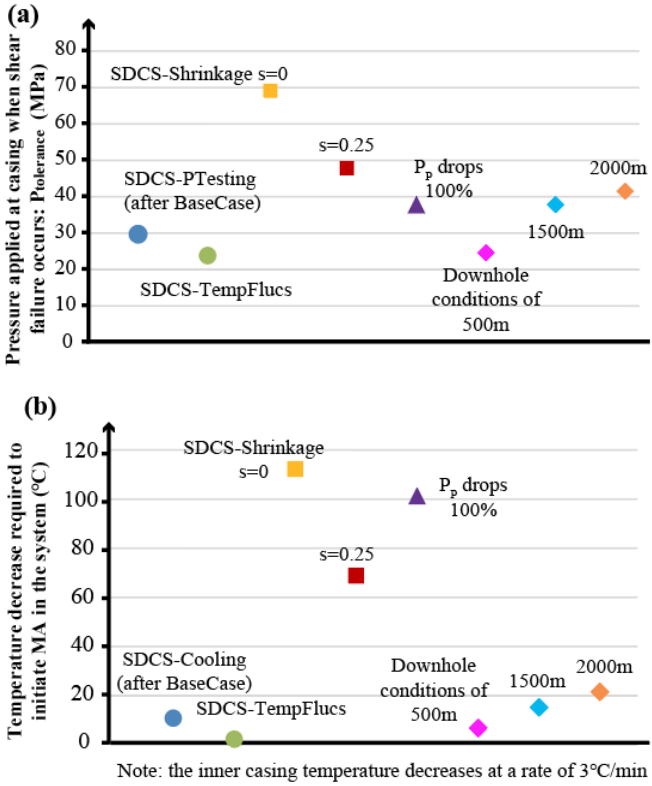

Figure 35. (a) The maximum inner casing pressure the wellbore system can withstand without shear failure ($P_{tolerance}$) for staged downhole conditions scenarios. (b) The temperature decrease required to initiate MA during injection-related cooling for staged downhole conditions scenarios.

Observations with respect to the temperature drop which initiates debonding, Figure 35b shows that:

- The poro-elastic bulk shrinkage (degree of cement bulk shrinkage during hardening) also affects the resistance of the system to debonding due to injection-related cooling. For s=0, 0.25, and 0.5 (SDCS-Cooling, the blue dot), debonding occurs at the cement-formation interface after a temperature decrease of 112℃, 68℃, and 10℃, respectively. If cement bulk shrinkage is minimized, the wellbore system can maintain integrity under a higher temperature difference during cooling.
- The cement pore pressure decrease has a significant influence on the tolerance of the system to debonding induced by injection related cooling. For a pore pressure decrease from 22% (SDCS-BaseCase) to 100%, debonding occurs at the cement-formation interface after temperature decreases of 10℃ and 103℃. (i.e., lower cement pore pressure allows higher temperature differences to be sustained). Further research efforts on the downhole conditions and the resulting cement pore pressure drop during hardening are recommended.

- Cement temperature fluctuations during hardening promote the initiation of debonding failure. When a cooling effect occurs during the hardening step, tensile thermal stresses are introduced, and the contact pressure at the cement-formation interface is reduced. Ignoring cement temperature fluctuations may lead to the underestimation of MA occurrence and resulting MA aperture. This factor is important when the contact pressure at the interface is close to debonding, but it is not enough to initiate MA at the interface under large compression by itself.
- Cement integrity increases with increasing depth. Due to the increasing confining pressure, the degree of compression in the cement increases with depth [5].

CONCLUSIONS

The status of cement is key to maintaining wellbore integrity during the life cycle of a well that is exposed to CO_2. Knowledge and understanding of cement hardening and cement failure from the investigation of the Mont Terri CO_2 injection well can aid the estimation of cement condition in field scale CO_2 injection wells. The cement system design needs to account for actual curing conditions (downhole conditions), the potential cement-formation and cement-formation fluid interactions, and the loads arising during the well life cycle. Minimizing the degree of cement bulk shrinkage during hardening is crucial to creating a compact cement matrix and maintaining integrity. This requires inhibiting fluid loss from the cement, providing abundant external water supply, maintaining compression during hardening, and adding an expansive agent in moderation. Cement temperature fluctuations and pore pressure decrease (especially for a field scale injection well) during hardening also have influence on the onset of shear and debonding failure, which need to be considered during upscaling to the field scale. Measuring and characterizing cement properties under representative downhole conditions is crucial to evaluate and select the proper cement system. The CO_2-cement interaction has been shown in this study to slightly promote wellbore integrity in the short-term, but significant cement failure and severe leakage hazard would be induced after the long-term degradation.

For new wells planned in the Mont Terri rock laboratory or similar conditions, several suggestions are provided based on this study:

- Fluid loss control agents should be added into the cement to inhibit the fluid loss at the early stage of hardening to guarantee the hydration reaction of the cement has enough water supply. This ensures the cement develops the desired mechanical properties and reduces the likelihood of failure occurrence.
- Additional hydrostatic pressure is suggested to be maintained in the well annulus during cement hardening to increase the compressional stress in the cement. This inhibits the onset of tensile failure (debonding and cracking) and improves the bonding quality at interfaces [13]. In addition, air bubbles existing in the cement slurry during mixing and grouting will remain in the hardened cement matrix, which may act as “weak points” and can significantly reduce the strength of the cement. Increasing pressure applied to the cement slurry is an effective method to mitigate the influence of air bubbles.
- Expansive cement can be used for cementing the shallow section of the wellbore. The expansive agents can provide additional compression during cement hardening, which counteracts the tensile stress resulting from cement shrinkage, and thus inhibits the onset of tensile failure (i.e., debonding failure and radial cracks).
- Moderately increasing the temperature of the injection fluid (e.g., during winter or cold offshore conditions) can be considered. High temperature fluids add additional thermal stresses at the cement-formation interface, which can further close the MA and promote wellbore integrity. However, a very rapid increase of the injection fluid temperature can

induce thermal shock (e.g., peaks of the contact pressure curve in Figure 26a), which may further induce shear failure in cement and formation rock. Hence, the temperature of the injection fluid should be increased slowly to avoid thermal shock.

- The long-term reaction between CO_2 and cement should be taken into consideration of the cement slurry design. Additives that promote the hydration reaction and inhibit shrinkage should be added.
- The wellbore integrity damage due to the cement CO_2 degradation can be inhibited by maintaining a compressional curing condition for the cement slurry during hardening. Preventing fracture onset due to the insufficient water and shrinkage is vital to the long-term integrity of CO_2 injection wells.
- The safety pressure and temperature ranges of the well should be modified according to the period of CO_2 injection. After long-term injection of CO_2 (e.g., >6 months), the strength cement sheath would decrease dramatically, operations associated with excessive magnitudes and abrupt variations of pressure and temperature should be avoided or prudently implemented.

ACKNOWLEDGEMENTS

We acknowledge the support of the Energetic Materials, Rock Characterization and Geomechanics (EMRGe) research center at Missouri University of Science and Technology. We also acknowledge the financial support of BP America and the CCP consortium (Award #: 0059964) and the technical discussion and suggestions from Chevron ETC.

REFERENCES

1. Lavrov, A., & Torsæter, M. (2016). *Physics and Mechanics of Primary Well Cementing,* Springer.
2. Stormont, J. C., Fernandez, S. G., Taha, M. R., & Matteo, E. N. (2018). Gas flow through cement-casing microannuli under varying stress conditions. *Geomechanics for Energy and the Environment*, *13*, 1-13.
3. Nelson, E.B. and Guillot, D. Well Cementing, 773 Sugar Land, Texas: Schlumberger. 2006.
4. Levine, D. C., Thomas, E. W., Bezner, H. P., & Tolle, G. C. (1979, January). Annular gas flow after cementing: A look at practical solutions. In *SPE Annual Technical Conference and Exhibition*. Society of Petroleum Engineers.
5. Sabins, F. L., & Sutton, D. L. (1991). Interrelationship between critical cement properties and volume changes during cement setting. *SPE Drilling Engineering*, *6*(02), 88-94.
6. Bois, A. P., Garnier, A., Rodot, F., Sain-Marc, J., & Aimard, N. (2011). How to prevent loss of zonal isolation through a comprehensive analysis of microannulus formation. *SPE Drilling & Completion*, *26*(01), 13-31.
7. Boukhelifa, L., Moroni, N., James, S., Roy-Delage, L., Thiercelin, M. J., & Lemaire, G. (2005). Evaluation of cement systems for oil and gas well zonal isolation in a full-scale annular geometry. *SPE Drilling & Completion*, *20*(01), 44-53.
8. Zhang, W., Eckert, A., & Liu, X. (2017, August). Numerical simulation of micro-annuli generation by thermal cycling. In *51st US Rock Mechanics/Geomechanics Symposium*. American Rock Mechanics Association.
9. Orlic, B., Chitu, A., Brunner, L., Koenen, M., Wollenweber, J., & Schreppers, G. J. (2018, August). Numerical investigations of cement interface debonding for assessing well integrity risks. In *52nd US Rock Mechanics/Geomechanics Symposium*. American Rock Mechanics Association.

10. Nygaard, R., Salehi, S., Weideman, B., & Lavoie, R. G. (2014). Effect of dynamic loading on wellbore leakage for the wabamun area CO2-sequestration project. *Journal of Canadian Petroleum Technology*, *53*(01), 69-82.
11. Li, Y., & Nygaard, R. (2018). A numerical study on the feasibility of evaluating CO_2 injection wellbore integrity through casing deformation monitoring. *Greenhouse Gases: Science and Technology*, *8*(1), 51-62.
12. De Andrade, J., & Sangesland, S. (2016). Cement sheath failure mechanisms: numerical estimates to design for long-term well integrity. *Journal of Petroleum Science and Engineering*, *147*, 682-698.
13. Zhang, W., Eckert, A., Hilgedick, S., & Goodman, H. (2021, March). Integrated Laboratory and Numerical Investigation of Leakage Pathways Development in CO_2 Injection Wells. In *Proceedings of the 15th Greenhouse Gas Control Technologies Conference* (pp. 15-18).
14. Zhang, W., Eckert, A., & Ma, H. (2021, June). Integrated Experimental and Numerical Evaluation for Wellbore Integrity of Wells Under Downhole Conditions. In *55th US Rock Mechanics/Geomechanics Symposium*. OnePetro.
15. Barlet-Gouedard, V., Rimmele, G., Goffe, B., & Porcherie, O. (2006, February). Mitigation strategies for the risk of CO_2 migration through wellbores. In *IADC/SPE drilling conference*. OnePetro.
16. Omosebi, O., Maheshwari, H., Ahmed, R., Shah, S., & Osisanya, S. (2017). Experimental study of the effects of CO_2 concentration and pressure at elevated temperature on the mechanical integrity of oil and gas well cement. *Journal of Natural Gas Science and Engineering*, *44*, 299-313.
17. Kashef-Haghighi, S., Shao, Y., & Ghoshal, S. (2015). Mathematical modeling of CO_2 uptake by concrete during accelerated carbonation curing. *Cement and Concrete Research*, *67*, 1-10.
18. Li, Q., Lim, Y. M., Flores, K. M., Kranjc, K., & Jun, Y. S. (2015). Chemical reactions of portland cement with aqueous CO_2 and their impacts on cement's mechanical properties under geologic CO_2 sequestration conditions. *Environmental Science & Technology*, *49*(10), 6335-6343.
19. Wolterbeek, T. K., Hangx, S. J., & Spiers, C. J. (2016). Effect of CO_2-induced reactions on the mechanical behaviour of fractured wellbore cement. *Geomechanics for Energy and the Environment*, *7*, 26-46.
20. Manceau JC, Tremosa J, Audigane P, Lerouge C, Claret F, Lettry Y, Fierz T, Nussbaum C. Well integrity assessment under temperature and pressure stresses by a 1: 1 scale wellbore experiment. *Water Resources Research*. 2015 Aug;51(8):6093-109.
21. Zhang, W., & Eckert, A. (2020). Micro-annulus generation under downhole conditions: Insights from three-dimensional staged finite element analysis of cement hardening and wellbore operations. *Journal of Rock Mechanics and Geotechnical Engineering*.
22. Bourissai, M., Meftah, F., Brusselle-Dupend, N., Lécolier, É., & Bonnet, G. (2013). Evolution of the elastic properties of an oilwell cement paste at very early age under downhole conditions: Characterization and modelling. *Oil & Gas Science and Technology–Revue d'IFP Energies nouvelles*, *68*(3), 595-612.
23. Kurdowski, W. (2014). *Cement and concrete chemistry*. Springer Science & Business.
24. SIMULIA, 2017. *Abaqus Version 2017 Analysis User's Guide. Providence*, RI, USA: Dassault Systemes. 2017.
25. Zhang, W., & Eckert, A. (2018, August). Numerical Investigation of the Influence of Cement Failure to Micro-Annuli Generation. In *52nd US Rock Mechanics/Geomechanics Symposium*. American Rock Mechanics Association.
26. Zhang, W. (2020). Integrated approach to investigate the wellbore integrity under downhole conditions. PhD Dissertation, Missouri Univ. of Science and Tech.

27. Zoback, M. D. (2010). *Reservoir geomechanics*. Cambridge University Press. Postler, D. P. (1997, March). Pressure integrity test interpretation. In *SPE/IADC drilling conference*. OnePetro.
28. Bossart, P., & Wermeille, S. (2003). Paleohydrological study on the surroundings of the Mont Terri rock laboratory. *Mont Terri Project–Geology, Paleohydrology and Stress Field of the Mont Terri Region. Reports of the Federal Office for Water and Geology (FOWG), Geology Series*, *4*, 45-64.
29. Amann, F., Kaiser, P., & Button, E. A. (2012). Experimental study of brittle behavior of clay shale in rapid triaxial compression. *Rock Mechanics and Rock Engineering*, *45*(1), 21-33.
30. Justnes, H., Van Loo, D., Reyniers, B., Skalle, P., Sveen, J., & Sellevold, E. J. (1995). Chemical shrinkage of oil well cement slurries. *Advances in cement Research*, *7*(26), 85-90.
31. Therond, E., Bois, A. P., Whaley, K., & Murillo, R. (2017). Large-scale testing and modeling for cement zonal isolation in water-injection wells. *SPE Drilling & Completion*, *32*(04), 290-300.
32. Nygaard, R. (2010). Wabamun area CO_2 sequestration project (wasp). *Energy and environmental systems group (EES)*.
33. Zhang, W., Eckert, A., Hilgedick, S., Goodman, H., & Meng, M. (2021). Wellbore Integrity: An Integrated Experimental and Numerical Study to Investigate Pore Pressure Variation during Cement Hardening under Downhole Conditions. *SPE Journal, 1*-16.
34. Appleby, S., & Wilson, A. (1996). Permeability and suction in setting cement. *Chemical Engineering Science*, *51*(2), 251-267.
35. Amziane, S., & Andriamanantsilavo, N. (2004). Prediction of cement paste pore water pressure variations during setting period. *Advances in cement research*, *16*(1), 23-28.
36. Cheung, P. R., & Beirute, R. M. (1985). Gas flow in cements. *Journal of petroleum technology*, *37*(06), 1-041.
37. Reddy, B. R., Xu, Y., Ravi, K. *et al.* 2009. Cement Shrinkage Measurement in Oilwell Cementing–a Comparative Study of Laboratory Methods and Procedures. *SP E Drill & Compl* 24 (1): 104–114. SP E-103610-PA. https://doi.org/10.2118/103610-PA.
38. Chenevert, M.E. and Shrestha, B.K. Chemical Shrinkage Properties of Oilfield Cements (includes associated paper 23477*). SPE Drilling Engineering* 1991; 6(01): 37-43.

Carbon Dioxide Capture for Storage in Deep Geological Formations, Volume 5
Karl F. Gerdes (Editor)
© 2022 BP. All rights reserved.

Chapter 31

IMAGING LEAKAGE ASSOCIATED WITH CAPROCK FAULT ACTIVATION: RESULTS FROM THE FAULT SLIP EXPERIMENT IN MT. TERRI OPALINUS CLAY ANALOGUE CAPROCK

Yves Guglielmi[1], Jonathan Ajo-Franklin[2], Jens Birkholzer[1], Frédéric Cappa[3], Paul Cook[1], Chet Hopp[1], Christophe Nussbaum[4], Antonio Pio Rinaldi[5], Michelle Robertson[1], Veronica Rodriguez-Tribaldos[1], Jonny Rutqvist[1], Tanner Shadoan[2], Florian Soom[1], Todd Wood[1], Alba Zappone[5]
[1]Energy Geosciences Div., Lawrence Berkeley National Laboratory, Berkeley, CA, USA
[2]Department of Earth, Enviro. and Planetary Sciences, Rice University, Houston, TX, USA
[3]Univ. Côte d'Azur, CNRS, Observ. de la Côte d'Azur, IRD, Géoazur, Sophia Antipolis, FR
[4]Federal Office of Topography, Swisstopo, St-Ursanne, CH
[5]Swiss Seismological Service, and Department of Mechanical Engineering, ETHZ, CH

ABSTRACT: The Fault Slip (FS) experiment FS-B at the Mont Terri Underground Laboratory in Switzerland was designed to study faulted caprock integrity. Repeated seismic imaging of fluid flow and stress variations were conducted during 6 constant flowrate water injections directly into the fault zone. A high correlation between pore pressures, displacement-strain data, induced earthquakes, and P-wave velocity images was observed. Results show that a fluid leak is coupled to fault deformation complexity. Signals an order of magnitude smaller were observed in the non-leaking fault zones compared to the leaking ones within the spatially heterogeneous fault zone. Instantaneous decrease in P-wave velocity with injection pressure correlated with mechanical opening and shearing of fractures within the fault zone. Outside the leakage zone, fault displacements are too small to induce a P-wave velocity variation. A rupture front, or process zone, of several meters precedes the fluid leakage front. The rupture front occurs where compressive strain favors dilatant shear on pre-existing fault structures. Periods of rapid pore pressure increase that produce the fastest displacement and strain rates of ~20 microstrain (micrometer/s) generate a sparse seismicity. The seismic velocity images show an asymmetric leakage pathway propagation, highlighting stress and strength heterogeneities distributed along the fault zone. Long-term apparent irreversible change in the P-wave travel times matches with the irreversible fault shear displacement. Given the protocol adopted in the FS-B experiment, fault activation mechanisms appear highly complex resulting in a surprisingly directional, fast, and large magnitude fluid leak within the fault zone.

KEYWORDS: cap rock; fault; fluid injection; leakage; field scale experiments; active seismic imaging

INTRODUCTION

This work is aimed at improving the understanding of top-seal integrity for CO_2 storage. Earthquakes exceeding a moment magnitude (M_w) of 5.0 triggered at approximately the CO_2 storage depth could create migration pathways in seals (or caprocks) overlying the storage formation [1]. These pathways could manifest via slip or opening of existing, or unidentified faults, leading to permeability enhancement and eventually leakage of CO_2 [2,3]. *In situ* experiments at the tens-of-meter scale allow controlled activation of pre-existing faults by fluid injection, provide access to the complex

architecture of the entire fault, and with high-resolution monitoring in place, offer an opportunity for tracking fault slip, induced seismicity and leakage close to the nucleation zone [4].

The FS-B experiment utilized repeated seismic imaging of fluid flow and stress variations during a controlled fault activation experiment by fluid injection. Monitoring was continued several months after the activation sequence to characterize the three-dimensional long-term permeability evolution of the stimulated fault. FS-B is building on the results of a previous FS experiment performed in 2015.

FS demonstrated that a 0.4 mm fault slip could be triggered and continuously monitored while the pore pressure was increased by ~2.0 MPa above the initial pressure in the Mont Terri Main Fault affecting the Opalinus clay. The Opalinus clay is considered to be a perfect caprock analogue [5]. The effective normal stress perturbation proved to be high enough to reactivate the fault, but not sufficient to explain the exponential fault permeability increase from 10^{-17} to 10^{-13} m^2 that occurred during the ~30 minutes long injection period. We observed that such high magnitude permeability increase occurred during fault slip events and a low magnitude -2.3 earthquake, highlighting that permeability variation also depends on the fault slip rate and can be associated with induced seismicity [5,6,7,8]. Thus, high slip rate yielded high permeability increase while low slip rates, led to lower permeability increases. In more detail, similar ruptures can create or destroy the fluid diffusion pathways, since the creation of too high or too low diffusivity by the main rupture prevents secondary rupture events from occurring, whereas 'intermediate' diffusivity favors the initiation of a secondary rupture associated with the fluid diffusion. The FS experiment utilized an injection well and three monitoring wells – two vertical boreholes where fault three-dimensional displacements and pore pressure were continuously monitored and one additional vertical borehole with two three-components accelerometers. This arrangement did not allow an estimation of the fault activated volume size, geometry and seismic events localization because there were not enough seismic sensors and not enough boreholes to give a three-dimensional view of the stimulated volume. Nevertheless, the results showed that the effective normal stress on the fault has to be drastically lowered for the fault to leak and that there was a significant closing of the leakage pathway as soon as the injection pressure was decreased [4].

The new FS-B experiment, compared to FS, is combining more extensive direct measurements of fault movements and pore pressures with indirect time-lapse seismic imaging of the evolution of the dimensions of the stimulated patch. In this chapter, we first describe the physical setting of the FS-B experiment. Next, we show preliminary results of fault displacements, deformations, induced seismicity and variations of P-wave velocities during activation. Finally, we briefly discuss the consistency between the different measurements that leads to the observation of the complex coupling between the fault rupture propagation and the growth of a tens-of-meter long leakage flow path.

FAULT ZONE GEOLOGY

The instrumented volume for the FS-B experiment is about 70 m x 70 m x 70 m and is centered on the Mont Terri Main Fault zone (Fig. 1). The Main Fault zone is cutting all the laboratory's galleries which means that its extension is at least several hundreds of meters. It is the most extensive tectonic structure observed in the Mont Terri underground research laboratory. In the Northeastern side of the FS-B volume, the gallery excavated in 2008 intersects the Main Fault zone. Two windows in the gallery wall (meaning two zones where there is no shotcrete has been applied) allow direct observation of the fault zone and comparison with other galleries.

The experiment is set below the gallery floor in 23 fully-cored boreholes that were used to localize and characterize the fault zone architecture, and then to deploy the instrumentation (Fig. 1a). Ten boreholes were drilled for the 2020 fault slip (FS-B) experiment (BFSB boreholes in Fig. 1a). In

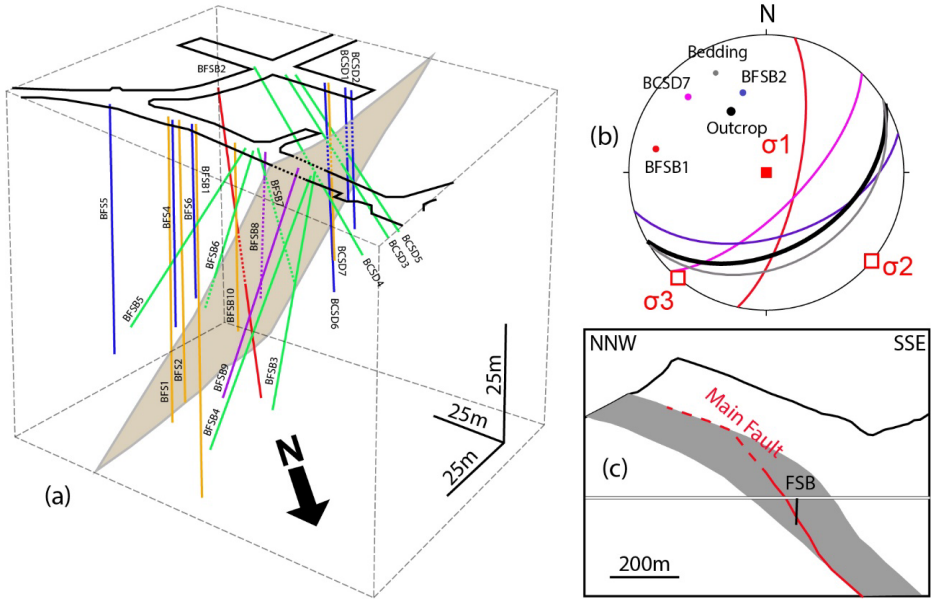

Figure 1. Fault zone geology. (a) Three-dimensional view of the FS-FSB-CSD experiments borehole setting (Main Fault is shown as the light grey, tilted surface and access galleries are shown as black outlines on top of the cube). (b) Stereographic projection of Main Fault principal slip surface intersected in different zones, respectively BFSB2, BFSB1, BCSD7 and gallery 2008 outcrop. Bedding plane orientation is also projected in grey. (c) Vertical cross section of the Mont Terri anticline with the Opalinus clay layer in grey affected by the Main Fault in red.

addition, the experiment benefits from 6 pre-existing boreholes drilled in 2015 for the first fault activation experiment (BFS boreholes in Fig. 1a) and from the 7 boreholes drilled in 2019 for the CSD project [9] that aimed at studying the potential for CO_2 leakage into the inactive fault (BCSD boreholes in Fig. 1a). Core recovery was higher than 90%. All borehole deviations (azimuth and inclination from vertical) were logged. Then, borehole diameter was measured with a 4 arm caliper and imaged with an oriented optical borehole televiewer (OPTV), natural gamma ray, conductivity, and, for some boreholes, full waveform sonic. The cores were mapped and scanned in the field. The correlation between cores mapping and the logs allowed an accurate reconstruction of the oriented geological log for each borehole.

The Mont Terri Main Fault zone displays spatial strike, dip and thickness variations of N040°-to-N075°, 40-to-65° SE and 1 to 6 m, respectively (Fig. 1c). It is extremely difficult to interpolate the fault zone top and bottom limits between all the observation points that correspond to intersections between boreholes, galleries and the Main Fault. The top of the Main Fault seems easier to identify on cores while the bottom in general seems more progressively vanishing in the intact rock [10]. The fault zone is composed of fault gouge, shear bands, meso-scale folds, microfolds, numerous fault planes and apparent undisturbed parts. The fault zone architecture displays a small damage-zone-vs-core ratio, suggesting a strong localized deformation [4]. Large amounts of “scaly” fabric that form an anastomosing network of polished surfaces where clay-rich rock splits into progressively smaller flakes are observed. Scaly clay is considered as a product of intense strain in locked positions such as

relay zones linking shear bands. Core observations show that almost all of the fault plane strike and dip belong to the same directional family. This family belongs to the Jura deep decollement structures. These structures are part of a shear fault-bend fold [11]. The fault-bend fold passively steepens from 20° to around 40°-45° in sequence with the folding of the Mont Terri anticline (Fig. 1b). The fault shear offset is ~10 m. Fault initial permeability is 10^{-19} to 6×10^{-17} m^2 [9]. The ambient pore pressures are ~2 MPa and the current state of stress is characterized by σ_1 =7.8±1MPa, dip direction of 89±5° and dip of 40±2°; σ_2 =5.4±0.6MPa, dip direction of 200±10° and dip of 37±10°; σ_3 =4.7±0.2MPa, dip direction of 310±1° and dip of 34±10° (Fig. 1c). Given this state of stress, the fault and most of the features contained in the fault zone are not optimally oriented versus stress for shear slip activation. Outside the fault zone, the Mont Terri tectonic deformations are mostly characterized by a large density of faults parallel to bedding with a 2-4 m spacing and a length >10 m. These reverse faults crosscut all the other structures including the Main Fault. They are related to the late installation of the Mont Terri anticline.

INSTRUMENTATION

The FS-B test volume is accessed by 23 instrumented boreholes, creating a unique fault-testing field laboratory. The test patch is monitored by a large array of instruments including local and distributed strain measurements, pore pressure measurements, passive acoustic and seismic events detection, and active seismic imaging (Figure 1a). BFSB2 is the high-pressure water injection hole in the FS-B experiment. BCSD1 is the low pressure and low flowrate CO_2 brine injection in the CSD experiment [9]. Green boreholes are instrumented with active seismic systems such as the Continuous Active-Source Seismic Monitoring (CASSM, [13]) for the FS-B experiment. Orange boreholes are instrumented with SIMFIP 3D fault displacement instruments and DAS, DSS and DTS optical fibers for distributed strain and temperature monitoring. Blue boreholes are used to measure pore pressures. Many measurements are coupled (Figure 2a). For example, all the boreholes are instrumented with optical fibers that capture the borehole axial strain and the temperature distribution with very fine sampling (sub-meter) and spatial resolution depending on the sensing system (DSS/DTS about 1 m, DAS 10 m gauge-length). The fibers are cemented behind the borehole casing. In the injection borehole (BFSB2) and in the two monitoring boreholes, BCSD7 and BFSB1, local pore pressure and fault three-dimensional displacements are monitored with hydromechanical probes [12]:

- In the injection hole, BFSB2, one SIMFIP probe (Step-Rate Injection Method for Fracture In-Situ Properties [12] is sealing a 2.43 m long injection interval between two inflatable packers. The interval is set across the top principal shear zone (PSZ) of the Main fault observed on cores at a depth of 41.2 m. The sealed borehole segment is set between 39.7 and 41.93 m. In this segment, the borehole PVC casing is screened to allow for injection into the formation. Inside the interval, the SIMFIP displacement sensor is anchored across the PSZ between 40.2 and 41.43 m. Thus, the SIMFIP probe monitors the relative three-dimensional displacement between the hanging wall and the foot wall of the top main fault PSZ, in addition to interval pressure and injection flowrate. Note that the injection interval is not straddling the entire thickness of the fault zone that spans between 41.2 and 42.7 m in BFSB2. Behind the BFSB2 casing, the DTS-DSS-DAS fibers monitor continuous strains and temperatures.

- In BCSD7, one SIMFIP probe is sealing a 6.3 m long interval between two inflatable packers. The interval is straddling the entire fault zone thickness observed between 21.15 and 26.95 m in BCSD7. The SIMFIP is thus monitoring the relative displacements between the hanging and the footwall of the entire fault zone, in addition to interval pressure. BCSD7 is an open hole. Four nearby boreholes (BCSD3-6) are instrumented with distributed DSS strain fibers.

- In BFSB1, 4 DORSA probes (Downhole Robotic Stress Analyzer) are deployed at 31, 34.9, 38.55 and 42.2 m depths. The DORSA probe is an evolution of the SIMFIP probes. They are more compliant than the SIMFIP, allowing measurements over a broader range. At 31 m depth, the DORSA-1 monitors the relative three-dimensional displacement between two borehole anchoring points at 30.4 and 31.6 m set in intact rock. At 34.9 m depth, the DORSA-2 is monitoring the relative displacement between two anchoring points at 34.3 and 35.15 m set across the top Main Fault shear surface which has a dip direction N143.1 and a dip angle 56.3°. At 38.55 m depth, the DORSA-3 is monitoring

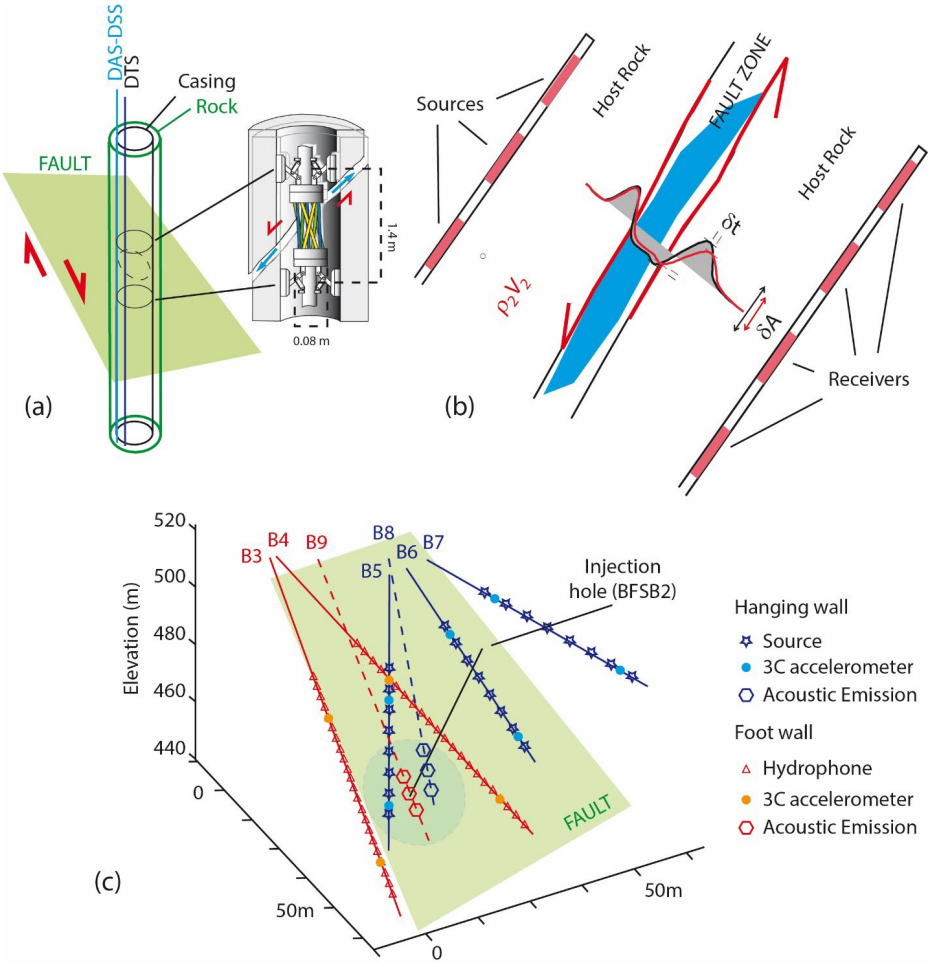

Figure 2. Experiment setting. (a) Borehole strain, temperature and pressure instrumentation. (b) Schematic vertical cross section showing the concept of active seismic source-receiver p-waves velocity monitoring across the activated fault zone. (c) CASSM and passive seismic monitoring setting (blue are borehole instruments set above the fault, red are borehole instruments set below the fault).

the relative displacement between two anchoring points at 37.95 and 39.15 m set across a second major slip surface within the Main fault zone that displays a dip direction and dip angle of N145.1 and 65.3°, respectively. DORSA-2 and DORSA-3 are anchored across the two principal slip surfaces of the main fault zone. In both locations, the footwall of the shear surface is made of highly deformed scaly clay while the hanging wall is made of intact rock. At 42.2 m, the DORSA-4 is monitoring the relative displacement between two anchoring points at 41.6 and 42.8 m set across a 0.1 m thick shear zone parallel to the bedding with a dip direction and dip angle of N158 and 30°, respectively. The four DORSA sensors are set inside the borehole's PVC casing. Behind the borehole casing and at the same depths, 4 pore pressure sensors are deployed within 1 m long sand intervals (the remaining behind casing annular zone is cemented). In addition, DTS-DSS-DAS fibers monitor continuous strains and temperatures.

During the fault activation period, the displacements, strains, pore pressures and flowrate are continuously monitored over a broad band of frequencies (0.5-to-1 kHz for the SIMFIP and DORSA, and 0.1 Hz to >5 kHz for the distributed optical fibers). The sensitivities of the measurements are micro-meters for displacement, micro-strains for strain, 10^{-3} Pa for pore pressure, and 0.1 L/min for flowrate.

The cross-well Continuous Active-Source Seismic Monitoring (CASSM) technology is deployed to monitor P- and S-wave velocity changes related to fluid-driven aseismic deformations triggered during the activation of the fault (Fig. 2b). The CASSM method has been applied to detect seismic velocity changes induced by tectonic stresses [13,14}, reservoir fluid saturation [15], CO_2 injection [16] and shallow hydraulic fractures [17]. Here, the CASSM setting includes five dedicated monitoring wells to monitor the volume of 70 x 70 x 70 m^3 crosscut by the Mont Terri Main Fault (Figure 1a and 2c). Three boreholes have a total of 24 piezoelectric seismic sources (8 each); the other two boreholes have 44 hydrophones in two arrays (22 each). The receiver boreholes (B3 and B4) are in the foot wall of the fault, while the source boreholes (B5, B6, and B7) are in the hanging wall. During CASSM acquisition, each source is activated 16 times, while all 44 hydrophones are recording at 48 kHz and stacking to increase signal to noise ratio (SNR). The acquisition process cycles through all sources to generate a single CASSM epoch. The time to complete each full sequence is about 8 minutes, the temporal resolution of this system.

The passive seismic monitoring system tracked the seismic events induced by fault activation. In addition to the 44 hydrophones, a set of three-component accelerometers (3C) were deployed in each of the five CASSM boreholes with one accelerometer installed above and one below each source and receiver array (Figure 2c), for a total of ten elements. Compared to the hydrophone sensors which have a 360-degrees sensitivity that does not allow distinguishing the direction of incident waves, each accelerometer is sensitive to particle motion in longitudinal, transverse, and vertical orientations. The accelerometers display a response between 2 and 20 kHz. An inflatable bladder is activated to mechanically bind each accelerometer to the formation through the borehole casing. Accelerometers signals are recording at 48 kHz with the CASSM system. In addition, 12 acoustic emission sensors with a 1-50 kHz sensitivity are cemented in two dedicated boreholes B8 and B9 drilled about 3 m away from the injection interval in BFSB2. Acoustic sensors capture high frequency rupture events in the injection near field. Acoustic sensors are recording at 200 kHz on a dedicated system provided by GMuG (Gesellschaft für Materialprüfung und Geophysik: http://www.gmugmbh.de).

RESULTS

Injection Protocol

The first FS-B fault stimulation experiment took place on November 21st, 2020 and consisted of 6 injections at constant flowrates of 2 l/min (injection 1), 6 l/min (injection 2), 9.8 l/min (injection 3), 9.94 l/min (injection 4), 9.55 l/min (injection 5) and 10 l/min (injection 6, Fig. 3a). The duration of the first 5 injections was 10 minutes each and the 6th was 20 minutes. The injection interval was shut-in between injection periods. The total time elapsed from the start of injection 1 and completion of injection 6 was 8 hours and 10 minutes. The fault hydraulically opened at injection pressures between 5 and 6 MPa. After a total injected volume of 80 liters (after cycle 2), a hydraulic connection occurred across the 1.5 m thick fault zone crosscut by the injection borehole BFSB2 (this was detected in injection borehole BFSB2 below the sealed injection interval, Fig. 1a). After a cumulative injected volume of 178 liters (during cycle 3), another hydraulic connection occurred with boreholes set in gallery 2008 (Boreholes BFSB1, BFS1, BFS2 and BFS3 in Fig. 1a), intersecting the fault 15 – 18 m away along strike from the injection point. No clear hydraulic connection was observed in boreholes intersecting the fault in the CSD borehole (Fig. 1a), which is 8-10 m up-dip and 15-20 m along strike from the injection point. These observations show an apparent heterogeneity in the fault leakage that preferentially initiated parallel to the fault strike where outflow from the boreholes BFSB2 lower part, BFS1 and 2 was measured to about 26% of the injected flowrate. The outflow rate was quasi steady state and stopped several minutes after the injection stopped.

Fault Hydromechanical Response

Instantaneous fast displacements correlated with injection pressure increase at injection borehole BFSB2 corresponding to a dilatant shear activation of the fault zone (Fig. 3b-d). During the shut-in periods and after cycle 2, slow decays in displacements correspond to apparent over shearing and over closing of the fault. The over shearing and closing are qualified as apparent because they are calculated from the projection of the east-North-Vertical borehole displacements on one given fault plane identified as a principal shear surface between the two anchoring zones of the SIMFIP probe. The fact that over-displacement occurs must mean that other planes within the injection interval or even outside of it may be activated when water is leaking in the fault zone during shut-in (and not only along the principal shear surface). Indeed, such propagation of strains to the entire fault zone thickness was observed on the DSS and DAS optical fibers.

Figure 3 also shows significant differences between the fault hydromechanical responses of the non-hydraulically connected point (BCSD7) and the hydraulically connected point (BFSB1). During injection cycle 3, pressure in BFSB1 suddenly increased to about 2 MPa when the hydraulic connection was established with the injector BFSB2 (Fig. 3b). BCSD7 shows slight decreases in pressure of 0.3 10^3Pa starting at injection cycle 2 (Fig. 3b, green pressure scale on the right Y-axis). The largest displacements were measured at the injector and at BFSB1, with a fault normal opening of 130 to 133 microns and tangential displacement of 111 to 77 microns at BFSB2 and BFSB1, respectively (Fig. 3c-d). In comparison, BCSD7 displayed very small normal and tangential displacements of 0.22 and 0.43 microns, respectively (Fig. 3c-d). At the end of the stimulation cycles, all points displayed an irreversible shear and normal displacement component. In addition, an irreversible pressure drop is observed at BCSD7 (Fig. 3b).

At BFSB1, normal and tangential displacements initiated before the hydraulic connection with

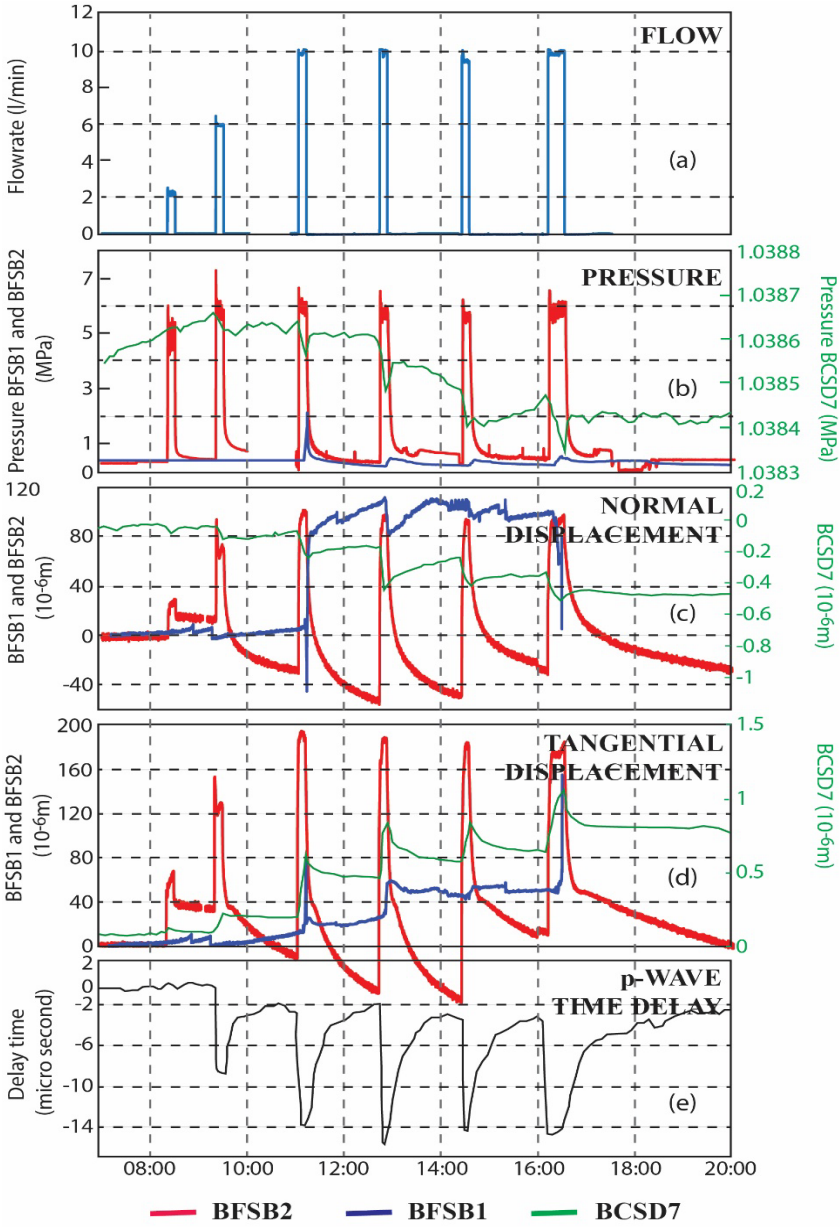

Figure 3. Time variation of (a) Injection flowrate, (b) Pore pressure, (c) Displacement normal to the fault plane, (d) Displacement tangential to the fault plane and (e) P-wave time delay measured along a linear ray path perpendicular to the injection point. Measurements at injection (BFSB2), and at monitoring points BCSD7 and BFSB1 are colored in red, green, and dark blue, respectively.

BFSB2. Normal and tangential displacement variations were also measured at BCSD7 beginning with cycle 1. Significant, but reversible, p-wave arrival time delay variations were recorded by the CASSM during the injection cycles (Fig. 3e). These changes correspond to the reversible displacements observed at injector and at BFSB1. Nevertheless, no p-wave arrival time delays were observed during cycle 1, which may be due to the stimulated volume after cycle 1 being too small to be detected given the CASSM resolution. After, the stimulation, there is a residual time delay value that can be related to the irreversible fault displacements.

Low-frequency DAS and DSS optical fiber measurements along all boreholes also showed a clear spatial-temporal progression of the strain recorded because of the injection (Fig. 4). During cycle 1, positive strain (extension possibly indicating "fracture opening") was limited to the point of injection along borehole BFS-B2. Strain magnitude was also small, with values in the order of 10-20 micro-strain. In cycle 3, when hydraulic connection was established with borehole BFS-B1, positive strain in the order of 30-40 micro-strain was recorded within the Main Fault along borehole BFS-B1, as expected. However, the interpolated image also reveals that positive strain is not confined to the immediate area surrounding boreholes BFS-B2 and BFS-B1, but some smaller magnitude deformation was recorded up-dip from the injection and hydraulic connection points. This deformation "patch" is constrained by strain recorded along borehole BFS-B9, which also intersects with the Main Fault (Fig. 2c for location of BFS-B9). For cycles 3 and 6, the spatial pattern of strain is similar, with strain magnitudes becoming larger for both the injection and the hydraulic connection points during cycle 6. No significant strain is detected in any other regions of the fault zone.

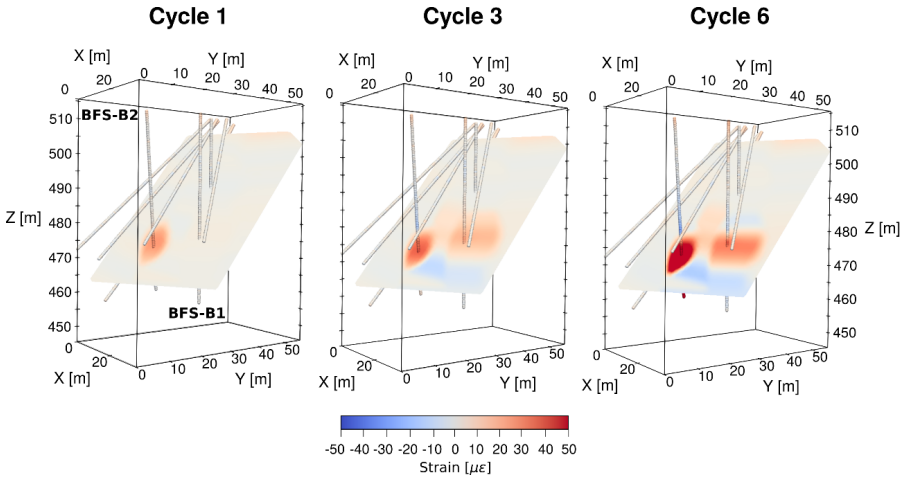

Figure 4. Low frequency DAS fiber strain signal evolution from injection cycles 1 to 6.

First, low-frequency DAS measurements along all boreholes were combined in a 3D interpolation scheme. An "inverse distance weighting interpolation" approach has been used, in which each unknown point is calculated based on a weighted average of the known points, and the weights are proportional to the inverse of the distance between the data point and the prediction location. Figure 4 shows a slice through the 3D interpolated volume that is parallel to the Main Fault average orientation.

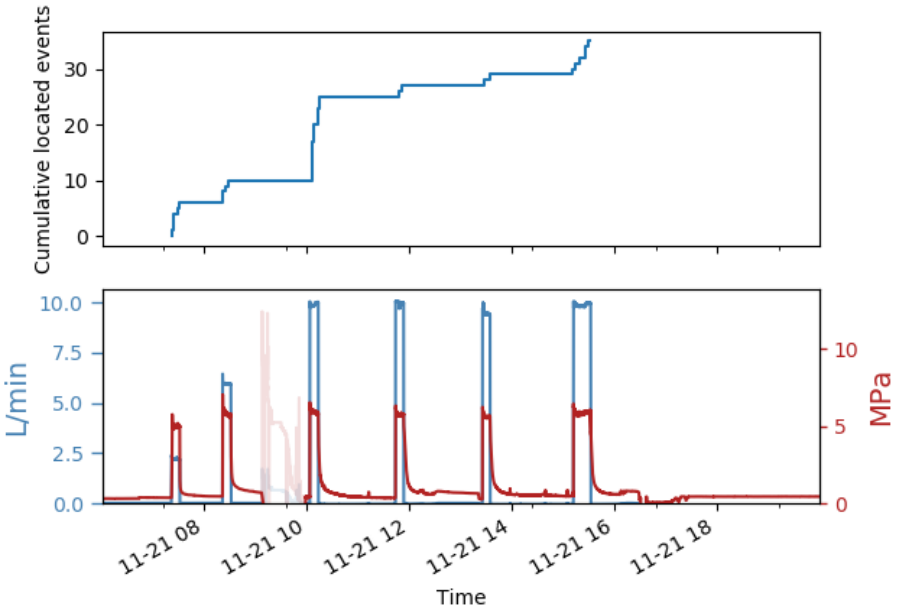

Figure 5. Cumulated number of located seismic events (upper graph) compared to injection cycles (lower graph where injection pressure is red and injection flowrate is blue).

Induced Seismicity

Passive seismic data were first processed using standard observational techniques to identify impulsive signals that were cleaned of noise sources and subsequently sorted into groups of known and unknown sources. Second, two more advanced noise filtering methods–the matched filtering and SVD filtering methods–were applied to further reduce the noise level. Seismicity was sparse during the experiment, with 36 events detected, and only 6 events qualified as major events because they were detected on all sensors. Three of these major events occurred during injection cycle 1, at the onset of fault activation, while the three remaining events occurred during the last injection cycles 5 and 6. Figure 5 shows that when considering the complete catalog of 36 events, seismicity occurred during each of the injection cycles, and particularly during cycle 3.

Continuous Active-Source Seismic Monitoring of Brine Injections

To compute a three-dimensional time-lapse travel-time tomography (fig. 6), four main components were used – a three-dimensional background absolute-velocity model, accurate raypath geometry, the delay-time data, and a spatially variable regularization term. For the three-dimensional background velocity model, first arrivals were hand-picked from the background dataset to create a homogeneous p-wave velocity model. The background dataset was gathered on November 21, 2020, right before the first injection cycle. Then an eikonal code was integrated to calculate accurate ray path geometries from the p-wave velocity models. These results were used to update the three-dimensional background

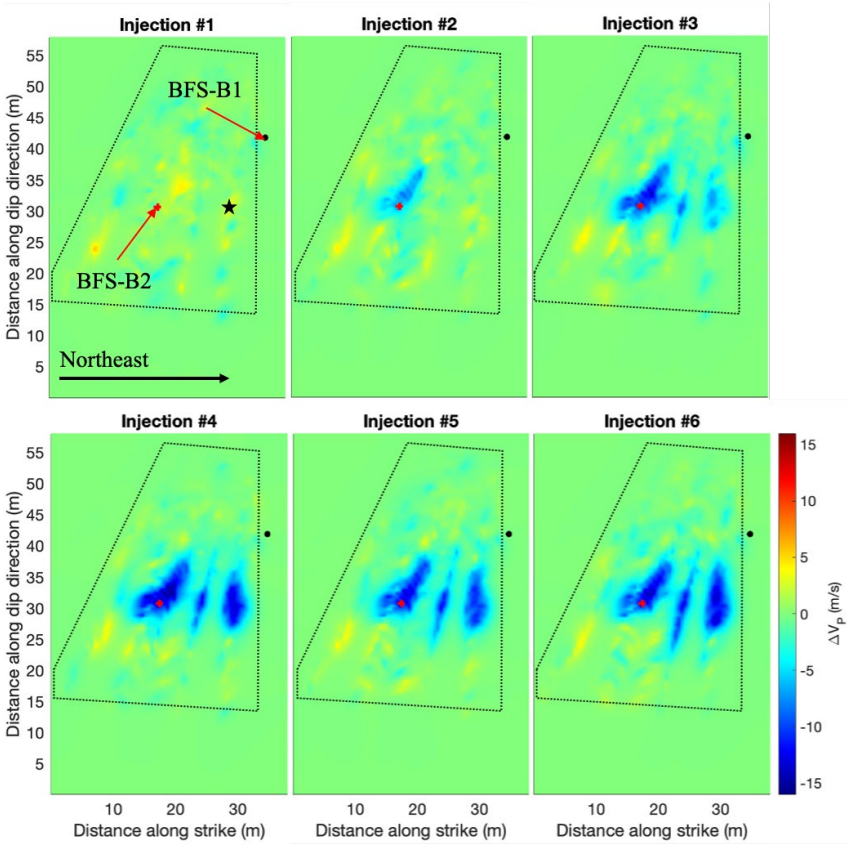

Figure 6. p-wave velocity tomography images calculated after each injection cycle. The trapezoidal shape shows the limits of the measurement's validity.

p-wave velocity model. Multiple iterations were computed until an appropriate fit was reached. The delay-time data was used as the primary measurable for the time-lapse tomography. There are 1056 delay-time curves, one for every source-receiver pair in this system. Some delay-time curves were noisy due to the low signal-to-noise ratio of the first arrival, likely a result of large source-receiver pair offsets. We removed these noisy delay-time curves which would otherwise dominate the tomography results. The last component used in the tomography analysis was the spatially variable regularization term. Since the ray paths between the sources and receivers are primarily perpendicular to the fault there is little constraint in that direction. We also assume that during the injections, the primary change in p-wave velocity is going to occur in the fault zone. This regularization term allows us to constrain the velocity changes to within that fault zone itself.

Six tomograms are shown in figure 6 corresponding to the shut-in period immediately following each injection cycle. Dark blue colors in the tomograms are negative changes in velocity, which we interpret as showing the part of the fault that has been reactivated. After the first injection, there are no major anomalies, suggesting that the fault reactivation is spatially limited at this time. For the second injection tomogram, there is a small blue patch that starts to develop around the injection well.

This patch is not symmetric around the borehole, suggesting that there is a preferred direction of fault reactivation. A large change in the tomogram occurs after injection three, when the injection rate increased to 10 l/min. The third injection tomogram shows a larger patch near the injection well and two smaller patches north-easterly along the fault for a total of three patches. These three 'streaks' were also observed in the checkerboard tests, suggesting this behavior is CASSM acquisition geometry related and not geologic in nature. Therefore, we interpret these three patches as a single patch that is moving north-easterly along the fault zone. Tomograms for injection cycles 4 through 6 appear to show that the outer edges of the patch have not grown, but rather show that the patch itself has intensified with greater negative ΔV_P values. Hydraulic connection was made with BFS-B1 after the third injection cycle, suggesting that the fault reactivated there as well. Unfortunately, BFS-B1 is located just outside the imaging area (dot shown in figure 6). Therefore, we interpret the reactivated patch to extend at least to BFS-B1. Overall, the reactivated patch is not symmetric around the injection well (BFS-B2), which again suggests that there is a preferred direction of fault reactivation and therefore will have implications on the direction of leakage along the fault.

INTERPRETATION-DISCUSSION

Instruments Complementarity

The amplitude of the DAS and DSS signals recorded along all boreholes with respect to the location of the injection point reveals that the largest signals were recorded along boreholes intersecting the fault, but the signals were visible elsewhere. Although DSS measurement sensitivity is lower than that of DAS, spatial resolution for DSS is better, and it helps localize the location of maximum deformation along each of the boreholes, including the point of hydraulic connection in BFS-B1. A comparison of the DAS and DSS signals reveals the challenges associated with recovering true strain amplitude from DAS due to the differences in gauge length, which smears the signal in the space domain given the 10 m moving window. At the injection interval, the comparison between the DAS-DSS distributed strains and the SIMFIP discrete displacements measurements shows positive strain associated with fault shear and opening when pressure increases at each injection cycle, as well as some degree of permanent strain and displacement. The changes observed could indicate either permanent damage to the fault or a permanent fault offset (or both). Outside the pressurized flow path, (above and below the injection interval in BFSB2), along the fault at BCSD7 (SIMFIP measurement interval) and outside the fault zone in BFSB1 (DORSA-1 measurement interval), DAS and DSS show negative strain, with a small degree of permanent negative strain. This corresponds to reverse shear and fault closing at the BCSD7 SIMFIP interval and to strike slip shear at the BFSB1 DORSA-1 interval. This is interpreted as compression of the rock surrounding the Main Fault stimulated zone.

The induced seismicity is clearly associated with the periods of fast fault shearing during pressure increase. The "instantaneous" variations in p-waves delay time with injection pressure correlated with the mechanical opening and closing of compliant fractures within the fault zone. A decrease in P-wave velocity (increase in delay time) as a function of injection pressure is consistent with laboratory data showing similar reductions as a function of decreased normal stress [18]. Likewise, similar signatures are observed during hydraulic fracturing operations, albeit at lower accuracies in the context of time-lapse VSP studies [19]. During a similar shale fault activation experiment, Rivet *et al.* [20] produced P- and S-wave velocity images highlighting perturbations in and around a minor fault using a prototype active seismic source system in the ISRN Tournemire Underground Research Laboratory (France). Like in the Mont Terri experiment, seismic velocity perturbations dramatically increased (1 to 5%) while permeability was enhanced by fault rupture. In both experiments, these observations are consistent with an increase of fluid flow associated with a dilatant shearing of the fault. Finally, the apparent long-term change in travel times observed in the Mont Terri experiment matches the irreversible fault deformations recorded on the strain monitoring array. This long-term

change in travel times might relate to fault zone shear-induced damage or to delayed leakage of the injected fluid volume in this low permeability clay fault environment.

Time Evolution of Fault Deformation and Leakage

The fault hydraulically opened in the nearfield of the pressure source when the injection pressure induced a drop of the effective normal stress on the fault to almost zero. This is consistent with previous theoretical studies on clay-rich faults that demonstrated that the local fluid pressure must get close to the total fault normal stress before fault slip is triggered [21]. One reason for this behavior is that the faults studied in the shale experiments were not "favorably enough" oriented towards the principal stress state, "requiring" more fluid pressure to reactivate as described in previous theoretical works [22-25]. Perhaps more importantly, models show that this effect is amplified by the very low initial permeability of the shale fault and by the low rigidity of the rock surrounding the fault, which together create conditions for a mixed opening and shearing rupture mode where fluids force their way through ruptured patches within the fault [4,26-29]. As a result, the fault experiences a relatively large normal displacement measured at the injection point compared to the shear displacement.

The spatiotemporal evolution of the p-wave velocity is consistent with the observed hydraulic connection between the injector BFSB2 and the BFSB1 zone that occurred at injection cycle 3. It is reasonable to consider that the low p-wave region corresponds to the high fluid pressure leakage region that connected the two boreholes during injection cycle 3. Dilatant shear was observed at BFSB1 during injection cycle 2 before the hydraulic connection formed, and no p-wave velocity anomaly was observed. Indeed, during cycle 2, the low p-wave velocity region boundary is about 10 meters away from BFSB1. Thus, a dilatant shear front preceded the high-pressure leakage front by several meters along the fault. When the high-pressure leakage front reaches the BFSB1 point, a large fault normal opening component adds to the dilatant shear fault movements. This is consistent with theoretical models that show that failure in the pressurized fault patch increases the shear stress beyond the pressure front where the shear strength reduces as a function of the slip characteristics (magnitude and velocity), according to Cappa *et al.* [27,30]. This mechanism is intimately linked to the reduction in fault strength being more pronounced in the pressurized zone than in the immediate surrounding region.

Seismicity was associated with periods of large slip rate when pressure was increased quickly at the onset of each injection cycle. The largest number of seismic events was also associated with the main period of leakage path growth from cycle 2 to cycle 3. After cycle 3, there is little spatial growth of the leakage path (from cycles 3 to 6) and relatively less seismicity. During cycles 4 and 5, it is possible that leakage out of BFSB1 into the gallery may have "controlled" the fault pore pressure and "limited" rupture growth. The largest earthquakes (detected on all sensors) occurred during cycle 1 at the onset of fault rupture, which was characterized by a significant irreversible shear displacement at BFSB2 after cycle 1. Large seismic events also occurred during cycle 6 when sufficient water volume had been injected into the fault to re-initiate rupture growth. Nevertheless, most of the measured seismic events were small (not detected on all the sensors) at a time when the local fault shear displacements are of the order of hundreds of micrometers in the pressurized zone. Thus, the observed seismicity cannot explain the observed fault shear, which highlights a significant aseismic component of fault rupture. This is consistent with other fault reactivation experiments where the importance of injection-induced aseismic deformation has been estimated to represent about 80-to-100% of the energy dissipated at rupture [26,31]. Yet, the reasons for aseismic fault reactivation by injection of fluid remain complex because of multiple controlling factors [4].

Influence of Fault Strength and Stress Heterogeneity on Rupture Directionality

The p-wave velocity images show that the growth of the leakage pathway displays a preferential North-Eastward direction. This highlights a significant heterogeneity that may reflect complex rupture mechanisms involving the heterogeneous spatial distribution of stress and strength along the fault. For example, previous numerical studies showed an almost symmetrical rupture patch developing on a single plane fault with homogeneous mechanical properties and imbedded into a homogeneous stress field (with a stress gradient induced by gravity). In the context of the Mont Terri Main Fault, the principal shear surface (corresponding to the fault top limit) displays spatial dip direction and dip angle variations, with the BFSB1 zone being better oriented for shear failure than the BCSD7 zone. In addition, the 2015 fault reactivation experiment was executed in the BFSB1 zone. Damage by that experiment may have resulted in lower strength in the BFSB1 zone compared to the BCSD7 zones or to changes caused by the injection. Stress and/or strength gradients between the injection point and the BFSB1 zone may thus have induced the rupture on the main fault plane to propagate in the direction favorable to meeting failure (away from areas of low stress or high fault strength). Finally, the fault zone is three times thicker in the BFSB1 zone as compared to the injection zone. This means that the fault is more compliant and contains a larger density and variety of fracture orientation in the BFSB1 zone. The BFSB1 zone may thus be more elastic and/or more permeable which may either favor the propagation of dynamic rupture and/or fluid leakage towards that zone.

CONCLUSION AND PERSPECTIVES

The primary objective of the FS-B experiment was achieved – to create a significant fluid leak into an initially low permeability fault zone. The data measured for pore pressure, displacement-strain, induced earthquakes and P-wave velocity images were highly consistent. The leak appears tightly coupled to variations in the orientation of the fault rupture surface and to stress gradient. Borehole displacements and deformations were observed at many 20 different locations. Displacement signals a factor-of-ten smaller were observed in the non-hydraulically connected zones compared to the hydraulically connected ones. We correlate the “instantaneous” decrease in P-wave velocity (increase in delay time) with injection pressure as related to mechanical opening and shearing of fractures within the fault zone. Outside the high-pressure zone, fault displacements may be too small to generate a detectable p-wave velocity variation. We observe fault shear preceding the pressure increase corresponding to the arrival of injection water, showing that fault hydromechanical activation generates two successive fronts – a rupture front preceding a fluid pressure front. The rupture front is associated with compressive strain which favors dilatant shear on pre-existing fault structures. The occurrence of induced seismicity correlated with the periods of fast pore pressure increase that produce the fastest displacement and strain rates. The velocity images show that the growth of the leakage pathway displays a preferential North-eastward direction. Long-term apparent irreversible change in the P-wave travel times matches either the irreversible fault shear displacement that caused fault zone shear-induced damage (fault offset), or the delayed leakage of the injected fluid volume in this low permeability clay fault environment that caused delayed mechanical closing of the pressurized patch.

The preliminary results shown here highlight that a significant leakage pathway can occur in a shale fault affecting an analogue cap rock. Mechanisms involved appear highly complex, resulting in a fast-developing, asymmetrical high permeability leakage flow path within the fault zone. Analyses that are more detailed will allow exploring the sensitivity of these mechanisms to the distribution of hydro-mechanical properties and stress within the fault zone. They will be compared to other case studies of leakage development in caprocks. The post activation evolution of the fault is the next challenge. The aim now is to characterize how the observed P-wave travel time variations will evolve over longer time scales of months to years. We will correlate with pore pressure and strain to better understand the mechanisms of clay fault zones initial low permeability recovery (self-sealing). This work is part

of the continuing program at Mont Terri including injection of CO_2 charged brine and further instrumentation.

ACKNOWLEDGEMENTS

This work was part of jointly funded project by Mont Terri, Shell, Total, Chevron, DoE, ETH Zurich, ENSI, swisstopo, BGR, JAEA, IRSn and phase 4 of the CO_2 Capture Project (CCP).

REFERENCES

1. Verdon, J.P., Stork, A.L. (2016). Carbon capture and storage, geomechanics and induced seismic activity. *Journal of Rock Mechanics and Geotechnical Engineering* 8, 928-935.
2. Zoback, M.D., Gorelick, S.M. Earthquake triggering and large-scale geologic storage of carbon dioxide. PNAS, June 26, 2012; vol. 109; no. 26; 10164–10168, 2012; https://doi.org/10.1073/pnas.1202473109.
3. Vilarrasa, V., Carrera, J. Geologic carbon storage is unlikely to trigger large earthquakes and reactivate faults through which CO_2 could leak, P. Natl. Acad. Sci. USA, 112, 5938–5943. 2015; https://doi.org/10.1073/pnas.1413284112, 2015.
4. Guglielmi,y. C., Nussbaum, F., Cappa, L. De Barros, J., Rutqvist, J., Birkholzer. Field-scale fault reactivation experiments by fluid injection highlight aseismic leakage in caprock analogs: Implications for CO_2 sequestration. International Journal of Greenhouse Gas Control 111, 103471. 2021.
5. Guglielmi, Y., Nussbaum, C., Jeanne, P., Rutqvist, J., Cappa, F., Birkholzer, J. Complexity of fault rupture and fluid leakage in shale: Insights from a controlled fault activation experiment. *Journal of Geophysical Research: Solid Earth*, **125**, e2019JB017781. 2020a; https://doi.org/ 10.1029/2019JB017781.
6. Guglielmi Y., Cappa F., Avouac J.P., Henry P., Elsworth D. Seismicity triggered by fluid-injection-induced aseismic slip. *Science* **348**, 1224. 2015; DOI: 10.1126/science.aab0476.
7. Jeanne, P., Guglielmi, Y., Rutqvist, J., Nussbaum, C. and J. Birkholzer. Field characterization of elastic properties across a fault zone reactivated by fluid injection. *J. Geophys. Res. Solid Earth*, **122**, 6583–6598. 2017; doi: 10.1002/2017JB014384.
8. Jeanne, P., Guglielmi, Y., Rutqvist, J., Nussbaum, C., Birkholzer, J. Permeability variations associated with fault reactivation in a claystone formation investigated by field experiments and numerical simulations. *Journal of Geophysical Research: Solid Earth*, **123**, 1694–1710. 2018; https://doi.org/10.1002/2017JB015149.
9. Zappone, A., Rinaldi, A.P., Grab, M., Wenning, Q.C., Roques, C., Madonna, C., Obermann, A.C. , Bernasconi, S.M., Brennwald, M.S., Kipfer, R., Soom, F., Cook, P., Guglielmi, Y., Nussbaum, C., Giardini, D., Mazzotti, M. and Stefan Wiemer. Fault sealing and caprock integrity for CO_2 storage: an in situ injection experiment. Solid Earth, 12, 319–343. 2021; https://doi.org/10.5194/se-12-319-202.
10. Jaeggi, D., Laurich, B., Nussbaum, C., Schuster, K., Connolly, P. Tectonic structure of the ‘‘Main Fault’’ in the Opalinus Clay, Mont Terri rock laboratory (Switzerland). Swiss J Geosci. 2017; DOI 10.1007/s00015-016-0243-2.
11. Nussbaum, C., Bossart, P., Amann, F., Aubourg, C. Analysis of tectonic structures and excavation induced fractures in the Opalinus Clay, Mont Terri underground rock laboratory (Switzerland). Swiss J Geosci 104. 2011. 187-210. 2011.
12. Guglielmi Y., Cappa F., Lançon H., Janowczyk, Rutqvist J., Tsang C.F. and Wang J.S.Y. ISRM Suggested Method for Step-Rate Injection Method for Fracture In-Situ Properties (SIMFIP): Using a 3-Components Borehole Deformation Sensor. Rock Mechanics and Rock Engineering. 2013 ; DOI 10.1007/s00603-013-0517-1.

13. Silver, P.G., Daley, T.M., Niu, F., Majer, E.L. Active source monitoring of crosswell seismic travel time for stress induced changes, Bulletin of Seismological Society of America, v97, n1B, p281-293. 2007.
14. Niu, F., Silver, P.G., Daley, T.M., Cheng, X., Majer, E.L. Preseismic velocity changes observed from active source monitoring at the Parkfield SAFOD drill site, Nature, 454, 204-208. 2008; DOI:10.1038/nature07111, LBNL-717E.
15. Daley, Thomas M., Jonathan B. Ajo-Franklin, Christine Doughty. Constraining the reservoir model of an injected CO_2 plume with crosswell CASSM at the Frio-II brine pilot, International Journal of Greenhouse Gas Control, 5, pp. 1022-1030. 2011; DOI information: 10.1016/j.ijggc.2011.03.002.
16. Marchesini, P., J.B. Ajo-Franklin, T.M. Daley. In-Situ Measurement Of Velocity-Stress Sensitivity Using Crosswell Continuous Active-Source Seismic Monitoring (CASSM), Geophysics 82 (5), 1-27. 2017.
17. Ajo-Franklin, J. B., Thomas Daley, Belinda Butler-Veytia, John Peterson, Yuxin Wu, Bob Kelly, and Susan Hubbard. Multi-level continuous active source seismic monitoring (ML-CASSM): Mapping shallow hydrofracture evolution at a TCE contaminated site, SEG Expanded Abstracts 30, 727. 2011; DOI:10.1190/1.3627980.
18. Pyrak-Nolte, L. J., Myer, L. R. and N.G.W. Cook. Journal of Geophysical Research, volume: 95 issue: (B6), pages: 8617-8638. 1990.
19. Binder. G., Titov, A., Tamayo, D., Simmons, J., Tura, A., Byerley, G., Monk, G. Time delays from stress-induced velocity changes around fractures in a time-lapse DAS VSP. 88th Annual International Meeting, SEG, Expanded Abstracts, 5328–5332, doi: 10.1190/segam. 2018; 2998082.1.
20. Rivet D., De Barros L., Guglielmi Y., Cappa F., Castilla R. and Henry P. Seismicity velocity changes associated with aseismic deformations of a fault stimulated by fluid ibnjection. Geophys. Res. Lett., 43, 9563-9572. 2016.
21. Viesca, R. C., and J. R. Rice. Nucleation of slip-weakening rupture instability in landslides by localized increase of pore pressure, J. Geophys. Res., 117, B03104. 2012; doi:10.1029/2011JB008866.
22. Axen GJ. Pore pressure, stress increase, and fault weakening in low-angle normal faulting. J. Geophys. Res. 97, 8979–8991. 1992; doi: 10.1029/92JB00517, 35.
23. Rice, JR. Fault stress states, pore pressure distributions, and the weakness of the San Andreas fault. In Fault mechanics and transport properties in rocks (eds B Evans, T-F Wong), pp. 475–503. London, UK: Academic Press. 144, 39-58. 1992.
24. Faulkner, D.R., Rutter, EH. Can the maintenance of overpressured fluids in large strike-slip fault zones explain their apparent weakness? Geology, 29, 503–506. 2001; doi:10.1130/ 0091-7613(2001)029<0503:CTMOOF>2.0.CO2.
25. Garagash, D.I., Germanovich, L.N. Nucleation and arrest of dynamic slip on a pressurized fault, J. Geophys. Res., 117, B10310. 2012; doi:10.1029/2012JB009209.
26. Guglielmi, Y., Elsworth, D., Cappa, F., Henry, P., Gout, C., Dick, P. and J. Durand. In situ observations on the coupling between hydraulic diffusivity and displacements during fault reactivation in shales, J. Geophys. Res. Solid Earth, 120, 7729–7748. 2015b; doi:10.1002/ 2015JB012158.
27. Cappa, F., Guglielmi, Y., Nussbaum, C., Birkholzer, J. On the Relationship between Fault Permeability Increases, Induced Stress Perturbation, and the Growth of Aseismic Slip During Fluid Injection. Geophysical research letters, Volume45, Issue20, 28 October 2018, Pages 11,012-11,020.
28. Rutqvist, J., Graupner, B., Guglielmi, Y., Kim, T., Maßmannd, J., Son, T., N., Park, J.-W., Shiu, W., Urpi, L., Yoon, J.S., Ziefle, G., Birkholzer J. An international model comparison study of controlled fault activation experiments in argillaceous claystone at the Mont Terri

Laboratory. International Journal of Rock Mechanics and Mining Sciences, Volume 136, December 2020, 104505. 2020.
29. Park, J.W., Guglielmi, Y., Graupner, B., Rutqvist, J., Taehyum, K., Park, E.-S., Changsoo, L. Modeling of fluid injection-induced fault reactivation using coupled fluid flow and mechanical interface model. International Journal of Rock Mechanics and Mining Sciences. 132. 104373. 10.1016/j.ijrmms.2020.104373. 2020.
30. Cappa, F., Scuderi, M.M., Collettini, C., Guglielmi, Y., Avouac, J.P. Stabilization of fault slip by fluid injection in the laboratory and in situ. Science Advances, 13 Mar. 2019, EAAU4065.
31. De Barros, L., Cappa, F., Guglielmi, Y., Duboeuf L., Grasso, J.L. Energy of injection-induced seismicity predicted from in-situ experiments. Nature, Scientific Reports volume 9, Article number: 4999. 2019.

Carbon Dioxide Capture for Storage in Deep Geological Formations, Volume 5
Karl F. Gerdes (Editor)
© 2022 BP. All rights reserved.

Chapter 32

CO_2 STORAGE MONITORING AT AQUISTORE USING 3-AXIS BOREHOLE GRAVITY

Francis Neill, Zhijun Du, Ashwin Seshia
Silicon Microgravity Limited, Cambridge, CB25 9GL, United Kingdom

ABSTRACT: To assess the potential of borehole gravity response as a CO_2 storage monitoring tool, Silicon Microgravity Limited (SMG) carried out modelling of the in-well gravity response to changes in CO_2 saturation within the reservoir. Surveys were planned to use a prototype wireline-deployed gravimeter tool at the Canadian Petroleum Technology Research Center's Aquistore CO_2 storage project [1]. Following the initial baseline survey, further modelling was planned to be done and a second gravity survey performed approximately six months after the baseline survey to deliver a time-lapse record of the changes in gravity.

Gravity is a direct measurement of density as it changes through substitution of water by CO_2. The gravity measurement detects changes in mass in the subsurface, such that time-lapse wireline-based surveys will give a picture of fluid movements at 100's of meters from the wellbore. By measuring gravity in all three axes, it is possible to determine directional information about the spatial movement of fluid, even when data are acquired from just a single borehole.

SMG's 3-axis borehole gravity technology enables the recording of gravitational acceleration at very high sensitivity (targeted at ~5 μGal) using an innovation in resonant Microelectromechanical system (MEMS) vibrating beam technology. This approach aims to produce small, cheap, but highly stable and highly sensitive field and borehole-deployable relative gravimeters. The vibrating beam gravimeter consists of a suspended mass connected to a vibrating beam, such that the inertial force experienced by the mass in a gravitational field is communicated as an axial load on the beam.

Initial forward modelling of the reservoir demonstrated that expected changes in CO_2 saturations would deliver changes in gravity detectable by a tool with a sensitivity of 10 μGal.

In September 2019, SMG's prototype tool was deployed in well PTRC OBS 5-6-2-8 in Estevan, Saskatchewan, Canada. Three deployments were made into the well and on each occasion technical problems resulted in a tool measurement response significantly inferior to that required for baselining of the gravity response. Components of the tool string were changed between runs, but the temperature control circuits required to keep the sensor at a constant temperature did not function as expected. As a result, the trial was abandoned without acquiring viable gravity data.

After the equipment was returned to the UK for repair it was planned to revisit the CCP4 site in Q2 2020 for further tests. However, the global COVID-19 pandemic prevented this and by November 2020 the wireline deployed gravity project was postponed by SMG due to technical and funding issues and as a result the trials supported by CCP were terminated.

KEYWORDS: borehole gravity, CO_2 storage, monitoring

INTRODUCTION

Monitoring CO_2 storage at the Aquistore CO_2 storage project includes both surface and subsurface monitoring, a unique permanently installed sparse seismic array, groundwater and soil gas sampling

and 3D seismic. However, gravity measurements have a unique advantage among other geophysical methods because changes in mass density are detected directly and are uniquely related to reservoir fluid changes. The desire to use gravity measurement to detect reservoir fluid changes has resulted in development of ever more sensitive gravimeters, and the MEMS-based three-axis sensor is the culmination of many years of research [2].

The results of a feasibility study aimed at monitoring CO_2 at Aquistore show that the gravity variation due to density changes is likely to be within the sensitivity of the sensor during a 5-year period of CO_2 injection from April 2015 to January 2020. Borehole gravity logging of the displacement and substitution of the aquifer water at the storage site over time is referred to as a 4D gravity survey. The cost effectiveness of a 4D wireline gravity survey compared to a 4D seismic survey conducted recently is highly attractive in smaller carbon storage programs. Where the project size or complexity allow both to be run, the complementary nature of the measurements has been noted by several operators.

In this chapter, survey feasibility modelling and a workflow are presented that together provide important information for planning and acquiring a successful gravity survey, as well as the best time interval (given the planned injection rate), and which well location is most suitable to use. The workflow for conducting borehole gravity simulations from time-lapse reservoir models starts with a 3D model of reservoir porosity, saturation, and fluid constituent density, which is used to generate a time-lapse density model from the reservoir simulation data. Vector gravity anomaly responses (g_z, g_x, and g_y) along the wellbore in a variety of well locations are then predicted through forward modelling. The density changes due to fluid substitution are measured by the vertical, g_z, gravity anomaly with respect to the reference gravity field. The fluid front progress through the field is assessed through the horizontal gravity anomalies (g_x, and g_y). Modelling shows plume growth is detectable even over a short time interval of 1 year. With MEMS technology lifetime monitoring is possible.

We conclude that gravity technology has the potential to provide a solution for long term monitoring of CO_2 plume growth within the likely numerous wells required for the CO_2 storage requirements resulting from the IPCC pathway scenarios to 1.5°C.

BOREHOLE GRAVITY METHOD AND ITS APPLICATION TO CO_2 MONITORING

The advantages of measuring gravity have been well established in the literature. These measurements can be very effective for directly imaging mass distributions at depth in the subsurface and at large distances from well bores. However, the challenge faced by gravity measurements is the inherently minute signal observable at a distance, such as from the surface above a deep reservoir, due to the small changes in mass density. For this reason, a borehole gravimeter is desirable, so the measurement sensor is closer to the reservoir mass. However, the measurement of gravity in a borehole has been somewhat limited by the form-factor (i.e., sensor size), sensitivity, stability, and noise floor. Emerging gravity sensor technology has resulted in a MEMS accelerometer with a resolution of a billionth of the Earth's gravity (1 nano g = 0.981 μGal). The scale of the silicon sensor device provides significant size, weight, and power (SWaP) advantages, which enable the sensor to be packaged as a 3-axis arrangement in a standard 2-1/8" (54 mm) logging tool.

Borehole gravity measures the gravitational field produced by the mass of the formation at locations in the borehole. The response is a volumetric effect sensing the mass around the gravity sensor. Therefore, the measured gravity data detect the density change as a function of spatial position, which is composed of the background density, such as a sequence of layers of the sedimentary rocks, and the 3D perturbations, such as a reservoir and its interval density variations, superimposed on the background. The premise behind the measurements is that the static element of the rock matrix is assumed not to change over time (i.e., changes in porosity due to changes in pressure and/or

geochemical reactions with CO_2 acidified water are assumed to be negligible) and dynamic flow processes cause alteration of the saturation of fluids within the rock matrix, resulting in density changes which create a detectable gravity anomaly.

The formation density change, Δρ, due to displacing water in a formation with porosity, φ, with CO_2 is:

$$\Delta\rho = \varphi\rho_g - \rho_w\Delta S_w \quad (1)$$

where ΔS_w is the change in water saturation. The CO_2 density, ρ_g, is estimated to be between 0.7 g/cm^3 to 0.8 g/cm^3 at formation temperature and pressure conditions. The density of the formation water, ρ_w, will be that of the water displaced by the CO_2 plume at that depth.

Consider two instances in time at which we acquire gravity measurements at a particular location, where the difference between the two sets of measurements would capture the signal. Furthermore, the difference is assumed to be devoid of any gravity effect that is unrelated to the dynamic target. For the source of the gravity anomaly, all mass produces a gravity attraction that leads to the variation of the gravity field in spatial locations. In a time-lapse sense, a change in mass over time produces a change in gravity attraction that leads to variations of the gravity field over time. Given this understanding and the fact that the gravity field obeys linear superposition, the time-lapse gravity anomaly can be rewritten as [3]:

$$\Delta g_z(r^o, \Delta t) = \gamma \int_V \rho_{\Delta t}(r^s, \Delta t) \frac{z' - z}{|r^s - r^o|^3} dv \quad (2)$$

Where r^s and r^o are respectively, the source and observation positions, $\rho_{\Delta t}(r^s, \Delta t)$ is the density change over the time interval, $\Delta t = t_2 - t_1$, and $\Delta g_z(r^o, \Delta t)$ is the corresponding time-lapse gravity signal. Here we only show the vertical component (z dimension) for simplicity. One of the objectives of a time-lapse gravity survey is to image the temporal density change, $\rho_{\Delta t}(r^s, \Delta t)$, away from the measurement boreholes and infer that the density change is due to fluid saturation change.

CO_2 STORAGE MONITORING USING 3-AXIS BOREHOLE GRAVITY

The Energy & Environmental Research Center (EERC) constructed a static geologic model to assess the potential storage capacity of the Aquistore site using a combination of reservoir characterization data provided by PTRC and independently acquired information [4]. The University of Alberta subsequently updated the dynamic reservoir simulations to history-match field data, using seismic tomographic images, well data and additional reservoir properties such as pressure and temperature [5]. Both a baseline density model of April 2015 data and a porosity model are shown in Figure 1. Porosities of the reservoir sandstones range from 0.04-0.17 with mean values of 0.058 and 0.068 in the injection well for the Black Island and Deadwood sands, respectively.

To model density changes in the reservoir, we defined a baseline model based upon data from the start of CO_2 injection in April 2015. To examine the time-lapse response, reservoir properties of water saturation, CO_2 saturation and their densities were extracted from the reservoir simulation models at intervals of 9, 12, 18 and 24 months following the start of injection in April 2015. In the simplest form, the 3D bulk density distribution within a reservoir at a given time interval, ρ_b, can be defined by two fundamental contributions:

$$\rho_b\left(\underset{r}{\rightarrow}\right) = (1 - \varphi)\rho_{ma} + \varphi\left[(S_w \cdot \rho_w) + (S_g \cdot \rho_g)\right] \quad (3)$$

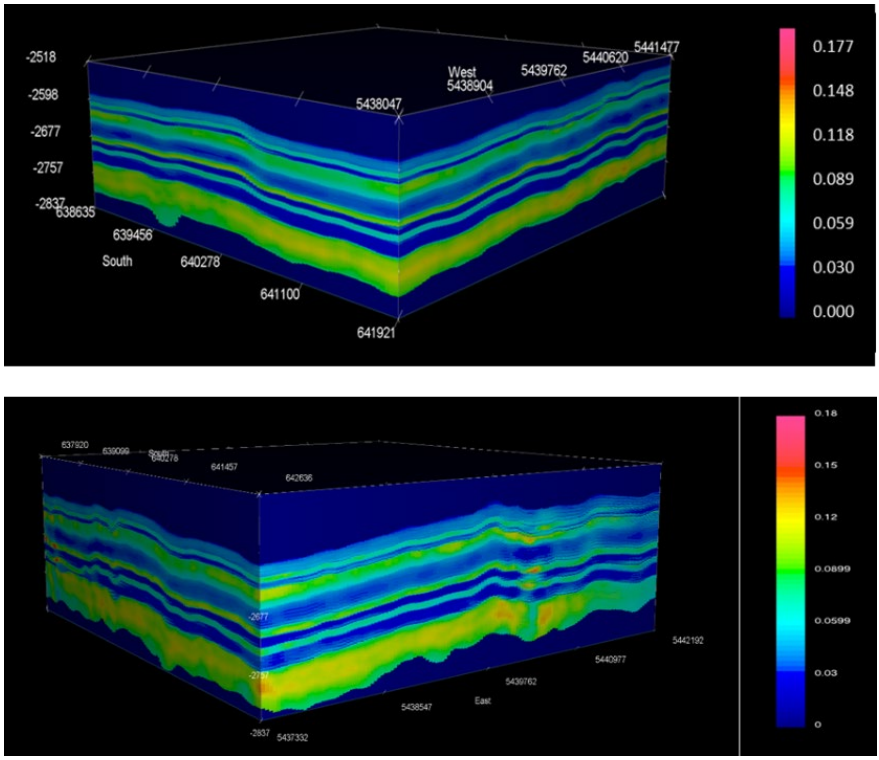

Figure 1. Top, Density model of EERC/UofA reservoir simulation in April 2015; Bottom, Porosity distribution extracted from same model.

The first term in equation 3 defines the contribution to bulk density from the rock matrix, which is assumed to be a static element within a reservoir model. The second term defines the remaining contribution from the combination of possible pore fluids (water and CO_2).

The 3D bulk density distribution within a reservoir can therefore be constructed by merging the 3D distributions of porosity (φ), matrix density (ρ_{ma}), saturations of water/gas (S_w/S_g), and the densities of the water/gas (ρ_w/ρ_g) through equation 3 at any time. The density change throughout the reservoir between two time-states can then be defined by the changes in fluid saturations and densities within the pore volumes:

$$\Delta\rho\left(\underset{r}{\rightarrow}\right) = \varphi\{[(S_w^f \cdot \rho_w^f) + (S_g^f \cdot \rho_g^f)] - [(S_w^i \cdot \rho_w^i) + (S_g^i \cdot \rho_g^i)]\} \quad (4)$$

where the first term in equation 4 represents the fluid saturation and density at a final time, f, and the second term is the state of reservoir fluids at an initial time, i. We construct time-lapse density models from the PTRC reservoir simulation models using conditions at several time intervals.

Using the 3D gravity forward modelling approach described by equation 2 [6], forward modelling was undertaken to understand the time-lapse gravity signal [3] resulting from water displacing CO_2 during 5+ years period of CO_2 injection at Aquistore.

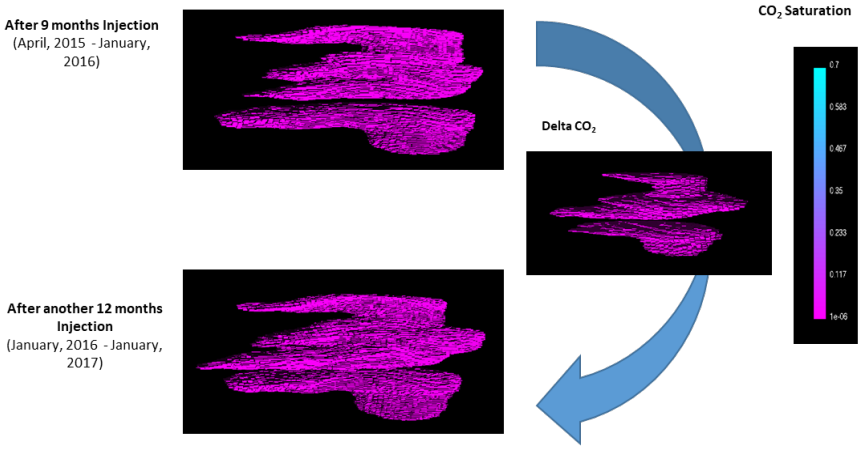

Figure 2. Reservoir fluid density change resulting from CO_2 displacing water. Two instances are shown (top) a baseline scenario (time *i*), and (bottom) after 12 months (time *f*) of CO_2 injection. Where the volume on the right is the total volume of CO_2 that displaced water (refer to text for details).

In this illustration of the workflow, the density reservoir simulation model (from previous section) was used to build two time-lapse density contrast models (Figure 2), one representing a baseline (time *i*) and the other, for example, after 12 months (time *f*) injection. The density contrast models could thus be used to evaluate the changes in the gravity field arising from reservoir dynamic flow processes when CO_2 replaces water.

Results for First 2 Years of Injection (04/2015–06/2017)

The 3-axis borehole gravity tool enables measurement of gravity responses in three orthogonal components (g_x, g_y, g_z) producing a vector gravity anomaly, where g_z measures the magnitude of the gravity change in the vertical direction while the two horizontal components (g_x and g_y) are indicative of the possible directionalities of the CO_2 plume movement.

The gravity modelling for the five time-lapse density contrast models (baseline and 9, 12, 18 and 24 months after start of injection) built in the previous section predicts that the change in the gravity signal from CO_2 displacing water around the Aquistore Observation well (150 m offset from injector) at a short time-lapse interval of 9 months (04/2015–01/2016) is less than 10 μGal (Figure 3a). In contrast, over a longer time interval of 12 months (01/2016–01/2017), the g_x (north-south) and g_z (vertical) anomalies are predicted to be more measurable, with g_z = ~20 μGal and a relatively large northward pull, g_x =18 μGal, accompanied by a smaller, g_y = -7 μGal in the easterly direction.

In Figure 3b, we show the modelling results from two additional datasets: 06/2016–06/2017 (12 months) and 04/2015–06/2016 (14 months), together with the result from the time-lapse: 01/2016–01/2017. By comparing the two 12-months results of the 01/2016–01/2017 (cyan) and 06/2016–06/2017 (red), we observe the gravity anomaly from the model of 06/2016–06/2017 is much smaller. The magnitude of the gravity anomaly is closely related to the amount of density change resulting from the CO_2 injection volume, which for the two 12-month intervals was ~34 kt and ~71 kt, respectively. So, this explains the smaller 10 μGal gravity anomaly for the case of the 06/2016–06/2017 time-lapse interval.

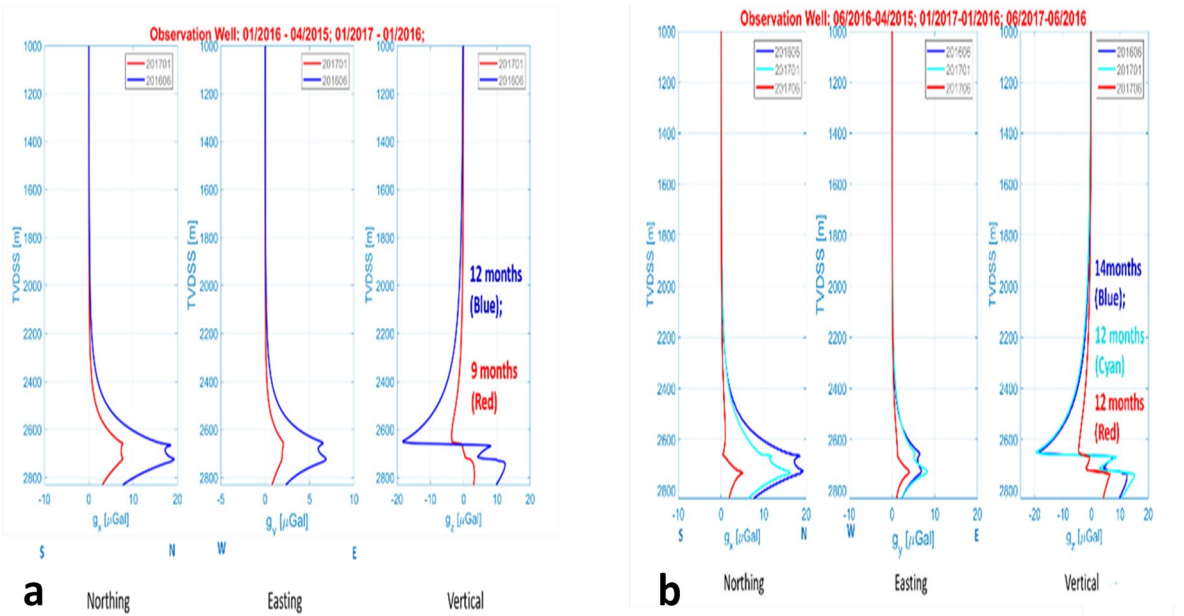

Figure 3. Time-lapse borehole vector gravity data predicted in PTRC OBS 5-6-2-8 well. (**a**) time-intervals of 9 months (01/2016-04/2015) and 12 months (01/2017-01/2016); (**b**) additionally shows 12 months (06/2017-06/2016) and 14 months (06/2016-04/2015).

In Figure 4, results of the modelling of the 19-month time-lapse model of 04/2015–01/2017 are shown. To further increase the resolution of the modelling and decrease ambiguities, two notional additional observation points were modelled at locations: ObsA1 and ObsA2, allowing more points to constrain the spread of the CO_2 plume. The modelling results from the four locations show a consistent CO_2 plume migration trend, determined by the responses of the horizontal components. Specifically, we observe the CO_2 plume migrating towards the NE direction and passing the observation well, whereas at the injection well, we observe the plume growing westward as indicated at ObsA2 [7]. The CO_2 plume is going to pass the observation point and expanding away from both injection and observation wells.

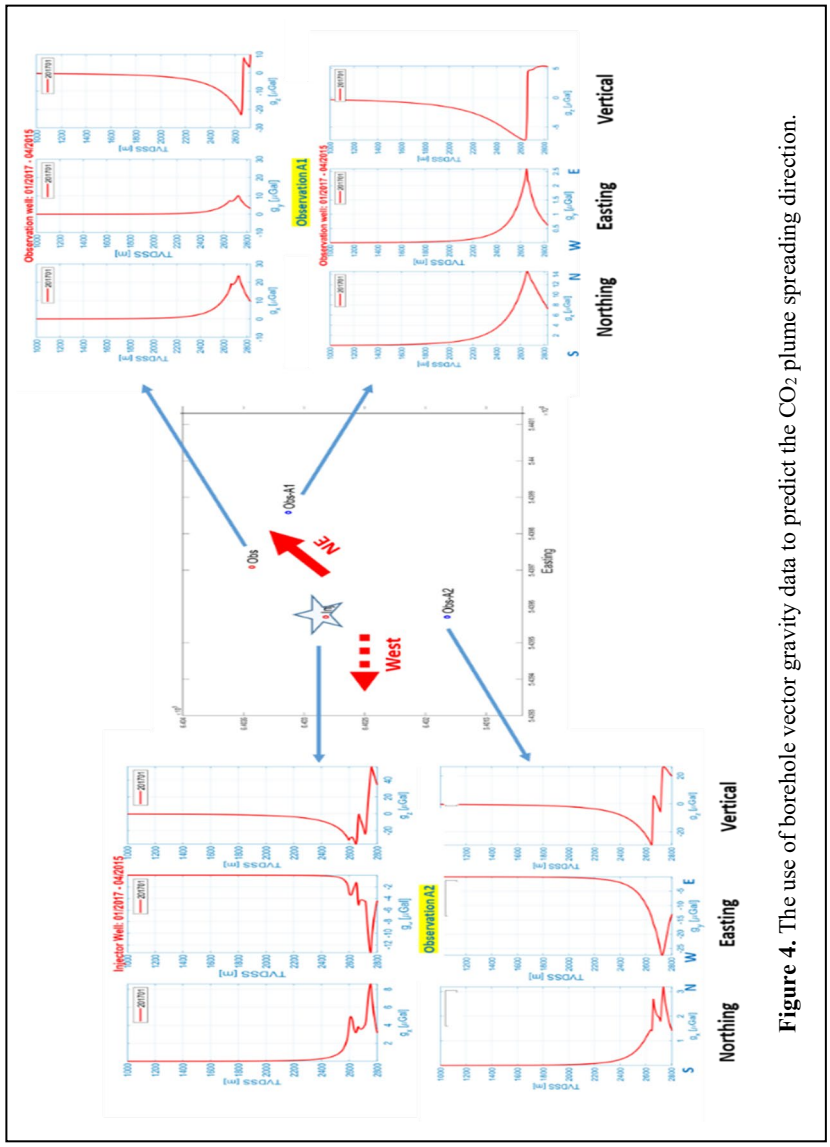

Figure 4. The use of borehole vector gravity data to predict the CO_2 plume spreading direction.

Results for Most Recent Injection Period (06/2017–01/2020)

For injection into the Aquistore reservoir, PTRC receives changeable rates of CO_2 from the Boundary Dam power station CO_2 capture plant, which vary seasonally and with changing volumes for commercial use for EOR. In Figure 5, variable time periods of injection of CO_2 into the reservoir are divided into three time-periods with similar cumulative injections of ~50 kt and which coincide with the latest reservoir simulation data periods. The simulated gravity response for each survey time period is presented (dark blue, cyan, and red) reflecting the increase in injected CO_2 from the 3 periods, denoted as T1 (12 months), T2 (24 months) and T3 (30 months).

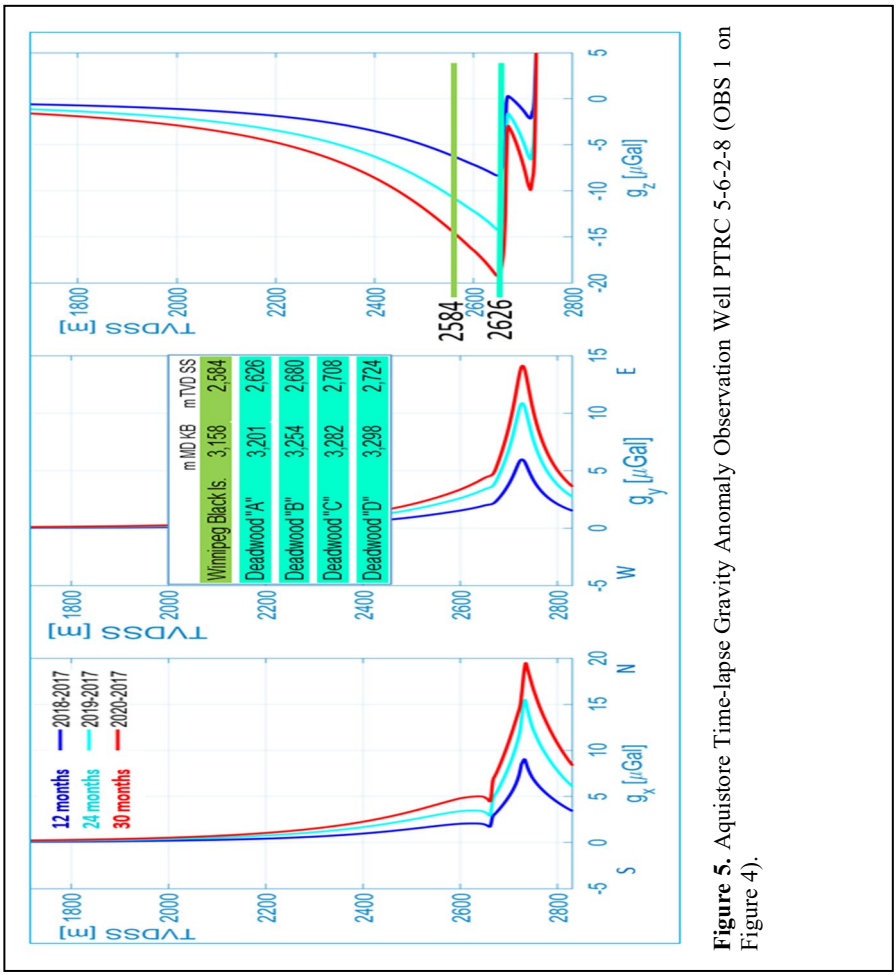

Figure 5. Aquistore Time-lapse Gravity Anomaly Observation Well PTRC 5-6-2-8 (OBS 1 on Figure 4).

As expected, the vertical gravity anomaly g_z has a well-defined zero-crossing at the central depth of the plume and two peak locations that approach the top and bottom boundaries of the plume as it reaches the monitoring well [8]. The peak value increases with the radius of the plume as it approaches the well and then becomes constant after the plume envelopes the well [9].

The horizontal components g_x and g_y exhibit different behavior than the vertical component, having their maximum response at the central depth of the plume for all radii. The peak values increase as the plume front approaches the observation well and achieve their maximum values when the fluid front reaches the observation well. Further expansion of the plume results in decreased peak values and broader anomalies. The vector gravity measurement allows us to monitor and characterize fluid injection more effectively than the scalar only vertical gravity measurement.

Focusing on period T3 (30 months), the vertical gravity $g_z = 20$ μGal peak coincides with the majority of CO_2 injection into the Deadwood A formation coinciding with a depth of 2626 m TVDSS. The lateral gravity response g_x and g_y have peaks indicating Northerly and Easterly movement of the CO_2 plume.

The gravity feasibility modelling predicts the expected CO_2 plume growth behavior as shown in Figure 6. As injection continues, the main CO_2 accumulation expands to the SW of the observation well. The front of the CO_2 plume grows in a predominantly ENE/NE direction with respect to both the injection and observation wells, as shown by the g_x plots in Figure 6.

A measurable gravity signal depends on the magnitude and proximity of the gravity anomaly, which in turn depends on the volume of CO_2 injected and the position of the CO_2 plume growth. By considering current CO_2 plume front position at Aquistore, a desirable gravity signal (>10 μGal) could be obtained after a 1.5 to 2-year injection period assuming an average injection rate of at least 50,000 tonne/year is maintained.

To further illustrate the far-field nature of the gravity measurement, Figure 7 shows how g_z, responds to the accumulated CO_2 injection; the magnitude of g_z at T1, T2, and T3 were chosen to correspond to multiples of ~50 kt injections. Since the front of CO_2 plume is some distance away from the observation well at the end of T3, a further well will eventually be required to enable continued monitoring.

This study shows despite using a single observation location, the three component gravity data contain sufficient information to enable the reconstruction of the plume front with clear definition of its growth.[1] Ongoing operations are designed to acquire a series of 3-axis gravity measurements in the observation well enabling comparison of the modelled vector gravity responses to verify the growing pattern of the CO_2 plume as delineated with the current study.

[1] Editor's note: One reviewer felt that this had not been demonstrated.

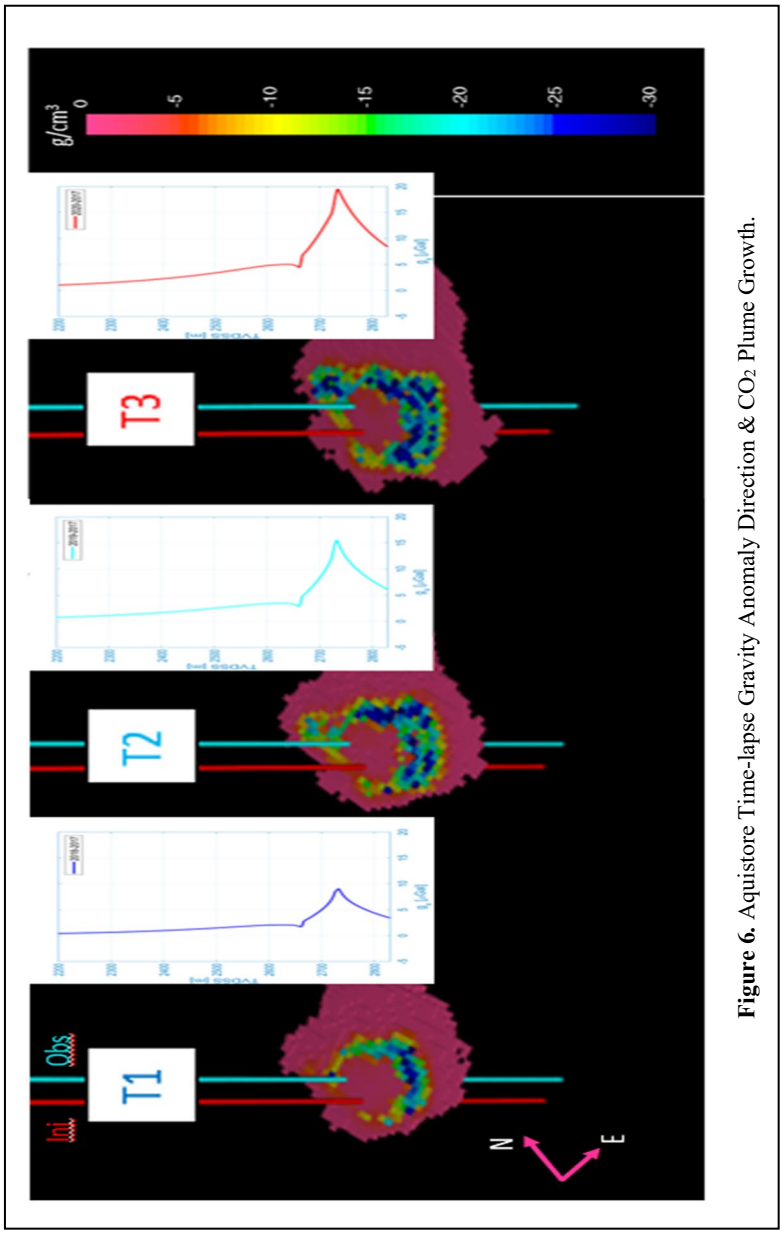

Figure 6. Aquistore Time-lapse Gravity Anomaly Direction & CO_2 Plume Growth.

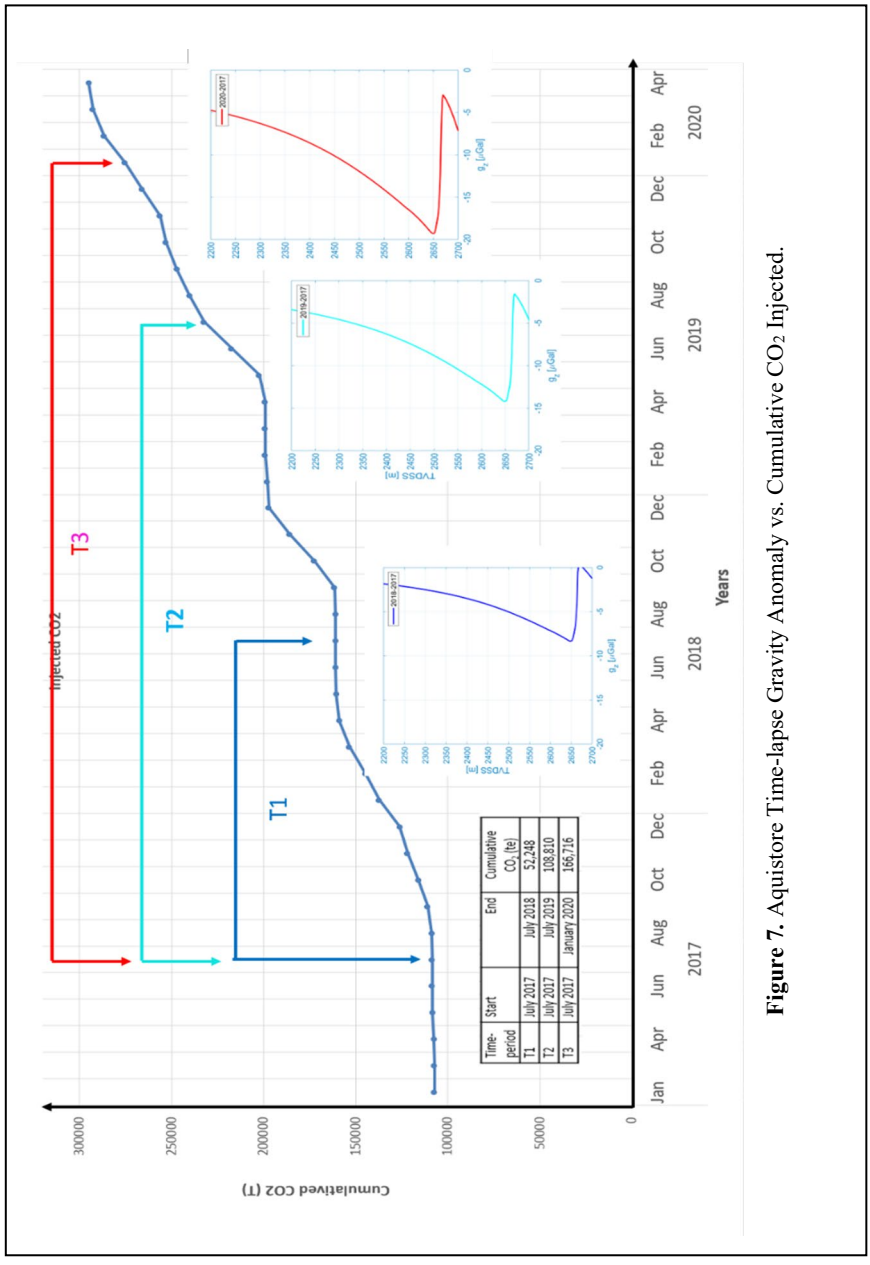

Figure 7. Aquistore Time-lapse Gravity Anomaly vs. Cumulative CO_2 Injected.

COMPARISON WITH SEISMIC MEASUREMENTS

The Aquistore project has used seismic surveys extensively as a major tool for CO_2 monitoring. Recently updated high quality 4D seismic images were obtained by combining use of permanent installed seismic geophones on the surface with well DAS-based VSP in 2018 [10]. We here compare the results of gravity responses predicted from reservoir modelling to the preliminary results from seismic inversion [10], where the CO_2 injection periods correspond approximately to the time-periods used in the gravity modelling.

The following comparison figures show a map of CO_2 plume growth as estimated from a history matched reservoir model at different CO_2 volumes injected. In Figure 8, the left image shows the modelled gravity response (reflecting the density difference between the two injection periods) and the right image is the corresponding seismic response. Figure 8 shows the position of the CO_2 plume after the first 36 kt of CO_2 were injected and both responses are qualitatively similar. Note that the gravity response is discernible over a 10m thick interval whereas the seismic can only be averaged over a 30m interval.

Figure 9 shows the CO_2 plume growth at the end of time period T3 (cumulative injection of 272,000 te). The gravity response, shown as a red polygon superimposed on the seismic, accounts for only the last 18 months of injection (~114,000 te). The two measurements match and clearly indicate an unswept zone, with no CO_2 change over the period, which is shown as white on the seismic. This unswept region may be caused by a region of low permeability blocking CO_2 expansion.

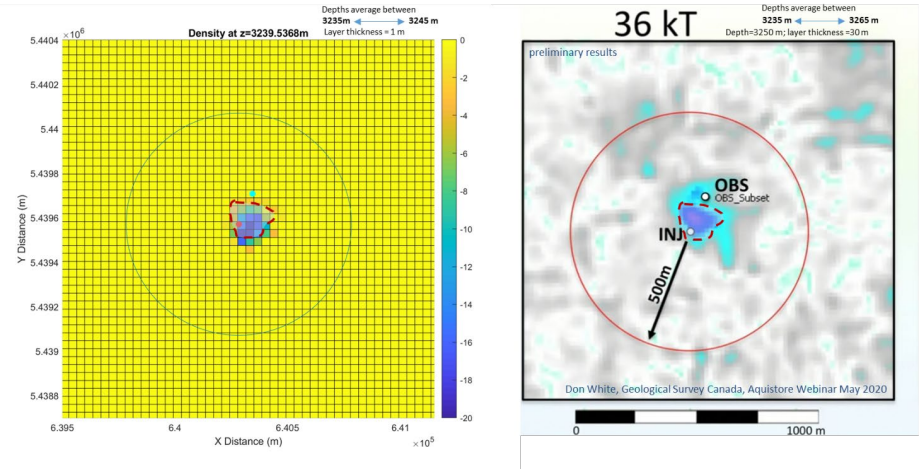

Figure 8. Fluid density change after 9 months injection (01/2016–04/2015) compared to Seismic imaged CO_2 plume at 02/2016.

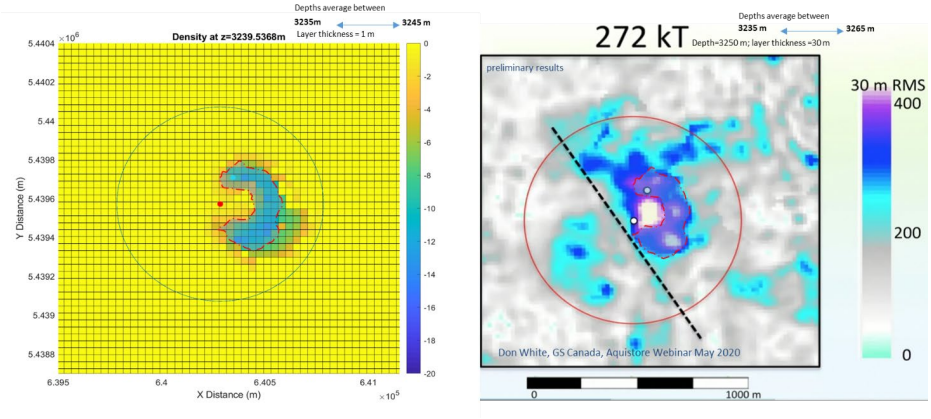

Figure 9. Fluid density change after 18 months injection (01/2020–07/2018) compared to Seismic imaged CO_2 plume at 01/2020.

The value of information brought by the gravity measurement is further illustrated by the direct relationship of gravity to density change, while the seismic shows indications of a noisy response as evidenced by the discontinuous patches of change in the SW. The seismic response in the SW is interpreted as noise since this area around the SW of the well is seen (also from seismic) to be disconnected from the injector by a sealing fault running NW-SE between this region and the injector (dashed line on Figure 9 right side).

TESTING PROGRAM

During August 2019 SMG's prototype wireline gravity tool was deployed in a test well in Cornwall, UK to determine functionality with satisfactory results (Figure 10). It was then shipped to Canada in September 2019 for deployment in well PTRC OBS 5-6-2-8.

The equipment was tested at the surface in preparation for downhole deployment. The tool string consisted of a telemetry module, a GammaRay tool, a Casing Collar Locator, a Clamp and a 3-axis gravity sensor. The tool was deployed by Eclipse Wireline using a standard wireline logging truck with a wireline mast. The tool was deployed to 1,000 m and the functionality of the clamping system confirmed and data acquired. The tool was then left acquiring data overnight. It became apparently that there were unexpected issues with tool temperature stability which was impacting data quality. The tool was pulled out of the well and replaced by a back-up tool. However, the back-up tool experienced a failure which resulted in no data being acquired. As a result, it was decided to stop the planned program and send the equipment back to the UK for troubleshooting.

When returned to the UK, issues were discovered with the functionality of the tools and a program to correct these issues was initiated. The global COVID-19 pandemic arose and made it impossible to return to Canada for further trials during 2020. In Q4 2020, SMG suspended its wireline deployed gravimeter project due continuing uncertainties.

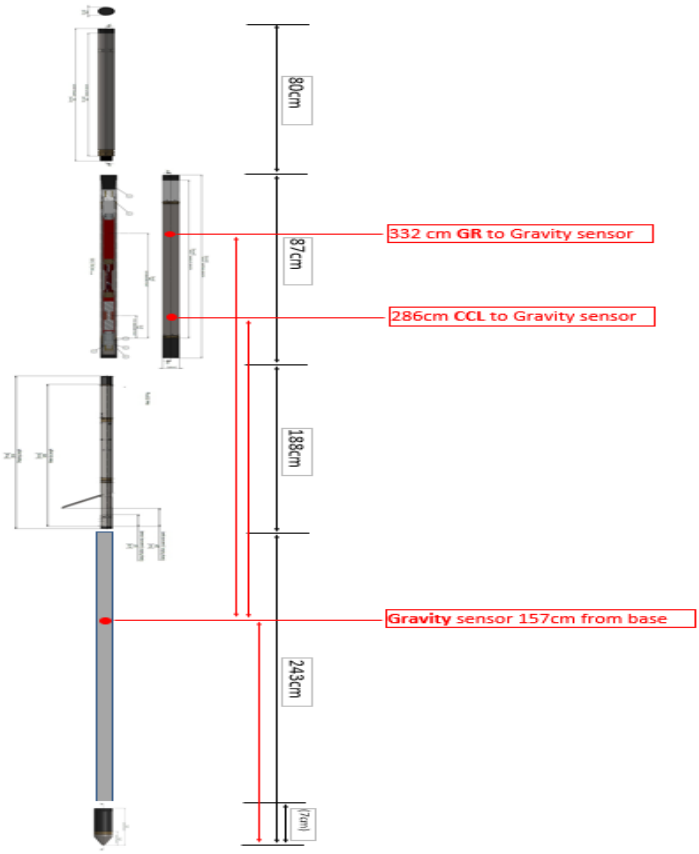

Figure 10. Wireline tool string.

CONCLUSIONS

The project has shown the advantage of using gravity for CO_2 monitoring through a feasibility study, and that a time lapse gravity survey has the potential to detect both the magnitude and the directionality of fluid substitution.[2]

The study has shown that it should be possible for a measurable time-lapse gravity response to be detected when the CO_2 plume front is 0.5 km away from the logged well. Simulation of the target Aquistore reservoir showed the response is large enough to detect after 75 kt CO_2 has been injected into the reservoir at a reservoir temperature of 110–129°C. The gravity response arises from the displacement of water by CO_2 with a density contrast of 0.36–0.41 g/cm^3. The modelling was able to delineate the current CO_2 plume position at Aquistore, and that a gravity signal >10 µGal can be obtained after a 1.5 to 2-year injection period, assuming an average injection rate of >50 kt/year is maintained.

[2] Editor's note: One reviewer felt that this statement had not been demonstrated in this study.

Direct comparison of simulated gravity data to field seismic data demonstrates the complimentary nature of the 4D type gravity response to 4D seismic for CO_2 storage monitoring. Further, it shows that, when CCUS is deployed at scale, gravity logging could offer a cost-effective alternative to reduce uncertainties further.

Unfortunately, the full scope of work could not be completed due to a combination of technical, commercial, and COVID-19 issues and as a result the project was unable to demonstrate a working 3-axis gravimeter in the CCP4 well.

REFERENCES

1. PTRC, Aquistore Project, https://ptrc.ca/projects/co2-eor-and-storage/aquistore .
2. Pandit M, Mustafazade A, Zhao C, Sobreviela G, Zou X, Steinmann P, Seshia A, 2019. An ultra-high resolution resonant MEMS accelerometer. 32nd IEEE International Conference, Seoul.
3. Krahenbuhl R, Martinez C, Li Y, Flanagan G, 2015. Time-lapse monitoring of CO_2 sequestration: A site investigation through integration of reservoir properties, seismic imaging, and borehole and surface gravity data. *Geophysics*, 80(2), WA15-WA24.
4. Peck W, Bailey T, Liu G, Klenner R, Gorecki C, Ayash S, Steadman E, Harju J, 2014. Model development of the Aquistore CO_2 storage project. *Energy Procedia*, 63, 3723-3734.
5. Shokri A, Chalaturnyk and Nickel, E, 2020. Non-Isothermal Injectivity Considerations for Effective Geological Storage of CO_2 at the Aquistore Site, Saskatchewan, Canada. SPE Annual Conference and Exhibition DOI: 10.2118/196110-MS.
6. Rim H and Li Y, 2015. Advantages of borehole vector gravity in density imaging. *Geophysics*, Vol. 80, No. 1, G1-13.
7. Du Z., A. Topham, J. Lofts and A. Seshia. 2020 Three-axis borehole gravity feasibility method and its application to CO_2 storage monitoring. 82nd EAGE Conference & Exhibition 2020, Expanded Abstract.
8. Topham, A., Lofts, J., Du, Z., Zett, A., Espie, T., Li, Y., Krahenbuhl, R., 2020. 3-axis borehole gravity: Method and application to CO_2 storage monitoring and oil/gas production, ATCE (SPE-201441-MS).
9. Dodds K, Krahenbuhl R, Reitz A, Li Y, Hovorka S, 2013. Evaluating time-lapse borehole gravity for CO_2 plume detection at SECARB Cranfield: *International Journal of Greenhouse Gas Control*, 18, 421–429.
10. White D, Harris K, Roach L, Robertson M, 2019. 7 years of 4D seismic monitoring at the Aquistore CO_2 storage site, Saskatchewan, Canada. Society of Exploration Geophysicists. SEG Expanded Abstract.

NOMENCLATURE

1 Gal = 1 cm/sec^2
1 µGal = 10^{-6} Gal
Earth's gravity field = 981 Gal (cm/sec^2) = 1 g (earth)
1 ng = 0.001 µg = 0.981 µGal
4D seismic = time-lapse three-dimensional seismic
4D gravity = time-lapse triaxial gravity
1 kt = 1000 tonne

Carbon Dioxide Capture for Storage in Deep Geological Formations, Volume 5
Karl F. Gerdes (Editor)
© 2022 BP. All rights reserved.

Chapter 33

ELECTROMAGNETIC MONITORING AT AQUISTORE

Patrick Belliveau[1], Mike McMillan[1], Eldad Haber[1,2]
[1]Computational Geosciences Inc.
[2]University of British Columbia

ABSTRACT: This chapter describes research into the use of surface to borehole electromagnetics (BSEM) for the monitoring of CO_2 injection at the Aquistore sequestration project in southern Saskatchewan. The Aquistore project is injecting CO_2 into a saline reservoir at approximately 3 km depth below surface. A BSEM forward modelling study determined the signal to be very small but above instrument noise levels. We found that the plume was not resolvable by inversion of BSEM data from a single survey. A subsequent synthetic study indicated that time-lapse BSEM imaging of the Aquistore plume should be possible but is still unlikely to succeed unless significant measures to reduce sensor positioning errors, such as the installation of permanent sensors, are undertaken.

KEYWORDS: electromagnetics, inversion, monitoring, time-lapse

INTRODUCTION

Monitoring and management of subsurface fluid flow is essential to the success of CO_2 sequestration, and geophysical methods can be important tools in this monitoring process. Physical properties such as density, electrical conductivity, and seismic wave velocity are sensitive to changes in fluid volumes within the subsurface rock matrix–see Annetts *et al.* [1] and NETL [2]. Therefore, by inverting geophysical data sensitive to these physical properties, changes to the subsurface fluid volumes can be recovered, providing valuable information about the volume and movement of the injected fluid. It is also beneficial to include information about the physics that describes the movement of the fluid, such as multiple phase flow models [3], into the geophysical modelling/inversion process.

Here, we focus on electromagnetic monitoring at the Aquistore CO_2 sequestration project, which is an experimental CO_2 sequestration project in Saskatchewan, Canada, led by the Petroleum Technology Research Council (PTRC) [4]. The work described here was originally conceived as part of a project to assess the ability of joint geophysical inversion coupled with fluid flow simulation to image the injected CO_2 plume at Aquistore. Lack of time-lapse electromagnetic data precluded following the original joint inversion plan and the project was refocused on electromagnetics.

Aquistore is capturing CO_2 from a coal-fired power plant and injecting it into a deep saline aquifer approximately 3 km below the earth's surface. Previous theoretical work [5] had indicated the potential feasibility of direct current resistivity methods to image injected CO_2 at Aquistore, and as such, borehole-to-surface electromagnetic (BSEM) surveying had been planned before the beginning of this project. The supercritical CO_2 injected into the Aquistore reservoir has a much higher electrical resistivity than the brine that occupies the pore space in the reservoir rock. Therefore, as CO_2 displaces brine in the pore space, the bulk resistivity of the reservoir increases.

Electromagnetic (EM) geophysical methods are sensitive to the electrical resistivity of the earth, making them potentially useful for the monitoring of CO_2 sequestration. Several research studies have

been done regarding EM monitoring of CO_2 injection in saline aquifers, indicating that in principle it is a feasible exercise [6-8]. Tietze *et al.* [9] used a borehole-to-surface EM survey configuration similar to the one discussed herein to assess oil saturation in the closely related problem of determining oil saturation in an oil reservoir injected with brine. That study included a field test that had promising results. The main difficulties in applying EM imaging at the Aquistore site are the depth of the target and the complexity of modelling surface-to-borehole EM in the presence of steel cased wells. The casing helps to amplify the signal at depth but it requires special modelling techniques. These are extremely computationally expensive, but critical. The steel in the well acts as a strong conductor which channels electrical current along its surface. Therefore, precise modelling of the location, geometry and thickness of the well is of the utmost importance to represent the current flow and resulting electromagnetic (EM) fields in a suitable manner. See Um *et al.* [10], Puzyrev *et al.* [11], Schwarzbach and Haber [12], and Commer *et al.* [13] for references on geophysical electromagnetic modelling in the presence of steel casing.

This project began with a forward modelling study designed to assess the detectability of the Aquistore CO_2 plume by the BSEM method and to inform the survey design for the BSEM data collection. A BSEM survey was subsequently conducted at Aquistore in July 2019. After processing the data, we inverted the field data. The field data inversion determined that the CO_2 plume could not be resolved by a single EM survey alone and could not distinguish between multiple plausible CO_2 saturation models derived from fluid flow modelling. In light of this we performed a synthetic time-lapse inversion study using the same survey configuration that was used for the 2019 BSEM survey, in order to assess what might have been possible with time-lapse BSEM data.

This report will summarize these three main phases of the project: the forward modelling study, inversion of the 2019 field data set, and the synthetic time-lapse inversion study.

FORWARD MODELLING

The forward modelling process simulates the electromagnetic data that result from a given resistivity model and survey configuration. We constructed 3D electrical resistivity models representing the Aquistore site before the start of CO_2 injection and after two years of injection. We then simulated the BSEM data that would arise from surveys, given those models.

The Conductivity Models

The Aquistore site is located in the Williston basin, a large sedimentary basin underlying parts of Montana, the Dakotas, and southern Saskatchewan. CO_2 is injected into the Winnipeg and Deadwood formation sandstones at the bottom of the basin. The injection zone is bounded from below by impermeable Precambrian basement. The icebox shale unit in the upper Winnipeg formation forms the caprock. For more details on the geology of the Aquistore site, see White *et al*. [14].

We constructed a detailed conductivity model based on a combination of resistivity well-log data, porosity and permeability models derived from seismic and a post injection CO_2 saturation model derived from two-phase fluid flow modelling [15]. Outside the CO_2 reservoir, the resistivity was assumed to be unchanged over the injection period. In a real world time-lapse EM experiment, there will likely be changes in the near-surface resistivity due to changes in water content, introducing potential error into the time-lapse data. Investigation of such errors is beyond the scope of this study. We constructed a one-dimensional (1D) resistivity model by averaging well-log resistivity data onto our computational mesh. A cross-section of the model in the plane of the CO_2 injection well is shown in Figure 1. The lateral variations appear because we discretize the model more finely near the well than away from it. Therefore, model cells far from a well represent the resistivity averaged over a greater depth extent than cells near a well.

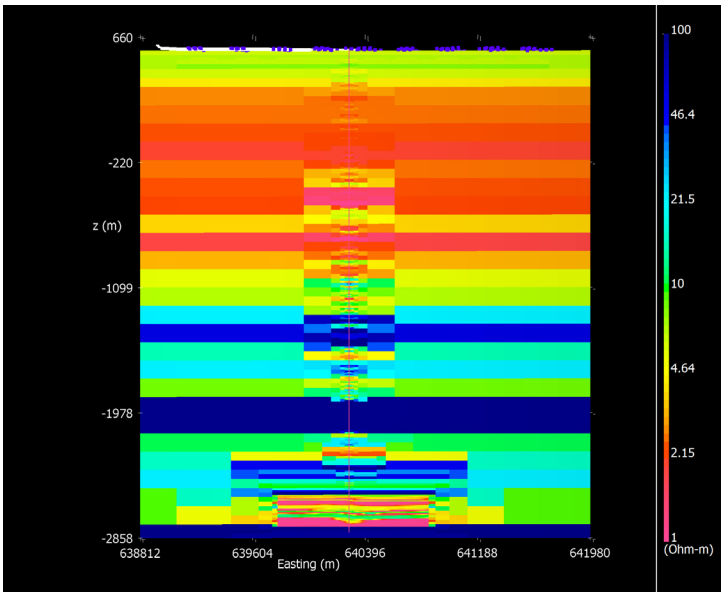

Figure 1. A-priori resistivity (Ωm) model. East-West cross-section at injection well.

Inside the reservoir, we computed the pre- and post-injection resistivities from the 3D porosity and CO_2 saturation models provided to us using the empirical relation known as Archie's law. Archie's law may be written as

$$R_t = a R_B S^{-n} \Phi^{-m}, \tag{1}$$

where R_t is the bulk resistivity of the reservoir, Φ is porosity, S_B is brine saturation, a is called the tortuosity factor, R_B is the brine resistivity, and n and m are the saturation and cementation exponents. We used $a = 0.62$, $n = 2$, $m = 2$, and $R_b = 0.014$. These values were reported by Daley *et al*. [5], who investigated the application of direct-current resistivity methods to CO_2 monitoring at Aquistore. The pre-injection reservoir model consisted of a fully brine-saturated reservoir. The post-injection CO_2 saturation model was derived from a two-phase flow simulation of two years of CO_2 injection [15].

The final, crucial component of our resistivity model is the steel casing of the production and injection wells. We incorporated the casing resistivity and susceptibility using an upscaling method developed by Schwarzbach and Haber [12].

EM Forward Modelling Methodology

Forward modelling of EM fields requires the numerical solution of Maxwell's equations. Our in-house forward modelling software uses a finite volume discretization technique—see Haber and Ascher [16], Schwarzbach and Haber [17].

Maxwell's equations in the frequency domain can be written as

$$\nabla \times \mathbf{E}_{jk} = -i\omega_j \mathbf{B}_{jk}, \tag{2}$$

$$\nabla \times \mu^{-1} \mathbf{B}_{jk} = \sigma \mathbf{E}_{jk} + \mathbf{v}_k \tag{3}$$

$$\mathbf{n} \times \mathbf{B}_{jk} = 0, \qquad j = 1, \ldots, n_f; \quad k = 1, \ldots, n_s \tag{4}$$

where $\mathbf{E}_{jk}$ and $\mathbf{B}_{jk}$ are electric fields and magnetic fluxes, respectively, that result from the j-th frequency and k-th source, μ is the magnetic permeability, σ is the conductivity (inverse of resistivity), ωj is the j-the angular frequency, and vk represents an external current density source. To compute the predicted electric field data due to a given resistivity model, Maxwell's equations are solved approximately for the electric field on the cell edges of our computational mesh, and the electric field values are integrated along the lengths of the receiver dipoles and normalized by the dipole length.

A time-lapse signal is produced by differencing the simulated pre- and post-injection data. The BSEM method is successful only if the time-lapse signal is detectable in the presence of noisy measurements. For this reason, we looked at the simulated time-lapse signals, d^{tl}, relative to the noise, ϵ:

$$d^{tl} = \frac{|d^{post} - d^{pre}|}{\epsilon} \tag{5}$$

To estimate the noise, we averaged the values extracted from Figures 2 and 3 [18] at frequencies matching those used in each experiment. The noise estimates of Hibbs [18] were derived by measuring fluctuations in the voltages recorded by EM receivers in the absence of a transmitted EM signal. These noise estimates have not been published but were provided to us by ANLEC.

Finally, to compare the results of our synthetic modelling experiments we measured the root-mean-square of the signal to noise ratio:

$$RMS = \sqrt{\frac{\Sigma(d_i^{tl})^2}{n}}, \tag{6}$$

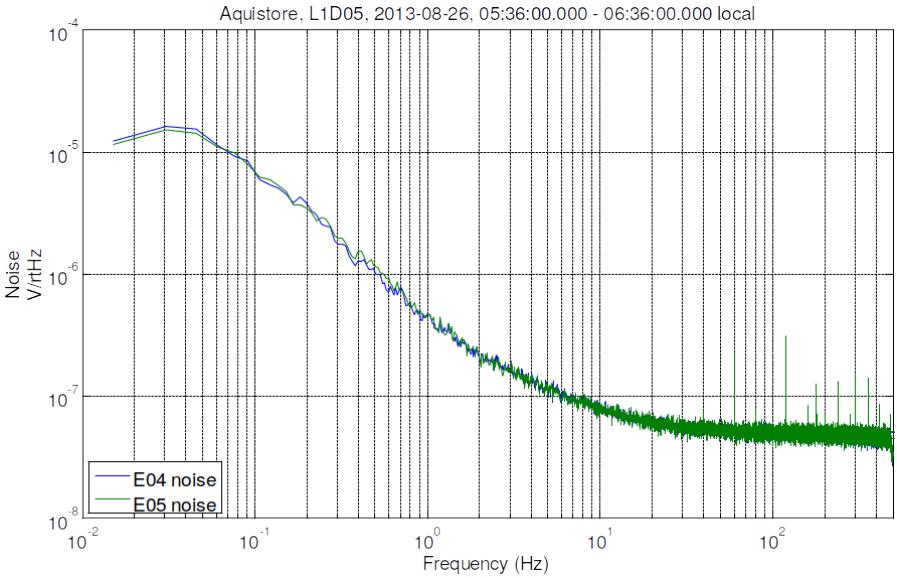

Figure 2. Environmental noise measured on site in the early morning (taken from Hibbs [18]).

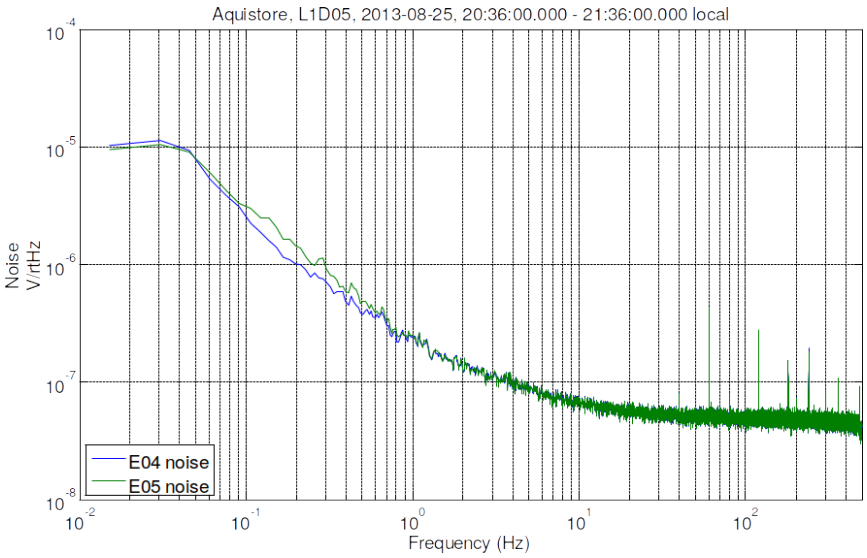

Figure 3. Environmental noise measured on site in the evening (taken from Hibbs [18].

Forward Modelling Results

We designed a set of experiments to test various transmitter configurations and frequencies. The transmitter configurations consisted of a downhole electrode connected to a remote surface electrode. We varied the positions of the surface electrode and the depth of the downhole electrode, for a total of 168 configurations per frequency, testing at frequencies of 0.2Hz, 0.5Hz, and 1.0Hz. Data were simulated on a regular 7 × 7 grid of measurement locations covering a 2.5 km × 2.5 km area centered about the injection well.

For each experiment, the signal to noise RMS was computed for each frequency on the concatenation of all combinations of x-dipole, y-dipole, real and imaginary data as well as the concatenation of all frequencies. We used the RMS to determine the best survey designs since a large RMS implies that the average time-lapse signal is large relative to the noise and therefore more likely to be detectable in a real-world survey.

To decide which experiment contains the most information about conductivity changes, we also used the A-optimal design criterion to find a transmitter configuration that provides the most independent data to the strongest RMS experiment. A-optimal experimental design is a well-established statistical technique used to assess the information content of the data from a given experiment [19]. Both the A-optimal experimental design analysis and the RMS sorting revealed that the most useful configuration consists of a transmitter operating at 1Hz, with a downhole electrode at a depth of -2800 m elevation (immediately below the reservoir, see the left side of Figure 4) with the surface electrode placed to the southwest of the observation well.

Figure 4 compares the time-lapse signal relative to the noise at 1.0Hz (the frequency which produces the higher RMS) for the highest RMS experiment and the experiment with the most independent data. The empty circles represent the receiver locations used for the RMS calculations over the survey area.

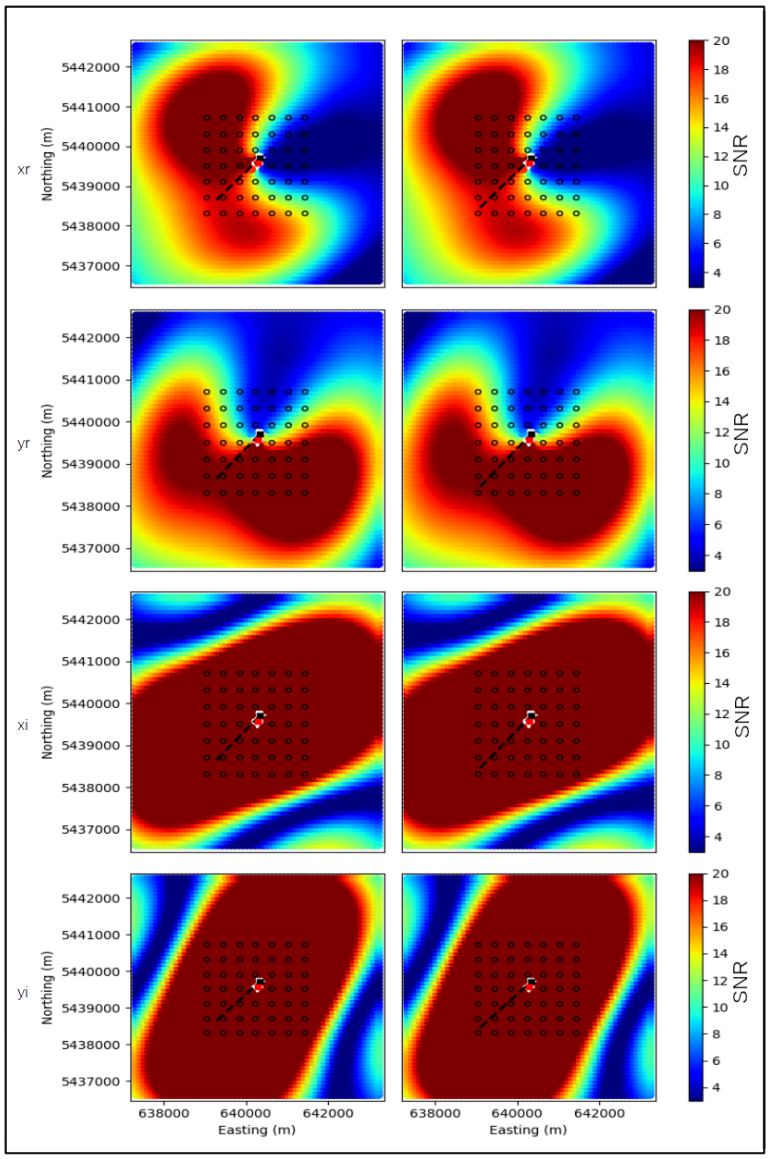

Figure 4. Signal to noise ratio for the survey with the highest RMS signal to noise ratio (left) at 1.0Hz and the experiment selected as the next most important configuration (right) by the A-optimal design. The black dashed line shows the transmitter wirepath, which is slightly different between the two experiments. The transmitter terminates at the observation well, shown by a black square. The injection well is shown by a red circle.

Forward Modelling Conclusions

Although the above-mentioned configuration provided the highest RMS, some other configurations gave comparable values. In general, the RMS was not particularly sensitive to the transmitter electrode locations. Surface transmitters at the longest offset, and in more south-westerly directions tended to produce larger RMS. Downhole transmitters in the middle and below reservoir positions also tended to produce larger RMS, but the improvement over even the smallest RMS configurations was small. The frequency of the experiment strongly affected the resulting RMS calculation due to the frequency dependent noise. Higher frequencies produced lower noise levels as reported by Hibbs [18], resulting in a 6-fold increase in the RMS for the top ten 1.0Hz experiments compared to the top ten 0.2Hz experiments.

When we compute time-lapse data by differencing the pre- and post-injection data for each transmitter configuration, we remove the effect of the source. The time-lapse signal can be thought of as the secondary field generated by eddy currents circulating within the reservoir, and since the reservoir is roughly symmetric about the injection well, it is not surprising that the different transmitter configurations produced such similar results.

It is important to note that the RMS values discussed above refer only to instrument measurement noise. Many other sources of noise exist that are not accounted for in our analysis and which may easily exceed the noise sources we have modelled here. Many of these other sources of noise are difficult or impossible to control, such as: changes to the water table, vegetative growth, and cultural sources. However, one crucial aspect of controlling the noise is positional error in the wire paths and electrode locations. Great care must be taken to accurately measure not only the transmitter and receiver electrode locations but also the wire path that connects the transmitter electrodes. Great care must also be taken to accurately re-occupy these locations at each new time interval of time-lapse surveying. See Tietze *et al.* [9] for a thorough discussion.

EM FIELD DATA INVERSION

A BSEM survey using a configuration based on results from the forward modelling study described above and on discussions with the data acquisition contractor was performed at the Aquistore site in July 2019. Unfortunately, no pre-injection BSEM data were available to form a baseline for the 2019 survey and currently no follow-up EM survey is planned. Therefore, we attempted to image the CO_2 plume using the data from the single survey alone.

Survey

The survey measured the earth's response to an alternating electrical current source excitation. EM energy was transmitted into the ground using two grounded wire source configurations: a surface transmitter and a surface to borehole transmitter. The two transmitters utilized the same surface wire-path, running from a remote electrode approximately 3 km to the southwest of the observation well, to the top of the observation well casing. The first transmitter, labelled the top casing source (TCS) terminated at the top of the casing and the second down-hole source (DCS), terminated with an electrode coupled to the casing at a depth of 3 km below surface. A schematic diagram showing the transmitter wire-paths in plan and section view is shown in Figure 5. Each transmitter produced a 100% duty cycle square wave signal with an amplitude of approximately 10 Amps.

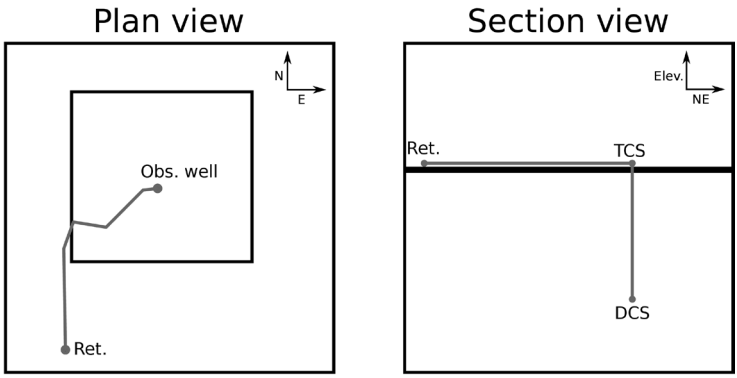

Figure 5. Diagram showing the transmitter wire-path and survey area. The rectangle in the plan-view diagram shows the bounding box of the receiver grid. Ret. is the transmitter return electrode. TCS is the positive electrode location for the top of casing source and DCS is the down-hole electrode location.

The electric fields generated in the earth by each transmitter configuration were measured at a series of receivers arranged in a grid pattern at the earth's surface. A satellite image showing the survey area and receiver layout is shown in Figure 6.

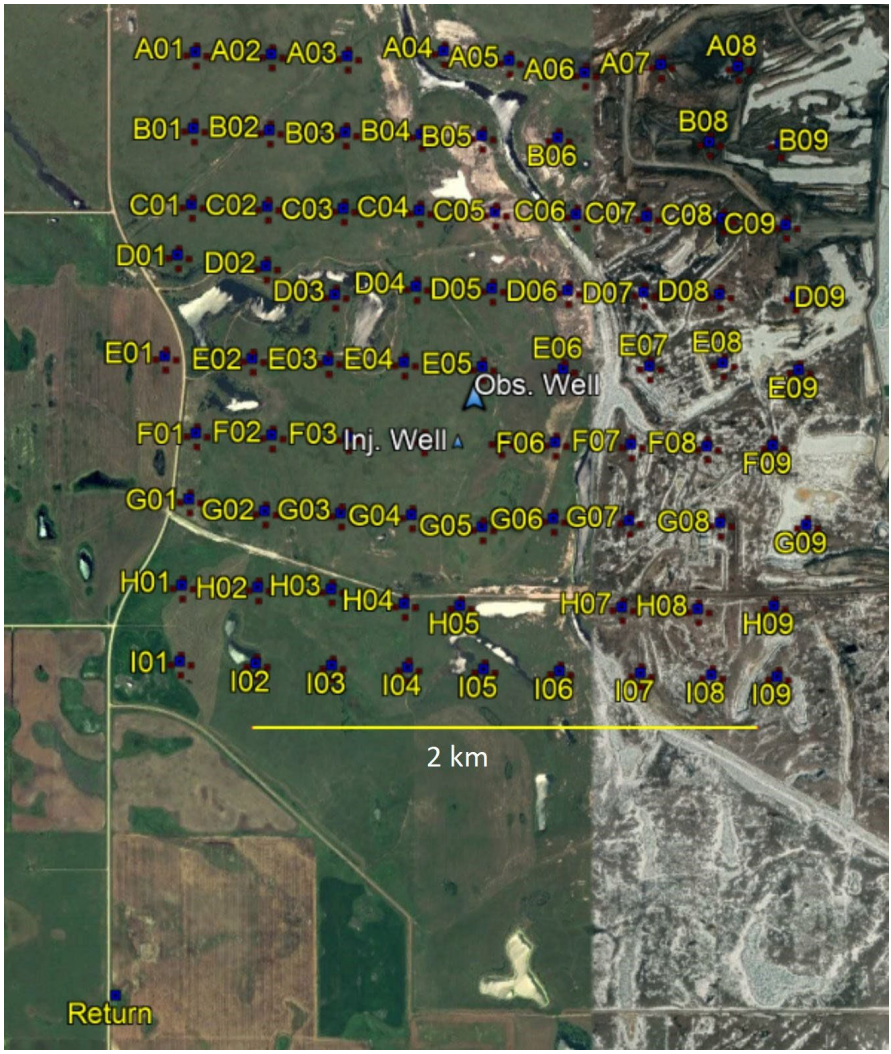

Figure 6. Satellite image showing survey layout. Well locations and return transmitter electrode labelled. Data recorder locations are shown in dark blue and receiver electrode locations in red.

The injection well represents the location where CO_2 is injected into the earth, whereas the observation well is where the downhole electrode is connected to monitor the injection process. At each measurement station, the electric fields were measured by electric dipole receivers at three orientations, labelled channel 1 (south-north orientation), channel 2 (southwest-northeast), and channel 3 (west-east). The electrode layout is shown in Figure 7. The data were processed to the frequency-domain. Unfortunately, the exact transmitter (TX) wire-path was not recorded during the survey as only the end electrode locations were measured. Due to EM induction generated by time-varying currents moving through the TX wire, the largest effect seen in the imaginary part of the electric field data is the geometric decay of these inductive effects away from the wire. It is therefore crucial to model the wire-path correctly. Outside the survey area, the wire followed a road, so we

could easily determine its path from satellite imagery. Inside the survey area, we were forced to estimate the wire-path from the frequency-domain EM data from the four frequencies used for modelling (1Hz, 5Hz, 9Hz, and 13Hz). Since EM induction primarily affects the imaginary part of the data at these frequencies [20], to assess the most likely wire-path we computed the magnitude of the imaginary horizontal electric field at each station at 13Hz. We then manually plotted a wire path based on the assumption of the magnitude at that higher frequency being maximized near the wire.

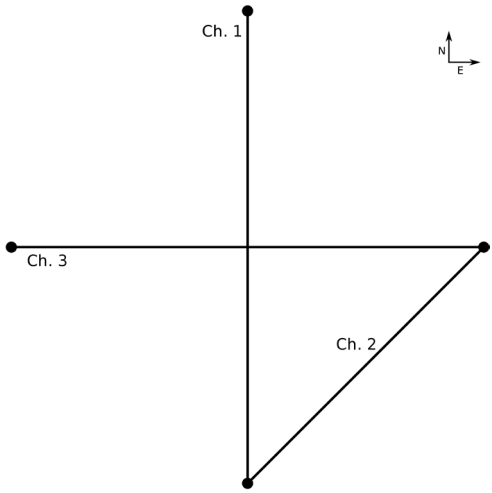

Figure 7. Diagram showing the approximate arrangement of the electric dipole receivers at each measurement station.

Inversion Methodology

EM inversion is the process of estimating the spatial distribution of EM physical properties in the earth from observed EM data. In this case, we seek to estimate the electrical resistivity of the earth from the electric field measurements taken at the earth's surface. Although imaging CO_2 at depth is the main goal of this project, the EM data are sensitive to the resistivity of the overlying geology as well, so this must be modelled if we are to find a resistivity that explains the observed data. We divide the earth into a set of discrete volumes called cells or voxels and assume the physical properties of the earth to be constant in each cell. The goal of the inversion is then to estimate the resistivity of each cell.

We formulate the inverse problem as an optimization problem. We seek to minimize an objective function that contains a data misfit term, which measures how well the estimated resistivity model explains the observed data, and a regularization term that measures how well the model matches *a priori* information regarding the resistivity. The objective function $\Phi(m)$ is:

$$\Phi(m) = \frac{1}{2}\|W(F(m) - d)\|_2^2 + \gamma R(m) \quad (7)$$

$$\text{subject to } m_l < m < m_u,$$

where m is the estimated resistivity model, m_u and m_l are upper and lower bounds on the resistivity values, d is the observed data, W is a diagonal matrix holding the standard deviations of the data, F is the forward modelling operator, R is the regularization operator, and γ is the scalar regularization

parameter that balances the relative importance of the data misfit and regularization terms in the objective function.

The problem of finding the voxel resistivity model that minimizes the data misfit is severely ill-posed as there are multiple models that may agree with the observed data equally well. Regularization is therefore required to make the inverse problem well posed. Our regularization operator is written as

$$\int_V \alpha_s W_s (m - m_r)^2 + \alpha_x \left(\frac{\partial}{\partial x}(m - m_r)\right)^2 + \alpha_y \left(\frac{\partial}{\partial y}(m - m_r)\right)^2 + \alpha_y \left(\frac{\partial}{\partial y}(m - m_r)\right)^2 + \alpha_z \left(\frac{\partial}{\partial z}(m - m_r)\right)^2 dv \quad (8)$$

where m_r is the reference model, which represents our best *a priori* estimate of the resistivity model. The first regularization term encourages the inverted resistivity model to stay close to the reference model, and W_s is a diagonal matrix that weights the importance of the reference model in each cell. The remaining terms encourage spatially smooth variations of the model, preventing the inversion from introducing spurious structure. Finally, the α values are scalars that balance the relative weights of the individual terms in the regularization functional.

All our inversions presented here used αs = 0.1, αx = αy = 10.0 and αz = 1.0. This encodes the fact that the geology at the Aquistore site consists of flat lying sedimentary layers and, therefore, we expect the resistivity to vary more smoothly in the horizontal directions than it does vertically. A systematic study of the effect of regularization weights was not performed specifically for the Aquistore project. Based on experience from other projects, we would expect the varying of these coefficients to affect the near-surface conductivity but not to have a significant impact at depth in the reservoir.

Inversion Workflow and Results

We employed a two-part inversion modelling workflow in an attempt to fit the small signals from the changing reservoir. The first stage of the inversion workflow was designed to find the best fitting background resistivity model outside the reservoir area, in addition to finding the optimal electrical resistivity and magnetic permeability value for the two steel cased wells. This step was done using the surface transmitter electrode data, as this set of data had the maximum sensitivity to near-surface information. The first stage was required since most of the signal in the data can be attributed to near-surface effects which are not accounted for in the *a priori* model. These additional near-surface features are therefore needed in the model to fit the signal coming from everywhere except for the growing CO_2 plume in the reservoir.

The second stage of the workflow involved using the background model obtained in the first stage as a reference model and inverting for only the reservoir cells, using the down-hole electrode data. Since the background model was optimized in the first stage, keeping only the reservoir cells active in the second stage constrained the inversion to change only the reservoir resistivities in order to extract the most information possible out of the small signal levels in the observed data.

The starting model for the background inversion was the post injection resistivity model used in our forward modelling study. Even without inversion, this *a priori* model does a reasonable job at fitting the large wavelength features of the data, but the first stage of the inversion workflow is needed to fit the finer details of the observed data. Once this step has been carried out, the stage 2 analysis is meant to extract the reservoir signal out of the downhole dataset. Overall, there is a good agreement between the final observed and predicted downhole data. The reduction in data misfit achieved by the stage 1

inversion is plotted in Figure 8. The inversion reduced the root mean squared data misfit error from a starting value of 8.7 to a final value of 0.99. The root mean squared error is

$$RMS = \sqrt{\frac{1}{n}\frac{\sum i\left(d_{obs}^{i} - d_{pred}^{i}\right)^{2}}{(w^{i})^{2}}} \tag{9}$$

where n is the total number of data, d_{obs}^{i} is the ith observed datum, d_{pred}^{i} the corresponding predicted datum and w^{i} the uncertainty assigned to the ith datum. The uncertainties assigned to the data reflect both data measurement and modelling uncertainty.

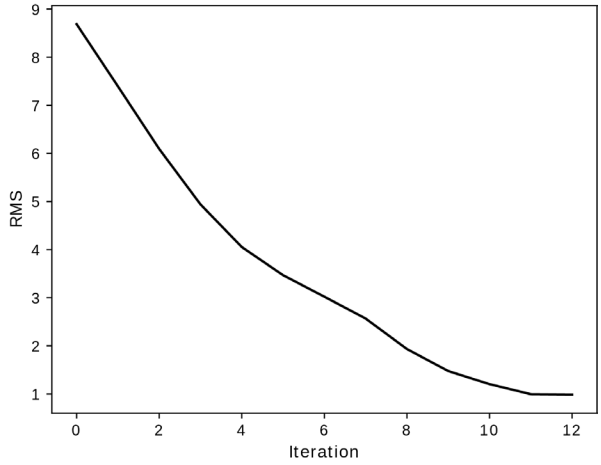

Figure 8. Convergence curve showing the reduction in the root-mean-squared error between observed and predicted data over the course of the stage 1 inversion.

Figures 9-10 show selected slices through the starting model and resulting best-fitting background model.

For the second stage of the workflow, it was necessary to fix the resistivity model outside the reservoir in order for the inversion to update the resistivity values in the area of interest. Even with added sensitivity at depth from the downhole transmitter, there is still a high sensitivity to near-surface conductivity and, therefore, cells outside the reservoir need to be fixed to obtain the best reservoir result. To illustrate the scale of the reservoir signal, we ran two additional forward simulations representing end member reservoir resistivity models–one with the entire reservoir set to a resistivity of 1000 Ωm and the other with the reservoir at 1 Ωm. The former value is more resistive than if the reservoir was entirely CO_2 saturated and the latter more conductive than a fully brine-saturated reservoir. We compared the synthetic data from these two end member data sets and found the relative difference between the two datasets at each receiver location to be 3.6% different on average, with a median difference of 0.6%. We computed the relative error at each point using the formula:

$$relativeerror = \left|\frac{d_c - d_r}{d_c}\right|,$$

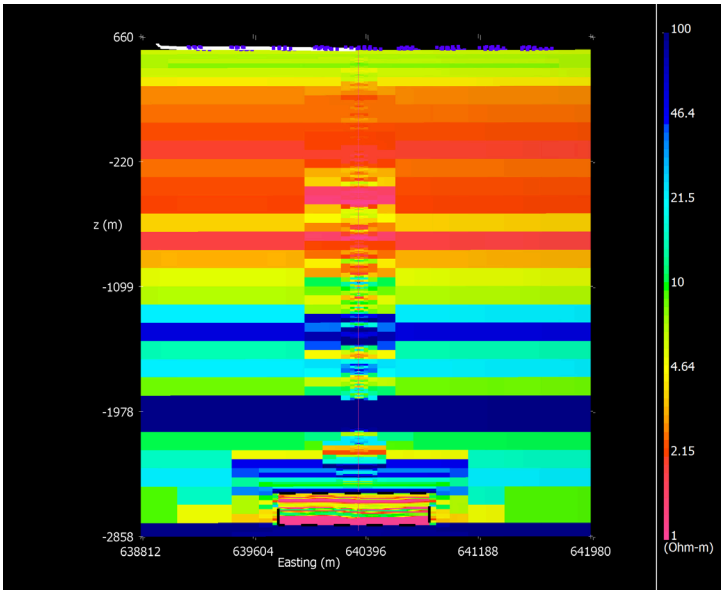

Figure 9. Starting resistivity (Ωm) model. East-West cross-section at observation well. Reservoir zone active in inversion marked by thick black dashed line. The downhole electrode is at an elevation of -2432 m.a.s.l.

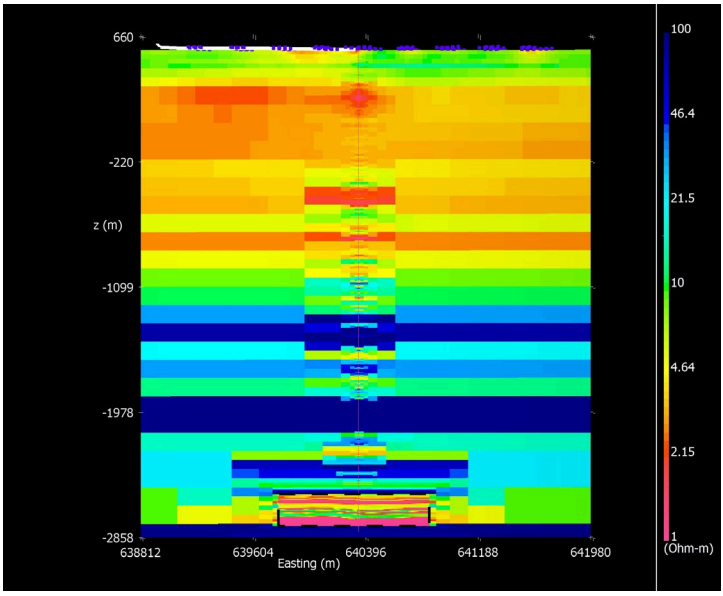

Figure 10. Background resistivity (Ωm) inversion model. East-West cross-section at observation well.

where d_c is a datum from the conductive model and d_r is the corresponding datum from the resistive model. These differences are only for the down-hole source at the fundamental frequency of 1Hz, whereas the other frequencies and the top casing source data have even less sensitivity to the reservoir. Such a large difference in reservoir properties represents an extreme example, but it shows that even with this scenario the relative errors are quite small. The difference in signal from the actual reservoir changes where CO_2 injection has occurred will be much smaller.

In addition to fixing the resistivity model outside the reservoir, we also fixed the resistivity in reservoir regions with hydraulic permeability values less than 1 millidarcy and porosity values less than 0.08. These regions represented areas in the reservoir with the lowest likelihood of changing, and these constraints were needed to provide the inversion with the best chance of producing a plausible model. Recall that the starting reservoir model was based on converting the modelled June 2017 CO_2 saturation to resistivity using Archie's law. As CO_2 replaces brine in the reservoir rock pore space, the overall resistivity of the rock is increased. The final inversion created a large volume of high resistivity (low conductivity) rock, which is interpreted as the growing CO_2 plume.

An East-West cross-section through the final resistivity model at the injection well is shown in Figure 11, while a similar cross-section at the observation well is displayed in Figure 12. Focusing only within the reservoir area, an East-West cross-section comparison at the injection well between the results from stage 1 and stage 2 of the inversion workflow is shown in Figures 13 and 14, and a similar cross-section comparison at the observation well in Figures 15 and 16. Figures 17 and 18 show depth slices of the stage 1 and final resistivity models at elevation of -2650 meters above sea level (MASL). Figures 19 and 20 show depth slices of the stage 1 and final resistivity models at elevation of -2730 MASL. These comparison figures show the small, relatively uniform expansion of the resistive CO_2 plume from the 2017 model to the inversion model based on the 2019 EM data.

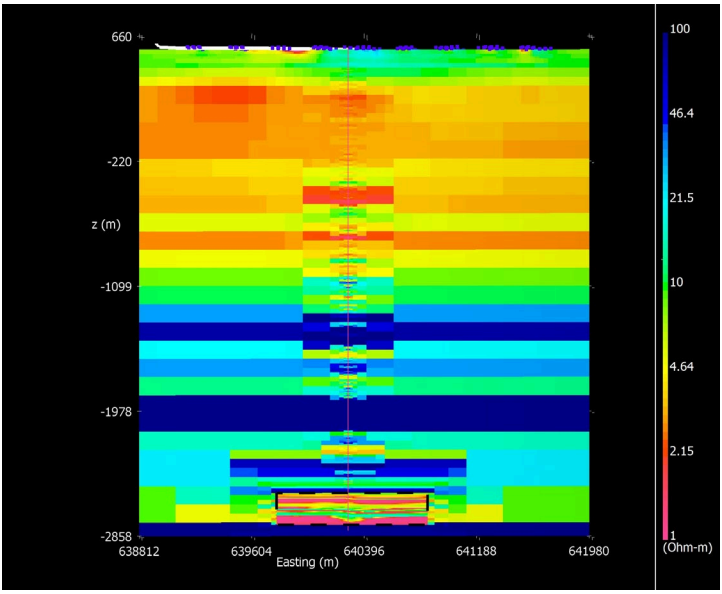

Figure 11. Final resistivity (Ωm) model. East-West cross-section at injection well. Reservoir zone active in inversion marked by thick black dashed line. The downhole electrode is at an elevation of -2432 m.a.s.l.

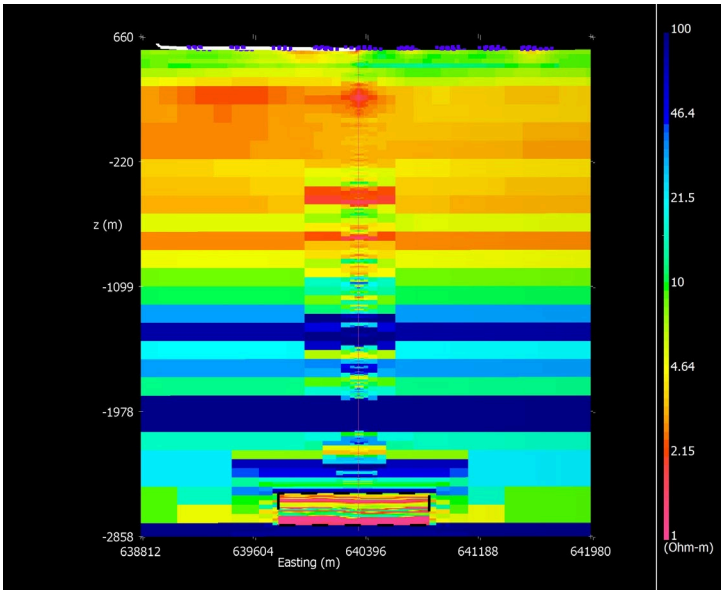

Figure 12. Final resistivity (Ωm) inversion model. East-West cross-section at observation well.

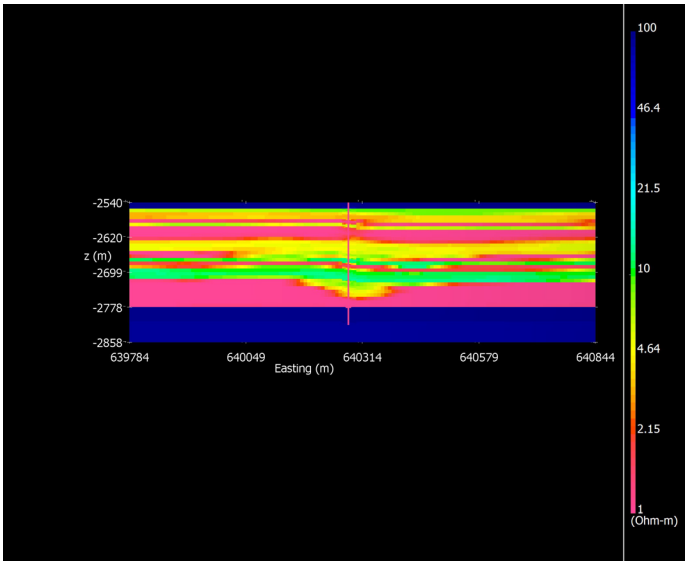

Figure 13. Stage 1 resistivity (Ωm) inversion model. East-West cross-section at injection well.

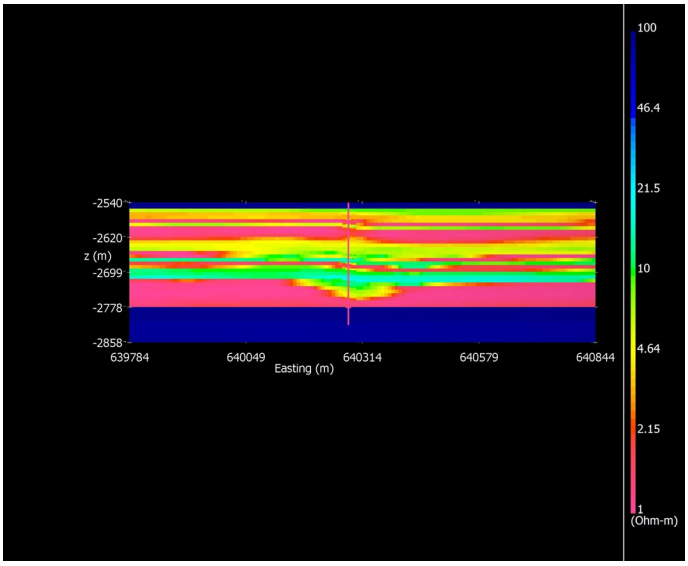

Figure 14. Final reservoir resistivity (Ωm) model. East-West cross-section at injection well.

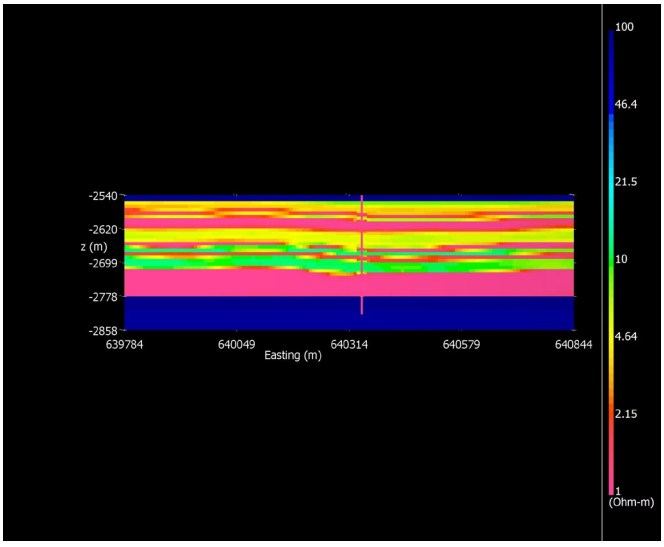

Figure 15. Stage 1 resistivity (Ωm) inversion model. East-West cross-section at observation well.

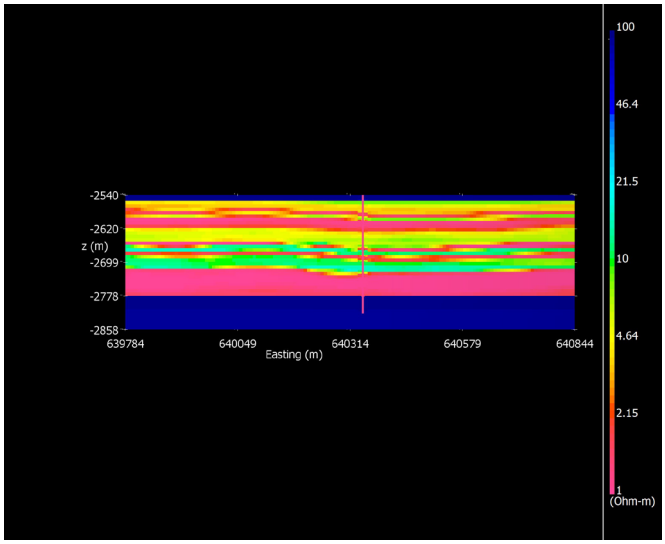

Figure 16. Final reservoir resistivity (Ωm) model. East-West cross-section at observation well.

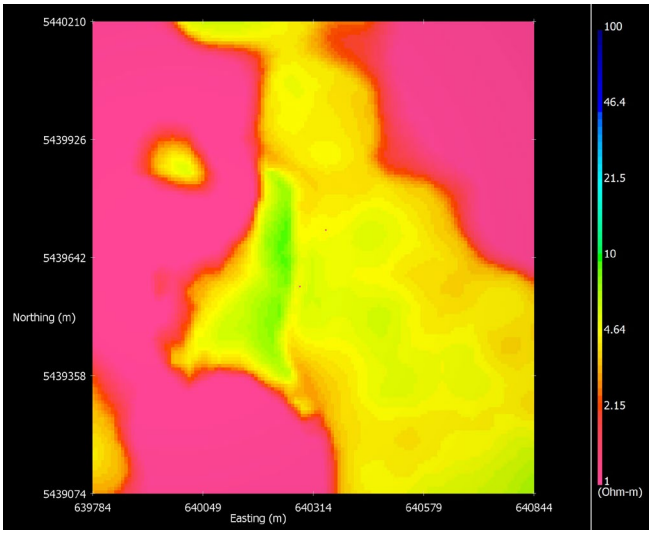

Figure 17. Stage 1 resistivity (Ωm) inversion model. -2650m Elevation slice.

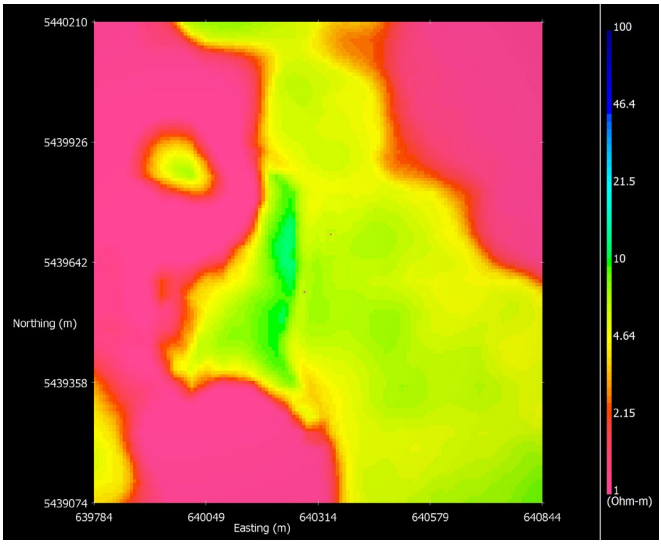

Figure 18. Final reservoir resistivity (Ωm) model. -2650m Elevation slice.

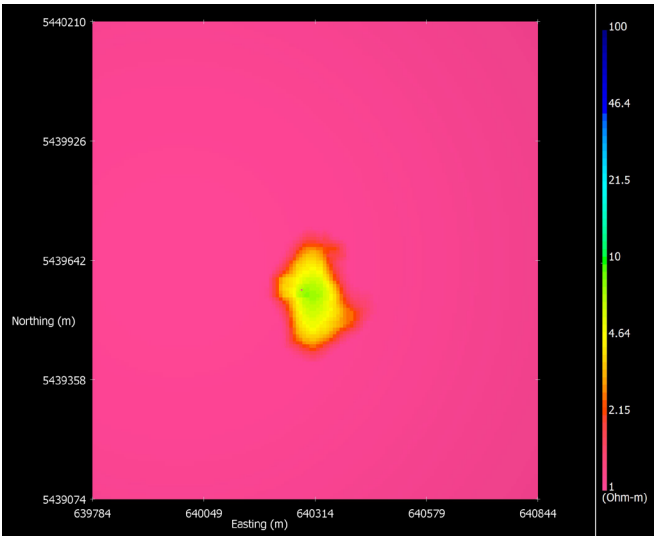

Figure 19. Stage 1 resistivity (Ωm) inversion model. -2730m Elevation slice.

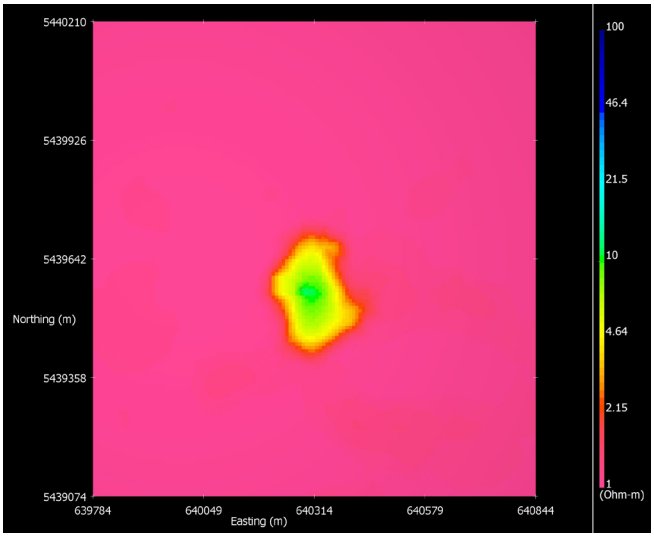

Figure 20. Final reservoir resistivity (Ωm) model. -2730m Elevation slice

Overall, our modelling and inversion study indicates that the 2019 Aquistore borehole to surface EM data did not contain sufficient signal to allow accurate single EM dataset imaging of the CO_2 reservoir. The inversion result from stage 2 of this workflow represents our best estimate of the CO_2 plume, and the predicted data agrees well with the observed data. Most of this signal is from near-surface features, which are fit in the first stage of the inversion workflow. The inversion results indicate a small expansion of the CO_2 plume relative to its extent in the 2017 saturation model that formed the basis for our starting conductivity model, but many other configurations of the plume are consistent with the data.

Without baseline data, the survey only has one time-stamp of measurements to model, which reduces the amount of signal in the data. This is because a baseline data set with transmitters and receivers in the same place allows for the two surveys to be subtracted from one another, which removes unwanted signal and focuses on the reservoir signal, which is changing over the time-lapse period. However, the wire-path was not recorded for the 2019 Aquistore survey. Without this knowledge it would be virtually impossible to replicate the initial design, and this transmitter positioning uncertainty would introduce too much error into the time-lapse data for it to be worth collecting. Therefore, any future time-lapse survey would have to involve a new baseline survey and an additional survey at a later time with the same survey layout.

We further tested the ability of the inversion to distinguish between CO_2 saturation models by running the stage-two inversions with starting models based on improved flow modelling of the CO_2 plume. These starting models were constructed by modelling the flow of CO_2 in the reservoir out to the time of the BSEM survey in July 2019. These flow models were then converted from CO_2 saturation to conductivity using Archie's law, as with the 2017 saturation model used above. The initial RMS data misfits for each of those two starting models and the 2017 saturation model were within 0.02%, with our flow modelling result having the best data fit. However, the extremely subtle difference between the initial data misfits suggests that the EM data alone do not have the sensitivity to evaluate which saturation model is best. Final data misfit results for the three models were identical, showing that all of them are equally viable models according to the EM data.

SYNTHETIC TIME-LAPSE EM INVERSION

Without time-lapse field data, it is not possible to fully assess the suitability of BSEM methods for monitoring of the Aquistore CO_2 plume. A time-lapse field study was originally envisioned for this project but was not carried out. Lacking appropriate field data, the decision was made to perform a synthetic study to demonstrate the capabilities of time-lapse EM inversion.

This synthetic study used the same survey configuration that was used for the single electromagnetic dataset at the Aquistore site but simulated what would happen if a baseline EM survey (using the same configuration as the 2019 survey) had been conducted prior to the commencement of CO_2 injection, in order to produce time-lapse data. The earth models used to generate synthetic data were based on the previous electromagnetic work done at the site and on fluid-flow modelling work used to predict the evolution of the CO_2 plume.

Time-lapse Inversion Methodology

We perform time-lapse inversion using the double-difference technique, which was developed for time-lapse seismic imaging [21, 22] and has also been applied to EM inversion [23, 24].

Double difference inversion is a two-stage procedure. First, a baseline dataset is collected before the physical property changes of interest occur (i.e., before CO_2 injection begins in the Aquistore case). The baseline data are inverted, generating a baseline conductivity model. Then after sufficient CO_2 injection, a second survey is performed keeping the survey parameters as close to the baseline values as possible. It is therefore essential to accurately record the baseline survey parameters, such as the transmitter and receiver layouts and the transmitter current waveform. After the follow-up survey, the change in the observed data between the two surveys is computed and used to form what's known as the double-difference dataset. This dataset is then inverted to estimate the change in the subsurface conductivity between the two surveys.

Survey and Results

In this synthetic study, we used the true survey layout and parameters used in the field survey conducted at the Aquistore site in July 2019. If a time-lapse EM field study were to be carried out at Aquistore in the future, we would recommend keeping the previous survey layout intact, and that is what is represented in this synthetic scenario. The time-lapse inversion solves for changes in electrical conductivity, the inverse of resistivity. To better illustrate small changes in the model over the time-lapse period, the inversion results below are presented as electrical conductivities in units of Siemens per metre (S/m) as opposed to resistivities, which have been used in this report up to now. Far from the injection well we expect zero change in conductivity. In converting conductivity to resistivity, its inverse, small variabilities in the model will be over-enlarged by the inverse operation. Therefore, we keep all values as conductivities.

As with the survey layout, the conductivity models used in this synthetic study were made as realistic as possible. Outside the reservoir region, where the conductivity is assumed to remain unchanged over the time-lapse period, we used the model recovered from the inversion of the 2019 field data. For the baseline pre-injection inversion, the reservoir was assumed to be 100% brine saturated, and its conductivity was computed using Archie's law with the same parameters used throughout this project. The post-injection reservoir model used the CO_2 2019 saturation model provided by the University of Alberta, discussed in the previous section. The pre- and post-injection conductivity models inside the reservoir region are shown in Figure 21. The responses from these two models are subtracted, yielding synthetic time-lapse data. These data can now be inverted to recover a change in conductivity model in the reservoir region.

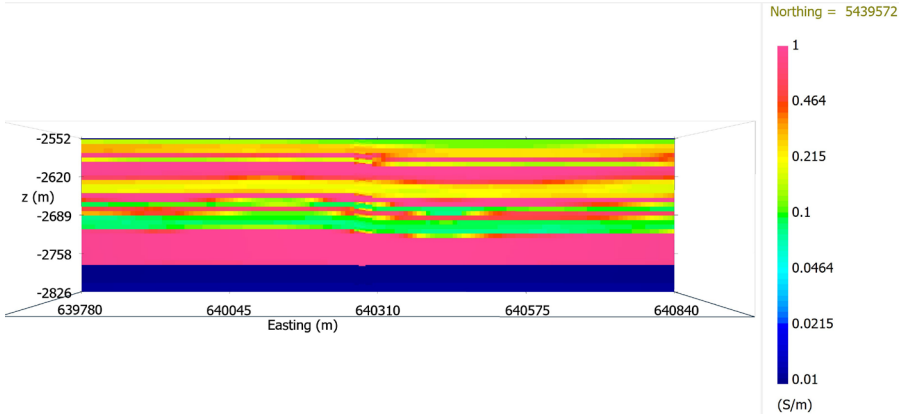

(a) Pre-injection conductivity model at the injection well.

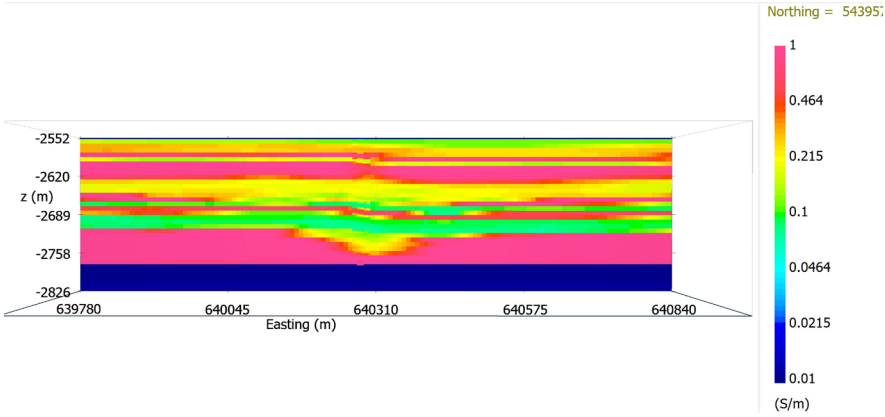

(b) Post-injection conductivity model at the injection well.

Figure 21. East-West cross-sections at the injection well through the pre- and post-injection conductivity models used to create the synthetic time-lapse data. Reservoir region only.

Results

We computed the "true" pre- and post-injection data for our synthetic experiment using the conductivity models described above and added artificial Gaussian noise. This added noise represents only the sensor measurement noise. We expect this to be Gaussian and I.I.D at each frequency of interest. The measurement noise spectrum was estimated by the data acquisition contractor based on field measurements of the ambient noise level. The time-lapse signal in our synthetic experiment was well above the instrument noise level. This is consistent with our previous forward modelling work, discussed in section 1 of this chapter, which was done before the 2019 field survey. The ratio of the absolute value of the imaginary 1Hz time-lapse signal to the instrument measurement noise level is plotted in Figure 22a, where values above one are shown in red and signify that at these locations more signal exists compared to noise. Conversely, locations shown in blue have ratios below one and represent locations where the noise has greater magnitude than the signal.

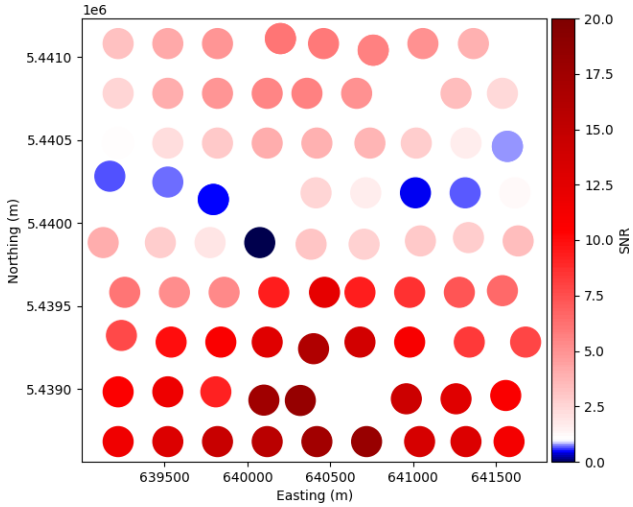

(a) Signal to noise ratio for instrument measurement noise.

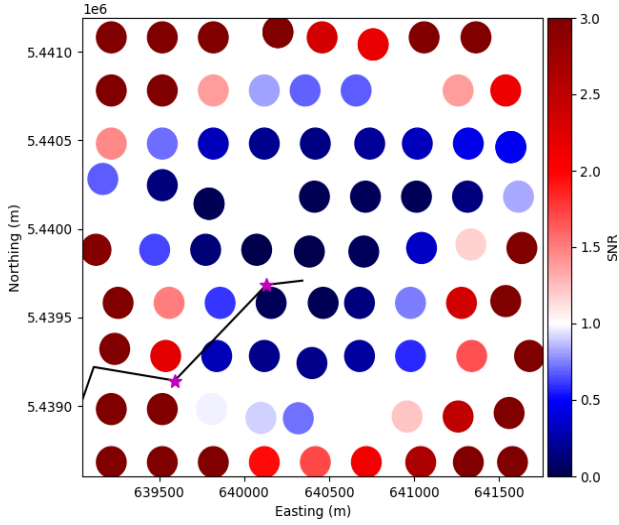

(b) Signal to noise ratio for a 20 cm transmitter positioning error. True transmitter wire path shown as black line. Stars show the points defining the wire path that were moved.

Figure 22. Signal to noise ratios for the imaginary data due to individual sources of error.

There are other important sources of error in the time-lapse experiment. The two most significant are changes in the near-surface conductivity (due to changes in soil moisture or the water table for example) and errors in sensor placement. Ideally, the EM transmitter and receivers would be installed permanently, or their locations marked by permanent survey markers. If that is not possible, great care must be taken to place the transmitter and receivers for the follow-up survey as close as possible to their baseline survey positions, as small errors in sensor placement can easily overwhelm the time-lapse signal for very deep, difficult targets, such as the Aquistore CO_2 plume. A rigorous analysis of the noise associated with near-surface conductivity changes was beyond the scope of this study, but we performed an analysis of the errors introduced due to sensor placement changes.

The sensor placement analysis was based on forward modelling the response due to an earth model consisting of steel cased wells embedded in a homogeneous half-space. Using a half-space model allowed us to isolate the effect of sensor geometry from variations in near-surface conductivity. We kept the receiver locations fixed and varied the position of a key section of the transmitter wire path. Figure 22b shows the result of moving the main section of the transmitter wire running through the study area by 20 cm. It shows the ratio of the true synthetic time-lapse signal to the change in the data caused by moving the transmitter wire. We see that a movement of 20 cm eliminates much of the signal in the area as the signal-to-noise ratio is below one in much of the survey area.

To verify this conclusion independently, we looked at the rate of change of the observed data with respect to distance from the transmitter and came to the same conclusion. Namely, that positioning errors in the transmitter wire or receivers of 20 cm or more is enough to yield a signal-to-noise ratio of less than 1 at the majority of receiver locations less than 500 m from the transmitter wire. Errors in placement of the transmitter wire will change the data in a spatially smooth manner, but random errors in the positioning of individual receiver electrodes could lead to a much more spatially heterogeneous distribution of errors.

In our synthetic time-lapse inversion, we assumed to know the location of the transmitter and receivers perfectly and data were contaminated with artificial Gaussian noise representative of instrument noise only. These data were inverted to recover an estimate of the change in conductivity $\delta\mathbf{m}$ due to CO_2 injection. The starting model for the inversion corresponds to a CO_2 free (fully brine saturated) reservoir. This corresponds to a $\delta\mathbf{m}$ of 0 everywhere. We then perform a voxel inversion with a limited number of subsurface cells active to find a final $\delta\mathbf{m}$ model. The active cells are chosen as three horizontal layers of the reservoir containing zones of sufficient permeability to allow CO_2 flow (based on the permeability model provided by EERC). These active cell layers are presented in Figure 23.

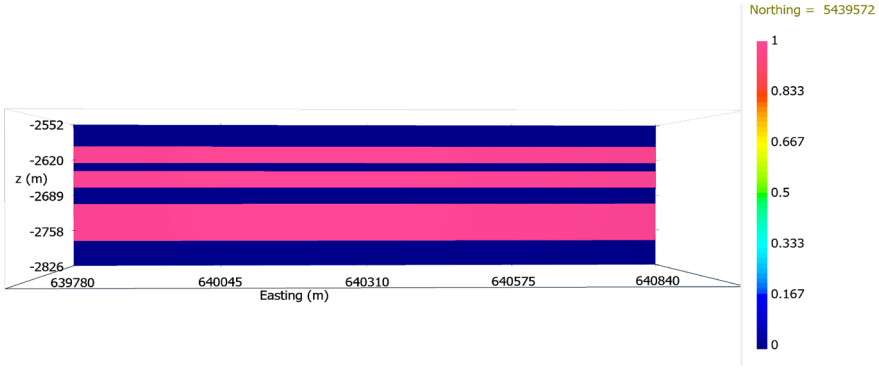

Figure 23. Active cell region in the reservoir for the time-lapse inversion. An active cell value of 1 refers to an active cell where the change in conductivity is allowed to vary and 0 refers to an inactive cell where the value cannot change.

The true and recovered change in conductivity models are displayed in East-West cross-section form in Figure 24 at the injection well location, with the true model in 24(a) and the recovered model in 24(b). Here we see that the time-lapse data enables recovery of a realistic estimate of the true CO_2 plume with EM data alone without relying on a flow model for a starting guess. This represents what one might hope to recover with time-lapse data in the field. Even with time-lapse data, the signals at the surface are still extremely small, and thus the ability to model the exact size of the various plumes is far from perfect, as the recovered top plume is too large compared to the true model and the middle plume does not extend far enough. But this exercise shows that there the time-lapse approach shows much more promise compared to non-time lapse data. In the field example discussed above, the data misfit decreased by only 0.2% during the course of the inversion, which demonstrates the inability to meaningfully fit much signal in the inversion process. In this synthetic trial, the data misfit drops by over four orders of magnitude or 99.99%. This shows that the initial guess does not adequately fit the data and the inversion can produce many changes in the model that cause it to better fit the time lapse data.

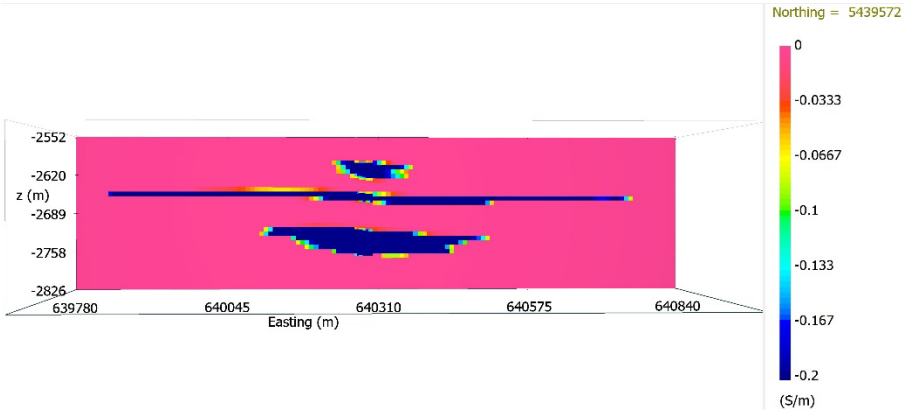

(a)True change in conductivity.

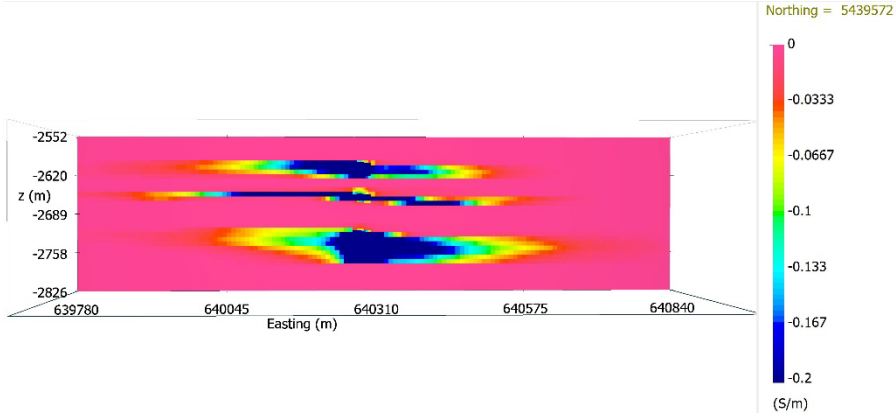

(b)Recovered change in conductivity

Figure 24. East-West cross-sections at the injection well through the true and recovered change in conductivity models in the reservoir region.

A caveat to these results is that, in this example, we presumed to know the near-surface conductivity values and the physical properties of the casing perfectly. In a true field scenario, this will not be the case. However, if a reasonable guess for the near-surface conductivity can be developed, as is the case at Aquistore, the observations from this synthetic study should be generally applicable to a field setting. We also presumed to know the transmitter wire and receiver location perfectly for both the baseline and follow-up surveys in this study. As we have shown, this is key to acquire reliable time-lapse data since small errors in these locations can quickly eliminate any signal from the reservoir of interest. As such, we recommend the installation of permanent sensors to minimize this location uncertainty as much as possible.

CONCLUSIONS AND RECOMMENDATIONS

This project studied electromagnetic monitoring at the Aquistore CO_2 sequestration site. The first phase of the project showed that the time-lapse BSEM signals from the Aquistore CO_2 plume (based on two years of injection) were well above instrument noise levels. This study provided guidance on choosing a survey design that would maximize the signal from the plume. However, it did not address all potential sources of error in the BSEM data, such as sensor reoccupation positioning errors, and did not address whether the plume could be resolved by inversion. This question of detectability versus resolvability is a crucial one. The forward modelling study addressed only the question of whether a survey could produce an EM signal from the CO_2 plume that could be detected by the receivers, not whether an inversion could robustly separate that plume response from the full EM response of the earth and reliably image the plume.

Following that work, a BSEM survey was conducted at Aquistore in July 2019. The BSEM data were inverted. We were able to fit the BSEM data, but a wide range of reservoir resistivities were found to be consistent with the data, and we could not be confident that our results accurately imaged the plume. The BSEM data are sensitive to the resistivity of the entire subsurface in the survey area and not just the injected CO_2. With a single survey, it was not possible to separate the plume signal from other effects in the data.

Further inversions were then performed using starting resistivity values computed from updated flow modelling. The results of these inversions were highly dependent on their respective starting models and yielded extremely similar data fits. We concluded that the single survey BSEM data could not help to discriminate between the different estimates of the plume provided by the different flow simulations.

The final stage of the project was a synthetic time-lapse inversion study. With the knowledge gained from the baseline BSEM inversion, our synthetic study sought to assess how well the plume could have been recovered, had a follow-up survey using the same configuration as the 2019 survey been performed. We found that a time-lapse inversion could image the CO_2 plume but only with extremely careful time-lapse surveying. An analysis of the potential impact of sensor positioning errors between the baseline and follow-up surveys showed that positioning discrepancies of as little as 20 cm might be enough to wipe out the signal from the plume. However, unlike in the single survey case, with careful surveying, the time-lapse data should show a signal from the plume that may be distinguished from other effects in the data and thereby used in an inversion to image the CO_2 plume.

In our view, time-lapse BSEM imaging at Aquistore would be highly unlikely to succeed without a reliable way to eliminate sensor positioning errors, such as permanent sensor placement or marking of sensor locations using permanent survey markers. Even without sensor positioning errors, imaging will be difficult and not guaranteed to succeed. Multiple factors, including seasonal variations in surface moisture and imperfect knowledge of well casing physical properties, will affect the background conductivity and introduce error into even a very well executed time-lapse survey. Ideally, baseline and follow-up surveys would be conducted at similar times of year under similar conditions to minimize these discrepancies. Additional surveys between the baseline and main follow-up survey would also be very useful in assessing the nature and magnitude of near surface

fluctuations. Using data at multiple frequencies should also be beneficial. Higher frequency data will be more sensitive to near-surface features than lower frequency data and unaffected by the reservoir. A full analysis of all factors that might confound a time-lapse survey is beyond the scope of this project. It is also important to note that even if careful time-lapse surveying definitively indicates change in the CO_2 plume, this is no guarantee that EM alone can image that change at sufficient resolution to constrain the geometry of the plume to a degree that is adequate for monitoring of carbon sequestration. EM is more likely to be useful in drawing quantitative conclusions about the plume if used in conjunction with other geophysical techniques.

Overall, monitoring CO_2 injection at Aquistore with single survey BSEM data is not feasible. It is possible to generate a reservoir EM signal well above instrument noise levels, but the signal is far too small to be separated from other electromagnetic effects and resolved by inversion. With time-lapse surveying, many of these other effects in the data are eliminated. In this case, electromagnetically imaging a target comparable to the Aquistore plume at such a large depth should be possible but will still be extremely difficult, especially if used a standalone technique rather than as part of a multi-modal imaging strategy. For a shallower reservoir, the signal from a comparable plume will be much larger, and we believe that borehole to surface electromagnetics can be an effective monitoring technique, especially when combined with other geophysical modalities.

ACKNOWLEDGMENTS

The authors wish to acknowledge financial assistance provided through Australian National Low Emissions Coal Research and Development. ANLEC R&D is supported by Low Emission Technology Australia (LETA) and the Australian Government through the Department of Industry, Science, Energy and Resources.

REFERENCES

1. David Annetts, Juerg Hauser, James Gunning, Boris Gurevich, Andrej Bona, Brett Harris, Milovan Urosevic, Mamdoh Ajami, John Cant, and David Annetts (2012*), A deployment strategy for effective geophysical remote sensing of CO_2 sequestration: Final report*, Technical report, CSIRO.
2. NETL (2009), *Monitoring, verification, and accounting of CO_2 stored in deep geologic formations*, Technical report, National Energy Technology Laboratory.
3. Jennifer Fohring (2016), *Adaptive optimal experimental design and inversion of a coupled fluid flow and geophysical imaging model for reservoir monitoring*, PhD thesis, The University of British Columbia.
4. PTRC (2015), *Aquistore Project Summary Report*, Technical report, Global Carbon Capture and Storage Institute.
5. T. Daley, J. Smith, J. Beyer, and D. Labreque (2015), Borehole em monitoring at aquistore with a downhole source, in *Carbon Dioxide Capture for Storage in Deep Geological Formations–Results from the CO_2 Capture Project Volume 4: CCS Technology Development and Demonstration; Results (2009-2014),* CPL Press.
6. M. Hoversten, R. Gritto, R. Washbourne, and T. Daley (2003), Pressure and fluid saturation prediction in a multicomponent reservoir using combined seismic and electromagnetic imaging, *Geophysics*, **68**:1580–1591.
7. E. Vilamajo, B. Rondeleux, P. Queralt, A. Marcuello, ,and J. Ledo (2015), A land controlled-source electromagnetic experiment using a deep vertical electric dipole: experimental settings, processing, and first data interpretation, *Geophysical Prospecting*, **63**: 1527–1540.
8. J. Borner, F. Wang, J. Weirflog, M. Bar, I. Gorz, and K. Spitzer (2015), Multi-method virtual electromagnetic experiments for developing suitable monitoring designs: A fictitious CO_2 sequestration scenario in northern germany, *Geophysical Prospecting*, **63**:1430–1449.

9. K. Tietze, O. Ritter, and P. Veeken (2015), Controlled-source electromagnetic monitoring of reservoir oil saturation using a novel borehole-to-surface configuration. *Geophysical Prospecting*, **63**:1468–1490.
10. E. Um, M. Commer, and G. Newman (2015), Finite element modelling of transient electromagnetic fields near steel-cased wells, *Geophysical Journal International*, **202**: 901–913.
11. V. Puzyrev, E. Vilamajo, and P. Queralt (2017), Three-dimensional modeling of the casing effect in onshore controlled-source electromagnetic surveys. *Surveys in Geophysics*, **38**: 527–545.
12. C. Schwarzbach and E. Haber (2018), Improved upscaling of steel-cased wells through inversion. *SEG Technical Program Expanded Abstracts*, pages 888–892.
13. M. Commer, M. Hoversten, and E. Um (2015), Transient-electromagnetic finite-difference time-domain earth modeling over steel infrastructure, *Geophysics,* **80**:E147–E162.
14. D. White, C.D. Hawkes, and B.J. Rostron (2016), Geological characterization of the aquistore CO_2 storage site from 3D seismic data, *Int J GHG Control*, **54**:330–344.
15. W. Peck, R. Klenner, G. Liu, C. Gorecki, and E. Steadman (2014), Geologic modeling and simulation report for the aquistore project, *Technical Report Task1 D93*, Energy and Environmental Research Center.
16. E. Haber and U. Ascher (2001), Fast finite volume simulations of 3D electromagnetic problems with highly discontinuous coefficients, *SIAM Journal on Scientific Computing*, **22**(6): 1943–1961.
17. C. Schwarzbach and E. Haber (2011), Finite element based inversion for electromagnetic problems using stochastic optimization. *SEG Technical Program Expanded Abstracts*, 567–572.
18. A. Hibbs (2013), Test of a new BSEM configuration at aquistore, and its application to mapping injected CO_2. *Technical Report Contract no. SMV-039*, Groundmetrics.
19. E. Haber, Z. Magnant, C. Lucero, and L. Tenorio (2012), Numerical methods for a-optimal designs with a sparsity constraint for ill-posed inverse problems, *Computational optimization and applications*, pages 293–314.
20. E. Haber (2014), *Computational methods in geophysical electromagnetics*. SIAM, 1 ed.
21. Z. Zhang and L. Huang (2013), Double-difference elastic-waveform inversion with prior information for time-lapse monitoring, *Geophysics*, **78**:R259–R27.
22. D. Yang, M. Meadows, P. Inderwiesen, J. Landa, A. Malcolm, and M. Fehler (2015), Double-difference waveform inversion: Feasibility and robustness study with pressure data, *Geophysics*, **80**(6):M129–M141.
23. G.M. Hoversten and C. Schwarzbach (2021), Monitoring hydraulic fracture volume using borehole to surface EM and conductive proppant. *Geophysics,* **86**(1).
24. M. Ayani, D. Grana, and M. Liu (2020), Stochastic inversion method of time-lapse controlled source electromagnetic data for CO_2 plume monitoring. *Int J GHG Control*, **100**:103098.

Carbon Dioxide Capture for Storage in Deep Geological Formations, Volume 5
Karl F. Gerdes (Editor)
© 2022 BP. All rights reserved.

Chapter 34

SMV KEY FINDINGS, CONCLUSIONS AND OUTLOOK

Scott Imbus[1] and Dean Thornton[2]
[1]Chevron CCP SMV Team Lead 2003-19, Houston TX
[2]Chevron Technology Center, Aberdeen, UK

ABSTRACT: CCP's Phase 4 Storage Monitoring and Verification (CCP4-SMV) program continued its role in identifying and developing risk reduction technologies and processes to ensure that CCUS is a safe and effective GHG mitigation approach. A range of technologies across the characterization, surveillance and "contingencies" space were executed to fill well-known and anticipated assurance gaps, or to achieve a substantial improvement in economics or field application. Chapter 21 of this volume outlines the background and results of each of the projects, whereas the present chapter seeks to place the findings in context of prevailing uncertainties in and, thus barriers to widespread, large-scale CCUS deployment.

INTRODUCTION

At the conclusion of CCP3 in 2014 [1], the SMV team recognized a number of continued technical challenges to widespread, large-scale deployment of CCUS:

- Realistic static/dynamic models and experimental approaches
- Integration and interpretation of M&V data
- Well integrity, particularly new P&A and mitigation techniques
- Contingencies
- Costs (including CCUS)

Applying its long-held strategy, the team identified specific knowledge gaps and sought to address them at an appropriate scale and venue. An assessment of the key project results and their significance to advancing CCUS is outlined below.

DISCUSSION

Chapter 21 of the present volume outlines results of CCP4 SMV technical projects by theme: Subsurface Assurance, Contingencies, Optimization and Surveillance and Field Trials. Although convenient from an organizational point of view, a more useful approach to describing CCP4-SMV's project accomplishments is to rank them in the context of significance to long-term CCUS assurance:

1. **Mont Terri Scale Well (CS-A)**: Injection of novel sealants to mitigate cement and annular defects allowed specific mechanisms of failure and their mitigation to be documented (Chapters 28 and 29) and modelled (Chapter 30) at the bench-field scale. The work links measured performance outcomes and analytics applied in such a way as to support further development of these sealants for deep storage site application. Furthermore, in addition to opening up new options for sealing CO_2-involved well leaks (at least temporarily until a permanent mitigation is in place), the study results indicate a greater role of cement / host rock annulus development than previously assumed. The

potential applicability to the broader storage system (seal leakage and thief zone) and modifications to improve permanence are future areas of investigation (note the related seal enhancement study in Chapter 24).

2. **CO_2 EOR as De Facto Storage**: Although CO_2 EOR has been deployed economically for over forty years, CO_2 disposition has only been empirically implied and comparisons of various flood mechanism only indirectly compared. The University of Texas, Austin, study (Chapter 25) also comprises the basis for describing short- and long-term trapping mechanisms relative to operations and ultimately, post-closure. The study did in fact launch expanded studies by UT which quantified carbon neutrality by carbon capture technology and EOR / storage process. A related study (Chapter 27) modelled cost considerations for first of a kind (FOAK) versus Nth of a kind (NOAK) based on project infrastructure and surveillance considerations.

3. **Mont Terri Fault Slip Experiment (FS-B)**: One of the key uncertainties in CO_2 storage assurance is the effect of faulting on seal permeability and thus CO_2-involved fluid containment. The exceptional, multi-scale surveillance of induced micro-seismicity (Chapter 31) showed the extent to which prodromal phenomena (rupture front) and permeability changes relative to hydraulic connectivity with the fault can be detected. The study provides critical data to model system resilience to induced seismicity from CO_2 storage or any subsurface fluid injection operations.

4. **Storage Project Start-Up/Early Operations Experience**: The study topic presented in Chapter 26 was of seemingly obvious necessity but not yet attempted (i.e., consider lessons learned before proceeding). For those saline CO_2 storage projects at any scale that had unexpected outcomes or even had to be terminated, the most frequent reason was inadequate subsurface characterization. This should be the most critical beginning and interim step in any storage project given that errors here are compounded in subsequent evaluations (e.g., reservoir simulation, surveillance design and even operational contingencies) and thus result on untoward events or project abandonment.

5. **Field Trials of Novel Surveillance Techniques (Aquistore)**: R&D wouldn't be R&D if all projects were successful. CCP4-SMV attempted to take advantage of the well-characterized and monitored saline storage project at Aquistore (Saskatchewan) to test two high risk technologies with a potential for enhancing established monitoring techniques (e.g., seismic) or as low cost alternatives to these. The borehole gravity tool deployed to detect the CO_2 plume (Chapter 32) could not achieve the stability to acquire useful data (i.e., not field-ready) and the electromagnetic surveillance project (Chapter 33) was thought to be feasible without a pre-injection baseline. A repeat survey was planned but modelling showed that fluid substitution in the near subsurface and slight offsets in receiver locations (from the prior survey) would overwhelm any useful survey.

The unique approach that the SMV team has applied to CCUS-related assurance and economic R&D has had outsized results for the investment level and has substantially influenced larger programs.

SUMMARY AND CONCLUSIONS

Introduction of Net Zero targets since the beginning of CCP4 has only enhanced the importance of CCUS owing to the reliance of negative emissions (e.g., BECCS, DACCS) to achieve these targets. Continued advancement of CCUS technologies and assurance processes has therefore become more critical given the anticipated, needed scaling from numerous individual projects to regional hubs.

Over the last 20 years, the CCP-SMV program has made substantial contributions to both the approach to tacking difficult technical problems but also anticipating how processes might improve acceptance of CCUS as a major GHG mitigation technique (e.g., risk assessment, surveillance technologies, and contingencies).

REFERENCES

1. Imbus, S., (2015) Chapter 49 "CCP3-Storage Monitoring & Verification (SMV): Implications of Key Findings and the Path Forward," in *Carbon Dioxide Capture for Storage in Deep Geologic Formations – Results from the CO_2 Capture Project*, Vol 4 *Development and Demonstration Results (2009-2014).* Gerdes, K.F. (editor) ISBB 978-1-872691-68-8, CPL Press, UK.

Carbon Dioxide Capture for Storage in Deep Geological Formations, Volume 5
Karl F. Gerdes (Editor)
© 2022 BP. All rights reserved.

Chapter 35

DEVELOPMENT OF CCS POLICIES AND REGULATIONS IN THE ENERGY TRANSITION

Arthur Lee[1], Ashleigh Ross[2], Poh Boon Ung[2], Vinicius Lima[3], Vicky Hudson[4], Lee Solsbery[5]
[1]Chevron Services Company, 6001 Bollinger Canyon, San Ramon, California 94583 USA
[2]BP, 501 Westlake Park Blvd., Houston, Texas 77079
[3]Petrobras, 28 Avenida Henrique Valadares, Rio de Janeiro, RJ 20231-030 BR
[4]Enviro. Resource Mgmnt (ERM), 33 St Mary Axe, London EC3A 8AA, UK
[5]ERM, 840 West Sam Houston Parkway North, Suite 600, Houston, TX 77024-392 USA

ABSTRACT: Phase 4 of the CO_2 Capture Project (2016-2022) was conducted in a time of increasing level of interest in CCS technology development and increasing activity in policymaking and creating incentives to enable project development. This chapter describes the key results, in detail, of the four studies carried out by the Policy & Incentives Team of the CO_2 Capture Project in support of CCS deployment.

BACKGROUND

Carbon Capture and Storage (CCS) has increasingly been recognized as a critical technology to achieve the long-term goals of the Paris Agreement since the release of the 2014 Intergovernmental Panel on Climate Change (IPCC) report [1]. The IPCC acknowledged the role of CCS as part of a portfolio of energy technologies and concluded that without CCS, the cost of GHG emissions reductions could be as much as 138% of the costs of an energy portfolio with CCS. In addition, in October 2018, the IPCC Special Report on Global Warming at 1.5 °C was released [2]. This report stated plainly in at least two of the four indicative low carbon transition pathways that CCS and negative emissions technologies (coupled to CCS) are critical to achieving both the 2°C and 1.5 °C goals. Both these reports, along with the International Energy Agency's [3], and others have raised the profile of CCS and generated significant interest among policy makers worldwide over this time period.

Phase 4 of the CO_2 Capture Project (2016-2022) coincided with this period of increasing interest in CCS technology development and increasing activity in policymaking and creating incentives to enable CCS project deployment. The CO_2 Capture Project's Policy & Incentives (CCP P&I) Team's focus also matched with this growing, evolving interest to understand policies and incentives that could enable wider deployment of CCS projects around the world. The CCP P&I Team surveyed existing and emerging policies and incentives, and analyzed both national and subnational policies. The team examined how policies and regulations could be leveraged from CO_2 enhanced oil recovery regulations transitioning into CO_2 storage regulations, executed a deep dive on the detailed regulations at two subnational jurisdictions of interest to the CCP member companies, and conducted a global analysis of whether CCS commitments and deployments are included in the "nationally determined contributions" of nations that are Parties to the Paris Agreement.

This chapter summarizes the goals and key findings from the four studies conducted in Phase 4:

- Best Practice in Transitioning from CO_2 EOR to CO_2 Storage

- Review of CO_2 EOR Transitioning to CCS in Texas and Alberta
- Role of CCS in the Energy Transition
- Survey of CO_2 Storage Regulations

STUDY: BEST PRACTICE IN TRANSITIONING FROM CO_2 EOR TO CO_2 STORAGE

Enhanced oil recovery (EOR) projects are primarily implemented to increase oil and gas production (tertiary recovery) with any long-term storage of CO_2, an ancillary benefit. When CO_2 injection projects are designed with CCS from the start, there is typically a site characterization process to review the storage formation according to best practice criteria for CCS.

CO_2 EOR regulations were not written to cover long-term underground storage of CO_2 as a CCS project. In oil and gas producing countries, there will be a body of laws, policies, rules, and regulations for hydrocarbon extraction including EOR activities. The legal/regulatory framework governing EOR anticipates that CO_2 injection will end and producing wells will be decommissioned, plugged, and abandoned after CO_2 EOR has ceased. Typically, EOR regulations do not account for what happens to the injected CO_2 after EOR activities have ceased.

An EOR project seeking to be treated as a CCS project presents a special case which must satisfy both oil and gas production rules and the rules for CCS storage sites. Regulations that govern CCS projects typically assume that the project was designed for the purpose of CCS from the beginning based on site selection criteria that emphasize permanence in underground CO_2 retention. Since the underground reservoir in an EOR project is pre-determined by the location of the existing oil and gas producing formation (i.e., not selected from the beginning for CO_2 storage purposes) then a separate process will likely be required to evaluate the oil and gas reservoir undergoing EOR to determine its viability for long-term underground storage of CO_2 under CCS rules and regulations.

EOR operators who focus on the commercial benefit of EOR and not on any additional environmental benefit, have their own concerns over any new legal requirements that they perceive could impose cost or impede their ability to continue to grow their EOR portfolios in line with traditional oil and gas activities. To encourage EOR, any proposed changes to policy and legal frameworks in relation to transitioning to CO_2 storage should take these concerns into account, provide clear legal guidance addressing uncertainties, and recommend cost-effective solutions.

Thus, the key question addressed in this study is:

'*How should best practices and regulatory frameworks for CCS project site characterization and monitoring be considered in cases where the underground pore space has been pre-determined as an existing oil and gas reservoir where CO_2 will be or is being injected for purposes of CO_2 EOR?*'

Challenges for Transitioning CO_2 EOR to CCS Storage

Most of the CO_2 injected into the reservoir for EOR remains permanently trapped under ground. It is this characteristic of EOR operations which makes them potential candidates for CCS project designation. Also, CO_2 costs are offset by revenues generated from the sale of recovered hydrocarbons. This is especially beneficial when comparing against the higher cost of standalone CCS projects that generally do not have an associated revenue stream.

As a basis for understanding the key practical challenges for a transition, it is helpful to identify the main fundamental differences between CO_2 EOR and CCS storage projects, as set out in Table 1.

Table 1. Fundamental differences between CO_2 EOR and CO_2 storage projects.

Aspect	*CO_2 EOR*	*CO_2 Storage*
Purpose	Increase oil and gas production efficiency (tertiary recovery) to optimise the hydrocarbon-bearing reservoir.	Reduce greenhouse gas (GHG) emissions to the atmosphere in support of climate change mitigation activities/obligations.
CO_2 Lifecycle	Captured from a natural or anthropogenic source, transported, injected into the hydrocarbon-bearing formation, and recycled through a closed-circuit process. [1]	Captured from an anthropogenic source, transported, and injected into the depleted hydrocarbon formation or saline for safe and permanent sequestration.
Primary Regulatory Framework	Oil and gas or petroleum legislation.	Ranges between: • CCS/GHG storage-specific legislation • Mining and mineral legislation • General environmental management/impact assessment legislation
Competent Authority	Oil and gas or energy regulator	Oil and gas or energy regulator; mineral resources regulatory; and/or environmental management regulator.

Site Characterization, Integrity, and Monitoring

CO_2 EOR projects are not required to investigate the structure of the oil and gas producing fields in which they operate to the same extent required by CCS site characterization rules because the oil and gas producing formation was not originally developed for the stated purpose of CCS.

As such, CO_2 EOR operations wishing to transition to CCS are not likely to have undertaken the technical analysis and site characterization called for in a built-for-purpose CCS project. Therefore, claiming credit for the CO_2 which has been stored underground from CO_2 EOR presents a special case.

The appropriateness of a potential CO_2 storage site needs to be carefully assessed to ensure safe and permanent storage of CO_2. This is determined primarily by three principal requirements:

- ***Capacity***–whether there is sufficient storage volume and whether it can be accessed
- ***Injectivity*** - whether suitable reservoir properties exist for sustained injection of CO_2 at economical industrial supply rates
- ***Integrity***–whether the site is secure with negligible risk of unintended migration or leakage

[1] Consensus on the incidental retention rate of the injected CO_2 ranges from 50-60% sequestration to 99%. See further *n.24* in *'Bridging the Gap: An Analysis and Comparison of Legal and Regulatory Frameworks for CO2–EOR and CO2–CCS*', Global CCS Institute (October 2013).

Given that depleted oil and gas fields are considered some of the best storage site options for CCS, capacity and injectivity are unlikely to be an issue in the transition from CO_2 EOR to CCS.

Integrity, on the other hand, could be a challenge given the need to ensure permanent storage of CO_2 to achieve climate change mitigation aims. Although the original geological traps that allowed the hydrocarbon to accumulate in the first place are still there, CO_2 EOR activities result in the drilling of numerous injection wells across an oil field to enhance production. Therefore, "*injection wells and abandoned wells have been identified as one of the most probable leakage pathways for CO_2 storage projects."* [4]

A key element related to the long-term nature of CCS projects is monitoring. The long-term monitoring of CO_2 storage sites required by CCS regulations goes beyond the post-closure and decommissioning requirements for CO_2 EOR projects. CO_2 EOR/CCS projects will need to ensure that appropriately robust monitoring regimes are in place to detect leakage, to account for losses in the project's overall emissions inventory and to ensure that measures are put in place to stop leaks when detected. Maintaining well integrity is important throughout the well's life cycle, from drilling to plugging and abandonment.

An issue that could affect well integrity and the occurrence of fractures is the potential impact of seismicity. Along with public perception risk, increased seismicity (even seismicity due to legacy disposal wells, unrelated to EOR) could potentially impact well integrity or result in leakage from CO_2 storage facilities, thereby reducing the climate change mitigation benefit of activities, or potential legal liabilities. While the seismicity issue is still being researched, the uncertainties, potential future regulatory changes, and risk context should be considered when addressing the transition from CO_2 EOR to CCS.

Any CO_2 EOR project seeking to transition to a CCS project will have to address the long-term monitoring requirements for CCS storage sites.

Pore Space Issues Likely to Arise in CO_2 EOR Transition to CCS

A CO_2 EOR project ends when oil production ceases, the production facilities are decommissioned, wells are plugged and abandoned and the lease to produce oil from that field is terminated. Any CO_2 EOR operation seeking to transition to a CCS project and receive credit for long-term underground storage of CO_2 as a GHG mitigation activity will likely need to address issues regarding the use of the pore space for CO_2 storage purposes beyond decommissioning of oil production.

The challenges associated with pore space ownership in a CO_2 EOR project are not insurmountable barriers to claiming credit for long-term underground storage of CO_2 from EOR. But the success of a CO_2 EOR project transitioning to a CCS project will likely require addressing these issues in the broader context of a clear, legal framework and possibly including engagement with the pore space owner to assess and deal with concerns.

Post-Closure Liability and CO_2 Ownership

Given the nature of CCS projects and the long term need to remove CO_2 permanently from the atmosphere, the issue of liability and ownership of CO_2 over time is important in ensuring that effective measures are put in place to ensure the efficacy of the projects. Liability issues arise with respect to any impacts that might occur to persons or property from operation of a CO_2 underground storage facility and in the worst (but highly unlikely) case of catastrophic release of CO_2 from the site.

Aspects which have been considered by government authorities in the context of a liability framework for CCS include:

- Management of leakage and permanence
- Stewardship of the storage site
- Costs and financial provision(s)

GHG Emissions Accounting Considerations

For a CO_2 EOR/CCS project, the GHG emissions during the production stage of the project have added complexity due to the nature of the EOR operations. In CO_2 EOR operations, a minority fraction of the injected CO_2 becomes miscible with the oil and will eventually be recovered in production wells when the oil is produced, sometimes referred to as 'break through' of CO_2.

The process of recovering, separating, recompressing, and reinjecting the CO_2 in an EOR operation is often referred to as 'CO_2 recycle.' Because there are energy requirements and potential losses of CO_2 during the CO_2 recycle process, the GHG emissions associated with CO_2 EOR/CCS need to account for the energy use and fugitive emissions inherent in the operation.

Several GHG accounting guidelines addressing CCS and specifically, CCS with EOR, have been published in the last several years. Most of these guidelines do address accounting for emissions associated with CO_2 EOR, especially in the recycle phase of production. The 2006 *IPCC Guidelines for National GHG Inventories* [5] address the geological storage of CO_2 within emission inventories. CCS projects have requirements to assess the potential for CO_2 to be emitted via leakage pathways, as follows:

- Properly and thoroughly characterize the geology of the storage site and surrounding strata
- Model the injection of CO_2 into the storage reservoir and the future behavior of the storage system
- Monitor the storage system
- Use the results of the monitoring to validate and/or update the models of the storage system

The 2019 Refinement to the 2006 IPCC Guidelines for National GHG Inventories did not change the CCS provisions [6].

Legal and Regulatory Review and Gaps Analysis

Over the course of the past 40 years, the application of CO_2 EOR has proven to be an effective technology for the purposes of maximising the oil-bearing reservoir output and incidentally sequestering the majority of the injected CO_2. Experience has been gained from over 130 commercial CO_2 EOR operations globally. Based on a mature regulatory regime and decades of industry practice, active CO_2 EOR projects exist primarily in the United States and Canada, with further commercial and demonstration projects, operating in Asia, Latin America, Middle East, and the North Sea.

This legal and regulatory review focused on the regimes in the USA, Canada, EU, Australia, and Brazil. The regions presented varying degrees of stakeholder attention and progression to potentially enable the transition process from a CO_2 EOR operation to the long-term sequestration of CO_2 as a CCS project.

There is currently widespread CO_2 EOR activity in North America, underpinned by decades of technical and regulatory experience in the oil and gas sector. In the US, the Environment Protection Agency (EPA) has produced a draft transition guidance document [7] pertaining to the Underground Injection Control (UIC) Well Programme and a memorandum [8] with key implementation principles to this effect. CO_2 EOR and CCS projects are currently feasible in terms of existing regulatory framework in the US (Federal); Canada (Alberta and Saskatchewan), the EU, and the UK. However,

further regulatory direction is required in terms of an efficient and legitimate approval pathway for transitioning from one to the other. This relates both to the primary laws for oil, gas and CO_2 injection and sequestration activities such as the UIC Well Programme, but also secondary or 'incidental' environmental, health and safety regulations.

In Australia, petroleum and GHG storage legislation exists at a federal and state level, with specific provision for CO_2 EOR. However, there is minimal evidence of any current or planned CO_2 EOR activity in the country and no explicit guidance for the prospective transition to long-term CO_2 storage.

In Brazil, CO_2 EOR activities are regulated under the environmental permitting processes of O&G projects at the federal and state levels. Although the current National Climate Change Policy allows for technological processes such as CCS/EOR to be considered as GHG 'sinks' in the National GHG Inventory, no further aspects or transition rules for EOR to CCS are detailed under a specific guidance or regulation.

Table 2 summarizes the CO_2 EOR and CCS regulations and the potential (theoretical at least) for a transition between these projects, to the extent these exist, across focus regions. The indicator key is as follows:

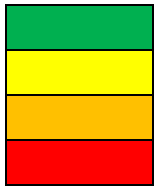

Regulations/process in place

Regulations/guidance in development

Policy discussions under way

No information available

Table 2. Overview of regulatory status of each country/region.

Type of Regulation	USA	Canada			European Union	Australia	Brazil
		Alberta	Saskatchewan	British Columbia			
EOR							
Transition							
CCS							

Key Findings of the Study: Best Practice in Transitioning from CO_2 EOR to CO_2 Storage

The analysis conducted and the information compiled in this report regarding the transition of CO_2 EOR to CCS support the 2013 CSLF [9] finding that:

> "*There are no specific technological barriers or challenges* per se *in transitioning and converting a pure CO_2 EOR operation into a CO_2 storage operation.*
>
> *The main differences between the two types of operations stem from legal, regulatory and economic differences between the two."*

There is a clear regulatory framework for CO_2 EOR and for CCS in most regions but there are insufficient provisions that would allow a CO_2 EOR operator to follow a clear transition pathway for legal and regulatory approval of a CCS project. Permitting requirements for design, commissioning,

operational management, decommissioning, and post-closure site stewardship, if any, differ for CO_2 EOR and CCS projects.

It is important to note that no existing policies or regulatory provisions in the regions studied explicitly prohibit the prospect of CO_2 EOR projects transitioning to CCS projects.

The main differences that require particular attention from regulators, policy makers and relevant legal authorities for CO_2 EOR transitioning to CCS are:

1. Storage site characterization and geological modelling
2. Monitoring of the storage site, reporting and verification
3. Site closure conditions and post-closure stewardship and liability
4. Conformance with national GHG inventory guidelines for CCS

Practically, these areas of difference are likely to have greater implications for existing CO_2 EOR projects that have been operating in accordance with the applicable oil and gas legislative framework before any attention was placed on CO_2 EOR becoming a candidate for transition to CCS. The legal and technical provisions for CCS projects to meet the requirements of the issues outlined above are such that an existing CO_2 EOR project may have difficulty complying, particularly in relation to site characterization and monitoring requirements.

In theory, and if incentivized, a proponent of a *new* CO_2 EOR project should be in a better position to design and plan for such a project to transition to CCS based on the evaluation of issues such as site characterization and monitoring requirements in the design of the entire project life (i.e., planning for both the CO_2 EOR and CCS phases).

It is recommended that specific guidance or regulation be provided setting out the specific requirements on new and existing CO_2 EOR projects which may wish to transition to CCS.

STUDY: REVIEW OF CO_2 EOR TRANSITIONING TO CCS IN TEXAS AND ALBERTA

The CO_2 Capture Project conducted a deeper analysis of the issues of CO_2 EOR transitioning to CCS in two jurisdictions: Texas in the U.S.A. and Alberta in Canada.

Texas

The Texas state government supports CCS to reduce greenhouse gas (GHG) emissions via financial incentives. These include incentives for advanced energy projects, which include CCS, and an authorization for CO_2 pipelines to become a common carrier. The United States Internal Revenue Service also provides a tax credit under Section 45Q of its regulations for CCS projects, which may also apply.

The regulatory pathway for a CCS project is in place for Texas, though no projects have yet applied for or been permitted under the U.S. Environmental Protection Agency's Underground Injection Control Program's Class VI well requirements [8], which may be required for the protection of underground drinking water.

For GHG emissions reporting, the EPA recently approved the first Monitoring, Reporting, and Verification (MRV) plan under Subpart RR regulations for CO_2 storage for the Oxy Denver Unit. This unit is a CO_2 EOR project since 1983 but is now intending to be recognised as a CCS project, noting that the facility will still be producing oil. Subpart RR reporting is required for all CCS projects to report GHG emissions under EPA's GHG Reporting Program. In the post-closure period, responsibility for GHG reporting of any leaks of CO_2 to the atmosphere is not explicitly addressed. This ambiguity is a potential gap or uncertainty in the current regulatory pathway.

Alberta

The government of Alberta supports CCS with financial incentives. Financial disincentives are also set to encourage reduction of greenhouse gas emissions. Alberta introduced a carbon tax, starting at $20 per tonne in 2017 and increasing to $30 per tonne in 2018. Further, the federal government of Canada proposed a carbon tax of $50 per tonne by 2022.

The regulatory pathway for CCS in Alberta is established and in place. The Carbon Capture and Storage Statutes Amendment Act, (2010) has promoted and simplified the regulatory process for CCS. In addition, several legislative changes have been made recently, and more are expected. In particular, the CCS project closure process is new in Alberta and more development is needed. In summary, a measurement monitoring verification (MMV) plan must be approved and updated every three years. The project operator must demonstrate that the MMV plan is being executed in compliance with regulations. A closure plan is also required as part of the MMV plan. When the criteria for closure are met, the operator of the project can apply for a closure certificate.

A regulatory framework exists in Alberta for approving and operating EOR projects. The government of Alberta has further identified a need to supplement the EOR regulations with the expectation that EOR projects will mature into CCS. However, the applicable regulations have not yet been supplemented. Therefore, the framework to transition CO_2 EOR to CCS is not yet in place.

STUDY: ROLE OF CCS IN THE ENERGY TRANSITION

Transition to a low carbon economy requires near zero emissions in the coming decades and will also need technologies that will "...achieve a balance between anthropogenic emissions by sources and removals by sinks of greenhouse gases in the second half of this century …," as stated in the Paris Agreement. Therefore, CCS should be central to the discussion of mitigating future GHG emissions from fossil fuels because CCS can remove CO_2 emissions from combustion or remove the carbon even prior to combustion, thus providing low or zero carbon emission fossil fuel usage.

This study presents three key areas of findings about the role of CCS in:

- Nationally determined contributions and mid-century strategies
- Global scenarios

Of the 163 submitted nationally determined contributions (NDCs) to the UN Framework Convention on Climate Change (UNFCCC), 14 specifically mention CCS, and five nations submitted mid-century strategies (MCS) that include some description of CCS. Those handful of nations that do mention CCS do so with extensive discussion about barriers to investments in CCS projects including the cost of CCS, the lack of finance and the lack of implementation of government policies and incentives.

The International Energy Agency, Massachusetts Institute of Technology, Intergovernmental Panel on Climate Change, Global CCS Institute, Deep Decarbonisation Pathways Project, and the EU Joint Research Centre have all projected the need for CCS to achieve the Paris Agreement goals. The contributions of CCS to scenarios that could successfully achieve the Paris Agreement goals range from 10 to 25 percent of the total GHG emissions response effort depicted in those scenarios. This points to the critical need for the rapid scale-up of CCS in the coming decades, which has yet to begin. The pipeline of major CCS projects has dried up in recent years, though a few projects in the U.S. are now being incentivized by the renewal of Section 45Q tax incentives and California's low carbon fuel standards. Further, because of costs and a range of issues, such as lack of policy framework, policy uncertainty, public perception, and potential long-term storage site stewardship, some business leaders in a World Energy Council survey have expressed negative sentiments about the prospect of deploying CCS. These difficult challenges point to a fundamental gap between the ambitious goal of the Paris Agreement and the reality of deployment of CCS projects.

This study also points out that even if nations did not mention CCS in their nationally determined contributions or in a mid-century strategy, they should consider CCS as part of future actions. As nations go through the every-five-year global stocktake, it could be beneficial for nations to analyse for and plan the conditions that would help in the future deployment of CCS to reduce emissions significantly.

The 'energy transition' is a widely used term referring to the evolution of the global energy mix toward a low-carbon (many activists say near zero-carbon) footprint for the production, transformation, delivery and end-use of energy in all its forms and applications. The biggest challenge for the energy sector, both producers and consumers in both developed and developing countries, is to confront the reality of the dominant share of fossil fuels in today's energy mix and consider viable pathways for the transition over time to a more climate-friendly energy mix. With the dominance of oil today in all modes of transport and the growing share of gas in power generation and petrochemicals, not to mention the many other end-uses for oil and gas, it is challenging to imagine in practical terms the low-carbon energy mix envisaged across all global energy scenarios. Logically, CCS should be central to the discussion of mitigating future GHG emissions from fossil fuels.

Thus, this study looks in some detail at current views on and projections for the role of CCS in the energy sector and what aspects need to be addressed for CCS to play a significant role in the energy transition.

Nationally Determined Contributions and Mid-Century Strategies

Across the 163 parties which have submitted NDCs to the UNFCCC, only 13 countries and the European Union on behalf of its 27 member states, have mentioned Carbon Capture and Storage. These are: Bahrain, China, Egypt, Iran, Iraq, Japan, Malawi, Mexico, Montenegro, Norway, Saudi Arabia, South Africa, United Arab Emirates, and the EU. The extent to which CCS is discussed varies considerably, from a mention as part of the scope, to its own section in the NDC as noted in Table 3.

It is useful to remember that countries may have more interest and focus on CCS than what is mentioned in their NDC, which is only a short document. For example, this is shown by the larger extent to which the EU comments on CCS within its Low Carbon Economy Roadmap for 2050, which is discussed later in this report.

The main messages from the 14 parties' NDCs are summarised in Table 4.

Table 3. The inclusion of CCS by different UNFCCC Parties in their NDCs.

Party	In table or list	In text with other policies	Own section of text	No data
Bahrain			✓	
China		✓		
Egypt		✓		
EU	✓			
Iran		✓		
Iraq				✓
Japan	✓			
Malawi	✓			
Mexico	✓			
Montenegro	✓			
Norway		✓		
Saudi Arabia			✓	
South Africa		✓		
UAE			✓	

Table 4. Main points of interest from select NDCs that mention CCS (2018 analysis).

Topic included in NDC	Number of Countries	Countries	Comments
R&D or technological needs	4	China, Iran, Malawi, Saudi Arabia	China and Saudi Arabia aim to invest in R&D, while Iran says CCS could address its technological needs. Malawi needs better technology to install CCS.
Investment required	3	Iran, Malawi, South Africa	All three countries state that investment is required for CCS to be successful.
Cost of CCS	2	Iran, South Africa	These two countries attempt to estimate the cost needed to install CCS in their country, US$0.45 billion for South Africa, whilst Iran estimates up to US$52.5 billion for their 6 plans to be introduced, but do not mention an individual CCS cost.
Importance of CCS for tackling Climate Change	3	Egypt, Iran, Norway	Egypt claim CCS is essential, Iran state it has high potential, while Norway class CCS as a priority in their NDC.
Mention specific projects	3	Bahrain, Saudi Arabia, UAE	Bahrain: BAPCO Carbon Recovery Plan and GPIC Carbon recovery plan. Saudi Arabia: Enhanced Oil Recovery project. UAE: project relating to steel industry and enhanced oil recovery.
Other benefits of CCS addressed	2	Saudi Arabia, UAE	Both these countries talk about the potential economic benefits and the opportunities for enhanced oil recovery.
Aims to be leading countries for CCS	2	Saudi Arabia, UAE	Saudi Arabia wants to build the world's largest CCS plant, while UAE wants to build the region's first commercial-scale network for CCS.
Minimal coverage of CCS	5	EU, Japan, Malawi, Mexico, Montenegro	These countries only mention CCS as an option within certain sectors or for mitigation without giving much further detail.

The Paris Agreement calls for Parties to create a long-term plan, or a mid-century strategy (MCS) [11], looking at how their 2050 goals can be achieved. As of December 2021, Andorra, Australia, Austria, Belgium, Canada, China, Chile, Colombia, Costa Rica, Czech Republic, Denmark, the European Union, Fiji, Finland, France, Germany, Guatemala, Hungary, Iceland, Indonesia, Japan,

Korea, Latvia, Luxembourg, Marshall Islands, Macedonia, Mexico, Malta, Nepal, Netherlands, Norway, New Zealand, Portugal, Singapore, Slovak, Slovenia, South Africa, Spain, Sweden, Switzerland, Thailand, Tonga, United Kingdom, Ukraine, and the United States have submitted plans.

CCS is mentioned in several of these MCSs, including now the United Kingdom and the United States with more details in their strategies compared to even three years ago. However, the uses for CCS in the plans to 2050 vary considerably, including for oil and gas, coal, EOR and industrial sectors such as chemicals, steel, and cement.

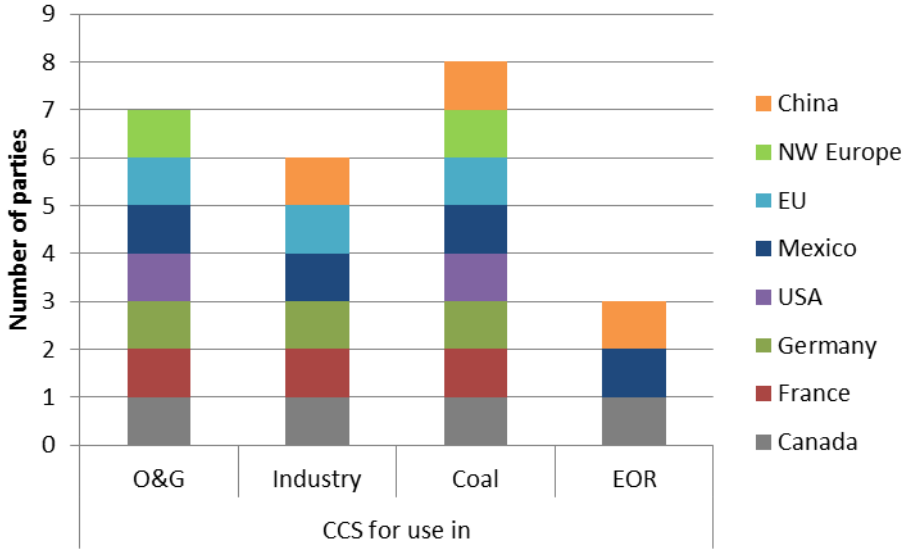

Figure 1. Summary of the different uses of CCS in key countries' MCSs and roadmaps.

In Figure 1, NW Europe refers to data from a report published by the PBL Netherland Environment Assessment Agency. This focuses on Belgium, Denmark, France, Germany, the Netherlands, and the UK.

Despite CCS being mentioned in five of the six mid-century strategies as well as three roadmaps to 2050, only four of these documents use scenarios to model emission reductions up to 2050 which include CCS. Furthermore, only three documents quantify the reductions which could be achieved by CCS.

In addition, most countries or parties consider there to be barriers to CCS implementation in their MCSs, whether it is present challenges or those faced when scaling up in the future.

Global Scenarios

The Deep Decarbonisation Pathways Project (DDPP) is a global research initiative looking at how countries can limit global temperature rise to 2 degrees [12]. With research teams in 16 countries responsible for 74% of global CO_2 emissions, the scenarios developed by this work are well respected and are used by many of the countries, for example in Canada's MCS. In contrast to methods used by others to develop scenarios, the DDPP uses back casting methods to determine steps required to get to the 2050 target. Country reports were released in 2015, of which 13 of the 14 included CCS in their scenarios. Ten of the 13 reports included values for CCS which are summarized in Table 5.

Table 5. Values for the contribution of CCS to limit global temperature rise to 2 degrees in the DDPP individual country reports.

Country	Findings on CCS
Australia	- Up to 21% of electricity supply with CCS in 2050 (9% gas, rest is coal) - CCS will capture 25-50% of emissions from non-energy sectors by 2050
Canada	- 23 Mt CO_2e captured and stored by 2050
China	- In 2050, CCUS is projected to annually remove 2737 Mt CO_2 (1867 Mt CO_2 from the power generation sector and 807 Mt CO_2 from industry emissions) - Accumulated CO_2 capture is approximately 27 Gt CO2 between 2010 and 2050
France	- By 2050, about 10 Mt CO_2 will be stored annually using CCS, equating to 20% of gas and 40% of coal consumed
Germany	- 57 Mt CO_2 captured from industrial sector in their 90% GHG reduction scenario by 2050
India	- 7099 to 9929 Mt CO_2 captured depending on the scenario (mainly coal) by 2050
Indonesia	- Power supply in 2050 in renewable and CCS scenario: 19% coal with CCS and 18% natural gas with CCS
Japan	- Decarbonisation in power sector "notably thanks to large deployment of CCS" approximately 97% reduction in carbon intensity of electricity from 2010 level by 2050
UK	- 318 Mt CO_2 captured between 2033 and 2050 in the industrial sector
US	- In the mixed scenario, 12.2% of electricity generation is from natural gas with CCS -In the high CCS scenario, 26.3% of the supply is from gas with CCS, 28.6% is from coal with CCS

The Joint Research Centre (JRC), a European Union academic consortium, published the Global Energy and Climate Outlook (GECO) [13], which assesses different countries' abilities to reduce emissions to stay within the 2-degree scenario. This paper estimated coal will fall to 10% of the global energy mix in 2050, most of which is associated with CCS, while total energy with CCS is 30%. This 30% includes all forms of CCS including biomass.

The International Energy Agency (IEA) sees a large role for CCS, accounting for 14% of emission reductions in the 2-degree scenario (2DS) [14] and 19% of reduction emissions in the BLUE Map scenario, in which energy-related CO_2 emissions are reduced by 50% by 2050 from 2010. However, the IEA raises concerns about several barriers which need to be addressed for CCS to be able to store the 7000 Mt CO_2 required by 2050 in the 2DS. Expansion of the current global CCS network is required, including significant research and development, investment, and the backing of governments through such actions as the implementation of laws and incentives.

In 2017, the IEA introduced a new scenario in their World Energy Outlook [15], the Sustainable Development Scenario, which focuses on achieving aims relating to climate change, reducing air pollution and universal energy access security. Therefore, its main aim is not to limit global surface temperature rise to two degrees, but it is useful to compare CCS contributions in this report. The trajectory of CO_2 emissions over time for this scenario is shown in Figure 2. The other main scenario introduced by IEA in 2017 is the New Policies Scenario, which uses existing policies and announced intentions, which overall leads to a slight increase in CO_2 emissions by 2040. In 2019, the IEA renamed the 'New Policies Scenario' to 'Stated Policies Scenario' to reflect the reality that what was considered new policies in 2016-2017, are now thought of as having been stated and are no longer that new in 2019.

CCS is projected to account for a further 9% of the cumulative reductions in emissions in the IEA Sustainable Development Scenario in comparison to the New Policies scenario. However, a value for CCS reductions in the New Policies Scenario is not given. Therefore, this scenario is excluded from the final conclusion that CCS accounts for more than 10% in all scenarios covered in this report, to reach the Paris Agreement 2-degree goal, as it is unclear what the total reductions from CCS would be.

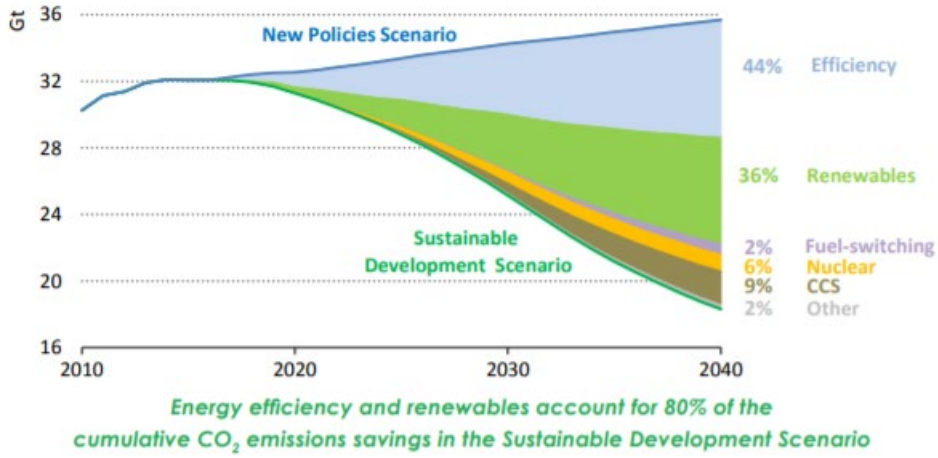

Figure 2. Global CO_2 emissions reductions in the 2017 IEA New Policies and Sustainable Development Scenarios.

The most recent MIT report, *Climate stabilisation at 2 degrees and net zero carbon emissions,* published in 2017, explores possible emission pathways to keep warming below 2 degrees [16]. It focuses on different climate sensitivities: high, medium, and low, equating to sensitivity of 4.5, 3.0, and 2.0 degrees C respectively.

One reference to CCS in the MIT 2017 report is made in a comparison of global energy use, using Integrated Global System Model (IGSM) calculations with estimates for CCS technology costs from the MIT future of coal study from 2007[17]. The 2017 MIT paper concludes that in comparison to the 2007 report on the future of coal, there is now an expected "reduced role for CCS and biomass" and an increased role of renewables (wind and solar), nuclear and energy efficiency. However, CCS could still supply up to 20% of energy use up to 2100.

The *Role of CCS in Meeting Climate Policy Targets*,[18] commissioned by the Global CCS Institute (GCCSI) in 2017, looks at the importance of CCS in meeting GHG targets. Research in this GCCSI report, focusing on the scenarios used in the IPCC 5th Assessment report, comments that "without large scale CCS, most models cannot produce pathways consistent with the 2°C goal." Comparisons between the role of CCS for 2 degrees, 1.5 degrees and INDC targets are shown in the figure below:

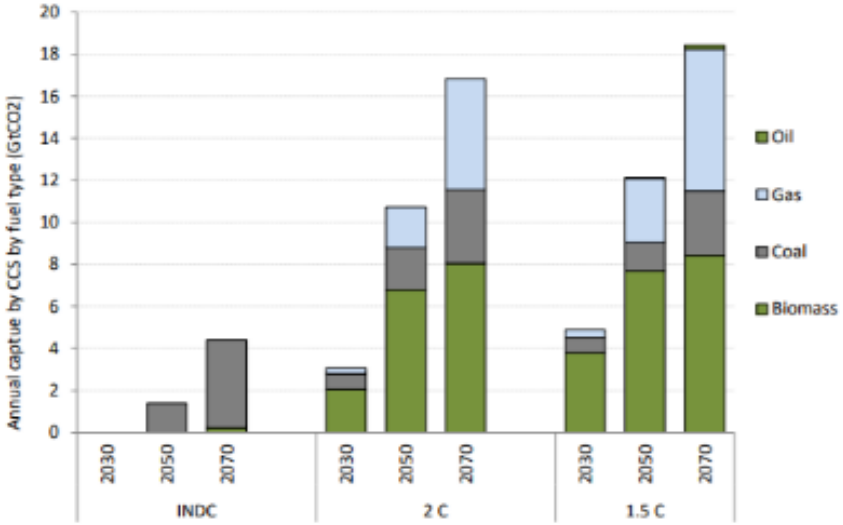

Figure 3. Annual carbon captured through CCS by fuel type, dependent on selected scenarios, for 2030, 2050 and 2070 (From GCCSI [18]).

The GCCSI report concludes that the "risks of CCS not being available as part of a portfolio of mitigation options to address climate policy targets are greater than the risks associated with attempting to develop it."

Summary Observations on CCS in Key Energy Scenarios

An important observation of this project is that the five leading scenarios reviewed all include CCS, and all of which estimate CCS will contribute 10 % or more of the reduction needed to reach a 2-degree world. This supports the conclusion that CCS has a sizeable role in emission reductions (see Figure 4).

In the DDPP report, CCS accounts for 10% of electricity capacity, whereas all the other studies state CCS contributions in relation to total emission reductions. While the DDPP (blue bar, Figure 4) is not directly comparable, it is collected here to show that such analysis still shows significant CCS contributions.

Figure 4 summarizes the contribution of CCS to various scenarios as compiled by ERM for CCP [19]. The MIT 2017 value in Figure 4 is taken from MIT's 'high optimism CCS scenario.' For the GECO 2015 report, the CCS contribution includes application to coal, gas, and biomass usage. The values from different models in the GCCSI report range from 3.7% to 24.3%. The IEA 2017 Sustainable

Development Scenario is not included in the figure as it is not a 2DS and no temperature rise is given, although it is expected to be in line with Paris Agreement objectives.

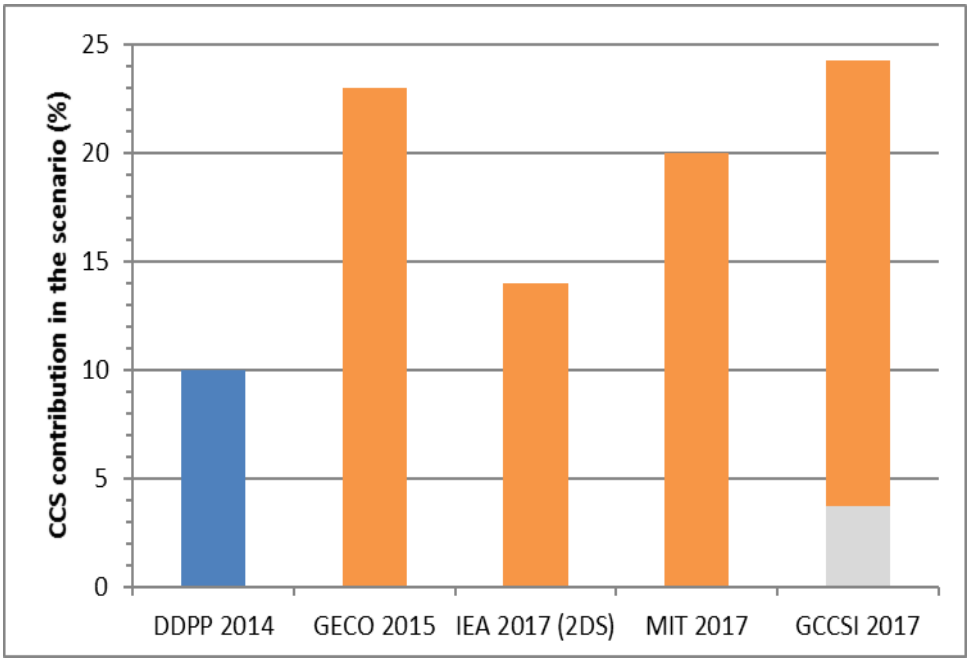

Blue bar: electricity contribution, Orange bar: total emission reduction contribution, Grey bar: minimum reductions contribution from range of models

Figure 4. ERM Summary: CCS contributions for the different scenarios to 2050 [19].

Figure 5 compares the energy mix predicted for 2050 across different models. The IEA scenario suggests that the energy mix in 2050 would be comprised of 12% coal and 16% gas. The IEA comments that the future contribution of coal and gas in their scenario is only so high due to CCS.

The main findings from ERM's review of key energy scenarios include [19]:

- The IEA 2DS expects CCS to account for 14% of carbon reductions against the reference transition scenario.
- All scenarios which include a contribution from CCS to reach a 2-degree scenario project that CCS will account for more than 10% of emission reductions, which is a substantial role in the future.
- 13 of 14 DDPP country scenarios include CCS.
- Current NDC commitments are not enough to reach a 2-degree world; there is an emission gap, which requires solutions which could include CCS.

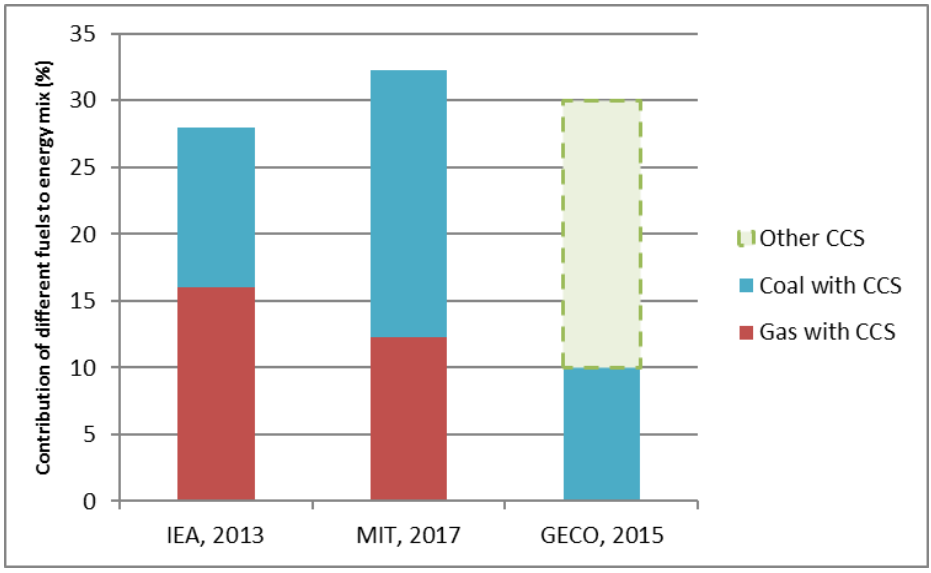

Figure 5. ERM: Selected Global energy mix projections with CCS for 2050 [20].

CCS in the Public Domain

From ERM's assessment of publicly available information on potential impact of CCS [19], it is clear that most sources are in agreement that CCS will be required to play a pivotal role in the energy transition. An outlier is the World Energy Council (WEC) *World Energy Issue Monitor* report [20], where energy leaders surveyed by WEC hold the opinion that CCS is decreasing in importance and its future is seen as uncertain.

Across most of the sources reviewed there are several barriers seen as holding back CCS development (although the GCCSI does not see some of these as significant, or disagrees on the numbers):

- CCS technology has been mature for some time, however large-scale projects to prove its application across the energy and industrial sectors, are few compared to earlier projections.
- Costs are currently too high on the whole, especially given low carbon prices. This could be mitigated by financial incentives, and any such support policies should be stable and long term.
- Regulation is absent (e.g., on coal sector emissions), which would support CCS deployment if retrofitting is to become more common or more plants that are CCS-ready are to be built.

Carbon pricing could serve as an effective policy for enabling investment in CCS and could serve to create a more level playing field with other low-carbon technology options.

Successful operational projects have typically benefitted from project-specific policy and financial support, there are lessons to be learned from these cases:

- Responsibility and accountability across the value chain will have to be more clearly defined to reduce risk premiums.

- Support for CCS will likely have to come from the national government level in the first instance, addressing some of the barriers above, before the private sector will become interested again.

Overall, the various leading energy scenarios cited in this report all conclude that current commitments are not enough and more must be done in order to increase our chances of meeting the 2-degree goal. This should leave an opportunity for CCS, especially with the high level of fossil fuel reliance predicted to continue into the future.

At the same time, the share of CCS's contribution to the transition to a low-carbon energy mix has gone down somewhat when the latest scenarios are compared to earlier scenarios, and energy sector leaders surveyed by WEC expect CCS to play a lesser role from their view of today's energy trends.

The challenge suggested by ERM's findings, and an area potentially ripe for further analysis, is how to 'square the circle' of CCS still needing to provide an estimated 10%+ of the projected GHG reductions required by 2050 in a 2-degree pathway when energy executives surveyed by WEC are not optimistic about CCS.

STUDY: SURVEY OF CO_2 STORAGE REGULATIONS

In 2019, the CO_2 Capture Project completed its final Phase 4 policy and incentives study: "Survey of CO_2 Storage Regulations." The following is a summary with key findings.

There is now a wide range of regulations that govern CO_2 storage projects across the globe. This study focuses on rules and regulations for CO_2 storage projects with an emphasis on key learnings, potential gaps, and main findings to support the viability of CO_2 storage projects, both onshore and offshore, in a practical and commercial context. This assessment is limited to CO_2 injection and long-term storage.

Regulators are aiming to promote transparency and generally considering public comments from key stakeholders when developing regulations. Although many of these regulations have yet to be rigorously tested due to a low level of deployment of actual CCS projects, reviews of regulations have been carried out using hypothetical projects (e.g., Victoria, Australia) or recommendations from technical panels (e.g., Alberta CCS).

Regulations for CCS have been shaped by multiple regulators, operators, and key stakeholder groups. We looked at regulations for permitting and for qualifying CO_2 storage projects for incentives. These regulations are not consistent across the globe, with various disparities in the treatment of long-term liability and post-injection monitoring requirements. Despite this, there are some areas, such as the need for proof of financial ability to cover potential liabilities and public engagement which are, on the whole, being approached in a similar way.

In general, there has been a growth in CCS policy confidence. This can be seen in the development of new regulatory frameworks, for example, the tax incentives provided by the Internal Revenue Service's 45Q provisions in the United States. This is also reflected in the growing ambition of certain countries such as the UK, who have created the CCS Council and CCUS Cost Challenge Taskforce with the aim to make CCUS economically feasible.

The GCCSI legal and regulatory indicator ranks only five countries as having legal and regulatory models which are sophisticated enough to address novel aspects of the CCS process: Australia, Canada, Denmark, the UK, and the USA. This shows there is still a considerable amount of development required in many countries, such as Japan and Indonesia, as highlighted in this study.

Key Findings

This study looks at selected recent developments in regulations for CO_2 storage projects with particular emphasis on any key developments, outstanding issues or gaps that might help or hinder commercial success of CCS. Two broad categories of policies and regulations are addressed:

- CCS incentives and funding
- Detailed comparison between key regulations

There is now a wide range of regulations that govern CO_2 storage projects across the globe. These regulations have been influenced by multiple regulators, operators, and key stakeholder groups. This study includes regulations for permitting and for qualifying CO_2 storage projects for incentives. The focus is on rules and regulations for CO_2 storage projects relevant to the oil & gas as well as other industries, with an emphasis on key learnings, potential gaps, and main findings to support the viability of CO_2 storage projects both onshore and offshore in a practical and commercial context. The research is limited to CO_2 injection and long-term storage.

CCS Incentives and Funding for CO_2 Storage

Significant developments have recently occurred in relation to incentives and funding for CO_2 storage projects. Most notable are developments in California, the European Union and at the federal level in the USA.

California

From January 1st, 2019, the CCS Protocol comes into force as part of the latest amendments to the California Low Carbon Fuel Standard (LCFS). The California Air Resources Board (CARB) aimed for the CCS Protocol to be the most robust regulation released to date, for the benefit of environmental integrity but also reputation of the technology. If the first CCS project fails, it could damage the viability of deployment of CCS, which CARB acknowledged is potentially very important for climate change mitigation. CARB indicated that California is *"willing to pay a premium"* for complying with the LCFS protocol, compared to the value of incentives of the California cap and trade system or with the highest value of credits of any program, which currently range from \$180-200/tCO_2e (referring to the market price of California LCFS credits, awarded for sequestered CO_2 by qualified CA LCFS CCS projects).

As part of the CA LCFS CCS Protocol, monitoring to ensure the stability of the CO_2 plume and track leakage, if relevant, must occur for 100 years post injection. Whilst the plume is stabilising, significantly more stringent monitoring is required. Once the plume is stable, the wells can be plugged and abandoned, with monitoring reduced to a lower level, which remains in force at this lower level for the rest of the 100-year period. The CA LCFS CCS Protocol has a buffer account, which is an assurance pool of credits that all projects contribute to. The credits paid into the buffer account depend on the project's risk rating, which is dependent on project specifics. The operator is only liable to pay back credits for the first 50 years if leakage occurs. Prior to 50 years post injection, credits from the buffer account up to and including the project's total contribution can count towards leakage-related credit invalidation. If the leakage exceeds this contribution to the buffer account, the project operator must retire any outstanding credits. After 50 years post-injection, the CCS project operator is no longer responsible for credits found to be invalid due to leakage. Other credits from the buffer account can be used to cover this leakage. Thus, the burden on CCS project proponents under the CA LCFS after 50 years is only lower-level monitoring, not liability for credits if there is post-closure leakage after 50 years.

European Union

As part of the latest amendments to the Directive for the EU Emissions Trading System, which occurred in March 2018, the European Commission developed an Innovation Fund that launched in 2021. A total of 450 million EU ETS Allowances have been put aside to support low-carbon technologies including carbon capture and utilisation as well as products substituted for carbon intensive ones. The fund is also available to help stimulate the construction and operation of CCS projects as well as innovative renewable energy and energy storage technologies. Projects in all EU member states including small-scale projects are eligible for the new fund.

USA

In the USA, the FUTURE Act provides additional financial certainty for private investors and developers of carbon capture projects by lifting the current cap on available 45Q tax credits and increasing their value for each ton of CO_2 captured and safely stored or put to beneficial use. The tax credit seeks to incentivise private investment in commercial deployment of technologies to capture CO_2 from power plants and industrial facilities for enhanced oil recovery (CO_2-EOR), other forms of geologic storage and for beneficial uses of CO_2. The incentive is performance-based, so only projects that successfully capture and store CO_2 can claim the credit. The updates to the tax credit include:

- 10-year ramp up to $35 per ton for CO_2 stored geologically through EOR
- 10-year ramp up to $35 per ton for other beneficial use such as converting carbon emissions into fuels, chemicals, or useful products like cement
- 10-year ramp up to $50 per ton for CO_2 stored in other geologic formations and not used in CO_2-EOR or for other purposes
- No cap on total credits that can be claimed under 45Q
- Eligible projects that begin construction within seven years of the enactment of the FUTURE Act (i.e., before January 1, 2024) can claim the credit for up to 12 years after the carbon capture equipment is placed in service.

Detailed Comparison between Key Regulations

As part of the research, a detailed comparison was undertaken of five different regulatory frameworks that best address the key regulatory issues:

- EPA UIC Class VI Well Permits
- California LCFS
- Alberta CCS Regulatory Framework Assessment recommendations
- EU CCS Directive
- Australian Offshore Petroleum Amendment

The study examined a broad international spectrum of regulations from the USA, Canada, the EU, the UK, Netherlands, Norway, Indonesia, Japan, and Australia.

Post-Injection Site Care (PISC) and Site Closure

The period for Post-Injection Site Care (PISC) varies from a maximum of 100 years monitoring for the CA LCFS to a minimum of 15 years in the Australian Offshore Petroleum Amendment. This is certainly a key area where there is disparity between regulations, while there is also flexibility in some regulations on the length of PISC. The extent to which the variation in PISC regulations may be a barrier to CCS project viability depends on the overall context of each regulatory regime. Project developers who operate globally will certainly need to take into account that such wide variations in the CCS regulatory regimes do exist.

Financial Requirements

Mandatory regulations such as the EU CCS Directive or the US EPA Underground Injection Control (UIC) Class VI regulations require proof of financial resources to cover any obligations relating to corrective measures or leakages. Proof of financial ability to cover potential liabilities is fairly standard across various CCS regulations, except in California. The CA LCFS considers this aspect out of scope because CCS project operators apply for CA LCFS credits as a financial incentive, rather than to satisfy regulatory compliance.

Long Term Liability

There is considerable disparity among regulations in relation to long-term liability. For the US EPA UIC Class VI well permits, site closure does not eliminate responsibility or liability, and the EPA cannot transfer this liability between entities. For the CA LCFS, the operator is liable for leakage during the first 50 years (to buy credits to offset leakage), after which any liability is paid from the CA LCFS buffer pool of credits.

Liability is transferred to the Member state authority after at least 20 years after site closure in the EU CCS Directive unless there are concerns over permanence of the CO_2 storage. Liability is also transferred back to the Commonwealth under the Australian Offshore Petroleum Amendment, depending on when a closure assurance period occurs, which is after at least 20 years. In summary, not all regulations allow a transfer of liability back to the state or relevant authority, and those which do have differing time frames for when this can occur.

Liability for Leakage and Environmental Damage

In all regulations, there is a level of financial liability for environmental damage or leakage of CO_2. How this is paid depends on whether there is a credit system in place. For example, under the EU CCS Directive, surrender of emission trading allowances can cover the liability. The Alberta RFA recommends creation of a post-closure stewardship fund which all projects contribute to, which has a similar role to the buffer pool which has been established in the CCS Protocol of the CA LCFS. The remaining regulations mainly require the operators to correct the physical damage and pay any fines.

Public Engagement

In general, the regulators all aim to be transparent and engage the public and other key stakeholders. The US EPA is required to respond to comments made on UIC Class VI permit applications. For the CA LCFS, the applicants must respond to comments on applications to qualify. The Commonwealth Minister will consider comments made concerning applications in Australia. Under the EU CCS Directive, provisions must be put in place by member states to engage the public, in addition to allowing public access to the EU Commission's reviews of all CCS permit applications within member states.

Thresholds

Some regulations apply only to projects meeting certain requirements. For example, the EU CCS Directive and the Australian Offshore Petroleum Amendment do not apply to projects storing less than a cumulative 100 kilotonnes of CO_2. The other regulations do not have any thresholds; all projects which are undertaking geologic storage of CO_2 must have a valid permit.

Monitoring and Reporting

Monitoring and reporting plans and requirements vary considerably between regulatory regimes. Most regulators require an annual report, but others have more demanding requirements. For example, the CA LFCS requires semi-annual reporting from CCS projects, in addition to informing CARB every quarter of details relating to quantities of fuels sold for the CA LCFS. In general, most regulators require a monitoring or environmental plan to be submitted with the application. Elements of the plan include how the plume is monitored, what technologies are used, and how this will be recorded and verified if appropriate. In addition, there may be other monitoring requirements for the surface, water sources or subsurface, with the duration of the monitoring period varying between regulations.

Pore Space Access

Issues relating to access to pore space for storage are considered out of scope for both the EPA UIC Class VI well permits and the CA LCFS. This is because both programs see pore space access as the CCS project developers' commercial responsibility (i.e., if there is no pore space access negotiated by the developer, then there is no CCS project for the US regulators to review.)

The EU CCS Directive requires member states to ensure measures are taken to allow operators to obtain pore space access. In Australia, operators must apply for access to acreage through the Commonwealth Minister for offshore storage.

In many cases, access to pore space and duration of that access for specific projects may be seen by regulators to be a commercial siting issue for project developers governed by local laws for mineral rights or sub-surface activities, and not a permitting issue *per se*.

Flexibility

The CA LCFS CCS Protocol is a very prescriptive regulation. CARB has concluded that the philosophy for fixed regulatory requirements has been validated by credits granted through the protocol receiving the highest market value of credits of any current program. The LCFS credits were valued in January 2021 at approximately US$200/tonne and are currently priced at approximately $145/tonne (as of December 2021). The value of sequestered CO_2 emissions under the LCFS is a proportion of the equivalent number of LCFS credits minus loses from breakthrough gases and operational emissions. CARB felt that rewarding CCS project developers with this level of benefit is in line with regulations to ensure certainty for long-term underground retention of CO_2.

Many other regulations do allow some form of discretion in certain permit conditions by a senior regulator such as the EPA Program Director or the Commonwealth Minister, depending on project-specific circumstances.

Other Variations Between Regulations

There are some other variations between regulations worth noting. In the USA, states can apply for primacy to regulate the UIC permits themselves instead of the EPA. This could lead to inconsistency between implementation of the regulation between states but could also streamline or speed up CCS project applications in some states compared to others.

In contrast, to maintain consistency in the EU CCS Directive, the EU Commission intends to review all CCS project applications across all member states.

Finally, in line with the stringent nature of the CA LCFS regulations, operators must have their projects verified every year in order to assure the CO_2 is being stored safely.

UIC Class VI and Class II Comparison

The US EPA UIC Class VI well regulations for CCS are quite extensive, much more so than the UIC Class II regulations for EOR projects. The main additional requirements for Class VI permit regulations over Class II are greater financial responsibility, continuous monitoring during operations, more rigorous testing, and 50 years post-injection site care (PISC). In more detail:

- Class II requires financial responsibility until the closing, plugging, or abandoning of the well. Class VI responsibility addresses corrective action, PISC, site closure, emergency, and remedial response.
- Class VI requires installation of continuous recording devices, alarms and surface or down-hole shut-off systems or other safety devices.
- PISC–This is not a requirement for Class II and is stated as 50 years for Class VI, but depends on the director's discretion.
- Class VI Regulations specify the depths of casing strings and cementing to the surface. Well materials must be compatible with fluids with which they come into contact.

Other Regulatory Developments

This study also looked at other regulations or standards which are not part of national frameworks. A key finding was that the London Protocol amendment to allow transboundary movement of CO_2 is still to be ratified, but the legal framework has been in place since 2009, with the amendment to sub-surface offshore storage approved in 2006. In 2011, ISO/TC 265 for carbon dioxide capture, transportation and geological storage was created. The role of the ISO standards is advisory, since they are not binding government requirements, but they have the potential to be useful in a number of different situations, such as informal guidelines for CCS project developers to follow in countries that are still developing their own government regulatory frameworks for CCS.

GCCSI Legal and Regulatory Indicator

Since the last publication of the GCCSI legal and regulatory indicator in 2015, 11 countries have introduced new legislation or made legislative amendments related to CCS, but only seven of those countries have had a change in their GCCSI rating score, out of the 55 countries included in the assessment. The top five countries for CCS regulation are Australia, Canada, Denmark, the UK, and the USA, referred to as Band A. The GCCSI states that legal and regulatory models in these countries are "sophisticated and address novel aspects of the CCS process," although the results show these nations have seen little to no change since the 2015 publication. Overall, the GCCSI report concludes there has been little to no material change in the status of CCS legal and regulatory models in many countries worldwide between 2015 and 2018.

Expected Developments

Many significant developments are expected to occur in the next few years. In particular, these could be the inclusion of avoided emissions from CCS in the US National GHG inventory, update of the British Colombia LCFS to include CCS, the development of a Canadian Clean Fuel Standard at federal level, and the publication of more ISO standards for CCS. In addition, in the USA, the National Petroleum Council was requested by the US Secretary of Energy to undertake a study on CCUS and the potential pathways leading to CCUS deployment at scale, which resulted in a "Roadmap for CCUS Implementation," published in December 2019.

Key Themes from Interviews with Regulators and Industry Experts

This study is primarily based on an approach of policy and regulatory reviews supported by interviews with policymakers and regulators from the jurisdictions of interest. Key themes were identified from the 15 interviews conducted for this study, which included a range of regulators and industry experts (See Appendix for a full list of the interviewees). Regarding the overall maturity of the CCS regulatory environment, there was a divergence of opinions among the interviewees about whether such regulations are sufficiently advanced for broad deployment of CCS. Many interviewees believed that some key barriers remain including the insufficient clarity and support around ownership of pore space. Some interviewees felt some regulations were too detailed or too prescriptive.

The majority of the people interviewed considered current tax credits to be insufficient. One person interviewed suggested implementing an investment tax credit in order to further CCS research and development.

When discussing the key barriers, the main issue raised by interviewees was a lack of experience of regulators, a barrier that was also recognised by regulators themselves. As there have been a limited number of projects to date, agencies lack experience in implementing the regulations, so it can be a long process. In addition, identifying gaps or issues in regulations is difficult until enough projects have tested the regulations.

When discussing next steps for the CCS regulatory landscape during the series of interviews undertaken for this report with CCS experts, the following suggestions were put forward by the interviewees:

- Incentives such as 45Q are not attractive enough; more money is required to incentivise CCS projects over a longer time horizon.
- Projects need subsidising so pilots can be successful and build momentum, to enable future projects and regulatory agencies to learn from pilot projects.
- More practicality relating to regulations such as 50-year default opposed to 100 years, or more flexibility–it should be acknowledged this was not the view of all interviewees, with one commenting legal flexibility can make industry nervous since they prefer certainty.
- Streamlining the regulations while finding the balance among acceptability, protection, and project liability.
- There is a role for governments to push CCS; for example, a role for avoided emissions from CCS to be expressly included in national GHG inventories.

The following themes were key discussion points of the interviews, and the summary of the key findings of the research and differing viewpoints of the interviewees are summarised below.

Where are the general consistencies in CO_2 storage regulatory approaches?

When comparing the details of CO_2 storage regulations, there are many areas with consistent approaches. Most regulations require some form of proof of financial resources for liability purposes, with operators liable for leakage during the project lifetime and expected to mitigate such leakage. In general, CCS regulations have a very transparent process for reviewing applications and publishing comments from stakeholders and the responses from CCS project proponents. Many regulators commented that this feedback process was a critical part of developing regulations and approving applications. Apart from the CA LCFS, most regulations include some level of flexibility and discretion in relation to aspects of the framework, for example not mandating a fixed period for PISC, or allowing approved of monitoring plans on a case-by-case basis.

Where are the greatest differences or inconsistencies in regulatory approaches? And what are the reasons for these disparities?

One of the key differences among the regulatory approaches is the duration of Post-Injection Site Care (PISC), varying from 15 to 100 years of monitoring. Another is the approach to long-term liability, with some (but not all) regulations allowing transfer back to the state or regulator, but the time frame when this occurs does vary. The CA LCFS CCS Protocol probably entails the most extensive regulations, with the highest level of monitoring requirements. This is due to the desire by CARB to ensure the success of the LCFS and to not damage the reputation of CCS by having a failed project due to insufficiently rigorous requirements. As noted previously, in return for fixed regulatory requirements, CARB indicated that California is "*willing to pay a premium"* compared to the incentives in the cap-and-trade system for CCS projects complying with the LCFS protocol for sequestered CO_2 emissions, The LCFS credits have the highest value of credits of any program and currently range from \$180-200/tCO_2e. It is worth noting the price of LCFS credits is market driven and does fluctuate. In July 2016 credits dropped to \$67 per tCO_2e, but recently has had a higher value, with a low of \$124 per tCO_2e in the period March 2018 to February 2019, and a low of \$171 per tCO_2e in the period September 2018 to February 2019.

Another difference in regulatory approach is the value of incentives such as 45Q versus CA LCFS. In general, there has been an increase in funding recently, despite withdrawal of other funding mechanisms to encourage CCS since the previous CO_2 Capture Project (CCP) regulatory review published in 2015 [21]. Overall, this variation in incentives is due to countries or states having different priorities or being in different stages of developing their regulatory frameworks. For example, the EU Fuel Quality Directive included CCS as part of fuel pathways since 2009. In comparison, the CA LCFS introduced CCS in 2018, and British Columbia and Canada are still developing fuel quality standards and considering the basis for including CCS projects.

Where are there potential conflicts posed by regulatory requirements?

It is most likely conflicts will occur where operators are looking to introduce projects in the same region or country where states or member states have differing frameworks. One example would be in the USA, where the CA LCFS CCS requirements are more stringent than those of the EPA UIC Class VI well regulations or where states with primacy differ in implementing regulations. However, the CA LCFS is an optional scheme offering an incentive, so this is not necessarily a conflict but a decision to be made by the operator if they are willing to address these issues. In the USA the more likely conflict would come from states which have primacy having slight differences in regulations to the EPA. However, this is hard to determine at the time of this writing, with only one state having primacy for Class VI. However, any discrepancies are expected to be minor.

Another possible conflict could be in the EU, with differing legal and regulatory regimes available to support the implementation of the CCS Directive. However, no major conflicts have been identified to date and the final EU Commission review of applications should help to promote consistency.

Finally, another potential conflict is the difference in long-term liability across Australia. The federal regulations allow transfer of liability back to the state, but the state regulations do not allow this.

Overall, there are differences in monitoring or well requirements, but these are usually between countries, and are only likely to become material as deployment grows. These disparities are also likely to be tested as more projects are approved and as the regulations get trialled by actual projects and the regulators gain experience.

Conclusions of this Study of CO_2 Storage Regulations

Overall, regulators are aiming to promote transparency and generally seem to be taking into account comments from key stakeholders when developing regulations. Although many of these regulations have yet to be rigorously tested due to a relatively low level of CCS project deployment, reviews of regulations have been carried out using hypothetical projects (Victoria, Australia) or recommendations from technical panels (Alberta CCS).

Regulations that have been developed are not consistent across the globe, with key disparities relating in particular to the long-term liability and post-injection monitoring requirement. Despite this, there are some areas such as the need for proof of financial ability to cover potential liabilities and public engagement which, on the whole are being approached in a similar way.

In general, there has been a growth in CCS policy confidence. This can be seen by the development of new regulatory frameworks, highlighted by inclusion of incentives such as 45Q. This is also reflected in the growing ambition of certain countries such as the UK, who have created the CCS Council and CCUS Cost Challenge Taskforce to aim to make CCUS economically feasible.

The GCCSI legal and regulatory indicator ranks only five countries as having legal and regulatory models which are sophisticated enough to address novel aspects of the CCS process, showing there is still a considerable amount of development required in many countries, such as Japan and Indonesia, as highlighted in this review.

POLICY AND INCENTIVES CHAPTER CONCLUSIONS

The Policy and Incentives Team of the CO_2 Capture Project has provided policy studies and surveys of incentives in different jurisdictions of interest to the CCP member companies since 2004, when the team was first formed to support the CO_2 Capture Project's technology-based work. We concluded very early on that, without policies, incentives, and public acceptance of CO_2 capture and geological storage, there would not be widespread deployment.

Phase 4 of the CO_2 Capture Project (2016-2022) coincided with a period of increasing level of interest in CCS technology development and increasing activity in policymaking and creating incentives to enable CCS project deployment. This chapter is a detailed summary of the four studies carried out in this period, supporting the results of the Paris Agreement, and analyzing the detailed policies, regulations, and incentives that nations are continuing to develop. As we found, there are still gaps and inconsistencies, but the fact is that these are either narrowing or, as intended, remain different because of national, regional, and local circumstances. These developing policies, incentives, and regulations will either pose barriers to, or they will encourage more widespread deployment. The CO_2 Capture Project is not a lobbying organization; the studies we have conducted have helped us illuminate the gaps and inconsistences so that other organizations will take these insights forward to facilitate that widespread deployment of CO_2 capture and geological storage.

REFERENCES

1. IPCC (2014) *Climate Change 2014: Synthesis Report. Contribution of Working Groups I, II and III to the Fifth Assessment Report of the Intergovernmental Panel on Climate Change* [Core Writing Team, R.K. Pachauri and L.A. Meyer (eds.)]. IPCC, Geneva, Switzerland, 151
2. IPCC (2018) Global Warming of 1.5°C. An IPCC Special Report on the impacts of global warming of 1.5°C above pre-industrial levels and related global greenhouse gas emission pathways, in the context of strengthening the global response to the threat of climate change, sustainable development, and efforts to eradicate poverty [Masson-Delmotte, V., P. Zhai, H.-O. Pörtner, D. Roberts, J. Skea, P.R. Shukla, A. Pirani, W. Moufouma-Okia, C. Péan, R.

Pidcock, S. Connors, J.B.R. Matthews, Y. Chen, X. Zhou, M.I. Gomis, E. Lonnoy, T. Maycock, M. Tignor, and T. Waterfield (eds.)].
3. International Energy Agency, Energy Technology Perspectives 2017; https://webstore.iea.org/download/direct/1058
4. IPCC (2005) IPCC Special Report on Carbon Dioxide Capture and Storage. Prepared by Working Group III of the Intergovernmental Panel on Climate Change [Metz, B., O. Davidson, H. C. de Coninck, M. Loos, and L. A. Meyer (eds.)]. Cambridge University Press, Cambridge, United Kingdom and NewYork, NY, USA, 442 pp.
5. IPCC, 2006 IPCC Guidelines for National Greenhouse Gas Inventories, Prepared by the National Greenhouse Gas Inventories Programme, Eggleston H.S., Buendia L., Miwa K., Ngara T. and Tanabe K. (eds). Published: IGES, Japan.
6. IPCC, 2019 Refinement to the 2006 IPCC Guidelines for National Greenhouse Gas Inventories, Calvo Buendia, E., Tanabe, K., Kranjc, A., Baasansuren, J., Fukuda, M., Ngarize, S., Osako, A., Pyrozhenko, Y., Shermanau, P. and Federici, S. (eds). Published: IPCC, Switzerland.
7. US EPA Guidance on UIC transition from EOR to CCS. https://www.epa.gov/uic/class-vi-guidance-documents
8. US EPA Memorandum on implementation of EOR to CCS transition for UIC. https://www.epa.gov/uic/class-vi-wells-used-geologic-sequestration-co2
9. Carbon Sequestration Leadership Forum (CSLF) Task Force on CCS Technology Opportunities and Gaps, Final Report. https://www.cslforum.org/cslf/sites/default/files/documents/CO2-EORtoCCS_FinalReport.pdf November 2013
10. All countries NDCs available at http://www4.unfccc.int/ndcregistry/Pages/All.aspx
11. All Mid-Century Strategies available at: https://unfccc.int/process/the-paris-agreement/long-term-strategies
12. DDPP report (2014) http://deepdecarbonization.org/wp-content/uploads/2015/12/DDPP_EXESUM-1.pdf
13. GECO (2015) Road to Paris. https://ec.europa.eu/jrc/en/publication/eur-scientific-and-technical-research-reports/geco2015-global-energy-and-climate-outlook-road-paris-assessment-low-emission-levels-under
14. IEA (2017) Tracking Clean Energy Progress http://www.iea.org/publications/freepublications/publication/TrackingCleanEnergyProgress2017.pdf
15. IEA (2017) World Energy Outlook
16. Sokolov *et al.* (2017) Climate stabilisation at 2 degrees and net zero carbon emissions (MIT) https://globalchange.mit.edu/sites/default/files/MITJPSPGC_Rpt309.pdf
17. MIT (2007) *The Future of Coal.* https://web.mit.edu/coal/The_Future_of_Coal.pdf
18. GCCSI (2017) The role of CCS in meeting climate policy targets http://hub.globalccsinstitute.com/sites/default/files/publications/201833/report-role-ccs-meeting-climate.pdf
19. Campbell, L. *et al.* (2018) *The role of CCS in the Energy Transition*, prepared by Environmental Resources Management for CCP.
20. World Energy Council (2017) World Energy Issues Monitor: 2017 http://wec-italia.org/wp-content/uploads/2017/04/1.-World-Energy-Issues-Monitor-2017-Full-Report-v1-Embargoed.pdf
21. Lee, A., *et al*. (2015) "Issues, Barriers and Opportunities in Policies, Incentives and Stakeholder Acceptance," in Gerdes, K. (ed), *Carbon Dioxide Capture for Storage in Deep Geologic Formations–Results from the CO_2 Capture Project Volume 4: CCS Technology Development and Demonstration; Results (2009-2014),* CPL Press 2015.

22. UNFCCC, downloads of long term low emissions development strategies submitted by nations in the 'Documents and Decisions' section of the website, with search terms 'LT-LEDS,' https://unfccc.int/documents

APPENDIX A

As part of this project, representatives of the following organisations were interviewed and contacted:

- US EPA
- University of Edinburgh
- Battelle
- US Department of Energy
- Global CCS Institute
- University of Calgary
- Natural Resources Defense Council
- Ministry of Energy, Mines and Petroleum Resources
- British Standards Institution Technical Committee
- ISO Technical Committee 265
- California Air Resources Board
- Independent Consultants

Carbon Dioxide Capture for Storage in Deep Geological Formations, Volume 5
Karl F. Gerdes (Editor)
© 2022 BP. All rights reserved.

Chapter 36

CCP4 COMMUNICATIONS SUMMARY

Simon Taylor and Mona Ishaq
Pulse Brands, 1-3 Langley Court, London WC2E 9JY

ABSTRACT: Following the creation of a range of communications platforms during Phase 3 of CCP (CCP3), CCP4 continued the sharing of updates and results from the work of the Technical and Policy teams through these platforms. In addition, increased focus was placed on peer-to-peer communication through conferences and events. As the 20-year CCP program came to a close, the establishment of a lasting legacy of CCS knowledge and insights, derived from the entire body of CCP work and available to all, became an overarching aim.

KEYWORDS: CCP, CCS, communications, reports

CONTEXT

After environmental issues had slipped down the order of international priorities in the wake of the 2008 financial crisis, something of an upswing in CCS momentum emerged during the course of CCP4. This was driven by several events:

- The COP21 Paris agreement in 2015, as a result of which governments across the world committed to significant cuts in man-made CO_2 emissions.
- Policy changes in Europe and, especially in the US, where the Budget Bill of 2018 contained an extension and enlargement to the US tax credit for CCS and CCUS, known as 45Q.
- The coming to prominence in 2018 of Extinction Rebellion and other movements–which, allied with major climate-linked events over recent years, focused attention like never before on our changing environment.
- Publication of the sixth Climate Change Assessment Report by the IPCC in 2021, with its stark warnings about the threats facing mankind.

As Lord Nicholas Stern said of CCS in the GCCSI 2020 Global Status of CCS report: “Low-carbon technologies, including renewables and CCUS, point toward a viable pathway for achieving net-zero GHG emissions by 2050, even in sectors that were considered ‘too difficult’ to decarbonise just a few years ago.”

In light of this renewed interest, the work carried out and documented by CCP over the last two decades provides a crucial source of learnings and insights regarding technical and policy challenges, as well as paves the way for the development of future capture and storage solutions.

The CCP Communications programme has played an important role in ensuring that this knowledge is available to all interested parties. This should prove invaluable in helping project developers and authorities worldwide as they move into deploying CCS and bringing it to the scale needed to help the world meet its CO_2 reduction targets.

LEAVING A LEGACY: TECHNICAL KNOWLEDGE, PROJECT RESULTS, ACCESS

The CCP Communications programme during the fourth phase of CCP ran on dual tracks–continuing to provide background and updates on the latest CCP4 initiatives, while at the same time ensuring that a comprehensive body of technical project information would be available for wider access to industry, academia, and the public, once CCP formally finished.

One of the founding principles of CCP when it was set up was that the results of its work should be made widely available to support the ongoing development of CCS. Since 2000, when CCP was founded, communications technology has developed in such a way as to make this aim easier to achieve than might otherwise have been the case.

During the course of CCP, a range of communications materials has been produced in print, and then digitally, to explain the work of the Technical and Policy teams–including results books, technical factsheets, policy reports, annual reports, conference presentations, as well as brochures, leaflets and posters.

Apart from being made available at conferences, these materials have also been available to a wider audience via the CCP website– www.co2captureproject.org –and awareness has been further raised through media coverage as well as alerts to website subscribers. Although the CCP program is now completed, the CCP website is planned to be kept open and maintained as a resource accessible to all until 2026.

CCP4 Project Communication

Technical Literature

Technical factsheets were published on a range of CCP4 Capture and Storage initiatives. These factsheets provide a snapshot of individual CCP projects, summarising the aims and results of each one. In CCP4, brand-new technical factsheets were created for 3D Caps (3D printed structures for

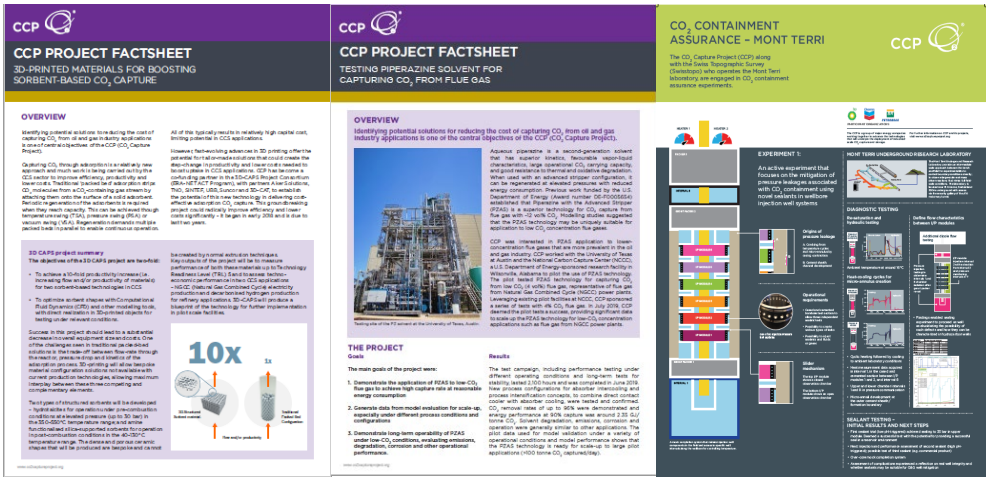

Figure 1. Project Factsheets–3D-Printed Sorbents, Piperazine Solvent Testing–and Mont Terri Sealant Testing poster.

adsorption of CO_2), Piperazine (solvent for CO_2 capture) and Mont Terri sealant testing–as well as results updates being made to pre-existing factsheets. Management briefings on selected projects were also created for issue to member company senior managers.

Annual Reports

Individual annual reports were created summarising each year of CCP4's activity. Interactive functionality was introduced, and each report contains Capture, Storage, Policy, and Communications updates along with selected photography and graphics. The final CCP annual report–covering the year of 2019–also contains a summary of the history, partnerships, and key achievements of CCP over the course of the last 20 years.

Figure 2. CO_2 Capture Project 2019 Annual Report.

Results Books

As well as this book covering CCP4, the phase 3 results book (Carbon Dioxide Capture for Storage in Deep Geologic Formations: Volume 4) was published at the beginning of this phase, in 2015, and contains full details of all CCP3 projects. These volumes complement those produced for Phases 1 and 2 of CCP.

Policy Reports

A number of insightful policy reports were developed by the Policy Team during CCP4. These were published in an accessible format and included: *Best Practice in Transitioning from CO_2 EOR to CO_2 Storage*; *Review of CO_2 EOR transitioning to CCS in Texas and Alberta*; *Role of CCS in the Energy Transition*; and *Survey of CO_2 Storage Regulations*. Further details of these can be found in the Policies & Incentives chapter of this volume.

Spreading the Word

Conferences

A renewed emphasis was placed on conference support during the fourth phase, allowing CCP members and partners the opportunity to personally share latest insights from ongoing projects and engage with interested parties.

CCP's participation included sponsorships, presentation of papers, exhibition stand presence and hosting of poster sessions across several prominent events, each attracting hundreds of visitors. These included the GHGT bi-annual conferences in Lausanne (2016), Melbourne (2018), and Abu Dhabi in 2021. The latter was a virtual event due to COVID-19 restrictions, and CCP took on Diamond-level sponsorship of the show to mark the pending completion of its programme. CCP was also present at various other events during CCP4, including the CCUS conferences in Pittsburgh (2015), Washington

DC (2016), Chicago (2017) and Nashville (2018); the 2018 Geosciences conference in Vienna; and the 2017 SINTEF Trondheim conference on CCUS.

Media and Broader Awareness

Figure 3. Recent CCP Policy Reports.

CCP continued to work with industry bodies, media, and academia during CCP4 to drive awareness of significant developments in the CCP programme. Regular alerts were issued to the CCP website's 4,500-strong database of regular users, while the sharing of information with CCS and oil and gas

industry media led to editorial coverage which helped to spread the message more widely about CCP's work to advance the deployment of CCS.

A Digital Legacy

The CCP website–www.co2captureproject.org–was updated throughout CCP4 to provide the latest news of CCP project progress.

The site attracted a monthly average of around 1,300 visitors–many of them new to the site–for the duration of CCP4. Notable traffic peaks of up to ten times normal were experienced during significant CCP initiatives, such as participation at conferences and the publication of annual reports and factsheets. The CCS Browser (www.ccsbrowser.com), which was developed during CCP3 as a CCS education tool, also continued to attract regular daily visitors.

With the closure of the CCP4 program, the website has been updated to ensure it remains relevant and accessible to everyone. CCP results books, annual reports, policy reports, videos, press releases, technical factsheets and leaflets are available to download from the site, along with a selection of conference papers.

Functionality of and access to the site is planned to be maintained until 2026, although the site itself will not be updated once CCP completes at the end of 2022.

With the close of CCP4 and the programme as a whole, the legacy of pioneering work carried out by the Technical and Policy teams has been assured through a broad range of communications channels and tools, all now available online. This will ensure that the important learnings from CCP's work will remain accessible to all as CCS develops over the coming years.

Figure 4. CCP Website.

Carbon Dioxide Capture for Storage in Deep Geological Formations, Volume 5
Karl F Gerdes (Editor)
© 2022 BP. All rights reserved.

CONTRIBUTORS TO CCP4

Karl F. Gerdes
Editor, Karl F. Gerdes Consulting, Davis, California, US

The successful completion of the 4th and final phase of the CO_2 Capture Project required the efforts of many people. In this section, the contributions of CCP Member companies, technology providers, and chapter reviewers are acknowledged.

CCP STRUCTURE AND STAFFING

The individuals making up the management structure, advisory body, and the technical teams of CCP are listed in Tables 1 and 2.

TECHNOLOGY PROVIDERS & CHAPTER AUTHORS

A variety of technology providers were commissioned by CCP4 to execute the projects making up the technical program. These providers included academic institutions, research companies, CCP4 participants, national laboratories, and expert consulting firms, who worked together with the CCP Technical Teams to deliver the program results. Authors of each chapter are listed in the Author Index.

CO_2 Capture

The technology providers for CCP4 Capture-related projects are:

- Aker Carbon Capture (NO)
- Amec Foster Wheeler (UK)
- Babcock and Wilcox (US)
- BP International (UK)
- C-Capture (UK)
- FuelCell Energy (US)
- GTI Energy (US)
- IEA Greenhouse Gas Research Programme (FR)
- Imperial College London (UK)
- Mitsubishi Heavy Industries (JP)
- Nederlandse Organisatie voor Toegepast Natuurwetenschappelijk Onderzoek (TNO) (NL)
- Politecnico di Milano (IT)
- Rensselaer Polytechnic Institute (US)
- Stiftelsen for Industriell og Teknisk Forskning (SINTEF) (NO)
- Svante, Inc. (CA)
- Trimeric Corporation (US)
- University of Leeds (UK)
- University of Texas at Austin (US)

Storage, Monitoring, and Verification

Organizations which carried out SMV projects for CCP4 are:

- Advanced Resources International (US)
- Bureau of Economic Geology (BEG)-University of Texas, Austin (US)
- Computational Geosciences Inc (CA)
- CGG Geo-Consulting (CA)
- Eidgenössische Technische Hochschule Zürich (ETHZ) (CH)
- GroundMetrics Inc. (US)
- Lawrence Berkeley National Laboratory (US)
- Los Alamos National Laboratory (US)
- Missouri University of Science and Technology (US)
- Noetic Engineering (CA)
- Rice University (US)
- Silicon Microgravity Limited (CA)
- Solexperts AG (CH)
- Stanford University (US)
- SWISSTOPO (CH)
- Texas A&M University (US)
- University of British Columbia (CA)
- Univ Côte d'Azur, CNRS (FR)
- University of Calgary (CA)
- University of Texas, Austin (US)

Policy & Incentives and Communications

Work for CCP4 related to Policy and Incentives and to Communications was carried out by:

- Environmental Resources Management (UK)
- Pulse Brands (UK)

REVIEWERS

On behalf of CCP4, the editor expresses profound gratitude to reviewers of the technical chapters in this volume. Their advice and perspective measurably improved the usefulness of this volume to the CCS community. Special thanks to several reviewers who helped us with more than one chapter.

CO_2 Capture

The reviewers for CCP4 Capture-related chapters are:

- Jurriaan Boon, TNO (NL)
- Joel Cizeron, Svante (CA)
- Paul Feron, CSIRO (AU)
- Manuele Gatti, Politecnico di Milano – LEAP (IT)
- Hossein Ghezel-Ayagh, FuelCell Energy (US)
- Sandra Kentish, University of Melbourne (AU)
- Dan McCartney, McCartney Gas Advisors (US)
- Juliana Garcia Monteiro, TNO (NL)
- Frank Morton, National Carbon Capture Center (US)

- Paul Webley, Monash University (AU)
- Tony Wu, National Carbon Capture Center (US)

Storage, Monitoring and Verification

Reviewers for the SMV chapters are:

- Andreas Busch, Heriot-Watt University (UK)
- Chris Consoli, GCCSI (AU)
- Kaveh Dehghani, Emeritus Chevron (US)
- Andrew Duguid, ARI (US)
- Jenny Gao (US)
- Mike Hoversten, LBNL (US)
- Franklin M. Orr, Stanford University (US)
- Adriana Paluszny, Imperial College (UK)
- Antonio Pio Rinaldi, ETH Zūrich (CH)

Table 1. Management structure of CCP4.

CCP4 EXECUTIVE BOARD	PROGRAM MANAGER	CCP4 ADVISORY BOARD	
Jonathon Forsyth/ Tony Espie (Chair) *BP*	**Mark Crombie/ Tony Espie** *BP*	**Vello Kuuskraa (Chair)** *President, Advanced Resources Int'l Inc., US*	
Rodolfo Dino/ Ana Musse *Petrobras*	***Dave Gilbert (project support)*** *Sustainable Tech*	**Michael Celia** Prof. and Chair, *Civil & Enviro. Engr., Princeton Univ, US*	**Dale Simbeck** *Consultant Palo Alto, CA, US*
Stephen Kaufman *Suncor*[*]			
Vincent Kwong/ Raja Jadhav *Chevron*			

[*]Suncor withdrew from CCP during Phase 4.

Table 2. Working teams of CCP4.

CAPTURE	STORAGE, MONITORING & VERIFICATON	POLICY & INCENTIVES	COMMUNICATIONS
Raja Jadhav (lead) Chevron	**Scott Imbus/ Dean Thornton (lead)** Chevron	**Arthur Lee (lead)** Chevron	**Mark Crombie/ Tony Espie (lead)** BP
Stuart Lodge BP	**Subhash Thakur** BP	**Mark Crombie** BP	**Lilas Allen** BP
Mark Sankey BP	**Tony Espie** BP	**Ashleigh Ross** BP	**Melissa Ritchie** Chevron
Ibrahim Ali BP	**Juan Anguiano** BP	**Poh Boon Ung** BP	**Sean Comey** Chevron
Betty Pun Chevron	**Rodolfo Dino** Petrobras	**Vinicius Lima** Petrobras	**Vinicius Lima** Petrobras
Ana Musse Petrobras	**Moema Martins** Petrobras	**Dan Burt** Suncor*	**Mona Ishaq** Pulse Brands
Gustavo Moure Petrobras	**Fatima Rosario** Petrobras		**Simon Taylor** Pulse Brands
Paulo Prunzel Petrobras	**Milene França** Petrobras		**Tanis Short** Suncor*
Dan Burt Suncor*	**Mark Chan** Suncor*		
Iftikhar Huq Suncor*	**John Graham** Suncor*		
	Dave Gilbert Sustainable Tech		
	Brian Williams D. Brian Williams Associates		

*Suncor withdrew from CCP during Phase 4.

AUTHOR INDEX

KEYWORD INDEX

Carbon Dioxide Capture for Storage in Deep Geologic Formations

CCP (CO_2 Capture Project) has been a pioneering organisation in the world of CO_2 capture and storage (CCS) for more than two decades. It was set up in 2000 as a partnership of eight major energy companies – with the aims of:

- Driving down the cost of CO_2 capture in oil and gas applications through R&D and demonstration
- Advancing knowledge of CO_2 storage and monitoring
- Informing the development of legal and policy frameworks.

This volume marks the completion of the fourth and final phase of CCP activity. It contains detailed results of work in the fields of storage and capture, as well as summaries of important activity in policy analysis and communications. The work was undertaken by CCP teams – comprising member company specialists in subsurface geology and chemical engineering – along with partners from research institutions, universities, government bodies and commercial organizations.

It contains 36 peer reviewed chapters – and includes, among others, the results of techno-economic assessments, pilot scale technology tests, research studies and modeling carried out during the seven years of CCP4.

The completion of CCP4 marks the end of the CCP program as a whole. CCP thanks all its member companies and partners who have supported it over the past two decades in advancing the cause of CCS. The results from Phases 1, 2 and 3 are contained in four separate volumes, all available online at www.co2captureproject.org.

"The CO_2 Capture Project (CCP) grew out of a meeting organised by BP, IEAGHG and US Department of Energy in 1999 on 'CO_2 Capture and Geologic Sequestration: Progress through Partnership'. As a research programme, the CCP has achieved a lot since then in advancing capture, storage and monitoring technologies. What has impressed me the most about the work of the CCP, including this final phase CCP4, is that it has been driven by the energy companies who are delivering CCS projects, so the broad range of topics worked on are very much needs-driven from a user's perspective (in a similar way to the IEAGHG technical programme). This means that the results are what industry needs and will enable better, more effective and lower-cost CCS projects. Congratulations to all involved in CCP for an excellent CCS research programme over 22 years."

Tim Dixon, General Manager IEAGHG.

"Over the last two decades, the Carbon Capture Project has documented detailed knowledge and experience developed by teams working around the world on the design and operation of safe and effective carbon capture and storage projects. From project planning to operating experience, from well design to problem detection and mitigation, or from project verification to expected project costs, the results reported in this fifth volume in the series are required reading for those working to deploy CCS at the scale required for deep reductions in greenhouse gas emissions."

Franklin M Orr Jr, Professor Emeritus, Department of Energy Science and Engineering, Stanford University, and former Under Secretary for Science and Energy, U.S. Department of Energy.

CCP4 Participant Organizations

www.co2captureproject.org

ISBN: 978-1-3999-4078-8